FOP 2026

FRONTIERS IN OPTICS AND PHOTONICS

XLIX OSI SYMPOSIUM

25 – 28 SEPTEMBER 2026 | IIT DELHI | NEW DELHI, INDIA

BOOK OF ABSTRACTS



INDIAN INSTITUTE OF TECHNOLOGY DELHI

OPTICAL SOCIETY OF INDIA

CSIR-NATIONAL PHYSICAL LABORATORY

XLIX OSI SYMPOSIUM

FRONTIERS IN OPTICS AND PHOTONICS (FOP) 2026

September 25 - 28, 2026

File ID	Presenting Author	Title of paper	Page no.
		DAY-1	
KYN001	Ranjan Singh	From Chips to Full Space Wireless: Intelligent Topological Terahertz Photonics	1
		DAY-2	
PLN001	G. Ravindra Kumar	Intense Light-Matter Interaction: Sculpted Pulses, Structured Targets, Brighter Sources	2
PLN002	A. Erdmann	3D Mask Effects in EUV Lithography: From Limitation to Opportunity	3
INV001	Goutam K Samanta	Quantum sensing using single and entangled photons	4
INV002	C.M. Chandrashekhar	Photonic Quantum Computing Platform Using Multi-Degree-of Freedom of Photons	5
FOP326	Priyanka Kandankel	Characterisation of A Biphoton Source for Quantum Super-Resolution Imaging	6
FOP327	Priyanka Kannath	Quantum dual-interferometer using non-degenerate two-mode squeezed states	7
INV003	Anand Kumar Jha	High-dimensional quantum state measurement: foundation and applications	8
INV004	R. P. Sing	Free-Space Quantum Communication: Effect of Turbulence	9
FOP316	Rahul Dhankhar	Optical control of NV center charge states for stable quantum sensing	10
FOP322	Kripali Jain	Experimental Realization of a Magneto-Optical Trap for Atom Interferometry-Based Quantum Sensing Applications	11
INV005	Balpreet Singh Ahluwalia	Photonic chips based integrated microscopy and spectroscopy	12
INV006	Renu John	Artificial Intelligence in Clinical Microscopy: Applications	13
FOP027	Keerthana A	Near Infrared Imaging system for Tissue Oxygenation and Perfusion Assessment for Diabetic Foot Ulcer	14
FOP035	Abritty Kisku	Quantitative assessment of retinal microvasculature density changes in metabolic dysfunction-associated steatotic liver disease with OCT Angiography	15
FOP043	Chetna Patel	Classification of Red Blood Cells using Photothermal Holography	16
INV007	Sivarama Krishnan	Bio-inspired Femtosecond Laser Microstructuring of Polypropylene Surgical Meshes for Biomedical Applications	17
FOP030	Shivam	Polarization-Resolved Wide Field-of-View Digital Holographic Microscope	18

FOP033	Nripesh Dixit	Low-Power Sono-Neurophotonic Control of Calcium-Dependent Synaptic Plasticity in the Brain	19
FOP039	Praveen Kumar	One-Dimensional Photonic Crystal Sensor for Early MGUS Screening Using Tamm Plasmon Resonance	20
FOP044	Pritam Pradhan	Customization of the through-focus visual Strehl ratio in extended depth of focus intraocular lenses	21
FOP051	Mridul Verma	Benchmarking Deep Learning Reconstruction Models for SparseView Photoacoustic Tomography on OADAT Dataset	22
INV008	Rajan Jha	Integrated Processed Fiber-Cavity: Advanced Optical Sensing and Single-Photon Guidance	23
INV009	Ravi Pant	Demonstration of efficient Brillouin nonlinearities in silica microresonators in the 2 μm wavelength region	24
FOP169	Sayan Chaki	On-Chip Polarization-Independent Edge Coupler Design for O-Band Operation	25
FOP172	Shiva Kondeti	Inverse-Designed Ultra-Compact Photonic Logic Circuit for Half Adder Implementation on an SOI Platform	26
FOP397	Varnam Sherawat	Geometric Bloch-Sphere Interpretation of Complete Mode Conversion in a Detuned Directional Coupler	27
INV010	Sergey Babin	High-beam-quality narrowband lasers based on multimode and multicore fibers with FBG cavity	28
INV011	Anirban Dhar	Photodarkening-Resistant Yb-Doped Optical Fibers through Host Glass Engineering	29
FOP094	Elisa Mathew	Experimental Demonstration of Fading Mitigation Using Spatial Diversity in Multi-Core Fiber	30
FOP107	Sharashti Saxena	Bandwidth Evolution under Co- and Counter-Propagating Brillouin Gain and Loss	31
INV012	Ryoichi Horisaki	Computational Imaging with Randomness	32
INV013	Rakesh Singh	Single pixel microscopy: Creating images without a sensor grid	33
FOP057	Nishant Goyal	3D Phase Imaging using Single-View Structured Illumination	34
FOP059	Jasleen Birdi	Learning Phase Diversity for Robust Computational Imaging	35
INV014	Lakshminarayan Hazra	Principal Azimuths in a General Image-Forming Optical System and Their Uses in Image Assessment	36
INV015	Bosanta R. Boruah	Vectorial Exact Ray Tracing: Advancements in the modeling of complex objective lens systems and experimental validation	37
FOP060	Totan Chand	Optical design of a compact prime focus wide-field corrector using aspherical optics with atmospheric dispersion compensation	38

FOP061	Umesh Dhatrak	Optimal support to minimize the self-weight deformation for a cylindrical Fabry-Perot cavity	39
INV016	Shriganesh Prabhu	Far-Field, Near-Field and Time Resolved Terahertz (THz) Spectroscopy of Materials	40
INV017	Dibakar Roy Chowdhury	Symmetry-protected bound states in the continuum in terahertz metasurfaces	41
FOP201	Mukundadev Behera	Photon-Energy-Dependent Terahertz Emission Spectroscopy of Ferrimagnetic Spintronic Heterostructures	42
FOP204	Divya Sree K	Experimental Demonstration of an Opto-Electronic Self-Interference Cancellation System for 5G In-Band Full Duplex Communication	43
INV018	A K Chowdry	Development of THz-based spectroscopy and imaging techniques for characterization of optical, dielectric and surface roughness properties of explosive composites	44
INV019	Dhanvir Rana	Emergent Terahertz Functionalities Enabled by Quantum Materials	45
FOP199	Md Afroz	A Self-Adaptive Microwave Photonic Anti-Jamming Architecture Based on Stimulated Brillouin Scattering	46
FOP200	Bhawana Andola	Engineering Ultra-Broadband Terahertz Absorption in Flexible Metamaterials	47
Day 3			
PLN003	Roberto Morandotti	Classical and Quantum Photonics for Smart Technologies	48
PLN004	Osamu Matoba	Potential of Holographic Microscopy for Neuroscience	50
INV020	Amarendra Sarma	Beyond the Standard Quantum Limit: Coherent Quantum Noise Cancellation in Hybrid Cavity Optomechanics	51
INV021	Shailendra K Varshney	Integrated Nanophotonic Components and Devices for Quantum Computing and Sensing Applications	52
FOP323	Milan Jana	Broadband polarization entanglement via spatial multiplexing of Type-0 SPDC photons	53
FOP328	Chahat Kaushik	Quantum sensing by tunable exchange symmetry control using geometric phase	54
INV022	Ashok Kumar	Quantum Noise of Bright Light: Enabling Quantum Communication and Cryptography	55
INV023	T. Schoenbeck	Event-driven single-photon cameras based on Timepix3 and Timepix4 for quantum optics	56
FOP331	Ayan Nai	Spatial division-multiplexing-based high-rate, quantum communication networks	57

FOP337	Rachita Nandan	Impact of Detector Noise on Experimental Free-Space Unidimensional Continuous-Variable Quantum Key Distribution	58
INV024	B. N. Upadhyaya	Recent advances in high power fiber laser activity at RRCAT	59
FOP179	Debasish Mishra	3kW Narrow Linewidth Fiber LASER for Multi-Wavelength LASER Beam Combining Based DEW System	60
FOP182	Anirban Ghosh	High-Power femtosecond Dual-Pulse OPO with Tunable Polarization, Wavelength, Delay, and Repetition Rate	61
FOP195	Shweta Verma	Glow discharge spectral data analysis with machine learning for accurate identification of gas mixture compositions for CO2 lasers	62
FOP198	Manjesh Bhaskar	Optical PAM-16 Signal Generation Using Mach–Zehnder Interferometer	63
INV025	Jagannath Nayak	High-Energy Ultrafast Laser Technology: Frontiers, Breakthroughs, and Emerging Applications	64
INV026	Sanjay Mishra	High Speed De-blurring Technology for Wide-area Surveillance System	65
FOP388	Anuj Varshney	Modeling and Simulation for COIL Unstable Resonator	66
INV027	Kanik Palodhi	Interferometric Approaches to Refractive Index Measurement	67
INV028	Raj Kumar	Retinal display for vergence accommodation conflict elimination in augmented reality applications	68
FOP164	Saumya Sarkar	Design of a Long Working-Distance, High-Numerical-Aperture Objective Lens for Optical Trapping and Fluorescence Imaging	69
FOP165	Parag Sharma	Establishment of Luminous Flux Scale using Recently Created Facility at CSIR-NPL India	70
FOP 167	Harupjit Singh	Reduction of the Laser Intensity Noise for the Optical Setup of Quantum Frequency Standard	71
INV029	Senthil Kumar M	Aspects of System Design for a Satellite based Optical Remote Sensing	72
INV030	Sanjay Mittal	Photonics for Space Autonomy: Range and Velocity to 3D perception	73
FOP277	Sirisha J	Diamond Like Carbon Antireflection coatings for optical C-Band Applications	74
FOP278	Madhavi Thakre	Design of Compact multispectral imaging system for remote sensing applications	75
INV031	Pavan Kumar G V	Multipolar Optical Binding and Rotational Jamming in Plasmonic Optical Matter	76
INV032	Nirmalya Ghosh	Spin Orbit Interaction and Weak measurements in Plasmonic Metasurfaces	77

FOP226	Shyambhargav Jodidar	Surface plasmon polaritons guided nanoparticle assembly beyond the metal–dielectric interface	78
FOP240	Vivek Semwal	Detection of small molecules Using a Plasmonic Chip on an Optical Fiber Microfluidic Platform	79
INV033	Prem Bisht	Parametric fluorescence, amplification and autocorrelation: A Beginner's perspective	80
INV034	Partha Roy Chaudhuri	Photonic Crystal Fibers: Designing Fibers, Active and Nonlinear Fiber Devices	81
FOP116	Arannya Ghosh	All-optical anti-skyrmions and anti-merons in Difference frequency generation	82
FOP125	Priyanshu Pandey	Kramers–Kronig Receiver for Direct-Detection Measurement of Fiber Kerr Nonlinearity	83
INV035	Tapajyoti Das Gupta	Metalenses for Advanced Wavefront Engineering: From Achromatic Imaging to Sub-Diffraction Nanofabrication	84
FOP216	Golak Bage	External Grating-induced Band Inversion Trapped State on Optical Nanofiber	85
FOP229	Faizan Lone	Control of Nitrogen-Vacancy Center Emission Using Compact Disc-Derived Plasmonic Gratings	86
FOP237	Sahil Rathi	Deterministic strong light matter interaction in QDs-Bowtie on Silver substrate	87
FOP249	Vendamani V S	Flexible SERS-based Hybrid ZIF-8@Copper Nanodendrite Substrates for Real-time Monitoring of Hazardous Molecules	88
INV036	Subhasish Dutta Gupta	Beam Shifts with Structured Light	89
INV037	Shanti Bhattacharya	Tailored Bessel Beams and Their Applications	90
FOP360	Abhishek Dutta	Susceptibility-Engineered Polarization Shaping of Structured Light in Rubidium Vapor	91
FOP375	Sonu Rao	Optical vortices-based pseudo-DNA logic and its applications	92
FOP382	Dileep Upadhyay	Determination of 3-D Spin Densities	93
INV038	T. Sasaki	Effect of the Structure of the Chiral Moiety of the Photoconductive Dopant on the Photorefractive Effect of Liquid Crystal Blends	94
INV039	Yasuhiro Awatsuji	Quantitative phase imaging of dynamic object by parallel recording technique	95
FOP140	Deepak Kumar	Single-Shot Jones Matrix Extraction Using a Common-Path Intensity Measuring Techniques	96
FOP142	Shadiya M P	Development of a Programmable Quadriwave Interferometric Wavefront Sensor for Aspheric Testing	97
INV040	Ganesan Angarai	Anisoplanatism in Adaptive Optics and Advancements in Wavefront Sensing	98

INV041	Chaitanya Kumar Suddapalli	Deep-Infrared Ultrafast Femtosecond Parametric Oscillator at $7\mu m$	99
FOP070	Alex Singh	Development of Low-cost Spectrometer for Pesticide detection using ML	100
FOP083	Diksha Karnatak	Generation and Validation of Phase Screen using Zernike Based Method	101
INV042	Amit Agrawal	Scalable Metasurface Photonics for Quantum Computers and Sensors	102
INV043	S R K Chaitanya Indukuri	Light-Matter Interactions with Hyperbolic Materials	103
FOP288	Abel Joseph	Reconfigurable Dielectric Metasurface for Polarization Switching	104
FOP291	Raghwendra Kumar	Switching of bands in a graphene assisted metamaterial absorber	105
INV044	Deepa Venkitesh	On-Demand SOA-Based Optical Phase Conjugation for Adaptive Coherent Optical Networks	106
FOP271	Bingi Kiran	FPGA-Based Wideband Pre-Emphasized LFM Waveform Generation for Photonic Filters	107
FOP072	Mohit Sisodiya	Millimeter Wave Over Fiber System with Nakagami-m Fading and Adaptive Equalization for 5G C-RAN	108
FOP400	Afreen	Co-Alloyed Perovskite Quantum Dots for Controlled Hot-Carrier Dynamics and Phase Stable Optoelectronics	109
INV045	Nithyanandan Kanagaraj	Ultrafast Fiber Lase-An Avenue for Photonic Intelligence	110
INV046	Vishwa Pal	Laser solver for computationally hard optimization problems	111
FOP019	Kritarth Srivastava	Selective-State Residual-Based DSP for 2.24 Tbps Coherent DWDM Transmission	112
FOP021	Nikhil Vangety	Robust 64-Ary Optical Communication through Multimode Fiber Using Scaled LG Modes and Deep Learning	113
Day 4			
INV047	Rajesh V. Nair	Diamond Color Centers as Solid-State Quantum Platforms	114
INV048	Anshuman Kumar	Making Quantum Light: Deterministic Defect Engineering in Hexagonal Boron Nitride	115
FOP339	Nisha	Portable Optically Pumped Atomic Magnetometer for Geophysical Surveys	116
FOP340	Chirangbhai Patel	Towards Demultiplexing of OAM-Multiplexed Bright Twin Beams	117
INV049	Supradeepa V. R.	Engineering Nonlinearities in High Power Narrow Linewidth Fiber Lasers	118
FOP180	Rajneesh Fulara	Ground-State Search via Intrinsic Feedback Annealing in Coupled Laser Arrays	119

FOP187	Neethu K	Spatial Coherence Control of Structured Beams in a Degenerate Cavity Laser: Binary versus Gaussian Fourier Filtering	120
FOP192	Diksha Sharma	On-chip random lasing from clusters of quasi-monodispersed microdroplets in amplifying medium	121
FOP197	Bhanu Yadav	Tunable modulation depth in multimode-interference saturable absorbers for $2\ \mu m$ fiber lasers.	122
INV050	Anirban Pathak	Interference, Interferometer and Fock States: Revisiting old Concepts from the Perspectives of New Applications	123
FOP347	Ikshvaku Shyam	Hexagonal Boron Nitride Spin Defects for Quantum Photonics: Annealing-Free Generation by Krypton Ion Implantation	124
FOP351	Sandra Susil	Coherence transfer in bright twin beams	125
FOP129	Love Sharma	Negative-Temperature States in Multimode Solitons	126
INV051	Rajib Chakraborty	Perspective on Photonic and Electronic Devices using Oxide-based thin films	127
FOP001	Jhuma Dutta	Excitation and Momentum Resolved Multi-Polaritonic Emission Mapping in Hybrid Organic-2D Material Microcavity	128
FOP003	James Singh Konthoujam	Advancing Light Emission from 2D Semiconductor Devices Through Van der Waals Contact Engineering	129
FOP004	Palash Makumuria	Molecular Resonance- and Charge-Transfer-Assisted Surface-Enhanced Raman Scattering using Molybdenum Oxide Nanoparticles	130
FOP005	Meera V	Sb_2S_3 Films for Low-Loss Reconfigurable Photonics	131
INV052	Moumita Dutta	Design and Development of Hyperspectral Imaging instruments for India Earth and planetary missions	132
INV053	A Raja Bayanna	Optical Instrumentation for Solar astronomy: Overview of observational facilities at Udaipur Solar Observatory	133
FOP279	Anjitha Viswanath	Active-Medium-Induced Scale Factor Variations in Prism-based Ring Laser Gyroscopes for Space Navigation	134
INV054	Balaji Srinivasan	Advances and Challenges in Nested Loop Cascaded Stage Tiled Aperture Coherent Beam Combining	135
INV055	Sudhir Khare	Next Generation Electro-optical Systems	136
FOP264	Chinmay Khattar	Neuromorphic Event Data Acquisition for High-Speed Vision Applications	137
INV056	Vipul Rastogi	Epsilon-Near-Zero Materials and Their Photonic Applications	138

INV057	Sebabrata Mukherjee	Observation of Chiral s-p Orbital Topological Edge States in Femtosecond Laser-Written Photonic Floquet Lattices	139
FOP253	Vikram Bhandari	LWIR all-Silicon ultrathin spherical metalens design and numerical simulations	140
FOP394	Shubhrakanta Panda	Monte Carlo Analysis of MgO Nanoparticles dispersed in PDMS Matrix for Passive Day time Radiative Cooling	141
INV058	Sachin K Srivastava	A plasmonic metagrating based dual-mode infrared sensor for label-free detection of traces of water in ethanol	142
INV059	Arup Lal Chakraborty	Probing narrow photonic resonances using tunable diode lasers - applications in gas sensing, FBG interrogation and nanobiosensing	143
INV060	Vyas Akondi	Advanced ocular wavefront sensing methods and towards customized ophthalmic solutions	144
INV061	Dinesh N Naik	Temporal Phase Unwrapping with Under-sampled Spectral Signal using Tilted Interference	145
FOP143	Harikrishnan P	Comparison of Fourier Transform Speckle Profilometry and Temporal Phase Unwrapping using a Recursive Algorithm in Wavelength-tuning Interferometry	146
FOP147	Chhavi Verma	Optimal contrast criterion for accurate classification of phase objects from their in-line holograms	147
FOP168	Aniket Pandey	Projection-based Grayscale Photolithography for Beam Shaping	148
FOP393	Munindra Kushwaha	Modelling of Three-Dimensional Refractive Index Map in Optical Diffraction Tomography	149
INV062	C Narayanamurthy	Atmospheric Turbulence impacted light beam scintillation mitigation using PMMA Rod(s)	150
FOP067	J. Sreekantha Reddy	A Plenoptic Wavefront Sensing Framework for Atmospheric Turbulence Characterization and Adaptive Optical Imaging	151
FOP076	Anitta Jomy	Holographic Modal Wavefront Sensing Using Spatial Intensity Distribution and Convolution Neural Network	152
FOP082	Anuvratha Vijay	Adaptive Wavefront Shaping for Optical Focusing and Imaging Through Scattering Media	153
FOP085	Bhoomika Saxena	A Real-Time Implementation of an Adaptive Autofocus Algorithm leveraging NVIDIA Jetson AGX Orin	154
INV063	Yoko Miyamoto	Non-separable light beams and scattering	155
INV064	Somnath Ghosh	Exceptional-Point Photonics for Application-Specific System Design	156
FOP381	Mohammad Umar	SU(2) walk on higher-order Poincaré sphere	157

FOP062	Ratnabali Ghosh	Investigation of Detector Translation for Refocusing in a Compact Imaging System	158
INV065	Vijay Kumar	Speckle-Learned Single-Shot Regression of Complex OAM Superposition States	159
FOP017	Anushree Khisti	Multimodal Optical Feature Extraction with a Free-Space Photonic Extreme Learning Machine	160
FOP020	Vishal Srivastava	Virtual Staining Microscope for Label-Free Liver Cancer Histopathology	161
INV066	Rajesh Kumar	HRFZ SOI Platform for Selected THz Guided Wave Active Devices	162
INV067	N. Yogesh	Terahertz Optical Devices Based on Tunable Metamaterials	163
FOP295	Vanlal Rinfela	Light-Controlled Lattice Engineering for Reconfigurable Terahertz Metadevices	164
FOP297	Mitali Sahu	Plasmonically Hybridized Broadband Graphene Metasurface for Terahertz Dual-Band Four-Wave Mixing	165
INV068	Akhilesh Mishra	Probing Spatial Coherence with a Terahertz Metasurface	166
FOP299	Parul Sharma	Observation of Exceptional Points in non-Hermitian Photonic Crystal	167
FOP205	Atul Khanna	Centre Frequency Tuneable Linear Frequency Modulated Dual-Chirp generation for Microwave Photonic FMCW Radar	168
Poster Day-2			
FOP002	Kalaivani H	Machine Learning prediction and experimental analysis of Potassium-thiourea complexes for Optical limiters	169
FOP008	Mohammad Adnan	Hysteretic Piezochromism in a Lead Iodide-Based Two-Dimensional Inorganic-Organic Hybrid Perovskite	170
FOP009	Deepak Kumar	Synthesis and Multifunctional Luminescence Properties of Mn^{2+} Activated $Ca_2KZn_2(VO_4)_3$ Phosphors for White LEDs, Latent Fingerprint Visualization and Anti-Counterfeiting Applications.	171
FOP010	Riddhi Palan	Bias Tunable Negative-to-Positive Photoresponse Transition in Anisotropic $ReSe_2$ Single Crystals	172
FOP011	Km. Jyoti Singh	Photoluminescence Characterization of SrNaKBiB: Dy^{3+} Glasses for w-LED Applications	173
FOP012	Kalpit Kumar Vaniya	Direct Vapour Transport Grown WS_2 Single Crystals for Multifunctional Visible-Light Photodetection and Photocatalytic Degradation Applications	174
FOP013	Ritwik Watsh	Photoluminescence Studies of $SrBi_2Ta_2O_9$: Dy^{3+}/Eu^{3+} Phosphors for w-LED Applications	175
FOP016	Zoya Fatima	Free-Space Optical Neural Network Using a scalable Mach-Zehnder Interferometer Mesh	176

FOP018	Suman Mandal	Machine Learning Assisted Predictive Model of Fano Resonances in Waveguiding Plasmonic Crystals	177
FOP022	Lavi Vaswani	Engineering Multipurpose Terahertz Metamaterials Using a Machine Learning Approach	178
FOP023	Abhishek Verma	Learned ADMM for Fast Image Reconstruction in Digital Lensless In-line Holographic Microscopy	179
FOP024	Vinay Yadav	Physics-Consistent Direct Modal Regression for High-Order Clinical Wavefront Retrieval from Shack–Hartmann Sensors	180
FOP025	Nandana Rs	Hybrid AI-Assisted Laser Guide Star Adaptive Optics for High-Resolution Astronomical Imaging	181
FOP026	Vimod Kumar	Residual GAN With Spectral Normalization for Image Dehazing	182
FOP028	Vivek Bohane	Influence of Optical Excitation Geometry on Photoacoustic Sectional Imaging: A Numerical Study.	183
FOP029	Saumya Chakraborty	An Explainable Learning Framework for Early Detection of Chronic Kidney Disease	184
FOP031	Sneham Dey	Non-invasive Analysis of Sweat Sample using Optical Methods	185
FOP032	Pratik Dhar	Design of a Confocal Hyperspectral Scanning Microscope for Label-Free Multiscale Structural and Spectral Imaging	186
FOP034	Gaurang Garg	Brenner gradient topology-based autofocusing framework for Fourier ptychography microscopy	187
FOP036	Dhanush Koodi M	Handheld Microscopic Imaging System for Subsurface Tissue Characterization	188
FOP037	Akshay Kumar	Lightsheet fluorescence microscopy (LSFM) using an engineered line diffuser	189
FOP038	Bipeen Kumar	Scattered light-based detection of cell membrane fluctuations without tracer particles	190
FOP040	Clint Mathew	Detection of thiamine in infantile blood sample using High-Performance Liquid Chromatography-LED- Induced Fluorescence system	191
FOP041	Monisha Mohan	Design of a laser printed paper-based microfluidic platform for colorimetric detection of oral cancer biomarkers	192
FOP042	Dhritiman Nath	Effects of ocular pupil dynamics on Zernike polynomial coefficients	193
FOP045	Vidya Rastapur	Comprehensive Raman Analysis of Functional RBCs with Structured Optical Traps	194
FOP046	Sahil Sharma	Low-Intensity Nonlinear Structured Illumination Microscopy Using Photochromic Absorption Modulation	195
FOP047	Paresh Sahoo	Evaluation of pyramid wavefront sensing artifacts due to reflectivity variations across thick layered samples	196

FOP048	Dinesh Saini	Field of view characterization using slanted-edge MTF method	197
FOP049	Santhosh Chidangil	Micro-Raman Spectroscopy of Extracellular Vesicles Derived from Stored Blood Components: Towards Label-Free Molecular Characterization	198
FOP050	Shalni Srivastava	Silicon Photonic based Grating Assisted Microring Resonator for Biosensing Application	199
FOP052	Mridul Verma	Coupling Optical Fluence and Acoustic Geometry: Physics-Informed Geometry-Adaptive Reconstruction for Quantitative Photoacoustic Imaging	200
FOP053	Hari Singh	Design and Simulation of a Terahertz-Based Sensor for Early Breast Cancer Detection	201
FOP054	Deepika PT	Design and Development of an Intraoral Imaging Probe for Early Detection of Oral Premalignant Lesion	202
FOP055	D Qaiser	FTIR Spectroscopy in serum sample of breast cancer Patients	203
FOP056	Annwesha Bhattacharya	Improving finite bit-depth of any low-cost CMOS camera sensor using Quantitative Exposure Fusion	204
FOP058	Muskan Kularia	Optimization-based Phase Retrieval in Cryo-Electron Microscopy	205
FOP064	Khushi	Stray Light Analysis and Optimization of a Double Gauss Imaging System Using Non-Sequential Ray Tracing in ANSYS Zemax OpticStudio	206
FOP065	Neeraj Kumar	An affordable Multimodal Optical Scanning Microscope (MOSM)	207
FOP066	Suvadeep Maji	Design of Zoom Lens in LWIR for Surveillance Purposes	208
FOP068	Rajarshee Roy	Glass Optimization for a Wide Field-Of-View Lens Assembly Design for Camouflage Detection in IR bands	209
FOP069	Rohit Sala	Performance Analysis Comparison of PIN and APD based Receivers in Free-Space Optical Communication Systems	210
FOP071	Amarendra Singh	Impact of Thermal and Mechanical Stress on Optical Performance of a large aperture Long Wave Infrared Catadioptric Telescope	211
FOP074	Nandan Bhat	Sidelobe suppression of Airy beams	212
FOP077	Abanish Maity	Integral Imaging Using Programmable Lenslet Array	213
FOP078	Sarita.	Design and development of a wavefront sensor using a lenslet array	214
FOP079	Sruthy Sebastian	A Unified Chromium Wet-Etch Process for Fabricating Compact Photon Sieves and Fresnel Zone Plates	215
FOP080	Emi Shine	Fourier Ptychography Microscopy using Different Imaging Modalities and Multi-plane Illumination	216

FOP081	Ananthakrishnan V	Flat-Top Beam Shaping Under Phase Perturbations: Comparative Analysis of IFTA, Adjoint Gradient Descent, and Optimal Transport	217
FOP084	Soumya Kumari	Automation and Performance Evaluation of a Digital Micromirror Device	218
FOP086	Arti Yadav	SERS based indirect sensing of glial fibrillary acidic protein (GFAP): a brain injury biomarker	219
FOP087	Supankar Das	Autonomous Electrostatic Force-Induced Fiber Bragg Grating Sensing Module for High-Voltage Discharge Monitoring	220
FOP088	Maryann Mampilly	Cladded Plastic Optical Fibre based U-Bent Sensors with Enhanced Coupling Efficiency for Robust Biosensing	221
FOP089	Rahul Gangwar	Sensitivity Enhancement in a D-Shaped Optical Fiber SPR Sensor via GeO_2 Doping	222
FOP090	Avdhesh Kumar	Design and development of a 4×1 fiber optic laser signal combiner using tapered fiber bundle technique	223
FOP091	Manjeet Kumar	A Portable System Incorporating a Microfabricated Chip for Detecting Metal Ions Using Glow Discharge in Open Air	224
FOP092	Anupam Kushwaha	Machine Learning-Assisted Colorimetric Paper Sensor for Smartphone-Based Detection of Pb^{2+} and Fe^{3+} Ions	225
FOP093	Souryadipta Maiti	Comparative Chirp Profile Engineering in Apodized Fiber Bragg Gratings for Narrowband Reflection and Dispersion Compensation	226
FOP095	Shrishty Mishra	Distance-Dependent Class Asymmetry in CNN-Based OTDR Fault Detection	227
FOP096	Saikat Mondal	Optical Liquid-flow Sensing via Mechanically Amplified Etched Fiber Bragg Grating	228
FOP097	Anjali Nehra	A Compact Single-FBG Platform for Early Parkinsonian Tremor Detection	229
FOP098	Nirlesh Singh	Modeling, Design, and Implementation of an FPGA-Based MZM Bias point controller for High-Speed Optical Transmitters in Intersatellite Laser Communication Links	230
FOP099	Pratishtha Pandey	Engineering Third-Order Exceptional Points in Photonic Time Crystals	231
FOP100	Sabila Parveen	Exceptional Point Engineering in Photonic PT-Symmetric Systems	232
FOP101	Surabhi Raj	Hybrid Φ-OTDR/BOTDA-Based Distributed Acoustic and Strain Sensing for Geohazard Monitoring	233
FOP102	Abhimanyu Roy Chaudhuri	Experimental Demonstration of a Polarization-Based Fiber-Optic Torsion Sensor for Open-Channel Flow Velocity Measurement	234

FOP103	Kishore S	Improving Detection Bandwidth in Distributed Acoustic Sensing using Frequency Division Multiplexing	235
FOP104	Pavithra S	Mechanical tensor recovery from Few-Mode Fiber Rayleigh backscatter using complex intermodal covariance	236
FOP105	Shikha Sachdeva	Surface Plasmon Resonance based optical fiber refractive index sensor using molybdenum disulfide and Gold	237
FOP106	Shubhakanta Sahoo	Linear stability analysis for Optical Bistable Gyrosensor	238
FOP108	Nikita Sharma	Fabrication and experimental evaluation of a 7×1 fiber optic pump combiner for high power fiber laser	239
FOP109	Della Vincent	Accurate estimation of gas parameters using an automated 1f wavelength modulation spectroscopy system	240
FOP110	Pramod Watekar	Analysis of temperature-dependent stress in nano-fibers for coupling applications	241
FOP111	Neha Ahlawat	Machine Learning based Multi-Parameter Sensing Using SMS Fiber Structure	242
FOP112	Hareesh Panakkal	A Gold–Titanium-Dioxide Bimetallic Bowtie Photonic-Crystal-Fiber SPR Biosensor for Wide-Range Refractive-Index Detection	243
FOP113	Akash Battu	Evolution of Pure Quartic Soliton in Graded-index Multimode Fiber	244
FOP114	Somen Adhikary	Relative Phase-Induced Spectral Shaping in Three Temporal Cavity Solitons for Flat Kerr Frequency Comb	245
FOP115	Milenia Basumatary	Simulations on higher-order optical nonlinearities	246
FOP117	Aakash Gupta	Understanding ultrafast-photoinduced reaction dynamics of methyl iodide on TiO_2 (110) and TiO_2 (100) surfaces	247
FOP118	Prabhakar Gupta	Generation of Second Order Meron in Nonlinear Photonic Crystal Using $\mathbf{LG_{02}}$ Beam	248
FOP119	Atiq Iqbal	Exceptional-Point Signatures and Geometric Phase in Anti-PT-Symmetric Difference-Frequency Generation	249
FOP120	Abhinav Kumar	Effect of pump wavelength on parametric gain in three-segment electro-optic quasi-phase-matched device for widely tunable optical parametric oscillator	250
FOP121	Bindu Kumar	Topological Transition in Difference Frequency Generation	251
FOP122	Aanaya Maheshwari	Quality Evaluation of a Laser Writing System Using Direct Microscopic Analysis	252

FOP123	Mohd Mehkoom	Enhanced Photothermal Nonlinearity in Dye-Doped PolymerStabilized Liquid Crystals for Low-Power Photonics	253
FOP124	Dileep M S	Structural, Optical and Second Harmonic Generation Studies of NaCl-Doped L-Ascorbic Acid Crystals for Quantum Photonic and Nonlinear Optical Device Applications	254
FOP126	K. Mani Rahulan	Optical Limiting characteristics of Flexible MXene/PVA Nanocomposites: A Synergistic Approach	255
FOP127	Abhisek Roy	Raman-Induced Frequency Shift Suppression of Solitons in an Engineered Oscillatory Dispersion-Waveguide	256
FOP128	Ashutosh Sharma	Statistical characterization of phase depth variations in quasi-phase matching device	257
FOP130	Ugrasen Singh	Analytical Modeling of Electro-Optically Controlled Second-Harmonic Generation in Three-Segment Quasi-Phase-Matched $LiNbO_3$ Crystals	258
FOP131	Neel Tripathi	Design of an Efficient JavaScript-Based Algorithmic Framework for Chirped Structure Generation in Laser-Writing Fabrication	259
FOP132	Mukesh Shukla	Nanosecond optical parametric oscillator for 2 μm and 4 μm wavelength generation	260
FOP133	Arathi Babu	Low-Cost Biocompatible Flexible WS_2-Based Photodetector on a Paper Substrate	261
FOP134	Harsh Chatwani	Lensless Fourier Holography for Dual Sample via Multiplexing	262
FOP135	Jignasha Dangar	Holographic detection of Thalassemia	263
FOP136	Dhaval Hadiya	Spectral Analysis of Red Blood Cell Lateral Fluctuations: A Comparative Study	264
FOP137	Neha Joshi	Single-Shot Anisotropic Jones Matrix Microscopy	265
FOP138	Ritish Kamboj	Phase Recovery from Single-shot, Undersampled Diffraction Intensity Measurement using Object Support-Constraints	266
FOP139	Harman Kaur	Design and fabrication of 2D Holographic Grating for Exit Pupil Expansion of Maxwellian-type AR Display	267
FOP141	Kuldeep Kumar	Interferometric Refractometry of Water Under Temperature Variation.	268
FOP144	Miss Sharma	Design and Fabrication of Holographic Trichroic Combiner	269
FOP145	Rahul Kumar Sharma	Shape Identification Technique Based on Speckle Correlation and Phase Measuring Deflectometry	270
FOP146	Vidhi Singh	Label-Free Classification of Morphologically Similar Yeast Strains Using Digital Holographic Microscopy and Machine Learning	271

FOP148	Haneen V N	Phase Shifting of the Spatial Coherence Function Using Rotating Amplitude Sinusoidal Radial Grating	272
FOP149	Deepak Kumar	Categorization and Analysis of Cross-Spectral Purity for Partially Polarized Light Fields	273
FOP006	Periyasamy THILAKAN	Synthesis of pure and doped Sb_2Se_3 nanocrystallites and study on their optical phase change characteristics	---
FOP007	Nikita Nagar	Slow Evaporation Growth of Pure ZTS Crystal: Structural, Optical, and SHG Studies for Nonlinear Optical Applications	---
FOP015	Ranu KR Dutta	AI Rare-Earth Nanophotonic Platforms for Next-Generation Molecular Imaging and Precision Theranostics	---
FOP073	Vikas Dua	Optical Design of Long Focal Length MWIR Continuous Zoom Optics	---
FOP075	Chinmay Chittaranjan Deo	A Deterministic, Microsecond CPU Wavefront Processing Pipeline for Edge-Deployable Adaptive Optics	---
Poster Day 3			
FOP272	Vikas Agrawal	Energy-Efficient Optical Transceiver Architecture for Intersatellite Links.	274
FOP273	Binayak Dasmohapatra	Design and Performance Evaluation of a Compact 3U-Class MWIR Catadioptric Imaging Payload with Exit Pupil Matching and Stray-Light Suppression for CubeSat Earth Observation	275
FOP274	Sreelakshmy K	Investigation of Photolytic Degradation in Fused Silica Optics for Ring Laser Gyroscopes	276
FOP275	Praveen K C	Realization of Tapered Cavity Layer in a Narrow Bandpass Filter Designed for Hyperspectral Applications	277
FOP280	Mayank Garg	Design of transportation system and criticalities during transportation of space borne glass mirror	278
FOP281	Milind Bagul	Photonic Ising Machine for Image Denoising	279
FOP282	Jyoti Mohapatra	Optical frontend neural network for image classification	280
FOP283	Ayush Soni	Second Order Differential Equation Solver Using Programmable Integrated Photonic Circuits	281
FOP284	Rahul Verma	Angle-Insensitive High-Q Metasurface for Infrared	282
FOP285	Debashri Saha	Design and Development of a 2×4 Optical Demultiplexer based on a Photonic Band Gap (PBG) Crystals	283
FOP286	Faisal Ishaq	Designing Hyperbolic Metasurfaces for Enhanced Light-Matter Interaction and Efficient Radiation Outcoupling	284
FOP287	Geetanjali Jena	Quantifying the loss characteristics of a valley-assisted microwave beam splitter	285
FOP289	Sarang Joshi	Half-Wave Plate Characteristics of 2A3NPCl in the Terahertz Range	286

FOP290	Chandan Kumar	Polarization-Independent All-Dielectric Metasurface-Based Ultra-Narrow Bandpass Filter in Telecom Band Regime	287
FOP292	Sanket Kumar	Broadband Four-Winged Bowtie Metasurface for Passive Radiative Cooling through Enhanced Mid-Infrared Emissivity	288
FOP293	Santosh Nayak	Transmittance Tunability in Topological Waveguide	289
FOP294	Soorya N	An Orion-shaped Infrared Metamaterial Absorber for Greenhouse Gas Sensing Applications	290
FOP296	Abhisek Roy	A multipolar decomposition approach for resonant phase control in all-dielectric metasurfaces	291
FOP298	Siya Pallath	Dielectric Chiral Metafoil Structures with Bisignate Circular Dichroism for Terahertz Waveband Applications	292
FOP301	Neha Singh	High-temperature photothermal conversion using a selective refractory metamaterial absorber for efficient solar energy harvesting	293
FOP302	Riya Soni	Four-Fold Symmetric Metasurface for Dual-Band Terahertz Near-Perfect Absorption	294
FOP304	Praveen Vishwakarma	Graphene-Embedded all-dielectric metamaterial absorber	295
FOP305	Rakesh Kumar	Broadband Visible Region Absorber Using Dual-Shaped Tungsten Resonator Metasurfaces	296
FOP306	Rajneesh Joshi	Coherence control in Young's two-pinhole interferometer with incoherent electromagnetic fields	297
FOP307	Mansoor Ahmed	High-Q Silicon Carbide Ring Resonator for Purcell-Enhanced Emission from Erbium Defect Centers at Telecom Wavelengths.	298
FOP308	Sagar Ailawadhi	Effects of Anisotropic Atmospheric Turbulence on the Polarization Stability of C-Point and V-Point Vector Beams	299
FOP309	Jayeta Banerjee	High Photon Pair Generation Rate in SiN Microring Resonator for O-Band Photonic Integrated Circuit	300
FOP310	Aadi Bharatia	Mid-Infrared Absorption Spectroscopy Using a Folded Quantum Nonlinear Interferometer	301
FOP311	Harshita Bose	Pulse-Programmable Processing in Coulomb-Blockaded Triple Quantum Dots for Hybrid Quantum Optical Architectures	302
FOP312	Ipsita Chakraborty	Quantum Weak-Value Amplification of Chiral Phase-SPR for Zeptomolar Enantiomer Detection	303
FOP313	Rajnandan Choudhury Das	A grating-chip cold-atom CPT clock with Raman phase mapping	304
FOP314	Rup Chowdhury	Tuning the Dimensionality of NbTiN Meander Structures for Near-Infrared Single Photon Detection	305

FOP315	Manoj Das	Optical Interferometer for Transferring Optical Carrier Frequency with High Stability	306
FOP317	Purvesh Garge	Weak-Measurement Enhanced Two-Photon Polarization Spectroscopy of 5S-5D Transition in Rubidium	307
FOP318	Shubham Ghosh	Pancharatnam-Berry Phase Metasurfaces for Two Entangled Photon State Generation	308
FOP320	Gya Prasad	Voltage-Controlled Quantum Coherence Engineering via Birefringence-Frequency Coupling in Nematic Liquid Crystals	309
FOP321	Harshal Jain	Non-monotonic Dependence of the Angular Schmidt Spectrum on Crystal Thickness in Spontaneous Parametric Down-Conversion	310
FOP324	Amrutha K	Quantum Metrology with Displaced Squeezed vacuum state in Mach - Zehnder Interferometer	311
FOP325	Swetha K	Thickness Dependent Optical Effects in Hexagonal Boron Nitride	312
FOP329	Shahan Ulla Khan	Generation of Three-Component Mechanical Schrödinger Cat States in an Optomechanical Platform	313
FOP330	Khushboo	Polarization Entanglement Distribution through Existing Fiber Infrastructure	314
FOP332	Rohit Kumar	Deterministic Single-Photon Emitter Arrays in Hexagonal Boron Nitride by Carbon-Assisted Focused Ion Beam Engineering	315
FOP333	Simanshu Kumar	OAM-Induced Lattice Rotation Reveals a Fractional Optimum in Fault-Tolerant GKP Quantum Sensing	316
FOP334	Sugar Meena	Robust Continuous-Variable Multipartite Entanglement Using Arrays of Nonlinear Waveguides	317
FOP335	Soumyadip Mukherjee	Cavity Enhanced Steady State Quadrature Squeezing in Spontaneous Four-Wave Mixing Regime	318
FOP336	Uddipta Mukherjee	Design of QPM crystal-based source for Quantum Ghost Imaging	319
FOP338	Sayan Nayak	Purcell Enhancement of Green CdSe QDs Using a Bullseye Cavity	320
FOP341	Muppalla Prakash	Schmidt-Mode Impurity as Visibility Ceiling in a Folded Nonlinear Interferometer with Undetected Photons	321
FOP342	Siva Karri	Investigating the Emergence of Entanglement in an Atom-Cavity System	322
FOP343	Rachana	Towards Magnetically Tunable Laser Locking Using Polarization Spectroscopy of the Cs D_2 Line	323
FOP344	Aryan Raj	Design and Optimization of a High-Resolution TOF Absorption Imaging System for a 2D Magneto-Optical Trap	324

FOP346	Naincy Shrivastava	Helical Ince-Gaussian Beam Assisted Six-Wave Mixing in a Coherent Atomic Medium	325
FOP348	Parul Singh	Height-Driven Modulation of Single-Photon Emission in $Al_{0.4}Ga_{0.6}As$ Bullseye Cavity	326
FOP349	Shashank Srivastava	Decoherence Analysis of $^{167}Er:Y_2SiO_5$ at the ZEFOZ Operating Point: Bath Regime Diagnostic and Motional Narrowing in a Telecom-Wavelength Quantum Memory	327
FOP350	Shilpi Srivastava	Interplay of Environmental and Target Reflectivity in Quantum Illumination	328
FOP353	Vijay	Detection Parameter Optimization for Efficient Photon-Correlation Measurements	329
FOP354	Gunjan Sinha	Underwater topological charge detection of optical vortices	330
FOP355	Gaurav Kumar Yadav	Multi-Metric Analysis of Many-Body Quantum Interference in Integrated Photonic Boson Sampling	331
FOP356	Upasana Baishya	Quantification of Weak Crystal Anisotropy Using Extreme Cross-Polarization Extinction	332
FOP357	Sunny Bajaj	Generation of Single-Photon Needle Beams Using a Flat Lens	333
FOP358	Bharat	Comparative Study of Vector Beam Encoding Using Twisted Nematic and Parallel Aligned SLM	334
FOP359	Neha Choudhary	Engineered Vector Vortex Beams with Multiple Radial Zones and Controllable Topological Charges	335
FOP361	Gayathri P	Tightly focusing of circular airy femtosecond pulse with binary axicon	336
FOP362	Aroma Indus	Tailoring Orbital Angular Momentum Spectra with Angular Slit Masks	337
FOP363	Aditya Jena	Frozen Whirlpools of Light: An Optical Analogue of Abrikosov Vortex Pinning Using Discrete Vortex Landscapes	338
FOP364	Ankita Karmakar	Dynamic Transformation of Optical Bimerons using Enantiomeric Excess	339
FOP365	Laxminarayan	Methods of Structured beam characterization	340
FOP366	Priya Malik	Quantification of Rotational Speed Using Laser Speckle Contrast Imaging and 3D Convolutional Neural Networks	341
FOP367	Md Ansari	Propagation characteristics of scattered Hermite-Gaussian beams	342
FOP368	Brijesh Mishra	Formation of High-Order Hollow Vector Beams with Invariant Dark-Core	343
FOP369	Lucky Nagar	Speckle Correlation Method for Non-Contact Force Sensing using a Disc-Type Cross-Beam Transducer	344
FOP370	Sushanta Pal	Generation of Homogeneous Polarization Singularity Array	345

FOP371	Rudrashis Panda	Vortex Evolution in Composite Optical Field	346
FOP372	Aman Pandey	Non-Contact detection of small deflection on a Cantilever Beam Using Laser Speckle Pattern Imaging	347
FOP373	Yukti Pandey	Interferometric Complex-Field Approach for Reconstruction Through Scattering Media	348
FOP374	Sakthi Maheswari R	Topological and Polarization Effects in the Tight Focusing of Hybrid Vector Vortex Beams through Uniaxial Crystals	349
FOP376	Kanishka S	Vectorial Diffraction Analysis of Tightly Focused Hybrid Poincaré Beams Through an Oil Immersion Objective	350
FOP377	Rohit Shimpi	Programmable Liquid Crystal Vortex Beam Generation Using Independently Addressable Ring Sector Electrodes	351
FOP378	Tileshwar NLN	Secure Optical Image Authentication Based on C-Point Singularities	352
FOP379	Kushal Tripathi	Optimized simultaneous generation of dual-wavelength phase and polarization singularities	353
FOP380	Athira T S	Point singularities in Spectral Interference	354
FOP383	Ganesh Velagala	Tailoring the properties of coherence vortices: control functional engineering of Laguerre-Gaussian beams.	355
FOP384	Anil Kumar Nirala	Spatiotemporal Enhancement of Dynamic Laser Speckle Activity Maps for Low-Contrast Fine Structural Visualisation	356
FOP385	Shouvik Sadhukhan	Fourier-Space Theory of Turbulence Broadening and Scintillation Reduction in Vortex Beams	357
FOP386	Mirza Baig	Development of a Reflectance Speckle Contrast Optical Spectroscopy System for Quantitative Flow Imaging	358
FOP387	Ramesh Kumar	Finite Difference Vector Analysis of the Arbitrary Waveguides	359
FOP389	Geetanjli	Dual-Adaptive Physics-Informed Neural Networks for Optical Waveguide Eigenvalue Problems	360
FOP390	Aayush Deole	Quantum Simulator for RC Circuit Analysis using Unitary Dilation and Strang Splitting	361
FOP391	Kannal Amudhu K	Inverse designed non-volatile phase change varifocal metalens at the edge of the visible spectrum	362
FOP392	Ajay Kumar	Spectral Characterization of Large Hollow-Core Bragg Fibers: A New Approach	363
FOP395	Rajnish Singh	Design and Stray Light Simulation of Star Sensor Baffle for Interplanetary Missions	364
FOP396	Anupam Shaw	Numerical Investigation of Enhanced Alpha-Particle Generation in Laser-Driven Proton-Boron Fusion	365

FOP398	Deepanshi Singh	Stability Analysis of the Effective index of Bent Optical Waveguide Operators with Perfectly Matched Layer	366
FOP399	Agniva Das	$NaBiF_4$:Yb, Er UCNPs: Temperature Sensing with off-resonant 1064 nm light	367
FOP401	Km Shivani Bhardwaj	Relativistic Compression Optimization of Negatively Chirped Super-Gaussian Laser Pulse in Plasma	368
FOP403	Mandeep	Halide-Organic Spacer Interplay as energy funneling knob to tailor optical response in 2D Ruddlesden-Popper Perovskites	369
FOP404	Subrata Manna	Harmonically Mode-Locked Bright-Dark-Bright Vector Soliton Complexes in an Erbium-Doped Fibre Laser	370
FOP405	Supriya Pradhan	Femtosecond Vortex Beam Nanostructuring of Plasmonic Silver Surface and Application in SERS-based Trace Detection	371
FOP407	Tuhina Sultana	Intensity-dependent Nonlinear Optical Behavior of $MoSe_2$ Nanoparticles Prepared by Femtosecond Laser Ablation in Liquid	372
FOP408	Aanchal Tyagi	Synthesis of few layers WS_2 sheets via liquid assisted ultrafast laser ablation for SERS applications	373
FOP409	Pooja Chugh	Generation of few-micron thick liquid sheet using single jet impingement on knife-edge	374
FOP410	Nisha	Asymmetric frequency-mode coupling for discrete spectral diffraction	375
FOP411	Shailesh Mohine	Primary Vibration Calibration Using Laser Interferometer	376
FOP412	B.S. Bhargava Ram	Characterization of Off-Axis Aspheric Mirrors of Three Mirror Anastigmatic (TMA) Telescope	377
FOP413	Snehita Ghosh	Effect of Nonlinearity in branched flow of light in quasi-periodic photonic lattices	378
FOP414	Priyanshu Singh	Fiber Bragg gratings in Multi-mode ZBLAN fiber for environmental temperature sensing	379
FOP415	Divya Mishra	Tunable Bandgap - Assisted Nonadiabatic Dynamics in an Optomechanical Array	380
FOP300	Vishakha Sharma	High-Q Dual-Resonant Chirality Engineering through Cavity Rotation in Bilayer Dielectric Metasurfaces	---
FOP303	Sreeman Narayanan T	Magnetically Homogeneous Mu-Zero Metamaterial for Microwave Applications	---
Poster Day 4			
FOP150	Kamal Tewari	Measurement of displacement using shadow-based Opto-Mechanical Analysis	381
FOP151	Biprav Chetry	A Portable Low-Cost Smartphone-Based Microspectrophotometer for Integrated Microscopic Imaging and Spectroscopy	382

FOP152	Chunuranjan Dutta	Portable Electrochemiluminescence Sensor with Smartphone-Controlled Imaging for Antioxidant Capacity Determination	383
FOP153	Surya Gautam	Interferometric Force Measurement System Based on Fringe Displacement Tracking	384
FOP154	Md Haque	Investigation on Post-Processing of Diamond-Turned Chalcogenide Glass using Chemical Mechanical Polishing	385
FOP155	Virendra Jaiswal	Estimation of spectral mismatch factor for broadband UV radiometers	386
FOP156	Elizabeth James	Optoelectronic arrangement and beat frequency measurement of the optical pressure standard	387
FOP157	Adarsh Mishra	Theoretical Analysis of Pressure Dependent Beat-Frequency Sensitivity in Optical Refractometry: Helium and Nitrogen	388
FOP158	Nandini Mondal	Polarization-multiplexed dual-frequency finite-difference discriminator for frequency locking	389
FOP159	Ojaswi Jangra	An Indigenously Developed Photodiode Preamplifier Array for Reliable and Sustainable Operation of a Laser- Cooled Cesium Primary Frequency	390
FOP160	Diganta Rabha	A Systematic Comparison of Retroreflective Background-Oriented Schlieren and Retroreflective Shadowgraph Imaging	391
FOP161	Anirban Roy	A Hot-Extractive Fourier Transform-based UV-DOAS System for SO_2, NO and NH_3 Monitoring in Industrial Plants	392
FOP163	Shibu Saha	Blue Light Hazard Measurement Facility for Photobiological Safety Assessment of Lamps, Luminaires and Electronic Display Devices	393
FOP166	Harsh Singh	Investigation of Optical Polishing of Single Crystal Sapphire and Polycrystalline Spinel	394
FOP170	Binshati Chatterjee	Single - layer silicon-nitride edge coupler for short-wavelength NIR PIC architecture	395
FOP173	Divyanshu Tiwari	Rapid Designing of Silicon Nitride Frequency Combs via Integrated Tidy3D and PyLLE Simulations	396
FOP174	Nithin Vogirala	Dispersion-Engineered Asymmetric Directional Coupler on InP for Routing 1310 nm and 1550 nm	397
FOP175	Poonam Yadav	Hollow core Arrow Waveguide	398
FOP176	Gayathri Nair	Analysis of Kerr lens modelocking Ti:Sapphire laser under CW operation	399
FOP177	Nikita Choudhary	V-shaped millibot integrated with FRET-assisted random lasing tip	400
FOP178	Christy P	Breaking Plastic with Light: Resonant Energy Transfer-Driven Near-Infrared Degradation of PET Polymer	401

FOP181	Avantika Gautam	Experimental and theoretical understanding on the role of Xenon in laser gas mixture towards sealed off CO_2 laser development	402
FOP183	Ipshit Ghosh	Analytical Evaluation of Atmospheric Propagation for High-Power CW and Pulsed Lasers	403
FOP185	Kriti Gupta	Ge-based Cylindrical Meta-Atoms on a ZnSe substrate for focusing at 10μm Wavelength	404
FOP186	Dr Joshi	Studies on the Effect of Nanosecond Pulse Laser Irradiation on Layered Mylar Sheet	405
FOP188	Dixit Kumar	Competing Noise-Driven Operating Regimes in a Free-Running GHz-rate Actively Harmonic Mode-Locked Fiber Laser	406
FOP189	Mrutyunjaya Rath	Metal-nanoparticle assisted simultaneous self-assembly and phase change at air-water interface	407
FOP190	Kethiri Reddy	The Effect of CW Laser on Silicon Based Optical Sensor	408
FOP191	Priyabrata Senapati	Realization of Optical Bench for Intersatellite Laser Communication Terminal	409
FOP193	Purva Sharnagat	Investigation of Damage Morphology in Multilayer Dielectric Mirrors Induced by High-Power Laser Irradiation	410
FOP194	Hasna K T	Picosecond Laser Pulse Propagation Through Aerosols Under Atmospheric Conditions	411
FOP196	Swati Verma	Laser Power Beaming through Multi-spectral Muti-beam Power Transfer	412
FOP202	Khushboo Bishnoi	Terahertz Antiferromagnetic Resonance Tuning in Zn-Doped NiO via Cationic Doping and Temperature	413
FOP203	Parvathy J P	THz Plasmonic Photoconductive Antennas on Semi-Insulating and Ion-Implanted GaAs: Fabrication and Characterisation	414
FOP206	Aryansingh Kushwah	Fabrication, Characterization, and Comparative Study of Unimplanted and Ion Implanted GaAs-Based Terahertz Photoconductive Antennas	415
FOP207	Shakti Mahato	Dual-Resonant Graphene Split-Ring Metamaterial for Terahertz Refractive Index Sensing	416
FOP208	Neha	A High Resolution Switchable and Tunable Microwave Photonic Multi-Notch Filter	417
FOP209	Shivansh Sharma	High-Q Terahertz Electromagnetically Induced Transparency in Silicon Metamaterials	418
FOP210	Shruti	A WDM-RoF Framework for Hybrid Wired-Wireless Networks	419
FOP211	Ram Yadav	Effect of Length and Conductivity of PCM VO_2 on the Performance of the On-Chip Guided Wave THz Modulator	420
FOP212	Sapana Yadav	Engineering a Quartz-Supported Terahertz Gold Nano rod Metasurface for Enhanced Refractive Index Sensing	421

FOP213	Amitkumar Pandey	Terahertz Investigation of Tunable Natural Ferromagnetic Resonance in Rare Earth Substituted $CoFe_2O_4$	422
FOP217	Aseefhali Bankapur	In-situ SERS detection of gaseous benzaldehyde: A prospective breath analysis method	423
FOP218	Soumita Chakraborty	Machine Learning assisted Graphene-Coated Quantum-Enhanced Photonic Crystal Waveguide Biosensor for blood Cancer Detection	424
FOP219	Satyam Dalmiya	Fourier investigation of Surface-Plasmon Polariton coupled Emission	425
FOP220	Ritwik Dhara	Fourier domain imaginary weak value amplification of small birefringence effects	426
FOP221	Divyanshu Suthar	Engineering of a Perovskite-based Ultrasensitive Multilayer Plasmonic Sensor	427
FOP222	Mohammed Eesa S M	Slot-Engineered Split Cylindrical TiO_2 Metasurfaces for Enhanced Refractive Index Sensing	428
FOP223	Hemant Beniwal	Engineering of Multimode Excitation on Multilayer Flat Plasmonic Geometry by Integrating with Spherical Nanoparticles	429
FOP224	Sourabh Jain	Integrated Long-Period Grating-Coupled SPR Sensor for High-Sensitivity Refractive Index Sensing	430
FOP225	Bablu Jatav	Engineering of Extraordinary Transmission via Fano Resonance for Selective Wavelength Filtering with Ultra-high Q-factor	431
FOP227	Aashirya Kanwar	Analyte Thickness Engineering for Enhanced Localized Plasmonic Sensing through Resonance Hybridization	432
FOP228	Deepak Kumar	Scalable Reproduction of Plasmonic Quasicrystals via Thermal Nanoimprint Lithography for Label-Free Detection of Cotinine	433
FOP230	Shubham Mahanta	Protein detection in real-time using whispering gallery modes and comparative analysis of modes and photonic nanojets in bare and multilayer dielectric microspheres	434
FOP231	Arani Maiti	Probing the Broken Spatial Symmetry of a Stratified Medium with Structured Light	435
FOP232	Meenakshi	In-Situ Detection of Micro/Nano Plastics in Water Using Surface Enhanced Raman Spectroscopy	436
FOP233	Srikant Moharana	Optics of Finite Self-Assembled Disordered Sphere Arrays	437
FOP234	Sherep Dukpa	Free-Carrier Tunable and Reconfigurable Mid-Infrared Meta-Atoms	438
FOP235	Srijith Kanakambaran	Influence of Analyte Thickness on Refractive Index Sensing Performance of Silicon Cylindrical Metasurfaces	439
FOP236	Sujit Rajak	Spin-split dispersion in symmetric and symmetry-broken plasmonic Metasurfaces	440

FOP238	Ananya Rout	Exploring Resonant Metasurfaces for Extreme Light Matter Interaction	441
FOP241	Nikhil Shrivas	Multichannel photon correlation simulation of fast spectral dynamics of single fluorophores	442
FOP242	Arya Siddharth	Optical properties of single magnetic micro and nanoparticles using a transmission-based darkfield microscope	443
FOP243	Laksh Sharma	Graphene-Coated Nanomatryoshka for Cholesterol Detection	444
FOP244	Ojasvi Singh	Dual-mode SEIRA detection of microplastics from disposable paper cups using a plasmonic metagrating	445
FOP245	Subanya Saravanan	Numerical Analysis of Pd/$HfSe_2$ Based Surface Plasmon Resonance Biosensor with Enhanced Sensitivity for Biomolecular Detection	446
FOP246	Surendra Prasad	Modelling Surface Plasmon Polaritons in double layers Graphene Elliptical Waveguide	447
FOP247	Vinod Parmar	Design Optimization of Plasmonic Metasurfaces for Sensing Applications	448
FOP248	M. Lavanya	Performance Analysis of SPR Biosensor for Colorectal Cancer Diagnosis Using TMDC layers	449
FOP250	Dheeraj Yadav	Fourier domain enhancement of Chiro-optical signal in Plasmonic Nanostar using Structured light	450
FOP251	Naveen Yadav	Investigating Optical Excitons in Two-Dimensional Inorganic-Organic Hybrid Perovskites	451
FOP254	Siddharaj Gadge	Tailoring soft cavities for robust molecular strong coupling	452
FOP255	Rakshith Kamath	Electric Double Layer–Driven Flow Focusing in Laser-Induced Liquid Microjets	453
FOP257	Arnab Bhattacharyya	Beaconless Adaptive Wavefront Shaping by MEMS-based Deformable Mirror	454
FOP258	Sankar Davuluri	Entanglement based LiDAR for ranging moving targets	455
FOP259	Sayantan Gantait	Rapid laser beam focusing and lateral scanning through scattering media using a gradient descent algorithm	456
FOP260	Lt Colonel Kabir Kohli	Design & Development of Minimum Resolvable Temperature Difference (MRTD) Test Station for Field Performance Evaluation of Thermal Imagers	457
FOP261	Sourav Paul	Parametric Studies of an Optical Telescope System for Tracking of Low Earth Space Objects	458
FOP262	Pooja P M	Effect of Maritime and Terrestrial Atmospheric Turbulence on Coherent Beam Combination	459
FOP263	Krishnendu Roy	Narcissus analysis of a Ge-free Mid Wave Infrared Cooled System	460
FOP265	Naresh Sothuku	A High-Speed Time Interleaved Photonic-Assisted Analog-to-Digital Converter (Ph-ADC) Architecture for Defense Applications	461

FOP266	Aditya Khudiwal	Visible-Near Infrared Photodetection using large area grown SnS_2 Thin Film on Quartz Substrate	462
FOP267	Manjeet Kumar	Disposable microplasma generating chip for aqueous sample analysis, fabricated on a PET substrate.	463
FOP268	Anjali Sharma	Synergistic improvement of narrow bandgap PbS quantum dot solar cells through surface ligand engineering and enhanced electrode transparency	464
FOP183	Deepika Porwal	Development of System Electronics of 1 KW High Power Fiber Laser	---
FOP214	Mohammed Ashahar Ahamad	Dynamical control of light-matter interaction through broken symmetry metasurface	---
FOP215	Indhu AR	Solar-Driven Photothermal conversion using non-oxidative Plasmonic Cu nanostructures	---
FOP239	Basudev Roy	Comparison of viscoelasticity measurement between optical tweezers and rheometer	---
FOP256	Anirudh Bharadwa	Phase Controller Bandwidth Optimization in 7-Channel Tiled Aperture Coherent Beam Combining	---

From Chips to Full Space Wireless: Intelligent Topological Terahertz Photonics

[1,#]Ranjan Singh
[1]Department of Electrical Engineering, University of Notre Dame, IN 46556, USA
[#]*rsingh3@nd.edu*

The terahertz spectrum offers enormous bandwidth for future wireless systems, but realizing its potential requires integrated technologies that can efficiently route, beamform and connect signals between chips and free space. In this talk, I will present our recent progress toward intelligent topological terahertz photonic systems that combine robust wave transport, silicon integration and AI-assisted design [1]. We first demonstrate silicon topological beamformers that protected scale protected waveguiding into complex phased-array architectures, enabling programmable 360° beamforming, 72-Gbps chip-to-chip links and multiple simultaneous 40-Gbps wireless channels. I will then describe topological leaky-wave antennas that deliberately harness radiation from topological edge states, enabling frequency-controlled beam scanning across 75% of the three-dimensional solid angle, spatial demultiplexing of multiple THz links and simultaneous bidirectional transmission and reception [2]. Together, these results point to a new paradigm in which topology is used not only to protect terahertz transport, but to engineer how information flows through space. I will conclude with a vision for AI-enabled, reconfigurable THz integrated systems that unite communications, sensing and intelligent control for 6G and beyond.

References:

[1] W. Wang, Y. J. Tan, T. C. W. Tan, A. Kumar, P. Pitchappa, P. Szriftgiser, G. Ducournau, R. Singh, *Nature* 632, 522 (2024).
[2] W. Wang, Y. J. Tan, P. Szriftgiser, G. Ducournau, R. Singh, *Nature Photonics* 20, 317 (2026).

.

Intense Light-Matter Interaction: Sculpted Pulses, Structured Targets, Brighter Sources

[#]G. Ravindra Kumar
Tata Institute of Fundamental Research, Homi Bhabha Road, Colaba, Mumbai 400005
[#]*grk@tifr.res.in*

We examine the latest trends in enhancing the coupling of high intensity, femtosecond laser pulses to matter, involving both shaping of the light pulses in space and time as well as fabricating structures on target surfaces.

Extreme light interaction with matter has emerged as a major frontier of contemporary physics. Ultrashort, ultra-intense laser pulses can create extreme states of matter on a laboratory tabletop for scientific study, simultaneously providing compact sources of high-energy, high-flux and directional electrons, ions, x-rays and other forms of radiation.

A central challenge—and opportunity—in this field is the controlled coupling of extreme light to matter. Traditionally, considerable effort has been devoted to delivering the highest possible intensity to the target. Propagation through a complex amplifier chain introduces spatial and phase distortions, requiring sophisticated wavefront correction and adaptive optics to recover near-diffraction-limited focusing. Equally important is the temporal structure of an ultrashort pulse. Over the past two decades, enormous progress has been made in improving **temporal intensity contrast**, suppressing picosecond and nanosecond pedestals and pre-pulses that can substantially modify a target before the arrival of the principal femtosecond pulse. Increasingly, however, these apparently undesirable degrees of freedom can be viewed instead as **control parameters**. Rather than merely eliminating temporal structure, one can deliberately sculpt it. The importance of pulse shaping is already well established in laser-driven fusion, where the temporal profile determines compression, shock formation and energy deposition. In fast-ignition concepts, for example, control of the intense driving pulse may provide a route towards tailoring the resulting relativistic-electron distribution for efficient energy transport into an independently compressed fuel core.

A corresponding transition is occurring in the spatial domain. Adaptive optics has conventionally sought to remove wavefront distortions to produce the sharpest, cleanest possible focal spot. Structured light suggests the complementary possibility of **creating spatial structure deliberately**. Optical vortices and beams carrying orbital angular momentum, extensively explored at conventional intensities for applications including particle trapping and manipulation, are now entering the relativistic-intensity regime. Generating such structures across the large-aperture beams of high-power laser systems remains challenging, but rapid advances point towards extreme-light fields whose amplitude, phase, polarization and angular momentum can be engineered in space as well as in time.

The third component of this emerging picture is the **structured target**. Periodic and sub-wavelength structures have long been known to enhance electromagnetic coupling to matter. Modern nanofabrication now allows this idea to be extended to nanowires, gratings, tailored surfaces and increasingly sophisticated metasuface architectures. At extreme intensities these structures can influence not only the absorption of the incident light but also the generation, transport and directionality of energetic charged particles and radiation.

References:

[1] G. Ravindra Kumar, Amita Das, Prashant K. Singh and M. Krishnamurthy, *J. Opt. Soc. Am. B 43* (2026) B407-B462

[2] M. Piccardo, M.O. Cernaianu, J.P. Palastro, A. Arefiev, C. Thaury, J. Vieira, D.H. Froula, and V. Malka. *Optica, 12(2025)732*

[3] C. Aparajit *et. al., Phys. Rev. Res*. 7 (2025) L032063

[4] S. Dam *et. al., Phys.Rev.Res*. 8 (2026) 023017

3D Mask Effects in EUV Lithography: From Limitation to Opportunity

A. Erdmann[#], V. Jadhav, P. Evanschitzky and C. Schwemmer
Fraunhofer IISB, Schottkystr. 10, 91058 Erlangen, Germany

[#]*email: Andreas.Erdmann@iisb.fraunhofer.de*

EUV lithography relies on reflective masks where thick absorbers and oblique illumination produce complex three-dimensional imaging effects. Using rigorous simulation and physical modeling, we analyze these effects and demonstrate advanced strategies to mitigate or exploit them, enabling high-contrast imaging with improved depth of focus across current and next-generation EUV systems.

Extreme ultraviolet (EUV) lithography[1] uses light at a wavelength of 13.5 nm to fabricate the most advanced semiconductor devices for mobile, high-performance, and AI computing. Bragg-type multilayer mirrors filter and guide EUV light from a laser-produced plasma source through the illumination system, providing uniform, coherence-controlled illumination of a reflective mask. The reflective mask carries absorber patterns several wavelengths thick, deposited on top of a multilayer stack. The projection system's multilayer mirrors then form a demagnified image of the mask in a photoresist layer coated on a silicon wafer.

The combination of thick absorbers, reflective multilayers, and oblique illumination gives rise to so-called **three-dimensional mask (M3D) effects**[2]: orientation-dependent imaging, non-telecentricity, feature-specific best-focus shifts, and contrast fading caused by superposition of laterally shifted images from different source points. Accurate understanding and modeling of these effects is essential for maintaining image quality in EUV systems. Simplified analytical approaches such as a **double diffraction model** and a **waveguide model** (Fig. 1) provide physical insight into the underlying imaging mechanisms, while highly efficient rigorous electromagnetic field solvers combined with multi-objective optimization identify optimum combinations of illumination source and mask geometry, maximizing contrast, depth of focus (DoF), and EUV throughput.

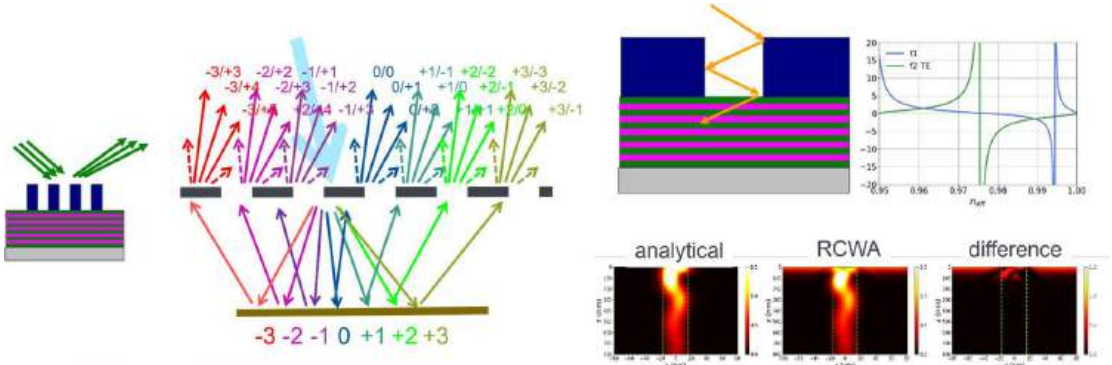


Figure 1: Double diffraction model (left) and waveguide model (right) of a mask for EUV lithography.

The mask and image simulation models of our Fraunhofer development and research simulator **Dr.LiTHO** are applied to identify imaging solutions for EUV systems with numerical apertures of 0.33, 0.55, and 0.75. Key findings include: **split-pupil exposures** to mitigate contrast fading; **low-refractive-index absorber materials** that channel light through mask openings for more efficient EUV utilization; and a **volume-hologram analogy** for 3D EUV masks, demonstrating that M3D effects—widely regarded as a fundamental limitation—can in fact be harnessed to improve imaging performance[3].

References:

[1] J. van Schoot, *IEEE Electron Devices Magazine*, 2 (2024) 8.
[2] A. Erdmann, D. Xu, P. Evanschitzky, V. Philipsen, V. Luong, E. Hendrickx, *Advanced Optical Technologies,* 6 (2017).
[3] A. Erdmann, G. Bottiglieri, C. Schwemmer, P. Evanschitzky, P. Dhagat, T. Brunner, M. van de Kerkhof, *J. Micro/Nanopatterning, Materials and Metrology,* 25 (2026).

Quantum sensing using single and entangled photons

[1,#]G. K. Samanta
[1]Photonic Sciences Lab. Physical Research Laboratory, Navrangpura, Ahmedabad 380009, Gujarat, India
[#]*gsamanta@gmail.com*

Quantum sensing and imaging are emerging as powerful technologies for achieving measurement precision beyond classical limits. Here, we will present our recent advances in Hong–Ou–Mandel interferometry-based quantum sensing, including high-precision measurements of optical delay, birefringence, and group refractive index, along with their potential applications in real-time quantum metrology.

Quantum sensing and imaging are emerging as key quantum technologies that exploit nonclassical states of light, quantum correlations, and entanglement to enable measurements beyond the capabilities of conventional optical techniques. Among these quantum resources, Hong–Ou–Mandel (HOM) interference, arising from the bunching of two indistinguishable photons at a balanced beam splitter, has become a powerful tool for precision metrology, imaging, and sensing. When one photon of a pair generated through spontaneous parametric down-conversion is delayed with respect to the other, the coincidence counts measured at the two output ports of the beam splitter exhibit a characteristic bell-shaped interference dip, whose width is determined by the spectral bandwidth of the photon pairs. Consequently, the spectral bandwidth plays a crucial role in determining the resolution of HOM-based sensors. Conventionally, broadband photon pairs are generated using bulky and expensive ultrafast laser systems, limiting the deployment of HOM-based sensors outside laboratory environments.

We demonstrate the generation of high-brightness photon pairs with tunable spectral bandwidth using a compact single-frequency continuous-wave diode laser, enabling high-precision and real-time sensing. Using a 1-mm-long periodically poled KTP crystal, we generate broadband degenerate photon pairs that produce a narrow HOM dip, allowing measurements of displacements as small as 60 nm and vibration amplitudes of 205 nm at a frequency of 8 Hz. We further employ the HOM interferometer to measure temperature-dependent refractive-index changes in nonlinear crystals, demonstrating its potential for precision-augmented in-field quantum sensing.

Exploiting the sensitivity of HOM interference to polarization indistinguishability, we also demonstrate a projection-free method for mapping two-dimensional polarization distributions. Unlike conventional polarization characterization techniques, such as Stokes polarimetry, which require multiple polarization projections and are susceptible to calibration errors and finite extinction ratios, our approach directly maps spatially varying polarization transformations onto coincidence counts. Using a HOM interferometer driven by a high-brightness photon-pair source at 810 ± 2 nm, we characterize a birefringent q-plate exhibiting spatially varying polarization rotations and reconstruct the polarization distribution with a fidelity of approximately 95% and an angular resolution of about 0.4°. Fisher-information-based analysis can further improve the resolution at the expense of increased acquisition time.

Finally, by exploiting the controllable transition between symmetric and antisymmetric Bell states, we demonstrate a quantum sensing modality based on entangled-state symmetry. Phase shifts introduced through birefringence, optical delay, or pump-phase modulation are directly mapped onto the symmetry of the entangled state and read out through HOM interference. Using this approach, we measure thermo-optic birefringence changes on the order of 10^{-6}/°C and static and dynamic optical delays with amplitudes as small as 10 nm. In this talk, I will introduce the fundamentals of HOM interference and present our recent advances in HOM-based quantum sensing and imaging.

References:

[1] S. Singh, V. Kumar, V. Sharma, D. Faccio, and G. K. Samanta, “Near-video frame rate quantum sensing using Hong-Ou-Mandel interferometry”, Adv. Quant. Tech. 6, 202300177 (2023).
[2] S. Singh, V. Kumar, and G. K. Samanta, “Fast measurement of group index variation with optimum precision using Hong-Ou-Mandel interferometry”, APL Quantum 1, 046117 (2024).
[3] Chahat Kaushik, Vimlesh Kumar, and G. K. Samanta, “Quantum sensing through bosonic-fermionic Bell-state transitions in two-photon interference”, arXiv:2606.14408 (2026).

Photonic Quantum Computing Platform Using Multi-Degree-of-Freedom of Photons

C. M. Chandrashekar
Quantum Optics and Quantum Information Processing Group, Department of Electronic Systems Engineering, Indian Institute of Science, Bengaluru 560012, India
chandracm@iisc.ac.in

We present a deterministic photonic quantum computing platform that encodes multiple qubits per photon using polarization and path degrees of freedom via discrete-time quantum walks, and demonstrate universal quantum gates, a six-qubit GHZ state, linear-complexity quantum phase estimation, and gate-based emulation of boson sampling, all with high experimental fidelity.

Photonic qubits are attractive for quantum computation as they operate at room temperature, but deterministic two-qubit gates are difficult since photon-photon interactions are inherently probabilistic. We address this by encoding multiple qubits within a single photon, combining its polarization and path (spatial-mode) degrees of freedom via a single-photon discrete-time quantum walk (DTQW), realized using polarizing beam displacers and wave plates in a Galton-board-like arrangement. A single photon thus carries a three-qubit register, and SPDC photon pairs entangle multiple such registers, scaling qubit count without a proportional increase in photon number. Gate operations, implemented deterministically through these transformations rather than probabilistic dual-rail KLM schemes, give fully deterministic, high-fidelity single- and two-qubit gates at room temperature, characterized via quantum state tomography (QST).

Using this encoding, we experimentally realized a universal gate set — Phase (P), Hadamard (H) and CNOT — with high fidelity (QST-measured Bell-state fidelity ≈ 98.1%). Two three-qubit modules, each carried by one photon of an SPDC-entangled pair, were joined by two consecutive CNOT gates to prepare the genuinely entangled six-qubit GHZ state

$$|GHZ\rangle = (1/\sqrt{2})\,(\,|000000\rangle + |111111\rangle\,) \tag{1}$$

confirmed via entanglement-witness measurement. The quantum-walk operations were also mapped onto standard circuit gates, providing a resource-efficient route to scale qubit number using fewer photons [1].

Quantum phase estimation (QPE) underlies Shor's, HHL and many eigenvalue-estimation algorithms, but its standard circuit — an n-qubit control register, controlled-U2^k operations and an inverse quantum Fourier transform — scales as $O(n^2)$. For the practically important class of structured (diagonal) unitaries arising in QFT-based protocols, cyclic-group representations and periodic evolutions, we introduced a QPE construction reducing this to O(n), implemented on a 4-qubit photonic system from a single photon pair (2 qubits in polarization, 2 in path). Unlike earlier dual-rail/KLM photonic QPE demonstrations with inherently probabilistic controlled operations, ours is fully deterministic and scalable to higher-dimensional unitaries preserving the same structure [2].

Boson sampling — multiphoton interference in a linear-optical network — is a prominent non-universal model of quantum computation, naturally expressed in bosonic Fock space rather than qubits. We developed a scalable quantum-circuit framework mapping boson sampling onto a universal, gate-based qubit platform: from balanced beam-splitter transformations on the single- and two-photon sectors, we derive equivalent quantum-circuit implementations unified via ancilla-assisted encoding. This generalizes to arbitrary interferometers by replacing each beam splitter with a repeating circuit unit acting within the relevant local-interference subspace, needing only N+1 qubits for a two-photon, N-mode interferometer. We built and experimentally implemented the gate-based circuit for a four-mode boson-sampling instance on our four-qubit platform [3].

Together, these results establish a deterministic, room-temperature, multi-degree-of-freedom photonic quantum-walk platform, turning a resource generally regarded as probabilistic — linear optics — into a deterministic, gate-based, scalable route to photonic quantum computing.

References:

[1] K. Sengupta, S.P. Dinesh, K.M. Shafi, S. Asokan, C.M. Chandrashekar, Physical Review Applied 24, 024012 (2025).
[2] M. Midhuna, A. Jayachandran, K. Sengupta, A.T. Krishnan, C.M. Chandrashekar, arXiv:2607.13404 (2026).
[3] A.P. Zalone, S.P. Dinesh, C.M. Chandrashekar, arXiv:2608.09509 (2026).

Characterisation of a Biphoton Source for Quantum Super-Resolution Imaging

[1, *]Priyanka Kandankel, [1, *]Shrutija Swain, [1, *]Gargi Joshi, [2, #]Tanmoy Chakraborty and [1, #]Anshuman Kumar

[1]Laboratory of Optics of Quantum Materials (LOQM), Department of Physics, Indian Institute of Technology Bombay, Mumbai 400076, India

[2]Raman Research Institute, C. V. Raman Avenue, Sadashivanagar, Bengaluru 560080, Karnataka, India

[#]anshuman.kumar@iitb.ac.in, tanmoy@rri.res.in

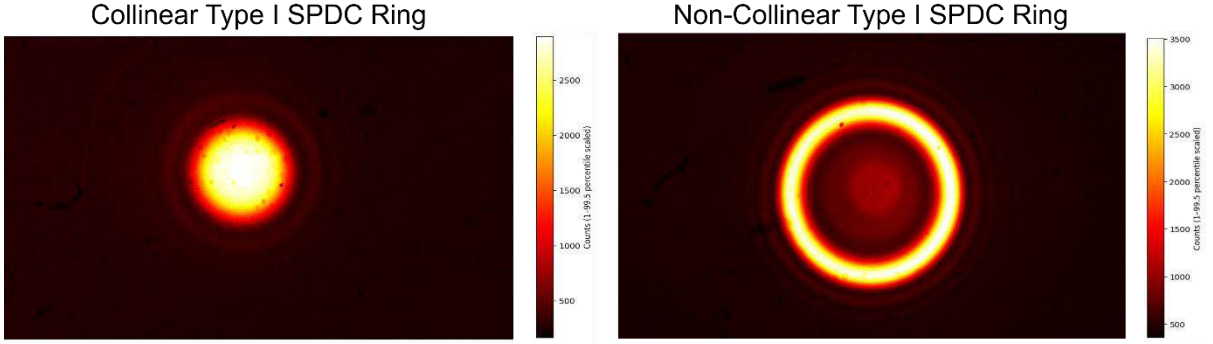
*Equal author contribution

We report the characterisation of a biphoton source generated via spontaneous parametric down-conversion (SPDC) in a Type-I beta barium borate (BBO) crystal pumped by a $405\ nm$ continuous-wave laser. Degenerate photon pairs at $810\ nm$ were detected on an sCMOS camera, revealing both collinear and non-collinear ring emission, establishing the basis for a multicentre $G^{(2)}$ quantum super-resolution imaging system.

Quantum imaging using spatially entangled biphoton pairs generated through SPDC enables resolution beyond the classical diffraction limit [1], quantified through the second-order spatial correlation function

$$G^{(2)}(\boldsymbol{\rho}_1, \boldsymbol{\rho}_2) = \langle E^{(-)}(\boldsymbol{\rho}_1) E^{(-)}(\boldsymbol{\rho}_2) E^{(+)}(\boldsymbol{\rho}_2) E^{(+)}(\boldsymbol{\rho}_1) \rangle$$

which narrows the effective point-spread function by a factor of two relative to classical imaging [2]. A multicentre $G^{(2)}$ Integration strategy using a thick nonlinear crystal, recently demonstrated by He *et al.* [3], reduces the required frame count by a factor of 20 for quantum super-resolution imaging. In this work, spatially correlated photon pairs at 810 nm were generated via SPDC in a 3-mm-thick Type-I BBO crystal pumped by a 405 nm continuous-wave diode laser. Energy conservation between the pump photon and the down-converted signal and idler photons requires $1/\lambda_s + 1/\lambda_i = 1/\lambda_p$ which, for the degenerate case $\lambda_s = \lambda_i$, gives $\lambda_s = \lambda_i = 2\lambda_p = 810nm$, matching the observed emission wavelength. The pump beam was spatially filtered using a 4f relay, producing a Gaussian beam of waist $\approx 0.8\ \mathrm{mm}$ at the crystal. Pump polarisation was set using a half-wave plate, while the phase-matching angle was tuned via the BBO crystal orientation; residual pump light was removed with spectral filters before recording the SPDC photons on an sCMOS camera. Background-subtracted images of the collinear degenerate emission and the non-collinear Type-I SPDC ring were obtained (Fig. 1). The transition from collinear to non-collinear emission with crystal orientation matches the expected phase-matching behavior of Type-I BBO, confirming successful generation of degenerate SPDC photon pairs and providing the experimental basis for a multicenter $G^{(2)}$ quantum super-resolution imaging system.



Fi g. 1. Background-subtracted SPDC images showing collinear degenerate emission (left) and the non-collinear Type-I emission ring (right)

Next, we will integrate a 4f Fourier-plane relay to collect spatially entangled photon pairs on the sCMOS camera, with imaging of a resolution target and biological samples planned to demonstrate multicenter $G^{(2)}$ integration for faster correlation acquisition in quantum super-resolution imaging [3].

Acknowledgement: The authors acknowledge the financial support from the National Quantum Mission (NQM), Department of Science and Technology (DST), Government of India.

References:

[1] M. D'Angelo, Y.H. Shih, *Laser Phys. Lett.* 2 (2005) 567.
[2] Z. He *et al.*, *Nat. Commun.* 14 (2023) 2441.
[3] Z. He *et al.*, *ACS Photonics* 12 (2025) 6530.

Quantum dual-interferometer using non-degenerate two-mode squeezed states

†Priyanka M Kannath, and #Ashok Kumar
Department of Physics, Indian Institute of Space Science and Technology,
Thiruvananthapuram, Kerala, India, 695547

†*priyankakannath@gmail.com*, #*ashokkumar@iist.ac.in*

We propose a quantum correlated dual-interferometric scheme to improve the average phase sensitivity in two Mach-Zehnder interferometers using two non-degenerate two-mode squeezed states. We establish quantum correlations among the two interferometers by swapping the modes of the two-mode squeezed states and show quantum-enhanced average phase sensitivity independent of the phase values.

Highly sensitive optical sensors, like interferometers, traditionally use lasers for various metrology and sensing tasks, but their accuracy is limited by the shot-noise limit of the lasers. This limit can be surpassed using quantum resources such as squeezed states and entanglement, thereby achieving the ultimate precision limit, called the Heisenberg limit.

In this work, we present an efficient distributed quantum sensing scheme to estimate the average phase of a dual-interferometer system with quantum-enhanced sensitivity by leveraging squeezing and entanglement. As shown in Figure 1 (a), two Mach-Zehnder interferometers (MZI) are probed by a pair of two-mode squeezed states generated via two nonlinear parametric amplifiers, PA1 and PA2,

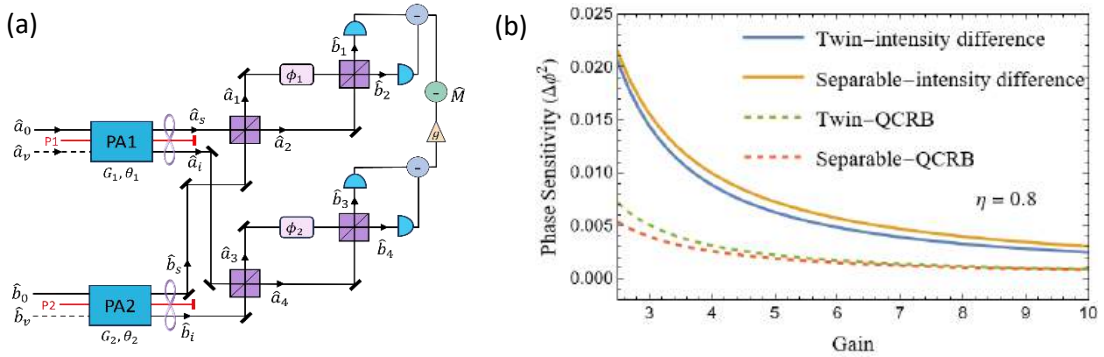


Figure 1 (a) Twin interferometer using swapped two-mode squeezed states, (b) Phase sensitivity plots of the twin interferometer and separable interferometer along with their corresponding quantum Cramér-Rao bound (QCRB), as a function of the parametric gain.

characterised with parametric gains and squeezing angles G_1, θ_1 and G_2, θ_2 respectively. Both PAs are seeded with coherent states to generate a pair of quantum-correlated bright two-mode squeezed states, called the signal and idler modes. We swap the idler mode of PA1 with the signal mode of PA2 and send the two signal modes to one MZI and the idler modes to the other MZI. This way, we establish quantum correlations among the two MZIs, making them twin interferometers and sensing the unknown phases, ϕ_1 and ϕ_2, using intensity difference measurement.

We compare the results with an equivalent dual-interferometer, sensed by two separate two-mode squeezed states whose modes are not swapped. Our results show that both the twin and separable interferometer configurations show similar quantum-enhanced average phase sensitivity; however, the sensitivity in the separable case depends on the unknown phases in the MZIs, which is not the case with our proposed twin interferometer design. Also, we calculate the quantum Cramér-Rao bound in phase sensitivity of both setups and plot along with the corresponding intensity difference detection results in Fig. 1 (b), in the presence of 20% photon loss in both MZIs. We can observe from the figure that at higher parametric gain, both setups can approach the Heisenberg limit in sensitivity.

Therefore, the twin interferometric scheme can be utilised for the quantum-enhanced estimation of the average phase of two interferometers without the need for precise control over the phases.

References:

[1] B.J. Lawrie, P.D. Lett, A.M. Marino, & R.C. Pooser, *ACS Photonics* 6, (2019) 1307-1318.
[2] Q. Zhuang, Z. Zhang, J. H. Shapiro, *Physical Review A* 97, (2018) 032329.
[3] Du, Wei, et al., *Science Advances* 11, (2025) 44.

High-dimensional quantum state measurement: foundation and applications

[1,#]Anand K. Jha
[1]Department of Physics, Indian Institute of Technology Kanpur, Kanpur, UP 208016, India
[#]*akjha@iitk.ac.in*

The high-dimensional orbital angular momentum (OAM) states have several unique advantages for photonic quantum technologies compared to two-dimensional states. In this talk, I will discuss how partial coherence properties could be utilized for efficient measurements of high-dimensional OAM quantum states, and as well as for enhanced imaging capabilities.

The high-dimensional basis of orbital angular momentum (OAM) offers significant advantages for photonic quantum technologies compared to the two-dimensional polarization basis. These include terabit-scale data transmission using OAM-mode multiplexing for long distance communication [1, 2], enhanced security and error tolerance for quantum communication protocols, efficient gate implementation, super-sensitive measurement in quantum metrology, and fundamental tests of quantum mechanics. The most-widely used process for generating high-dimensional OAM entangled two-photon state is spontaneous parametric down-conversion (SPDC)—a second-order nonlinear process in which a pump photon at higher frequency down-converts into two photons of lower frequencies, referred to as the signal and idler photons. In most applications involving SPDC photons, the OAM is assumed to be conserved, which means that the sum of the OAMs of the down-converted signal and idler photons equals the OAM of the pump photon. However, the OAM conservation in SPDC has remained an unsettled question.

However, till date, there has been no experimental demonstration of OAM non-conservation in either Type-I or Type-II SPDC. In this talk, we present our work utilizing the coherence properties of entangled two-photon field for making a novel two-photon OAM spectrum detector (see Fig. 1). Using this detector, we report first experimental observations of non-conservation of OAM in Type-I SPDC [3]. We further show that the coherence properties of fields can be utilized not only for high dimensional quantum state measurement but also for enhanced imaging capabilities.

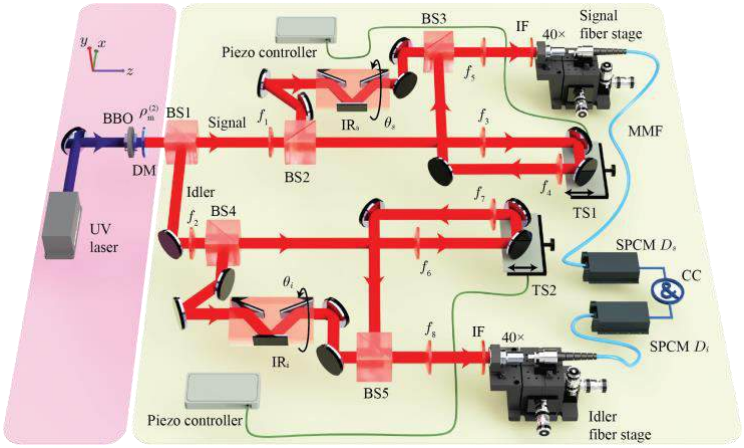


Fig. 1: Experimental setup. (a) schematic of the experimental setup for generating the two-photon state. (b) Schematic of the experimental setup for measuring the two-photon OAM spectrum.

We acknowledge financial support from the Science and Engineering Research Board through grant CRG/2022/003070, and from the Department of Science & Technology, through the National Quantum Mission (NQM) grant DST/FFT/NQM/QSM/2024/3.

References:

[1] J. Wang, J.-Y. Yang, I. M. Fazal, N. Ahmed, Y. Yan, H. Huang, Y. Ren, Y. Yue, S. Dolinar, M. Tur, and A. E. Willner, Nature Photonics 6, 488 (2012).
[2] N. Bozinovic, Y. Yue, Y. Ren, M. Tur, P. Kristensen, H. Huang, A. E. Willner, and S. Ramachandran, Science 340, 1545 (2013).

[3] Observation of OAM non-conservation in entangled photon generation; S Karan, A K Jha arXiv preprint arXiv:2604.23550.

Free-Space Quantum Communication: Effect of Turbulence

[1,#]Pooja Chandravanshi, [1]Rachita Nandan, [1]Jayanth R, [2]Pravalika P L, [3]Ayan Biswas,[1]Shashi Prabhakar and [1]RP Singh
[1]Physical Research Laboratory, Navrangpura, Ahmedabad
[2]PhD in Physics, Heriot Watt University, Edinburgh, Scotland, UK
[3]C-DOT, Chhatarpur Internal Path, Chattarpur Enclave, Mehrauli, New Delhi

[#]*pooja@prl.res.in*

We will discuss some of the experiments carried out in the direction of free-space quantum communication at PRL, Ahmedabad including our recent results on the effect of turbulence in free-space quantum communication.

To provide unconditional security to the encryption keys, and subsequently to the message, Quantum Key Distribution (QKD) comes to the rescue. QKD is one of the most ubiquitous applications of quantum mechanics in modern times [1].

Though QKD provides unconditional security, its practical implementation deviates from the ideal one, affecting the security of the encryption key. Prepare and measure protocols such as BB84 consider the satellite as a trusted device, which is fraught with danger looking at the current trend for satellite based optical communication. Therefore, entanglement-based QKD (EB QKD) protocols must be preferred since, along with overcoming the distance limitation, one can take the satellite as an untrusted device [2]. The most well-known EB QKD protocol is the E91 protocol, but the achieved key rate is less as maximum of the bits are sacrificed for measuring Bell parameter. This key rate can be increased without compromising the security provided by EB QKD, if one uses the BBM92 protocol with a pre-characterized relation between S and QBER. Thus, an estimate of QBER provides a simultaneous measurement of entanglement without sacrificing the bits used in proving the Bell's inequality violation [3].

Long distance quantum communication through optical fibers is not possible with the present technology as the loss of quantum signal due to attenuation in the fiber cannot be recovered, since quantum states cannot be cloned i.e., they cannot be amplified like classical signals. Therefore, one needs to have a network combining free-space and fiber quantum communication. Satellite-based quantum communication provides the best option for long distance quantum communication as the atmospheric losses happen only in the region covering average height of atmosphere that is just 12-15 kms. However, realizing satellite-based quantum communication has challenges in its implementation. The first and the foremost is availability of suitable optical ground stations and development of a fine pointing, acquisition, and tracking system with accuracy better than one micro-radian.

In this talk, we will discuss some of the experiments carried out in this direction at PRL including our recent results on the effect of turbulence in free-space quantum communication through an indigenously designed turbulence chamber spanning low to high turbulence.

We acknowledge the support of DOS and DST in setting up the laboratory for free-space quantum communication.

References:

[1] P. Chandravanshi, J. Ramakrishnan, T. Sharma, A. Biswas & R.P. Singh, Quantum Information Processing 24 (2025) 306.
[2] S. Mishra, A. Biswas, S. Patil, P. Chandravanshi, V. Mongia, T. Sharma, A. Rani, S. Prabhakar, S. Ramachandran and R.P. Singh, Journal of Optics 24 (2022) 074002.
[3] A. Biswas, S. Mishra, S. Patil, A. Banerji, S. Prabhakar, R.P. Singh, arXiv:2307.02149v2.

Optical control of NV center charge states for stable quantum sensing

Rahul Dhankhar,[1] Durga Bhaktavatsala Rao Dasari,[2] and Rajesh V Nair,[1*]
[1]Quantum Photonic and Sensing group, Department of Physics, Indian Institute of Technology Ropar, Rupnagar, Punjab, India
[2]3rd Institute of Physics, IQST, and Research Centre SCoPE, University of Stuttgart, Stuttgart, Germany

[*]Email: rvnair@iitrpr.ac.in

We demonstrate that controlled optical excitation stabilizes the charge environment of nitrogen-vacancy (NV) centers in nanodiamonds, reducing spectral fluctuations and improving sensing stability. A macroscopic model explains the observed behaviour, while incoherent sensing achieves $\mu T/\sqrt{Hz}$ sensitivity under strong decoherence, enabling robust quantum sensing applications.

Nitrogen-vacancy (NV) center in diamond is a leading platform for quantum sensing and quantum information technologies owing to their long spin coherence times and room-temperature optical addressability [1–3]. The negatively charged NV^- state is particularly important because its spin-dependent emission enables efficient spin initialization, manipulation, and readout [4,5]. However, the stability of the NV^- state is governed by the local defect environment, particularly substitutional nitrogen (P1) centers, which act as electron donors, mediate charge-transfer processes, and can serve as quantum memory resources through hyperfine interactions. Since these charge dynamics directly influence the sensitivity and stability of NV-based sensors, controlling the local charge environment is essential for advancing diamond quantum technologies. The optical excitation stabilizes the local charge environment, suppressing charge fluctuations and enhancing the stability of NV-based quantum sensing. Spin-state-dependent emission measurements reveal reduced spectral fluctuations across nanodiamonds with varying sizes and impurity concentrations under controlled optical excitation. To explain these observations, we develop a macroscopic theoretical model that captures the ensemble-averaged response of large NV populations without explicitly simulating microscopic charge dynamics. Guided by these results, we propose sensing protocols that remain effective in strongly fluctuating charge environments, providing new insights into the interplay between charge dynamics, spin coherence, and quantum sensing [6]. Our findings establish optical control of charge environments as a practical strategy for improving robustness of diamond-based quantum sensing.

References

[1] S. Pollok et al., “Magnetic microscopy for operando imaging of battery dynamics,” Nat. Commun. 16, 8303 (2025).

[2] J. Wang, F. Sciarrino, A. Laing, and M. G. Thompson, “Integrated photonic quantum technologies,”Nat. Photonics 14, 273–284 (2020).

[3] N. Singh, D. Sehgal, A. Venkatesan, and R. V. Nair, “Enhancing N-V-center coherent emission using the weak-coupling regime of a hybrid metal-dielectric architecture,” Phys. Rev. Appl. 22, 064069 (2024).

[4] R. Dhankhar, N. Singh, and R. V. Nair, “Probing the electronic ground state of the nitrogen-vacancy center in nanodiamonds at room temperature,” Optik 315, 172038 (2024).

[5] A. Redhu, R. Dhankhar, S. Dey, and R. V. Nair, “The strong spectral- and time-dependent emission of NV center charge state in bulk diamonds,” J. Appl. Phys. 137, 223107 (2025).

[6] R. Dhankhar, D. B. R. Dasari, and R. V. Nair, “Optical control of charge environments in nanodiamonds for enhanced quantum sensing stability,” Phys. Rev. A 113, 053725 (2026).

Experimental Realization of a Magneto-Optical Trap for Atom Interferometry-Based Quantum Sensing Applications

[1,#]Kripali Jain, [2]Ranjeet Maurya, [2]Srijan Chatterjee and [2]Bodhaditya Santra
[1]School of Interdisciplinary Research, Indian Institute of Technology, New Delhi, 110016, India
[2]Department of Physics, Indian Institute of Technology, New Delhi, 110016, India
[#]*srz238153@sire.iitd.ac.in*

We demonstrate the implementation of a Magneto-Optical Trap (MOT) that captures approximately 10^6 cesium atoms at 137.2 ± 5.4 μK using a six-beam configuration. This stable cold-atom test mass provides the foundation for sub-Doppler cooling and subsequent high-accuracy gravity measurements using a cold-atom interferometer.

Gravimetry plays a crucial role across geophysics, geodesy, and fundamental physics by providing insights into Earth's subsurface structures, tectonic activity, and general relativity. Quantum gravimeters based on atom interferometry [1,2] offer unprecedented accuracy by measuring the acceleration of free-fall test masses, in this case, cold atoms, against a local ground reference frame. This work aims to construct a high-precision atom interferometer tailored for field applications.

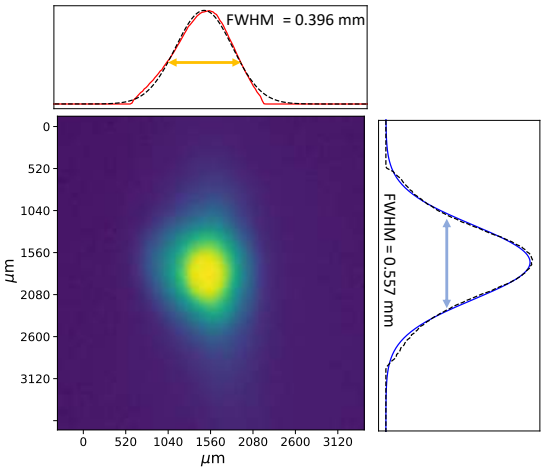


Fig. 1: The image shows the Magneto Optical Trap.

Atom interferometry is a precision measurement technique that exploits the wave nature of atoms to achieve extremely accurate measurements of physical quantities. Current commercial inertial measurement devices suffer from long-term drift and are often limited in portability and sensitivity. Cold-atom-based systems overcome these limitations by enabling high-precision measurements of gravity. Cold atoms, cooled to temperatures in the microkelvin range, exhibit wave-like behavior due to their extremely low thermal energy. This enables them to behave as coherent matter waves, similar to de Broglie waves, essential for interference effects.

The proposed measurement framework implements a Mach-Zehnder geometry for atoms in free fall. In this scheme, three phase-coherent optical pulses, separated by a pulse interval T, coherently manipulate the quantum state of an ensemble of cold atoms. The resulting output population is directly proportional to the gravitational acceleration experienced by the atoms. Here, P_i is the transition probability of an ensemble of atoms in any one of the ground states.

$$P_i = \frac{C_0}{2} cos(\Delta\theta + \Delta\phi)$$

$$\Delta\theta = (k_{eff} g - \alpha_0) T^2$$

To experimentally realize the coherent matter waves required by this framework, a cloud of approximately 10^6 ^{133}Cs atoms is consistently trapped and cooled using a stabilized six-beam laser configuration. Daily operations confirm the system's exceptional stability and repeatability, yielding a reliable atom cloud temperature of 137.2 ± 5.4 μK.

With the primary atom-trapping stage successfully established, the next steps involve implementing polarization-gradient cooling to drive the atom temperature well below the Doppler limit. Following this, the generation of Raman pulses optimized via the Rabi oscillation frequency will be used to realize absolute gravity measurements.

References:

[1] Wu, X., Pagel, Z., Malek, B.S., Nguyen, T.H., Zi, F., Scheirer, D.S. and Müller, H., Science Advances, (2019), 5(9).
[2] Ménoret, V., Vermeulen, P., Le Moigne, N., Bonvalot, S., Bouyer, P., Landragin, A. and Desruelle, B., Scientific reports, (2018), 8(1).

Photonic chips based integrated microscopy and spectroscopy

Balpreet Singh Ahluwalia
Department of Physics & Technology, UiT The Arctic University of Norway, Tromsø, Norway
Department of Physics, University of Oslo, Norway

#balpreet.singh.ahluwalia@uit.no

Abstract: *Photonic integrated circuits offer a transformative platform for compact, scalable, and multimodal bioimaging. This talk will present advances in photonic-chip-based microscopy and spectroscopy, integrating super-resolution imaging, quantitative phase imaging, and Raman spectroscopy. These technologies enable enhanced sensitivity, large-field imaging, and molecular characterization, opening new opportunities for biomedical research and diagnostics.*

In this talk, an overview of photonic chip-based multi-modal super-resolution microscopy is presented. Instead of a glass coverslips, the sample is seeded directly on top of an optical waveguide, (photonic-chip), that delivers the evanescent field illumination directly to the sample via total internal reflection (TIR). The core of chip is made of high-refractive index material ensuring excellent optical sectioning via ultra-thin (decay <50nm), ultra-large and clean TIR illumination over entire length of the chip (centimeter scale) and supports broad spectral range. The photonic-chip based microscopy not only reduces the footprint, and complexity but enables integration of different microscopy platforms such as on-chip single molecule localization optical microscopy (SMLM) [1], on-chip TIRF-structured illumination microscopy (TIRF-SIM) [2], light intensity fluctuation based optical super-resolution microscopy [3] and its compatibility with correlative light-electron microscopy [4]. The chip-based SMLM enabled super-resolved images over millimetre field-of-view scale; a 100-fold increase in imaging area as compared to conventional SMLM platforms, thus opening the opportunities of high-throughput optical nanoscopy. The compatibility of photonic-chip for different biological applications have been demonstrated on living (5) and delicate cells such as neurons (6). Similarly, the photonic-chip withstands standard preparation protocols of histopathology (7). This makes photonic-chip optical microscopy an attractive platform for application looking for scanning large areas with super-resolution and ultra-high contrast.

I will also present, recent development of harnessing dark-field alike TIR-illumination from a photonic-chip for label-free superior contrast imaging (8) and label-free super-resolution imaging (9) of nanosized extra-cellular vesciles and tissue sections. By exploiting the photoluminence of the silicon nitride waveguide platform in tandem with the autofluoroscence of tissue sections, we proposed novel incoherent label-free super-resolution optical microscopy.

Beyond microscopy, we are extending the photonic-chip concept towards integrated optical spectroscopy, particularly waveguide-enhanced Raman spectroscopy (10). Here, the same evanescent field used for imaging can interact with molecules located at the waveguide surface over millimetre- to centimetre-scale propagation distances, substantially increasing the effective light–matter interaction length.

Reference

1. R. Diekmann, O.I. Helle, C. Oie, P. McCourt, T. R. Huser, M. Schuttpelz, B. S. Ahluwalia, Nature Photonics 11, 322 (2017).
2.. Ø.I. Helle, F.T. Dullo, M. Lahrberg, J.C.Tinguley, O.G. Hellesø and B. S. Ahluwalia, Nature Photonics **14,** 431–438 (2020).
3. N. Jayakumar, Ø.I. Helle, K. Agarwal and B. S. Ahluwalia, Opt. Express, 28, 35454, 2020.
4. J. Tinguely, A. Steyer, C. Øie, Ø.Helle, F. Dullo, R.Olsen, P. McCourt, Y. Schwab, B Ahluwalia, Commun. Bio. 3, 739 (2020).
5. J.C. Tinguely, Ø. I. Helle, and B. S. Ahluwalia, Opt. Express 25, 27678-27690 (2017).
6. I. S. Opstad, F. Ströhl, M. Fantham, C. Hockings, O. Vanderpoorten, F. W. van Tartwijk, J. Q. Lin, J.C. Tinguely, F. T. Dullo, G. S. Kaminski-Schierle, B S. Ahluwalia, C F. Kaminski, "A waveguide imaging platform for live-cell TIRF imaging of neurons over large fields of view", Journal of Biophotonics, 13, 6, e201960222, 2020.
7. Villegas-Hernández, L.E., et al., Chip-based multimodal super-resolution microscopy for histological investigations of cryopreserved tissue sections. Light: Science & Applications, 2022. 11(1): p. 1-17.
8. N. Jayakumar, F.T. Dullo, V. Dubey, A. Ahmad, F. Ströhl, J. Cauzzo, E. M. Guerreiro, O. Snir, N. Skalko-Basnet, K. Agarwal, B. S . Ahluwalia, "Multi-moded high-index contrast optical waveguide for super-contrast high-resolution label-free microscopy" Nanophotonics, vol. 11, no. 15, 2022.
9. N. Jayakumar, L E. Villegas-Hernández, W. Zhao, H. Mao, F. T Dullo, J.C Tinguley, K. Sagini, A. Llorente, B. S. Ahluwalia, Light: Science & Applications 14 (1), 259, 2025,
10. D. A. Coucheron, D. N. Wadduwage, G. S. Murugan, P. T. C. So and B. S. Ahluwalia, IEEE Photonics Technology Letters, 31, 14, 1127-1130, 2019.

Artificial Intelligence in Clinical Microscopy: Applications

Jyothika V Ganesan, Partha P Pal, Renu John[#]
[1]*Medical Optics and Sensors Laboratory, Department of Biomedical Engineering,*
Indian Institute of Technology Hyderabad, Telangana, India
Email:renujohn@bme.iith.ac.in

[#] renujohn@bme.iith.ac.in

This talk will address the clinical applications of Artificial Intelligence in microscopy with few examples. Extensive work carried out on reconstruction of quantitative phase, creation of virtual staining and classification of images for digital cytology will be addressed in this paper

Artificial intelligence (AI) is rapidly transforming microscopy from a primarily image-acquisition technique into an intelligent platform for automated visualization, quantitative analysis, and clinical decision support. This transformation is particularly significant in quantitative phase microscopy techniques, where, label-free quantitative phase information provides access to cellular morphology, refractive index, dry mass, dynamic cellular changes and overall 3D volumetric information of cells without conventional staining [1]. When integrated with deep learning and computer vision, techniques like Digital Holographic Microscopy (DHM) can enable automated cell detection, segmentation, classification, phenotyping, and disease-associated morphological analysis, creating new opportunities for clinical microscopy and point-of-care diagnostics.

In this paper, we discuss the evolution of DHM platforms that are compact, portable and AI-enabled. We focus on advanced reconstruction algorithms for quantitative phase as well as automation, autofocus, and classification of images. We apply DHM mainly to three clinical scenarios: digital cytology, In vitro fertilization applications and pseudo-staining applications for cytology [2]. In digital cytology, AI-assisted quantitative phase and holographic imaging can support automated identification and classification of abnormal cells based on subtle morphological and biophysical features that conventional intensity microscopy may not readily capture. Applications are emerging in cancer cytology, blood-cell analysis, cervical and oral cytology, and virtual staining.

AI-enabled microscopy also has considerable potential in in-vitro fertilization (IVF) and embryology. Automated analysis of sperm morphology and motility, oocyte assessment, embryo segmentation, developmental-stage recognition, and prediction of embryo quality can provide quantitative information complementary to conventional embryologist assessment. We demonstrate in this talk, the combination of DHM with AI for label-free, non-invasive, longitudinal monitoring of spermatozoa, oocytes, and embryos without introducing any labels or potentially disruptive staining procedures.

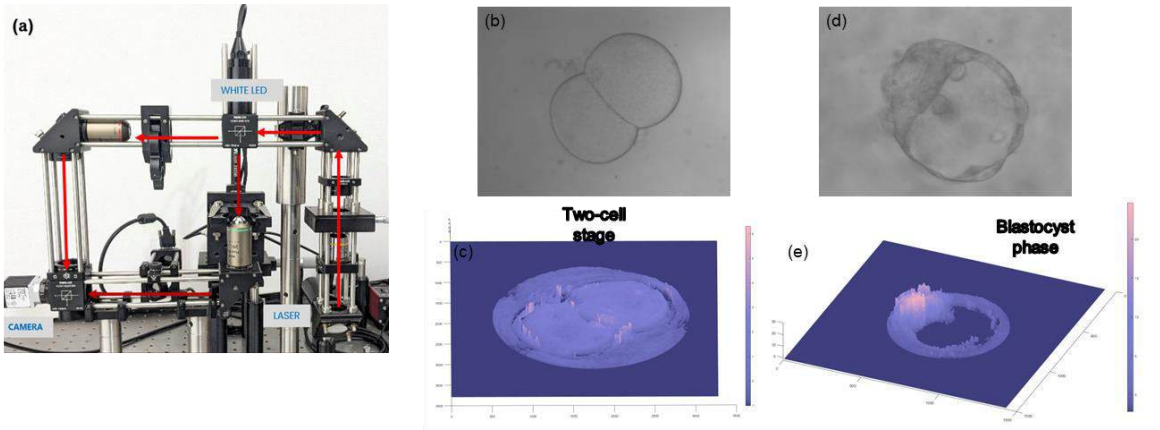


Fig. 1: A Digital holographic microscopy of Embryos in division
(a) Multimodal DHM Microscope (b) Two cell stage under a regular microscope (c) DHM reconstruction of a two-cell stage (d) A Blastocyst phase under a regular microscope (e) DHM reconstruction of blastocyst phase

References:

[1] AS Galande, V Thapa, A Vijay, R John, Journal of Biomedical Optics 29 (10), 106502
[2] JV Ganesan, PP Pal, S Karunakaran, R John, , IEEE Applied Sensing Conference (APSCON), 1-4 (2026)

Near Infrared Imaging system for Tissue Oxygenation and Perfusion Assessment for Diabetic Foot Ulcer

[1,] A.Keerthana, [2,] Arpitha Anantharaju,[1#]Uttam M Pal
[1]Department of Electronics and Communication Engineering, IIITDM, Kancheepuram
Dept. of Gynecology and Obstetrics, JIPMER, Puducherry, India 605006
[#]*uttampal@iiitdm.ac.in*

This work presents a portable Near- infrared (NIR) imaging system for non-invasive assessment of tissue oxygenation and perfusion to facilitate early detection of ischemic conditions and chronic wound complications. The system was validated using a controlled vascular occlusion on index finger and ROI based perfusion showed a perfusion ratio of 1.27, while tissue oxygen saturation (StO_2*) increased from approximately 20% during occlusion to 50% following reperfusion, demonstrating the system's sensitivity to hemodynamic changes.*

Reduced blood flow results in ischemia and tissue hypoxia, which contribute to delayed wound healing [1,2] and are commonly associated with diabetic foot complications. Conventional perfusion assessment techniques are often expensive, contact-based, or unsuitable for continuous monitoring. Near infrared (NIR) [3] imaging provides a non-invasive alternative by exploiting the differential absorption characteristics of oxygenated and deoxygenated hemoglobin. In this work, portable, non-contact NIR imaging system was developed to quantify tissue oxygen saturation (StO_2) and perfusion changes under controlled vascular occlusion conditions.

The Pilot study was performed with the proposed system (Fig 1a) employs NIR illumination at 740nm, 850nm and, 940nm, monochrome imaging sensor, and single board computer for image acquisition and processing. Oxygenated and deoxygenated hemoglobin exhibit distinct absorption characteristics. A modified Beer lamberts-based approach was employed to estimate tissue oxygenation from NIR images as shown in Eq 1. and subsequently normalized to find the percentage of StO_2. The hand was occluded and then released, and the images were captured at 740nm and 850 nm during both conditions. The resulting StO_2 heatmaps (Fig. 1b) demonstrate a reduction in tissue oxygen saturation during vascular occlusion, followed by recovery after reperfusion, increasing from approximately 20% to 50%.

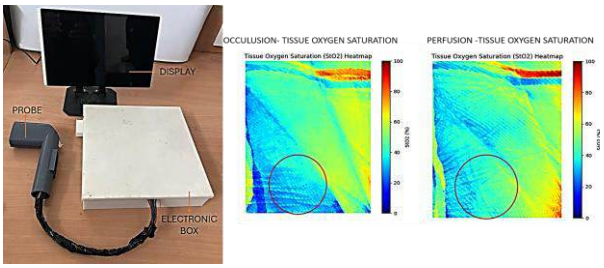


*Fig 1a; Setup of the Imaging Probe Fig. 1b: Tissue oxygen saturation (StO_2) heatmaps acquired under **normal perfusion (left)** and **vascular occlusion (right)** conditions.*

$$\mathrm{StO2} = \frac{(I_{850} - I_{740})}{(I_{850} + I_{740} + \in)} \qquad \text{-----Eq 1}$$

Vascular occlusion experiments under clinical supervision were performed by applying a rubber band constriction around the finger to temporarily restrict blood circulation. Images were acquired under normal perfusion and occluded conditions. Following acquisition, preprocessing steps including noise reduction, background correction, and image normalization were performed using 940nm. The Perfusion Index (PI) was estimated from the ROI intensity, and the perfusion ratio was calculated by comparing the occluded and normal conditions. The mean perfusion index increased from 0.713 under normal conditions to 0.910 during vascular occlusion, corresponding to a perfusion ratio of 1.27.

The developed wavelength NIR imaging platform successfully identified changes in tissues oxygenation and perfusion induced by controlled vascular occlusion. These findings establish a foundation for future clinical investigations involving diabetic foot ulcer assessment, peripheral vascular disease monitoring, and early detection of tissue ischemia.

References:

[1] *Basiri A, Nabili M, Mathews S, et al. Use of a multi-spectral camera in the characterization of skin wounds. Opt Express. 2010;18(4):3244*
[2] Lin CL, Wu MH, Ho YH, Lin FY, Lu YH, Hsueh YY, Chen CC. Multispectral Imaging-Based System for Detecting Tissue Oxygen Saturation With Wound Segmentation for Monitoring Wound Healing. IEEE J Transl Eng Health Med. 2024 May 9;12:468-479.
[3] *Neidrauer M, Zubkov L, Weingarten MS, Pourrezaei K, Papazoglou ES. Near infrared wound monitor helps clinical assessment of diabetic foot ulcers. J Diabetes Sci Technol. 2010;4(4):792-798..*

Quantitative assessment of retinal microvasculature density changes in metabolic dysfunction-associated steatotic liver disease with OCT Angiography

[1,] Abritty Kisku,[2]Naval K Vikram, [3]Shorya Azad, [1]Kishore K Deepak, [3]Pradeep Venkatesh and [1#]Pradipta Mukherjee
[1]Centre for Biomedical Engineering, IIT Delhi
[2]Department of Medicine, AIIMS, Delhi
[3]Dr. RP Centre for Ophthalmic Sciences, AIIMS, Delhi
[#] pmukherjee@cbme.iitd.ac.in

We measured the retinal optical coherence tomography angiography (OCTA) of 30 Metabolic Dysfunction Associated Steatotic Liver Disease (MASLD) Grade-3 and 30 healthy subjects. Based on the OCTAVA software [1], we analysed the microvasculature parameters from the superficial macular OCTA enfaces images. Analysis shows significant decrease in vessel length and perfusion density of MASLD subjects compared to healthy subjects.

Metabolic dysfunction associated steatotic liver disease (MASLD) is a chronic liver disorder that is affecting 38% of the world population [2]. Existing diagnostic methods are either invasive or require clinical interpretation. It has been reported that during metabolic stress, the retina undergoes microvascular changes [3] but has not been studied in MASLD patients exclusively.

We collected blood, liver elastography and retinal imaging data of 30 MASLD Grade-3 and 30 healthy subjects. The cohorts were recruited to achieve a comparable sex ratio. We recruited MASLD Grade 3 subjects by testing for a Controlled attenuation parameter (CAP) >290 dB/m using vibration-controlled transient elastography (FibroScan).

Macular OCT and OCTA in a 3x3 mm field of view centred on the fovea were measured using the SPECTRALIS SD-OCT system with a wavelength of 815nm and 5.7 µm lateral resolution, 3.9 µm/ pixel axial resolution [4]. We analysed the OCTA en face images using the open-source toolbox OCTA Vascular Analyser (OCTAVA) [1]. OCTAVA calculates perfusion density as the ratio of vessel pixels to the total image area. Vessel length is obtained by summing the lengths of connected components. Branch point density is calculated as the ratio of the number of branchpoints to the total vessel length. Retinal parameters were statistically compared using a two-tailed unpaired Student's t-test.

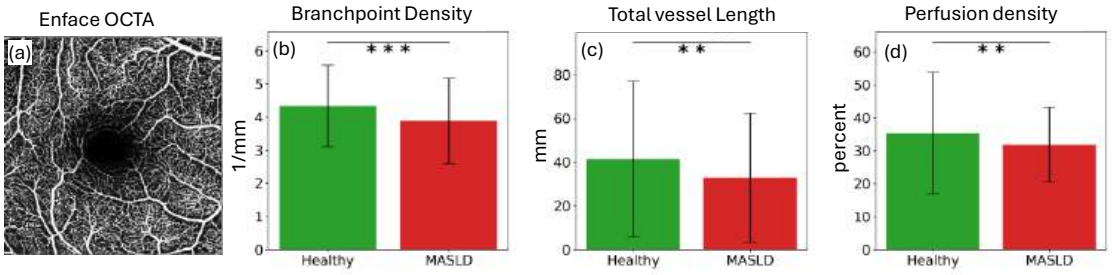


Figure 1. *(a)-Representative image of superficial macular OCTA measured in SPECTRALIS. (b-e)-Comparison of microvascular parameters based on OCTA extraction using OCTAVA;(b) Branchpoint density; (c)Total Vessel length; (d)Perfusion density. N = 30 for each cohort. All plotted values represent mean ±SD. P values derived from two tailed, unpaired t-test. ns – no significant difference; ** p<0.01; *** p<0.001.*

We see a 10% decrease in the branchpoint density ($p<0.001$) (fig 1b), 20% decrease in the total vessel length ($p<0.01$) (fig 1c) and 9% decrease in the vessel area density ($p<0.01$) (fig 1d) in MASLD condition. The results can be explained by capillary death as one reason for the observed trend. Hence, we conclude that microvasculature density can be used as a parameter for MASLD detection.

References:

[1] G. R. Untracht, R. S. Matos, N. Dikaios, M. Bapir, A. K. Durrani, T. Butsabong, P. Campagnolo, D. D. Sampson, C. Heiss, and D. M. Sampson, PLoS ONE 16, (2021)
[2] V. W.-S. Wong, M. Ekstedt, G. L.-H. Wong, and H. Hagström, Journal of Hepatology 79, 842–852 (2023).
[3] K. T. Fahnehjelm, B. Fischler, L. Martin, and A. Nemeth, Acta Ophthalmol 89, 143–150 (2011).
[4] "SPECTRALIS®," https://www.heidelbergengineering.com/en-US/products/spectralis.

Classification of Red Blood Cells using Photothermal Holography

[1,2,#]Chetna Patel, [3]Harsh Chatwani,[3]Rahul Sharma and [3]Arun Anand
[1]Applied Physics Dept., The M. S. University of Baroda, Vadodara 390001, Gujarat
[2]V. P. & R. P. T. P. Science College, Vallabh Vidyanagar, Anand 388120, India
[3]Optics Lab, Department of Physics, Sardar Patel University, Vallabh Vidyanagar, Gujarat
[#]chetnapatel290@gmail.com

Photothermal excitation was integrated with a lateral shearing digital holographic microscope (LSDHM) to investigate the photothermal response of red blood cells (RBCs). The findings show that the approach has potential for label-free biophysical characterisation of hematological diseases and can offer complementary information on the optical and thermal properties of RBCs.

Lateral shearing digital holographic microscopy (LSDHM) employs a compact, self-referencing common-path geometry with excellent temporal stability. The technique has been applied to quantitative phase imaging and characterisation of biological cells, including red blood cells (RBCs), by extracting morphological, optical, and biomechanical data [1, 2]. The great phase sensitivity and temporal stability of LSDHM make it ideal for monitoring minor photothermally generated phase fluctuations. The combination of LSDHM and Photothermal excitation effect gives additional information, resulting in better characterisation of healthy and diseased cells.

Photothermal excitation occurs when a sample absorbs laser energy, causing a localized increase in temperature via non-radiative relaxation mechanisms [3, 4]. The thermo-optic effect causes the medium's refractive index to alter as the temperature rises. As a result, the optical path length of a probe beam passing through the sample is altered, resulting in a detectable phase shift. The phase change $\Delta\phi_{PT}(x, y, t)$ is obtained from the phase maps reconstructed from the recorded holograms. Its time evolution is utilized to study the photothermal response of different locations in the sample.

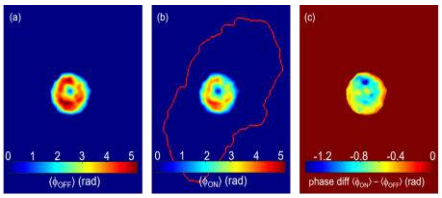


Fig. 1: Photothermal response recorded as before, during and after exposure for a healthy red blood cell

Figure 1 depicts representative phase maps obtained before and during photothermal excitation, demonstrating the photothermal phase response of RBC in thin blood smears. The phase maps represent a 2-second temporal average over the beam OFF (Fig. 1a) and beam ON (Fig. 1b) conditions, respectively, to reduce noise and increase signal-to-noise ratio. The phase difference map ($\Delta f = \langle f_{ON} \rangle - \langle f_{OFF} \rangle$) in Fig. 1c illustrates the quantifiable phase change caused by photothermal excitation. Phase differences were compared between healthy and β-thalassemia minor RBCs.

To analyze the photothermal response of healthy RBCs, both the spatial and temporal variations in phase were used. Amplitude-based, spatial and temporal features were then analyzed and compared to show differences for RBCs that are healthy and those from β-thalassemia minor samples.
The results demonstrate that photothermal phase measurements can detect changes in the biophysical properties of cells.

References:

[1] B. Javidi et. al., Optics Express, 26, (2018) 13614.
[2] C. Patel *et al.*, *Journal of Optical Society of America A,* 43, (2026) D1.
[3] H. Cabrera, B. Abbasgholi-NA, et. al., Applied Physics Letters **123**, (2023) 041101.
[4] S. Utadiya, V. Singh, et. al., Optics Express **33**, (2025) 53028.

Bio-inspired Femtosecond Laser Microstructuring of Polypropylene Surgical Meshes for Biomedical Applications

Nickita Acharya, Sivarama Krishnan[1,#]
[1]Indian Institute of Technology Madras, Chennai – 600036, Tamil Nadu

[#]srkrishnan@physics.iitm.ac.in

A scalable femtosecond laser-based, chemical-free fabrication strategy was developed to engineer bio-inspired polypropylene surgical meshes with tunable wettability (124°–82°). Laser-structured surfaces enhanced HEK 293 cell viability (96.7%), adhesion, and proliferation, demonstrating their potential for next-generation biomedical implants and scalable manufacturing.

Polypropylene (PP) surgical meshes are widely used for soft tissue repair but possess limited surface bioactivity. In this work, fs laser microstructuring was employed as a single-step, chemical-free technique to engineer functional surface topographies for biomedical applications. Bio-inspired patterns were generated from optical images of stingray skin, plant pith and human osseous tissue and translated into laser scan paths using digitally scaled templates. Laser processing was performed using an industrial fs laser integrated with galvanometric scanning, enabling rapid and scalable fabrication. By systematically varying the characteristic surface area of the patterned features, the water contact angle was tuned from approximately 124° to 82°**,** demonstrating precise wettability control through hierarchical surface structures [1, 2]. Biological evaluation using HEK 293 cells showed enhanced cytocompatibility on hydrophilic laser-structured surfaces, with a cell viability of **96.7%** after 72 h. Fluorescence microscopy and SEM revealed extensive cell spreading, strong filopodial anchorage, and improved proliferation compared with untreated polypropylene, consistent with previous reports that biomimetic surface topography and controlled wettability enhance cell attachment and tissue integration [3–5]. Preliminary antibacterial studies also indicated reduced bacterial adhesion on hydrophobic surfaces. These results demonstrate that bio-inspired femtosecond laser microstructuring provides a versatile and scalable route for tailoring the biological performance of polypropylene surgical meshes, making it a promising platform for implant manufacturing.

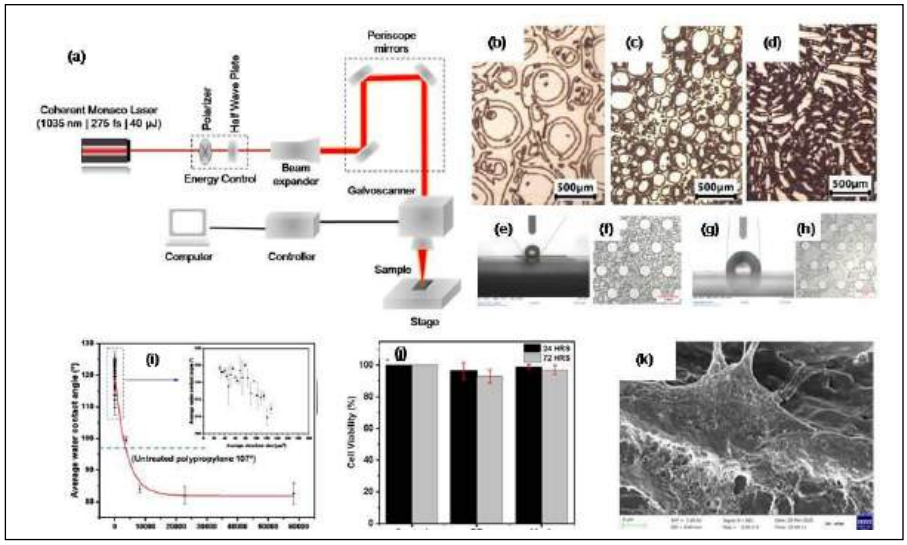


Figure 1: (a) Experimental setup showing 1035 nm laser used for surface patterning via a galvo scanner, Femtosecond laser-microstructured microscopic images on polypropylene for (a) stingray skin scales (b) plant pith cells and (c) osseous bone cells. (e) and (g) show the water contact angle and (f) and (h) display the mesh with bio-inspired structuring for hydrophobic and hydrophilic structures respectively, (i) shows the average structure size vs. average water contact angle for plant pith cells varying above and below the water contact angle for untreated polypropylene set at 107°, (j) swos the biocompatibility test results for controlled cell growth (control), plain polypropylene sheet (PP) and the laser microstructured polypropylene mesh (Mesh), for 24 and 72 hours cell cultures of normal human kidney embryonic cells (HEK 293), and (k) shows the SEM images of cell adhesion observed on hydrophilic polypropylene mesh (CA = 82°) performed with 72 hr cell culture of normal human kidney embryonic cells (HEK 293).

References:

[1] A. Y. Vorobyev and C. Guo, Laser & Photonics Reviews **7**, 385 (2013).
[2] S. A. Jalil *et al*., Applied Surface Science **506**, 144952 (2020).
[3] S. Lanzalaco *et al.*, J. Mater. Chem. B **8**, 1049 (2020).
[4] Y. Bilsel and I. Abci, Journal of Surgery **10**, 317 (2012).
[5] O. Neděla et al., Materials (Basel) **10**, 1115 (2017).

Polarization-Resolved Wide Field-of-View Digital Holographic Microscope

#Shivam Kumar Chaubey, Mohit Rathor, Rakesh Kumar Singh

Laboratory of Information Photonics and Optical Metrology, Department of Physics, Indian Institute of Technology (Banaras Hindu University), Varanasi, 221005, India

#*shivamkumarchaubey.rs.phy21@itbhu.ac.in*

We present a single-shot polarization-resolved digital holographic microscope with double field-of-view acquisition. Two distinct sample regions are folded onto a single detector by angular multiplexing, while a Sagnac interferometer provides orthogonal reference beams with spatial carriers, enabling Fourier filtering to recover amplitude and phase for both polarization states simultaneously. Validation on a USAF resolution chart confirms imaging across both fields, promising label-free biomedical and metrology applications.

Digital holographic microscopy (DHM) is a powerful quantitative imaging tool for capturing optical wavefronts' amplitude and phase information in a single measurement. Its non-invasive, label-free nature makes it suitable for dynamic biological imaging and phase-sensitive characterization. While single-shot DHM systems have individually achieved either extended field-of-view [1] or polarization-resolved imaging [2], their simultaneous integration has not yet been realized. This limits wide-area polarization imaging in applications such as live-cell analysis of birefringent biological cells and tissue. To address these challenges, we present a digital holographic microscopy (PDHM) system integrated with an extended double field-of-view (DFoV) acquisition capability. This compact and efficient optical configuration combines angular spatial multiplexing for FoV extension with a polarization-encoded reference beam generated via a Sagnac interferometric geometry. The system enables simultaneous retrieval of polarization-resolved phase and amplitude information from two distinct sample regions. The result of the proposed DFoV-PDHM is validated using a 1951 USAF resolution chart under a 40×/0.65 NA objective. From a single multiplexed hologram [Fig. 1(a)] and its Fourier spectrum [Fig. 1(b)], phase for both X and Y polarization components is reconstructed across two spatially separated FoVs. Fig. 2(c, d) reports FoV1 X and Y phase maps, and Fig. 2(e, f) reports FoV2 X and Y phase map. The close agreement between channels within each FoV and consistency across FoVs indicate negligible crosstalk and accurate polarization separation, confirming robust channel isolation and DFoV operation in a single shot.

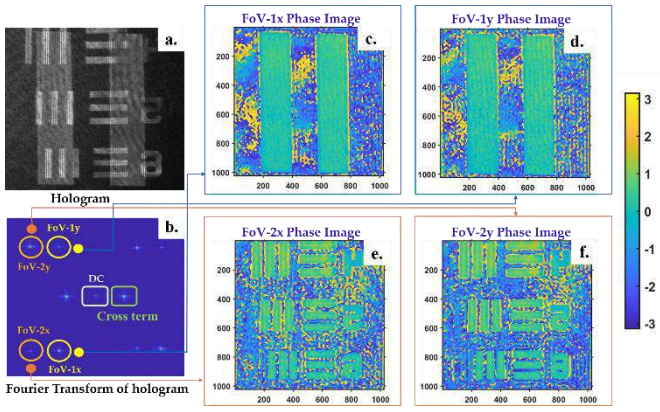


Fig. 1. USAF resolution chart experimental result

In summary, we have presented a compact and efficient single-shot digital holographic microscopy system that combines angularly multiplexed double field-of-view imaging with polarization-resolved phase reconstruction. The system enables label-free, high-resolution imaging of anisotropic samples across spatially extended regions without mechanical scanning or multiple acquisitions. This approach holds strong potential for advancing quantitative biomedical imaging, polarization metrology, and the study of complex anisotropic materials across multiple scientific and industrial domains.

Acknowledgments:
This work is supported by I-DAPT HUB (IIT-BHU), grant no. I-DAPT/IIT-BHU/2023-24/PROJECT SANCTION/46.

References:

[1] Kumar, M., et al. Opt. Laser Technol. 2024, 176, 110961.
[2] Rathor, M., et al. ACS Photonics **10**(10), 3755–3762 (2023).
[3] Takeda, M., Appl. Opt. **52**(1), 20–29 (2013).

Low-Power Sono-Neurophotonic Control of Calcium-Dependent Synaptic Plasticity in the Brain

[1]Nripesh Dixit,[2#]Sukhdev Roy
[1,2] Dayalbagh Educational Institute, Agra, 282005.
[#]sukhdevroy@dei.ac.in

A theoretical study of synergistic sono-optogenetic control of calcium-dependent synaptic plasticity using CapChR2 is presented. Combined electrical, ultrasound and optogenetic stimulation achieves robust synaptic modulation at an irradiance of 7 μW/mm², reducing the optical power requirement by 61.11% compared with a previously reported optogenetic-only approach.

Intracellular calcium (Ca^{2+}) signaling plays a fundamental role in synaptic plasticity, learning and memory in the brain. This work presents a theoretical model of synergistic sono-optogenetic control of calcium-dependent synaptic plasticity using calcium-permeable channelrhodopsin CapChR2 and mechanosensitive channel MscL-I92L, enabling efficient modulation of postsynaptic calcium dynamics at low optical irradiance [1-3]. The computational model integrates presynaptic neurotransmitter release, postsynaptic receptor activation, calcium influx through NMDA receptors and CapChR2 and ultrasound (US)-evoked activation of MscL-I92L. Postsynaptic intracellular calcium concentration ($[Ca^{2+}]_i$), leaky calcium integrator (C*), and synaptic efficacy (ρ) were used to quantify synaptic plasticity within a calcium-based modeling framework [4]. The strongest synergistic effect was observed when presynaptic electrical stimulation, postsynaptic electrical stimulation, CapChR2 activation and US stimulation were applied simultaneously. The synaptic efficacy crossed the potentiation threshold at an irradiance of only 7 μW/mm², compared with the previously reported requirement of 18 μW/mm² for optogenetic stimulation alone corresponding to a 61.11% reduction in optical power [1,2]. Calcium dynamics were described by [2]:

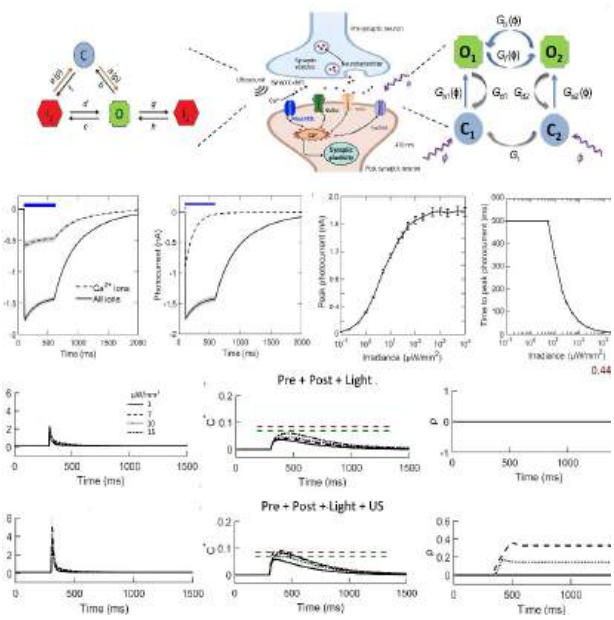


Figure 1. (a) Schematic of synaptic transmission showing neurotransmitter release from the presynaptic terminal. (b) CapChR2 photocurrents (all ions and Ca^{2+} only) at 10^3 μW/mm² for 10 ms and 500 ms light pulses, with irradiance-dependent peak photocurrent and time-to-peak photocurrent (t_{peak}). (c) Coincident presynaptic and postsynaptic electrical stimulation with optogenetic activation of the postsynaptic spine. (d) same as (c), with additional ultrasound-evoked MscL-I92L activation at 0.44 MPa.

$$\frac{d[Ca^{2+}]_i}{dt} = -\frac{([Ca^{2+}]_i - [Ca_0^{2+}]_i)}{\tau_{Ca}} - \xi(\beta_{NMDA}\, I_{NMDA} + \beta_{VDCC}\, I_{VDCC} + \beta_{CapChR2}\, I_{CapChR2})$$

where, τ_{Ca} is single exponential time constant and $[Ca_0^{2+}]_i$ is calcium resting concentration. The optimal response was obtained at an US-pressure of 0.44 MPa well within the safe range [3]. The proposed synergistic sono-optogenetic framework enables efficient low-power modulation of calcium-dependent synaptic plasticity and offers a promising approach for neuromodulation and studies of learning and memory.

References:

[1] N. Dixit, S. Roy, *Scientific Reports* 16, (2026) 16832.
[2] N. Dixit, G. Pyari, H. Bansal, S. Roy, *Scientific Reports* 15(1), (2025) 11166.
[3] S. Roy, G. Pyari, H. Bansal, *Communications Biology* 8(1), (2025) 379.
[4] M. Graupner, N. Brunel, *PLoS Computational Biology* 3 (11), (2007) e221.

One-Dimensional Photonic Crystal Sensor for Early MGUS Screening Using Tamm Plasmon Resonance

[1]Praveen Kumar, [2]Laxmi Shiveshwari, [3]Suneet Kumar Awasthi.

[1]Department of Physics, Vinoba Bhave University, Hazaribag, 825301, India.
[2]Department of Physics, Vinoba Bhave University, Hazaribag, 825301, India.
[3]Department of Physics and material Science & Engineering, Jaypee Institute of Information technology, Noida, Uttar Pradesh 201304, India.
ypk538500@gmail.com

MGUS is a premalignant plasma cell disorder characterised by the presence of M-protein in blood plasma. Variations in M-protein concentration alter the optical properties of blood plasma. we investigate theoretically a 1D-PC biosensor based on the HfO_2/BaF_2/Cavity/Ag structure. The results demonstrate the potential of the proposed biosensor for M-protein sensing.

Monoclonal Gammopathy of Undetermined Significance (MGUS), a precursor to multiple myeloma, is marked by serum M-protein < 3 g/dL. Tracking small rises in M-protein is vital for assessing progression risk, but standard electrophoresis is limited to 0.5 g/dL, missing early changes [1]. For blood plasma the refractive index (RI) varies linearly with M-protein concentration: $n_{Plasma} = n_0 + \alpha \cdot C$, Where n_{Plasma}= RI of plasma with M-protein, n_0 = 1.3338 = RI of M-protein-free plasma, α = 0.00185 RIU/(g/dL) = RI increment for immunoglobulins [2], C = M-protein concentration in g/dL, enabling optical sensing [3]. Tamm plasmon structures provide sharp resonances and strong field confinement, ideal for detecting minute RI shifts [4].

The proposed 1D-PC consists of 10 alternating layers Hafnium Oxide (HfO_2) and Barium Fluoride (BaF_2), with optimized thicknesses of 70 nm and 100 nm, respectively. A 440 nm cavity containing the sensing medium is introduced, followed by a thin Ag layer to support electromagnetic-field confinement and Tamm plasmon resonance. The optical response is calculated using the Transfer Matrix Method (TMM). The reflection coefficient is obtained from the resultant transfer matrix and the reflectance is R = |r|². The resonance wavelength (λ_{res}) is determined from the reflectance minimum. Sensor performance is evaluated in terms of sensitivity ($S = \Delta\lambda_{res}/\Delta n_{Plasma}$), Quality factor ($Q = \lambda_{res}/FWHM$), where FWHM is the full width at half-maximum of the reflectance dip, and limit of detection ($LOD = FWHM/(20 * S)$).

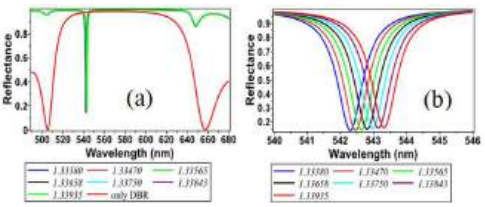


Fig.1 *Reflectance spectra of (a) 1D-PC with/without defect layer (b) An enlarged view*

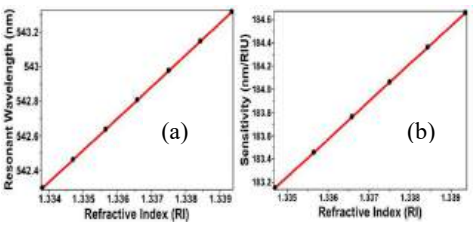


Fig. 2 (a) *Resonance Wavelength vs Plasma RI (b) Sensitivity vs Plasma RI.*

Increasing M-protein concentration increases the plasma RI, and produces a systematic red shift of the Tamm resonant wavelength as shown in fig 1(b). This behaviour results from the increased effective optical path length of the cavity, which modifies the resonance condition. The distinct separation of successive resonance dips indicates strong interaction between the confined electromagnetic field and the sensing medium. The corresponding spectral shifts and sensitivity values are presented in Fig.2 for a quantitative evaluation of the sensor performance.

The obtained sensing performance suggests that the proposed sensor has the potential to detect smaller M-protein-induced RI variations than those typically detectable by conventional electrophoretic techniques, making it a promising platform for early MGUS screening and monitoring.

References:

[1] R. A. Kyle et al., *Blood Cancer Journal* 11, 108 (2021).
[2] R. Barer and S. Joseph, *Quarterly Journal of Microscopical Science* 95, 399 (1954).
[3] H. Zhao, P. H. Brown, and P. Schuck, *Biophysical Journal* 100, 2309 (2011).
[4] M. Kaliteevski et al., *Physical Review B* 76, 165415 (2007).

Customization of the through-focus visual Strehl ratio in extended depth of focus intraocular lenses

[1,#]Pritam Kumar Pradhan, [1]Suman Sangiri, [2]Chinmaya Kumar Dehury, and [1,*]Vyas Akondi

[1]*Department of Physical Sciences, Indian Institute of Science Education and Research (IISER) Berhampur, Berhampur, Odisha 760003, India*
[2]*Department of Computer Science, Indian Institute of Science Education and Research (IISER) Berhampur, Berhampur, Odisha 760003, India*

[#]*pritam22@iiserbpr.ac.in*, [*]*vakondi@iiserbpr.ac.in*

Abstract: In this work we developed a machine learning framework for inverse designing patient-specific EDOF intraocular lens profiles directly from target VSOTF curve. Two neural architecture – 1D CNN and transformer are tested against benchmarked brute force grid search method. The transformer model predicts the best VSOTF profile for EDOF lens

Intraocular lenses (IOL) are artificial lens design to replace the crystalline lens of the eye during cataract and refractive surgery. During surgery, the cloudy crystalline lens is replaced with an IOL to restore the vision of the eye. Conventional monofocal IOL is designed to focus at a single distance (typically far). An Extended Depth of Focus (EDOF) lens [1] overcomes this limitation by enabling patients to see near, intermediate and far visions simultaneously. The depth of focus can be extended by adding selective primary, secondary and higher-order spherical aberrations. Introducing primary and secondary spherical aberrations (z_4^0, z_6^0) have been proved to significantly increased the depth of focus [2].

This study presents a framework to optimize custom EDOF lens profiles under varying aberration conditions, evaluating performance using the neural-weighted visual Strehl ratio based on the optical transfer function (VSOTF) [3]. Through-focus (TF) visual Strehl ratios were computationally evaluated across a comprehensive parameter space of radially symmetric Zernike coefficients, with range of coefficients as follows: $a_2^0(0.27\ to\ 0.72\ \mu m)$, $a_4^0 = (-0.50\ to 0.50\ \mu m)$, $a_6^0(-0.20\ to\ 0.20\ \mu m)$– sampled at 24,21,21 discrete points.

We compared a traditional brute force grid search method with a data driven approach that takes a target VSOTF curve as input and directly predicts the corresponding Zernike coefficients. We train and evaluate two neural network architectures for this mapping namely – a 1D Convolution Neural Network (1D CNN) and a Transformer – train on the same dataset. The two approaches are against predefined “target” TF profiles using two primary metrics: the root mean square (RMS) error relative to the target profile, and an EDOF benefit metric.

The transformer model performed equally good as traditional method, achieving low prediction errors and maximizing the EDOF benefit metric. The authors thank Indian Council of Medical Research (DEV/SG-2025/08_PN); Indian Institute of Science Education and Research Berhampur (AFS5L/SRLRI/VA, Seed grant).

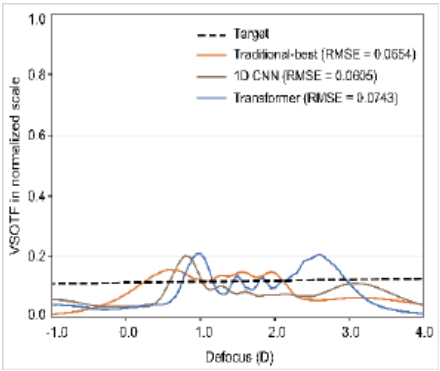


Figure 1.VSOTF profiles (a) x and y axis represent defocus and VSOTF respectively (b)The dashed black line indicates the target through-focus VSOTF profile; (c) colored lines show reconstructions obtained from the traditional grid-search-best solution, the 1D CNN, and the Transformer model. (d) RMSE values relative to the target are indicated in the legend for each method.

References:

[1] P. Kanclerz, F. Toto, A. Grzybowski, J.L. Alio, Asia Pac. J. *Ophthalmol. (Phila.)* 9 (2020) 194–202.
[2] F. Yi, D.R. Iskander, M. Collins, *Vision Research* 51 (2011) 1648–1658.
[3] D.R. Iskander, *Optometry and Vision Science* 83 (2006) 57–59.

Benchmarking Deep Learning Reconstruction Models for Sparse-View Photoacoustic Tomography on OADAT Dataset

[1]Mridul Verma, [2]Yash Thakre, [1,#]Renu John

[1]Department of Biomedical Engineering,
Indian Institute of Technology Hyderabad, Telangana, India

[1]Department of Biotechnology,
National Institute of Technology Warangal, Telangana, India

[#]renujohn@bme.iith.ac.in

Sparse-view acquisition introduces severe artifacts in photoacoustic tomography when conventional Filtered Back-Projection is used. We benchmark six deep learning reconstruction models, spanning image-domain, dual-input fusion, and model-based strategies, trained from scratch under matched conditions on the OADAT dataset, and show that measurement-domain information consistently improves reconstruction fidelity.

Photoacoustic Tomography (PAT) converts optical absorption contrast into acoustic signals through laser-induced thermoelastic expansion, combining rich optical contrast with the high spatial resolution of ultrasound detection in deep tissue. Sparse-view acquisition introduces severe reconstruction artifacts when conventional Filtered Back-Projection (FBP) is used, motivating deep-learning-based reconstruction methods capable of restoring fine structural details.

Extending the comparison framework [1], we compare six models spanning three strategies: (i) U-Net and FD-UNet operate on reconstructed images (FD-UNet via dense skip connections); (ii) Y-Net, FD-YNet, and AS-Net [2] jointly use reconstructed images and raw measurements (AS-Net via attention-based fusion); (iii) DeepMB [3] reconstructs directly from measurement data via a model-based projection framework. All six models were trained from scratch on the OADAT dataset [4], using the multisegment array sparse-sampled to 128 of 256 elements, with a 70/30 train-test split and a fixed training budget of 50 epochs per model for fair comparison.



Fig. 1: Visual comparison of Ground Truth and the six reconstruction methods, with PSNR/SSIM annotated per panel.

Table 1 summarizes the quantitative comparison. DeepMB achieves the highest PSNR by preserving measurement-domain information throughout the pipeline; AS-Net and FD-YNet achieve competitive intermediate performance via dual-input fusion, while U-Net and FD-UNet record lower PSNR. Fig. 1 supports these PSNR-based findings.

Table 1: PSNR and SSIM Comparison

Model	PSNR (dB)	SSIM
DeepMB	38.97	0.9154
AS-Net	36.86	0.8901
FD-YNet	34.90	0.8291
Y-Net	34.46	0.8131
U-Net	34.19	0.8426
FD-UNet	33.93	0.8411

Measurement-domain information thus improves PSNR substantially, consistent with raw acoustic measurements retaining phase and amplitude information lost during FBP. SSIM, however, is more mixed: U-Net outperforms FD-YNet and Y-Net despite being purely image-domain, suggesting structural similarity here is not solely set by measurement-domain access. Whether this reflects training dynamics, dataset characteristics, or a limitation of SSIM here is unclear and needs future work, including testing this pattern across OADAT's other sparse-view configurations before extending to experimental PAT data.

References

[1] Ko-Tsung Hsu, Steven Guan, and Parag V. Chitnis, *Photoacoustics*, 23, 100271 (2021).

[2] Mengjie Guo, Hengrong Lan, Changchun Yang, and Fei Gao, *IEEE Transactions on Computational Imaging*, 7, 1180–1192 (2021).

[3] Christoph Dehner, Guillaume Zahnd, Vasilis Ntziachristos, and Dominik Jüstel, *Medical Image Analysis*, 84, 102715 (2023).

[4] F. Ozdemir, B. Lafci, X. L. Deán-Ben, D. Razansky, and F. Perez-Cruz, *Transactions on Machine Learning Research (TMLR)* (2023).

Integrated Processed Fiber-Cavity: Advanced Optical Sensing and Single-Photon Guidance

Rajan Jha
Nanophotonics and Plasmonics Laboratory, Department of Physics, IIT Bhubaneswar, Khordha 752050, Odisha, India

rjha@iitbbs.ac.in

Integrated optical-fiber interferometers enable advanced sensing and imaging, including harsh-environment applications. Meanwhile, optical nanofiber cavities coupled with quantum emitters enhance light–matter interactions, enabling efficient unidirectional and bidirectional coupling of single photons.

Inline optical fiber interferometers, owing to their compact geometry, intrinsic compatibility with optical fibers, high sensitivity, and potential for integration with multifunctional photonic architectures, have emerged as an important platform for the development of advanced and next-generation optical sensing systems. Their inherent integrability and reconfigurability enable the realization of highly compact and application-specific photonic structures in which the propagation, interference, and modal characteristics of light can be precisely engineered. In particular, advances in fiber processing techniques have enabled the development of high-resolution fiber, micro/nanofiber, and specialty-fiber interferometers, as well as their hybrid combinations, with precisely controlled geometries and optical properties. High-resolution processed fiber/micro-nano fiber/specialty fibers interferometers and their combinations based on controlled excitation of fundamental/higher order core modes and cladding modes have been developed and demonstrated for potential use in surface profiling/imaging, harsh environment hydrophone industrial and beyond [1-4]. One such cavity formation steps along with cavity has been shown in the fig.1 It utilizes different types of fiber under controlled environment to form a customized cavity with different major and minor dimension. Beyond conventional sensing applications, the ability to strongly confine and manipulate optical fields within micro- and nanostructured fiber cavities has opened new opportunities in the field of light–matter interaction. In particular, optical nanofiber cavities provide strong electromagnetic-field confinement and enhanced evanescent-field interactions, making them attractive platforms for coupling guided optical modes with nanoscale emitters and quantum systems. The integration of optical nanofiber cavities with quantum emitters has therefore enabled enhanced and controllable light–matter interactions, with potential applications in quantum photonics, cavity quantum electrodynamics, quantum communication, and single-photon technologies [4,5]. The enhanced optical confinement and engineered modal properties of these cavity structures can significantly modify the interaction between the optical field and quantum emitters. Cavity-enhanced nanostructures can provide efficient coupling of emitted photons into guided optical modes, while the spatial and directional characteristics of the cavity modes can be engineered to control photon propagation. Consequently, unidirectional and/or bidirectional coupling of single photons can be realized, providing an important route toward efficient photon collection, routing, and manipulation [6]. Such capabilities are particularly relevant to the development of integrated quantum photonic systems, where efficient generation, coupling, transmission, and control of single photons are essential.

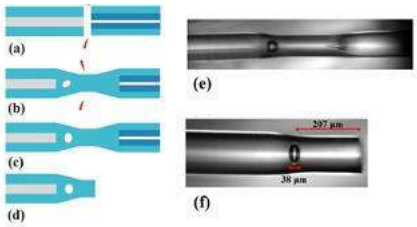


Fig. 1: Different steps involved in cavity formation and its microscopic images.

References:

[1] A. K. Maurya, K. Chatterjee, R. Jha, Optics Letters 49 (2024) 3588-3591.
[2] K. Chatterjee, S. K. Pal, R. Jha, Advanced Optical Materials 9 (2021) 2001547.
[3] S. Dass, S. Kachhap, R. Jha, IEEE Transactions on Instrumentation and Measurement 69 (2019) 4015-4020.
[4] S. Murmu, T. Srivastava, S. Sahu, R. Jha, Advanced Quantum Technologies 8 (2025) e00408.
[5] S. Sahu, K. P. Nayak, K. R. Mangipudi, R. Jha, Applied Physics Letters 124 (2024) 034002.
[6] S. Murmu, A. Kumar, R. Jha, Advanced Quantum Technologies 5 (2022) 2100160.

Demonstration of efficient Brillouin nonlinearities in silica microresonators in the 2 μm wavelength region

#Ravi Pant

Laboratory for Phoxonics and Nonlinear Optics in Nanostructures (PHONON),
School of Physics, Indian Institute of Science Education and Research (IISER)
Thiruvananthapuram, Trivandrum, 695551, Kerala, India

#rpant@iisertvm.ac.in

Abstract*:* Large loss of silica in the 2 μm wavelength region prohibits use of silica-based waveguides in nonlinear optics. Here we exploit high-Q of silica-based microspheres to overcome large loss at 2 μm to demonstrate low-threshold Brillouin lasing and frequency comb generation.

Spectral window around 2 μm is useful for the molecular fingerprinting of greenhouse gases and industrial pollutants e.g. CO_2, NH_3 [**1,2**]. The 2 μm wavelength region is also emerging as a potential candidate for free-space communications and for gravitational wave sensing. All these applications necessitate development of coherent sources in this wavelength region using material platforms compatible with existing fiber-optic network, which is based on silica-based fibers. However, silica has high loss at wavelengths ≥ 2 μm, which has restricted the use of silica-based fibers for propagation, processing, and generation of signals in and around 2 μm wavelength.

In this talk, we will present generation and processing of 2 μm signals using specialty silica fibers and silica-based microspheres. We will demonstrate Brillouin lasing and multi-Stokes generation in silica-based fibers [**3**]. Since the large loss of silica above 2 μm wavelength restricts the use of long length fiber cavities to reduce the Brillouin lasing threshold, we will show high-Q microsphere cavities for reducing the Brillouin lasing threshold and to create multi-Stokes Brillouin lasing at sub 100 mW powers [**4**]. We then use high-Q silica microsphere cavities to report the first demonstration of low-threshold tunable Brillouin pumped 2 um Kerr comb [**5**].

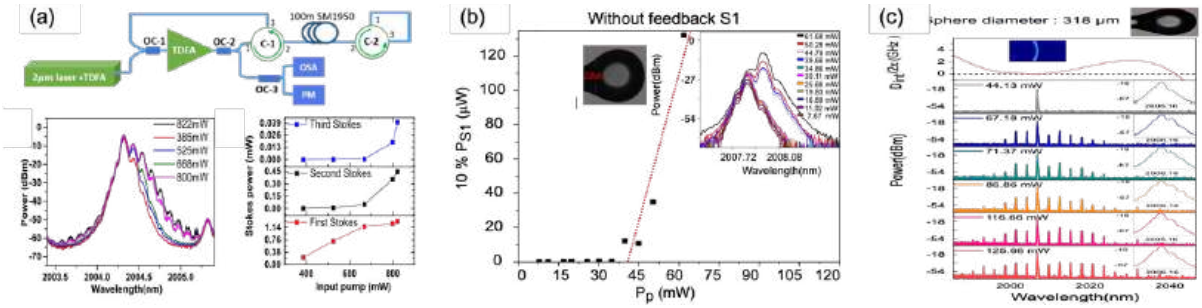


Figure 1 (a) Demonstration of multi-Stokes Brillouin lasing using SM1950 fiber-based resonator [**3**]. (b) Low-threshold Brillouin lasing in a silica microsphere [**4**]. (c) Sub-100 mW Brillouin pumped 2 μm frequency comb [**5**].

In conclusion, we have demonstrated efficient Brillouin lasing and multi-Stokes generation in fiber cavities and silica-based microspheres. Tunable low-threshold Brillouin pumped Kerr combs were demonstrated exploiting intracavity pumping in silica microspheres.

Acknowledgements: These works were carried out with funding support from the Department of Science and Technology through Grant #s: EMR/2015/000363, SB/S2/RJN-069/2014, CRG/2023/001165, and funding from the Ministry of Education through Grant #: MoE-STARS/STARS-2/2023-0415.

References:

[1] Albert Schliesser, Nathalie Picqué, and Theodor W. Hänsch, " Mid-infrared frequency combs," Nature Photonics, 6(7):440–449, (2012).

[2] Rémi Bizot *et al.*, "All-fiber supercontinuum absorption spectroscopy for mid-infrared gas sensing. APL P " APL Photonics, 9 (11), (2024).

[3] Akhileshwar Mishra and Ravi Pant, “Efficient Brillouin lasing and multi-Stokes generation at 2004 nm” OSA Continuum 2, 2826-2833 (2019).

[4] Kanad Pathak, Satyam Puri, and Ravi Pant, "Microresonator Brillouin laser and multi-Stokes generation at 2 um," Physical Review Research 6, 023062 (2024).

[5] Kanad Pathak and Ravi Pant, "Brillouin laser pumped tunable low-threshold Mid-IR Kerr Comb at 2 μm," APL Photonics Vol.9, Issue 10, (2024).

On-Chip Polarization-Independent Edge Coupler Design for O-Band Operation

[1] Sayan Chaki , [2] Binshati Chatterjee, and [2]Shailendra K. Varshney

[1] Department of Physics , National Institute of Technology Warangal, Warangal, Telangana 506004, India
[2] Department of Electronics and Communication Engineering, Indian Institute of Technology Kharagpur, Kharagpur, West Bengal 721302, India

[#]*Correspondence :* sayanchaki28@gmail.com

Abstract : *A polarization-insensitive Si_3N_4 edge coupler employing a novel slanted-corner trapezoidal inverted taper is proposed for O-band operation. Compared with conventional trapezoidal and semi-conical tapers, the design achieves below 1 dB coupling loss, low polarization-dependent loss, broadband performance, and large fabrication tolerances, making it suitable for high-performance photonic integrated circuits.*

Efficient fiber-to-chip coupling is essential for achieving low-loss, high-performance Photonic Integrated Circuits (PICs). In this work, *a polarization-insensitive Si_3N_4 edge coupler* based on a novel slanted-corner trapezoidal inverted taper is proposed for O-band (1270–1320 nm) operation. The proposed geometry combines the advantages of conventional trapezoidal and semi-conical tapers, resulting in improved coupling efficiency, reduced polarization dependence, and enhanced fabrication tolerance. The structure was designed and optimized using Ansys Lumerical FDTD, EME, and FDE solvers.

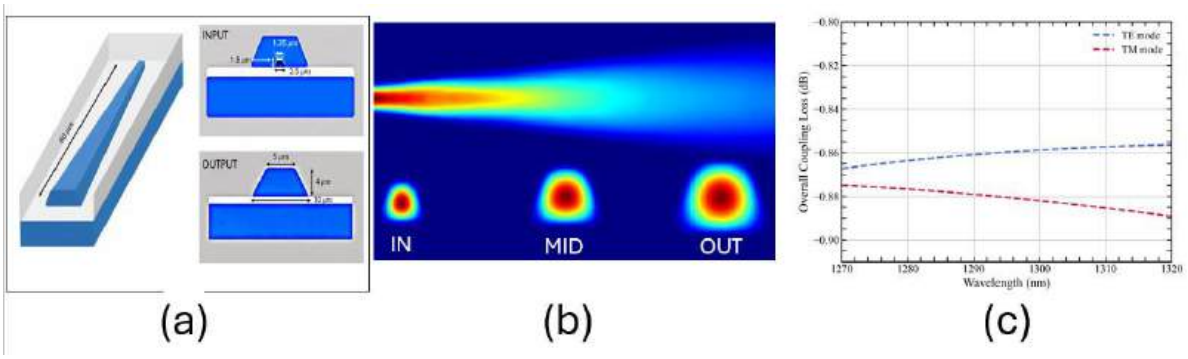


Figure 1: (a) 3D schematic model and optimized geometrical design parameters , (b) Mode propagation and Mode field profiles for TE mode and (c) Overall Coupling loss variation of the Slanted corner trapezoidal inverted taper for O-band.

The optimized edge coupler with a 60 μm taper length and 2.5 μm tip width achieves insertion losses of 0.26 dB (TE) and 0.22 dB (TM), with 94–95% transmission, and mode-overlap losses of 0.60 dB (TE) and 0.66 dB (TM), corresponding to >86% coupling efficiency. The overall coupling loss remains below 1 dB [Fig. 1(c)] for both polarizations, while the TE–TM difference is only 0.025 dB, demonstrating excellent polarization-insensitive O-band operation.

Fabrication robustness analysis shows 1 dB horizontal tolerances of ±1.7 μm (TE) and ±2.2 μm (TM), with corresponding vertical tolerances of ±1.1 μm (TE) and ±1.2 μm (TM). Under the 3 dB criterion, the horizontal tolerances increase to ±2.8 μm (TE) and ±3.2 μm (TM), while the vertical tolerances reach ±1.8 μm (TE) and ±2.0 μm (TM), demonstrating excellent alignment tolerance. These results confirm that the proposed slanted-corner inverted taper is a simple, fabrication-friendly, and highly efficient solution for polarization-insensitive O-band fiber-to-chip coupling.

References:

[1] Mengdie Sun, Ruxue Wang, Aimin Wu, Andshuowang, “Single-layer silicon nitride-based coupler with sub-dB coupling loss to a standard SMF-28 by an engineering refractive index of the upper cladding oxide”, *Optics Express*, vol.34, no. 10, pp. 18179-18189 (2026).

[2] Shengtao, Xiaoyu Li, Chengqun Gui, "3D SOI edge coupler design for high tolerance", *AIP Advances*, vol. 13, no. 2, p.025365 (2023).

[3] Nathan C. Lin , Sakib Hassan , Xuan Zhao , Ashok Veeraraghavan , Jacob T. Robinson, “Visible-range silicon nitride edge coupler with U-groove passive alignment”, in *IEEE Photonics Conference*, pp. 1-2 (2020).

[4] Nathan C. Lin , Sakib Hassan , Xuan Zhao , Ashok Veeraraghavan , Jacob T. Robinson, “Visible-range silicon nitride edge coupler with U-groove passive alignment”, in *IEEE Photonics Conference*, pp. 1-2 (2020).

[5] Yuhan Du, Yu He, Zhen Wang, Yong Zhang, Weiqiang Xie, Yikai Su, “High-Efficiency Fiber-Chip Edge Coupler Design for Visible Light on Alumina-on-Insulator Photonics”, in *Asia Communications and Photonics Conference (ACP)*, p. T4A.213 (2021).

Inverse-Designed Ultra-Compact Photonic Logic Circuit for Half-Adder Implementation on an SOI Platform

[1,3]Kondeti Shiva Narasimha, [1,2]Ritesh Kumar and [1,3,#]Vinod Parmar

[1]Optics and Photonics Instrumentation, CSIR-Central Scientific Instruments Organisation, Chandigarh, 160030, India.

[2]Centre of Excellence for Intelligent Sensors and Systems, CSIR-Central Scientific Instruments Organisation, Chandigarh, 160030, India.

[3]Academy of Scientific and Innovative Research (AcSIR), Ghaziabad, 201002, India.

[#]*email id of the corresponding author: kondeti.csio25j@acsir.res.in, vinodparmar.csio@csir.res.in*

We demonstrate an ultra-compact silicon photonic half-adder, designed using inverse methods, with a footprint of 2.8 × 2.8 μm² on a CMOS-compatible Si-on-Insulator (SOI) platform at 1550 nm. The design uses a minimum feature size (MFS) of 100 nm to ensure it can be fabricated, while still retaining the required half-adder functionality. This makes it a compact building block for large-scale photonic integrated computing.

Photonic processors are a promising alternative to traditional electronic processors because they can overcome limits in bandwidth, latency, and energy use by using the unique properties of light. Silicon photonics offers a CMOS-compatible way to create compact, high-density photonic integrated circuits for optical computing [1,2]. Photonic half-adders are important building blocks for arithmetic logic units (ALUs) and are essential for scalable all-optical computing. However, simultaneously achieving compact footprints, high transmission, and fabrication-compatible feature sizes remains a key challenge in inverse-designed photonic circuits [3].

This study introduces an ultra-compact silicon photonic half-adder that can perform both XOR (SUM) and AND (CARRY) operations at the same time. To achieve this, we used two optimization methods: density-based adjoint topology optimization (Adjoint TO) and a fabrication-aware approach [4] that combines Adjoint TO, Constrained Majority Voting Optimization (CMVO), and Direct Binary Search (DBS). This second method makes sure the device has a MFS of 100 nm, which is compatible with fabrication limits. We tested the device using 2D FDTD simulations in Ansys Lumerical, launching a TE-polarized 1550 nm source into silicon waveguides that are 0.5 μm wide. The simulations used effective refractive indices of 2.8 for Si, 1.44 for SiO_2, and 1.0 for air, along with PML boundaries and a transmission threshold of 0.4 to evaluate logic performance.

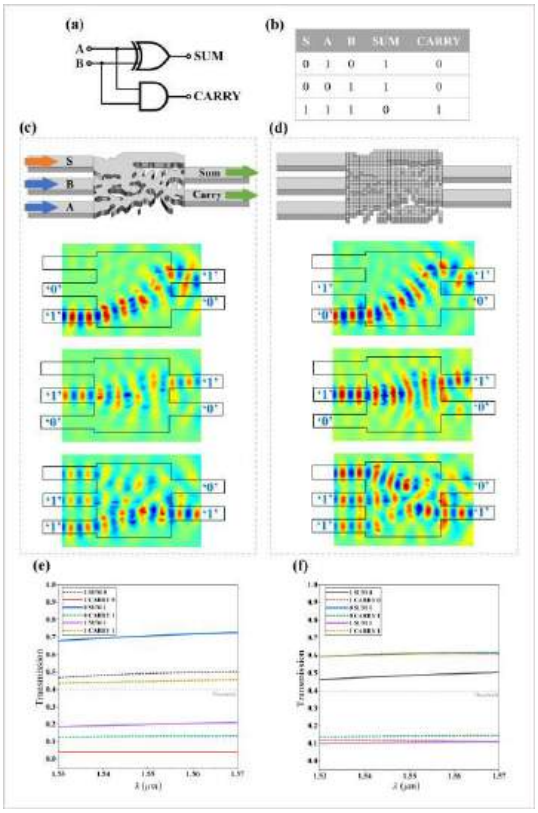


Fig. 1: Comparison of structural optimization approaches and their performance. (a) Representation of half-adder components. (b) Truth table. Optimized schematics and the corresponding E field distributions for a half adder using (c) density-based Adjoint TO and (d) the multi-stage method. Transmission spectra for (e) Adjoint TO and (f) the multi-stage method.

Fig. 1 compares the optimized structures, E-field distributions, and transmission spectrums. The fabrication-aware optimization increases the average logic contrast ratio from 6.88 dB to 7.40 dB while preserving a 100 nm minimum feature size, enabling compact photonic logic circuits for next-generation optical computing platforms.

References:

[1] D. A. B. Miller, *Nature Photonics* 4, 3–5 (2010).
[2] A.Y. Piggott, J. Lu, K.G. Lagoudakis, J. Petykiewicz, T.M. Babinec, J. Vučković, *Nature Photonics* 9 (2015) 374–377.
[3] Z. Zhang, H. Yang, M. Luo, *Journal of the Optical Society of America* B 40, 3032–3037 (2023).
[4] Z. Wang, Z. Luo, M. Lai, Z. Peng, Y. Yuan, Z. Zhang, J. Chen, *Optics Express* 33 (2025) 48381–48392.

Geometric Bloch-Sphere Interpretation of Complete Mode Conversion in a Detuned Directional Coupler

[1#]Varnam Sherawat,[1]Nisha,[1]Priya Shrivastava,[1]Sushma Kumari,[1]Chanakya Kolli,
[1]Kushagra Chikara,[1]Awanish Pandey
[1]Optics and Photonics Centre, Indian Institute of Technology Delhi, New Delhi-110016, India
[#]Corresponding author: ird601551@iitd.ac.in

Propagation constant detuning in non-identical waveguides prevents complete mode conversion in conventional directional couplers by tilting the Bloch-sphere rotation axis. We show that phase switching of the coupling coefficient restores complete transfer by creating intersecting trajectories on the Bloch-sphere, leading to a simple analytical criterion for detuned two-mode systems.

Efficient mode conversion is central to integrated photonics, but propagation-constant or frequency mismatch between coupled supermodes limits the achievable transfer efficiency [1]. Let Δ denote the detuning, κ the complex coupling coefficient, φ the phase difference between two coupling intervals, and define $\Omega = (\Delta^2 + |\kappa|^2)^{1/2}$. For constant coupling, maximum transferred power is $|\kappa|^2/(\Delta^2 + |\kappa|^2)$, so complete conversion is forbidden whenever $\Delta \neq 0$ [1]. Mapping the coupled-mode dynamics onto a Bloch sphere provides a direct geometric interpretation of this limitation [2-4]. The Bloch vector represents the normalized optical state, while the north and south poles correspond to complete excitation of supermodes A_1 and A_2, respectively as shown in Fig. 1. The rotation axis

$$\hat{n} = \frac{(Re\{\kappa\}, Im\{\kappa\}, \Delta)}{\Omega} \tag{1}$$

is tilted by detuning, confining the trajectory to a latitude that cannot reach the target pole [2-4]. Complete mode conversion is achieved by temporally switching the phase of the coupling coefficient while maintaining a constant coupling magnitude. The phase switch rotates the precession axis, with 2Ω being the precession frequency. This allows the second trajectory to intersect the first. Using spherical geometry, the geodesic angle Θ_Ω between the rotation axes must satisfy $\Theta_\Omega \geq 2\psi$, where 2ψ defines the angular aperture of a cone of inaccessibility centered at the South pole. This represents the feasibility condition for the intersection of the trajectories which can further be written as (2).

$$\cos(\Theta_\Omega) \leq \cos(2\psi) \tag{2}$$

The inequality in (2) defines the exact angular gap (2ψ) the switching event must bridge to link the two distinct trajectories. For $\Delta/\kappa = 0.5$ and $\varphi = \pi$, complete transfer occurs for $\Omega t_1 \approx 0.29\pi$ and $\Omega t_2 \approx 0.71$, demonstrating that trajectory engineering provides an intuitive framework for designing dynamically controlled detuned directional couplers.

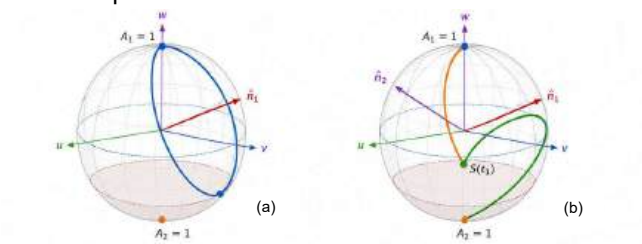


Fig. 1. Bloch-sphere representation of mode conversion in a detuned directional coupler with the orthogonal axes u, v, w denoting the Bloch-vector components. (a)Static detuning tilts the rotation axis, while (b) temporal phase switching rotates the precession axis to enable complete power transfer from state A_1 to A_2.

References:
[1] A. Yariv, IEEE J. Quantum Electron. 9, 919–933 (1973).
[2] R. Ulrich, Opt. Lett. 1, 109–111 (1977).
[3] N. Frigo, IEEE J. Quantum Electron. 22, 2131–2140 (1986).
[4] S. Korotky, IEEE J. Quantum Electron. 22, 952–958 (1986).

High-beam-quality narrowband lasers based on multimode and multicore fibers with FBG cavity

[1,#]Sergey A. Babin
[1]Institute of Automation and Electrometry SB RAS, 1 Koptyug Ave., Novosibirsk 630090, Russia

[#]*babin@iae.nsk.su*

We review recent developments on multicore and multimode fiber lasers with direct laser diode (LD) pumping and cavity based on FBG arrays inscribed by femtosecond pulses allowing for the comprehensive control of spatial and spectral output characteristics involving new physical effects (combined Raman and Kerr beam cleaning, FBG filtering, beam shaping/stirring, spectral collapse).

Multimode and multicore fibers (MMF&MCF) were initially proposed for spatial division multiplexing of future high-capacity optical communications, which may overcome the limitations of conventional singlemode fibers [1]. At the same time, such fibers are treated as potential media for high-power fiber lasers which may outperform large-mode-area (LMA) singlemode fibers [2]. MMF/MCF lasers with direct LD pumping (both Yb-doped and Raman) and implementation of special fiber components allowing for their high-power operation, all-fiber structure and comprehensive control of spatial and spectral output characteristics are reviewed below. At the same time, we have revealed and studied new physical effects as well as obtained unique performance and parameters of such lasers.

For graded-index (GRIN) MMF lasers, we have developed all-fiber laser structure involving LDs coupled through a spliced fiber combiner, femtosecond point-by-point (PbP) inscription of fiber Bragg grating (FBG) and FBG arrays with 3D control of their position in MMF. In the all-fiber LD-pumped 100-μm GRIN MMF with FBG cavity, a Raman lasing in the spectral range of 950-976 nm at the level of ~100 W which is hardly possible with conventional Yb-doped fiber lasers, has been demonstrated [3]. At that, the highly multimode pump beam (M^2~34) is efficiently converted into the high-quality (M^2<2) Stokes beam with narrow (<0.4 nm) spectrum that is defined by the combined action of Raman and Kerr cleaning effects and spatio-spectral FBG filtering. Use of thin-film mirror deposited on the central part of GRIN-fiber endface is shown also possible for beam cleaning in MMF Raman laser [4], that makes also possible tunable operation. More complex spatio-spectral filtering effects have been observed with fs-inscribed regular/random FBG arrays. Scaling capabilities of such lasers to ~1 kW have been demonstrated [5].

For MCF lasers, with fs-inscribed FBG array cavity, the effect of spectrum collapse to ~0.1 nm at >30 W has been observed for 2- and 7-core Yb-doped fibers with coupled cores, which is explained by supermode formation and hybridization at geometric mean FBG reflection wavelength [6]. Whereas in 4-core active and 7-core passive fibers spatial localization of output beam in single core has been demonstrated. Alternatively, a new effect of spatiotemporal beam stirring when the power is equally redistributed between weakly-coupled cores at the presence of Kerr nonlinearity for kW-level sub-ns narrowband pulses has been observed and explained [7].

Thus, high power, high beam quality, narrowband, wavelength-tunable, CW and pulsed operation has been demonstrated for multimode and multicore fiber lasers.

This work was supported by the Russian Science Foundation, project №21-72-30024-П

References:

[1] D.J. Richardson, J.M. Fini & L.E. Nelson, *Nature Photonics* 7 (2013) 354..
[2] A. Klenke, et al., *Progress in Quantum Electronics* 84 (2022) 100412.
[3] S.A. Babin, et al., *Scientific Reports* 11 (2021) 21994.
[4] A.G. Kuznetsov, et al., *Micromachines* 15 (2024) 940.
[5] C. Fan, et al., *Opt. Las. Techn.* 172 (2024) 110507.
[6] A.Yu. Koplesnikova et al. *High Power Las. Sci. and Eng.* (2026) https://doi.org/10.1017/hpl.2026.10157.
[7] A.Yu. Koplesnikova et al. *Opto-Electronic Advances* 9 (2026) 260036.

Photodarkening-Resistant Yb-Doped Optical Fibers through Host Glass Engineering

Anirban Dhar
[1]Fiber Optics & Photonics Division, CSIR-Central Glass & Ceramic Research Institute, 196 Raja S. C. Mullick Road, Jadavpur, Kolkata-700032, West-Bengal, India
anirband.cgcri@csir.res.in

An Yb-doped alumino-fluorophosphosilicate (AFPS) fiber with ~4000 ppm Yb^{3+} and a near 1:1 Al:P ratio was fabricated using the Vapor Phase Chelate Delivery (VPCD) technique. Tailoring the host glass composition improved photodarkening (PD) resistance by 5.4-fold and 3.5-fold compared with aluminosilicate (AS) and aluminophosphosilicate (APS) fibers, respectively.

Yb^{3+}-doped fiber lasers (YDFLs) have attracted significant attention for applications in medical treatment, precision material processing, defense, and scientific research owing to their excellent beam quality, high efficiency, low thermal load, and compact design. Further power scaling in YDFL is limited by photodarkening (PD)—a light-induced increase in near-infrared core loss under high-power operation. PD progressively degrades laser efficiency, output stability, and device lifetime, making its mitigation a critical challenge for the next generation of high-power YDFLs. The microscopic origin of PD remains obscure, with proposed mechanisms including possible formation of color-center, two-photon absorption, presence of trace Tm impurities, and Yb–Yb pair-induced defect-mediated charge transfer. Beyond this ongoing debate, it is widely accepted that minimizing defect precursors and rare-earth clustering within the host glass is key to suppressing PD and as a result various mitigation strategies, such as hydrogen/oxygen loading, tuning host glass composition or co-doping of some specific ions, waveguide engineering, and thermal or photobleaching, have been investigated. However, among all possible techniques, tailoring the core glass composition offers the most practical and scalable approach that can helps to enhance rare-earth solubility, reduce ion cluster, stabilize the glass network, and overall helps to achieve reduce color-center formation.

In this work, the host glass composition was engineered by optimizing the different fabrication parameters of the Vapor Phase Chelate Delivery (VPCD) technique to fabricate an alumino-fluorophosphosilicate (AFPS) glass with Yb^{3+} concentrations up to 4000 ppm while minimizing the unwanted central refractive-index dip in a reproducible manner. Different material and optical characterization of developed fibers revealed that the core numerical aperture (NA) is strongly governed by the Al_2O_3:P_2O_5 ratio in ultimate preform/fiber, reaching a minimum near 1:1 due to extensive formation of $AlPO_4$ unit that stabilizes the glass network. PD measurements demonstrated (Fig 1) that the optimized AFPS fiber exhibits ~5.4-fold and ~3.5-fold lower PD-induced loss than conventional aluminosilicate (Al–Si–Yb) and P_2O_5-rich aluminophosphosilicate fibers, respectively. These results highlight the synergistic effect of $AlPO_4$ network formation and fluorine incorporation in enhancing Yb^{3+} solubility, suppressing defect generation, and improving glass-network stability. The proposed AFPS composition therefore provides a robust host platform for developing highly photostable, high-power Yb-doped fiber lasers.

Thus tuning of host glass composition is found to be an effective method to improve PD resistivity as it has been evident in the present investigation. The authors express their sincere gratitude to the Director, CSIR–CGCRI, for his encouragement and support from colleagues of the entire Fiber Optics & Photonics Division.

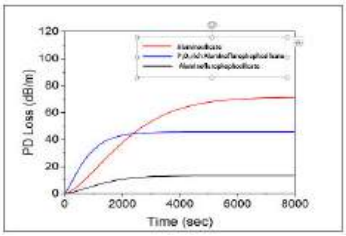


Fig 1: Comparison of PD of different host glass

References:

[1] *D.J. Richardson, J. Nilsson, W.A. Clarkson, J. Opt. Soc. Am. B 27, (2010) B63.*
[2] *M. Engholm, L. Norin, D. Åberg, Opt. Lett. 32, (2007) 3352.*
[3] *N. Choudhury, R. Sen, A. Dhar, J. Am. Ceram. Soc. 109, (2026), 70947.*

Experimental Demonstration of Fading Mitigation Using Spatial Diversity in Multi-Core Fiber

[1]Elisa Prathibha Mathew and [1,#]Balaji Srinivasan
[1]Department of Electrical Engineering, Indian Institute of Technology, Madras, India
[#]*balajis@ee.iitm.ac.in*

We experimentally demonstrate intensity fading mitigation in distributed acoustic sensing (DAS) using the spatial diversity of a 10 km multi-core fiber. Complex backscattered signals from independent cores are coherently combined using a Rotated Vector Sum (RVS) algorithm, improving backscattered intensity at fading locations, enhancing phase stability, and enabling more reliable detection.

The ability to continuously monitor acoustic and vibrational disturbances over long distances has made Distributed Acoustic Sensing (DAS) a promising technology for applications such as structural health monitoring, pipeline surveillance, and perimeter security. DAS operates by analyzing Rayleigh backscattered light in standard telecommunication fibers to provide distributed measurements with high spatial resolution. However, its performance is significantly affected by intensity fading, a phenomenon in which the backscattered signal intensity falls below the detection threshold due to the random destructive interference of Rayleigh backscatter. These fading regions result in reduced signal-to-noise ratio, inaccurate phase estimation, and, in severe cases, complete loss of sensing information, thereby limiting the overall sensitivity and reliability of DAS systems.

Multi-core fibers (MCFs) provide an effective approach to mitigating intensity fading by incorporating multiple independent sensing cores within a single fiber cladding [1]. Since each core possesses a unique Rayleigh scattering profile, fading occurs at different spatial locations across the cores. This spatial diversity enables the selection or combination of signals from multiple cores, thereby reducing the impact of fading and improving the overall reliability and sensitivity of DAS systems.

By applying the Rotated Vector Sum (RVS) algorithm [2] to the complex backscattered signals from two cores, the backscattered intensity at fading locations is increased above the detection threshold, thereby enabling reliable extraction of the corresponding phase information.

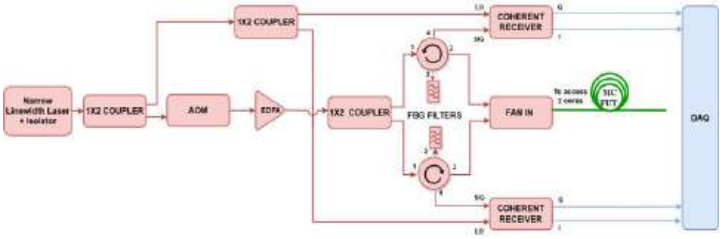


Fig. 1: Schematic of the experimental setup

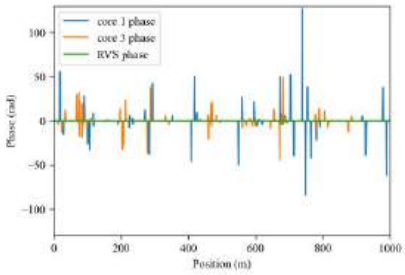


Fig. 2: Experimental results showing spatial diversity of fading points in core 1 and core 3 of a multicore fiber (MCF), and the corresponding phase improvement after applying the Rotated Vector Sum (RVS) method.

In this work, we experimentally demonstrate fading mitigation in DAS using the spatial diversity provided by a 10 km MCF (Fig.1). Owing to the independent Rayleigh scattering characteristics of each core, fading occurs at different spatial locations across the MCF. To coherently combine the signals, the RVS method is used, where the phase of each core is aligned with respect to its first slow-time sample using

$$\widetilde{i_k} = i_k \frac{i_k^*(0)}{|i_k(0)|}, \qquad k = 1, 2$$

where i_k^* denotes the complex conjugate. The aligned signals are then summed, which increases the backscattered intensity at locations affected by fading, allowing reliable phase recovery (Fig.2). By exploiting the complementary fading characteristics of the two cores, the proposed spatial diversity approach improves phase stability, mitigates intensity fading, and enhances the robustness of DAS for practical sensing applications.

References:

[1] Y. Liu, H. Liu, Y. Xiao, X. Shen, J. Li, H. Dang, *et al*., *IEEE 8th Optoelectronics Global Conference (OGC 2023)* (2023)
[2] K. Cui, F. Liu, K. Wang, X. Liu, J. Yuan, B. Yan, *et al*., *IEEE Photonics Journal* 13 (6) (2021) 1–6.

Bandwidth Evolution under Co- and Counter-Propagating Brillouin Gain and Loss

[1, #]Sharashti Saxena, Harsh Vaid and Amol Choudhary
Ultrafast Optical Communication and High-performance Integrated Photonics (UFO-CHIP), Indian Institute of Technology (IIT), Delhi, New Delhi-110016, India

[#]eez228479@iitd.ac.in

We present a comprehensive experimental study of SBS gain-loss interactions in single-pass configurations, demonstrating that SBS loss is a key parameter governing Brillouin bandwidth engineering for microwave engineering.

Stimulated Brillouin Scattering (SBS) provides a gain/loss response that can be exploited for bandwidth engineering in microwave filtering [1]. Previous studies have shown the effect of SBS gain alone on the evolution of Brillouin bandwidth; however, the influence of SBS-loss propagation on bandwidth evolution remains largely unexplored [2]. In this work, we experimentally investigate the evolution of the Brillouin bandwidth under the combined action of SBS gain and co-/counter-propagating SBS loss in a single-pass configuration.

Figure 1 shows the setup used to investigate SBS gain interacting with co- and counter-propagating SBS loss. An external cavity laser at f_{p1} is equally split into upper (gain) and lower (loss) arms. The gain arm launches light into a 10-km SMF, generating backward Stokes waves that provide SBS gain. SBS loss at the same frequency is produced by red-shifting the loss-arm carrier by 21 GHz, isolating the sideband, and launching it into the same SMF.

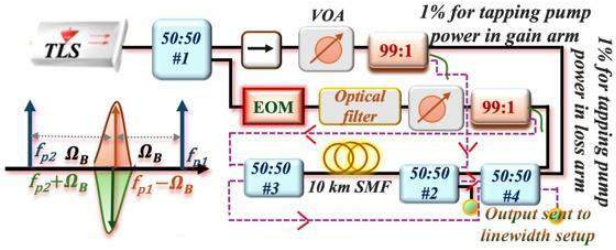


Fig 1 The experimental setup for the investigation of the interaction between SBS gain and co/ counter-propagating SBS loss

In the co-propagating (solid lines) and counter-propagating (dotted lines) configurations, signals travel in the same and opposite directions and are detected at couplers 50:50 #2 and #4, respectively. Brillouin spectra at each detection port are characterized via self-heterodyne linewidth measurements [3].

Figures 2(a) and 2(b) present the Brillouin bandwidth evolution under co- and counter-propagating SBS gain-loss interaction. In the co-propagating scheme, the detection-port output power decreases significantly with increasing loss-arm pump power (PP), limiting bandwidth characterisation at high loss and low gain PP. This restriction is absent in the counter-propagating scheme due to opposing propagation directions. In both configurations, increasing gain-arm PP at fixed loss narrows the Brillouin bandwidth, consistent with standard SBS behaviour [2]. However, at higher loss, the arm PP bandwidth saturates, as shown in Fig 2(b). Notably, in the co-propagating scheme, gain-arm PP is limited to 16–20 dBm due to another coupler (50:50 #4) insertion loss. The insets of Figs. 2(a) and (b) compare RF spectra at 3.5 and 15.5 dBm loss-arm power. We experimentally investigate the evolution of the Brillouin bandwidth under co- and counter-propagating SBS gain-loss in a single-pass configuration. Both configurations reveal bandwidth narrowing at low SBS loss and saturation at high loss, establishing SBS loss as a key bandwidth-engineering parameter. Future work will focus on bandwidth investigation in a ring-cavity configuration.

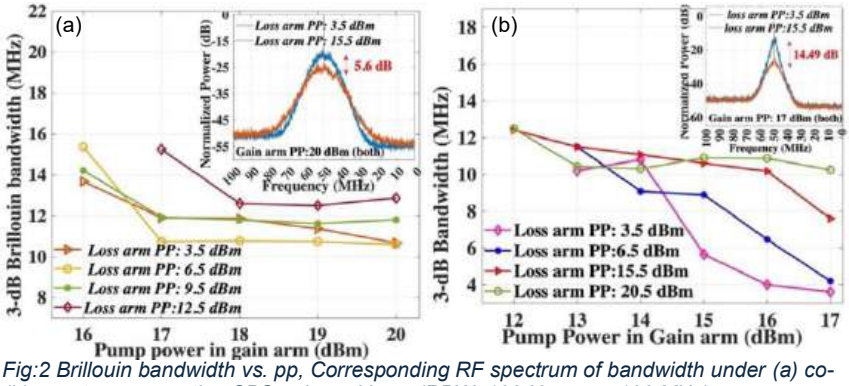


Fig:2 Brillouin bandwidth vs. pp, Corresponding RF spectrum of bandwidth under (a) co- (b) counter propagating SBS gain and loss. (RBW: 100 Hz, span:100 MHz)

Acknowledgement: Department of Telecommunication (DoT), India, through the Advanced Optical Communication Testbed Project.

References:

[1] S. Preußler, A.Wiatrek, K. Jamshidi and T.Schneider, *Optics Express* 19 (9), 8565-8570, (2011).
[2] Y. Eniay, Aydin, J.M. Delavaux, and J. Toulouse, *Journal of Lightwave Technology*, 20.8, 1425 (2002).
[3] I.V. Kabakova, R. Pant, S. Debbarma, B. L.-Davies, S. J. Madden, and B. J. Eggleton, *Optics Letters*, 38.17, (2013).

Computational Imaging with Randomness

[1,#]Ryoichi Horisaki
[1]Graduate School of Information Science and Technology, The University of Tokyo, 7-3-1 Hongo, Bunkyo-ku, Tokyo 113-8656, Japan
[#]*horisaki@g.ecc.u-tokyo.ac.jp*

Computational imaging integrates optics and information science to design advanced imaging systems. Recent progress in information science, including compressive sensing and deep learning, has significantly accelerated this field. In this talk, I will present our recent studies on computational imaging using random optical modulations, such as those induced by scattering media.

Computational imaging encodes object information optically and decodes it computationally [1]. Randomness can arise from scattering media, be introduced through designed modulation, or provide a statistical description of incoherent illumination. These connections between optics and information science support efficient sensing and computational wavefront control. Here, we discuss quantitative phase imaging and computer-generated holography (CGH) within this framework.

Quantitative phase imaging visualizes transparent specimens without fluorescent staining. Zernike phase-contrast microscopy is laser-free and reference-free, requiring no separate reference arm. We recover quantitative phase from a single image acquired with an off-the-shelf Zernike phase-contrast microscope by inverting a physical model of image formation, without modifying the optical hardware [2]. Partially coherent illumination is represented by random wavefronts, connecting the reconstruction to stochastic optimization. Experiments on polymer microbeads and biological cells validate the approach. A physics-informed learning extension jointly estimates phase and unknown optical parameters from measured Zernike images, without separately acquired phase data for training [3].

For optical phased arrays, unknown antenna phase biases can distort the illumination used in computational ghost imaging. We use random phase modulation and jointly estimate the object and these biases from multiple single-pixel measurements [4]. Numerical simulations demonstrate image recovery and an extension to complex-amplitude objects without reference light, using an iris in front of the detector.

In CGH, randomness also makes incoherent light propagation computationally tractable. Compressive propagation represents spatially partially coherent or incoherent light using coherent random wavefronts and combines this representation with stochastic gradient descent [5]. We apply this framework to hologram synthesis under spatiotemporally incoherent illumination [6]. Using a white light-emitting diode and a cascade of amplitude and phase holograms, we demonstrated color image reproduction [6]. This approach was extended to an ordinary display: a smartphone display and a spatial light modulator form a two-layer cascade that enables three-dimensional color reproduction using the display's incoherent illumination [7].

We further address the sampling requirements of CGH with a continuous implicit neural representation of a hologram [8]. A neural network with multi-resolution hash encoding represents the hologram phase as a function of spatial coordinates. Training across randomly selected pixel pitches allows the same representation to be sampled at the spatial light modulator's pixel pitch. Numerical and optical demonstrations validate this flexible approach to hologram synthesis.

Related studies exploit speckle correlations for imaging through scattering media [1]. Together, these examples show how optical randomness and computational models can be combined for sensing and light control.

References:

[1] R. Horisaki, *Optical Review* 31 (2024) 282–289.
[2] R. Kurata, K. Toda, G. Ishigane, M. Naruse, R. Horisaki, T. Ideguchi, *Optics Express* 32 (2024) 2202–2211.
[3] R. Kurata, K. Toda, T. Ideguchi, R. Horisaki, *Optics Letters* (2026), early posting, doi:10.1364/OL.611085.
[4] S. Hirata, N. Matsuda, K. Komatsu, T. Tanemura, R. Horisaki, *Optics Express* 33 (2025) 21132–21141.
[5] R. Horisaki, T. Aoki, Y. Nishizaki, A. Röhm, N. Chauvet, J. Tanida, M. Naruse, *Optics Letters* 47 (2022) 613–616.
[6] R. Suda, M. Naruse, R. Horisaki, *Optics Letters* 47 (2022) 3844–3847.
[7] O. Shigematsu, M. Naruse, R. Horisaki, *Optics Letters* 49 (2024) 1876–1879.
[8] O. Shigematsu, R. Horisaki, *Photonics Research* 14 (2026) 3338–3352.

Single pixel microscopy: Creating images without a sensor grid

[#]Rakesh Kumar Singh
Laboratory of Information Photonics and Optical Metrology, Department of Physics, Indian Institute of Technology (Banaras Hindu University), Varanasi, 221005, Uttar Pradesh, India

[#]krakeshsingh.phy@iitbhu.ac.in

We discuss recent progress in single-pixel imaging (SPI) and one of our recent works on single-pixel microscopy. This is implemented by shifting the sampling from the camera to the source plane and imaging the target using a single-pixel detector (SPD) and the intensity correlation.

The SPI is a novel imaging technique that uses a single-pixel rather than a sensor-grid camera. In SPI, an object is illuminated with structured patterns, and intensities corresponding to each pattern are recorded by an SPD. After correlating the patterns with intensities, the object is reconstructed [1].

In this work, we discuss recent developments in the SPIE and one of our recent works on single-pixel microscopy (SPM) and 3D imaging with an incoherent source. This SPM is achieved by recording the objects' holograms in terms of the complex coherence function [2]. Three-phase-shifted Fourier-basis-structured patterns with different spatial frequencies are used to encode the incoherent source, and the temporally averaged intensities are measured with the SPD. The temporally averaged intensities are employed to reconstruct the complex coherence function via a phase-shifting relation. The complex coherence function enables the reconstruction of microscopic images.

Fig. 1(a) presents the experimental configuration of our SPM. Here, the structured detection strategy is adopted. The incoherent light beam is transmitted through a USAF resolution test chart (Thorlabs R1DS1N) placed on a 3D translation stage. The object beam is relayed to the spatial light modulator (SLM) plane through the BS by a 4f imaging system comprising a 20X microscope objective and lens L_1. The resolution chart is imaged to the SLM plane. The SLM displays the structured patterns to modulate the object. The modulated beam is Fourier transformed by lens L2, and an SPD placed at the back focal plane collects the light. The complex coherence function is retrieved by time-averaged intensities recorded by SPD. The complex coherence is digitally inverse Fourier transformed to reconstruct the incoherent test object in the Fourier plane. Fig. 1(b) and (c) show the reconstruction of group 6 of the resolution chart using our proposed SPM.

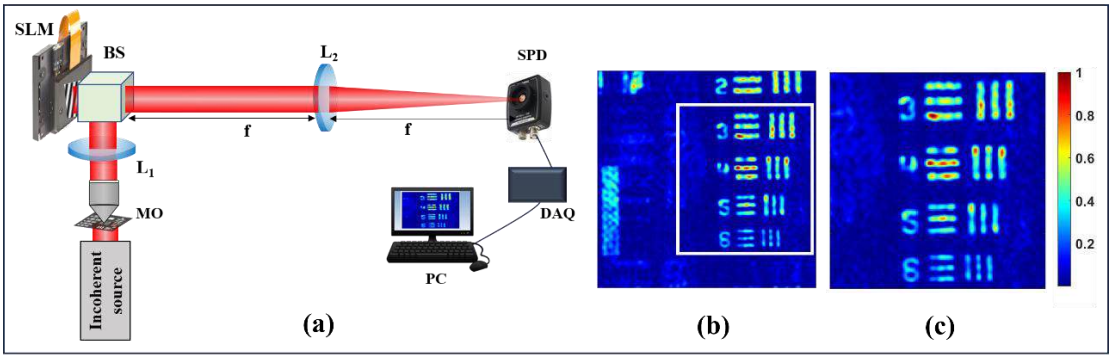


Fig. 1: (a) Experimental configuration of SPM. Experimental results: (b) & (c) reconstruction of group 6 of the resolution chart

In conclusion, we highlight a new class of microscopic techniques with the SPD. The use of SPD enables the system to be extended to a wide range of applications, including imaging in non-visible spectral regions, imaging through scattering media, and imaging under low-light conditions.

Acknowledgement: Support is acknowledged from ANRF/ARG/2025/000135/PS.

References:

[1] G. M. Gibson, S. D. Johnson, M. Padgett, *Optics Express* **28** (2020) 28190-28208.

[2] T. Karmakar, Satish, Sarita, Z. Zalevsky, R. K. Singh, *J. Phys. Photonics* **8** (2026) 025039.

3D Phase Imaging using Single-View Structured Illumination

[1,#]Nishant Goyal and [1,2]Kedar Khare
[1]Department of Physics, Indian Institute of Technology Delhi, New Delhi 110016 India
[2]Optics and Photonics Centre, Indian Institute of Technology Delhi, New Delhi 110016 India
[#]phz218060@iitd.ac.in

This work shows that on-axis phase structured illumination(s) with sparsity-driven reconstruction enables cross-talk–free 3D label-free refractive index/phase imaging of transparent samples, presenting the core idea and a complete practical guideline for building such a simpler and leaner coherent tomography system without conventional multi-angle illumination(s).

Holographic tomography (HT) aims to provide a 3D refractive index (RI) distribution of transparent objects, such as biological cells. While the phase map generated by a traditional digital holographic microscopy (DHM) system is a 2D function representing the phase accumulated by a plane wave transmitted through a 3D sample, HT systems can potentially provide more detailed information about the internal structure of transparent or unstained 3D objects. Following Wolf's early treatment [1], HT systems have largely employed a system approach, where several digital holograms of the 3D object are recorded by varying the direction of illumination.

In this work, we examine whether multiple angled illuminations can be replaced by axial structured illumination(s) to achieve high-quality tomographic reconstructions with minimal slice-to-slice cross-talk. We propose Axial Structured Illumination Tomography (ASIT), where axial illumination(s) with phase structuring can be practically implemented in a manner that avoids the hardware and calibration complexity associated with various illumination angles. The central idea is that the structured field evolves during propagation, so that different axial slices interact with different wavefronts. This provides useful depth-dependent diversity, which helps in separating the information from different object slices during reconstruction. The required decorrelation between different slices is related to the effective spatial bandwidth of the illuminating field. For this purpose, the bandwidth ratio, BWR, is used as a practical design parameter to decide whether a given illumination structure is suitable for a chosen inter-slice distance. For experimental validation, we used two lithographically fabricated phase objects containing simple phase patterns placed at different axial planes. The wavelength of the laser is 532 nm, and NA is 0.01. First, plane-wave illumination was used to study the effect of axial separation on the reconstruction. When the axial separation is sufficiently large, the reconstructed phases show only a very faint and minimal amount of cross-talk between the slices (column1). However, when the separation is reduced, substantial cross-talk appears in the reconstructed phase maps. This happens because there is insufficient decorrelation between the propagating fields at the individual slices, and TV sparsity alone fails to remove the cross-talk information (column2).



Fig. 1. Experimental slice-by-slice phase reconstruction for two phase objects (a) and (b), respectively.

A randomly structured illumination of suitably chosen BWR is then employed. Since this illumination evolves more strongly during propagation, it reduces the required decorrelation distance and improves the separation of information from different slices. The reconstructed phase maps obtained with structured illumination show cross-talk-free phase recovery again (column3) as compared to the plane-wave case. In conclusion, ASIT provides a practical label-free tomographic imaging methodology in which regular DHM systems can be converted into RI tomography devices by adding simple elements such as a diffuser mask or an SLM before the sample stage.

References:

[1] E. Wolf, Optics Communications 1, 153–156 (1969).
[2] N. Goyal and K. Khare, Journal of Physics: Photonics 7, 035012 (2025).

Learning Phase Diversity for Robust Computational Imaging

[1,#]Jasleen Birdi, and [1]Kedar Khare
[1]Optics and Photonics Centre, Indian Institute of Technology Delhi, Hauz Khas, New Delhi 110016 India
[#]*ird601366@iitd.ac.in*

We present a physics-informed deep learning data augmentation framework that introduces measurement diversity to improve inverse problem robustness. By generating reliable pseudo-data from a standard single measurement, the proposed method achieves higher-quality reconstructions while reducing hardware complexity and measurement requirements.

Computational imaging recovers object information from optical measurements by jointly designing acquisition and reconstruction strategies for solving inverse problems. These problems are inherently ill-posed, making them susceptible to reconstruction artifacts. Examples include image deblurring in incoherent imaging and Fourier phase retrieval (FPR) in coherent imaging. While optimization- and deep learning-based approaches improve reconstruction quality, they do not fundamentally address the ill-posedness. Measurement diversity offers a promising solution by providing complementary information, but typically requires multiple acquisitions and additional hardware. Recent studies have shown that phase-diverse measurements exhibit strong spatial correlations that can be learned using deep neural networks [1]. Leveraging this, we present a physics-informed deep learning framework that generates pseudo phase-diverse measurements from a single acquired image, thereby augmenting the available data without requiring additional measurements or hardware (Fig. 1). The generated pseudo-data are then combined with the original measurement to improve inverse reconstruction, as demonstrated for two representative imaging problems: incoherent image deblurring and coherent FPR.

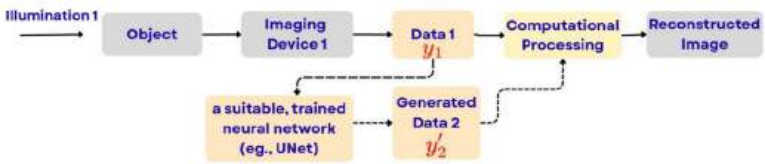


Fig. 1: Schematic overview of the presented approach. Figure adapted from [1].

For incoherent imaging, a standard image y_1 and a phase-diverse image y_2 are simulated using an open-aperture 4F system and a charge-1 spiral phase plate, respectively. Their complementary frequency responses are fused using a generalized Wiener filtering framework for deblurring. For coherent imaging, a standard diffraction pattern y_1 and a phase-diverse counterpart y_2 are generated using plane-wave and vortex-beam illumination, respectively. The measurement pair is incorporated into a spiral phase retrieval framework based on the Gerchberg–Saxton algorithm to suppress twin-image artifacts [2].

To avoid acquiring the second measurement, a U-Net is trained to learn the mapping between the standard y_1 and phase-diverse y_2 measurements. During inference, the network predicts a pseudo phase-diverse measurement y'_2 from a single input image y_1.

The predicted pseudo-data closely match the true phase-diverse measurements, achieving an SSIM of 0.97 and PSNR of 37.84 dB for incoherent imaging, and an SSIM of 0.89 and PSNR of 33.62 dB for coherent imaging. Reconstructions obtained using the predicted measurement pair (y_1, y_2') are visually indistinguishable from those using the true measurements (y_1, y_2). The proposed method effectively suppresses grainy artifacts in deblurring and eliminates the twin-image ambiguity in FPR.

These results demonstrate that high-fidelity pseudo phase-diverse measurements can be generated from a single acquisition and used to augment inverse reconstruction without additional hardware. The proposed framework offers a practical route toward robust, single-shot computational imaging systems with improved reconstruction quality.

Acknowledgements: JB: support from National Post Doctoral Fellowship from ANRF, India. KK: support from the National Quantum Mission, DST, India

References:

[1] J. Birdi, T. Majumder, D. Halder, M. Kularia, and K. Khare, *Journal of Physics:Photonics* (2025)

[2] M.K. Sharma, C. Gaur, P. Senthilkumaran, and K. Khare, *Applied Optics* 54, 3979-3985 (2015)

INV_DES_Hazra_Lakshminarayan_FOP_2026

Principal Azimuths in a General Image-Forming Optical System and Their Uses in Image Assessment

#Lakshminarayan Hazra
Department of Applied Optics and Photonics,
University of Calcutta
JD2 Sector 3, Salt Lake, Kolkata 700064
India

Lnhaphy@caluniv.ac.in; Lakshminarayanhazra@gmail.com:

Abstract: Using coordinate axes aligned with the principal azimuths in object and image spaces facilitates the aberrational treatment of general image-forming optical systems. This enables utilisation of image assessment procedures akin to those for axially symmetric systems. The existence and derivation of these principal azimuths will be described.

A general image-forming optical system may include one or more unconventional optical components, for example, tilted and/or decentered spherical surfaces, crossed cylindrical lenses, eccentric portions of nonspherical surfaces, freeform surfaces, refracting prisms, gradient-index lenses, etc. In most general optical systems, the object and image may also be curved surfaces. Conventional techniques for aberrational analysis and image assessment have been developed for tackling image-forming optical systems that possess a unique axis of symmetry. They cannot be directly extended to general optical systems. However, it is seen that with a suitable choice of axes for the object and image spaces, principal azimuths always exist for the object-space and image-space parts of the base ray. Pupil exploration determines the base ray for each object point numerically.

Let the local coordinates in the object space and the image space be represented by the rectangular coordinate systems $(\mathrm{X}, \mathrm{Y}, \mathrm{Z})$ and $(\mathrm{X}', \mathrm{Y}', \mathrm{Z}')$.The Z and Z' axes are aligned with the base ray in the object space and the image space, respectively. The $(\mathrm{X}, \mathrm{Y}) \text{ and } (\mathrm{X}', \mathrm{Y}')$ planes are perpendicular to the Z and Z' axes. If the coordinate axes $(\mathrm{X}, \mathrm{Y}) \text{ and } (\mathrm{X}', \mathrm{Y}')$ are rotated around the Z and Z' axes, we get new axes, say $(\mathrm{X_S}, \mathrm{Y_T}) \text{ and } (\mathrm{X_S'}, \mathrm{Y_T'})$. For a specific rotation, the new axes will lie in such azimuths that all rays entering the optical system with $\mathrm{Y_T} = 0$ emerge (to a first order in the aperture) with $\mathrm{Y_T'} = 0$; and, similarly, all rays entering the optical system with $\mathrm{X_S} = 0$ emerge with $\mathrm{X_S'} = 0$ to first order accuracy. These azimuths are the principal azimuths in the object space and in the image space for the particular object point. The existence of these principal azimuths requires only that the surfaces of the optical system encountered by the rays during its propagation through the optical system are continuous and smooth. For a general optical system, the principal azimuths differ with object position. The principal azimuths can also be defined for any intermediate image space. Note that the principal azimuths are perpendicular to each other.

The principal azimuths around the base ray from an object point provide suitable coordinate axes for the object/entrance pupil in the initial object space and image/exit pupil in the final image space. All image assessment criteria based on ray-optical and wave-optical theories of image formation, widely used for axially symmetric systems, can be suitably formulated around these coordinate axes for applications to general optical systems. This talk establishes the existence of the principal azimuths, and then presents an analytical approach to deriving these principal azimuths.

Vectorial Exact Ray Tracing: Advancements in the modeling of complex objective lens systems and experimental validation

Shilpa Singh and #Bosanta R Boruah
Department of Physics
IIT Guwahati,

Guwahati-781039, Assam

#brboruah@iitg.ac.in

Abstract: In this talk I will present our recent work on vectorial exact ray tracing, which is used first to compute the focal intensity distributions corresponding to the three cartesian components due to a complex objective lens system. This is then extended to compute the optical force on a trapped microsphere.

Optimization of any experimental setups using a tightly focused beam requires a correct description of the focal field. One such setup is the optical trap. Single beam optical traps also called optical tweezers are used to move and manipulate objects suspended in a given medium. They find widespread applications in biology which involve trapping of micron sized particles. Although there are different optical force calculation models, geometrical optics based models provide a simple yet efficient way to compute the optical force on objects of size larger than the wavelength of light. However most of the models predicting the focal field and the resulting optical force profile use the minimal number of parameters such as the numerical aperture (NA) and aperture diameter to describe the objective lens. In contrast the objective lens system invariably has multiple optical sub-elements whose role in describing the focal field can not be ignored.

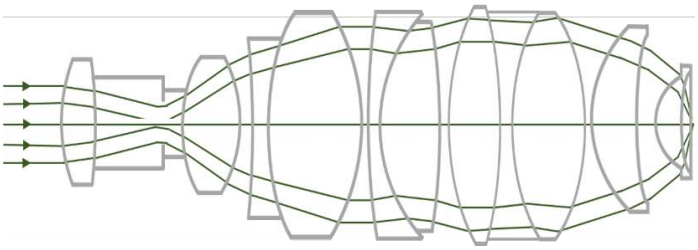


Fig. 1 Tracing of rays through a complex lens system.

We have developed a geometrical exact ray tracing [1] based scheme that takes into account each lens element of the objective lens system and obtains the focal field by associating each ray with the respective electric field as the ray is traced from the pupil plane to the focal volume. Figure 1 shows tracing of a few representative rays through a complex lens system inclusive of an objective lens. Later we extended the scheme to compute the optical force on a trapped micro-sphere. The vectorial nature of the focal spot diagrams for normal gaussian beam [2] and vortex beam [3] obtained using our scheme has interesting resemblance to those given by vectorial diffraction theory. The proposed force calculation model clearly demonstrates that use of only the NA is not sufficient to describe the objective lens and two different objective lenses with the same NA not necessarily correspond to the exact same optical force profile. Key findings of our vectorial exact ray tracing scheme have been validated by performing experiments.

References:

[1] Born M, Wolf E. Principles of optics. Oxford: Pergamon press; 1964.

[2] Singh, Shilpa, and Bosanta R. Boruah. "Vectorial ray tracing scheme for arbitrary complex amplitude profiles through a given optical system." *Journal of the Optical Society of America A* 42.11 (2025): 1835-1845.

[3] Singh, Shilpa, Karuna Sindhu Malik, and Bosanta Ranjan Boruah. "Tight focusing of aberrated vortex beams using the vectorial ray tracing scheme." *Journal of Optics* 28.5 (2026): 05560
.

Optical design of a compact prime focus wide-field corrector using aspherical optics with atmospheric dispersion compensation

[1] Totan Chand, [1] S. Sriram

[1]*Indian Institute of Astrophysics, Koramangala, Bangalore 560034, India.*

totan.chand@iiap.res.in

We present design of a compact wide field corrector(WFC)system with a circular field of view of 1.5degee in wavelength ranges from 0.35μm-1.6μmfor the proposed 3.7m segmented mirror telescope. The design consists of six optical elements with two aspheric surfaces. The two spherical lens with wedging can be rotated and moved laterally by a small amount to compensate the atmospheric dispersion.

Over the past two decades the observational astronomy largely relies on wide field imaging and spectroscopy. This facilitate astronomer further to map the larger area of the sky for studying various scientific phenomena for multiple astronomical objects. This telescopes require to cover a large angular field of view (FOV) and high optical etendue. In order to achieve this the imaging detectors are placed at the prime focus of the telescope. The large size primary mirror use for high FOV is inherently suffers from the off-axis optical aberration such as coma, astigmatism and field curvature which caused the degradation of image quality. In order to get control over these aberrations a refractive lens system commonly known as wide field corrector(WFC) is placed before the focal length of the primary mirror. The stringent optical design requirements of such system such as maximum size of the corrector lens, compactness, lightweight, good color correction, high fractional encircled energy, contrast with low distortion makes them challenging to the designer.

The WFC presented in this paper is design for a RC type cassegrain telescope of primary mirror of size 3.7m and the focal ratio(F#) of 1.51 working on prime focus mode. The primary mirror is segmented with 7 hexagonal segments of 1.44m size each. The first lens element is located at a distance of 500mm from the location of the secondary mirror of size equivalent to less than one segment for mechanical mounting feasibility. The maximum size of the corrector lens of the WFC system is 400mm and the total track length is 530mm.The WFC is optimized using six lens element and two lower order aspheric surfaces to get rid of higher order aberration. The optical design gives a flat focal plane of size 173mm which is positioned at 40mm from last surface of the corrector. The final F# of the design system is 1.7 which provides a plate scale of 32μm/arcsec. A micro lens array based focal ratio converter is planned to be used to feed the beam suitable for fiber coupling useful for spectroscopic survey application. The optical layout and the important image quality performance plot such as spot diagram and encircled energy of the design system is shown in figure1.The 80% encircled energy of the system falls within 12μm size which is about 0.37”design residual of 1” FWHM atmospheric seeing. The two spherical lens with wedge shown in Fig.1 will be counter rotated and also moved laterally to correct the atmospheric dispersion and also keep the image stationary without introducing any extra optical element.

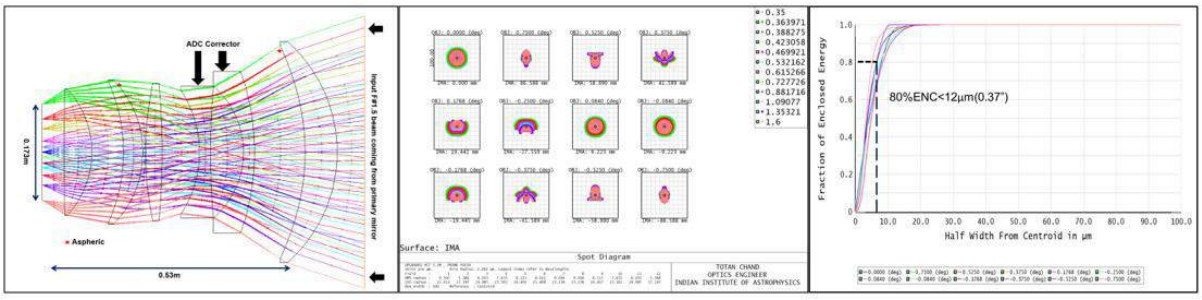


Fig.1:(From Left to right) WFC Optical Layout Spot Diagram Encircled energy Plot

References

[1] Prasanna Deshmukh, Sriram S., Totan Chand *etal*"Design and simulation of 6.2m wide-field telescope for spectroscopic survey", Proc. SPIE 13094, Ground-based and Airborne Telescopes X, 130941V.
[2] Cody Nelson, Vipender Singh Negi, Carson Fuls etal “Wide-field prime-focus corrector design: application to the Catalina Sky Survey”Opt Express 2026 May 18;34(10):18022-18036.

Optimal support to minimize the self-weight deformation for a cylindrical Fabry-Perot cavity

[1]Umesh Dhatrak,[1#]Sandip Haldar and [2*]Subhadeep De
[1]School of Mechanical Sciences, Indian Institute of Technology Goa, Farmagudi, Goa 403401, India
[2]The Inter-University Centre for Astronomy and Astrophysics (IUCAA), Post Bag 4, Ganeshkhind, Pune 411007, India

[#] sandip@iitgoa.ac.in, [*]subhadeep@iucaa.in

Ultra-stable Fabry–Pérot (FP) cavities are essential for linewidth narrowing of laser as required for high-precision spectroscopy, quantum communication etc. The choice of geometric parameters of FP cavity is an open design space. In this work, a finite element analysis based parametric study of cylindrical FP cavities is carried out to determine optimal geometry of a cylindrical cavity to minimize gravity-induced self-weight deformation therefore enhancing its stability.

Ultra-stable Fabry–Pérot (FP) cavities have wide range of applications [1, 2]. Disturbances such as gravity, thermal fluctuations and vibrations induce mechanical deformation in Fabry-Pérot (FP) cavities resulting in instability given by $\frac{\Delta\upsilon}{\upsilon}=\frac{\Delta L}{L}$, where υ is frequency of the laser and L is the cavity length. Therefore, significant effort is invested into mechanical design of the cavities to reduce deformation. In the design of FP cavities, while the spacer length is determined from the wavelength of the working laser, there is no standard to choose the shape or lateral dimensions [2, 3]. In this work, a finite element analysis (FEA) based work is presented to determine the optimal diameter and support position to minimize gravity induced deformation of a cylindrical cavity. A cylindrical geometry is selected in this work because of its symmetry and ease of fabrication. FEA was performed in ANSYS for horizontally mounted cylindrical cavities for L varying from 150 mm to 500 mm. The cavities are symmetrically 3-points×2 supported on either of its sides at the theoretical Airy points x = 0.2113×L, measured from its faces. Ultra-Low Expansion (ULE) glass and Fused Silica are used as spacer and mirror materials, respectively [3]. Spacer diameter and support position have been varied parametrically under transverse gravitational load (g) to determine the configuration corresponding to minimum fractional instability.

At first, with ideal Airy point supports, the variation of fractional instability (dL/L) with spacer diameter for different cavity lengths are studied. The optimum diameter (d) has been determined from zero crossing, i.e. dL/L=0. A similar trend can be observed for all cavity lengths. It has been reported in literature that the support point for the cavity for the best stability may not be the Airy point, since it is defined based on 1D geometry. Therefore, using the optimized diameters, the support locations are further analyzed, as shown in Fig. 1. The minimum instability occurs very close to the theoretical Airy point for all cavity lengths, validating it as the optimal support position (x). For reference, the Bessel point is also shown. At the end, the optimal ratios of d/L and x/L are found to be 0.26 and 0.2115, respectively.

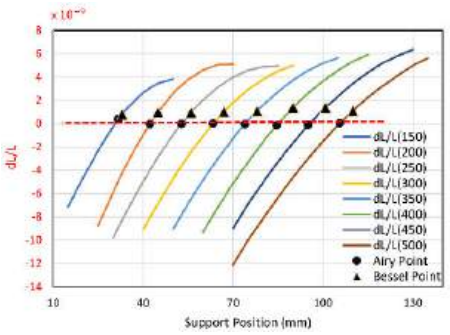


Fig. 1: Fractional instability for cylindrical cavities with optimal diameter with different support positions.

The results provide insight into the choice of cavity dimensions for optimal frequency stability and support positions to reduce gravity-induced deformation, enabling fractional frequency instability approaching the order of $10^{-12}/g$. Detailed simulation results and optimal designs will be presented in the conference.

References:

1. J. A. Boyd, T. Lahaye, *American Journal of Physics* 92, 50–58 (2024)
2. L. Jin et al., *Optics Express*, 26 (14), 18699-18707 (2018)
3. S. Banerjee et al., *International Journal of Mechanical Sciences* 250, 108299 (2023)

Far-Field, Near-Field and Time Resolved Terahertz (THz) Spectroscopy of Materials

Shriganesh S. Prabhu

DCMPMS, Tata Institute of Fundamental Research, Mumbai 400005, India

prabhu@tifr.res.in

This study explores Terahertz (THz) spectroscopy applications across diverse materials. Using OPTP and THz-TDS, we observed extended exciton relaxation (3.87 ps) and robust thermal conductivity in graphene-MoS_2 heterostructures. Additionally, we demonstrated high Q-factor (up to 107) quasi-BIC modes in metamolecules using selective symmetry breaking, verified via Near Field Scanning THz Microscopy.

Terahertz (THz) spectroscopy offers large opportunities in the ultrafast study of materials of various kinds. We have developed several Terahertz (THz) spectroscopic techniques to study different materials from single crystals to metamaterials. We investigated photo-induced intraband transitions and real-time charge carrier transfer dynamics across the interfaces of single-layer graphene and monolayer molybdenum disulfide (MoS_2) heterostructures. Utilizing optical pump terahertz probe (OPTP) spectroscopy, we observed an extended interfacial exciton relaxation lifetime of approximately 3.87 picoseconds inside the combined heterostructure compared to a much faster decay in isolated graphene[1].

We have also studied Metamaterials of different types for various applications. We studied THz transmission through such surfaces. We developed a Near Field Scanning THz Microscope for this purpose. We studied numerically and experimentally excited bound state in the continuum (BIC) mode with a high Q-factor in the THz meta-molecule (composition of meta-atoms) system, leveraging a unique method of selective symmetry breaking in a ring-shaped metamolecule system. Unlike conventional strategies that uniformly disrupt the symmetry across all resonators to excite a quasi-BIC mode, this innovative technique targets only half of the unit cell for symmetry perturbation. This selective symmetry breaking minimizes radiative losses and enhances the Q-factor of the quasi-bound states in continuum (quasi-BIC) modes. The results depict a notable improvement in the Q-factor, achieving values as high as 107 in simulation, a significant enhancement compared to the uniformly symmetry-breaking approach, which exhibits Q-factors around 25.80. The experimental transmission spectrum and the near-field scanning images firmly validate[2] the existence of the high Q BIC mode under this strategic symmetry-breaking approach.

Germanium (Ge) is emerging as a promising material for terahertz (THz) devices due to its non-polar nature, which enables gapless, broadband radiation. In this work, we demonstrate the compatibility of Ge films deposited by DC magnetron sputtering on high-resistive silicon and on low-cost insulating substrates, glass and Kapton, for the detection of free-space THz pulses. With the growing interest in the field of flexible electronics, we demonstrate THz detection using Ge-on-glass and Ge-on-Kapton photoconductive antennas (PCAs) with ZnTe as a THz emitter, achieving spectral bandwidths of 1.5 and 1.2 THz with signal-to-noise ratios (SNRs) of 27 and 23 dB, respectively.

We wish to acknowledge financial support from DAE, India and TIFR, Mumbai vide grant No.RTI4003

References:

[1] Sharma, Saloni, Singh, Divyansh Pratap, Rane, Shreeya, Srivastava, Shubhda, Puthirath, Anand B, Puranik, Ruturaj, Pandey, Utkarsh, Haldankar, Snehal, Parkar, Vibhavari, Faseela, Fathimath, Prabhu, Shriganesh S., Chowdhury, Dibakar Roy, Ajayan, P. M., Gupta, Bipin Kumar "Probing into Intraband Transitions Enabled Charge Carrier Dynamics of THz Response Generated in Graphene/MoS2 Heterostructures" Advanced Materials 37.26 (2025).

[2] B. Kumar Bhowmik, K. M. Rohith, S. John, S. Prabhu, and G. Kumar, “High-quality factor Quasi-BIC mode via selective symmetry-breaking approach in a terahertz metasurface,” New J Phys, vol. 26, no. 6, p. 063024, Jun. 2024, doi: 10.1088/1367-2630/ad570e.

[3] Dhanashree Chemate, Abhishek Singh, Utkarsh Pandey, Ruturaj Puranik, Gaurav Mota, Niranjan Jadhav, Siddhartha P. Duttagupta, Shriganesh S. Prabhu; Terahertz detection using germanium-based photoconductive antennas on various substrates. J. Appl. Phys. 28 May 2026; 139 (20): 203105. https://doi.org/10.1063/5.0331931

Symmetry-protected bound states in the continuum in terahertz metasurfaces

Dibakar Roy Chowdhury*

Anurag University, Ghatkesar, Hyderabad, 500088, India
*dibakar@anurag.edu.in

Bound states in the continuum (BIC) are discrete non-radiating eigenstates of a system that lie within the continuum of the radiation, characterized by the zero linewidth and theoretically infinite Q-factors[1]. The BICs in photonics provide a unique pathway for the implementation of various applications such as sensing, lasing, detection, and non-linear enhancements[2]. Symmetry-protected bound stated in the continuum (SP-BIC) are one of the BIC realization pathways widely explored in the terahertz (THz) metasurfaces due to their simpler yet exceptionally flexible implementation approaches. The SP-BICs arise due to the symmetry incompatibility of the state with respect to the incident radiation, thereby restricting the coupling of the mode to the radiation channel. Through symmetry perturbations of the system, introduced either by breaking structural symmetry of the system with respect to incident radiation or by asymmetric excitation of the system, these states can be accessed as leaky resonances with strong field confinements. Various unit cell geometries such as cut-wires, split ring resonators (SRR), and discs are utilized for the demonstration of SP-BICs in the THz metasurfaces. A metasurface design consisting of a pair of parallel cut-wires is employed to demonstrate the emergence of BIC from Fano resonance through symmetry restoration[3]. In another work, a pair of parallel SRRs are utilized to demonstrate the evolution of quasi-BIC resonances into BICs via dual excitation pathways. Here, the near-field coupling induced resonance mode hybridization of inductive-capacitive (LC) resonances leads to emergence of BIC for one probe polarization, while the near-field coupling of the dipolar resonances leads to emergence of BIC for orthogonal probe polarization[4]. These works highlight the emergence of SP-BICs and excitation of high Q-factor Fano-type resonances at the quasi-BIC conditions, providing enhanced light-matter interactions, which can pave the way for promising applications in the domains of THz functional devices and materials.

References:

[1] D.C. Marinica, A.G. Borisov, and S. V. Shabanov, “Bound States in the Continuum in Photonics,” Phys. Rev. Lett. **100**(18), 183902 (2008).

[2] N. Acharyya, Y. Pulagam, Y. S N, and D. Roy Chowdhury, “Bound states in the continuum: A study on metasurface engineering and photonic maneuvering,” APL Eng. Phys. **1**(1), (2026).

[3] Y. Pulagam, N. Acharyya, Y. S N, S. Rane, D.S. Rana, and D. Roy Chowdhury, “Fano resonance: a route to bound states in the continuum,” J. Opt. Soc. Am. B **42**(5), 1085 (2025).

[4] Y. Pulagam, Y. S N, U. Pandey, V. Parkar, S. Haldankar, N. Acharyya, S.S. Prabhu, and D. Roy Chowdhury, “Dual bound states in the continuum in near-field coupled terahertz metasurfaces,” J. Phys. Photonics **8**(1), 015019 (2026).

Photon-Energy-Dependent Terahertz Emission Spectroscopy of Ferrimagnetic Spintronic Heterostructures

[1]Mukundadev Behera,[1]Hrittik Kumar Roy, [2]Piyush Agarwal, [3]Chandrasekhar Murapaka, [1,#]Yogesh Kumar Srivastava

[1]Department of Physics, Indian Institute of Technology Hyderabad, Kandi, Sangareddy, Telangana, India, 502284.
[2]*Institute of Materials Research and Engineering (IMRE), Agency for Science, Technology and Research (A*STAR), Singapore.*
[3]Department of Materials Science and Metallurgical Engineering, Indian Institute of Technology Hyderabad, Kandi, Sangareddy, Telangana, India, 502284.

[#]*email id: yogesh.srivastava@phy.iith.ac.in*

The impact of excitation photon energy on spintronic terahertz (THz) emission is investigated in DyCo/Pt ferrimagnetic heterostructures using 400 nm and 800 nm femtosecond laser pulses. A wavelength-dependent shift in THz polarization reversal is observed across compositions, which shows photon energy significantly influences ultrafast spin-current generation in ferrimagnetic heterostructures.

Ultrafast laser-driven spintronic THz emitters (STE) have emerged as compact broadband THz sources due to their efficient optical generation of ultrafast spin current [1]. Upon femtosecond laser excitation, a transient spin current generated in the magnetic layer diffuses to adjacent heavy-metal layer and is converted into a transverse transient charge current through the inverse spin Hall effect (ISHE), $\mathbf{J}_c = \boldsymbol{\theta}_{\mathbf{SH}}(\mathbf{J}_s \times \boldsymbol{\sigma})$, where $\mathbf{J}_s$ and $\boldsymbol{\sigma}$ are the spin current and spin polarization direction of magnetic layer respectively, and $\boldsymbol{\theta}_{\mathbf{SH}}$ is the spin Hall angle of heavy metal layer. The resulting ultrafast charge current radiates a broadband THz pulse. While many efforts have been made for material optimization [2,3] and interface engineering, the influence of excitation photon energy on spin-current formation and THz generation in ferrimagnetic spintronic heterostructures remains mostly unexplored.

In this work, THz emission from Dy_xCo_{1-x}/Pt, ferrimagnetic and heavy metal heterostructures is investigated using 800 nm (1.55 eV) and 400 nm (3.1 eV) femtosecond laser excitation, as shown in Figure 1. Co rich compositions of Dy_xCo_{1-x}/Pt exhibit identical THz polarization under both excitation wavelengths, whereas Dy-rich compositions show a different excitation-wavelength-dependent evolution of the emitted THz signal, which includes changes in signal polarity and suppression at specific alloy compositions. These observations demonstrate that the ultrafast THz generation is strongly influenced by the excitation photon energy in addition to the alloy composition.

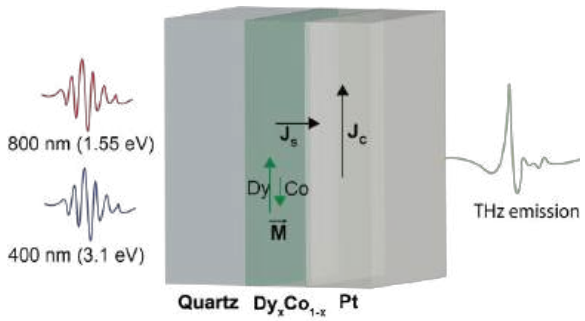


Figure 1: Schematic representation of THz generation in a DyCo/Pt ferrimagnetic spintronic emitter under 400 nm and 800 nm femtosecond laser excitation.

The observed photon-energy-dependent behaviors show that optical excitation plays an important role in determining the ultrafast spin-current generation process in DyCo/Pt ferrimagnetic heterostructures. These observations show excitation photon energy as an important parameter for investigating and engineering spintronic THz emitters and provide new insight into ultrafast light induced spin current generation in ferrimagnetic spintronic THz emitters.

Acknowledgement: I would like to acknowledge the Council of Scientific and Industrial Research (CSIR), Government of India, for awarding me the Junior Research Fellowship (JRF), which supported this research.

References:

[1] T. Seifert, T. Kampfrath, *Nature Photon* **2016**, *10*, 483.
[2] R. Schneider, R. Bratschitsch, *ACS Photonics* **2018**, *5*, 3936.
[3] Z. Ji, Y. Song, Z. Zhang, Q. Jin, *Applied Physics Letters* **2023**, *123*, 132401.

Experimental Demonstration of an Opto-Electronic Self-Interference Cancellation System for 5G In-Band Full Duplex Communication

[1]Divya Sree K, Rupam Biswas, Mahesh Lunavath, Chiranjeevi D and Ranu Tyagi
Electro-Optics and Photonics Group, Central Research Laboratory, Bharat Electronics Ltd
Bangalore, India

[1]*divyasreek@bel.co.in*

An opto-electronic assisted RF self-interference cancellation (SIC) system utilizing a Dual-Parallel Mach-Zehnder Modulator (DP-MZM) is demonstrated for 5G New Radio (NR) In-Band Full Duplex (IBFD) applications. Experimental results at 2.4GHz with QPSK modulation yielded cancellation depths of 46dB (10MHz bandwidth) and 25dB (100MHz bandwidth). Post-SIC analysis confirms successful recovery of Signal of Interest (SOI) and Error Vector Magnitude (EVM) performance within 3GPP-specified limits, validating the system's efficacy for wideband 5G transceivers.

As 5G networks evolve towards IBFD to maximize the spectral efficiency, co-locating Tx-Rx antennas cause the high-power Tx signal to leak into the Rx path, masking low-power SOI, thus necessitating SIC [1]. Photonics-based SIC [2] offers numerous advantages such as immunity to electro-magnetic interference (EMI) and high-precision phase manipulation of the signal, overcoming the limitations of electronic alternatives. This work investigates an opto-electronic assisted DP-MZM based SIC architecture, as shown in Fig.1(a), for QPSK modulated 5G NR frequencies. The core principle is to match the time delay and amplitude of a reference Tx signal copy to the Self-Interference (SI) signal, while inverting its relative phase. A CW Laser generates the optical carrier for DP-MZM electro-optic modulation. The upper and lower sub-MZMs of the DP-MZM are fed with the received signal (SOI+SI) and the RF domain amplitude and delay adjusted reference signal, respectively. Precise tuning of DC bias voltages of DP-MZM achieves the required phase inversion. The upper sub-MZM and the parent MZM are biased at quadrature to maximize the recovered SOI power and induce a π phase shift between the two branches, while the lower sub-MZM bias is fine-tuned for exact phase matching. Consequently, destructive interference of SI and reference signal at the DP-MZM combining branch achieves SIC in optical domain before the cancelled signals are detected by the photodetector.

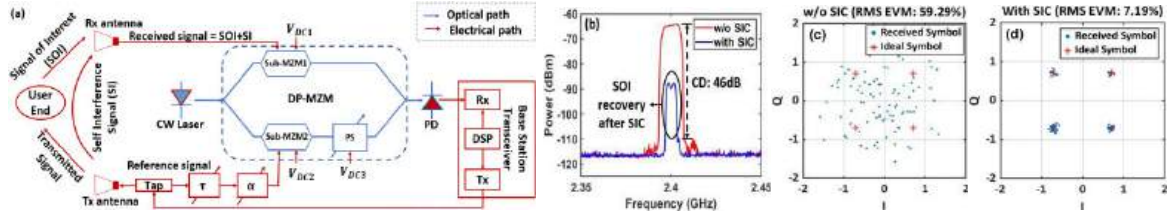


Fig. 1 (a) Block diagram of the proposed DP-MZM based SIC architecture. (b) RF spectrum without and with SIC, (c) Constellation diagram without SIC and (d) Constellation diagram with SIC for QPSK modulated 2.4GHz SOI and SI with 5MHz and 10MHz bandwidth, respectively.

TABLE I. SIC performance evaluation across various 5G frequencies and bandwidths

Center Frequency	SI Signal		Cancellation Depth	EVM without SIC	EVM with SIC
	Bandwidth	Input Power			
2.4GHz	10MHz	15dBm	46dB	59.29%	7.19%
	100MHz		25dB	51.44%	9.75%
5.6GHz	10MHz	15dBm	24dB	55.06%	9.02%
	100MHz		12dB	47.70%	12.44%

Experimental results show that while the SI initially masks the SOI into an unrecoverable, scattered constellation with high EVM as in Fig.1(b, c), successful SIC restores the SOI, yielding a tightly cluttered QPSK constellation in Fig.1(d) with low EVM. Performance across 5G frequencies is tabulated in Table I, which indicates that the cancellation depth decreases as the center frequency and bandwidth of the signal increases. The results demonstrate that the design is well suited for emerging 2.4GHz (Wi-Fi), 4GHz (C-Band) and 5.6GHz (sub-6) 5G NR frequency bands without requiring hardware modifications.

References:

[1] D. Wang et al., *Journal of Lightwave Technology*, vol. 40, no. 3, pp. 607-614, 1 Feb.1, 2022.

[2] X. Han, B. Huo, Y. Shao and M. Zhao, *IEEE Photonics Journal*, vol. 9, no. 2, pp. 1-8 (2017).

Development of THz-based spectroscopy and imaging techniques for characterization of optical, dielectric and surface roughness properties of explosive composites

P. Naveen Kumar[1], K. Rajesh[1], Chandan Ghorui[1], A.K. Chaudhary[1]*and Bikash Ghose[2]

1-DIA-CoE (Advanced Centre for Research in High Energy Materials), School of Physics, University of Hyderabad, Telangana, 500046, India.

2-HEMRL, Sutarwadi, Pashan, Pune -411021

* Email: akcsp@uohyd.ac.in, anilphys@yahoo.com

This paper reports the use of time domain Terahertz spectroscopy techniques for the measurement of optical and dielectric properties of sensitive explosives like RDX, TNT, AN etc. in composites form using an Effective Medium Theory. In addition, the indigenously developed 2D/3D imaging technique used for the recording of surface roughness of rusted metallic and explosive surfaces.

Terahertz Time-Domain Spectroscopy (THz-TDS) is a powerful spectroscopic technique used to study the optical and electronic properties of materials in the frequency range of 0.1–10 THz. It plays a significant role in security and defense, facilitating the detection of concealed explosives, narcotics, and hazardous substances through non-invasive imaging[1–2].

In the present work, we validated the applicability of EMT for the characterization of sensitive explosives. We prepared a mixture of three premium secondary explosives, RDX, HMX, and TNT, in a Teflon matrix and extracted the dielectric and optical properties of these explosives using EMT methods such as Landau-Lifshitz-Looyendga (LLL), Bruggeman (BG), and Maxwell Garnett (MG) methods[3–4].

In the next part, we have discussed the design aspects of 2D/3D imaging cum profilometer in terahertz (THz) frequency domain in reflection geometry. It is employed for surface roughness measurements of painted and unpainted metallic and explosives surfaces. The signal was recorded in the frequency range f = 0.5, 1.0, 1.5 and 2.0 THz frequency range respectively [5].

Acknowledgements: The authors gratefully acknowledge the financial support provided by DFTM/05/3454/THEX-2, DRDO, Ministry of Defense, Govt. of India, and Dr. S.C. Bhattacharyya, Director for full logistic support.

References:

[1] P.U. Jepsen, D.G. Cooke, M. Koch, Laser Photonics Rev. 5 (2011) 124. https://doi.org/10.1002/lpor.201000011.

[2] M. Naftaly, Terahertz Metrology, 2016.

[3] S.O. Nelson, T.S. You, J. Phys. D. Appl. Phys. 23 (1990) 346 https://doi.org/10.1088/0022 3727/23/3/014.

[4] K. Rajesh, A.K. Chaudhary ,Infrared Physics&Technology151(2025)106129

[5] C. Ghorui, P.Naveen Kumar and A.K. Chaudhary, J Infrared Milli Terahz Waves (2026) 47. https://doi.org/10.1007/s10762-026-01142-3

Emergent Terahertz Functionalities Enabled by Quantum Materials

Dhanvir Singh Rana

Department of Physics, Indian Institute of Science Education and Research (IISER) Bhopal, India

Abstract

The terahertz (THz) spectrum (0.1-10 THz) offers promising opportunities in the development of next-generation data processing, quantum memory and communication technologies. These aspirations are driven by simultaneous developments in the THz spectrum and, the area of spintronics, magnonics, caloritronic, and some emergent quantum materials. In ordered magnets, magnons - the quanta of spin waves - envisage the prospects of non-Boolean-based spin wave computation, magnon logic gates, and so on. Magnonics has been widely explored in ferromagnets resulting in gigahertz magnons. However, the area of magnonics is being extended to ultra-low dissipation and ultrafast THz region exploiting the antiferromagnet magnons in this region. This offers THz radiation-based technological utility of antiferromagnets which, so far, have played only a passive role in conventional magnetic devices. THz radiation couples mainly with the magnetic-dipole moment of the spins unveiling not only the low-energy antiferromagnetic magnons but an interplay of magnons with other quasiparticles such as phonons, polaritons, and many more. A control over such magnon can be contemplated in magnetoelectric/multiferroic systems, wherein the spin and electric orders are entangled, resulting in electric as well as magnetic control of magnons. These facets of magnon along with a control of the dielectric medium via magnetic phase transition offer several new THz functions which are potentially relevant in futuristic computational and communication technologies, In this talk, I'll present our recent work in exploration of a variety of non-collinear magnets for magnon and magnon-phonon excitation modes in the THz spectral region, considering some examples; i) the $A_4B_2O_9$ (A=Co and B=Nb, Ta) family of non-collinear magnetoelectric antiferromagnetic exhibit a multitude of low-energy antiferromagnetic resonances comprised of magnons, phonons, and hybridized spin-phonon coupled modes and the notion of beyond conventional magnon, that is, electromagnon, ii) the second example is based on $RCrO_3$ (R=rare-earth) orthochromates in which weak magnetic moment is accompanied by sub-THz magnon modes along with complex crystal-field excitations, and *iii)* using magneto-elastic and magnetoelectric transition induced drastic changes in dielectric medium to modulate THz phase in sub-THz region – a much desired attribute for wave propagation relevant for 6G and beyond technologies.

References:

1. Jayaprakash Sahoo *et al*, Advanced Functional Materials 36, e76416 (2026)
2. B. S. Mehra *et al*, Advanced Science e75555 (2026)
3. Santhosh Kumar *et al*, Advanced Optical Materials 8, 1900958 (2020)
4. B. S. Mehra and D. S. Rana, Nature Physics 20, 687 (2024) [News and Views]
5. A Shyam *et al*, Applied Physics Reviews 12, 021420 (2025)
6. Sanjeev Kumar *et al*, Applied Physics Reviews 12, 031423 (2025)
7. B Mehra *et al*, Physical Review Applied 23, 054081 (2025)

A Self-Adaptive Microwave Photonic Anti-Jamming Architecture Based on Stimulated Brillouin Scattering

[#]Md Kamran Afroz, Chowdhury Kamruzzaman and Amol Choudhary
Department of Electrical Engineering, Indian Institute of Technology Delhi,
New Delhi 110016 India

[#]*eez238570@iitd.ac.in*

We demonstrate a self-tracking stimulated Brillouin scattering (SBS)-assisted microwave photonic anti-jamming system in which the received jammer generates the SBS pump responsible for its own suppression. Image transmission over a 6 GHz carrier experimentally verifies autonomous interference suppression, achieving Peak Signal-to-Noise Ratio (PSNR) improvement from 11.5 dB to 19 dB.

Microwave photonic signal processing provides an attractive approach for mitigating narrowband radio-frequency (RF) interference owing to its wide bandwidth and high spectral selectivity [1-2]. Although stimulated Brillouin scattering (SBS)-based microwave photonic notch filters enable high-performance RF cancellation, most reported approaches require prior knowledge of the jammer frequency or active tuning [3]. Here, we demonstrate a self-tracking SBS-assisted microwave photonic anti-jamming system in which the received jammer itself is utilized to generate the SBS pump required for its suppression.

Figures 1(a)–(c) illustrate the operating principle of the proposed self-tracking anti-jamming system. The received RF signal, containing both the desired message and a strong narrowband jammer, is divided into probe and pump branches. In the probe branch, the received signal phase-modulates an optical carrier, while a programmable optical filter introduces the sideband imbalance required for RF cancellation. In the pump branch, the same received RF signal modulates a Brillouin-frequency-shifted optical carrier using a single-sideband suppressed-carrier modulator. Because the jammer is significantly stronger than the desired signal, it dominates the SBS interaction and automatically generates an SBS gain response centered at its own frequency. The SBS-induced restoration of the optical sideband balance enables destructive RF interference after photodetection, selectively suppressing the jammer while preserving the desired signal. Consequently, the notch response automatically tracks the interference frequency without requiring frequency estimation or adaptive feedback. The proof-of-concept experimental results for a 6.2 GHz jammer are presented in Figs. 1(d) and (e). Before SBS processing, the strong jammer dominates the received RF spectrum and severely degrades the reconstructed image, as shown in Fig. 1(d). After SBS-assisted self-tracking cancellation, the jammer is selectively suppressed by approximately 20 dB while preserving the desired 6 GHz message signal, resulting in a significantly improved recovered image, as shown in Fig. 1(e). Quantitative image analysis further confirms the effectiveness of the proposed system, with the peak signal-to-noise ratio (PSNR) improving from 11.5 dB to 19.0 dB and the structural similarity index (SSIM) increasing from 0.09 to 0.46, demonstrating effective autonomous jammer suppression and faithful image recovery.

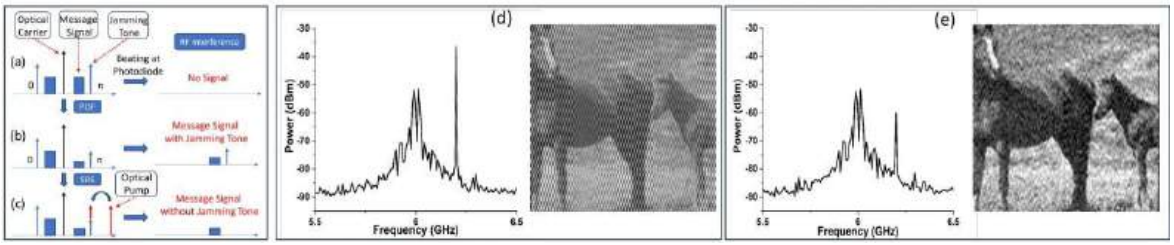


Fig. 1: Concept and experimental demonstration of the proposed self-tracking SBS-assisted microwave photonic anti-jamming system. (a)–(c) Operating principle. (d) RF spectrum and recovered image before jammer suppression. (e) Corresponding results after jammer suppression.

Acknowledgements: This work was supported by the Department of Telecommunications (DoT), India through the Advanced Optical Communications (AOC) Testbed Project.

References:

[1] J. Yao, IEEE Microw. Mag. 16(8), 46–60 (2015).
[2] B. J. Eggleton, C. G. Poulton, and R. Pant, Adv. Opt. Photon. 5(4), 536–587 (2013).
[3] D. Marpaung, M. Pagani, B. Morrison, and B. J. Eggleton, Optica 2(2), 76–83 (2015).

Engineering Ultra-Broadband Terahertz Absorption in Flexible Metamaterials

[1]Bhawana Andola, [2]Abhishek Kumar, [1#]Yogesh Kumar Srivastava

[1]Ultrafast Terahertz Photonics Laboratory (UTPL), Department of Physics, Indian Institute of Technology Hyderabad, Kandi, Sangareddy, Telangana, 502284, India

[2]Chemistry and Physics of Materials Unit (CPMU), Jawaharlal Nehru Centre for Advanced Scientific Research (JNCASR), Bangalore, 560064, India

[#]Email: yogesh.srivastava@phy.iith.ac.in

We experimentally demonstrate a structurally simple and flexible ultra-broadband terahertz meta-absorber based on an arc-shaped metal-dielectric-metal (MDM) architecture, exhibiting >90% absorption from 0.54-1.25 THz, robust bending and angular stability, and numerically predicted VO_2 enabled thermal tunability, offering a compact platform for adaptive THz photonic applications.

The rapid advancement of wireless communication systems, high-frequency electronics, and terahertz (THz) technologies has developed a growing demand for efficient electromagnetic wave management [1]. Metamaterial absorbers, particularly metal-dielectric-metal (MDM) structures, offer a promising solution owing to their subwavelength thickness and strong light-matter interactions. However, simultaneously achieving ultra-broadband absorption, mechanical flexibility, angular stability, and active tunability remain challenging [2,3].

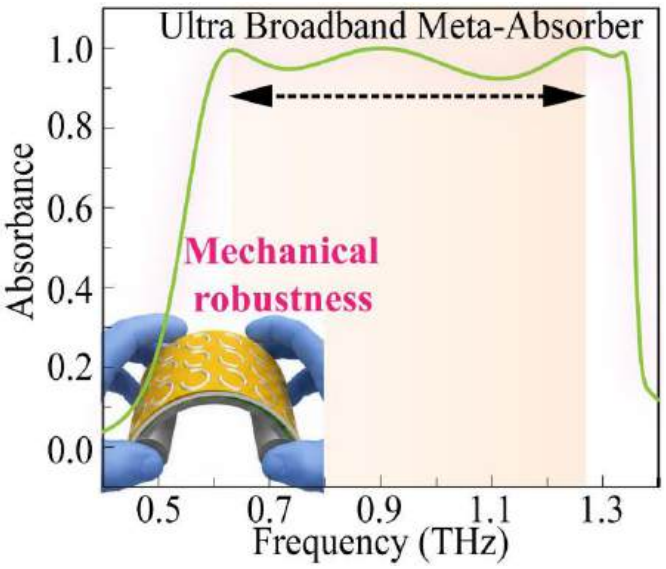


Figure 1: (a) Shows the broadband near-unity absorption (0.5-1.10 THz) and (b) photographs of the flexible device under different bending curvatures (k = 0-0.80 cm^{-1}), demonstrating excellent absorption stability against mechanical deformation.

Here, we experimentally demonstrate a flexible ultra-broadband THz meta-absorber based on a simple MDM architecture consisting of symmetric arc-shaped aluminum structure, a Kapton dielectric spacer, and a metallic ground plane. By carefully optimizing the geometry, multiple resonant modes are strongly coupled, resulting in broadband impedance matching with free space. The fabricated absorber exhibits experimentally measured absorbance exceeding 90% over a broad frequency range of 0.54-1.10 THz, in excellent agreement with numerical simulations. Furthermore, the device maintains high absorption under different bending curvatures and oblique incidence angles. Numerical investigations further reveal that incorporating the phase-change material vanadium dioxide (VO_2) enables efficient thermal tunability of the absorption characteristics. Owing to its combination of ultra-broadband absorption, mechanical robustness, structural simplicity, and active tunability, the proposed meta-absorber represents a promising platform for THz sensing, imaging, wireless communications, stealth technologies, and adaptive photonic systems.

Acknowledgement: Bhawana Andola would like to gracefully acknowledge the funding support received from the Department of Science and Technology (DST), Government of India, under the INSPIRE Fellowship.

References:

[1] R. Chávez-Santiago, M. Szydełko, A. Kliks, F. Foukalas, Y. Haddad, K. E. Nolan, M. Y. Kelly, M. T. Masonta, I. Balasingham, Wireless Pers Commun **2015**, 83, 1617.

[2] K. Chen, Z. Wang, M. Guan, S. Cheng, H. Ma, Z. Yi, B. Li, *Photonics* **2025**, *12*, 987.

[3] L. Zheng, R. Feng, H. Shi, X. Li, *Micromachines* **2023**, *14*, 1715.

Classical and Quantum Photonics for Smart Technologies

Luigi Di Lauro[1], Domenico Bongiovanni[1], Xutong Wang[1], Imitiaz Alamgir[1],Celine Mazoukh[1], Nicolas Perron[1], Yang Liu[1], Benjamin Crockett[1], Masnad Md. Mahadi[1], Pavel Dmitriev[1], Hosne Shamim[1], Hao Yu[1], Bennet Fischer[1,2], Mario Chemnitz[1,2], Monika Monika[1,3],Evgeny A. Viktorov[4], Anton V. Kovalev[4], ShervinVakili[1], Brent E. Little[5], Zhiming Wang[6], Ulf Peschel[3], Sai T. Chu[7], José Azaña[1], David J. Moss[8], and Roberto Morandotti[1,#]

[1]Institut National de la Recherche Scientifique, Centre Énergie Matériaux Télécommunications (INRS-EMT), Varennes (QC), Canada
[2]Leibniz Institute of Photonic Technology, Jena, Germany
[3]Institute of Condensed Matter Theory and Optics, Friedrich-Schiller-University, Jena, Germany
[4]ITMO University, St. Petersburg, Russia.
[5]QXP Technology Inc., Xi'an, China
[6]Shimmer Center, Tianfu Jiangxi Laboratory, Chengdu, China
[7]City University of Hong Kong, Hong Kong, China
[8]ARC Center of Excellence in Optical Microcombs for Breakthrough Science (COMBS), Swinburne University of Technology, Hawthorn, Australia

[#]Roberto.Morandotti@inrs.ca

We report on fiber- and integrated-photonic platforms that use time and frequency control for quantum communication and classical processing. High-dimensional entanglement, ultrafast time-bin encoding, dispersion-resilient quantum key distribution, reservoir computing, spectral machine learning, and microcomb optimization support scalable smart photonic technologies

Integrated and fiber-based photonic systems provide powerful platforms for classical information processing, optical computing, machine learning, and quantum communication [1,2]. Their compatibility with telecom infrastructure, together with precise control of the time and frequency degrees of freedom of light, enables scalable approaches for fast signal processing, photonic optimization, and high-dimensional quantum-state generation.
Here, we summarize our results in telecom-compatible photonic platforms for smart applications, including time-domain reservoir computing, spectral machine learning, learning-assisted microcomb control, frequency-bin and time-bin entanglement, and high-dimensional quantum key distribution. Our achievements rely on CMOS-compatible devices that exploit a highly doped silica glass platform, as shown in Fig. 1 (a-c).

For classical information processing, we demonstrate time-domain photonic reservoir computing using a Sagnac interferometric cavity incorporating an integrated spiral waveguide (see Fig. 1 (b)). The reservoir combines Kerr nonlinearity and cavity delay dynamics to generate high-dimensional temporal responses with fading memory. Wavelength-division multiplexing enables parallel processing of independent data streams in the same system. The platform achieves a normalized root-mean-square error below 6% for Mackey-Glass prediction and a bit-error rate below 10^{-4} for optical telecom signal recovery, with an effective processing speed of 32.5 GHz [3].

We further demonstrate learning-driven control of integrated microcombs using a genetic algorithm applied to high-Q microring resonators (see Fig. 1 (a)). The algorithm uses the measured optical spectrum and power trace as feedback to control key spectral features, including line spacing, spectral envelope, bandwidth, and spectral flatness. By optimizing the laser scan parameters and amplifier current, the system targets distinct comb regimes, including microcombs with line spacings of 48.9 GHz and about 150 GHz. This closed-loop approach also enables soliton-crystal states with line-to-line intensity variations reduced to about ±3 dBm across the telecom C-band. Coherence measurements confirm high spectral coherence across the generated combs, with average fringe visibility above 91% at short delay and above 83% after one photon lifetime [4].

In quantum photonics, we exploit CMOS-compatible integrated microring resonators and spiral waveguides to achieve high-dimensional frequency-bin entanglement. Spontaneous four-wave mixing in microring resonators generates broadband photon-pair frequency combs, where photons occupy

coherent superpositions of discrete frequency modes. These devices provide compact and stable sources of frequency-bin-entangled qudit states. By combining them with dispersive propagation, electro-optic modulation, and time-resolved detection, we extend control to hybrid time-frequency encoding for measurement-based quantum processing and complex entangled photonic resources [5].

Time-bin encoding provides a complementary route for quantum-state processing. In fiber-based systems, two coupled loops of different lengths form synthetic temporal photonic lattices, in which controlled delays and tunable coupling define discrete time bins [6]. This architecture enables photonic quantum walks with entangled photon pairs and high two-photon interference visibility, reaching 97.82% for d = 2 and 91.55% for d = 4. Integrated systems further improve compactness, stability, and speed.

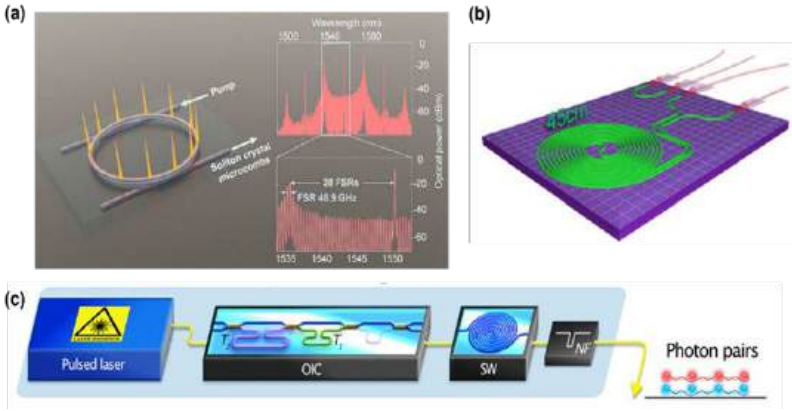


Fig. 1: Integrated devices on our CMOS-compatible platform. (a) Schematic representation of an integrated MRR for the generation of a comb spectrum from four-wave mixing. (b) Schematic representation of an integrated spiral waveguide. (c) Setup for photon state generation via on-chip cascaded interferometers.

Using programmable on-chip interferometric cascades and spiral waveguides (see Fig. 1 (c)), we generate and manipulate time-bin-entangled qudits with picosecond-scale spacing, including 64 ps for d = 4 and 32 ps for d = 8. This supports dense temporal multiplexing and high-rate entanglement-based quantum key distribution over 60 km fiber links [7]. We address dispersion, a key limitation for long-distance time-bin quantum communication. Instead of receiver-side compensation, we exploit nonlocal correlations in entangled photon pairs. By using sum-time correlations in the joint arrival-time distribution, high two-photon interference visibility is recovered even with large accumulated dispersion [8].

In conclusion, these results show how time and frequency control provide a shared framework for classical photonic information processing and quantum-state engineering. In the classical domain, temporal reservoirs, spectral processors, and learning-assisted microcomb control enable high-speed optical computing, signal recovery, and photonic machine learning. In the quantum domain, integrated frequency-bin sources, time-bin encoding, synthetic temporal lattices, and resilience to nonlocal dispersion support scalable, telecom-compatible quantum communication. Fiber platforms provide reconfigurability, while integrated devices provide compactness, stability, and precise control. Hybrid architectures combining both approaches offer a flexible route toward next-generation smart photonic technologies.

References:

[1] F. Flamini, N. Spagnolo, and F. Sciarrino, “Photonic quantum information processing: a review,” Reports on Progress in Physics 82, 016001 (2018).
[2] A. Argyris, “Photonic neuromorphic technologies in optical communications,” Nanophotonics 11, 897–916 (2022).
[3] A. Aadhi, L. Di Lauro, B. Fischer, P. Dmitriev, I. Alamgir, C. Mazoukh, N. Perron, E. A. Viktorov, A. V. Kovalev, A. Eshaghi, S. Vakili, M. Chemnitz, P. Roztocki, B. E. Little, S. T. Chu, D. J. Moss, and R. Morandotti, “Scalable photonic reservoir computing for parallel machine learning tasks,” Nature Communications 17, 1225 (2026).
[4] C. Mazoukh, L. Di Lauro, I. Alamgir, B. Fischer, N. Perron, A. Aadhi, A. Eshaghi, B. E. Little, S. T. Chu, D. J. Moss, and R. Morandotti, “Genetic algorithm-enhanced microcomb state generation,” Communications Physics 7, 1–11 (2024).
[5] C. Reimer, S. Sciara, P. Roztocki, M. Islam, L. Romero Cortés, Y. Zhang, B. Fischer, S. Loranger, R. Kashyap, A. Cino, S. T. Chu, B. E. Little, D. J. Moss, L. Caspani, W. J. Munro, J. Azaña, M. Kues, and R. Morandotti, Nature Physics 15, 148–153 (2019).
[6] M. Monika, F. Nosrati, A. George, S. Sciara, R. Fazili, A. L. Marques Muniz, A. Bisianov, R. Lo Franco, W. J. Munro, M. Chemnitz, U. Peschel, and R. Morandotti, Nature Photonics 19, 95–100 (2025).
[7] H. Yu, S. Sciara, M. Chemnitz, N. Montaut, B. Crockett, B. Fischer, R. Helsten, B. Wetzel, T. A. Goebel, R. G. Krämer, B. E. Little, S. T. Chu, S. Nolte, Z. Wang, J. Azaña, W. J. Munro, D. J. Moss, and R. Morandotti, Nature Communications 16, 171(2025).
[8] H. Yu, B. Crockett, N. Montaut, S. Sciara, M. Chemnitz, S. T. Chu, B. E. Little, D. J. Moss, Z. Wang, J. Azaña, and R. Morandotti, Physical Review Letters 134, 220801 (2025) .

Potential of Holographic Microscopy for Neuroscience

[1,2#]Osamu Matoba,[1,2]Naru Yoneda, [3]Xiangyu Quan, [4]Manoj Kumar, [5]Mitsuo Morita, [1]Luis Ordóñez
[1]Center for Life Photonic Innovation, Kobe University, Rokkodai 1-1, Nada, Kobe 657-8501, Japan
[2]Graduate School of System Informatics, Kobe University, Rokkodai 1-1, Nada, Kobe 657-8501, Japan
[3]Department of Fundamental Engineering, Utsunomiya University, 7-1-2 Yoto, Utsunomiya, Tochigi 321-8585, Japan
[4]Amity School of Physical Sciences, Amity University Punjab, Mohali, Sector 82 A, IT City Rd, Block D, Punjab 140306, India
[5]Graduate School of Science, Kobe University, Rokkodai 1-1, Nada, Kobe 657-8501, Japan
[#]*matoba@kobe-u.ac.jp*

We will present the development of holographic microscopes for neuroscience, equipped with optogenetics-based cellular manipulation technology and calcium fluorescence imaging. Three generations of holographic microscopes developed to date were presented.

In recent neuroscience, efforts are underway to observe and manipulate the mechanisms of brain functional networks using two main approaches: optogenetics-based cell activity manipulation and calcium fluorescence imaging using calcium-sensitive fluorescent proteins. Because conventional optical microscopes are specialized solely for fluorescence observation, there is an essential need to develop novel optical microscopes equipped with an input system for optogenetic cell activity manipulation. We have developed holographic microscopes those enable parallel optogenetic manipulation through simultaneous formation of multiple 3D light spots using computer-generated holography, while incorporating computational optical imaging technology to perform fast and highly efficient 3D fluorescence imaging with a reduced number of measurements [1-3].

In this presentation, we will introduce three generations of holographic microscopes. The first-generation system utilizes one-photon excitation to enable wide field-of-view (FoV) of the brain surface. The second-generation system employs two-photon excitation to achieve single-cell resolution, allowing observation at a depth of 0.5 mm from the brain surface. The third-generation system utilizes a giant objective lens with two-photon excitation to enable both a wide FoV and deep-tissue imaging. Figure 1 shows a photograph of the second-generation holographic microscope system. In this presentation, future prospects will also be discussed.

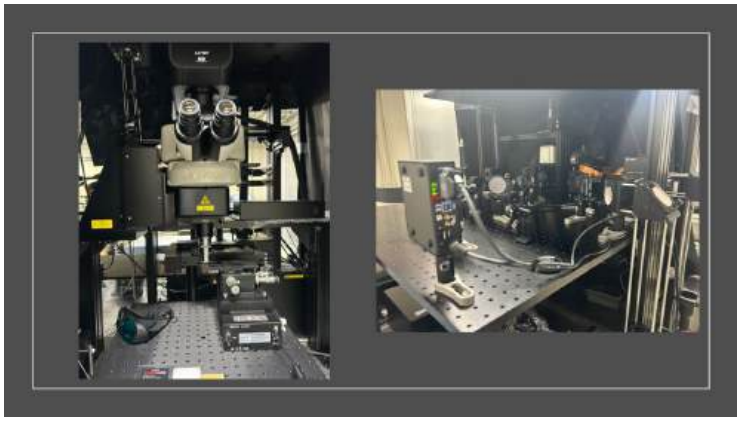


Fig. 1 Photograph of second-generation holographic microscope.

This work was supported by JST CREST JPMJCR22P6 and JPMJCR25R1, and Japan Society for the Promotion of Science (JSPS) KAKENHI (20H05886, 25H00854).

References:

[1] X. Quan, M. Kumar, O. Matoba, Y. Awatsuji, Y. Hayasaki, S. Hasegawa, H. Wake, Optics Letters 43 (2018) 5447.
[2] T. Okada, D. Kato, Y. Nomura, N. Obata, X. Quan, A. Morinaga, H. Yano, Z. Guo, Y. Aoyama, Y. Tachibana, A.J. Moorhouse, O. Matoba, T. Takiguchi, S. Mizobuchi, H. Wake, Science Advances 7 (2021) eabd8261.
[3] X. Quan, D. Kato, V. Daria, O. Matoba, H. Wake, Neuroscience Research 179 (2022) 57.

Beyond the Standard Quantum Limit: Coherent Quantum Noise Cancellation in Hybrid Cavity Optomechanics

Amarendra K. Sarma
Department of Physics, Indian Institute of Technology Guwahati, Guwahati-781039, Assam

Precision measurement has played a transformative role in physics, enabling stringent tests of fundamental interactions and driving the development of modern quantum technologies. Many of the most significant scientific discoveries have resulted not only from theoretical advances but also from the ability to measure physical quantities with extraordinary precision. A notable example is the direct detection of gravitational waves in the so-called LIGO, where kilometer-scale laser interferometers achieved displacement sensitivities far below nuclear length scales, allowing the observation of compact-binary mergers.

Beyond fundamental physics, precision measurement has become indispensable in condensed matter physics, nanoscale metrology, and emerging quantum technologies, where the detection of extremely weak forces, minute displacements, tiny magnetic and electric fields, or subtle mass changes provides access to new physical phenomena and enables advanced quantum devices. Among the leading platforms for precision sensing is cavity optomechanics, in which the motion of a mechanical resonator is inferred through its interaction with an electromagnetic cavity field, enabling ultrasensitive measurements of forces and displacements [1]. However, in continuous measurements, quantum fluctuations of the probe impose a fundamental trade-off between measurement imprecision and radiation-pressure backaction. This trade-off gives rise to the Standard Quantum Limit (SQL), which ultimately constrains the sensitivity of force and displacement measurements.

In this talk, we will discuss *coherent quantum noise cancellation (CQNC)* [1] as a strategy to overcome the SQL by engineering destructive interference of measurement backaction noise. The theoretical framework of linearized cavity optomechanics to derive the relevant noise spectra, and establish the matching conditions required for broadband backaction cancellation will be elaborated. Building on this framework, we analyze and compare a couple of hybrid CQNC architectures in which the mechanical resonator is coupled to an auxiliary system, such as an additional cavity mode, an effective negative-mass oscillator, or an electromechanical (microwave) subsystem. We further examine the impact of realistic imperfections—including optical loss, finite auxiliary bandwidth, cavity detuning, and parameter mismatch—on the performance of CQNC and identify the practical limits they impose on achievable sensitivity.

Overall, this talk will elucidate the key design trade-offs governing coherent quantum noise cancellation and identifies experimentally accessible regimes for suppressing measurement backaction and achieving force sensitivities beyond the Standard Quantum Limit [2,3]. The results provide valuable guidelines for the realization of next-generation quantum-limited sensors with applications in force microscopy, precision metrology, and advanced optomechanical sensing technologies.

References:

[1] Amarendra K. Sarma, Subhadeep Chakraborty and Sampreet Kalita, Continuous Variable Quantum Entanglement in Optomechanical Systems: A Short Review, AVS Quantum Science (AIP) 3, 015901 (2021).

[2] Alolika Roy and Amarendra K. Sarma, Overcoming the Standard Quantum Limit with Electro-Optomechanical Hybrid System for Enhanced Force Sensing, Physical Review A 111, 013509 (2025).

[3] Alolika Roy and Amarendra K. Sarma, Force Sensing Beyond the Standard Quantum Limit in a Hybrid Optomechanical Platform, Journal of Optical Society of America B 43, 1692 (2026).

Integrated Nanophotonic Components and Devices for Quantum Computing and Sensing Applications

Shailendra K Varshney
Fiber Optics, Nano & Quantum Photonics Group, Dept. of E&ECE, IIT Kharagpur
skvarshney@ece.iitkgp.ac.in

This talk will provide an overview of photonic waveguides and resonators for quantum photonic applications in the near-IR wavelength range, with a focus on quantum computing.

Quantum technologies have seen a rapid surge across multiple disciplines due to significant advantages and practical engineering solutions, such as powerful quantum computers capable of solving complex problems beyond the reach of even supercomputers, and quantum cryptography for ultra-secure communication. Quantum technologies are also poised to revolutionize precision measurement and quantum sensing, potentially transforming medical diagnostics and environmental monitoring. Most quantum technologies operate in cryogenic environments, whereas photonics-based platforms can operate at room temperature; therefore, they can play a pivotal role in turning these quantum breakthroughs into reality. From generating and manipulating light to precisely controlling it at the quantum level, photonic technologies are critical for improving the efficiency, security, and precision of quantum systems. The miniaturization of optical components is also helping to integrate these technologies into practical devices. Optical waveguides made from silicon or silicon-compatible materials have gained significant attention over the last few years due to their potential for data centers, healthcare, defense, and high-speed on-chip connectivity. Microring resonators (MRRs) are important building blocks for linear, nonlinear, and quantum computing applications. The microring resonator comprises a straight waveguide in proximity to a circular waveguide. The MRR can be used as a filter, modulator, and to generate a quantum frequency comb, squeezed entangled photon pairs for quantum computing and sensing applications.

I will provide an insight into our contribution to achieving the objectives of the National Quantum Mission.

Acknowledgment: We acknowledge the Department of Science and Technology (DST), Government of India, for financial support under the National Quantum Mission (NQM) Project

Broadband polarization entanglement via spatial multiplexing of Type-0 SPDC photons

[1,2,#]Milan Jana,[1,2]Swagata Sarkar and [1,2]Ayan Nai and [1]G. K. Samanta
[1]Photonic Sciences Lab, Physical Research Laboratory, Ahmedabad, Gujarat 380059, India
[2]Department of Physics, Indian Institute of Technology, Gandhinagar, Gujarat 380009, India

[#]*milanepsilon@gmail.com*

We have demonstrated polarization entanglement between Type-0 parametric down-converted (SPDC) broadband (130 nm in our setup) photons from bulk crystal in a single-pass setup, resulting in ultrashort spatial coherence (6.97μm). We have further demonstrated the generalized dependency of typical quantum parameters of the generated state over the spatial coherence of the SPDC photons.

A broadband bi-photon entanglement is a useful resource due to its wide spectral range, high photon flux, and ultrashort correlation time in fields like wavelength-multiplexed multiparty quantum network, high-resolution quantum metrology, quantum lithography, and many more. The existing scheme [1] to generate such source from bulk crystal often uses birefringence-phase compensation to compensate the ultrashort path-indistinguishability from the source. Here we have taken a different approach, more straight-forward and simple. The intrinsically random and correlated transverse bi-photon momentum states [2] of a spontaneous process from a thin-2mm ppKTP crystal, generate photons in broad spectral bandwidth with negligible group-velocity mismatch. The generated state is studied further via the two-photon spatial amplitude governed by Two-photon interference of the entangled-state [3].

We are selecting two diagonally transverse momentum states from the generated SPDC ring, followed by geometrical superposition these two pairs of photons (points) from two different random SPDC events to interfere in the final state experimentally via a polarizing beam-splitter. The superimposed states generate the entanglement over the full spectral range ~130 nm (Fig 2(a)), corresponding to an ultrashort spatial coherence (6.97 μm), which is managed by the relative delay (δx) between the bi-photon states with motorized stage with sub-micron precision. The perfect temporal superposition of the states maximizes the quantum parameters, measured at every delay position (Fig 2(b)). We have demonstrated the generalized dependency (Eq 1) of quantum state parameters (purity and Bell-CHSH value) over the spatial spectrum ($\gamma(\delta x)$) of the generated photons.

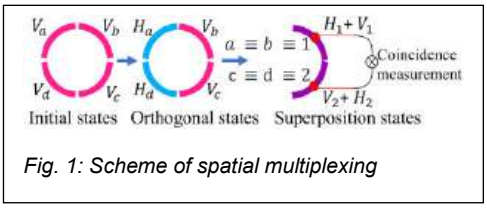


Fig. 1: Scheme of spatial multiplexing

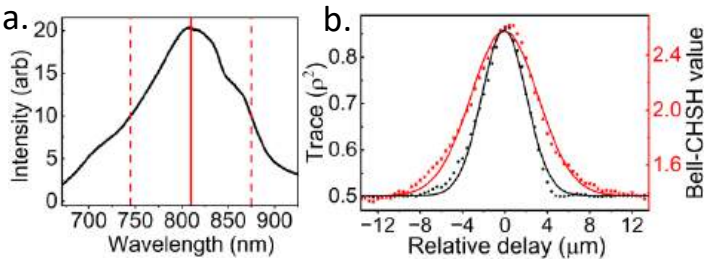


Fig. 2: (a) Broad SPDC spectrum (130 nm) leads to (b) very thin (6.97 μm) spatial coherence

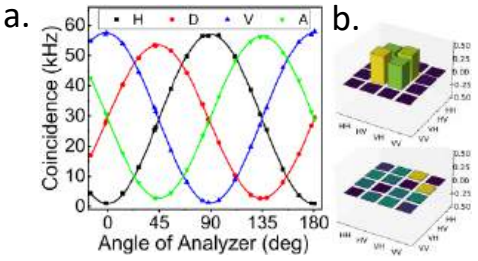


Fig. 3: (a) Polarization correlation, (b) real (top) and img (bottom) part of reconstructed density

$$Trace\ (\rho^2) = \frac{1}{2}(1 + |\gamma(\delta x)|^2) \text{ and } S = \sqrt{2}(1 + |\gamma(\delta x)|) \quad (1)$$

Fixing the stage at the zero delay, we have measured the interference visibility of 98.05 ± 0.06 % in H/V bases and 90.7 ± 0.1 % in D/A bases corresponding to Bell-CHSH value of 2.526 ± 0.005 (Fig 3(a)), along with state fidelity of 96.3 % from the reconstructed density matrix (Fig 3(b)). The pair-rate of the source goes to 0.5745 MHz/mW over full spectral range. The work has been performed with 810 bi-photons, and expected to be useful in other wavelengths as required for various applications.

References:

[1] A. Lohrmann, C. Perumangatt, A. Villar, and A. Ling, Appl. Phys. Lett. 116, 021101 (2020).
[2] J. Schneeloch and J.C. Howell, J. Opt. 18, 053501 (2016).
[3] P. G. Kwiat, A. M. Steinberg, and R. Y. Chiao, Phys. Rev. A. 45, 7729-7739 (1992).

Quantum sensing by tunable exchange symmetry control using geometric phase

[1,2,#]Chahat Kaushik,[1]Vimlesh Kumar and [1]Goutam K. Samanta
[1]Photonic Sciences Lab., Physical Research Laboratory, Ahmedabad 380009, Gujarat, India
[2]Indian Institute of Technology Gandhinagar, 382055, Gujarat, India

[#]*kaushik.28chahat@gmail.com*

We present a symmetry-engineered quantum sensing approach in which a geometric phase imprinted on the pump is transferred to polarization-entangled photon pairs. This phase coherently controls exchange symmetry, driving Hong–Ou–Mandel interference from bosonic bunching to fermionic-like anti-bunching while preserving indistinguishability, enabling birefringence sensing and quantum-state manipulation.

This paper presents a quantum sensing method based on the controllable exchange symmetry in Hong–Ou–Mandel interference [1,2]. A geometric phase introduced between the polarization components of a classical pump is transferred to polarization-entangled photon pairs generated by spontaneous parametric down-conversion. Varying this phase continuously transforms the two-photon state between symmetric and antisymmetric Bell states, producing a transition from bosonic bunching to fermionic-like anti-bunching without changing the photons' temporal delay, spectrum, or indistinguishability. The experiment uses a polarization-Sagnac source, Bell-state control, and a balanced beam splitter for HOM interference. Quantum-state tomography verifies the generation of all four Bell states, while the phase-dependent coincidence signal provides a stable sensing response whose linewidth is independent of photon bandwidth.

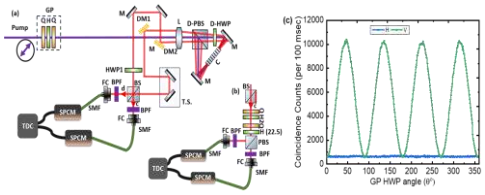


Fig. 1: (a) Schematic experimental setup for tunable exchange symmetry control using geometric phase in two-photon interference. (b) Verification of N00N state generated as a byproduct of HOM interference. (c) Variation of coincidence counts in HOM interferometry as a function of the geometric phase half-wave plate.

The measured HOM response evolves continuously from a dip to an anti-dip as the geometric phase changes. While the temporal width of the HOM feature remains determined by the photon coherence length, the phase-domain modulation width remains fixed and independent of photon bandwidth. This separates phase sensitivity from the spectral properties of the down-converted photons and allows the geometric phase to act as a tunable control parameter for positioning the sensor in its maximum-slope, high-sensitivity region. As a sensing demonstration, birefringent crystals are placed in the pump beam rather than inside the two-photon interferometer. Their temperature-dependent birefringence changes the pump phase and is detected through the HOM coincidence signal. The approach reduces disturbance to the entangled photons and establishes exchange symmetry as a useful resource for robust quantum metrology and photonic-state manipulation [3]. The results will be presented at the time of the conference.

References:

[1] C. K. Hong, Z. Y. Ou, and Leonard Mandel. Measurement of subpicosecond time intervals between two photons by interference. Phys. Rev. Lett., 59:2044–2046, 1987.
[2] B. Pittman, D. V. Strekalov, A. Migdall, M. H. Rubin, A. V. Sergienko, and Y. H. Shih. Can two-photon interference be considered the interference of two photons? Phys. Rev. Lett., 77:1917–1920, Sep 1996.
[3] Michael A Nielsen and Isaac L Chuang. Quantum computation and quantum information. Cambridge university press, 2010.

Quantum Noise of Bright Light: Enabling Quantum Communication and Cryptography

Ashok Kumar*
Department of Physics
Indian Institute of Space Science and Technology, Thiruvananthapuram, Kerala 695547, India
*Email: ashokkumar@iist.ac.in

Quantum fluctuations, traditionally viewed as noise, can serve as a resource for quantum technologies. Using bright quantum-correlated twin beams generated in hot rubidium vapor, we demonstrate correlated quantum random number generation, ultrafast extractor-free spatial quantum randomness, and information encoding within quantum noise.

Quantum fluctuations of light are often regarded as an unavoidable source of noise. However, our recent work demonstrates that these intrinsic quantum fluctuations can themselves serve as a powerful physical resource for quantum optical technologies. By generating bright quantum-correlated twin beams through four-wave mixing in hot rubidium vapour [1], we explore how quantum noise can be harnessed for secure communication, information encoding, and high-speed quantum random number generation [2-5].

The first part of work focuses on correlated quantum random number generation using bright twin beams. Owing to their strong quantum intensity correlations, the twin beams produce highly correlated random number sequences with more than 95% correlation while exhibiting intensity-difference squeezing below the shot-noise limit. These quantum correlations enable the generation of identical high-quality random keys, providing a promising platform for quantum cryptography and secure key generation [2].

The second part extends this concept by introducing an extractor-free quantum random number generator based on the spatial quantum noise of coherent light**.** Instead of relying on temporal quantum fluctuations, the approach exploits the two-dimensional spatial distribution of shot noise recorded using a high-speed EMCCD camera. By employing combinatorial frame processing and direct extraction from spatial quantum fluctuations, the system achieves an instantaneous entropy generation rate of 5.92 Gbps without algorithmic randomness extraction while successfully passing standard NIST and Diehard statistical tests. This demonstrates a scalable route toward ultrafast quantum entropy sources [3].

Finally, we present a new paradigm for information encoding directly within the intrinsic quantum noise of bright entangled twin beams [4]. Unlike conventional continuous-variable quantum communication protocols that encode information in optical field quadratures, the proposed approach conceals weak modulation signals beneath the excess quantum noise of individual beams while exploiting quantum correlations for faithful message recovery through joint detection. We experimentally demonstrate multiple encoding protocols based on time-bin, frequency, composite-frequency, and digital phase encoding, establishing quantum noise itself as an information-bearing medium for secure continuous-variable quantum communication.

Together, these studies demonstrate a unified vision in which the intrinsic quantum noise of bright optical fields is transformed from a measurement limitation into a valuable quantum resource. This platform combines macroscopic optical powers, robust quantum correlations, multimode operation, and compatibility with atomic systems, opening exciting opportunities for practical quantum communication, quantum cryptography, and future quantum networks.

References:

[1] J.A. Thachil, C.R. Patel, U. Ashwin, and A. Kumar, Physical Review A 112 (2025) 053718
[2] A. Shekar, C.R. Patel, J.A. Thachil, and A. Kumar, Applied Physics Letters 127 (2025) 104002
[3] M.A. Shaliq, and A. Kumar, Applied Physics Letters 129, (2026) 074002.
[4] C.R. Patel, J.A. Thachil, and A. Kumar, (Under Review) (2026)
[5] G. Nirala, S.T. Pradyumna, A. Kumar, and A.M. Marino, Science Advances 9 (22), eadf9161 (2023).

Event-driven single-photon cameras based on Timepix3 and Timepix4 for quantum optics

[1,#]T. Schoenbeck, [1]E. Hogenbirk, S. Farroq and [1]B. Ferrando
[1]Amsterdam Scientific Instruments, Science Park 106, 1098 XG Amsterdam, The Netherlands

[#]*thorbjoern.schoenbeck@amscins.com*

Hybrid pixel detectors read out in event mode record every photon as a separate (x, y, t) event with nanosecond time stamps and no frame clock. We describe intensified Timepix3 and Timepix4 cameras and show how per-photon time stamping turns photon-pair correlation measurements from sequential mode scans into single parallel acquisitions.

Measurements in quantum optics are often not of intensity. The observable is a correlation between two detection events: the joint probability that two photons arrive at a given pair of positions within a given time. A frame-based sensor cannot record this directly: within one exposure the pairing between photons is lost, so correlations must be recovered statistically over many frames with an estimated accidental contribution subtracted [1]. Mode-by-mode projection avoids that, but is lossy and scales quadratically with the dimension of the state [2].

Hybrid pixel detectors from the Medipix collaborations at CERN offer a different route. Sensor and readout chip are separate dies joined by bump bonds, and every pixel has its own amplifier, discriminator and timing circuitry. Timepix3 has 256 × 256 pixels on a 55 µm pitch and records, per hit, a time of arrival in 1.56 ns bins and a time over threshold proportional to the deposited signal [3]. Readout is data-driven and sparse: only pixels that register a hit are transmitted, as a continuous stream of up to 80 Mhits/s with no frame clock and no dead time. Timepix4 extends this to 512 × 448 pixels and a 195 ps time bin [4].

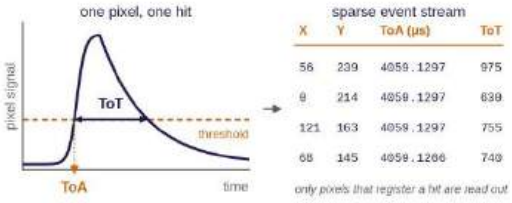


Fig. 1: Each pixel records a time of arrival and a time over threshold; only hit pixels are read out.

At optical wavelengths the bare sensor requires of order 10^3 photons per hit, so single-photon sensitivity comes from coupling an image intensifier to it. Each detected photon produces a small cluster of pixels, most commonly seven, centroided with the time-over-threshold weights to give sub-pixel position [5]. The intensifier also sets the limits: 20–30 % quantum efficiency in the visible, a 400–950 nm range, and single-photon timing of about 2.4 ns rms with Timepix3 and 0.6–1.5 ns with Timepix4, set by the ≈ 7 ns rise time of the P47 phosphor rather than by the chip [5,6].

Coincidence identification then becomes post-processing on the event list, applied across the whole sensor at once: 65 536 pixels correspond to some 2×10^9 pixel pairs measured simultaneously, with the coincidence window chosen in software afterwards. Biphoton digital holography has used this to recover the full amplitude and phase of spatial biphoton states — orbital-angular-momentum, radial and Hermite–Gauss correlations alike: from one-minute acquisitions, three orders of magnitude faster than projective tomography [2]. Because the window can be made short, entanglement across more than 6000 spatial modes has been certified without subtracting accidental coincidences [7].

Event-driven detection therefore changes what can be measured, not only how quickly. We summarise the architecture, the intensified implementation and its measured limits, and where larger tiled sensors and improved Timepix4 timing should matter. We thank the groups whose results are cited here.

References:

[1] A. D'Errico, E. Karimi, *Advanced Functional Materials* 36 (2026) e26562.
[2] D. Zia, N. Dehghan, A. D'Errico, F. Sciarrino, E. Karimi, *Nature Photonics* 17 (2023) 1009.
[3] T. Poikela et al., *Journal of Instrumentation* 9 (2014) C05013.
[4] X. Llopart et al., *Journal of Instrumentation* 17 (2022) C01044.
[5] A. Nomerotski et al., *Journal of Instrumentation* 18 (2023) C01023.
[6] E. Hogenbirk et al., *Journal of Instrumentation* 21 (2026) P02004.
[7] B. Courme, C. Vernière, P. Svihra, S. Gigan, A. Nomerotski, H. Defienne, *Optics Letters* 48 (2023) 3439.

Spatial division-multiplexing-based high-rate, quantum communication networks

[1,2,#] Ayan Kumar Nai, and [1]G. K. Samanta
[1]Photonic Sciences Lab., Physical Research Laboratory, Ahmedabad 380009, Gujarat, India
[2]Indian Institute of Technology Gandhinagar, Palaj, Gandhinagar 382055, Gujarat, India
[#] *ayankrnai@gmail.com*

We demonstrate a free-space multi-user quantum network based on spatial multiplexing of entangled photons generated from a single source. The proposed architecture establishes twelve quantum communication channels among six users, achieving high coincidence count rates, strong entanglement fidelity, and a scalable framework for future quantum communication networks.

Quantum communication networks are becoming increasingly important for connecting multiple users across large distances while enabling secure information exchange through entanglement-assisted Quantum Key Distribution (QKD). Most demonstrations of quantum networks with untrusted nodes have relied on optical fiber systems, employing wavelength-division multiplexing (WDM) [1] of entangled photon sources operating at 1550 nm together with commercially available WDM components designed for classical communication.

In this work, we present a quantum network architecture (Fig. 1(a)) specifically designed for free-space communication using only a single entangled-photon source, an essential requirement for realizing long-distance quantum communication via satellite-based links. By exploiting the inherent spatial and temporal correlations, along with the quantum randomness generated during the spontaneous parametric down-conversion (SPDC) [2] process, the annular emission ring of an 810 nm entangled photon source is spatially divided into six diametrically opposite sections (S1–S6), as illustrated in Fig. 1(a), creating three identical entangled photon sources. The three sources were multiplexed by recombining two non-opposite sections of the ring using beam splitters. Further, we distribute the photons through free-space channels to six users. Each user receives photons from two different sources and is connected to four other users through the corresponding correlated photon pairs, thereby forming a fully connected twelve-channel quantum network [3]. In general, a network with N users can establish N(N−2)/2 communication links using N/2 entangled photon sources. The proposed network achieves average coincidence count rates greater than (3×10^4 s^{-1}) between every pair of users (Fig. 1(b)). It can deliver a total sifted key rate of 407 kbps, despite employing silicon avalanche photodiode detectors. The measured entangled-state fidelity across all 12 network links ranges from 91% to 95%, as shown in Fig. 1(c). At the same time, Fig. 1(d) highlights the scalability of the proposed architecture to support a larger number of users.

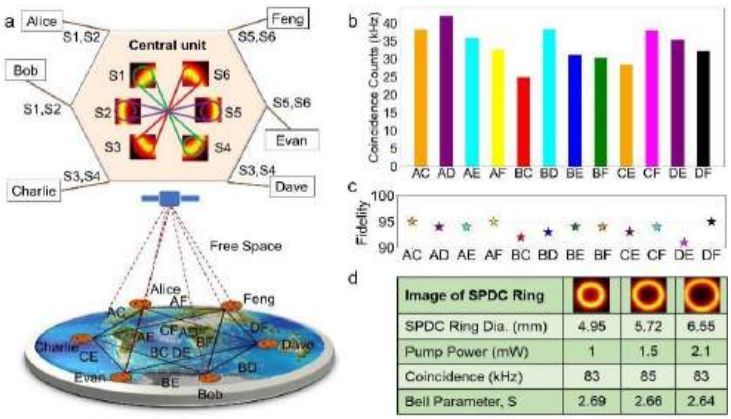


Fig. 1: (a) Representation of the network topology with the free space channels and users. (b) Coincidence rate (c) Entangled state fidelity for each link connecting two users, and (d) Scalability in the twelve-channel network.

In conclusion, our proposed architecture offers a scalable, resource-efficient, high-key-rate multi-user connectivity, making it well-suited for both terrestrial and satellite-based quantum communication networks.

References:

[1] S. Wengerowsky, S.K. Joshi, F. Steinlechner, H. Hübel, R. Ursin, *Nature* 564 (2018) 225–228.
[2] M.V. Jabir, G.K. Samanta, *Scientific Reports* 7 (2017) 12613.
[3] A.K. Nai, G.K. Samanta, *arXiv preprint* arXiv:2511.00466 (2025).

Impact of Detector Noise on Experimental Free-Space Unidimensional Continuous-Variable Quantum Key Distribution

[1,2,#]Rachita Nandan,[1]Jayanth Ramakrishnan, [1]Shashi Prabhakar and [1]R. P. Singh
[1]Physical Research Laboratory, Ahmedabad, India 380009.
[2]Indian Institute of Technology, Gandhinagar, India 382355.

[#]*rachita@prl.res.in*

We experimentally demonstrate free-space unidimensional continuous-variable quantum key distribution under high detector electronic noise. Security analysis shows finite secure key rates under trusted detection in low-loss channels, demonstrating feasibility under realistic high-noise detector conditions, depending on detector trust and channel transmittance.

Continuous-variable quantum key distribution (CV-QKD) enables secure communication using standard optical technologies [1, 2]. Unidimensional CV-QKD (UD-CVQKD) simplifies implementation by encoding information in a single quadrature [3], reducing system complexity while maintaining security [4]. In practice, detector noise plays a critical role [5], as high electronic noise can degrade secret key rates and may prevent secure key generation depending on the assumed security model. In this work, we experimentally investigate the performance of a free-space UD-CVQKD system under high detector electronic-noise conditions.

As shown in Fig. 1, a 780 nm continuous-wave laser at Alice prepares a vertically polarized state $|V\rangle$ using polarization optics (HWP1, PBS1), which is modulated to $[i\sin(\theta/2)\,|H\rangle + \cos(\theta/2)\,|V\rangle]$ by an amplitude modulator (AM). For $\theta \ll 1$, the weak $|H\rangle$ carries the signal while the strong $|V\rangle$ serves as the local oscillator (LO). Gaussian modulation with variance V_A is applied at 2.5 MHz using an arbitrary waveform generator (AWG). At Bob, polarization-based Stokes measurements are performed, where S_2 and S_3 correspond to the X- and P-quadratures, respectively. A QWP–HWP–QWP (Q-H-Q) configuration enables quadrature selection. The polarization components are separated using HWP2 (at $+22.5^{\circ}$) and PBS2, and detected using a balanced homodyne detector (BHD). The X-quadrature is used for key generation, while the P-quadrature is used for security analysis.

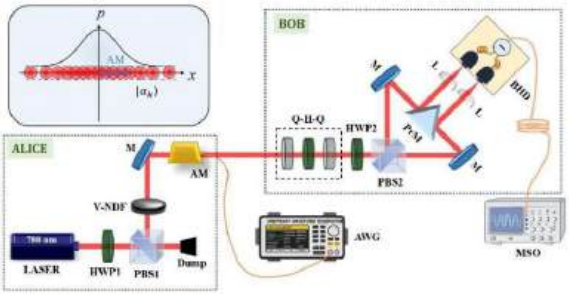


Fig. 1: Schematic setup of the implemented UD-CVQKD protocol.

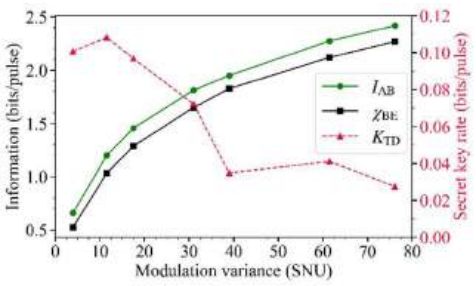


Fig. 2: Obtained secret key rates with modulation variances

The system operates in an electronic-noise-dominated regime with $V_{el} = 1.397$ shot-noise unit (SNU). The prepared states exhibit Gaussian distributions with ~98% correlation between Alice and Bob in the X-quadrature. The channel transmittance and excess noise are found to be $T_x \approx 0.88$ and $\epsilon_x \approx 0.01$ SNU. The secret key rate K_{TD} initially increases with modulation variance, reaching a maximum of ~ 0.108 bits/pulse (~ 270 kbps) at $V_A \approx 11.57$ SNU, and strongly decreases at higher modulation, as shown in Fig. 2, due to reduced effective transmission. A cutoff transmittance of $T_x \leq 0.85$ defines the boundary of the theoretical secure region, highlighting the requirement of a low-loss, high-transmittance channel. We find that secure key generation is not achievable under the untrusted detector model, whereas the trusted detector model yields positive key rates. This study demonstrates the feasibility of free-space UD-CVQKD under realistic detector constraints and emphasizes detector noise as a critical limiting factor in practical systems.

References:

[1] F. Grosshans and P. Grangier, *Phys. Rev. Lett.* 88, 057902 (2002).
[2] C. Weedbrook, S. Pirandola, R. Garc´ıa-Patr´on, N. J. Cerf, T. C. Ralph, J. H. Shapiro, and S. Lloyd, *Rev. Mod. Phys.* 84, 621–669 (2012).
[3] V. C. Usenko and F. Grosshans, *Phys. Rev. A* 92, 062337 (2015).
[4] A.Leverrier, *Phys. Rev. Lett.* 118, 200501 (2017).
[5] S. Pan, D. Monokandylos, and B. Qi, *Phys. Rev. A* 112, 052607 (2025).

Recent advances in high power fiber laser activity at RRCAT

[1,2] #B. N. Upadhyaya

[1] Advanced Laser Development & Applications Division, Raja Ramanna Centre for Advanced Technology, Indore-452013

[2] Homi Bhabha National Institute, Training School Complex, Anushakti Nagar, Mumbai

#bnand@rrcat.gov.in

kW-class Yb-doped fiber lasers find enormous applications in industry and defence. We have developed monolithic single-mode Yb-doped CW fiber lasers of 1kW output power at 1080nm directly from oscillator configuration. This talk will cover details of high power fiber laser development activity at RRCAT along with limitations and their mitigation.

High power fiber lasers have been adopted in most of industrial applications due to their inherent advantages in terms of high efficiency, high beam quality, ruggedness, compactness and reliable operation. Power scaling from Yb-doped fiber lasers is limited due to onset of transverse mode instability (TMI) and nonlinear effects such as stimulated Raman scattering (SRS) and stimulated Brillouin scattering (SBS) [1]. The onset of TMI is the main limitation in achieving power scaling in single mode high power fiber lasers, which leads to a rollover in output laser power and beam quality degradation. There are two main pump bands in Yb-doped fiber, one at 915 nm and another at 975 nm. The pump band at 915 nm is broader with lower absorption cross-section and it is narrow at 975 nm with high absorption cross-section. Thus, pumping at 915 nm requires longer fiber length, whereas pumping at 975 nm requires shorter fiber length for efficient pump absorption. Further, due to broader pump band at 915 nm, pump wavelength shift due to temperature and pump current variation is not critical, whereas at 975 nm it is very critical due to sharp decrease in absorption cross-section. Although worldwide, tens of kW single mode and hundreds of kW multimode fiber lasers have been reported in literature [2,3]. However, in Indian context development of kW-class fiber lasers are important for various industrial and defence applications. In view of this, we have developed 500 W, 1 kW and 2 kW CW fiber lasers by pumping at 915 nm as well as by pumping with 975 nm wavelength stabilized diodes and a maximum optical-to-optical conversion efficiency of ~82% has been achieved [4]. TMI has been observed even at 300 W of output power and mitigated by bend-induced losses to higher order modes. Figure 1(a) shows schematic of 1 kW Yb-doped CW fiber laser, Fig.1(b) shows laser output variation as a function of input pump power and Fig. 1(c) shows laser output spectrum peaked at 1080 nm with a linewidth of 0.8 nm. In view of micromachining applications of ns pulsed fiber lasers, a 100 W average power Yb-doped Q-switched ns fiber laser has also been developed. This talk will cover the details of different fiber laser configurations, their limitations and mitigation strategy to these limitations.

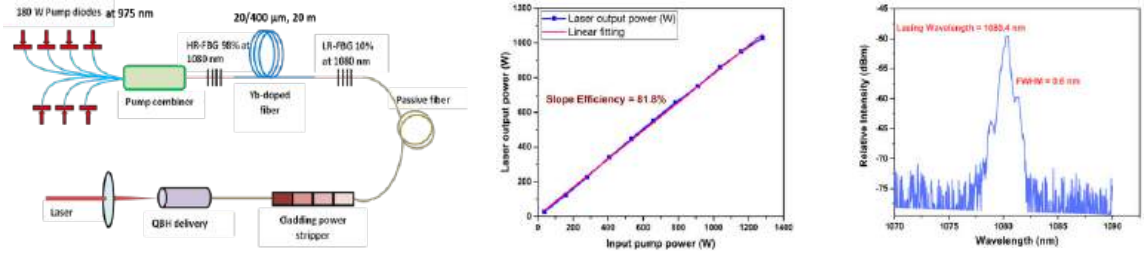


Fig. 1: (a) *Schematic of 1 kW Yb-doped CW fiber laser, (b) laser output variation as a function of input pump power and (c) laser output spectrum at 1080 nm.*

Fiber optic pump combiners and signal combiners are key components of high power fiber lasers. We have also optimized process parameters for in-house fabrication of pump and signal combiners. The talk will cover the details of fabrication of these fiber optic components. Further, in view of absorption peak in water at 1940 nm and its uses in medical applications as well as non-metal cutting and welding applications, Tm-doped CW fiber laser of 100 W output power and ns pulsed fiber laser of 30 W average power have been developed. This talk will provide the details of these Tm-doped fiber lasers.

References:

[1] C. Jauregui C. Stihler, and J. Limpert, *Adv. Opt. Photonics* 12(2), (2020) 429.

[2] B. Shiner *et al., CLEO: 2013*, San Jose, California: OSA, p. AF2J.1 (2013).

[3] E. A. Shcherbakov *et al., Advanced Solid-State Lasers Congress*, Paris: OSA, (2013).

3kW Narrow Linewidth Fiber LASER For Multi-Wavelength LASER Beam Combining Based DEW System

Debasish Mishra, Rishabh, Abhishek Tiwari, Praveen Samuel, Renuka Sehgal
Center of Excellence-EW & P
Bharat Electronics Limited
Bangalore, India.

debasishmishra@bel.co.in

Realization of modular narrow linewidth fiber laser giving an optical output power of 3kW with a spectral linewidth of ~40 GHz having excellent beam quality is presented which serves as a building block for Directed Energy Weapon(DEW) system involving lethal beam generation using multi wavelength laser beam combining technique.

Current world warfare scenario has shown increased attention towards development of LASER based DEW systems as part of defense competency building to have a low cost, highly precise and reliable non kinetic weapon solution featuring high speed multi target engagement capability to be utilized for cheap and deadly aerial threats such as drones. Multiple high power fiber laser having a calculated wavelength separation are used in multi wavelength beam combining (Spectral Beam Combining) to generate single high power combined laser beam to fulfill the requirement of DEW systems [1]. SBC system is a simple wavelength combining technique where multiple low power laser channels with slightly varying wavelength are first collimated and directed onto a diffraction grating using an off axis parabolic mirror acting as a transform mirror. Very narrow spectral linewidth and good beam quality are two of the mostly required specifications to be catered during the development of such high power fiber lasers to be used in SBC architecture[2].

Developed fiber laser consists of a seed and an amplifier module operating at 1070nm wavelength giving out 3kW of laser power with a beam quality(M^2) of 1.2 at an output linewidth of ~40GHz. The seed module consists of depolarized DFB laser which is line broadened using cascaded phase modulation [3]. The Amplifier module houses multiple amplification stages to boost the laser power coming from seed module from mW to kW level. The amplification stages make use of optimized length of doped fiber being pumped using wavelength stabilized laser diodes spliced to pump combiners. The high power pump diodes and gain fiber grooves are placed on a Liquid Cold Plate (LCP) to dissipate the residual thermal load out of the system using a water chiller.

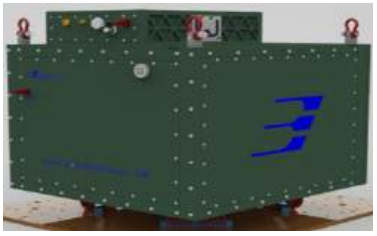


Fig. 1: Developed 3kW laser showing seed(Top) and amplifier (Bottom) modules



Fig.2 : Output power of laser shown in power meter

The laser output is finally taken to the SBC system through a beam delivery cable being spliced to an inhouse designed lensed endcap having a radius of curvature (ROC) intended for divergence control as per system requirement. Safety interlocks are provided for protection of the laser system and the operator from unforeseen system failures. Continuous operation even over 1hour has shown excellent power stability of ±3%.

The developed laser is first of its kind in world which qualifies for both environmental and military grade performance specification requirements. Multiple such lasers with varying operational wavelengths can be realized by changing the seed module and slightly modified amplifier units which serve as building block for enhancing the SBC power to multi kilowatt regime. Further research activities are going on to scale the laser output beyond the current value with rigorous methodical attempts to lessen the output linewidth as much as possible.

References:

[1] Eric Honea, Robert S. Afzal, Matthias Savage-Leuchs, Jason Henrie, Proc. SPIE 9730, 97300Y (22 April 2016)
[2] *Thejna Ros Joseph, Mahesh Lunavath, Renuka Sehgal, and Ranu Tyagi,Advances in Photonics Integrated Circuits(pp.19-27,2025)*
[3] V. R.Supradeepa and A. M. Weiner, Opt. Lett. 37, 3066-3068 (2012)

High-Power femtosecond Dual-Pulse OPO with Tunable Polarization, Wavelength, Delay, and Repetition Rate

[1,2 #]Anirban Ghosh, and [1]G.K. Samanta
[1]Photonic Sciences Lab, Physical Research Laboratory, Ahmedabad, Gujarat 380009, India
[2]Indian Institute of Technology-Gandhinagar, Gujarat 382355, India
[#]*email id: anirbang@prl.res.in*

We present a two-crystal OPO generating dual-pulse outputs with independent control of wavelength, polarization, repetition rate, and delay within a single-beam path, ensuring superior stability and versatility across the visible-to-mid-infrared range.

Ultrafast pump–probe spectroscopy has revolutionized the study of transient phenomena in materials, molecules, and biological systems, providing femtosecond temporal resolution for processes such as carrier relaxation, molecular vibrational dynamics, and energy transfer [1]. Traditional implementations rely on a single laser source with mechanical delay lines or dual-comb laser systems, each offering specific advantages but also notable limitations [2]. To overcome those limitations, here, we demonstrate a two-crystal optical parametric oscillator (OPO) that produces a dual-pulse output enabling pump–probe spectroscopy with unprecedented flexibility in a single-beam, single-system configuration. Both pulses are independently tunable in wavelength, polarization, and relative delay, while inherently sharing the same optical path, which significantly reduces instability compared to conventional split-beam or dual-comb methods.

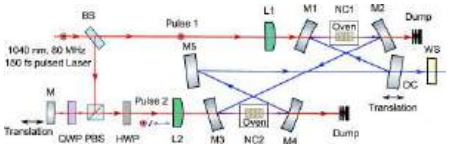


Fig. 1: Schematic of the experimental figure for the generation of dual pulse OPO

Figure 1 illustrates the experimental setup. A 1040 nm, 150 fs, 80 MHz Yb:fiber laser pumps two 50-mm-long MgO: PPLN crystals placed at separate foci inside a common ring cavity. The pump is divided into two beams that independently excite the crystals. The cavity length (940 mm) is synchronized to the fourth harmonic of the pump repetition rate, producing a 320 MHz singly resonant OPO [3]. Initially, both crystals were maintained at 40°C, generating vertically and horizontally polarized signal pulses at 1555 nm. RF measurements confirm stable 320 MHz operation for both outputs. Introducing an optical delay in one pump arm enables continuous tuning of the temporal separation between the two signal pulses. Optical delays of 21.6, 46.8, 78.0, and 93.9 cm produce relative delays of 0.72, 1.56, 2.60, and 3.13 ns, respectively. Orthogonally polarized pulses permit arbitrary delay tuning, whereas co-polarized pulses exhibit coherent coupling within the pump coherence length. Power-scaling measurements show oscillation thresholds of approximately 105 mW and 110 mW for OPO1 and OPO2. At 2 W pump power, both OPOs generate ~180 mW signal power, corresponding to ~9% conversion efficiency. Independent wavelength tuning is achieved by varying the temperature of the second crystal from 35°C to 60°C, continuously tuning the second signal from 1550–1575 nm while maintaining the first signal fixed at 1555 nm. Autocorrelation measurements yield pump and signal pulse durations of 175 fs and 1.49 ps, respectively.

In conclusion, we demonstrate a compact dual-crystal femtosecond OPO capable of independently controlling wavelength, polarization, delay, and power within a single shared cavity. The architecture provides a stable and flexible source for ultrafast pump–probe spectroscopy, with extension from the visible to the mid-infrared.

References:

[1] C. van M. D. Anderson, S. T. Velez, K. Seibold, et al., Phys. Rev. Lett. 120, 233601 (2018).
[2] Y. Jin, S. M. Cristescu, F. J. M. Harren, and J. Mandon, Opt. Lett. **39**, 3270–3273 (2014).
[3] A. Ghosh, N. Das, S. C. Kumar, K. Devi, and G. K. Samanta, Opt. Lett. **50**, 4906-4909 (2025).

Glow discharge spectral data analysis with machine learning for accurate identification of gas mixture compositions for CO_2 lasers

[1,#]Shweta Verma,[1]Avantika Gautam, [2]Anunay Gupta, [1]B.Tirumala Rao,[1]Manoj Kumar
[1]CO_2 Laser Technology Section, Raja Ramanna Center for Advanced Technology, Indore, Madhya Pradesh 452 013
[2]Center of Quality, Reliability, and Maintainability Engineering, Marvin, USA

[#]*shwetaverma@rrcat.gov.in*

This work presents a reliable method for identification of laser gas mixture compositions from glow discharge based optical emission spectroscopy data obtained from in-house developed experimental set-up combined with machine learning. Classification accuracy of >98% was achieved for 66 binary and tertiary gas mixtures using support vector machine and logistic regression models.

Optimum ratio of CO_2, N_2, and He gas mixture composition is crucial in determining laser output power and operating conditions of a CO_2 laser. Hence, precise gas composition determination with a simple and reliable method is important to ensure the performance of sealed-off CO_2 lasers. In this direction, glow discharge based optical emission spectroscopy is a rapid and economic diagnostic technique for monitoring gas compositions. For multi-component complex spectral data analysis, machine learning is effective for accurate classification in various domains [1-2]. Therefore, this work presents an in-house developed direct-current glow discharge based optical spectroscopy method for identification of various compositions of binary and tertiary mixtures of CO_2, N_2, and He gases.

The experimental set-up consists of a portable dc power supply (35 kV, 45 mA) and a compact double wall glass tube for creating glow discharge in the pressure range of 10-30 mbar. Three cylinders of individual gases, each with a pressure gauge and mass flow controller (MFC), were connected to glass discharge tube. Different gas mixture compositions were obtained by controlling the gas flow through MFC and a coaxial flowing water jacket around the glass tube was used to maintain the temperature. Optical emission spectra were recorded using a fiber optic portable spectrometer (Avantes 2048) by fixing the fiber probe near discharge region.

The emission spectra collected of the three gases and their 27 binary and 36 tertiary mixtures at three operating pressures was processed with principal component analysis (PCA) for feature extraction. Fig. 1(a) presents the spectra of N_2-CO_2 gas mixture of different compositions showing complex and overlapping peak patterns. For such cases, use of PCA a dimension reduction method becomes important for ML analysis. 3D PCA plot of N_2-CO_2 gas mixtures shown in Fig. 1(b), presents a well-separable clusters for 09 different binary mixture compositions. Also, the data could be categorized into distinct clusters for 10 and 30 mbar pressures, reveals that PCA could identify the spectral difference arising from pressure variations. The spectral charactersitcs of other mixtures and the role of number of principal components is also studied. Classification accuracy for three models: logistic regression, k-nearest neighbor and support vector machine (SVM) for the binary and terrtiary mixtures was studied and the best performance of more than 98% was obtained with SVM. The developed method is suitable for wide range of applications which require gas composition monitoring such as pre-mixed laser-gases, welding and cutting gas mixtures, industrial safety monitoring etc.

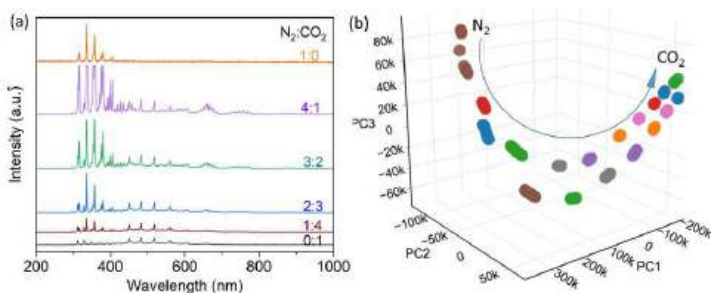


Fig.1(a) Emission spectra and (b) 3D PCA plot of N_2-CO_2 gas mixtures

Acknowledgement: The authors thank Shri P. U. Sangale for his help during experiments.

References:

[1] S. Liu, D. Sun, J. Cheng, L. Shang, Z. Liu, *Physics of Plasmas* 33 (2026) 063509.
[2] V.S. Bitra, S. Verma, B. T. Rao, *Microchemical Journal* 219 (2025) 116054.

Optical PAM-16 Signal Generation Using Mach–Zehnder Interferometer

Manjesh Bhaskar[1,#] and E. S. Shivaleela[2]

[1]Department of Electronics and Communication Engineering,
University of Kalyani, Kalyani, West Bengal, India

[2]Department of Electrical Communication Engineering,
Indian Institute of Science, Bengaluru, Karnataka, India

[#]manjeshbhaskar65@gmail.com

Several techniques for improving the spectral efficiency of a carrier are in practice. Among them, Pulse Amplitude Modulation-N (PAM-N) is useful in Passive Optical Networks (PONs) as a simple and elegant intensity modulation/direct detection method. This work presents the experimental generation of PAM-4, 8 and 16 optical signals using a lithium-niobate Mach–Zehnder Interferometer (MZI) with an automatic bias control board (BCB-4), evaluated after 10 km single-mode fiber transmission.

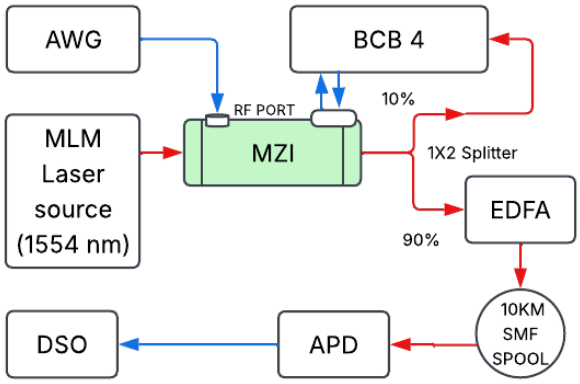


Fig. 1: Experimental setup for optical PAM-4, 8 and 16 generation using MZI.

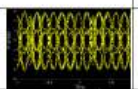
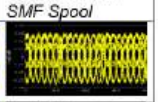
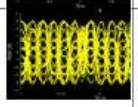
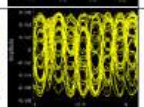
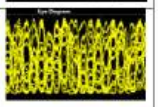
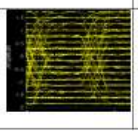
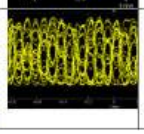
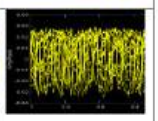
PAM	AWG Signal	Before EDFA	*EDFA+10km SMF Spool*
4			
8			
16			

Table 1: Eye diagrams for the PAM signals.

The schematic diagram for optical PAM signal generation and transmission is shown in Fig. 1. Multilevel PAM formats have attracted significant attention for short-reach IM/DD links, with recent demonstrations of high-order PAM generation using Mach–Zehnder modulators [1, 2]. A multi-longitudinal mode laser operating at 1554 nm is employed as the optical source. The optical signal/carrier is fed into the MZI intensity modulator, which is biased at the Q-point, and the electrical PAM signal generated by the arbitrary waveform generator (AWG) is fed to the RF port of the MZI for modulation. The output of the MZI is connected to a 90/10 1×2 optical splitter; 10% of the optical power is directed to the PD of the BCB, which continuously monitors and stabilizes the operating point of the MZI. The 90% optical power is amplified using an Erbium-Doped Fiber Amplifier (EDFA) before transmission through a 10 km Single Mode Fiber (SMF). At the receiver, an Avala liode (APD) converts the received optical signal into the electrical domain, which is subsequ red using a Digital Storage Oscilloscope (DSO) for eye-diagram analysis. The PAM signal e of the AWG and APD outputs are listed in Table 1. The obtained eye diagrams verify the feasibility of high-order PAM modulation for optical communication systems.

Our future work will be focused on improving the performance and also on generating the PAM signals at high bit rates.

References:

[1] K. Chen, H. Yue, J. Huang, T. Chu, Optics Letters 49 (2024) 2045.
[2] Q. Hu, R. Borkowski, Y. Lefevre, J. Cho, F. Buchali, R. Bonk, K. Schuh, W. Heni, B. Baeuerle, C. Hoessbacher, et al., Journal of Lightwave Technology 40 (2022) 3338.

High-Energy Ultrafast Laser Technology: Frontiers, Breakthroughs, and Emerging Applications

[1#]Jagannath Nayak, [2]Gaurav Singal and [2]S Veerabuthiran
[1]O/o Director General (Missile & Strategic System), DRDO, Hyderabad
[2]Centre for High Energy System and Science (CHESS), DRDO, Hyderabad
[#]e-mail: director.chess@gov.in

This paper reviews the current frontiers and major technological breakthroughs in high-energy ultrafast lasers and examines emerging applications including the defence sector.

Ultrafast laser technology working in the pulse durations from picoseconds to attosecond regime has undergone a great transformation from laboratory based scientific instruments toward high energy, high average power systems capable of defence and industrial applications. Rapid advances in chirped-pulse amplification, optical parametric amplification, thin-disk and fiber-based architectures, coherent beam combining, and high-damage-threshold optical materials have enabled the generation of ultrashort pulses with increasingly high peak and average powers. These systems now combine short duration, high repetition rate, and increasingly robust beam quality, opening routes to compact, reliable platforms for demanding applications. Their core advantage is the ability to deposit energy on timescales faster than thermal diffusion, enabling extreme precision, minimal collateral damage, and access to nonlinear light–matter interactions. In manufacturing, ultrafast lasers are now used for micromachining, 3D micro and nanostructuring, transparent-material processing, and fabrication of photonic, biomedical, and optical devices with sub-micrometer precision. In aerospace, semiconductors, and medical engineering, they support high-value processing of hard and brittle materials, precision drilling, waveguide writing, and advanced surface functionalization. Also, high-energy ultrafast sources are increasingly important for compact accelerators, high-brightness radiation generation, cargo inspection, medical imaging, and potentially laser-driven therapy etc.

Despite remarkable progress, major challenges remain in scaling pulse energy and average power while maintaining excellent beam quality, temporal contrast, pointing stability, optical-damage resistance, and overall wall-plug efficiency. Thermal management, nonlinear effects, component lifetime, system complexity, and cost remain critical barriers to widespread deployment. The future of high-energy ultrafast laser technology will therefore depend on the integration of advanced amplifier architectures, intelligent control, robust optical engineering, and efficient energy-management strategies.

A plausible case study of effectively utilizing ultrashort pulse laser in defence application will be presented in this talk.

References:

[1]. Kasparian J, Sauerbrey R, Chin S L, *Appl Phys B*, 71(2000)877–879.
[2]. Durand M, Houard A, Prade B, Mysyrowicz A, Durécu A, Moreau B, Fleury D, Vasseur O, Borchert H, Diener K, Schmitt R, Théberge F, Chateauneuf M, Daigle J-F, Dubois J, *Opt Exp*, 21(2013)26836–26845.
[3]. Sibo Niu et al., Photonics, 11(2024), 857.

High Speed De-blurring Technology for Wide-area Surveillance System

SK Mishra
Instruments R&D Establishment, Dehradun-248001, Uttarakhand (INDIA)
e-mail: skmishra.irde@gov.in

The system involves MWIR cooled for day/ night or SWIR for day surveillance under poor weather conditions. The camera is designed for 90 deg Field-of-regard coverage in one second which is equivalent to 25 static staring camera. Fast-steering mirror based motion deblurring mechanism is being used for achieving blur free frames from camera. The talk will cover the technologies for wide-area surveillance.

Scanning camera in IR spectral band is being used for the wide-area surveillance, detection and tracking. Such scanning camera can be used for ground based, airborne or marine environment surveillance. The main technologies involved are the Scanning camera payload with FSM based de-blur technology, high-speed image processing, frame stitching, GP-GPU/ FPAGA based hardware for detection and tracking, communication link and command control stations. A typical conceptual schematic of the system is illustrated in the figure 1. *The raw data video transmission require atleast 1.*66 Gbps bandwidth corresponding to 13-bit radiometric depth of the pixel. Thus the raw data cannot be transmitted directly over the typical tactical UAV link. The talk will cover the scanning camera technologies and high-speed link requirement.

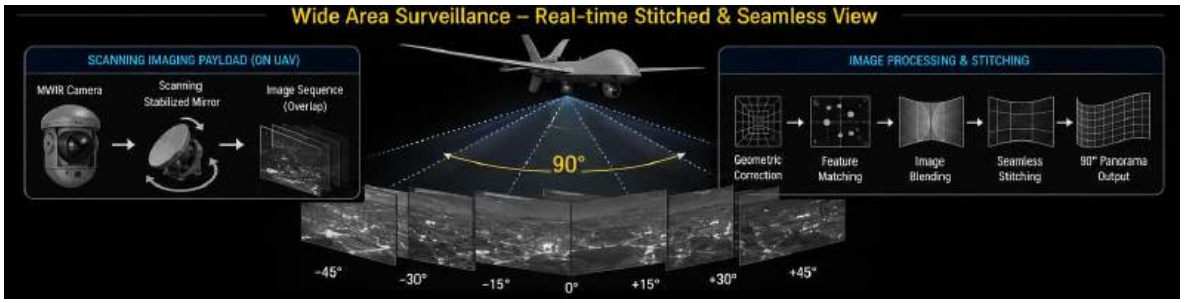


Fig. 1: Schematic of UAV based wide-area surveillance system

Typical specifications of the Scanning camera are 1280 x 1024 HD detector, 10 um pixel size, 13-bit pixel depth and video output via high-speed Camlink. Motion blur compensation is based on the Fast Steering Mirror which is integrated in the relay optics of the camera. The required acceleration of the actuators is fulfilled by the APSs suitably designed for the large stroke and high speed operation. Customized FSM and the deblurring results for two cases are shown in the figure 2. Further, GP-GPU/ FPGA hardware will take camera input through Camlink interface and the output panorama video data will be through 10G ethernet /or HDMI 2.1. Video transmission bandwidth for 5 Hz refresh rate is of the order of 1.66 Gbps which is generally a typical tactical UAV links does not support. This data rate scaleup with the number of the ground stations.

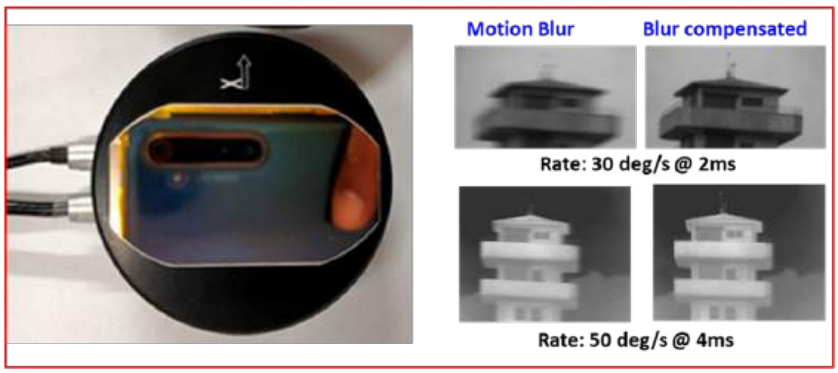


Fig. 2: Customized FSM and the deblurring results for two cases

References:

1. Edward K Huang, et al, "Recent advancements in high-definition HOT MWIR and eSWIR camera cores with 5um pixel pitch", *Proc. SPIE*, 1346900 (2025).
2. S. K. Mishra, Vikash Porwal, Sushil Chaukiyal, J. S. Rawat, and Ajay Kumar, *"Real-time deblurring of known motion blurs using optical means"*, OSI Symposium, P 400-285 (2015)

Modeling and Simulation for COIL Unstable Resonator

[1,#]A K Varshney,[1]Gaurav Singhal, [1]Jagannath Nayak and [2]Kedar Khare
[1]Centre for High Energy Systems and Sciences, Hyderabad
[2]Optics & Photonics Centre, IIT, Delhi

[#] *anujkumar.chess@gov.in*

In present work, wave optics model has been applied to calculate the intensity and phase profile at the output of the unstable resonator using Fox and Li iteration convergence for determining the optimal laser beam characteristics.

A gas laser source such as Chemical Oxygen Iodine Laser (COIL) [1] with an output power in multi-hundred-kilowatt range typically expands the laser gases supersonically into the rectangular laser cavity resulting into low laser gain coefficient ranging 0.005-0.009 cm^{-1} and cross-section more than 100 cm^2. In such a COIL source, positive branch confocal unstable resonator configuration is typically chosen as it produces in-situ a collimated output laser beam.

Wave-optics model as shown in Fig. 1 has been applied to calculate the intensity and phase profile at the output of the unstable resonator. Box represents bare laser cavity with resonator mirror separation of 2.5 m. Here, in order to model and simulate laser cavity, multiple round paths for propagation of random phase wavefront have been used in accordance with Fox and Li method, which leads to a stable cavity field profile [2]. The laser cavity and resonator mirror parameters have been incorporated in Python code. The computation window size of 30 mm x 30 mm with pixel size of 20 μm has been chosen for simulation. The angular spectrum method has been used for the propagation of field in the laser cavity.

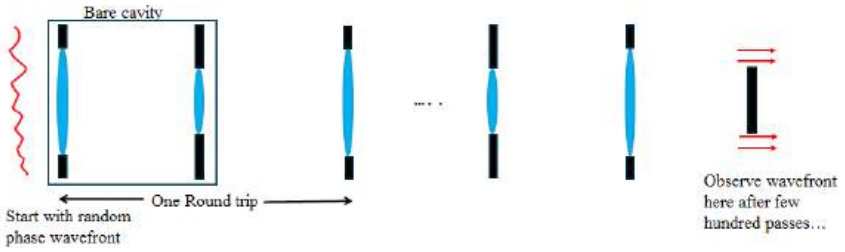


Fig. 1: Schematic of bare laser cavity and its modeling

The simulation prediction in terms of the obtained output intensity and its electric field phase are shown in Fig. 2. The intensity and phase maps after 1000 iterations are observed to converge to a circularly symmetric annular beam profile with 99% of output energy contained within 21.2 mm diameter region at the output port of the cavity for magnification of 1.7.

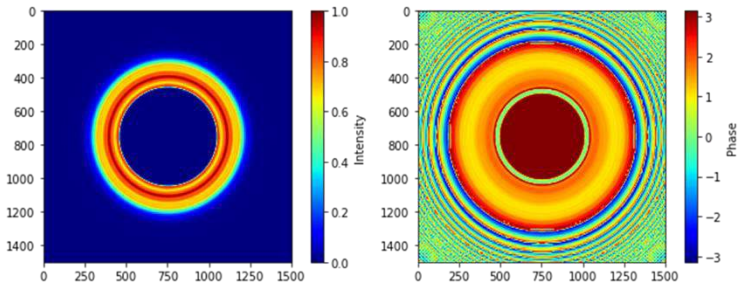


Fig. 2: Output intensity pattern and its phase after 1000 iterations for cavity design with magnification factor of 1.7

The beam quality (M^2) factor of annular beam is computed with the help of far field intensities as shown in Fig. 3 for the annular beam and the reference Gaussian beam with standard deviation equal to mean radius of annular ring [3]. We find that the confocal unstable resonator design gives an annular output laser beam with M^2 factor of ~ 1.2 at magnification of 1.7.

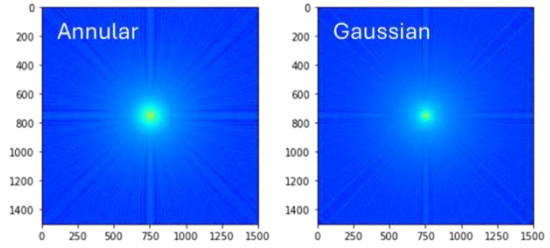


Fig. 3: Far field intensity profiles

References:

[1] A.K.Varshney, Rajeev K.Dohare, Gaurav Singhal, Mainuddin, *Defence Science Journal* 69(3), 298 (2019).
[2] A.G.Fox and T.Li, *Bell Syst. Tech.J.* 40, 453 (1961).
[3] M.H.Griessmann et. al., *Optics Continuum* 2(8), 1833 (2023).

Interferometric Approaches to Refractive Index Measurement

[#]Kanik Palodhi
Department of Applied Optics and Photonics, University of Calcutta, Kolkata-700106.
[#]Email id: kpaop@caluniv.ac.in

Abstract: *The accurate determination of the refractive index is a fundamental requirement across diverse fields, ranging from thin-film characterisation in microelectronics to the study of fluid properties in photonics. Interferometric methods are increasingly becoming the standard for such high-precision measurements, for their smarter and faster methods that combines effective computation techniques.*

Coherence Scanning Interferometry (CSI) is a robust technique for three-dimensional topographic and thickness mapping. Recent advancements demonstrate that frequency-domain analysis of CSI signals enables the simultaneous reconstruction of a sample's surface reflectivity spectrum and refractive index. By utilizing the Fresnel reflection model, this approach achieves high lateral resolution, with relative errors within ±2% compared to theoretical values, making it an effective tool for thin-film analysis.

Beyond CSI, differential white-light interferometry has been established as a precise method for the simultaneous measurement of thickness and group refractive index in transparent specimens, offering expanded uncertainties as low as $\sim 10^{-5}$ refractive index units (RIU). For specialized applications, particularly in the short-wave infrared (SWIR) region, Rayleigh interferometry has been successfully implemented to characterize the refractive index of various liquids.

A distinct and sensitive alternative involves Moiré interferometry. Studies have proposed novel techniques in which the mechanical superposition of periodic structures—such as gratings or repetitive lines—generates incoherent Moiré patterns. These patterns shift in response to changes in the refractive index of an intercepted liquid medium, providing a versatile, high-sensitivity tool for characterizing fluid properties and detecting potential adulteration.

Collectively, these interferometric strategies demonstrate a transition toward robust, multi-modal characterization tools that deliver high precision measurements of refractive indices in both industrial and research settings.

References:

1. **X. Guo and T. Guo**, "Measurement of reflectivity and refractive index based on coherence scanning interferometry," *IEEE Photonics Technol. Lett.*, vol. 38, no. 9, pp. 592-595, May 2026.
2. **X. Lu et al.**, "Simultaneous measurement of thickness and group refractive index based on differential white light interferometry," *IEEE Trans. Instrum. Meas.*, vol. 72, pp. 1-13, 2023.
3. **H.-J. Chang et al.**, "Refractive index measurements of liquids from 0.5 to 2 μm using Rayleigh interferometry," *Opt. Mater. Express*, vol. 14, no. 5, pp. 1253-1267, May 2024.
4. **S. De, J. Chatterjee, S. Chakraborty, and K. Palodhi**, "Refractive index measurements of liquids using moiré pattern," in *Recent Advancements in Photonics*, 2020.
5. **J. Coupland, R. Mandal, K. Palodhi, and R. Leach**, "Coherence scanning interferometry: linear theory of surface measurement," *Appl. Opt.*, vol. 52, no. 16, pp. 3662-3670, 2013.

Retinal display for vergence accommodation conflict elimination in augmented reality applications

[1,2,#]Raj Kumar
[1]Holography Group, Optics & Photonics Instrumentation, CSIR – Central Scientific Instruments Organisation, Sector 30C, Chandigarh 160030, India
[2]Academy of Scientific & Innovative Research (AcSIR), CSIR-HRDC Campus, Sector 19, Kamla Nehru Nagar, Ghaziabad 201 002, India

[#]*Email ID: raj.optics.csio@csir.res.in*

Augmented reality (AR) displays are finding applications across diverse areas of science, technology, healthcare, and society. When displaying 3D information, these displays suffer from the vergence-accommodation conflict (VAC), causing headache and nausea, and hindering long-term wearability. We discuss the retinal display scheme to solve the VAC issue in AR displays.

Optical displays have become an integral part of society as they are extensively used in our day-to-day life, such as television, smart boards, advertisements, personal electronic gadgets, healthcare, defence, entertainment, education, etc. Among optical displays, the augmented/ virtual reality (AR/VR) displays are the fast-emerging technologies [1]. AR displays augment the viewer's vision through mixing digital information with real-world information in the field of view of the wearer. On the other hand, VR displays provide a more immersive experience by shutting the viewer off from the real world. As AR displays provide additional information to the viewer, they are finding newer applications day-by-day and are among the world's fastest-emerging technologies of the 21st century. Due to their ability to provide personalized information to the viewer only, it is expected that AR near-eye wearable displays would replace the smartphone in the near future.

When displaying 3D information, most currently available stereoscopic AR displays suffer from vergence-accommodation conflict (VAC), a mismatch between the eye's convergence and the focal depth of the displayed image [2]. VAC causes discomfort for the wearer and may lead to fatigue and even nausea, making it difficult to wear for extended periods. A number of optical schemes, including varifocal displays, multiple depth planes, lightfield displays, retinal displays, and holography, have been developed over the years to alleviate the VAC issue. In retinal displays, the image is directly formed at the retina of the eye. Here, the light passes through the pupil of the eye by bypassing the eye's focusing system to project an image directly onto the retina, rendering perfectly sharp images. This scheme provides always focused images and therefore does not suffer from VAC.

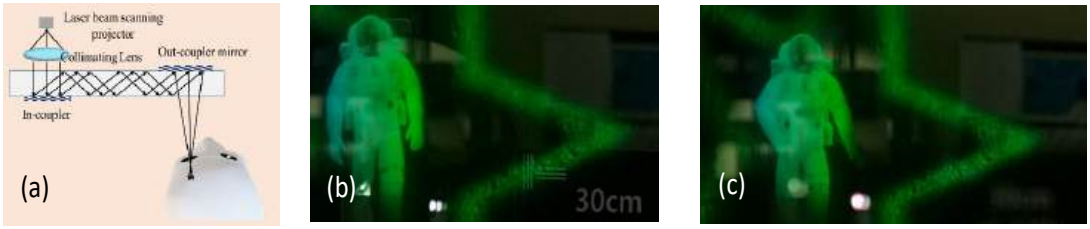


Fig. 1 (a) Scheme of retinal displays, (b) focused images at 30cm, (c) focused image at less than 30cm

The Fig. 1 shows the scheme and results of a retinal display system [3]. Here it may be noted that the digital information is in focus for different focusing distance of the photographic camera. In Fig. 1(b), the marked information, i.e., 30cm, is in focus, whereas in Fig. 1(c), it becomes defocused. This shows that retinal displays are suitable for alleviating the VAC problem in AR displays.

Acknowledgement: This work was supported by CSIR India under project FTT010506. The author thanks Prof. JH Park, Seoul National University, South Korea, for his support of this work.

References:

[1] C. Chang, K. Bang, G. Wetzstein, B. Lee, L. Gao, *Optica* 7 (2020) 1563.
[2] D.M. Hoffman, A.R. Girshick, K. Akeley, S. Banks, *J. Vis.* 8 (2008) 33.
[3] R. Kumar, M.H. Choi, R. Kaur, J.H. Park, *J. Info. Display*, 26 (2025) 483-492.

Design of a Long Working-Distance, High-Numerical-Aperture Objective Lens for Optical Trapping and Fluorescence Imaging

[1, #]Saumya Jyoti Sarkar, [1]Arjun Duhoon, [1]Surya Narayan Sahoo and [1]Ashok Kumar Mohapatra

[1]National Institute of Science Education and Research (NISER) Bhubaneswar

[#]*Email: saumya_js@niser.ac.in*

We present a custom objective lens design optimized for both the optical trapping and the high-resolution fluorescence imaging of neutral rubidium atoms at 780 nm. Achieving a high numerical aperture of 0.414 alongside a 32.6 mm working distance, the system provides diffraction-limited performance from outside the vacuum chamber.

High-numerical-aperture (NA) objectives are essential in atomic physics for confining atoms in optical traps and capturing single-atom fluorescence. Because these experiments occur under vacuum, observation requires imaging through a glass viewport that introduces significant spherical aberrations. Externally mounting the objective maximizes optical access but necessitates a long working distance and rigorous aberration correction. We present a custom external objective design that corrects for a 3.5 mm thick Pyrex viewport while balancing an exceptionally long working distance with a high NA, significantly improving upon existing designs for cold atom experiments [1,2].

Optimized for 780 nm, our Zemax simulations demonstrate an effective focal length of 39.30 mm and a practical working distance of 32.6 mm. The optomechanical assembly (Fig. 1(a)) utilizes an internally threaded barrel separated by precise spacers (5.71 mm, 30.58 mm, and 29.23 mm) to ensure accurate optical alignment. This configuration achieves an NA of 0.414, substantially outperforming comparable ex vacuo designs that typically offer NAs between 0.17 and 0.32 [1,2].

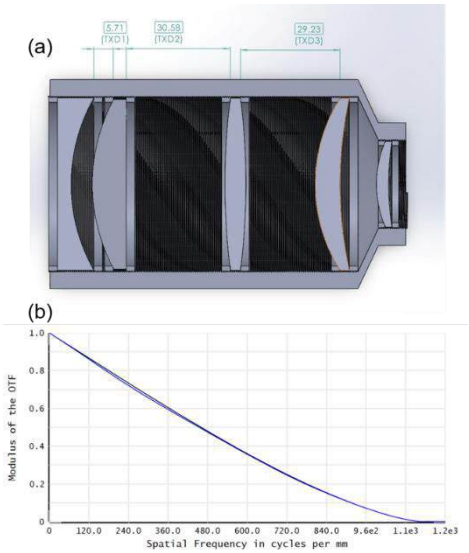


Fig 1: (a) CAD model of the objective lens assembly with precise threaded spacer distances (5.71 mm, 30.58 mm, 29.23 mm); (b) simulated MTF curve demonstrating near diffraction-limited contrast.

The system exhibits a 300 μm diffraction-limited field of view, to achieve extended atom arrays, with an Airy radius of 1.054 μm, confirming excellent diffraction-limited focusing. Furthermore, the nominal design maintains near diffraction-limited Modulation Transfer Function (MTF) contrast up to a spatial frequency of approximately 1100 cycles/mm (Fig. 1(b)).

While tolerance analysis shows MTF degrades faster than spot size under extreme alignment errors, our specified tolerances maintain the required diffraction-limited performance bounds. This objective provides a robust solution for demanding applications requiring high collection efficiency and tight focusing without sacrificing optical access. Fabrication is currently underway in our laboratory, with comprehensive optical characterization in progress to experimentally validate these results.

References:

[1] Pritchard, J. D., Isaacs, J. A., & Saffman, M. (2016). *Review of Scientific Instruments*, *87*(7).

[2] Bennie, L. M., Starkey, P. T., Jasperse, M., Billington, C. J., Anderson, R. P., & Turner, L. D. (2013). *Optics express*, *21*(7), 9011-9016.

Establishment of Luminous Flux Scale using Recently Created Facility at CSIR-NPL India

[1,2,#]Parag Sharma, [1,2]V.K. Jaiswal, [1,2]Shibu Saha, [1]Naval Manchalwar, [1]Mukul Singh
[1]Optical Radiation Metrology, CSIR-National Physical Laboratory,
New Delhi 110012, India
[2]Academy of Scientific and Innovative Research (AcSIR), Ghaziabad- 201002, India

[#]*Email: sharmap2.npl@nic.in*

Luminous flux scale has been established through recently established C-type goniophotometer with direct traceability from SI base unit candela. In sphere-spectroradiometer, scale has been realized through spectral radiant flux. Further, intercomparison of flux is done using goniophotometer and integrating sphere, and results are found within 1.5% of the reference value.

Artificial illumination is an integral part of our life. LED based lighting systems have already revolutionized the illumination technology, due to their high energy efficiency, robustness, long life and illumination and color tuneability etc. However, due to some atypical characteristics of the LEDs e.g. non-uniform illumination and color distribution, dependence of illumination characteristics on junction temperature etc., measurement systems and written standards were also updated, and still research is in progress for further improvements. The performance of the LED based lighting is evaluated through radiometric, photometric and electrical characterization. The most important parameter for illumination sources, 'luminous flux' is defined as total visible light emitted by a light source as sensed by human eye. Absolute measurement of flux is done using gonio-photometric techniques, which is expensive and time consuming, whereas quick relative measurements are performed using integrating spheres.

Presently, CSIR-NPL is creating an apex level calibration and testing facility for LED based lighting as per National/International standards [1-3]. Recently, NPL have established a C-type gonio-spectroradiometer/photometer (Fig.1(a)), a Mirror based C-type gonio-spectroradiometer/photometer (Fig.1(b)), and 2m sphere-spectroradiometer system (Fig.1(c)), as per latest international standard ANSI/IES LM-79-19 [1].





Fig. 1(a): C-type goniophotometer (b): C-type mirror goniophotometer (c): 2m Sphere-spectroradiometer

The traceability of luminous flux scale was established by calibrating the photometer of goniophotometer using luminous intensity Wi 41/G reference lamps. In case of the sphere-spectroradiometer the traceability is established through spectral radiant flux scale, which is realized using spectral irradiance scale and luminous flux scale [4]. *Further, intercomparison of luminous flux parameter is done using goniophotometers and integrating sphere, and results are found within 1.5% of the reference value.*

Acknowledgement: Authors thank Director, CSIR-NPL, for encouragement and support. Financial support from the Bureau of Energy Efficiency (BEE), India, and Council of Scientific and Industrial Research (CSIR), India, for the LED testing and calibration facility is acknowledged.

References:

[1] ANSI/IES LM-79-19, Optical and Electrical Measurements of Solid State Lighting Products.
[2] CIE S 025/E:2015 Test Method for LED Lamps, LED Luminaires and LED Modules.
[3] IS 16106: 2012 Method of Electrical and Photometric Measurements of Solid-State Lighting (LED) Products.
[4] Vijeta, N. Manchalwar, S. Saha, V.K. Jaiswal, P. Sharma, *MAPAN-JMSI* 38 (2023) 629.

Reduction of the Laser Intensity Noise for the Optical Setup of Quantum Frequency Standard

[1,2]Harupjit Singh, [1,2]Anjali Bisht, [1,2]Manoj Das,[3]Amitava Sengupta, and [1,2,#]Poonam Arora
[1]CSIR – National Physical Laboratory, New Delhi, Delhi - 110012
[2]The Academy of Scientific and Innovative Research, Ghaziabad, Uttar Pradesh - 201002
[3]The NorthCap University, Gurugram, Haryana - 122017

[#]*arorap.nplindia@csir.res.in*

We present the scheme to reduce noise in laser intensity using a commercial liquid crystal amplitude modulator (LCAM) and an in-house designed active feedback control. The setup was successfully tested by integrating into existing optical layout of NPLI-CsF1 and it significantly stabilized laser intensity in presence of cyclic thermal variation.

The operation of caesium fountain quantum frequency standard require a complex optical layout for deriving various laser beams for cooling, trapping, launching and detection of atoms [1],[2]. Therefore, the laser intensity of each beam must be stable for reliable operation of the fountain. Althought, inherently low noise lasers are used for varitey of scientific application, however, the lasers could still manifest instability in intensity due to environmental dynamics such as thermal fluctuations, mechanical vibrations etc [3]. Hence, a liquid crystal amplitude modulator was employed for laser power stabilization. While its internal feedback loop effectively suppresses laser power fluctuations over its specified operating range, the residual intensity fluctuations were still greater than the our experimental requrements. Therefore, an external active digital feedback controller was developed to achieve the fine power stabilization required for fountain operation.

Fig. 1 presents the basic schematic of the system wherein the linearly polarized laser beam was fed to LCAM for stabilizing the laser power. The input power of the laser was kept sufficient enough for covering the working range of the LCAM and the power of the stabilized beam was continuously monitored using the photodiode (PD). The PD received a tiny fraction of the collimated D1 (detection beam) laser light immediately upon its exit from the beam expander optics [4]. The PD output was amplified using transimpedance amplifier and converted to digital signal using 16 bits ADC. A 32-bit system on chip (SoC) compared PD output to a set point and generated an error. A PI-based control algorithm computed the corrected voltage using proportional and integral gains to drive a 10-bit onboard PWM chip, which generated a 10 kHz PWM output that is subsequently smoothed by a low-pass filter which is continuously fed to LCAM through a voltage buffer. The closed loop continuously performs corrections every 2 seconds (fountain cycle) for stabilizing the laser power in the detection beams. Finally, the setup was evaluated for extended hours (>12 hours) for validating the efficacy of the developed digital control system. The complete results will be presented at the time of the oral presentation.

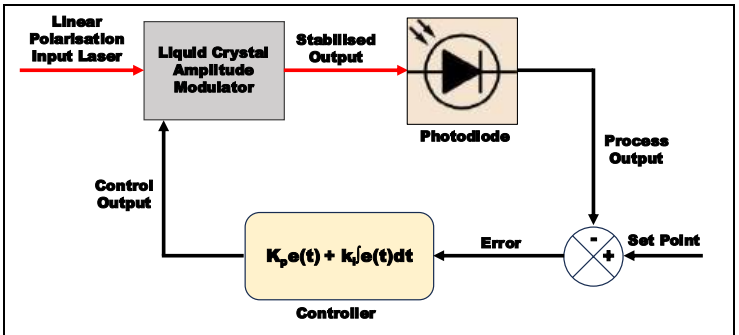


Fig. 1: The schematic of the control hardware designed and implemented

References:

[1] A. Sen Gupta, A. Agarwal, P. Arora, K. Pant, Current Science 100 (2011) 1393-1399.
[2] P. Arora, S.B. Purnapatra, A. Acharya, A. Agarwal, S. Yadav, K. Pant, A. Sen Gupta, IEEE Transactions on Instrumentation and Measurement 62 (2013) 2036-2041.
[3] Y. Wang, K. Wang, E.F. Fenton, J.D. Hood, Optics Express 28 (2020) 3120
[4] A. Bisht, M. Das, P. Arora, Atoms 13 (2025) 26.

Aspects of System Design for a Satellite based Optical Remote Sensing

Senthil Kumar M
Distinguished Scientist and Former Deputy Director
Space Applications Centre, ISRO, Ahmedabad

email: senthiliist@gmail.com

Earth observation from space provides a synoptic view and global coverage which helps in monitoring, forecasting and managing earth resources, urbanization and other activities taking place on earth. In this talk the system design aspects of a satellite based optical remote sensing having various major modules developed with contemporary approach will be presented.

Earth observation from space provides a synoptic view and global coverage which helps in monitoring, forecasting and managing earth resources, urbanization and other activities taking place on earth. In the present scenario of India's new policy on space program, a lot of private companies and startups are venturing into or actively involved in synergizing the existing business with the space program, investing in the development of technology on various satellite systems and involved in the innovation on niche segment of space technology.

Remote sensing is a method of acquiring information about an object or its phenomena without making a physical contact. The interested object or phenomena are mostly inferred by measuring some other parameter that object or phenomena exhibits rather than that itself. Observation of earth from space can be made through the measurement of properties of electromagnetic radiation interaction with its surface. The earth's atmosphere plays a significant role in the selection of electromagnetic spectrum for a sensor and also interpretation of observation (fig. 1). In general, optical remote sensing is represented by observation carried out over the wavelength span from 400 to 900 nm of electromagnetic spectrum, however in certain context it is extended into Infrared spectrum up to 13000 nm.

In this talk various parameters that form the system of an optical remote sensor having major subsystem namely optical, detector, electronics and mechanical with their salient parameters. This talk will also provide various aspects, requirements and specifications in general, needs to be complaint for a space borne optical remote sensor.

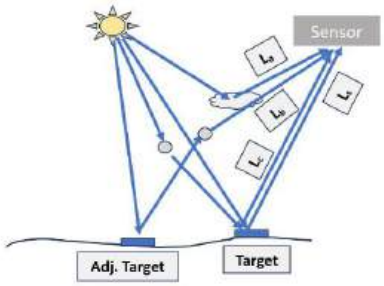


Fig. 1: Earth observation from Space

Photonics for Space Autonomy: Range and Velocity to 3D perception

Sanjay Mittal
Laboratory For Electro-Optics Systems (LEOS)
Indian Space Research Organization(ISRO)
Bengaluru, Karnataka, India-560058

skmittal@leos.gov.in

Future space missions demands increasing levels of onboard autonomy for navigation, rendezvous, docking and planetary landing and robotic exploration. High precision, low latency and information-rich sensing is therefore critical. Photonics sensing, particularly laser-based technologies, offers a unique combination of high precision, spatial resolution, compactness, making a key enables for autonomous space systems. This talk presents the evolution of laser-based space sensing from precision range and velocity measurement to multidimensional perception.

Time of Flight laser ranging provides accurate line-of-sight distance, while Laser Doppler Velocimetry enables direct and absolute measurement of relative velocity with high precision. The integration of these complementary observables through FMCW coherent LiDAR architecture enables simultaneous range and velocity measurement, enhancing relative navigation during proximity operation. Moving beyond the range and Doppler measurements, the integration of ToF range with angle information (3D LiDAR) and integration of FMCW technique with multi beam LiDAR provide dense spatial information for target detection, geometry estimation, and 6-DOF pose estimation. These capabilities are particularly relevant to autonomous rendezvous, proximity and docking operation where robust perception of target geometry and relative motion is essential for close loop guidance and control.

With successful Landing of Chandrayaan-3, India has achieved three developmental milestone of lunar exploration: Lunar Orbiting, Lunar Surface Landing and Rovering. Further ISRO has envisaged its next mission “Lunar Sample Return Mission”: Chandrayaan-4. Laser technology being employed in these missions are: (1) Laser Altimeter for altitude measurement (2) Laser Doppler Velocimeter for precise 3-axis velocity measurement (3) 3D imaging LiDAR designed for terrain mapping, Hazard Detection and Avoidance

Also, through its **SPA**ce **D**ocking **EX**periment (SPADEX) mission in 2025, ISRO has demonstrated the technology needed for spacecraft rendezvous, docking, and undocking using two small satellites in Low Earth Orbit. Further, push towards a robust autonomous rendezvous and docking (AR&D) to support a host of different mission application such as in Chandrayaan-4, Bhartiya Antrix Station and ISRO Servicing Mission (ISM), has led developments of state-of-the-art LiDAR sensors capable of providing insight to relative state (3DoF/6D0F estimation) of two spacecraft.

This talk will highlight the underlying principles, technological evolution and system level challenges associated with Laser based sensing. Talk will explore emerging directions such as 3D LiDAR, FMCW LiDAR, multidimensional 4D perception, compact photonics architectures and intelligent processing, highlighting how photonics can form sensing backbone of future autonomous space missions.

I sincerely thank Director, LEOS, for providing this opportunity to present on LiDAR technology developed at LEOS on global platform. It is a privilege to share our experiences and perspectives before such a distinguished audience. The valuable interactions, knowledge exchange and technical discussion with the expert from across the domain on this platform will further enrich our understanding and contribute to the advancement of LiDAR technologies for future space missions.

References:

[1] Francois Blais, *Journal of Electronic Imaging,*January 2004/Vol.13(1)/231-243
[2] Goodman,J., *Journal of Spacecraft and Rockets*, Vol. 43, No.5, September-October 2006, pp 944-959
[3] Andrew E Johnson, James F, Montgomery, IEEAC, Paper #1657, Version2, January 2008
[4] Cornelius J. Dennehy, *NESCT1-11-00753*, 11 April 2013
[5] Christian, J.A; Cryan, A., *Proceeding of the AIAA Guidance, Navigaion and Control Conference*; Amrican Institute of Aeronautics And Astronautics: Reston, VA, USA, 2013; P.4641
[6] Genghua Huang, Weiming Xu, *Remote Sens, MDPI*, 2024,26,4354.

Diamond-like Carbon Antireflection Coatings for Optical C-Band Applications

#Sirisha J., Sumesh M. A., Giridhar M. S. and S. P. Karanth
Laboratory for Electro-Optics System (LEOS), Indian Space Research Organisation (ISRO), Peenya Industrial Estate, Bengaluru-560058 ,

#Corresponding author e-mail id: sirisha_j@leos.gov.in

Diamond-like carbon (DLC) antireflection coatings were deposited on silicon substrates using Radio Frequency Plasma Enhanced Chemical Vapor Deposition (RF-PECVD) for optical C-band applications. Optical and structural characterization confirmed the formation of high quality coatings. Double-sided DLC enhanced maximum transmission to 94.3% at 1550 nm. The coatings passed environmental durability tests, indicating their suitability for LiDAR, silicon photonics, and space borne optical systems.

Diamond-like carbon, comprising of sp^3 and sp^2 bonded carbon, combines high hardness, chemical inertness, optical transparency, low friction, and excellent environmental durability. These properties make DLC a promising antireflection (AR) coating for reducing Fresnel reflection at the silicon-air interface in the optical C-band (1530-1565 nm), thereby enhancing optical transmission. This makes DLC attractive for various applications such as FMCW LiDAR systems [1], fiber-optic communication components [1], silicon photonic integrated circuits [2], and space-borne optical payloads [3].

In this work, DLC films were deposited on double-side-polished monocrystalline silicon and fused silica substrates, using an in-house 13.56 MHz RF-PECVD system established at LEOS, ISRO under the Make-in-India initiative, as shown in Fig. 1. The coatings were deposited using methane gas at 100 W RF power and 25 mTorr pressure at room temperature. The coating thickness was optimized for enhanced transmission in the C-band using the quarter-wave condition. Based on the measured refractive index of 1.86 at 1550 nm, an optimum thickness of approximately 208 nm was obtained.

Optical characterization in the 200–2000 nm wavelength range yielded an optical band gap of 2.28 eV as determined by Tauc's plot shown in Fig. 2. Raman spectroscopy showed D and G bands at 1355.3 cm^{-1} and 1606.4 cm^{-1}, respectively as evident from Fig. 3. The low I_D/I_G ratio of 0.56, indicates a relatively high sp^3 bonding fraction [4] and improved mechanical robustness. The anti-reflection properties of DLC were demonstrated by an enhancement in optical transmission from 56% for bare silicon to 70% after single-side coating and to 94.3% at 1550 nm after coating both surfaces, as shown in Fig. 4. Environmental qualification tests performed as per MIL-C-48497A [5], included relative humidity (55°C; 96%; 24 hrs.), thermal cycling (-75°C to 75°C ;15 cycles at 3°C / min), salt solution immersion test (NaCl: 7.5g + H_2O 1L for 24 hrs), adhesion testing (Scotch Tape Peel Test), and abrasion resistance testing (Eraser,10 strokes). Less than 1% variation was observed before and after environmental tests in optical transmission, with no visible coating damage or delamination. These results demonstrate the excellent environmental stability and mechanical durability of the DLC coatings, confirming their suitability for space-borne and harsh-environment optical applications.



Fig 1: PECVD system established at LEOS, and DLC deposited on silicon and fused silica substrate (inset)

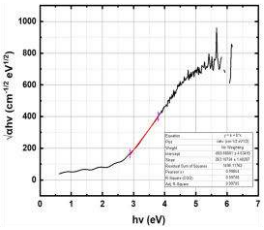


Fig. 2: Optical bandgap measurement using Tauc's plot

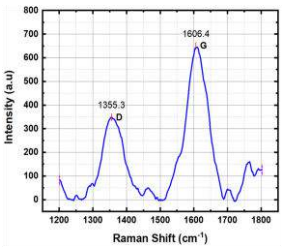


Fig. 3: Raman analysis of DLC coating deposited on Si substrate

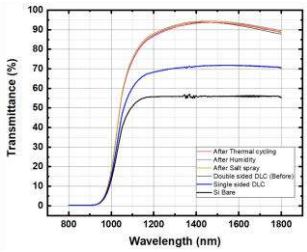


Fig. 4: Transmission spectra for uncoated silicon, single side coated and double side coated DLC (before and after environmental tests).

References:

[1] M. J. R. Heck, Nano photonics,6, 93–107 (2017).
[2] B. Jalali and S. Fathpour, *Journal of Lightdewave Technology*, 24(12), 4600–4615 (2006).
[3] J Fontaine, Proceedings of Institution of Mechanical Engineers (Journal of Engineering Tribology), 222,1015-1029 (2008).
[4] Eder. C. Oliveira, Sandra A. Cruz, Paulo H. L. Aguiar, Journal of the Brazilian Chemical Society, 23 (9), 1657-1662 (2012)
[5] Jung H. Ina, Min W. Seoa, Haeng Y. Junga, Seon H. Kima, Ju H. Choi, Infrared Sensors, Devices, and Applications IX, 11290H-1-7 (2019)

Design of Compact Multispectral Imaging System for Remote Sensing Applications

Madhavi Thakre[1]
[1]Space Applications Centre, ISRO, Ahmedabad, Gujrat – 380015

Corresponding author: madhavi.isro@gmail.com

This work presents the optical design and performance analysis of single-lens assembly for a miniaturized multispectral camera. The system is optimized to minimize chromatic aberrations while maintaining high image quality across multiple spectral bands. The designed optical system is lightweight and low cost. Performance is validated using MTF, spot size, distortion and ray-tracing analysis.

For earth observations, multi band imaging systems have significant advantages of capturing target features across multiple spectral dimensions and enhancing imaging capabilities. This paper describes the optical design of single lens assembly catering to four multi-spectral bands (B1: 450 - 520 nm, B2: 520 – 590 nm, B3: 620 – 680 nm and B4: 770 – 860 nm). The designed lens assembly (Figure 1) caters to effective focal length of 116 mm, F/No of 4.5 and 2-dimensional field of view ± 3.0° in X-direction and ± 6.4° in Y-direction. Field distributed in X-direction gives spectral coverage and in Y-direction gives spatial information.

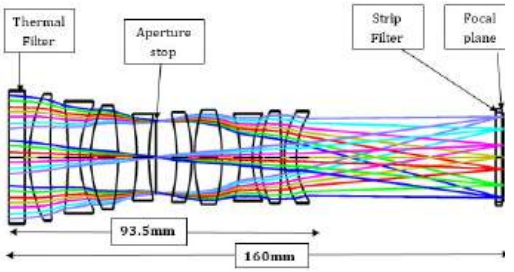


Fig 1: Optical schematic of lens assembly

The main goal of the optical design is to achieve the best image quality, both in terms of geometric and radiometric performance, having minimum package dimensions and weight. The single lens assembly with nine lens elements are used to minimize system aberrations and to get diffraction limited performance. Efforts were put to make lens design less sensitive to fabrication tolerances and thermal gradients [1, 2 & 3].

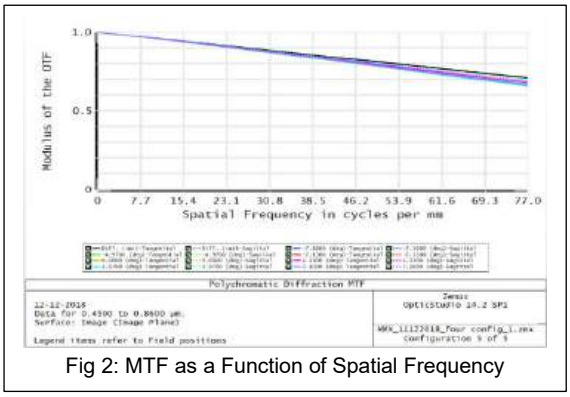


Fig 2: MTF as a Function of Spatial Frequency

Figure 2 shows the polychromatic (450 to 860 nm) design MTF curves as a function of spatial frequency for different field angles. The minimum design MTF obtained at 77 lp/mm is 65 % which is close to the diffraction limit value of 71%. The distortion of the lens assembly is extremely small, less than 0.01% over the entire spectral range of operation (Figure 3).

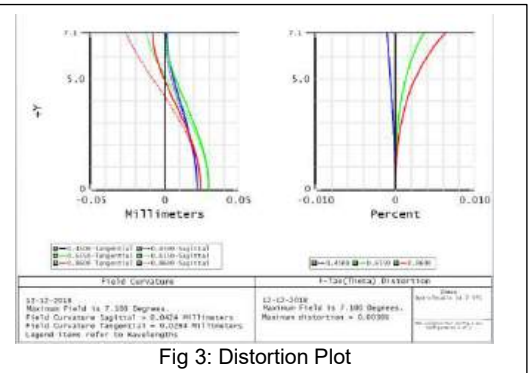


Fig 3: Distortion Plot

In conclusion, designed single lens assembly minimizes system aberrations to get diffraction limited performance. At nyquist frequency, obtained minimum design MTF is 65% which is close to diffraction limited MTF (71%) and distortion less than 0.01% over full spectral range and entire field of view.

I would like to express my sincere gratitude to Ashish Mishra, DD SEDA and S. S. Sarkar, Director, SAC for their invaluable guidence, encouragement and continuous support throughout this work.

References:

1. R. Kingslake, R Barry Johnson: Lens design fundamentals, Academic Press in an imprint of Elsevier, 2010.
2. R Sandhu, Status and trends of small satellite missions for earth observation, Elsevier, 2009.
3. J Rienstra and M Ballard, Multispectral focal plane assembly for satellite remote sensing, IEEE Aerospace conference, 1998.

Multipolar Optical Binding and Rotational Jamming in Plasmonic Optical Matter

G. V. Pavan Kumar[1,#], A. Shukla[1] and S. Boby[1]

[1]Department of Physics, Indian Institute of Science Education and Research (IISER) Pune, Dr. Homi Bhabha Road, Pune 411008, Maharashtra, India

[#]*pavan@iiserpune.ac.in*

We examine how plasmonic optical matter is assembled and driven by light. Generalized multiparticle Mie theory reveals that multipolar mode symmetry governs binding-force nodes and dimer stiffness, while experiments on chiral-light-driven assemblies show a symmetry-loss transition that arrests rotation, a rotational jamming analogue relevant to optical micromachines.

Optical matter (OM) is a non-equilibrium phase in which light-induced interactions bind free-standing particles into ordered, reconfigurable assemblies. Metallic nanoparticles are attractive building blocks, because plasmon resonances amplify both the scattering that mediates optical binding and the momentum light deposits on the assembly. Two questions govern how far such systems can be pushed towards functional micromachines: what sets the interparticle force landscape beyond the point-dipole limit, and what happens to that order once the assembly is driven to rotate. We address both, combining electrodynamic calculations of optically bound gold nanoparticle (AuNP) pairs with experiments on assemblies driven by chiral light.

Optical binding of AuNPs has conventionally been treated within the Rayleigh limit using dipole approximations. For particles in the 100-500 nm range, however, the dipole approximation is insufficient and a complex landscape of multipolar resonances must be considered, which can in turn be leveraged to engineer richer forms of optical matter. Using generalized multiparticle Mie theory, we compute the optical binding force landscape experienced by a pair of AuNPs, and evaluate the total binding forces together with the mechanical trap stiffness

$$k_i = -\,\mathrm{d}F_i / \mathrm{d}i \tag{1}$$

at the specific resonance wavelengths where the electric dipole, quadrupole and octupole modes reach their respective scattering peaks and dominate the mechanical response. We find that the symmetry of the driven plasmonic mode greatly influences the spatial distribution of zero-force nodes and the rigidity of the optically bound dimer, so that the equilibrium separations and the stiffness holding the pair together can be selected by wavelength alone.

Scaling from a pair to a crowded assembly introduces a distinct constraint. Circularly polarized light carries spin angular momentum (SAM) that is transferred to a plasmonic OM assembly and sets it into rotation, the mechanism behind optical micromachines for plasmofluidics and soft robotics. Through experiments supported by numerical simulations, we find assemblies with well-defined hexagonal or triangular symmetry that efficiently harness the SAM of the incident chiral light, resulting in stable rotation. As the assembly grows and its dimensions approach the beam waist, however, newly recruited particles disrupt this order. The system crosses into a fluid-like state of less well-defined symmetry, correlated with a substantial reduction in transferred torque, causing rotation to stagnate or cease. We interpret this arrest as analogous to a jamming transition, with crowding competing directly against optical driving.

Taken together, the two studies connect structure to mechanics across scales: multipolar mode symmetry fixes the binding landscape at the level of a particle pair, while assembly symmetry fixes the capacity to harness SAM at the collective level. This provides a mechanical framework for programmable metafluids and reconfigurable micromachines, and identifies the dynamic regimes in which optically driven assemblies are susceptible to jamming.

The authors acknowledge financial support from the Indian Institute of Science Education and Research (IISER) Pune, and thank members of the Photonics and Optical Nanoscopy Laboratory for discussions.

References:

[1] A. Shukla, S. Boby, R. Chand, G. V. Pavan Kumar, *ACS Photonics* 13 (2026) 1919-1929.

[2] A. Shukla, S. Boby, G. V. Pavan Kumar, *J. Opt. Soc. Am. B* 43, 7 (2026).

Spin Orbit Interaction and Weak measurements in Plasmonic Metasurfaces

[,#]Nirmalya Ghosh
Department of Physical Sciences, IISER Kolkata

[#nghosh@iiserkol.ac.in](mailto:nghosh@iiserkol.ac.in)

Intriguing Spin orbit interaction (SOI) of light and Rashba-like spin-split dispersion of leaky surface plasmon modes observed in a symmetric plasmonic metasurface will be discussed. Realization of the quantum mechanical concept of weak measurements and weak value amplification using the platform of SOI metasurfaces will also be presented.

Spin (SAM) and orbital angular momentum (OAM) of photons are usually ascribed to the quantum nature of light. However, classical light beams can also carry both SAM and OAM, which are associated with circular / elliptical polarization and phase vortex, respectively. Thus, the evolution of polarized light beam in curved trajectory mimics the spin orbit interaction (SOI) effects of a massless spin 1 particle (photon). In this talk, I shall present some of our recently observed intriguing SOI effects of classical light beam, photonic spin-momentum locking and spin-split dispersion in plasmonic metamaterials etc. Specifically, I shall present our recent findings on an unconventional spin orbit coupling phenomenon revealing an unusual Rashba-like spin splitting of leaky surface plasmons in an *inversion-symmetric* plasmonic metasurface. I shall also illustrate how the extraordinary quantum mechanical concept of weak measurement and weak value amplification (WVA) can be formulated within the realm of classical optics and discuss its implementation for the amplification of weak SOI effects. In this regard, some other interesting manifestations of weak measurements in the classical optics domain realized using different degrees of freedom of light, will be presented. These include realization of WVA in standard path interference, natural WVA of Faraday effect in spectral domain interference of Fano resonance in magneto-plasmonic crystals, measurement of joint weak value and the emergence of position-position classical entanglement of light. Finally, I shall discuss how these advancements in the domain of SOI and weak measurements are fostering a new paradigm in photonics, enabling next-generation "quantum-inspired" nanophotonic meta-devices.

References:

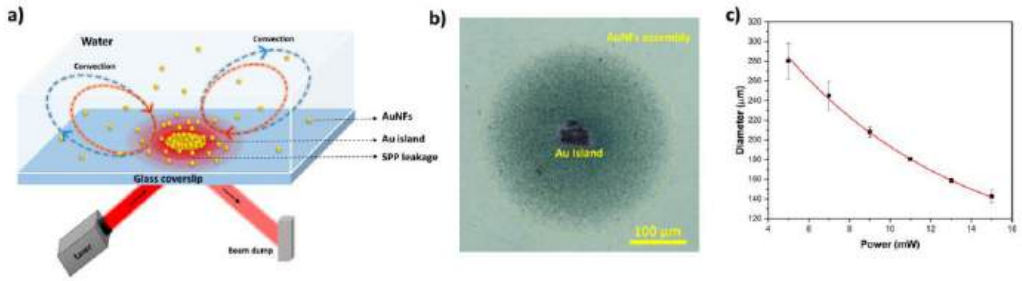
1. JK Nayak et al, *Physical Review Letters* 131 (19), 193803 (2023).
2. R. Dhara et al, Physical Review A 112, 023524 (2025).
3. JK Nayak et al, Applied Physics Letters 126, 030501 (2025)
4. N. Modak, et al, Physical Review A 110 (2), 023528 (2024).
5. N Modak et al, Laser & Photonics Reviews, 17 (9) 2300166 (2023).
6. JK Nayak et al, Communications Physics, 4, 102 (2021)
7. S. Bhunia et al, Science, Vol 373, 6552, 321-327 (2021).
8. SK Ray et al, ACS Nano, 11, 1641-1648 (2017).

Detection of Surface Plasmon Polariton leakage via nanoparticle assembly

J. S. Shyambhargav[a], K. S. Mahadeva Prasad[a], Rajeev K. Sinha[b], Aseefhali Bankapur[a]*
[a] Department of Atomic and Molecular physics, Manipal Academy of Higher Education, Manipal 576104, Karnataka, India
[b]Department of Physics, Birla Institute of Technology, Mesra 835215, Ranchi, India
asif.bankapur@manipal.edu

The leakage of surface plasmon polaritons (SPPs) and its behavior beyond the metal-dielectric interface represents a significant advancement in photonics, enhancing near-field studies. By leveraging nanoparticle (NP) assemblies driven by SPP forces, we successfully manipulated these assemblies on gold islands. Our results demonstrate that gold nanoflowers (AuNFs) assembly can extend beyond the metal boundary and be regulated by excitation power, contributing to progress in photonics and subwavelength investigations.

Surface plasmon polaritons (SPPs) are surface-bound electromagnetic waves that propagate along metal–dielectric interfaces and generate highly confined near fields, enabling applications in sensing, nanomanipulation, and surface-enhanced Raman scattering (SERS). Understanding their behaviour beyond the metal boundary remains challenging. In this work, we investigate the leakage of SPPs and their role in guiding nanoparticle (NP) assemblies beyond the metal–dielectric interface. A dove-prism-based Kretschmann configuration was employed to excite SPPs at a gold–water interface using a 785 nm laser. Gold nanoflowers (AuNFs) synthesized via a chitosan-mediated reduction method were assembled on Au islands. Under laser excitation, nanoparticles assembled at the illumination spot due to the combined effects of fluid convection and SPP-induced trapping forces. Similar to the assemblies on continuous gold films, the assemblies on Au islands was observed but extended beyond the metal boundary onto the surrounding glass surface, indicating SPP leakage and possible nanoparticle-assisted plasmon propagation.



Systematic experiments performed at excitation powers between 5 and 15 mW revealed that the assembly size decreases with increasing power, exhibiting an exponential dependence on Au islands, while planar films showed a linear trend. Lower powers produced loosely packed assemblies, whereas higher powers resulted in compact structures with reduced interparticle spacing. Electromagnetic (EM) simulations further support the experimental observations, showing that leaked SPP fields can extend several micrometers beyond the island edge and guide nanoparticles through localized field gradients and interparticle plasmon coupling. The assemblies also demonstrated dynamic and reversible behavior, dispersing when the laser was turned off and reforming upon re-excitation. These findings provide experimental and computational evidence of SPP leakage and nanoparticle-guided plasmon propagation, offering new insights into plasmonic field distribution and enabling controlled nanoparticle manipulation for advanced near-field photonic applications.The abstract could end with a concluding paragraph and a statement on acknowledgements.

References:

[1] M. Riswan, E. Widianto et al, “Tuning optical properties of Au thin film using electric field for surface plasmon resonance biosensor application,” Opt Mater (Amst), vol. 150, (2024).
[2]C. Ghanashyam, R. K. Sinha, and A. Bankapur, “Surface-Plasmon-Polaritons for Reversible Assembly of Gold Nanoparticles, In Situ Nanogap Tuning, and SERS,” Small Methods, (2023).
[3] P. P. Patra, R. Chikkaraddy, R. P. N. Tripathi, A. Dasgupta, and G. V. P. Kumar, “Plasmofluidic single-molecule surface-enhanced Raman scattering from dynamic assembly of plasmonic nanoparticles,” Nat Commun, vol. 5, (2014).
[4] M. Y. Deng and X. Zhu, “A historical overview of nano-optics: From near-field optics to plasmonics,” Chinese Physics B, vol. 33, no. 5, (2024).

Detection of small molecules Using a Plasmonic Chip on an Optical Fiber Microfluidic Platform

[1,#]Vivek Semwal and Jakob Janting[2]
[1]Manipal Institute of Applied Physics, Manipal Academy of Higher Education (MAHE), Manipal- 576104, Karnataka, India
[2]DTU Electro, Department of Electrical and Photonics Engineering, Technical University of Denmark, 2800 Kongens Lyngby, Denmark

[#]*corresponding author: vivek.semwal@manipal.edu*

In this study, we developed a label-free plasmonic biosensor chip that can detect PFOA in real-time. A microfluidic chamber was used to increase precision and stability.

Perfluorooctanoic acid (PFOA) is a perfluorinated compound used as a surfactant in various industries [1]. It is a carcinogenic compound that can induce serious diseases, such as liver damage, thyroid hormone secretion, immune system damage, and brain damage, and is also responsible for cancers of the liver, testicles, and prostate [1,2]. Therefore, it is important to detect PFOA with a high sensitivity. Existing traditional technologies for detecting PFOA, such as high-performance liquid chromatography (HPLC), high-performance liquid chromatography-mass spectrometry (HPLC-MS), and gas chromatography-mass spectrometry (GC-MS) have several limitations [3]. They are expensive, time-consuming, and require extensive pre-treatment steps. In addition, these are off-site analyses available only in professional laboratories. Therefore, a highly sensitive sensor is required for PFOA detection. The sensing principle is based on localized surface plasmon resonance (LSPR) [3]. Aptamers have been used to capture PFOA molecules because they have several advantages, such as high affinity and selectivity, binding to a broader range of targets including small molecules, higher purity, superior stability, and lower production price [4]. The PFOA aptamers were immobilized on a gold nanoparticle (AuNP)-coated glass coverslip through a thiol chemical bond, and the chip was fixed inside the microfluidic chamber using adhesive tape. The microfluidic chamber was connected to a pump to dispense a controlled amount of analyte. The microfluidic chamber was fixed inside a modified Ocean Optics cuvette holder to record absorbance spectra. Inside the chamber, PFOA molecules were captured by PFOA aptamers. Therefore, the effective RI around the AuNPs changes, which changes the resonance wavelength of the AuNPs. The experimental setup is shown in fig.1, consists of a light source, modified cuvette holder with homemade fixtures, optical fiber cables to send and receive the light, microfluidic chamber, peristaltic pump, and spectrometer. In this study, we used a microfluidic chamber because it provides various benefits, such as reduced sample volume, multiple microchannels preventing cross-contamination, reduced system size, and improved LSPR signal [4]. We presented a microfluidic fiber-optic plasmonic chip platform for PFOA sensing. We demonstrated PFOA sensing at 100 µM and 500 µM concentrations. The preliminary results demonstrate good sensing capability of the fiber-optic microfluidic LSPR setup.

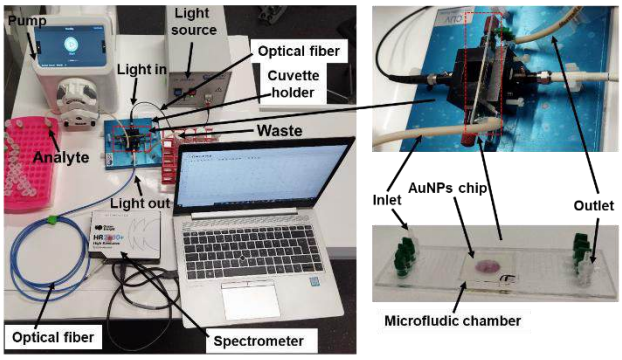


Fig. 1: Experimental setup

References:

[1] H. Park, J. Park, W. Kim, W. Kim, J. Park, "Ultra-sensitive SERS detection of perfluorooctanoic acid based on self-assembled p-phenylenediamine nanoparticle complex," J. Hazard. Mater. 453 (2023) 131384.
[2] E.T. Chang, H.O. Adami, P. Boffetta, H.J. Wedner, J.S. Mandel, "A critical review of perfluorooctanoate and perfluorooctanesulfonate exposure and immunological health conditions in humans," Crit. Rev. Toxicol, 46 (2016) 279-331.
[3] K. Saito, E. Uemura, A. Ishizaki, H. Kataoka, "Determination of perfluorooctanoic acid and perfluorooctane sulfonate by automated in-tube solid-phase microextraction coupled with liquid chromatography–mass spectrometry," Anal. Chim. Acta. 658 (2010) 141–146.
[4] S. Kastner et al., "LSPR-Based Biosensing Enables the Detection of Antimicrobial Resistance Genes," Small (2023) 2207953.

Parametric fluorescence, amplification and autocorrelation: A Beginner's perspective

Prem B Bisht

Department of Physics, Indian Institute of Technology, Madras, Chennai, 600 036, India

bisht@iitm.ac.in

This talk will present the basics of the parametric processes and bring out the correlations of their use in quantum optics, tunable ultrafast lasers and their characterisation techniques.

In the parametric process of difference frequency generation (DFG)., the pump photon ω_p splits in to two frequencies known as signal (ω_s) and idler (ω_i) depending on the type of the crystal (fig. 1, left panel). Following this, the interesting world of quantum optics opens up as the properties of the the latter two photons are correlated with each other. The phenomenon of DFG is related to spontaneous parametric down conversion (SPDC) and optical parametric amplifiers (OPA). In OPA, a weak signal beam with frequency spectrum around ω_s is amplified along with the generation of an idler beams of frequency ω_i when pumped with a fixed pump frequency ω_p.

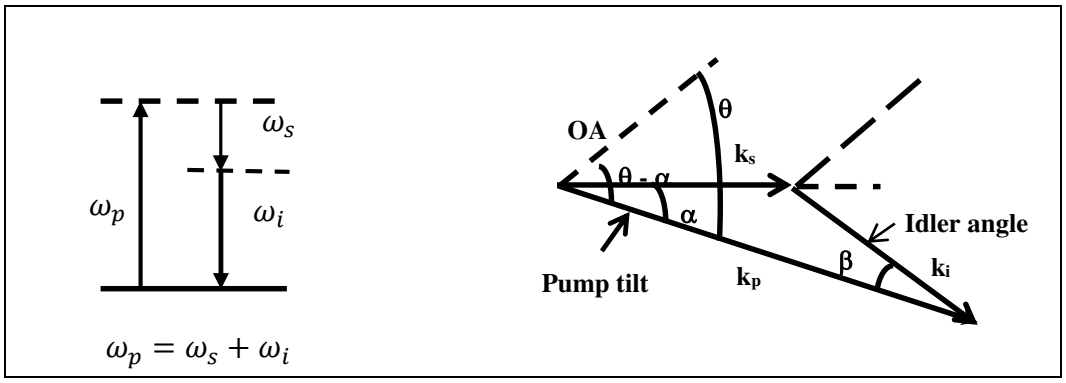


Fig.1. Energy level diagram for the case of DFG and SPDC (Left panel); OPA process on the right panel. OA is the optic axis. k_p, k_s and k_i are the wave vectors of pump, single and idler beams.

In a simple experimental schematic (fig. 1 , right panel) based on the phase matching angle of the $\chi^{(2)}$ material, temporal and spatial overlap of the pump and signal beams interacting at an angle (α), OPA process can be used to obtain tunable, intense femtosecond pulses. On the other hand in SPDC, since the generated frequencies are strongly correlated and are entangled, it can be used for imaging at low photon numbers without damaging the samples. This also is helpful in improving signal to noise ratio beyond the shot noise of electronic. A special case of sum-frequency generation (SFG) is autocorrelation measurement, which stands in contrast to coincidence measurements performed in a Hong–Ou–Mandel (HOM) setup. These interrelated terms will be discussed in this lecture.

Photonic Crystal Fibers: Designing Fibers, Active and Nonlinear Fiber Devices

Partha Roy Chaudhuri
Department of Physics, IIT Kharagpur, Kharagpur- 721 302, India

Email: roycp@phy.iitkgp.ac.in

Photonic crystal fibers offer remarkable flexibility for tailoring modal confinement and propagation characteristics through their microstructured geometry. A finite-difference-based numerical approach is presented for designing PCFs and active fiber devices. An optimized Er^{3+}-doped triangular-lattice PCF amplifier demonstrates spectral gain exceeding 51 dB using a fiber length of approximately 2.5 m.

Photonic crystal fibers (PCFs) offer unusual propagation characteristics and extensive design flexibility for realizing advanced fiber devices. Their optical properties can be tailored through geometrical parameters such as air-hole diameter, pitch, core size, and material distribution. Accurate determination of electromagnetic propagation characteristics is therefore essential for PCF design. A finite-difference (FD) mode-convergence approach is employed to determine the modal field distribution, effective refractive index, effective mode area, and related propagation characteristics. As a representative application, an Er^{3+}-doped triangular-lattice PCF amplifier is investigated by varying geometrical and operating parameters. The designed PCF amplifier host is shown in Fig. 1(a). Tailoring the PCF geometry enables control of effective numerical aperture, modal confinement, and pump and signal field overlap with the Er^{3+}-doped region. The modal characteristics obtained from FD analysis are incorporated into standard population and propagation rate equations to evaluate amplifier performance.

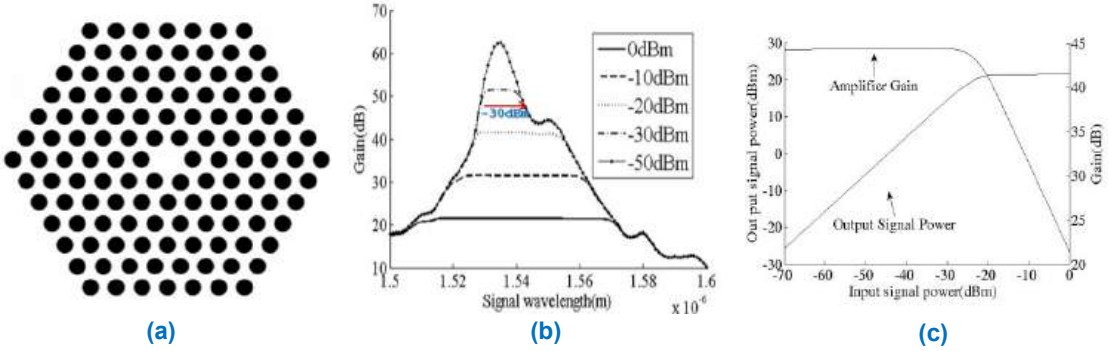


Fig. 1: (a) Designed triangular-lattice PCF structure considered as the Er^{3+}-doped amplifier host; (b) gain spectrum at different input signal powers and (c) output signal power and amplifier gain as functions of input signal power

The calculated amplifier characteristics are illustrated in Figs. 1(b) and 1(c). The gain spectrum shows strong amplification in the communication wavelength region and its dependence on input signal power. As the input signal power increases, the output power initially increases while high gain is maintained. At higher signal powers, depletion of population inversion reduces the gain, eventually leading to amplifier saturation. These results demonstrate the importance of optimizing the PCF geometry and operating conditions for efficient amplification. Optimization of the PCF parameters shows that a spectral gain exceeding 51 dB can be achieved with an Er^{3+}-doped PCF length of approximately 2.5 m. Other important all-fiber characteristics, including beam divergence, bending loss, nonlinearity, and splice/coupling loss, are also evaluated. Tailoring the PCF geometry improves mode matching with standard telecom-grade SM28/G.652 fiber and considerably reduces splice loss without compromising amplifier gain. The numerical methodology thus provides a useful framework for designing compact, high-performance PCF-based active fiber devices.

References:

[1] K. Mondal, P. Roy Chaudhuri, *Optics & Laser Technology* 43 (2011) 1436–1441.
[2] P. Roy Chaudhuri, A.K. Ghatak, B.P. Pal, C. Lu, *Optics and & Laser Technology* 37 (2005) 61-67.
[3] K. Mondal, P. Roy Chaudhuri, *Journal of Modern Optics* 60 (2013) 1247-1252.
[4] P. Roy Chaudhuri, V. Paulose, C. Zhao, C. Lu, *IEEE Photonics Technology Letters* 16 (2004) 1301-1303.

All-optical anti-skyrmions and anti-merons in Difference frequency generation

[1,#]Arannya Ghosh,[1]Mukesh K. Shukla and [1]Ritwick Das
[1]Optics and Photonics Centre, Indian Institute of Technology Delhi, Hauz Khas New Delhi,110016

[#]*arannya.ghosh@opc.iitd.ac.in*

The paraxial difference frequency generation (DFG) process, which could be modelled as a two-level atomic system interacting with laser field, exhibits an anti-$\mathcal{PT}$ symmetric dynamics. In the broken anti-$\mathcal{PT}$ symmetric phase, we show the existence of nontrivial antiskyrmionic and antimeronic pseudo-magnetization textures for negative phase-mismatched and phase-matched DFG interactions.

Skyrmions represent topological quasiparticles that are in a stable equilibrium in an excited state and were initially conceptualized within the realm of nuclear physics by T. Skyrme [1]. Subsequently, it has been incorporated in the field of spintronics owing to its significant applications in racetrack memory, neuromorphic computing, and construction of robust spin-valves [2]. Optical skyrmions, antiskyrmions, and merons, have been introduced in the context of spin-orbit coupling, utilizing the polarization degree of freedom. In this paper, we demonstrate an anti-skyrmionic pseudo-magnetization texture in a paraxial difference-frequency-generation (PDFG) process where signal and idler modes constitute the basis.The interaction Hamiltonian of PDFG process in Fourier space could be expressed as

$$\tilde{H} = \begin{pmatrix} h_z & h_x + ih_y \\ -h_x + ih_y & -h_z \end{pmatrix}$$

Where, $h_x = -\left|\tilde{\kappa}\right| cos\phi, h_y = \left|\tilde{\kappa}\right| sin\phi, h_z = 4\pi^2 f^2 + \Delta k'/2$ and coupling coefficient $\left|\tilde{\kappa}\right|$ is proportional to Fourier transform of pump amplitude ($\tilde{A_p}$), while $\Delta k'$ is the normalized phase mismatch and $f^2 = f_x^2 + f_y^2$with f_x, f_y being the spatial frequencies along x, y directions respectively. The non-Hermitian Hamiltonian $\tilde{H}$ exhibits an anti-$\mathcal{PT}$ symmetric character [3]. In the broken anti-$\mathcal{PT}$ symmetric region where the eigen spectrum is real, the Skyrmion number is defined through $N = \frac{1}{4\pi}\int_0^\infty df \int_0^{2\pi} d\phi \hat{h}.(\partial_f \hat{h} \times \partial_\phi \hat{h})$. This could be simplified through the characteristics of spatial beam structure which turns out to be $N = 1/2[1 - sgn(\Delta k')][\,4]$. Therefore, for negative phase mismatch, we obtain $N = 1$ and for a phase-matched interaction, we got $N = 1/2$, that essentially manifests as anti-skyrmionic and anti-meronic pseudo-magnetisation textures. We explore this via an experimental configuration where a paraxial DFG is carried out in a periodically-poled lithium tantalate crystal pumped by a green beam ($\lambda_p = 532nm$) with a signal beam of $\lambda_s = 820nm$, that generates idler with $\lambda_i = 1515nm$ [5]. At a cystal temperature of $200℃$, for a grating period of $\Lambda = 7.77\ \mu m$ the pseudo-magnetization vector shows the anti-skyrmion texture which corresponds $\Delta k' = -0.004$(see Fig.1(a)). At the same crystal temperature, $\Delta k' = 0$ is achieved when $\Lambda = 8.22\ \mu m$ and this corresponds to an anti-meronic pseudo-magnetisation texture (Fig. 1(b)). Positive phase mismatch such as $\Delta k' = 0.002$ ($\Lambda = 8.5\ \mu m$) is a signature of trivial topology (or N = 0) (see Fig.1(c)).Here, we have shown that a paraxial DFG process, under the undepleted pump approximation, could give rise to the nontrivial anti-skyrmionic (for negative phase mismatch) and antimeronic (for perfect phase match) pseudo-magnetization textures in the anti- $\mathcal{PT}$ broken symmetry spectrum which corresponds to purely real eigenvalues of the non-Hermitian system Hamiltonian.

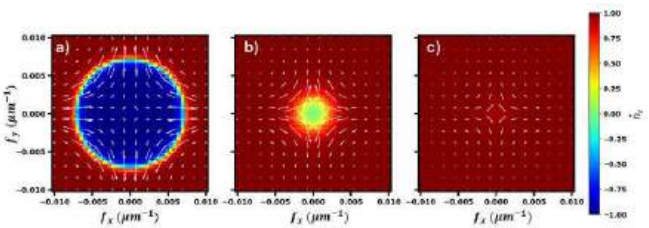


Figure 1 (a) shows antiskyrmion (b) shows anti meron (c) shows trivial skyrmionic textures.

References:

[1] T. Skyrme, Nucl. Phys. 31, 556 (1962).
[2] A. Fert, N. Reyren, and V. Cros, Nat. Rev. Mater. 2, 17031 (2017).
[3] C. M. Bender and S. Boettcher, Phys. Rev. Lett. 80, 5243 (1998).
[4] M. Lin, L. Du, and X. Yuan, IEEE Photonics J. 15, 1 (2023).
[5] G. Kulkarni, J. Rioux, , et al., Phys. Rev. Res. 4, 033098282 (2022)

Kramers–Kronig Receiver for Direct-Detection Measurement of Fiber Kerr Nonlinearity

[1,2,#]Priyanshu Kumar Pandey, [1,3]Kritarth Srivastava, [1,3]Dixit Kumar and [1,2,3]Amol Choudhary
[1]UFO-CHIP Group, IIT Delhi
[2]Bharti School of Telecommunication Technology and Management, IIT Delhi
[3]Department of Electrical Engineering, IIT Delhi
#priyanshu.kumar.pandey@dbst.iitd.ac.in

We demonstrate phase-sensitive measurement of the fiber Kerr coefficient using a direct-detection Kramers–Kronig receiver. A receiver-side optical pilot enables complex-field recovery of a propagated three-tone probe from a single photodiode waveform. The launched-power slope of the recovered differential phase yields γ values matching expected fiber specifications at milliwatt powers.

Fiber Kerr nonlinearity is a key parameter in predicting power-dependent impairments in optical links, but its measurement normally benefits from access to optical phase. This work shows that the required phase information can be obtained without a coherent front end. A three-tone optical probe is transmitted through the fiber under test, combined with a detuned optical pilot at the receiver, and detected using a single photodiode. Kramers–Kronig (KK) digital processing then reconstructs the complex field, allowing the carrier and sideband phases to be used for nonlinear coefficient extraction [1].

An intensity modulator generates the three-tone probe near 1550 nm with first-order sidebands at ±2 GHz. After propagation through the FUT, the received signal is combined with a receiver-side pilot offset by about −10 GHz.

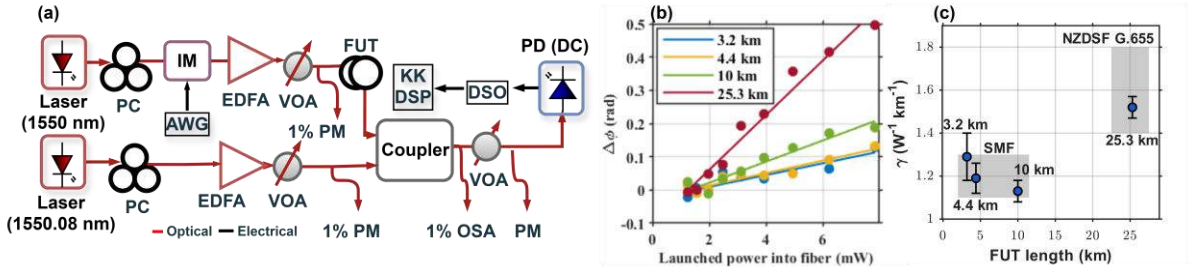


Fig. 1: (a) KK Receiver direct-detection γ-measurement chain. (b) Differential phase Δϕ vs. launched power for different fiber spans; solid lines show linear fits. (c) Extracted γ for SMF and G.655 fibers with error bars and expected fiber-class ranges.

A pilot-to-signal power ratio of about 14–15 dB maintains the minimum-phase condition needed for KK reconstruction [2]. The recovered tone phases are combined as $\Delta\phi = \phi_{usb} + \phi_{lsb} - 2\phi_{carrier}$. where ϕ_{usb}, ϕ_{lsb}, and $\phi_{carrier}$ are the upper-sideband, lower-sideband, and carrier phases respectively. This differential phase suppresses common phase drift and retains the Kerr-induced phase contribution. In the weakly nonlinear regime, $\Delta\phi$ varies linearly with launched carrier power P_0. At fixed f a linear fit $\Delta\phi \approx sP_0 + c$ gives [3]

$$s = \gamma L_{eff} K_{eff}\,, \quad \gamma = s/\left(L_{eff} K_{eff}\right) \tag{1}$$

where, $c = \beta_2(2\pi f)^2 L$, $L_{eff} = (1 - e^{-\alpha L})/\alpha$ and s is the slope. $K_{eff} = 2 + \sqrt{r_-/r_+} + \sqrt{r_+/r_-}$ is the effective correction factor (dimensionless; ≈ 4 for symmetric, chirp-free case) where, r± are the sideband-to-carrier power ratios. Because the extraction uses the slope rather than the absolute phase offset, static KK phase constants, filtering phase and small chirp-induced offsets do not dominate the final γ estimate.

Experiments were performed on 3.2, 4.4, and 10 km SMF spans and a 25.3 km G.655 span over 1–8 mW launched power. The extracted γ values were 1.29±0.11, 1.19±0.07, and 1.13±0.05 $W^{-1}km^{-1}$ for the SMF spans, and 1.52±0.05 $W^{-1}km^{-1}$ for the G.655 fiber. The consolidated $\Delta\phi$-power trends show clear linearity, and the extracted values lie within the expected fiber-class ranges.

The result establishes that coherent reception is not required for three-tone Kerr-coefficient metrology. By moving phase recovery into KK-DSP while retaining a single-photodiode front end, the method offers a compact and practical route for nonlinear fiber characterization, laboratory validation, and field-oriented γ measurement.

Acknowledgement: Department of Telecommunication (DoT), India, through the Advanced Optical Communication Testbed.

References:

[1] P.K. Pandey, K. Srivastava, D. Kumar, A. Choudhary, Optics Letters 51, 2860-2863 (2026), doi:10.1364/OL.599867.
[2] A. Mecozzi, C. Antonelli, M. Shtaif, Optica 3, 1220-1227 (2016).
[3] G.P. Agrawal, Nonlinear Fiber Optics, 6th ed., Academic Press, Oxford (2019).

Metalenses for Advanced Wavefront Engineering: From Achromatic Imaging to Sub-Diffraction Nanofabrication

[1,#]Tapajyoti Das Gupta, Santanu Mondal, Shubham Meena, S Ramnistahnth and Jerin Geogy
LANSPE, IAP IISC Bangalore

[#]tapajyoti@iisc.ac.in

Metasurfaces have emerged as a transformative platform for manipulating light using ultrathin arrays of subwavelength nanostructures, enabling compact optical components with unprecedented control over phase, amplitude, and polarization. Among these, metalenses have attracted significant attention as lightweight alternatives to conventional refractive optics, with applications spanning imaging, sensing, augmented reality, optical communications, and nanofabrication. In this talk, I will present our recent advances in the design, optimization, and application of dielectric metalenses operating in the visible and infrared spectral regions. Particular emphasis will be placed on super-oscillatory metalenses capable of generating sub-diffraction focal spots beyond the conventional diffraction limit. I will discuss the underlying design principles, optimization strategies, and the trade-offs between resolution, efficiency, and fabrication complexity. The integration of metalenses into emerging optical systems, including high-resolution lithography, computational imaging, and photonic devices, will also be highlighted. These results demonstrate the potential of metasurface optics to bridge fundamental wavefront engineering and practical optical technologies, paving the way for next-generation miniaturized and multifunctional photonic systems..

Metasurfaces have revolutionized optical wavefront control by enabling ultrathin optical elements that can manipulate the phase, amplitude, and polarization of light with subwavelength precision. Among these devices, metalenses have emerged as a powerful alternative to conventional refractive optics, offering compactness, multifunctionality, and compatibility with integrated photonic systems. In this talk, I will present our recent research on dielectric metalenses spanning imaging, beam shaping, and nanofabrication applications.

The presentation will begin with our work on high-efficiency visible-wavelength metalenses, including a bilayer achromatic RGB metalens architecture that mitigates chromatic aberrations while maintaining high focusing performance across the red, green, and blue spectral bands. The design exploits multilayer metasurface engineering to achieve broadband wavefront control and improved fabrication tolerance, providing a pathway toward compact imaging and display systems.

I will then discuss our investigations into super-oscillatory metalenses, where advanced optimization strategies are employed to generate focal spots significantly smaller than the diffraction limit. A comparative study of zonal and modal optimization approaches reveals the fundamental trade-offs between resolution, efficiency, robustness, and scalability in super-oscillatory focusing.

Finally, I will present the integration of metalenses into laser direct-write lithography systems, where a high-numerical-aperture dielectric metalens replaces conventional bulky microscope objectives to achieve compact, high-resolution optical patterning. This approach enables subwavelength feature fabrication over large areas while significantly reducing system complexity and cost. Together, these advances highlight the growing role of metalenses as versatile optical platforms capable of bridging fundamental photonics research with practical technologies in imaging, display engineering, optical manufacturing, and integrated photonic systems.

References:

[1] Santanu Mondal, Tapajyoti Das Gupta, Optica Open, https://doi.org/10.1364/opticaopen.32144296

[2] Srijeeta Biswas, Renu Raman Sahu, Omkar Deokinandan Nayak Shinkre, Shubham Meena, Ramnishanth S, Mark Vailshery & Tapajyoti Das Gupta, Communication Materials, 2026.

External Grating-induced Band Inversion Trapped State on Optical Nanofiber

[1]Golak Bihari Bage, [1,#]Rajan Jha
[1]Nanophotonics and Plasmonics Laboratory, School of Basic Sciences, IIT Bhubaneswar, Khorda, 752050, Odisha, India

[#]*rjha@iitbbs.ac.in*

We realize a zero-dimensional trapped state on an optical nanofiber platform using an external grating structure. By fusing two external grating-induced inverted domains, we realize a localized zero-dimensional trapped state. Using finite-element methods, we study the cavity response of the realized state to external perturbations.

Optical nanofibers (ONFs) are promising platforms for quantum information and quantum optics applications, and are well suited for realizing high-quality photonic crystal cavities (PhCC) [1,2]. Considerable theoretical and experimental studies have been reported in this aspect, including composite photonic crystal cavities [1], femtosecond-laser fabricated cavities and slot waveguide enhanced cavities [3]. These studies, however, realize cavity effects using a finite, localized '*defect'* within an otherwise periodic photonic structure. Here, we report the realization and characterization of a '*zero defect*' cavity on an ONF platform realized by fusing two photonic band inverted domains.

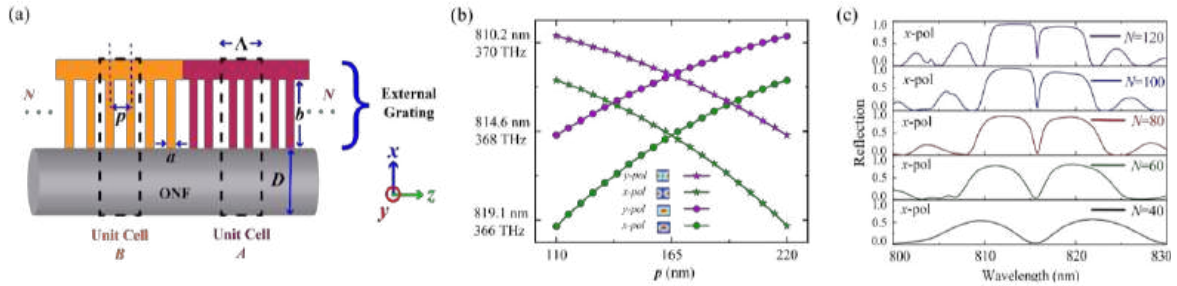


Fig. 1: (a) Schematic the device with p = center-to-center distance of two slats in a Unit Cell, a = 50nm, Λ = 330 nm, b = 2 μm, D = 580 nm, N = Number of Unit Cell repetitions of on both sides. Yellow and Red color refers to PhC realized by repetition of Unit Cell-A and Unit Cell-B, respectively. (d) Variation of bandedge points with 'p'. Here, UB: Upper Band, LB: Lower Band, Xpol: x-pol mode, Ypol: y-pol mode; green (violet) band highlights the bandgap for x-pol (y-pol) mode. (e) Cavity reflection profile of the trapped state with variation of N.

The proposed structure consists of an ONF, in which the modulation to the ONF guided modes is induced externally via a grating structure. Exact dimensions of the device are described in the caption of Fig. 1. Fig. 1(a) shows the external modulating structure, which consists of two photonic crystals (PhC) realized by repetition of two Unit Cells: Unit Cell-*A* and Unit Cell-*B*. These two Unit Cells have distinct inter-slat distances of 220 nm (yellow-marked) and 110 nm (red-marked), respectively. Fig.1(b) shows the inversion characteristics, where the variation of '*p*' leads to flipping of band order. As '*p*' varies from 110 nm to 220 nm, one can see the band character inverts for both *x*-pol and *y*-pol modes, and at *p* = 165 nm, there is closure in the bandgap. Fig. 1(c) shows the normalized reflection spectrum of the structure, where a reflection dip for the *x*-pol mode centered at ~ 815 nm is observed. Notably, an increase in the repetition of Unit Cell-*A* and Unit Cell-*B* leads to a sharper linewidth of the dip in the reflection spectrum. The reversible, structure-preserving nature of external grating-based fiber modulation, which enables the realization of a zero-dimensional trapped state, may invite advanced photonic applications.

Acknowledgments: RJ acknowledges support from the National Quantum Mission (NQM), Govt. of India.

References:

[1] R. Yalla, M. Sadgrove, K. P. Nayak, K. Hakuta, Phys. Rev. Lett. **113** (2014) 143601.
[2] K. P. Nayak, M. Sadgrove, R. Yalla, F. Le Kien, K. Hakuta, Journal of Optics **20** (2018) 31500.
[3] S. Sahu, K. P. Nayak, K. R. Mangipudi, R. Jha, Appl. Phys. Lett. **124** (2024) 034002.

Control of Nitrogen-Vacancy Center Emission Using Compact Disc-Derived Plasmonic Gratings

Faizan H. Lone and Rajesh V. Nair*

Quantum Photonics Sensing Group (QPS), Department of Physics, Indian Institute of Technology Ropar, 140001, India

*email: rvnair@iitrpr.ac.in

Deterministic control of quantum emitter emission is central to next-generation quantum enabled technologies. We propose a plasmonic metal grating platform derived from a compact disc to tailor the spectral and polarization characteristics of nitrogen-vacancy (NV) centers in diamond, offering a scalable route toward integrated quantum photonic devices.

The ongoing quantum technology revolution relies fundamentally on quantum emitters, which serve as the building blocks for quantum communication, sensing, and information processing. Among the various solid-state quantum emitters, the nitrogen-vacancy (NV) center in diamond [1] has emerged as one of the most promising candidates owing to its room-temperature spin coherence, optical spin addressability, and exceptional photostability. However, the spontaneous emission of NV centers is intrinsically broadband, with less than 4% of the emission concentrated in the zero-phonon line at room temperature. Moreover, the emitted photons are largely unpolarized and radiate into multiple optical modes, limiting deterministic control over their spectral and characteristics.

In this work, we engineer the electromagnetic environment of NV centers using a thin plasmonic grating [2] with periodic groove structure taken from the commercially available compact discs. The periodic metallic grooves provide the additional in-plane momentum required to overcome the intrinsic momentum mismatch between photons and surface plasmon polaritons (SPP), thereby enabling efficient excitation of propagating plasmonic modes [3]. The SPP resonance for the grating structure is governed by:

$$\frac{\omega}{c}\sqrt{\frac{\varepsilon_m \varepsilon_d}{\varepsilon_m + \varepsilon_d}} = \frac{2\pi}{\lambda}\sin\theta \pm \frac{2\pi m}{P},$$

where P is the grating periodicity. Reflectivity measurements reveal pronounced resonance dips, confirming the excitation of surface plasmon polaritons within the NV emission band and the extracted grating periodicity of ~ 4.6 microns. NV centers coupled to the structure exhibit pronounced spectral modification [Fig.1] with polarization selective photoluminescence peaks matching with the plasmonic resonances. Spectral decomposition reveals a dominant plasmon-assisted emission channel near 600 nm, confirming efficient SPP-mediated light–matter coupling. This cavity-free approach provides a scalable route for tailoring spontaneous emission with polarization selectivity in diamond quantum emitters, opening new opportunities for integrated quantum photonics and quantum sensing.

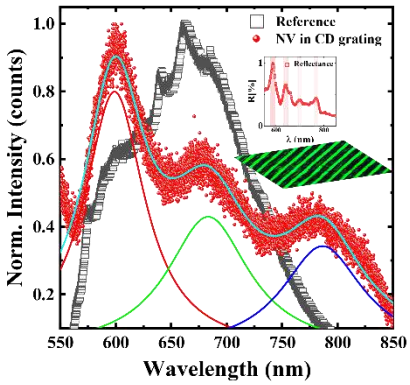


Fig 1. Normalized photoluminescence spectra of NV centers coupled to a plasmonic grating (closed circles), showing pronounced spectral modification induced by surface plasmon resonances in comparison to reference NV (open squares). Inset: Micro-reflectivity spectrum of the metallic grating, revealing the multiple plasmonic resonance dips.

References:

1. Doherty, M. W. *et al.* The nitrogen-vacancy colour centre in diamond. *Phys. Rep.* 528, 1–45 (2013).

2. Francs, G. C. des *et al*. *Journal of Optics* 18, 094005 (2016).

3. Dai, C., Wan, S., Li, Z., Shi, Y., Zhang, S. & Li, Z. Commun. Mater. 5, 15 (2024).

Deterministic strong light matter interaction in QDs-Bowtie on Silver substrate

[1,2,#]Sahil Rathi,[2,1]Satyam Dalmiya and [1]Satyendra Nath Gupta

[1]Physical Research Laboratory, Ahmedabad,380009
[2] Indian Institute of Technology, Gandhinagar

[#]*sahil@prl.res.in*

Strongly coupled polaritonic states can enable emerging quantum technologies such as quantum communication, sensing, and low-threshold lasers. This work shows strong coupling between QDs and silver Bowtie nanocavity on silver substrate and provides a way to achieve deterministic strong coupling at room temperature.

Strong light–matter interactions between quantum emitters and nanoscale optical cavities provide a powerful platform for exploring cavity quantum electrodynamics and enabling emerging quantum photonic technologies. Plasmonic nanocavities offer extreme electromagnetic field confinement beyond the diffraction limit; however, their practical implementation is often hindered by low quality factors due to intrinsic metallic losses. Here, we demonstrate strong exciton–plasmon coupling between a few CdSe/ZnS quantum dots (QDs) and lithographically fabricated silver bowtie nanocavities integrated on a silver substrate separated by a 2 nm dielectric spacer with precise positioning of QDs in between the tips of the nanotriangle of the bowtie cavity using overlay lithography. The engineered silver substrate significantly enhances the cavity quality factor from 30 to 110 by reducing the plasmon linewidth by approximately 70%.

Strong coupling is evidenced by pronounced Rabi splitting observed in both dark-field scattering and photoluminescence (PL) measurements of the coupled QD–bowtie system. Polarization-resolved scattering measurements confirm that the observed mode splitting originates from exciton–plasmon coupling, as only the horizontally polarized plasmon mode interacts with the QDs. Analysis using a coupled-oscillator model reveals a maximum Rabi splitting of 195 meV and a coupling strength of 181 meV, both of which substantially exceed the strong-coupling threshold. Furthermore, a PL splitting of 43 meV directly confirms the formation of hybrid light–matter states. These results demonstrate a practical substrate-engineering strategy for achieving robust strong coupling in plasmonic nanocavities and establish a promising route toward room-temperature quantum nanophotonic devices.

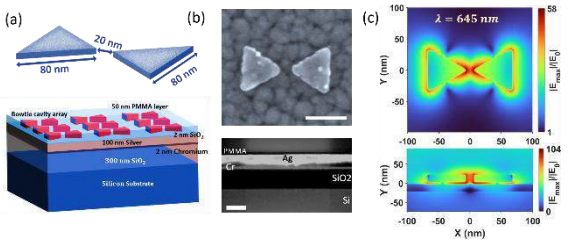


Fig.1: (a) Shows a schematic of the fabricated substrate and Bowtie nanostructure dimensions. (b) SEM image of Bowtie and cross-section profile of the substrate.

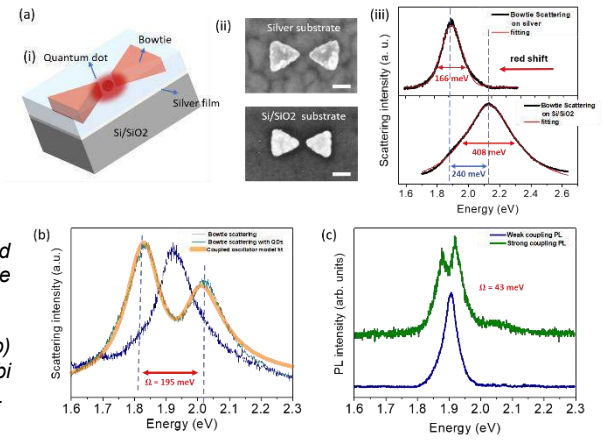


Fig. 2: (a) Schematic of the QDs-Bowtie system. (b) scattering of the Bowtie with and without QDs. (c) Rabi splitting in the photoluminescence of strongly coupled QDs.

References:

[1] Rathi, S., & Nath Gupta, S. (2025). Narrowing the linewidth of the plasmonic cavities for strong light-matter coupling. Plasmonics, 20(8), 6279-6287.

[2] Bitton, O., Gupta, S. N., & Haran, G. (2019). Quantum dot plasmonics: from weak to strong coupling. Nanophotonics, 8(4), 559-575.[3] S. Sunder, A. Sharma, *Workshop on Recent Advances in Photonics, (WRAP 2019)* 19 (2019).

Flexible SERS-based Hybrid ZIF-8@Copper Nanodendrite Substrates for Real-time Monitoring of Hazardous Molecules

[1,2]V.S. Vendamani, [1,2,#]Soma Venugopal Rao
[1]DRDO Industry Academia - Centre of Excellence (DIA-COE; formerly ACRHEM)
[2]School of Physics, University of Hyderabad, Hyderabad, India.
[#]*corresponding author: soma_venu@uohyd.ac.in*

Reported the flexible ZIF-8@Cu-nanodendrites on filter-paper for trace detection of hazardous-molecules present in the environment. FESEM/TEM analyses confirm the high-density CuNDs fabricated on filter paper. HRTEM/SAED confirm the crystalline-quality of CuNDs with 0.2 nm d-spacing. Furthermore, the capability of the substrate was tested with CV, TNT, RDX, and AN molecules.

In today's rapidly advancing world, the detection of hazardous species has gained broad significance across a wide range of disciplines, including medical diagnosis, homeland security, environmental, and industrial monitoring [1,2]. In this scenario, for rapid and reliable detection of hazardous molecules, cost-effective and highly sensitive detection techniques are highly appreciated. The existing conventional analytical techniques, like gas chromatography-mass spectrometry, high-performance liquid chromatography, and ion mobility spectrometry, require expensive sample preparation and sophisticated instrumentation. Surface-enhanced Raman spectroscopy (SERS) has established itself as a promising analytical and nondestructive technique owing to its specific molecular fingerprint, ultra-high sensitivity, and rapid detection [3]. The SERS signal enhancement is primarily driven by the characteristics of plasmonic nanostructures, which are capable of amplifying intense localized electromagnetic fields, called hotspots. The hotspots are highly significant for possessing superior Raman scattering signals. Therefore, plasmonic structures with different architectures attained considerable importance in SERS-based molecular detection [3].

Copper nanodendrites (CuNDs) are a hierarchical plasmonic nanostructure with trunks, branches, sharp tips, and numerous nanoscale junctions that offer abundant hotspot-rich spots for electromagnetic field confinement [4]. The CuNDs are prepared on Whatman filter paper to make them flexible and effective for analyte adsorption and diffusion by attaching the filter paper to the cathode and the Cu spiral to the anode in a DC power supply in the two-electrode electrochemical setup. The electrolyte is composed of 10 mM $CuSO_4$, and 100 mM HCl at 4V for 15 minutes deposition time. Despite the advantages of CuNDs, the detection abilities are further improved by integrating porous, chemically stable zeolitic imidazolate framework-8 (ZIF-8) by a seed-mediated approach, which is highly capable for molecular adsorption due to its high specific surface area. The field emission scanning electron microscope (FESEM) provides the image of CuNDs deposited on filter paper. The highly branched CuNDs and ZIF-8@CuNDs are visualized in Figures 1(a) and 1(b). High-resolution transmission electron microscope (HRTEM) and corresponding IFFT images confirm the crystalline Cu with a d-spacing of 0.2 nm, as shown in Figure 1(c). Figure 1(d) gives the selected-area electron diffraction (SAED) pattern. These flexible SERS-based hybrid ZIF-8@CuNDs are further used for real-time monitoring of hazardous molecules like CV (in Figure 1(e)), TNT, RDX, and AN.

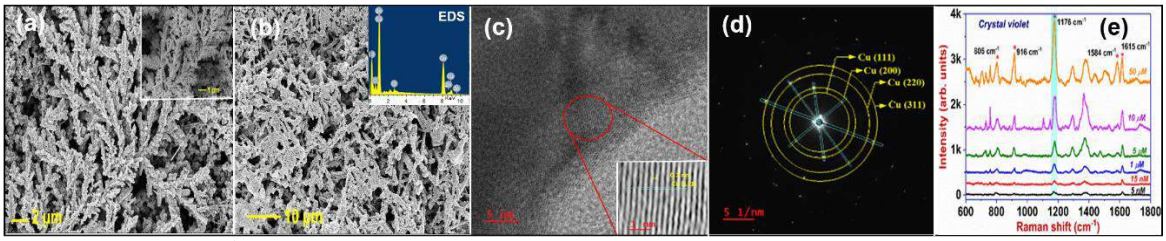


Fig.1: (a) CuNDs, (b) ZIF-8@CuNDs, (c) HRTEM [Inset: IFFT], (d) SAED pattern, and (e) SERS signals of CV molecules

VSV thanks to DST for WISE-PDF fellowship and research allowances (DST/WISE-PDF/PM-30/2023). We thank DIA- COE, School of Physics, Center of Nanotechnology, University of Hyderabad, for the infrastructure and instrumentation facilities provided.

References:

[1] J. J. Gooding, K. Gaus, *Angew Chem Int Ed Eng* 55 (2016) 11354.
[2] J. M. Emory, *LSU Doctoral Dissertations* (2010) 1-197.
[3] M. Moskovits, *Journal of Chemical Physics* 69 (1978) 4159.
[4] V.S. Vendamani, Pardhu Yella, Sathi Das, Venugopal Rao Soma, *Spectrochimica Acta Part A* 353 (2026) 127597.

Beam Shifts with Structured Light

[1,2,#]Subhasish Dutta Gupta
[1]Department of Physical Sciences, IISER Kolkata, Mohanpur 741246, India
[2]Tata Institute of Fundamental Research, Hyderabad, Telangana 500046, India

[#]sdghyderabad@gmail.com, *sdg@tifrh.res.in*

We study both Goos-Hanchen and Imbert-Feodorov beam shifts with structured light with or without orbital angular momentum. We show how these shifts can be magnified by resonant local fields as well as by weak value amplification. Coupled with symmetry considerations we show that non-reciprocity in reflection for illumination from opposite ends can result in different shifts with opposite signs for tiny imbalance resulting from the broken symmetry. Our methodology is responsive to any entity that may cause such symmetry breaking – including refractive index, displacement etc. - thus ushering a new paradigm in ultra-high precision sensing using structured light.

We present a rigorous theoretical study of nonreciprocal[1] Goos–Hänchen (GH) and Imbert–Fedorov (IF) beam shifts in reflection from asymmetric stratified media. The study focuses on the effect of broken spatial symmetry on reflected beams for opposite directions of illumination[2]. Unlike previous approaches based mainly on stationary-phase approximations or scalar beam descriptions, a fully vectorial angular-spectrum method is developed [3,4]. The theory is applicable to arbitrary stratified media composed of homogeneous and isotropic layers, with asymmetry arising from displacement, refractive-index mismatch, or other perturbations. The method allows the analysis of both linearly polarized beams and beams carrying spin or orbital angular momentum. Tiny deviations from an ideal symmetric structure are shown to produce giant differential GH shifts for opposite propagation directions. Small IF and vortex-induced shifts can further be enhanced through projective measurements based on weak-value amplification. The proposed nonreciprocal beam-shift mechanism is explored for sensing small refractive-index mismatches and displacements. A theoretical sensitivity of approximately $\geq 10^{-9}$ RIU/nm is obtained, indicating significant potential for high-sensitivity optical sensing. A table (Table 1) containing the recent advancements are given for comparison of the sensitivity achieved so far in different platforms. Although practical implementation will be affected by fabrication and detection limitations, the results provide a promising foundation for further experimental investigations.

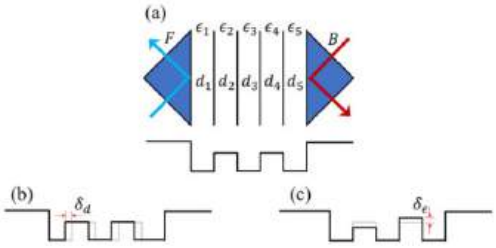


Figure 1: (a) Schematic of the symmetric coupled-waveguide structure, with $\epsilon_i = \epsilon_f$, $\epsilon_1 = \epsilon_3 = \epsilon_5 = \epsilon_s$, $\epsilon_2 = \epsilon_4 = \epsilon_g$, $d_1 = d_5 = d$, and $d_2 = d_4 = d_g$. The layers of widths d_2 and d_4 serve as high-index guiding layers. (b) Translation induced asymmetry. (c) RI mismatch induced asymmetry. Forward (backward) propagation is indicated by blue (red) arrows in FIG:1(a). $F(B)$ denotes forward (backward) incidence.

No	Type	Sensitivity reported in paper	Converted in `RIU/nm' unit	Paper
1	Theoretical GH/BIC	$3.58 \times 10^6\ \mu m/RIU$	$2.79 \times 10^{-10}\ RIU/nm$	[5]
2	Theoretical PCF-SPR	$1.2 \times 10^5\ nm/RIU$	$8.13 \times 10^{-6}\ RIU/nm$	[6]
3	Experimental GH/BSW	$2.0 \times 10^{-9} RIU/nm$	$2.0 \times 10^{-9} RIU/nm$	[7]
4	Experimental Au-SPR	$1.82 \times 10^{-8}\ RIU/nm$	$1.82 \times 10^{-8} RIU/nm$	[8]
6	Our prediction	$\geq 5.7799 \times 10^{-9} RIU/nm$	$\geq 5.7799 \times 10^{-9} RIU/nm$	

References:

[1] G. S. Agarwal et al., Opt. Lett. 27, 1205 (2002)
[2] M. Kumari et al., Opt. Commun. 285, 617 (2002)
[3] S. Sinha Biswas et al., J. Opt. 25, 095401 (2023)
[4] S. S. Biswas et al., Opt. Commun. 569, 130766 (2024)
[5] X. Jiang et al., Micromachines 14, 10.3390/mi14061109 (2023)
[6] M. Al Mahfuz et al., IEEE Access 12, 64727 (2024)
[7] W. Kong et al., Sensors and Actuators A: Physical 276, 62 (2018)
[8] X. Yin et al., Appl. Phys. Lett. 89, 261108 (2006).

Tailored Bessel Beams and Their Applications

[1,#]Shanti Bhattacharya

[1]*Department of Electrical Engineering, IIT Madras, Chennai, India,*

#shanti@ee.iitm.ac.in

Bessel beams are diffraction-resistant structured light fields with self-healing properties. However, their applications are limited by non-uniform axial intensity and strong sidelobes. We show how to design and generate beams using diffractive and meta-elements. We demonstrate custom axial shaping and sidelobe suppression below 6% for advanced imaging such as light-sheet microscopy.

Bessel beams (BBs) maintain their transverse profiles over long distances and self-heal, making them attractive for optical trapping, high-aspect-ratio laser processing, and light-sheet fluorescence microscopy (LSFM). However, practical BBs exhibit significant axial intensity variation and strong concentric sidelobes. To resolve the former problem, we present a cascade of two diffractive optical elements (DOEs) that can be used to tailor the longitudinal intensity over centimeters [1]. The proposed technique is used to demonstrate a BB with linear, uniform, or parabolic axial intensity variation.

In the case of sidelobes, an earlier reported technique [2] is adapted to create an element that simultaneously generates, a field comprising two slightly different BBs. Concentric sidelobes are suppressed by the superposition of the two co-propagating BBs with slightly different radial wavevectors as given below:

$$U(r, z) = A_1 J_0(k_{r1} r) \exp(jk_{z1} z) + A_2 J_0(k_{r2} r) \exp(jk_{z2} z) \quad (1)$$

Amplitudes and wavevectors are optimized to preserve the core intensity while minimizing sidelobe energy [2, 3]. The optimized phase functions are spatially multiplexed into a single-phase element using a random binary matrix virtual mask. For a design wavelength of 633 nm and radial wavevector ratio kr1/kr2 = 0.61, a sidelobe suppressed (SSBB) generated using a phase-only spatial light modulator achieved a $1/e^2$ core radius of 44 μm and a propagation-invariant range of 39 mm. Crucially, the first sidelobe peak intensity was reduced from 13.36% (for a standard BB) to just 5.92% [4]. Experimental results are given in Fig. 1. The phase mask can also be fabricated as a static meta-optical element utilizing silicon nanopillars.

For one-photon LSFM, an SSBB designed with m = 0.57 maintained a 4.8 ± 0.3 μm core thickness up to a depth of 430 μm in scattering phantoms [4]. Imaging early-stage zebrafish larvae (4-5 dpf) expressing GCaMP eye and notochord structures revealed a two-fold contrast-to-noise ratio improvement over standard BBs without requiring deconvolution, demonstrating high-performance, single-shot volumetric depth imaging.

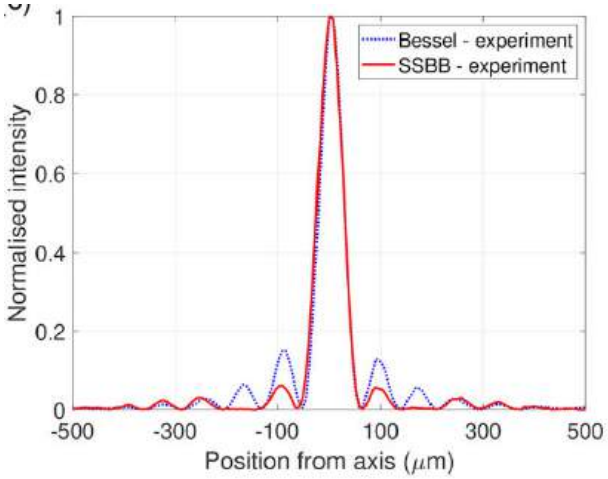


Fig. 1 On-axis experimental intensity profiles realized with an SLM. The cross section of both a standard Bessel beam and a sidelobe-suppressed Bessel beam optimized with wavevector ratio of 0.61. or a $1/e^2$ radius of 44 μm are plotted.

References:

[1] R. Dharmavarapu, *S. Bhattacharya* S. Juodkazis, Journal of Optics 20 (2018) 085606.

[2] S. Mori, "Side lobe suppression of a bessel beam for high aspect ratio laser processing," Precis. Eng. 39, 79–85 (2015).

[3] J.G. George, *K. Dholakia* S. Bhattacharya, Optics Continuum 2 (2023) 1649.

[4] C. Taneja, *J.G. George* S. Corsetti, P. Wijesinghe, G.D. Bruce, M.F. Zwart, S. Bhattacharya, K. Dholakia, Biomedical Optics Express 15 (2024) 6183.

Susceptibility-Engineered Polarization Shaping of Structured Light in Rubidium Vapor

[#]Abhishek Dutta, Vivek Venkataraman
Department of Electrical Engineering, Indian Institute of Technology Delhi

[#]*eez248411@iitd.ac.in*

We investigate radially polarized vector vortex beams propagating through a four-level rubidium tripod system under a longitudinal magnetic field. Simulations show conversion of the radial state toward azimuthal vector beams with position-dependent transmission, tunable through the magnetic field and spatially varying atomic susceptibility.

Structured light has become a key area of modern quantum optics [1] owing to its inhomogeneous polarization distribution and the underlying phase structure of its transverse profile. In atomic media, the propagation of such light depends strongly on the medium's quantum coherence and susceptibility. Here we drive D_2 line of rubidium vapor with a radially polarized beam, whose local polarization decomposes into equal amplitude σ_+ and σ_- components, imprinting a spatially dependent coherence distribution on the medium. This coherence yields a position-dependent susceptibility. In the presence of a longitudinal magnetic field, Zeeman splitting introduces a differential phase shift between the circular polarization components, resulting in a spatial rotation of the local polarization and reshaping the transverse vector beam structure.

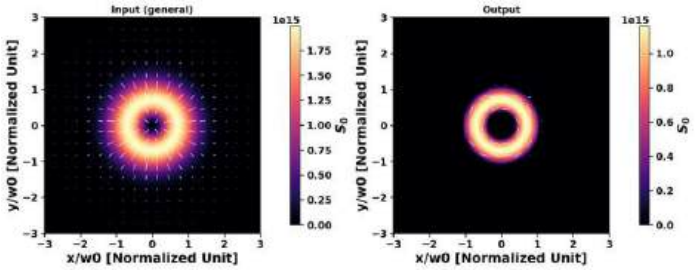


Fig. 1: Magnetically controlled conversion of a radially polarized vortex beam (left) into an azimuthally polarized beam (right) via the engineered atomic susceptibility of the tripod Rb system.

The theoretical model is based on the semiclassical Lindblad master equation [2] and is solved numerically in the steady-state regime for the non-perturbative case ($\Omega > \Gamma$), where analytical solutions are generally unavailable. We incorporated the realistic broadening mechanism such as time-of-flight and Doppler effect. A fully thermal-average susceptibilities is obtained, showing magnetic field dependent rotation of the vector beam.

Under experimentally realistic conditions, numerical simulations demonstrate the complete conversion of a radially polarized beam into an azimuthally polarized beam after propagation through a 75 mm rubidium vapor cell, as illustrated in Fig. 1. The field intensity is represented in terms of the corresponding Rabi frequency. Both the probe and coupling beams have an input power of 200 μW, corresponding to a peak Rabi frequency of both beams is 11.728 MHz, with a beam diameter of 3.5 mm. The vapor cell is maintained at a temperature of 30 °C. The output intensity is reduced by resonant absorption in the atomic medium, while ground-state coherence partially suppresses the absorption (EIT-like transparency), resulting in an overall transmission of approximately 29.56%.

In conclusion, we have demonstrated the conversion of a radially polarized beam into an azimuthally polarized beam through propagation in a coherently prepared rubidium tripod system. The transformation arises from the spatially varying ground-state coherence induced by the vector beam, combined with the longitudinal magnetic field, which sets the differential phase between the circular components and hence the local polarization rotation. The same spatial coherence structure produces position-dependent transmission, indicating that both the polarization texture and the intensity profile of structured light can be engineered through the atomic susceptibility.

References:

[1] Qiu, S. et el, *Photonics Research, 9(12), 2325-2331*.
[2] Manzano, D. (2020). A short introduction to the Lindblad master equation. *Aip advances*, *10*(2).

Optical vortices-based pseudo DNA logic and its applications

Sonu Kumar Rao and #Naveen K. Nishchal
Indian Institute of Technology Patna, Bihta, Patna, Bihar 801106, India
#E-mail: nkn@iitp.ac.in

The availability of large number of mutually orthogonal modes of optical vortex beam offers a promising platform for realizing pseudo-deoxyribonucleic acid (DNA) exclusive-OR (XOR) operation. This study provides a versatile framework for optical vortices-based DNA XOR, demonstrating its potential for both optical security and bioinformatics applications.

Optics has drawn considerable attention of researchers due to its attractive features such as parallel processing, high speed, and several degrees of freedom [1]. The increasing importance of optical sensing and imaging in the modern world is the cause of the increase in light-related security requirements. Optical techniques would be especially useful in biometrics, inspection, surveillance, and health and medical monitoring. The classical and quantum characteristics of light provide powerful means to securely store or transmit information to authorized users. Various degrees of freedom of light such as polarization, amplitude, phase, and orbital angular momentum (OAM) are used to encode the information, thereby enabling advanced optical communication and security applications [1,2]. The inherent characteristics of OAM of light, such as its robustness in turbulent atmospheric media and large number of orthogonal modes, offer versatile platform for wide range of applications [2,3].

By leveraging the unique properties of OAM beams, this study presents a novel approach for implementing pseudo-deoxyribonucleic acid (DNA) exclusive-OR (XOR) operations using a Mach-Zehnder interferometer. The DNA consists of four bases; adenine (A), thymine (T), guanine (G), and cytosine (C) that obey the Watson-Crick complementary base-pairing rule, where A pairs with T and G pairs with C [3]. In the proposed technique, DNA bases A, T, C, and G are encoded into OAM beams having topological charges (TCs) l_1, - l_1, l_2, and - l_2, respectivley. The OAM-based pseudo-DNA XOR utilizes superposition of two beams U_1 and U_2, having TCs l_1 and l_2, respectively and can be expressed as,

$$I = |U_0^1|^2 + |U_0^2|^2 + 2U_0^1 U_0^2 \cos\{(l_1 - l_2)\phi - \phi_1\} \quad (1)$$

where ϕ: azimuth angle and $\phi_1 = \frac{2\pi}{\lambda}(x\sin\alpha + y\sin\beta)$. The mirror tilt angles along the *x*- and *y*-directions are denoted by α and β, respectively [3], while λ represents the wavelength of the optical beam. The parameters U_0^1 and U_0^2 represent the amplitudes of the individual OAM beams. Table 1 presents the encoding rule that maps DNA bases into OAM beam, whereas DNA XOR rule is listed in Table 2.

Table 1. OAM beam encoding from DNA base

DNA base	**A**	**T**	**C**	**G**
TC	l_1	$-l_1$	l_2	$-l_2$

Table 2. OAM-based DNA XOR rule (X_i & Y_i =DNA bases)

$X_i \oplus Y_j$	**A =** l_1	**T =-** l_1	**C=** l_2	**G=-** l_2
A = l_1	$\lvert l_1 - l_1\rvert$, **A**	$\lvert 2\,l_1\rvert$, **T**	$\lvert l_1 - l_2\rvert$, **C**	$\lvert l_1 + l_2\rvert$, **G**
T=- l_1	$\lvert -2\,l_1\rvert$, **T**	$\lvert -l_1 + l_1\rvert$, **A**	$\lvert -l_1 - l_2\rvert$, **G**	$\lvert -l_1 + l_2\rvert$, **C**
C= l_2	$\lvert l_2 - l_1\rvert$, **C**	$\lvert l_2 + l_1\rvert$, **G**	$\lvert l_2 - l_2\rvert$, **A**	$\lvert 2l_2\rvert$, **T**
G=- l_2	$\lvert -l_2 - l_1\rvert$, **G**	$\lvert -l_2 + l_1\rvert$, **C**	$\lvert -2l_2\rvert$, **T**	$\lvert -l_2 + l_2\rvert$, **A**

The developed pseudo-DNA XOR operation has been experimentally validated, demonstrating its suitability for applications such as image security, authentication, and bioinformatics.

Acknowledgement: The funding from the Council of Scientific and Industrial Research (03/1492/23/EMR-II) and Anusandhan National Research Foundation (ANRF/ARG/2025/012264/PS), Govt. of India are acknowledged.

References:

[1] N. K. Nishchal, Optical Cryptosystems, IOP Publs. Ltd. Bristol, UK, 2019.
[2] K. A. Forbes, D. L. Andrews, Opt Lett. 43, (2018) 435-438.
[3] S. K. Rao, R. Kumar, N. Singh, N. K. Nishchal, A. Alfalou, Opt. Laser Eng. 197 (2026) 109483.

Determination of 3-D Spin Densities

Dileep Kumar Upadhyay# and Nirmal K. Viswanathan
School of Physics, University of Hyderabad, Gachibowli, Hyderabad 500046, India

#23phph14@uohyd.ac.in

Tight focusing of light produces all three field components ($\boldsymbol{E_x}$, $\boldsymbol{E_y}$ and $\boldsymbol{E_z}$) in the focal region. Their simultaneous presence results in the appearance of longitudinal ($\boldsymbol{S_z}$) and transverse ($\boldsymbol{S_x}$ and $\boldsymbol{S_y}$) spin densities. In this work, we determine these quantities using experimental measurements and the field reconstruction technique and verify the results via simulation.

The presence and significance of the longitudinal field component ($\boldsymbol{E_z}$) in nonparaxial focus is unavoidable. This component can be measured or extracted using various experimental techniques, such as nanoprobe scanning, near-field scanning optical microscope (NSOM), or an interferometer-based reconstruction technique. Transverse spin densities are the quantities that are directly connected to the presence of $\boldsymbol{E_z}$ and helps us to study these quantities and understand their role in various experimental scenarios. Transverse spin densities are also useful for achieving 3-D control over dipole excitation (in a quantum dot or a single atom), in optical tweezers, and in experiments aimed at determining the force and torque in an optical particle trap, where a map of the individual angular momentum is crucial [1].

The electromagnetic field in free space satisfies the Maxwell equation, and especially Gauss's theorem ($\boldsymbol{\nabla}.\boldsymbol{E} = \boldsymbol{0}$), which describes the transversality condition for plane waves [2]. In the case of a nonparaxial focused beam, this condition is no longer satisfied due to the presence of $\boldsymbol{E_z}$. So, by using Gauss' law, one can determine $\boldsymbol{E_z}$ with the help of the reconstructed amplitude and phase of $\boldsymbol{E_x}$ and $\boldsymbol{E_y}$. The field reconstruction is carried out using $\boldsymbol{E_i} = \sqrt{I_i}\, e^{\varphi i}$ from which $\boldsymbol{E_z}$ is calculated using [3]:

$$\boldsymbol{E_z} = IFT\left[\frac{-1}{k_z}\left(k_x\, FT[\boldsymbol{E_x}] + k_y\, FT[\boldsymbol{E_y}]\right)\right] \tag{1}$$

Using all three field components, the spin densities calculated using [1]:

$$\mathbf{S} = \frac{\varepsilon_0}{\omega}\,\mathrm{Im}[\boldsymbol{E}^* \times \mathbf{E}] \qquad \text{Where } \mathbf{E} \text{ is the total field.} \tag{2}$$

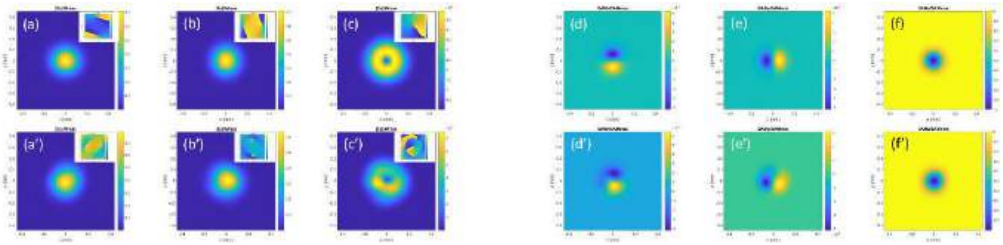


Fig. 1: *(Left Column) Simulated (a, b, c) and experimentally measured (a', b', c') field components $\boldsymbol{E_x}$,$\boldsymbol{E_y}$ and $\boldsymbol{E_z}$ with their phase plot in the inset. (Right Column) Simulated (d, e, f) and calculated (d', e', f') spin densities $\boldsymbol{S_x}$, $\boldsymbol{S_y}$ and $\boldsymbol{S_z}$.*

The field component $\boldsymbol{E_x}$ (Fig. 1 (a')) and $\boldsymbol{E_y}$ (Fig (b')) are reconstructed from the experimentally measured interferograms and $\boldsymbol{E_z}$ (Fig (c')) is extracted from the reconstructed fields using equation (1). From these extracted total field (**E**), the spin densities ($\boldsymbol{S_x}$ (Fig (d')), $\boldsymbol{S_y}$ (Fig (e'), $\boldsymbol{S_z}$ (Fig (f')) are determined using equation (2) and are shown to match well with the simulated results obtained using the Richards and Wolf formalism [3].

From experimentally measured complex transverse-field components, we determined the longitudinal component of the electric field and, using that, calculated 3-D spin densities in a tightly focused circularly polarized Gaussian beam.

Acknowledgment: The authors acknowledge SERB for the support to carry out this work.

References:

[1] Neugebauer, M., Bauer, T., Aiello, A., & Banzer, P, *Physical Review Letters*, *114*(6), (2015) 063901.
[2] Maluenda, D., Aviñoá, M., Ahmadi, K., Martínez-Herrero, R., & Carnicer, A, *Scientific Reports*, *11*(1), (2021) 17992.
[3] Herrera, I., & Quinto-Su, P. A., *Journal of Optics*, *25*(3), (2023) 035602.

Effect of the Structure of the Chiral Moiety of the Photoconductive Dopant on the Photorefractive Effect of Liquid Crystal Blends

[1,#] Takeo Sasaki, [1]Kengo Ishihara, [2]Yusuke Tajima, [1]Khoa V. Le, [1]Yumiko Naka
[1] Department of Chemistry, Faculty of Science, Tokyo University of Science, 1-3 Kagurazaka, Shinjuku-ku, Tokyo 162-8601, Japan

[2]Department of Environment and Sustainability, Mukogawa Women's University, 11-68 Koshien Kyuban-cho, Nishinomiya, Hyogo 663-8179, Japan

[#]*sasaki@rs.tus.ac.jp*

Photorefractive liquid crystal blends exhibiting the flexoelectric effect were prepared, and the photorefractive effect, dielectric properties, and optical properties of these materials were investigated. These mixtures showed either only flexoelectricity or both flexoelectricity and ferroelectricity. The former mixtures exhibited a faster and larger photorefractive effect than the latter ones.

The photorefractive effect is one of the phenomena that enable the formation of dynamic holograms. Because the photorefractive effect can be used not only for optical recording but also for optical amplification, Fourier optics, and the detection of phase changes in light, it is expected to serve as one of the operating principles for optical devices. In particular, asymmetric energy exchange is a characteristic phenomenon. In a photorefractive material, one of two interfering light beams is amplified by the other. The photorefractive effect occurs in materials that exhibit both photoconductivity and electro-optic properties. To date, various substances, including inorganic crystals, organic crystals, polymeric compounds, and liquid-crystal (LC) mixtures, have been investigated as photorefractive materials [1]. Photorefractive LCs exhibit fast photorefractive response times, making them suitable for use in laser ultrasonics. [2]. In this study, photorefractive liquid crystal blends exhibiting the flexoelectric effect were prepared (Fig. 1), and their photorefractive, dielectric, and optical properties were investigated. These blends comprised mixtures of smectic liquid crystals, chiral photoconductive compounds, and an electron-trap reagent. Depending on the molecular structure of the chiral compound, these mixtures showed either only flexoelectricity or both flexoelectricity and ferroelectricity.

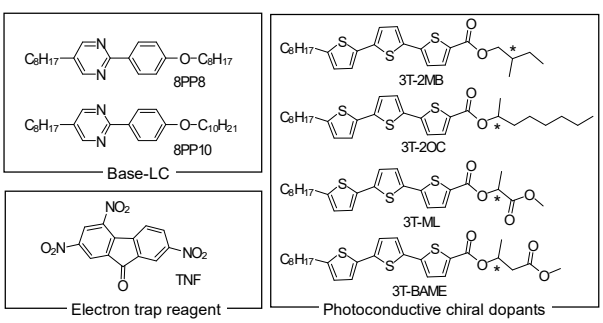


Fig. 1 Structures of the base LC compounds, the photoconductive chiral compounds, and the electron trap reagent.

The chiral photoconductive compounds 3T-ML and 3T-BAME were synthesized, and photorefractive smectic LC blends were prepared using these compounds. The LC blend made with 3T-ML exhibited both flexoelectricity and ferroelectricity, whereas the one incorporating 3T-BAME showed only flexoelectricity. The LC blend with 3T-BAME provided a larger photorefractive two-beam coupling gain coefficient than the 3T-ML mixture. The difference in the photorefractive effect between these LC blends is attributed to variations in the fineness of LC molecular alignment in cells with a polyimide alignment layer. The LC blends that showed only flexoelectricity exhibited larger gain coefficients and faster response times. Further evaluation of the difference between LC blends showing ferroelectricity and those showing flexoelectricity in terms of the photorefractive effect will require identifying additional chiral dopants that induce flexoelectricity solely in such blends.

References:

[1] Maho Hirakawa, Atsushi Seki, Khoa Van Le, Yumiko Naka, Takeo Sasaki, *ACS Appl. Opt, Mater*. 3, 284-295 (2025).
[2] Takeo Sasaki, Takaaki Yagami, Toshinobu Takashi, Kaita Suzuki, Gouta Ikeda, Yukihiro Ishii, Khoa Van Le, and Yumiko Naka, *Opt. Mater. Express*, 13, 728-738 (2023).

Quantitative phase imaging of dynamic object by parallel recording technique

[1,#]Yasuhiro Awatsuji, [2,3]Tomoyoshi Inoue,[1]Kenzo Nishio,[4]Hou Natsu,[5]Sudheesh K. Rajput, [6]Manoj Kumar, and [7]Osamu Matoba
[1] Kyoto Institute of Technology, Matsugasaki, Sakyo, Kyoto, 606-8585, Japan
[2] Hiroshima University, Higashi-Hiroshima, Hiroshima, 739-8521, Japan
[3] Japan Science and Technology Agency, 4-1-8 Honcho, Kawaguchi, Saitama 332-0012, Japan
[4] National Institute of Advanced Industrial Science and Technology, Central 2, 1-1-1 Umezono, Tsukuba 305-8568, Japan
[5] Koneru Lakshmaiah Education Foundation, Vaddeswaram, 522302, Guntur, Andhra Pradesh, India
[6] Amity University Punjab, Sector 82A, Mohali 140306, India
[7] Kobe University, Rokkodai 1-1, Nada, Kobe 657-850, Japan
[#] *awatsuji@kit.ac.jp*

The authors introduce two parallel techniques for recording complex amplitude images of dynamic objects: parallel phase-shifting digital holography and parallel transport of intensity equation. Both techniques use spatially division multiplexing technique for single-shot recording multiple images. Dynamic quantitative phase-imaging has been demonstrated by each technique.

A variety of techniques have been developed for quantitative phase imaging (QPI) of objects. Among them, one representative approach is digital holography [1]. Another representative approach is the transport of intensity equation (TIE) [2]. To enable QPI of dynamic objects, the authors have developed parallel phase-shifting digital holography (PPSDH) [3] and the parallel TIE (P-TIE) [4].

Figure 1(a) illustrates the principle of PPSDH [3]. The technique simultaneously records the multiple holograms required for phase-shifting digital holography [5] using a single image sensor based on space-division multiplexing (SDM). Because the complex amplitude is reconstructed from a single hologram, instantaneous phase imaging of dynamic objects can be achieved. Since the technique is based on holographic interferometry, it generally requires coherent illumination.

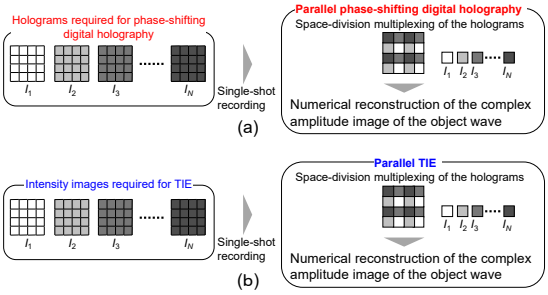


Fig. 1: Schematic of the basic concept of parallel recording technique for complex amplitude imaging. (a) PPSDH, (b) P-TIE

Figure 1(b) shows the principle of the P-TIE [4]. Similar to the PPSDH, this technique employs SDM to simultaneously record the multiple diffraction intensity images, required for TIE-based phase retrieval [2], with a single image sensor. As the complex amplitude is reconstructed from a single recorded image, the technique enables instantaneous QPI of dynamic objects. Unlike digital holography, the parallel TIE is a non-interferometric technique and therefore does not require coherent illumination.

We have reviewed PPSDH and the P-TIE for quantitative phase imaging of dynamic objects. To date, QPI at 1 million fps has been achieved using both techniques [6,7]. Both techniques can be regarded as powerful tools for the observation, inspection, and measurement of dynamic objects.

This study was partially supported by the Japan Society for the Promotion of Science KAKENHI Grant-in Aids for Research Activity Start-up 23K19121, Scientific Research (B) 23H01422 and 23K26117.

References:

[1] J. W. Goodman, R. W. Lawrence, *Appl. Phys. Lett.* 11 (1967) 77.
[2] M. R. Teague, *J. Opt. Soc. Am.* 73 (1983) 1434.
[3] Y. Awatsuji, M. Sasada, T. Kubota, *Appl. Phys. Lett.* 85 (2004) 1069.
[4] P. Xia, Y. Awatsuji, S. Ura, K. Nishio, O. Matoba, *2013 OSA Topical Meeting, Digital Holography and Three-Dimensional Imaging (DH)* (2013) DTh5A.3.
[5] I. Yamaguchi T. Zhang, *Opt. Lett.* 22 (1997) 1268.
[6] P. Xia, Y. Awatsuji, K. Nishio, O.Matoba, *Electron. Lett.* 50 (2014) 1693.
[7] S. K. Rajput, Y. Kumon, K. Nishio, H. Natsu, A. Sanpei, O. Matoba, Y. Awatsuji, *Optica* 12 (2025) 350.

Single-Shot Jones Matrix Extraction Using a Common-Path Intensity Measuring Techniques

Deepak Kumar[1*], Dinesh N. Naik[1], Biswajit Pathak[1], Sooraj Ravindran[2] and C.S. Narayanamuthy[1]

[1]Applied and Adaptive Optics Laboratory, Department of Physics, Indian Institute of Space Science and Technology (IIST), Valiamala, Thiruvananthapuram 695547, Kerala, India.

[2]Optoelectronics and Photonics Lab, Department of Avionics, Indian Institute of Space Science and Technology (IIST), Trivandrum 695547, Kerala, India

*deepakkumarsvc@gmail.com

In this work, we propose a compact polarisation single-shot common-path digital holographic microscopy (PSC-DHM) system for Jones matrix extraction of anisotropic specimens. Simulation results of the proposed experiment are obtained by considering a birefringent test specimen to validate the effectiveness of the proposed system.

Quantitative polarisation microscopy through Jones matrix imaging characterises birefringent and dichroic specimens, but conventional multi-frame implementations are vulnerable to vibration. The proposed common-path architecture differs from two-arm polarisation holographic techniques [1], which generate the object and reference fields in separate stages. The feasibility of single-shot Jones matrix extraction using a common-path interferometry is investigated by considering the following four beam interference [2].

$$I(\mathbf{r}) = O_x R_x^* E_{11} + O_x R_y^* E_{12} + O_y R_x^* E_{21} + O_y R_y^* E_{22} + \text{c.c.}$$

Where O_x and O_y are the x and y components of the simulated field after the specimen when it was simultaneously illuminated with +45° and −45° linearly polarised and relatively tilted coherent beams, yielding the object beams O_x and O_y, in the reference beams; R_x and R_y are x and y components of the reference field with a relative tilt. Here $E_{11} = J_{11} + J_{12}$, $E_{21} = J_{11} - J_{12}$, $E_{12} = J_{21} + J_{22}$, and $E_{22} = J_{21} - J_{22}$ are complex combinations of the Jones elements, each carried on a distinct spatial-frequency carrier. Fourier filtering of each carrier isolates the corresponding E_{ij} term, and the Jones elements follow from,

$$J_{11} = \frac{1}{2}(E_{11} + E_{21}),\ J_{21} = \frac{1}{2}(E_{12} + E_{22}),\ J_{12} = \frac{1}{2}(E_{11} - E_{21}),\ J_{22} = \frac{1}{2}(E_{12} - E_{22})$$

The PSC-DHM reconstruction pipeline is validated through simulation using a QWP mosaic with quadrant orientations of 0°, 30°, 45° and 90°. The same has also been validated through experimental implementation. Figure 1 shows the simulated multiplexed hologram (a), its Fourier spectrum (b), and the reconstructed Jones matrix amplitude (top) and phase (bottom) for each quadrant.

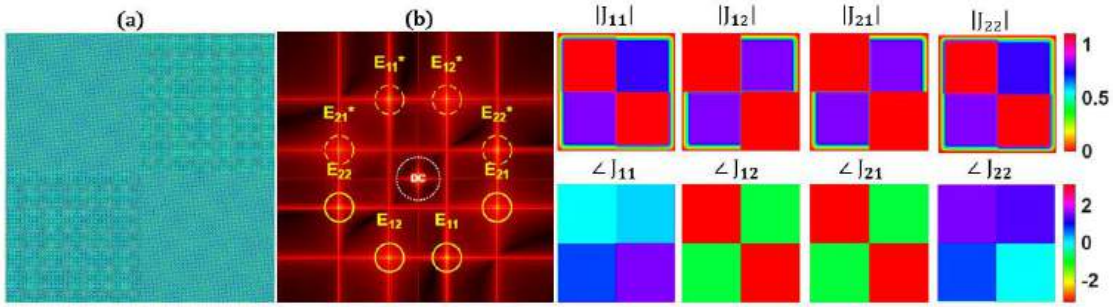


Fig. 1. Multiplex hologram(a), corresponding Fourier spectrum (b), and retrieved amplitude (top row) and phase (bottom row).

Preliminary results confirm that the common-path, single-shot geometry has capability to retrieve all four complex Jones matrix elements, offering a vibration-insensitive approach to polarisation microscopy. The proposed scheme can be implemented using a single Sagnac interferometer that generates orthogonally polarised (H and V) beams, which is then passed through a non-polarising beam splitter (NPBS) rotated along the diagonal axis. This duplicates the beams into two angularly offset copies to form the object beams and reference beams. In the object beams, a half-wave plate at 22.5° converts the H and V components into +45° and −45° linearly polarised. A Fresnel biprism introduces angular deviation between carriers forming a single multiplexed hologram, and the Jones matrix elements can be recovered using the Fourier-domain extraction approach.

References:

[1] Z. Wang, L.J. Millet, M.U. Gillette, G. Popescu, *Optics Letters* 33, 1270 (2008).

[2] M.M. Sreelal, R.V. Vinu, R.K. Singh, *Optics Letters* 42, 5194 (2017).

Development of a Programmable Quadriwave Interferometric Wavefront Sensor for Aspheric Testing

[1,*]Shadiya MP, [2]Akankshya Patel Choudhury, [3]Arjun A S and [4,#]Biswajit Pathak
[1] Department of Physics, Indian Institute of Science Education and Research, Tirupati-517619, Andhra Pradesh, India
[2] Department of Physics and Astronomy, National Institute of Technology Rourkela-769008,Odisha, India
[3] Department of Physics, Cochin University of Science and Technology South Kalamassery-682022, Kerala, India
[4] Department of Physics, Indian Institute of Space Science and Technology, Thiruvananthapuram -695547, Kerala, India
Corresponding Author(s): *shadiya_20221137@students.iisertirupati.ac.in ; # biswajitpathak@iist.ac.in

Abstract: *We develop a high-sensitivity programmable quadriwave lateral shearing interferometry system capable of testing aspheric surfaces with high accuracy, utilizing different diffraction orders of a multiplexed phase grating (MPG).*

Summary: The accurate testing of aspheric surfaces is essential in optical metrology because even small surface deformations can significantly affect the performance of precision optical systems. Reliable measurement requires a wavefront sensing technique capable of providing high accuracy, sensitivity, and spatial resolution. Traditional Shack-Hartmann wavefront sensor (SHWS) uses microlens arrays to sample the incident wavefront and estimate deformations based on the relative slope measurements of focal spots. However, the limited number of microlenses restricts sampling ability, resulting in poor resolution and reduced sensitivity. Meanwhile, a quadriwave lateral shearing interferometry (QLSI) system achieves high sampling through its small grating pitch, enabling the incident wavefront to be sampled at a very high resolution. However, conventional QLSI techniques rely on fabricated gratings with fixed shear and transmittance, limiting flexibility and optimization. Existing methods struggle to simultaneously tailor shear, suppress unwanted diffraction orders, and balance beam intensity.

In view of the limitations mentioned above, we propose a programmable QLSI (pQLSI) system that leverages an MPG implemented on a spatial light modulator (SLM) to achieve accurate, high-sensitivity wavefront sensing. This system allows precise control of shear and mitigates unwanted diffraction effects through random binarization, and enhances sensitivity by exploiting higher orders. Key advantages include uniform beam intensity and compatibility with various wavefront aberrations. In the present work, we perform theoretical analysis, numerical simulations, and optimization of critical parameters, culminating in the development of an experimental pQLSI system for accurate aspheric surface measurements. The proposed approach is expected to provide a compact and highly sensitive wavefront sensing system. Such a system holds significant potential in optical testing and precision metrology.

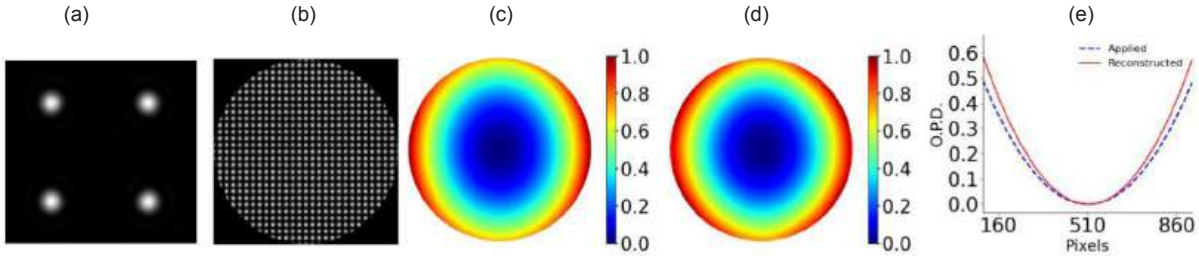


Fig. 1: Simulation results of programmable wavefront sensing of an aspheric surface: (a) Fourier spectrum showing the four isolated +1 diffraction orders produced by the multiplexed programmable phase grating, (b) corresponding interferogram, (c) applied aspheric wavefront profile, (d) reconstructed aspheric wavefront profile, and (e) its corresponding line plot across the center.

References:
[1] Baffou, G., *J. Phys. D: Appl. Phys.* 54 (2021), 294002.
[2] Jacob, J. and Pathak, B., *J. Phys. D: Appl. Phys.* 59 (2026), 205104.

Anisoplanatism in Adaptive Optics and Advancements in Wavefront Sensing

#A.R. Ganesan, Jaspal Singh
Applied Optics Laboratory, Indian Institute of Technology Madras, Chennai 600036, Tamil Nadu, India
#*arg@faculty.iitm.ac.in*

In our study, we have investigated angular anisoplanatism using a pseudo-random phase plate that mimics atmospheric turbulence in a laboratory environment. We also introduce a grating array-based multiplex wavefront sensor that captures multiple wavefronts in a single camera frame. Finally, we present a reference-less wavefront sensing that uses the shifts of the +1 and -1 diffraction orders to determine local slopes and reconstruct the wavefront.

The field of view (FoV) of adaptive optics (AO) correction is limited by angular anisoplanatism and focal anisoplanatism. In a typical AO system, the wavefront is sensed along the path of a laser guide star (LGS), but the correction is applied along the direction of the target object. When the guide star is angularly offset from the target, it samples a different turbulence volume, resulting in incomplete correction and reduced AO performance. Furthermore, since LGSs are generated either in the mesospheric sodium layer or at finite altitudes in the case of Rayleigh guide stars, they cannot fully sample the upper atmospheric turbulence. As a result, residual uncorrected turbulence further degrades image quality and system performance [1].

We have developed a laboratory setup to experimentally study angular anisoplanatism using a pseudo-random phase plate (PRPP) that simulates atmospheric turbulence. Various parameters, including Zernike coefficient correlations, mean square error, and centroid displacements, are analysed to characterise the effect of angular separation on AO correction performance [2].

To mitigate the limitations of angular and focal anisoplanatism, Multi-conjugate adaptive optics (MCAO) systems are often used to improve the effective FoV. However, MCAO requires multiple wavefront sensors to sample the volumetric turbulence, increasing the system complexity. To address this, we have developed a multiplexed wavefront sensing scheme based on a grating array-based wavefront sensor (GAWFS). This approach enables simultaneous sensing of multiple wavefronts using a single sensor with a single camera frame [3].

Another limitation of the conventional Shack–Hartmann wavefront sensor (SHWFS) is its dependence on a pre-recorded reference wavefront. It first records reference spots and then estimates local slopes from the displacement of the spots in the test wavefront. This requirement limits its use in scenarios where obtaining a high-quality reference is difficult or impossible. To overcome this, we employ the GAWFS in a reference-less configuration that utilises both +1 and −1 diffraction orders to determine the local slopes directly from the test wavefront, thereby eliminating the need for a separate reference measurement [4].

References

[1] R. Tyson, and B. Frazier, *Principles of Adaptive Optics,* CRC Press, 5th ed. (2022).
[2] J. Singh, L. Mandal, B.Pathak, C. S. Narayanamurthy, and A. R. Ganesan, *Optics Communications* **557**, 130360 (2024).
[3] J. Singh, B. Pathak, C. S. Narayanamurthy, and A. R. Ganesan, *Optics Express* **33**, 4437-4445 (2025).
[4] B. Pathak, J. Singh, C. S. Narayanamurthy, and A. R. Ganesan, *Optics Letters* **50**(21), 6798-6801 (2025).

Deep-Infrared Ultrafast Femtosecond Parametric Oscillator at 7 μm

[1,#]*Chaitanya Kumar Suddapalli*
[1]Tata Institute of Fundamental Research, 36/P Gopanpally, Hyderabad-500 046, Telangana, India

[#]chaitanya.suddapalli@tifrh.res.in

Ultrashort deep-infrared laser pulses are crucial for spectroscopy and sensing, yet direct generation is constrained by the lack of suitable gain media. This lecture discusses the development of efficient, high-power deep-infrared optical parametric oscillator at 7 μm and its power scaling capabilities, enabling access to this otherwise inaccessible spectral region.

The 6-8 μm spectral window encompasses characteristic absorption bands of numerous molecules relevant to environmental monitoring [1] and biomedical diagnostics [2]. However, direct generation of ultrafast pulses in the deep infrared (deep-IR) using conventional lasers is limited by the lack of suitable gain media. On the other hand, deep-IR femtosecond sources based on nonlinear frequency conversion, particularly optical parametric oscillators (OPOs), have emerged as practical alternatives. Among the available nonlinear materials, Cadmium Silicon Phosphide, $CdSiP_2$ (CSP), is particularly attractive due to its large effective nonlinearity (d_{36}~84 pm/V), broad transparency ranges from 1 to ~ 8 μm, and compatibility with 1 μm ultrafast pump lasers [3]. Earlier reports on femtosecond deep-IR OPOs based on CSP were limited to pumping <4 W due to thermal effects, constraining achievable deep-IR output [4]. In this lecture, I will discuss the power scaling and full characterization of a deep-infrared parametric oscillator with average output power exceeding 400 mW in few-cycle pulses [5].

References:

[1] N. J. Bareza, K. K. Gopalan, R. Alani, B. Paulillo, and V. Pruneri, “Mid-infrared gas sensing using graphene plasmons tuned by reversible chemical doping,” *ACS photonics*, vol. 7, no. 4, pp. 879–884, 2020.

[2] M. J. Walsh, R. K. Reddy, and R. Bhargava, “Label-free biomedical imaging with mid-IR spectroscopy,” *IEEE Journal of selected Topics in quantum electronics*, vol. 18, no. 4, pp. 1502–1513, 2012.

[3] P. G. Schunemann, K. T. Zawilski, L. A. Pomeranz, et al., "Advances in nonlinear optical crystals for mid-infrared coherent sources," *J. Opt. Soc. Am. B* 33, D36–D43 (2016).

[4] S. Chaitanya Kumar, J. Krauth, A. Steinmann, K. T. Zawilski, P. Schunemann, H. Giessen, and M. Ebrahim-Zadeh, “High-power femtosecond mid-infrared optical parametric oscillator at 7 μm based on CdSiP2,” *Optics letters*, vol. 40, no. 7, pp. 1398–1401, 2015.

[5] Kiran K. Panigrahi, B. Chauhan, K. Zawilski, et al., "High-power, broadband, deep-IR femtosecond optical parametric oscillator based on $CdSiP_2$," in Laser Science, *Optica Technical Digest (Optica Publishing Group, 2025)*, pp. JW4A–9.

Development of Low-cost Spectrometer for Pesticide detection using ML

[1,#]Alex Kumar Singh,[2]Arun Anand and [1]Gyanendra Sheoran
[1]AROMA Lab, Department of Applied Sciences, National Institute of Technology, Delhi, India
[2]Department of Physics, Sardar Patel University, Anand, Gujarat, India

[#]alexsingh@nitdelhi.ac.in

A compact smartphone camera based visible spectrometer is made using a razor-blade, cardboard and DVD-R. Automated wavelength calibration, absorbance extraction and Machine learning analysis enabled reliable estimation of pesticide concentration and classification is performed.

Detecting pesticide residues remains an important challenge in agriculture and food surveillance industry. Conventional analytical techniques such as Gas Chromatography-Mass Spectrometery(GC-MS) and high performance liquid chromatography (HPLC) provides excellent sensitivity but require expensive laboratory infrastructure and trained personnel. Consequently, there is increasing interest in portable optical spectroscopic systems capable of providing rapid, low-cost screening measurements.

In this work, first a compact visible spectrometer is developed using inexpensive readily available items like White LED, cardboard enclosure, razor-blade and DVD-R. For the capturing device, Samsung Galaxy A125 smartphone camera is used (which can further be replaced by any imaging camera or USB device including webcams based on the resolution requirements). As the instrument mainly operates over the visible spectral region (approximately 400-750nm) with an experimentally determined dispersion of nearly ~1.8 nm pixel^{-1} (for the chosen Samsung Smartphone camera) using CFL bulb in lab, while independent validation employed Solar Fraunhofer absorption features, resulting in wavelength residuals below ~2nm.

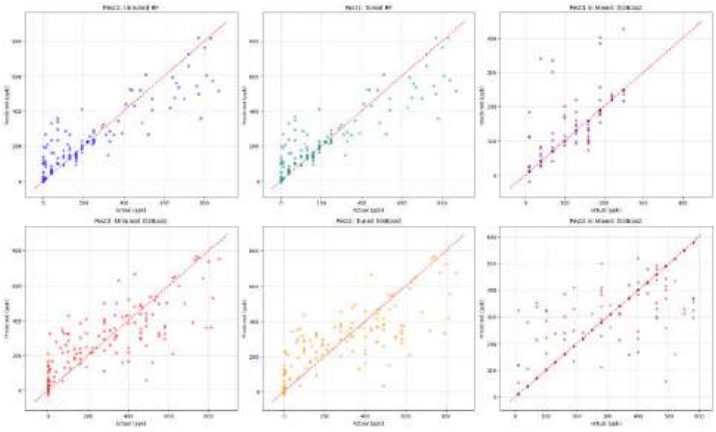


Figure 1: Predicted vs Actual concentration best ML outputs for Pesticides

An automated Python-based processing pipeline was developed to perform spectral extraction, image tilt-correction, wavelength calibration, absorbance computation using Beer-lambert relation and feature extraction. Fourteen engineered spectral features are further singled out, including peak intensities, peak ratios, spectral contrasts, integrated areas, and spectral slopes and were extracted from each normalized spectrum. These features are used for quantitative regression and pesticide classification using Random Forest, K-Nearest Neighbor (KNN) and Extreme Gradient Boosting (XGBoost) models.

Experimental investigations were carried out on aqueous solutions of two commercially available pesticides, Hamla 550 (Chlorpyrifos + Cypermethrin) and Kemcron (Profenofos) covering concentrations between 10 ppb and 4 ppm together with binary mixtures of the two. The developed system achieved concentration prediction with coefficient of determination exceeding R^2 = 0.82 for individual pesticide estimation and classification accuracy of 97.6%, demonstrating that meaningful quantitative information can be extracted despite the simplicity of the hardware. The results further indicate that ensemble learning methods outperform conventional linear regression due to the nonlinear relationship between spectral response and pesticide concentration. Owing to its material cost of less than ₹50 (excluding the smartphone), the proposed approach has potential point-of-measurement applications in agriculture, environmental water-quality monitoring, educational spectroscopy, and preliminary pesticide residue screening before laboratory confirmation.

The authors acknowledge research funding through Department of Science and Technology DST/TTI/TDP-12/2024.

References:

[1] Crocombe, R. A. (2018). Portable spectroscopy. Applied Spectroscopy, 72(12), 1701–1751.
[2] Mäntele, W., & Deniz, E. (2017). UV-VIS absorption spectroscopy: Lambert-Beer reloaded. Spectrochimica Acta Part A: Molecular and Biomolecular Spectroscopy, 173, 965–968.

Generation and Validation of Phase Screen using Zernike Based Method

#Diksha Karnatak, Sarita and Rakesh Kumar Singh
Laboratory of Information Photonics and Optical Metrology, Department of Physics, Indian Institute of Technology (Banaras Hindu University), Varanasi, India, 221005

#*dikshakarnatak.rs.phy25@itbhu.ac.in*

A static phase screen is generated to simulate atmospheric turbulence using Zernike-based method following modified von Kármán statistics. Correlated Zernike coefficients are obtained from a covariance matrix, which reconstructs turbulence-induced wavefront distortions. Validation of the phase screen is performed using the wavefront structure function parameter, which shows good agreement *with the modified von Kármán model.*

Atmospheric turbulence introduces random phase distortions in optical wavefronts. These effects are simulated by static phase screen generated using Zernike based method [1], following modified von Kármán turbulence statistics. The atmospheric wavefront is represented as a linear combination of Zernike Polynomials

$$\phi(r) = \sum_{j=2}^{N} a_j \, Z_j \left(\frac{r}{R}\right) \tag{1}$$

where a_j represents Zernike coefficients and $Z_j \left(\frac{r}{R}\right)$ signifies Zernike polynomial following Noll indexing [2] and *N* denotes the highest retained Zernike mode. These Zernike coefficients determine the contribution of individual aberration modes. j = 1, is excluded as it does not contribute to phase distortion. These coefficients satisfy the covariance statistics derived from the modified von Kármán turbulence model. Hence, the covariance matrix is decomposed using the Cholesky factorization, enabling the generation of correlated Zernike coefficients from independent Gaussian random variables.

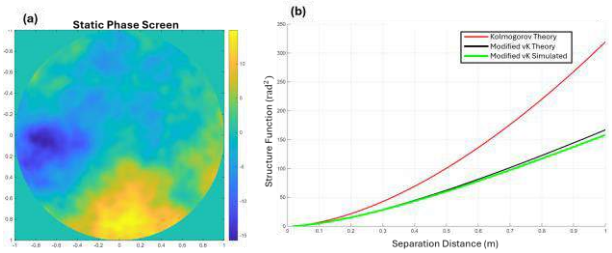


Fig. 1: (a) Generated Phase Screen (b)Validation of Phase Screen

Let B denote a vector of independent standard Gaussian variables, and U be the lower triangular matrix obtained from the Cholesky factorization of the covariance matrix. The correlated Zernike coefficient vector A is then generated as

$$\mathrm{A} = \mathrm{UB} \tag{2}$$

These coefficients are substituted in Eq. (1), to reconstruct the atmospheric phase screen while preserving the covariance statistics imposed by the modified von Kármán model. The generated static phase screen is shown in Fig. 1(a), and its validation is performed using the wavefront structure function [3] as presented in Fig. 1(b), which agrees with the theoretical modified von Kármán model.

A static atmospheric phase screen is generated using Zernike based method following modified von Karman turbulence statistics. Correlated Zernike coefficients derived from the covariance matrix are used to reconstruct realistic wavefront distortions induced by atmospheric turbulence.

The authors acknowledge the support from IIT(BHU), Varanasi and DRDO sponsored project (DGTM/DFTM/GIA/24-25/426).

References:

[1] B. Lu, D. Cai, *Optics Express* 21 (2024) 38609.
[2] K. Niu, C. Tian, *Jornal of Optics* 24 (2022) 123001.
[3] V.I. Tatarski, R.A. Silverman, N. Chako, *Wave propagation in a turbulent medium*, Dover, New York, (1961).

Scalable Metasurface Photonics for Quantum Computers and Sensors

Amit Agrawal[1,*]

[1]*Department of Engineering, University of Cambridge, Cambridge CB3 0FA, UK*
**Corresponding author: aka59@cam.ac.uk*

Development of compact, robust and scalable experimental systems that produce cold atomic ensembles or single neutral atoms would enable real-world, deployable applications in quantum sensing and precision measurement. In particular, transportable optical clocks based on the ultra-narrow optical transition of ^{87}Sr require a liter-scale, fully monolithic, alignment-free apparatus to produce a magneto optical trap (MOT). However, straightforward miniaturization of the traditional optical infrastructure necessary to implement multi-step laser cooling has proven prohibitively complex.

Multifunctional metasurface (MS) optics, planar photonic elements consisting of periodic arrays of dielectric nanopillars, are capable of exquisite control of the optical phase and offer the potential to perform the function of multiple traditional optics simultaneously using a single semiconductor wafer-thickness optic, greatly reducing the system footprint. Here, we demonstrate the use of TiO_2 metasurfaces to simultaneously generate all the laser beams required for trapping and cooling of Sr in a fully monolithic, alignment-free platform, and use it to experimentally realize a two-stage cooled MOT for ^{87}Sr.

Our Sr MOT platform consists of a custom geometry of twelve optical beams for the two wavelengths involved with cooling and trapping Sr (six each at 461 nm and 689 nm), integrated and controlled with twelve MS optics nanofabricated on two fused silica wafers. Each metasurface optic acts equivalent to several bulk optics in positioning, expanding or collimating the beam, deflecting the beam to the center of the trap, and rotating the beam's polarization to the circular polarization needed for atom trapping. The platform contains circular arrays of six co-fabricated MS optics on each of the two fused-silica wafers illuminated directly with optical fibers in an engineered, fixed geometry. We demonstrate the capability of our platform to cool and trap all four naturally occurring isotopes of strontium, including ^{87}Sr, the isotope of preference for most optical lattice clocks. The temperature of the atoms in the Sr MOT was determined to be less than 2 mK with time-of-flight measurements.

These results demonstrate a CMOS foundry compatible, metasurface optics-based approach for laser cooling and trapping of strontium as a scalable, monolithic platform towards realization of a compact, fully integrated strontium optical lattice clock. The multifunctional beam control offered by meta-optics further paves the way for manufacturable miniaturized photonic systems that enable scaling of future quantum systems including quantum computers and sensors.

Light-Matter Interactions with Hyperbolic Materials

[1] S R K Chaitanya Indukuri
[1]Department of Physics
Indian Institute of Technology
Jammu, Jammu and Kashmir, India
[#] *chaitanya.Indukuri@iitjammu.ac.in*

Transition metal di chalcogenide (TMDC) monolayers, with atomic-layer thickness and a direct band gap, are considered for diverse optoelectronic applications. However, due to their atomic-layer thickness, light interacts weakly with TMDCs. We proposed a mechanism in which TMDC couples to a hyperbolic material, enhancing light-matter interactions.

Transition metal dichalcogenides (TMDCs) are direct-band-gap semiconductors in the monolayer limit that exhibit strong excitonic photoluminescence (PL), making them highly attractive for next-generation photonic and optoelectronic devices.

However, their practical implementation is limited by several limitations, including low quantum efficiency, weak optical absorption due to their atomic-scale thickness, and limited light–matter interaction. These factors hinder the performance of TMDC-based photonic and optoelectronic systems.

Enhancing light–matter interactions is therefore essential to fully exploit the potential of TMDCs. Hyperbolic metamaterial (HMM) nano-cavities and natural hyperbolic materials provide a promising platform for this purpose due to their unique hyperbolic dispersion and high photonic density of states. These properties can significantly enhance both optical absorption and spontaneous emission of the TMDC layers.

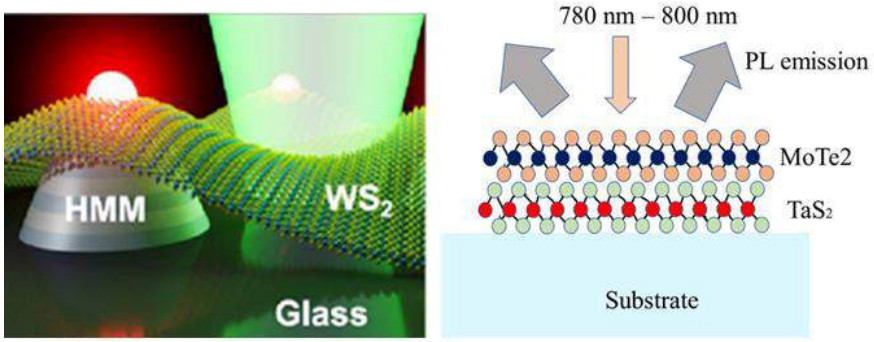


Figure 1: Schematic diagram of TMDC monolayer on top of the HMM Nano cavities and Natural hyperbolic materials.

Motivated by these challenges, we propose integrating monolayer TMDCs with engineered hyperbolic metamaterial nano cavities and naturally hyperbolic materials to achieve enhanced light–matter interactions. By exploiting the hyperbolic dispersion of the High-K vector in these platforms, we proposed a mechanism to improve the absorption, emission, and photo detection efficiency of TMDC-based optoelectronic devices.

References:

[1] S. R. K.Chaitanya Indukuri, Christian Frydendahl, Jonathan Bar-David, Noa Mazurski, Uriel Levy; WS2 Monolayers Coupled to Hyperbolic Metamaterial Nanoantennas: Broad Implications for Light–Matter-Interaction Applications. *ACS Appl. Nano Mater.* 23 October 2020; 3 (10): 10226–10233.

[2] Sakal Singla, Christian Frydendahl, Pragya Joshi, Noa Mazurski, S. R. K. Chaitanya Indukuri, Biswanath Chakraborty, Uriel Levy; Enhancing Broad Band Photoresponse of 2D Transition-Metal Dichalcogenide Materials Integrated with Hyperbolic Metamaterial Nanocavities. *ACS Photonics* 16 October 2024; 11 (10): 4398–4406.

[3] S. R. K. Chaitanya Indukuri, Jonathan Bar-David, Noa Mazurski, Uriel Levy; Ultrasmall Mode Volume Hyperbolic Nanocavities for Enhanced Light–Matter Interaction at the Nanoscale. ACS Nano 22 October 2019; 13 (10): 11770–11780.

Reconfigurable Dielectric Metasurface for Polarization Switching

[1]Abel Paul Joseph, [1#]Harish N. S. Krishnamoorthy
[1]Tata Institute of Fundamental Research Hyderabad, Hyderabad, Telangana 500046
[#]*harishk@tifrh.res.in*

We leverage topological properties and symmetry-breaking dynamics of bound states in the continuum (BICs) to design and fabricate metasurfaces on a phase change material platform (Sb_2S_3) for switchable orbital angular momentum (OAM) beam generation and circular to nearly linear polarization control.

Dielectric metasurfaces (MS) have garnered considerable interest due to their low losses and ability to support high Q-factor resonances. However, such systems once fabricated are constrained to operate within a fixed wavelength range, determined by the geometry and refractive indices of the constituent meta-atom. This limitation can be circumvented by using phase change materials (PCMs) such as Sb_2S_3 which exhibit high refractive index contrast between their amorphous and crystalline phases. In this work, we show that Sb_2S_3 MS which support symmetry-protected bound states in the continuum (BICs) can be used for switchable orbital angular momentum (OAM) beam generation. We also show reversible control over polarization of states in a symmetry-broken MS.

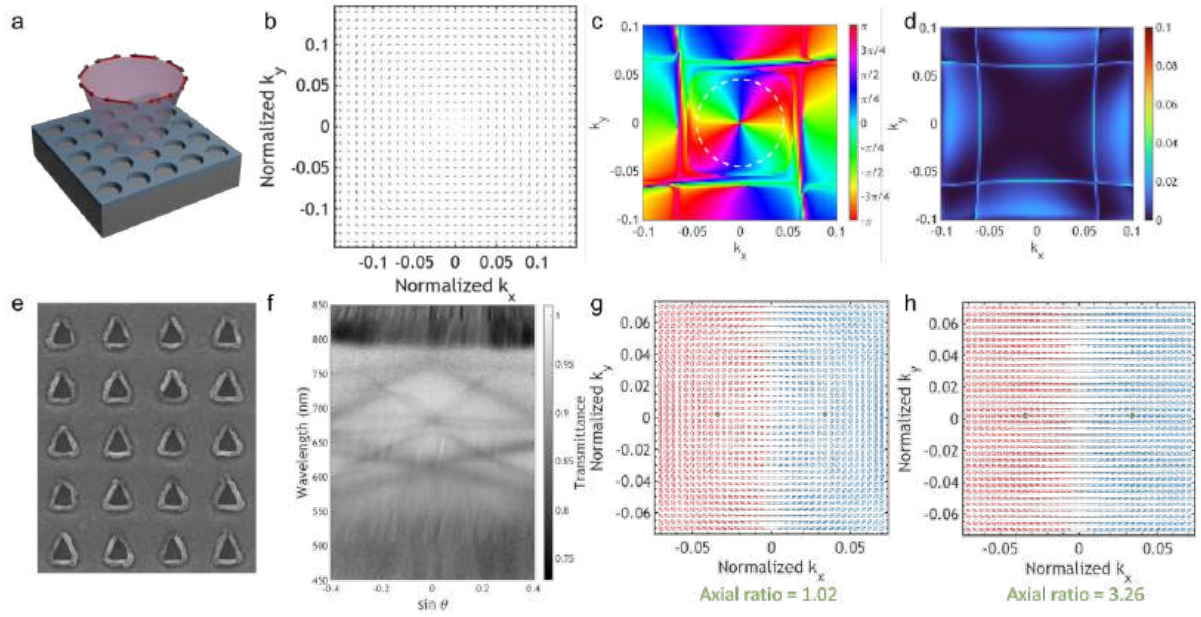


Fig 1: a. Geometry of symmetry-protected metasurface. b. Simulated momentum-space polarization map of a. showing vortex polarization. c(d). Momentum-space phase(amplitude) map of reflected beam at λ = 680 nm in amorphous(crystalline) state. e. SEM image and f. measured band structure of fabricated symmetry-broken metasurface. g(h). Computed momentum-space polarization map of amorphous(crystalline) metasurface showing circular(nearly linear) polarization at (k_x, k_y) = (±0.034, 0).

The designed MS has C_4 symmetry and consists of circular air holes in a thin film of Sb_2S_3 on glass substrate (Fig. 1a), which supports a BIC at λ = 683 nm, with charge $q = 1$. Momentum-space polarization map of the band shows vortex polarization (Fig. 1b). When a circularly polarized beam is incident on the MS, the orthogonally polarized component of reflected/transmitted beam acquires OAM $l = -2q$ [1] at λ = 680 nm in the amorphous phase (Fig. 1c). Upon crystallization, the linear dependence of phase on azimuthal angle is lost, and reflected amplitude becomes zero (Fig. 1d), demonstrating switchable OAM beam generation.

In another MS with broken C_2 symmetry (SEM image in Figure 1e, experimentally determined band structure in Fig. 1f), the annihilation of symmetry-protected BIC generates a pair of C points with circular polarization of opposite handedness in the momentum space [2]. Crystallization causes the C points to shift from λ ~ 680 nm in the amorphous state (Fig. 1g) to λ ~ 779 nm, whereas the new band at λ = 680 nm supports elliptical (nearly linear) polarization (Fig. 1h), thus enabling dynamic polarization control.

References:

[1] B. Wang, W. Liu, M. Zhao, J. Wang, Y. Zhang, A. Chen, F. Guan, X. Liu, L. Shi, J. Zi, *Nature Photonics* 14 (2020), 623–628.
[2] W. Liu, B. Wang, Y. Zhang, J. Wang, M. Zhao, F. Guan, X. Liu, L. Shi, J. Zi, *Physical Review Letters* 123(11) (2019) 116104.

Switching of bands in a graphene assisted metamaterial absorber

Raghwendra Kumar
Department of Physics, Bihar National College, Patna University, Patna, Bihar-800005
Email id of the corresponding author: raghaviitk0@gmail.com

We present a novel switchable multi-band graphene-based metamaterial absorber. Numerical simulations are carried out using the finite integration technique in CST Microwave Studio, while coupled mode theory (CMT) is employed to validate the results and explain the absorption mechanism. The proposed design enables electrical control of the number of absorption bands, making it promising for bands switching applications.

Metamaterials are artificially engineered structures that exhibit unique electromagnetic properties unavailable in naturally occurring materials. Among their various applications, metamaterial absorbers (MMAs) have attracted significant interest because of their potential use in sensing, thermal emission control, infrared detection, and energy harvesting systems. However, conventional metamaterial absorbers generally suffer from limited tunability and lack of dynamic control over their absorption characteristics. Graphene has emerged as a promising material for tunable photonic devices due to its electrically controllable optical conductivity and excellent optoelectronic properties. The integration of graphene with resonant dielectric and metallic structures can substantially enhance light absorption through strong light–matter interaction. Although several graphene-based absorbers have been reported, most of them are designed for a single functionality and provide limited switching capabilities [1, 2].

In this work, a graphene-based multi-band metamaterial absorber consisting of a perforated silicon layer, monolayer graphene, and a metallic substrate is proposed and numerically investigated. The proposed absorber exhibits electrically controlled switching between multi-band, triple-band, double-band, single-band absorption, and perfect reflection, making it suitable for optical switching, modulation, filtering, and communication applications.

Figure 1 shows the three-dimensional schematic of the proposed graphene-based metamaterial absorber unit cell. The switching behavior of the absorption bands for different chemical potentials is shown in Fig. 2.

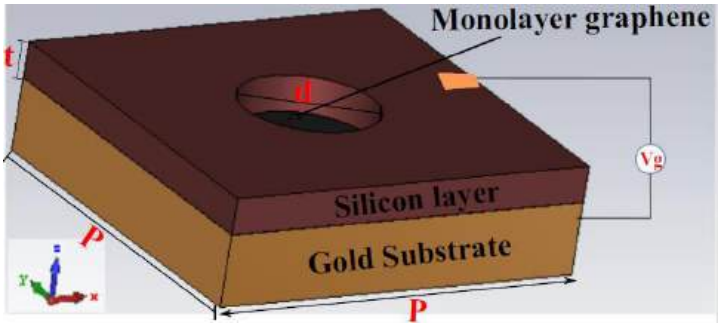


Figure 1 Three-dimensional view of the schematic diagram of the metamaterial absorber.

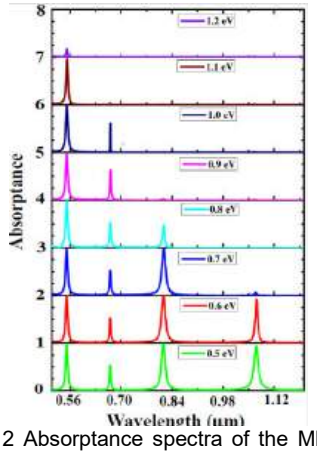


Figure 2 Absorptance spectra of the MMA for different graphene chemical potential.

The proposed simple and actively switchable absorber offers significant potential for graphene-based photonic devices, such as optical switches, modulators, high-performance optoelectronic detectors, and narrowband selective filters. Its ability to dynamically control the absorption bands also makes it promising for radar communication systems requiring selective signal transmission and reception, as well as electromagnetic interference applications involving tunable frequency bands and adjustable interference levels.

References:

[1] Kumar, Raghwendra. "Electric-controlled switching ON/OFF of bands in a graphene-based multi-band metamaterial absorber." *Plasmonics* 20.6 (2025): 3313-3323.
[2] Kumar, Amrendra, et al. "Graphene-supported all-dielectric metamaterial absorber for refractive index sensing at optical frequencies." *Physica Scripta* 100.11 (2025): 115506.

On-Demand SOA-Based Optical Phase Conjugation for Adaptive Coherent Optical Networks

[#]Deepa Venkitesh, Mrudula Pai
[1]Department of Electrical Engineering, Indian Institute of Technology Madras, Chennai 600036,
[#]*deepa@ee.iitm.ac.in*

We present a compact on-demand semiconductor optical amplifier (SOA) based optical phase conjugator supporting three software-selectable modes : conjugation, low-distortion amplification and transparent pass-through, on a single hardware platform. Validation over a 320 km link with PM-56 GBaud 16QAM signals shows stable constellation recovery in every mode with 5–10 ms switching.

As coherent optical networks evolve toward higher data rates and dynamically reconfigurable transmission paths, flexible optical impairment compensation is essential to reduce the reliance on power-hungry digital signal processing (DSP). Optical phase conjugation (OPC) offers an attractive route to mitigating chromatic dispersion and Kerr nonlinearity in the optical domain, but conventional conjugators are fixed-function subsystems that occupy a node whether or not conjugation is required. We report a compact, packaged on-demand SOA-based OPC prototype that resolves this limitation by supporting three software-selectable modes on a single hardware platform, allowing the module to adapt its role to the instantaneous needs of a reconfigurable network.

In this talk, we discuss working principle of SOA as distortion-free conjugator and an amplifier, the corresponding mathematical models and the system design details of the multi-functional prototype built in our laboratory. In conjugate mode, a strong optical pump generates a phase-conjugated replica of the signal through four-wave mixing, providing dispersion and nonlinearity compensation. In amplifier mode, the same laser is repurposed as a holding beam that suppresses gain saturation to enable low-distortion amplification. In transparent mode, the SOA is bypassed using optical switches. Mode selection is performed in real time under software control, with a measured switching time of 5–10 ms. The packaged unit is shown in Fig. 1. The prototype is experimentally validated in a 320 km (4 × 80 km) standard single-mode fibre coherent link carrying PM-56 GBaud 16QAM signals. Dynamic switching between all three modes are demonstrated without interrupting the link, and stable constellation recovery was obtained in each mode (Fig. 2). Transparent operation introduced a negligible penalty relative to the reference (average EVM of 8.4 % against 8.17 %), while the conjugate and amplifier modes both operated near 10 % EVM, well within the recovery threshold for 16QAM. Holding-beam-assisted amplification performs similar to the conjugator.



Fig. 1: Packaged on-demand SOA-based OPC prototype.

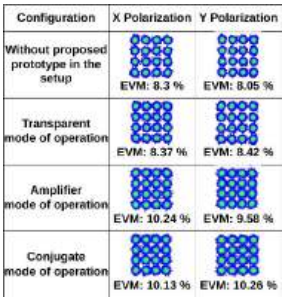


Fig. 2: Recovered constellations and EVM per mode after 320 km.

These results establish that impairment compensation, amplification and pass-through can be consolidated into one field-deployable module, reducing the DSP burden of electronic dispersion compensation and enabling adaptive all-optical signal processing. Target applications include intelligent ROADM nodes, flexible coherent transport networks, and energy-efficient coherent communication systems.

Acknowledgements: The authors acknowledge the support of IIT Madras, AOC Testbed project and IITM Pravartak Technologies Foundation.

References:

[1] G.P. Agrawal, *Fiber-Optic Communication Systems*, Wiley, New York (2010).
[2] A. Yariv, D. Fekete, D.M. Pepper, *Optics Letters* 4 (1979) 52.
[3] S. Sunder, A. Sharma, *Workshop on Recent Advances in Photonics (WRAP 2019)* 19 (2019).

FPGA-Based Wideband Pre-Emphasized LFM Waveform Generation for Photonic Filters

[1,2#]Bingi Uday Kiran, [2]Arun Malik, [1,2]Md Kamran Afroz, and [1,2]Amol Choudhary
[1]Ultrafast Optical Communications and High-performance Integrated Photonics (UFO-CHIP)
[2]Department of Electrical Engineering, IIT Delhi, New Delhi 110016, India

[#]*bingiudaykiran@gmail.com*

FPGA-driven broadband LFM waveform synthesis with programmable pre-emphasis is experimentally demonstrated for SBS-based photonic filtering. Integrated architecture replaces external AWGs, enabling compact implementation, real-time control, and GHz-range signal generation for reconfigurable microwave photonic processing.

Broadband SBS photonic filters typically rely on external AWGs for wideband LFM generation, increasing system cost and limiting integration. Integrated FPGA-based digital pre-emphasis for broadband SBS photonic filtering has received limited experimental investigation, motivating the proposed architecture.

The experimental platform is implemented on an RFSoC 4×2 board based on the AMD-Xilinx Zynq UltraScale+ RFSoC Gen3. A 14-bit RF DAC generates waveforms in real output mode at 9.34 GSPS using a 583.68 MHz AXI4-Stream interface. As shown in Fig. 1(a), the architecture integrates the MPSoC, AXI interconnect, custom RTL waveform engine, and RF Data Converter IP. A dual-RAM streaming engine [Fig. 1(b)] combines two 128-bit RAM outputs into a 256-bit data stream, enabling deterministic continuous waveform generation across independent write and DAC clock domains.

A 10 MHz–1 GHz, 2 µs linear frequency modulated (LFM) waveform is synthesized and stored in FPGA memory to drive an electro-optic modulator in an SBS-based microwave photonic filter. The broadband RF sweep shapes the optical pump spectrum, broadening the SBS gain spectrum beyond its intrinsic linewidth and enabling programmable broadband filter responses. The photonic setup is shown in Fig. 1(f). Direct application of the DAC-generated waveform results in frequency-dependent amplitude variation caused by electro-optic nonlinearities, reducing spectral flatness.

To compensate for this effect, the measured filter response is analyzed to compute a digital amplitude pre-emphasis profile, which is applied within the FPGA before waveform regeneration. Figures 1(d) and 1(e) demonstrate preserved linear time-frequency evolution and improved spectral uniformity after pre-emphasis. The optimized waveform is then applied to the photonic filter, achieving a 1 GHz bandwidth response with ripple within 2 dB, as shown in Fig. 1(g). Figure 1(c) further demonstrates reconfigurable LFM bandwidths from 200 MHz to 1 GHz.

The proposed RFSoC framework enables deterministic waveform generation with integrated digital pre-emphasis, eliminating external AWGs. Experimental results demonstrate stable operation, broadband reconfigurability up to 1 GHz, compact implementation, and efficient waveform synthesis for programmable microwave photonic filtering.

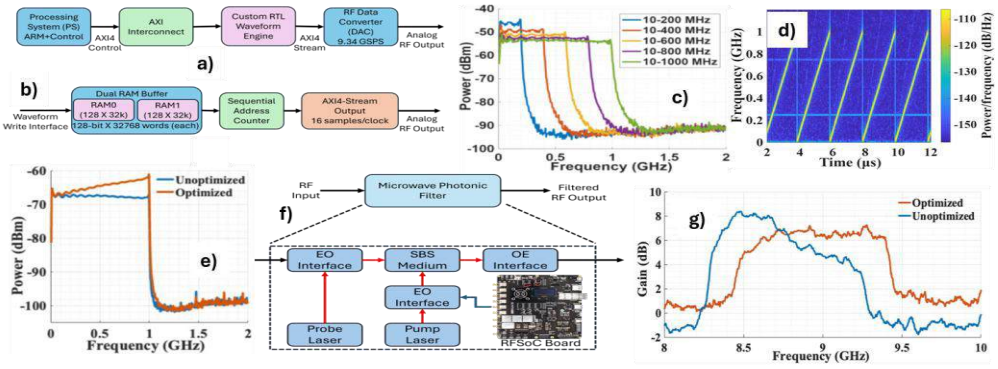


Fig. 1: a) RFSoC waveform synthesis architecture, b) Dual-RAM streaming architecture, c) DAC-generated LFM spectra (200-1000 MHz), d) Measured LFM spectrogram, e) Measured LFM spectrum with and without pre-emphasis, f) RFSoC-driven SBS photonic filter setup, g) SBS photonic filter response

Acknowledgement: Department of Telecommunication (DoT), India, through the Advanced Optical Communication Testbed Project.

References:

[1] S. Y. Cruz-Nava et al., IEEE Embedded Systems Letters 17 (2025) 365–369.
[2] J. Goldsmith et al., IEEE Access 8 (2020) 129012–129031.
[3] A. Choudhary et al., Optics Letters 41 (2016) 436–439.

Millimeter Wave Over Fiber System with Nakagami-m Fading and Adaptive Equalization for 5G C-RAN

[1]Mohit Kumar Sisodiya [1]Simranjit Singh [2]Arun Kumar Singh
5G Use Case Lab, Department of ECE, Punjab Engineering College, Chandigarh
SRC Lab, Department of ECE, Punjab Engineering College, Chandigarh
Mohitkumarsisodiya.phd24ece@pec.edu.in , simranjit@pec.edu.in , arun@pec.edu.in

The millimeter wave over fiber is simulated for 5G cloud radio access network (C RAN) modeling both the optical fronthaul segment and wireless access link followed by Nakagami-m fading using Optisystem 23 software. Further, the adaptive automatic gain control (AGC) based equalizer used to compensate fading distortion and Q factor improved across different fading levels.

The advancement of network happening on regular basis which requires high capacity, low latency fronthaul links for better results in terms of speed, capacity, BER and QoS. The Analog Radio over Fiber (RoF) technology plays crucial role in transporting radio signal over fiber which is stated as most bandwidth efficient fronthaul solution. For dense urban area MMwave preferred to boost network flexibility and match the capacity of 5G network [1]. In this paper, MMwave over fiber is proposed in which downlink is divided into two parts BBU to RRH by SMF (optical ROF fronthaul) and wireless scenario which is from RRH to all users. The wireless part is implemented through fading channel i.e. Nakagami-m distribution statistical model [2].

For MMwave generation, optical heterodyne beating of two CW lasers at 193.1THz and 193.16 THz are used for 60 GHz MMwave carrier. After sending QAM data at 10 Gbps through SMF followed by the heterodyne receiver, the signal is transmitted through Nakagami-m fading channel based on the standard Probability density function (PDF) of nakagami-m stated below.

$$f(x;\ m, \Omega)\ =\ \frac{2m^m}{\Gamma(m)\,\Omega^m}\ x^{2m-1}\ \exp\left(-\frac{mx^2}{\Omega}\right),\ \ \text{for}\ x \geq 0$$

Where the “x” represents received signal amplitude, m is fading factor Ω mean square value and Γ(m) is the Gamma function. By varying m(fading parameter) as per the standard from (0.5,1,2,5 to10) , where m<1(severe fading) m=1 (rayleigh fading) and as m value increases it experience milder fading. To recover the distorted signal from different conditions an adaptive AGC equalizer is implemented bt introducing python signal processing component placed after nakagami-m fading in Optisystem. Architecture of system is shown in Fig1.

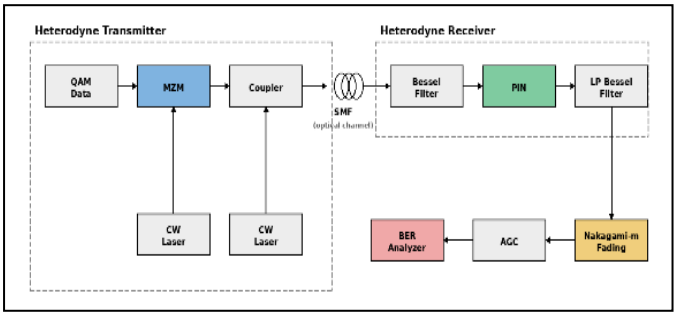


Fig. 1: Architecture of Radio over system

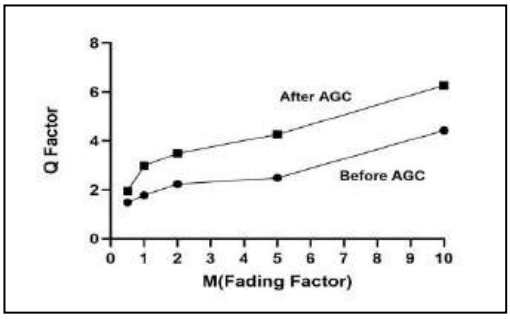


Fig. 2: Q Factor variation wrt AGC

Behavior of AGC equalizer is evaluated and compared with Q factor before equalizer shown in Fig2.

In conclusion, 5G C-RAN MMwave over fiber Fronthaul with Nakagami-m wireless channel simulated with software. The AGC equalizer proposed method improves Q factor across different fading. In future can be extended to multi-users fronthaul and upgradation in recovering method by including machine learning algorithms.

References:

[1] C. Vázquez, R. Altuna, Y. Jung, J. Barco-Alvárez, D. McCulloch and P. Petropoulos, "*Photonics Breakthroughs 2024 Advances in B5G Radio-Power Over Fiber Fronthaul,"* in IEEE Photonics Journal, vol. 17, no. 3, pp. 1-10, June 2025
[2] Q. -N. Van *et al*., "*Multiple RISs for Enhancing the Secrecy Performance of NOMA Systems Over Realistic Nakagami-m Fading Channels*," in IEEE Transactions on Vehicular Technology, vol. 73, no. 5, pp. 6584-6599, May 2024

Co-Alloyed Perovskite Quantum Dots for Controlled Hot-Carrier Dynamics and Phase Stable Optoelectronics

[1]Afreen,[2]Shekhar Mondal,[2]Abhijit Hazarika and [1,#]K. V. Adarsh
[1] Department of Physics, Indian Institute of Science Education and Research, Bhopal, 462066, India
[2]Polymers and Functional Materials Division, CSIR-Indian Institute of Chemical Technology, Uppal Road, Tarnaka, Hyderabad, 500007, India

[#]*adarsh@iiserb.ac.in*

Tunable bandgap along with strong carrier-phonon coupling, long carrier lifetime and controlled hot-phonon bottlenecks in co-alloyed $FAPbI_3$ and $CsPbBr_3$ quantum dots unveiled from the temperature-dependent photoluminescence and ultrafast transient absorption spectroscopy, emphasizing their potential for next-generation optoelectronics.

Metal halide perovskite quantum dots (QDs) have emerged as a highly promising material for a plethora of futuristic and efficient optoelectronic devices [1] owing to their high absorption coefficient, color purity and defect tolerance [2,3]. However, conventional metal halide perovskite QD systems often face limitations of phase instability and rapid carrier thermalization [4].

In this work, we investigate the temperature-dependent optoelectronic properties of co-alloyed QDs, consisting of formamidinium lead iodide ($FAPbI_3$) and cesium lead bromide ($CsPbBr_3$) in various ratios. Using ultrafast transient absorption spectroscopy in along with steady-state and time-resolved photoluminescence (PL) over a 10-300 K range, we characterize the carrier dynamics and lattice interactions of these systems. Our results exhibit excellent composition-dependent bandgap tunability (Fig. 1(a)) and incredibly long-lived carrier lifetimes (~ 30 ns), substantially surpassing their pure-inorganic $CsPbBr_3$ counterparts (Fig. 1(b)). We observe a strong carrier-phonon coupling indicated by a Fröhlich interaction energy of nearly 47 meV (Fig. 1(c)). Crucially, at high excitation fluences, these co-alloyed QDs exhibit a pronounced hot-phonon bottleneck.

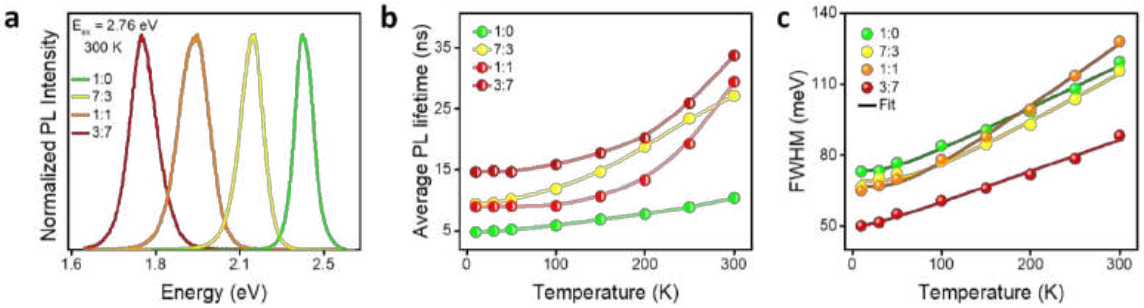


Fig. 1: (a) Normalized PL intensity of $FAPbI_3$:$CsPbBr_3$ = 1:0; 7:3; 1:1; & 3:7 QDs showing bandgap tunability, (b) their average PL lifetime and (c) corresponding PL fwhm fit for carrier-phonon coupling.

We show that the strength of this bottleneck and the resulting carrier cooling rate can be systematically tuned through the formamidinium/cesium ratio, as the rotational degrees of freedom of the organic cation provide additional channels for phonon-bottleneck enhancement.

References:

[1] Sutherland, Brandon R., and Edward H. Sargent. *Nature Photonics* 10.5: 295-302 (2016).
[2] Protesescu, Loredana, et al. *Nano letters* 15.6: 3692-3696 (2015).
[3] Kang, Jun, and Lin-Wang Wang. *The journal of physical chemistry letters* 8.2: 489-493 (2017).
[4] Bodnarchuk, Maryna I., et al. *ACS energy letters* 4.1: 63-74 (2018).

Ultrafast Fiber Laser – An Avenue for Photonic Intelligence

Nithyanandan KANAGARAJ,
Ultrafast Fiber Optics and Smart Photonic Technologies Lab, Indian Institute of Technology Hyderabad, Telangana – 502285, India

nithyan@phy.iith.ac.in

Ultrafast fiber lasers reveal diverse nonlinear pulse dynamics such as soliton molecules, molecular complexes, and noise-like pulses. Integrating AI and machine learning enables automated optimization, real-time stability control, and intelligent spectral shaping, significantly enhancing performance and adaptability in next-generation photonic systems for sensing, communication, and advanced scientific applications.

Ultrafast fiber lasers have become indispensable tools for exploring light–matter interactions on extremely short timescales. Their guided-wave architecture enables precise control over dispersion, nonlinearity, gain, and filtering, allowing for the generation of diverse pulse regimes within a compact and stable platform. This work brings together recent developments in understanding how different physical mechanisms in a fiber cavity cooperate or compete to produce a rich spectrum of pulse behaviors [1]. Particular attention is given to bound multi-pulse states, broadband stochastic emissions, and vectorial soliton formations—each revealing unique aspects of nonlinear intracavity dynamics. These regimes provide a window into phenomena such as phase-locked pulse binding, long-range temporal correlations, and polarization-dependent coupling, offering insights that are valuable for both fundamental studies and practical implementations.

Alongside these physical investigations, the work emphasizes the growing role of computational intelligence in shaping the next generation of photonic systems. Modern fiber lasers often feature many tunable elements whose combined influence on pulse formation is highly nonlinear. Traditional trial-and-error tuning struggles to exploit the full capability of such systems [2]. By incorporating modern data-driven strategies—including training-based prediction models, adaptive control algorithms, and learning-enabled feedback mechanisms—fiber lasers can be guided toward desired operating states with improved speed, consistency, and resilience to perturbations. These approaches enable dynamic optimization that would be difficult to achieve manually, particularly in high-dimensional parameter landscapes.

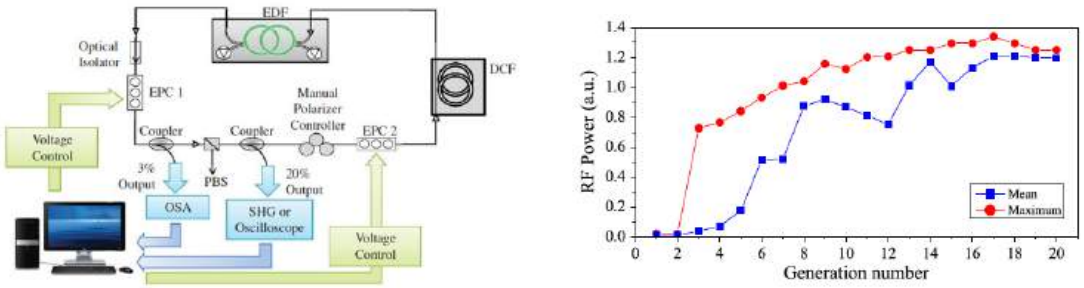


Fig. 1 (a) A fiber laser cavity mode-locked through nonlinear polarization rotation through an electronically controlled PC with AI/ML algorithm (b) Convergence curve of the merit function for stable mode-locking

The convergence of advanced laser physics with machine-based optimization marks a shift toward intelligent optical platforms that can sense, adapt, and respond to changes in their environment [3]. The broader implication of this work is the emergence of photonic systems that exhibit both high performance and operational autonomy, supporting opportunities in precision measurement, optical communication, biomedical diagnostics, and other fields where reliable ultrafast light sources are essential.

References:

[1]. Grelu, P. Akhmediev, N. : Dissipative solitons for mode-locked lasers. Nat. Photonics 6, 84–92 (2012).
[2] Krupa, K., Nithyanandan, K., Andral, U., Tchofo-Dinda, P. Grelu, P. : Real- time observation of internal motion within ultrafast dissipative optical soliton molecules. Phys. Rev. Lett. 118, 243901 (2017).
[3] ZQ Wang, K Nithyanandan, A Coillet, P Tchofo-Dinda, Ph Grelu: Optical soliton molecular complexes in a passively mode-locked fibre laser, Nat. Commun. (10), 830 (2019).

Laser solver for computationally hard optimization problems

[1,#]Vishwa Pal,[1]Rajneesh Fulara, [3]Fabien Bretenaker [4]Asher Friesem and [5]Nir Davidson
[1]Department of Physics, Indian Institute of Technology Ropar, Ropar, Punjab 140001, India
[2]Université Paris-Saclay, ENS Paris-Saclay, CNRS, CentraleSupélec, LuMIn, Orsay, France
[3]Department of Physics of Complex Systems, Weizmann Institute of science, Rehovot, Israel

[#]*vishwa.pal@iitrpr.ac.in*

We present a rapid laser solver for computationally hard optimization problems arising across diverse domains of science and technology. Experimental and simulation results demonstrate rapid, fair sampling of the XY spin Hamiltonian and efficient solutions to phase retrieval problems. We further introduce an internal feedback-driven annealing mechanism that enables the solver to escape locally stable states, significantly enhancing its optimization performance.

Optimization problems are ubiquitous across social science, biology, chemistry, physics, engineering, computer science, big data, and artificial intelligence [1]. Many of these problems belong to the class of computationally hard problems, motivating the search for physical systems capable of solving them efficiently. A promising approach is to map optimization problems onto spin Hamiltonians and implement them in physical platforms that emulate spin dynamics, such as Bose-Einstein-condensate polaritons, superconducting circuits, optical parametric oscillators, integrated photontic circuits, spatial light modulators, and coupled laser networks [2]. In these systems, the solution to the optimization problem is encoded in the ground state of the corresponding spin Hamiltonian. Among the available platforms, coupled lasers are particularly attractive because their intrinsic gain-dissipation dynamics naturally drive the system toward phase-locked minimum-loss configurations, which are analogous to the ground-state of a spin Hamiltonian [2-4].

We present a rapid and efficient optimization solver based on coupled laser arrays, generated in a degenerate cavity, as shown in Figs.1(a,b). By incorporating a self-imaging telescope and a near-field binary amplitude mask with circular holes arranged in a desired geometry, the cavity can generate thousands of nearly identical lasers in various network configurations. The lasers are coupled through Talbot diffraction, and the dissipative coupling drives the system toward phase-locked, minimum-loss states. Figures 1(b-f) demonstrates rapid fair sampling in a negatively coupled square laser array with a unique ground state (Fig. 1(c)). The far-field diffraction pattern exhibits sharp peaks and a central intensity null, indicating long-range out-of-phase phase ordering (Fig. 1(d)). This ordering is further confirmed by the measured coherence (Fig. 1(e)) and phase distribution (Fig. 1(f). The results show that the entire ensemble of experiments, realized through multiple longitudinal modes, converges to the same nondegenrate ground state, consistent with the single minimal-loss manifold shown in Fig. 1(c).

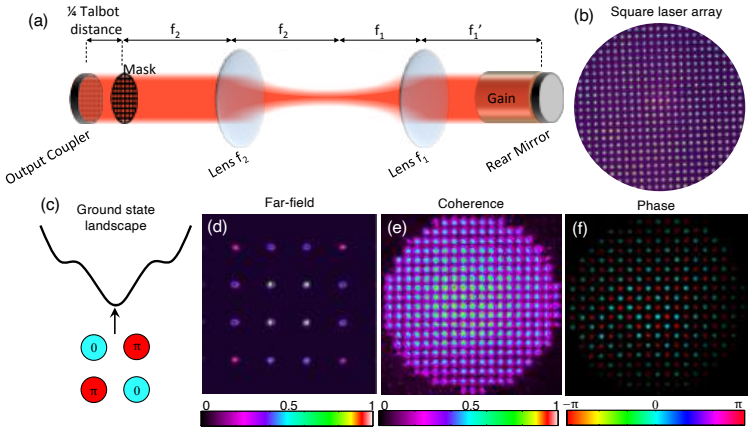


Figure 1. Rapid fair sampling of a negatively coupled square laser array. (a) Setup, (b) square laser array (near field), (c) ground state landscape, (b) far-field, (d) coherence function, and (d) phase distribution.

Experiments on systems with doubly degenerate and highly degenerate ground state manifolds further demonstrate the efficiency of the laser solver [2]. The solver has also been applied to phase retrieval problems, enabling object reconstruction from scattered intensity distribution [3]. More recently, an internal feedback-driven annealing mechanism was shown to help the system escape locally stable states, significantly improving optimization performance [4].

References:

[1] C. H. Papadimitriou and K. Steiglitz, *Combinatorial Optimization: Algorithms and Complexity* (Dover, NY, 1998)
[2] V. Pal, S. Mahler, C. Trandonsky, A. A. Friesem, and N. Davidson, Physical Review Research 2, 033008 (2020).
[3] C. Tradonsky, I Gershenzon, V. Pal, R. Chriki, A. A. Friesem, O. Raz, and N. Davidson, Science Advances 5, eaax4530 (2019)
[4] R. Fulara, F. Bretenaker, and V. Pal, arXiv:2602.18368 (2026).

Selective-State Residual-Based DSP for 2.24 Tbps Coherent DWDM Transmission

[1]Priyanshu Kumar Pandey,[2,#]Kritarth Srivastava and [1,2]Amol Choudhary
[1]Ultrafast Optical Communications and High-performance Integrated Photonics (UFO-CHIP)
Bharti School of Telecommunication Technology and Management, IIT Delhi
[2]Department of Electrical Engineering, IIT Delhi, New Delhi-110016, India

[#]*kritarthsrivastava4@gmail.com*

We propose a machine learning-inspired digital signal processing (DSP) framework for coherent optical communications. By utilizing Selective-State Residual Receiver, our approach achieves significant improvements in bit error rate (BER) and error vector magnitude (EVM) compared to standard commercial DSP software.

Due to rapid surge in data traffic, the demand for high-capacity optical communications network has increased significantly. In recent years, a lot of focus has been on WDM based systems to increase the capacity of long haul-optical networks [1]. In this work, we experimentally demonstrate 10 channels 50 GHz spacing WDM coherent transmission over 200 km distance and 224 Gbps bit rate per channel using dual polarization (DP) 16-QAM 28 GBaud modulation format. The schematic of coherent WDM setup is shown in Fig. 1 (a). The process flow of in-house DSP chain is illustrated in Fig. 1 (b).
The classical coherent DSP receiver includes chromatic dispersion compensation, timing synchronization, carrier frequency offset compensation, and MIMO equalization. While the classical DSP chain compensates for major impairments, residual distortions may persist. These include residual ISI, nonlinear impairments, phase estimation errors, amplitude compression, WDM-dependent distortions, and imperfect convergence of MIMO equalization and carrier phase estimation algorithms. The proposed Selective-State Residual Receiver (SSR) [2] is designed to learn and mitigate these remaining impairments. In the proposed implementation, SSR is used as a post-DSP residual-correction stage. It predicts a small correction to the classical DSP output using local symbol-memory, nonlinear intensity-dependent terms, WDM-channel features, and compact state features. The final performance was evaluated using measured PRBS SER in addition to EVM.
The EVM was computed using both our in-house DSP implementation and commercial software (Keysight VSA). The results, shown in Fig. 2, indicate that in-house DSP outperforms commercial solutions. The X- and Y-polarization constellation diagrams for all channels were computed using the in-house DSP, with only channels 3 and 5 shown in the inset of Fig. 2.

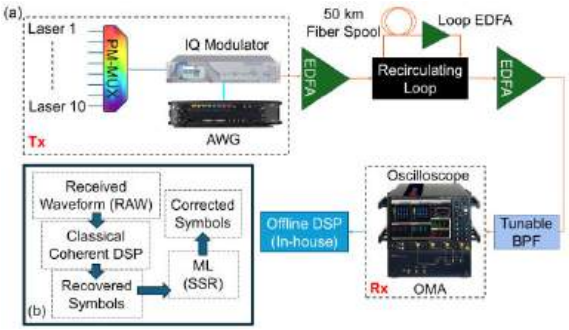


Fig. 1: (a) Schematic of 10 channels coherent WDM setup (b) Process flow of In-house DSP Chain

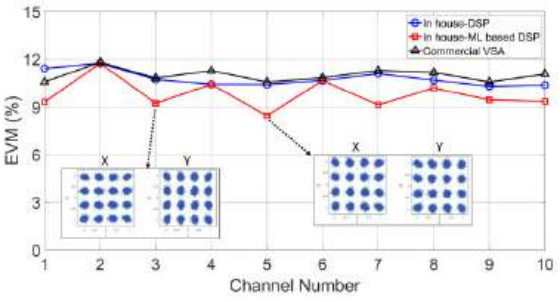


Fig. 2: Comparison of EVM (%) for various Channels

The BER was evaluated using direct bit-by-bit comparison. The pre-FEC BER is better than 1.64×10^{-4} for all the 10 channels. The fluctuation in the EVM arises from the wavelength dependent impairments and DSP convergence sensitivity; hence SSR is used only when it improves reliability, while classical DSP is retained otherwise.

Acknowledgement: Department of Telecommunication (DoT), India, through the Advanced Optical Communication Testbed Project.

References

1. G. Bennett et al., IEEE Commun. Mag., vol. 52, no. 10, pp. 102–110, Oct. 2014.
2. A. Gu et al., arXiv preprint arXiv:2312.00752, 2023.

Robust 64-Ary Optical Communication through Multimode Fiber Using Scaled LG Modes and Deep Learning

[1,#]Nikhil Vangety, Vidhi Patel[2], Rachita Nandan[3], Jayanth Ramakrishnan[1], Salla Gangi Reddy[4] and Shashi Prabhakar[1]
[1]QST Laboratory, Physical Research Laboratory, Ahmedabad 380009, India
[2]Adani University, Ahmedabad 382421, India
[3]Indian Institute of Technology Gandhinagar, Gandhinagar 382355, India
[4]SRM University-AP, Amaravati 522502, India

vnikhil@prl.res.in

We demonstrate a CNN-assisted framework for robust identification of 64 constant-size-scaled Laguerre–Gaussian modes transmitted through a multimode fiber. A modified AlexNet achieves 99.84% classification accuracy and enables high-fidelity image transmission and reconstruction over complex fiber channels, highlighting a scalable approach for high-capacity optical communication.

Orbital angular momentum (OAM) modes offer a high-dimensional platform for optical communication. However, propagation through multimode fibers (MMFs) leads to strong modal mixing and complex speckle formation, making reliable mode identification challenging. In this work, we employ 64 constant-size-scaled orthogonal Laguerre–Gaussian (LG) modes (ℓ = −32 to +32, excluding zero) to implement a 64-ary communication scheme over a 1 m MMF.

The transmitted LG modes generate deterministic speckle patterns classified using a modified AlexNet-based CNN. Trained on 6,400 experimental speckle images, the model achieves 99.84% classification accuracy in real time, while size-scaled LG beams ensure nearly uniform coupling efficiency across all OAM orders.

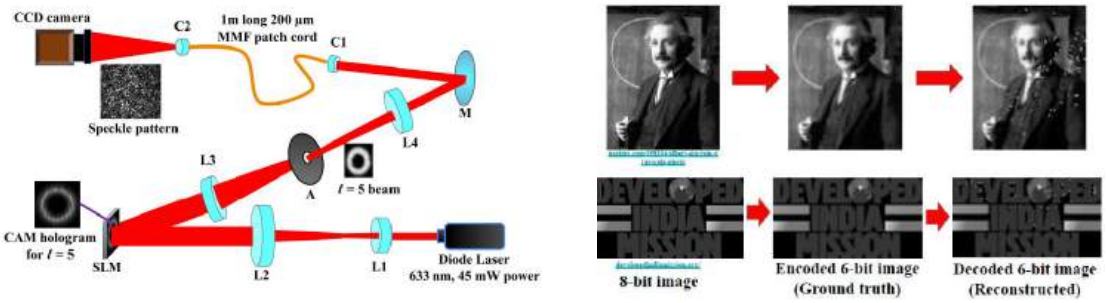


Fig.1 Left: Experimental demonstration of 64-ary optical communication through a 1 m multimode fiber. Constant-size-scaled Laguerre–Gaussian modes are generated using an SLM, transmitted through the MMF, and decoded from output speckle patterns using a CNN. Right: Grayscale images are encoded into 64 spatial modes and reconstructed with high fidelity after transmission.

To demonstrate practical communication, grayscale images were quantized into 64 intensity levels and mapped directly to the 64 LG modes. After MMF transmission, the trained CNN decoded the speckle patterns to reconstruct the original images The recovered images achieved PSNR > 26 dB and SSIM > 0.96.

The results demonstrate that deep learning can effectively recover high-dimensional spatial information from seemingly random MMF speckle patterns, providing a scalable route toward high-capacity optical communication and information processing. The proposed framework is readily extendable to larger mode sets, enabling higher channel capacity and secure key generation rates. The proposed approach eliminates explicit modal decomposition, enabling efficient high-dimensional mode decoding.

References:

[1] A. Trichili et al., *IEEE Commun. Surveys Tuts.* 21 (2019) 3175–3203.
[2] V. Cocotos and A. Forbes, *J. Opt.* 27 (2025) 07LT01.
[3] N. Vangety et al., *Results Opt.* 14 (2024) 100602.

Diamond Color Centers as Solid-State Quantum Platforms

Rajesh V. Nair#

Quantum Photonics and Sensing Group, Department of Physics, Indian Institute of Technology Ropar, 140001, India

#rvnair@iitrpr.ac.in

We discuss methodologies for tailoring the emission properties of NV^- centers by coupling them to structured photonic environments that enhance their emission intensity and rate at room temperature. Such emission engineering is essential for improving the sensitivity of NV-center based quantum sensing and for realizing bright, high-purity single photon sources.

The negatively charged nitrogen-vacancy (NV^-) center in diamond is a promising emitter due to its unique optical and spin properties at room temperature. The NV^- center emission is characterised by a pure electronic transition at 637 nm, the zero phonon line (ZPL), assisted with broad phonon-induced sideband (PSB) emission. It is widely used as a single photon source operating at room temperature and has long spin coherence times, making it an excellent candidate for various quantum technologies. However, it is required to enhance the NV^- center emission for various quantum technologies and depending upon specific required, spectrally-selective or broadband emission enhanced is desirable.

Here, we investigate the coupling of NV^- centers in nanodiamonds to cavity modes in both open and closed cavity architectures. Cavity coupling significantly enhances the spontaneous emission rate, reducing the emission lifetime from approximately 25 ns for uncoupled emitters to as low as 6 ns, corresponding to a Purcell enhancement factor of approximately 4. These results are in good agreement with theoretical predictions based on a point-dipole model. We further perform optically detected magnetic resonance (ODMR) measurements on the cavity coupled NV^- centers and observe substantial improvements in spin-state readout arising from cavity-induced localized emission enhancement. In addition, we discuss the influence of charge-noise induced spectral fluctuations in nanodiamond-hosted NV^- centers and their implications for quantum sensing in noisy environments. Finally, we present the generation of bright, high-purity single-photon sources using diamond nano-pillar structures, highlighting their potential for scalable quantum photonic applications.

We thank funding from IIT Ropar, DST, ANRF, and SERB.

Making Quantum Light: Deterministic Defect Engineering in Hexagonal Boron Nitride

[1]Anshuman Kumar

[1]Laboratory of Optics of Quantum Materials (LOQM), Department of Physics, Indian Institute of Technology Bombay, Powai, Mumbai 400076, India

[#]*[anshuman.kumar@iitb.ac.in]*

Solid-state single-photon sources are the currency of quantum photonics, and hexagonal boron nitride (hBN) offers a rare combination — room-temperature emission, van der Waals integrability, and bright, photostable defects — that makes it uniquely suited to the metasurface and nanophotonics community. Realising this promise demands deterministic control: placing an emitter where you want it, as the defect you want, with device-scale yield. Framed through Fermi's golden rule, this talk addresses the emitter side of that problem — the transition matrix element — through three maskless engineering routes. Carbon-assisted focused-ion-beam milling produces site-controlled single-photon emitter arrays at ~89% yield. Electron-beam dose engineering gives quantitative control of single-photon purity, with emitters that survive the thermal budget of device integration. Krypton-ion implantation extends the platform from photons to spin, producing near-infrared, spin-active defects with a resolvable magnetic-resonance signature. I close on the second knob — the photonic density of states — and the route to metasurface integration.

References:

[1] Akkanaboina, Mangababu, Rohit Kumar, Brijesh Kumar, Hrushikesh Gawali, Parul Sharma, Ikshvaku Shyam, and Anshuman Kumar. "Deterministic Single-Photon Emitter Arrays in Hexagonal Boron Nitride by Carbon-Assisted Focused Ion Beam Engineering." arXiv preprint arXiv:2606.12304 (2026).

[2] Majumder, Amrita, Janhavi Khunte, Ikshvaku Shyam, Rohit Kumar, and Anshuman Kumar. "Deterministic single-photon sources in hexagonal boron nitride with electron-dose-tuned purity and reversible thermal quenching." arXiv preprint arXiv:2606.16977 (2026).

[3] Shyam, Ikshvaku, Raj Singh, Mangababu Akkanaboina, A. M. Sonawane, Muthu Satheeshkumar, Amrita Majumder, Janhavi Jayawant Khunte et al. "Hexagonal Boron Nitride Spin Defects for Quantum Photonics: Annealing-Free Generation by Krypton Ion Implantation." arXiv preprint arXiv:2606.23334 (2026).

Portable Optically Pumped Atomic Magnetometer For Geophysical Surveys

Nisha[1], Karishma Devi[1], Shubham Utreja[2] and Bodhaditya Santra[1,2]

[1]Department of Physics, Indian Institute of Technology Delhi, New Delhi-110016, India

[2] Prenishq Pvt. Ltd., Synergy building, TBIU complex, Indian Institute of Technology Delhi, New Delhi 110016, India

Bodhaditya.Santra@physics.iitd.ac.in
Nisha@physics.iitd.ac.in

We experimentally demonstrate a portable optically pumped atomic magnetometer based on room-temperature alkali atomic vapor. By controlling the magnetic resonance with a transverse magnetic field, we observe polarization-dependent resonance splitting that provides a sensitive probe of the magnetic field. The compact architecture makes this technique well suited for portable quantum sensing and geophysical applications.

Atomic magnetometers based on optically pumped alkali atoms offer high magnetic sensitivity at room temperature without requiring cryogenic cooling, unlike SQUIDs, making them attractive for portable quantum sensing and geophysical applications. Here, we experimentally demonstrate a portable optically pumped atomic magnetometer based on ground-state Hanle resonances in a room-temperature ^{133}Cs vapor cell using a simple single-beam configuration on the $6S_{1/2}(F=4) \rightarrow 6P_{3/2}(F'=4)$ D_2 transition. Owing to the strong dependence of atomic spin coherence on the polarization of the interacting laser, we examine the magnetic resonance using both circularly and linearly polarized light. While circularly polarized excitation produces a single resonance, linearly polarized excitation exhibits symmetric resonance splitting in the presence of a transverse magnetic field. In the unshielded Earth's magnetic field, the proposed scheme achieves a magnetic-field sensitivity of $28.50\ \mathrm{pT}/\sqrt{\mathrm{Hz}}$.

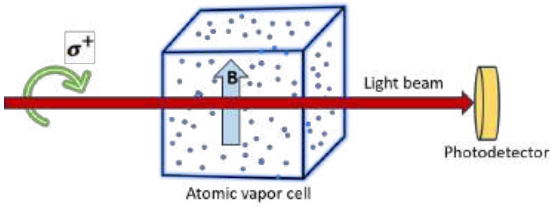


Figure 1: Schematic of the experimental setup for room-temperature optical atomic magnetometry.

The demonstrated portable optically pumped atomic magnetometer provides a compact and robust platform for high-sensitivity magnetic field measurements, making it well suited for navigation, geomagnetic surveys, and other field-deployable sensing applications.

Acknowledgement: We acknowledge the Indian Institute of Technology Delhi, for providing the research facilities and thank Prof. Bodhaditya Santra for his guidance and support.

References

[1] D. Budker and M. Romalis, *Nature Physics*, 3, 227–234 (2007).

[2] D. Budker and D. F. J. Kimball, *Optical Magnetometry*, Cambridge University Press, Cambridge (2013).

[3] R. S. Grewal and M. Pattabiraman, European Physical Journal D, 70, 240 (2016).

Towards Demultiplexing of OAM-Multiplexed Bright Twin Beams

#Chirang R. Patel, Jerin A Thachil *Ashok Kumar
Department of Physics, Indian Institute of Space Science and Technology (IIST), Thiruvananthapuram, Kerala 695547, India
#chirangpatel648@gmail.com and *ashokkumar@iist.ac.in

Abstract: We demonstrate the generation of orbital angular momentum (OAM)-multiplexed bright twin beams through four-wave mixing in hot ^{85}Rb vapor and implement OAM demultiplexing using a Sagnac-based mode sorter, establishing a scalable platform for parallel quantum information processing.

Orbital angular momentum (OAM) of light provides a high-dimensional basis for encoding quantum information and has attracted considerable interest for applications in quantum communication, quantum imaging, and quantum information processing [1]. Because different OAM modes are mutually orthogonal, multiple such modes can be multiplexed onto a single optical beam and later demultiplexed. Extending this concept to quantum-correlated twin beams would enable each OAM mode to act as an independent quantum channel, providing a scalable resource for parallel quantum information processing. Four-wave mixing (FWM) in hot atomic vapor provides a promising platform for generating such OAM-multiplexed twin beams, as the process does not require an optical cavity and therefore naturally supports multi spatial modes [2].

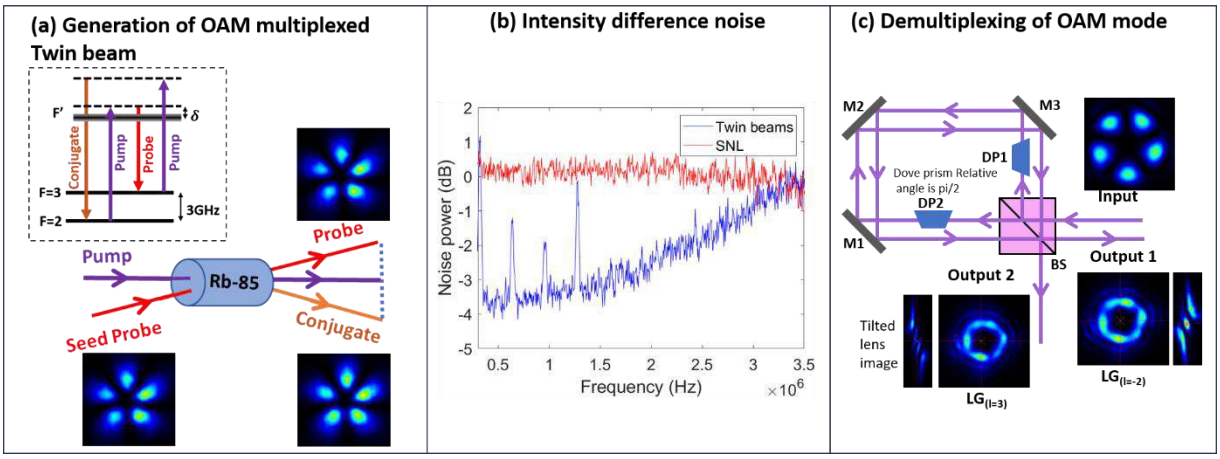


Fig. 1 (a) Generation of OAM-multiplexed twin beams via four-wave mixing in hot ^{85}Rb vapor (inset: energy levels of ^{85}Rb involved in FWM). (b) Intensity difference noise power vs noise analysis frequency. (c) Demultiplexing of the multiplexed OAM beam using a modified Sagnac interferometer separating into corresponding LG (l = +3) and LG (l = −2) modes.

In this work, we employ FWM in a double-Λ configuration in hot ^{85}Rb vapor to generate quantum correlated twin beams [2]. Two photons from the pump beam are converted into a probe-conjugate photon pair, as shown in the inset of Fig. 1(a). In the presence of a weak seed probe beam, the FWM process is stimulated and generates macroscopically bright twin beams. Here, the pump is Gaussian and the seed probe is prepared in a superposition of Laguerre-Gaussian modes with topological charges $l_1 = +3$ and $l_2 = -2$, resulting in a beam with a five-petal spatial intensity profile [Fig. 1(a)]. The resulting twin beams inherit this same petal structure, confirming that the OAM superposition is transferred through the FWM process. Intensity-difference noise measurements reveal a noise reduction of about 3.7 dB (blue trace) below the shot-noise limit (SNL) (red trace) as shown in Fig. 1(b), confirming that the twin petal beams are quantum correlated.

To investigate whether these quantum correlations are preserved within the individual OAM modes of the multiplexed twin beams, we first demonstrate an OAM mode sorter based on a modified Sagnac interferometer as shown in Fig. 1(c). Two Dove prisms, oriented at a relative angle of π/2, are placed in each arm of the interferometer [3]. The OAM-dependent phase shift introduced by the Dove prisms causes the $l_1 = +3$ and $l_2 = -2$ modes to interfere constructively at different output ports, separating them into two distinct outputs with high purity [Fig. 1(c)]. The topological charge of each output beam after the mode-sorter was confirmed using the tilted-lens method. Using this OAM mode sorter, we plan to demultiplex the probe and conjugate twin beams and examine quantum correlations independently in the OAM-matched pairs (probe l=+3 with conjugate l=−3, and probe l=−2 with conjugate l=+2). This capability of multiplexing and demultiplexing of twin beams offers a route toward parallel encoding and decoding of quantum information.

References:

[1] A. Forbes, F. Nothlawala, A. Vallés, Nature Photonics 19 (2025) 1291–1300.
[2] V. Boyer, A.M. Marino, P.D. Lett, Physical Review Letters 100 (2008) 143601.
[3] J. Leach, M.J. Padgett, S.M. Barnett, S. Franke-Arnold, J. Courtial, Physical Review Letters 88 (2002) 257901.

Engineering Nonlinearities in High Power Narrow Linewidth Fiber Lasers

[1,#]V. R. Supradeepa
[1]Centre for Nano Science and Engineering, Indian Institute of Science

[#]supradeepa@iisc.ac.in

We present multi-kW narrow-linewidth fiber lasers in polarized and depolarized formats enabled by systematic management of nonlinearities. We identify polarization-dependent loss and Kerr nonlinearity as the origin of power-dependent spectral broadening and environmentally driven linewidth fluctuations in depolarized systems, and propose architectures to suppress these effects while retaining depolarization benefits.

High-power, narrow-linewidth fiber lasers are essential building blocks for beam-combined systems. Scaling the power of individual modules reduces the number of channels required, but is constrained by stimulated Brillouin scattering (SBS) and transverse modal instabilities. Achieving multi-kilowatt output while preserving spectral and spatial beam quality therefore requires systematic management of nonlinear effects throughout the laser system.

We have developed multiple versions of multi-kW-class narrow-linewidth fiber lasers in polarized and depolarized formats by engineering the seed, modulation and amplification stages. Our work addresses the statistical limits of noise-based SBS suppression [1] and introduces dual sinusoidal and noise modulation to improve SBS suppression through line-shape control [2,3]. We will also discuss how nonlinear saturation of RF drivers can reduce SBS thresholds even at a fixed optical linewidth, emphasizing the need to control modulation statistics as well as spectral width.

A central scientific focus is the unwanted spectral broadening observed as the power of depolarized narrow-linewidth lasers increases. Although depolarization can raise the SBS and modal-instability thresholds, the output linewidth can also fluctuate on timescales of seconds to minutes. We investigate these effects in packaged 2 kW laser modules operating with approximately 10 GHz linewidth and show how the power dependence and temporal fluctuations can be understood within a common physical framework.

We identify the interplay of polarization-dependent loss (PDL) and Kerr nonlinearity as the origin of this behavior [4]. PDL in the amplifier chain converts polarization interference into residual intensity noise, which drives Kerr-induced spectral broadening during amplification. Ambient perturbations, including temperature variations and fiber motion, change the polarization orientation relative to the principal axes of PDL. The resulting variation in intensity noise makes the linewidth time dependent, even at a fixed output power. Residual PDL can therefore affect spectral stability even when individual components with appreciable PDL have been eliminated.

Finally, we propose alternative architectures to suppress this broadening mechanism while retaining the power-scaling benefits of depolarization. One approach uses a polarization-maintaining amplifier chain supporting both orthogonal polarization modes, with equal input powers and PDL axes aligned to the maintained polarization axes. We will discuss how such architectures can reduce polarization-to-intensity-noise conversion and enable more stable narrow-linewidth operation at multi-kilowatt powers.

References:

[1] V. R. Supradeepa, *Optics Express* 21(4), 4677-4687 (2013).
[2] R. Prakash, B. S. Vikram, V. R. Supradeepa, *IEEE Photonics Journal* 13(5), 1500106, 1-6 (2021).
[3] V. R. Supradeepa, R. Prakash, S. V. Bhagavatula, Indian Patent No. 555435 (2021).
[4] V. R. Supradeepa, M. Harsha, A. S. Thakur, C. J. Sreenath, S. Varghese, *Proc. SPIE* 13874, 138740R (2026).

Ground-State Search via Intrinsic Feedback Annealing in Coupled Laser Arrays

[1,#] Rajneesh Fulara,[2] Fabien Bretenaker and [1] Vishwa Pal

[1] Department of Physics, Indian Institute of Technology Ropar, Rupnagar 140001, Punjab, India

[2] Université Paris-Saclay, ENS Paris-Saclay, CNRS, CentraleSupélec, LuMIn, Orsay, France.

[#]rajneesh.22phz0011@iitrpr.ac.in

Coupled laser arrays lase in their lowest-loss mode, corresponding to the ground state of a spin Hamiltonian. However, sometimes system gets trapped in higher-loss topological defect states. We identified an intrinsic feedback driven annealing in semiconductor lasers that suppresses topological defects, enabling the system to reach the ground state efficiently.

Many computationally hard optimization problems that appear in different domains, such as artificial intelligence, resource allocation, and social networking, can be mapped onto ground-state search of the spin Hamiltonian and can be solved using physical platforms that emulate spin dynamics [1]. In coupled laser arrays, spins are encoded in the laser phases, while the coupling between lasers represents spin interactions. The laser array intrinsically lases in the lowest-loss phase configuration, corresponding to the ground state of the spin Hamiltonian. However, during evolution, the system can become trapped in local minima corresponding to higher-loss states, also known as topological defect states, instead of reaching the ground state [2]. In this work, we demonstrate an intrinsic feedback-driven annealing mechanism in 1D ring class-B semiconductor laser arrays that enables efficient ground-state search [3]. This feedback mechanism arises from the interplay between the internal linewidth enhancement factor (α) and external coupling between different lasers (η), where the instantaneous phase configuration of lasers modulates amplitude fluctuations. These fluctuations act as a dynamical temperature, reshaping the effective potential and allowing escape from local minima.

Fig.1(a) shows the probability of defect formation across the α–η parameter space, revealing an optimal regime where the ground state is reached with ~100% probability. The feedback loop, whose strength can be controlled independently by α and η, suppresses defects by modifying the two competing timescales: amplitude stabilization time (t_{amp}) and phase locking time (t_{phase}). Fig. 1(b) demonstrates the universality of this mechanism in defect formation by showing that, when the feedback yields the same t_{phase} / t_{amp} ratio, the defect probability is identical regardless of the α value. This confirms that relative timescales determine defect formation, analogous to the Kibble–Zurek mechanism. Our results establish internal feedback-driven annealing as a practical, scalable route to ground-state search in laser-based spin simulators for hard optimization problems.

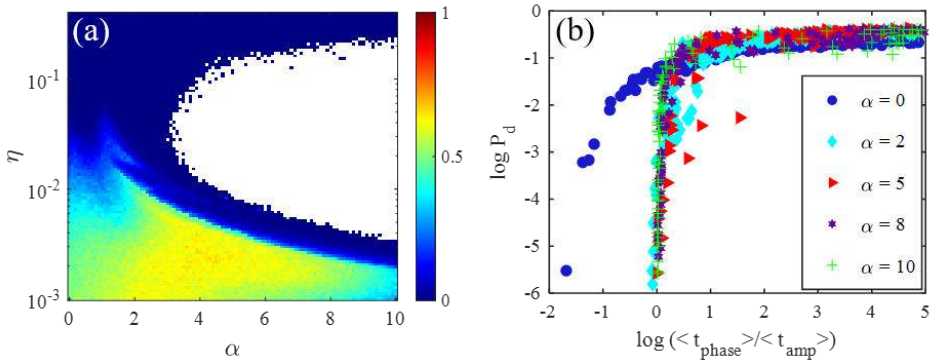


Fig.1 (a) Probability of topological defects with α and η for a 20 lasers ring array of semiconductor lasers. The white region indicates where the lasers are unstable, and phase locking is not achieved. **(b)** The probability of topological defects with the ratio of amplitude stabilization time (t_{amp}) and phase locking time (t_{phase}) for different values of α. Different points along the curve represent the probability of defects for different pump powers and coupling strengths η.

References:

[1] N. G. Berloff, M. Silva, K. Kalinin, A. Askitopoulos, J. D. Töpfer, P. Cilibrizzi, *et al.*, Nature Materials **16** (2017) 1120..
[2] V. Pal, C. Tradonsky, R. Chriki, A. A. Friesem, and N. Davidson, Physical Review Letters **119** (2017) 013902.
[3] R. Fulara, F. Bretenaker, and V. Pal, arXiv:2602.18368 (2026)..

Spatial Coherence Control of Structured Beams in a Degenerate Cavity Laser: Binary versus Gaussian Fourier Filtering

[1, #]Neethu K,[1]Raja Mondal, [2]Vasu Dev and [1]Vishwa Pal
[1]Laser Research Lab, Department of Physics, Indian Institute of Technology Ropar, Rupnagar 140001, Punjab, India
[2]Centre for Disruptive Photonic Technologies, Nanyang Technological University, Singapore 637371, Singapore

[#]*staff.neethu@iitrpr.ac.in*

We investigate spatial coherence control of structured beams in degenerate cavity lasers (DCLs) using Fourier filtering. Gaussian filtering more effectively suppresses spatial modes, enabling high-resolution and high-quality structured beams with tunable spatial coherence. These results demonstrate the potential of DCLs as ultraviolet pump (UV) sources for SPDC and quantum imaging.

Degenerate cavity lasers constitute a powerful platform for structuring light with spatial coherence control by supporting around 10^5 spatial modes with nearly identical quality factors [1, 2]. Their ability to tailor amplitude and coherence through intracavity near-field and far-field filtering while maintaining nearly constant output power makes them promising UV sources for spontaneous parametric down-conversion (SPDC), where pump coherence governs the properties of entangled photon pairs [3].

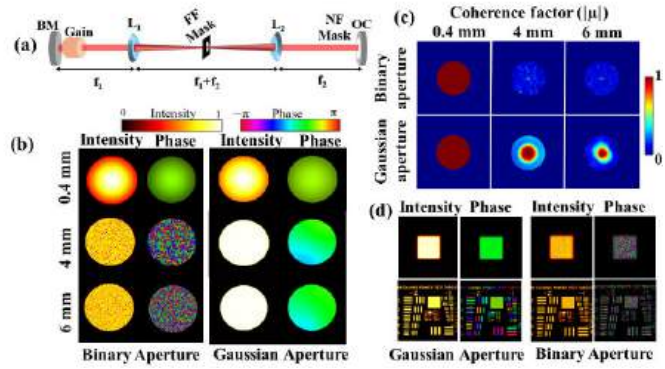


Fig. 1: (a) Schematic of the degenerate cavity laser. (b) Intensity and phase profiles of the output beam for binary and Gaussian Fourier filters with different aperture diameters. (c) Complex coherence factor as a function of aperture diameter for binary and Gaussian Fourier filters. (d) Intensity and phase profiles of various complex-shaped beams generated using binary and Gaussian Fourier filters, each with a diameter of 6 mm. BM: Back mirror; FF Mask: Far-field amplitude mask; NF Mask: Near-field amplitude mask; OC: Output coupler; and L_1 and L_2: Plano-convex lenses with focal length f_1 and f_2, respectively.

Motivated by the growing demand for structured light with controllable spatial coherence in ultraviolet pump sources for SPDC-based quantum imaging, we investigate intracavity amplitude and coherence engineering in a degenerate cavity laser using near-field (NF) mask and far-field (FF) Fourier filtering (Fig. 1(a)). The beam profile is defined by an intracavity NF mask, while its spatial coherence is tailored through FF filtering. Binary and Gaussian Fourier filtering schemes are systematically compared to evaluate their effectiveness in controlling spatial coherence. Gaussian filtering more effectively suppresses spatial modes, generating high-resolution and high-quality structured beams with reduced intensity defects and rapid convergence toward a spatially coherent phase front (Fig. 1(b)). In contrast, a binary circular Fourier filter with the same aperture size retains residual phase randomness and pronounced intensity defects, thereby limiting the achievable beam quality (Fig. 1(b)). Analysis of complex coherence factor further shows that Gaussian filtering maintains a high degree of spatial coherence over a broad range of aperture sizes, whereas coherence with binary filtering deteriorates rapidly as the aperture diameter increases (Fig. 1 (c)). The versatility of Gaussian filtering is further demonstrated by the generation of complex structured beams (Fig. 1(d)). A comprehensive analysis of the supported spatial modes and beam propagation confirms that Gaussian Fourier filtering provides superior control of spatial coherence, yielding enhanced beam quality and spatial resolution, both of which are essential for imaging applications.

Overall, this study demonstrates that the combination of an intracavity NF mask and Gaussian Fourier filtering enables precise spatial coherence control and generation of high-quality, high-resolution structured beams in degenerate cavity lasers, highlighting their potential as ultraviolet pump sources for SPDC-based quantum imaging. This work was supported by the Department of Science and Technology (DST), Government of India, under the National Quantum Mission (NQM).

References:

[1] A.N. Kumar Reddy, S. Mahler, A. Goldring, V. Pal, A.A. Friesem, N. Davidson, *Optics Express* 30 (2022) 1114.
[2] R. Chriki, M. Nixon, V. Pal, C. Tradonsky, G. Barach, A.A. Friesem, N. Davidson, *Optics Express* 23 (2015) 12989.
[3] W. Zhang, R. Fickler, E. Giese, L. Chen, R.W. Boyd, *Optics Express* 27 (2019) 20745.

On-chip random lasing from clusters of quasi- monodispersed microdroplets in amplifying medium

[1,#]Diksha Sharma,[1]Nikita Choudhary and [1,2]Anjani Kumar Tiwari
[1]Department of Physics, Indian Institute of Technology Roorkee, Roorkee, 247667, Uttarakhand, India
[2]Centre for Photonics and Quantum Communication Technology, Indian Institute of Technology Roorkee, Roorkee, 247667, Uttarakhand, India

[#]*diksha_s@ph.iitr.ac.in*

We demonstrate on-chip random lasing from the clusters of quasi-monodispersed microdroplets distributed in a dye-doped amplifying liquid. The microdroplets act as scatterers, while the surrounding dye-doped liquid acts as an amplifying medium. Upon optical pumping, the system enables random lasing emission above a well-defined threshold.

Random lasers are unconventional optical sources in which randomly distributed scatterers provide the desired optical feedback. Random lasing has been explored in a variety of systems, including semiconductor powders, optofluidic channels, and arrays of microdroplets [1-4]. The size, shape and distribution of the scatterers provide a versatile platform for investigating various ensemble-averaged quantities, including spectral and intensity fluctuations, distribution of spatial confinement, and threshold statistics of the random lasing modes.

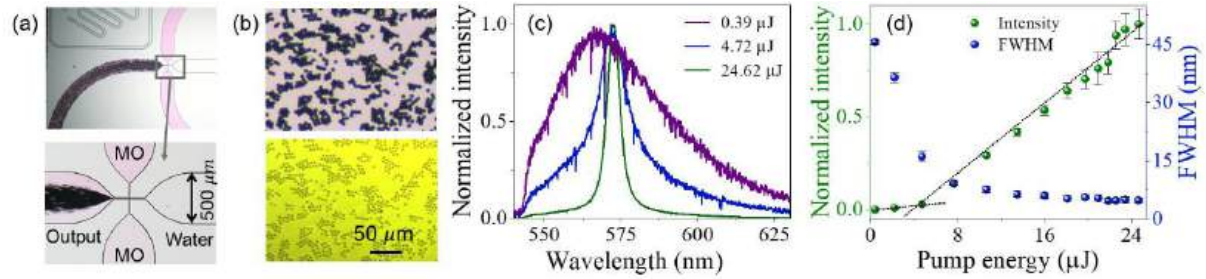


Fig. 1: (a) Top panel: image of a microfluidic channel, bottom panel: zoomed view of the junction. (b) Image of the microdroplet sample, illuminated with a white light (top panel) and with a laser (bottom panel). (c) Emission spectra at three pump energies. (d) Plot of emission intensity and FWHM versus pump energy.

In this work, we generate quasi-monodisperse microdroplets of water-in-oil from a microfluidic chip, as shown in Fig. 1(a). One input channel of the chip was used for the droplet phase, and two input channels for the oil phase. Deionized water (n = 1.33) was used for the droplet phase, while a fluorescent dye-doped mineral oil (n = 1.467) was used for the carrier phase. Microdroplets of different sizes and distributions were generated by adjusting the pressure of the liquids using pumps integrated with the microfluidic system. To obtain the steady samples, the flow of all liquids was simultaneously stopped. In the steady state, the sample contains clusters of quasi-monodispersed microdroplets, distributed randomly throughout the output channel as shown in Fig. 1(b). Due to refractive index contrast, these clusters act as scatterers. The microdroplet clusters were optically excited by a 532 nm subnanosecond Nd:YAG laser. The beam was focused on the sample using a cylindrical lens to excite the microdroplet clusters in the form of a stripe. The emission from the stripe was collected in-plane using a convex lens and analyzed using a CCD-based spectrometer. Single-shot emission spectra of the sample at three different pump energies are shown in Fig. 1(c). At low pump energy (0.39 μJ), a standard fluorescence profile of the dye is obtained. As pump energy increases, the bandwidth narrows down. The variation of the emission intensity and full width at half maxima (FWHM) with input pump energy is shown in Fig. 1(d). Below threshold (E_{th} = 4.7 μJ), the emission intensity increases gradually, and above threshold, it rises rapidly, accompanied by a sharp reduction in FWHM, a characteristic signature of random lasing. Such optofluidic coherent sources offer a promising platform for integrated lab-on-chip optical devices.

References:

[1] D. S. Wiersma, Nature physics 4 (2008) 359–367.
[2] H. Cao, Y. Zhao, S. Ho, E. Seelig, Q. Wang, and R. Chang, Physical Review Letters 82 (1999) 2278.
[3] B. Shivakiran Bhaktha, N. Bachelard, X. Noblin, and P. Sebbah, Applied Physics Letters 101 (2012) 151101.
[4] A. K. Tiwari and S. Mujumdar, Physical Review Letters 111 (2013) 233903.

Tunable modulation depth in multimode-interference saturable absorbers for 2 μm fiber lasers

[#]Bhanu Yadav and Gayathri Bharathan
Optics and Photonics Centre, Indian Institute of Technology Delhi, New Delhi 110016, India.
[#]*opz248271@opc.iitd.ac.in*

We numerically investigate a multimode-interference (MMI) saturable absorber whose modulation depth (MD) can be continuously tuned by adjusting the offset from characteristic self-imaging position within a multimode fiber, enabling stable mode-locking in a 2 μm thulium fiber laser.

Saturable absorbers (SAs) are key components for passively mode-locking fiber laser cavities to generate ultrashort pulses across mid-infrared spectral regions. Real SAs exhibiting intrinsic intensity-dependent transmission, include semiconductor saturable absorber mirror (SESAM) and low-dimensional nanomaterials including carbon nanotubes, graphene etc. They are generally less suitable for high peak power operations and ultrashort pulse generation because of relatively low damage thresholds and slow recovery times [1]. In contrast, fiberized artificial SAs mimic intensity-dependent transmission through techniques, based on Kerr non-linearity of silica fiber, such as nonlinear polarization rotation (NPR) and multimode interference (MMI) inside a multimode fiber (MMF). They offer broad wavelength coverage (1-2 μm), all-fiber integration, cost-effectiveness, high damage thresholds, faster recovery time, and supports even femtosecond pulse generation.

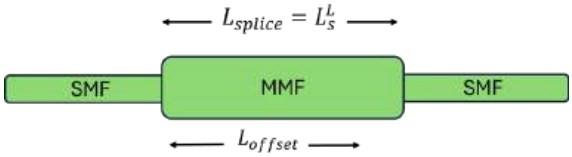


Fig. 1: MMI-SA Structure

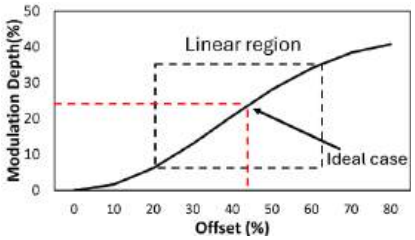


Fig.2 MD vs offset percentage

In this work, we investigate the saturable absorber properties of a MMI based SA whose structure comprises splicing a MMF in between two single mode fibers (SMF), as shown in Fig.1. Spliced MMF length is crucial for SMF-MMF-SMF structure to behave as a saturable absorber. The launched single mode gaussian field excites multiple guided modes within the multimode fiber. When these excited modes become phase matched, a self-image of the launched field is periodically formed along the MMF at intervals known as linear self-imaging distance (L_s^L) [2]. These intervals shift in distance with high input signal power due to additional phase introduce by non-linear self-phase modulation (SPM) [3]. A properly chosen MMF (50 μm core diameter, 0.22 NA) splice length (L_{splice}) equal to some offset (L_{offset}) from linear self-imaging (L_s^L) will result in high coupling efficiency and transmission of input field from MMF to SMF at higher power and low coupling and transmission at low powers. Hence, this configuration provides vital intensity-dependent transmission and mimics saturable absorber behavior.

Offset length was systematically varied and corresponding modulation depth was calculated for each case, and results were plotted in Fig.2. Increase in modulation depth (MD) with offset percentage could be attributed to availability of distance for self-imaging planes to migrate at higher powers. Subsequently, MMI-SA was inserted into thulium doped linear fiber laser cavity and stable mode-locked single as well as twin pulses were obtained numerically for MD in the region of 10-25 %.

In conclusion, the MMI-SA was numerically demonstrated to function as a MD tunable device, with the MD controlled by varying the MMF splice offset from the linear self-imaging distance. Simulation results further indicate that the optimized SA can support stable mode-locking in a thulium-doped fiber laser cavity operating at 2 μm.

References :

[1] Yani Zhang, *Laser Photonics Rev*. 2024, *18*, 2300786, Wiley-VCH GmbH.
[2] X. Zhu,Phd Thesis (University of Arizona, 2008).
[3] Tao Chen, et al Vol. 6, No. 11 / November 2018 / Photonics Research.

Interference, Interferometer and Fock States: Revisiting Old Concepts from the Perspectives of New Applications

[#]Anirban Pathak
Department of Physics and Materials Science & Engineering, Jaypee Institute of Information Technology, A10, Sectro 62, Noida, UP-201309, India

[#]*anirban.pathak@gmail.com*

With the advent of quantum technologies and quantum state engineering, well-known concepts related to interference, interferometer and Fock states have recently been revisited by us using new formalism and/or frameworks. Such new ideas are discussed with specific focus on recent works related to quantum foundation, quantum communication and quantum sensing.

In the last few years, different groups have revisited the old concepts of classical optics and quantum optics, like interference, interferometer and Fock states from different angles. For example, in Ref. [1], a new formalism to look at the double slit interference pattern using the concept of bright and dark state was introduced. Extending the formalism introduced in [1], recently we have studied the effect of a which-path memory ancilla on the three-slit interference pattern [2]. Some of the result discussed in [2] are discussed here with specific attention to the idea of quantum eraser within this framework.

Going beyond interference, interferometers have recently been used as testbeds for many new ideas and frameworks. Here, we have restricted ourselves to two particular aspects. First, we have discussed that quantum delayed choice experiment and counterfactual measurement which are apparently disjoint ideas and till now studied independently, can be studied within a single unified quantum interferometric framework involving Mach Zehnder interferometer (MZI) [3]. Further, it is shown that in quantum sensing, MZI can be used to achieve robust phase sensitivity by using photon added and subtracted squeezed coherent states [4]. Generation of states like photon added and subtracted squeezed coherent states is now part of an emerging subarea of quantum optics known as quantum state engineering. In that particular area, a problem of specific relevance is how to generate relatively large Fock states. This question is addressed here in line with our recent work [5], where a scheme for the generation of large Fock states of near unit fidelity is proposed using Kerr nonlinearity and displacement.

Acknowledgements: Contribution of all the students and collaborators in obtaining some of the results presented here are gratefully acknowledged.

References:

[1] C.J. Villas-Boas, C.E. Máximo, P. J. Paulino, R. P. Bachelard, G. Rempe, *Physical Review Letters* 134 (2025) 133603.
[2] A. Kumar, G. Kadam, A. Pathak, arXiv:2608.24243 (2026).
[3] H. Awasthi, S. Mishra, A. Pathak, arXiv:2608.12268 (2026).
[4] S. Singh, P. Malpani, A. Pathak, arXiv:2607.02984 (2026).
[5] N. Meher, Nilakantha, A. Pathak, S. Sivakumar, *Physical Review A* 113 (2026) 033704.

Hexagonal Boron Nitride Spin Defects for Quantum Photonics: Annealing-Free Generation by Krypton Ion Implantation

[1]Ikshvaku Shyam, [2]Raj Singh, [1]Mangababu Akkanaboina, [3]A. M. Sonawane, [2]Muthu Satheeshkumar, [1]Amrita Majumder, [1]Ekta, [1]Janhavi Jayawant Khunte, [3]Akash Khaire, [4]Kenji Watanabe, [4]Takashi Taniguchi, [2,§]Gopalan Rajaraman, [3,†]S. S. Dahiwale, and [1,‡]Anshuman Kumar

[1]Laboratory of Optics of Quantum Materials, Department of Physics, Indian Institute of Technology Bombay, Mumbai, INDIA
[2]Department of Chemistry, Indian Institute of Technology Bombay, Mumbai 400076, INDIA
[3]Department of Physics, Savitribai Phule Pune University, Pune 411007, INDIA
[4]National Institute for Materials Science (NIMS), Tsukuba 305-0044, JAPAN

§ *ssd@physics.unipune.ac.in*

† *rajaraman@chem.iitb.ac.in*

‡ *anshuman.kumar@iitb.ac.in*

We report annealing-free generation of near-infrared spin defects in hBN using 40 keV Kr^+ implantation. Structural and optical characterisation reveal implantation-induced defect centres that exhibit near-infrared emission around 830 nm. Electron paramagnetic resonance measurements, supported by first-principles calculations, confirm the presence of optically active paramagnetic defects.

Hexagonal boron nitride (hBN) has emerged as a promising platform for solid-state quantum emitters owing to its room-temperature operation, high photostability, and compatibility with integrated photonic architectures. However, scalable and deterministic generation of optically active defect centres remains a major challenge. Here, we demonstrate an annealing-free approach to engineer near-infrared luminescent spin defects in hBN via 40 keV Kr^+ ion implantation.[1]

SRIM simulations predict a projected ion range of approximately 30.5 nm, enabling controlled defect formation within exfoliated hBN flakes.[2] Raman spectroscopy reveals the characteristic hBN E_{2g} phonon at $\sim$1366 cm^{-1} together with an implantation-induced defect mode near $\sim$1295 cm^{-1}, confirming irradiation-induced lattice disorder. Photoluminescence (PL) measurements reveal a stable near-infrared emission band centred at $\sim$830 nm, whose intensity increases systematically with implantation fluence from 10^{11}–10^{15} ions cm^{-2}. No comparable emission is observed in pristine hBN or irradiated quartz control samples in that region, establishing the defect-related origin of the luminescence.

Temperature-dependent PL between 20 and 300 K reveals linewidth broadening that scales as T^3, consistent with acoustic-phonon-mediated dephasing. Time-resolved photoluminescence measurements yield sub-nanosecond decay components with lifetimes of $\tau_1 = 0.80 \pm 0.03$ ns and $\tau_2 = 0.195 \pm 0.007$ ns.

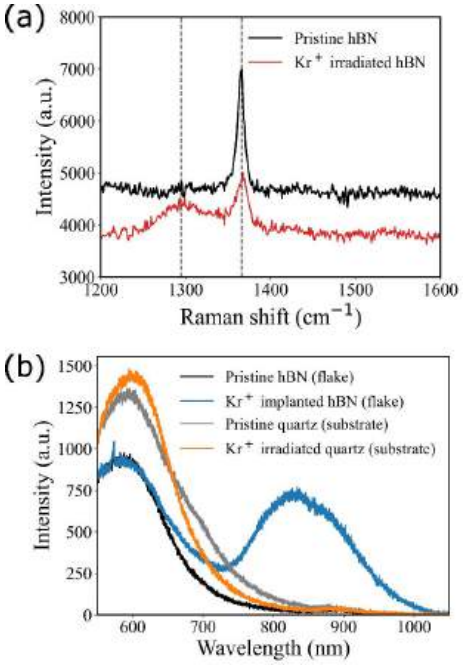


Figure 1: Optical characterisation of Kr^+-implanted hBN. (a) Raman spectra showing the E_{2g} mode at $\sim$1366 cm^{-1} and an implantation-induced defect mode at $\sim$1295 cm^{-1}. (b) PL spectra of the implanted hBN flake (blue), pristine hBN (black), and quartz control samples (grey and orange). A near-infrared emission band centred at $\sim$830 nm appears exclusively in the implanted hBN flake.

X-band EPR measurements at 9.386 GHz reveal a paramagnetic defect centre with $g = 2.003$, absent in pristine hBN and irradiated quartz controls. EasySpin simulations and spin-polarised density functional theory calculations are consistent with a spatially separated V_N–C_B donor–acceptor pair as a plausible microscopic origin of the observed optical and magnetic signatures.

These results establish Kr^+ implantation as a clean, scalable, and annealing-free route for generating stable near-infrared spin defects in hBN, providing a promising platform for future optically detected magnetic resonance studies and integration with quantum-photonic cavities.[3,4]

Acknowledgements. This work was supported by the National Quantum Mission (NQM), Department of Science and Technology, India, and ANRF Grant No. SPR/2023/000175. Related intellectual property is protected under Indian Patent Application No. 202621071884.

References:

[1] I. Aharonovich, D. Englund, and M. Toth, *Nature Photonics* **10**, 631–641 (2016).

[2] M. Toth and I. Aharonovich, *Annual Review of Physical Chemistry* **70**, 123–142 (2019).

[3] J. F. Ziegler, M. D. Ziegler, and J. P. Biersack, *Nucl. Instrum. Methods Phys. Res. B* **268**, 1818–1823 (2010).

[4] S. Li, A. Pershin, and A. Gali, *Nature Communications* **16**, 5842 (2025).

Coherence transfer in bright twin beams

† Sandra Susil, Jerin A Thachil, and *Ashok Kumar

Department of Physics, Indian Institute of Space Science and Technology
Thiruvananthapuram, Kerala, 695547, India.

†*sandrasusiln@gmail.com*, **ashokkumar@iist.ac.in*

We theoretically investigate the coherence properties of bright twin beams generated via a four-wave mixing process and demonstrate how the coherence from the seed probe can be transferred to the generated conjugate beam. Such control of coherence transfer in bright twin beam can be potentially useful for quantum sensing, metrology, and biological imaging applications.

The control of coherence properties of correlated light fields is of fundamental importance for the field of quantum sensing and metrology. A quantum source with tunable coherence properties makes it an ideal candidate for applications like biological imaging [1]. In the current work, we theoretically investigate the generation and temporal evolution of bright twin beams generated via the four-wave mixing (FWM) process in a double-Λ configuration. In particular, our study investigates how the coherence of the seeded probe is transferred to the unseeded generated beam.

To study the temporal evolution and coherence transfer in twin beams, we adopt a semi-classical approach. The atom-light interaction is modeled using a three-level atomic system comprising two hyperfine ground states, $|1\rangle$ and $|2\rangle$, and an excited state $|3\rangle$ as shown in the Fig. 1(a). The transitions governed by a strong pump field with rabi frequency Ω_p, and two weak fields, the probe and conjugate denoted by Ω_{pr} and Ω_c respectively. The Hamiltonian of the system is given by,

$$\begin{aligned}\hat{H} = \hbar\omega_1|1\rangle\langle 1| + \hbar\omega_2|2\rangle\langle 2| + \hbar\omega_3|3\rangle\langle 3| - \hbar\left(\Omega_c e^{-i\omega_c t} + \Omega_p e^{-i\omega_p t}\right)|3\rangle\langle 1| \\ - \hbar\left(\Omega_{pr} e^{-i\omega_{pr} t} + \Omega_p e^{-i\omega_p t}\right)|3\rangle\langle 2| + \text{c.c.}\end{aligned} \tag{1}$$

We followed the density matrix formalism to study the evolution of the system, including the effects of spontaneous emission and collisional damping phenomenologically [2]. The optical response of the system is determined through polarization of atomic medium. Substituting the polarization terms in Maxwell's equations, the temporal evolution of the generated fields obtained as coupled differential equations. These equations are solved numerically to investigate the first-order coherence function, $g^{(1)}(\tau)$ of the generated conjugate field for different spectral widths of the seed probe beam as,

$$g^{(1)}(\tau) = \frac{\langle E^*(t)\, E(t+\tau)\rangle}{\sqrt{\langle |E(t)|^2\rangle \langle |E(t+\tau)|^2\rangle}}, \tag{2}$$

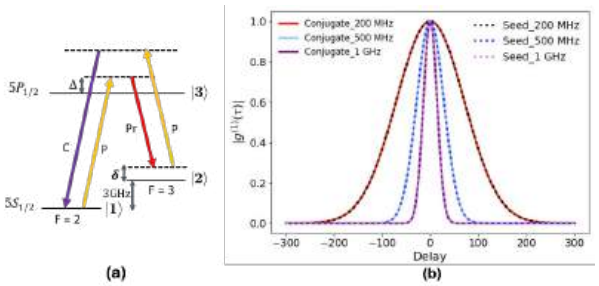


Figure 1: (a) Energy levels of the Rb atom involved in four-wave mixing in a double-Λ configuration. (b) First-order coherence function of seed probe and conjugate fields as a function of time delay for different spectral widths of 200 MHz, 500 MHz and 1 GHz.

where $E(t)$ and $E(t+\tau)$ are the fields at time t and $t+\tau$, respectively, and τ is the time delay between the fields.

Figure 1(b) shows that the coherence functions of the seed probe and generated conjugate fields overlap for all spectral widths, confirming the complete transfer of coherence from the seed probe to the unseeded conjugate beam. The experimental realization of the theoretical investigations are currently under progress. This opens a way to develop a coherence tunable bright quantum twin light beam source for quantum technology applications.

References

[1] Magued B Nasr, Bahaa EA Saleh, Alexander V Sergienko, and Malvin C Teich. *Physical Review Letters*, 91(8):083601, 2003.

[2] Jerin A Thachil, Chirang R Patel, Onkar N Verma, and Ashok Kumar. *Physical Review A*, 110(5):053520, 2024.

Negative-Temperature States in Multimode Solitons

[1,#]Love Kumar Sharma,[1]Vishwa Pal
[1]Laser Research Laboratory, Department of Physics, Indian Institute of Technology Ropar, Rupnagar 140001, Punjab, India

[#]love.21phz0018@iitrpr.ac.in

We report the emergence of inverted modal condensates in multimode (MM) solitons propagating in graded-index multimode fibers (GRIN-MMFs) with non-parabolic refractive-index profiles. The preferential occupation of higher-order mode groups suggests the existence of negative-temperature states in a finite modal spectrum. A thermodynamic framework incorporating positive- and negative-temperature branches is developed to describe the observed population inversion.

Negative-temperature states constitute one of the most intriguing predictions of statistical mechanics and arise in systems possessing a bounded energy spectrum, where entropy decreases with increasing energy beyond a maximum-entropy configuration. Such states are characterized by population inversion and preferential occupation of high-energy levels [1]. The finite modal spectrum supported by MMFs suggests that they may provide a suitable platform for realizing such exotic thermodynamic states.

Recent studies have established connections between multimode wave dynamics and statistical physics through Rayleigh–Jeans and Bose–Einstein-like equilibrium distributions in weakly nonlinear MMFs [2]. However, the existence of negative-temperature states in strongly nonlinear multimode systems remains largely unexplored. In particular, MM solitons represent highly coherent self-organized structures sustained by the interplay of chromatic dispersion, modal dispersion, and Kerr nonlinearity, placing them beyond the scope of existing weak-wave thermodynamic descriptions [3].

Here, we investigate MM soliton dynamics in GRIN-MMFs with tailored refractive-index profiles and observe a transition from conventional low-order-mode condensation to an inverted modal distribution in which higher-order mode groups become preferentially occupied [4]. Remarkably, this inversion occurs despite the preservation of the underlying linear modal ordering. Motivated by this observation, we develop a thermodynamic framework based on finite-spectrum statistical mechanics that supports both positive- and negative-temperature MM-soliton condensates. The proposed framework identifies the observed inverted modal condensate as a negative-temperature MM-soliton state and establishes MM solitons as a promising platform for exploring exotic thermodynamic states in strongly nonlinear optical systems.

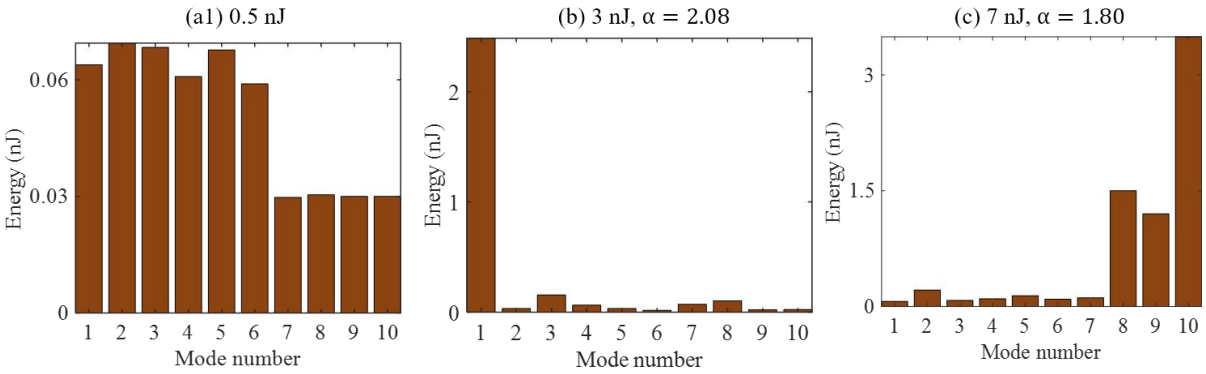


Fig. 1: Modal energy distribution at the fiber output. (a) Initial modal excitation (0.5 nJ). (b) Conventional MM soliton condensation into the fundamental mode at 3 nJ for an ideal parabolic index distribution. (c) Inverted modal condensation into higher-order modes at 7 nJ for non-parabolic index distribution, indicating a population-inverted MM soliton state.

References:

[1] E. M. Purcell, R. V. Pound, Phys. Rev. 81, 279 (1951).
[2] K. Baudin, J. Garnier, A. Fusaro, N. Berti, K. Krupa, G. Millot, A. Picozzi, Phys. Rev. Lett. 130, 063801 (2023).
[3] W. Renninger, F. Wise, Nat. Commun. 4, 1719 (2013).
[4] L. K. Sharma, V. Pal, arXiv:2605.02511 (2026).

Perspective on Photonic and Electronic Devices using Oxide-based thin films

Rajib Chakraborty
Department of Applied Optics and Photonics, University of Calcutta
JD-2, Sector-III, Kolkata-700106, INDIA
Email: rcaop@caluniv.ac.in

Abstract: Oxide materials are versatile and fundamental platform for photonic and electronic devices. Here we focus mainly on the development, fabrication, characterization, and optimization of different oxide-based thin films for improving device performance using low-cost and scalable fabrication techniques while addressing important challenges in light management, sensing and high-k dielectric technologies.

SUMMARY

Modern optoelectronics, photovoltaics, and microelectronic semiconductor technologies heavily depend on the strategic engineering of high-quality functional thin films. Silicon (Si) remains crucial for both the photovoltaic (PV) industry and complementary metal-oxide-semiconductor (CMOS) architectures due to its high abundance, exceptional mechanical stability, and compatibility with highly mature fabrication ecosystems. Despite these fundamental advantages, current advancements in both optical energy conversion and nanoscale transistor scaling are encountering severe physical constraints.

In optical applications such as photovoltaics and organic light-emitting diodes (OLEDs), severe optical losses occurring at material interfaces fundamentally limit overall performance. For instance, bare silicon displays a massive refractive index mismatch with air ($n \approx 3.5 – 4$ versus $n \approx 1$), causing it to reflect approximately 30% of incident solar radiation. This restricts the front-surface light coupling, directly lowering the short-circuit current density (J_{sc}) and power conversion efficiency. Similarly, bottom-emitting OLEDs suffer from poor light extraction efficiency (LEE), where nearly 80% of internally generated photons remain trapped within the active layers due to total internal reflection occurring at the substrate/air and indium-tin-oxide (ITO)/substrate boundaries [4]. Periodic layers of two different oxide layers when used along with metal layer can generate tamm-surface plasmon hybrid mode with improved sensing figure of merit.

Concurrently, in the electronics device, the aggressive dimensional scaling down of field-effect transistors (MOSFETs) has reduced the physical thickness of standard silicon dioxide (SiO_2) gate dielectrics to a few atomic layers. This scaling triggers an exponential surge in quantum tunneling, causing unacceptable gate leakage currents and elevated static power dissipation. To mitigate these interconnected challenges, transition metal oxide thin films, most notably titanium dioxide (TiO_2), have emerged as highly versatile candidates capable of addressing constraints across both photonic and electronic device architectures.

The research work to be discussed will involve the development, fabrication, characterization, and optimization of different oxide-based thin films for applications in photonic and microelectronic devices. The main objective is to improve device performance using low-cost and scalable fabrication techniques while addressing important challenges in light management and high-k dielectric technologies. Another objective is to use it along with metal for sensing application using the concept of tamm plasmon.

Excitation and Momentum Resolved Multi-Polaritonic Emission Mapping in Hybrid Organic- 2D Material Microcavity

[1,#]Jhuma Dutta,[2]Nitin Yadav, [3]Ben Johns and [4]Jino George

[1]*Department of Physics & Materials Science, Thapar University, Patiala – 147004, India*
[2]Department of Chemical Sciences, Indian Institute of Science Education and Research (IISER) Mohali, Punjab-140306, India

[#]*Corresponding authors E-mail address Email: jhuma.dutta@thapar.edu*

Organic Frenkel excitons in layer-by-layer assembled TDBC and Wannier–Mott excitons in monolayer WS_2 strongly couple to form hybrid multi-polaritonic states. Excitation- and momentum-resolved spectroscopy reveals their polaritonic emission properties. These concepts are further exploited to realize a room-temperature cavity-QED quantum phototransistor with efficient energy transfer to atomically thin MoS_2.

Hybridization of organic Frenkel excitons (layer-by-layer assembled TDBC J-aggregates) with inorganic Wannier–Mott excitons in a WS_2 monolayer forms a hybrid multi-polaritonic system that enables emission engineering through strongly coupled states. Excitation- and momentum-resolved Fourier-plane micro-spectroscopy is employed to map the polaritonic dispersion, revealing a strong correlation between the photonic fraction and emission from different polariton branches, with enhanced middle-

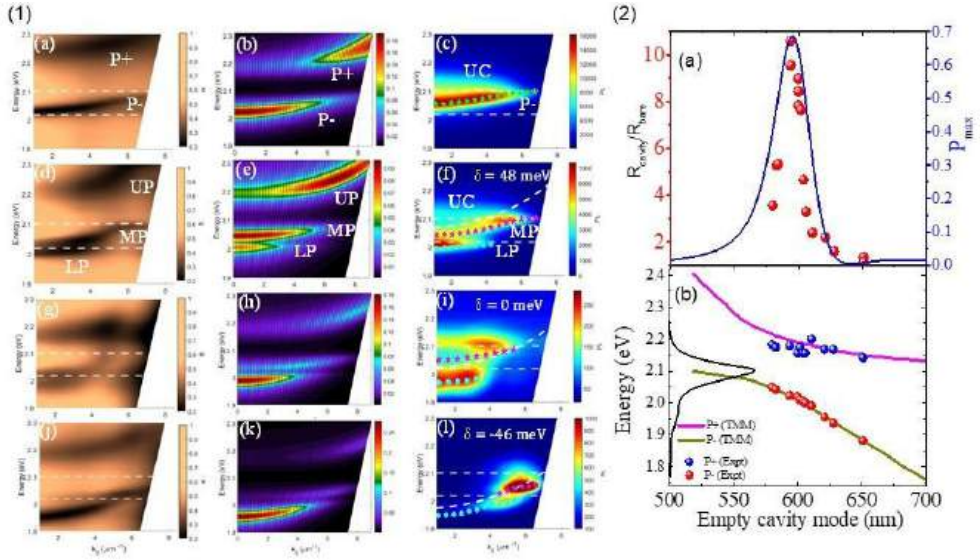


Fig.1: Energy/in-plane momentum dispersion: (a, b, c) TDBC-hBN within a λ cavity, (d, e, f) TDBC-hBN-WS_2 within a λ cavity with δ =48 meV, (g, h, i) TDBC-hBN-WS_2 within a λ cavity with δ =0 meV, (j, k, l) TDBC-hBN-WS_2 within a λ cavity with δ =-46 meV. **Fig.2**:(a) Relative photoresponsivity (R_{cavity}/R_{bare}) measured at 590 nm plotted against the empty cavity mode position (red spheres), with quantum mechanically calculated probability of energy transfer (blue line). (b) Experimental (blue and red solid spheres) and TMM-simulated (pink and green solid lines) polariton dispersion, with bare TDBC absorbance (black curve).

polariton emission at specific momenta due to its increased photonic character. This approach also provides direct estimates of the group velocity and effective mass of the polaritonic states. These insights facilitate the design of tailored hybrid polaritonic systems and are further exploited to realize a room-temperature cavity-QED quantum phototransistor based on a single-MOSFET architecture, demonstrating efficient energy transfer to an atomically thin MoS_2 monolayer.

References:

[1] **J. Dutta**, N. Yadav, B. Johns, and J. George, *Adv. Optical Mater.* (2025) e02324.
[2] K. Kaur, **J. Dutta**, and J. George, *J. Chem. Phys.* 163 (2025) 050902.
[3] **J. Dutta,** N. Yadav, P. Bhatt, K. Kaur, D. E. Gómez, and J. George, *J. Phys. Chem. Lett.*, 15 (2024) 8211.

Advancing Light Emission from 2D Semiconductor Devices Through Van der Waals Contact Engineering

[1]Konthoujam James Singh, [1]Pin-Jie Pu, [1]Cha-Jia Chang, [1]Shih-Yen Lin, [2]Kuan-Bo Lin, [1]Chao-Cheng Kaun, [1]Min-Hsiung Shih
[1]Research Center for Applied Sciences (RCAS), Academia Sinica, Taipei, 11529, Taiwan
[2]International College of Semiconductor Technology, National Yang Ming Chiao Tung University, Hsinchu 30010, Taiwan

[#]*mhshih@gate.sinica.edu.tw*

We demonstrate that low-temperature (75 °C) growth crystalline antimonene van der Waals contacts form defect-free interfaces, reducing the Schottky barrier height and boosting electroluminescence in 2D semiconductors, addressing defect-induced interface limitations and underscoring their promise for efficient, high-performance 2D optoelectronic devices.

Transition metal dichalcogenides (TMDCs) have emerged as promising materials for next-generation optoelectronic devices owing to their exceptional physical and electronic properties [1,2]. However, conventional metal contacts formed by direct deposition often exhibit high contact resistance, poor carrier injection efficiency, and strong Fermi-level pinning, thereby degrading device performance [3]. Furthermore, the atomically thin nature of TMDCs makes them particularly susceptible to the formation of undesirable Schottky barriers at metal-semiconductor interfaces [4]. Van der Waals (vdW) contacts provide an effective route to overcome these limitations.

In this study, we systematically compared the performance of WSe_2-based devices employing two contact materials: antimony (Sb) and titanium (Ti), with distinct work functions. The Sb electrode was deposited at 75 °C, the onset temperature for the formation of antimonene layer. Fig. 1(a) shows the evidence of vdW interface formation between antimonene and the WSe_2 monolayer having a clear vdW gap of about 0.5 nm, while the direct contact interface shows noticeable defect formation. Fig. 1(b) shows the room-temperature EL comparison of WSe_2-based devices with two different contact materials. Compared to the Ti/Ag device, the vdW Sb/Ag device exhibits a significant enhancement of approximately 173% in EL intensity, with a peak emission centered around 750 nm. We used temperature-dependent I_d-V_g measurements to examine the electrical behavior of the WSe_2-based FET devices. We extracted SBHs using the slope of the Arrhenius plot of $\ln(I_d/T^{3/2})$ versus 1000/T derived from the conventional thermionic emission equation for both devices. This method yields SBHs of 0.86 and 0.45 eV for the vdW Sb/WSe_2 and direct Ti/WSe_2 contacts, respectively as shown in Fig. 1(c), leading to improved carrier injection. By leveraging weak vdW interactions between the TMDC monolayer and the contact electrode, this approach avoids chemical bonding and suppresses defect and trap formation at the interface, thereby enhancing the electroluminescence and the SBH reduction.

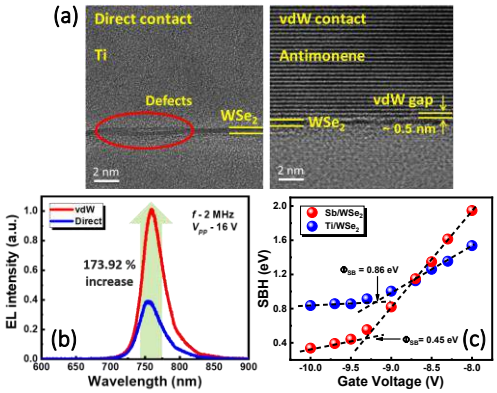


Fig. 1 Comparison between direct and vdW contacts. (a) TEM images. (b) EL spectra. (c) SBH comparison.

In summary, this study demonstrates that vdW contact engineering offers a highly effective strategy for improving carrier injection and light emission in TMDC-based LEDs highlighting the potential of vdW contact integration toward high-performance, scalable, and defect-free 2D optoelectronic devices.

Acknowledgement: This work was supported by the research funding National Science and Technology Council (NSTC) in Taiwan under contract number NSTC 113-2112-M-001-040- and NSTC 114-2112-M-001-021.

References:

[1] T. Ahmed, J. Zha, K. K. Lin, H.-C. Kuo, C. Tan, D.-H. Lien, Advanced Materials 2023, 35, 2208054.
[2] Aleksander A. Tedstone, David J. Lewis, and Paul O'Brien, Chemistry of Materials 2016, 28, 1965-1974.
[3] X. Liu, M. S. Choi, E. Hwang, W. J. Yoo, J. Sun, Advanced Materials 2022, 34, 2108425.
[4] Shen, PC., Su, C., Lin, Y. et al., Nature 2021, 593, 211–217.

Molecular Resonance- and Charge-Transfer- Assisted Surface-Enhanced Raman Scattering using Molybdenum Oxide Nanoparticles

[1,#]Palash Makumuria, and [1]Ashwini Kumar Sharma
[1]Department of Physics, Indian Institute of Technology Guwahati, Guwahati-781039, Assam, India

[#]*email id: p.makumuria@iitg.ac.in*

In this work, SERS performance of MoO_{3-x} nanoparticles synthesized via PLAL technique are evaluated using RhB as the probe molecule. The maximum SERS enhancement factor of 10^7-10^8 obtained with limit of detection 10^{-8} M for RhB. The enhancement mechanism is attributed to molecular resonance and charge-transfer between RhB-MoO_{3-x} complex.

Surface enhanced Raman scattering (SERS) is a highly sensitive, label free molecular detection technique that works by enhancing the Raman signal of molecules adsorbed on nanostructured surface. Unlike conventional SERS substrates such as gold and silver nanoparticles which enhances Raman signal of molecules adsorbed via plasmonic resonance, semiconductor-based SERS substrate primarily enhances via chemical enhancement mechanism originating from charge transfer between analyte molecule and substrate, and via molecular/excitonic resonance in molecule/substrate. The semiconductor-based SERS substrates has multiple advantages such as tunable electronic structure, chemical stability, molecular selectivity, and low cost. In this work, the SERS performance of sub-stoichiometric molybdenum oxide nanoparticles synthesized via pulsed laser ablation in liquid (PLAL) method is investigated using Rhodamine B (RhB) as the molecule. PLAL possesses several advantages over conventional wet chemical synthesis routes, including the generation of high-purity nanoparticles without the use of surfactants or capping agents, ambient-temperature synthesis, and rapid processing. Additionally, PLAL enables the formation of defect-rich, sub-stoichiometric, metastable nanoparticle phases through the rapid quenching of the ablated species, which is difficult to achieve using conventional wet chemical synthesis routes. The schematic of the experimental set up of the PLAL used in this work is provided in our previous work [1]. The synthesized nanoparticles were characterized via FETEM, Raman, XPS and UV-Vis-NIR spectroscopy.

The Raman spectrum of the synthesized MoO_{3-x} nanoparticles was observed to be matching with reported sub-stoichiometric phase Mo_8O_{23} ($MoO_{2.875}$) [1]. XPS and UV-Vis-NIR absorption analysis also supports the formation of MoO_{3-x} nanoparticles. Fig.1 shows the SERS spectra of RhB adsorbed on the synthesized nanoparticles. The Raman intensity of 1647 cm^{-1} mode increased from 2260 counts for RhB bulk powder to 43073 counts for 10^{-4} M RhB adsorbed on the synthesized nanoparticles, indicating their excellent SERS enhancement capability. The enhancement factors were calculated to be 1.95×10^5 and 1.18×10^6 for RhB concentration of 10^{-4} and 10^{-5} M, respectively, using the eq provided in Ref. [2]. The maximum SERS enhancement factors of 4.5×10^7 and 2.02×10^8 were obtained for RhB concentration of 10^{-7} and 10^{-8} M. The strong SERS enhancement is attributed to molecular resonance of the RhB molecule, where the laser excitation of 514 nm lies within the primary absorption band of RhB molecule. Additionally, change transfer between RhB-MoO_{3-x} complex is also contributing to strong SERS enhancement. The charge transfer mechanism is validated via steady state photoluminescence measurement, where strong quenching is observed for RhB-MoO_{3-x} complex as compared to RhB, when acquired using 514 nm excitation. Furthermore, charge transfer mechanism is validated by measuring the UV-Vis and ultraviolet photoelectron spectroscopy of synthesized nanoparticles. These results demonstrate the ability of PLAL to produce sub-stoichiometric MoO_{3-x} nanoparticles and its utility as efficient SERS substrates for detection of RhB molecule.

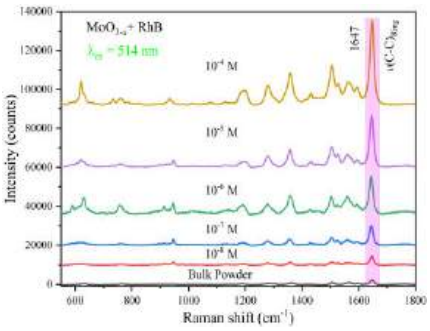


Fig. 1: SERS spectra of RhB adsorbed on MoO_{3-x} nanoparticles

References:

[1] P. Makumuria, A.K. Sharma, *Applied Surface Science* 720 (2026) 165226

[2] A. Kaushik et al, *ACS Applied Nano Materials 6 (2023)9236-9246*

Sb_2S_3 FILMS FOR LOW-LOSS RECONFIGURABLE PHOTONICS

[1]Meera V, [1,#]Harish N S Krishnamoorthy
[1]Tata Institute of Fundamental Research Hyderabad, Telangana, India
[#]*harishk@tifrh.res.in*

Sb_2S_3 is a promising phase-change material for reconfigurable photonics, but device performance is often compromised by sulphur loss, oxidation, and dewetting. We demonstrate mitigation of these degradation mechanisms using wetting and capping layers. We also design an ITO-based microheater to facilitate reliable, reversible phase transitions, advancing practical Sb_2S_3 photonic devices.

Phase change materials (PCMs) have gained significant interest in reconfigurable photonics applications due to their ability to rapidly switch between amorphous and crystalline states, showing huge optical contrast. GST and Sb_2Te_3, two of the widely used non-volatile PCMs, face the problem of high optical loss in the visible region. The wide-bandgap material Sb_2S_3 known for its earth abundance and low toxicity, has been identified as a PCM showing high refractive index contrast and low losses in the visible region. Getting stoichiometric Sb_2S_3 thin films is often considered a challenging task due to the volatile nature of sulphur. Several factors in the workflow of the film fabrication process are critical to the crystallization behaviour, phase change characteristics of the films as well as wettability on different substrates.

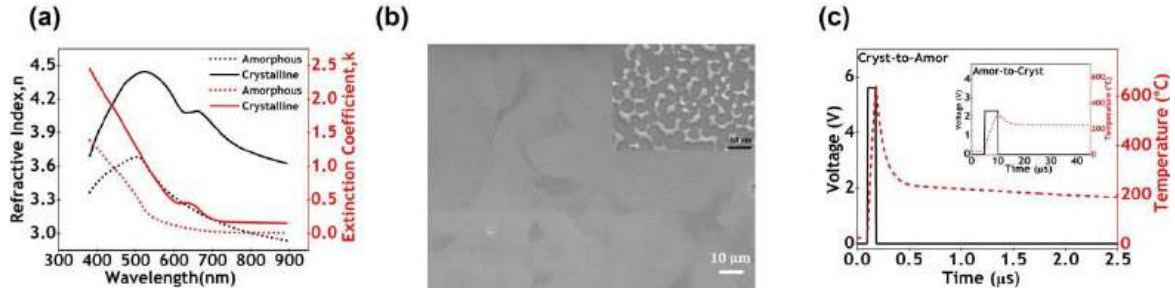


Fig. 1: (a) Optical properties of 85 nm amorphous and crystalline Sb_2S_3 thin films (b) SEM image of annealed Sb_2S_3 in a multi-layer configuration consisting of Ti and ZnS-SiO_2 layers and the inset shows the dewetting of annealed Sb_2S_3 deposited on Si without wetting and capping layers. (c) The temporal heat profiles generated by the voltage pulse for phase transition.

In this work, we used RF magnetron sputtering technique to deposit Sb_2S_3 thin films. The optimisation of sputtering conditions, including RF power and sputtering duration [1], was carried out to obtain stoichiometric, low-loss and uniform Sb_2S_3 thin films. For the as-deposited films, which are amorphous in nature, the k value goes to zero beyond λ=650 nm. Sb_2S_3 films were annealed at 300°C for 30 minutes in order to facilitate the phase change. During this process, the films dewetted irrespective of the substrates they were deposited on. An ultrathin layer of Ti was introduced to provide better adhesion and prevent dewetting. Sulphur loss as well as oxidation were prevented by suitably choosing a capping layer, ZnS-SiO_2 of thickness 40 nm. The addition of wetting and capping layers significantly reduced the dewetting of Sb_2S_3 thin films deposited on Si. The thermal switching of Sb_2S_3 from amorphous to crystalline states in this multilayer configuration was confirmed with both XRD and Raman analysis. We also observed that multiple optical states can be achieved by annealing Sb_2S_3 at different intermediate temperatures. In order to demonstrate electrical switching, an ITO-based microheater was designed to perform reversible phase switching operations. Further optimisations yielded excellent heater metrics resulting in a melt-quench rate of 4 X 10^9 K/s, which is close to the reported values [2] and low switching energy phase transitions, which points towards improved endurance of Sb_2S_3-based photonic devices.

References:

[1] Yuto Miyatake, Tomohiro Anda, Yosuke Wakita, Kotaro Makino, Shogo Hatayama, Makoto Okano, Kasidit Toprasertpong, Shinichi Takagi, and Mitsuru Takenaka, *Optical Materials Express* 15 (2025) 1972-1986.
[2] Jayita Dutta, Rui Chen, Virat Tara, Arka Majumdar, *APL Photonics* 10 (2025) 020803.

Design and Development of Hyperspectral Imaging instruments for India's Earth and planetary missions

[1]Moumita Dutta, Archit Dube, Ashish Mishra
Space Applications Centre, Indian Space Research organization

[1]duttamoumita@sac.isro.gov.in

Space applications Centre is developing Hyperspectral Imagers operating in VNIR, SWIR and LWIR range for Earth observation and planetary missions. The development was initiated with a plane grating based airborne instrument and subsequently wedge filter based hyperspectral in VNIR was developed. However due to some limitations of wedge filter based systems, we migrated to convex grating based offner and recently DYSON based hyperspectral imagers.

The first offner based spectrometers were developed to provide 30-meter ground resolution operating to 0.4 micron to 2.5-micron wavelength range catered by two separate instruments. The fore optics were made of a Tri mirror anastigmat (TMA) and two fold mirrors were used to direct the beam towards the spectrometer. The convex grating used was a single blazed grating for VNIR. Similarly, for SWIR, the same configuration with metal optics was developed. The instrument (f/8) was catering to a range of 0.8 to 2.5 micron. It was a three-blazed grating. All the metal mirrors and metal gratings were designed in SAC and developed through Indian industries. The performance of the optical design was diffraction limited meeting high MTF requirement at Nyquist. However, fabrication tolerance had its own impact on the integrated performance. Two separate instruments in VNIR and SWIR providing sub meter resolution from airborne platforms are also developed for vegetation and mineralogical studies.

The same offner based configuration was used to design hyperspectral imager in MWIR catering from 0.8 micron to 5 micron for Chandrayaan-2 mission. Infrared Imaging Spectrometer (IIRS) used a five-blazed convex grating to cater to the said wavelength range and provided around 22 nm spectral resolution. All the optics were fabricated on Aluminum metal. IIRS strongly confirmed presence of water molecule on lunar surface.

Recently a LWIR imaging spectrometer, f/2 system is developed using DYSON configuration. The instrument caters to a field of view of +/-7 degree. The wavelength range of optical system is 7 micron to 12 micron. The single blazed concave grating used in DYSON spectrometer is shown in Figure1.

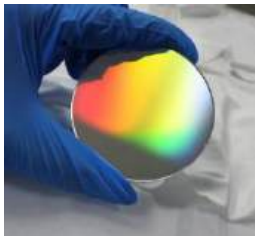


Figure1: Concave grating for DYSON

The DYSON lens made of ZnSe is shown in figure 2. The spectral sampling of the instrument is 7.63 nm, which is measured using spectral filters. The blazed grating designed in SAC and developed through industry.



Figure2: DYSON lens

The measured spectral dispersion of the instrument is summarized in table below.

Central Wavelength	Band Number	Spectral dispersion measured	Spectral dispersion expected
7.5 µm	90	7.5 nm /pixel	7.63 nm /pixel
8.5 µm	226		
9.6 µm	376		
10.5 µm	491		

The most challenging part of the development is fabrication of ZnSe DYSON lens and metal grating with required surface figure. The other offner spectrometers use higher order aspheric mirrors designed with conic. The surface figure strongly depends on the mirror material. Lower surface figure degrades the image quality and leads to poor MTF of the optical system. A surface figure as good as λ/33 is achieved for a mirror of 100 mm diameter. Use of higher order aspheric surface helps to make the instrument compact and lightweight and as well as to achieve diffraction limited MTF performances at higher Nyquist frequency. The ultimate goal is to achieve much better spatial and spectral resolution and catering longer spectral range with single instrument.

References:

[1] Various Design Documents and reports of SAC.

Optical Instrumentation for Solar astronomy: Overview of observational facilities at Udaipur Solar Observatory

[1,#]A Raja Bayanna,[1]Shibu K Mathew
[1]Physcial Research Laboratory, Udaipur Solar Observatory, Dewali, Udaipur-313004

[#]*bayanna@prl.res.in*

India has a rich history of solar physics research spanning over a century, through ground and space-based facilities dedicated to the continuous monitoring of solar activity in the photosphere and chromosphere. Udaipur Solar Observatory is one of the ground-based observational facilities that has significantly contributed to solar astronomy by developing optical instrumentation to observe solar active regions for decades. Details of the instrumentation facilities at Udaipur Solar Observatory are summarized here.

India has a rich heritage in solar astronomy, highlighted by the discovery of helium during a total solar eclipse in 1868 and the identification of the Evershed effect in 1909 at the Kodaikanal Solar Observatory (KSO). Ground-based optical facilities such as the Udaipur Solar Observatory (USO), KSO, and the Devasthal Observatory have enabled continuous monitoring of solar activity, particularly in the photosphere and chromosphere, significantly advancing solar physics in the country. Additionally, the recent success of the Aditya-L1 mission for studying Sun demonstrated our capabilities in space-based instrumentation.

Udaipur Solar Observatory has been developing optical instrumentation for observing Solar active regions for decades. The Multi-Application Solar Telescope (MAST) [1] is the recent one. MAST is a 50 cm off-axis Gregorian telescope designed for near-simultaneous high-resolution observations of solar active regions in the solar photosphere and chromosphere. The important back-end instrument of the telescope is a Fabry-Perot-based narrow-band imaging spectro-polarimeter. In addition, at USO, a low-order solar adaptive optics system is in operation to counter the effects of atmospheric seeing.

The imaging-based Spectrometer of MAST [2] is intended to obtain near-simultaneous line-scan observations of the solar photosphere and chromosphere in the Fe I 6173 and Ca II 8542 spectral lines, respectively. It employs two $LiNbO_3$-based Fabry-Perot etalons (FP) to achieve a larger FSR and a narrower bandwidth. The thicknesses of the etalons are 226 μm and 577 μm, respectively. Two FPs are used in tandem for photospheric lines, while a single FP is used for broader chromospheric lines along with their respective pre-filters. The Free spectral range (FSR) and Full-width at Half-Maximum (FWHM) of the at 6173 Å are 6.5 Å and 85 mÅ, respectively, while at 8542 Å they are 7 Å and 170 mÅ, respectively. A recent study on bidirectional flows in a quiescent prominence and associated dynamics suggested a potential link to magnetic reconnection within the prominence. [3].

To improve the resolution of MAST beyond the seeing limit, an Adaptive Optics (AO) system has been developed at USO. A Shack-Hartmann Wavefront Sensor (SHWFS) consists of 37 lenslets and a 15 mm membrane deformable mirror with 37 actuators — used as the wavefront sensor and corrector, respectively. Closed-loop update rate of the system is about 1 kHz. Improvement up to 0.6-0.7 times of the diffraction limit is achieved with the system. The granulation contrast increased by 16-36% relative to that without AO correction over a wide field of view in the science camera.

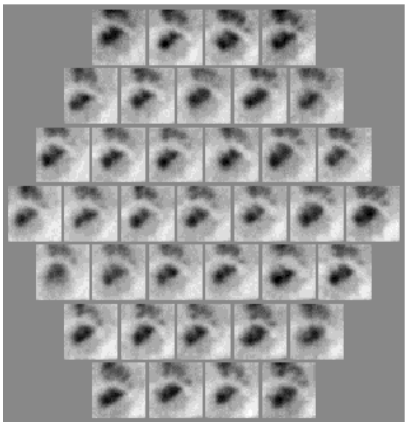


Fig. 1: Shck-Hartmann wavefront sensor at USO for MAST

Acknowledgements: This work includes contributions from entire MAST team at Udaipur Solar Observatory.

References:

[1] P. Venkatakrishnan, S. K. Mathew, N. Srivastava, *et al.*, *Curr. Sci.* 113(4), 686, (2017)
[2] S. K. Mathew, A. R. Bayanna, A. R. Tiwary et.al. *Solar Phys.* 292(8), 106 (2017)
[3] S. K. Dubey, A. Hillier, S. K. Mathew, The Astrophysical Journal 985 (2025)

Active-Medium-Induced Scale Factor Variations in Prism-based Ring Laser Gyroscopes for Space Navigation

#Anjitha Viswanath, Bindu John, Rajesh George, Pradeep K, Joji J Chaman
Inertial Sensors Entity, ISRO Inertial Systems Unit, Thiruvananthapuram-695013

#anjithavssc@gmail.com

A unified analytical model based on semi-classical Lamb theory is presented to quantify active-medium-induced scale factor variations in a total internal reflection prism-based ring laser gyroscope. The influences of frequency detuning, gain, temperature and pressure are systematically analyzed, providing theoretical insight into scale factor stability and space navigation performance optimization.

Ring Laser Gyroscopes (RLGs) continue to represent one of the most accurate inertial rotation sensors for strategic navigation owing to their exceptional bias stability, long-term accuracy and reliability. Despite significant advances in resonator design and control electronics, the achievable navigation accuracy remains strongly dependent on scale factor stability, which is influenced not only by the resonator geometry but also by the characteristics of the active laser medium. Recent developments in high-performance RLGs continue to emphasize accurate modeling and compensation of laser dynamics to achieve navigation-grade performance [1–3]. However, a comprehensive analytical understanding of the influence of active-medium parameters on the scale factor of total internal reflection (TIR) prism-based Ring Laser Gyroscopes (RLGs) remains limited.

In this work, a unified analytical model based on the semi-classical Lamb formalism is developed to quantify the contribution of the active medium to scale factor (SF) variations in a TIR prism-based RLG. The laser dynamics are represented by the coupled Lamb equations describing the amplitudes and frequencies of the counter-propagating laser beams, where the Lamb coefficients $(\alpha, \beta, \theta, \tau, \sigma \; and \; \rho)$ are evaluated using the plasma dispersion function. The resulting gyroscope output is expressed as $\Delta f = K\Omega + \Delta f_{ns} + \Delta f_{bs}$, where K denotes the SF, Ω is the applied angular rate, Δf_{ns} represents the null-shift contribution and Δf_{bs} accounts for backscattering. The scale factor is further expressed as $K = K_R + K_A$, where $K_R$is determined by the resonator geometry and K_A represents the active-medium contribution. Mathematically, active medium contribution to scale factor is given by

$$K_A = \frac{1}{\Delta\omega_D}\left[\frac{\partial\sigma}{\partial\xi} + \left(\frac{\partial\rho}{\partial\xi} + \frac{\partial\tau}{\partial\xi}\right)I + \frac{\rho-\tau}{\beta-\theta}\left(\frac{\partial\alpha}{\partial\xi} - \frac{\partial\beta}{\partial\xi}I\right)\right]$$

where $\Delta\omega_D$is the Doppler broadening and ξ the frequency detuning.

The developed model is employed to investigate the effects of frequency detuning, gain, temperature and pressure on the gyroscope scale factor. At operating conditions, the change in SF for (i) 10% change in active medium gain is 376 ppm, (ii) 27 to 77 deg Celsius change in temperature is 354 ppm, (iii) 680 MHz detuning is 50 ppm and (iv) 10% variation in active medium pressure is 83 ppm. These results providing a clear theoretical basis for prioritizing gain and path length stabilization to achieve superior scale factor stability. For illustration, the change in SF in arcs/s for different active medium gain values is shown in *Fig. 1*.

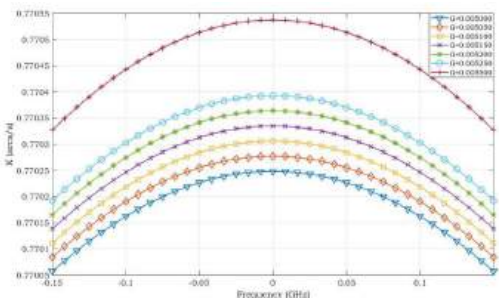


Fig. 1: Active medium gain induced SF variations

The presented analytical framework systematically establishes how active-medium parameters govern the scale factor of a TIR prism-based Ring Laser Gyroscope through a unified semi-classical Lamb-theory formulation. The results provide quantitative insight into the relative sensitivity of the scale factor to operating conditions and cavity parameters, offering a theoretical basis for analysing and improving scale factor stability in high-precision navigation-grade inertial laser gyroscopes.

References:

[1] A. O. Sinelnikov, et al., Photonics Russia, 18-6 (2024)
[2] E. Maccioni, et al., Applied Optics, 61-31 (2022).
[3] D. Cuccato et al., Physical Review, 2013.

Advances and Challenges in Nested Loop Cascaded Stage Tiled Aperture Coherent Beam Combining

#B. Srinivasan, S. Maji, P. Gorai, A. Bharadwaj, and H. Ilangovan
Department of Electrical Engineering, IIT Madras, Chennai 600036

#*balajis@ee.iitm.ac.in*

Nested loop tiled aperture coherent beam combining (NLTA CBC) with cascaded stages promises to be a scalable configuration for realizing directed energy sources capable of generating 100 kW and beyond in a diffraction-limited beam. In this talk, we will discuss the recent advances and the challenges involved in the implementation and control of such sources.

Coherent beam combination based on tiled aperture configuration (TA-CBC) has excellent potential for multiple applications including space exploration, material processing, additive manufacturing and defense applications due to its scalable architecture [1]. One of the most challenging issues in TA-CBC is the development of a robust and scalable closed loop feedback algorithm for phase synchronization. Conventional approaches rely on the power in the diffraction limited main lobe region, commonly referred to as the Power-in-Bucket (PIB). However, such a feedback mechanism is susceptible to issues with local maxima, especially when the number of beams is relatively high. In this work, we propose and experimentally demonstrate a novel approach based on feedback from one of the off-center locations in the far field pattern.

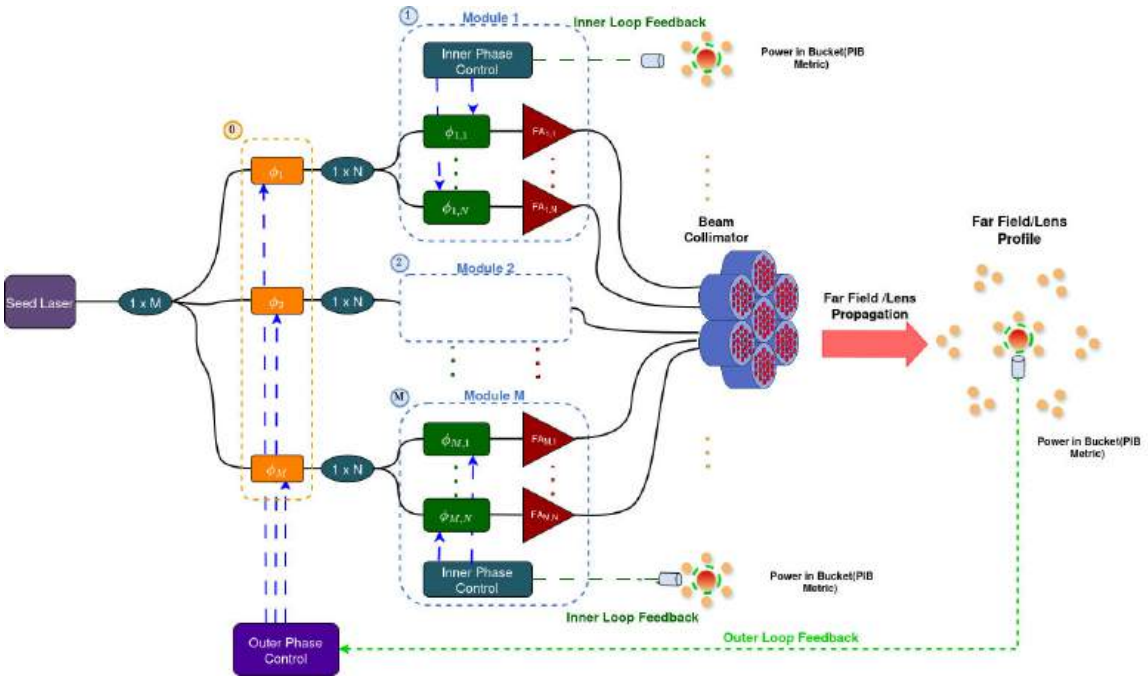


Fig. 1: Schematic diagram of the nested loop tiled aperture CBC system.

Another challenge is the design of the optical phased array block, which includes the hexagonal steering mirror unit. In this talk, we will also discuss the key design parameters and how they impact the overall CBC efficiency. Yet another challenge is the development of an engineered 7x7 CBC unit consisting of 49 polarization-maintaining amplifiers each of which needs to demonstrate uniform output power, polarization extinction ratio (PER) and M^2 values. This will also be discussed during this talk.

The authors would like to acknowledge DRDO for financial support.

References:

[1] L. Linslal et al.,"Challenges in coherent beam combining of high power fiber amplifiers: a review", ISSS Journal of Micro and Smart Systems **11**, 277 (2022).

Next Generation Electro-optical Systems

Sudhir Khare

Instruments Research and Development Establishment, Dehradun 248008, India

email: sudhirkhare.irde@gov.in

Electro-optical (EO) systems are true force multiplier as it allows the weapon and equipment's to be used effectively during day and night in fair and bad weather conditions. It is an emerging technology which has evolved in last 40 years. Infrared imagers has become favourite of military forces since World War-II and it performed exceptionally well during past few wars. The development in the infrared imaging technology changes the concept of conventional war.

Keywords: Infrared Imaging, IDDCA, Image Processing, Hyper-spectral, Dual Color, Hot Detector

Infrared imaging systems are finding wide range of applications as they work in truly passive manner, utilizes the target to background thermal contrast [1]. It allows the operator to see and acquire the targets in total darkness including adverse weather conditions (poor ambient light). With the advancement in detector, optics and image processing technologies, infrared imagers are finding new areas of exploration. Today, there is a demand in the market for high resolution, more compact, low power and light weight EO systems with higher Field of View (FOV).

Advancements in the IR detector technologies always governed the performance and application of infrared imaging system. Started with first generation single detector technology, now matured third generation FPA based technology detectors are available. With the increasing market demand for compact and low powered infrared imagers, advancement in the detector technologies is still progressing. Latest trends in detector technologies is low pitch, high format, broad band high operating temperature detectors.

Infrared Optics module collects the radiations from the targets and form images on to the detector. The available optical materials which transmit infrared radiations are very limited. In IR region Silicon (Si), Germanium (Ge), Zinc Selenide (ZnSe) and Zinc Shulphide (ZnS) are the few common materials. ZnSe being a non RoHs complained materials, therefore,unfriendly material during processing. In LWIR spectral band, chalcogenide, Amorphous Materials Transmitting IR (AMTIR) are the new invention.The modeling [2] and simulation software reduces the cost, time and risk in R&D. The new optimization technique for Diffractive Optical Element (DOE) is helpful to reduce the optical components in the optics module for better performance.

With the advancement of detector technology, a compatible image processing technologies for high format and high frame rate is required. To cater for this high amount of real time data processing, FPGA based parallel processing technique is required. The performance of infrared imager can further be enhanced using advance image processing features like through fog imaging, real time turbulence correcting algorithms. Different spectral window have different advantage and disadvantages. Weighted image fusing technique provides high quality video in different weather and different time with the advantage of each spectral window. Image processing on FPA is the futuristic technique to reduce system noises and power consumption requirement.

Future EO systems would be designed towards being more compact, low power and low cost with improved observation capabilities like detection, and identification in difficult conditions (low contrast, camouflage etc.). The requirements are posing new challenges to infrared imaging technology, so today, only rely on radiation intensity is not enough, there is a need to exploit additional attributes of incoming radiation like spectral characteristics, polarisation etc.

3. References

[1] M. S. Seán, "Analysis of the relative merits of the 3-5 μm and the 8-12 μm spectral bands using detected thermal contrast," in Proceedings of SPIE 9485 on Thermal Infrared Applications XXXVII, 2015.

[5] S. Keßler, R. Gal, W. Wittenstein, "TRM4: Range performance model for electro-optical imaging systems." In Proceedings of the Infrared Imaging Systems: Design, Analysis, Modeling, and Testing XXVIII, Anaheim,CA, USA, 11–12,vol. 10178, pp. 2–12, 2017.

Neuromorphic Event Data Acquisition for High-Speed Vision Applications

[1,#]Chinmay Khattar,[1]Neeraj Pandey, [1] Harshit Singh, [1]L M Pant
[1]Instruments Research & Development Establishment (IRDE)
[#]*ckhattar.1999@gov.in*

Event-based vision sensors enable asynchronous imaging with microsecond resolution, high dynamic range, and low latency. This paper presents a practical framework for sensor configuration, calibration, bias tuning, accumulation time, and noise filtering. Experimental results analyze their impact on event generation and data quality. The study provides guidelines for reliable event data acquisition in detection, tracking, and real-time vision applications.

Conventional CCD/CMOS cameras capture complete frames, leading to motion blur, latency, limited dynamic range, and data redundancy. Event cameras, inspired by the biological retina, operate asynchronously at the pixel level. They generate events only when brightness changes, enabling microsecond temporal resolution, low latency, and high dynamic range. These features make event cameras highly suitable for high-speed vision applications.

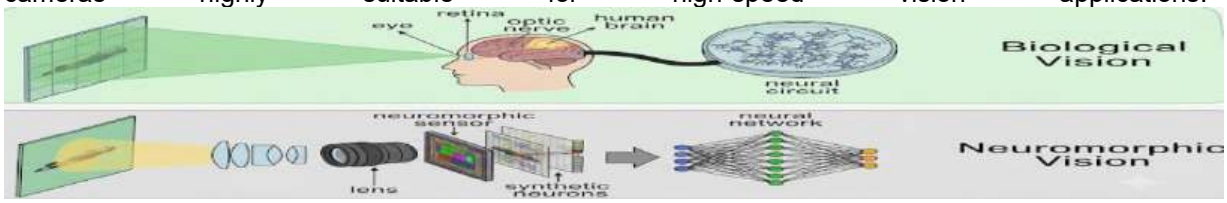


Fig. 1. Biological vision and neuromorphic vision



Event-based vision sensors generate an asynchronous stream of events instead of conventional image frames. Each event is represented by the tuple

$$e=(t,x,y,p),$$

where (t) is the event timestamp, (x) and (y) are the pixel coordinates, and (p) denotes the polarity of the brightness. The quality of the acquired event data is influenced by sensor parameters such as **accumulation time**, **bias**, and **bias difference (Diff**).

Fig. 3: Demonstrates the HDR capability of the event camera, clearly detecting objects under strong sunlight where conventional cameras suffer from overexposure.
Fig. 4: Demonstrates the high-speed motion capture capability, effectively recording a rotating fan and fired bullet without motion blur.

Accumulated event frames preserve important motion and structural information, making them suitable for detection, tracking, and real-time vision applications.

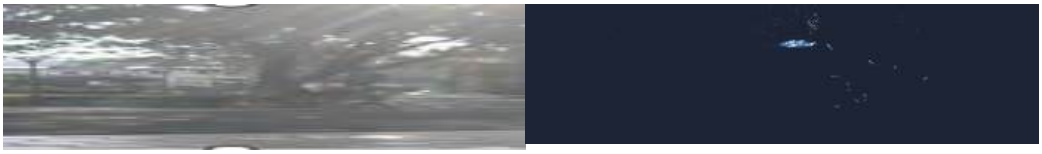


Fig 3: Comparison between HDR Frames & HDR Events (HDR-High Dynamic Range)

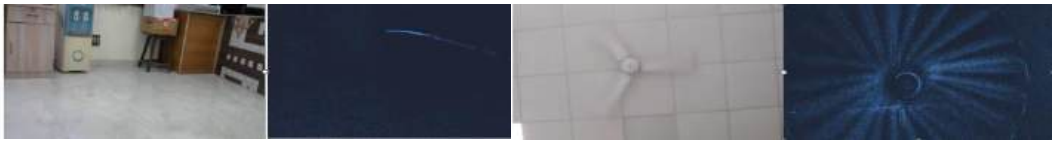


Fig 4: Comparison between Motion blur Frames & Motion blur Events for the above 2 pictures

References:

[1] P. Lichtsteiner, C. Posch, and T. Delbruck, "A 128×128 120 dB 15 μs latency asynchronous temporal contrast vision sensor," IEEE Journal of Solid-State Circuits, vol. 43, no. 2, pp. 566–576, Feb. 2008.
[2] C. Brandli, R. Berner, M. Yang, S.-C. Liu, and T. Delbruck, "A 240×180 130 dB 3 μs latency global shutter spatiotemporal vision sensor," IEEE Journal of Solid-State Circuits, vol. 49, no. 10, pp. 2333–2341, Oct. 2014.

Epsilon-Near-Zero Materials and Their Photonic Applications

[1]Shakti P. Mahato, [1,2 #]Vipul Rastogi
[1]Department of Physics, Indian Institute of Technology Roorkee, INDIA 247667
[2]Centre for Photonics and Quantum Communication Technology, Indian Institute of Technology, Roorkee, Uttarakhand, INDIA 247667

[#]*vipul.rastogi@ph.iitr.ac.in*

The epsilon-near-zero (ENZ) concept in photonics has gained considerable interest due to its remarkable linear and nonlinear optical properties. Here, we present recent advances in ENZ nanophotonics and its prospects for light–matter interactions, optical communications, and emerging photonic applications.

Epsilon-near-zero (ENZ) materials are a class of optical materials whose real part of the dielectric permittivity approaches zero at a specific frequency. The unique linear and nonlinear optical characteristics, relatively high tuning flexibility, and CMOS compatibility make ENZ materials a competitive platform for integrated photonics and nanophotonic devices. ENZ materials can be realised using both naturally occurring materials and artificially engineered metamaterials, enabling ENZ operation across a broad spectral range extending from the ultraviolet (UV) and visible regions to the near-infrared (NIR), mid-infrared (MIR), and far-infrared (FIR). By tailoring the material composition, carrier concentration, or structural geometry, the ENZ wavelength can be engineered to meet the requirements of different spectral regimes and applications [1]. Furthermore, at ENZ wavelength, the continuity of the normal electric displacement field across interfaces requires a corresponding increase in the electric field inside the ENZ medium. These characteristics make ENZ materials highly attractive for linear, nonlinear, and tunable photonic devices [2]. Here, we present an overview of recent advances in epsilon-near-zero (ENZ) materials and showcase some research contributions from our group.

Over the past decade, epsilon-near-zero (ENZ) materials have attracted significant attention, leading to the development of a wide variety of nanophotonic devices. Early research primarily focused on integrating ENZ materials into waveguide platforms for all-optical and electro-optical modulation, as well as thin-film structures for perfect absorption, frequency conversion, and enhanced nonlinear optical responses [3,4]. More recently, the integration of ENZ materials with metasurfaces has considerably broadened their functionality. In particular, the coupling of ENZ effect with resonant modes such as Fabry-Parot, plasmonic, guided-mode, and bound-state-in-the-continuum (BIC) resonances has enabled improved device efficiency and new opportunities for tunable, compact, and multifunctional photonic devices [5,6]. We have recently explored several ENZ-based photonic structures, and selected results from these studies will be presented in this talk. Our research has focused on the design and development of ENZ-enabled photonic devices for diverse applications. We designed a broadband directional thermal emitter based on ENZ polar dielectrics, demonstrating its potential for passive radiative cooling and energy-efficient smart window applications [7]. Furthermore, we investigated ENZ-integrated free-space optical devices based on electrical and optical tuning strategies, achieving high modulation depth, low-power operation, and fast switching [8,9]. Our current efforts are directed toward theoretical modelling and experimental characterisation of the nonlinear optical properties of ENZ materials, which will provide deeper insight into their nonlinear response and facilitate the realisation of advanced nonlinear photonic and all-optical switching devices.

References:

[1] J. Wu, Z. T. Xie, Y. Sha, et al., *Photon. Res*. 9, 1616–1644 (2021).
[2] A. Anopchenko, S. Gurung, S. Bej, et al., *Nanophotonics* 12(14), 2913–2920 (2023).
[3] L. Jin, Q. Chen, W. Liu, and S. Song, *Plasmonics* 11, 1087–1092 (2016)
[4] J. Yoon, M. Zhou, M. A. Badsha, et al., *Sci. Rep.* 5(1), 12788 (2015).
[5] B. Johns, *Nanophotonics* 12, 3301 (2023).
[6] H. Zheng, Y. Zheng, M. Ouyang, et al., *Opt. Express* 32, 7318–7331 (2024).
[7] S. P. Mahato and V. Rastogi, *Appl. Opt.* 64, 7176-7185 (2025).
[8] S. P. Mahato and V. Rastogi, *JOSA B.* 43, B141-B149 (2026).
[9] S. P. Mahato and V. Rastogi, *Progress in Electromagnetic Research Symposium (PIERS-2025)*, (2025).

Observation of Chiral s-p Orbital Topological Edge States in Femtosecond Laser-Written Photonic Floquet Lattices

[1]Gayathry Rajeevan, and [1, #]Sebabrata Mukherjee
[1]Department of Physics, Indian Institute of Science, Bengaluru 560012, India

[#] mukherjee@iisc.ac.in

We experimentally realize a higher-orbital Floquet topological insulator by periodically modulating s-p orbital couplings in a photonic square lattice with a synthetic π-flux. We demonstrate unidirectional s-p orbital topological edge states, establishing the orbital degree of freedom as a versatile platform for exploring novel topological phases in photonic systems.

Waveguide-based photonic systems provide a powerful platform for exploring novel topological phenomena and realizing robust light transport [1]. Specifically, two-dimensional topological waveguide networks can support unidirectional, backscatter-immune edge states that are robust against defects and disorder [2]. Such topological systems have been widely investigated using arrays of single-mode optical waveguides, each supporting only the fundamental (s) orbital. The role of higher orbitals in topological systems has remained largely unexplored.

Here, we consider a bipartite square lattice of s-p orbitals, where nearest-neighbor couplings are periodically modulated along the z direction. In our waveguide network, shown in Fig. 1(b,c), the A waveguide supports only the s orbital that is in resonance with the p orbital of the neighboring B sites. The evanescent couplings J_{1-4}^{sp} are switched on and off in a four-step clockwise manner [3,4]. Owing to the odd parity of the p orbital, one of the couplings in each plaquette of the lattice acquires a negative sign, producing a uniform synthetic π-flux per plaquette.

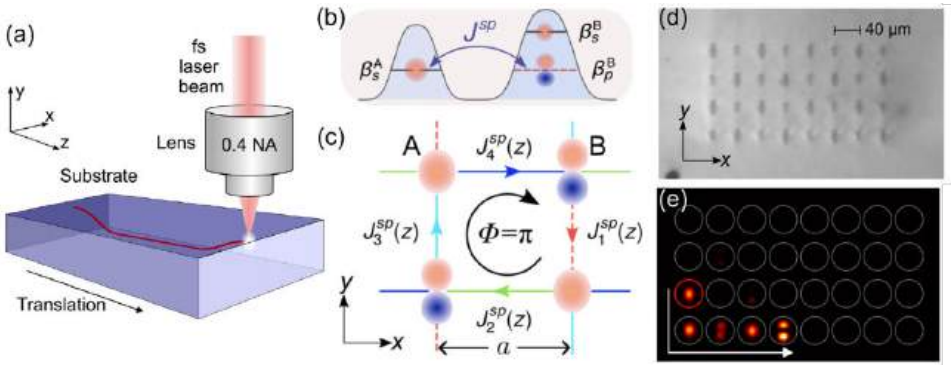


Fig. 1.(a) Schematic of femtosecond laser-writing. (b) Sketch of the refractive index profile of two neighboring waveguides and the resonance condition, $\beta_s^A = \beta_p^B$. (c) Schematic of a square lattice of s-p orbitals. (d) Micrograph of a femtosecond laser-fabricated s-p orbital square lattice. (e) Experimentally observed unidirectional topological edge state of s-p orbital. [5]

The waveguide lattices were fabricated inside a 120-mm-long borosilicate (BK7) glass material using 260 fs laser pulses at 1030 nm wavelength, 500 kHz repetition rate, and 380 nJ pulse energy [5]. We launch low-power light at 980 nm wavelength into a single edge waveguide and image the output intensity pattern after a propagation of two driving periods. Fig. 1(d, e) show a white-light micrograph of the lattice facet and the measured output intensity distribution, respectively. Unidirectional propagation of topological s-p orbital edge states, traveling around a lattice corner, is clearly visible. We further demonstrate that turning off the flux makes the system trivial over a range of driving parameters. These results establish higher-orbital photonic lattices as a promising platform for exploring nonlinear, non-Hermitian, and quantum topological physics.

We acknowledge funding from the STARS program, Ministry of Education, Government of India (MoE-STARS/STARS-2/2023-0716), the Indian Institute of Science, and the Infosys Foundation, Bangalore.

References:

[1] T. Ozawa et al., Reviews of Modern Physics **91**, 015006 (2019).
[2] M. C. Rechtsman et al., Nature **496**, 196 (2013).
[3] M. S. Rudner et al., Physical Review X **3**, 031005 (2013)
[4] S. Mukherjee et al., *Nature Communications* **8**, 13918 (2017).
[5] G. Rajeevan and S. Mukherjee, Communications Physics (2026). https://doi.org/10.1038/s42005-026-02756-8

LWIR all-Silicon ultrathin spherical metalens design and numerical simulation

[1]Vikram Singh Bhandari,[1]Deblina Sabui, [1]Arpit Gupta, [1]Purva Sharnagat, [1]Md Shanu, [1]Md Talha Ateeque,[2]Amit Kumar Agarwal and [1, #]Gufran Sayeed Khan
[1]Centre for Sensors, INstrumentation and Cyber-physical Systems Engineering, Indian Institute of Technology Delhi
[2]Instruments Research and Development Establishment, Dehradun, India
[#]*gufranskhan@sense.iitd.ac.in*

Nano-structured optics can replace bulky optical lenses in optical systems, enabling significant size reduction while maintaining phase modulation capabilities. A metalens with a 300 µm diameter and 500 µm focal length was designed and numerically evaluated using finite-difference time-domain simulations at a wavelength of 10 µm. In the silicon metalens design the unit cell library generation achieve an average transmission of ~78% and a continuous phase shift from 0 to 2π by varying the radius from 0.5 µm to 1.4 µm.

Ultrathin metalenses in the long-wavelength infrared (LWIR) range enable compact and efficient optical imaging systems. These metalenses are well-suited for thermal sensors, non-contact thermal imaging, and optical devices used in space and defence applications. Their thin design and precise phase control make them ideal for advanced LWIR imaging technologies [1]. Metalens design begins with creating a unit cell library, varying the dimensions of the structures on the substrate surface. The selection of the dimension range should be such that the output phase varies from 0 to 2π with high transmission. For the LWIR source, 10 µm wavelength is chosen, and accordingly, the material of nanostructures chosen is silicon (Figure 1a). The silicon material was low in cost, and availability is versatile. The designed parameters for the silicon unit cell are given in Table1. The transmission and phase map achieved from a parametric sweep of radius with height, which is illustrated in Figures 1 (b) and (c). The optimized height of 6 µm for the desired phase variation is chosen, which is shown in Figure 1 (d). The average transmission is ~78%, and the phase varies from 0 to 2π for the generated library.

Table 1

S.No	Parameters	Value
1	Wavelength (λ)	10 µm
2	Period (P)	3.0 µm
3	Radius (R)	0.5-1.4 µm
4	Height (h)	0.1-8.0 µm
5	Material	Silicon

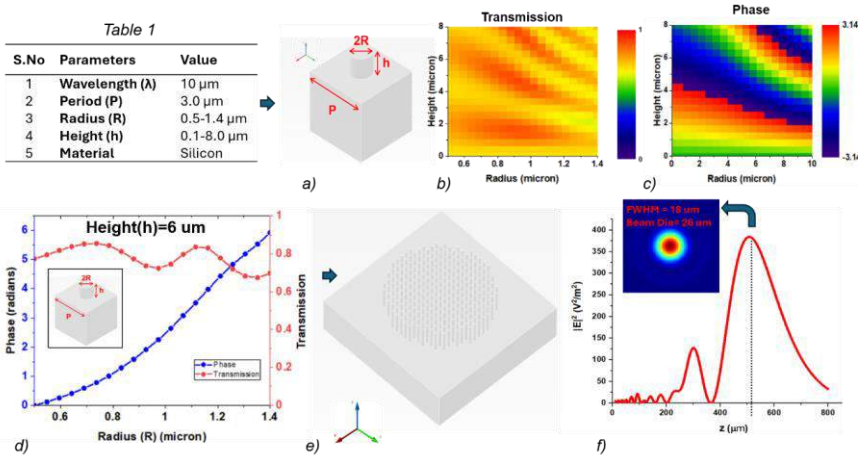


Figure 1 design workflow of ultrathin all Silicon metalens

In process of metalens design the next step is the nanostructures placement on the surface based on the required phase profile for the lens as shown in *figure1 e)*. Each location is assigned a nanostructure from the phase library that matches the desired local phase, as given by the spherical lens phase equation (1). This setup allows the metalens to focus light like a conventional spherical lens [2].

$$\phi(x,y) = \frac{2\pi}{\lambda}\left(\sqrt{r^2+f^2} - f\right) \quad (1)$$

Here, ϕ (x, y) represents the phase at position (x, y) on the lens, r is the position vector, f is the focal length, and λ is the wavelength. The targeted phase profile is designed for a spherical lens with a 300 µm diameter and a 500 µm focal length. The focal length and the beam diameter achieved ~507 um and 26 um. This can be designed for the achromatic lens as well.

References:

1. Borlido, J. M., Vieira, E. M. F., Correia, J. H., & Rodrigues, J. A. (2024). Germanium Metalens for longwave infrared applications. Optik, 317, 172087.
2. Wirth-Singh, A., Brook, A. M., Johnson, R., Fröch, J. E., & Majumdar, A. (2026). Meta-optical imaging at thermal wavelengths. *Journal of Physics: Photonics*, *8*(1), 012003.

Monte Carlo Analysis of MgO Nanoparticles dispersed in PDMS Matrix for Passive Daytime Radiative Cooling

[2,#]Shubhrakanta Panda,[1,2]Anjani Kumar Tiwari and [1,2]Vipul Rastogi

[1]Department of Physics, Indian Institute of Technology Roorkee, Roorkee, 247667 Uttarakhand, India

[2]Centre for Photonics and Quantum Communication Technology
Indian Institute of Technology Roorkee, Roorkee 247667, Uttarakhand, India

[#]*shubhrakanta_p@cpqct.iitr.ac.in*

We investigate solar reflectance and absorptance of 100nm diameter MgO nanoparticles dispersed in a 100μm PDMS film using Monte Carlo radiative transfer model. The optimized film exhibits <0.7% solar absorptance, 0.93 emissivity in the 8–13μm range, and a net cooling capability of 99-102W/m² across the design space.

Passive daytime radiative cooling (PDRC) enables heat dissipation to the 3K cold sink of outer space by combining high solar reflectance (0.3–2.5μm) with strong thermal emission within the atmospheric transparency window (8–13μm), without requiring any electrical power [1]. Dielectric nanoparticle–polymer composites are attractive PDRC materials because they are low-cost, scalable, and compatible with paintable coatings [2,3]. Among these, MgO is particularly attractive due to its wide bandgap (negligible solar absorption) and its Mg–O phonon resonances, which overlap with the atmospheric window. MgO-polymer nanocomposites have shown >96% solar reflectance and sub-ambient cooling outdoors [1]. Most designs use PVDF or polydisperse fillers; a systematic monodisperse MgO-in-PDMS volume-fraction study is comparatively scarce and, in this work, we address that gap.

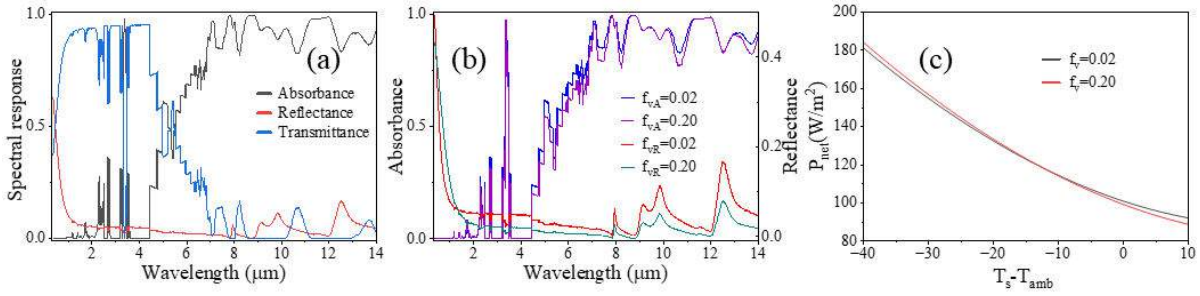


Fig. 1: (a) Spectral response of PDMS-MgO Coating at f_v=0.04, (b) Absorbance and reflectance spectra with varying volume fraction. (c) Plot of the net cooling power (P_{net}) vs. surface-ambient temperature difference ($T_s - T_{amb}$).

In this work, we simulate a semi-infinite PDMS slab (100μm thick) embedded with monodisperse, spherical MgO nanoparticles (r = 50nm) at volume fractions (f_v) ranging from 0 to 0.20.To model this behaviour, the complex refractive indices of both MgO and PDMS are processed through Mie theory to determine single-particle absorption (Q_{abs}) and scattering (Q_{sca}) efficiencies, which are subsequently used by the Monte Carlo simulation to calculate the total slab reflectance, transmittance, and absorptance in the wavelength range 0.36μm to 14μm. Fig. 1(a) shows the spectral response of the PDMS-MgO coating, demonstrating high absorbance in the thermal infrared region (8-13μm) for efficient heat emission and low absorbance in the solar spectrum (0-2.5μm) to minimize solar heating. Fig. 1(b) shows that solar reflectance increases as the MgO volume fraction (f_v) increases, while maintaining a high emissivity near 0.93. Moreover, under AM1.5G at 300K, the structure achieves approximately 100W/m² net cooling power at ambient thermal equilibrium, as depicted in Fig. 1(c), which provides the structure's robustness for PDRC applications.

References:

[1] A.P. Raman, M.A. Anoma, L. Zhu, E. Rephaeli, S. Fan, Nature 515 (2014) 540.
[2] P. Das, S. Rudra, K.C. Maurya, B. Saha, Advanced Materials Technologies 8 (2023) 2301174.
[3] B.R. Mishra, S. Sundaram, K. Sasihithlu, ACS Omega (2024);9(50):49494-502.

A plasmonic metagrating based dual-mode infrared sensor for label-free detection of traces of water in ethanol

[1,2,#]Sachin Kumar Srivastava and [1]Jhuma Pan
[1]Department of Physics, Indian Institute of Technology Roorkee, Roorkee-247667, Haridwar, Uttarakhand, India
[2]Centre for Photonics and Quantum Communication Technology, Indian Institute of Technology Roorkee, Uttarakhand, India
#sachin.srivastava@ph.iitr.ac.in

We report a dual-mode infrared sensor for small water impurities in ethanol using a plasmonic metagrating. The plasmonic mode enhances -OH bending and stretching bands of water, while the Berreman mode (BEIRA) enhances ethanol's C=O stretching peak. This multi-modal sensing approach provides a reliable, label- and receptor-free method of sensing.

Pure ethanol (C_2H_5OH) with a purity of at least 93-95% is required in biofuel, chemical synthesis, analytical laboratories, and food and beverage processing [1]. Water and methanol come as two major impurities while ethanol is manufactured from molasses. The developed sensor combines refractive index (RI)-based sensing, plasmon and Berremen (BE)-enhanced IR absorption (BEIRA) spectroscopy to detect traces of water in ethanol with high sensitivity and reliability. A metagrating absorber (MGA) was designed and developed, as shown in Fig. 1, which depicts a sinusoidal periodic structure with a bottom Ag layer and a top SiO_2 thin film on a polydimethylsiloxane (PDMS) substrate. The MGA was fabricated using physical vapor deposition, following a scalable and cost-effective nanoimprint lithography. A picture of the fabricated MGA confirms the flexibility, high fidelity, and large-area, uniform coating of the nanostructures.

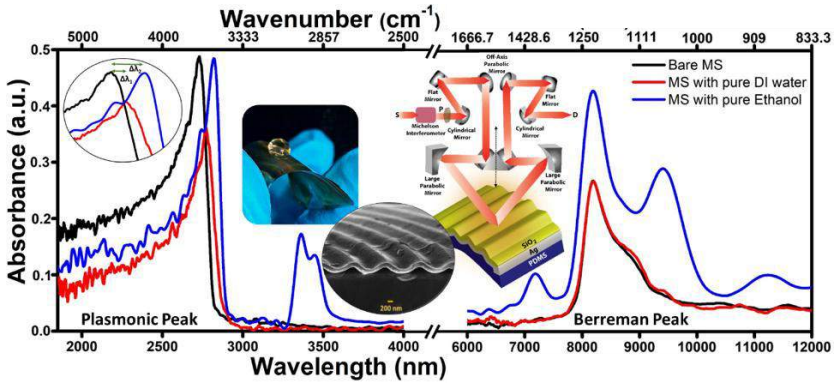


Fig. 1. The multimodal sensing approach based on plasmonic resonance shift and BEIRA.

The MGA exhibits two distinct absorption peaks in the NIR and LWIR regions with absorbance values of 80 and~99.5%, respectively, due to the excitation of plasmons and phonons [2]. Finite element method (FEM) simulations reveal strong electromagnetic field confinement at both plasmonic and phononic resonances, leading to enhanced vibrational fingerprints of water and ethanol. The sensing functionality of this dual-mode MGA was first demonstrated through plasmonic RI sensing, where a red shift in the NIR peak is observed when the RI of the surrounding medium is changed from pure water (1.33) to pure ethanol (1.36). Subsequently, BEIRA is observed when the BE absorption peak induced by LO phonons at the ENZ wavelength of SiO_2 overlaps with the C═O stretching mode of ethanol. This enhancement enables the detection of molecular vibrational features, confirming efficient plasmon-phonon-molecular coupling [3]. The plasmon–Berreman coupled MGA demonstrated a high RI sensitivity of 14.64 nm/(% v/v) with an LOD of 1.14% (v/v), whereas BEIRA provided high molecular selectivity for reliable detection of trace water and other common impurities in ethanol.

The authors acknowledge financial support from ISRO, the Ministry of Education (STARS), and SERB, Government of India.

References:

[1] F. B. Xiong and D. Sisler, Optics Communications, 283 (2010) 1326–1330.
[2] D. W. Berreman, Physical Review, 130 (1963) 2193–2198.
[3] J. Pan and S. K. Srivastava, ACS Sensors, 2026, DOI:10.1021/acssensors.6c00663.

Probing narrow photonic resonances using tunable diode lasers – applications in gas sensing, FBG interrogation and nanobiosensing

Arup Lal Chakraborty
Department of Electrical Engineering, Indian Institute of Technology Gandhinagar
Gandhinagar – 382055, Gujarat, India

arup@iitgn.ac.in

Narrow linewidth, precisely tunable and frequency agile distributed feedback semiconductor lasers can be used to probe narrow photonic resonances encountered in physical and chemical sensing. This talk will describe some applications in which such laser-based interrogation can be used to build cost-effective interrogation solutions with extremely high spectral resolution.

Injection current modulated tunable diode lasers are very widely used in the field of trace gas sensing. Precision tunable diode laser absorption spectroscopy (TDLAS) and photoacoustic absorption spectroscopy (PAS) with wavelength modulation have proved to be extremely successful in the development of rapid, highly accurate and sensitive field-deployable sensor systems that have been used in laboratory-based experiments, in vehicle-mounted sensor systems and in airborne monitoring systems with great success. Rapid advancements in the development of narrow linewidth lasers emitting from the near-infrared region to deep into the mid-infrared region has accelerated this field. The emission wavelength of a typical edge-emitting distributed feedback lasers can be tuned very precisely over 1 - 2 nm by keeping its temperature constant and varying the injection current. Vertical cavity surface-emitting lasers (VCSELs) offer as much 10 nm of tuning. This precise tuning together with the laser's spectral purity (linewidth of 1-2 MHz) allows one to probe the molecular or atomic resonances of gases with very high spectral resolution. This characteristic is used in trace gas sensing to recover individual absorption lines of the rotational-vibrational spectrum of a molecule, and extract the mole percent, pressure and temperature of the gas. High-frequency modulation of the laser's wavelength and phase-sensitive harmonic detection increases the detection sensitivity significantly [1].

Interestingly the same interrogation strategy can be used to probe other narrow photonic resonances such as the transmission (or reflection) spectrum of a fiber Bragg grating (FBG), and the longitudinal surface plasmon resonance (LSPR) of gold nanostructures. Although the FBG itself is very small and lightweight, the overall FBG sensor system can often be sizeable because commercial interrogators are bulky. Tunable diode lasers can be used to build small and low-power interrogators for FBG-based wearable sensors [2] that can achieve wavelength resolution as low as 0.5 pm [3].

Plasmonic sensors have also emerged as excellent candidates for miniaturized nanobiosensing platforms. The spectral shift of the longitudinal surface plasmon resonance (LSPR) of gold nanostructures due to changes in surrounding refractive index is typically measured with a spectrometer that is often the most expensive part of the setup. In this case too, frequency agile tunable lasers can be readily used to accurately detect the LSPR shifts. Spectral shift-based detection is far superior to intensity-based detection that are more prone to noise. The limited tuning range but the precision of tuning of these laser diodes makes them better suited for applications in which very small spectral changes need to be detected. This talk will elaborate on this topic, present some results and discuss the possibilities.

References:

[1] A. Roy and A. L. Chakraborty, *IEEE Sensors Journal, 20*(2020),12691.
[2] L. Lu, J. Cui, L. Hin Cho and H. -Y. Tam, *IEEE Transactions on Instrumentation and Measurement*, 75 (2026). 700480
[3] A Roy, A L Chakraborty and C K Jha, Applied Optics, 56(2017), 35629.

Advanced ocular wavefront sensing methods and towards customized ophthalmic solutions

[1,#]Vyas Akondi
[1]*Department of Physical Sciences, Indian Institute of Science Education and Research (IISER) Berhampur, Berhampur, Odisha 760010, India*
[#]*vakondi@iiserbpr.ac.in*

We present recent advancements in ocular wavefront sensing and customized ophthalmic optics, featuring physics-informed Shack–Hartmann and dual-plane sensing techniques designed to overcome cataract opacities and asymmetric intraocular lens artifacts. Alongside multilayer pyramid and curvature sensing models, we introduce a machine learning framework that optimizes patient-specific extended-depth-of-focus lenses to restore continuous vision.

Measurement and correction of ocular aberrations are required for personalized ophthalmic optics and vision restoration. Standard wavefront sensing and lens design face constraints under variable pupil apertures, scattering media, multilayer reflections, and phase asymmetries. We present theoretical, computational, and experimental methods addressing these diagnostic and therapeutic challenges.

On the diagnostic side, pupil size variations alter measured aberration coefficients. Analysis of monochromatic aberrations (655 nm) across 2.0 to 6.0 mm pupil diameters using an iTrace aberrometer and numerical simulations demonstrates that reducing pupil diameter redistributes higher-order aberrations into lower-order Zernike terms via power-law scaling. Obtaining mean values requires averaging 20 consecutive scans to reduce ocular measurement variability.

When measurements are corrupted by pathology or scattering, gradient-based algorithms fail. In nuclear cataracts, localized scattering disrupts Shack–Hartmann wavefront sensor (SHWS) spots, increasing reconstruction errors. Applying a machine learning model trained on 10,000 aberrated wavefronts with cataract masks (radii 0.1–0.7) maps spot patterns to 25 Zernike coefficients, yielding low root-mean-square (RMS) errors across evaluated cataract sizes. In stratified tissues like the retina, secondary reflections modify focal-plane intensity distributions in Pyramid Wavefront Sensors (PWFS). A Fourier optics simulation incorporating circular modulation and layer superposition demonstrates that axial layer separation and reflectivity introduce systematic reconstruction artifacts. To evaluate alternative phase-retrieval methods, we modeled a Curvature Wavefront Sensor (CWS) based on the Transport of Intensity Equation, reconstructing phase from intensity differences across two defocus planes using an iterative Fourier algorithm with Neumann boundary conditions.

Rotationally asymmetric refractive bifocal intraocular lenses (IOLs) produce vertical coma artifacts (~0.57 μm RMS) on standard SHWS due to out-of-focus light. We developed a dual-plane SHWS method that isolates and fuses in-focus spot centroids from near and far focal planes, reducing residual RMS errors well below the diffraction limit. Benchtop integration is underway following characterization of an electrically tunable lens, a spatial light modulator, and an in-house SHWS. Finally, a Transformer model driven by the visual Strehl ratio based on the optical transfer function (VSOTF) was developed to calculate custom extended depth-of-focus (EDOF) lens profiles, optimizing target through-focus performance across 0 to 3 D.

References:

[1] A. K. Tarai, S. Sangiri, L. K. Pampana, S. K. Shukla, and V. Akondi, Journal of the Optical Society of America A, 43(8), D64-D74 (2026)
[2] P. K. Sahoo, Arjun Raj M R, and V. Akondi, Biomedical Optics Express, 17(8), 4115-4130 (2026)
[3] S. Sangiri and V. Akondi, Journal of Refractive Surgery, 42(8), e759-e769 (2026).

Temporal Phase Unwrapping with Under-sampled Spectral Signal using Tilted Interference

Harikrishnan. P and # Dinesh N Naik
Applied and Adaptive Optics Laboratory, Department of Physics,
Indian Institute of Space Science and Technology, Thiruvananthapuram, Kerala, 695547, India

#*dineshnnaik@iist.ac.in*

Recent advances in surface profiling and ranging using Fourier-transform speckle profilometry, as well as an iterative temporal phase-unwrapping algorithm, are presented. The extension of the schemes for an undersampled spectral-intensity signal, recently achieved by relaxing the stringent path-difference constraint in interferometry, will be discussed.

Optical interferometry enables measurement of path differences as small as a fraction of a wavelength of light, accessing phase from the intensity modulation in the recorded interferogram. However, for quantifying path delays longer than the wavelength of light, either the elapsed fringes need to be counted, or the correct order of the fringes must be known. Since the resulting phase depends on the wavelength of the light used, using multiple wavelengths allows the determination of the fringe order.

Fourier transform speckle profilometry utilizes the spectral intensity modulation resulting from the interference of optical fields with a finite path delay to directly access the optical path delay utilizing the Fourier transform relation between them [1]. On the other hand, the iterative approach of temporal phase unwrapping relaxes the requirement to record the spectral intensity signal at equi-spaced wavenumbers. It relies on generating a synthetic wavelength long enough to obtain an unambiguous phase map to begin with, and on improving measurement accuracy through subsequent iterations with gradually reduced synthetic wavelengths [2]. Recording the interferograms as off-axis holograms of the object's far field enables access to the phase and propagation of the recorded field to focus on surfaces of a 3D object or on non-planar objects. In either case, the wavelength tuning must be gradual and limit the maximum path delay that can be measured [3].

It is recently shown that the two under-sampled spectral intensity signals recorded with the path differences that differ by a specific value enabling the observation of a beat signal when added, can indeed allow profile measurement through an analysis akin to Fourier transform speckle profilometry on the envelop of the beat signal obtained [4]. Possibility of range extension beyond the longest synthetic wavelength possible by continuous tuning of the source wavelength and with the use of tilted interference for excess fraction extraction from a spectrally undersampled signal [5,6]. This allows for the unique measurement of the extended range. For a correctly assumed fringe order for the initial source wavelength, the non-divergence of the estimated range as a function of wavelength tuning provides the potential range locations. These are further zeroed in on by repeating the analysis with varying tuning steps.

In summary, for profiling in the sampled-data regime, an improvement in the measurement resolution of Fourier Transform Speckle Profilometry and a recursive algorithm-based temporal unwrapping are presented. The importance of fringe order detection was shown using holography. Surface profiling in undersampled data via envelope detection and absolute distance measurement (ranging) beyond the synthetic wavelength, using phase differences obtained from the spatial Fourier transform of tilted interference, are achieved.

One of the authors, HP, acknowledges the research fellowship from the Council of Scientific and Industrial Research, India.

References:

[1] M. Takeda, H. Yamamoto, *Applied Optics,* 33 (1994) 7829-7837.
[2] A. Wada, *Advanced Holography - Metrology and Imaging*, edited by I. Naydenova, InTech (2011).
[3] P. Harikrishnan, D.N. Naik, *Measurement,* 242 (2025) 115838.
[4] P. Harikrishnan, D.N. Naik, *Proceedings of SPIE*, (2025) 1352907.
[5] P.J. De Groot, *Applied Optics*, 33 (1994) 5948--5953.
[6] P. Harikrishnan, D.N. Naik, *Optics Letters*, 51 (2025) 213-216.

Comparison of Fourier Transform Speckle Profilometry and Temporal Phase Unwrapping using a Recursive Algorithm in Wavelength-tuning Interferometry

[#]Harikrishnan. P, and Dinesh N Naik
Applied and Adaptive Optics Laboratory, Department of Physics,
Indian Institute of Space Science and Technology, Thiruvananthapuram,
Kerala, 695547, India

[#]harikrishnanp.21@res.iist.ac.in

Surface profiling with micro-level fluctuations can be achieved using either Fourier Transform Speckle Profilometry (FTSP) or Temporal Phase Unwrapping. Employing a recursive approach in wavelength-tuning interferometry (TPU). The objective of this work is to conduct a comparative analysis of the two methodologies.

2π phase ambiguities arise when profiling a surface with a height variation greater than the light source's wavelength. Interferometry-based schemes, such as Fourier Transform Speckle Profilometry or Temporal Phase Unwrapping, can be implemented using a recursive algorithm with a continuously tunable wavelength source to overcome the ambiguity and measure surface variation [1,2]. A comparative analysis of the two methodologies is performed. The interference equation is given by,

$$I(x,y,\lambda) = \left|\sum_{j=1,2,} U_i(x,y,\lambda) e^{i\left(\frac{2\pi}{\lambda}\left(\alpha_j x+\beta_j y+d_j(x,y)\right)\right)}\right|^2 \quad (1)$$

Where, two fields $U_i(x,y,\lambda)$ are fields with a relative tilt between them. α_j and β_j determine the extent of linear phase, and $d_j\ (x,\ y)$ denotes the residual path-dependent optical phase. FTSP recovers the phase at each pixel by applying temporal Fourier filtering of the +1 order, whereas TPU uses spatial Fourier filtering. The phase obtained Phase difference is given by,

$$\left(\phi(x,y)\right)_n + 2\pi m_n(x,y) = \frac{2\pi}{\lambda_n}\left(\Delta\alpha x + \Delta\beta y + \Delta d(x,y)\right) \quad (2)$$

where m_n is the integer fringe, $\phi(x,y)$ is the experimentally obtained phase and $\Delta\alpha = \alpha_1 - \alpha_2, \Delta\beta = \beta_1 - \beta_2$ and$\Delta\alpha = d_1(x,y) - d_2(x,y)$.

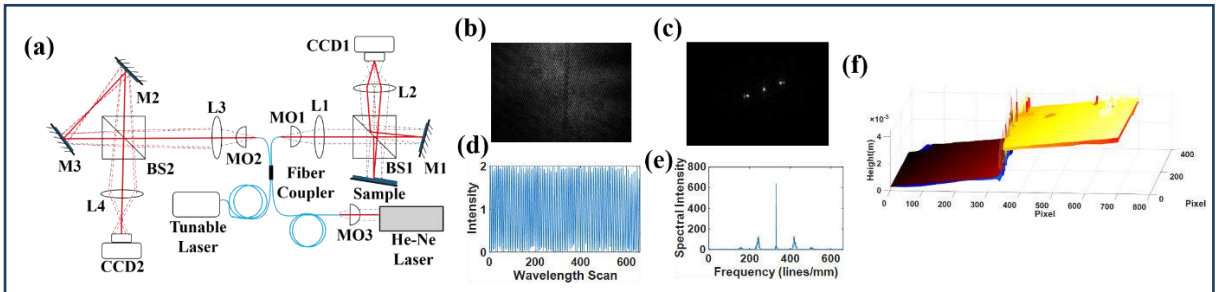


Fig.1 (a) Experimental Setup, (b) Recorded Interferogram, (c) Spatial FFT of (b), (d) recorded spectral interferogram as a function of wavelength change, (e) spectral FFT (d), and (f) Height variation of the sample obtained using FTSP and TPU

The experimental setup is shown in Fig. 1(a). The light is concurrently fed to the Michelson and Sagnac interferometers from the tunable laser and the He-Ne laser. By tuning the laser's wavelength, interferograms are captured. Fig. 1(b) shows the recorded interferogram corresponding to 900nm, Fig.1 (c) shows the spatial FFT of 1. (b), the spectral modulation as a function of wavelength change for the pixel is shown in Fig. (d), the spectral FFT of Fig. 1(d) is shown in Fig. 1(e), and the height variation obtained using FTSP and TPU is shown in Fig. 1(f). Though they are almost identical, FTSP requires a carrier in the spectral FFT, and TPU outperforms FTSP by a factor of two in range measurements.

HP acknowledges the Council of Scientific and Industrial Research, India, for the research scholarship.

References:

[1] M. Takeda, H. Yamamoto, Fourier-transform speckle profilometry: three-dimensional shape measurements of diffuse objects with large height steps and/or spatially isolated surfaces, Appl. Opt. 33 (34) (1994) 7829, https://doi.org/10.1364/AO.3.

[2] Harikrishnan, P., & Naik, D. N. (2025). Tunable wavelength laser surface profilometry through tilted interference. Measurement, 242, 115838.https://doi.org/10.1016/j.measurement.2024.115838.

Optimal contrast criterion for accurate classification of phase objects from their in-line holograms

[1]Chhavi, [1]Ritish Kamboj, [1,2] Kedar Khare[1,2] and [1#]Satish Kumar Dubey
[1]SeNSE, IIT Delhi, New Delhi 110016, India
[2]Optics and Photonics Centre (OPC), IIT Delhi, New Delhi 110016, India
[#]satishdubey@sense.iitd.ac.in

We present a simulation study establishing a contrast-based criterion to find an optimal object to sensor distance (z)-range for recording in-line holograms of phase objects for reconstruction free classification. The results may be valuable for designing DLIHM systems for classification of phase objects.

Digital Lens less In-Line Holographic Microscopy (DLIHM)[1] is a compact, low-cost, and label-free imaging technique that provides large field of view (equal to image sensor area) without imaging lenses. In-line hologram encodes information of complex amplitude transmittance of the object, which is conventionally recovered by numerical image reconstruction to form visually meaningful phase and amplitude image. Image reconstruction is computationally intensive and time-consuming and limits the practical utility of DLIHM under low resource settings. However, when the main objective is classification rather than imaging, numerical reconstruction may be unnecessary, since all the diffraction limited information for automatic decision-making is implicitly encoded in the hologram itself. Also, the reconstructed image is algorithm dependent, that nominally may not give the identical numerical phase maps for same samples, due to differences in algorithmic steps used for reconstruction. while a raw in-line hologram recorded under a standardized protocol is algorithm independent. Although reconstruction-free classification from raw holograms[2,3] has been demonstrated, an optimal physical criterion for recording distance (*z*) that maximizes classification accuracy is still not standardized. Since the spatial-frequency content present in the hologram strongly depends on the *z* as shown in (Fig.1(a)): at small *z*, phase information is not modulated into intensity measurements, thus contrast and distinguishing class information is low. At large *z*, angular spectrum spreads beyond the sensor resulting in loss of high spatial frequencies and contrast is again poor. At *z* -range where phase information is sufficiently modulated in the intensity variations with highest contrast can be used as optimality criteria. To find the optimal *z* range, in-line holograms of the MNIST dataset images as pure phase objects with phase range [0, π/2] were simulated using angular spectrum method with sampling pitch Δx = 2 μm over a normalized distance $z = \alpha DoF_{eff}$, where DoF_{eff} is the effective depth of focus derived from the object's spatial bandwidth for $\alpha \in [0.125, 200]$, with additive white gaussian noise. The classification performance of multinomial logistic regression (LR)[4] model is shown in (Fig.1(b)). The mean contrast ($\bar{C}$) of dataset at each *z* is given by $\bar{C} = \left(\frac{1}{N}\right)\sum_{(i=1)}^{(N)}\left(\frac{\sigma_i}{\mu_i}\right)$ where, σ_i is the standard deviation and μ is the mean of ith image in the dataset with N =70,000 images. The classification accuracy and mean contrast follow the same trend with *z* (Fig.1(c)), showing a peak in an intermediate range for α = [2,5]. Using this criterion, highest test accuracy for noisy hologram dataset is 89.9% at $z = 5DoF_{eff}$, which is close to the accuracy 92% for noiseless MNIST hologram and raw MNIST images. We demonstrated using simulations that the maximum classification accuracy can be achieved in a *z* -range where object information is sufficiently spread across the detector window with high contrast. This criterion provides a practical, standardized benchmark for choosing *z* in reconstruction-free DLIHM based classification systems, enabling comparable accuracy across different groups and setups for the same class of samples.

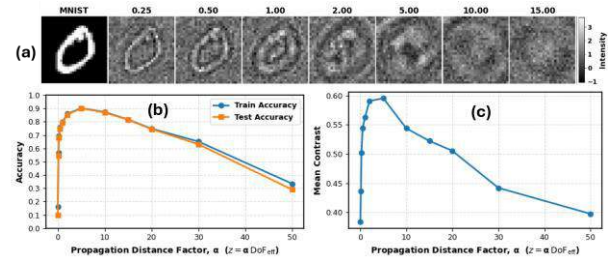


Figure1. (a) Simulated inline holograms recorded at different normalized z (b) Classification accuracy versus normalized z (c) Mean hologram contrast versus normalized z.

References:

[1] D. Gabor, *Nature* **161** (1948) 777.
[2] T.-H. Song, M. Cao, J. Min, H. Im, H. Lee, K. Lee, *APL Bioeng.* **9** (2025).
[3] S.-J. Kim, C. Wang, B. Zhao, H. Im, J. Min, H. J. Choi, J. Tadros, N. R. Choi, C. M. Castro, R. Weissleder, H. Lee, K. Lee, *Sci. Rep.* **8** (2018) 17003.
[4] C.-Y. J. Peng, K. L. Lee, G. M. Ingersoll, *J. Educ. Res.* **96** (2002) 3.

Projection-based Grayscale Photolithography for Beam Shaping

[1,#]Aniket Pandey,[1]Jerin Geogy George and [1]Tapajyoti Das Gupta
[1] *LANSPE, Department of Instrumentation & Applied Physics, IISc Bengaluru*
[#]*paniket@iisc.ac.in*

We demonstrate a projection-based grayscale photolithography technique that enables the fabrication of microstructures with continuous height variation through calibrated grayscale-to-height mapping. Using this calibration, we fabricated phase elements to generate structured light beams such as Bessel, Airy and OAM beams. This approach offers an alternate pathway for efficient beam shaping compared to meta-optics-based approaches.

Beam shaping using flat optics, particularly metasurfaces, has gained popularity over the past decade. Highly efficient meta-optical elements have been demonstrated, but their fabrication in the visible and NIR typically needs e-beam lithography and associated pattern-transfer steps, which are expensive, complex, and scale poorly for large-area or rapid-prototyping applications [1]. For many single-wavelength beam-shaping applications, grayscale lithography can achieve comparable results with a much simpler process: arbitrary phase variation in a single exposure step, without photomasks [2,3]. In this work, we calibrate a DLP-based grayscale lithography system and use it to fabricate phase profiles for structured-light generation, thereby demonstrating its capability for continuous-phase micro-optic fabrication.

Initially, for calibration, a grayscale test pattern was generated with pixel values varying linearly from 0 to 255 (black to white) along the horizontal direction. Glass substrates spin-coated with ma-P 1200G photoresist at 3000 rpm and pre-baked for 2 minutes were used for patterning. The pattern was then projected onto the resist using our in-house DLP-based projection system, which employs a Texas Instruments DLP9000 micro-mirror, with exposure times ranging from 0.3 to 1.2 s and varying intensities. After 1 minute of development, profilometry measurements were taken on the samples to establish the calibrated grayscale-to-height mapping.

Based on the established grayscale-to-height calibration, an operating wavelength of 630 nm was selected, as the maximum fabricated height variation corresponds precisely to a 0 to 2π phase modulation. For this wavelength, target phase profiles for the desired structured light beams were generated and mapped onto the calibrated grayscale values to achieve the required physical heights.

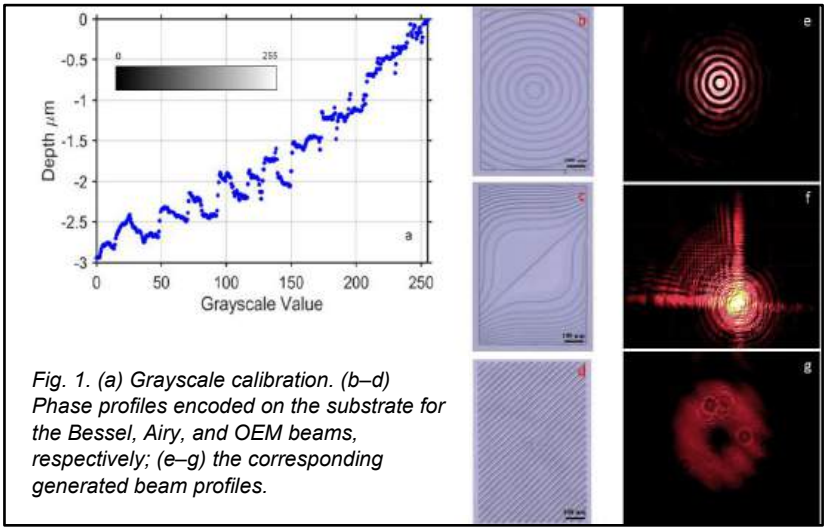


Fig. 1. (a) Grayscale calibration. (b–d) Phase profiles encoded on the substrate for the Bessel, Airy, and OEM beams, respectively; (e–g) the corresponding generated beam profiles.

A depth of 3 μm was achieved at a grayscale value of 255 using an exposure time of 0.5 s and a pulse-width modulation (PWM) value of 64 (Fig. 1a). This optimised exposure-dose calibration was subsequently used to fabricate the phase elements. Upon characterising the fabricated elements (Fig. 1b-d), we successfully demonstrated the generation of Bessel, Airy and OAM beams (Fig. 1e-g).

DLP-based grayscale photolithography enables single-step, maskless fabrication of continuous-phase (2.5D) micro-optics. This offers a simpler, lower-cost alternative to conventional multi-step metalens fabrication for rapid prototyping and large-area applications.

References:

[1] Yu, Nanfang, and Federico Capasso. *Nature materials* 13.2 (2014): 139-150.
[2] Banerji, Sourangsu, et al. *Optica* 6.6 (2019): 805-810.
[3] Engelberg, Jacob, and Uriel Levy. *Nature communications* 11.1 (2020): 1991.

Modelling of Three-Dimensional Refractive Index Map in Optical Diffraction Tomography

#Munindra Kushwaha, Rakesh Kumar Singh
Laboratory of information photonics and optical metrology, Department of Physics, Indian Institute of Technology (Banaras Hindu University), Varanasi, India 221005

#munindrakushwaha.rs.phy23@itbhu.ac.in

Optical Diffraction Tomography (ODT) enables three-dimensional reconstruction of the refractive index of microscopic samples. Reconstruction accuracy depends on the forward-scattering model and on mitigating missing-cone artefacts caused by the limited numerical aperture. This study compares the First-Born Approximation and the Beam Propagation Method (BPM) for 3D reconstruction.

Optical Diffraction Tomography (ODT) is a label-free imaging technique that reconstructs the 3D refractive index (RI) of a sample from multiple-angle illumination measurements [1]. Reconstruction quality in ODT depends on the accuracy of the forward-scattering model. It is often degraded by the missing-cone problem arising from the limited numerical aperture of the imaging system. Linear reconstruction methods based on the First-Born Approximation (FBA) are computationally efficient but may exhibit reconstruction artefacts and reduced accuracy. In contrast, nonlinear approaches such as the Beam Propagation Method (BPM) can account for multiple-scattering effects and improve reconstruction quality. This work presents a simulation-based comparison of these two approaches for reconstructing a spherical bead. The FBA is a linear forward-scattering model in which we assume the scattered field is weak relative to the incident field [2]. Under this assumption, multiple-scattering effects inside the sample are neglected, and the total field within the object is approximated by the incident field. This simplification establishes a linear relationship between the measured scattered field and the refractive index distribution, enabling efficient reconstruction in ODT.

The BPM is a nonlinear forward model that simulates light propagation through a sample by dividing it into multiple thin slices [3]. The optical field is sequentially updated through propagation and phase modulation in each slice, allowing the model to account for multiple-scattering and wave propagation effects. As a result, BPM provides a more accurate representation of light–matter interaction and can improve reconstruction quality while reducing missing-cone artefacts in ODT.

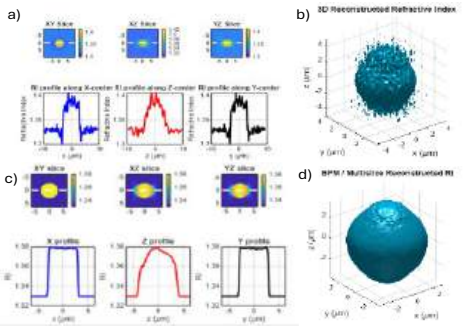


Fig1.a) Reconstructed XY, XZ and YZ slice and corresponding line plot to the center using FBA b)3D reconstructed RI using FBA C) Reconstructed XY, XZ and YZ slice and corresponding line plot to the center using BPM d) 3D reconstructed RI using BPM

In this simulation, our test object is a spherical bead with a refractive index 1.38, and a size of 6 microns, and RI of the immersion liquid $n_0 = 1.33$. We employed the Born approximation and BPM to simulate in an inhomogeneous medium and generate 200 scattered fields corresponding to various illumination directions. We applied a golden-rule scenario with a maximum illumination angle of 45 °. Another assumed parameter is the wavelength of light $\lambda = 532nm$. The size of the simulated object is 128x128x128 with a sampling interval $0.15\mu m$.

We have highlighted that the FBA is not valid for multiple scatter objects; however, BPM provides a reconstruction closer to the original object and mitigates the missing-cone problem.

Acknowledgement: Support is acknowledged from the I-DAPT/IIT(BHU)/2025-25/project sanction/69, and the challenge grant IIT(BHU)/R&D/2025-26/CPCG-01/608.

References:

[1] Kim, Kyoohyun, et al. "*Optical diffraction tomography techniques for the study of cell pathophysiology*." Journal of Biomedical Photonics & Engineering 2.2 (2016).
[2] E. Wolf, "*Three-dimensional structure determination of semi-transparent objects from holographic data," Optics Communications* 1, 153-156 (1969).
[3] Kamilov, Ulugbek S., et al. "*Optical tomographic image reconstruction based on beam propagation and sparse regularization*." *IEEE Transactions on Computational Imaging* 2.1 (2016): 59-70.

Atmospheric Turbulence impacted light beam scintillation mitigation using PMMA Rod(s)

Shouvik Sadhukhan and *C S Narayanamurthy

Applied and Adaptive Optics Laboratory, Department of Physics, Indian Institute of Space Science and Technology, Valiamala(PO), Trivandrum – 695547, Kerala State, India

Abstract

Whenever light beam propagates through the atmospheric turbulence, it introduces random fluctuations in intensity(scintillation), phase, and polarization [1] which severely disturb Free-space optical (FSO) communication. These distortions introduce aberrations like beam wander, scintillation, and coherence loss, resulting in significant communication link losses. To correct these adaptive optical technologies using complex wavefront sensing and active correction [2] are used. In this work we report a new technique using passive PMMA(Poly Methyl Meta Cryolite) rods without any external filed for mitigating the scintillation of light beam impacted with dynamic atmospheric turbulence. Fig.1 shows a typical experimental geometry used in our analysis where the light beam from a laser source passes through a spatial filter assembly then through a dynamic(Rotating) Pseudo Random Phase Plate(PRPP) mimicking atmospheric turbulence mounted on a rotating stage powered by a stepper motor. Then after passing through the rotating PRPP the light beam intensity fluctuates randomly and it is allowed to pass through PMMA rod. Finally the turbulence impacted laser beam after passing through the PMMA reaches CCD camera. The intensities are measured using the CCD camera and the scintillation index

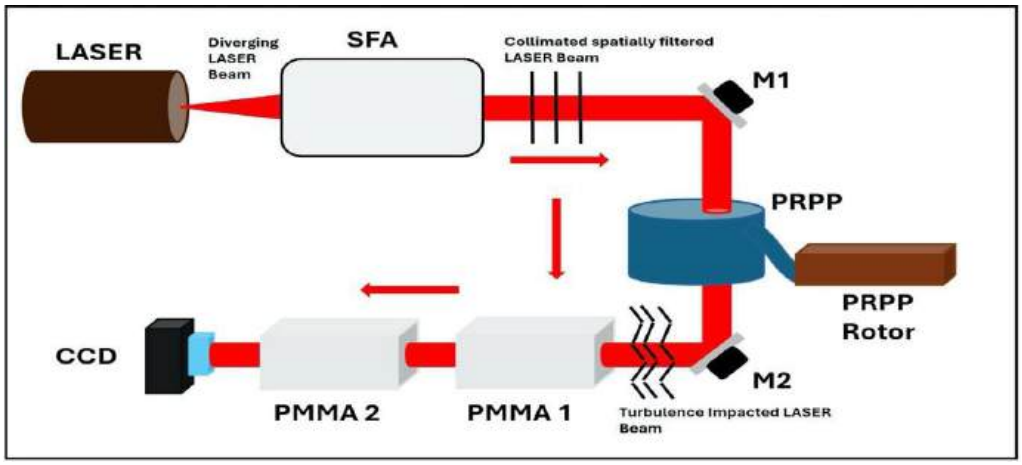


Fig. 1. Experimental set up for common path beam propagation through turbulence and its compensation methodology. Experimental setup showing laser source (L), spatial filter assembly (SFA), mirrors (M1, M2), pseudo-random phase plate (PRPP), PMMA rods, and CCD camera. Total propagation distance: 1.5 m.

mitigations are studied. We used two distinct methods to analyse the results i) The first one uses manifold-based statistical framework for analyzing turbulence-affected optical beam propagation and compensation in free-space communication systems and the second one ii) Using a coupled anharmonic dipole synchronization model for passive tur-bulence mitigation in PMMA media—a mechanism distinct from beam- shaping or spatial filtering. In both these methods we show the mitigation of turbulence impact clearly with detailed experimental results.

Acknowledgement : The authors acknowledge ANRF(Formerly SERB/DST, (Govt. of India) for providing the financial support via project grant CRG/2020/003338 to carry out this work.

References

[1] O. Korotkova, Changes in the intensity fluctuations of a class of random electromagnetic beams on propagation, J. Opt. A: Pure Appl. Opt. 8 (1) (2005) 30, http://dx.doi.org/10.1088/1464-4258/8/1/005.

[2] O. Korotkova, Scintillation index of a stochastic electromagnetic beam propagating in random media, Opt. Commun. 281 (9) (2008) 2342–2348, http: //dx.doi.org/10.1016/j.optcom.2007.12.047.

A Plenoptic Wavefront Sensing Framework for Atmospheric Turbulence Characterization and Adaptive Optical Imaging

[1,] Snehal Tonpe,[2#]J. Sreekantha Reddy,[3]Amit Pratap and [4]Jagannath Nayak
[1,2,3]Center of High Energy System and Sciences (CHESS), DRDO, Hyderabad
[4]O/o Director General, Missiles & Strategic Systems, DRDO, Hyderabad

[#]jsreddy.chess@gov.in

Atmospheric turbulence degrades the performance of imaging systems. Conventional wavefront sensing techniques relay on adaptive optics hardware, reference sources, and complex optical setups, which limits their applicability in dynamic imaging. To address these limitations, plenoptic camera provides a way to compensate for turbulence through image processing, thus avoiding the need for adaptive optics hardware like deformable mirrors. This study explores the use of a plenoptic camera as a wavefront sensor allowing direct measurement of wavefront distortions in free-space optical (FSO) systems. Its dual role supports both passive digital image restoration and active wavefront sensing, all within a single imaging system. Its dual functionality enables both passive digital image restoration and active wavefront sensing within a single imaging platform.

Atmospheric turbulence is one of the primary factors that limits the performance of optical imaging systems. It caused image degradation through deformation of wavefront, blurring, and loss of spatial information [1]. Conventional wavefront sensing techniques, require active optical components, reference sources, and adaptive optics systems, making them unsuitable for several practical applications involving weak illumination, extended objects, or dynamic environments [2]. The approach adopted in this research focuses on evaluating the ability of a plenoptic camera to characterize atmospheric turbulence, restore images, and measure wavefront distortions through a fully digital processing system. Initially, a digital image processing pipeline is developed to mitigate the effects of atmospheric turbulence without relying on active adaptive optics hardware. The acquired turbulence-degraded plenoptic images are then processed using image restoration techniques to recover scene quality and reduce distortions introduced by atmospheric propagation. To further enhance image quality, a super-resolution algorithm is implemented to improve the spatial resolution of the restored images and recover fine structural details that are otherwise lost due to turbulence and the inherent resolution limitations of plenoptic imaging.

Additionally, the potential of plenoptic camera as an active wavefront sensor is explored for free-space optical correction and adaptive optics applications by utilizing the directional light field information captured by the microlens array. Finally, the methodology includes the estimation of atmospheric and imaging parameters, such as Fried's coherence diameter (ro), the number of image sensor pixels corresponding to each microlens array (MLA), and the operating wavelength λ to characterize atmospheric turbulence and evaluate the performance of the proposed imaging and correction framework under turbulent conditions. These parameters provide a quantitative understanding of turbulence strength and guide the design and optimization of plenoptic wavefront sensing systems

The results demonstrate that plenoptic camera offers a versatile and computationally efficient alternative to conventional wavefront sensing by enabling both passive digital turbulence correction and active wavefront measurement within a single imaging architecture. This research demonstrates that a plenoptic camera can serve as both a computational wavefront sensor and an active wavefront sensing device. The proposed digital turbulence mitigation approach eliminates the need for expensive adaptive optics hardware while improving image quality. The integration of turbulence correction, super-resolution, and wavefront estimation into a single plenoptic imaging framework offers a robust, cost-effective, and versatile solution for next-generation optical imaging systems operating in turbulent environments.

The proposed research has potential applications in astronomical imaging, medical imaging, free-space optical communication, surveillance and security systems, target tracking, remote sensing, defence imaging systems, adaptive optics, computational photography, autonomous vision systems. As a result, it provides a compact, cost-effective, and flexible solution for turbulence mitigation, making it particularly suitable for dynamic and field-deployable imaging applications where conventional adaptive optics systems are impractical.

References:

[1] F. Di Lena, F. V. Pepe, A. Garuccio, and M. D'Angelo. Correlation plenoptic imaging: *An overview. Applied Sciences*, 8(10), 2018. ISSN 2076-3417. doi: 10.3390/app8101958.

[2] N. Anilmi¸s Baci and A. Yeniay. Wave-front Aberrations of Laser Beams Propagating through the Atmosphere. *In COAT-2019*.

Holographic Modal Wavefront Sensing Using Spatial Intensity Distribution and Convolution Neural Network

[1,*]Anitta Jomy, [1]Aryan Chand, [1]Dinesh N. Naik and [1,#]Biswajit Pathak
[1]Indian Institute of Space Science and Technology, Thiruvananthapuram, Keralam 695547, India

Corresponding Author E-mail IDs: *anittajomy@outlook.com , #biswajitpathak@iist.ac.in

Abstract: *We propose an improved holographic modal wavefront sensing (HMWS) technique with a quality metric parameter based on spatial distribution co-occurrence matrix. The technique addresses constraints such as dependence on aperture diameter, bias value and position of point spread function. We have also employed machine learning approach for faster wavefront estimation.*

Summary: We propose an improved holographic modal wavefront sensing (HMWS) technique with quality metric parameter (QMP) based on spatial distribution co-occurrence matrix known as gray level co-occurrence matrix (GLCM). The conventional mean intensity based HMWS (MI-HMWS) provides accurate wavefront estimation upon certain constraints such as optimum bias value, pinhole diameter placed in front of detector and the position of point spread function (PSF). The proposed GLCM based HMWS (GLCM-HMWS) addresses these constraints of MI-HMWS. Since the GLCM image metric follows quadratic optimization curve as shown in Fig. 1, GLCM can be used for wavefront estimation using HMWS. The experimental result corresponding to the proposed GLCM-HMWS is shown in Fig. 2. The PSF corresponding to combination of 4 Zernike modes, corrected using MI-HMWS and GLCM-HMWS are shown in Fig. 2 (a)→(c). The intensity line plot across the maximum intensity point in the PSF is shown in Fig. 2 (d). In addition, we have proposed GLCM based convolution neural network (GLCM-CNN) for wavefront estimation and the corresponding conceptual diagram is shown in Fig. 3. In basic-CNN architecture, high resolution image of PSF is used as input layer. But, in GLCM-CNN, GLCM which has smaller dimension compared to raw PSF image is used as input layer. This makes the GLCM-CNN faster and independent of position of PSF. The experimental result corresponding to the proposed GLCM-CNN is shown in Fig. 4. The PSF corresponding to combination of 4 Zernike modes, corrected using basic-CNN and GLCM-CNN are shown in Fig. 4 (a)→(c) and corresponding intensity line plot is shown in Fig. 4 (d).

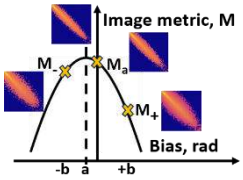


Fig. 1 The quadratic optimization curve of GLCM image metric with bias value.

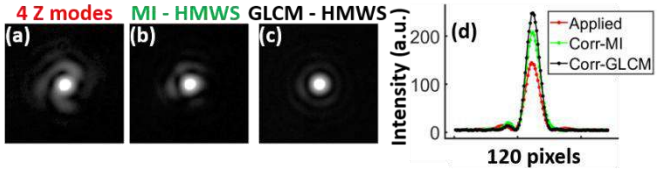


Fig. 2 The experimental result corresponding to proposed GLCM-HMWS.

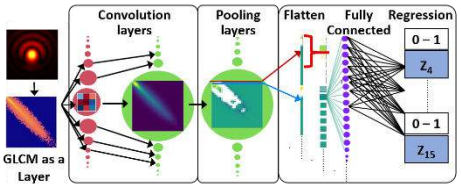


Fig. 3 The conceptual diagram of proposed GLCM-CNN.

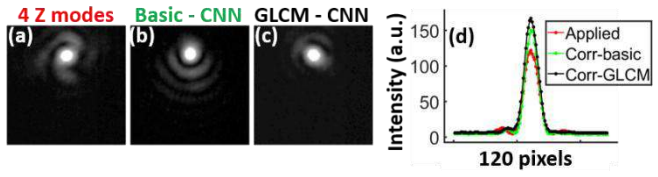


Fig. 4 The experimental result corresponding to proposed GLCM-CNN.

The proposed GLCM- HMWS and GLCM-CNN technique could efficiently address the major constraints of conventional approaches. The provided experimental results validate that the proposed GLCM-HMWS and GLCM-CNN technique gives improved estimation of wavefront in comparison to the conventional approaches.

References:

[1] M. A. Neil, M. J. Booth, and T. Wilson, *Journal of Optical Society of America A* 17 (2000) 1098
[2] B. Pathak, *Optics Express* 30 (2022) 17953.
[3] A. Jomy, A. Chand, D. N. Naik and B. Pathak, *Optics Letters,* 51 (2026) 2520.

Adaptive Wavefront Shaping for Optical Focusing and Imaging Through Scattering Media

[1,*]Anuvratha Vijay, [2]Affreena A K, [3]Diksha and [1,#]Biswajit Pathak

[1] Applied and Adaptive Optics Laboratory, Department of Physics, Indian Institute of Space Science and Technology, Thiruvananthapuram - 695547, Kerala
[2] Department of Physics, National Institute of Technology, Warangal - 506004, Telangana
[3] Department of Natural Sciences, GNA University, Phagwara -144401, Punjab

*Corresponding Author(s): *anuvrathavijay@gmail.com ; #biswajitpathak@iist.ac.in*

Adaptive wavefront shaping technique is proposed for focusing and imaging in the presence of scattering medium. The optical transmission characteristics of the scattering medium is measured to obtain a sequence of tightly focused beam that restores the optical resolution and intensity required for high-contrast imaging in a laser scanning microscopy.

Wavefront shaping is a technique used to achieve focusing of a light beam, passing through a scattering medium, at a predetermined target location. Wavefront shaping is performed by delaying different parts of the incident wavefront in a controlled way, such that it counteracts the impact of the scattering medium. To determine the transmission matrix (TM) of the scattering medium, a four-step phase-shifting interferometry technique is employed. Sequentially applying controlled phase shifts of $0°, 90°, 180°$, and $270°$ yields four intensity equations per matrix element, enabling the retrieval of the full complex field. Iterating this process across all input channels systematically measures the complete TM, where the linear relation between input and output field and the formulation of each element of the TM is defined by

$$E_m = \sum_{n=1}^{N} t_{mn} A_n e^{i\phi_n} \quad ; \quad TM_{(i,j)} \approx \left(\frac{I^{0°} - I^{180°}}{4}\right) + i\left(\frac{I^{270°} - I^{90°}}{4}\right)$$

where t_{mn} is the transmission matrix and $I^{0°}$, $I^{90°}$, $I^{180°}$and $I^{270°}$ represents the measured intensities corresponding to the controlled phase shifts of 0°, 90°, 180° and 270°, respectively.

The input plane wavefront, when passing through a highly scattering medium creates speckle pattern as the output. By four-step phase shifting via a spatial light modulator (SLM), the TM of the scattering medium is acquired. Taking the complex conjugate transpose of the TM allows the SLM to shape the input wavefront, to cancel out the effect of scattering and to obtain a focused spot at a target location. By sequentially generating a focus at each discrete location of the sample, we synthesize a structured illumination field. Point-by-point illumination of these focused spots is performed to obtain the image.

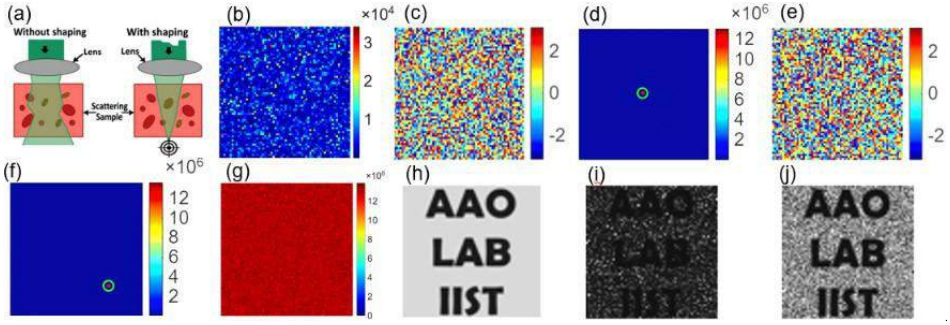


Fig: (a) Concept figure showing effect of scattering sample, without wavefront shaping and with wavefront shaping, (b) scrambled beam profile, (c) measured TM to focus spot at (32, 32), (d) focused beam at (32, 32), (e) measured TM to focus spot at (48, 50), (f) focused beam at (48, 50), (g) intensity distribution matrix of all focussed spots combined, (h) ground-truth object, (i) image formed without wavefront shaping, and (j) image formed with wavefront shaping.

References:
[1] I. Vellekoop and A. Mosk, *Opt. Lett.* 32, 2309-2311 (2007).
[2] Popoff, S.; Lerosey, G.; Carminati, R.; Fink, M.; Boccara, A.; Gigan, S. *Phys. Rev. Lett.*, 104, 100601 (2010).

A Real-Time Implementation of an Adaptive Autofocus Algorithm leveraging NVIDIA Jetson AGX Orin

BhoomikaSaxena[1][0009-0005-5033-5460] Deepak Singh[1][0009-0003-1038-2006] Nitin Agrawal[1][0009-0001-1977-9451]

[1] IRDE, DRDO, Dehradun, India

Corresponding author: deepak.irde@gov.in

Real-time autofocus in cameras remains tedious due to the trade-off between continuous frame acquisition and focus peak stability. This paper presents a lightweight, real-time autofocus algorithm for electro-optical systems, incorporating Sobel-filter-based focus estimation, coarse-to-fine adaptive lens motor control with multithreaded processing to achieve a real-time focus correction method.

The proposed framework comprises of an autofocus algorithm implemented using NVIDIA Jetson AGX Orin ensuring portability and seamless field-deployment for edge computing while also making it optimal for power-constrained environments leveraging dynamic power management capabilities of Jetson Orin, designed particularly for deployment on electro-optical systems such as CMOS Day Camera and MWIR (Medium Wave Infrared) Camera. This system provides minimal latency with a convergence time of 25 ms on average with a frame rate of over 40 fps.

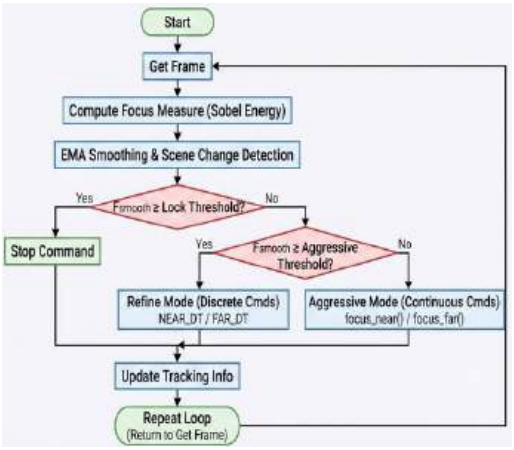


Fig. 1: Autofocus Loop

The focus score thread calculates the edge energy for continuous frames. The acquired frame is subdivided into pixel blocks of 128x128 to minimize computational overhead. The image edge-sharpness is computed for each block, aggregated using exponential moving average. To stabilize tracking against sensor noise, the resulting focus score is normalized via a sigmoid mapping.

To maintain real-time, autofocus control, the whole framework comprises of separate threads employing independent image acquisition and Sobel-filter-based [1] frame processing and lens motor control via serial transmission. A thread-safe communication layer interfaces with the camera, enabling continuous serial command transmission via MOXA cable for lens motor actuation parallel to frame processing with a rolling double ended-queue-based focus score buffer storing focus scores of last few frames to compute scene-sensitive thresholds for locking mechanisms trigger and continuous-to-discrete mode switching facilitating a coarse-to-fine peak search strategy [2][3], shifting to refinement mode (discrete commands) upon reaching near the estimated peak focus, while also determining the motor speed dynamically in accordance with the current scene when in aggressive search mode (continuous command mode) with adaptive speed control for the motor movement step-size [4] (as shown in Figure 1).

The image edge sharpness is computed using Tenengrad gradient energy for each block as shown in (1), (2):

$$T(x,y) = \sum_{x=1}^{M}\sum_{y=1}^{N}\left[G_{x(x,y)}^{2} + G_{y(x,y)}^{2}\right] \quad (1)$$

$$E_{log(x,y)} = log\left(1 + T(x,y)\right) \quad (2)$$

Experimental results demonstrate an optimized focus score of 0.9220 upon implementing this autofocus algorithm on CMOS Day camera while observing an outside scenery, compared to 0.9285 as observed by manually focusing the same frame to the best possible focus indicating an error of 0.0075 which is acceptable for practical applications whereas an error of 0.0065 was observed upon testing it with MWIR camera.

References:

[1] C.C. K. S., S. G. S., N. K. R., C. A. L., *Proc. Third Int. Conf. Inventive Syst. Control (ICISC)* (2019) 526–531.
[2] C. Ma, Q. Zhang, M. Zhang, J. Ma, Z. Chen, Y. Yan, *Applied Optics* 64 (2025) 8255–8265.
[3] Z. Ding, S. Zheng, F. Zhang, Q. Li, C. Guo, *Optics and Lasers in Engineering* 181 (2024) 108366.
[4] J. He, R. Zhou, Z. Hong, *IEEE Transactions on Consumer Electronics* 49 (2003) 257–262.

Non-separable light beams and scattering

[#]Yoko Miyamoto
Department of Engineering Science, The University of Electro-Communications,
1-5-1 Chofugaoka, Chofu, Tokyo 182-8585 Japan
Institute for Advanced Science, The University of Electro-Communications,
1-5-1 Chofugaoka, Chofu, Tokyo 182-8585 Japan

[#] *yoko.miyamoto@uec.ac.jp*

Classical non-separable light beams have non-separable states of polarization and spatial distribution. The non-separability can be assessed in the form of concurrence. We have experimentally evaluated the change in concurrence for scattering by single ground glass plates and by multiple scattering layers.

Classical non-separable light beams have attracted attention in recent years, due to both the mathematical similarity to quantum entanglement and the potential for application. The non-separability is usually that between states of polarization and spatial distribution, meaning that the beams have position-dependent states of polarization across their cross-sections.

An important feature of these non-separable beams is that they become unpolarized when position is ignored, and that they lose their spatial profile when states of polarization are ignored. This allows the non-separability to be assessed in the form of concurrence, which quantifies the loss of polarization information when averaged over space. Lossless processes that affect either only the states of polarization or only the spatial profile (i.e. the phase distribution) do not change this value.

This raises the question how non-separability is affected by scattering by inhomogeneous media and subsequent propagation through space. If, as in the case of an ideal weak scatterer, only the phase distribution is modified, then concurrence values should not change. Change in non-separability during scattering can provide a new means of characterizing scattering media.

Experimentally evaluating the change in concurrence during scattering involves an accurate evaluation of states of polarization. Unphysical values for the Stokes parameters can lead to imaginary values for concurrence, which can be avoided by introducing constraints to the Stokes parameter estimation. Change in concurrence was evaluated both for the case of single ground glass plates and the case of multiple scattering layers. A small increase in concurrence was observed for single ground glass plates. For the multiple layers the current results are still unconclusive.

Exceptional-Point Photonics for Application-Specific System Design

Somnath Ghosh[#]
Department of Physics, École Centrale School of Engineering, Mahindra University,
Hyderabad 500043, India
[#]*somiit@rediffmail.com*

Exceptional points (EPs) in non-Hermitian photonics enable unconventional state evolution, asymmetric mode conversion, and nonreciprocal responses. This talk explores EP topology, dynamical encirclement, conjugate and higher-order EPs, and their applications in waveguides and microcavities for controllable lasing, absorption, and photonic functionality.

Exceptional points (EPs) have emerged as one of the most intriguing features of non-Hermitian systems, providing a unique connection between non-Hermitian physics, topology, and wave dynamics. Unlike conventional degeneracies, an EP represents a singular point in parameter space at which not only the eigenvalues but also the corresponding eigenstates of a system coalesce. The associated branch-point topology gives rise to unconventional phenomena when system parameters are varied around an EP, including state permutation, asymmetric mode evolution, and direction-dependent dynamical responses. These properties have made EPs particularly attractive in photonics, where gain, loss, coupling, and structural parameters can be engineered with considerable flexibility [1].

In this talk, I will provide an overview of EP physics from both non-Hermitian and topological perspectives, with particular emphasis on the consequences of encircling these singularities in multidimensional parameter spaces. The distinction between quasistatic and dynamical encirclement will be discussed, highlighting how the interplay between adiabatic evolution and nonadiabatic transitions can lead to unusual state-conversion phenomena [2]. I will also briefly discuss how these concepts have motivated potential applications in asymmetric mode conversion, direction-dependent light transport, optical isolation in suitably designed nonreciprocal systems, sensing, and the controlled manipulation of photonic states.

Against this broader background, I will present some of our studies on engineering EPs in application-oriented photonic platforms. These include gain–loss-assisted and all-lossy waveguide systems exhibiting encirclement-induced asymmetric light dynamics, extensions to fiber geometries, and the interplay of nonlinearity with EP-mediated mode evolution toward nonreciprocal photonic functionalities.

Particular attention will be given to conjugate EPs, formed by time-reversal-related pairs of exceptional points, and to the correlated transport and nonreciprocal responses that can emerge from their associated dynamical encirclement [3]. I will further discuss the manifestation of conjugate EP topology in optical microcavities, where suitable encirclement schemes around conjugate EPs provide a reconfigurable mechanism for controlling lasing and absorbing states within the same photonic system, including dual-state control of lasing and absorption. This illustrates how the topology of multiple related singularities can be used not only for state conversion but also to control fundamentally different optical responses [4].

Finally, the discussion will extend beyond conventional second-order EPs to systems with multiple interconnected EPs and higher-order branch-point structures. Using optical microcavities as a representative platform, I will illustrate how the topology associated with such structures can enable richer state-permutation and switching scenarios involving multiple interacting states for new functionalities in integrated and application-specific photonic systems.

Acknowledgment: I acknowledge the contributions of Y. D. Chong, A. Laha, S. Dey, S. Bhattacherjee, A. Das, A. Miranowicz, R. K. Varshney, B. P. Pal, L. Wu, A. Roy, S. Ghosh, D. Beniwal, A. Paul, and H. K. Gandhi.

References:

[1] C. Wang, Z. Fu, W. Mao, J. Qie, A. D. Stone, and L. Yang, Adv. Opt. Photon. **15**, 442 (2023).
[2] S. Ghosh and Y. D. Chong, Scientific Reports **6**, 19837 (2016)
[3] A. Laha, A. Miranowicz, R. K. Varshney and S. Ghosh, Physical Review A **109**, 033511 (2024)
[4] A. Laha, S. Ghosh, A. Miranowicz, and L. Wu, Physical Review A **113**, 063521, (2026)

SU(2) walk on higher-order Poincaré sphere

Mohammad Umar and Paramasivam Senthilkumaran

Optics and Photonics Centre
Indian Institute of Technology Delhi, New Delhi 110016, INDIA

mohd.umar@opc.iitd.ac.in

Abstract: *Analogous to the universal SU(2) gadget for the Poincaré sphere, we show two quarter-wave q-plates and one half-wave q-plate realize arbitrary SU(2) walks on the higher-order Poincaré sphere. We also demonstrate that sandwiching this gadget between spiral phase plates of appropriate charges enables arbitrary transformations on hybrid-order Poincaré sphere.*

The Poincaré sphere (PS) provides a geometric framework for representing the polarization of light, where every polarization state is bijectively mapped onto its surface via the Stokes parameters as Cartesian coordinates. The poles of the PS correspond to the two orthogonal circular polarization states, $|R\rangle$ and $|L\rangle$, and each point on the PS represents a homogeneous state of polarization (SOP), with transformations between such states corresponding to elements of the SU(2) group, equivalent to rotations on the PS under SO(3), reflecting the two-to-one homomorphism between the two groups. Birefringent waveplates are the practical realization of these SU(2) elements; however, a single waveplate cannot achieve all possible SU(2) transformations. It has been shown that a combination of two quarter-wave plates (QWPs) and one half-wave plate (HWP), arranged coaxially in any order, forms a minimal SU(2) gadget [1] capable of realizing all polarization transformations on the PS.

The concept of the Poincaré sphere is further generalized as the higher-order Poincaré sphere (HOPS) [2], extending the framework to structured light beams. Here, the poles correspond to circularly polarized vortex modes with equal and opposite orbital angular momentum (OAM), $|R, +\ell\rangle$ and $|L, -\ell\rangle$, and their superpositions map bijectively onto a sphere of order ℓ. The equator yields cylindrical vector beams (e.g., radial and azimuthal for $\ell = 1$), while other points represent vector vortex beams with inhomogeneous elliptical polarization; $\ell = 0$ recovers the fundamental PS. A further generalization, the hybrid-order Poincaré sphere (HyOPS) [3], allows the two basis modes to carry unequal OAM, $|R, +\ell_1\rangle$ and $|L, -\ell_2\rangle$ with $\ell_1 \neq \ell_2$, breaking the symmetric spin–orbit locking of the HOPS and yielding a broader class of hybrid-order vector vortex beams, with the HOPS and PS recovered as special cases.

While the standard PS admits a universal SU(2) gadget, no analogous construction has so far been established for the HOPS until our work [4, 5]. In search of an SU(2) gadget compatible with the HOPS, we investigated various configurations of inhomogeneous waveplates, particularly q-plates, and obtained promising results. A q-plate is a structured birefringent element whose fast-axis orientation varies azimuthally in a well-defined manner. Depending on its retardance, a q-plate operates as a half-wave q-plate (q^H-plate) when the retardance is π, or as a quarter-wave q-plate (q^Q-plate) when the retardance is $\pi/2$. The HOPS and the q-plate share a common topological character, in that one of their defining parameters is azimuthally varying, which renders the q-plate a natural SU(2) optical element for transformations on the HOPS surface. Building on this correspondence, we show that, using the Euler angle parameterization of the SU(2) group [4] and the effective waveplate concept [5], an arbitrary SU(2) transformation can be realized using three q-plates — two q^Q-plates and one q^H-plate — independent of their sequential ordering. This configuration thus realizes all SU(2) transformations on the HOPS and constitutes the corresponding SU(2) gadget. Extending this result further, we demonstrate that sandwiching this SU(2) gadget between spiral phase plates of appropriate topological charge yields a new composite gadget capable of realizing the full set of polarization transformations on the HyOPS.

References

[1] R. Simon, N. Mukunda, *Physics Letters A* 143 (1990) 165-169.

[2] G. Milione *et al.*, *Physical Review Letters* 107 (2011) 053601.

[3] X. Yi *et al.*, *Physical Review A* 91 (2015) 023801.

[4] M. Umar, P. Senthilkumaran, *arXiv:2509.10964* (2025).

[5] M. Umar, S. Bansal, P. Senthilkumaran, *Optics Express* 34 (2026) 15632-15647.

Investigation of Detector Translation for Refocusing in a Compact Imaging System

[1,#]Ratnabali Ghosh,[1]Mohammad Sinad,[1]Akshat Sharma,[1]Arun Sharma,[1]Nitin Shahi ,
[1]Prabhu Balasubramanian, [1]Ravikrishnan Elangovan
[1]Indian Institute of Technology Delhi, Hauz Khas, New Delhi – 110016
[#]Corresponding email: ratnabalighosh97@gmail.com

Abstract: Automated microscopy requires reliable refocusing to compensate for sample topography variations and imaging-system drifts. This work investigates detector translation (Z+) as an alternative focusing mechanism on infinity-corrected microscopy systems. Experimental results demonstrate detector-assisted refocusing, enabling a compact approach to focus and control in a single system.

Automated microscopy systems require reliable refocusing to compensate for sample topography variations, mechanical tolerances and thermal drift during image acquisition. Conventional approaches typically rely on translation of either the sample stage or the objective lens. In this work, we investigate a third degree of freedom – axial detector translation, termed the Z+ axis.

The proposed Z+ focusing strategy is based on first-order imaging theory, which predicts that produced magnified image plane shifts according to:

$$dv = M^2 . du$$

Where, dv = distance change in image plane; du = distance change in object plane; M = magnification

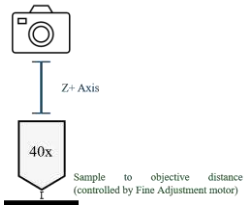


Fig (1): Diagram of Z+ Axis

To investigate this experimentally, controlled sample defocus (1–30 μm) was introduced using the microscope fine adjustment, previously calibrated using a digital dial gauge (~1 μm per division). Detector translation was then used to recover focus in an infinity-corrected microscope equipped with a 40× NA 0.65 objective (180mm design tube length; ~22x/28x actual magnification with 100mm/125mm tube lenses) and a SONY IMX477 detector and focus quality was assessed using edge-based metrics, like Tenengrad and Laplacian variance, as a parameter for sharpness.

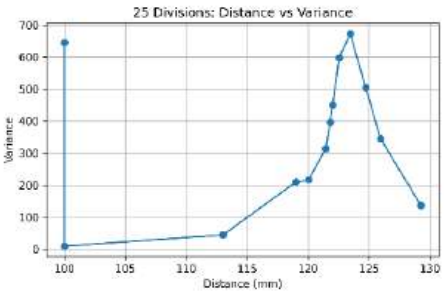


Fig (2): Change in sharpness variance with increasing Z+ distance (for 100mm TL)

Figure (2) shows the plot between variance (sharpness) and the distance in Z+ required to travel to recover focus after a 25μm (25 division) defocus from the initial focus plane. Detector translation successfully restored focus over a limited range of sample displacements at a fixed objective position, with larger object-space defocus requiring progressively larger Z+ translation. Beyond approximately 20-25μm object displacement however, Z+ movement alone could no longer fully compensate for defocus, reaching a plateau [fig (3)]. Repeating the set-up with a finite objective resulted in steep change in magnification when Z+ was moved and thus was abandoned in lieu of a infinity-corrected system, that showed a more tolerable range of magnification change over a large detector translation length.

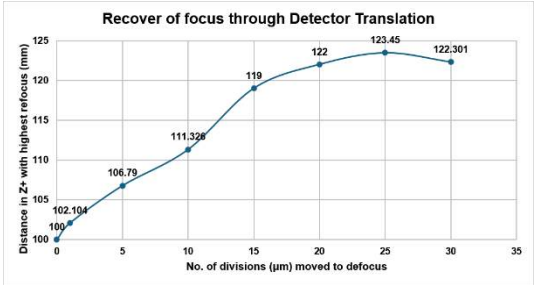


Fig (3): Z+ range reaches a saturation after a certain defocusing displacement range

The proposed Z+ approach establishes detector position as an additional optical degree of freedom in microscopy, recovering image sharpness in agreement with first-order imaging theory. Unlike stage/objective based refocusing, Z+ translation also shifts magnification (~dv/f_tube, ~10% here) and field of view – relevant to stitching and calibration in a scanner. These findings support a compact, low-cost, adaptable imaging platform now being incorporated into our in-house scanner – Autoscope.

References:

[1] V.N. Mahajan, *Optical Imaging and Aberrations, Part I: Ray Geometrical Optics*, SPIE Press Monograph PM45, SPIE Press, Bellingham, WA (1998)

[2] S.Pertuz, D. Puig, M.A. Garcia, *Pattern Recognition* **46** (2013) 1415–1432.

Speckle-Learned Single-Shot Regression of Complex OAM Superposition States

Chayanika Sharma, Purnesh Singh Badavath, and Vijay Kumar*
Department of Physics, National Institute of Technology Warangal, Hanamkonda, Telangana-506004
*vijay@nitw.ac.in

Structured light propagating through scattering media produces complex speckle patterns that encode information about the incident optical field. We demonstrate a speckle-learned regression approach for single-shot characterization of complex orbital angular momentum (OAM) superposition states. The approach provides accurate complex coefficient retrieval from single-short intensity speckle measurements for high-dimensional structured-light characterization.

Structured light beams, including Laguerre–Gaussian (LG), Hermite–Gaussian (HG) have emerged as key resources for optical communications, imaging, metrology, quantum information processing, and sensing. Their rich spatial degrees of freedom enable high-dimensional information encoding. However, when structured light propagates through scattering media such as diffusers, multimode fiber, atmospheric turbulence channels, its spatial structure becomes severely distorted, producing seemingly random speckle patterns. Extracting the original optical information from these scattered intensity distributions remains a major challenge in modern photonics.

Here, we present a machine-learning framework for the regression of structured light through scattering media. We adopt the speckle-learned approach, where the scattered speckle field acts as an encoded representation of the incident structured light. Instead of relying on interferometric measurements or complex modal decomposition techniques, information of complex coefficients is recovered from single-short intensity speckle pattern.

While classification enables reliable identification of structured-light modes from scattering-induced speckle patterns, it is limited to assigning discrete mode labels [1-3]. A more complete characterization requires regression, where continuous complex coefficients are estimated directly from the intensity speckle pattern. This transition from classification to regression enables quantitative retrieval of high-dimensional OAM superposition states from a single intensity speckle measurement.

An arbitrary OAM superposition state U can be expressed as a weighted sum of constituent Laguerre-Gaussian modes: $U = c_{p,l} LG_p^l$, here $c_{p,l}$ are the complex coefficients representing relative amplitude and phases among the constituent modes. A customized deep neural network is trained to learn the inverse mapping between the measured intensity speckle pattern and these complex modal coefficients. The network performs simultaneous regression of both amplitude and phase parameters, enabling complete characterization of the OAM superposition state from intensity-only measurements [4,5].

In summary, we demonstrate that scattering-induced speckle patterns can serve as information-rich fingerprints of complex OAM superposition states. By combining speckle learning with deep regression, the modal amplitudes and relative phases can be retrieved directly from a single intensity measurement. The proposed framework provides a compact, alignment-robust, and non-interferometric approach for high-dimensional structured-light characterization, with potential applications in optical communications, quantum information processing, and intelligent photonic sensing.

Acknowledgement: SERB India Project: SERB/SRG/2021/001375; ANRF India Project: ANRF/ARG/20256/007273/PS.

References:

[1] V. Raskatla, P. S. Badavath, S. Patil, V. Kumar, and R. Singh, “Speckle-Based Deep Learning Approach for OAM Modes Classification,” JOSA A 39, 759 (2022).
[2] P. S. Badavath, Venugopal Raskatla, T. Pradeep Chakravarthy, and Vijay Kumar, “Speckle-based structured light shift-keying for non-line-of-sight optical communication,” Appl. Opt. 62, G53 (2023).
[3] C. Sharma, P. S. Badavath, P. Supraja, R. Rakesh Kumar, and V. Kumar, "Machine-learning-assisted orbital angular momentum recognition using nanostructures," J. Opt. Soc. Am. A 41, 1420-1425 (2024)
[4] C. Sharma, V. Raskatla, V. Kumar,“Speckle-learned Regression of Orbital Angular Momentum Superpositions,” in in Laser Congress 2024 (ASSL, LAC, LS&C) , Technical Digest Series (Optica Publishing Group, 2024), paper JD1.4.
[5] C. Sharma, P. S. Badavath, and V. Kumar, "Speckle-Learned Regression for Complete Characterization of Orbital Angular Momentum Superposition States" APS Open (2026).

Multimodal Optical Feature Extraction with a Free-Space Photonic Extreme Learning Machine

[1,*]Anushka Kumari, [1,*]Anushree Khisti, [1,2,*]Abhinav Choube, [1]Devansh Satra, [1]Srivatsa Murali, and [1,#]Anshuman Kumar

[1]Laboratory of Optics of Quantum Materials, Department of Physics, Indian Institute of Technology Bombay, Mumbai 400076, India
[2]Department of Physics and Electronics, Institute for Excellence in Higher Education, Bhopal 462042, India
[#] *anshuman.kumar@iitb.ac.in*

We demonstrate a single free-space photonic extreme learning machine, using SLM phase encoding, Fourier-like propagation, and camera intensity readout, that unifies image, audio-derived, tabular, and regression tasks [1]. The platform reaches 96.56% accuracy on MNIST, 95.67% on spoken-digit spectrograms, 100.00% on Mushroom classification, and 0.0699 NRMSE on Abalone regression.

Rising computational and energy demands of modern AI have made optical computing an attractive alternative, since free-space propagation naturally implements high-dimensional linear operations without incurring the memory-computation bottleneck of conventional digital hardware; photonic extreme learning machines (PELMs) exploit this by using a fixed optical transformation as an untrained hidden layer, with only a simple linear readout trained on the resulting features.

To our knowledge, this is the first free-space PELM to span image, audio-derived, and tabular tasks within one physical pipeline. Diagnostics based on distance preservation and kernel alignment further reveal two distinct regimes underlying this generalization: geometry preservation for image and regression tasks, and distributed class-mean accumulation for audio spectrograms, offering concrete design rules for building multimodal optical feature extractors.

Our experimental platform (Fig. 1) comprises a 532 nm laser, a phase-only spatial light modulator, a $4f$ optical system that expands the beam to uniformly illuminate the entire SLM, an iris for first-order spatial filtering, and a CMOS camera that records $M = 4096$ intensity features per input. The same optical pipeline is applied identically across all datasets.

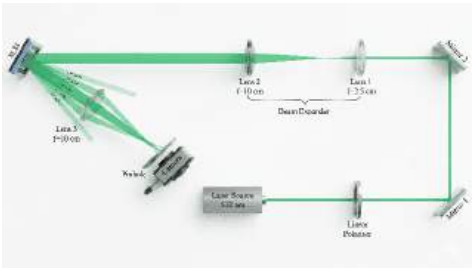


Figure 1: Free-space PELM setup

Only the ridge-regression readout is trained digitally,

$$\beta = \left(H^\top H + \lambda I\right)^{-1} H^\top T, \tag{1}$$

where β denotes the trained readout weights, H the measured optical feature matrix, T the target matrix, and λ the ridge regularization parameter optimized independently for each dataset.

Each dataset is reshaped into a 2D grid, combined with a fixed embedding mask, and displayed as a single SLM phase pattern. Since the camera samples only a small subset of the optical Fourier spectrum, an unembedded phase pattern would make neighboring inputs produce nearly identical responses; the embedding mask decorrelates this subsampled transform, preserving pairwise input distances and keeping the readout matrix well-conditioned. A multi-frequency Fourier mask slightly outperformed a random noise mask across all datasets, showing that a simple, fabrication-free free-space apparatus can serve as a general-purpose multimodal feature extractor.

A.C. acknowledges financial support from the Industrial Research and Consultancy Centre (IRCC) internship fund at IIT Bombay.

References

[1] A. Kumari, A. Khisti, A. Choube, D. Satra, S. Murali, A. Kumar, *arXiv preprint* arXiv:2605.29043 (2026).

Virtual Staining Microscope for Label-Free Liver Cancer Histopathology

[1,]Anant Gupta, [1,]Meenaakshi Rana, [1,#]Vishal Gupta, [1]Hari Shankar Singh, [2]Asit Ranjan Mridha, [3]Uman Nahar Saikia and [1,#]Vishal Srivastava

[1]Thapar Institute of Engineering and Technology, Patiala (Arial 11 point)
[2]All India Institute of Medical Sciences, New Delhi
[3]Postgraduate Institute of Medical Education and Research, Chandigarh

[#]email id of the corresponding author: vsrivastava@thapar.edu

Histopathology relies on H&E staining for cancer diagnosis, but conventional staining is labor-intensive and time-consuming. We propose a U-Net-based deep learning framework that virtually stains label-free autofluorescence liver images into realistic H&E images. The generated images closely match conventional histology, demonstrating strong potential for rapid, cost-effective, and clinically applicable digital pathology.

Liver cancer is a major cause of cancer-related mortality worldwide, with a rapidly increasing burden in India. Although H&E-stained histopathology remains the gold standard for diagnosis, conventional staining is labor-intensive, time-consuming, and reagent-dependent. Label-free autofluorescence imaging provides a rapid, non-destructive alternative but lacks the color and contrast required for routine pathological assessment. To address this limitation, we propose a U-Net-based deep learning framework for automated virtual staining of label-free autofluorescence images of human liver tissue. As shown in Fig. 1, the proposed method directly transforms unstained autofluorescence images into realistic H&E-equivalent images. The generated virtual stained images demonstrate strong agreement with conventionally stained sections, achieving a correlation of 91.07%, SSIM of 77.27%, and PSNR of 18.98 dB, while preserving diagnostically relevant morphological features. The proposed AI-assisted framework offers a rapid, reagent-free, and cost-effective alternative to conventional histopathology, with significant potential to accelerate liver cancer diagnosis and advance stain-free digital pathology.

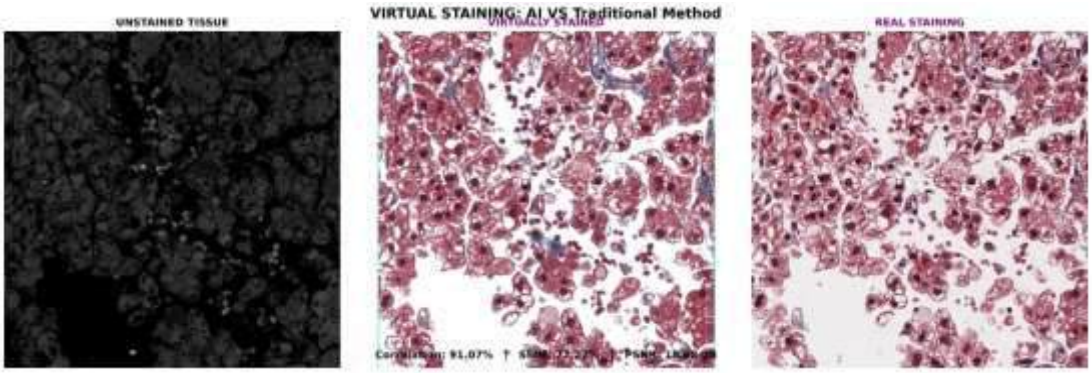


Figure 1: Deep learning-based virtual staining of label-free autofluorescence liver tissue images.

In summary, we developed a U-Net-based deep learning framework for virtual H&E staining of label-free autofluorescence images of human liver tissue. The proposed method generates realistic H&E-equivalent images while preserving diagnostically relevant morphological features, offering a rapid, non-destructive alternative to conventional staining. This approach has the potential to enable faster, standardized, and cost-effective histopathological assessment, advancing stain-free digital pathology and supporting improved clinical decision-making.

References:

[1] M. Boktor, B.R. Ecclestone, V. Pekar, et al., Scientific Reports **12** (2022) 10296.

[2] L. Kang, X. Li, Y. Zhang, T.T.W. Wong, Photoacoustics **25** (2022) 100308.

HRFZ SOI Platform for Selected THz Guided Wave Active Devices

Rajesh Kumar
Department of Physics, Indian Institute of Technology Roorkee, Uttarakhand 247667, India.
Centre for Photonics and Quantum Communication Technology, Indian Institute of Technology Roorkee, Uttarakhand 247667, India.
rajesh.kumar@ph.iitr.ac.in

The THz active components, including a PCM GST-based switch, a PCM VO_2-based modulator, and a tunable filter, enabled using the low-loss SOI waveguide platform with HRFZ-Si as the guiding medium and silica as the substrate, are investigated that form building blocks of the THz PICs on the SOI waveguide platform.

The terahertz (THz) electromagnetic spectrum (0.1-10 THz) has diverse applications, including futuristic wireless communication (6G and beyond), non-invasive biomedical diagnostics and spectroscopy, non-destructive industrial testing, and security screening [1]. However, there is a lack of an on-chip platform accommodating the THz devices and components required for these use cases. CMOS-compatible on-chip THz integrated photonic circuits (THz PICs) that enable switching, modulation, and spectral filtering within a single guided-wave platform can address this technology gap. A strip waveguide with high-resistivity float-zone silicon (HRFZ-Si) as the guiding material, air as the upper cladding, and silica as the substrate, with a waveguide cross-section of 195μm×95μm (width X height), supports a single TE mode in the frequency range of 0.5 to 0.6 THz, and exhibits an average propagation loss of 0.24 dB cm^{-1}. This platform serves as a fundamental building block of the proposed THz PICs [2]. A novel micro-fin heater enables the energy-efficient electro-thermal phase transformation of phase change materials (PCMs) by concentrating heat within the PCM while minimizing thermal diffusion to surrounding regions.

Using this waveguide platform, a PCM $Ge_2Sb_2Te_5$ (GST) based CMOS-compatible broadband THz waveguide switch operating in the 0.5-1.0 THz frequency band is demonstrated. The amorphous-to-crystalline electro-thermal phase switching of GST integrated on top of the HRFZ-Si strip waveguide is induced by a novel micro-fins heater through localized thermal heating. For a GST volume of 1500μm×195μm×2 μm (Length×width×thickness), the switch exhibits a broadband extinction ratio exceeding 10 dB and an insertion loss below 2.6 dB across the 0.5-1.0 THz frequency range. The electro-thermal study exhibits that the crystallization is achieved with an electrical pulse of 11 ms and 350 V, while re-amorphization of crystalline GST is achieved with a pulse as short as 4 μs and 350 V. The corresponding energy consumption for crystallization and re-amorphization is 61.73 mJ and 19.84 mJ, respectively. The switching speed is 100 times better than previously reported metamaterial-based THz photonic switches based on electro-thermally induced phase transformation of GST [3]. The device consumes no power to hold its state, making it well-suited for THz photonic switching networks and reconfigurable signal routing on THz PICs [2].

A guided-wave THz modulator employing a 150-nm-thick, 1000-μm-long volatile PCM VO_2, integrated atop the THz waveguide, is demonstrated. In the operating frequency band of 0.5 to 0.6 THz, the modulation depth exceeding 90%, and the insertion loss is below 1 dB. The electro-thermally driven reversible insulator-to-metal (IMT) phase transformation of VO_2 is enabled using two distinct heater configurations: a conventional direct micro-fins heater and a graphene-assisted micro-fins heater. The direct micro-fins heater requires 250 V to trigger IMT of VO_2, achieving a modulation speed of 2.45 ms, while the graphene-assisted heater reduces the required actuation voltage to just 8 V and attains a modulation speed of 0.79 ms, making it one of the fastest electro-thermally driven VO_2-based THz modulators reported to date [4]. A tunable THz filter is a key element required for THz signal routing, spectral shaping, and multiplexing. A thermally tunable waveguide Bragg grating filter (WBGF) operating in the frequency range of 0.5-0.6 THz is designed using the same waveguide platform. For the total grating length of 5.475 mm, it exhibits an extinction ratio of 18 dB and a full-width-at-half-maximum bandwidth of 12 GHz. The Bragg resonance frequency shifts by 8 GHz as the temperature of HRFZ-Si increases to 100 °C. Taken together, the demonstrated THz devices constitute a coherent and synergistic set of active THz components required for THz PICs.

Acknowledgment: DST, India (DST/QTC/NQM/QMD/2024/4); SERB, India (CRG/2023/001094).

References:

[1] J. Xie, W. Ye, L. Zhou, X. Guo, X. Zang, L. Chen, Y. Zhu, Nanomaterials, 11(7), 1646, (2021).
[2] R. A. Yadav, C.B. Sirish, G. Morthier, R. Kumar, and Kumar. Optik, 311, p.171889, (2024).
[3] P. Pitchappa, A. Kumar, S. Prakash, H. Jani, T. Venkatesan, & R. Singh, Advanced Materials, 31(12), 1808157 (2019).
[4] R. A. Yadav, V.B. Palekar, G. Morthier, R. Kumar, Advanced Theory and Simulations 9, e01200 (2026).

Terahertz Optical Devices Based on Tunable Metamaterials

N. Yogesh*

Metamaterials and Photonic Structures Laboratory, National Institute of Technology Calicut, Kozhikode-673601, Kerala, India

*yogesh@nitc.ac.in

Tunable materials such as graphene, bulk Dirac semimetals, VO_2, and GST phase-change materials offer intuitive control of wavefront and polarization engineering of THz waves when combined with metamaterial structures. In this talk, I'll highlight the potential of tunable metamaterial THz devices for plasmonic, imaging, and sensing applications.

Metamaterials (MTMs) are artificial sub-wavelength periodic structures that offer unprecedented control over the amplitude, phase, and polarization state of light. In particular, MTMs offer rich optical responses in the THz band, including magnetism, giant optical activity, strong nonlinear susceptibility, surface-plasmon polariton resonances, a coherent Cerenkov radiation source, zero and negative refraction, and near-unity absorption. Though the metamaterial research is well established for THz applications, the ability to tune THz wave properties, such as wavefront engineering, polarization control, and amplitude modulation, is emerging with respect to the introduction of tunable materials. In this talk, I'll highlight the physics and applications of THz-tunable metamaterials formed from tunable materials such as graphene, bulk Dirac Semimetals, VO2, and GST phase-change materials, in the realization of innovative THz optical and photonic devices for imaging, sensing, and communication applications.

Keywords: **THz Tunable Metamaterials, Surface Plasmon Polariton Resonances, Bulk Dirac Semimetal, Graphene, VO_2, and GST phase change materials.**

References

1. B. Asrafali, Fahim Khan, Deepika Tyagi, M.S. Syam, M. Pavithra, N. Yogesh, and Z. Ouyang, Optics Communications 583 131770 (2025).
2. Tony Mathew Blessan, C. Venkateswaran, and N. Yogesh, Optik 257, 168795 (2022).
3. Tony Blessan Mathew and N. Yogesh, JOSA B, Vol. 38, 2261-2266 (2021).
4. L. P. Abhishek and N. Yogesh, "Graphene Assisted Tunable Electromagnetically Induced Transparency Metasurface for Spatial Modulation Applications in THz Regime," 2025 Photonics & Electromagnetics Research Symposium - Spring (PIERS-Spring), Abu Dhabi, United Arab Emirates, 2025, pp. 1-5.

Light-Controlled Lattice Engineering for Reconfigurable Terahertz Metadevices

[1,2]Vanlal Rinfela, [2]Prem Pal, [3]Abhishek Kumar, [4]Manoj Gupta and [1#]Yogesh Kumar Srivastava

[1]*Ultrafast Terahertz Photonics Laboratory (UTPL), Department of Physics, Indian Institute of Technology Hyderabad, Kandi, Sangareddy, Telangana, 502284, India*

[2]*MEMS & Micro/Nano Systems Laboratory, Department of Physics, Indian Institute of Technology Hyderabad, Kandi, Sangareddy, Telangana, 502284, India*
[3]*Chemistry and Physics of Materials Unit (CPMU), Jawaharlal Nehru Center for Advanced Scientific Research (JNCASR), Bangalore, 560064, India*
[4]*Department of Electrical Engineering, Indian Institute of Technology Jodhpur, Karwar, Jodhpur, Rajasthan, 342030, India*

[#] *Email: yogesh.srivastava@phy.iith.ac.in*

Surface lattice resonances enable high-Q light confinement but are intrinsically fixed by structural periodicity. We demonstrate light-controlled, reversible lattice-mode engineering in a terahertz metasurface using photoactive silicon, dynamically switching the effective lattice periodicity from 70 to 140 µm to achieve ultrafast, reconfigurable resonance splitting without structural modification.

Surface lattice resonances (SLRs) [1], arising from Rayleigh diffraction in periodic resonator arrays, support high-quality resonances and strong electromagnetic field confinement through collective lattice-mediated interactions [2]. However, their spectral characteristics are fundamentally dictated by the lattice periodicity, making them fixed after fabrication and limiting dynamic tunability [3]. Here, we demonstrate a **light-controlled lattice engineering** that dynamically controls lattice modes in a terahertz (THz) metasurface without altering its physical geometry. The platform comprises a complementary asymmetric split-ring resonator (cASRR) metasurface integrated with selectively patterned photoactive silicon. Optical excitation generates photocarriers that selectively suppress every alternate resonator channel, switching the effective lattice periodicity from **70 µm to 140 µm**. This reversible process activates a previously inaccessible lattice mode that strongly couples with the intrinsic magnetic dipole resonance, producing pronounced resonance splitting. Numerical simulations and experimental measurements confirm that the additional splitting occurs only under optical excitation, verifying its purely light-induced, lattice-driven origin. This approach enables ultrafast, reversible, and reconfigurable control of lattice-mediated THz photonic functionalities.

Acknowledgment: Vanlalrinfela gratefully acknowledges the University Grants Commission (UGC), Government of India, for the financial support of the research fellowship

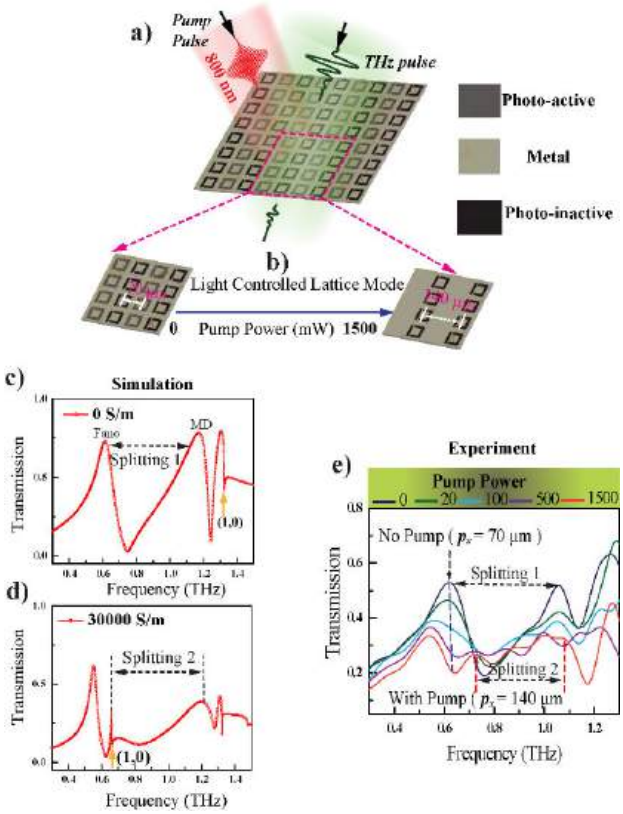


Fig 1. Light-Controlled Lattice Mode Switching. *(a) Experimental configuration (b) Optical switching of the effective lattice periodicity from* ***70 µm*** *to* ***140 µm****. (c,d) Simulated and (e) Measured THz transmission spectra under different optical pump powers.*

References:

[1] T. C. Tan, E. Plum, R. Singh, in *Photonics*, MDPI, 2019, p. 75.
[2] T. C. Tan, Y. K. Srivastava, M. Manjappa, E. Plum, R. Singh, *Appl. Phys. Lett.* 2018, *112*, 201111.
[3] M. Manjappa, Y. K. Srivastava, R. Singh, *Phys. Rev. B* 2016, *94*, 161103.

Plasmonically Hybridized Broadband Graphene Metasurface for Terahertz Dual-Band Four-Wave Mixing

[1]Mitali Sahu, and [1,#]Partha Roy Chaudhuri
[1]Department of Physics, Indian Institute of Technology Kharagpur, India, 721302
[#]*roycp@phy.iitkgp.ac.in*

A new wideband nonlinear graphene metasurface comprising three concentrically coupled graphene rings is proposed for efficient terahertz four-wave mixing (FWM). Plasmonic mode hybridization enables broadband (>90%) absorption over nearly 1 THz and mode-selective dual-band FWM generation at 1.7 and 2.5 THz, providing an efficient platform for THz nonlinear frequency conversion.

Graphene-based metasurfaces have emerged as an attractive platform for compact nonlinear terahertz (THz) devices owing to their strong third-order optical nonlinearity, exceptional plasmonic field confinement, and deep-subwavelength light manipulation. In this work, a wideband nonlinear graphene metasurface is designed using three concentrically coupled graphene rings placed above a metallic ground plane separated by a dielectric spacer. Strong near-field coupling among the graphene rings induces plasmonic mode hybridization, resulting in broadband absorption exceeding 90% over the 1.5-2.5 THz frequency range. The broad absorption band enables simultaneous excitation of multiple input frequencies required for nonlinear frequency conversion processes such as four-wave mixing (FWM), while the enhanced local electromagnetic field significantly strengthens the nonlinear interaction. Unlike conventional narrowband nonlinear metasurfaces, the proposed design supports broadband excitation while maintaining spectrally selective nonlinear emission governed by the hybrid plasmonic modes. Consequently, the metasurface produces mode-selective dual-band FWM output with two dominant peaks at approximately 1.7 THz and 2.5 THz.

The proposed metasurface and its calculated responses are illustrated in Fig. 1. Figure 1(a) shows the design of the proposed graphene metasurface together with the degenerate FWM excitation scheme using two obliquely incident THz waves. Figure 1(b) presents the calculated linear response, demonstrating broadband absorption produced by plasmonic mode hybridization among the coupled graphene rings. The corresponding nonlinear response is shown in Fig. 1(c), where two dominant FWM output bands are observed within the broadband absorption window. The nonlinear emission is governed by the radiative hybrid plasmonic modes rather than the specific pump frequencies, demonstrating broadband excitation together with mode-selective dual-band frequency conversion. These results highlight the potential of the proposed graphene metasurface as a compact platform for THz nonlinear frequency conversion and integrated nonlinear photonic devices.

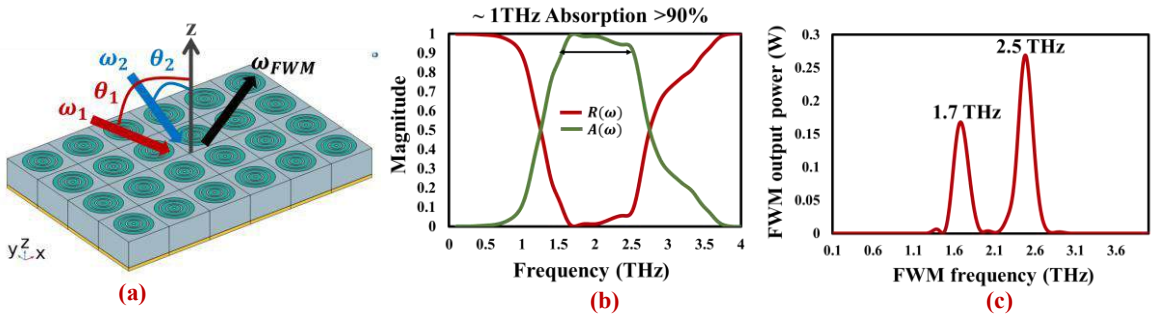


Fig. 1. (a) Design of the proposed triple-ring graphene metasurface comprising periodic concentric graphene rings placed above a dielectric spacer and a metallic ground plane. Two obliquely incident THz waves at frequencies ω_1 and ω_2 generate the FWM signal at ω_{FWM}. (b) Calculated reflectance and absorptance spectra of the metasurface, showing broadband absorption exceeding 90% over the 1.5-2.5 THz range due to plasmonic mode hybridization. (c) Calculated FWM output spectrum of the proposed metasurface exhibiting two dominant peaks at 1.7 THz and 2.5 THz, demonstrating mode-selective nonlinear emission.

References:

[1] B. Jin, C. Argyropoulos, *Scientific Reports 6 (2016) 28746.*
[2] T. Guo, B. Jin, C. Argyropoulos, *Physical Review Applied* 11 (2019) 024050.
[3] J. W. You, Z. lan, N. C. Panoiu, *Science Advances 6 (2020) 3910.*

Probing Spatial Coherence with a Terahertz Metasurface

[1]Manish Kala, [2]Lavi Kumar Vaswani, [2]Anuraj Pawar, [3,4]Gagan Kumar, [1,5,#] Akhilesh Kumar Mishra

[1]Department of Physics, Indian Institute of Technology Roorkee, Roorkee 247667, Uttarakhand, India

[2]Department of Physics and Materials Science and Engineering, Jaypee Institute of Information Technology, Noida 201309, Uttar Pradesh, India

[3]Department of Physics, Indian Institute of Technology Guwahati, Guwahati 781039, Assam, India

[4]Department of Physics, Indian Institute of Technology Ropar, Rupnagar 140001, Punjab, India

[5]Centre for Photonics and Quantum Communication Technology, Indian Institute of Technology Roorkee, Roorkee 247667, Uttarakhand, India

[#]akhilesh.mishra@ph.iitr.ac.in

This study investigates coherence effects on THz metasurface transmission, comparing coherent and partially coherent illumination via the Van Cittert–Zernike theorem. Fabricated zigzag-slit aluminum-on-SiC metasurfaces show experiment-simulation agreement, revealing coherence-dependent resonance behavior critical for realistic THz device design.

With the continuous progress in terahertz (THz) science and technology, metasurfaces have emerged as powerful platforms for tailoring electromagnetic wave propagation through accurate control of their amplitude, phase, and polarization characteristics. These engineered two-dimensional structures consist of periodically arranged subwavelength resonant elements whose electromagnetic response is determined by their geometry, spatial configuration, and material composition [1]. Although the interaction of metasurfaces with perfectly coherent THz illumination has been studied extensively, their response under realistic operating conditions involving partially coherent or incoherent THz radiation remains comparatively underexplored. This aspect is of considerable practical importance because many THz systems employ spatially extended radiation sources that inherently exhibit limited coherence, making it essential to understand the influence of source coherence on metasurface performance.

In this study, the transmission characteristics of a THz metasurface are systematically investigated under both coherent and partially coherent illumination conditions. The analysis is founded on the Van Cittert–Zernike theorem, which establishes the relationship between the spatial coherence width of an optical field and its corresponding distribution of wavevector (k) components [2]. Under coherent illumination, the incident field is represented by a single normally incident (k)-component, resulting in uniform phase excitation across all metasurface unit cells. Conversely, partially coherent illumination is described by a superposition of multiple mutually out-of-phase (k)-components distributed within the finite spatial coherence width. The overall transmission spectrum is then determined by averaging the spectral responses associated with these individual (k)-components.

The metasurface, featuring a complementary zigzag slit pattern of aluminum (Al) on a silicon carbide (SiC) substrate, was fabricated using a laser writing lithography process in a cleanroom environment. Transmission measurements were performed using THz time-domain spectroscopy (THz-TDS) with a LUNA Innovations Terametrix 5000 T-Ray system. Experimental results exhibit excellent agreement with full-wave simulations, validating our theoretical approach. The study reveals that the degree of spatial coherence significantly alters the observed resonance features [3]. These findings provide essential insights for the design and optimization of metasurface-based THz devices operating under realistic illumination conditions, enabling improved performance in sensing, imaging, and communication applications.

References:

[1] J. Zhang, et al. “An ultrathin directional carpet cloak based on generalized Snell’s law,” Appl. Phys. Lett. 103, 151115 (2013).

[2] M. Born, E. Wolf, “Principles of Optics,” Cambridge University Press, Cambridge, 1998.

[3] M. Kala, L. Vaswani, A. Panwar, G. Kumar, and A. K. Mishra, “Probing beam coherence via terahertz metasurface”, Opt. Lett. 51, 1069 (2026).

Observation of Exceptional Points in non-Hermitian Photonic Crystal

[1]Parul Sharma, [2]Anuj Kumar Singh, [1]Rohit Kumar, [1]Brijesh Kumar, [1,*]Anshuman Kumar
[1]Laboratory of Optics of Quantum Materials (LOQM), Department of Physics,
IIT Bombay, Mumbai, 400076
[2]Technical Physics, University of Würzburg, Am Hubland, Germany, 97074

[*]*anshuman.kumar@iitb.ac.in*

We realize exceptional points in silicon nitride photonic crystal nanohole arrays using band-structure engineering, nanofabrication, and cross-polarized k-space imaging. Coupling quantum dot emitters to the exceptional point modes enables enhanced spontaneous emission, establishing a low-loss, CMOS compatible platform for integrated non-Hermitian photonics.

Exceptional points (EPs) are the spectral singularities of the non-Hermitian system where both the eigenvalues and eigenvectors coalesce, giving rise to unconventional optical phenomena such as enhanced light-matter interactions [1], spontaneous emission enhancement [2], and high sensitivity. Implementing EPs in low-loss, CMOS compatible photonic platforms remain an important step toward practical integrated photonic devices. Silicon nitride (Si_3N_4) photonic crystals provide an attractive platform owing to their low optical loss, mature fabrication processes, and versatile dispersion engineering, making them well suited for realizing non-Hermitian photonic functionalities.

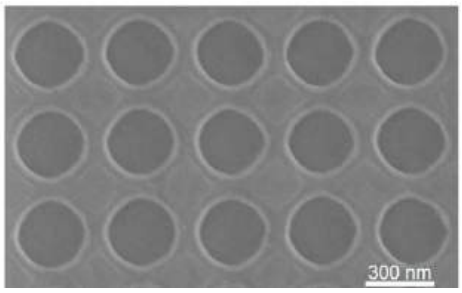


Fig.1 SEM image of fabricated photonic crystal

The photonic band structure is calculated using full-wave finite element method in COMSOL Multiphysics. The simulated dispersion reveals two symmetric EPs located at $\pm k_{EP}$, originating from the coupling of bright and dark Bloch modes. Isofrequency contour maps are further computed under cross-polarized detection, which suppresses specular reflection and selectively isolates the coupled modes associated with the EPs, providing clear signatures for experimental identification. The designed nanohole arrays are subsequently fabricated using electron-beam lithography followed by reactive ion etching. To experimentally probe the engineered non-Hermitian modes, a polarization resolved Fourier space imaging setup operating under cross polarization is developed. The measured isofrequency contours and momentum-space spectra show excellent agreement with the simulated band structure, confirming the realization of exceptional points in the fabricated photonic crystals.

To investigate light-matter interactions near EP, colloidal quantum dots emitting at the EP wavelength are spin-coated onto the photonic crystal, and angle-resolved photoluminescence (PL) spectra is measured. The measurements probe the interaction between the quantum emitters and the engineered non-Hermitian photonic modes, demonstrating the suitability of this platform for studying enhanced spontaneous emission.

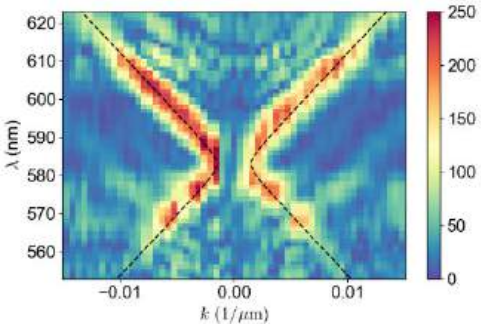


Fig.2 Angle-resolved reflectance showing band dispersion with EP

This work demonstrates a CMOS compatible route to realizing exceptional points in photonic crystals, bridging non-Hermitian band engineering with quantum emitter integration. The proposed platform provides new opportunities for manipulating light-matter interactions in next-generation integrated photonic devices.

I acknowledge the support by the Prime Minister Research Fellowship (PMRF), Govt. of India. We acknowledge funding support from the National Quantum Mission (NQM), an initiative of the Department of Science and Technology, Govt. of India.

References:

[1] V. A. Nguyen, V. H. Le, E. Sarelli, L. Malgrey, etal., *Applied Physics Letters* 123, 191105 (2023).
[2] L. Ferrier, P. Bouteyre, A. Pick , S. Cueff, etal., *Physical Review Letters* 129, 083602 (2022).

Centre Frequency Tuneable Linear Frequency Modulated Dual-Chirp generation for Microwave Photonic FMCW Radar

[1,2,#]Atul Khanna,[2]Praveen Jha, [2]Mukund Jha, and [2]Amol Choudhary
[1]UltraFast Optical Communications and High-performance Integrated Photonics (UFO-CHIP) group, Department of Electrical Engineering, Indian Institute of Technology (IIT) Delhi
[2]Optics & Photonics Centre, IIT Delhi, Hauz Khas, Delhi - 110016, India

[#]*opz228314@iitd.ac.in*

We demonstrate a frequency modulated continuous wave (FMCW) microwave photonic (MWP) radar system with frequency-agile linear frequency modulated (LFM) dual-chirp generation for seamless multi-band operation in various RF bands. The system makes use of optical heterodyning between two lasers for shifting the central frequency of the generated RF waveform.

Radar applications require diverse frequency bands, from long-range surveillance (0.3-4 GHz) and SAR/ISAR imaging (4-18 GHz) to automotive radars (76-81 GHz). MWP radars are making significant advancements in their RF tuneability, form factor, system complexity, and high-bandwidth capabilities [1]. MWP FMCW radars use RF LFM chirps for range measurements. Additionally, V-shaped RF LFM dual-chirps are frequently utilised for simultaneous range and velocity detection [2,3]. However, switching between the distinct RF bands typically demands significant hardware modifications to the system [4].

In this work, we demonstrate the tuneable frequency up-conversion of an RF baseband LFM chirp for radar RF band tuneability. By mixing a laser modulated with a 1 GHz 10μs baseband LFM chirp with a tuneable laser at a frequency offset, f_o, we generate a frequency up-converted V-shaped LFM dual-chirp centred at frequency f_o. Utilizing this method, we generated waveforms across the RF C-band (4-8 GHz), X-band (8-12 GHz), and Ku-band (12-18 GHz) and successfully did the ranging of static targets at distances up to 43 metres. The range variation across the three used RF bands was minimal as shown in figure 1(b). The RF LFM chirp's central frequency tuneability is governed by the frequency offset between the LFM chirp modulated laser and the tuneable laser (Laser 2 from figure 1(a)). The overall bandwidth of the waveform generation system is limited only by the bandwidth of the photodetector. The system can very well operate with low-bandwidth Mach-Zehnder Modulators (MZM), used at the transmitter for the electro-optic modulation, and low bandwidth RF waveform generators for operation in much higher bandwidth RF bands thereby saving cost on expensive high-frequency equipment.

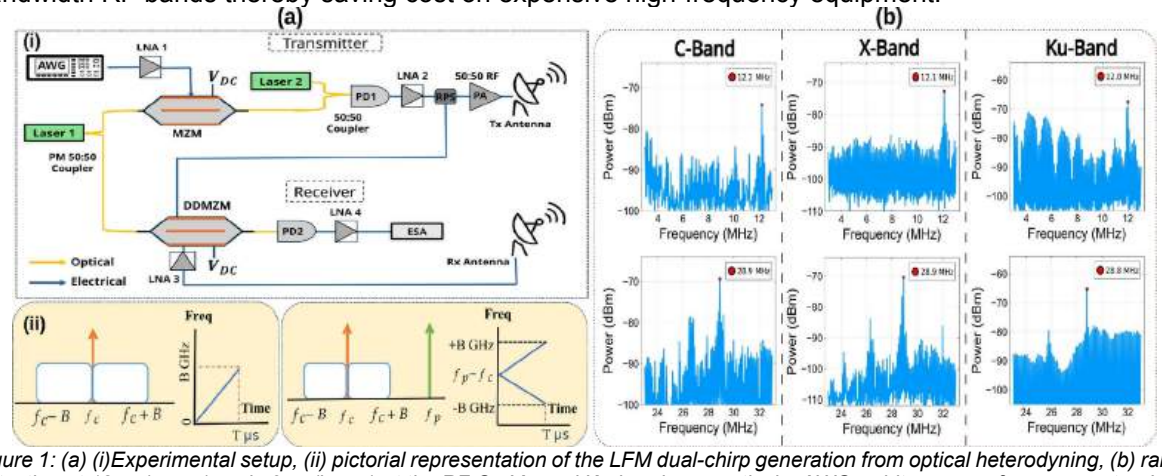


Figure 1: (a) (i)Experimental setup, (ii) pictorial representation of the LFM dual-chirp generation from optical heterodyning, (b) range detection at 18 m (upper) and 43 m (lower) at the RF C-, X-, and Ku-band, respectively. AWG: arbitrary waveform generator, LNA: low noise amplifier, MZM: Mach-Zehnder modulator, PD: Photodetector, RPS: RF Power Splitter, PA: power amplifier, PM: polarisation maintaining, DDMZM: dual-drive MZM, ESA: electronic spectrum analyser.

This approach provides an electronics' hardware-independent and cost-effective approach to MWP FMCW multi-band radar operation with high frequency-agility. The system's overall RF tuneability helps using the same MWP radar system across multiple RF bands helping reduce the overall cost and size footprint of the multi-band FMCW radar system.

This work is sponsored by the I-Hub Foundation for Cobotics (IHFC), IIT Delhi

References:

[1] J. Yao, J. Light. Technol. 40, 6595 (2022).
[2] M. Jha, L. Kumar, R. Dhawan, et al., Applied Optics 64, 6746 (2025).
[3] D. Liang, L. Jiang, and Y. Chen, J. Light. Technol. 39, 6470 (2021).
[4] M. Jha, A. Khanna, L. Kumar, et al., in *CLEO/Europe - EQEC*, (*Optica Publishing Group*, 2025).

Machine Learning prediction and experimental analysis of Potassium-thiourea complexes for Optical limiters

[1]Kalaivani H and [1, #]Chitra M
[1]Anna University, Chennai, India
[#] chitrashadrach@annauniv.edu

This work presents machine learning-enabled optical properties prediction in metal ion-incorporated potassium-thiourea complexes. The complexes were prepared using the solution evaporation method. The structural and optical characteristics were studied. The optical constants were ML-predicted and experimentally determined. The average error in ML prediction is 7.1%. The optical-limiting FOM is 11.89.

There is an ever-present demand for efficient NLO materials in the field of optics and laser technology. Metal-organic NLO materials possess the required high nonlinearity with added metallic stability, especially metal-thiourea complexes, which exhibit superior performance in various NLO applications, such as frequency doublers and optical limiters [1]. The experimental trial and error in finding efficient materials is time-consuming. A machine learning model which predicts the optical constants would be desirable.

A machine learning model was designed using the XGBoost method. A dataset of 2000 observations was used in designing the model. The workflow is shown in Figure 1. The algorithm would predict the optical constants such as refractive index, dielectric constant, optical bandgap, and third-order susceptibility. The average coefficient of determination R^2 was found to be 0.70.

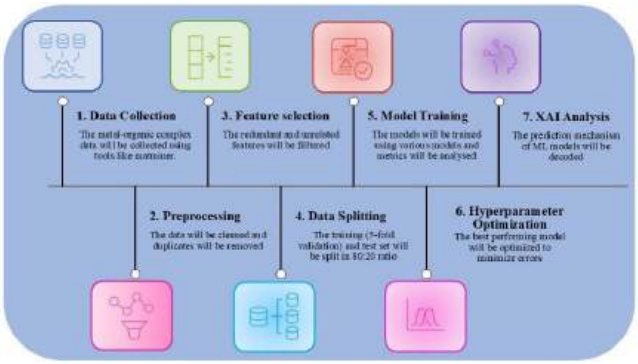


Fig 1: Machine Learning workflow

The experimental part of the work deals with the preparation of potassium-thiourea chloride (PTC) complexes using the solvent evaporation technique. The copper doping was done in different concentrations (5 mol% and 10 mol% CPTC). The complexes were studied using XRD, SEM, Optical absorption, and Z-Scan. The structural orientation was found to be more ordered with increased dopant concentration. The optical absorption analysis revealed that the complexes have a wider transparency window and a large band gap, essential for optical limiters [2]. The optical constants, such as bandgap, refractive index, extinction and absorption coefficient, and optical and electrical conductivity, were also calculated. The dopant shows a positive impact on the optical constants. The machine learning predictions and the experimental results were compared. The average error in prediction was found to be around 7.1%. The optical limiting figure of merit (FOM) [2] can be calculated using equation (1),

$$FOM = \frac{\beta\lambda}{n_2} \tag{1}$$

β, λ, and n_2 are non-linear absorption coefficient, non-linear refractive index, and wavelength of the laser respectively. These non-linear constants were calculated using the Z-Scan method. The figure of merit increased to 11.89 from 2.50 with doping. The copper doping aided in the increased performance in the linear and non-linear optical regimes, with the added advantage of improved stability. The ML model can be used for predicting properties in other complex combinations.

References:

[1] Albert, H. M., Shibu, S., Gupta, A., Ganganagunta, S., Neelima Patnaik, D., Rajagopalan, N. R., & Manoj Kumar, N *Journal of Nonlinear Optical Physics & Materials*, (2025). *34*(06), 2450019.

[2] S.M. Azhar, M. Anis, S.S. Hussaini, S. Kalainathan, M.D. Shirsat, G. Rabbani, Opt. Laser Technol. 87 (2017) 11–16

Hysteretic Piezochromism in a Lead Iodide-Based Two-Dimensional Inorganic-Organic Hybrid Perovskite

Mohammad Adnan[1,2], Paul Steeger[1], Thorsten Deilmann[1], Rudolf Bratschitsch[1] and G. Vijaya Prakash[3]
[1]Institute of Physics and Center for Nanotechnology, University of Münster, 48149 Münster, Germany
[2]Department of Physics, Aligarh Muslim University Aligarh 202002 India
[3]Nanophotonics Lab, Department of Physics, Indian Institute of Technology Delhi, New Delhi 110016, India
Author e-mail address: mohdadnan898@gmail.com

Abstract: Two-dimensional inorganic-organic hybrid perovskites are interesting due to their potential applications in photonics and optoelectronics. They are environmentally stable, and their chemical composition variations offer a wide range of bandgap energies. Alternatively, crystal deformation enables *in situ* control over their optical properties. Here, we investigate one of the two-dimensional hybrid perovskites $(C_6H_9C_2H_4NH_3)_2PbI_4$ (CHPI) containing alternate organic and inorganic layers. Pressure-dependent optical absorption and emission spectroscopy reveal a hysteretic piezochromism that was not reported for other lead iodide-based 2D perovskites. We combine our optical studies with high-pressure X-ray diffraction experiments and first-principles calculations to demonstrate that the deformation of the inorganic lead iodide layers is the main reason for the observed changes in the optical bandgap.

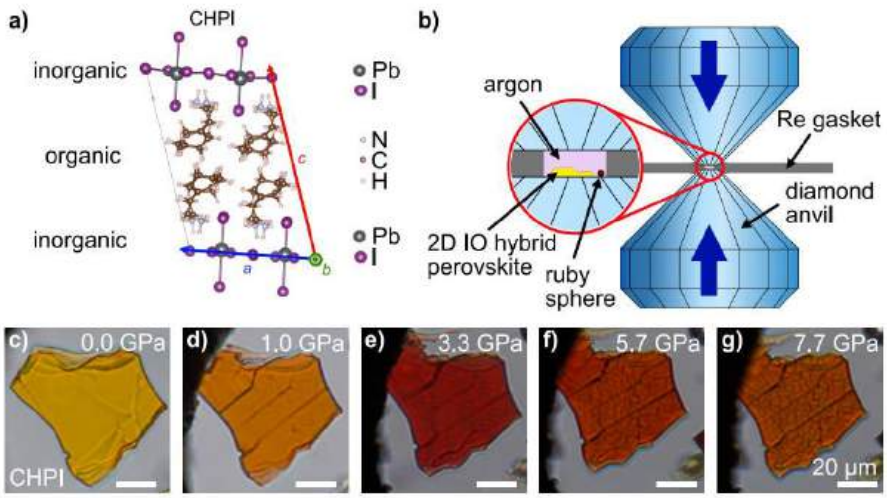


Figure 1. (a) Crystal structure packing of the 2D inorganic-organic hybrid perovskite CHPI. (b) Sketch of the diamond anvil cell (DAC). The sample is enclosed in argon, which is compressed between two diamond anvils creating quasi-hydrostatic pressure. (c-g) Piezochromism of CHPI crystals as seen in bright-field microscopic images at different pressures. The crystals change color from yellow to red upon compression. This trend reverses above 5 GPa.

References

[1] P. Steeger, M. Adnan, T. Deilmann, X. Li, S. Müller, K. Skrzyńska, M. Hanfland, E. Kolesnikov, J. Kösters, T. Block, R. Schmidt, I. Kupenko, C. Sanchez-Valle, G. Vijaya Prakash, S. M. Vasconcellos, and R. Bratschitsch, "Hysteretic Piezochromism in a Lead Iodide-Based Two-Dimensional Inorganic-Organic Hybrid Perovskite" J. Am. Chem. Soc. **146**, 23205-23211 (2024).

[2] L. Zhang, K, Wang, Y, Lin, B, Zou, "Pressure Effects on the Electronic and Optical Properties in Low-Dimensional Metal Halide Perovskites" J. Phys. Chem. Lett. **11**, 4693-4701 (2020).

Synthesis and Multifunctional Luminescence Properties of Mn^{2+}-Activated $Ca_2KZn_2(VO_4)_3$ Phosphors for White LEDs, Latent Fingerprint Visualization and Anti-Counterfeiting Applications

[1]Deepak Kumar,[1]Praveen Chandra Pandey
[1]Department of Physics, IIT (BHU), Varanasi, 221005, India

E-mail: pcpandey.app@iitbhu.ac.in

Mn^{2+}-activated $Ca_2KZn_2(VO_4)_3$ (CKZVO) phosphors were synthesised via solid-state reaction and investigated for multifunctional photonic applications. The phosphors exhibit broad visible luminescence, demonstrating potential for phosphor-converted white LEDs, latent fingerprint visualisation, and anti-counterfeiting, and for use as a promising rare-earth-free phosphor for sustainable optoelectronic and security technologies.

Rare-earth-free luminescent phosphors have emerged as promising alternatives for solid-state lighting and optical security owing to their low cost, environmental friendliness, and tunable emission characteristics. In this work, Mn^{2+}-activated CKZVO phosphors were synthesised by a conventional high-temperature solid-state reaction. Phase purity and crystal structure were confirmed by X-ray diffraction, while the optical properties were investigated using photoluminescence spectroscopy.

The Mn^{2+}-doped phosphors exhibit strong visible emission under ultraviolet excitation, originating from Mn^{2+} ions incorporated into the CKZVO host lattice. The luminescence intensity varies with dopant concentration, indicating the importance of optimising Mn^{2+} content to achieve maximum emission efficiency. The broad emission band and favourable optical characteristics suggest that the phosphor is suitable for phosphor-converted white light-emitting diode (pc-WLED) applications.

The multifunctional capability of the phosphor was further explored through forensic and security applications. Under ultraviolet illumination, the optimised phosphor produces high-contrast latent fingerprint images with clearly distinguishable ridge details on different substrates, demonstrating its potential for forensic identification. In addition, luminescent security patterns prepared using the phosphor exhibit bright emission under UV light while remaining inconspicuous under ambient conditions, making the material suitable for anti-counterfeiting and information encryption.

The simple synthesis route, efficient luminescence, and multifunctional performance demonstrate that Mn^{2+}-activated CKZVO is a promising rare-earth-free phosphor for emerging photonic applications, including solid-state lighting, forensic science, and optical security.

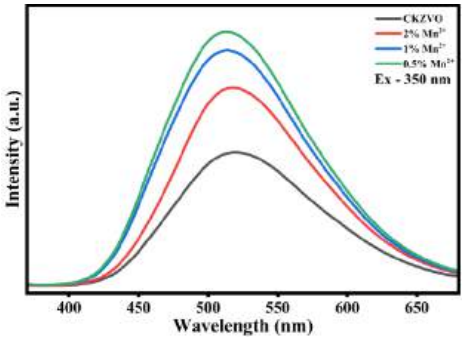


Figure 1 Photoluminescence emission spectra of $Ca_2KZn_2(VO_4)_3$ and Mn^{2+} doped *$Ca_2KZn_2(VO_4)_3$* phosphor under excitation of 350 nm.

Reference:

[1] Bharat, L. Krishna, Soo-Kun Jeon, Kurugundla Gopi Krishna, and Jae Su Yu. "Rare-earth free self-luminescent Ca2KZn2 (VO4) 3 phosphors for intense white light-emitting diodes." *Scientific Reports* 7, no. 1 (2017): 42348.

[2] Li, Junfu, Kehui Qiu, Junfeng Li, Wei Li, Qian Yang, and Junhan Li. "A novel broadband emission phosphor Ca2KMg2V3O12 for white light emitting diodes." *Materials Research Bulletin* 45, no. 5 (2010): 598-602.

Bias Tunable Negative-to-Positive Photoresponse Transition in Anisotropic $ReSe_2$ Single Crystals

Riddhi B. Palan[1*], Bhavesh Socha[2], Aamir Khatri[1], Trusha D. Ahir[1], Kaushal Agheda[2], K. D. Patel[1], G. K. Solanki[1#],

[1]Department of Physics, Sardar Patel University, Vallabh Vidyanagar-388120, Gujarat, India

[2]Department of Materials Science, Sardar Patel University, Vallabh Vidyanagar -388120, Gujarat, India

Email: [*] riddhipalan10@gmail.com ,[#] solankigunvant@yahoo.co.in

High-quality triclinic $ReSe_2$ single crystals synthesized by direct vapor transport were comprehensively characterized and integrated with DFT analysis. Anisotropic photodetectors exhibited a novel bias-tunable negative-to-positive photoresponse transition, achieving 1.68 μA/W responsivity, 1.43 ×10^8 Jones detectivity, 52 ms response, enabling multifunctional optoelectronic applications through crystal chemistry-guided device engineering with excellent stability.

Two-dimensional (2D) transition metal dichalcogenides (TMDCs) have emerged as promising materials for next-generation optoelectronics owing to their unique electronic and optical properties[1]. Among them, triclinic $ReSe_2$ remains relatively unexplored despite its pronounced in-plane anisotropy, weak interlayer coupling, and biaxial optical characteristics[2].

Herein, high-quality $ReSe_2$ single crystals were synthesized via direct vapor transport (DVT) and comprehensively characterized using PXRD, SEM, DRS, Raman spectroscopy, and HRTEM. Notably, this work presents the first systematic crystallite size and microstrain analysis of triclinic $ReSe_2$ using multiple PXRD models, together with the first integrated Hirshfeld surface and density functional theory (DFT) investigation to establish the crystal chemistry optoelectronic property relationship. A single crystal photodetector was systematically investigated under different crystallographic orientations, illumination intensities, excitation wavelengths, and bias conditions. Remarkably, a previously unreported bias-tunable negative-to-positive photoresponse transition was observed, demonstrating dual photodetection and photomemory functionality[3]. Under 633 nm illumination, the device exhibited a responsivity of 1.68 μA W^{-1}, a detectivity of 1.43 × 10^8 Jones, and a rapid response time of 52 ms, together with excellent operational stability. These findings establish anisotropic $ReSe_2$ as a promising platform for multifunctional, high-performance optoelectronic devices and provide fundamental insights into crystal chemistry-guided device engineering[4].

References:

[1] B. Peng, P.K. Ang, K.P. Loh, Two-dimensional dichalcogenides for light-harvesting applications, Nano Today 10 (2015) 128–137. https://doi.org/10.1016/j.nantod.2015.01.007.

[2] H. Tian, J. Tice, R. Fei, V. Tran, X. Yan, L. Yang, H. Wang, Low-symmetry two-dimensional materials for electronic and photonic applications, Nano Today 11 (2016) 763–777. https://doi.org/10.1016/j.nantod.2016.10.003.

[3] Y. Wang, E. Liu, A. Gao, T. Cao, M. Long, C. Pan, L. Zhang, J. Zeng, C. Wang, W. Hu, S.-J. Liang, F. Miao, Negative Photoconductance in van der Waals Heterostructures-Based Floating Gate Phototransistor, n.d.

[4] A. Rani, A. Verma, B.C. Yadav, Advancements in transition metal dichalcogenides (TMDCs) for self-powered photodetectors: challenges, properties, and functionalization strategies, Mater. Adv. 5 (2024) 3535–3562. https://doi.org/10.1039/d3ma01152f.

Photoluminescence Characterization of SrNaKBiB: Dy^{3+} Glasses for w-LED Applications

[1#]Jyoti Singh, [2]Sk. Mahmuda, [1]Sukhdev Roy, [1]Aman Prasad

[1]Department of Physics and Computer Science, Dayalbagh Educational Institute, Agra, 282005.

[2]Department of Physics, K.L. University, Green Fields, Vaddeswaram 522502, AP.

#jyotisingh1@dei.ac.in

SrNaKBiB: Dy^{3+} glasses were synthesized, characterized and the Judd-Ofelt theory was used to obtain various radiative parameters that include transition probability (A_R), radiative lifetime (β_R), branching ratio (τ_R) and stimulated emission cross-sections (σ_{se}). The results show their suitability for lasing applications with improved properties.

White light emitting diodes (w-LEDs) have almost replaced incandescent and fluorescent lamps due to their advantages like, high reliability, high luminous efficiency, long lifetime and low energy consumption. In general, rare earth (RE) ions doped glasses can improve w-LED characteristics such as color purity and color reproduction range and are widely used in various applications, such as optical detectors, bulk lasers, optical lenses and fibers for high-speed data transmission. In this research work, we have synthesized Strontium Sodium Potassium Bismuth Borate (SrNaKBiB) glasses doped with Dy^{3+} ions to improve luminous efficiency, thermal stability and color tunability. Boron trioxide (B_2O_3) is an excellent glass former, which helps to manufacturing glass, but it has high phonon energy. This drawback is removed by adding heavy metal oxides like Bi_2O_3, which enhances infrared emission. Heavy-metal glasses (Bi, Ba) further improve refractive index, density, and radiation resistance. SrO improves density, refractive index and thermal stability and also reduces hygroscopicity of borate glass, which enhances its durability. Na_2CO_3 and K_2CO_3 have lower cost, moderate phase transition temperature and low corrosivity. K_2CO_3 provides K_2O, which modifies the glass network, lowers melting temperature, and enhances optical quality. Na_2O helps in enhancing the glassy nature and improves the optical and shielding properties of prepared glasses. Considering these advantages, SrNaKBiB glasses have been developed as potential materials for w-LEDs, lasing and other solid-state lighting applications. Here, a series of SrNaKBiB glasses of varying concentrations of dysprosium (Dy^{3+}) has been prepared. The photoluminescence spectra of Dy^{3+} ions doped SrNaKBiB glasses exhibit intense emission at 575 nm corresponding to the transition $^4F_{9/2} \rightarrow {}^6H_{13/2}$ under 388 nm excitation wavelength. Optimized concentration of Dy^{3+} was observed to be 1.0 mol%. The CIE chromaticity coordinates and color correlated temperature (CCT) values of optimized glass sample are (0.3443, 0.3578) and 5048 K respectively, which imply natural cool white light. According to temperature dependent photoluminescence (TDPL) spectra, the glasses retain 53.5% of their luminescence intensities at 175^0C demonstrating excellent thermal stability. The Judd-Ofelt intensity parameters indicate high asymmetry and covalency of Dy^{3+}-O bond, with $\Omega_2 > \Omega_6 > \Omega_4$ being observed for all prepared samples. Branching ratio (β_R) is more than 60%, which confirms the lasing potential of the of SrNaKBiB: Dy^{3+} glasses.

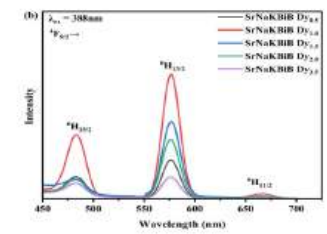


Fig.1: Emission Spectra

References:

[1] P. Kumari, A. Kumar, S. Kumari, S. Mahamuda, S. Roy, A. Prasad, A. S. Rao, *Ceramics International,* 52, 4614-4624 (2025).

[2] S. Kumari, P. Rohilla, A. Prasad, A.S. Rao, R.K. Sinha, *Journal of Luminescence,* 275 120791 (2024).

Direct Vapour Transport Grown WS_2 Single Crystals for Multifunctional Visible-Light Photodetection and Photocatalytic Degradation Applications

[1,#]Kalpitkumar V. Vaniya,[1]Devang R. Dhorada, [1]Kevin K. Bhander, [1]Jay B. Ka. Patel, [1]Gunvant K. Solanki, [1,##]Kireetkumar D. Patel

[1]Department of Physics, Sardar Patel University. Vallabh Vidyanagar 388120, Anand, Gujarat, India

[#]Kalpitkumar V. Vaniya: kalpitkumarvaniya77@gmail.com,

[##]Kireetkumar D. Patel: kdpatel-phy@spuvvn.edu

WS_2 single crystals synthesized by direct vapour transport exhibited excellent structural and optical quality with bifunctional performance in photodetection and photocatalysis. The crystal photodetector achieved 425 μA/W responsivity and 2×10^8 Jones detectivity, while powdered WS_2 degraded methylene blue and acridine orange by 93.97% and 93.06%, respectively.

Transition metal dichalcogenides (TMDCs) have attracted considerable attention for next-generation optoelectronic and environmental applications owing to their unique layered structure and excellent electronic, optical, and catalytic properties. In this work, high-quality **WS_2 single crystals** were successfully synthesized by the **Direct Vapour Transport (DVT)** technique and investigated for bifunctional applications in **visible-light photodetection** and **photocatalytic dye degradation**. The as-grown crystals were employed for photodetector fabrication, whereas finely ground crystal powder was utilized for photocatalytic studies.

The structural, morphological, elemental, and optical properties of the synthesized crystals were systematically characterized using **X-ray diffraction (XRD), scanning electron microscopy (SEM–EDAX), UV–Visible diffuse reflectance spectroscopy (UV–DRS), and Raman spectroscopy**. The characterization results confirmed the formation of highly crystalline hexagonal WS_2 with layered morphology, near-stoichiometric composition, and strong visible-light absorption.

The optoelectronic performance was evaluated using a crystal-based photodetector with an active area of **2 mm²** under **white, red, green, and blue LED** illumination over an intensity range of **20–100 mW/cm²** at applied biases of **0, 0.05, and 0.1 V**. The device exhibited stable photo-switching with rise and decay times of approximately **100 ms**. The highest performance was achieved under **100 mW/cm² white-light illumination** at **0.1 V**, delivering a responsivity of **425 μA/W** and a detectivity of **2×10^8 Jones**.

The photocatalytic activity of finely ground WS_2 crystal powder was investigated under visible-light irradiation using **Methylene Blue (MB)** and **Acridine Orange (AO)** dyes with a catalyst loading of **1 g/L** and dye concentration of **0.1 g/L**. The photocatalyst achieved degradation efficiencies of **93.97% for MB within 300 min** and **93.06% for AO within 140 min**.

Overall, the successful realization of **low-voltage photodetection** and **efficient visible-light photocatalysis** using the same DVT-grown WS_2 crystal demonstrates its potential as a multifunctional material for advanced optoelectronic devices and environmental remediation.

Acknowledgement

The authors acknowledge the financial support from the Department of Science and Technology (DST), Government of India, through the INSPIRE Fellowship (IF230131), and the Department of Physics, Sardar Patel University, for research facilities.

References:

[1] T. Ma *et al.*, “Recent Progress in Photodetectors: From Materials to Structures and Applications,” Oct. 01, 2024, *Multidisciplinary Digital Publishing Institute (MDPI)*. doi: 10.3390/mi15101249.

[2] M. Long, P. Wang, H. Fang, and W. Hu, “Progress, Challenges, and Opportunities for 2D Material Based Photodetectors,” May 09, 2019, *Wiley-VCH Verlag*. doi: 10.1002/adfm.201803807

[3] R. B. Palan, T. D. Ahir, S. A. Bhakhar, S. Sharma, and G. K. Solanki, “Enhanced photocatalytic performance of two-dimensional NixRe1-xSe2 (x = 0 & 0.25) crystalline material: Exploring its potential as a high-efficiency catalyst,” *Journal of Physics and Chemistry of Solids*, vol. 195, Dec. 2024, doi: 10.1016/j.jpcs.2024.112285.

Photoluminescence Studies of $SrBi_2Ta_2O_9$: Dy^{3+}/Eu^{3+} Phosphors for w-LED Applications

[1#]Ritwik Raj Watsh, [1]Ashok Jangid, [1]Aman Prasad

[1]Department of Physics and Computer Science, Dayalbagh Educational Institute, Agra, 282005.

[#]ritwikraj2400783@dei.ac.in

$SrBi_2Ta_2O_9$:Dy^{3+}/Eu^{3+} phosphors were synthesized via solid-state reaction. Under UV excitation, Dy^{3+}-doped samples emitted blue light (480 nm) and yellow light (572 nm) whereas Dy^{3+}/Eu^{3+} co-doped phosphors showed enhanced red emission (615 nm and 651 nm) due to energy transfer. These phosphors are suitable for red emitting component in w-LEDs.

In recent years,w-LEDs have emerged as a promising lighting technology due to their high energy efficiency, long lifetime, excellent reliability, and eco-friendly nature. Among the various phosphor materials, rare-earth (RE) ion-doped phosphors have attracted considerable attention due to their high luminescence efficiency, excellent thermal and chemical stability, and tunable emission characteristics. By selecting appropriate RE activator ions, the emission color can be effectively controlled, leading to improved color purity and correlated color temperature.In the present work, Dy^{3+}/Eu^{3+}-doped $SrBi_2Ta_2O_9$ phosphors were synthesized to investigate their structural, morphological and luminescence behaviour along with thermal stability for potential solid-state lighting applications.It is an attractive host lattice owing to its excellent chemical and thermal stability, low phonon energy, and efficient energy transfer capability. The incorporation of Dy^{3+} ions produces characteristic blue and yellow emissions, enabling efficient white-light.Eu^{3+} ions were incorporated into the $SrBi_2Ta_2O_9$ lattice as an efficient red-emitting activator for white LED (w-LEDs) applications. It exhibits intense red emission around 615 nm due to the characteristic $^5D_0 \rightarrow {}^7F_2$ transition. In co-doped Dy^{3+}/Eu^{3+} phosphors, energy transfer takes place as emission bands of Dy^{3+} overlap with the excitation bands of Eu^{3+} and, part of the energy stored in excited Dy^{3+} ions is transferred non-radiatively to nearby Eu^{3+} ions through dipole–dipole interaction. The combined emissions enable tunable luminescence with improved CRI and warm white light along with excellent thermal stability and high luminescence efficiency.Here, a series of $SrBi_2Ta_2O_9$:Dy^{3+}/Eu^{3+} phosphors has been prepared via a solid state reaction method.These samples were then characterized by using techniques like XRD,SEM,FTIR,Photoluminescence (PL), Temperature dendent PL, UV-Vis and Time decay (TRPL) spectroscopies. The photoluminescence spectra of Dy^{3+} ions doped $SrBi_2Ta_2O_9$ phosphor exhibit intense emission at 572 nm corresponding to the transition $^4F_{9/2} \rightarrow {}^6H_{13/2}$ under 352 nm excitation wavelength. Optimized concentration of Dy^{3+} was observed to be 3.0 mol%. After fixing Dy^{3+} at 3 mol% and varying the concentration of Eu^{3+} in the Dy^{3+}/Eu^{3+} co-doped phosphor, intense emission at 615 nm corresponding to the transition $^5D_0 \rightarrow {}^7F_2$ under 352 nm excitation wavelength was seen whose intensity increased till 5.0 mol% of Eu^{3+}. The optical energy band gaps for the co-doped samples were found to be in the range of 5.21-5.33 eV using Tauc's plot. To study concentration quenching mechanism, a Dexter plot was drawn that showed a slope of 5.3 implying dipole-dipole interaction between the RE ions. CIE confirmed the reddish-orange to yellow emission suitable for w-LEDs applications to improve CRI and create warm white light proving it potential candidates for red emitting components in w-LEDs and solid-state lighting applications.

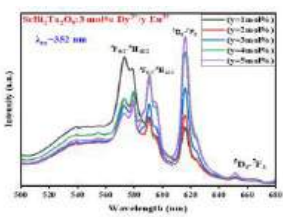


Fig.1: Emission Spectra

References:

[1] P. Rohilla, S.Kumari, Anu, S. Barik, K.kumar, G. Ahmad, A. S. Rao, & A.Prasad , *Materials Science and Engineering* B, 319 18368 (2025).

[2] S. Kumari, P. Rohilla, A. Prasad, A.S. Rao, R.K. Sinha, *Journal of Luminescence,* 275 120791 (2024).

Free-Space Optical Neural Network Using a Scalable Mach-Zehnder Interferometer Mesh

[1,*]Zoya Fatima,[1,#]Biswajit Pathak and [2]Deepak Mishra

[1]Department of Physics Indian Institute of Space Science and Technology, Thiruvananthapuram-695547, Keralam

[2]Department of Avionics Indian Institute of Space Science and Technology, Thiruvananthapuram-695547, Keralam

*Corresponding Author(s): *zoya.sc25m119@pg.iist.ac.in; #biswajitpathak@iist.ac.in*

This work demonstrates a scalable free-space Mach-Zehnder interferometer (MZI) mesh framework for optical matrix multiplication using singular value decomposition (SVD). Three progressive training configurations are evaluated, on Fashion-MNIST, with the trained configuration surpassing the electronic MLP baseline on Fashion-MNIST. Energy conservation and hardware viability are validated with numerical simulation.

Optical Neural Networks (ONNs) exploit the passive energy efficiency and parallelism of photonic systems as a compelling alternative to electronic AI hardware [1]. This work presents a scalable free-space Mach-Zehnder interferometer (MZI) mesh for optical matrix-vector multiplication. Using singular value decomposition (SVD) [2], any real matrix is factorized as $A = U\Sigma V^{T}$, where U and V are unitary matrices physically realized by cascaded MZI layers and Σ by optical attenuators. Each MZI implements the transfer matrix, which is unitary by construction, guaranteeing energy conservation. Alternating even-odd pair coupling across successive layers approximates a dense random unitary transformation, consistent with Johnson-Lindenstrauss theory, providing the theoretical basis for effective classification without phase training. Scalability is demonstrated via a 4×4 optical unitary core as shown in Fig. (1) implementing $E' = U^{4}E$ through cascaded MZI layers with alternating pair coupling, confirming hardware viability for N×N architectures. The ONNs execute computations at high speeds, consume minimal power, and offer inherent parallelism compared to traditional electronic neural networks.

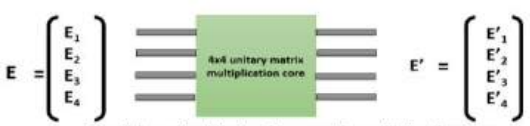
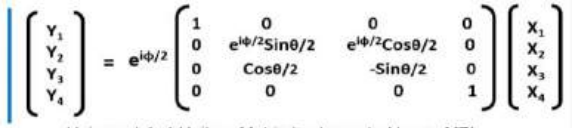


Fig. 1 An optical 4x4 unitary matrix multiplication core



Universal 4×4 Unitary Matrix implemented by an MZI

Three progressive configurations are evaluated on MNIST and Fashion-MNIST against electronic MLP baselines of 98.4% and 87.1% respectively. Stage I — random MZI phases with nearest-neighbor classification achieves 96.57% on MNIST and 85.53% on Fashion-MNIST, demonstrating remarkable untrained optical feature extraction. Stage II — same random phases with a trained hidden-layer readout improves to 97.24% and 88.70%, the Fashion-MNIST result exceeding the electronic MLP baseline without hardware modification. Stage III — joint phase perturbation and readout optimization achieves 97.34% on MNIST and 88.77% on Fashion-MNIST as shown in Fig. (3). Classification accuracy scales as shown in Fig. (2) from 79.2% (4x4) to 97.34% (28x28), confirming pixel resolution as key performance parameter.

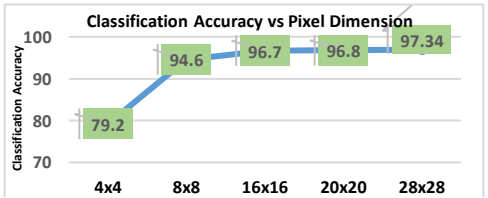


Fig. 2 Classification accuracy vs pixel dimension (MNIST)

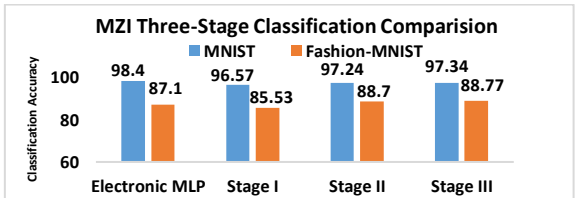


Fig.3 Three-stage accuracy comparison with Electronic MLP

References:

[1] Fu, T., Zhang, J., Sun, R., Huang, Y., Xu, W., Yang, S. *Light: Science & Applications 13(1),p.263,* (2024).
[2] Reck, M., Zeilinger, A., Bernstein, H. J., & Bertani, P. *Physical Review Letters*, *73*(1), 58, (1994).

Machine Learning Assisted Predictive Model of Fano Resonances in Waveguiding Plasmonic Crystals

[1,#]Suman Mandal, [1]Apuroop Vaidyam, [2]Kripabandhu Ghosh and [1]Nirmalya Ghosh

[1]Department of Physical Sciences, Indian Institute of Science Education and Research Kolkata, Mohanpur, West Bengal 741246, India

[2]Department of Computational and Data Sciences, Indian Institute of Science Education and Research Kolkata, Mohanpur, West Bengal 741246, India

[#]*sm22rs100@iiserkol.ac.in*

We are numerically investigating Fano resonances in waveguiding plasmonic crystals using finite-element method simulations. Systematic variations in structural and illumination parameters are being used to generate a comprehensive resonance dataset. The predictive performance of least-squares, random-forest and XGBoost regression models is being evaluated for previously unseen grating configurations.

In a waveguiding plasmonic crystal, the Fano response arises from interference between a broad plasmonic resonance and a narrow quasiguided resonance under TM illumination, whereas under TE illumination, it results from interference between the narrow quasiguided resonance and the broad photon continuum. This interference produces an asymmetric line shape characterized by a sharp peak followed by a pronounced dip. Refractive index-induced spectral shifts and sharp, tunable asymmetric line shapes make Fano resonances attractive for sensing, narrowband filtering, and tunable nanophotonic applications.

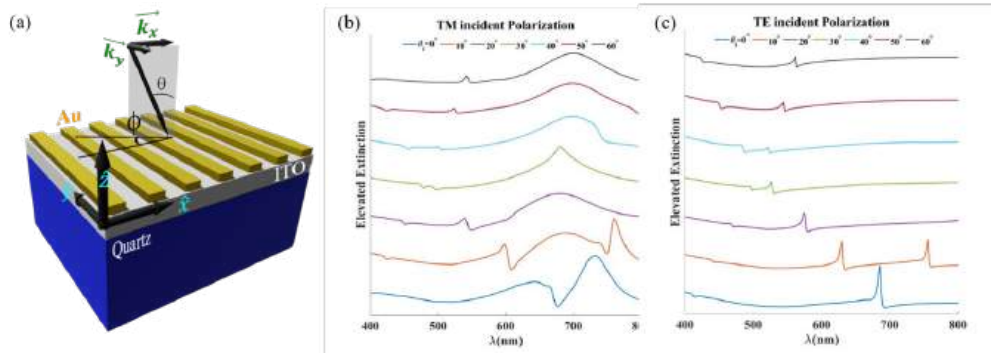


Fig. 1: (a) Schematic illustration of the WPC geometry, consisting of a periodic gold grating deposited on an ITO waveguiding layer above the substrate. (b) and (c) Extinction spectra of the WPC for angles of incidence varied from 0° to 60° in steps of 10° under incident TM polarization (b) and TE polarization (c), over the wavelength range 400–800 nm.

The periodicity, width and height of the gold grating, together with the incident polarization and angle of incidence, are being systematically varied, and the optical response of a waveguiding plasmonic crystal is computed using the finite-element method. For each configuration, the Fano dip wavelength is extracted from the simulated spectrum. The results reveal no simple linear relationship between the Fano resonance wavelength and the input parameters, making the system suitable for machine-learning applications.

A randomly selected 70% of the simulated data is being used to train the predictive models, while the remaining 30% is kept unseen during training and used only for testing. In this poster, we present a comparative study of three regression approaches: the conventional least-squares method, random-forest regression and XGBoost regression. The least-squares method provides a simple baseline, whereas the two ensemble-learning methods are capable of capturing more complex nonlinear relationships among the structural parameters, illumination conditions and Fano dip wavelength.

This simulation-assisted machine-learning framework enables rapid prediction of Fano dip wavelengths for unseen configurations, reducing the need for repeated full-wave simulations and facilitating the optimization of waveguiding plasmonic crystals.

References:

[1] S. Mandal, A. Vaidyam, N. Kumar, S. Rajak, S. Guchhait and N. Ghosh, *Journal of the Optical Society of America B* 43(8) (2026) B58–B65.

[2] S.K. Ray, S. Chandel, A.K. Singh, A. Kumar, A. Mandal, S. Misra, P. Mitra and N. Ghosh, *ACS Nano* 11(2) (2017) 1641–1648.

Engineering Multipurpose Terahertz Metamaterials Using a Machine Learning Approach

[1,#]Lavi Kumar Vaswani,[2]Ali Nawaz, [3]Bhagwat Singh Chouhan, [1]Anuraj Panwar, [2]Amir Ahmad and [3,4]Gagan Kumar

[1]Department of Physics and Materials Science and Engineering, Jaypee Institute of Information Technology, Noida, 201309, Uttar Pradesh, India

[2]Department of Information Systems and Security, College of Information Technology, United Arab Emirates University, Al Ain, United Arab Emirates

[3]Department of Physics, Indian Institute of Technology Guwahati, Guwahati, 781039, Assam, India

[4]Department of Physics, Indian Institute of Technology Ropar, Rupnagar, 140001, Punjab, India

[#] *corresponding author: lavivaswani37@gmail.com*

The advancement of terahertz technology requires the development of multipurpose metamaterials. In this study, we utilize a machine-learning framework for rapid and efficient design of multipurpose metamaterials, enabling bidirectional prediction of transmission responses and structural parameters. Predicted results are validated through simulations and experiments, showing strong agreement with target spectra.

To realize a multipurpose metamaterial design, we propose a novel metamaterial (MM) structure comprising seven variable parameters. The MM is patterned on a quartz substrate with a relative permittivity of 4.4. The metallic layer is aluminum with a thickness of 200 nm, as shown in Fig. 1. The seven geometric parameters include r_1 to r_6, representing the distances from the center to each edge of the star-shaped resonator, and the gap (g), which varies with g_1 according to g1 = 28 micron - g. Approximately 2200 EIT and BIC datasets are generated using numerical simulations in CST Microwave Studio for machine-learning training. Simulations are performed using the frequency-domain solver with unit-cell boundary conditions along the X and Y directions. At the same time, a y-polarized THz wave is incident along the positive Z direction. Adaptive mesh refinement is applied during simulations.

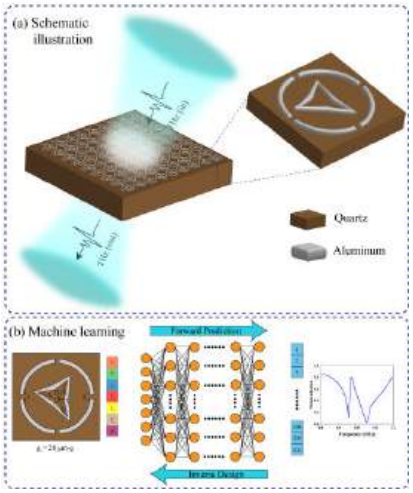


Fig. 1: a) Schematic illustration of the designed MM and unit cell of the MMs. (b) Machine learning framework for forward and inverse prediction of transmission and structural parameters.

The forward and inverse-design capability of the trained machine-learning model to predict the different transmission spectra and target EIT and BIC structural parameters is evaluated [1,2]. The simulated and target spectra exhibit good agreement with predicted results. Subsequently, the predicted parameters of inverse modelling are used to fabricate the metamaterial via photolithography, and the fabricated samples are experimentally characterized using terahertz time-domain spectroscopy (THz-TDS). The experimentally obtained transmission spectra also demonstrate good agreement with both simulations and target spectra.

In conclusion, this work demonstrates the integration of machine learning with terahertz metamaterials for the rapid and precise development of multipurpose devices. The resulting simulated and experimental transmission spectra show good agreement with the target responses. This approach significantly accelerates the design and fabrication of multipurpose metamaterials and provides a promising pathway for advancing terahertz technologies.

References:

[1] C. S. Ha, D. Yao, Z. Xu, C. Liu, H. Liu, D. Elkins, M. Kile, V. Deshpande, Z. Kong, M. Bauchy, and X. Zheng, *Nature Communications* 14 (2023) 5765.

[2] B.S. Chouhan, A. Nawaz, A. Das, Rohith KM, A. Ahmad, G. Kumar, *Journal of Lightwave Technology* 43 (2024) 2734-2744.

Learned ADMM for Fast Image Reconstruction in Digital Lensless In-line Holographic Microscopy

[1]Abhishek Verma, [1]Ritish Kamboj, and [1#]Satish Kumar Dubey

[1]SeNSE – Centre for Sensors, Instrumentation and Cyber-Physical System Engineering, Indian Institute of Technology Delhi, Hauz Khas, New Delhi 110016, India

[#]satishdubey@sense.iitd.ac.in

We present a fast image reconstruction framework for Digital Lensless In-line holographic microscopy (DLIHM). We use 10 ADMM unrolled iterations and train iteration parameters. The proposed method provides reconstruction in ~10 iteration steps of ADMM with only 30 (3/iteration) learnable parameters and takes around 5ms for images of size 512x512.

DLIHM is a computational imaging technique that provides quantitative phase imaging without needing any imaging lenses. It provides a large field of view, numerical refocusing capability, and a compact, low-cost system architecture, making it highly suitable for biomedical and point-of-care imaging applications [1-2,9]. DLIHM encodes the objects complex amplitude information as intensity modulations in the diffraction intensity measurements (I_z). However, the image reconstruction in DLIHM remains computationally intensive and parameter-sensitive. Recently, deep learning-based image reconstruction methods have been proposed [3,4,7] which generally lack convergence guarantees or domain generalizations, this motivates physics-aware learned reconstructions [6]. However, most supervised learned methods require large datasets, while untrained methods avoid this at the cost of slow per-image optimization. In this work we solve this problem by using unrolled alternating direction method of multipliers (ADMM) iterations [5,6] by learning 30 parameters, 3 per iteration for image reconstruction. Since the number of learnable parameters is very small, only a small training dataset is needed. The model learns optimal step sizes and regularization weights from paired simulated holograms and ground-truth complex object fields generated from approximately 100 natural images (512×512) [8]. The holograms were simulated using the angular-spectrum method with 2μm pitch, 500nm wavelength, and five axially shifted diffraction intensity measurements at z ∈ {1,2,3,5,10} mm. Training needs only a few (~50) epochs and training time is around 5 minutes using a single NVIDIA RTX 4090 GPU. The learned ADMM reconstruction takes around 5ms (≈200 reconstructions/s); a representative reconstruction is shown in Fig. 1 validates the performance of proposed reconstruction method.

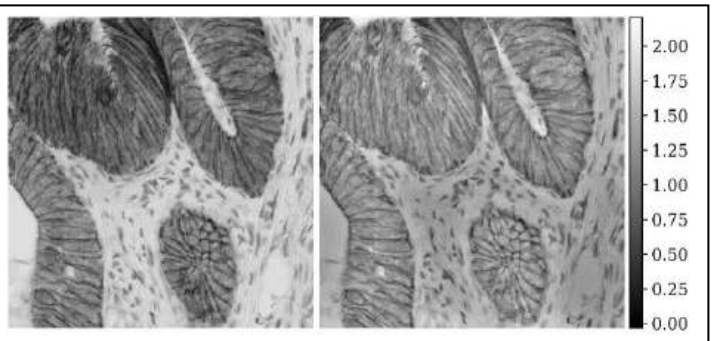


Figure 1 Image reconstruction using learned ADMM from simulated data. Ground truth object phase on the left and corresponding reconstructed from image diffraction intensity measurements shown on right on the right.

In summary, the lightweight unrolled-ADMM framework for DLIHM learns only 30 parameters from minimal training data and reconstructs holograms in ~5 ms, making it a potential candidate for near real-time point-of-care lensless imaging. Future work will focus on validating the method on experimental data.

References

[1] Y. Wu, A. Ozcan, *Methods* 136, 4–16 (2018).
[2] A. Greenbaum, W. Luo, T.-W. Su, Z. Göröcs, L. Xue, S. O. Isikman, A. F. Coskun, O. Mudanyali, A. Ozcan, *Nat. Methods* 9(9), 889–895 (2012).
[3] K. Monakhova, J. Yurtsever, G. Kuo, N. Antipa, K. Yanny, L. Waller, *Opt. Express* 27, 28075–28090 (2019).
[4] G. Ongie, A. Jalal, C. A. Metzler, R. Willett, R. Heckel, *IEEE J. Sel. Areas Inf. Theory* 1(1), 39–56 (2020).
[5] Y. Yang, J. Sun, H. Li, Z. Xu, *Adv. Neural Inf. Process. Syst. (NeurIPS)* 29 (2016).
[6] M. Mel, P. Springer, P. Zanuttigh, Z. Haitao, A. Gatto, Computer Vision – ECCV 2024, LNCS 15129, Springer, Cham (2025)
[7] K. Wang, E. Y. Lam, *Adv. Photonics Nexus* 3(5), 056006 (2024).
[8] R. Singh, 130k Images (512×512) *Universal Image Embeddings*, Kaggle (2023).
[9] R. Kamboj, B.S. Ahluwalia, S. K. Dubey, in Appl. Opt. 65, 6093-6103 (2026)

Physics-Consistent Direct Modal Regression for High-Order Clinical Wavefront Retrieval from Shack–Hartmann Sensors

[1]Vinay Yadav, [1]Navaneeth V Munavalli, [1]Gungun Agarwal, [1]Sakshi, [1]Sushma Chaudhary and [1]Nagendra Kumar*
[1]Indian Institute of Information Technology Vadodara

*nagendra_kumar@iiitvadodara.ac.in

We present a physics-consistent deep learning framework for retrieving ocular Zernike coefficients directly from Shack-Hartmann intensity images. By bypassing centroiding bottlenecks, our direct regression approach (DR-CNN, DR-ResNet) achieves superior reconstruction fidelity (0.015–0.018 μm RMSE) against spatial reconstructors (SR-UNet) and classical methods under noisy clinical conditions.

Adaptive optics (AO) relies on Shack–Hartmann wavefront sensors (SHWS) to measure optical aberrations. However, classical reconstruction algorithms (e.g., Southwell, Modal, FFT based) are bottlenecked by sequential spot localization, centroid estimation, and slope calculation. Under realistic conditions, sensor noise and localized spot deformations introduce centroiding errors that propagate into phase integration, severely degrading high-order spatial reconstructions.

To overcome this gradient bottleneck, we propose a direct image-to-coefficient regression mapping. To ensure practical realism, we developed a high-fidelity forward model configured to match a commercially available SHWS (Thorlabs WFS20-7AR with a 46 × 46 hexagonal array). By encompassing diffraction-limited spot formation, photon shot noise, and electronic read noise, this model generates realistic, bias-free training data. The incident aberrated wavefront over the pupil is represented using orthonormal Zernike polynomials:

$$W(\rho,\theta)=\sum_{j=1}^{N} a_j Z_j(\rho,\theta)$$

We trained direct regressors (DR-CNN, DR-ResNet) to map raw intensity directly to 36 Zernike coefficients (Z4 to Z39), using a weighted Huber loss to balance the ocular power-law energy distribution. These were evaluated against a hybrid spatial reconstructor (SR-UNet) that relies on an intermediate phase map.

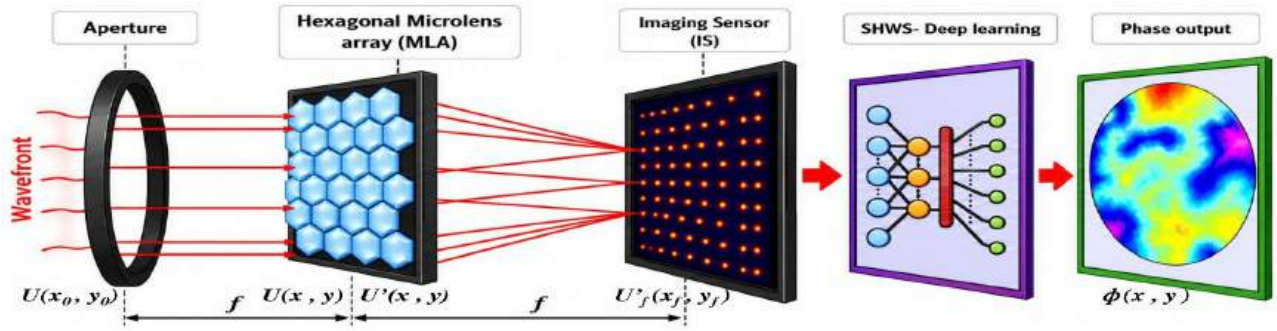


Fig. 1: Overview of the proposed framework for direct ocular wavefront estimation from Shack–Hartmann wavefront sensor measurements.

Validation on clinically acquired wavefronts from diseased eyes confirmed the superiority of direct modal regression. DR-CNN and DR-ResNet achieved mean root-mean-square errors (RMSE) of 0.015 μm and 0.018 μm respectively, drastically outperforming SR-UNet (0.108 μm) and traditional gradient-based solvers.

By bypassing conventional center-of-mass (CoM) slope extraction, the direct regressors implicitly function as non-linear, noise-aware estimators. They preserve high-frequency spatial morphology and prevent classical modal instability, providing a robust, highly scalable solution for real-time wavefront characterization in challenging AO environments.

References:

[1] Noll, Robert J. , *Journal of the Optical Society of America* 66.3 (1976): 207-211.
[2] N. Kumar, P. Choudhury, and S. G. Buddha, IEEE Sensors Journal, vol. 25, no. 3, pp. 4769–4776, 2024
[3] Platt, Ben C., and Roland Shack. , *Journal of refractive surgery* 17.5 (2001): S573-S577.

Hybrid AI-Assisted Laser Guide Star Adaptive Optics for High-Resolution Astronomical Imaging

NANDANA RS

Department of Physics, National Institute of Technology Karnataka (NITK), Surathkal, Srinivasnagar, Mangaluru – 575025, Karnataka, India

rsnandana553@gmail.com

Laser Guide Stars provide artificial reference sources for adaptive optics systems to correct atmospheric wavefront distortions in astronomical observations. However, residual aberrations and noise continue to limit image quality and resolution. While AI-based reconstruction enhances image clarity, it may introduce artifacts. A hybrid AI framework is proposed to improve fidelity, resolution, accuracy, and reliability.

.

Laser Guide Stars (LGS) provide artificial reference sources for Adaptive Optics (AO) systems to correct atmospheric wavefront distortions in astronomical observations. Despite significant improvements, residual aberrations and detector noise continue to limit image quality and angular resolution.

One of the greatest challenges in ground-based astronomy is atmospheric turbulence, which distorts incoming starlight and degrades image sharpness. Adaptive Optics systems employ wavefront sensors and deformable mirrors to compensate for these distortions in real time, producing images approaching space-based quality.



Figure 1: Four laser guide stars projected from ESO's Very Large Telescope (VLT) at Paranal Observatory, Chile. Image credit: F. Kamphues/ESO.

A Laser Guide Star is generated by projecting a powerful laser beam into the atmosphere, creating an artificial reference star. Modern observatories commonly employ Sodium Laser Guide Stars and Rayleigh Laser Guide Stars, operating at different atmospheric altitudes to characterize turbulence and improve wavefront correction.

Recent advances in Artificial Intelligence have opened new possibilities for astronomical image reconstruction. However, standalone AI techniques may introduce artifacts or non-physical structures that affect scientific reliability. To overcome this limitation, a Hybrid AI framework is proposed in which Adaptive Optics corrections are combined with physics-aware deep-learning approaches.

.

References:

1. J.W. Hardy, *Adaptive Optics for Astronomical Telescopes*, Oxford University Press, New York (1998).
2. R.K. Tyson, *Principles of Adaptive Optics*, 4th Edition, CRC Press, Boca Raton (2015).
3. R.Q. Fugate, D.L. Fried, G.A. Ameer, et al., *Nature* 353 (1991) 144–146.
4. F. Roddier (Ed.), *Adaptive Optics in Astronomy*, Cambridge University Press, Cambridge (1999).

Residual GAN With Spectral Normalization for Image Dehazing

Vimod Kumar[#], Manish Kumar[*]
Centre for Sensors, Instrumentation and cyber physical system engineering (SeNSE)
Indian Institute of Technology Delhi, New Delhi 110016, India
[*]*E-mail: kmanish@iitd.ac.in*, [#]*vimodmech@gmail.com*

Image dehazing addresses an atmospheric phenomenon primarily caused by the scattering of light by particles such as dust, fog, or haze. This work presents dehazing technique with enhanced pix2pix-based conditional GAN to improve feature learning and training stability. Trained on RESIDE dataset, the proposed model achieves superior PSNR, SSIM, and visual quality over pix2pix on both synthetic and real images.

In our work, we have developed an enhanced pix2pix, a cGAN framework for the image dehazing problem, introducing a Residual GAN architecture combined with spectral normalization. The generator integrates residual blocks within a U-Net structure to facilitate more robust feature extraction and improved gradient propagation, which is critical for complex tasks such as haze removal. Spectral normalization has been systematically applied to stabilize the adversarial training, ensuring greater fidelity and removing classic issues like mode collapse and training instability. To the best of our knowledge, these techniques have been individually applied to the dehazing task [1,2,3], but have not been explored in combination. Other training parameters are same as in original pix2pix. We trained our model on RESIDE dataset [4]. The model is trained and evaluated on synthetic and real dehazing datasets, where it demonstrates consistent superiority over the original pix2pix.

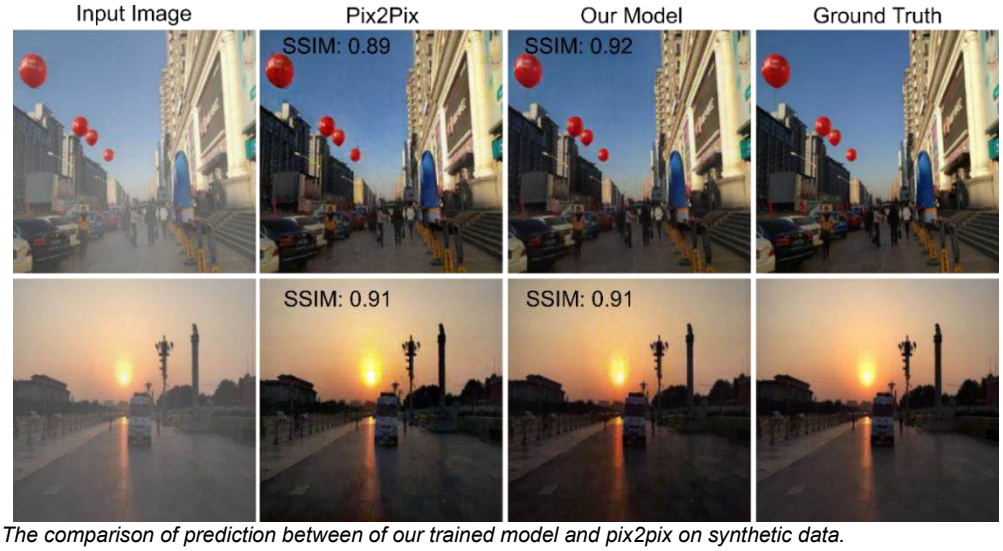


Fig. 1: The comparison of prediction between of our trained model and pix2pix on synthetic data.

Quantitatively, our approach achieves an SSIM of 0.93 and a PSNR of 31 on synthetic data (average over 100 images), indicating a significant enhancement in both structural preservation and image quality. These results are competitive when benchmarked against recent GAN-based dehazing methods, many of which report SSIM values in the range of 0.82–0.93 for similar tasks [2,3]. Notably, our Residual GAN with spectral normalization avoids the over-smoothing and colour distortion observed in standard approaches. On real data our model achieves 0.83 SSIM compared to 0.78 SSIM (average over 100 images) with original pix2pix model. The predicted image from original pix2pix and our network is shown in figure 1.

Acknowledgement: We thank IIT Delhi and ANRF for supporting and funding this research.

References

[1] Khatun, Amina, et al. "Dehazing using Generative Adversarial Network-A Review." *SN Computer Science* 6.1 (2024): 20.
[2] Khatun, Amina, et al. "Single image dehazing: an analysis on generative adversarial network." *Journal of Computer and Communications* 8.4 (2020): 127-137.
[3] Zheng, Yitong, et al. "Unpaired remote sensing image dehazing using enhanced skip attention-based generative adversarial networks with rotation invariance." *Remote Sensing* 16.15 (2024): 2707.
[4] Li, Boyi, et al. "Benchmarking single-image dehazing and beyond." *IEEE transactions on image processing* 28.1 (2018): 492-505.

Influence of Optical Excitation Geometry on Photoacoustic Sectional Imaging: A Numerical Study

[1]Vivek Bohane, [1]Mridul Verma, [1]Partha Pratim Pal, [2]Sri-Rajasekhar Kothapalli and [1,#]Renu John

[1]Medical Optics and Sensors Laboratory, Department of Biomedical Engineering, Indian Institute of Technology, Hyderabad, India

[2]Department of Biomedical Engineering, Pennsylvania State University, USA

[#]*renujohn@bme.iith.ac.in*

Photoacoustic signal quality is strongly influenced by the optical illumination used to excite the sample. In this work, we develop a numerical simulation framework that combines Monte Carlo–based light transport modeling (MCX) with acoustic wave propagation (k-Wave). This framework is used to study the impact of different optical source configurations on photoacoustic sectional imaging performed with a linear ultrasound array.

Photoacoustic imaging combines optical excitation with acoustic wave detection to provide images with high optical contrast and ultrasonic spatial resolution [1]. The distribution of absorbed optical energy within tissue determines the initial pressure distribution (p_0), making the illumination geometry an important factor that affects signal and image quality. To study these effects, a numerical simulation framework offers a flexible platform where tissue properties, source parameters, and detector configurations can be controlled independently.

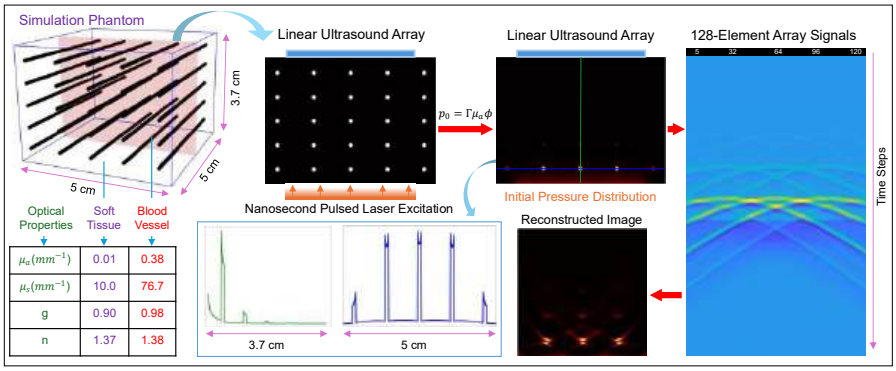


Figure 1: Workflow of the proposed photoacoustic simulation framework.

This work presents the numerical simulation framework integrating Monte Carlo eXtreme (MCX) [2] and k-Wave [3] to study the impact of different optical source configurations on cross-sectional photoacoustic imaging. A three-dimensional computational tissue phantom with embedded blood vessels was created using literature-based optical properties [4]. Light transport was simulated in MCX for various optical source configurations, such as planar, slit, disk, and Gaussian illumination. The absorbed optical energy distribution from the MCX simulation was then converted into the initial pressure distribution (p_0) using the photoacoustic relation

$$p_0 = \Gamma \cdot \mu_a \cdot \phi$$

where Γ is the Grüneisen parameter, μ_a is the absorption coefficient, and ϕ is the local optical fluence. The obtained initial pressure distribution was imported into k-Wave to simulate acoustic wave propagation. A 128-element linear ultrasound array was placed above the imaging volume to acquire the generated photoacoustic signals. The collected signals were then reconstructed to produce cross-sectional photoacoustic images.

The proposed simulation framework allows the study of different optical source configurations under identical tissue properties and acoustic detection conditions. This ensures a fair comparison of optical excitation strategies. *The simulation code is available at: https://github.com/vivekbohane/pai_matlab.*

References:

[1] L.V. Wang, S. Hu, *Science* 335 (2012) 1458–1462.
[2] Q. Fang, D.A. Boas, *Optics Express* 17 (2009) 20178–20190.
[3] B.E. Treeby, B.T. Cox, *Journal of Biomedical Optics* 15 (2010) 021314.
[4] N. Bosschaart, G.J. Edelman, M.C.G. Aalders, T.G. van Leeuwen, D.J. Faber, *Lasers in Medical Science* 29 (2014) 453–479.

An Explainable Learning Framework for Early Detection of Chronic Kidney Disease

[1,#]Saumya Chakraborty, [1]Rajib Chakraborty and [2]Surajit Bagchi
[1]Department of Applied Optics and Photonics, University of Calcutta
[2]Department of Electronics and Instrumentation Engineering, Heritage Institute of Technology, Kolkata

[#]smcaop_rs@caluniv.ac.in

Many existing ML models prioritize predictive accuracy taking large sets of clinical variables while offering limited interpretability. An explainable machine learning framework for early Chronic Kidney Disease detection was developed using significant clinical parameters. Ensemble models were comparatively evaluated on 3,431 patient records.

CKD is a progressive, irreversible disorder that may remain silent until advanced stages, causing irreversible kidney damage, cardiovascular complications, and costly renal replacement therapy [1]. Early diagnosis is therefore essential. Although ML can capture complex clinical patterns, many existing models operate as black boxes and rely on numerous variables, increasing computational complexity and limiting routine clinical deployment [2–4]. This study addresses these limitations by combining a compact set of statistically significant clinical parameters with ensemble learning and SHAP-based interpretation to achieve accurate, precise, and transparent early CKD prediction.

A clinical dataset of 3,431 patient records was processed using duplicate removal, categorical encoding, and natural-log transformation of Albumin and Sugar because of skewness. Exploratory analysis included correlation, skewness, kurtosis, variance inflation factor (VIF), and class-distribution assessment. Six clinically relevant predictors including age, gender, hypertension, eGFR, log albumin, and log sugar were selected for model development through feature engineering, thereby reducing dimensionality while preserving the most informative characteristics associated with CKD progression. The dataset was split in an 80:20 ratio, resulting in 2,744 records for training and 687 records testing. K-Nearest Neighbors, (KNN) Decision Tree (DT), Random Forest (RF), Gradient Boosting (GB), XGBoost (XGB), and Support Vector Machine (SVM) were trained under identical settings. A comparative assessment revealed that XGBoost attained the highest ROC-AUC (95.85%), while Gradient Boosting offered the most favorable overall balance among accuracy, precision, recall, F1-score, discrimination, and interpretability. Figure 1 shows the confusion matrix obtained using Gradient Boosting, Gradient Boosting recorded 91.56% accuracy, 89.33% precision, 76.14% recall, 82.21% F1-score, and 95.82% ROC-AUC). SHAP analysis highlighted eGFR, Log Albumin, Hypertension, Age, and Sugar as the most influential predictors, offering clinically meaningful explanations for individual predictions.

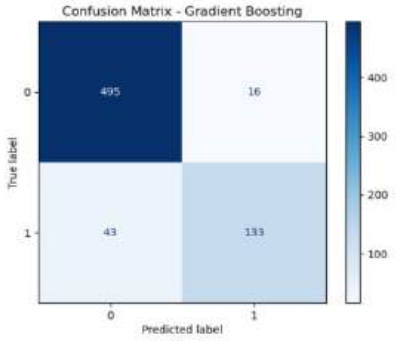


Fig. 1: A confusion matrix from Gradient Boosting

The proposed explainable ensemble learning framework enables accurate and transparent early CKD prediction using six clinically significant parameters. The framework shows considerable promise for intelligent clinical decision-support systems, facilitating timely intervention, improved patient outcomes, and efficient healthcare delivery.

References:

[1] T.K. Chen, M.P. Hoenig, D. Nitsch, M.E. Grams, *BMJ* 383 (2023) e074216.
[2] R. Borg, P. Rossing, *International Journal of Nephrology* (2023) 9609266.
[3] R. Gupta et al., *Scientific Reports* 16 (2026) 12679.
[4] P. Gogoi, J.A. Valan, *Computer Methods in Biomechanics and Biomedical Engineering* (2026).

Non-invasive Analysis of Sweat Sample using Optical Methods

[1]Sneham Dey, [1]Rajarshee Roy, [2]Semanti Chakraborty, [1#]Kanik Palodhi
[1]Dept. of Applied Optics and Photonics, University of Calcutta, Kolkata-700106
[2]Dept. of Electronics and Communications, Adamas University, Kolkata-700126
[#]*Email: kpaop@caluniv.ac.in*

Abstract: *Sweat samples containing various physiological constituents - electrolytes, metabolites and salts are prepared to mimic human sweat. Its' refractive indices are analysed by an Abbe Refractometer to investigate the relationship between optical properties and sweat biomarkers concentration, demonstrating potential applications in non-invasive health monitoring and wearable biosensing.*

Human Sweat contains various biomarkers, including electrolytes and metabolites [1] that provide important information regarding the respective human physiological condition and health status. Conventional biochemical analysis techniques often require complex instrumentation and laboratory procedures. Therefore, the development of rapid, non-invasive and cost-effective sensing methods are gaining significant research interest [2]. This work proposes an optical refractive index (RI)-based methodology for estimating the biomarker concentrations present in human sweat samples.

Sweat samples are prepared with different concentrations of Sodium Chloride (NaCl), Glucose ($C_6H_{12}O_6$), Potassium Chloride (KCl), Ammonium Chloride (NH_4Cl), Lactic Acid ($C_3H_6O_3$), Urea ($CO(NH_2)_2$) along with other chemicals dissolved in deionized water as solvent. The variations in human sweat composition provide health status under different physiological conditions [3]. The RI of the prepared samples are analysed using an Abbe Refractometer under suitable environmental conditions. Experimental results demonstrate a gradual change in RI with increasing biomarker concentration, indicating a strong relationship between optical properties (RI) and sweat biomarker composition.

Additionally, the measured RI values (function of biomarker concentration) has the potential to be utilized for developing predictive models towards non–invasive disease identification. The proposed method offers advantages such as simplicity, rapid response, non-invasive nature and low-cost implementation [4]. This study highlights the potential of RI-based optical sensing techniques for future wearable healthcare systems, continuous health monitoring devices and personalized biomedical diagnostics. In conclusion, the present study demonstrates the potential of RI-based analysis for biomarker concentration estimation in sweat samples, indicating its wide applicability. The support provided by the Department of Applied Optics and Photonics, University of Calcutta, in carrying out this work is gratefully acknowledged.

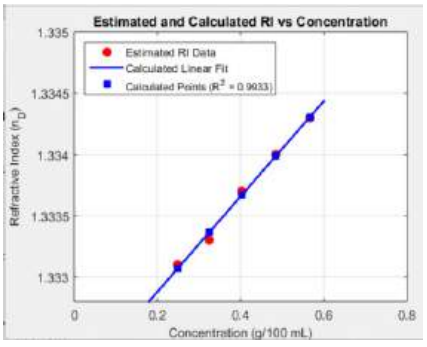


Fig. 1 Variation of Refractive Index with sample composition

References

[1]Changqi Shi, Ziyi Chen, LuLu Zhang, Xiaomeng Zhang, Xiaoyu Liang, Lan Yan, Xiaopeng Hao, Guoju Dong, Cheng Lu, Luqi Huang "Sweat components as a promising monitoring tool for systemic diseases" The Journal of Physiological Sciences Volume 76, Issue 2, (2026)

[2] Roozbeh Ghaffari, Da Som Yang, Joohee Kim, Amer Mansour, John A. Wright Jr., Jeffrey B. Mode, IDonald E. Wright, John A. Rogers, Tyler R. Ray" State of Sweat: Emerging Wearable Systems for Real-Time, Noninvasive Sweat Sensing and Analytics", ACS Sensors, Vol 6/Issue 8 (2021)

[3] Lindsay B Baker, Anthony S Wolfe "Physiological mechanisms determining eccrine sweat composition" Eur J Appl Physiol. 2020 Apr;120(4):719-752. doi: 10.1007/s00421-020-04323-7, Epub (2020)

[4] Wei Gao, et al."Fully integrated wearable sensor arrays for multiplexed in situ perspiration analysis" doi: 10.1038 Nature (2016)

Design of a Confocal Hyperspectral Scanning Microscope for Label-Free Multiscale Structural and Spectral Imaging

[1]Pratik Dhar and [2, #]Suchandra Banerjee
[1,2] Amity Institute of Applied Science, Amity University, Noida, Uttar Pradesh
[#]banerjee.suchandra@gmail.com

We present an optical design of a confocal hyperspectral scanning microscope over 400–700 nm with a spectral resolution of 9 nm. The system employs a 2D galvo-scanner with a switchable micro/macroscopic dual-mode configuration, enabling scalable imaging across fields of view from 2mm to 10 mm for label-free imaging.

Hyperspectral imaging (HSI) simultaneously acquires spatial (x, y) and spectral (λ) information from light interacting with a sample, generating spectral signatures shaped by intrinsic absorption, scattering, autofluorescence, and refractive-index heterogeneity of endogenous molecules [1,2]. Existing hyperspectral architectures are based on spatial-spectral acquisition but face key limitations: filter-based systems (LCTF/AOTF) rely on sequential band-by-band filtering makes the system slow with low spectral resolution, unsuitable for live/dynamic samples; snapshot imaging suffers an inherent spatial–spectral resolution trade-off, requiring bulky image-mapping optics or microlens arrays; and confocal hyperspectral systems typically depend on exogenous fluorescent labels which only detects the particular wavelength band sensitive to fluorophores, also dyes introduces photobleaching and phototoxicity that limit longitudinal imaging [3]. To overcome these limitations, we propose CHASM, which acquires spatial information via high-speed galvanometric scanning while spectral information is simultaneously collected using a reflective hyperspectral spectroscope coupled with a spectral detector, forming a three-dimensional data cube that encodes full-spectrum molecular information at each spatial point—unlike fluorescence, which is restricted to discrete emission bands specific to particular fluorophores.

Figure 1(a) represents the optical design of a confocal hyperspectral scanning microscope, designed using Zemax Optic Studio. A 2D galvanometric scanner raster-scans collimated broadband illumination (400–700 nm) in episcopic configuration for high-speed, non-contact scanning. The system's multiscale imaging capability, shown in fig.(b), comes from an interchangeable front-end in the probe arm: an f-theta scan lens gives a 10 mm × 10 mm field at around 10μm spatial resolution, while a standard objective (NA 0.25, 10x) gives a ~2 mm × 2 mm field at ~2.5 μm resolution for high resolution high magnified imaging. A reflective type of diffraction-grating spectrometer with slit size 20μmx1mm collects scattered light, acquisition pairs each (x, y) coordinate with a spectrum, forming the data cube upon full-field scanning. Fig.(c) shows the image plane dispersion at y-direction with respect to its five sets of field along x-direction represents the hyperspectral demonstration of designed CHASM. The spot sizes between two adjacent wavelengths with 9nm separation are well resolved which is shown in fig. 1(d). CHASM offers a versatile, multiscale platform for label-free characterization of structural and spectral across cellular and tissue-level applications.

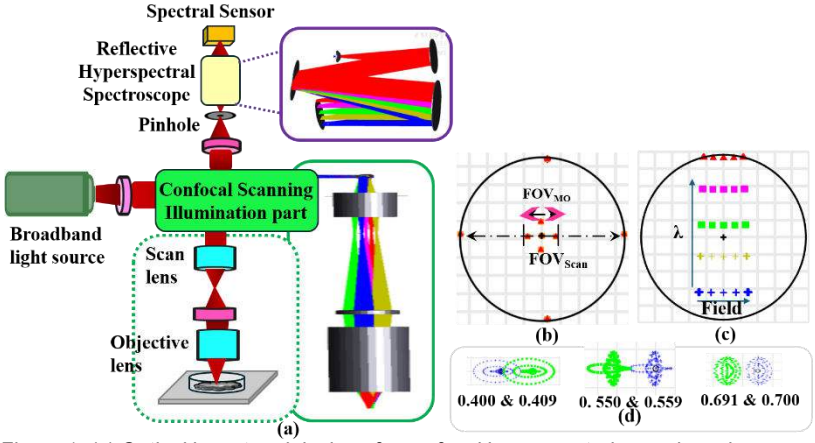


Figure 1: (a) Optical layout and design of a confocal hyperspectral scanning microscope (CHASM) for the label free imaging, (b) Footprint diagram of field of view (FOV) illustrating the dual-mode scalable imaging system at Microscope Objective (MO) and Scan lens image plane, (c) Footprint diagram in the image plane of the entire system, representing the hyperspectral capability of the designed system, & (d) Designed spectral resolution of Reflective Hyperspectral Spectroscope

References:

[1] Lu, G., & Fei, B., Journal of Biomedical Optics, 19(1), 010901 (2014).
[2] Gao, L., & Smith, R. T., Journal of Biophotonics, 8(6), 441–456 (2015).
[3] Icha, J., et al., BioEssays, 39, 1700003 (2017).

Brenner gradient topology-based autofocusing framework for Fourier ptychography microscopy

[1]Gaurang Garg and [1,#]Pradipta Mukherjee
[1]Centre for Biomedical Engineering, Indian Institute of Technology Delhi, New Delhi, 110016

[#]*pmukherjee@cbme.iitd.ac.in*

Accurate defocus estimation in Fourier ptychographic microscopy (FPM) remains challenging for transparent samples, where amplitude-contrast autofocus metrics fail. We introduce an object-aware framework that analyses the topology of Brenner gradient curve to decouple wave propagation from digital artifacts, enabling automatic sample classification and optimal focus selection for universal, label-free FPM reconstruction.

Fourier ptychography microscopy (FPM) is a powerful computational imaging technique, but its high-fidelity phase retrieval relies entirely on accurate initial defocus estimation[1]. In label-free biomedical applications, we deal with samples that may be transparent phase objects. Traditional autofocusing metrics, which maximize the Brenner gradient[2] to find amplitude contrast peaks, fail catastrophically on these phase objects due to complex wave-matter interactions[3,4].

In contrast to amplitude objects where amplitude-maximization criteria holds efficiently [Fig. 1(a)],this work identifies three non-linear topological phenomena on the Brenner curve that cause conventional algorithms to fail: Phase inversion, where the true focal plane manifests as a global minimum rather than a peak [Fig. 1(b)]; Gibbs anomaly, where finite numerical aperture (NA) clipping forces invisible diffraction boundaries to form deceptive, W-shaped false peaks [Fig. 1(c)]; and the amplitude-phase crosstalk in complex objects, which heavily skews the contrast curve and breaks symmetrical search rules [Fig. 1(d)]. This establishes that applying standard contrast maximization algorithms to transparent samples is flawed.

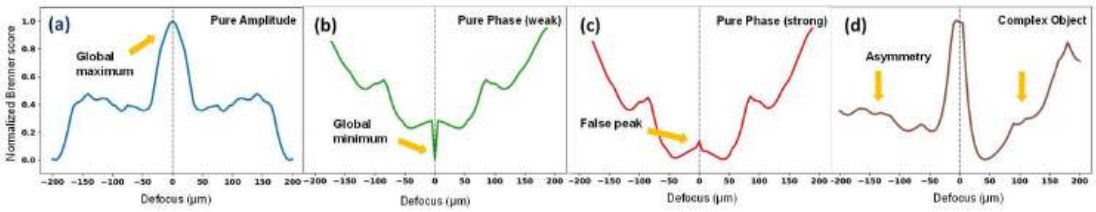


Figure 1: Brenner curve for different objects

To overcome this limitation, we propose an object-aware autofocusing framework that mathematically decouples macroscopic wave propagation from microscopic digital ringing artifacts. Following a rapid simulated Z-sweep, our multi-scale topological profiler functions as an autonomous logic gate. By extracting specific geometric parameters from the gradient curve; namely macro-curvature to capture broad transport of intensity equation physics, micro-curvature to detect sharp clipping artifacts, and a Brenner asymmetry index, the system successfully classifies the specimen's physical nature without prior knowledge.

Based on these parameters, the framework deterministically routes the data to the correct mathematical solution. It locks onto maximums for pure amplitude, minimums for weak phase, and immediately triggers a multi-LED universal fallback loop if Gibbs anomalies or heavy skews are detected. Ultimately, this approach eliminates local minima traps, providing a universal, highly accurate computational pre-step for robust, label-free FPM reconstructions.

References:

[1] G. Zheng, R. Horstmeyer, and C. Yang, *Nature Photonics* 7, 739–745 (2013).
[2] S. Yazdanfar, K. B. Kenny, K. Tasimi, A. D. Corwin, E. L. Dixon, and R. J. Filkins, Opt. Express, 16, 8670–8677 (2008).
[3] F. Dubois, C. Schockaert, N. Callens, and C. Yourassowsky, *Opt. Express*, 14, 5895–5908 (2006)
[4] S. Schoell, F. Mualla, B. Sommerfeldt, S. Steidl, A. Maier, R. Buchholz, and J. Hornegger, Journal of Microscopy 254, 65–74 (2014).

Handheld Microscopic Imaging System for Subsurface Tissue Characterization

Dhanush Koodi M[1], Keepa Manandhar[2], Apoorva Challa[2], Tanya Gupta[2], Sridhar A S[1], R Thanigaivel[1], Somesh Gupta[2], Uttam M Pal[1]

[1]Department of Electronics and Communication Engineering, IIITDM Kancheepuram, Chennai.
[2]Department of Dermatology and Venereology, AIIMS Delhi, New Delhi.

uttampal@iiitdm.ac.in

An epiluminescence device is a handheld imaging tool used to examine tissue lesions. By utilizing specialized illumination and magnification, it eliminates surface glare from the tissue's outer layer, allowing clinicians to visualize vital subsurface pigment networks and microvascular architectures that are completely invisible to the naked eye, significantly improving diagnostic accuracy.

This handheld microscopic system is designed for the visualization and characterization of hard-to-reach anatomical regions, integrating a high-resolution, sub-miniaturized camera with a 12 mm focal length imaging lens. The imaging system performance was quantitatively evaluated using USAF 1951 resolution test target and a micrometer calibration scale. Figure 1(a) evaluates the spatial resolution capabilities of the imaging system. Based on the USAF 1951 resolution target, the system successfully resolves Group 6 Element 3. Based on the standard resolution formula, the system achieves spatial resolution of 80.6 lines pair / mm, which translates to a minimum resolvable single line width of 6.20µm. Figure 1(b) evaluates the system's field of view (FOV) using a calibration scale 0.1 mm divisions. Based on the captured image, the system achieves a maximum lateral field of view of 2.6 mm. Notably, these optical performance metrics were characterized by a working distance of 0 mm.

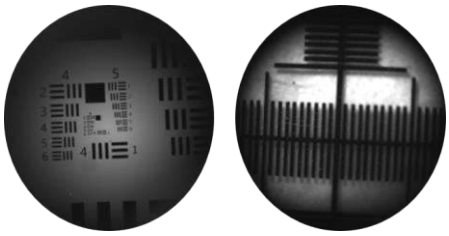


Fig. 1(a): USAF 1951 Target, 1(b): Micrometer Calibration Scale

Figure 2(a) presents a tissue image acquired by the developed imaging probe, revealing detailed subsurface tissue structures and micro-topographical texture that are unresolved in the commercial epiluminescence device image as shown in Figure 2(b). This enhanced subsurface visualization is seen because light penetrates the tissue, laterally from sides, the camera captures the backscattered photon to generate high-resolution subsurface image.

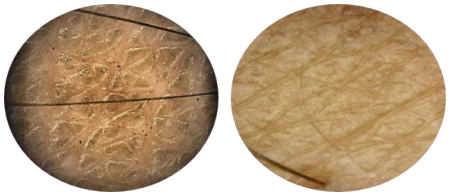


Fig. 2(a): Handheld Microscopic Image (FOV: 2.6 mm), 2(b): Commercial epiluminscence device (FOV: 7.4 mm)

Acknowledgement: The authors gratefully acknowledge the Indian Council for Medical Research (ICMR) for financial support under Grant No. DevRes/Onco/FIW-2024-01-00000135(227345).

References:

[1] Lam, Christopher T et al. "Design of a Novel Low Cost Point of Care Tampon (POCkeT) Colposcope for Use in Resource Limited Settings." PloS one vol. 10,9 e0135869. 2 Sep. 2015, doi:10.1371/journal.pone.0135869

[2] Rahaman, Alisha et al. "Optical imaging for early detection of cervical cancer: state of the art and perspectives." Journal of biomedical optics vol. 28,8 (2023): 080902. doi:10.1117/1.JBO.28.8.080902

Lightsheet fluorescence microscopy (LSFM) using an engineered line diffuser

Akshay kumar, and #Manish Kumar
Center for Sensors, Instrumentation and Cyber Physical System Engineering (SeNSE),Indian Institute of Technology Delhi, New Delhi 110016 India
#*kmanish@iitd.ac.in*

Lightsheet fluorescence microscopy (LSFM) has become a significant method that utilizes selective plane illumination. The objective is to attain improved axial resolution and reduce photobleaching in biological specimens. In this work we are presenting implementation of LSFM using an engineered line diffuser.

Light-sheet imaging, due to its superior axial resolution, is a favored technique for imaging biological specimens and colloidal suspensions [1]. It relies on a specialized illumination approach integrated into a conventional microscopy configuration [2]. The presence of absorbing and scattering particles in transparent biological specimens creates shadow artifacts that can degrade image quality [3]. This study seeks to rigorously quantify the shadows generated by absorbent particles, proposing essential factors for quantifying shadow length. Additionally, we investigated techniques [4] to reduce these shadow artifacts, thus improving the accuracy of light sheet imaging. Our approaches involving engineered line diffuser have been shown to effectively diminish shadow artifacts in agar-based fluorescence studies. By properly resolving these difficulties, we expect enhanced clarity in the information derived from biological samples.

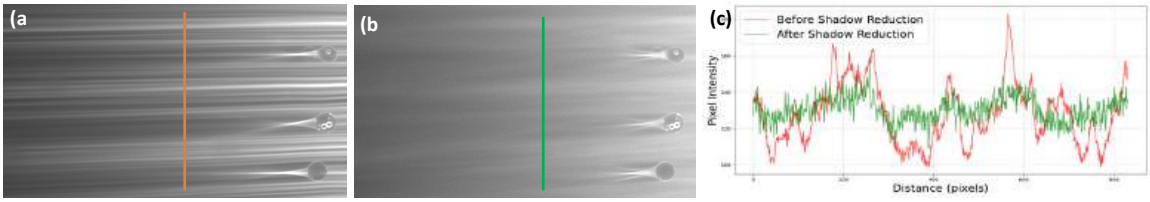


Fig. 1:2D fluorescence images captured using our LSFM system (a) with shadow artifacts, (b) after removing shadow artifacts, (c) intensity line profile along the line given in both (a) and (b).

We have implemented our LSFM system using an engineered line diffuser instead of a conventional cylindrical lens. That is a beam-shaping optical element; it accepts laser beams and transmits ray fans with finite divergence angles (100° in our case). We used it to create a light sheet at the sample plane by collimating and demagnifying the outcoming ray fan. Further to mitigate shadow artifacts, we require angular diversity in the light-sheet illumination at the sample plane. So, we added a line diffuser with a diffraction grating. This configuration produces an offset beam on the diffuser, yielding angularly varied light sheets at the working distance of the microscope objective. The offset generated by the grating is directly proportional to the angular diversity detected at the sample plane.

We made an agar-based sample to validate our system. To replicate biological materials, glass beads and fluorescein dye were added to agar. In a transparent cuvette, we could flash a light sheet from one side and detect it from the other. A laser source of 473 nm stimulated the fluorescein-filled sample, causing fluorescence emission at 515 nm from the region where the light-sheet interacts with the sample.

The results we obtained indicate that the proposed methodology is exceptionally effective in reducing shadow regions in the photographs. Fig. 1 (c) illustrates that the intensity variations induced by particles obstructing the light sheet are significantly diminished.

Akshay Kumar acknowledges Anusandhan National Research Foundation (ANRF) for funding this research under project no. SRG/2022/000930, and also IIT Delhi for the research fellowship.

References:

[1] H. Siedentopf, R. Zsigmondy, Annalen Der Physik 315 (1902) 1–39.
[2] P.A. Santi, J Histochem Cytochem. 59 (2011) 129–138.
[3] P. Ricci, V. Gavryusev, C. Müllenbroich, L. Turrini, G. de Vito, L. Silvestri, G. Sancataldo, F.S. Pavone, Progress in Biophysics and Molecular Biology 168 (2022) 52–65.
[4] O.E. Olarte, J. Andilla, E.J. Gualda, P. Loza-Alvarez, Adv. Opt. Photon. 10 (2018) 111.

Scattered light-based detection of cell membrane fluctuations without tracer particles

Bipeen Kumar and #Basudev Roy
Department of Physics, IIT Madras 600036

#basudev@iitm.ac.in

Cell membrane fluctuations provide information about cellular mechanics. We present a microscopy-based scattered light method to detect membrane fluctuations without tracer particles. Slope fluctuations were analyzed using power spectral density, showing signals above noise with a power-law exponent close to −1.2. This method enables length-scale-dependent studies of membrane mechanics.

Cell membranes are highly dynamic structures that continuously fluctuate due to thermal motion, ATP-driven processes, and cytoskeletal activity. These fluctuations reveal mechanical properties such as membrane tension and bending rigidity. These properties play key roles in cellular processes such as migration and division. Optical tweezer-based methods are widely used to study membrane fluctuations, but they often require tracer particles attached to the membrane. This may affect the natural state of the cell and limit measurement flexibility. This motivates the development of an optical method without tracer particles for studying membrane fluctuations across different length scales.

Figure 1 shows the schematic of the experimental setup. Experiments were performed on MCF-7 human breast cancer cells using a microscopy setup with a 532 nm laser and EMCCD camera. The laser was focused near the cell edge, where small membrane displacements modulate the scattered light collected by the objective and recorded by the EMCCD camera. In this way, nanometer-scale membrane motion is detected as measurable intensity fluctuations without tracer particles.

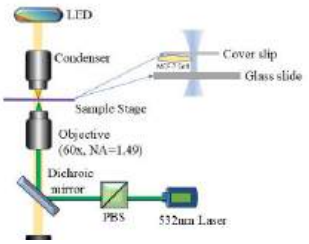


Fig 1: Schematic of the experimental setup

We recorded videos of the selected membrane edge at approximately 100 frames per second (fps) for 120 seconds. Slope fluctuation (angular deformation) was extracted by placing four boxes of size 2×2 pixels (0.54 × 0.54 μm²) across the membrane edge, as shown in Fig. 2. The slope fluctuation signal was defined using a QPD-like differential detection scheme [1]:

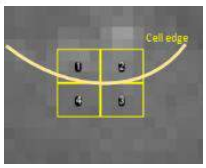


Fig 2: Slope fluctuation extraction

$$S_{s(t)} = \frac{I_{2(t)}+I_{4(t)}}{I_{1(t)}+I_{3(t)}}$$

The extracted signal was plotted as a time series and analyzed using Fourier analysis to obtain the power spectral density (PSD), which describes how fluctuation power is distributed over frequency.

Membrane fluctuation signals were observed above the background noise, as shown in Fig. 3. The PSD of the slope fluctuation showed a power-law behavior with an exponent close to −1.2. [1] This method enables studies of cell membrane mechanics across different length scales.

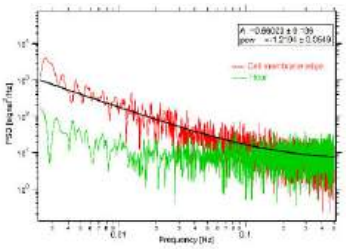


Fig 3: PSD of slope fluctuation

Reference:

[1] S. Roy et al., *Phys. Biol.* **20**, 046001 (2023)

Detection of thiamine in infantile blood sample using High-Performance Liquid Chromatography-LED- Induced Fluorescence system

Clint Mathew[1], Ajaya Kumar Barik[1], Jijo Lukose[1], Leslie Edward S. Lewis[2] and Santhosh Chidangil[1,3*]

1.Centre of Excellence for Biophotonics, Manipal Institute of Applied Physics, Manipal Academy of Higher Education, Manipal, Karnataka 576104, India.

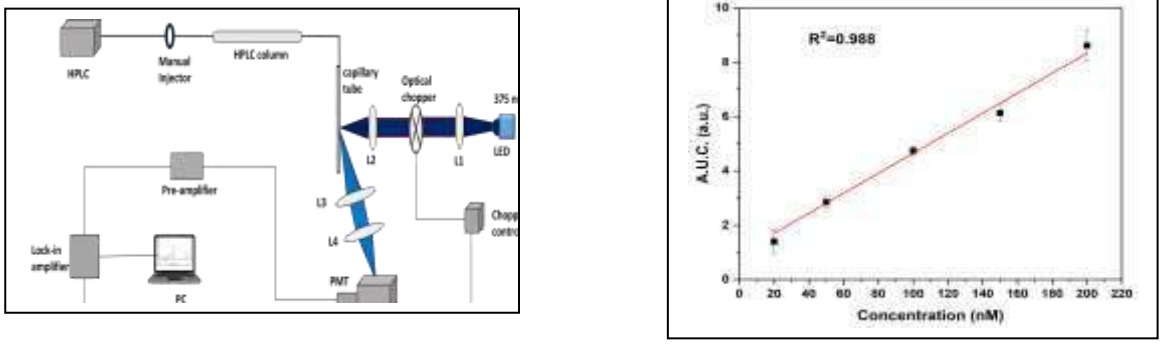
2. Department of Paediatrics, KMC, Manipal Academy of Higher Education, Manipal, Karnataka 576104, India.

3. Department of Physics, JSS Science and Technology University, Mysuru, Karnataka 570006, India.

**Corresponding author Email: santhosh.cls@manipal.edu, santhosh.cls@jssstuniv.in*

Abstract: *Thiamine is an essential nutrient, and thiamine diphosphate (TDP) its major active form. TDP was converted to fluorescent thiochrome and analyzed using a developed HPLC-LED-IF system. The method achieved a detection limit of 21.4nM, below the reference range. It successfully detected TDP in infant blood samples.*

Thiamine is one of the eight essential B vitamins required for the normal functioning of the central and peripheral nervous systems. Thiamine diphosphate (TDP) is the primary biologically active form of thiamine but a weakly fluorescent molecule. It can be oxidized to form thiochrome, a highly fluorescent compound. Thiochrome is unstable and degrades upon exposure to light and heat. Therefore, derivatization and subsequent analyses must be performed under controlled dark conditions [1]. Pre-column derivatization followed by fluorescence detection is the most commonly used approach for TDP analysis [2].



(a) (b)

Figure 1: (a) Schematic diagram of HPLC with LED induced fluorescence detection, (b) Calibration curve of TDP using the HPLC LED-IF system

In this study, TDP was converted into fluorescent thiochrome and analyzed using a high-performance liquid chromatography (HPLC) system coupled with an assembled LED-induced fluorescence (LED-IF) detection system (Figure 1(a)). The developed method achieved a limit of detection (LOD) of 21.4 nM for thiochrome (Figure 1(b)), which is well below the clinical reference range, demonstrating excellent analytical sensitivity. The method successfully detected TDP concentrations in infant blood samples, including levels below the normal reference range, highlighting its potential for the early detection and monitoring of thiamine deficiency. Considering that the clinical reference range of TDP in whole blood is 70–180 nM, the proposed system provides sufficient sensitivity for the detection and monitoring of thiamine deficiency while offering a cost-effective alternative to conventional fluorescence detection systems.

References

1. Lu, Jun, and Elizabeth L Frank. “Rapid HPLC measurement of thiamine and its phosphate esters in whole blood.” Clinical chemistry vol. 54,5 (2008): 901-6.

2. P.L.M Lynch, I.S Young, Determination of thiamine by high-performance liquid chromatography, Journal of Chromatography A, Volume 881, Issues 1–2, 2000

Design of a laser printed paper-based microfluidic platform for colorimetric detection of oral cancer biomarkers

[1]Divya Ramakrishnan, [1,#]Monisha Mohan

[1]School of Interdisciplinary Design and Innovation,

Indian Institute of Information Technology, Design and Manufacturing, Kancheepuram

Chennai, Tamil Nadu, 600127, India

[#]*monisha@iiitdm.ac.in*

Gold nanoparticle (AuNP)-integrated laser- printed paper microfluidic biosensor was developed for colorimetric detection of salivary oral cancer biomarkers. Exploiting the localized surface plasmon resonance (LSPR) of AuNPs, the platform enabled simultaneous detection of cysteine, glutathione and sialic acid with the limits of detection of 0.1845, 8.2284, and 77.5 µM, respectively.

Oral squamous cell carcinoma remains one of the leading causes of cancer related mortality worldwide, with delayed diagnosis significantly reduces patient survival. Salivary biomarkers offer a non-invasive and convenient alternative for early diagnosis of the disease. Gold nanoparticles (AuNPs) possess unique optical properties arising from localized surface plasmon resonance (LSPR), making them excellent candidates for colorimetric biosensing. In this work, an AuNP-integrated laser-printed paper-based microfluidic platform was developed for simultaneous detection of cysteine, glutathione and sialic acid.

Citrate-stabilised AuNPs were synthesized using Turkevich method and characterized using UV-Visible spectroscopy, Raman spectroscopy, DLS and FTIR analysis. UV-Visible spectroscopy exhibited a characteristic LSPR absorption peak at 533 nm, confirming successful nanoparticle synthesis. Functionalised AuNPs were integrated into a CO_2 laser-cut paper microfluidic device mounted within a 3D resin-printed holder. Interaction between the target biomarkers and AUNPs produced concentration-dependent optical color changes due to plasmonic coupling, which were quantified using RGB image analysis. The developed platform enabled simultaneous detection of cysteine, glutathione, and sialic acid with limits of detection of 0.1845 µM, 8.2284 µM, and 77.5 µM, respectively (Figure 1).

The developed plasmonic paper-based biosensor exploits the optical properties of AuNPs for rapid sensitive and simultaneous colorimetric detection of salivary oral cancer biomarkers. The combination of LSPR-based sensing with paper microfluidics provides a portable and cost effective platform with significant potential for point of care oral cancer screening.

Acknowledgement: The authors acknowledge the financial support provided by the HRD Scheme of the Department of Health Research“Start-up Grant for Induction into Biomedical & Health Research” (SUG 2025-1195).

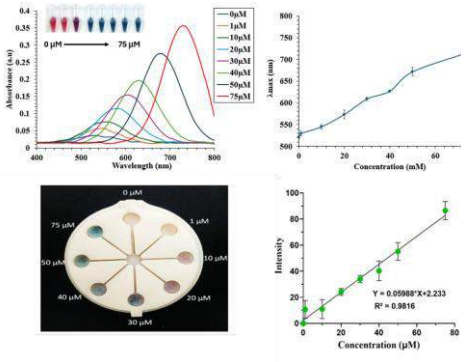


Figure 1: RGB analysis and calibration curves for AuNP-based paper microfluidic detection of cysteine, showing concentration-dependent color changes and the corresponding λmax shift.

References:

[1] E. Jeyasekaran, S. Venkatachalam, Can. J. Chem., 97, 233–237, 2019.
[2] J.-F. Li, P.-C. Huang, F.-Y. Wu, RSC Adv., 7, 13426–13432, 2017.
[3] S. Tang, L. Li, R. Wang, S. Regmi, X. Zhang, G. Yang, et al., Biosensors, 13, 164, 2023.

Effects of ocular pupil dynamics on Zernike polynomial coefficients

[1,*]Dhritiman Nath, [2]Suman Sangiri and [2,#]Vyas Akondi
[1]Department of Physics and Astrophysics, Central University of Haryana, Mahendergarh, Haryana, 123031, India
[2]Department of Physical Sciences, Indian Institute of Science Education and Research (IISER) Berhampur, Berhampur, Odisha, 760003, India

*ndhritiman1@gmail.com, #vakondi@iiserbpr.ac.in

Abstract: *We developed a simulation model to evaluate the variations in ocular aberrations with changing pupil diameter, via the evaluation of scaled Zernike coefficients over a pupil diameter range of 2 mm to 6 mm. The theoretically predicted wavefront maps were compared with those experimentally measured using the iTrace aberrometer, showing strong agreement in most cases.*

Zernike polynomials are widely used to represent ocular wavefront aberrations due to their orthogonality over a circular pupil and their direct association with clinically relevant aberration modes [1]. However, the pupil size depends on various light conditions (mesopic and photopic) and as a result the associated Zernike coefficient value also varies. This dependency poses a significant challenge for correct interpretation of longitudinal wavefront measurements, particularly in clinical settings. Although theoretical scaling relationships have been proposed [2], their practical validity under experimental conditions remains insufficiently explored and implemented. This study aims to investigate how wavefront aberrations change with varying aperture diameter and repeatability of ocular aberrations clinically.

For any given wavefront, the Zernike coefficients (a_i) for the reconstructed wavefront for a particular pupil size are obtained using:

$$a_i = (Z_i^T Z_i)^{-1} Z_i^T W_i$$

where $(\mathrm{Z}_i^T \mathrm{Z}_i)^{-1} \mathrm{Z}_i^T = Z^+$ represents the pseudo-inverse of the Zernike matrix and W_i refers to the wavefront vector [3].

To understand the effect of pupil size reduction on individual Zernike modes, we simulated single aberration mode with a coefficient value of 0.5 um. Fig. 1 illustrates the simulation results for coma and spherical aberration. It is observed that coma turns into tilt and spherical aberration gets transformed into defocus when the pupil diameter reduces from 5 mm to 3 mm. Experimental measurements of ocular aberrations have been carried out using the iTrace ray tracing aberrometer (Tracey Technologies) at 632 nm wavelength [4]. The largest experimentally measured pupil (6 mm) was considered as the reference wavefront. Using the corresponding Zernike coefficients, wavefronts were numerically reconstructed for smaller pupil sizes. These simulated wavefronts were then compared with the experimentally obtained wavefront maps at the same pupil sizes.

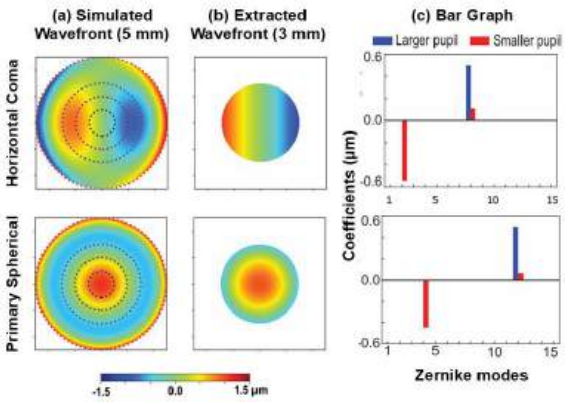


Fig. 1: Zernike coefficients for individual aberration modes (coma and spherical aberration) with pupil size reduction. (a) Simulated Wavefront (5 mm). (b) Extracted Wavefront (3 mm). (c) Bar Graph comparing the two sets of Zernike Polynomial coefficients.

The results show that the amount of aberration decreases with the decreasing pupil size. Significantly, we observed that a single aberration Zernike mode does not remain isolated when the pupil shrinks, instead it gets redistributed into multiple Zernike modes. Also, the Zernike coefficients follow a power-law behavior as the pupil shrinks, with higher-order aberrations showing a stronger dependence on the pupil diameter. This work demonstrates the significance of taking into account the effect of pupil size and pupil decentering while measuring ocular wavefronts at a clinical setup to accurately quantify the Zernike coefficients.

References:

[1] Kuo Niu, Chao Tian, *Journal of Optics,* 24.12 (2022): 123001.
[2] Jim Schwiegerling, *Journal of the Optical Society of America A,* 19.10 (2002): 1937-1945.
[3] S Sangiri, A Dubra, and V Akondi, *Optik*, 319 (2024), 172107.
[4] Nienke Visser, et al, *Investigative ophthalmology & visual science,* 52.3 (2011): 1302-1311.

Design of a laser printed paper-based microfluidic platform for colorimetric detection of oral cancer biomarkers

[1]Divya Ramakrishnan, [1,#]Monisha Mohan

[1]School of Interdisciplinary Design and Innovation,

Indian Institute of Information Technology, Design and Manufacturing, Kancheepuram

Chennai, Tamil Nadu, 600127, India

[#]*monisha@iiitdm.ac.in*

Gold nanoparticle (AuNP)-integrated laser- printed paper microfluidic biosensor was developed for colorimetric detection of salivary oral cancer biomarkers. Exploiting the localized surface plasmon resonance (LSPR) of AuNPs, the platform enabled simultaneous detection of cysteine, glutathione and sialic acid with the limits of detection of 0.1845, 8.2284, and 77.5 µM, respectively.

Oral squamous cell carcinoma remains one of the leading causes of cancer related mortality worldwide, with delayed diagnosis significantly reduces patient survival. Salivary biomarkers offer a non-invasive and convenient alternative for early diagnosis of the disease. Gold nanoparticles (AuNPs) possess unique optical properties arising from localized surface plasmon resonance (LSPR), making them excellent candidates for colorimetric biosensing. In this work, an AuNP-integrated laser-printed paper-based microfluidic platform was developed for simultaneous detection of cysteine, glutathione and sialic acid.

Citrate-stabilised AuNPs were synthesized using Turkevich method and characterized using UV-Visible spectroscopy, Raman spectroscopy, DLS and FTIR analysis. UV-Visible spectroscopy exhibited a characteristic LSPR absorption peak at 533 nm, confirming successful nanoparticle synthesis. Functionalised AuNPs were integrated into a CO_2 laser-cut paper microfluidic device mounted within a 3D resin-printed holder. Interaction between the target biomarkers and AUNPs produced concentration-dependent optical color changes due to plasmonic coupling, which were quantified using RGB image analysis. The developed platform enabled simultaneous detection of cysteine, glutathione, and sialic acid with limits of detection of 0.1845 µM, 8.2284 µM, and 77.5 µM, respectively (Figure 1).

The developed plasmonic paper-based biosensor exploits the optical properties of AuNPs for rapid sensitive and simultaneous colorimetric detection of salivary oral cancer biomarkers. The combination of LSPR-based sensing with paper microfluidics provides a portable and cost effective platform with significant potential for point of care oral cancer screening.

Acknowledgement: The authors acknowledge the financial support provided by the HRD Scheme of the Department of Health Research“Start-up Grant for Induction into Biomedical & Health Research” (SUG 2025-1195).

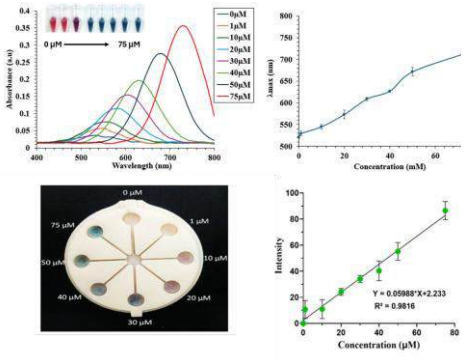


Figure 1: RGB analysis and calibration curves for AuNP-based paper microfluidic detection of cysteine, showing concentration-dependent color changes and the corresponding λmax shift.

References:

[1] E. Jeyasekaran, S. Venkatachalam, Can. J. Chem., 97, 233–237, 2019.
[2] J.-F. Li, P.-C. Huang, F.-Y. Wu, RSC Adv., 7, 13426–13432, 2017.
[3] S. Tang, L. Li, R. Wang, S. Regmi, X. Zhang, G. Yang, et al., Biosensors, 13, 164, 2023.

Low-Intensity Nonlinear Structured Illumination Microscopy Using Photochromic Absorption Modulation

[1,#]Sahil Sharma,[2]Balpreet Singh Ahluwalia [1,3,4]Joby Joseph
[1] Department of Physics, Indian Institute of Technology Delhi, New Delhi 110016, India

[2]Department of Physics and Technology, UiT-The Arctic University of Norway, Tromsø 9037,Norway
[3]Optics and Photonics Centre, Indian Institute of Technology Delhi, New Delhi 110016, India

[4]Indian Institute of Technology Delhi - Abu Dhabi, MZ29 Abu Dhabi, UAE

[#]*joby@opc.iitd.ac.in*

Nonlinear structured illumination microscopy (NL-SIM) offers resolution beyond conventional SIM but typically requires high optical intensities. We present a numerical study of photochromic absorption modulation for low-intensity NL-SIM, investigating illumination optimization, imaging robustness, and reconstruction performance. The results provide practical insights toward the experimental realization of absorption modulation-based nonlinear microscopy.

Structured illumination microscopy (SIM) is a widely adopted super-resolution imaging technique owing to its simple implementation, high imaging speed, and compatibility with live-cell microscopy. While conventional linear SIM provides a two-fold improvement in spatial resolution, further enhancement requires nonlinear structured illumination microscopy (NL-SIM). Existing NL-SIM techniques generally rely on fluorescence saturation or photoswitchable fluorophores, necessitating high optical intensities that increase photobleaching and limit their practical applicability.

To overcome these limitations, we investigate a low-intensity nonlinear structured illumination microscopy approach based on **photochromic absorption modulation**. In this method, a thin photochromic absorption modulation layer (AML) is illuminated using dual-wavelength sinusoidal excitation. The reversible photo-induced switching of photochromic molecules spatially modulates the absorption of the layer, producing nonlinear illumination patterns containing higher-order spatial frequency components. These harmonics extend the effective passband of the imaging system without requiring fluorescence saturation, enabling compatibility with continuous-wave laser sources and conventional fluorophores.

A detailed numerical investigation is performed to evaluate the imaging characteristics and practical feasibility of the proposed approach. The influence of excitation-to-confinement intensity ratio on harmonic generation is analysed, demonstrating that stronger nonlinear modulation leads to increased higher-order frequency content. Different photochromic materials are also compared, indicating that azobenzene produces significantly stronger nonlinear harmonic generation than diarylethene under comparable illumination conditions, making it a promising candidate for absorption modulation-based nonlinear imaging.

To assess robustness under realistic imaging conditions, reconstruction performance is further evaluated in the presence of photon noise, Gaussian noise, background fluorescence, and illumination pattern misalignment. The proposed method maintains high-quality super-resolution reconstruction with only modest degradation under moderate experimental imperfections. Reconstruction of simulated biological specimens further demonstrates improved recovery of fine structural features compared to conventional widefield and linear SIM. In addition, comparison with an existing nonlinear SIM reconstruction algorithm indicates that the proposed blind reconstruction approach provides competitive image quality while maintaining computational efficiency.

These studies provide a comprehensive evaluation of photochromic absorption modulation as a practical route toward low-intensity nonlinear structured illumination microscopy. The presented analyses establish useful design guidelines for future experimental implementation and optimization of absorption modulation-based super-resolution imaging systems.

References:

[1] Tsai H-Y, Moon E E and Menon R 2009 Far-field optical imaging at the nanoscale via Absorbance Modulation Advances in Imaging Novel Techniques in Microscopy (Vancouver: OSA) p NMA2
[2] Anon Switching from Molecules to Functional Materials: Breakthroughs in Photochromism With MOFs - Thaggard - Advanced Materials - Wiley Online Library
[3] S. Sunder, A. Sharma, *Workshop on Recent Advances in Photonics, (WRAP 2019)* 19 (2019).

Evaluation of pyramid wavefront sensing artifacts due to reflectivity variations across thick layered samples

[1,#] Paresh Kumar Sahoo and [2,] Vyas Akondi
Indian Institute of Science Education and Research (IISER) Berhampur
[#]*paresh23@iiserbpr.ac.in*

***Abstract**: Pyramid wavefront sensors (PWFS) are increasingly used in adaptive optics owing to their high sensitivity and adjustable dynamic range. In this work, we present a numerical framework to quantify artifactual wavefront errors in PWFS induced by out-of-focus reflections in multilayer retinal tissue and investigate their dependence on layer separation and relative reflectivity.*

Adaptive optics has become an indispensable tool for improving optical resolution in ophthalmoscopy and microscopy, where the Shack–Hartmann wavefront sensor (SHWS) and the pyramid wavefront sensor [1] are widely used for wavefront sensing. In thick biological samples such as the retina, multiple reflecting layers contribute out-of-focus scattered light that can introduce artefactual errors in wavefront estimation. While the influence of multilayer scattering on SHWS performance has recently been investigated [2,3], its impact on the PWFS remains largely unexplored despite its growing adoption in adaptive optics owing to its high sensitivity and adjustable dynamic range.

In this work, we present a numerical framework to investigate the performance of a PWFS in multilayer scattering media. The model simulates the incoherent contributions from multiple reflective retinal layers while accounting for the imaging geometry between the retina and the sensor. The optical field from each layer is propagated to the pyramid tip, modulated by the pyramidal prism phase mask, and propagated to the detector plane to generate the four-pupil intensity distribution. The wavefront is then reconstructed using a modal Zernike approach. Using a dual-layer retinal model, we systematically quantify artifactual wavefront errors as a function of axial layer separation and relative layer reflectivity.

Our simulations show that out-of-focus reflections from secondary retinal layers introduce artifactual aberrations in the reconstructed wavefront, even in the absence of additional optical aberrations. For a representative dual-layer (reflectivity ratio 1:1) retina with an axial separation of 10 μm, a noticeable defocus-like artifact is observed. The magnitude of these artifacts varies with the axial separation and relative reflectivity of the retinal layers, providing insights into the performance of pyramid wavefront sensors in multilayer retinal imaging.

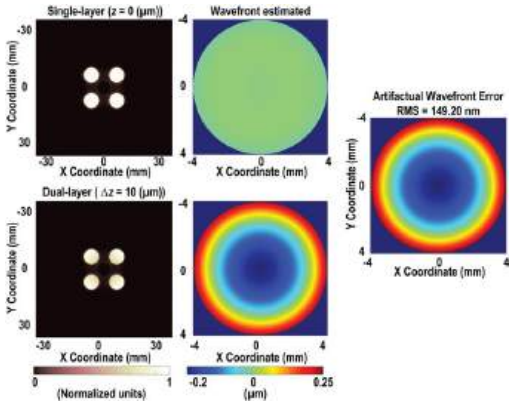


Fig.1:Simulated detector intensity distributions and reconstructed wavefronts for single-layer and dual-layer(1:1 reflectivity ratio) retinal models. The reconstructed wavefront difference demonstrates the presence of artifactual aberrations arising from secondary-layer reflections in the pyramid wavefront sensor.

References:

1. R. Ragazzoni, "Pupil plane wavefront sensing with an oscillating prism," J. Mod. Opt. **43**(2), 289–293 (1996).
2. V. Akondi, "Multi-layer Shack-Hartmann wavefront sensing in the point source regime," Biomed. Opt. Express **12**, 409–432 (2021).
3. P. K. Sahoo, A. Raj M R, and V. Akondi, "Evaluation of Shack-Hartmann wavefront sensing artifacts due to reflectivity variations across thick layered samples using the discrete Fourier transform," Biomed. Opt. Express **17**(8), 4115 (2026).

Field of view characterization using slanted-edge MTF method

[1,#]Dinesh Saini, and [2]Manish Kumar
[1]Optics and Photonics center, Indian Institute of Technology Delhi, Hauz Khas, New Delhi 110016, India
[2] Centre for Sensors, Instrumentation and Cyber Physical System Engineering, Indian Institute of Technology Delhi, New Delhi -110016

[#]*dineshsaini00786@gmail.com*

Modular Transfer Function (MTF) is a popular metric to evaluate the performance of an optical system. Generally, a single MTF curve is used for performance analysis of the system. Here we investigate field-dependent MTF curve across field of view (FOV) of a given system and use it to characterize FOV.

MTF is a widely used parameter to characterize a system's performance. It gives spatial frequency response of an optical system. MTF is defined as the modulus of the Optical Transfer Function (MTF) which is derived from Fourier transform of Point Spread Function (PSF). Here, in this paper, we have used slanted-edge based method to calculate MTF [1–3]. In this method, we use a slanted edge which blocks some part of the image to give a transition from dark to bright intensity values (shown in Fig. 1 top). The imperfections in system cause sloped edge at the intensity transition. In this method, the PSF is replaced by line spread function (LSF) of the sloped edge. It is a widely popular method for MTF calculation of digital imaging systems [2].

In this paper, we have used ImageJ plugin to calculate MTF from the slanted-edge [4]. We used a conventional microscopy system with 4x Nikon objective paired with tube lens with focal length of 200 mm. For imaging, we used Daheng CMOS sensor with pixel pitch of 3.45 micron and sensor size of 14x10 mm. The native FOV of 4x objective is 5.5 mm (radial 2.75 mm). However, with the sensor size, the system gives a reduced FOV of 3.5x2.5 mm. We used negative USAF target slanted at angle less than 5 degrees. Figure 1(Top) shows the captured image. We calculated MTF at the edge boundary of the highlighted region. The Field_0 corresponds to field point at center of FOV, whereas Field_1 corresponds to radial field point at 1.27 mm.

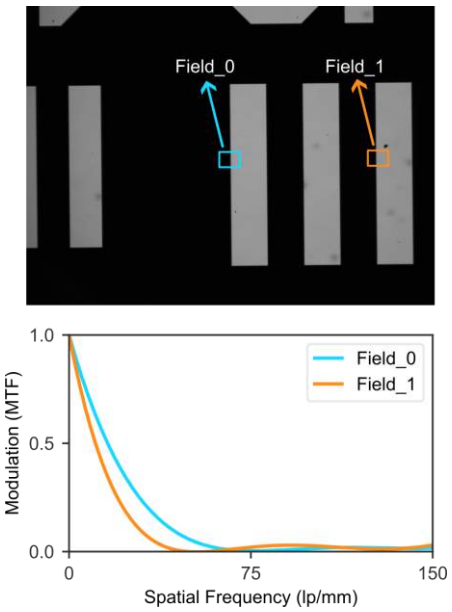


*Fig. 1: **Top –** slanted negative USAF target image recorded at the sensor. The MTF is calculated at highlighted two different field point windows. **Bottom** – corresponding MTF curve for two field points.*

Figure 1(Bottom) shows the corresponding MTF plots. We observe that The MTF curve degrades as we move away from the center of the FOV. We are using this method to characterize aberration free 3D FOV of remote focusing microscopy system [5]. Unlike the traditional MTF calculation from PSF, the slanted-edge method is easier to implement and provide super-sampling by combining data of edge spread from each row in the selected window.

D. Saini and M. Kumar acknowledge ANRF, Govt of India and IIT Delhi for financial support.

References:

[1] P.L. Smith, Appl. Opt., AO 11 (1972) 1424–1425.
[2] K. Nishi, J. Opt. Soc. Am. A, JOSAA 40 (2023) 259–269.
[3] X. Zhang, T. Kashti, D. Kella, T. Frank, D. Shaked, R. Ulichney, M. Fischer, J.P. Allebach, in: Image Quality and System Performance IX, SPIE, 2012, p. 64.
[4] C. Mitja, J. Escofet, A. Tacho, R. Revuelta, Computer Software. ImageJ. Vers 2 (2011).
[5] E.J. Botcherby, R. Juškaitis, M.J. Booth, T. Wilson, Optics Communications 281 (2008) 880–887.

Micro-Raman Spectroscopy of Extracellular Vesicles Derived from Stored Blood Components: Towards Label-Free Molecular Characterization

Mithun Nelliat[1] , Santhosh Chidangil[1,2*]

[1]Centre of Excellence for Biophotonics, Manipal Institute of Applied Physics, Manipal Academy of Higher Education, Manipal, Karnataka-576104, India

[2]Department of Physics, JSS Science and Technology University, Mysuru, Karnataka-570006, India

Email: santhosh.cls@manipal.edu, and santhosh.cls@jssstuniv.in

Extracellular vesicles (EVs) isolated from stored red blood cells and platelet concentrates were characterized using Micro-Raman spectroscopy. Distinct molecular fingerprints revealed differences in protein and lipid composition, while the absence of hemoglobin signatures in RBC-derived EVs indicated selective molecular packaging. The study highlights Micro-Raman spectroscopy as a rapid, label-free tool for EV characterization.

In the present study, we demonstrate the application of Micro-Raman spectroscopy for the molecular characterization of extracellular vesicles isolated from packed red blood cells (PRBCs) and platelet concentrates (PCs) during storage. EVs were isolated using polyethylene glycol (PEG)-based precipitation and characterized by nanoparticle tracking analysis (NTA), which confirmed mean particle sizes of approximately 120 nm for RBC-derived EVs and 170 nm for platelet-derived EVs. Raman spectra were acquired using a lab assembled micro-Raman system, enabling non-destructive biochemical analysis without the need for labels or molecular probes (1).

Distinct Raman signatures corresponding to proteins, lipids, and membrane-associated biomolecules were observed in both EV populations. Unlike their parent red blood cells, RBC-derived EVs exhibited negligible hemoglobin-specific Raman bands, indicating selective molecular packaging during vesicle formation. Comparative spectral analysis further revealed biochemical differences between RBC- and platelet-derived EVs, reflecting their unique cellular origins and biological functions. These findings demonstrate the capability of Micro-Raman spectroscopy to sensitively probe the molecular composition of nanoscale extracellular vesicles [2].

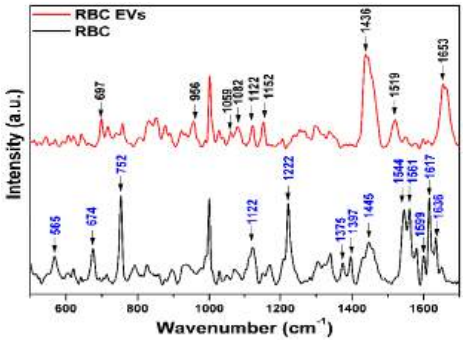


Figure 1: Micro-Raman spectra of a single live RBC and the RBC-derived extracellular vesicles

Micro-Raman spectroscopy provides a rapid, label-free platform for extracellular vesicle characterization. Combined with complementary analytical techniques, it holds significant promise for developing EV-based biomarkers for transfusion medicine and disease diagnosis.

References:

1. Van Niel G, d'Angelo G, Raposo G. Shedding light on the cell biology of extracellular vesicles, Nature Reviews Molecular Cell Biology. 2018;19(4):213-28.
2. Mithun N, Lukose J, Mohan G, Shastry S, Chidangil S. Single cell spectroscopy of red bloodcells in intravenous crystalloid fluids. Spectrochimica Acta Part A: Molecular and Biomolecular Spectroscopy. 2021;257:119726.

Silicon Photonic based Grating Assisted Microring Resonator for Biosensing Application

[1,2]Shalni Srivastava, [1,2]Shiva Kondeti, [1,2]Umesh K. Tiwari and [1,2,#]Vinod Parmar
[1]Optics and Photonics Instrumentation, CSIR-Central Scientific Instruments Organisation, Chandigarh, 160030, India.
[2]Academy of Scientific and Innovative Research (AcSIR), Ghaziabad, 201002, India.
[#]vinodparmar.csio@csir.res.in

An innovative design of grating assisted microring resonator is devised on silicon-on-insulator to determine the various stages of malaria in infected humans. A shift in resonant wavelength for healthy and infected individuals is observed in the proposed on-chip device with the maximum quality factor of 3411.65, and sensitivity of 450.057nm/RIU.

As per the World Health Organization's report on malaria, over 282 million people were affected in 2024 resulting in 610,000 deaths globally [1] therefore, appropriate and rapid detection of malaria is the primary focus of the doctors with increasing demand for advancements in biosensing technologies. In the last two decades, photonics has found immense potential in evanescent-field based biosensors [2]. The development of microring resonator (MRR) based silicon photonic lab-on-chip biosensor has aided in the holistic improvement of the healthcare sector. These resonators comprise an optically coupled loop and bus waveguide, separated by a micro or nanometre scale gap, to enable the propagation of resonant modes. They provide enhanced sensitivity, lower detection limits and robustness by leveraging the strong light-matter interactions between evanescent fields and analyte molecules [3], hence are able to detect subtle variations in analytes. The proposed research on label-free detection of malaria holds substantial importance due to its potential impact in advancing the domain of rapid point-of-care diagnostics and enables personalize treatment thus reducing the use of broad-spectrum antibiotics. This work, illustrates the analysis of a slotted grating assisted MRR designed on a silicon-on-insulator platform for efficient light coupling into the on-chip photonic biosensor. Furthermore, refractive index-based transmission wavelength shifts were observed corresponding to the detection of various stages of malaria with a maximum Q-factor of 3411.65 and sensitivity of 450.057 nm/RIU to function as a lab-on-chip label free biosensor for point-of-care diagnostics.

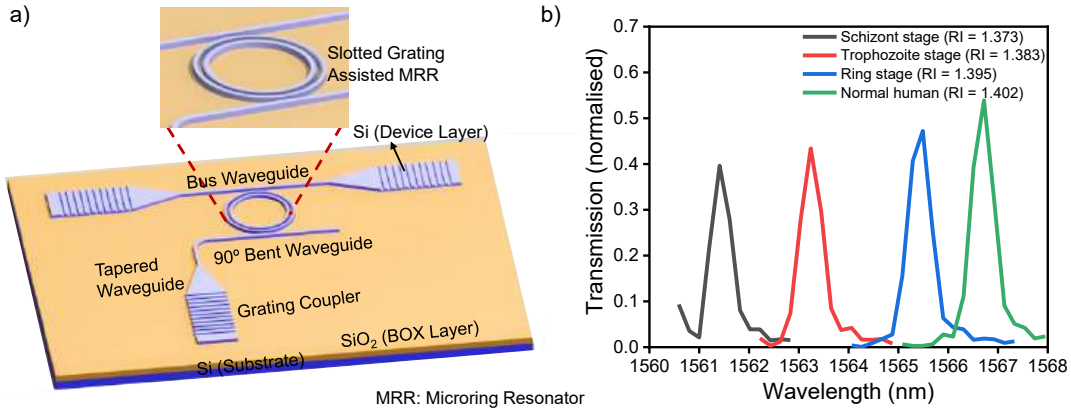


Fig. 1: (a)Perspective view of the proposed slotted grating assisted MRR-based photonic integrated biosensor, (b)Transmission spectra corresponding to the different malarial stages.

References:

[1] World Hhealth Organisation, (2025).
[2] S. Shekhar, W. Bogaerts, L. Chrostowski, J.E. Bowers, M. Hochberg, R. Soref, B.J. Shastri, Nat Commun 15 (2024) 751.
[3] W. Bogaerts, P. De Heyn, T. Van Vaerenbergh, K. De Vos, S. Kumar Selvaraja, T. Claes, P. Dumon, P. Bienstman, D. Van Thourhout, R. Baets, Laser & Photonics Reviews 6 (2012) 47–73.

Coupling Optical Fluence and Acoustic Geometry: Physics-Informed Geometry-Adaptive Reconstruction for Quantitative Photoacoustic Imaging

[1]Mridul Verma,[1]Partha Pratim Pal and [1,#]Renu John

[1]Medical Optics and Sensors Laboratory, Department of Biomedical Engineering, Indian Institute of Technology Hyderabad, Telangana, India

[#]*renujohn@bme.iith.ac.in*

We propose a physics-informed, geometry-adaptive reconstruction (PIGAR) framework for photoacoustic imaging that links optical fluence modelling with geometry-aware acoustic reconstruction. By jointly estimating the detector geometry and enforcing consistency between the optical and acoustic models, PIGAR targets the fluence and geometry dependent errors that limit quantitative accuracy in photoacoustic imaging.

In photoacoustic imaging (PAI), a short laser pulse is absorbed by tissue chromophores such as haemoglobin and melanin. The absorbed energy generates an initial pressure rise whose amplitude depends on local optical absorption and fluence, and the resulting ultrasound waves are recorded by an array of transducers [1]. Image accuracy therefore depends not only on acoustic inversion but on how well the optical fluence inside scattering tissue is modelled. Standard photoacoustic beamforming reconstructs the image from the detected signals while assuming uniform fluence and a fixed, exactly known detector geometry. In practice, light delivery is non-uniform and element positions are uncertain, so these assumptions break down and introduce quantitative error and limited-view artifacts.

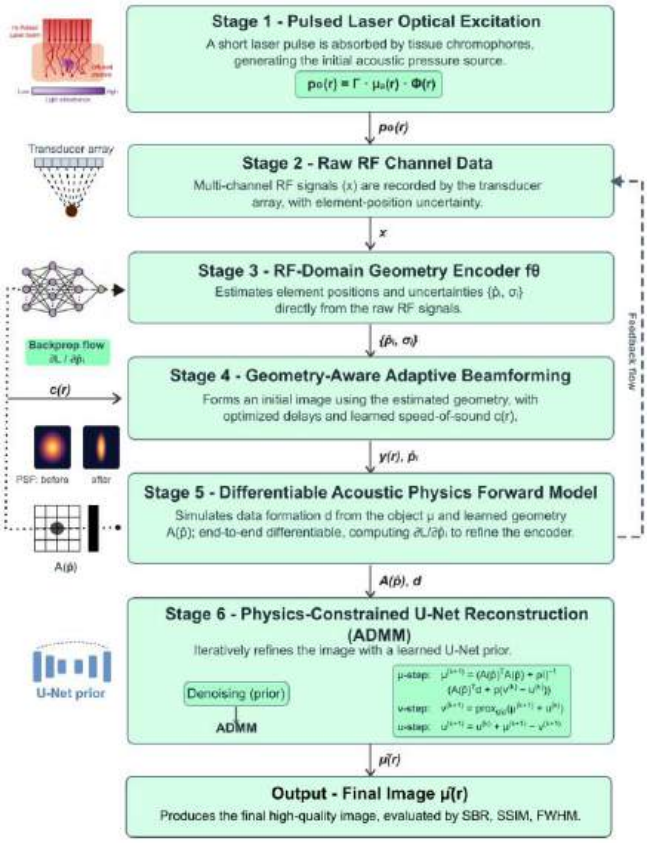


Fig. 1: PIGAR pipeline from pulsed-laser optical excitation through geometry-aware beamforming to physics-constrained reconstruction.

PIGAR couples optical excitation with geometry-aware acoustic reconstruction, following the pipeline in Fig. 1. From the raw multi-channel signals, a neural encoder f_θ estimates the effective detector geometry $\{\hat{p}_i, \sigma_i\}$. Geometry-aware beamforming then forms an initial image using the estimated geometry and a learned speed of sound c(r). A differentiable acoustic forward model $A(\hat{p})$ links the image back to the measured data, allowing the encoder to be refined end-to-end. A physics-constrained U-Net (PIGAR-Net) then refines the image using an ADMM scheme that alternates a data-consistency step, a learned U-Net prior, and a dual update, recovering the absorption map $\hat{\mu}(r)$ [2]. The networks will be trained on acoustic simulations [3] spanning a range of detector geometries and light-delivery conditions, with optical fluence modelled in tissue-mimicking media.

$$p_0(r) = \Gamma . \mu_a(r) . \phi(r) \qquad (1)$$

where p_0 is the initial acoustic pressure, μ_a is optical absorption coefficient, ϕ the local optical fluence and Γ is Grüneisen parameter.

The proposed PIGAR framework aims to improve quantitative accuracy and robustness to probe-position variation in photoacoustic imaging, with relevance to both preclinical and clinical use. The simulation and network-training pipeline is currently under development, and phantom validation is planned. Its core contribution is to treat detector geometry and optical fluence as jointly estimated quantities within a single differentiable reconstruction pipeline, rather than as separate, fixed assumptions.

References:

[1] L.V. Wang, S. Hu, *Science* 335 (2012) 1458–1462.
[2] A. Hauptmann, B.T. Cox, *Journal of Biomedical Optics* 25 (2020) 112903.
[3] B.E. Treeby, B.T. Cox, *Journal of Biomedical Optics* 15 (2010) 021314.

Design and Simulation of a Terahertz-Based Sensor for Early Breast Cancer Detection

[1#]Hari Shankar Singh,[2]Vishal Srivastava, [3]Asit Ranjan Mridha
[1]Department of Electronics and Communication Engineering, Thapar Institute of Engineering and Technology, Patiala, Punjab
[2]Department of Electrical and Instrumentation Engineering, Thapar Institute of Engineering and Technology, Patiala, Punjab
[3]Department of Pathology, All India Institute of Medical Science, New Delhi
[#]*harishankar1990@gmail.com*

Early diagnosis of breast cancer significantly improves treatment outcomes and patient survival. This work presents the design and simulation of a high-sensitivity terahertz (THz)-based sensor for non-invasive breast cancer detection. The proposed sensor exploits dielectric property variations between healthy and malignant tissues, demonstrating enhanced sensitivity, resonance characteristics, and strong potential for next-generation biomedical diagnostic applications.

Breast cancer is one of the leading causes of cancer-related mortality among women, highlighting the need for rapid, accurate, and non-invasive diagnostic techniques. Terahertz (THz) sensing has emerged as a promising modality due to its non-ionizing nature and high sensitivity to the dielectric properties of biological tissues. In this work, a compact metamaterial-inspired terahertz sensor is proposed for early breast cancer detection. The sensor operates in the 0.8–1.2 THz frequency range with a resonant frequency of 1.0 THz and employs a square split-ring resonator (SRR) with a central capacitive gap to achieve strong electric-field confinement. The sensor is designed on a 500 μm thick high-resistivity silicon substrate (ε_r=11.9) with a 200 nm gold conducting layer. The overall sensor dimensions are 1.5 mm × 1.5 mm, while the SRR has an outer length of 800 μm, strip width of 40 μm, and split gap of 20 μm. Breast tissue samples are placed within the sensing gap, where variations in dielectric properties produce measurable shifts in the resonance frequency and scattering parameters. The proposed sensor is modeled using CST Microwave Studio with a frequency sweep from 0.5 to 1.5 THz. Its performance is evaluated in terms of reflection coefficient (S11), transmission coefficient (S21), resonance frequency shift, quality factor (Q-factor), electric-field enhancement, sensitivity, and figure of merit (FOM). The proposed design is expected to exhibit distinct resonance shifts between healthy and malignant breast tissues, demonstrating its potential as a compact, high-sensitivity, and non-invasive THz sensor for early breast cancer diagnosis.

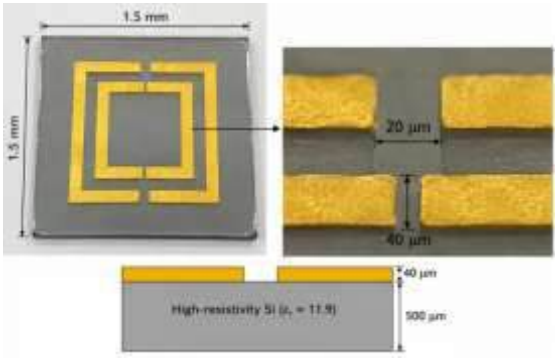


Fig. 1: Geometry of the proposed square split-ring resonator (SRR)-based terahertz sensor operating at 1.0 THz for early breast cancer detection.

Acknowledgement: The authors would like to thanks ANRF (Project Code: CRG/2022/001256) for providing financial support to carry out this research work.

References

[1] A.K. Ghatak, K. Thyagarajan, *Optical Electronics*, Cambridge University Press, Cambridge (1989).
[2] L.C. Venuti, T. Albash, D.A. Lidar, P. Zanardi, *Physical Review A* **93** (2016) 032118.
[3] S. Sunder, A. Sharma, *Workshop on Recent Advances in Photonics (WRAP 2019)* **19** (2019).

Design and Development of an Intraoral Imaging Probe for Early Detection of Oral Premalignant Lesion

Mohammed Ansar PT[*,1], Annavajhula Keerthana[*,1], Srikrishnan Senthilkumar[2], Vijayalakshmi Ramshankar[2], Arvind Krishnamurthy[2], Uttam Mrinal Pal[#,1]
[1] Department of Electronics and Communications Engineering, IIITDM Kancheepuram, Chennai
[2] Department of Surgical Oncology at the Cancer Institute (WIA), Chennai
[#]coressponding author: uttampal@iiitdm.ac.in
[*] Equal contribution

Abstract:
Oral cancer remains a major public health problem worldwide, driving high rates of patient illness and mortality. Early detection plays a crucial role in improving treatment outcomes and significantly increasing patient survival rates. However, conventional oral examinations rely primarily on manual visual inspections under standard dental white-light illumination. This approach has limited efficacty detect pre-malignant lesion. Furthermore, the accuracy of clinical screening depends significantly on the individual clinician's experience, leading to highly subjective variations in diagnostic assessment. An intra oral system has been developed using a low resolution camera (~ 1MP), achieving the spatial resolution of 20 lp/mm.

These limitations highlight a pressing clinical need for reliable, objective, and structurally refined technology-assisted screening tools that can streamline and significantly improve the early detection of suspicious oral premalignant lesions. To address these challenges, a handheld intraoral imaging probe was developed for diagnostic screening. Unlike standard commercial systems, this physical probe utilizes an architectural design that relocating the primary sensor elements away from the insertion end to keep the probe's profile compact and to keep the electronics parts away from the contacting tissue, avoiding heating issues. For significantly improved clinical ergonomics and ease of access to inaccessible posterior regions of the oral cavity, the distal end of the probe is specifically engineered with a pre-defined bent angle relative to its central axis. This physical angulation allows clinicians to navigate the oral cavity while maintaining a natural wrist posture. To thoroughly evaluate the optical and spatial characteristics of the imaging system, some pictures of a standard United States Air Force (USAF) 1951 (Fig 1) resolution test chart has been captured to quantify the system's spatial resolution limit and image-sharpness capabilities. Additionally, an experimental mapping of operational relationship between the probe's Field of View (FOV) and its Working Distance (WD) was done.

The quantitative relationship between the Field of View and Working Distance was systematically tabulated in Table 1. At close working distances (~ 3 cm), the probe successfully maintained magnified target capture, gradually retracting the probe increases the field of view, enabling imaging of the entire region of interest. The angled distal tip allowed consistent optical alignment with the tissue surface across these varying working distances. The system achieved resolution of approximately 20 lp/mm.

S.No	Working Distance (cm)	Field of View (cm)
1	3	2.5 × 4.25
2	3.5	3 × 5.5
3	4	3.5 × 6.2
4	5	4.5 × 7.5
5	6	4.6 × 8.1
6	7	5.2 × 9.5

Table 1: Field of View (FOV) VS Working Distance (WD)

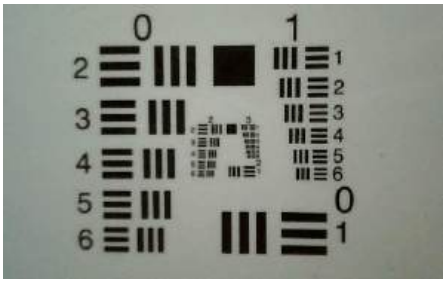


Fig 1: captured a standard USAF 1951 image

FTIR Spectroscopy in serum sample of breast cancer Patients

[1,#]D. Qaiser
[1]Department of Surgical Disciplines AIIMS New Delhi

#qaiser.d@gmail.com

Abstract

Breast cancer is regarded as the most malignant tumor among women throughout the world. Therefore, early detection and proper diagnostic methods have been known to help save women's lives. Fourier Transform Infrared (FT-IR) spectroscopy is a new technique to investigate the characteristics of serum in breast cancer.

Breast cancer is the second most common cancer worldwide and the leading cause of cancer death among women. Early detection and diagnosis can significantly improve patient outcomes. Fourier transform infrared (FTIR) spectroscopy is a non-invasive diagnostic tool that can provide valuable information on the molecular composition of biological samples. It has been shown to be effective in diagnosing various diseases, including cancer.

For the present study collected blood sample of breast cancer patients and separate out the serum from the blood and then we will record the FTIR spectra of serum sample. The spectra will be recorded in the mid-infrared region (4000-400 cm^{-1}) using a high-resolution detector.

Results indicates the spectral differences between breast cancer and normal patients sample using FTIR spectroscopy. Identification of differences in molecular composition between breast cancer patients and healthy controls using FTIR spectroscopy and evaluation of the accuracy of FTIR spectroscopy in diagnosing breast cancer.

There is spectral difference between the cancerous and non-cancerous group. This spectral difference is related to the difference in the protein conformation in the serum and tissue samples of two groups. It can be concluded that FTIR spectroscopy is able to discriminate between breast cancer and healthy serum sample.

.

References:

[1] Stewart, B.; Wild, C.P. World cancer report 2014. Public Health 2019; International Agency for Research on Cancer: Lyon, France, 2019.

[2] H. Ghimire, C. Garlapati, E.A.M Janssen, U. Krishnamurti, G. Qin, R. Aneja, A.G.U Perera, Cancer 12 (2020) 1708.

Improving finite bit-depth of any low-cost CMOS camera sensor using Quantitative Exposure Fusion

[1]Annwesha Bhattacharya,[2]Rajesh Kumar and [1]Kedar Khare
[1]Optics & Photonics Centre, Indian Institute of Technology Delhi, New Delhi 110016, India
[2]Department of Physics, Indian Institute of Technology Delhi, New Delhi 110016, India

E-mail: kedark@opc.iitd.ac.in

Affordable pixelated camera sensors are insufficient for observing well-known optical phenomena like diffraction due to their limited dynamic range. In this work, we demonstrate how to address the finite bit-depth problem using exposure fusion method to record quantitatively accurate diffraction patterns and implement the idea with a generic toolbox to turn it into a novel protocol for any imaging sensor.

Low-cost CMOS camera sensors with a typical dynamic range of 8 bits (256 grey levels) are now readily available in any research-based laboratory. The feature of interest in any Fraunhofer diffraction pattern spans the intensity values over a large dynamic range, which the two-dimensional pixelated array sensors are incapable of recording because of their limited bit-depth. Exposure fusion is a well-known technique for higher dynamic range (HDR) imaging and is already utilized in commercial mobile phone cameras for visually pleasing image display. However, such applications are usually not concerned with quantitative accuracy. In this work, we highlight the exposure fusion methodology along with appropriate camera sensor calibration.

For most commercially available camera sensors, the numeric pixel read-out value (Z) is not linear but rather a power-law function of the product ($E_0\Delta t$) of the native irradiance E_0, and exposure times Δt [1]. It is important to understand from the log-log plot in figure-1 that if another beam with a different native irradiance compared to the calibration is incident on the camera, then the plot simply results in a shift (Δ) from the response curve. Measurements do not follow the physical convolution model due to this nonlinear camera response. The profile plots through the central row of the recorded diffraction patterns of a stationary circular aperture, shown in Figure 2, illustrate our point. A linear model fit to the linear region of camera calibration is important to generate a reverse look-up table ($h^{-1}(log_{10}Z)$) that maps $log_{10}(\Delta t)$ values corresponding to all possible grey levels.

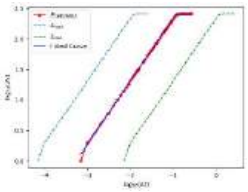


Fig.1: Nonlinear camera response

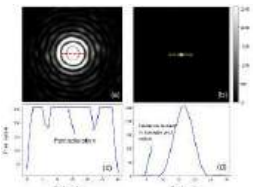


Fig.2: Airy patterns

Exposure fusion refers to an intelligent combining of multiple photographs of the same scene recorded over a range of exposure times. We assign equal weight ($w\,(log_{10}(Z))$ to those pixel values that lie in the linear region of the camera response to avoid the flat region of exposure values where the pixels get saturated. Weighted average of the shift (Δ_k) in irradiance for each pixel position (k) estimates the composite image with increased bit depth and that may be expressed as:

$$\Delta_k = \frac{\sum_{j=1}^{N} w\left(log_{10}(Z_{kj})\right)[h^{-1}(log_{10}(Z_{kj}))-log_{10}(\Delta t_j)]}{\sum_{j=1}^{N} w(log_{10}(Z_{kj}))} \quad (1)$$

A comparative study on the numerical energy ratio of the central peak to the higher-order peak in the composite image to the ground-truth ratio for the simulated pattern concludes that exposure fusion allows us to record quantitatively accurate diffraction patterns with enhanced dynamic range corresponding to 10-11 bits using an 8-bit camera sensor, shown in figure-3 [2]. We have further designed a high-performance multicore GUI using Python [3] to automate real-time image acquisition with multi-exposure camera sequence to construct the image after exposure fusion. This standardized toolbox is compatible across various camera platforms and can be extended to advanced quantitative imaging tools, such as high-end microscopy systems.

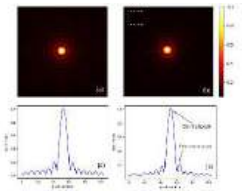


Fig.3: Theoretical vs composite Airy pattern

References:
[1] Paul E Debevec and Jitendra Malik, *In Seminal Graphics Papers: Pushing the Boundaries*, Volume 2, pages 643–652. (2023).
[2] A.Bhattacharya, Srishti, M. Kularia, and K. Khare, *European Journal of Physics*, 47(1), 015303 (2026).
[3] Hughes, M. R. *Applied Optics*, 64(20), 5837–5844 (2025).

Optimization-based Phase Retrieval in Cryo-Electron Microscopy

[1,#]Muskan Kularia,[2]Manidipa Banerjee and [1]Kedar Khare
[1]Optics and Photonics Centre, Indian Institute of Technology Delhi, Delhi, India
[2]Kusuma School of Biological Sciences, Indian Institute of Technology Delhi, Delhi, India
[#]*opz218644@iitd.ac.in*

We introduce an optimization framework for recovering the complex-valued exit wavefunction from Cryo-electron microscopy (*Cryo-EM) micrographs. By modeling the image formation process through the microscope's contrast transfer function and employing a Laguerre–Gaussian Total Variation penalty, the proposed method facilitates downstream image processing for improved 3D reconstruction in Cryo-EM.*

Cryo-electron microscopy (Cryo-EM) has revolutionized the field of structural biology by enabling determination of 3D structures of biological macromolecules at near-atomic resolution. In single-particle Cryo-EM, thousands to millions of randomly oriented biomolecules embedded in amorphous ice in their native hydrated states are imaged using a transmission electron microscope. Since biological specimens behave predominantly as weak-phase objects, the transmitted electron wave undergoes only small phase modulations with negligible amplitude variations, so an intentional defocus is introduced to enhance the amplitude contrast. The detector therefore records an intensity only image of the exit wavefunction modified by the effects of contrast transfer function (CTF) of the microscope that includes the effects of defocus, spherical aberration, chromatic aberration, astigmatism and other aberrations in the microscope. Also, these micrographs exhibit extremely low signal-to-noise ratios (SNR) as they are recorded under very low-electron-dose conditions to minimize radiation damage. The 3D reconstruction then relies on combining the Fourier information from numerous 2D projections through the Fourier projection (central slice) theorem. Recovering the accurate complex valued exit wavefunction which corresponds to the true 2D projections thus plays a pivotal role in achieving high-resolution 3D reconstructions.

In this work, we present an optimization-based framework for reconstructing the complex exit wavefunction from a Cryo-EM micrograph by reinterpreting the recorded image as an in-line Fresnel hologram of the specimen [1]. The forward model incorporates the microscope's CTF while the inverse problem is regularized using a novel Laguerre–Gaussian Total Variation (LGTV) penalty [2] that promotes physically plausible solutions under the extremely low signal-to-noise conditions of Cryo-EM imaging. The recovered exit wave can be numerically re-projected via Fourier optics model to the detector plane to obtain a denoised micrograph that retains intrinsic structural details while effectively suppressing noise. It can also be numerically propagated through different microscope transfer functions to synthesize images under different imaging conditions, enabling applications such as computational realization of virtual phase-plate imaging, improved particle picking and classification, and higher-fidelity 3D reconstruction.

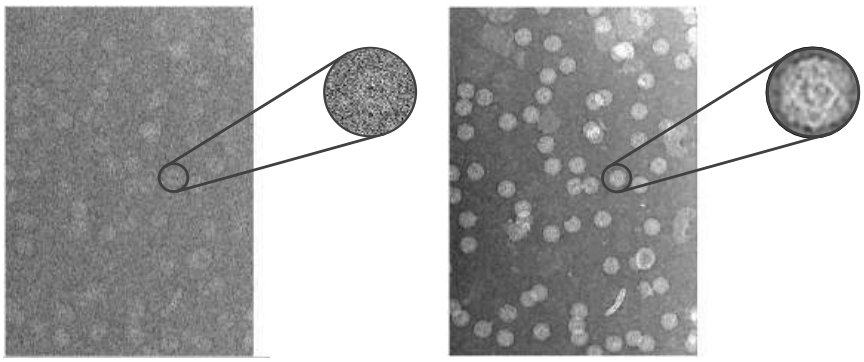


Fig. 1: (a) Original micrograph (b) Obtained denoised micrograph of Flockhouse Virus

References:

1. A. Pant, M. Banerjee,K. Khare, Optics Communications, 506, 127588 (2022).
2. M. Kularia, M. Banerjee, K. Khare, Journal of Optical Society of America A 43, D50-D63 (2026).

Stray Light Analysis and Optimization of a Double Gauss Imaging System Using Non-Sequential Ray Tracing in ANSYS Zemax OpticStudio

Khushi[1], Titir Bhattacharya[1], Sourabh Roy[1]

Department of Physics, National Institute of Technology Warangal, Warangal 506004, Telangana, India

kk24phc1r26@student.nitw.ac.in

titirbhattacharya28@gmail.com

Stray light impairs image performance by lowering contrast and creating ghost artifacts. This paper describes non-sequential stray light analysis and optimization of a Double Gauss imaging system in ANSYS Zemax OpticStudio. Mechanical suppression techniques and detector-based optimization greatly minimize stray irradiance, resulting in improved picture contrast and imaging performance.

Stray light from unwanted reflections, scattering, and ghost rays affects high-performance imaging systems, resulting in lower image contrast and higher detector noise. The Double Gauss lens is extensively employed because to its high imaging capability, yet it is still susceptible to stray radiation. A Double Gauss imaging system was studied in ANSYS Zemax OpticStudio's Non-Sequential Component mode and optimized using optical and mechanical stray-light suppression approaches.

The optical system was generated in ANSYS Zemax OpticStudio using non-sequential ray tracing. To minimize integrated stray irradiance, an absorbing housing, three annular baffles, VIS-NIR anti-reflection coatings, an optical filter, and detector-based merit function optimization using NSDD operands were implemented.

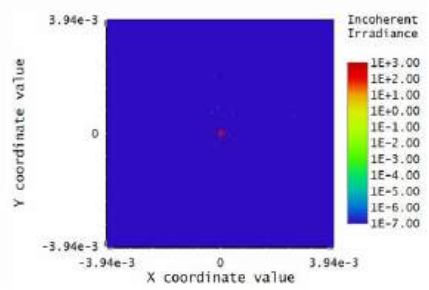


Fig. 1. Optimized detector irradiance distribution after stray-light suppression.

The baseline detector image showed significant background irradiance and ghost artefacts. Mechanical housing efficiently reduced peripheral stray radiation, while sequential annular baffles blocked ghost routes and dispersed rays. Anti-reflection coatings further reduced Fresnel reflections, and detector-based optimization resulted in a tightly restricted irradiance distribution with little stray-light contribution, improving contrast and overall imaging quality.

The proposed optical and mechanical suppression approach significantly reduced stray light in the Double Gauss imaging system. The revised design improved detector contrast, reduced ghost artifacts, and increased image performance, making it ideal for high-performance optical imaging applications.

Acknowledgement:

The authors would like to express their gratitude to Prof. Sourabh Roy, Head of the Physics Department at the National Institute of Technology Warangal, for his unwavering support and encouragement..

References:

[1] Lens Design Fundamentals, R. Kingslake and R. B. Johnson, Academic Press, 2010.

[2] ANSYS Inc.'s Zemax OpticStudio User Manual.

[3] Optical Electronics, A. K. Ghatak and K. Thyagarajan, Cambridge University Press, 1989.

An affordable Multimodal Optical Scanning Microscope (MOSM)

[1, #, $]Neeraj Kumar,[1, $]Anupam Bharadwaj, [1]Pranjal Choudhury, [1]Bosanta R. Boruah
[1]Department of Physics, Indian Institute of technology Guwahati-781039, India

[#]k.neeraj@iitg.ac.in

[$]Contributed equally

Here reported an affordable multimodal optical scanning microscope integrating Point Scanning Microscopy (PSM), Confocal Microscopy (CM), and Image Scanning Microscopy (ISM). Unlike conventional approaches that require separate experimental setups, the proposed system combines all three imaging modalities into a single, flexible, and cost-effective platform. Preliminary imaging of a USAF 1951 resolution target validates its feasibility.

Optical microscopy is a vital tool for exploring microscopic structures of biological and material sciences specimen. Although recent advances have significantly improved imaging performance, modern microscopy techniques are often associated with high cost, increased complexity, and dedicated experimental setups for each imaging modality. To improve accessibility, we have developed a low-cost, multimodal optical scanning microscope (MOSM) that integrates multiple imaging techniques within a single platform. The MOSM is capable of performing Point Scanning Microscopy (PSM), Confocal Microscopy (CM), and Image Scanning Microscopy (ISM), providing a versatile and cost-effective solution for advanced optical imaging [1-5]. The system is designed to be flexible, allowing hardware components to be replaced or upgraded according to user requirements while maintaining affordability. The MOSM utilizes galvanometer-based X–Y scanning mirrors, which scans a diffraction-limited laser beam on the sample. The reflected or emitted light from each scan position of the sample is descanned and recorded by the array of pixels on a CMOS camera, which are stored in the PC. The final image is reconstructed from the stored images using suitable algorithms, to produce PSM, CM, and ISM images. The developed microscope is evaluated by scanning a 64 × 64-pixel region corresponding to the alternating transparent and opaque strips of Group 0, Element 2 of a USAF 1951 resolution test target. The reconstructed images obtained using PSM, CM, and ISM are presented in Figure 1. Compared with PSM, CM effectively reduce out-of-focus background, resulting in improved image contrast. ISM further enhances contrast and signal-to-noise ratio, as confirmed by the intensity profiles shown in Figure 2 corresponding to yellow lines in Figure 1. These preliminary results demonstrate the successful implementation of three imaging modalities within a single, affordable optical scanning microscope.

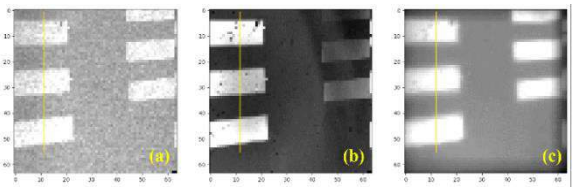


Figure 1: Implementation of **(a)** PSM, **(b)** CM and **(c)** ISM in a USAF 1951 test target.

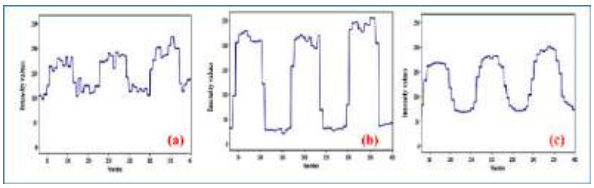


Figure 2: (a), (b) and **(c)** are the intensity plots corresponding to yellow lines as shown in figure **1 (a), (b)** and **(c)** respectively.

The proposed multimodal optical scanning microscope successfully combines PSM, CM, and ISM into a single, affordable platform thereby facilitating imaging of a common specimen area using each of the three different microscopy techniques. Preliminary results demonstrate its feasibility and potential as a flexible solution for advanced optical imaging.

Acknowledgements: The authors acknowledge the financial support from UGC.

References:

[1] A. D. Elliott, *Confocal Microscopy: Principles and Modern Practices*, *Curr. Protoc. Cytom.*, 2020.

[2] C. B. Müller and J. Enderlein, "Image Scanning Microscopy," *Phys. Rev. Lett.*, **104**, 2010.

[3] C. J. R. Sheppard and C. J. Cogswell, "Confocal Microscope with Array Detector," *J. Mod. Opt.*, **37**(2), 267–279, 1989.

[4] E. N. Ward and R. Pal, "Image Scanning Microscopy: An Overview," *J. Microsc.*, **266**, 221–228, 2017.

[5] I. Gregor and J. Enderlein, "Image Scanning Microscopy," *Curr. Opin. Chem. Biol.*, **51**, 74–83, 2019.

Design of Zoom Lens in LWIR for Surveillance Purposes

[1]Suvadeep Maji, [1]Rajarshee Roy and [1, #]Kanik Palodhi
[1]Department of Applied Optics and Photonics, University of Calcutta, Kolkata-700106.

[#]Email id: kpaop@caluniv.ac.in

Abstract: *Infrared imaging systems play a significant role in modern surveillance systems in the fields of defence, security, biomedical, target tracking, etc. This paper focuses on the design of a zoom lens and is simulated in Ansys OpticStudio with FOV of ±10° LWIR bands of IR to image the respective responses.*

Keywords: *Zoom lens, Imaging, LWIR.*

A multi-configuration infrared zoom lens assembly is designed in Ansys OpticStudio with a FOV of ±10º, an effective focal length of 60 mm, and an F/4.2 ratio in the LWIR (8-14 µm) wavelength band of the Infrared spectrum.

This zoom lens assembly consists of seven lens elements organised in two optical groups with four zoom configurations. Different types of infrared optical materials are utilised, such as Zinc Selenide (ZnSe), Cesium Bromide (CsBr), IRG25 (Infrared Chalcogenide glass), etc to attain high infrared transmission and enhanced imaging performance. The obtained 3D diagram is given in Fig. 1.

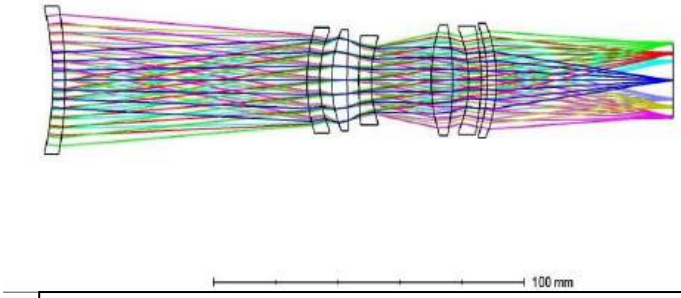


Fig. 1: Optical 3D Diagram of the IR Lens Assembly System

Using standard optical design parameters like spot diagram analysis, field of view variations, and modulation transfer function (MTF), the performance of the zoom lens assembly is evaluated. This lens assembly produce a continuous focal length variation while maintaining image quality and focus throughout the zoom range.

The design is further optimised for the lenses to obtain a good MTF of 40% for all the configurations, and the spot diagrams are within the airy radius for all the zoom configurations.

This lens assembly can be effectively used for defence applications particularly, for monitoring and surveillance purposes.

The authors gratefully acknowledge the support and facilities provided by the Department of Applied Optics and Photonics, University of Calcutta, which made this work possible.

References:

[1] Khaled Mowafy, Tawfik EL- Dessouky, Mohamed Medhat, " Design of IR Zoom Lens System for Long-range Detection in Uncooled LWIR Camera", J. Opt, (March 2023), 52(1), 281-289.
[2] K. Yamaji, "IV Design of Zoom Lens ", Progress in Optics, Vol 6, 105-170.
[3] G. C. Holst, "Infrared Imaging System Testing ". Bellingham, WA, USA: SPIE Press, 2008

Glass Optimization for a Wide Field-Of-View Lens Assembly Design for Camouflage Detection in IR bands

[1]Rajarshee Roy, [1]Agnija Dutta Gupta and [1,#]Kanik Palodhi
[1]Department of Applied Optics and Photonics, University of Calcutta, Kolkata-700106.

[#]Email id: kpaop@caluniv.ac.in

Abstract: *A Wide Field-of-View lens assembly is useful in camouflage detection through imaging in different Infrared bands through a single channel. A lens assembly is designed in Ansys OpticStudio with FOV of ±90º in SWIR, MWIR and LWIR for clear identification of objects through images recorded in this bands.*

Keywords: *Wide FOV, Imaging, IR bands.*

The Camouflage detection is the cognitive, biological, or technological process of identifying and segmenting hidden targets that blend into their background environment. By breaking through artificial or natural visual concealment—such as background matching, disruptive coloration, or mimicry—camouflage detection uncovers hidden threats, personnel, or assets. For a drone-based surveillance system employing wide FOV lens assembly, the effective mass of the system and the total axial extent of the system needs to be as minimal as possible.

A wide FOV lens assembly is designed in Ansys OpticStudio with a FOV of ±90º with effective focal length of 2.2 mm and F/2 in wavelength bands of SWIR (1.4-3.0 μm); MWIR (3-5 μm); and LWIR (8-14 μm) of the Infrared spectrum.

The design was initially done with glasses which has assigned transmittances in visible spectrum. Since, these glasses don't support the entire infrared spectrum, we had extended its transmittances to IR bands using Conrady equation, given in Eq. (1), in order to demonstrate that the entire spectrum could be covered with one setup only.

$$n = n_0 + \frac{A}{\lambda} + \frac{B}{\lambda^{3.5}} \quad (1)$$

Using glass substitution method, we are replacing these glasses to standard materials that have good IR transmittances. The radii of curvatures and the thicknesses were simultaneously optimized to obtain good imaging quality in the bands. The obtained 3D diagram after optimization is given in Fig. 1.

The design is further optimised for the lenses to obtain a good MTF of 40% for all the configurations and the spot diagram are within the airy radius.

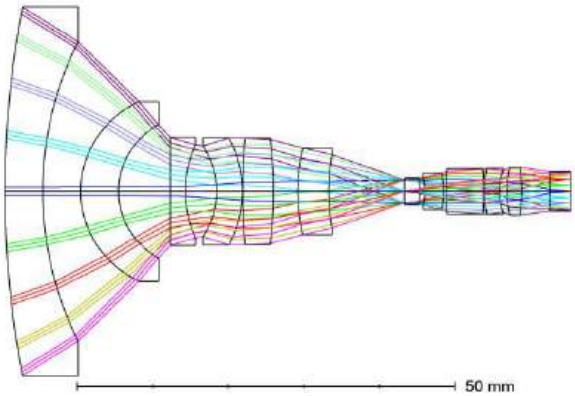


Fig. 1: Optical 3D Diagram of the IR Lens Assembly System

The authors gratefully acknowledge the support and facilities provided by the Department of Applied Optics and Photonics, University of Calcutta, which made this work possible.

References:

[1] Russell Hudyma, Michael Thomas, Navitar Industries, LLC. "Optical Assembly for a Wide Field of View Point Action Camera with Low Field Curvature", U.S. Patent 10,107,989 B1, issued October 23, 2018.
[2] Claudio Pernechele, Luca Consolaro, Geraint H. Jones, George Brydon, and Vania Da Deppo, "Telecentric F-theta fisheye lens for space applications," OSA Continuum 4, 783-789 (2021).
[3] Kumar, Vinay & Ghosh, Jayanta. (2016), Camouflage Detection Using MWIR Hyperspectral Images, Journal of the Indian Society of Remote Sensing. 45. 10.1007/s12524-016-0555-8.
[4] Leong, Ho C. "Imaging and reflectance spectroscopy for the evaluation of effective camouflage in the SWIR." (2007).

Performance Analysis Comparison of PIN and APD based Receivers in Free-Space Optical Communication Systems

Rohit Sai Nandu Venkat Sala and Srijith Kanakambaran#
Department of Electronics and Communication Engineering
IIITDM Kancheepuram, Chennai 600 127, India.
#email: srijith@iiitdm.ac.in

This study compares the performance of PIN and APD based receivers in a 1550 nm Free-Space Optical (FSO) communication system using OptiSystem. By analyzing thermal noise, shot noise, and their combined effects at different input powers, the results show that the APD provides higher Q-factor, lower BER, and better sensitivity under practical operating conditions.

The FSO channel transmits optical signals through free space, where attenuation and environmental effects influence the received signal quality. This work presents a comparative performance analysis of PIN and Avalanche Photodiode (APD) receivers in a 1550 nm Free-Space Optical (FSO) communication system using OptiSystem. The simulation setup includes a PRBS generator, NRZ pulse generator, MZM, CW laser, FSO channel, and PIN/APD receivers with BER analyzers [1]. Simulations were performed at 1550 nm, 800 m range, 0.44 dB/km attenuation, and −2 to 5 dBm input power, as shown in Fig.1

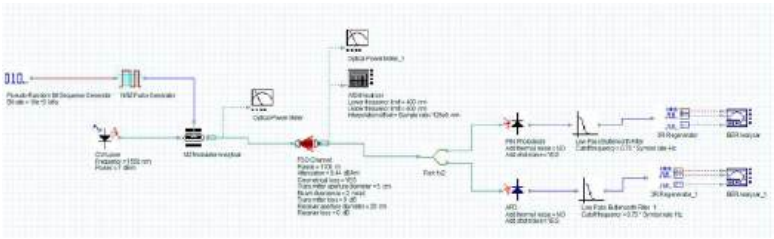


Fig 1: Layout of Simulation setup in OptiSystem

The performance of both photodetectors was evaluated by considering thermal noise, shot noise, and their combined effects. The Q-factor increased with input power for both receivers, while the APD achieved higher Q-factors and lower BER under combined noise conditions due to its internal avalanche gain. Under shot-noise-only conditions, the PIN receiver exhibited comparatively higher Q-factors because it is unaffected by APD multiplication noise, as shown in Fig.2 and Fig.3.

The simulation results show that the Q-factor increases with input power, while the BER decreases for both PIN and APD photodetectors [2]. The APD achieves higher Q-factors and lower BER under combined noise conditions due to its internal avalanche gain, whereas the PIN performs better only under shot-noise-only conditions because it is free from multiplication noise. These results demonstrate that the APD offers greater receiver sensitivity and more reliable performance for practical FSO communication systems.

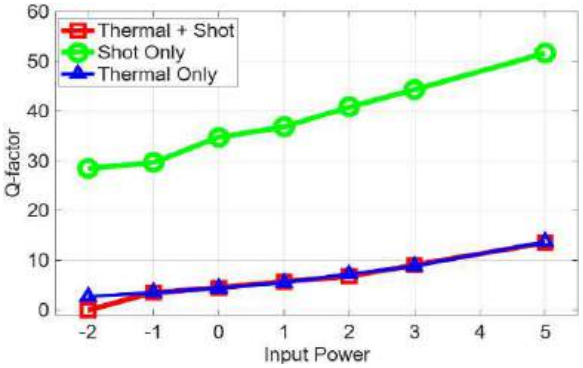


Fig 2: Q-factor vs Input power for PIN

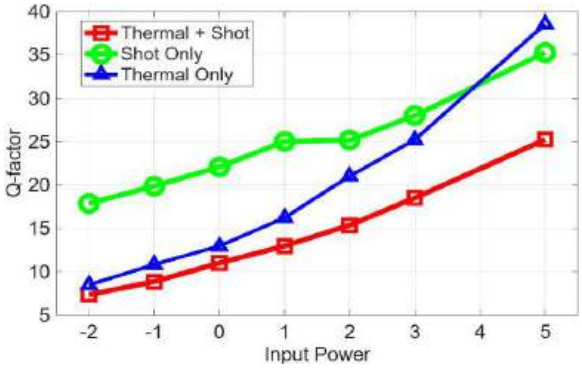


Fig 3: Q-factor vs Input power for APD

Overall, the simulation results confirm that the APD photodetector provides superior performance compared to the PIN photodetector under practical noise conditions. Its higher receiver sensitivity and lower BER make it a suitable choice for reliable long-distance 1550 nm FSO communication systems.

References:

[1] R. Challapalli and P. Chitra, “Investigating MIMO technology in free space optical communication systems for evaluating performance across various environment parameters,” Results in Engineering, vol. 25, p. 103617, 2025.
[2] E. I. Eltahir *et al*., "Performance Analysis of PIN and APD Photodetectors in an Optical Communication System under Adverse Conditions," *2025 10th International Conference on Computer and Communication Engineering (ICCCE)*, Kuala Lumpur, Malaysia, 2025, pp. 1-5.

Impact of Thermal and Mechanical Stress on Optical Performance of a large aperture Long Wave Infrared Catadioptric Telescope

[1,#]Amarendra Pratap Singh,[2]Neelam Verma and [3]Dr. Ravinder Reddy M
[1,2,3]Center of Excellence, EW&P, PDIC, Bangalore, Karnataka, 560013
[#]*apratap@bel.co.in*

High precision Catadioptric systems essentially use low expansion material and advanced mounting schemes. However, for cost-effective land based systems, use of Aluminum as substrate and housing material becomes imperative. This paper evaluates various load impacts on system's optical performance using Finite Element Analysis (FEA) and mapping results in optical software.

In multiple chemical and biological detection systems, large aperture telescopes are used for efficient capturing of low strength signals from the scene. [1][2] These afocal systems are further attached with core sensor for detection and analysis of such signals. For large aperture telescopic systems, catadioptric systems are anonymous choice to achieve smaller form-factor. But, it also brings complexity in the terms of structural integrity and robustness of system due to induced thermal and mechanical stresses under gravity, temperature and mounting loads.
Catadioptric Optical system was designed to achieve low obscuration ratio having diffraction limited performance. System parameters are shown in Table 1. Opto-mechanical modeling was done to house primary, secondary mirror as well as lenses. Designed opto-mechanical system was subjected to gravity; temperature and mounting point loads after finite element mesh modeling. Fig. 1 shows displacement map after structural analysis of long wave infrared (LWIR) telescope.

S.No.	Parameters	Value
1.	Aperture	200 mm
2.	Afocal Ratio	5x
3.	TOTR	300 mm
4.	Obscuration Area	<15 %
5.	Telescope type	Cassegrain

Table.1: System Parameters

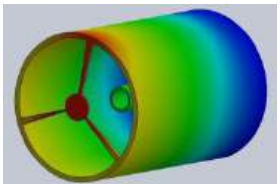


Fig. 1: Structural Analysis of LWIR telescope

Since, the system is intended to be used with further optics; exit pupil is maintained after the end element to avoid vignetting due to pupil mismatch. To achieve this Keplerian telescope approach was used with intermediate real image. Fig. 2 and Fig. 3 show optical performance in absence of stress.

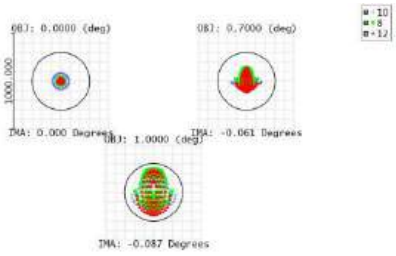


Fig. 2: Spot Diagram

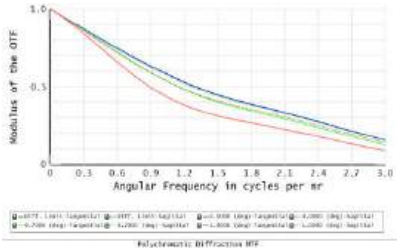


Fig. 3: Modulation Transfer Function

In this study, opto-mechanical housing was designed for LWIR catadioptric system. Finite Element Analysis was done by applying various loads such as gravity, temperature and mounting loads. Displacement map was imported in optical software for spot and MTF analysis. It was found that system is susceptible to minor displacement causing defocus as well as off-axis aberrations due to asymmetric deformation of optical surfaces making such analysis inevitable before finalizing mounting and tolerance parameters.
Authors would like to thank Head, Center of Excellence, EW&P and General Manager & Chief Technology Officer, EW&P, PDIC for providing necessary support and guidance for the work.

References:

[1] M. Kastek, T. Piatkowski, H. Polakowski, *WIT Transactions on Ecology and the Environemnt,* Vol 147 (2011).
[2] Rebecca J Hopkins, et. al., *Proc. of SPIE* Vol. 7484 748409 (2019).

Sidelobe suppression of Airy beams

[1,#]Nandan Satish Bhat, [1]Jerin Geogy George, and [1]Shanti Bhattacharya
[1]Department of Electrical Engineering, IIT Madras, Chennai, India
[#] *chikkadinandan@gmail.com*

Non-diffracting Airy beams possess significant sidelobes, which are detrimental in many applications, including light-sheet microscopy. We propose and experimentally demonstrate a sidelobe-suppressed Airy beam (SSAB) generated by random multiplexing two cubic phases. The SSAB shows considerably reduced sidelobe intensity while preserving its inherent properties.

light-sheet fluorescence microscopy overcomes out-of-plane signal and photo-bleaching limitations of conventional microscopy, but Gaussian beam based light-sheets suffer from non-uniform thickness. Non-diffracting beams offer a uniform light-sheet with self-healing properties, yet their sidelobes reintroduce photo-bleaching. Sidelobe suppression via multiplexing of two Bessel beams has been demonstrated [1]; we extend this approach to the Airy beam.

The cubic phase map is known to generate the Airy beams in the far field. If we generate two cubic phase maps such that the Airy beams they generate have their mainlobe undergoing constructive and the sidelobes undergoing destructive interference, then the resulting beam will have a variation of the Airy beam with reduced sidelobe intensity. The complex electric field is given by,

$$E(x,z) = E_1(x,z) + E_2(x,z)$$

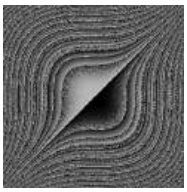


Figure 1: Cubic phase mask to generate an SSAB with beam diameter $50\mu m$

Where, $E_1(x,z)$ and $E_2(x,z)$ are the complex electric fields responsible for Individual Airy beams. To suppress the sidelobes, we have to minimize the integral,

$$\int_{z_1}^{z_2} \int_{-10\omega_0}^{-2.3\omega_0} |E(x,z)|^2 dx dz$$

where z_1 and z_2 are the distances along the z-direction over which the suppression lasts ideally, and ω_0 is the beam width of the resulting Airy beam.

Based on this, the information about the two individual Airy beams required is extracted, and the cubic phase mask to generate them is designed and multiplexed to obtain a phase mask (figure 1. This phase mask is loaded to a spatial light modulator (SLM) to experimentally generate the SSAB (figure 2).

The generated Airy beam is found to have its sidelobe reduced by more than 50% when compared to the Airy beam of a similar beam radius. Although not all sidelobes are suppressed simultaneously, the number of sidelobes that can be suppressed at once can be controlled. The suppression is periodic along its lobe direction.

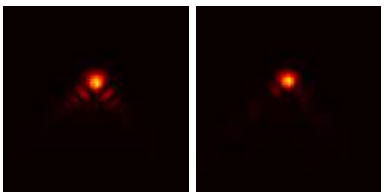


Figure 2: (a) Left: Cross-sectional view of Airy beam with beam diameter $50\mu m$. (b) Right: Cross-sectional view of SSAB with beam diameter $50\mu m$.

For the experimental analysis of light-sheets made up of Airy beams and SSAB, both beams were generated using a spatial light modulator (SLM) at a wavelength of 633 nm. Both of the beams were made to have a beam width of 50 µm. The beam was made to travel along the z-direction, and it was along the y-axis; as such, the light-sheet is made to lie in the yz plane. Then a camera was used to image the xy plane to study the effect of the beams on the thickness. It was observed that for the Airy beam, the mainlobe and the sidelobes both integrate to form a light-sheet, which results in the broadening of the light-sheet thickness. When SSAB was used to generate a light-sheet using the same setup, due to suppression of sidelobes at certain regions, the light-sheet generated had a lower full-width half-maxima(FWHM). For the current arrangement, the FWHM was reduced by 27% when SSAB was used instead of AB. An interesting point to note is that the null effectively separates the regions. In the current experiment, the second sidelobe effectively undergoes maximum suppression; as such, the resulting light-sheet contains the mainlobe and first sidelobe. This indicates a further possibility of reducing the FWHM by suppressing the first sidelobe.

References:

[1] J.G. George, K. Dholakia, S. Bhattacharya, *Optics Continuum* 2(7) (2023). https://doi.org/10.1364/optcon.493003

Integral Imaging Using Programmable Lenslet Array

[1,*]Abanish Maity and [1,#]Biswajit Pathak

Applied and Adaptive Optics Laboratory, Department of Physics, Indian Institute of Space Science and Technology, Thiruvananthapuram - 695547, Kerala, India

*Corresponding Author(s): *abanishmaity@gmail.com; #biswajitpathak@iist.ac.in*

Integral imaging is a robust technique for capturing 3D spatial and angular information. We design an array of reconfigurable lenslet on a SLM for integral imaging. This enables real-time, dynamic control over lens parameters to optimize elemental image overlap and enhance 3D reconstruction quality.

Integral imaging is a prominent three-dimensional (3D) display and capture technique that records the complete spatial and angular light field of a scene. By utilizing a microlens array, the system captures a set of 2D elemental images (EIs) from various perspectives. A key advantage of integral imaging is its single-shot capture capability, enabling full-parallax, glasses-free 3D visualization and computational depth reconstruction. However, traditional systems rely on physical microlens arrays with fixed optical properties. This static nature limits system flexibility and frequently leads to issues such as EI overlapping or aliasing when the scene depth varies, ultimately degrading the resolution of the reconstructed 3D volume.

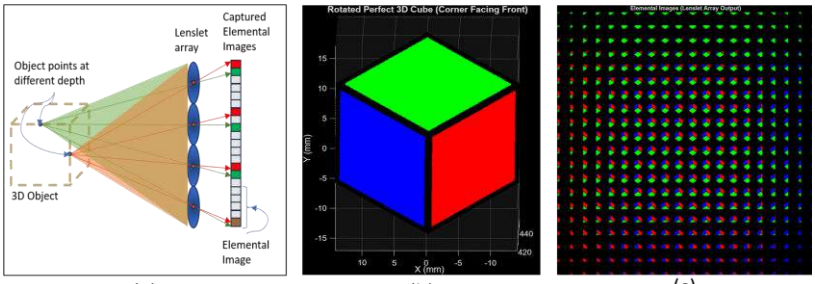


Fig. 1: (a) Ray diagram illustrating the capture of spatial and angular information for object points at varying depths. (b) Simulated 3D target volume. (c) Corresponding elemental images generated via the simulated lenslet array.

To overcome the limitations of fixed hardware, we propose the integration of a spatial light modulator (SLM) to act as a programmable lenslet array. The phase modulation capabilities of the SLM allow us to digitally synthesize a microlens array where the fundamental lens parameters can be dynamically altered. This programmable approach provides real-time control over the pitch, diameter, focal length, and even the shape of the individual lenslets. By actively tuning these parameters, we can precisely control the field of view of each lenslet and manage the overlap of the captured EIs in real-time. This adaptability ensures optimal sampling of the light field and tailor different parameters in real time as per requirement.

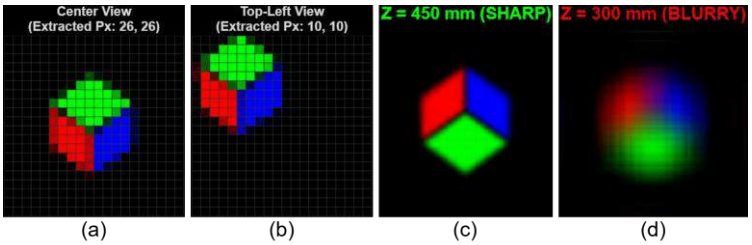


Fig. 2: Computational 3D reconstruction and perspective extraction. Orthographic views generated by extracting (a) center pixels and (b) top-left pixels from the elemental image array, demonstrating parallax. Digital refocusing results at (c) the original object depth of Z = 400 mm showing sharp focus, and (d) a defocused plane at Z = 300 mm.

We have developed a computational simulation to validate the proposed programmable capture system. The forward model simulates the generation of EIs using customized lenslet profiles, while the inverse model reconstructs the depth planes from the simulated sensor data. Our preliminary simulation results demonstrate that dynamically adjusting the lenslet pitch and diameter effectively mitigates EI overlap, resulting in higher fidelity and fewer reconstruction artifacts in the recovered 3D images compared to static array of lenslets.

References:

[1] Martínez-Corral, M., & Javidi, B. (2018). *Advances in Optics and Photonics*, *10*(3), 512-566.
[2] Arimoto, H., & Javidi, B. (2001). *Optics Letters*, *26*(3), 157-159.
[3] Lim, Y. T., Park, J. H., Kwon, K. C., & Kim, N. (2009). *Optics Express*, *17*(21), 19253-19263.

Design and development of a wavefront sensor using a lenslet array

#Sarita, Sayantan Gantait, Rakesh Kumar Singh
Laboratory of Information Photonics and Optical Metrology, Department of Physics, Indian Institute of Technology (Banaras Hindu University), Varanasi, India – 221005

#*sarita.ra.phy25@itbhu.ac.in*

Wavefront sensing and wavefront reconstruction are widely used in adaptive optics systems to measure and correct optical aberrations in real time. In this paper, we have designed a wavefront sensor using a microlens array and a CMOS camera. Wavefront reconstruction is performed using our developed slope-based algorithm.

Adaptive optics correction is an advanced optical technique used to compensate for wavefront distortions caused by atmospheric turbulence, optical imperfections, inhomogeneous media, and aberrated systems [1]. Wavefront sensing is an essential task in adaptive optics, used to detect induced distortions and provide correction signals to wavefront modulators to improve image quality. A slope-based wavefront sensor, such as a Shack-Hartmann wavefront sensor (SHWFS), is widely used and can be further used for wavefront phase reconstruction [2, 3].

This paper demonstrates our own wavefront sensor utilizing a lenslet array and a CMOS camera. Optical aberrations are introduced in the system by a phase-only spatial light modulator (pSLM). The image spot of the distorted wavefront is recorded by a camera that divides the beam into a number of beamlets with a two-dimensional lenslet array. Each sub-aperture provides a separate focus on the detector spatial position. A change in the centroid coordinates of the sub-aperture and its respective local optical path is evident due to system aberrations. For wavefront reconstruction, we have developed the Southwell algorithm, in which the wavefront phase values are estimated at the same grid points where the wavefront slopes are measured, typically by solving a set of least-squares equations that relate phase differences to measured gradients.

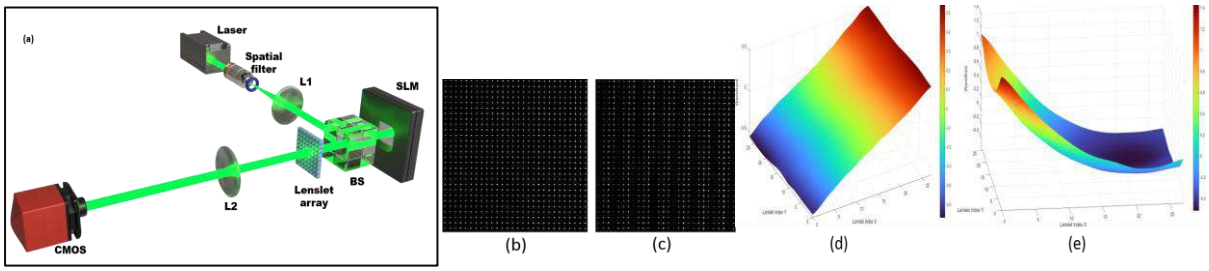


Fig 1: (a) Schematic of the experimental setup: L1-collimating lens, SLM-spatial light modulator, BS-beam splitter, L2-2f imaging lens. Spot images (b)reference, (c) distorted due to x-linear tilt aberration. Reconstructed wavefront for (d) x-linear tilt, (e)defocus

The designed wavefront sensor is shown in Fig. 1(a). A collimated laser beam of wavelength 532 nm (Coherent Sapphire, SF NX 100mW) passing through a high-quality microlens array (MLA150-7AR(-M) lenslet pitch of 150um, effective focal length is 5.2mm) is recorded by a CMOS camera (Thorlabs, Model no: DCC3240M). Initially, a reference spot image is recorded for a non-aberrated system. For linear tilt in x direction, defocus, and astigmatism aberrations introduced by pSLM (Holoeye LCOS Pluto 2.1), the distorted wavefront image spots are captured as shown in fig. 1(b) and (c), and the local gradients are determined. The reconstructed wavefront for the cropped second quadrant of the captured images, obtained using our developed wavefront reconstruction algorithm, is presented in Fig. 1 (d-e).

In conclusion, we demonstrated the designed wavefront sensor and developed wavefront reconstruction algorithm. Experimental results for the reconstructed wavefront of the distorted beam are also presented.

The authors acknowledge the support from the DRDO project (DGTM/DFTM/GIA/24-25/426).

References:

[1] Tyson, R.K., Principles of Adaptive Optics, CRC Press, (2010)
[2] Southwell, William H. Journal of the Optical Society of America 70, 8, 998-1006 (1980).
[3] Khosrow H., and Khajehhassanirabori V. American Journal of Physics 93, 3, 264-271 (2025).

A Unified Chromium Wet-Etch Process for Fabricating Compact Photon Sieves and Fresnel Zone Plates

[#]Sruthy Sebastian and Shanti Bhattacharya
Department of Electrical Engineering, Indian Institute of Technology Madras, Chennai, India

[#]*ee24d005@smail.iitm.ac.in*

We demonstrate a reliable fabrication process using a single wet-etch recipe to pattern continuous Fresnel Zone Plate (FZP) zones and dense Photon Sieve (PS) apertures with thousands of pinholes. Experimental focal properties agree well with simulation at designed wavelength of 632.8 nm. PS with hole diameter-to-zone-width ratio (d/w) = 1.53 shows the best focusing efficiency and side-lobe suppression.

Photon sieves extend FZPs by replacing transparent zones with pinholes, enabling improved resolution and sidelobe suppression. By controlling pinhole diameter and density, the focusing characteristics can be tailored for enhanced efficiency and high-contrast imaging. This work focuses on density optimization, development of a single-step fabrication process, and experimental validation at 632.8 nm. While large-area membrane PS have been widely studied, compact visible-wavelength implementations remain relatively unexplored.

A 100 nm chromium (Cr) layer was deposited on the quartz substrate using electron-beam evaporation, with the substrate temperature maintained below 60 °C during deposition. Positive photoresist (S1813) was spin-coated at 4000 rpm with an acceleration of 400 rpm/s for 50 s, followed by soft baking at 80 °C for 20 min. Pattern transfer was carried out using a 365 nm UV lithography system with an average exposure intensity of 6 mW/cm² for 25 s. The exposed resist was developed in MF-319 developer for 25 s and subsequently post-baked at 120 °C for 30 min. Chromium pattern transfer was achieved through wet chemical etching for 25 s using freshly prepared Cr etchant at room temperature, followed by photoresist removal. The process successfully realized FZP, PS and inverted PS with minimum feature sizes down to 16 µm as confirmed by confocal microscopy imaging. The FZPs with minimum feature sizes of 16 µm and 32 µm, as well as PS and inverted PS structures with d/w ratios of 1 and 1.53 and minimum feature sizes of 16, 24, 32, and 50 µm, were successfully fabricated with a dimensional error below 2%.

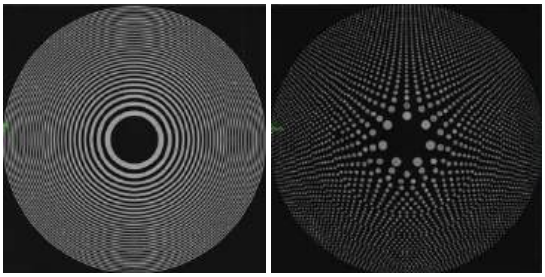


Fig. 1: Fabricated (FZP (left) and PS (right) with a minimum feature size of 16 µm.

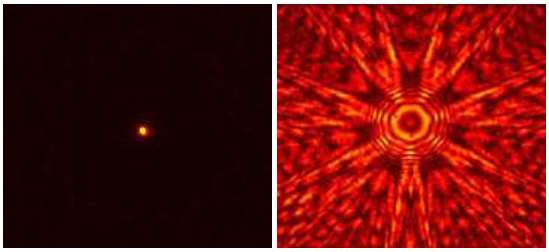


Fig. 2: PSF of PS with minimum feature size 16 µm and d/w = 1 at focal plane of 100 mm and out of focus plane of 120 mm respectively.

Experimental results tested at 632 nm closely matched simulations, with focal plane, Point Spread Function (PSF), full width half maximum, spot size, and side-lobe characteristics. Among the fabricated devices, the 16 µm PS with a d/w of 1.53 exhibited the best resolution consistent with the Bessel-function-based diffraction model governing the focal intensity contribution of individual pinhole. A spot size of 19 µm was achieved.

The authors acknowledge the Centre for Nano Scienceand Engineering (CeNSE), IISc Bangalore, for writing the photomask used for pattern transfer through photolithography in this work.

References:

[1] S. Hariharan, V. Singh, *Proceedings of the Workshop on Recent Advances in Photonics*, IEEE, 2017, pp. 14–18.
[2] F. S. Oktem, L. Huang, *Imaging and Applied Optics Congress*, OSA, 2016, p. IM4C.3.
[3] Q. Cao, J. Jahns, Proc. SPIE 6027 (2006) 602702.

.

Fourier Ptychography Microscopy using Different Imaging Modalities and Multi-plane Illumination

[1,*]Emi Susan Shine and [2,#]Biswajit Pathak

[1,]Department of Physics, Indian Institute of Science Education and Research, Tirupati-517619, Andhra Pradesh
[2,]Department of Physics, Indian Institute of Space Science and Technology, Thiruvananthapuram-695547, Kerala

Corresponding Author(s): *emisusanshine@gmail.com; #*biswajitpathak@iist.ac.in*

Fourier Ptychography Microscopy is a super-resolution imaging technique which bypasses the resolution limit imposed by a low numerical aperture (NA) objective lens. Here, we investigate the use of multi-plane illumination through programmable beams to improve spatial resolution while studying the impact of different illumination geometries on image fidelity and reconstruction.

Fourier Ptychography Microscopy (FPM) is a computational imaging technique that overcomes the trade-off between the resolution and field-of-view (FOV) of an imaging system in a conventional optical microscope. FPM addresses this by capturing a sequence of low-resolution intensity images under variable angular illumination and then stitching its corresponding Fourier spectrum. This results in the creation of a higher synthetic NA to produce a wide-field, high-resolution complex image [1]. However, traditional LED-based FPM system has various limitations including broad spectral bandwidth, non-uniform illumination, chromatic aberrations which degrade image quality. To overcome these limitations, we introduced programmable FPM (pFPM) to enable precise and dynamic control over the illumination profile and its positioning [2].

Multiple imaging modalities can be realized by programmable tailoring of the illumination geometries. From Fig 1., we observe that the central illumination beams correspond to brightfield imaging and the peripheral beams correspond to darkfield imaging. The phase contrast imaging is realized by taking the ratio of difference and summed images corresponding to each half of the annular illumination as shown in Fig. 1(d). In this work, we realize different illumination geometries and perform a comparative study to explore its effects on image fidelity. The realization of these geometries facilitates the user to seamlessly switch between various imaging modalities to dynamically optimize image quality as per requirement. Furthermore, we introduce a multi-plane illumination geometry which enables precise control of illumination angles in both the axial and lateral directions. This work paves the way for a new class of versatile, high-resolution and programmable computational microscopes, with potential applications in biomedical imaging, material science, etc.

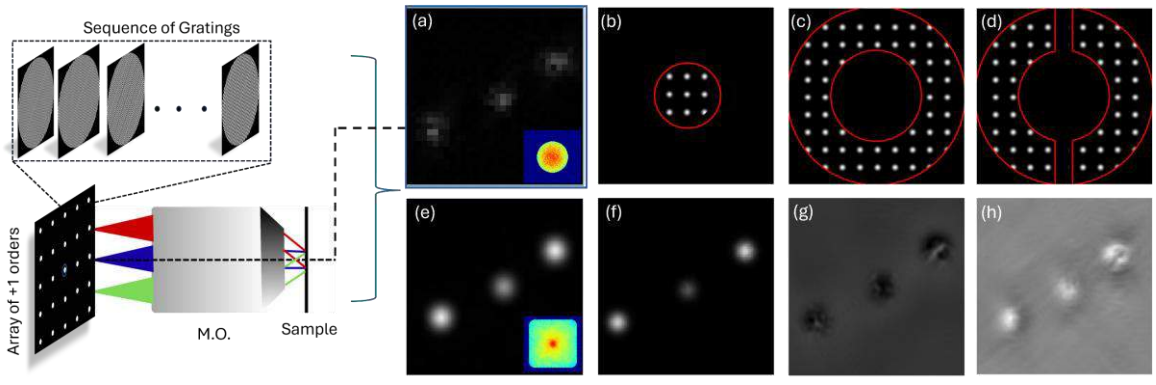


Figure1. The extreme left figure illustrates the concept of angular illumination using an array of +1 order beams. The right hand side figure demonstrates the (a) low-resolution image, (b) brightfield illumination, (c) darkfield illumination, (d) phase contrast illumination, (e) reconstructed high-resolution image, and (f)-(h) reconstructed image corresponding to illuminations for (b)–(d), respectively.

References:

[1] Zheng, G., Horstmeyer, R., & Yang, C. *Nature photonics*, *7*(9), 739-745 (2013).
[2] Mehta, S., & Pathak, B. *Optics Express*, *33*(5), 12071-12089 (2025).

Flat-Top Beam Shaping Under Phase Perturbations: Comparative Analysis of IFTA, Adjoint Gradient Descent, and Optimal Transport

[1,#]Ananthakrishnan V,[1]Tanish Nilesh Chudiwal,[1]Nandan Bhat and [1]Shanti Bhattacharya
[1]Department of Electrical Engineering, Indian Institute of Technology Madras, Chennai 600036, India

[#]*v8ananthakrishnan@gmail.com*

We compare three phase-only DOE design methods for flat-top beam shaping under phase noise. IFTA converges to speckled, noise-sensitive profiles with no independent control over uniformity or efficiency. Adjoint gradient descent suppresses speckle and decouples these trade-offs, but residual roughness persists across the flat top, along with sidelobes. Optimal transport eliminates this, giving near-ideal flatness robust well beyond the tested noise range.

Flat-top beam shaping with phase-only DOEs is conventionally handled by IFTA, which converges to whichever local minimum it finds with no principled control over the uniformity-efficiency-flatness trade-off. The far-field problem is well-posed under exact phase knowledge, but once the phase is known only probabilistically, no such guarantees survive. This motivates a direct comparison of IFTA, Adjoining Gradient Descent (AGD), and Optimal Transport (OT) under clean and noisy Gaussian inputs.

IFTA enforces amplitude constraints alternately at input and target plane [1], converging to a phase solution limited by inherent speckle with no independent control over uniformity or efficiency. AGD poses beam shaping as an optimization problem with independently weighted terms for uniformity and efficiency [2], with robustness built in through Monte Carlo averaging over phase-perturbed inputs. OT treats beam shaping as mass transport between input and target intensity distributions, giving the phase directly from cumulative distribution function (CDF) matching [3].

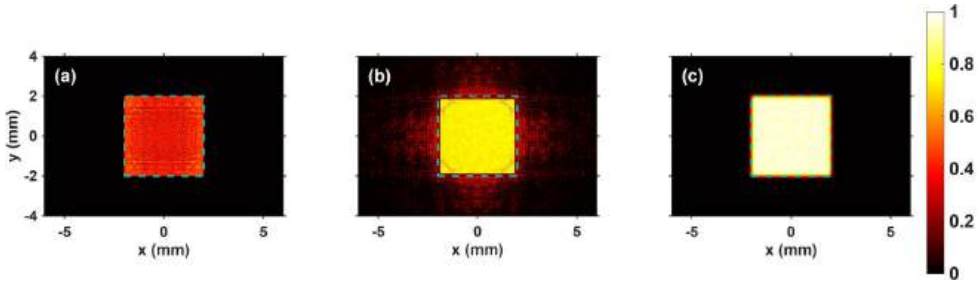


Fig. 1: Normalised intensity profiles at the target plane for (a) IFTA. (b) AGD, (c) OT under a randomly perturbed input wavefront with 15% phase noise

Fig. 1 summarizes performance across all three methods under phase-noisy input. IFTA achieves the highest power ratio (98.5%) but intensity across the flat top is severely non-uniform even on clean input, with a flatness error (defined as the standard deviation of intensity within the target region, normalised to the mean) of 0.25. AGD improves flatness to 0.17 under both clean and noisy input at 95% uniformity. OT achieves the lowest flatness error of 0.074 clean and 0.076 noisy, sidelobe-free and tracking the target almost exactly.

OT is the clear winner for noise-robust flat-top beam shaping, delivering near-ideal flatness that survives well beyond the tested noise range. AGD offers a useful middle ground where explicit control over the uniformity-efficiency trade-off is needed. Experimental validation on the SLM bench is in progress ahead of the conference.

References:

[1] A.K. Ghatak, K. Thyagarajan, *Optical Electronics*, Cambridge University Press, Cambridge (1989).
[2] L.C. Venuti, T. Albash, D.A. Lidar, P. Zanardi, *Physical Review A* 93 (2016) 032118.
[3] S. Sunder, A. Sharma, *Workshop on Recent Advances in Photonics, (WRAP 2019)* 19 (2019).

Automation and Performance Evaluation of a Digital Micromirror Device

[#]Soumya Kumari, Arnab Bhattacharyya, Sarita, Rakesh Kumar Singh
Laboratory of Information Photonics and Optical Metrology, Department of Physics, Indian Institute of Technology (Banaras Hindu University), Varanasi, Uttar Pradesh, INDIA

[#]*soumyakumari.rs.phy24@itbhu.ac.in*

An automated Digital Micromirror Device (DMD)-based display system was developed for high-fidelity optical reconstruction. The system performance was evaluated through the reconstruction of Lee and Local Diffraction Efficiency binary holograms. Both simulation & experimental results demonstrate accurate reconstruction quality, validating the effectiveness of the proposed DMD-based optical system.

Digital Micromirror Device (DMD)-based projection systems have become an effective approach for high-speed optical modulation, display, and structured-light generation [1]. In this work, we report the automation of the DMD projection and image acquisition system which uses MATLAB platform & the ALP API (Advanced Light Processing Application Programming Interface).It is the software control library developed by controlling DMD-based DLP projection systems. for real-time hologram display and CCD-based image capture. The automation framework includes image loading, preprocessing, hologram generation, binary conversion, DMD upload, projection control, image acquisition, and result storage. The binary amplitude modulation characteristic of DMDs requires efficient binarisation to convert grayscale holograms into binary ones while preserving reconstruction quality. In this work, we present a comparative investigation of the 'Lee hologram' and an 'advanced Adaptive Digital Hologram Binarization approach based on Local Thresholding, Block Division, and Error Diffusion' (LDE). Binary holograms generated by both methods are displayed on a DMD, and their reconstruction performance is evaluated. The generated holographic patterns were projected using DMD and captured through a CCD imaging system for validation.

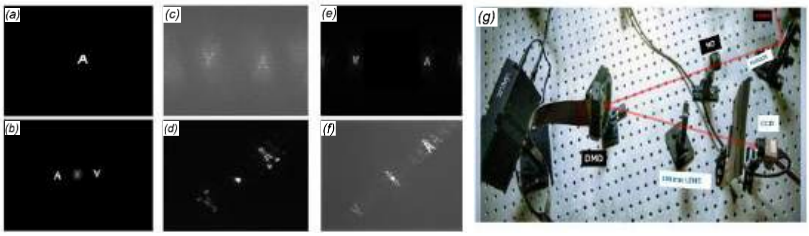


Fig: (a)Object; (b) Fourier Hologram; (c)&(e)Simulation Results for LEE & LDE respectively; (d)&(f) Experimental Results for LEE & LDE respectively; (g) Experimental Setup

$$\text{Binary Threshold: } B(x,y) = \begin{cases} 1, H(x,y) > T_{local} \\ 0, H(x,y) > T_{local} \end{cases}$$

$$\text{LEE Hologram: } H(x,y) = \frac{1}{2}[1 + A(x,y)\cos(2\pi f c^{x} + \Phi(x,y))]$$

$$\text{LDE Hologram: } T_{local} = \frac{1}{N}\sum H(x,y)$$

The experimental results show good outcomes and demonstrate that the LDE binary method [2] provides improved reconstruction quality and better optical performance compared with the conventional Lee hologram [3] approach. In addition, the use of DMD enables high-speed pattern switching (up to ~22.7 kHz, depending on configuration), making the system suitable for rapid optical projection and real-time beam-shaping applications. The developed automated DMD platform provides an efficient framework for high-speed beam shaping and advanced wavefront engineering applications.

Soumya Kumari acknowledges financial support from the University Grants Commission (UGC), Support is acknowledged from projects DRDO: DGTM/DFTM/GIA/24-25/426 and UPEIDA: R&D/UPEIDA/D.Corridor/2018-19/01/Phy/813.

References:

[1] S.A. Goorden, J. Bertolotti, A.P. Mosk, *Optics Express* 22 (2014) 17999–18009.
[2] P.A. Cheremkhin, E.A. Kurbatova, N.N. Evtikhiev, V.V. Krasnov, V.G. Rodin, R.S. Starikov, *Journal of Imaging* 8 (2022) 15.
[3] W.H. Lee, *Applied Optics* 18 (1979) 3661–3669.

SERS based indirect sensing of glial fibrillary acidic protein (GFAP): a brain injury biomarker

[1]Arti Yadav,[1]Sadhna Singh, [2]Palkin Arora, [2]Richa Trivedi, [3]Priyanka Sharma, [1,4,#]Sachin Kumar Srivastava
[1]Department of Physics, Indian Institute of Technology Roorkee, Roorkee, 247667, India
[2]Department of Neurobehavioral Research, INMAS, DRDO, India
[3]Traumatic Brain Injury and Metabolomics (TBIM) Department, INMAS, DRDO, India[2]
[4]Centre for Photonics and Quantum Technology, Indian Institute of Technology Roorkee, Roorkee, 247667, India

[#]*sachin.srivastava@ph.iitr.ac.in*

An Ag nano-sculptured thin film-based SERS biosensor is developed for detection of GFAP. An indirect SERS sensing mechanism is employed using changes in local dielectric environment due to GFAP - antibody binding, therefore enhancing SERS signal of 4-Aminothiophenol*. The biosensor works on real-world samples with 1 pg/ml limit of detection.*

Surface-enhanced Raman spectroscopy (SERS) is a highly sensitive analytical technique capable of detecting molecular signatures at trace levels via strong localized electric fields at plasmonic nanostructures [1]. Among SERS substrates, nano-sculptured thin films (nSTFs) fabricated by glancing angle deposition (GLAD) offer a cost-effective, scalable alternative to lithographically patterned or colloidal substrates, providing enhancement factors up to 10^9 [2], while avoiding the reproducibility limitations of colloidal nanoparticle assemblies. Since SERS is a short-range effect and cannot directly detect large biomolecules like GFAP protein. To detect large molecules, an indirect SERS-based sensing mechanism is employed, where SERS signal is collected from a Raman reporter 4-Aminothiophenol (4ATP), attached to the Ag-nSTF [3].

A SERS biosensor for GFAP is reported on a silver nSTF. A schematic of the biosensor chip is shown in Fig. 1(a). The chip is prepared by immobilizing an anti-GFAP antibody onto the 4ATP adsorbed over Ag-nSTF. Bovine Serum Albumin (BSA) is used to block any non-specific binding. The biosensor is based on the enhancement in the intensity of SERS signal of 4ATP. The enhancement arises due to GFAP binding-induced changes in local polarizability and dielectric constant near the plasmonic surface. A FE-SEM image of an nSTF is shown in Fig. 1(b). A plasmonic nanorod array provides uniform hotspots for reproducible enhancement. Fig. 1(c) shows the variation of SERS intensity of 4ATP at 1091 cm^{-1} for varying GFAP concentrations in phosphate buffer saline. The concentrations of GFAP in 3 blast-induced moderately injured rat sera are found to be 15, 24, and 37 pg/ml respectively, as shown using dotted lines. The biosensor has a dynamic range of 1-75 pg/ml with a 1 pg/ml limit of detection. It offers specificity, repeatability, reusability, minimal analyte requirement (3 µl), and rapid response (<1 minute) in comparison to ELISA and Western blot.

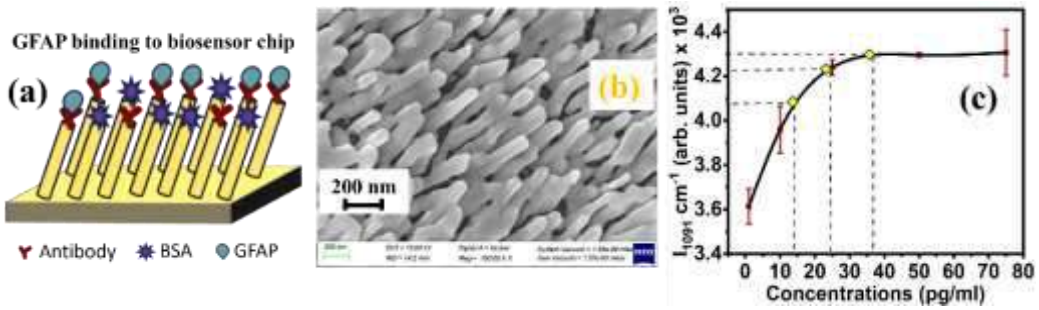


Fig. 1(a). Schematic of the biosensor chip, (b). FESEM image, and (c). Variation of SERS intensity with GFAP concentrations

Funding from SERB (), and Department of Science and Technology () is thankfully acknowledged. Arti Yadav thanks to Council of Scientific & Industrial Research, India for fellowship.

References:

[1] I. Abdulhalim, Small 10 (2014) 3499–3514.
[2] K. Robbie, M.J. Brett, J. Vac. Sci. Technol.: Vac., Surf. Films 15 (1997) 1460–1465.
[3] S. Singh, A. Yadav, P. Arora, R. Trivedi, P. Sharma, S.K. Srivastava, Biosens. Bioelectron. 305 (2026) 118677.

Autonomous Electrostatic Force-Induced Fiber Bragg Grating Sensing Module for High-Voltage Discharge Monitoring

[1,#]Supankar Das, [2]Jashan Preet, [3]Simranjit Singh,[4]Umesh Kumar Tiwari
[1]CSIR-Central Scientific Instruments Organisation, Sector-30C, Chandigarh-160030
[3] University Institute of Engineering and Technology (UIET), Sector 25, Chandigarh-160025
[3]Punjab Engineering College (PEC), Sector-12, Chandigarh-160012
[4]CSIR-Central Scientific Instruments Organisation, Sector-30C, Chandigarh-160030
[#]supankardas.csio@csir.res.in

Abstract

A self-powered electrostatic force sensor based on the spatial designed dielectric membrane and FBG is proposed for high-voltage discharge monitoring. Electrostatic force-induced membrane deflection is transduced to Bragg wavelength shifts, enabling passive, electrically isolated and EMI-immune sensing. The sensor has shown great potential for online condition monitoring of high voltage switchgear and power transmission equipment.

Summary

The reliable operation of high-voltage equipment, including gas-insulated switchgear (GIS), transformers, circuit breakers, and transmission systems, depends on the early detection of electrostatic discharge (ESD) and electric field abnormalities. Conventional electrostatic sensors, which utilize metallic electrodes and electronic circuits positioned near high-voltage sources, are susceptible to electromagnetic interference (EMI), insulation difficulties, and safety risks.

A passive Fiber Bragg Grating (FBG)-based electrostatic sensing module is introduced, employing a **spatially designed dielectric membrane surface** as an electro-mechanical transducer. The engineered dielectric membrane surface increases electrostatic force generation and charge interaction, resulting in enhanced mechanical sensitivity. When subjected to electrostatic excitation, the dielectric membrane deforms due to electrostatic attraction, and the induced strain is transferred to the attached FBG, producing a measurable Bragg wavelength shift.

The sensor functions without electrical connections at the sensing site, ensuring complete electrical isolation, immunity to electromagnetic interference, and enabling remote optical interrogation. Experimental results confirm the feasibility of the dielectric membrane–FBG sensor for electrostatic monitoring, presenting a compact, safe, and reliable approach for real-time diagnostics and predictive maintenance of high-voltage power assets.

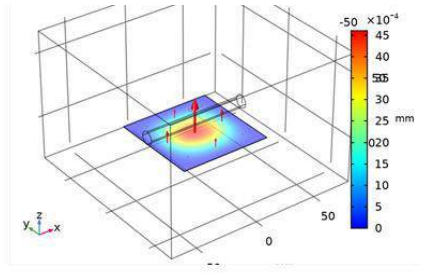


Fig.2- Total displacement (mm) Arrow Surface: Displacement Field

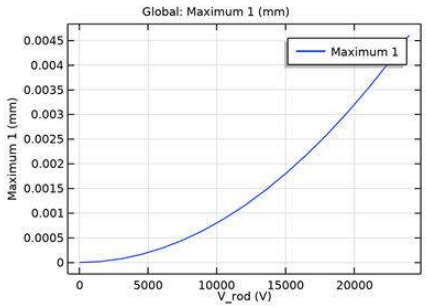


Fig.1- 1D Deflection plot

"To the best of the authors' knowledge, this is the first autonomous optical sensing architecture that employs electrostatic-force-induced Dielectric membrane deflection as the primary transduction mechanism for Fiber Bragg Grating-based high-voltage discharge monitoring." It is a highly challenging task to optimize the sensor design.

Cladded Plastic Optical Fibre based U-Bent Sensors with Enhanced Coupling Efficiency for Robust Biosensing

[1]Maryann EM,[2]Niranjan Sindu Das,Rishit V Nambiar and [1]V V R Sai

[1]Department of Applied Mechanics and Biomedical Engineering, Indian Institute of Technology Madras

[2]International School of Photonics,CUSAT,Kerala
vvrsai@iitm.ac.in

We demonstrate that cladded Plastic Optical Fibre (POF) can potentially achieve enhanced EWA/RI sensing by optimising LED–ball lens coupling that maximizes optical throughput by way over 5 times. They enable robust and reproducible U-bent sensors for low-cost biosensing.

Plastic optical fiber (POF) sensors based on evanescent wave absorption (EWA) and refractive index (RI) sensing are attractive for low-cost biosensing. While decladded POFs are proven to show RI and EWA sensitivity, their fabrication is labor-intensive and inconsistent. This raises the central question: Can cladded POFs achieve comparable sensitivity for EWA sensors if the light coupling bottleneck is resolved first?

Compared to decladded fibers, cladded fibers offer ease of manufacturing, reproducibility, mechanical robustness, and long-term stability, making them more suitable for point-of-care and field applications.Cladded POFs are proven to exhibit RI sensitivity.

Efficient coupling is critical in cladded U-bent fibre sensors, as any coupling loss reduces transmitted power and sensor sensitivity.So to improve performance of cladded U-bent sensors, coupling was improved by two methods - one by modifying the LED, another by using Ball lenses.Coupling efficiency studies were performed in three parts:1)Theoretical analysis using Fresnel equations and numerical aperture mismatch, 2) Experimental validation using a custom 3D-printed adapter with Thorlabs PM100 optical power meter, 3) Zemax Optic Studio ray-tracing simulations(n=1.54 lens model) under varied conditions: a) normal LED vs cut LED b)half ball lens 2 mm vs full ball lens 3 mm, c)green LED source 525 nm.

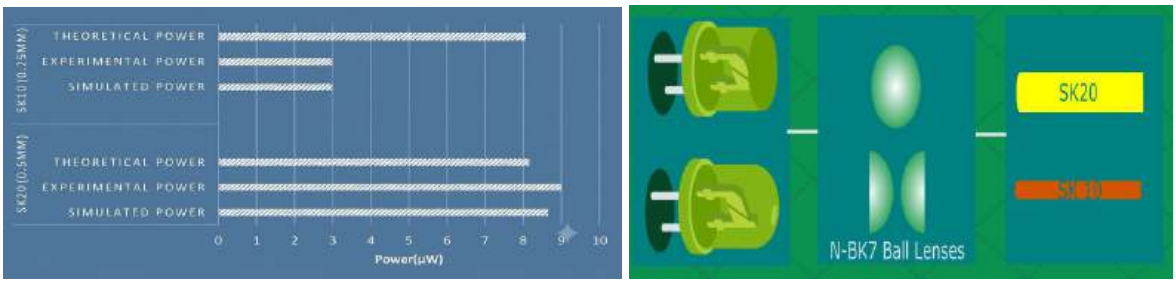


Fig. 1:a) Bar graph showing optimized coupling efficiency of SK20 and SK10 plastic optic fibers using Zemax software b)Experimental components kept at different positions on the optical axis

Experimentally, the adaptor ensured repeatable alignment to isolate lens and fibre effects. Maximum coupling efficiency for cladded SK10 and SK20 fibres was determined for each configuration as shown in Fig 1 a).

The results show that with optimized coupling, cladded POFs deliver sufficient optical power to the U-bent region for a measurable EWA/RI response while retaining manufacturing ease. This establishes a design pathway for robust, mass-producible POF sensors without compromising its performance.

References:

[1] Danny, Christina & Murugan, Divagar & V V, Raghavendra Sai. (2025). Evanescent wave absorption in U-bent fiber optic sensors—a ray-optics model for evanescent power and experimental validation. Applied Optics. 64. 5997-6005. 10.1364/AO.557577.

[2] Chaudhary, Ratan & Manoharan, Hariharan & Swain, Krishna & Madaboosi, Narayanan & V V, Raghavendra Sai. (2023). Investigations on cladded U-shaped fiber optic sensors for refractive index measurements. 106. 10.1117/12.2679729.

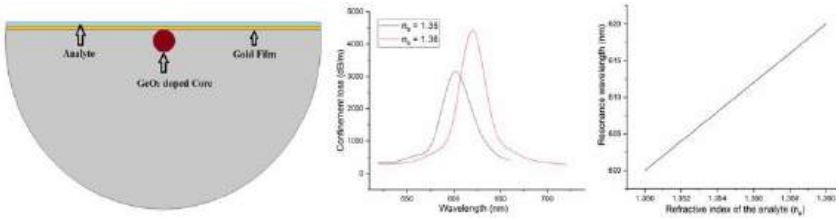
Sensitivity Enhancement in a D-Shaped Optical Fiber SPR Sensor via GeO_2 Doping

[1]Rahul Kumar Gangwar,[2]Dharmaendra Shakya and [2,#]Sourabh Jain
[1]Department of Physics, Indian Institute of Information Technology, Bhopal, Madhya Pradesh – 462003
[2]Department of Electronics and Communication Engineering, Indian Institute of Information Technology, Bhopal, Madhya Pradesh – 462003
[#]*sourabh.jain@iiitbhopal.ac.in*

We present an optical fiber refractive index sensor based on surface plasmon resonance effect. By using the wavelength interrogation method, the maximum sensitivity of the proposed sensor is found to be 2000 nm/RIU.

Surface plasmon resonance (SPR) is an optical phenomenon that can be used for the chemical and biochemical sensing. This technology has several advantages such as high sensitivity, convenient operation, label-free detection and real-time detection [1, 2]. In the SPR phenomena, a p-polarized light wave excites charge density oscillation (i.e., surface plasmon wave, SPW) along the metal-dielectric interface and it satisfied the resonance condition, i.e., the wavevector of the SPW wave equal to the propagation constant of incident light wave [3, 4]. In this paper, we study the D-shaped optical fiber SPR sensor for the refractive index sensing. We have investigated the different doping concentration of the GeO_2 for the core region of the sensor. It is observed that the GeO_2 concentration played a very effective role for improving the performance of our sensors.

The cross section of the proposed D-shaped optical fiber based plasmonic sensor is shown in Fig. 1(a). The core and cladding of the D-shaped fiber is made from GeO_2 doped silica and fused silica with the diameter of 8.2 μm and 125 μm, respectively. Gold film is coated on the flat surface of the fiber. This flat surface is just above on the boundary of the core region of the fiber and the thickness of the gold is fixed at 40 nm. We have numerically investigated a D-shaped optical fiber refractive index plasmonic sensor by using the COMSOL Multiphysics built-in finite element method. The key factor of this D-shaped optical fiber SPR sensor is the evanescent field of the TM (p-polarized) mode propagating through the core of the optical fiber. This evanescent field easily excites the metal surface electrons, resulting in a surface plasmon wave. Throughout our simulations, only the TM mode was considered. Fig. 1(b) depicts the variation of the confinement loss as a function of the wavelength for the different analyte having refractive index n_a = 1.35 and 1.36. With the increase in the n_a, the resonance wavelength increases towards the higher wavelength having higher value of the confinement loss. The sensitivity was calculated through the derivative of the linear fit of the fig. 1(c). As can be seen, the D-shaped optical fiber sensor has a sensitivity of 2000 nm/RIU for a refractive index ranging from 1.35 to 1.36 for 5% doping concentration of GeO_2 doped silica. We have also calculated another parameter of interest resolution defined as the ability of the proposed sensor in detecting small refractive index variations. Considering $\Delta\lambda_{min}$ = 0.1 nm, the resolution of the proposed sensor is found to be 5 × 10^{-5} RIU. We have observed the effect of the doping concentration of the GeO_2 in the core region on the performance of the proposed sensor. From this study, we gather that the proposed structure can be very useful for a broad scope of applications such as chemical and biochemical sensing. The authors acknowledge MPCST support under Grant No. 3852/CST/R&D/Phy.&Engg. and Pharmacy/2025–26.



(a) (b) (c)

Fig. 1: (a) Schematic diagram of the proposed D-shaped optical fiber SPR sensor, (b) Evolution of the confinement loss as a function of wavelength for analytes with different refractive indexes at t_g = 40 nm, (c) variation of the resonance wavelength with different refractive index analyte.

References

[1] J. Homola, S. S. Yee, and G. Gauglitz, Sens. Actuators B 54, 3–15 (1999).
[2] Y. Chen et al., Advanced Optical Materials, 1900479 (2019).
[3] W. Wei et al., Plasmonics, vol. 13, no. 2, pp. 483-491, (2018).
[4] R. K. Gangwar and V. K. Singh, Plasmonics 12, 1367 (2017).

Design and development of a 4×1 fiber optic laser signal combiner using tapered fiber bundle technique

[1,2] #Avdhesh Kumar, [1]Nikita Sharma, [3]Pankaj Roa, [1]Rajpal Singh, [1,2]B. N. Upadhyaya
[1]Raja Ramanna Centre for Advanced Technology, Indore
[2]Homi Bhabha National Institute, Training School Complex, Anushakti Nagar, Mumbai
[3]Samrat Vikramaditya University, Ujjain

#avdhesh@rrcat.gov.in

A 4×1 fiber laser signal combiner has been fabricated in-house using tapered fiber bundle (TFB) technique, employing four double-clad input fibers and an output fiber. Signal combiner has been actively tested up to combined output power of 415W at 1080nm using Yb-doped CW fiber lasers with a combining efficiency of 97%.

The output power from a single fiber laser oscillator or master oscillator power amplifier (MOPA) configuration is limited by nonlinear effects such as transverse mode instability (TMI) [1] and stimulated Raman scattering (SRS) [2]. All-fiber signal combiners [3, 4] offer an effective power scaling solution by combining multiple laser channels into a single output fiber, though often at the expense of beam quality. In this direction, in-house fabrication of a 4x1 fiber laser signal combiner has been carried out and characterized with the objective of developing the technology for future multi-kilowatt CW fiber laser systems. The efficiency of power combination from multiple input fibers into a single output fiber is governed by brightness conservation criteria: $\boldsymbol{D_{out}^2 . NA_{out}^2 \geq N . D_{in}^2 . NA_{in}^2}$.

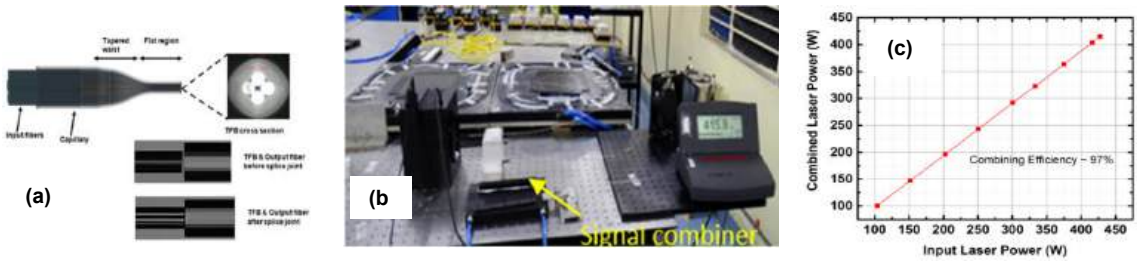


Fig. 1: (a) *In-house fabricated TFB, cleaved fiber bundle cross-section, and splice with the output fiber, (b) test setup for laser signal combining and (c) combined fiber laser power vs. total power from all input fiber lasers.*

A key challenge in the TFB technique is the simultaneous reduction of the core and cladding diameters during tapering process. Excessive core reduction increases the effective numerical aperture (NA_{eff}), leading to power leakage into the cladding and reduced transmission efficiency. To overcome this, the cladding diameter of all the 20/400 µm input fibers were first reduced from 400 µm to ~100 µm by hydrofluoric acid based etching over a 10 cm length. This limited the core diameter reduction during tapering process to ~9 µm, ensuring effective optical confinement. For fabrication, a low-index fluorine doped capillary tube was tapered from 800/1500 µm (ID/OD) to ~250/469 µm. The etched input fibers were bundled, inserted into the tapered capillary, and thermally tapered under axial tension to form the TFB. The combined fiber bundle at the cleaved position is confined within a 96 µm diameter, ensuring efficient coupling to the 100 µm output core. The taper and waist lengths were maintained to15 mm &5 mm, respectively. Figure 1(a) shows in-house fabricated TFB, cleaved fiber bundle cross-section, & splice joint with the output fiber, Fig. 1(b) shows test setup for laser signal combining, and Fig. 1(c) shows combined fiber laser power vs. total power from all input fiber lasers. The signal combiner has been packaged in aluminium housing for providing mechanical strength & heat removal during operation.

Testing with 1080 nm Yb CW fiber lasers having 20 µm core diameter yielded ~97% transmission efficiency for all input ports. A maximum output power of 415 W was achieved at 427 W of combined input power, which corresponds to an overall ~97% efficiency of the signal combiner. The signal combiner temperature remained below 40°C during continuous operation for more than half an hour, indicating good thermal stability of the device and a way to scale output power from fiber lasers.

References:

[1] Cesar Jauregui *et al.*, *Adv. Opt. Photon.*2020, *12* (2), 429.
[2] Lingfa Zeng *et. al., Optics & Laser Technology*2023, *159*, 108903
[3] Wu Weijun *et. al., Optik* 2021, *225*, 165353
[4] Fu Min *et. al., Opt. Express* 2021, *29* (17), 26658

A Portable System Incorporating a Microfabricated Chip for Detecting Metal Ions Using Glow Discharge in Open Air

Manjeet Kumar and Bhaskar Mitra
Indian Institute of Technology Delhi, India

Manjeet.Kumar@ee.iitd.ac.in

A portable, miniaturized glow-discharge optical emission spectroscopy (GD-OES) system is developed for liquid-phase ion detection. The platform combines an atmospheric-pressure microplasma device, a 3D-printed alignment holder, an Arduino-based control unit, and a handheld spectrometer. Operating in ambient, it enables a simplified, portable, low-cost elemental analysis system.

An optoelectronic device utilising microplasma discharge technology was fabricated via microfabrication, with dimensions of 5 mm × 5 mm. The device comprises metallic electrodes and a synthesised, sol–gel–derived porous silica layer patterned onto the cathode surface. This porous silica structure enables efficient liquid sampling and facilitates the formation of a wetted cathode upon contact with the analyte solution. In addition, the porous cathode improves the device's operational stability by reducing liquid splashing during plasma discharge.

The system operation is managed using LabVIEW software, while an Arduino-based controller is employed to generate high-voltage pulses and coordinate plasma ignition with spectral data acquisition. The enclosed device design incorporates optical self-alignment between the fibre-optic interface and the active cathode region, thereby enhancing light-collection efficiency.

A stable and visually observable microglow plasma is produced across a 55 μm interelectrode gap using a pulsed DC power supply. The application of short-duration DC pulses minimises power consumption and improves device lifetime. The analytical capability of the developed system was demonstrated by detecting sodium ions at 5 ppm and mercury ions at 10 ppm using less than 0.7 μL of a 5% HNO_3 solution. Furthermore, the approach can be extended to detect other elemental species. The developed device demonstrates significant potential as a low-cost, portable alternative to conventional large-scale inductively coupled plasma atomic emission spectroscopy (ICP-AES) systems.

References:

[1] C.G. Wilson and Y.B. Gianchandani, *IEEE Transactions on Electron Devices*, vol.49, no.12, pp.2317-2322, (2002)
[2] B. Mitra, B. Levey and Y. B. Gianchandani, *IEEE Transactions on Plasma Science*, vol. 36, no. 4, pp. 1913-1924, (2008).
[3] C. -C. Hsu, J. -H. Tsai, Y. -J. Yang, Y. -C. Liao and Y. -W. Lu, vol. 21, no. 5, pp. 1013-1015, (2012).
[4] J. Yu, K. Wang, Y. Feng, X.X. Hao, X.H. Li, Q.F. Lu, *Anal. Lett*., 58, pp. 1549-1563, (2025).

Machine Learning-Assisted Colorimetric Paper Sensor for Smartphone-Based Detection of Pb^{2+} and Fe^{3+} Ions

[1,2]Anupam Kushwaha, [1]Akanksha Mishra, [1,2,#]Roli Verma
[1]Department of Physics, University of Lucknow, Lucknow, 226007, India
[2]Department of Physics and Astrophysics, University of Delhi, New Delhi, 110007, India
[#]*roli@physics.du.ac.in*

We report a machine learning-assisted colorimetric paper sensor for smartphone-based detection of Pb^{2+} and Fe^{3+} ions. Green-synthesized copper oxide nanoparticles on filter paper produce colorimetric responses imaged across multiple smartphones, lighting conditions, and paper types. From RGB, HSV, and Lab spaces, 27 descriptors trained a Random Forest model achieving 99% (Pb^{2+}) and 98% (Fe^{3+}) accuracy and $R^2 \approx 0.96$, validated on spiked Gomti River water.

The growing threat of heavy metal contamination in water demands advanced sensing technologies that are not only accurate, but also rapid, portable, and affordable [1]. Paper-based colorimetric sensors are attractive for environmental monitoring due to their low cost, portability, and ease of use. However, their practical sensitivity is often limited when the color changes are subtle, variations in lighting conditions, differences in smartphone cameras, and the subjective nature of human visual detection [2]. In response to this need, we report a machine learning-enabled colorimetric paper-strip sensor for the detection of Pb and Fe ions, combining green nanomaterial synthesis, smartphone imaging, and intelligent data analysis into a single field-deployable platform.

In this study, copper oxide nanoparticles were green-synthesized and immobilized on filter paper to develop a low-cost sensing substrate [3]. The fabricated sensing strips were exposed to varying concentrations of Pb and Fe ions, and the resulting colorimetric responses were captured using multiple smartphones under six different lighting conditions and four types of filter papers. To move beyond subjective visual inspection, 27 global color descriptors were extracted from RGB, HSV, and Lab color spaces, allowing the model to capture complementary information related to intensity, chromaticity, and illumination-insensitive features [4]. These features were then used to train and compare three machine learning algorithms: Support Vector Machine (SVM), Logistic Regression (LR), and Random Forest (RF).

Among the tested models, the RF model demonstrated the best overall performance. For classification of ion concentration levels, it achieved cross-validation accuracies of 99% for Pb and 98% for Fe. In quantitative regression analysis, the model also showed strong predictive capability, with R^2 values of 0.9644 for Pb and 0.9588 for Fe [5]. To evaluate practical applicability, the sensor system was further tested using Gomti River water samples spiked with the target ions.

The proposed method demonstrates how computational intelligence can significantly enhance the performance of simple colorimetric sensors, transforming them into reliable tools for quantitative and field-deployable heavy metal detection.

Reference:

[1] A. Singh, S.S. Shah, C. Sharma, V. Gupta, A.K. Sundramoorthy, P. Kumar, S. Arya, Journal of Environmental Chemical Engineering (2024) 113032.
[2] D.M. Cate, J.A. Adkins, J. Mettakoonpitak, C.S. Henry, Analytical Chemistry 87 (2015) 19–41.
[3] A. Mishra, A. Kushwaha, R. Verma, Analytica Chimica Acta (2025) 344477.
[4] B. Khanal, P. Pokhrel, B. Khanal, B. Giri, ACS Omega 6 (2021) 33837–33845.
[5] A. Mishra, A. Kushwaha, R. Verma, Sensors and Actuators A: Physical (2025) 117380.

Comparative Chirp Profile Engineering in Apodized Fiber Bragg Gratings for Narrowband Reflection and Dispersion Compensation

[1] Souryadipta Maiti, [1#] Partha Roy Chaudhuri
[1] Department of Physics, Indian Institute of Technology Kharagpur, West Bengal, India, 721302

[1]souryadipta@phy.iitkgp.ac.in, [1#] roycp@phy.iitkgp.ac.in

A comparative numerical study of linear, quadratic, cubic, exponential, logarithmic, hyperbolic-tangent, and centred chirped fiber Bragg gratings near 1550 nm is presented. Transfer-matrix analysis shows that cubic and exponential chirp yield the minimum bandwidth, while cubic chirp provides the best combined reflectivity, group-delay, and local-dispersion performance.

Fiber Bragg gratings (FBGs) are widely employed for wavelength-selective filtering, sensing, and chromatic-dispersion compensation owing to their tunable spectral characteristics [1]. Chirped FBGs introduce wavelength-dependent reflection and delay through a spatially varying grating period. Although centred chirp has been extensively studied, a systematic comparison of different chirp profiles remains limited. In this work, seven chirp profiles—linear, quadratic, cubic, exponential, logarithmic, hyperbolic-tangent, and centred—are numerically analyzed to identify the optimum design for narrowband, high-reflectivity, and low-dispersion optical filtering in the C-band communication window.

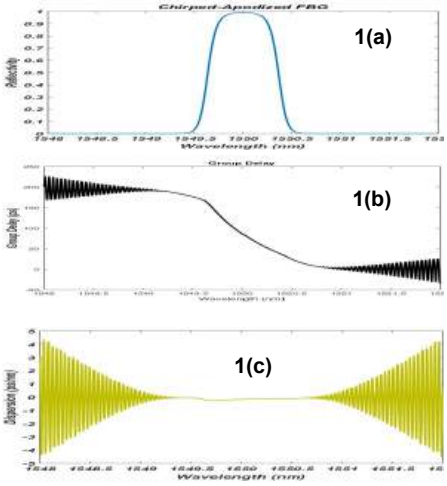


Fig. 1: Reflection spectrum (a), Group delay response (b), Dispersion (c) of Cubic Chirped–Raised Cosine Apodized FBG

The optical response is analyzed using coupled-mode theory (CMT) and the transfer matrix method (TMM). Grating parameters including the chirp profile, grating period $\Lambda(z)$, grating length (L) are optimized to tailor the reflectivity $R(\lambda)$, group delay $\tau(\lambda)$, and chromatic dispersion $D(\lambda)$. Raised-cosine apodization is employed to suppress sidelobes [2,3]:

$$g(z) = 0.5\left(1 + \cos\left(\frac{2\pi\left(z - \frac{L}{2}\right)}{L}\right)\right)$$

Simulation results show that quadratic, cubic, and exponential chirp profiles achieve near-unity reflectivity (~0.99998) with a significantly reduced FWHM (~0.322 nm), whereas linear, logarithmic, hyperbolic-tangent, and centred chirp profiles exhibit broader bandwidths (~0.72 nm). Among all profiles, the cubic chirp demonstrates the best overall performance, providing the minimum FWHM (~0.32192 nm), low group delay (~42.03 ps), and nearly zero local dispersion (~5.9×10⁻³ ps/nm) at the Bragg wavelength, established cubic chirp as the most suitable chirp profile for compact narrowband optical filters and dispersion-engineering. Although centred chirp exhibits lower overall dispersion variation over a wider spectral range, it is accompanied by increased bandwidth and higher delay.

Chirp Profile	Peak Reflectivity	FWHM (nm)	Group Delay at peak (ps)	Dispersion at peak (ps/nm)
Linear ($\Lambda = \Lambda_0 + Cz$)	0.98934	0.72459	86.73	0.1625
Quadratic ($\Lambda = \Lambda_0 + Cz^2$)	0.99998	0.32201	42.14	0.0279
Cubic ($\Lambda = \Lambda_0 + Cz^3$)	**0.99998**	**0.32192**	**42.03**	**0.0059**
Exponential ($\Lambda = \Lambda_0 \exp(Cz)$)	0.99998	0.32192	42.03	0.0066
Logarithmic ($\Lambda = \Lambda_0 + Clog(1+z)$)	0.98970	0.71933	86.09	0.1649
Tanh ($\Lambda = \Lambda_0 + \tanh(Cz)$)	0.98934	0.72459	86.73	0.1625
Centred ($\Lambda = \Lambda_0 + C(z - \frac{L}{2})$)	0.98934	0.72456	86.83	0.1624

Table 1: Comparative performance of different chirp profiles of Raised Cosine Apodized FBG

References:

[1] D. Tosi, *Sensors*, 18(2018), 2147.
[2] B. A.Naguib et al., *AIP Advances*, 11(2021), 015231.
[3] R. Kashyap, *Fiber Bragg Gratings,* 2nd ed., Academic Press, (2010).

Distance-Dependent Class Asymmetry in CNN-Based OTDR Fault Detection

[1]Shrishty Mishra, [1]Alok Singh
[1]Department of Physics, JSS University, Noida – 201301, India
#*shrishtymishra336@gmail.com* #*aloksinghphy@gmail.com*

Not all fault types fail at the same fibre length. In CNN-based OTDR classifiers, Fresnel reflection detection collapses beyond 20 km while splice and bend monitoring holds to ~40 km, and fault-free discrimination is unaffected by distance. We derive a closed-form SNR–distance model that predicts these per-class limits, and confirm it on 10,000 simulated SMF-28 traces across five fibre spans.

CNN classifiers applied to OTDR traces achieve high accuracy at short fibre ranges [1], but how performance degrades with distance — and whether all fault types fail together — has not been studied. At 1550 nm on SMF-28 (α = 0.2 dB/km) [2], round-trip propagation imposes a 0.4 dB/km double penalty: fault amplitude decays as $\exp(-2\alpha z_0)$ while the receiver noise floor rises with span L. We characterise how this penalty affects each fault class separately, across five fibre lengths from 5 to 80 km.

Four fault classes — Fresnel reflection (spike + insertion loss), splice loss (instantaneous step), fibre bend (distributed ramp, 2–5 km), and fault-free — were simulated across five spans (5, 10, 20, 40, 80 km) with per-trace SNR ~ Uniform (15, 35) dB. Gaussian noise plus polynomial baseline drift model instrument wander. Noise standard deviation $\sigma = \alpha L/\sqrt{3}\cdot 10^{-\mathrm{SNR}/20}$ scales with L, giving the effective SNR at fault position z_0:

$$\mathrm{SNR}^{\mathrm{eff}} = \mathrm{SNR}^{\mathrm{In}} - 2\alpha z_0\ (\mathrm{dB}) - 10\cdot\log_{10}(\alpha L/\sqrt{3}) \qquad (1)$$

A dataset of 10,000 traces (500 per class per span, 80/20 split) trained a single dual-output 1D-CNN (backbone: 64→128→256 filters; classification and position-regression heads) across all lengths simultaneously. Per-trace z-score normalisation removes absolute power level, so the model classifies by trace shape rather than amplitude — which is the appropriate choice when fibre length is unknown.

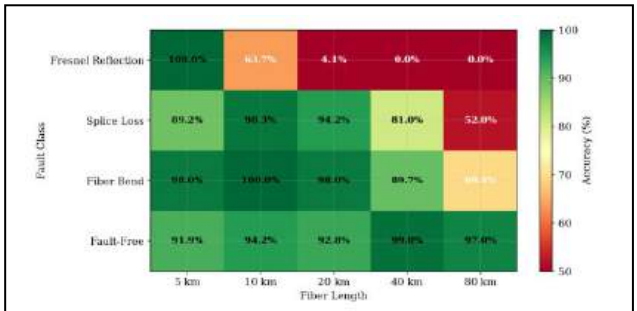


Fig.1: Per-class CNN accuracy (%) vs. fibre span. Fresnel reflection collapses beyond 20 km; splice loss, fibre bend, and fault-free detection remain viable at longer ranges.

The results follow the ordering Eq. (1) predicts: the fault class with the narrowest signature fails first. Fresnel accuracy falls from 100% at 5 km to 4.1% at 20 km and 0% beyond: its 3-sample spike is buried by the rising noise floor, leaving only the step-loss component, which the model correctly reclassifies as splice. Splice loss and fibre bend degrade more gradually — 89.2%→52.0% and 98.0%→69.4% over 5–80 km — because the step and ramp signatures span enough samples to remain detectable even as noise rises. Fault-free discrimination remains 91.9–99.0% at all spans since noise creates no systematic false pattern. Overall accuracy falls from 94.4% at 5 km to 55.4% at 80 km, the collapse driven entirely by Fresnel misclassification. Fault localisation RMSE rises from 0.58 km at 5 km to 15.6 km at 80 km. Grad-CAM attribution maps confirm the underlying mechanism: at 5 km, attribution concentrates within 0.1 km of the fault position (conf = 100%); at 80 km it becomes diffuse across the full trace yet the model remains 84–90% confident in its Splice prediction — it correctly identified the surviving insertion-loss step, not a noise artefact.

Equation (1) gives a practical design guideline before any classifier is deployed: Fresnel detection is reliable below ~20 km, splice and bend monitoring to ~40 km, and fault-free classification works at any span. An operator can use these bounds to decide which fault types a given link length can reliably support, without running exhaustive field trials.

Acknowledgements: Shrishty Mishra thanks Alok Singh, JSS University, Noida, for guidance and computational support.

References:

[1] K. Abdelli, H. Griesser, and S. Pachnicke, Proc. 22th ITG Symposium on Photonic Networks, Online, Germany, pp. 1–5 (2021).
[2] Corning Inc., *SMF-28 ULL Optical Fiber — Product Information*, PI1470, Corning, NY (2014).

Optical Liquid-flow Sensing via Mechanically Amplified Etched Fiber Bragg Grating

[1]Saikat Mondal, [2]Abhimanyu Roy Chaudhuri and [1,#]Partha Roy Chaudhuri
[1]Department of Physics, Indian Institute of Technology Kharagpur, India, 721302
[2]Department of Civil Engineering, Indian Institute of Technology Kharagpur, India, 721302
[#]*roycp@phy.iitkgp.ac.in*

We have proposed a lever assisted optical liquid-flowmeter utilizing etched-FBG, which converts flow induced drag-force into axial strain on FBG. The effect of dimensions, etching depth and elastic modulus of adhesive on strain transfer are computationally studied. The sensor offers an effective approach for liquid-flowmeter where conventional methods are limited.

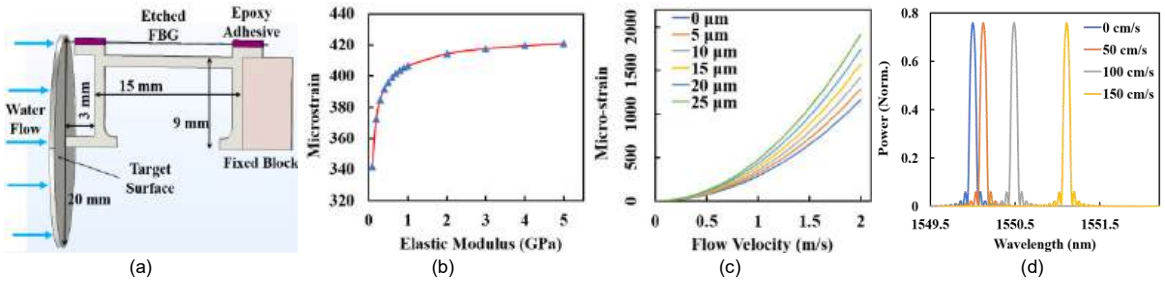
Liquid flow monitoring plays a crucial role in industrial process control, chemical plants, water resource management and distribution networks [1]. In this work we have proposed a compact flow sensor based on lever mechanism employing an etched FBG. The sensor is designed computationally where flow induced drag force generates axial strain on the FBG. The effects of key design parameters on the strain transfer efficiency are analyzed to optimize the sensor performance.

As illustrated in fig. 1(a), the flowing liquid exerts a drag force on a circular target plate attached to the sensing structure. This force deforms the compliant lever, generating an amplified axial strain on the etched FBG. The drag pressure due to a flowing liquid of velocity V, density ρ can be expressed as [2];

$$P_D = \frac{1}{2} C_D \rho V^2 \quad (1)$$

where C_D (~1.1 for a circular flat plate) is the drag coefficient. The drag force acting on the target plate is the area of the target surface (A) multiplied by P_D. Although increasing A enhances the sensor performance, a larger surface experiences non-uniform flow velocities, leading to inaccurate reading. Therefore, a circular target plate of radius 1 cm is selected. Now for ε strain generated on FBG the Bragg wavelength shift is; $\Delta\lambda_b = (1 - P_e) \times \lambda_b \varepsilon$, where P_e(~0.22) is the photoelastic coefficient [3]. Finite element simulations are employed to validate the strain amplification mechanism and optimize the geometric parameters of the compliant lever structure, as shown in fig. 1(a). The influence of adhesive elastic modulus and fiber etching thickness on strain transfer efficiency is systematically evaluated.

The simulation results presented in fig 1(b) demonstrate that the strain transfer efficiency increases with adhesive elastic modulus and approaches saturation at approximately 2 GPa, indicating that commercially available epoxy adhesives are suitable for practical implementation. Figure 1(c) illustrates the relationship between flow velocity and induced strain for different etching thickness. Increasing the etching depth improves strain transfer efficiency due to reduced cross-section area; however excessive etching compromises the sensor mechanical robustness. Based on this trade off, an acceptable etching depth of 20 μm is selected as optimum design. The corresponding reflection spectrum shifts under different flow conditions (using 20 μm etched FBG) are presented in fig 1(d).



(a) (b) (c) (d)

Fig. 1: (a) Schematic representation of the sensor; (b) strain experienced by FBG for different elastic modulus of adhesive; (c) strain transfer on FBG for different etching depth; (d) shift in reflection spectra with varying flow velocity.

The proposed compact sensor shows an efficient passive strain amplification mechanism for flow velocity measurement, promising an alternative where conventional flow-meter techniques are limited.

References:

[1] A. Rodriguez, P. Dieguez, J.C. Urroz *et al., Scientific Reports* 14 (2024) 13377.
[2] B. R. Munson et. al., *Fundamentals of Fluid Mechanics*, Wiley & Sons Incorporated, John, (2012).
[3] Q. Liu *et al.*, *IEEE Sensors Journal* 25 (2025) 28314-28322.

A Compact Single-FBG Platform for Early Parkinsonian Tremor Detection

#Anjali Nehra, Archana Thrikkaikuth Chalackal, Gayathri Bharathan
Optics and Photonics Centre Indian Institute of Technology Delhi, New Delhi,110016 India
anjali99.cstaff@iitd.ac.in

A novel single-FBG sensor embedded in an asymmetric PDMS structure is proposed for Parkinsonian tremor monitoring. The engineered geometry enables finger-specific wavelength responses using a single sensing element. Simulations demonstrate effective finger discrimination in the low-force regime, achieving a maximum sensitivity of 14.95 nm/N for optimized fiber placement.

Parkinson's disease is a progressive neurological disorder causing tremor, impaired motor control, and postural instability that adversely affect daily activities and quality of life . Early diagnosis and continuous monitoring are therefore essential for timely intervention and treatment. The earliest symptoms of Parkinson's constitute resting tremors of the fingers and hands. Accelerometers, IMUs, surface electromyography, and FBG-based wearable sensors have been explored by researchers for quantitative tremor assessment in Parkinson's disease. Fiber Bragg Grating (FBG)-based wearable sensors have attracted significant attention owing to their high sensitivity, lightweight nature, electromagnetic immunity, and suitability for real-time monitoring. However, most existing approaches employ multiple FBGs distributed across different fingers, increasing fabrication complexity, interrogation requirements, cost, and device bulkiness. Consequently, there is a growing need for compact and cost-effective solutions capable of finger-specific sensing. To address this challenge, a single-FBG embedded within an engineered asymmetric PDMS structure is proposed to generate distinguishable responses from individual finger movements.

Fig.1 presents the simulated wavelength shift as a function of applied force for different finger positions within the proposed embedding structure. The results demonstrate that the engineered asymmetric PDMS structure effectively tailors finger-specific strain transfer to the single embedded FBG. Thus, the proposed sensor gives distinguishable wavelength signatures from individual finger movements while minimizing sensing complexity. The non-uniform geometry enhances spatial selectivity in the clinically relevant low-force regime (<2 N), yielding a maximum sensitivity of 14.95 nm/N and improved wavelength separation for tremor-prone fingers. A slight overlap in sensitivities were observed, suggesting scope for further optimization of the PDMS. The proposed sensor placement on the hand for finger-specific tremor monitoring is illustrated in Fig.2. The sensor is positioned on the dorsal hand region to maximize strain transfer from finger motion. These results demonstrate the potential of engineered PDMS architectures for compact, wearable, and cost-effective Parkinsonian tremor monitoring. Future work includes fabrication and experimental validation of the proposed sensor, followed by development of a wearable prototype for continuous neurological monitoring.

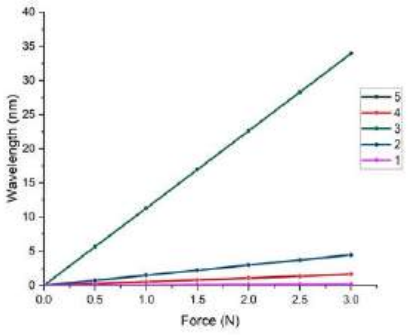


Fig.1: Wavelength shift with force for different fingers

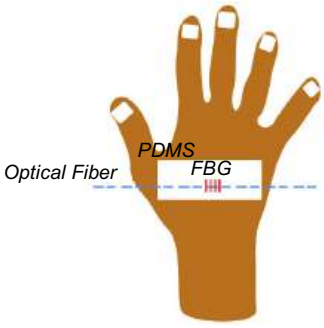


Fig.2: Proposed Sensor placement

References:

[1] D. M. Radhakrishnan and V. Goyal, "Parkinson's disease: A review," *Neurology India*, vol. 66, no. Suppl 1, pp. S26–S35, 2018
[2] R. De Fazio, C. Del-Valle-Soto, V. Mastronardi, M. De Vittorio, and P. Visconti, "A smart glove to evaluate parkinson's disease by flexible piezoelectric and inertial sensors," *Sensors International*, vol. 6, p. 100324, 2025.
[3]. S. P. G, S. Umesh, U. Asokan, and T. Srinivas, "Parkinsonian hand tremor measurement device based on fiber bragg grating sensor," in 2015 *International Conference on Smart Sensors and Systems* (IC-SSS), 2015, pp. 1-3.

Modeling, Design, and Implementation of an FPGA-Based MZM Bias point controller for High-Speed Optical Transmitters in Intersatellite Laser Communication Links

[1,#]Nirlesh Singh, [2]Sanjana Mohite, [3]Atharv Kulkarni, [1]Ravikumar K., [1]Sanjay Mittal, [1]Karanth S.P.
[1]Laboratory for Electro Optics Systems (LEOS)-ISRO
[2]Ramaiah University of applied sciences, Bengaluru
[3]Indian Institute of Technology, Dharwad
[#]nirleshsingh@leos.gov.in

This work deals with quadrature point bias correction in a Mach Zehnder Modulator (MZM) using a dither signal as tracker and PI controller, for bias point correction. Error signal for the controller is obtained by doing FFT on the output modulated beam converted to electric signals using photodiode.

High-speed optical communication systems employed in satellite applications require highly stable optical transmitters to ensure reliable long-distance data transmission. A key component of these transmitters is the Mach–Zehnder Modulator (MZM), whose operating bias point directly affects critical performance parameters such as extinction ratio (ER), optical power stability, linearity, chirp, and bit error rate (BER). In space optical communication terminals operating in LEO and GEO orbits, maintaining the optimum MZM bias point is particularly challenging due to temperature variations, component aging, radiation effects, and long mission durations. These factors cause gradual bias drift, resulting in degradation of transmitter performance and reduced communication link margin. The Mach–Zehnder Modulator operates based on the electro-optic effect, in which the refractive index of an electro-optic material such as lithium niobate ($LiNbO_3$) changes with the applied electric field. By selecting an appropriate bias voltage and superimposing the data modulation signal, modulation formats such as On-Off Keying (OOK) can be efficiently implemented. Since the modulation characteristics strongly depend on the operating bias point, continuous bias stabilization is essential for maintaining optimum system performance.

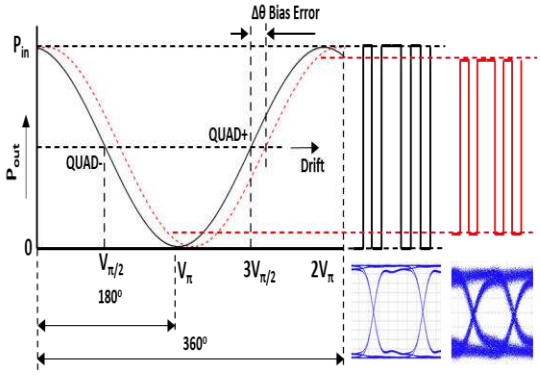


Fig. 1: MZM Bias point drift & ER reduction

This work presents an FPGA-based Automatic Bias Control (ABC) technique for maintaining the MZM at its quadrature operating point using a low-amplitude, low-frequency dither signal. The injected dither continuously tracks the operating point without significantly affecting the transmitted data. A small portion of the modulated optical output is monitored using a photodiode, converted into an electrical signal, and digitized by an Analog-to-Digital Converter (ADC). The digitized samples are processed in an FPGA to extract the harmonic components associated with the injected dither signal. When the MZM deviates from its quadrature point, harmonic components are generated in the detected signal. In the proposed method, the second harmonic component serves as the bias error indicator, with its amplitude being proportional to the deviation from the desired operating point. A narrow-band digital filter isolates the second harmonic, and Fast Fourier Transform (FFT)-based processing accurately estimates its amplitude. The extracted harmonic amplitude is used as the error signal for bias correction. A digital Proportional-Integral (PI) controller implemented in the FPGA processes the estimated error and generates the required correction voltage. This correction signal is converted to an analog voltage using a Digital-to-Analog Converter (DAC) and applied to the MZM bias input, thereby forming a closed-loop feedback system that continuously compensates for slow bias drift. The controller maintains stable operation at the quadrature point despite environmental variations and long-term device aging. The proposed bias tracking technique ensures stable optical transmitter performance, improved extinction ratio, and enhanced communication link reliability throughout the mission lifetime.

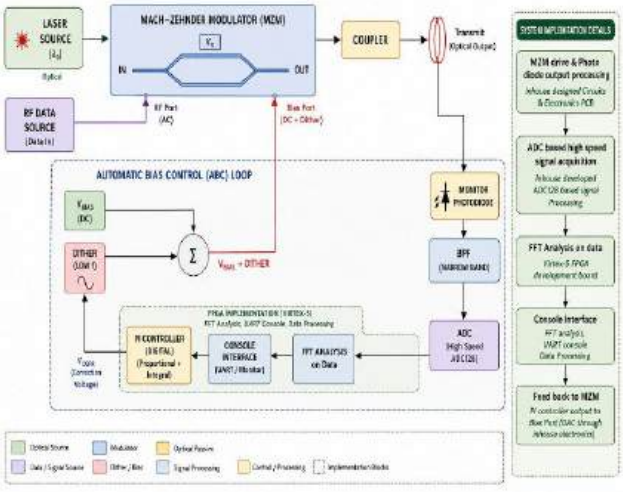


Fig. 2: Automatic Bias Control (ABC) Implementation

References:

[1] Cho, P.S., Khurgin, J.B., and Shpantzer, I., 2006. Closed-loop bias control of optical quadrature modulator. IEEE Photonics Technology Letters, 18(21), pp.2209–2211

[2] Ji, Y., Wu, B., Hou, Y., and Ding, A., 2020. A MZ modulator bias control system based on variable step P&O algorithm. IEEE Photonics Technology Letters, 32(23), pp.1473–1476.

Engineering Third-Order Exceptional Points in Photonic Time Crystals

[1, #]Pratishtha Pandey,[1]D.K. Dwivedi and [2]Saurabh Mani Tripathi

[1]Photonics and Photovoltaic Research Lab (PPRL),
[1]Madan Mohan Malaviya University of Technology, Gorakhpur-273010, India
[2]Optics and Photonics Centre, Indian Institute of Technology Delhi, New Delhi 110016, India

[#]*pandeypratishtha18@gmail.com*

We present a Floquet-based framework for realizing third-order exceptional points (EP3) in photonic time crystals through temporal refractive-index modulation. A reduced three-mode Hamiltonian predicts cube-root eigenvalue dispersion, cyclic mode state and fractional Berry phase accumulation under parameter encirclement, establishing a dynamically tunable non-Hermitian platform with enhanced sensing capabilities.

Photonic time crystals provide a dynamic platform for manipulating electromagnetic waves through periodic temporal modulation of material properties. In contrast to conventional photonic crystals, where periodicity is introduced in space, PTCs exploit temporal periodicity to induce frequency conversion and momentum bandgap formation through Floquet interactions [1]. The additional temporal degree of freedom enables the realization of wave phenomena that are inaccessible in static media, including non-Hermitian and topological effects. For time-periodically-driven dielectric materials, the permittivity becomes $\varepsilon(t) = \varepsilon_0 + \delta\varepsilon\cos(\Omega t + \phi)$, where Ω is the modulation frequency and ϕ is the modulation phase. This periodic modulation couples spectral components separated by integer multiples of the modulation frequency leading to floquet sideband hybridization and the opening of momentum bandgaps in the quasienergy spectrum [2]. Non-Hermitian photonics has revealed the importance of exceptional points (EPs) singular degeneracies at which both eigenvalues and eigenvectors coalesce. While most studies have focused on second-order EPs, higher-order exceptional points exhibit richer topology, stronger modal coalescence and enhanced sensitivity scaling [3]. Near the parametric resonance, coherent coupling among floquet sidebands induces strong mode hybridization leading to avoided crossings and momentum bandgap formation. The interaction of three resonant sidebands supports a third-order exceptional point (EP3). Projecting the Floquet-Maxwell equations onto the resonant three mode subspace yields the effective non-Hermitian Hamiltonian.

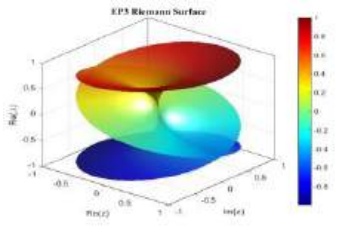


Fig. 1: Real part of eigenvalues near the EP3 in complex parameter space $z = \Delta + i\gamma$ showing three-sheeted riemann topology

$$H_F = \begin{pmatrix} \Delta_{-1} + i\gamma_{-1} & \kappa_- & 0 \\ \kappa_- & \Delta_0 + i\gamma_0 & \kappa_+ \\ 0 & \kappa_+ & \Delta_{+1} + i\gamma_{+1} \end{pmatrix} \quad (1)$$

Here, $\Delta_{-1}, \Delta_0, \Delta_{+1}$ represents floquet detunings, κ_- is temporal coupling between $\omega_0 - \Omega$and ω_0, $\kappa_+$is temporal coupling between $\omega_0$and $\omega_0 + \Omega$, γ_j represents effective gain/loss and zero corner terms represent negligible direct coupling between the two nonadjacent sidebands.

At the critical condition $\Delta_{-1} = \Delta_0 = \Delta_{+1} = 0, \gamma = \sqrt{2}\kappa$ the system reaches a third-order exceptional point, where all three eigenvalues and eigenvectors coalesce. At this point the Hamiltonian becomes non-diagonalizable which reduces to a third-order jordan block, eigenvalues exhibit cube-root dispersion $\lambda \sim \epsilon^{1/3}$.This leads to a three-sheeted riemann surface, where eigenvalues permute cyclically upon encircling the EP3.

References:

[1] E. Lustig, Y. Sharabi, M. Segev, Topological aspects of photonic time crystals, *Optica* 5 (2018) 1390.
[2] X. Wang, P. Garg, M.S. Mirmoosa, A.G. Lamprianidis, C. Rockstuhl, V.S. Asadchy, Expanding momentum bandgaps in photonic time crystals through resonances, *Nat. Photonics* 19 (2025) 149–155.
[3] H. Hodaei, A.U. Hassan, S. Wittek, H. Garcia-Gracia, R. El-Ganainy, D.N. Christodoulides, M. Khajavikhan, Enhanced sensitivity at higher-order exceptional points, *Nature* 548 (2017) 187–191.

Exceptional Point Engineering in Photonic PT-Symmetric Systems

Sabila Parveen[1,*], Bhavin Shastri[2], P. Senthilkumaran[1] and A. Aadhi[1]

[1]Optics and Photonics Centre, Indian Institute of Technology Delhi, New Delhi 110 016.

[2]Centre for Nanophotonics, Department of Physics, Engineering Physics, and Astronomy, Queen's University, Kingston, Ontario, Canada.

*sabila.cstaff@opc.iitd.ac.in

Abstract: *The high sensitivity and enhanced system responses at exceptional points (EPs) in non-Hermitian PT-symmetric photonic systems are useful for unconventional light transport and for optical sensing. We investigate the construction of generalized higher-order EPs in a coupled-cavity photonic system, analyze their perturbation-induced eigenvalue splitting and the resulting sensitivity enhancement.*

In recent years, PT-symmetric non-Hermitian systems have attracted much due to their real spectra in the Hamiltonians [1]. At the exceptional points (EPs), the non-Hermitian system has the unique property of coalescence of eigenvalues and eigenvectors, which plays an important role across various branches of physics, from classical mechanics and optics to quantum mechanics. As a result, the investigation and physical realization of PT-symmetric Hamiltonians have become major subjects of theoretical and experimental endeavor. Non-Hermitian photonic systems have been realized using integrated coupled microring lasers, coupled waveguide architectures, photonic crystal structures, Anderson localization, active metasurfaces and coupled fiber-based devices [3]. Among these photonic systems, coupled waveguides or resonators with appropriate gain and loss, and suitable coupling configuration exhibit PT-symmetric non-Hermitian dynamics. By properly controlling gain and loss and the coupling between the modes allows the non-Hermitian system to operate in three regimes, such as PT symmetry, PT broken, and exceptional points. Recently, it has been shown that non-Hermitian degeneracies can enhance the sensitivity of photonic systems to external perturbations [2]. In particular, an external perturbation around the EP splits the degenerate eigenfrequency ($\Delta\lambda$), enabling the detection of even small perturbations. As a result, the system provides ultra-sensitivity for detecting refractive index variations, temperature or pressure changes, and even the presence of biological molecules.

Higher-order PT-symmetric systems, such as ternary (D = 3) and quaternary (D = 4) support higher-order EPs (EP3 and EP4), in contrast to two-dimensional systems (EP2). The coalescence of multiple eigenstates in these higher-order systems shows higher response to perturbations. As a result, these systems enhance optical sensitivity by increasing the splitting between degenerate eigenfrequencies. However, the realization of higher-order non-Hermitian systems in photonic platforms is challenging due to their stringent requirements of system design and modelling. Here, we have developed a generalized higher-order non-Hermitian system using a microring-based coupled-cavity photonic platform. By properly applying the control parameters, the system shows higher-order non-Hermitian properties and higher-order exceptional points. Further, to study the enhancement in sensitivity, we introduced an external perturbation and observed the eigenvalue splitting for different EP orders (Fig.1). We noticed that under a small perturbation, *i.e.*, the refractive index variation, the eigenvalue splitting scales as $\varepsilon^{1/D}$ with increasing EP order D, thereby enhancing sensitivity. As evident from Fig. 1, we observe that higher EP order provides enhanced sensitivity for detecting refractive index variations (Δn). In conclusion, we develop an implementation of a higher-order photonic non-Hermitian system. Our investigation confirms that the higher-order photonic EP is attractive for practical applications, including nanoparticle detection, refractive-index sensing, and precision measurements.

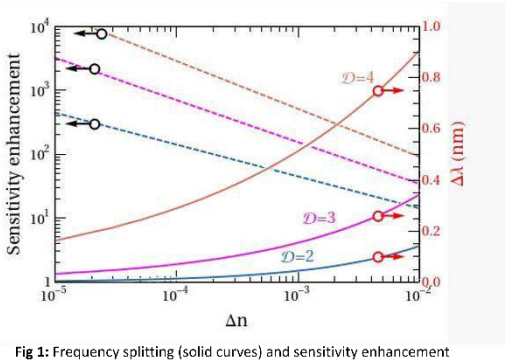


Fig 1: Frequency splitting (solid curves) and sensitivity enhancement (dashed curves) with different order of non-Hermitian system.

Acknowledgement: Funding support from 'ANRF/ARG/2025/001176/PS' is gratefully acknowledged.

References

[1] C.M. Bender, S. Boettcher, *Physical Review Letters* 80 (1998).
[2] H. Hodaei, A.U. Hassan, S. Wittek, H. Garcia-Gracia, R. El-Ganainy, D.N. Christodoulides, M. Khajavikhan, *Nature* 548 (2017).
[3] Miri, M. A., & Alu, A., *Science*, *363* (2018).

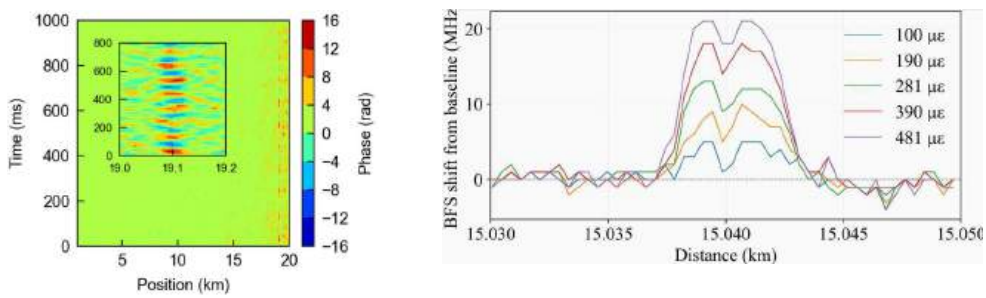
Hybrid Φ-OTDR/BOTDA-Based Distributed Acoustic and Strain Sensing for Geohazard Monitoring

Surabhi Raj[1], Subbash Padmanabhan[1,2], V.P Anand[1,3], Arsath Abbasali Ayubali[1], P.S Harrish[1], Balaji Srinivasan[1]*

[1]Department of Electrical Engineering, Indian Institute of Technology Madras, Chennai, India
[2]CSIR- Structural Engineering Research Center, Chennai, India
[3]CSIR-Central Scientific Instruments Organization, Chennai, India
*Email: balajis@ee.iitm.ac.in

This work presents a hybrid Φ-OTDR/BOTDA-based Distributed Acoustic and Strain Sensing (DASS) system for geohazard monitoring, integrating DAS for detecting dynamic events and DSS for monitoring long-term ground deformation using a single core of an optical fiber cable (OFC).

Distributed fiber-optic sensing (DFOS) has emerged as a powerful technology for continuous, real-time, and long-range monitoring by utilizing the optical fiber itself as a distributed sensing medium [1]. Among the various DFOS techniques, phase-sensitive optical time-domain reflectometry (Φ-OTDR) and Brillouin optical time-domain analysis (BOTDA) offer complementary sensing capabilities. Φ-OTDR realizes Distributed Acoustic Sensing (DAS) by detecting dynamic perturbations through Rayleigh backscattering, whereas BOTDA enables Distributed Strain Sensing (DSS) by measuring the Brillouin frequency shift (BFS) to quantify static or slowly varying strain and temperature distributions over extended distances [2]. Integrating both techniques on a single core of an optical fiber cable (OFC) enables simultaneous monitoring of dynamic events and progressive deformation, making the hybrid approach well suited for geohazard monitoring.



(a) (b)

Fig. 1. *Experimental validation of the hybrid Φ-OTDR/BOTDA-based DASS system.* ***(a)*** *Waterfall plot of the Φ-OTDR-based DAS response to dynamic strain induced by a piezoelectric transducer (PZT) at 19.10 km.* ***(b)*** *Brillouin frequency shift (BFS) measured by the BOTDA-based DSS under controlled mechanical static loading at 15.04 km.*

As a proof-of-concept laboratory demonstration, controlled dynamic and static strain are applied to a single core of the OFC to emulate slope instability. The Φ-OTDR subsystem is employed to detect dynamic strain events, while the BOTDA subsystem measures the Brillouin frequency shift under varying static loading, which is subsequently converted into distributed strain using a calibrated strain coefficient. The experimental results validate the proposed hybrid sensing approach and demonstrate its potential for distributed geohazard monitoring.

References

[1] A.H. Hartog, *An Introduction to Distributed Optical Fibre Sensors*, CRC Press, Boca Raton (2017).
[2] J. Pastor-Graells, H.F. Martins, A. Garcia-Ruiz, S. Martin-Lopez, M. Gonzalez-Herraez, *Optics Express* **24** (2016) 13121–13133.

Experimental Demonstration of a Polarization-Based Fiber-Optic Torsion Sensor for Open-Channel Flow Velocity Measurement

[1]Abhimanyu Roy Chaudhuri, [2]Saikat Mondal and [1,#]Prashanth Reddy Hanmaiahgari
[1]Department of Civil Engineering, Indian Institute of Technology Kharagpur, India, 721302
[2]Department of Physics, Indian Institute of Technology Kharagpur, India, 721302
[#]*hpr@civil.iitkgp.ac.in*

We present an optical flow sensor employing polarization modulation in a torsionally strained polarization-maintaining fiber for measuring open-channel water velocity. Hydraulic flume experiments show close agreement of the sensor-estimated velocities with Acoustic Doppler Velocimeter (ADV) reference measurements, demonstrating its potential for continuous long-term hydraulic monitoring.

Reliable determination of flow velocity is fundamental in hydraulic engineering, environmental monitoring, and water-resources management [1]. In the present work, we developed a polarization-based fiber-optic torsion sensor to measure open-channel flow velocity through optical intensity modulation.

The sensing system incorporates a lightweight submerged rectangular plate connected to a pendulum mechanism, as shown in Fig. 1(a). When flowing water acts on the plate, it exerts hydrodynamic drag and lift forces given by: $F_D = \frac{1}{2}\rho C_D \alpha V^2$; $F_L = \frac{1}{2}\rho C_L \alpha V^2$, where ρ is the fluid density, C_D and C_L are the drag and lift coefficients, α is the projected target area, and V is the flow velocity. The combined action of these forces causes the pendulum to undergo an angular displacement. This rotation introduces torsional deformation into a polarization-maintaining Panda fiber positioned along the hinge rotational axis and fusion-spliced between two single-mode fibers. This induced a change in polarization axis and alters the transmitted optical intensity after passing through crossed polarizers setup, providing a measurable response that is directly related to the flow velocity [2].

We first verified the optical response of the sensor by imposing controlled angular displacement, where the measured intensity exhibited the expected periodic variation associated with polarization rotation [3]. Following this calibration, we tested the device in a recirculating laboratory flume over water velocities ranging from approximately 0.01 to 0.38 m s^{-1}. The experimental observations established a stable relationship between normalized optical intensity and flow velocity. Velocity estimates obtained from the optical sensor showed close agreement with simultaneously recorded Acoustic Doppler Velocimeter (ADV) measurements, with the maximum deviation remaining below 3.4%.

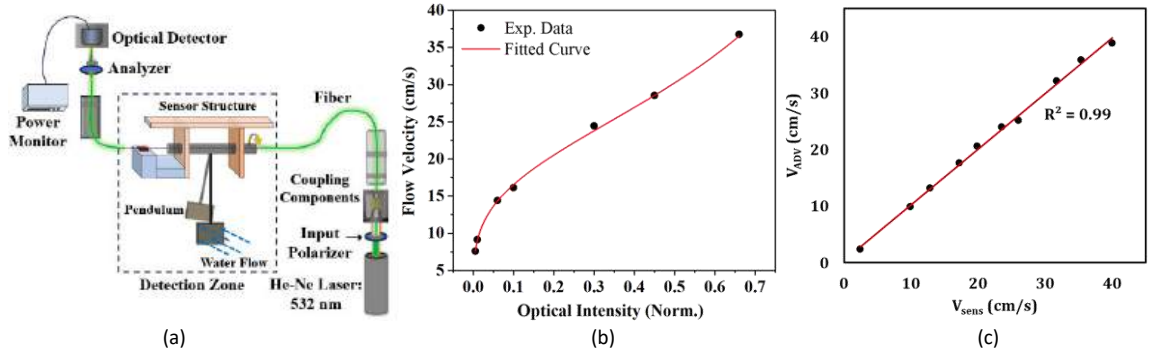


Fig. 1:(a) Schematic of the experimental set-up; (b) Experimental relationship between normalized optical intensity and measured flow velocity; (c) Comparison between sensor-estimated velocities (V_{sens}) and reference Acoustic Doppler Velocimeter (V_{ADV}) data.

The experimental results demonstrate that polarization-based torsional sensing can provide accurate flow-velocity measurements while avoiding the limitations associated with conventional electronic instrumentation.

References:

[1] V. I. Nikora, D. G. Goring, *Journal of hydraulic engineering*, 124(6) (1998), 630-634.
[2] V. Budinski, D. Donlagic, *Sensors*, *17*(3) (2017) 443.
[3] B. Culshaw, *Journal of lightwave technology*, *22*(1) (2004), 39-50.

Improving Detection Bandwidth in Distributed Acoustic Sensing using Frequency Division Multiplexing

[1]Kishore Kumar S, [2]Nayana Madhu Deshpande, [1]Elisa Prathibha Mathew and [1,#]Balaji Srinivasan

[1]Indian Institute of Technology Madras, India
[2]Cochin University of Science and Technology, India

[#]*balajis@ee.iitm.ac.in*

Conventional DAS is limited by the pulse repetition frequency (PRF), which depends on the sensing fiber length and restricts the measurable acoustic bandwidth [1]. This work employs frequency-division multiplexing using EOMs and AOMs to transmit multiple frequency pulses at overlapping intervals, increasing the effective interrogation rate and achieving a 3x improvement in detection bandwidth.

The pulse repetition frequency (PRF) in a distributed acoustic sensing (DAS) system is fundamentally constrained by the optical round-trip time of the sensing fiber to prevent overlap between consecutive Rayleigh backscattered signals. To increase the detection bandwidth without violating this constraint, a multi-frequency pulse interrogation scheme is employed. Since the Rayleigh backscattered signals associated with each modulation frequency can be independently separated during digital signal processing, two independent measurements are acquired within a single fiber round-trip time without introducing signal ambiguity. Consequently, the proposed multi-frequency interrogation technique effectively increases the sampling rate, improves signal fidelity, and better reconstruction of original acoustic signal compared with conventional single-frequency DAS interrogation.

The experimental setup is illustrated in Fig. 1. A narrow-linewidth laser with a linewidth of 1 kHz serves as the optical source. The laser output is divided by a 90:10 optical coupler, with 10% of the optical power directed to the local oscillator (LO) and the remaining 90% used for optical pulse generation. An arbitrary waveform generator (AWG) generates electrical pulse sequences at modulation frequencies of 30 MHz and 60 MHz. These signals drive the electro-optic modulator (EOM) which is biased at the null point and the acousto-optic modulator (AOM) driver, which subsequently drives the AOM to produce the corresponding frequency-shifted optical pulses. The optical pulses are amplified using an erbium-doped fiber amplifier (EDFA) before being launched into the fiber under test (FUT). The Rayleigh backscattered (RBS) light returning from the FUT is routed through an optical circulator to a coherent receiver, where it interferes with the local oscillator. The coherent receiver generates In-phase (I) and Quadrature (Q) electrical signals, which are digitized and recorded using a data acquisition (DAQ) system for subsequent signal processing. The length of the fiber under test (FUT) is 18 km and the multiplexed PRF was chosen to be 10 kHz, where a conventional DAS would be limited to 5kHz.

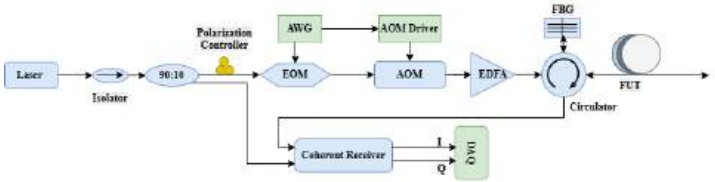


Fig. 1: Schematic of FDM DAS

The system was evaluated using 440 Hz, 3 kHz, and 4 kHz vibration signals. The DAQ data was filtered with a 20 MHz second-order digital band-pass filter, processed using the conventional DAS algorithm, and combined in the time domain. Fig. 2 shows successful detection of a 4 kHz acoustic signal using Frequency Division Multiplexing (FDM) DAS.

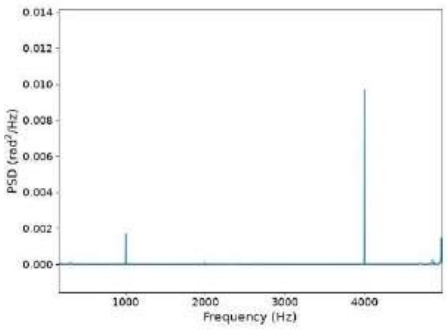


Fig. 2: PSD plot of DAS channel at 12 km showing detection of acoustic signal at 4 kHz with a multiplexed PRF of 10 kHz

The achievable improvement depends on the number of interrogation frequencies, the detector bandwidth, and the optical spectrum bandwidth, which is determined by the pulse shape.

References:

[1] L. Bouffaut, K. Taweesintananon, H.J. Kriesell, R.A. Rørstadbotnen, J.R. Potter, M. Landrø, S.E. Johansen, J.K. Brenne, A. Haukanes, O. Schjelderup, F. Storvik, Frontiers in Marine Science 9 (2022) 901348.

Mechanical tensor recovery from Few-Mode Fiber Rayleigh backscatter using complex intermodal covariance

[#]Pavithra S, Dinesh N Naik and Sudheesh Chethil

Indian Institute of Space Science and Technology, Valiamala, Thiruvananthapuram, Kerala

[#]*pavithras.23@res.iist.ac.in*

We demonstrate tensor-resolved mechanical sensing in a few-mode fiber via Rayleigh backscatter covariance measurement. Deriving the σ-flip backscatter selection rule analytically, we show that bend curvature, bend-plane orientation, twist rate, and axial strain imprint structurally distinct covariance fingerprints. With optimised dual-mode launch, the normalised Jacobian condition number is 1.32, confirming simultaneous identifiability of all four tensor components.

A fiber subjected to lateral force at an arbitrary angle is indistinguishable from axial strain, fundamentally limiting mechanical state reconstruction. We address this by exploiting the richer modal structure of few-mode fiber (FMF) and measuring the full complex intermodal covariance matrix Γ_{pq} rather than per-mode power [1]. The measured quantity is

$$\Gamma_{pq} = \mathbb{E}\left[B_p B_q^*\right] \qquad (1)$$

where $B_p$and B_q are backscattered modal fields. We derive analytically a hard selection rule for Rayleigh backscattering in an isotropic fiber: circular polarisation must flip on backscattering, while the orbital index remains unconstrained. This follows from the bilinear non-conjugated overlap governing contra-directional coupling [2],

$$(\hat{e}_{\sigma p} \cdot \hat{e}_{\sigma q}) = \frac{1 + \sigma_p \sigma_q}{2} \qquad (2)$$

which vanishes unless $\sigma_q = -\sigma_p$. Each perturbation type produces a structurally distinct coupling matrix: bend generates off-diagonal coupling (Δl = ±1, $\Delta\sigma$ = 0) [3,4], twist produces σ-dependent phase shifts [5], and strain produces diagonal β-proportional shifts [6]. Simulations for a step-index FMF ($a = 6.5\,\mu$m, NA $= 0.17, V = 4.48, \lambda$ 1550 nm, 12 vector eigenstates) reveal that twist and strain produce predominantly off-diagonal covariance signatures, demonstrating that power-only measurements are insufficient and that the full complex covariance is essential.

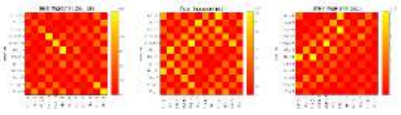


Figure 1 : Covariance fingerprints for bend (left), twist (center), and axial strain (right), showing distinct checkerboard-like σ-flip backscatter patterns that enable tensor identifiability.

The normalised Jacobian of the covariance measurement with respect to the four tensor components $(\kappa_b, \theta, \tau, \varepsilon_{zz})$ yields a condition number of 1.32 across 58 operating points spanning bend radii from 2 to 50 cm and V-numbers from 2.76 to 6.20. The optimal launch pair, HE_{21} $(l = +1, \sigma = +1)$and the TE/TM partner $(l = +1, \sigma = -1)$was identified by an exhaustive search over all 15 two-mode combinations [7]. The linear estimator achieves sub-0.05% reconstruction bias with an identity cross-talk matrix. Using the calibrated Rayleigh backscatter coefficient for silica [8], the minimum detectable perturbations are 7 nanostrain in axial strain and 0.001° in bend-plane orientation per measurement.

References:

[1] S. Ö. Arik, D. Askarov, and J. M. Kahn, *Journal of Lightwave Technology* 31(3), 423–431 (2013)

[2] A. Yariv, *IEEE J. Quantum Electron.* 9 (1973) 919–933.

[3] M. Heiblum, J. Harris, *IEEE J. Quantum Electron.* 11 (1975) 75–83.

[4] S.C. Rashleigh, J. Lightwave Technol. LT-1 (1983) 312–331.

[5] R. Ulrich, A. Simon, *Appl. Opt.* 18 (1979) 2241–2251.

[6] C.D. Butter, G.B. Hocker, *Appl. Opt.* 17 (1978) 2867–2869.

[7] S. Ramachandran, P. Kristensen, *Nanophotonics* 2 (2013) 455–474.

[8] P. Healey, *Electron. Lett.* 20 (1984) 30–32.

Surface Plasmon Resonance based optical fiber refractive index sensor using molybdenum disulfide and Gold

[1]Shikha Sachdeva and [2,#]Navneet K. Sharma
[1,2] Department of Physics and Materials Science and Engineering, Jaypee Institute of Information Technology, Noida, India

[#]Navneet.sharma@mail.jiit.ac.in

An experimental fiber optic surface plasmon resonance (SPR) sensor based on gold and molybdenum disulfide is presented. The method of wavelength interrogation is employed to analyze the sensor. The effects of the materials' thicknesses on the sensitivity of the sensor are elaborated. It is demonstrated that the presence of a molybdenum disulfide layer of specific thickness in the gold-based sensor enhances sensitivity.

One of the extremely effective optical techniques is surface plasmon resonance (SPR). It is widely employed in chemical sensing, environmental sensing, biological sensing, research on biomolecule interactions, and the detection of molecular events. Surface plasmons are typically excited using three different types of SPR sensing setups, such as prism couplers, grating couplers, and waveguide couplers. However, we have used fiber based waveguide coupler. It's quite difficult to handle the prism because of its size and mechanical features. To excite surface plasmons, generally metals like gold, silver, copper, etc. are used but in our presented study, we have used gold followed by molybdenum disulfide. It has been seen that it's a good plasmonic material. Molybdenum disulfide (MoS_2) is a transition metal dichalcogenide. Bulk layer has a indirect band gap of 1.23 eV and monolayer has direct band gap of 1.80 eV. We have analyzed how sensitivity of sensor varies with thickness of MoS_2 film keeping the gold film constant and also, we have shown that sensitivity is enhanced when we use MoS_2.

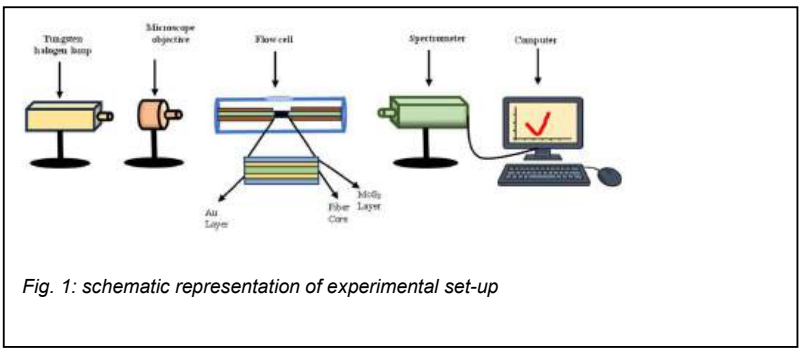


Fig. 1: schematic representation of experimental set-up

References:

[1] Y. Zhao, H. Zhang, X. Zhou, Y. Zhang, T. Cheng and X. Li, *Sensors and Actuators B: Chemical* 443 138262 (2025).

[2] J. Homola, S. S. Yee and G. Gauglitz, *Sensors and Actuators B: Chemical* 54 3–15 (1999).

[3] V. Kapoor and N. K. Sharma, *Optical and Quantum Electronics*, 54 475 (2022).

Linear stability analysis for Optical Bistable Gyrosensor

[1,#]Shubhakanta Sahoo, [2]Aranya Bhuti Bhattacherjee and [3]Pradip Kumar Jha
[1]Department of Physics & Astrophysics, University of Delhi, New Delhi - 110007, India,
[2]Department of Physics, Birla Institute of Technology and Science, Pilani, Hyderabad Campus, Hyderabad - 500078, India,
[3]Department of Physics, DDU College, University of Delhi, New Delhi - 110078, India.
[#]*sahooshubhakant@gmail.com*

This work presents the linear stability analysis of coupled twin resonating system, mapping bistability with critical transitions using Jacobian eigenvalues. A direct topological correspondence is established between steady state bistability hysteresis and eigenvalue crossings, validating the unstable intermediate branch and demonstrating that parameter tuning governs the unstable manifold's structure.

We investigate a system consisting of two rotating coupled microresonators operating at nonlinear Kerr regime. Dynamics of this system are studied under the influence of rotation induced Sagnac frequency shift with Kerr self phase modulation, while the stability is examined through Jacobian matrix for quantum noises fluctuations around steady state mean fields as shown in Fig.1 [1-3]. This study reveals the correlation between quantum fluctuation topology and macroscopic optical bistability transitions. We identify a Jacobian Exceptional Point (EP) occurring when Jacobian eigenvalues coalesce [3]. This Jacobian EP, which is different from real EP, physically signifies the topological transition from an underdamped oscillatory regime to an overdamped nonoscillatory regime. On the other hand, the bistable transition point corresponds to the saddle node bifurcation of the nonlinear steady state response, where the Jacobian develops a zero eigenvalue [4]. We further demonstrate that the derivative of the nonlinear equation of state is directly proportional to determinant of Jacobian matrix, thereby establishing an analytical connection between the loss of local stability and the macroscopic optical switching threshold.

The subsequent eigenvalue analysis verifies that the imaginary components of the Jacobian eigenvalues describe oscillatory variations, while the real parts remain negative on the lower and higher stable branches but turn positive along the intermediate branch as shown in Fig. 2. Further evidence that detuning structurally impacts the topology of the stability landscape and the formation of optical bistability comes from three dimensional stability maps, which demonstrate that increasing cavity detuning widens the unstable manifold and bistable region [5].

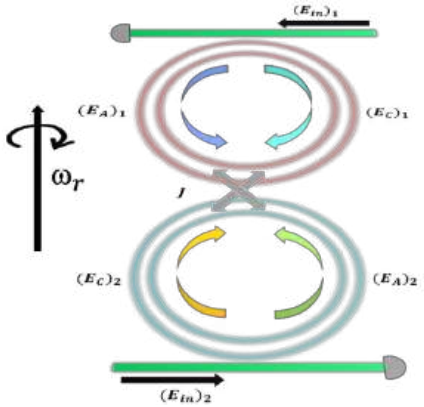


Fig. 1: Schematic diagram of nonlinear rotating twin resonating system with Kerr medium inside it and unidirectional input is supplied to it.

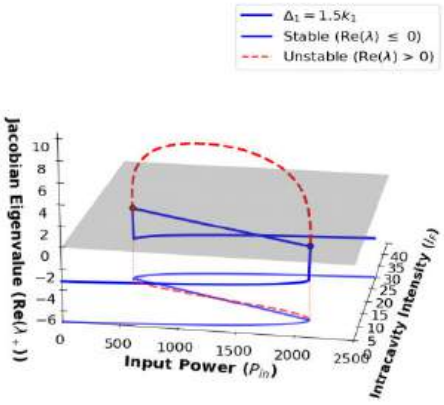


Fig. 2: Linear stability analysis of Jacobian eigenvalues showing stable and unstable regime and its projection gives optical bistability in input vs output planes.

References:

[1] Kaplan, A. E., & Meystre, P. *Optics letters*, *6*(12), 590-592.(1981).
[2] Pal, A., Ghosh, A., Zhang, S., Hill, L., Yan, H., Zhang, H., ... & Del'Haye, P. *Photonics Research*, *12*(11), 2733-2740. (2024).
[3] Cognée, K. G., Oumessoud, N., & Rahimzadeh Kalaleh Rodriguez, S. *ACS Photonics*, *13*(5), 1217-1224.(2026).
[4] Hill, L., Gohsrich, J. T., Ghosh, A., Fauman, J., Del'Haye, P., & Kunst, F. K. *arXiv preprint arXiv:2505.02691*. (2025).
[5] Uemura, T., Takata, K., & Notomi, M. *Physical Review Research*, *7*(4), 043266, (2025).

Fabrication and experimental evaluation of a 7×1 fiber optic pump combiner for high power fiber laser

[1, #]Nikita Sharma, [1,2]Avdhesh Kumar, [1]Rajpal Singh, [1,2]B. N. Upadhyaya

[1]Raja Ramanna Centre for Advanced Technology, Indore-452013
[2]Homi Bhabha National Institute, Training School Complex, Anushakti Nagar, Mumbai-400094,
[#]nikita@rrcat.gov.in

A 7×1 fiber optic pump combiner has been fabricated in-house using tapered fiber bundle technique employing seven input fibers and an output fiber. The taper geometry and splice parameters for combiner were optimized and combiner was tested up to 501W of output power with a pump combining efficiency of ~98%.

TFB-based pump combiners are widely used in high-power fiber lasers owing to their compact all-fiber architecture, low loss, and high power handling capability [1]. Xiao *et al.* demonstrated 7×1 TFB combiners with output powers up to 4.72 kW and efficiencies exceeding 95% [1], while Zhou *et al.* reported efficiencies approaching 99% with output powers up to 3.81 kW [2,3]. In this work, we report the in-house fabrication and experimental characterization of a 7×1 fiber pump combiner delivering 500 W output pump power.

For efficient power transfer, the combiner dimensions must satisfy the brightness conservation relation: $\boldsymbol{D_{out}^2 . NA_{out}^2 \geq N . D_{in}^2 . NA_{in}^2}$. Where, N is the no. of input fibers, D_{out}, D_{in} and NA_{out}, NA_{in} are the diameters and numerical apertures of the output fiber and input fibers, respectively. The 7×1 fiber pump combiner was fabricated using the tapered fiber bundle (TFB) technique employing a fluorine-doped low-index capillary. Seven input fibers of dimensions 100/125 µm (NA = 0.22) were inserted into a pre-tapered capillary (1100/800 µm to 532/538 µm) with a taper ratio of ~0.35 to a final diameter of ~390 µm. The tapered section consisted of a ~5 mm transition region and a ~10 mm straight waist to match the 400 µm cladding diameter of the 20/400 µm output double-clad fiber (NA = 0.46). Figures 1(a)–(c) show the tapered section, cross-sectional view of fiber bundle, and splice joint of the bundle with the 20/400 µm output fiber.

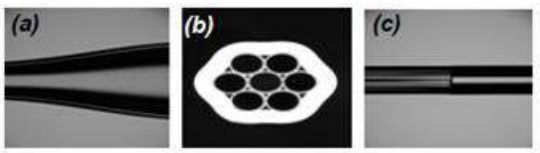


Fig. 1: *(a) Tapered section, (b) cross section, and (c) splice joint of the fabricated 7×1 pump combiner.*

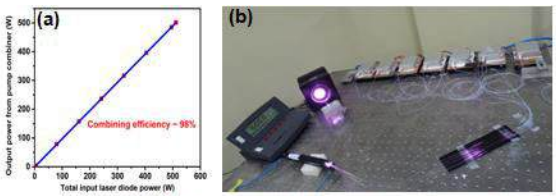


Fig. 2: *(a) Combined output power vs total input power and (b) experimental setup of the 7×1 pump combiner.*

The fabricated pump combiner delivered >500 W output power for a total input power of ~512 W from seven 976 nm fiber-coupled laser diodes, corresponding to a pump combining efficiency of ~98%. Temperature profiling showed a maximum temperature of ~38 °C at full power, with no appreciable increase during more than 1 h of continuous operation, indicating good thermal stability. Further optimization is underway to reduce losses and enable multi-kW operation.

References:

[1] Q. Xiao, Y. Wang, Z. Fan, et al., Frontiers of Optoelectronics, vol. 9, no. 2, pp. 301–306, 2016.
[2] H. Zhou, Z. Chen, X. Zhou, et al., Optics Communications, vol. 347, pp. 137–140, 2015.
[3] H. Zhou, Z. Chen, X. Zhou, et al., Applied Optics, vol. 54, no. 11, pp. 3090–3094, 2015.

Accurate estimation of gas parameters using an automated 1f wavelength modulation spectroscopy system

Della Vincent, Shruti De and Arup Lal Chakraborty
Department of Electrical Engineering, Indian Institute of Technology Gandhinagar, Gujarat, India
arup@iitgn.ac.in

Automated estimation of the mole percent and pressure of a gas using calibration-free $R_{1f}/\Delta I_1$wavelength modulation spectroscopy (WMS) is necessary for unattended real-time gas sensing applications. This paper shows how accuracy is affected by small errors in characterising the laser's modulation properties and in the time-to-frequency conversion technique used in such systems.

Tunable diode laser absorption spectroscopy (TDLAS) is widely used to accurately retrieve the mole fraction, pressure (and temperature) of gas by faithfully recovering the line shape of an isolated rotational vibrational transition. A recently developed calibration-free $R_{1f}/\Delta I_1$WMS technique [1] has proven to be effective for real-time, drone-based water vapour monitoring in which the algorithm simultaneously extracts the pressure and mole fraction within 3–5 s. In this system the measured 1f WMS signal is fitted with a model in a least squares to estimate the gas parameters. The model is generated by including the spectroscopic parameters of the gas taken from the HITRAN database [2], the amplitudes of the laser's intensity modulation (IM) and frequency modulation (FM), the phase shift (ψ_1) between the laser's IM and FM, and the variation of all these quantities across the wavelength scan range. The mole percent and the pressure are used as the free parameters. Additionally, the algiorithm requires that the acquired time-indexed data be converted to frequency-indexed values. This time-to-frequency conversion is done by constructing a frequency ruler made using a interferometer whose FSR is known accurately. Uncertainties in the variation of the peak FM deviation (Δv) across the wavelength scan range and in the value of the FSR leads to significant estimation errors.

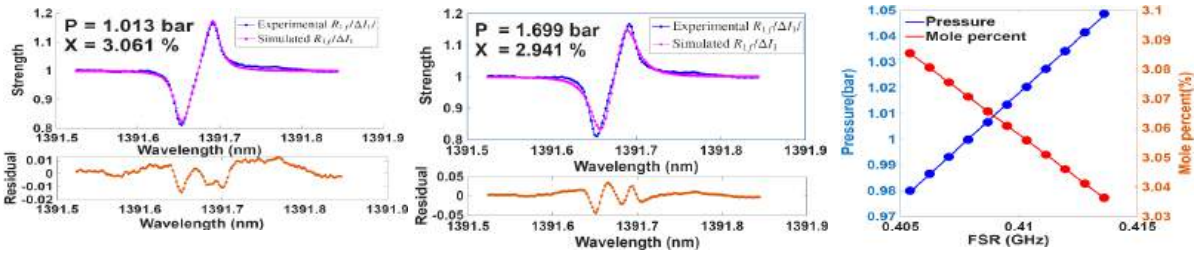


Fig. 1: (a) Experimental and simulated 1f WMS signal obtained for ambient water vapour for the correct FSR showing excellent fitting, (b) Worsening of the fit when the model did not account for the variation of Δv across the scan range, leading to large errors (c)Variation of pressure and mole percent when the FSR was changed by ±1% from its true value.

Figure (1a) shows the quantity $R_{1f}/\Delta I_1$ that is obtained experimentally and a good fit to it. In this case the correct values of the FSR (0.4095 GHz) and Δv were used. This led to accurate estimates of the ambient air pressure (1.013 bar) and the mole percent (3.061%). Notably, the value of $\Delta\nu$ for the DFB laser used in the study showed varied by 100% across the wavelength scan range. The variation of $\Delta\nu$ must be included in the model. Figure (1b) shows that when the value of Δv was not included in generating the model, the fit was poor, as is evident from the larger residuals. The estimated pressure was 1.699 bar (~68% error) and the estimated mole percent was 2.941% (~4% error). Next, the FSR was varied by ±1% keeping all other experimental and fitting parameters constant. Figure (1c) shows that when the FSR was intentionally changed from 0.4054 GHz and 0.4135 GHz (+2% change) to simulate an error, the pressure increased significantly from 0.98 bar to 1.0487 bar (+7% change), while the mole percent reduced a little from 3.0854% to 3.0364% (-1.58 % change). This shows the need to carefully characterize the system parameters to design a highly accurate trace gas sensing system for continuous and unattended measurements.

References:

[1] S. De, R. S., K. T. V. Grattan, A. L. Chakraborty, *Applied Optics* 62 (13) (2023) 3160–3168
[2] I. E. Gordon, L. S. Rothman, R. J. Hargreaves, F. M. Gomez, T. Bertin, C. Hill, *et al.*, *J. Quant. Spectrosc. Radiat. Transfer* 353, 109807 (2026)

Analysis of temperature-dependent stress in nano-fibers for coupling applications

#Pramod R. Watekar, Binshati Chatterjee, Jayeta Banerjee, Shailendra K. Varshney
National Quantum Mission, Department of Electronics and Electrical Communication Engineering, Indian Institute of Technology, Kharagpur, West Bengal, India 721302

#Corresponding author: drpramodwatekar@iitkgp.ac.in

Estimation of temperature-dependent stresses in optical nano-fibers used in quantum devices has been carried out. It is found that radial stresses in the nano-fiber gets affected by temperature change.

The Nanofibers are an ideal platform for quantum devices because their subwavelength diameters produce a strong evanescent optical field, enabling efficient interaction between single photons and quantum emitters while maintaining low-loss optical guidance [1-3]. For applications such as quantum sensors or coupling power to quantum devices, etc., applying a thin protective coating improves the nanofiber's mechanical robustness, environmental stability, and long-term reliability. A polymer coating can slightly perturb the optical mode and reduce the strength of the evanescent field, if the coating is too thick or has a relatively high refractive index. Despite this trade-off, an ultrathin low-index coating such as Teflon AF greatly improves the nanofiber's mechanical robustness, environmental stability, and long-term reliability while preserving most of its optical performance, making coated nanofibers practical for deployable quantum communication and quantum sensing systems.

The coated nanofiber exhibits temperature-dependent stress variations, which can lead to changes in propagation loss, similar to those observed in multilayer and multimaterial optical fibers [4]. An approximate opto-mechanical simulation was performed for a nanofiber with a 500 nm diameter, coated with a 20 nm-thick layer. Figure 1 shows the estimated radial and axial stress distributions corresponding to a temperature change from 60 °C to 20 °C. These stress distributions provide physical insight into the mechanism responsible for the enhanced propagation losses observed in the coated nanofiber.

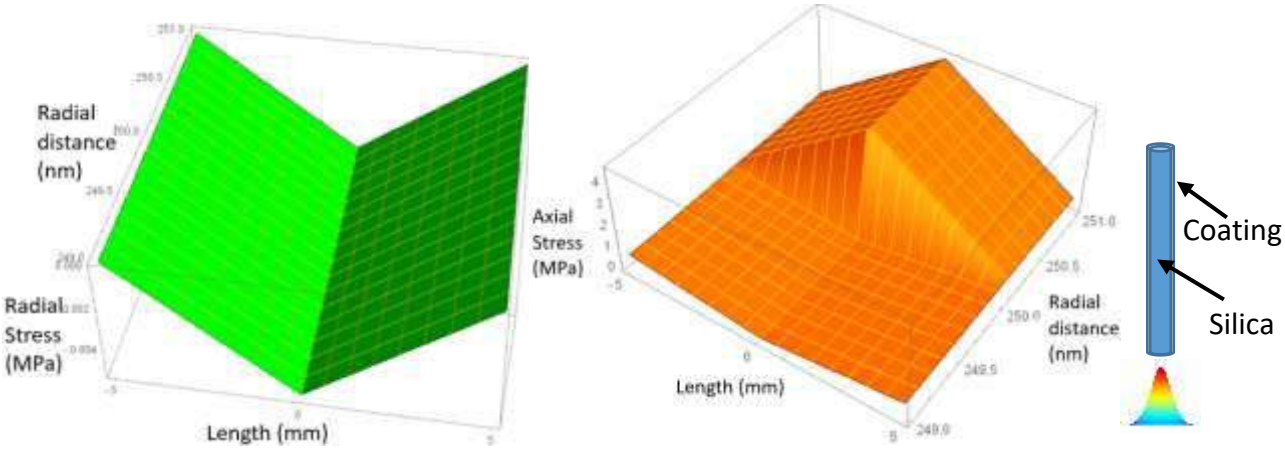


Fig.1. The schematic of stresses in coated optical nano-fibers, (Far right) Optical nano-fiber.

Further study shows that temperature-dependent stress changes occur in the Shear, Axial, Radial, and Tangential components, which will be discussed during the presentation.

Acknowledgment: The authors gratefully acknowledge the financial support received from the National Quantum Mission (NQM), Government of India, for carrying out this research.

References:

[1] S. Horikawa, S. Kato, R. Inoue, T. Aoki, A. Goban, and H. Konishi, "Low-loss telecom-band nanofiber cavity for interfacing Yb atomic qubits," Optics Letters, vol. 50, no. 17, pp. 5294–5297, Aug. 2025, doi: 10.1364/OL.570362.
[2] G. Tatel and X. Bao, "Resonant SAW–nanofiber acousto-optic coupling for high-sensitivity detection," Optics Letters, vol. 51, no. 11, pp. 3144–3147, Jun. 2026, doi: 10.1364/OL.599847.
[3] X. Zuo, Z. Tang, B. Li, X. Chen, and J. Sun, "Quantum-Empowered Fiber Sensing Metrology," Photonics, vol. 12, no. 8, Art. no. 763, Jul. 2025, doi: 10.3390/photonics12080763.
[4] S. Gaikwad, P. R. Watekar, "Stress Distribution in Metal Rods-in-cladding Electro-optic Fibers by Finite Element Analysis," Photonics India Conference, December 2014.

Machine Learning based Multi-Parameter Sensing Using SMS Fiber Structure

Neha Ahlawat,[1,*] and Saurabh Mani Tripathi,[1]

[1] *Optics and Photonics Centre, Indian Institute of Technology Delhi, New Delhi - 110016, India*

[*] *opz218645@iitd.ac.in*

Abstract: We report a compact, mode-engineered SMS fiber sensor for simultaneous refractive index and temperature sensing. Spectral features are extracted using principal component analysis (PCA) and analyzed with a regression-based artificial neural network (ANN) to decouple both parameters, demonstrating an effective machine-learning approach for simultaneous multi-parameter sensing using a limited experimental dataset.©2026 The Author(s)

1. Introduction

Simultaneous measurement of refractive index and temperature remains a significant challenge in optical fiber sensing, particularly for applications in biomedical diagnostics, chemical analysis, environmental monitoring, and industrial process control [1]. Variations in refractive index and temperature often occur simultaneously and influence the effective indices and modal interference patterns of optical fibers, leading to coupled and nonlinear spectral responses that are difficult to decouple using conventional calibration techniques.

The single-mode–multimode–single-mode (SMS) fiber configuration provides a robust platform for compact, low-cost interferometric sensors [2]. To decouple the two physical parameters, the measured spectra are processed using principal component analysis (PCA) for feature extraction, followed by a regression-based artificial neural network (ANN). This combined sensing and data-driven framework provides an effective approach for simultaneous multi-parameter sensing using a limited experimental dataset.

2. Results and Discussion

The measured transmission spectra were first normalized and analyzed using Principal Component Analysis (PCA) to extract a compact set of features that captures the dominant spectral variations.

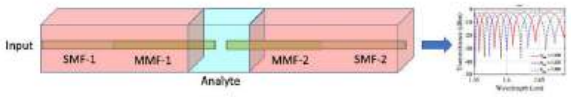


Fig. 1. Schematic diagram of the proposed SMS fiber-optic sensor comprising two single-mode fibers (SMF-1 and SMF-2) spliced to two multimode fibers (MMF-1 and MMF-2), separated by an analyte-filled gap.

3. Conclusion

The proposed framework combines PCA based dimensionality reduction and a regression based artificial neural network for effective separation of refractive index and temperature from the measured spectra. The results demonstrate the potential of the integration of machine learning with compact SMS fiber sensors for reliable multi-parameter sensing.

References

1. Yu Liu and Li Wei, "Low-cost high-sensitivity strain and temperature sensing using graded-index multimode fibers," Appl. Opt. **46**, 2516–2519 (2007)
2. Pengfei Wang, Gilberto Brambilla, Ming Ding, Yuliya Semenova, Qiang Wu, Gerald Farrell, "Investigation of single-mode–multimode–single-mode and single-mode–tapered-multimode–single-mode fiber structures and their application for refractive index sensing," J. Opt. Soc. Am. B **28**, 1180–1186 (2011)

A Gold–Titanium-Dioxide Bimetallic Bowtie Photonic-Crystal-Fiber SPR Biosensor for Wide-Range Refractive-Index Detection

Hareesh Panakkal,[1]Dr.Sajin C S

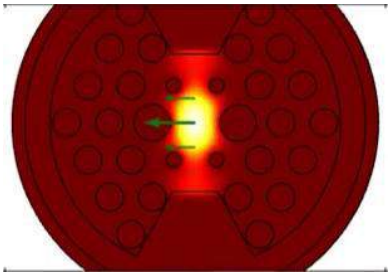
[1]Adishankara Institute of Engineering and Technology

hareeshpanakkal@gmail.com

This work presents the numerical design and performance evaluation of a bowtie photonic crystal fiber (PCF) surface plasmon resonance (SPR) biosensor incorporating a gold–titanium dioxide (Au–TiO_2) bilayer plasmonic coating. Unlike conventional SPR sensors that rely solely on a gold film, the addition of a thin TiO_2 layer improves optical field confinement near the sensing interface, enhances coupling between the guided mode and surface plasmon mode, and provides a chemically stable and biocompatible surface suitable for biomolecule attachment. These improvements contribute to higher sensing performance over a broad refractive-index range.

Surface plasmon resonance has become a powerful label-free optical sensing technique because of its exceptional sensitivity to changes in the refractive index of the surrounding medium. When a transverse magnetic (TM) polarized optical wave interacts with a metal–dielectric interface under phase-matching conditions, collective oscillations of conduction electrons generate surface plasmon polaritons (SPPs). The resonance characteristics are strongly influenced by the dielectric environment, allowing extremely small refractive-index variations to be detected through measurable wavelength shifts. Consequently, SPR technology has found widespread applications in biochemical sensing, environmental monitoring, medical diagnostics, and chemical analysis.

The proposed sensor consists of a fused-silica photonic crystal fiber with three hexagonal rings of air holes. Different air-hole diameters are employed to optimize optical confinement and regulate coupling between the guided core mode and the plasmonic interface. A comparatively larger air hole modifies the modal field distribution, whereas smaller air holes positioned adjacent to the sensing surface strengthen the evanescent field interaction. The central air hole is removed to improve light confinement within the core region. Perfectly matched layers (PMLs) are incorporated into the numerical model to eliminate unwanted boundary reflections and accurately represent an open computational domain.



The optical response of the gold coating is described using the Drude–Lorentz dispersion model

$$\varepsilon_{\{Au\}} = \varepsilon_{\{infty\}} - \frac{\{\omega_D^2\}}{\{\omega(\omega+j\gamma_D)\}} - \frac{\{\nabla\varepsilon Omega_L^2\}}{\{(\omega^2-\Omega_L^2)+j\Gamma_{L\omega}\}} \qquad (1)$$

while the refractive index of fused silica is represented by the Sellmeier equation

$$n^{2}_{(\lambda)} = 1 + \frac{\{A_1 lambda^2\}}{\{lambda^2-B_1^2\}} + \frac{\{A_2 lambda^2\}}{\{lambda^2-B_2^2\}} + \frac{\{A_3 lambda^2\}}{\{lambda^2-B_3^2\}} \qquad (2)$$

Simulation results indicate that increasing the analyte refractive index shifts the resonance wavelength toward longer wavelengths because of changes in the phase-matching condition between the guided mode and the plasmonic mode. The relationship between resonance wavelength and refractive index is expected to remain highly linear, enabling precise calibration for refractive-index sensing. Furthermore, the TiO_2 overlayer modifies the resonance characteristics by influencing sensitivity, resonance linewidth, and full-width at half-maximum (FWHM).

Although slight linewidth broadening may occur, the enhanced optical interaction can provide improved sensing performance. Future investigations will focus on alternative dielectric coatings, including graphene and transparent conducting oxides, as well as multiplexed sensing configurations for simultaneous detection of multiple analytes.

References:

[1] Md Abu Huraiya, Sankar Ganesh Ramaraj,Nanoscale Advances,Royal Society of Chemistry (2025).
[2] Jacob Wekalao, Ahmed Mehaney, Nassir Saad Alarifir,Elsvier, Physica E 172 (2025)
[3] Riadh A. Kadhim, Liming Yuan, Hao Xu, IEEE SENSORS JOURNAL(2020).

Evolution of Pure Quartic Soliton in Graded-index Multimode Fiber

[1]Akash Deep Battu and [1,2,#]Sudip Kumar Chatterjee
[1] Department of Physics, Bennett University-201310, Uttar Pradesh, India
[2] Photonics Research Centre, Bennett University-201310, Uttar Pradesh, India
[#]sudip.kumar@bennett.edu.in

In this work, we study the propagation of Pure-Quartic Solitons in a parabolic-index multimode fiber. A variational approach, combined with the Gauss-amplitude transformation, has been employed to obtain the evolution of the pulse width and quadratic chirp of the input pulse.

Pure-quartic solitons (PQSs), governed by the interplay between fourth-order dispersion (β_4) and Kerr nonlinearity, have attracted significant attention in the field of high-energy ultrashort lasers owing to their unique propagation characteristics [1,2]. However, PQSs measurements in silicon-based photonic crystal waveguides are strongly perturbed by two-photon absorption [3]. In this work, we extend the pure-quartic nonlinear Schrödinger equation to graded-index (GRIN) fibers, for the first time to the best of our knowledge, by incorporating the Periodic Nonlinearity arising from the self-imaging effect. The generalized nonlinear Schrödinger equation models the pulse evolution as shown:

$$i\frac{\partial \psi}{\partial z} - \frac{|\beta_4|}{24}\frac{\partial^4 \psi}{\partial T^4} + \frac{\gamma}{f(z)}|\psi|^2\psi = 0$$

Here, $f(z) = \cos^2\left(\frac{\pi z}{z_p}\right) + C^2\sin^2\left(\frac{\pi z}{z_p}\right)$ represents the periodic nonlinear modulation of the GRIN fiber in each self-imaging period (z_p) having a beam contraction factor $'C'$. After normalization,the above equation is, $i\frac{\partial \Psi}{\partial \xi} - \frac{1}{24}\frac{\partial^4 \Psi}{\partial t^4} + |\Psi|^2\Psi + ig(\xi)\Psi = 0$ Where $g(\xi) = \frac{L_{FOD}}{2}\frac{d(\ln \xi)}{d\xi}$. After the Gauge-amplitude transformation $\Psi(\xi, t) = m(\xi)u(\xi, t)$,[1] The governing equation is transformed into conservative form

$$i\frac{\partial u}{\partial \xi} - \frac{1}{24}\frac{\partial^4 u}{\partial t^4} + \frac{1}{f(\xi)}|u|^2 u = 0$$

Using the corresponding Lagrangian density, $\mathcal{L} = \frac{i}{2}(u^*u_z - uu_z^*) - \frac{1}{48}\left(uu_t^{*(4)} + u^*u_t^{(4)}\right) + \frac{1}{2f(\xi)}|u|^4$ and reduced lagrangian $L = \int_{-\infty}^{\infty}\mathcal{L}\,dt$ together with the Gaussian trial function $u(\xi, t) = A(\xi)\,exp\left(-\frac{t^2}{2a^2(\xi)} + iC_p(\xi)t^2\right)$, the conserved power $N = \int_{-\infty}^{\infty}|u|^2dt = \sqrt{\pi}A^2(\xi)a(\xi)$ and the averaged Lagrangian $L = \frac{N}{32a^4}\left(-16a^6\frac{dC_p}{d\xi} - \left(4a^4C_p^2 + 1\right)^2 + 8\sqrt{\frac{2}{\pi}}\frac{Na^3}{f(\xi)}\right)$ are obtained analytically. Here, a and C_p denote the temporal width and quadratic chirp of the pulse. The Euler-Lagrange equations $\frac{\partial L}{\partial q} - \frac{d}{dz}\left(\frac{\partial L}{\partial \dot{q}}\right) = 0$ $(q = a, C_p)$ yield the coupled evolution equations.

$$\frac{da}{d\xi} = \frac{c}{2a}\left(4a^4C_p^2 + 1\right) \qquad \frac{dC_p}{d\xi} = -2a^2C_p^4 - \sqrt{\frac{2}{\pi}}\frac{N}{4a^3f(\xi)} + \frac{1}{8a^6}$$

which completely describe the evolution of the pulse width and chirp in the variational framework. The derived model provides a reduced analytical framework for studying pure-quartic soliton dynamics in GRIN fibers. A comprehensive analytical explanation of the PQS in GRIN fiber and related observations will be presented at the conference.

References:

[1] C. Han, Q. Kong, M. Shen, and X. Chen, "Fast compression of pure-quartic solitons in nonlinear optical fibers via shortcuts to adiabaticity," Phys. Rev. A 113, (2026) 023511.
[2] Y. Li, J. Dai, J. Liu, Z. Weng, W. Hu, and D. Lu, "Evolution of pure-quartic solitons studied by the variational approach," Opt. Commun. 524 (2022) 128790.
[3] E. N. Tsoy and L. A. Suyunov, "Generic quartic solitons in optical media," Phys. Rev. A 109 (2024) 053528.

Relative Phase-Induced Spectral Shaping in Three Temporal Cavity Solitons for Flat Kerr Frequency Comb

[1,#]Somen Adhikary, and [1]Shailendra K. Varshney
[1]Dept. of Electronics and Electrical Communication, IIT Kharagpur, Paschim Medinipur - 721302, West Bengal, India.

[#]*E-mail:* somen@ece.iitkgp.ac.in

We propose and numerically demonstrate a three-temporal-cavity-soliton configuration as an extension of twin cavity solitons. The relative phase provides an effective control parameter for tailoring spectral interference. Compared with the in-phase case, ±π/2 phase differences markedly suppress spectral ripples, yielding flatter Kerr frequency combs for integrated nonlinear photonics.

Temporal cavity solitons (CSs) in Kerr-driven passive microresonators have emerged as fundamental building blocks for coherent Kerr frequency-comb generation owing to their remarkable stability and localised nature, which arise from a delicate balance among dispersion, Kerr nonlinearity, cavity detuning, external driving, and intrinsic loss. In this work, we extend the conventional twin temporal cavity soliton model to a phase-controlled three-soliton bound state within the framework of the normalized Lugiato–Lefever equation (LLE) [1,2]. We systematically investigate how the central soliton phase influences the spectral interference pattern and the resulting Kerr frequency-comb characteristics. The normalized LLE equation in such a system can be written as

$$\frac{\partial \psi}{\partial \tau} = -(1 + i\theta)\psi + i\frac{\partial^2 \psi}{\partial \tau^2} + i|\psi|^2\psi + \rho \quad (1)$$

Temporal cavity solitons can be controlled by the normalized cavity detuning (θ) and the normalized pump amplitude (ρ). To investigate the dynamics of the intracavity field associated with the bound state of three temporally separated cavity solitons, we consider the following initial field distribution:

$$\psi(0,t) = C + A_1 sech(t + \xi) + A_2 exp^{i\phi} sech(t) + A_3 sech(t - \xi) \quad (2)$$

Here, C represents the constant continuous-wave (CW) background, while ξ denotes the temporal separation between the interacting pulses, A_1, A_2, and A_3 represent relative amplitudes of the solitons, and ϕ represents the relative phase. For our simulations, we are using the normalized parameters as θ=1.5, ρ=1.1, C=0.1, ξ=50 and the relative amplitudes are also set to be equal [3].

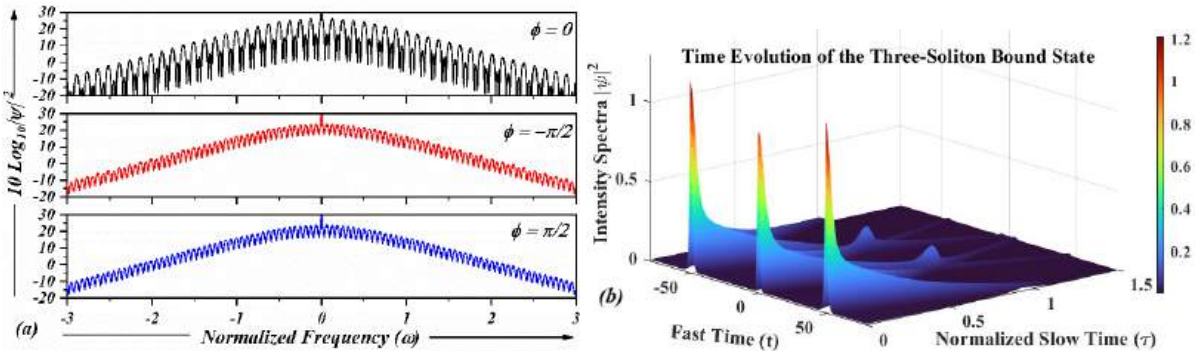


Fig. 1(a): *Spectrum generation for different relative phases of solitons,* ***(b)*** *Three soliton propagation for ϕ = -π/2.*

Compared with the in-phase configuration (ϕ=0), phase differences of ±π/2 significantly suppress spectral ripples, yielding flatter, more uniform Kerr frequency combs, which are highly desirable for integrated nonlinear photonic applications. This study demonstrates that phase-controlled three-soliton bound states provide a promising platform for tunable, high-quality Kerr frequency-comb generation in passive microresonators, offering an additional degree of freedom for precise spectral engineering.

References:

[1] Wang, Yadong, et al. "Universal mechanism for the binding of temporal cavity solitons." Optica 4.8 (2017): 855-863.
[2] Parra-Rivas, Pedro, et al. "Interaction of solitons and the formation of bound states in the generalized Lugiato-Lefever equation." The European Physical Journal D 71.7 (2017): 198.
[3] Saha, Maitrayee, et al. "Analysis of the Twin-soliton Bound States in Passive Microresonator." Frontiers in Optics. Optica Publishing Group, 2018.

Simulations on higher-order optical nonlinearities

[1,#]Milenia Basumatary and [2]Prem B Bisht
[1]Department of Physics, Indian Institute of Technology Madras, Chennai, India
[2]Centre of Excellence in Biochemical Sensing and Imaging Technologies (CenBioSIm), Indian Institute of Technology Madras, Chennai
[#]*ph24d028@smail.iitm.ac.in*

We present numerical simulations on the higher order optical nonlinearities. Simulations are based on the Z-scan formalism by incorporating third- and fifth-order nonlinear terms. The transmittance profiles how variations in various nonlinear coefficients influence the overall response of a Z-scan curve.

Nonlinear optical (NLO) materials are of significant interest for applications in photonic devices, optical switching and optical limiting. The Z-scan method is a widely used technique for determining the nonlinear absorption and nonlinear refractive properties. In this work numerical simulations are carried out to study the Z-scan transmittance profile in presence of third- and fifth-order nonlinear optical effects. The generalized transmission equation for Z-scan analysis is given as[1],

$$T_m(x,\phi_{0m}) = 1 + \frac{4mx\phi_{0m}}{(x^2+1)^m[x^2+(2m+1)^2]} + \frac{4m^2[3x^2-(4m+1)]\phi_{0m}^2}{(x^2+1)^{2m}[x^2+(2m+1)^2][x^2+(4m+1)^2]} \quad (1)$$

Here m represents the order of optical nonlinearity, $x = z/z_0$, $\phi_{0m} = kn_{2m}I^mL$ and $k = 2\pi/\lambda$ where L is the path length, I is the intensity of beam and λ is the wavelength.

Figure 1 shows the transmittance profiles simulated using equation (1). It can be seen that the transmittance profiles have different shape depending on the contributions of ϕ_1 and ϕ_2.

The simulated profiles provide a systematic framework for distinguishing the effects of third- and fifth-order nonlinearities in optical materials in the present case. The study serves as a valuable reference for interpreting experimental Z-scan data and identifying the dominant nonlinear processes[2]. The simulation approach can therefore aid in the characterization of nonlinear optical materials and improve the reliability of parameter extraction from experimental measurements. The applications of this technique in experimental data will be presented.

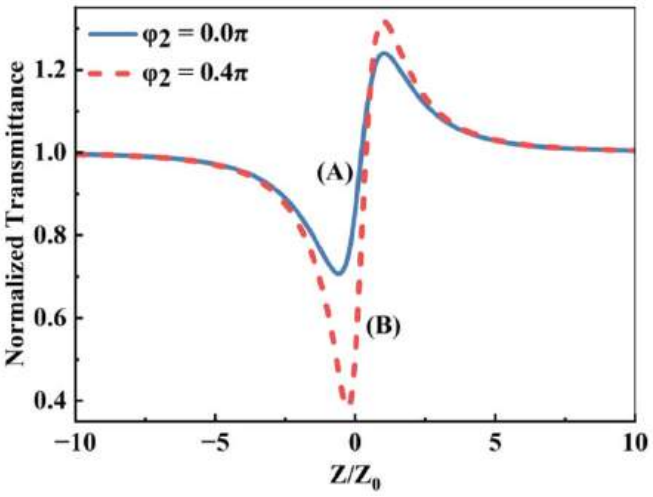


Figure 1: Simulated transmittance profile of Closed aperture (CA) Z-scan. The curve (A) has only third-order effects while (B) contains combined third- and fifth-order nonlinearities.

References:

[1] B. Gu, J. Chen, Y.-X. Fan, J. Ding, H.-T. Wang, J. Opt. Soc. Am. B **22** (12) (2005) 2651–2655.

[2] A. Bundulis, K. Leduskrasts, A. Sapne, RSC Adv. 15 (2025) 48109–48115.

Understanding ultrafast-photoinduced reaction dynamics of methyl iodide on TiO_2 (110) and TiO_2 (100) surfaces

[1,#]Aakash Gupta, [1]Keith Blackman, [1]Corine Smith and [1,2]Mihai E. Vaida
[1]*Department of Physics, University of Central Florida, Orlando, FL 32816, USA*
[2]*Renewable Energy and Chemical Transformations Cluster, University of Central Florida, Orlando, FL 32816, USA*

[#]*gp.aakash@gmail.com*

In this presentation, a technique that combines time-of-flight mass spectrometry with laser spectroscopy and fast surface preparation with molecules is employed to investigate the ultrafast photoinduced reaction of CH_3I on TiO_2(100) and TiO_2(110) surfaces. Evolution in reaction dynamics of intermediates and final products on both TiO_2 surfaces will be compared.

The detection of intermediate species during surface photoinduced reactions and the correlation of their dynamics with the surface composition is crucial to fully understand and control heterogeneous photoinduced reactions. In this study, a technique that combines time-of-flight mass spectrometry with laser spectroscopy and fast surface preparation with molecules is employed to investigate the mechanism of photoinduced reactions through the direct detection of intermediate species and final products.

The ultrafast photoinduced reaction of methyl iodide molecules on a TiO_2 surfaces is investigated under various conditions. On a freshly prepared TiO_2(110) sample, the photoinduced reaction dynamics of CH_3I follows similar trends that were observed on other metal oxide surfaces.[1-3] Specifically, the pump laser pulse at 266 nm excites the CH_3I molecule into the dissociative A-band. Subsequently, the CH_3I molecule dissociated within 110 fs and leads to the formation of CH_3 and I intermediate, which can further interact through collisions at the surface to form I_2 and reform the CH_3I parent molecule after their thermalization. The reaction intermediates and final products can be ionized via excitation through the probe laser pulse and detected with a time-of-flight mass spectrometer. Interestingly, during this whole process, a fraction of photofragments get trapped on to the active sites, resulting in passivation of TiO_2 surface.

On the TiO_2 surface that is irradiated with 266 nm laser pulses while dosing with CH_3I molecules for an extended period of time, the CH_3 fragment can react with another undissociated CH_3I to form a surface bound stable intermediate species, CH_3ICH_3. This alters the ultrafast surface dynamics, leading to another reaction pathway for the formation CH_3^+ via the dissociation of CH_3ICH_3 through an intermediate vibrational exited bound electronic state, i.e. also supported by the density functional theory calculations. The evolution dynamics of CH_3^+ and CH_3I^+ after the CH_3ICH_3 photoexcitation will be presented and compared with results obtained for CH_3I dosed on a TiO_2(100) surface. This type of experiments can provide rich physical insights into a variety of heterogeneous reactions with high technological and industrial importance, for instance catalytic reactions. This work is supported by NSF.

References:

[1] M. E. Vaida, T. M. Bernhardt, *ChemPhysChem* **2010**, *11*, 804-807.
[2] M. E. Vaida, T. M. Bernhardt, in *Ultrafast Phenomena in Molecular Sciences: Femtosecond Physics and Chemistry* (Eds.: R. de Nalda, L. Bañares), Springer International Publishing, Cham, **2014**, pp. 231-261.
[3] M. A. K. Pathan, A. Gupta, M. E. Vaida, *J. Phys. Chem. Lett.* **2022**, *13*, 9759-9765.

Generation of Second Order Meron in Nonlinear Photonic Crystal Using $\mathbf{LG_{02}}$ Beam

[1, #]Prabhakar Gupta,[2]Ritwick Das
[1]Department of Physics, Indian Institute of Technology Delhi, New Delhi 110016, India
[2]Optics and Photonics Centre, Indian Institute of Technology Delhi, New Delhi 110016, India
[#]*gupta2004prabhakar@gmail.com*

A meron is a two-dimensional topological spin texture, in which the magnetization continuously changes from an out-of-plane orientation at the core to an in-plane orientation at the boundary, resulting in a half-integer topological charge. In this work we explore the pseudo spin meronic structure in the sum-frequency generation (SFG) process with engineered nonlinear photonic crystals (NLPCs)[1-2]. By employing an LG_{02} pump beam, a propagation-dependent pseudo magnetization profile is engineered, leading to a second order meron texture at focal plane [1].

To describe the pseudo-spin dynamics in SFG, we employ the effective Pauli–Schrödinger formalism developed in Ref. [1],

$$i\frac{\partial \Psi}{\partial Z} = \left[\frac{(\mathbf{p}_T - \mathbf{A})^2}{2\bar{k}} + \boldsymbol{\sigma}\cdot\mathbf{M}\right]\Psi \qquad (1)$$

Where $\mathbf{p}_T = -i\nabla T$, $\Psi = (E_i, E_s)^T$ denotes the optical spinor, A is the synthetic vector potential, M is the effective magnetization, σ represents the Pauli matrices, $\bar{k}$ the mean wavenumber of the interacting waves. This analogy provides a unified framework to study 2-D spin dynamics in arbitrary magnetization textures using SFG. We define a radially symmetric pseudo magnetization texture as:

$$\hat{\mathbf{M}}(\rho,\phi) = \sqrt{1-m^2(\rho)}[\cos(n\phi+\eta)\,\hat{x} + \sin(n\phi+\eta)\,\hat{y}] + m(\rho)\hat{z} \qquad (2)$$

Where $m(\rho) = \Delta k(\rho)/2$ is the normalized phase mismatch, η is the phase factor, and n is the winding number. The electric field distribution of a LG_{02} at z=0 is given by:

$$E_{02}(\rho,\phi) = E_0\left(\frac{\sqrt{2}\rho}{w_0}\right)^2 \exp\left(-\frac{\rho^2}{{w_0}^2}\right)\exp(i2\phi) \qquad (3)$$

Where w_0 is beam waist and $m(\rho) = \sqrt{1-|\kappa|^2}$ .in κ ; E_p is E_{02}.

$$m(\rho) = \sqrt{1-\left(\frac{2\,d_{\text{eff}}\,\omega^2}{k\,c^2}|E_{02}|\right)^2} \qquad (4)$$

From Eq. (3), we put the value of E_{02} and take $C = \frac{2d_{\text{eff}}\omega^2}{kc^2}E_0$ then, for a meron-type configuration, the pseudo magnetization component out-of the plane must vanish at a finite radial distance. Therefore, we obtain the constrain that $C = e/2$.

$$m(\rho) = \sqrt{1-\frac{e^2\rho^4}{w_0^4}\exp\left(-\frac{2\rho^2}{w_0^2}\right)} \qquad (5)$$

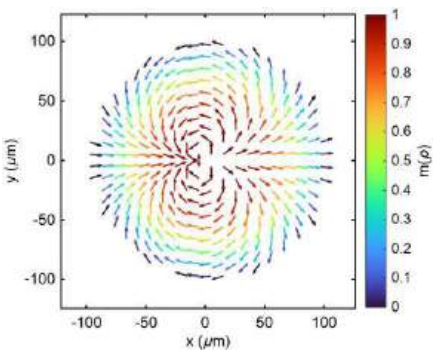


Fig: 1 Second order meron texture with topological charge $q_s = +1$ and vorticity = 2

Topological charge Q defined as

$$Q = \frac{n}{2}[m(0) - m(R)] \qquad (6)$$

Where R represents the boundary of the magnetization domain and n is winding number. Here we take $R = w_0$, and $n = 2$ for LG_{02} Beam. The topological charge becomes $Q = 1$.

References:

[1] Aviv Karnieli, Shai Tsesses, Guy Bartal, and Ady Arie. Emulating spin transport with nonlinear optics, from high-order skyrmions to the topological hall effect. Nature communications, 12(1):1092, 2021.
[2] Yijie Shen, Qiang Zhang, Peng Shi, Luping Du, Xiaocong Yuan, and Anatoly V. Zayats. Optical skyrmions and other topological quasiparticles of light, 2024.

Exceptional-Point Signatures and Geometric Phase in Anti-PT-Symmetric Difference-Frequency Generation

Atiq Iqbal[1,#], Ritwick Das[2]

[1]Department of Physics, Indian Institute of Technology Delhi, Hauz Khas, New Delhi 110016, India

[2]Optics and Photonics Centre, Indian Institute of Technology Delhi, Hauz Khas, New Delhi 110016, India

#[atiqiqbal604@gmail.com]

We investigate the intrinsic anti-PT-symmetric structure of difference-frequency generation. From an effective non-Hermitian Hamiltonian we derive the biorthogonal eigenstructure analytically and show that adiabatic pump-phase modulation imparts a geometric phase: real in the broken regime, and complex in the unbroken regime, where its real part is pinned to $-\pi$ and its imaginary part diverges at the exceptional point (EP).

Difference-frequency generation (DFG) feeds pump power into a signal and an idler inside a $\chi^{(2)}$ crystal. Grouping the signal with the conjugated idler into a single state $\Psi = (\Psi_s, \Psi_i^*)^{\mathrm{T}}$ collapses the coupled-wave equations to a two-level problem. For equal coupling ($\kappa_s = \kappa_i \equiv \kappa$), and once the phase-mismatch drift is removed, the field evolves along the crystal as

$$i\,\frac{d\Psi}{dz} = H\,\Psi, \qquad H = \begin{pmatrix} \beta/2 & -\kappa E_p \\ \kappa E_p^* & -\beta/2 \end{pmatrix}, \tag{1}$$

with β the phase mismatch and $E_p = r\,e^{i\theta}$ the pump. H is not Hermitian; instead it obeys the anti-parity-time relation $\sigma_x H^* \sigma_x = -H$, the gain-and-loss counterpart of PT symmetry.

Its eigenvalues $\lambda_\pm = \pm\alpha$, with $\alpha^2 = \beta^2/4 - \kappa^2 r^2$, are real for $\kappa r < \beta/2$ and imaginary ($\alpha = i|\alpha|$) for $\kappa r > \beta/2$; the two regimes meet at the exceptional point (EP) $\kappa r = \beta/2$. Being non-Hermitian, H carries distinct left and right eigenvectors,

$$|R_\pm\rangle = \begin{pmatrix} \dfrac{\kappa E_p}{\beta/2 \mp \alpha} \\ 1 \end{pmatrix}, \qquad \langle L_\pm| = \begin{pmatrix} \dfrac{-\kappa E_p^*}{\beta/2 \mp \alpha}, & 1 \end{pmatrix}, \tag{2}$$

and their overlap $\langle L_\pm | R_\pm \rangle = 2\alpha/(\alpha \mp \beta/2)$ vanishes at the EP ($\alpha \to 0$): there the left and right eigenvectors coalesce and the state becomes orthogonal to itself (self-orthogonality), so the modes are normalised by $z_\pm^2 = (\alpha \mp \beta/2)/2\alpha$ only away from the EP.

Cycling the pump phase through $\theta : 0 \to 2\pi$ traces a closed loop in parameter space; for a non-Hermitian system the geometric phase follows from the biorthogonal connection,

$$\gamma_n = i \oint_C \langle \tilde{L}_n |\, \partial_\theta\, |\tilde{R}_n\rangle\, d\theta. \tag{3}$$

The integrand is constant around the loop, with the complex weight $z_\pm^2$ (not $|z_\pm|^2$), so the integral collapses to a product:

$$\gamma_\pm = -\pi \left(1 \pm \frac{\beta}{2\alpha}\right), \qquad \alpha^2 = \beta^2/4 - \kappa^2 r^2. \tag{4}$$

In the broken phase ($\kappa r < \beta/2$) α is real, so $\gamma_\pm$ stays real. In the unbroken phase ($\kappa r > \beta/2$) it turns imaginary, $\alpha = i|\alpha|$ with $|\alpha| = \sqrt{\kappa^2 r^2 - \beta^2/4}$, and the geometric phase becomes complex,

$$\gamma_\pm = -\pi \pm \frac{i\pi\beta}{2|\alpha|}, \qquad \mathrm{Re}\,\gamma_\pm = -\pi, \quad \mathrm{Im}\,\gamma_\pm = \pm\frac{\pi\beta}{2|\alpha|}. \tag{5}$$

In summary, the geometric phase separates the two regimes — real below the EP, complex above it — with a real part quantised by anti-PT symmetry to $-\pi$ (mod 2π), independent of β, κ, r and θ, and an imaginary part diverging at the EP. This protected $-\pi$ establishes nonlinear frequency conversion as an accessible route to non-Hermitian topology and exceptional-point physics.

References

[1] C.M. Bender, S. Boettcher, *Phys. Rev. Lett.* **80**, 5243 (1998).
[2] R.W. Boyd, *Nonlinear Optics*, 4th ed., Academic Press (2020).
[3] M.V. Berry, *Proc. R. Soc. A* **392**, 45 (1984).
[4] J.C. Garrison, E.M. Wright, *Phys. Lett. A* **128**, 177 (1988).
[5] A. Karnieli, A. Arie, *Phys. Rev. Lett.* **120**, 053901 (2018).

Effect of pump wavelength on parametric gain in three-segment electro-optic quasi-phase-matched device for widely tunable optical parametric oscillator

Abhinav Kumar[1], Ugrasen Singh[2], Prashant Povel Dwivedi[1]*
[1]MUJ-NLO+ Research Lab, Department of Electronics and Communication Engineering, Manipal University Jaipur, Jaipur 303 007, Rajasthan India.
[2]Department of Physics, Manipal University Jaipur, Jaipur 303 007, Rajasthan India.303 007, Rajasthan India.

prashant.dwivedi@jaipur.manipal.edu

We present a theoretical investigation of three-segment electro-optic quasi-phase-matched optical parametric oscillator based on periodically poled lithium niobate. A generalized analytical gain model is derived and used to study on different pump-wavelength-dependent spectral tuning. Simulations show wide tuning bandwidth of ~315 nm for 0.94 μm, demonstrating efficient electro-optic wavelength control.

Optical parametric oscillators (OPOs) based on periodically poled lithium niobate (PPLN) are widely used for generating tunable coherent radiation across the infrared region [1-2]. Conventional quasi phase matching (QPM)-based OPOs employ uniform periodic poling, providing efficient parametric gain but limited flexibility in controlling the gain profile and phase evolution. In this work, a three-segment quasi-phase-matched (TSQ) device is analyzed for rapid and wide wavelength tuning. The structure consists of two outer periodically poled lithium niobate sections separated by a central single-domain electro-optic region as shown in Fig.1. The outer sections provide nonlinear parametric gain, while the central section acts as a phase-control region. By applying an external voltage across this segment, the refractive index changes through the electro-optic effect, modifying the relative phase between the interacting waves and controlling overall gain spectrum. The parametric gain (g) at the signal wavelength is given by

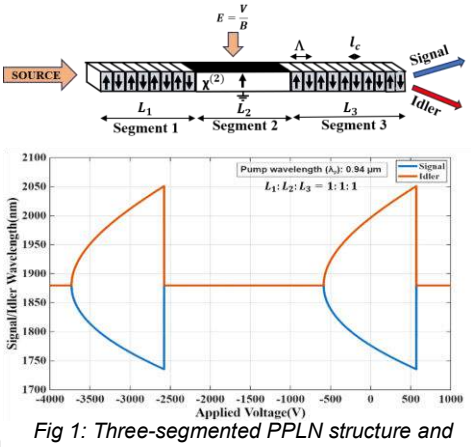


Fig 1: Three-segmented PPLN structure and signal and idler wavelengths as a function of applied voltage at pump wavelength 0.94 μm.

$$g \propto \left\{ \left(Sinc\left(\frac{\Delta k L_1}{2}\right) - Sinc\left(\frac{\Delta k L_3}{2}\right) \right)^2 + Sinc\left(\frac{\Delta k L_1}{2}\right) Sinc\left(\frac{\Delta k L_3}{2}\right) \left(Cos^2\left(\frac{\varphi}{2} - \frac{\Delta k L_2}{2} - \frac{\Delta k (L_1 + L_3)}{4}\right) \right) \right\} \quad (1)$$

Numerical simulations were carried out on a 57 mm long lithium niobate crystal using three practical pump wavelengths: 0.8044 μm, 0.94 μm, and 1.064 μm. For each pump wavelength, the applied voltage was varied while maintaining the equal-segment configuration. At a pump wavelength of 0.8044 μm [3], a tuning bandwidth of ~100 nm was observed with a voltage periodicity of ~1850 V. For a pump wavelength of 1.064 μm, the tuning bandwidth increased to ~ 207 nm with a periodicity of ~3531 V. The maximum infrared tuning bandwidth of ~315 nm was achieved at a pump wavelength of 0.94 μm over an applied voltage range of −590 to +570 V, corresponding to a voltage periodicity of ~1160 V.

These results indicate that the pump wavelength strongly influences both the achievable tuning bandwidth and the voltage required for electro-optic tuning. A periodic variation of the signal and idler wavelengths with applied voltage was observed, consistent with the underlying phase-modulation mechanism. Among the pump wavelengths investigated, 0.94 μm provided the broadest tuning range. In conclusion, the proposed TSQ OPO enables fast and wide infrared wavelength tuning without altering the grating period or operating temperature. OPO sources based on this segmented-crystal configuration may serve as highly wavelength-agile injection seeders for LiDAR systems.

Acknowledgment
The author1* wish to express his sincere thanks to the Defence Research and Development Organisation (D.R.D.O.), New Delhi, India for financial support (No. ERIP/ER/202302007/M/01/1830).

References
[1] R.W. Boyd, *Nonlinear Optics*, Academic Press, 3rd ed. (2008).
[2] M. Ebrahimzadeh, M.H. Dunn, *IEEE Journal of Quantum Electronics* 35 (1999) 784–798.
[3] P. Gross, M.E. Klein, H. Ridderbusch, D.-H. Lee, J.-P. Meyn, R. Wallenstein, K.-J. Boller Opt. Lett. 27 (2002) 1433-1435.

Topological Transition in Difference Frequency Generation

[1,#]Bindu,[2]Ritwick Das
[1,2]Optics & Photonic Centre, IIT Delhi, New Delhi 110016
[#]*opz238622@iitd.ac.in*

We study topological phase transition in second order nonlinear $\chi^{(2)}$ DFG process (non-Hermitian anti-PT symmetric). Analysis reveals $\mathbb{Z}_2$ topological phases: Topological Trivial anti-PT broken region($\Delta k > 2\Gamma$)and Topological invariant anti-PT unbroken phase($\Delta k < 2\Gamma$) with Exceptional point (EP) as transition boundary.

Nonlinear optical dynamics, including frequency-conversion processes, can be mapped onto non-Hermitian Hamiltonians. Amongst these, PT-symmetric [1],[2] and anti-PT-symmetric [3] systems exhibit exceptional point (EP) singularities, symmetry-breaking transitions, and nontrivial geometric and topological properties. The present work investigates the geometric evolution of a nonlinear optical process obeying PT-symmetry and anti-PT symmetry and shows that the dynamics could generate novel geometric phases, enabling a topological phase transition with enhanced stability, while the non-topological (geometric) phase remains useful for sensing applications.

Second order nonlinear $\chi^{(2)}$ process (SFG and DFG) with paraxial approximation can be written as Pauli-Schrodinger-type dynamical equation after rotating-wave approximation (RWA) using idler and signal spatial profile ($A_{1,2}$) modes. These coupling modes (function of $\Gamma(\boldsymbol{r}) = \frac{2\omega\, d_{eff}}{c\sqrt{n_1 n_2}}$, phase mismatch ($\Delta k$) can be mapped on Bloch space(θ, ϕ) as[4]

$$U = \Omega' \begin{pmatrix} cos\theta & isin\theta\, e^{-i\phi} \\ -isin\theta\, e^{i\phi} & -cos\theta \end{pmatrix}, \qquad tanh\, \frac{\theta}{i} = \left|\frac{2\Gamma}{\Delta k}\right|$$

Symmetry analysis of this model under PT-symmetry reveals the PT-symmetric and anti-PT symmetric phases that is divided into unbroken and broken regions. The dynamics is constrained by system variables with common transition boundary ($2\Gamma = \Delta k$) as Exceptional point(EP) is apparent in eigenspectrum.

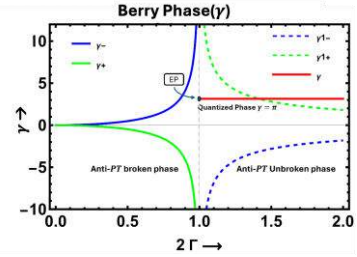


Fig. 1: Berry Phase spectrum of $\chi^{(2)}$ nonlinear process showing topological transition (Z_2) through EP ($\Delta k = 2\Gamma$)

On the other hand, geometric analysis reveals the properties like Berry curvature, Berry's connection, and Berry's phase of the parameter space. Berry phase accumulated over closed geometric path is

$$For\ |\Delta k| > 2|\Gamma| \quad \gamma\pm = \mp\pi\left(1 - \frac{1}{\sqrt{\sqrt{1-u^2}}}\right)$$

$$For\ |\Delta k| < 2|\Gamma| \quad \gamma_{\pm} = \pi\left(1 \pm \frac{i}{\sqrt{u^2-1}}\right)$$

These regions are Z_2 topological phases (Fig. 1) separated by an exceptional point (EP) as transition point. Region $|\Delta k| > 2|\Gamma|$ is topologically trivial (Z_2=0), where the Berry's phase is sensitive to geometric parameters, which makes it a potential candidate for sensing applications near EP. The region $|\Delta k| < 2|\Gamma|$ *is* topologically protected $(Z_2 = 1)$ with $\Re(\gamma\pm) = \pi$ with the imaginary component representing geometric amplification or attenuation arising from the non-Hermitian nature of the system.

References:

[1] A. A Zyablovsky, A P Vinogradov, A A Pukhov, A V Dorofeenko, and A A Lisyansky. Pt-symmetry in optics. Physics-Uspekhi, 57(11):1063, nov 2014.
[2] Carl M. Bender and Stefan Boettcher. Real spectra in non-hermitian hamiltonians having PT symmetry. Phys. Rev. Lett., 80:5243–5246, Jun 1998.
[3] Peng Peng, Wanxia Cao, Ce Shen, Weizhi Qu, Jianming Wen, Liang Jiang, and Yanhong Xiao. Anti-parity–time symmetry with flying atoms. Nature Physics, 12(12):1139–1145, December 2016.
[4] N. Westerberg, C. Maitland, D. Faccio, K. Wilson, P. ¨Ohberg, and E. M. Wright. Synthetic magnetism for photon fluids. Phys. Rev. A, 94:023805, Aug 2016

Quality Evaluation of a Laser Writing System Using Direct Microscopic Analysis

Aanaya Maheshwari[1], Ashutosh Sharma[1], Prashant Povel Dwivedi[2*]
[1]Department of Computer Applications, Manipal University Jaipur, Jaipur 303 007, Rajasthan India.
[2]MUJ-NLO[+] Research Lab, Department of Electronics and Communication Engineering, Manipal University Jaipur, Jaipur 303 007, Rajasthan India.

prashant.dwivedi@jaipur.manipal.edu

We have developed a laser writing system for the fabrication of quasi-phase-matching (QPM) devices. In this study, the domain width and grating period uniformity across the entire sample were evaluated using direct microscopic analysis to assess the fabrication accuracy and stability of the laser writing system.

A significant improvement in the development of mature QPM device fabrication has resulted in its employment in applications such as optical frequency conversion (OFC), optical dispersion compensation (ODC), optical parametric generating (OPG), and so on. The technological feature that permits nonlinear optical characteristics to be modified by varying the size, shape, and periodicity of ferroelectric domains. For example, a three-segment structure optical frequency converter based on a QPM device could operate as an electro-optic (EO) tuning method and provide a rapid wavelength selection method for the optical parametric oscillator (OPO) in the large infrared spectral region. The purpose of the work was to develop a laser writing system because the traditional fabrication process (mask technique) for QPM devices is expensive and time-consuming in most optical facilities. Getting effective feedback between the design and fabricating steps is another reason why cutting down on fabrication time is desirable. The maskless technology, which involves scanning the electrode pattern with a focused laser beam, can save time and money by eliminating the need for fabricating a photomask [1-6]. An advantage of this "laser writing" process is that it is easier and faster to modify the ferroelectric domains' structure to tailor the nonlinear optical properties. Examples of these structures include 2-D gratings, aperiodic (such as chirped gratings), tandem gratings, fan-out gratings, various gratings on the same wafer, and controlled distribution of deff and three-segment quasi-phase matching structures.

In this paper, we statistically analyzed microscopic images of the laser-written sample. Fig. 1 shows histograms of the exposed and unexposed domain widths measured along the 15 mm-long sample. For the exposed domains [Fig. 1(a)], the average domain width was 17.72 μm with a standard deviation (STD) of 0.52 μm. For the unexposed domains [Fig. 1(b)], the average domain width was 13.89 μm with a standard deviation of 1.06 μm.

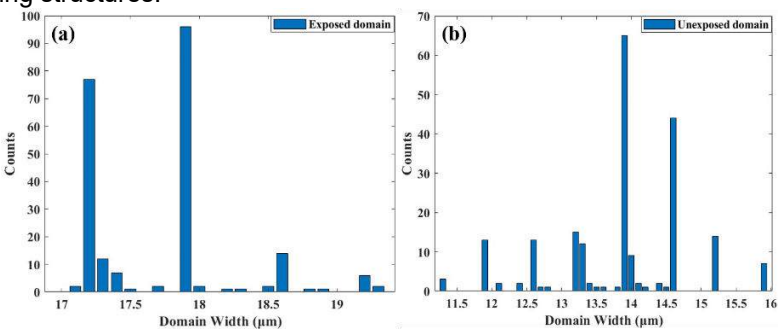


Fig.1. Histograms showing statistics of the widths of exposed (a) and (b) unexposed domains

Acknowledgment
The author[2*] wish to express his sincere thanks to the Defence Research and Development Organisation (D.R.D.O.), New Delhi, India for financial support (No. ERIP/ER/202302007/M/01/1830).

References:

[1] H. Ulrich, R. W. Wijnaendts-van-Resandt, C. Rensch, and W. Ehrensperger, “Direct writing laser lithography for production of microstructures,” Microelectron. Eng., 6, 77-84 (1987).
[2] C. Rensch, S. Hell, M. Schickfus, and S. Hunklinger, “Laser scanner for direct writing lithography,” Appl. Opt. 28, 3754-3758 (1989).
[3] H. Becker, R. Caspary, C. Toepfer, M. V. Schickfus, and S. Hunklinger, “Low-cost direct writing lithography system for the sub-micron range,” J. Mod. Opt. 44, 1715-1723 (1997).
[4] W. X. Yu, X. -C. Yuan, N. Q. Ngo, W. X. Que, W. C. Cheong, and V. Koudriachov, “Single-step fabrication of continuous surface relief micro-optical elements in hybrid sol-gel glass by laser direct writing,” Opt. Express, 10, 443-448 (2002).
[5] Y. Cheng, T. Huang, and C. C. Chieng, “Thick-film lithography using laser write,” Microsyst. Technol. 9, 17-23 (2002).
[6] P. P. Dwivedi and M. Cha, “Fabrication of periodically poled lithium noibate by direct laser-writing and its poling quality evaluation,” J. Opt. Soc. Korea 18, 762-765 (2014).

Enhanced Photothermal Nonlinearity in Dye-Doped Polymer-Stabilized Liquid Crystals for Low-Power Photonics

[1#]M. Mehkoom, [2]S. Donato, [1]D. Filippi, [1]D. S. Wiersma[2] S. Nocentini, [1,2,3]
[1]*European Laboratory for Nonlinear Spectroscopy (LENS), Via Nello Carrara, 1, 50019 Sesto Fiorentino, Italy*
[2]*National Institute of Metrological Research, Strada delle Cacce 91, Torino, Italy*
[3]*Department of Physics, University of Florence, Via Sansone 1, Sesto Fiorentino, Italy*

[#]*mehkoom.mohammad@lens.unifi.it*

Low-power nonlinear optical materials are essential for realizing compact and energy-efficient photonic devices. Here we demonstrate dye-doped polymer-stabilized liquid crystals that exhibit enhanced thermo-optic nonlinear refraction under CW excitation in pre-resonance conditions to minimize the optical losses through controlled polymer architecture, providing a versatile platform for nonlinear photonics.

The development of nonlinear optical materials capable of operating at low optical powers is fundamental to the advancement of integrated photonics, all-optical signal processing, optical switching, and adaptive beam manipulation. Among various nonlinear media, soft anisotropic materials offer exceptionally large refractive nonlinearities arising from strong light–matter interactions and thermally driven refractive index modulation [1]. Engineering their internal microstructure provides an effective route to tailor nonlinear optical performance while maintaining low operating power. In this work, we investigate the thermo-optic nonlinear response of dye-doped polymer-stabilized liquid crystals (PSLCs) under continuous-wave (CW) laser excitation. The polymer network serves not only to stabilize molecular alignment but also to regulate thermal diffusion and molecular reorientation, thereby directly influencing the nonlinear refractive response. A series of PSLC samples with tailored chemical formulations was fabricated to establish the relationship between polymer morphology, chemical and physical properties, and nonlinear optical response.

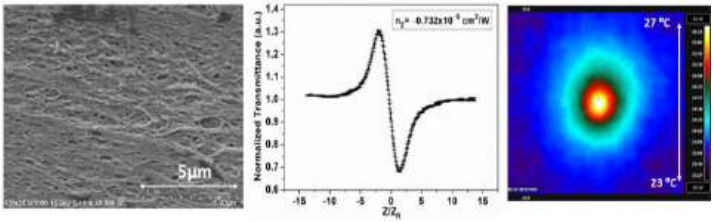


Fig. 1: SEM image (Left) representing the polymer network, Z-scan curve (Middle) demonstrating thermo-optic nonlinear refraction, and infrared thermal images (Right) illustrating laser-induced temperature distribution confirming the thermal origin of the nonlinear optical response.

The microstructure and thermal characteristics were examined using polarized optical microscopy, scanning electron microscopy (SEM) in Fig. 1, and differential scanning calorimetry, confirming uniform molecular alignment, well-defined polymer networks, and preserved liquid-crystalline phase behavior. The nonlinear refractive response was quantified using closed-aperture Z-scan measurements [2] with a low-power (5 mW) He–Ne laser (633 nm), while infrared thermal imaging was employed to visualize laser-induced temperature evolution and heat transport within the material as shown in Fig. 1, providing direct evidence of the thermo-optic processes responsible for the observed nonlinear refractive response. The PSLC samples exhibited nonlinear refractive indices (n_2) in the order of 10^{-6}–10^{-5} cm²/W (Fig. 1), together with enhanced thermo-optic performance and superior structural stability compared with the corresponding dye-doped liquid crystal (DDLC) systems reported in the literature [3].

The experimental results demonstrate that polymer stabilization enhances the thermo-optic nonlinear response under CW excitation, leading to larger refractive nonlinearity in PSLCs than in the corresponding DDLC systems. SEM confirms the morphology and formation of the polymer network, while thermal imaging and Z-scan measurements provide complementary evidence of enhanced laser-induced thermal effects and nonlinear refractive behavior. These findings establish dye-doped PSLCs as promising soft nonlinear optical materials for low-power photonic applications, including all-optical switching, tunable phase modulation, reconfigurable guided-wave photonic devices, and adaptive integrated photonic systems.

References:

1. Khoo, I. C. Nonlinear optics, *Prog. Quantum Electron.* 38, 77–117 (2014).
2. Sheik-Bahae, M., Said, A. A., Wei, T. H., Hagan, D. J. & Van Stryland, E. W., *IEEE J. Quantum Electron.* 26, 760–769 (1990).
3. Massarelli, F., Wiersma, D. S., Riboli, F. & Nocentini, S., *Liq. Cryst.* 52, 1541–1550 (2025).

Structural, Optical and Second Harmonic Generation Studies of NaCl-Doped L-Ascorbic Acid Crystals for Quantum Photonic and Nonlinear Optical Device Applications

[1,#]Dileep M.S., [2]Yashwanth H.J., Madhukara Naik M
[1,#]Centre of Excellence in Quantum Technologies, Department of Physics, R V College of Engineering, Bengaluru – 560059, India
[2]Department of Physics, Nitte Meenakshi Institute of Technology, Bengaluru – 560107, India
[3]Department of Chemistry, BMS Institute of Technology & Management, Bengaluru 560119, Karnataka, India
[#]*dileepms@rvce.edu.in*

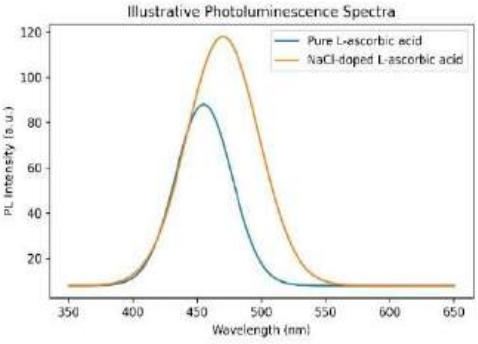
Abstract: *L-Ascorbic acid (LA) crystals (pure and 1 mol % NaCl doped) were grown by slow evaporation method. XRD confirmed monoclinic structure SEM-EDAX confirmed dopant incorporation. Doping resulted in enhanced photoluminescence and SHG efficiency with a minimal loss of thermal stability. This means that the doped crystals are promising for applications in nonlinear optical and photonic devices.*

Growth method: The pure LA and 1 mol% NaCl-doped LA solutions were prepared from LR grade reagents, stirred for 10 h and double filtered. The crystals were grown by slow evaporation in minimized rate for 28 days. The doped crystal was more transparent because there were less scattering solvent inclusions.

Structural analysis (single-crystal XRD): Both crystals were determined to be monoclinic (space group $P2_1$) by means of a Bruker Kappa APEX II diffractometer (Cu-Kα, λ = 0.71073 Å). The doping led to a small increase in the lengths of the a, b and c axes and the unit cell volume, and a slight decrease in β, which was attributed to the lattice distortion caused by the introduction of Na^+/Cl^-.[1]

Powder XRD: Powder XRD (Reich Seifert diffractometer, Cu-Kα, λ = 1.5418 Å, 5°–60°) confirmed the crystallinity of both the samples. Doping induced a slight shift in peak positions/intensities consistent with defect formation and strain, which is in accordance with single-crystal XRD results.

Compositional verification (SEM-EDAX): SEM images showed valley-like regions of dispersed microcrystals caused by growth-induced strain. The doped crystal composition was confirmed by EDAX (C: 46.70/53.99, O: 52.54/45.60, Na: 0.55/0.33, Cl: 0.21/0.08 wt%/at%) and the incorporation of Na and Cl into the lattice was confirmed.



Photoluminescence (PL): Pure LA shows a ~455 nm PL peak with a narrow linewidth (good crystallinity). Doped crystal exhibits higher intensity and red-shifted peak (~470 nm) indicating better crystal quality for optoelectronic/photonic application.[2]

Dielectric and Z-scan sections: Sections on dielectric and Z-scan describe expected trends (higher dielectric constant/loss and deeper Z-scan dips for the doped crystal from space-charge polarization and enhanced nonlinear absorption).

SHG efficiency: Kurtz-Perry powder method (1064 nm Nd:YAG laser, 1.2 mJ, 10 ns, 10 Hz) with oscilloscope output. Doped crystal showed higher SHG efficiency due to the enhanced crystallinity, which supports the use of the crystal in frequency-conversion and optical modulation devices.[3]

References:

[1] M. Ito, M. Izui, Y. Yamazaki, and M. Matsushita, *J. Physical Soc. Japan*, vol. 72, no. 6, pp. 1384–1389, 2003, doi: 10.1143/JPSJ.72.1384.
[2] S. K. Chandran, R. Paulraj, and P. Ramasamy, *Spectrochim. Acta A Mol. Biomol. Spectrosc.*, vol. 151, pp. 432–437, 2015, doi: 10.1016/j.saa.2015.06.113.
[3] L. R. Gabriya and A. Darlin Mary, *Results in Optics*, vol. 13, Dec. 2023, doi: 10.1016/j.rio.2023.100549.

Optical Limiting characteristics of Flexible MXene/PVA Nanocomposites: A Synergistic Approach

[1]Shabna S, [1]Kaviyarasan S, and [1,#]K. Mani Rahulan

[1]Nanophotonics Research Laboratory, Department of Physics and Nanotechnology, SRM Institute of Science and Technology, Kattankulathur – 603203, Tamil Nadu, India

[#]krahul.au@gmail.com

Nonlinear optics has undergone dramatic developments in the past 60 years, which has revolutionized the optoelectronic device applications with many essential applications such as electro-optic switching, optical limiting, and so forth. This study aims to investigate the third order nonlinear optical properties and optical limiting property of $Ti_3C_2T_x$ MXene using an open-aperture Z-scan technique at 532 nm pulsed laser.

This study focuses on the synthesize of pristine multilayer $Ti_3C_2T_x$ MXene using a HF-HCl-H_2O etching route, followed by the incorporation of MXene into PVA matrix through solution casting method to fabricate flexible optical limiting devices with the aim of improving the overall performance [1] The integration of MXene into PVA is expected to enhance the thermal stability of the MXene, while mitigating the vulnerability of MXene towards atmospheric conditions through the synergistic interaction of PVA with MXene through different interaction forces such as hydrogen bonding, electrostatic interactions, van der Waals interactions, and π–π stacking depending on the presence of various functional groups on the surface of both of them[2] The pristine material is comprehensively characterized using various techniques, including X-ray diffraction (XRD), SEM, UV-Visible absorption characteristics and analysed the optical limiting property of the same with 532 nm pulsed laser. Subsequently, the nanocomposite characterized using XRD to confirm the successful integration of MXene into the polymer matrix. The fabricated MXene/PVA composite with different weight percentage will be systematically investigated various morphological, linear and nonlinear optical properties under 532 nm pulsed laser excitation.[3]

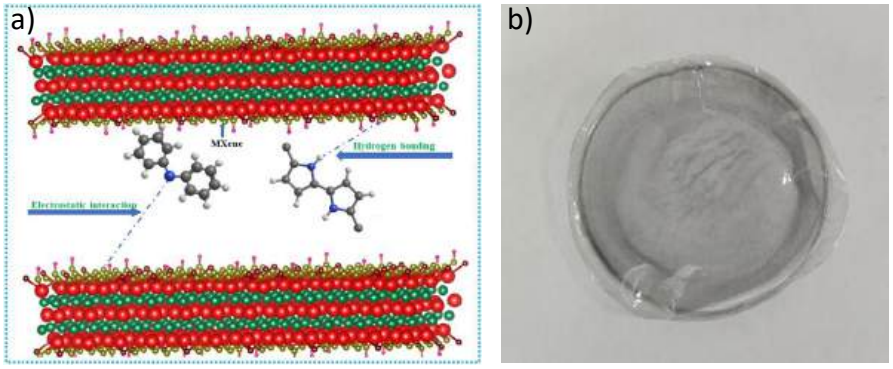


Figure 1: a) Schematic representation of synergistic interactions of polymer on MXene b) fabricated flexible MXene/PVA nanocomposite thin films

References:

[1] M. Downes, C.E. Shuck, B. McBride, J. Busa, Y. Gogotsi, Nat. Protoc. 19 (2024) 1807–1834.

[2] S. S, K. S, S. C. S, M. Saraf, M.R. K, Nanoscale 18 (2026) 12160–12200.

[3] K.M. Rahulan, S. Ganesan, P. Aruna, Appl. Surf. Sci. 258 (2012) 8439–8443.

Raman-Induced Frequency Shift Suppression of Solitons in an Engineered Oscillatory Dispersion- Waveguide

[1]Abhisek Roy, and [1,#]Partha Roy Chaudhuri
[1]Department of Physics, Indian Institute of Technology Kharagpur, India, 721302
[#]*roycp@phy.iitkgp.ac.in*

We demonstrate active control of Raman-induced frequency shift in two interacting solitons by spatially engineering the waveguide dispersion. We realize three distinct dispersion regimes: a constant anomalous dispersion, an anomalous-to-normal dispersion boundary, and complete stabilization via an oscillatory β_2 profile that creates a spectral trap.

Multiple soliton propagation in optical waveguides is accompanied by a continuous Raman-induced frequency redshift (RIFS, or intrapulse Raman scattering, a behavior inherent to the material's Raman response) and interpulse Raman scattering (the exchange of energy between two optical pulses). In contrast to conventional fibers, integrated waveguides permit longitudinal dispersion engineering to control this shift. Here, we investigate spatially varying second-order dispersion profiles. We show that an anomalous-to-normal dispersion boundary abruptly arrests the redshift, while a periodic β_2 oscillation $\beta(z) = -1 \times 10^{-26} + 1.6 \times 10^{-26} sin(2\pi z/\Lambda))$ creates a frequency trap that stabilizes the soliton against net drift. Adding β_3 facilitates blue dispersive wave emission that further compensates the Raman pull. These results position dispersion profiling as an effective strategy for spectral management, aiding stable frequency-comb generation.

The generalized nonlinear Schrödinger equation (GNLSE) is solved for a propagation length in fiber over 300 m. The input pulses are a set of two identical sech pulses having 100-fs pulse width at 1550 nm, with a time delay between them equal to 300 fs (enough for partial overlap of pulse tails). Raman scattering is included via a damped-oscillator model ($f_R = 0.18$, $\tau_1 = 12.2\,fs$, $\tau_2 = 32\,fs$). Three spatially varying waveguide dispersion profiles are tested: constant anomalous β_2, an anomalous-to-normal step, and a periodic β_2 oscillation combined with third-order dispersion β_3. Spatial dispersion engineering like this effectively controls Raman-induced frequency shifts in the two interacting solitons.

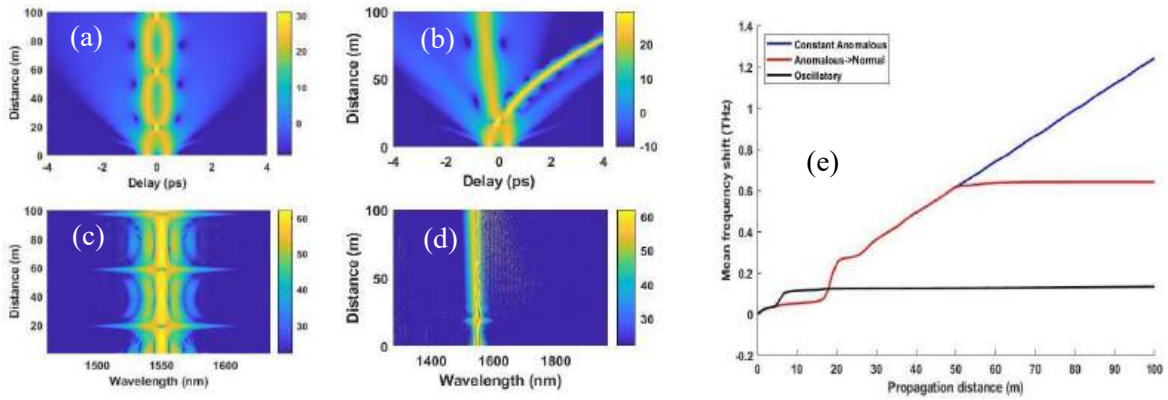


Fig. 1 Evolution of two identical and interacting solitons for (a) temporal, and (b) spectral intensity, for over 300 m of silica fiber for constant-anomalous case (in absence of Raman scattering), and (c—d) in presence of Raman scattering, (e) RIFS versus propagation distance for three dispersion profiles: constant anomalous (blue), anomalous-to-normal step (red), and oscillatory (black).

We demonstrate an anomalous-to-normal transition that halts the redshift, while a periodic β_2 profile creates frequency-trapped solitons. As evident from Fig 1. (e), complete RIFS compression is observed in the oscillatory β_3 profile. These strategies enable precise and robust soliton stabilization for integrated photonic applications.

References:

[1] Roy A. and Chaudhuri P.R., J. Appl. Phys., 135(24), (2024).
[2] Agrawal G.P., Nonlinear Fiber Optics. Academic Press, (2019).
[3] Balla P., Buch S. and Agrawal G.P., J. Opt. Soc. Am. B, 34(6), pp. 1247, (2017).

Statistical characterization of phase depth variations in quasi-phase matching device

Ashutosh Sharma[1], Aanaya Maheshwari[1], Prashant Povel Dwivedi[2]*

[1]Department of Computer Applications, Manipal University Jaipur, Jaipur 303 007, Rajasthan India.
[2]MUJ-NLO+ Research Lab, Department of Electronics and Communication Engineering, Manipal University Jaipur, Jaipur 303 007, Rajasthan India.

*prashant.dwivedi@jaipur.manipal.edu

Phase depth variation is an unavoidable feature in the fabrication of quasi-phase-matching (QPM) devcie, mainly resulting from non-uniformities and imperfections during the etching process. These variations can have a significant impact on the phase profile of QPM device and consequently affect device performance [1-2]. In this work, we investigate the phase depth of an etched QPM device and perform a statistical analysis to quantify its variation along a 10 mm-long QPM device. The measured phase depth exhibits a mean value of 29.4 nm with a standard deviation (STD) of 2.7 nm. The histogram analysis of the measured phase depth data indicates that the distribution closely follows a Gaussian profile. Any significant deviation from Gaussian behavior may introduce phase noise, potentially leading to reduced grating performance. This statistical characterization offers a reliable method for evaluating the fabrication uniformity and quality of the phase grating.

The narrow dispersion in phase depth validates the robustness and reproducibility of the poling and etching processes. Since the phase depth directly determines the phase modulation amplitude in QPM device, controlled statistical variation is essential to minimize phase noise and preserve diffraction efficiency. The demonstrated statistical conformity therefore confirms the suitability of the fabricated structures for high-quality QPM applications. QPM devices thus serve a dual role: in linear optics as phase gratings for diffraction-based characterization, and in nonlinear optics for efficient frequency conversion processes such as second-harmonic generation (SHG) and optical parametric oscillation (OPO). The presented methodology can further assist in optimizing fabrication parameters to ensure stable and reproducible performance of advanced nonlinear photonic components

We analysed the statistical evaluation of the phase depth in QPM device fabricated using electric-field poling and selective chemical etching has been presented. Surface profilometry measurements performed over a 10 mm-long grating reveal a mean phase depth of 29.4 nm with a standard deviation of 2.7 nm in Fig. 1, indicating low relative fluctuation and high fabrication uniformity. The extracted distribution closely follows Gaussian behaviour, confirming that the observed variations originate from small-scale random process effects rather than systematic fabrication errors.

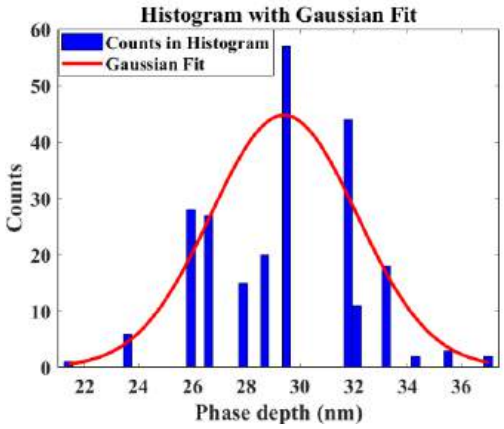


Fig.1. Histograms showing statistics of the phase depth of PPLN with corresponding Gaussian distribution.

Acknowledgment

The author[2]* wish to express his sincere thanks to the Defence Research and Development Organisation (D.R.D.O.), New Delhi, India for financial support (No. ERIP/ER/202302007/M/01/1830).

References

[1] José María Rico-García and Luis Miguel Sanchez-Brea, "Binary gratings with random heights," Appl. Opt. 48, 3062-3069 (2009).
[2] Abhinav Kumar, Ugrasen Singh, Prashant Povel Dwivedi, Ajay Mishra, Nimish Dixit, “Statistical analysis of phase depth in periodically poled lithium niobate gratings” Photonics and Nanostructures-Fundamentals and Applications, 71, 10155 (2026).

Analytical Modeling of Electro-Optically Controlled Second-Harmonic Generation in Three-Segment Quasi-Phase-Matched $LiNbO_3$ Crystals

Ugrasen Singh[1], Abhinav Kumar[2], Prashant Povel Dwivedi[2*]
[1]Department of Physics, Manipal University Jaipur, Jaipur 303 007, Rajasthan India.
[2]MUJ-NLO[+] Research Lab, Department of Electronics and Communication Engineering, Manipal University Jaipur, Jaipur 303 007, Rajasthan India.

*prashant.dwivedi@jaipur.manipal.edu

We present a generalized analytical model for electro-optically controlled second-harmonic generation (SHG) in a three-segment quasi-phase-matched $LiNbO_3$ crystal. An external applied voltage induces phase modulation in the central segment, enabling SHG control. Simulations at 1653 nm show that segment-length ratios significantly influence intensity modulation, spectral tuning, and phase-matching behavior.

Quasi-phase-matched (QPM) [1] lithium niobate is widely used for efficient nonlinear frequency conversion however, conventional wavelength tuning methods based on temperature control are relatively slow and require bulky thermal systems. In this work, a three-segment QPM $LiNbO_3$ structure is theoretically investigated, where the two outer poled segments generate second-harmonic (SH) waves [2], while the central unpoled segment acts as an electro-optic phase shifter. By applying an external electric field to the middle segment, the refractive index changes through the Pockels effect, enabling voltage-controlled modification of the SHG response without changing the crystal temperature or poling period [3].

A generalized analytical expression for SHG intensity is derived for arbitrary segment-length ratios while maintaining a fixed crystal length of 57 mm. Unlike previous studies restricted to specific geometries, the proposed model remains valid for both symmetric and asymmetric configurations. The analysis shows that the SH output is governed by coherent interference between the SH fields generated in the two nonlinear end segments, while the central segment controls their relative phase through voltage-induced modulation.

Figure a shows the three segmented Periodic Poled $LiNbO_3$ Device, while figure b shows that the SHG intensity strongly depends on both the applied phase shift and the segment-length ratio. Maximum intensity occurs at zero phase shift due to constructive interference, while increasing the phase shift reduces the SHG output. These results demonstrate that segment-length engineering provides an effective approach for optimizing electro-optically controlled SHG devices and other tunable nonlinear optical applications.

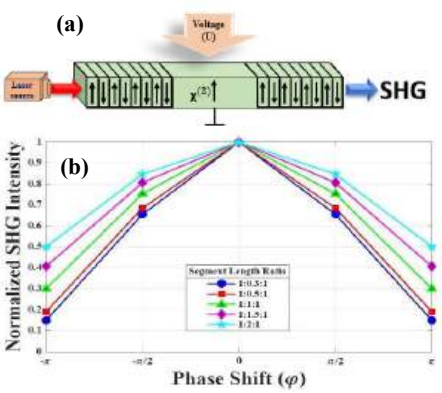


Figure 1: (a) Three segmented Periodic Poled $LiNbO_3$ Device (b) SHG intensity variation as a function of imposed phase shift for different crystal segment length ratios.

Acknowledgment
The author1* wish to express his sincere thanks to the Defence Research and Development Organisation (D.R.D.O.), New Delhi, India for financial support (No. ERIP/ER/202302007/M/01/1830).

References:

[1] Bahabad, A., Murnane, M. & Kapteyn, H. Quasi-phase-matching of momentum and energy in nonlinear optical processes. *Nature Photon* **4**, 570–575 (2010). https://doi.org/10.1038/nphoton.2010.122

[2] Duan Feng, Nai-Ben Ming, Jing-Fen Hong, Yong-Shun Yang, Jin-Song Zhu, Zhen Yang, Ye-Ning Wang; Enhancement of second-harmonic generation in $LiNbO_3$ crystals with periodic laminar ferroelectric domains. *Appl. Phys. Lett.* 1 October 1980; **37** (7): 607–609. https://doi.org/10.1063/1.92035

[3] Heiko Ridderbusch, Marvin E. Klein, Petra Gross, Dong-Hoon Lee, Jan-Peter Meyn, Richard Wallenstein, and Klaus-Jochen Boller, "Electro-optic modification of second-harmonic phase-matching spectra in segmented periodically poled $LiNbO_3$," J. *Opt. Soc. Am.* B **19**, 280-288 (2002).

Design of an Efficient JavaScript-Based Algorithmic Framework for Chirped Structure Generation in Laser-Writing Fabrication

Lapitsala Chimpad[1], Neel Tripathi[2], and Prashant Povel Dwivedi[3,*]
[1]Sirindhorn International Institute of Technology, Thammasat University, Thailand.
[2]JSS University, Noida
[3]MUJ-NLO+ Research Lab, Department of Electronics and Communication Engineering, Manipal University Jaipur, Jaipur 303 007, Rajasthan India.
[*]*prashant.dwivedi@jaipur.manipal.edu*

We have designed an efficient JavaScript-based algorithmic framework for chirped structure generation in laser-writing fabrication. Built on an affordable two-axis stepping-motor stage, it algorithmically generates chirped trajectories and compiles them into CRUX-D stage-controller commands, offering a fabrication-ready alternative to costly commercial laser direct-write lithography systems.

Chirped Quasi-Phase-Matching (CQPM) structures represent a significant advancement in nonlinear optical engineering, employing a spatially varying (chirped) grating period. Unlike conventional QPM's constant period to enable efficient phase matching over a broad wavelength range. This makes CQPM structures well suited for applications requiring wide spectral bandwidth, high conversion efficiency, and tunable optical responses, with growing importance in laser technology, optical communications, quantum photonics, spectroscopy, biomedical imaging, and integrated photonics. By compensating for wavelength-dependent phase mismatch, these devices support nonlinear interactions such as SHG, SFG, DFG, OPA, and supercontinuum generation.

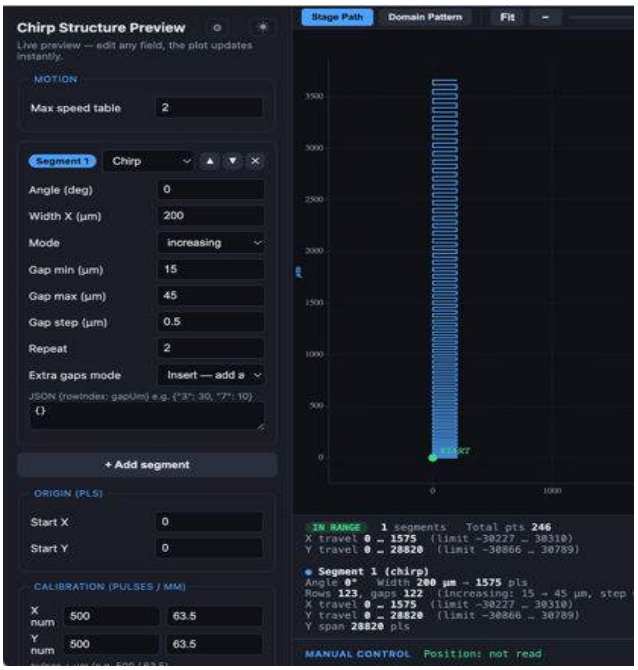


Fig. 1: Preview of the chirp structure for a gap tapering from 45 µm to 15 µm, repeated twice.

Realizing a CQPM device means translating an analytically defined chirp profile $\Lambda(z)$ into physical fabrication motion. Doing this with the manufacturer's own Chamonix Programmable software—the control software for our lab's maskless laser writing setup—requires working directly within its programmable grid environment, manually coding and computing each position and pulse value: a slow and inflexible process for the µm-scale trajectories we are targeting as in Fig. 1.

To address this, we developed Chirp Setup, a lightweight JavaScript framework (Electron desktop app) that automates the pulse calculation, converts a user-defined trajectory into a ready-to-execute list of commands for a Kohzu CRUX-D two-axis stage controller [1], and includes a preview feature so users can visualize the outcome before execution. This makes the workflow accessible even to non-technical users with no coding experience.

The core program builds N rows of width X, separated by a gap $\Lambda(i)$ chirped between GAP_MIN and GAP_MAX in steps of GAP_STEP $(Eq. 1)$, converted from μm to stage pulses and streamed to the controller in real time.

$$\Lambda(i) = GAP\_MIN + i \cdot GAP\_STEP,\ i = 0, \ldots, N-1 \quad (1)$$

In conclusion, we have developed Chirp Setup, a lightweight, preview-enabled program for automated chirped-structure generation that is accessible even to non-technical users, offering a simple, low-cost route to CQPM device fabrication.

References:

[1] Kohzu Precision Co., Ltd., CRUX-D Operation Manual, Rev. 1.0, KOSMOS series.

Nanosecond optical parametric oscillator for 2 μm and 4 μm wavelength generation

[1]Mukesh Kumar Shukla, [1]Arannya Ghosh and [1,#]Ritwick Das
[1]Optics and Photonics Centre, Indian Institute of Technology, Delhi
[#]*dasritwick@iitd.ac.in*

Optical parametric oscillators (OPO) are tunable optical sources which employ 'long' nonlinear crystals in an optimally designed optical cavity. We have designed and developed a nanosecond OPO for simultaneous generation of $2\ \mu m$ *and* $4\ \mu m$ *wavelength with a maximum power of* $1.2\ W$ *and* $0.4\ W$*, respectively.*

Wavelength-tunable mid-infrared (MIR) sources are of great importance by virtue of the atmospheric transmission window and the molecular fingerprint region. This band, in particular, is useful for military directional infrared countermeasures to jam and disable heat-seeking missiles by blinding their tracking cameras [1]. In general, high-power MIR sources are such that the generation of a particular wavelength takes place one at a time. Here, we report generation of tunable radiation in the MIR band by translating the nonlinear crystal in the OPO cavity.
In order to generate these tunable radiations we have used a nanosecond-pulsed laser operating at $1064\ nm$ *at a repetition rate of* $80\ kHz$ *with a pulse width of* $13\ ns$ *as a pump source. A combination of two half-wave plates (HWPs) sandwiching a polarizing beam splitter (PBS) is used to control both the pump power and the polarization of the incident pump beam [2]. A lens of focal length of* $f = 300\ mm$ *is used for focusing the pump beam to a waist of* $w_0 = 90\ \mu m$*. The nonlinear crystal is a 50 mm long periodically-poled Lithium Niobate (PPLN) containing multiple gratings. For* $2\ \mu m$ *and* $4\ \mu m$ *wavelength generation, we have utilized PPLN grating periods* $\Lambda = 31.59\mu m$ *and* $\Lambda = 28.67\mu m$ *at a fixed temperature of* 175^oC*. The chosen* Λ *facilitate the generation of the following wavelengths at* 175^oC *(i)* $1064(pump) \rightarrow 1450nm(signal) + 4000nm(idler)$ *and (ii)* $1064\ nm(pump) \rightarrow 2000\ nm(signal) + 2274\ nm(idler)$*. The singly resonant OPO cavity has been designed such that the signal for* $\Lambda = 31.59\mu m$ *and the idler for* $\Lambda = 28.67\mu m$ *oscillates within the cavity. In addition, the cavity is configured in a linear setting with two plane mirrors which allows transverse translation of PPLN crystal for simultaneous generation of both the wavelengths. The crystal translation could be remotely controlled which adds stability to the generation process.*

The power scaling was carried out by varying the pump power (at 80 KHz repetition rate) and the out-coupled signal and idler power at $4\ \mu m$ *and* $2\ \mu m$ *wavelength are measured (see Figs. 1(a) and (b)). The pump threshold for* $4\ \mu m$ *generation was* $\approx 2.5\ W$ *while that for* $2\ \mu m$ *generation, it was* $< 2\ W$*. We have generated a maximum of* $375\ mW$ *power at* $4\mu m$ *and* $1.2\ W$ *of power near* $2\ \mu m$ *wavelengths. In Fig. 1 (c) and (d), we have presented the measured spectral profiles of the beams which peaks at* $3.922\ \mu m$ *and* $1.954\ \mu m$ *wavelength using optical spectrum analyzer (Thorlabs OSA 205C) when the crystal temperature was* 175^oC*.*

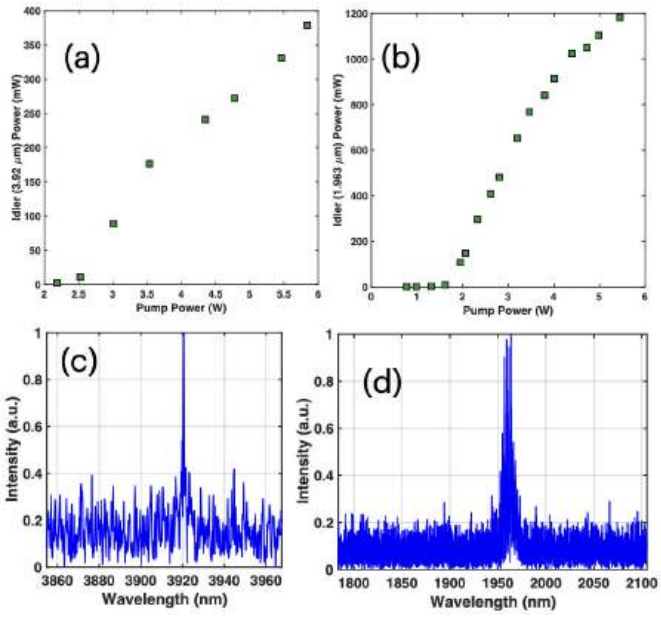


Fig. 1: Power scaling at (a) $4\mu m$ *and (b)* $2\mu m$*. The spectral profiles are given in (c) and (d) respectively.*

Acknowledgment*: The authors acknowledge the financial support received from DIA-CoE (DRDO, India) at IIT Delhi (Project no. P2QP18)*

References:

[1] I. T. Sorokina, K. L. Vodopyanov, Solid-State Mid-Infrared Laser Sources, Springer Berlin, Heidelberg (2003).
[2] M. K. Shukla, R. Das, IEEE Journal of Selected Topics in Quantum Electronics 24 (2018) 5100206.

Low-Cost Biocompatible Flexible WS_2-Based Photodetector on a Paper Substrate

[1]Arathi Babu, [1]Rahul Kumar R, [1]Vaishali Vashishtha, [2]Ranajit Mondal and [1,#]Satish Laxman Shinde

[1] Department of Physics, IIT Hyderabad, Sangareddy, India,502284

[2]Department of Chemical engineering, IIT Hyderabad, Sangareddy, India, 502284

[#]*shindesl@phy.iith.ac.in*

Advancements in technologies have parallelly leads to e-waste generation. Here, we demonstrate a solution to this challenge, by designing Tungsten disulfide (WS_2) paper-based flexible photodetector with biocompatible graphite paste as electrodes. Device exhibits high photoresponsivity with fast response and recovery times of 0.3s and 0.19s respectively under 650nm light illumination.

With the advancement in various flexible and wearable sensors that requires expensive design techniques, the generation of e-waste is one of the serious challenges. Devices fabricated on bio-degradable paper substrate provides a low-cost solution towards e-waste management [1]. Along with the substrates, the use of eco-friendly non-metallic conducting inks provides a great solution to the prevailing e-waste challenge. This work demonstrates Tungsten disulfide (WS_2) paper-based flexible photodetector with electrical contacts given by graphite paste prepared with plant-based biodegradable binder. Photodetector exhibits broadband range of photoresponsivity with fast response and recovery times of 0.3s and 0.19s respectively under 650nm light illumination. The prepared graphite paste gives moderately high conductivity of ~2400 S/m to 3200 S/m and exhibits good stability.

Device is fabricated on A4 sheet paper as substrate with WS_2 as the photo active material. The device outline is printed on the paper and WS_2 is deposited by rubbing method using cotton swab [2]. Electrodes are given using graphite-polymer nanocomposite paste, prepared by mixing graphite powder water-based organic solution. Final image of photodetector is shown in Fig. 1(a). The variation of the conductivity and resistivity with thickness of film prepared using graphite paste is represented in Fig. 1(b). The film exhibits good conductivity of ~2400 S/m to 3200 S/m. Fig. 1 (c) represents photo response of the device. Device shows moderately high photoresponsivity with nearly stable performance for over 30 days of air exposure. The magnified image of single pulse of photocurrent of the device under 650 nm light is shown in Fig. 1(d). The response time and recovery time are measured to be 0.3 s and 0.19 s respectively. This shows the good response of the device with light.

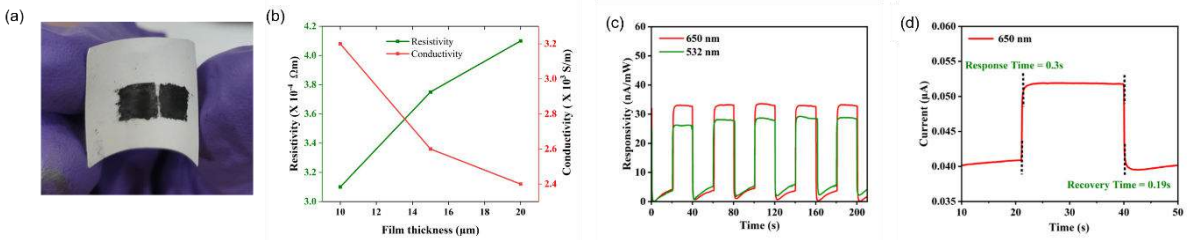


Fig. 1: (a) Picture of WS_2-based photodetector. (b)Variation of resistivity and conductivity with thickness of the film prepared using graphite ink. (c) Photoresponsivity of WS_2 photodetector under 650 nm and 532 nm light illumination at 5V external bias. (d) Magnified image of single pulse of photocurrent showing rise and decay time.

In summary, WS_2 photodetector on paper substrate was demonstrated with conductive graphite-biopolymer nanocomposite paste as electrodes. The moderately high photo response and stability of the device over days indicates the prepared paste can find applications in printed electronics that can help in e-waste management. Along with this, it can be an alternative to the prevailing expensive metallic contacts. Authors are thankful to for providing financial support from IIT Hyderabad through the project seed grant (SG-158) and DST-Inspire fellowship.

References:

[1] Pataniya, Pratik M, and C. K. Sumesh, ACS Applied Nano Materials 3, no. 7 (2020): 6935-6944.

[2] Ersu, Gulsum, Luke Doolan, Thomas Pucher, Jonathan N. Coleman, and Andres Castellanos-Gomez, Advanced Functional Materials 35, no. 44 (2025): e09505.

Lensless Fourier Holography for Dual Sample via Multiplexing

[1,#]Harsh Chatwani,[2]Arun Anand and [1]Gyanendra Sheoran
[1]Department of Applied Sciences, National Institute of Technology Delhi, Delhi, India
[2]Department of Physics, Sardar Patel University, Vallabh Vidyanagar, India

[#]harsh@nitdelhi.ac.in

We present a multiplexed lensless Fourier digital holography configuration for simultaneous recording and reconstruction of multiple Fourier holograms in a single acquisition. A transmission grating generates multiple object and reference waves, enabling spatial multiplexing. Fourier-domain reconstruction reliably separates individual object fields, enabling accurate, high-fidelity quantitative imaging of multiple samples.

Digital holography (DH) is a powerful quantitative phase-imaging technique that enables the retrieval of the full complex optical field of an object from a digitally recorded interference pattern. Lensless Fourier holography offers a simple optical configuration that eliminates the need for an imaging lens and enables direct Fourier-domain reconstruction [1]. However, the finite size and pixel pitch of image sensors fundamentally limit the amount of information that can be recorded in a single hologram. Multiplexing techniques have emerged as an effective solution to this limitation by encoding multiple object wavefronts onto the same sensor, thereby increasing the information capacity of a single acquisition [2]. Such techniques are particularly useful for comparative imaging of multiple samples under identical experimental conditions while reducing acquisition time.

In this work, an optical configuration for dual-sample multiplexed lensless Fourier holography is proposed and demonstrated. A transmission diffraction grating is used to split a collimated laser beam into three diffraction orders. The zeroth diffraction order serves as the reference wave, while the ±1st diffraction orders are employed as two independent object illumination beams. Mirrors redirect the object beams such that they interfere with the reference beam at distinct carrier frequencies on the image sensor. A 35 mm lens is inserted into the reference arm, and the object samples are positioned at the lens's front focal plane to generate Fourier holograms directly on the CMOS sensor. The recorded hologram, therefore, contains multiplexed Fourier information corresponding to both object fields within a single exposure.

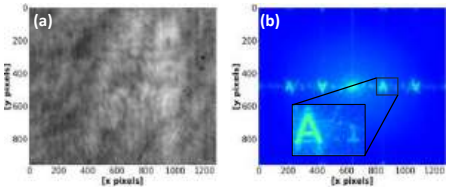


Fig 1. (a) Recorded multiplexed Fourier hologram (b) Retrieved information of distinct

The experimental results demonstrate successful simultaneous recording and reconstruction of two distinct samples from a single multiplexed Fourier hologram. The reconstructed Fourier spectra clearly exhibit spatially separated frequency components corresponding to the two object channels, confirming the effectiveness of the proposed multiplexing scheme. The technique eliminates the need for multiple sequential acquisitions while preserving reconstruction quality, thereby improving imaging efficiency and reducing computational overhead associated with repeated hologram acquisition and processing.

The proposed multiplexed lensless Fourier holography system provides a simple and robust approach for simultaneous imaging of multiple samples, as it is well-suited for comparative and differential studies that require identical illumination and environmental conditions.

References:

[1] J.W. Goodman, Introduction to Fourier Optics, 4th ed., W.H. Freeman, New York (2017).
[2] M. Kumar, L. Pensia, R. Kumar, O. Matoba, *Optics Letter* 50(6), 1909-1909 (2025).

Holographic detection of thalassemia

[1,#]Jignasha Dangar, [2]Chetna Patel, [1]Vidhi Singh, and [1]Arun Anand
[1]Optics Lab, Department of Physics, Sardar Patel University, Vallabh Vidyanagar, Gujarat
[2]V. P. & R. P. T. P. Science College, Vallabh Vidyanagar, Anand 388120, India

[#]jignashadangar@spuvvn.edu

Label-free identification of β-thalassemia minor is demonstrated using lateral shearing digital holographic microscopy combined with machine learning. Quantitative biophysical and biomechanical parameters extracted from red blood cell phase images enable accurate classification. The proposed approach provides a rapid, non-invasive, and cost-effective framework for thalassemia screening and diagnosis.

β-Thalassemia minor is one of the most prevalent inherited blood disorders and is characterized by altered red blood cell (RBC) morphology and hemoglobin content [1]. Conventional diagnostic techniques require specialized laboratory infrastructure and trained personnel. Quantitative phase imaging provides label-free measurements of cellular morphology and optical path length, enabling extraction of biophysical characteristics without staining. In this work, lateral shearing digital holographic microscopy (LSDHM) is combined with machine learning [2] for automated discrimination of healthy and β-thalassemia minor RBCs.

Figure 1 illustrates the complete workflow of the proposed label-free β-thalassemia detection framework, from hologram acquisition and phase reconstruction to feature extraction, feature selection, and machine learning-based classification. A compact LSDHM system employing a He-Ne laser (632.8 nm) was used to record off-axis holograms of individual RBCs. Numerical reconstruction yielded quantitative phase maps from which multiple biophysical and biomechanical features, including cell diameter, optical volume, surface area, mean thickness, eccentricity, and membrane fluctuation parameters, were extracted.

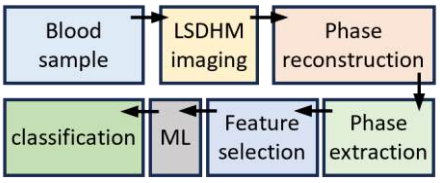


Fig. 1: Workflow of the proposed label-free β-thalassemia minor detection system using LSDHM and machine learning.

The dataset comprised RBCs collected from healthy individuals and β-thalassemia minor patients. To minimize the influence of cell-to-cell variability, feature values from ten randomly selected RBCs were grouped prior to classification. Fisher score analysis was employed to rank the extracted features according to their discriminative capability. The selected features were subsequently used to train and evaluate Logistic Regression (LR), Support Vector Machine (SVM), Decision Tree (DT), Random Forest (RF), k-Nearest Neighbour (KNN), Naïve Bayes (NB), and XGBoost classifiers. Among the evaluated models, the Random Forest classifier achieved the highest classification accuracy, demonstrating the effectiveness of combining quantitative phase imaging with machine learning for rapid, label-free detection of β-thalassemia minor. Figure 1 illustrates the overall workflow of the proposed methodology.

Quantitative phase imaging enables simultaneous measurement of multiple morphological and biomechanical properties of RBCs from a single hologram, providing richer diagnostic information than conventional intensity-based microscopy. The integration of feature selection with supervised machine learning facilitates identification of the most discriminative features while reducing data dimensionality. The proposed system is entirely label-free, requires minimal sample preparation, making it a promising approach for automated hematological screening.

References:

[1] A. Cao and R. Galanello, *Genetics in Medicine,* 12, (2010) 61.
[2] C. Patel *et al., Journal of Optical Society of America A,* 43, (2026) D1.

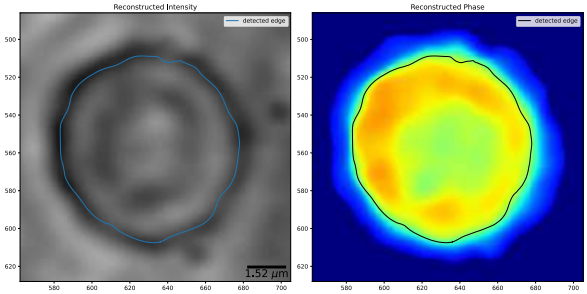
Spectral Analysis of Red Blood Cell Lateral Fluctuations: A Comparative Study

[#]Dhaval Hadiya, Jignesh Pandya and Arun Anand
Department of Physics, Sardar Patel University, Vallabh Vidyanagar

[#]*dhavalhadiya@spuvvn.edu*

We present a digital holographic microscopy study focusing on the membrane fluctuations of healthy red blood cells. Lateral membrane fluctuations were extracted directly from recovered holograms using contour tracking. These experimental fluctuations are compared with an in-house RBC simulation via spectral analysis.

Digital holographic microscopy (DHM) is a non-invasive imaging technique used to investigate the dynamic behaviors of biological specimens. In this study, we use a Lateral-Shearing DHM (LS-DHM) to analyze the lateral membrane fluctuations of healthy red blood cells (RBCs). Studying these edge fluctuations provides critical information regarding membrane elasticity [1], which is necessary for differentiating between healthy and pathological states[2].



Time series data of holograms were taken in an LS-DHM setup. The lateral fluctuations were measured from recovered images of this time series data with the help of a contour tracking algorithm from the scikit-image Python library. The temporal data of these fluctuations (edge displacements) were then transformed into a frequency spectrum for further analysis.

The red blood cell (RBC) simulation is a spring-particle based simulation that minimizes the total free energy of the RBC membrane. The viscoelasticity of RBC is modeled by dissipative particle dynamics (DPD) [2–4]. Similar to the experiments, the edge fluctuations were measured and transformed into a frequency spectrum.

$$V_{Total\ Energy} = V_{spring} + V_{Bending} + V_{Area+Volume}$$

The primary focus of this study is the comparison of experimentally measured fluctuation spectrum with those from the computer simulation. By matching the fluctuation spectrum peaks, the simulation parameters were validated[5].

In conclusion, the integration of DHM imaging, contour analysis, and in-house simulations provides a framework for studying RBC membrane dynamics. The authors acknowledge the Department of Physics, Sardar Patel University, for providing the computational and experimental facilities.

References:

[1] **H. Strey, M. Peterson, E. Sackmann, Biophys. J. 69 (1995) 478–488.**

[2] **D.A. Fedosov, B. Caswell, G.E. Karniadakis, Comput. Methods Appl. Mech. Eng. 199 (2010) 1937–1948.**

[3] **D.A. Fedosov, B. Caswell, G.E. Karniadakis, Biophys. J. 98 (2010) 2215–2225.**

[4] **Z.L. Liu, H. Li, Y. Qiang, P. Buffet, M. Dao, G.E. Karniadakis, Biophys. J. 120 (2021) 4663–4671.**

[5] **T. Yamamoto, H. Watanabe, Journal of Chemical Physics 159 (2023).**

Single-Shot Anisotropic Jones Matrix Microscopy

[1]Neha Joshi, [2]Munindra Kushwaha, [2]Rakesh Kumar Singh and [3,#]Nandan S. Bisht
[1]Applied Optics & Spectroscopy Laboratory, Department of Physics, SSJ University Campus, Almora (263601), Uttarakhand, India
[2]Laboratory of Information Photonics and Optical Metrology, Department of Physics, Indian Institute of Technology(BHU), Varanasi (221005)
[3]Department of Physics, Kumaun University Nainital (263001), Uttarakhand, India
[#]*bisht.nandan25@gmail.com*

We demonstrate a single-shot Jones matrix microscopy for quantitative extraction of anisotropic properties of complex samples. By utilizing angular multiplexing, this non-invasive and label-free method accurately retrieves the fully spatially resolved 2×2 Jones matrix from a single interferogram.

Quantitative polarization microscopy most effectively provides anisotropic variations as well as morphological and structural orientations in birefringent samples [1]. Jones matrix microscopy contains significant and most effective properties of non-invasiveness and label-freeness for extracting complex optical responses of a sample [2], and also provides valuable insights into the polarization properties of light [3].

We multiplexed orthogonal signals into distinct carrier frequencies in single interferograms by using angular splitting and applying Fourier fringe analysis for the extraction of complete Jones matrix elements. Jones matrix (J_{ij}) formalism is based on the assumption that the output field, which emerges from the object field (E_{0x}, E_{0y}) and the input field(E_{ix}, E_{iy}), is related to the following formula:

$$\begin{bmatrix} E_{0x} \\ E_{0y} \end{bmatrix} = \begin{bmatrix} J_{11} & J_{12} \\ J_{21} & J_{22} \end{bmatrix} \tag{1}$$

The interference pattern can be mathematically written as:

$$I = \left| JE_{45} + JE_{-45} + R_x + R_y \right|^2 \tag{2}$$

$JE_{\pm 45}$ and R_i represent the output field from the object arm and reference arm, respectively. We extract the Jones matrix elements of a highly characterized birefringent resolution chart and characterize the corresponding amplitude and phase of the Jones matrix elements.

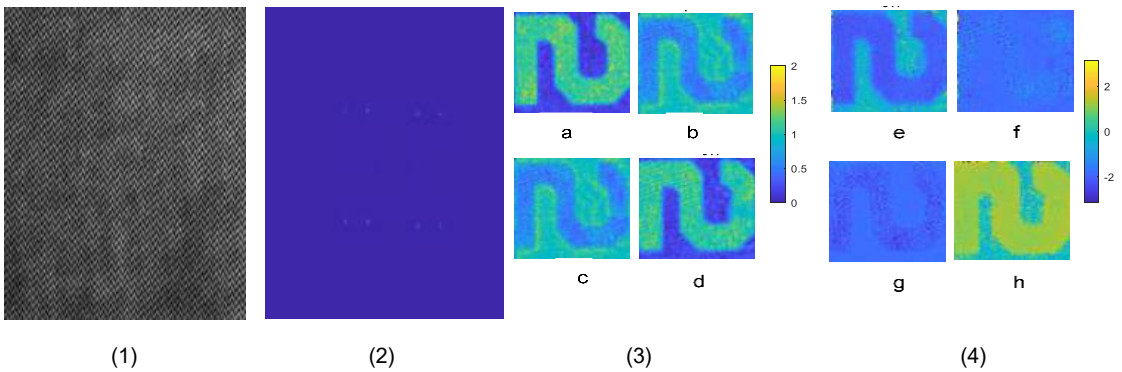


Fig.1 Recorded interferogram, Fig.2 Fourier Spectrum, Fig. 3 (a-d) Amplitude distribution of Jones matrix elements Fig.4 (e-h) Phase Distribution of Jones matrix elements

We have successfully developed and validated a robust single-shot Jones matrix microscope using spatial frequency multiplexed interferometry. This method provides a powerful framework for the real-time and non-invasive investigations of anisotropic samples.

References:

[1] M. Rathor, S. Chaubey, A. Debnath, R. Tamang, B. Koch, and R.K. Singh, J. Opt. Soc. Am. A 43(8) (2026) D10-D18
[2] S.K. Chaubey, M. Rathor, A. Debnath, R. Tamang, B.Koch, and R.K. Singh, Opto-Electronics Plus 1 (2025) 250007
[3] M. M. Sreelal, R. V. Vinu, and R. K. Singh, Optics Letters 42(24) (2017) 5194-5197

Phase Recovery from Single-shot, Undersampled Diffraction Intensity Measurement using Object Support-Constraints

[1]Ritish Kamboj, [2]Balpreet Singh Ahluwalia, and [1]Satish Kumar Dubey

[1]SeNSE – Centre for Sensors, Instrumentation and Cyber-Physical System Engineering, Indian Institute of Technology Delhi, Hauz Khas, New Delhi 110016, India[2]

Department of Physics and Technology, UiT The Arctic University of Norway, Tromsø, Norway

#satishdubey@sense.iitd.ac.in

In this work, we demonstrate that, for an object with sufficiently compact support, phase can be recovered with sub-pixel resolution from a single-shot measurement in digital lensless in-line holographic microscopy (DLIHM). This is achieved by explicitly modelling finite pixel integration effect and known object support in the forward model.

DLIHM enables compact, wide field-of-view quantitative phase imaging by numerical reconstruction of recorded Fresnel diffraction intensity [1,2]. Absence of imaging lens and optical magnification provides large field of view but limits resolution due to pixel averaging and aliasing of high spatial frequencies caused by the finite pixel size of the image sensor. Conventional pixel super-resolution (PSR) [2,3] recovers them from multiple sub-pixel-shifted or defocused measurements, but requires mechanical scanning, which adds complexity and sacrifices temporal resolution. We propose support constraint aliasing reduction pixel super-resolution (SCAR-PSR) [4] which provides phase recovery with sub-pixel resolution from a single shot undersampled measurement by modeling pixel-integration through pixel binning (B_b) in the forward model (Eq. (1)) and enforcing a tight, known object support via a binary mask (S). The propagation operator (P_z) is implemented using the angular spectrum method. Reconstruction is posed as a variational inverse problem combining data fidelity with total-variation regularization, solved with the Fast Iterative Shrinkage-Thresholding Algorithm (FISTA) [4].

$$I_z^{(b)} = B_b(|P_z(O \odot S)|^2) \quad (1)$$

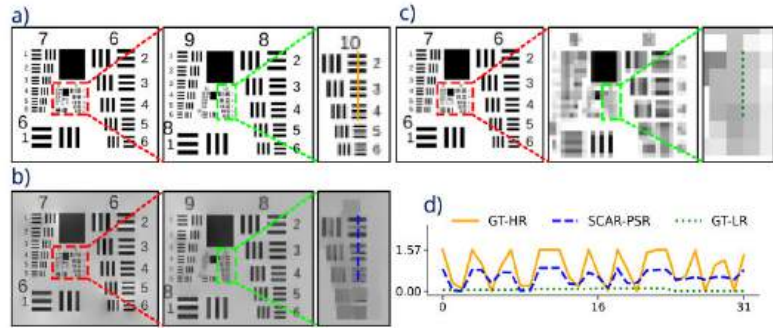


Fig. 1. USAF-1951 chart reconstruction with SCAR-PSR (8× binning, 2μm pixel, z = 0.6 mm). (a) Ground-truth chart. (b) SCAR-PSR reconstruction resolving Group 10, Element 3. (c) Pixel-limited camera image, unresolved beyond Group 8, Element 2. (d) Line profiles confirming ~5× resolution gain.

We validated SCAR-PSR using a calibrated USAF-1951 chart as a test image (1024x1192 pixels) with pixel size of 0.25μm. Reconstruction is performed using a single shot measurement at 8× pixel binning (effective pitch 2μm), z = 0.6 mm, with the object support 8× smaller than the measurement window (Fig. 1). The ground truth object image downsampled to camera resolution (2μm pixel size) shown (in Fig. 1c) fails to resolve beyond Group 8, Element 2, whereas SCAR-PSR resolves bars down to Group 10, Element 3, a half-period of ~0.4μm and a ~5× resolution gain over native sampling. Line profiles confirm clear feature separation and preserve contrast.

These simulation results establish SCAR-PSR as a deterministic and hardware-minimal technique for single-shot pixel super-resolution in DLIHM. By trading field-of-view for resolution gain through object support constraints, it offers a practical path toward high-speed, motion-free super-resolved phase imaging. Future work will aim to validate the proposed method experimentally.

References:

[1] D. Gabor, *Proc. Royal Soc. Lond. A* 197, 454–487 (1949).
[2] O. Mudanyali, D. Tseng, C. Oh, et al., *Lab Chip* 10, 1417–1428 (2010).
[3] W. Bishara, T.-W. Su, A. F. Coskun, A. Ozcan, *Opt. Express* 18, 11181–11191 (2010).
[4] R. Kamboj, B.S. Ahluwalia, S. K. Dubey, in Appl. Opt. 65, 6093-6103 (2026)

Design and fabrication of 2D Holographic Grating for Exit Pupil Expansion of Maxwellian-type AR Display

Harman Kaur[1,2], Raj Kumar[1,2.#]
[1]Holography Group, Optics & Photonics Instrumentation, CSIR-Central Scientific Instruments Organisation, Sector 30C, Chandigarh 160030, India
[2]Academy of Scientific and Innovative Research (AcSIR), Ghaziabad 201002, India
[#]*Corresponding author: raj.optics.csio@csir.res.in*

Abstract: We present a Maxwellian near-eye display configuration that resolves the typical eye-box constraints through a 2D transmission holographic grating. Operating at a recording angle of 5º, the system achieves seamless horizontal and vertical pupil replication, preventing disappearing of image during eye movements.

The architectural evolution of near-eye display (NED) platforms for immersive computing is heavily bottlenecked by architectural trade-offs between form-factor and visual ergonomics. While standard holographic or geometric waveguide displays frequently induce physiological discomfort due to the vergence-accommodation conflict (VAC), Maxwellian-view display architectures bypass the ocular lens accommodation state entirely. By forming a focal spot at the entrance pupil of the human eye, this technique delivers focus-free virtual imagery directly onto the retinal plane. Unfortunately, this pinpoint delivery establishes a highly constrained exit pupil, causing immediate visual occlusion upon sub-millimeter eye displacements or systemic shifts [1]. Existing approaches to widen the viewing window rely on bulky arrays of partial mirrors or multi-directional spatial light modulator (SLM) filtering, which inherently compromise system compactness. This work circumvents these limitations by implementing a compact waveguide display integrated with a 2D transmission holographic grating to generate a wide, two-dimensional array of viewpoints.

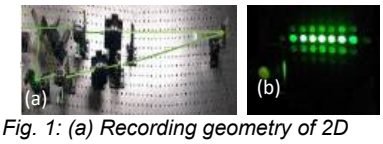


Fig. 1: (a) Recording geometry of 2D transmission grating. (b) Reconstruction of 2D transmission grating.

To transition away from high-efficiency single-order Bragg diffraction towards a distributed multi-order output, the grating must satisfy the condition

$$\rho = \frac{\lambda^2}{\Lambda^2 n \delta n}$$

For a 16µm photopolymer layer, this is enforced by lowering the inter-beam recording angle to 5º. Inside substrate, the information-bearing 532 nm light propagates via total internal reflection until striking the holographic lens which serve as the out-coupler. This holographic lens focuses the beam at a point , which is subsequently modulated by the 2D grating to yield a 3 X 3 viewing matrix. The fabrication of 2D grating pattern utilizes a two exposure peristrophic multiplexing technique in transmission configuration [2]. The recording geometry is depicted in Fig. 1(a) and the optical reconstruction of the 2D grating is depicted in 1(b).

Experimentally, a spatial light modulator (SLM) was used to feed digital imagery ("CSIR") into the proposed waveguide display. The display setup for the holographic waveguide system is shown in Fig. 2(a) and the Fig. 2(b) represents the digital information reconstructed by the SLM, which will be superimposed on real scene through waveguide display.



Fig.2: (a)Set-up for displaying proposed Maxwellian-based waveguide. (b) Photograph of image reconstructed by the SLM.

References:

[1] T. Lin, T. Zhan, J. Zou, F. Fan, S.T. Wu, Opt. Express 28 (2020) 38616.
[2] R. Kaur, R. Kumar, Proc. SPIE 13041 (2024) 1304108.

Interferometric Refractometry of Water Under Temperature Variation

[1, 2, #]Kuldeep Kumar, [1,2]Surya Kumar Gautam, [1,2]Vikas, [1,2]Kamal Tewari, [1,2]Mukesh Kumar, [1,2]Mayank Mathur, [1,2]Manoj Das, [1,2]Mukesh Jewariya
[1]CSIR-National Physical Laboratory (CSIR-NPL), New Delhi, Delhi 110012, India.
[2]Academy of Scientific and Innovative Research (AcSIR), Ghaziabad, 201002, India.

[#]*Corresponding author: Kuldeep20051995@gmail.com*

We present an environmentally stable interferometric approach to measure the temperature-dependent refractive index of water. Unlike conventional setups, this configuration inherently suppresses vibration-induced phase noise to ensure stable and highly accurate measurements. Using a helium-neon laser (wavelength = 632.8 nm), we successfully recorded highly repeatable phase differences across a temperature range of 44 °C to 50 °C. This robust technique offers high precision for liquid refractometry and thermally dependent optical sensing applications.

We present an environmentally stable approach for the interferometric refractometry of water under temperature variation. In contrast to conventional interferometers, which are highly susceptible to environmental perturbations, our setup inherently suppresses vibration-induced phase noise, enabling highly stable and accurate measurements [1,2]. Using a helium-neon laser (λ = 632.8 nm) as the coherent light source, we record the phase difference across a temperature range of 44 °C to 50 °C, acquiring seven distinct data points as shown in Table 1. We evaluated measurement repeatability across multiple trials to ensure experimental reliability, observing a highly consistent and reproducible trend in the temperature-dependent phase difference. From these data, the precise change in the refractive index of water can be determined if the thickness of the sample is known. The results, as shown in Figure 1, highlight the effectiveness of the proposed technique for high-precision optical sensing and the characterization of thermally dependent optical properties in liquid samples [1-3].

Table 1: Experimental Data	
Temperature	Phase Difference
50	0
49	0.2322
48	0.4826
47	0.8325
46	1.2907
45	1.8294
44	2.2698

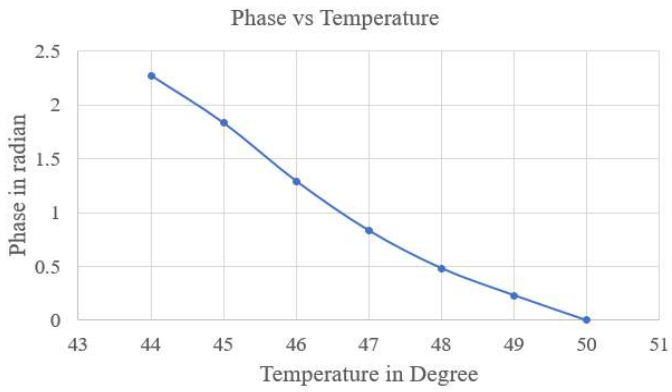


Figure 1: Phase vs Temperature

References:

[1] Yanan, Z., Qihang, G., Xiaodong, H., Junsheng, L., Changqing, L., Xiaopan, F., ... & Jianbo, L. (2025). Measurement, 248, 116822.
[2] An, X., Guo, T., & Wan, Y. (2026). Measurement, 269, 120837.
[3] Zhuang, F., Wang, J., Zhang, B., Yin, B., & Wang, S. (2026). *IEEE Transactions on Instrumentation & Measurement*.]

Design and Fabrication of Holographic Trichroic Combiner

Neeru Sharma[1,2], Raj Kumar[1,2]*

[1]Holography Group, Optics & Photonics Instrumentation, CSIR-Central Scientific Instruments Organisation (CSIR-CSIO), Sector 30-C, Chandigarh 160030, India

[2]Academy of Scientific and Innovative Research (AcSIR), Ghaziabad 201002, India

raj.optics.csio@csir.res.in

We propose a trichroic holographic combiner that combines 488 nm, 532 nm, and 660 nm laser beams using a stacked-grating configuration. In which the 532 nm grating was recorded first, then the 660 nm grating was recorded and stacked directly over it. Collinear output is achieved through an independent slant-angle design for each grating, with all beams having a diameter of 5 mm. The co-linear output is experimentally confirmed by projecting the combined beam onto a 25cm long white screen, where the three wavelengths overlap into a single mixed-colour spot.

Combining multiple laser wavelengths into a single collinear output beam is a critical requirement for compact photonic systems in holographic displays, multi-wavelength spectroscopy, augmented reality (AR) displays and bio-sensing. Conventional beam-combining approaches using dichroic mirrors introduce mechanical complexity. Volume holographic gratings (VHGs) recorded in photopolymer film offer a fundamentally different approach, in which wavelength- and angle-selective diffraction enables multiple beams at distinct wavelengths to be directed along a common output axis. This paper presents a trichroic holographic beam combiner for the collinear combination of 488 nm, 532 nm, and 660 nm laser beams, based on a stacked volume holographic grating design. To generate a single output beam, the stacked grating design is used, with a 532 nm grating as the first layer and a 660 nm grating as the second layer.

In a VHG, a plane wave is efficiently diffracted only when it satisfies the Bragg match condition. For collinear output from all three sub-gratings, all diffracted beams must emerge in the same direction. This is achieved by designing a different slant angle φ for each sub-grating. All three laser beams have a diameter of 5 mm. The 488 nm beam enters at 0° (normal incidence), diffracts from a symmetric grating. The 660 nm beam is incident at an angle of 30.5° and diffracts from a grating inclined at φ = 9.89°. The 532 nm beam is incident at an angle of 24.15° and diffracts from a grating tilted at φ = 7.87°. The laser source positions are fixed at 125 mm from the recording plane, with lateral distances of 73.6 mm (660 nm) and 55.6 mm (532 nm) from the normal. Recording beam powers for the stacked gratings were 1.21 mW (beam 1) and 1.15 mW (beam 2) for the 532 nm grating, and 1.32 mW (beam 1) and 1.25 mW (beam 2) for the 660 nm grating, with exposure times of 6 s (532 nm) and 4 s (660 nm), respectively. VHGs are fabricated in a transmission geometry; the grating period is calculated by Eq. (1), where

$$\Lambda = \lambda / [2n \sin((\theta_{2m} - \theta_{1m}) / 2)] \quad \ldots(1)$$

The gratings are designed with the same grating period and different slant angles to achieve wavelength-selective diffraction. The designed trichroic combiner is thinner than a conventional dichroic mirror, because each grating layer is limited by the film thickness (16 µm). Collinear output was verified by projecting the diffracted beams onto a white screen at a grazing angle, alongside a 25 cm ruler positioned at a distance of 10 cm from the recorded trichroic combiner, as shown in Fig. 1(c). The red, green, and blue beams overlap into a single mixed-colour, co-linear spot, confirming all three wavelengths emerge along a common axis. The green and red gratings, recorded with different beam powers and exposure times, show diffraction efficiencies of 55.4% (532 nm) and 61.9% (660 nm), respectively

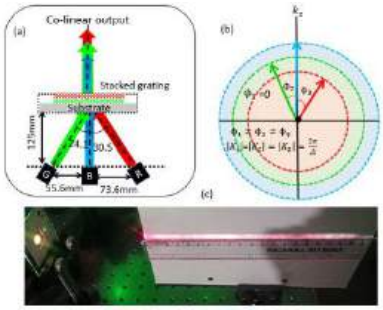


Fig. 1: (a) Recording geometry of a stacked holographic grating (b) Corresponding k-vector diagram. (c) A white screen placed at a grazing angle, with a 20 cm ruler at a distance of 10 cm from the recorded trichroic combiner.

This paper experimentally demonstrates a compact trichroic holographic combiner using a stacked-grating configuration. It offers an ultra-compact solution for multi-wavelength beam combining with direct relevance to RGB laser sources, holographic display engines, AR displays and multi-colour confocal systems.

References:

[1] H. Kogelnik, *Bell Syst. Tech. J.* 48 (1969) 2909.

[2] Z. Wang, J. Schwanke, D. Theobald, A. Herkommer, U. Lemmer, *Optical Sensors, SPIE* 13527 (2025).

Shape Identification Technique Based on Speckle Correlation and Phase Measuring Deflectometry

[1,#]Rahul Sharma,[1]Vidhi Singh and [1]Arun Anand

[1]Department of Physics, Sardar Patel University, Vallabh Vidyanagar, India

[#]*rahulsharma@spuvvn.edu*

Phase Measuring Deflectometry (PMD) combined with correlation-based image processing enables non-contact measurement of shape, optical thickness, and refractive index variations. Modulated fringe patterns are analyzed using Fourier phase retrieval and cross-correlation to reconstruct three-dimensional profiles with high sensitivity, providing a robust approach for optical metrology and industrial inspection.

Phase Measuring Deflectometry (PMD) is a non-contact optical technique used to measure the shape, slope, and optical thickness of transparent and reflective objects by analyzing modulation in projected sinusoidal fringe patterns [1]. In the proposed system, sinusoidal fringes are projected through the test object, and a digital camera captures the modulated fringe images. Fourier-based phase retrieval is then employed to extract the phase distribution, which is converted into gradient phase information and numerically integrated to reconstruct the three-dimensional surface profile.

As a complementary approach, a correlation-based image processing method is used for displacement-based gradient estimation and robust distortion detection using arbitrary patterns, including random, speckle, and fringe patterns. The method estimates local displacements through cross-correlation analysis and reconstructs the object shape from the resulting gradient phase information [2]. It does not require phase unwrapping, operates with both sinusoidal and non-sinusoidal patterns, and provides a robust implementation for optical shape measurement.

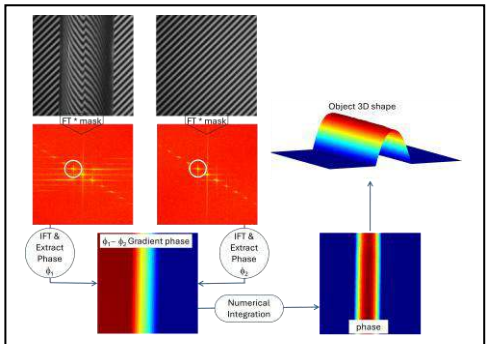


Fig 1. Fourier-Based Phase Extraction and 3D Surface Reconstruction in PMD

Overall, the combined PMD and correlation-based approach provides a robust methodology for non-contact shape measurement and optical characterization. With potential applications in laser heating and welding, thermal mapping, heat-flow visualisation, refractive-index and concentration mapping, optical-thickness reconstruction, and hybrid photothermal–PMD systems.

REFERENCES:

1. Anand, A., Chhaniwal, V. K., Almoro, P., Pedrini, G. and Osten, W. *Opt. Lett.* 34(10), 1522 (2009).
2. Trivedi, V., Joglekar, M., Mahajan, S., Chhaniwal, V., Javidi, B. and Anand, A., *Opt. Eng.* (2019).
3. Scott, W. R., Roth, G. and Rivest, J. F., *ACM Comput. Surv.* (2003).
4. Wu, Z., Guo, W., Li, Y., Liu, Y. and Zhang, Q., *Photonics Res.* (2020).
5. Wallace, A., Csakany, P., Buller, G. and Walker, A., *British Machine Vision Association* (2000).

Label-Free Classification of Morphologically Similar Yeast Strains Using Digital Holographic Microscopy and Machine Learning

[1,#]Vidhi Singh, [2]Sohan Sadhukhan, [1]Rahul Sharma, [1]Arun Anand

[1]Optics Lab, Department of Physics, Sardar Patel University, Vallabh Vidyanagar 388120, Gujarat, India
[2]Ramakrishna Mission Vivekananda Centenary College, Rahara, Kolkata 700118, India

Corresponding author: vidhisingh@spuvvn.edu

Digital Holographic Microscopy (DHM) enables label-free quantitative phase imaging of transparent biological cells. This work classifies morphologically similar Saccharomyces *yeast strains (KT-D22 and ID) using Mach-Zehnder DHM and machine learning. Phase-based features achieved approximately 90% classification accuracy, demonstrating potential for automated microbial identification.*

Digital Holographic Microscopy (DHM) is a label-free quantitative phase imaging technique that enables non-invasive characterization of transparent biological specimens by measuring their optical thickness and morphology without staining or fluorescent labeling. Unlike conventional brightfield microscopy, DHM reconstructs both the amplitude and phase of the optical field, providing quantitative information related to cellular morphology and intracellular structure [1]. In this study, a transmission-mode Mach-Zehnder DHM was used in inverted mode to differentiate two morphologically similar Saccharomyces yeast strains, KT-D22 and ID, which cannot be reliably distinguished using brightfield microscopy.

Off-axis digital holograms were recorded using a He–Ne laser (632.8 nm), and quantitative phase maps were reconstructed using the angular spectrum method after background phase subtraction. Individual yeast cells were automatically segmented using thresholding and binary masking, followed by extraction of phase-derived morphological features, including optical thickness, projected area, volume, eccentricity, skewness, and histogram-based descriptors. Fisher score analysis was used to identify the most discriminative features, and the selected features were employed to train several classical machine learning algorithms [2].

Logistic Regression achieved the highest classification accuracy of approximately 90%, demonstrating that quantitative phase imaging combined with machine learning provides a rapid, reliable, and label-free approach for automated yeast strain identification with potential applications in microbial diagnostics and biomedical research [3].

The author would like to acknowledge research funding from ANRF, CII, and ASKY instruments through the Prime Minister’s Fellowship for Doctoral Research.

References:

[1] Anand, A., Chhaniwal, V. K., & Javidi, B. Tutorial: Common path self-referencing digital holographic microscopy. *APL Photonics* 3 (2018) 071101.
[2] Kuhn, M., & Johnson, K. *Feature Engineering and Selection: A Practical Approach for Predictive Models*. Chapman and Hall/CRC, Boca Raton (2019).
[3] Sharma, R., Chatwani, H., Singh, V., Chhaniwal, V. K., Sheoran, G., Javidi, B., & Anand, A. Three-dimensional optical imaging for label-free sensing and classification of microorganisms and microparticles in fluidic environments: A review. *Optics Express* 34 (14) (2026) 25480–25507.

Phase Shifting of the Spatial Coherence Function Using Rotating Amplitude Sinusoidal Radial Grating

Haneen V N and Dinesh N Naik

Applied and Adaptive Optics Laboratory, Department of Physics,
Indian Institute of Space Science and Technology, Thiruvananthapuram, Kerala, 695547.

haneenvn.22@res.iist.ac.in

We propose a novel method of source-based phase shifting in the far-field spatial coherence function using the rotation of sinusoidal radial gratings under spatially incoherent illumination. Asymmetric illumination of the grating enables phase modulation while maintaining constant coherence magnitude, demonstrating a promising approach for phase shifting in rotational and radial shearing interferometers.

Spatial coherence engineering is an effective approach for manipulating optical fields for imaging, interferometry, and metrology. Recently, controlled phase shifting of the far-field spatial coherence function was demonstrated using a translating diffraction grating placed at the source plane [1]. The present work extends this concept to rotating radial gratings, motivated by their unique diffraction properties and rotational symmetry. Sinusoidal radial gratings generate characteristic petal-like diffraction patterns under coherent Gaussian beam illumination over propagation [2]. Moreover, the rotation of such gratings has been shown to produce Doppler frequency shifts in different diffraction orders [3]. However, such investigations in the incoherent regime remain unexplored.

A sinusoidal radial amplitude grating is simulated using the following equation

$$t(\theta) = \frac{1}{2}[1 + \cos(m\theta)]$$

Where, m is the number of spokes structures in the grating. A spatially incoherent source is simulated to pass through the radial grating, and the far-field spatial coherence function is obtained by correlating the radially sheared copies of the far-field.

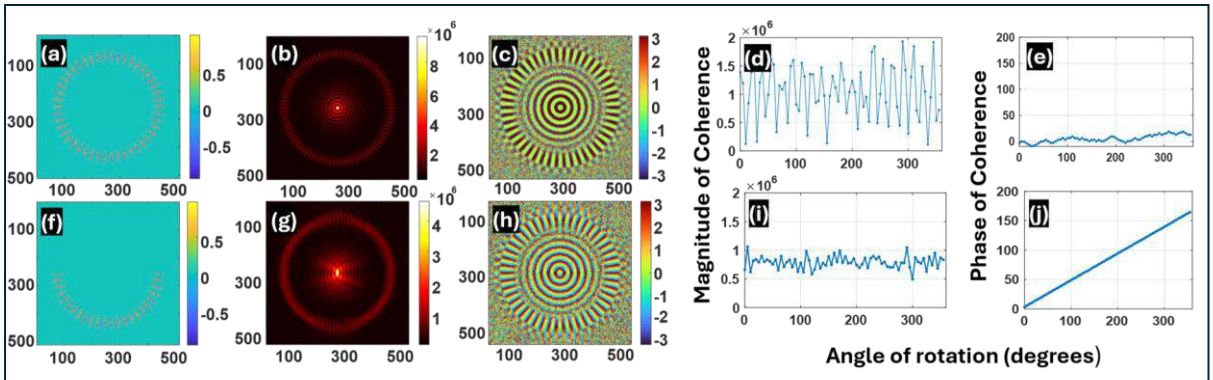


Fig. 1. Simulation results showing the effect of rotating a sinusoidal radial grating under symmetric (top row) and asymmetric (bottom row) illumination. (a), (f) Real part of the field after grating. (b), (g) Magnitude of the far-field spatial coherence function (arbitrary units). (c), (h) Phase of the far-field spatial coherence function (radians). (d), (i) Variation of the coherence magnitude for a fixed point on the ring, and (e), (j) variation of the phase of coherence function with the angle of grating rotation.

When the grating is illuminated by a spatially incoherent annular source, the far-field coherence function exhibits a ring-shaped distribution with petal-like modulation in its magnitude with zero phase. When the illumination is made asymmetric, the magnitude of the distribution becomes constant with azimuthally varying phase. The rotation of the sinusoidal radial grating in the former case produces only an amplitude modulation and the latter case produces a linear phase modulation in the far-field spatial coherence function, while keeping the magnitude same. The technique has potential applications in radial and rotational shearing interferometers.

HVN acknowledges University Grants Commission for research fellowship.

References:

[1] Haneen, V.N., D.N. Naik, *Optics Letters* 50 (2025) 4278–4281.
[2] R. Azizkhani, D. Hebri, S. Rasouli, *Optics Express* 31 (2023) 20665–20682.
[3] W.H. Stevenson, *Applied Optics* 9 (1970) 649–652.

Categorization and Analysis of Cross-Spectral Purity for Partially Polarized Light Fields

[1,2]Deepak Kumar and [2,3,#]Nandan S. Bisht

[1]Department of Physics, Government P.G. College Kapkote (Bageshwar), Uttarakhand, India

[2]Department of Physics, Soban Singh Jeena University Campus Almora, Uttarakhand, India

[3]Department of Physics, Kumaun University DSB Campus Nainital, Uttarakhand, India

[#]*bisht.nandan@gmail.com*

Cross spectral purity(CSP) for nonstationary electromagnetic (EM) is re-examined using normalized coherence Stokes parameters for partially polarized light fields and conditions for local CSP (LCSP) and global CSP (GCSP) are obtained. It is shown that the GCSP follows reduction formula while the specularity defines LCSP in terms of normalized coherence parameters .

CSP was first introduced by L. Mandel in 1961 for stationary scalar light fields. Non stationary light fields are more general fields whose statistical properties changes with time, frequency and space. CSP provides a generalized framework in describing the separability in correlation matrices. The field is LCSP if the cross spectral density (CSD) matrix is specular. Under separability condition if CSP shows all points on the wavefront then it is GCSP.

An ideal superposition of field in a wavefront shearing interferometer (WSI) can be realized at **r** due to interfering beams from two pinholes located at $\boldsymbol{\rho}_1$ and $\boldsymbol{\rho}_2$

$$\mathbf{E}(\mathbf{r},\omega) = \mathbf{E}(\boldsymbol{\rho}_1,\omega)\exp[\imath\omega\tau_1] + \mathbf{E}(\boldsymbol{\rho}_2,\omega)\exp[\imath\omega\tau_2] \tag{1}$$

The two-point Stokes parameters are given by

$$\mathcal{S}_{0,n}(\boldsymbol{\rho}_1,\boldsymbol{\rho}_2,\omega_1,\omega_2) = Tr[\mathbf{W}_0(\boldsymbol{\rho}_1,\boldsymbol{\rho}_2,\omega_1,\omega_2)\,.\,\sigma_p] \tag{2}$$

where $\mathbf{W}_0(\boldsymbol{\rho}_1,\boldsymbol{\rho}_2,\omega_1,\omega_2)$ is CSD matrix, σ_0 is unit matrix and $\sigma_p(p=1,2,3)$ are Pauli spin matrices.

Introducing normalized coherence Stokes parameters in space-frequency and space- time as

$$\mu_{0,n}(\boldsymbol{\rho}_1,\boldsymbol{\rho}_2,\omega_1,\omega_2) = \frac{\mathcal{S}_{0,n}(\boldsymbol{\rho}_1,\boldsymbol{\rho}_2,\omega_1,\omega_2)}{\sqrt{S_0(\boldsymbol{\rho}_1,\omega_1)S_0(\boldsymbol{\rho}_2,\omega_2)}} \quad \text{and} \quad \bar{\gamma}_n(\boldsymbol{\rho}_1,\boldsymbol{\rho}_2,\Delta t) = \frac{\bar{\mathcal{S}}_n(\boldsymbol{\rho}_1,\boldsymbol{\rho}_2,\Delta t)}{\sqrt{\bar{S}_0(\boldsymbol{\rho}_1,\boldsymbol{\rho}_1,0)\bar{S}_0(\boldsymbol{\rho}_2,\boldsymbol{\rho}_2,0)}} \tag{3}$$

Using CSP conditions $S_n(\boldsymbol{\rho}_2,\omega) = C_n S_n(\boldsymbol{\rho}_1,\omega) = D_n S_n(\mathbf{r}_n,\omega)$, where C_n and D_n are frequency independent factors, one lead to reduction formula; which is as

$$\bar{\gamma}_n(\boldsymbol{\rho}_1,\boldsymbol{\rho}_2,\Delta t) = \bar{\gamma}_n(\boldsymbol{\rho}_1,\boldsymbol{\rho}_1,\Delta t+\Delta\tau_n)\times\bar{\gamma}_n(\boldsymbol{\rho}_1,\boldsymbol{\rho}_2,-\Delta\tau_n)\times[\bar{\gamma}_n(\boldsymbol{\rho}_1,\boldsymbol{\rho}_1,0)]^{-1} \tag{4}$$

The first term depends on spatial coordinate, second term on temporal coordinate and the third one is on polarization at two input positions.

LCSP is followed if the normalized coherence Stokes parameter given by eq.(3) is specular i.e. $\mu_{0,n}(-\boldsymbol{\rho},-\boldsymbol{\rho},\omega,\omega) = \mu_{0,n}(\boldsymbol{\rho},\boldsymbol{\rho},\omega,\omega)$, while the condition for GCSP is separability i.e. $\mu_{0,n}(\boldsymbol{\rho}_1,\boldsymbol{\rho}_2,\omega_1,\omega_2) = \mu_n(\boldsymbol{\rho}_1,\boldsymbol{\rho}_2)\mu_n(\omega_1,\omega_2)$ and it also satisfies reduction formula.

References:

[1] J. Laatikainen, M. Luo, A. Halder, M. Koivurova, T. Setälä, J. Turunen, A. T. Friberg, *Journal of the Optical Society of America A 40* (2023) 1260.

[2] J. Laatikainen, A. T. Friberg, T. Setälä, *Optics Letters* 48 (2023) 5823.

[3] D. Kumar, R. Joshl, Gayaprasad N.S. Bisht, *Pramana- J. Phys (2026)* (under review).

Energy-Efficient Optical Transceiver Architecture for Intersatellite Links.

[1,#]Vikas Agrawal,[2]Pranav Pandey,[3]Chandra Prakash Sharma, [4]Dr. M Senthil Kumar
[1,2,3,4]Space Application Centre, ISRO Ahmedabad

#vikasagl, pranavpandey, cpsharma, senthil@sac.isro.gov.in

Abstract — *Next-generation satellite constellations require ultra-high data rates and minimal latency for global broadband and near-real-time Earth observation. Unlike spectrum-constrained, interference-prone RF channels, optical intersatellite links (OISLs) offer unlicensed bandwidth, spatial security, and optimized SWaP metrics. This paper introduces a reliable transceiver architecture operating from 100 Mbps to 10 Gbps across LEO/GEO constellations, utilizing an OOK transmitter globally favored for its structural simplicity and high reliability. Via modeling, simulation, and hardware, we evaluate this transmitter across intra- and inter-orbit paths, specifically comparing Mach-Zehnder versus electro-absorption modulator-based designs. Integrated with booster/low-noise amplifiers and high-sensitivity photodetectors, this framework quantifies how finite extinction ratios affect receiver sensitivity under ASE noise-limited conditions.*

Analytical Study — This work quantifies the impact of finite transmitter extinction ratios (r_{ex}) on optical eye closure within an amplified spontaneous emission (ASE) noise-limited regime—a phenomenon previously undocumented. To isolate this effect and mitigate baseline transmission impairments, external modulation is employed to maintain a static laser bias, thereby eliminating transient frequency chirp and subsequent chromatic dispersion penalties [1,2]. However, a finite (r_{ex}) inherently introduces a non-zero residual power offset during digital zeros ($P_0 \neq 0$). In band-limited preamplifier systems where signal-spontaneous beat noise dominates, this unmodulated offset severely amplifies the signal-dependent noise, ultimately degrading receiver sensitivity and imposing power penalty as per Equation 1-4, which includes noise variance σ^2,responsivity R, preamplifier gain G and spectral density S_{ASE}.

$$\sigma^2_{\,sig-sp,1} = 4R^2G\left(\frac{2\bar{P}}{1+r_e}\right)S_{ase}\Delta f = \left(\frac{8R^2GS_{ase}\Delta f}{1+r_e}\right)\bar{P} \quad (1)$$

$$\sigma^2_{\,sig-sp,0} = 4R^2G\left(\frac{2\bar{P}}{1+r_e}\right)S_{ase}\Delta f = \left(\frac{8R^2GS_{ase}\Delta f}{1+r_e}\right)\bar{P} = r_e.\,\sigma^2_{\,sig-sp,1} \quad (2)$$

$$\bar{P}_{sens}(r_e) = \frac{Q^2 8R^2GS_{ase}\Delta f(1+r_e)\left(\sqrt{r_e}+1\right)^2}{4R^2G^2(r_e-1)^2} \quad (3)$$

$$PP_{ex} = \frac{\bar{P}_{sens}(r_e)}{\bar{P}_{sens}(\infty)} = \frac{(1+r_e)(\sqrt{r_e}+1)^2}{(r_e-1)^2} \quad (4)$$

Results and Discussions — Measured results shows that due to escalating signal-ASE beat noise, a r_{ex} of 8 dB, imposes severe 2.7 dB penalty; however, improving r_{ex} to 10 dB restricts this penalty up to 1.5 dB relative to a baseline r_{ex} of 12.5 dB. Measured results depicts that MZM achieves r_{ex} greater than 12.5 dB over EAM which is limited to 10 dB. Across 42000 kms GEO ISL paths, upgrading r_{ex} from 10 dB to 12.5 dB, drops the required onboard EDFA power from 10W to 7.5W, saving 2.5W DC power; alternatively, it permits shrinking the terminal aperture from 100 mm to 85 mm at constant EDFA power.

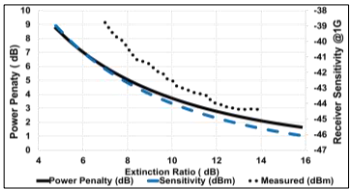


Fig. 1: Power Penalty in Finite Extinction in ASE Noise Regime

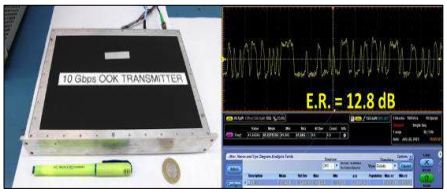


Fig. 2A: MZM Transmitter
Fig. 2B: Measured Extinction Ratio

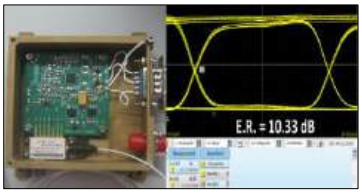


Fig. 3A: EAM Transmitter
Fig. 3B: Measured Extinction Ratio

Conclusions — This work successfully demonstrated that finite r_{ex} in ASE regime induce severe power penalties. The results establish a critical trade-off balancing transmission range against hardware complexity. For compact CubeSat's for LEO ISLs, the 10 dB r_{ex} EAM's satisfies the link budget while yielding a highly robust, monolithic chip-scale transmitter. For deep, long-range GEO trajectories, the 12.5 dB r_{ex} MZM capability remains an indispensable requirement to suppress noise and mitigate severe geometric path attenuation.

References:

[1] Franz, J. H. and J. V. Kumar "Optical Communications Components and Systems", 1st ed. New Delhi: Narosa Publishing House, 2000. ISBN 978-084930

[2] Eduard Sackinger "Broadband Circuits for Optical Fiber Communication", John Wiley & Sons, Inc., 2005.

Design and Performance Evaluation of a Compact 3U-Class MWIR Catadioptric Imaging Payload with Exit Pupil Matching and Stray-Light Suppression for CubeSat Earth Observation

*[1]**Binayak Das Mohapatra,** [2]**Ashutosh Verma,** [3]**Amitvikram Kurulkar**

Optics Department
SatLeo Labs Pvt. Ltd.
Ahmedabad, Gujarat 380059, India

Email: binayak@satleolabs.com

An integrated optical design methodology for a compact 3U-class MWIR CubeSat payload is presented. A Ritchey–Chrétien telescope with relay optics was optimized for exit pupil matching, diffraction-limited imaging, and stray-light suppression. The final design achieves an MTF greater than 27% at the detector Nyquist frequency while satisfying manufacturability and environmental performance requirements.

Mid-wave infrared (MWIR) imaging is widely employed in Earth observation for thermal anomaly detection, environmental monitoring, target surveillance, and quantitative thermal imaging. This work presents the design and performance evaluation of a compact 3U-class MWIR catadioptric imaging payload operating over the 3.7–4.8 μm wavelength range[1].

The optical system employs a Ritchey–Chrétien (RC) telescope integrated with a relay optics assembly to image onto a cooled mercury cadmium telluride (MCT) focal plane array comprising a 640×512 pixel detector. The system has an effective focal length of 300 mm, an F-number of 4, a total optical track length of 260 mm, and a central obscuration below 25%, achieving a ground sampling distance below 25 m from a 500 km sun-synchronous orbit. The relay optics were optimized to match the optical exit pupil with the detector cold stop located 24.7 mm from the focal plane array, minimizing parasitic flux and background thermal radiation while maintaining diffraction-limited imaging performance[2].

The optimized optical system achieves an MTF greater than 27% at the detector Nyquist frequency. Sensitivity and Monte Carlo tolerance analyses confirmed manufacturable tolerances while preserving the required optical performance. Ghost image and Narcissus analyses were performed to mitigate detector self-emission effects. Stray-light suppression below 1% was achieved using an analytical baffle design methodology implemented in Zemax OpticStudio through the Zemax Programming Language (ZPL). Detector-specific rectangular baffle apertures were adopted instead of conventional circular geometries to reduce baffle mass while maintaining equivalent stray-light suppression[3].

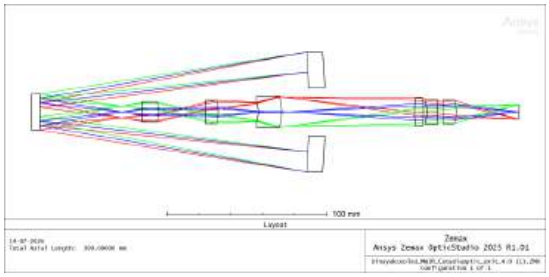


Figure 1: Optical layout of the compact 3U-class MWIR catadioptric imaging payload with relay optics and exit pupil matching.

The proposed optical architecture integrates exit pupil matching, tolerance-driven optimization, and detector-specific stray-light suppression into a compact and manufacturable MWIR payload suitable for next-generation CubeSat Earth observation missions.

References

[1] Compact, wide-angle catadioptric telescope design for MWIR imaging: optical performance analysis using Zemax® Sami D. Alaruri Independent Scholar P.O. Box 13123, Mill Creek, WA 98082, USA.

[2] Cold shield matching of cooled infrared system based on telecentric optical structure Xinrong Hu,1,a,* Jing Wang,1,b Su Chen,1,c Jing Li,2,d Ye Feng2,e 1China Academy of Space Technology (Xi'an), Xi'an, China, 710000 2 Xi'an Institute of Optics and Precision Mechanics, Chinese Academy of Sciences, Xi'an, China,710119

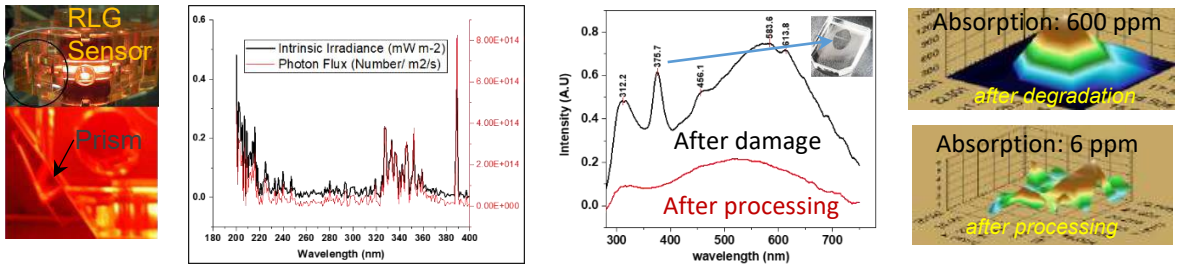
[3] Iterative method of baffle design for modified Ritchey–Chretien telescope M. Senthil Kumar, C. S. Narayanamurthy, and A. S. Kiran Kumar.

Investigation of Photolytic Degradation in Fused Silica Optics for Ring Laser Gyroscopes

Enni Krishna, Jagroop, Sreelakshmy K, Pradeep K.
ISRO Inertial Systems Unit, Thiruvananthapuram, Kerala
#krishna.enni@gmail.com

*A **failure analysis** of a malfunctioning prism-based ring laser gyroscope (RLG) revealed photolytic degradation of the fused-silica optics, which led to the formation of color centers. Through fluorescence, photothermal spectroscopy, and imaging, absorption was quantified at 600 ppm, and plasma photons were identified as the source of the degradation. Spectral irradiance analysis indicated that intense 200 nm photons were the primary cause. The implementation of mitigation measures restored normal RLG operation and increased the component lifetime fourfold, validating both the proposed degradation mechanism and the life-enhancement strategy.*

Ring Laser Gyro (RLG) devices are optical sensors used in launch vehicles, interplanetary missions, and human spaceflight missions due to their high dynamic range and precision. However, these devices have experienced premature failures, falling short of their intended operating lifetime and affecting sensor reliability. Various factors can limit the operational lifespan of RLG devices. An analysis of failed units revealed that Total Internal Reflecting (TIR) prisms, which contain plasma source and are crucial for laser generation, contribute to cavity loss. This loss was evidenced by a 60% increase in laser threshold voltage. Although literature documents on fused silica degradation under high-power laser interactions and plasma exposure exist[1–4], there is no evidence that low-fluence (5 μW/cm^2) He-Ne plasma damages fused silica optics [5]. This study presents a detailed root cause analysis, identifies the photolytic degradation mechanism, and validates it using advanced characterization tools and testing with an actual device.



(a) (b) (c) (d)

Fig. 1: (a) RLG device optical sensor with TIR prism, (b) spectral irradiance spectrum, (c) fluorescence spectrum, (d) photo thermal image after degradation and after chemical processing processing.

Figure 1 illustrates the optical sensing unit of the RLG sensor, featuring a plasma source confined by a TIR prism. Spectral irradiance measurements of the He Ne plasma (Fig. 1b) reveal a flux density of UV photons, with 200 nm photons exhibiting higher intensity than others. A photograph of the TIR prism (Fig. 1c) highlights the degraded area and its fluorescence spectrum following degradation and showing significant reductions in optical defect precursors such as optical deficiency centers (ODC) at 200 nm and nonbridging oxygen hole centers (NBOHC) at 650 nm after chemical polishing [6]. Photothermal imaging (Fig. 1d) indicates a decrease in absorption centers post-chemical polishing. These results revealed that continuous exposure of fused silica optics to UV photons from HeNe plasma under vacuum causes photolytic degradation.

$$\eta = \frac{V_{work\ voltage} - V_{threshold}}{V_{threshold} - V_{discharge}} \quad (1)$$

Integrating these TIR prisms into the RLG sensor for performance validation, the device achieved a standard laser threshold of 5 V and a 100% increase in efficiency factor η (as per equ.1) relative to damaged prisms. These findings elucidate the failure mechanisms in prism-based RLG devices and demonstrate improvements in device longevity, relevant for interplanetary applications.

References:

[1] M. Rothschild, D.J. Ehrlich, D.C. Shaver, *Appl. Phys. Lett.* 55 (1989) 1276–1278.
[2] J.W. Chan, T. Huser, S. Risbud, D.M. Krol, *Opt. Lett.* 26 (2001) 1726.
[3] X. Zhou, X. Zhou, J. Huang, Q. Cheng, F. Wang, X. Ye, X. Jiang, W. Wu, *Adv. Condens. Matter Phys.* 2014 (2014).
[4] H.B. Lü, S.Z. Xu, H.J. Wang, X.D. Yuan, C. Zhao, Y.Q. Fu, *Adv. Condens. Matter Phys.* 2014 (2014).
[5] C. Gerhard, W. Viöl, M. Kretschmer, *Opt. Photonik* 7 (2012) 35–38.
[6] Krishna Enni; Sreelakshmy K and Joji J Chaman, *Appl. Acoust.* APAC-D-26- (2026) 1–30.

REALIZATION OF TAPERED CAVITY LAYER IN A NARROW BANDPASS FILTER DESIGNED FOR HYPERSPECTRAL APPLICATIONS

*Praveen K. C and Nishith A

Laboratory for Electro-Optics Systems (LEOS), ISRO, I Cross, I Stage, Peenya Industrial Area, Bengaluru – 560058, INDIA.

**Corresponding Author: kcp@leos.gov.in, Phone: 09740894773.*

Hyperspectral (HySp) coatings are a niche functional coating that offer linearly variable optical filter (LVOF) to distribute different wavelengths across the detector area. HySp camera modules enable remote sensing of same scene with multiple wavelengths providing HySp data cube. Tapered cavity layer is a technological unit step developed to realize HySp coatings for space applications.

Earth Observation Satellites have dedicated optics modules to capture specific wavelength bands for remote sensing applications. Several spectral bands spread over UV, VIS, NIR and SWIR regions are of importance to scientific community vis-à-vis remote sensing data for applications like water resource management, targeted remedial measures in agriculture, mineral mapping, pollution monitoring, etc. Accommodating multiple spectral bands in a single satellite to acquire images increases complexity in satellite payload construction, integration, testing and band-to-band image data matching. Novel approach is to acquire images in multiple wavelength bands in a single lens head assembly to reduce the complexities arising at the payload level. Hyperspectral coated components when assembled within a single lens head reduce the complexities arising at the payload level. Multiple wavelength bands may be realized by thin films coatings on detector window or directly on the detectors at the wafer level.

The tapering of cavity layer was employed in a narrow bandpass thin film design to achieve a hyperspectral design over the detector window. The thin film stack was designed in the spectral region 600nm to 750nm targets full width half maximum (FWHM) of 3nm to 5nm. The cavity layer in a narrow bandpass thin film design (Fabry-Perot Etalon design) was tapered to achieve a hyperspectral design [1]. Whereas, the Bragg layers that are covered on either side of the cavity layer were coated without tapering. According to the design, it was required to achieve a tapering of 125nm to 335nm over a length of 30mm, further extracting the required area by dicing. Intentional non-uniformity mask was designed, fabricated and used as coating mask during the thin film deposition to achieve the tapered cavity layer [2]. The metrology confirms the tapered thickness over the extended region compared to the required region. Further, the Bragg layers were coated on the tapered cavity layer to form linearly viable narrow bandpass filter. Indigenous metrology set-up was established with a monochromator output to the integrating sphere providing spectrally pure uniform light output. The glass wafer was placed closely in front of the CMOS imager to capture the spatial spectral variation for exposure to different wavelength. The images captured at different wavelength are presented in Fig. 1 which depict the shift in bandpass filter peak towards the inner radius of the sample as per the mask design. The drop in the transmission peaks correlate to the refractive index mismatch between the theoretical design and practically achieved results for stack of 25 layers (~2.6µm thick).

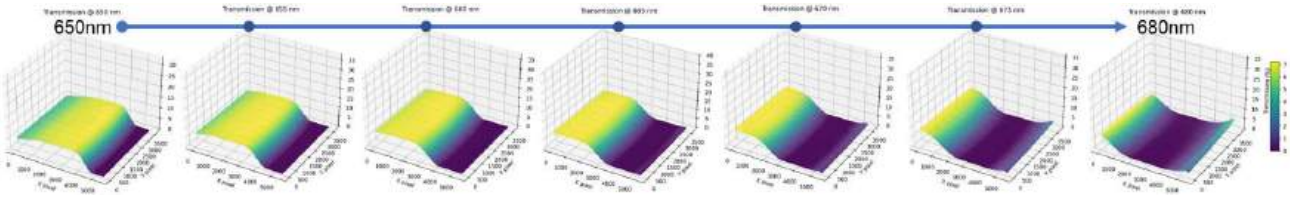


Fig. 1: The images captured at different wavelength show the shift in bandpass peak acting as linearly variable bandpass filter.

The design of non-uniformity mask and thin film stack along with realization of tapered layer and coating of complete stack will be presented in this paper. Further, the schema of dicing and mounting the coated sample for accurate positioning over the detector will be discussed.

We are thankful to LEOS management for identifying and funding the technology development program.

References:

[1] Arvin Emadi, Huaiwen Wu, Ger de Graaf and Reinoud Wolffenbuttel, *Optics Express, 20(1) (2012) 489-507*.
[2] Jiandong Pan, Fengshang zhang and Yixun Yan, *SPIE Vol. 2364* (1994) 225-228.

Design of transportation system and criticalities during transportation for space borne glass mirror

[1,#]Mayank Garg,[1]Ramajagol Rajkumar M., [1]Arvind Kumar Sharma, [1]Venkatesan B, [1]Vishweshwar Rao B, [1]Jiju John
[1] Laboratory for Electro Optics Systems, Indian Space Research Organization, 1st Cross 1st Cross, Peenya Industrial Estate, Bengaluru, Karnataka, India

[#]*mayank@leos.gov.in*

A reliable transportation system is essential for space borne glass mirrors used in space telescopes as these precise mirrors, which are realized with large capital investment, can easily get damaged during transportation. This paper presents the design of the transportation system done for a 1.2m diameter 85 kg mirror and details about its transportation which was done through road and air.

Realization of space borne glass mirrors used in space telescope is a capital and time intensive activity involving costly raw material, its grinding, polishing and interferometric testing under zero-g simulated environment. And a failure due to transportation for these mirrors before their integration to telescope structure needs to be prevented. Main reasons for failure are due to mechanical loads during transit and handling, and contamination of mirror's active surface. This paper covers the design of transportation system for a 1.2m diameter 85 kg glass mirror and with the aim to improve the design in future, shock-temperature data are recorded during mirrors' transportation. Further the paper presents the limitations of the work and discusses future scope.

Design - Expected environmental conditions like inertial loads, shock, humidity, temperature and their levels are identified and design is done to address them. System has a aluminium fixture which houses mirror. This fixture goes into a wooden box which has polyethylene foam with cutout to accommodate aluminium fixture In order to reduce mechanical shock going to the fixture. Inside fixture, mirror is placed horizontally on 50mm thick high density bonded foam to absorb shocks from handling and take off/landing of airplane in axial direction of mirror. Then 12 supports in mirror's radial direction is provided. Contact pad (for mirror) of radial support is of delrin material with polyurethane foam pasted on it to prevent scratches and provide cushioining to mirror when it experiences inertial load and shocks in radial direction. Radial gaps is filled with bonded form to provide arrestation if radial supports fail. For humidity control, silica gel is employed as passive control which are placed at various locations in fixture and wooden box. Provision of lifting the fixture and box using kevlar belts is included in design. FE Analysis is done to ensure design margins for transit inertial load of 5g. Figure 1 shows various images of transportation system.

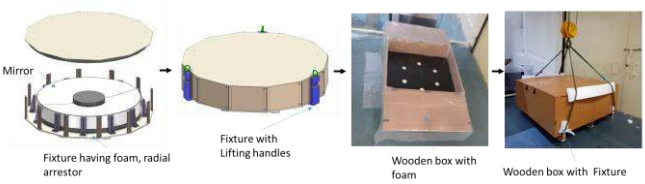


Fig. 1: Transportation system for 1.2m diameter 85 kg glass mirror

Transportation – Assembly and lifting trials are done to ensure seamless one time assembly (in clean room for preventing contamination) and loading of transportation system to truck. With the aim to build database which will help in designing the system better in future, a shock-temperature data logger is employed and mounted on aluminum fixture near mirror. During complete transportation, 196 shock events occurred with maximum amplitude of 23g occurring for 19 millisecond (majorly during handling of system) and temperature variation is from 20.9˚C to 26.2 ˚C.

Conclusion - Though the mirror is transported successfully but there exist numerous improvements which can be done in the system, like dedicated Environmental Data Acquisition System including location track, vibration, pressure and humidity data, active humidity control system, including live camera feed, designing mirror for transportation requirement, etc. The author like to thank the optics team for assembly of mirror to transportation system and courier service partner for ensuring damage free transportation of mirror.

Reference:

[1] Shashank Srivastava, Shreeniwas Sahu, A.Sekar, K.V.Govinda, *Advanced Materials Research* Vols. 588-589 (2012) pp 1161-116 (2012).

Photonic Ising Machine for Image Denoising

Milind Bagul[1,*], Nayem Al-Kayed[2], Bhavin J. Shastri[2], A. Aadhi[1]
[1]Optics and Photonics Centre, Indian Institute of Technology Delhi, New Delhi 110016, India
[2]Department of Physics, Engineering Physics & Astronomy, Centre for Nanophotonics, Queen's University, Kingston, ON, Canada

Email: *pha242131@physics.iitd.ac.in aadhi@iitd.ac.in

Here we propose a novel binary image denoising simulator using a cascaded modulator-based optoelectronic Ising machine. By mapping noisy binary images to an Ising model and minimizing the Ising energy, we achieve improvements in image quality. The mean squared error between the noisy and original images decreases from 40% to 5%.

Ising machine is an emerging hardware solver that has a wide range of applications in machine learning & AI, combinatorial optimization, and signal processing [1]. Typically, it consists of discrete binary variables called spins, each of which interacts with its nearest neighbours. Over iterations, the Ising machine gives optimal solutions to the problem defined by the coupling matrix and a local field. Photonic Ising machines offer the advantages of parallel processing, large scalability and energy efficiency.

In general, images are often affected by various noise sources and environmental factors such as camera sensor issues, electronic issues and transmission errors, leading to distortion from the original images. Image quality is vulnerable to degradation, which then limits the accuracy and precision of the image analysis, particularly in medical imaging or object identification. Image denoising is a computational technique commonly used to enhance the visual quality of images by reducing the presence of noise. Spatial domain methods, filtering techniques and variational models are traditional image denoising methods; however, they suffer from manual parameter tuning, lack detail preservation, and, in some cases, degrade visual quality. To address this, we propose a novel photonic simulator using the cascaded modulator based optoelectronic Ising machine, providing a fast and stable way to solve binary image denoising problems. By mapping noisy binary images to an Ising model, the original image can be recovered by minimizing the energy to the ground-state solution. The proposed implementation of image denoising algorithms using photonic Ising hardware exploits the advantages of fast vector-matrix multiplication and physical annealing.

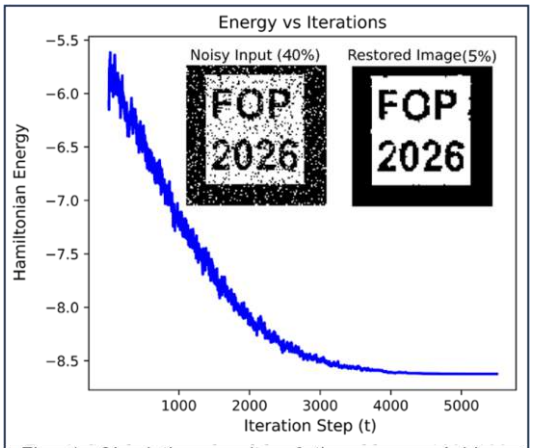


Fig. 1: Simulation results of the recovered binary 100×100 *pixel image.* E_{min} *= -8.59 was obtained after 4300 iterations, starting from an initial E = -7.47.*

Considering a noisy input image as an array of binary values $y_i \in \{-1,1\}$, where $i = 1,..,N$ indices all pixels in the image, and the pixels $x_i \in \{-1,1\}$ representing the recovered noise-free pixels of the image, the denoising Hamiltonian is expressed as $H = \gamma \sum_i x_i - \mu \sum_{\{i,j\}} x_i x_j - \eta \sum_i x_i y_i$, where the constants determine the penalties associated with adjacent pixel interactions and the corresponding minimum energy E_{min} is the noise-free image [2]. In our simulation of the 2D Ising model, each central pixel interacts with the four nearest neighbours. The energy of the system is minimized over iterations, leading to smoothing and the averaging of pixels with their neighbouring pixels to have similar values to obtain a high-quality image. To map the denoising problem onto photonic hardware, we reformulate the denoising Hamiltonian (H) as an iterative spin-update equation by applying gradient descent to the current spin state $x[t]$, allowing the energy to settle into its ground state. The iterative matrix-vector multiplication (MVM) is performed between a weight vector W and a spin vector σ(x[t]), where the adjacency matrix represents neighbouring pixel interactions. The injected Gaussian annealing noise $\eta'(\zeta)$ along with the feedback and coupling strengths α and β, respectively, is used for the implementation of a photonic Ising machine. As shown in Fig. 1, the system reduces the Hamiltonian energy by -1.12, corresponding to an 87.5% relative reduction in the mean squared error (MSE) of the image noise. Our findings pave the way for a scalable, low-power denoiser to support real-time imaging in medical and radar applications.

References:

[1] N. Al-Kayed, C. St-Arnault, H. Morison, et al., *Nature* 651 (2026) E16.
[2] M. Cherukuri, *IEEE 4th International Conference on Data Science and Computer Application*, (ICDSCA 2024) 266 (2024).

Optical frontend neural network for image classification

Jyoti Bikash Mohapatra and *Naveen K. Nishchal
Department of Physics, Indian Institute of Technology Patna, Bihar, India 801106
*nkn@iitp.ac.in

An optical frontend neural network processes visual data at the speed of light by performing optical convolution operated with the principle of Fourier optics by reframing the AI acceleration. The subsequent operations are executed digitally and this hybrid combination of optical and electronic processes enable ultrafast, energy efficient, and real-time pattern recognition.

Image recognition and classification are among the most important tasks in computer vision and artificial intelligence. In recent times, convolutional neural networks (CNNs) have achieved great success in pattern recognition problems. Neural networks are widely used in various applications such as object recognition, pattern analysis, medical imaging, autonomous vehicles, and surveillance systems. However, the increasing computational complexity of modern deep neural networks has led to high computational costs, high power consumption, and high latency. As the size of datasets and network architectures continues to grow, there is a need for faster and more efficient computing approaches.

Interestingly, there has been a recent surge in the adoption of optical techniques for AI/ML applications. Specifically, a CNN requires substantial computational resources to effectively classify large datasets. The total number of computations increases linearly with the network's depth. Convolving an input image of size $n \times n$ pixels with a kernel size of $k \times k$ pixels generate a computational complexity of $O(n^2k^2)$. This complexity also introduces latency into the system. In recent years, active research has been revitalized with demonstrations of optical frontend neural networks for image recognition and classifications

The proposed study presents a general optical frontend neural network framework for image classification. In this approach, the initial feature extraction stage is performed in the optical domain before the data is processed by an electronic neural network. An optical frontend based on Fourier optical processing is used to perform convolutional filtering and feature enhancement. The 4-*f* optical correlator can naturally implement convolution in real-time, which is significantly faster than electronic convolution. In the 4-*f* setup, two lenses of identical focal lengths are separated by a distance of 2*f*. The input is placed at the front focal plane of the first lens and in the back focal plane, a filtering mask is used to convolve with the input signal to produce the feature maps. Several spatial-frequency filtering operations, such as low-pass, high-pass, band-pass, and band-stop, can be used. Subsequent electronic processes follow the optical front end to make the final decision. Usual optical neural networks are feasible for a single layer of optical convolution.

Acknowledgement
The funding from the Council of Scientific and Industrial Research (03/1492/23/EMR-II) and Anusandhan National Research Foundation (ANRF/ARG/2025/012264/PS), Govt. of India are acknowledged.

References:

1. T. Fu, J. Zhang, R. Sun, Y. Huang, W. Xu, S. Yang, Z. Zhu, and H. Chen, Optical neural networks: progress and challenges," Light Sci. Appl. 13, 263 (2024).
2. X. Lin, Y. Rivenson, N. T. Yardimci, M. Veli, Y. Luo, M. Jarrahi, and A. Ozcan, "All-optical machine learning using diffractive deep neural networks," Science 361, 1004-1008 (2018).
3. S. Colburn, Y. Chu, E. Shilzerman, and A. Majumdar, "Optical frontend for a convolutional neural network," Appl. Opt. 58, 3179-3186 (2019).
4. X. Yuan, Y. Wang, and Z. Xu, "Training large-scale optoelectronic neural networks with dual-neuron optical-artificial learning," Nat. Commun. 14, 7110 (2023).
5. J. B. Mohapatra and N. K. Nishchal, "Data-driven classification in optical correlation systems," Opt. Lasers Eng. 201, 109719 (2026).
6. J. B. Mohapatra, R. Kumar, and N. K. Nishchal, "Transport of intensity-driven phase object recognition and classification," IEEE Photon. Technol. Lett. 38, 1395-1398 (2026).

Second Order Differential Equation Solver Using Programmable Integrated Photonic Circuits

[1#]Ayush Soni ,[2]Suman Dey and [3]Shailendra Kumar Varshney
[1]Indian Institute of Information Technology Tiruchirappalli, (Tiruchirappalli, TN)
[2,3]Indian Institute of Technology Kharagpur, (Kharagpur, WB)

[#]*soniayush312@gmail.com*

We designed a programmable photonic integrated circuit (PIC) based framework for implementing a second-order oscillatory differential equation solver using a voltage-controlled tunable basic unit (TBU) mesh architecture. The mathematical model is mapped onto the programmable TBU mesh by converting the computational parameters into electrical drive voltages for photonic implementation.

This work implements a second-order oscillatory differential equation solver on a Field Programmable Photonic Gate Array (FPPGA) using a matrix-based computational framework. The proposed approach is demonstrated for the second-order oscillatory differential equation

$$\frac{d^2x}{dt^2} + \omega^2 x = 0,$$

which is transformed into its first-order state-space representation before photonic implementation. The governing differential equation is first transformed into state-space representation, yielding a time-dependent state transition matrix that describes the evolution of the system's variables. This transition matrix is then decomposed using SVD, $A = U\Sigma V^{\dagger}$, where U and $V^{\dagger}$ are unitary matrices and Σ contains singular values.

The implementation consists of differential equation formulation, state-space modeling, SVD decomposition, normalization, transmission mapping, voltage assignment, photonic mesh programming, and optical output measurement, providing a mathematical-to-hardware framework for programmable photonic processors. The unitary matrices are mapped onto programmable optical coupling elements, while the singular values are implemented as optical attenuation within the tunable basic units (TBUs). The photonic mesh is programmed by converting the computed transmission coefficients into corresponding coupling ratios, phase shifts, and electrical control voltages. The programmed TBU mesh realizes the decomposed matrix optically, and the resulting optical power is measured to reconstruct the system response. A mean-square error of 6.5534×10^{-4} was achieved with respect to the analytical and RK4 solutions at an angular frequency of 9.4248 rad/s.

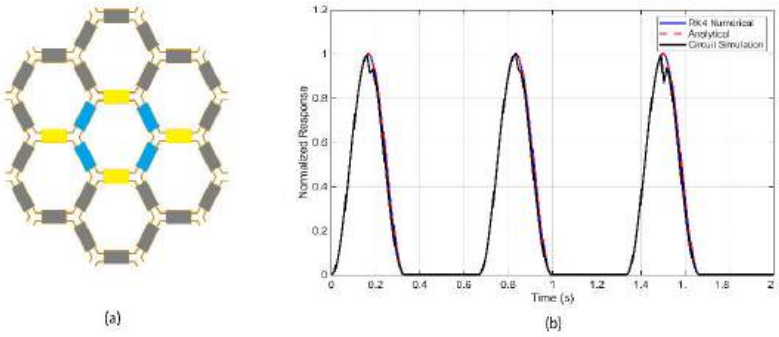


Fig 1: (a) Hexagonal programmable photonic mesh used for differential equation solving. (b) Comparison of analytical, RK4 numerical, and photonic circuit simulation results for the second-order oscillatory differential equation.

The present work bridges mathematical modeling and programmable photonic hardware, demonstrating the potential and capabilities of FPPGA-based processors for solving differential equations and other mathematical formulations. The framework is scalable and can be extended to a broader class of differential equations, making it suitable for applications such as real-time dynamical system simulation, photonic control engineering, photonic signal processing, and optical scientific computing.

References:

[1] Bogaerts, W., Pérez, D., Capmany, J., Miller, D. A., Poon, J., Englund, D., ... & Melloni, A. (2020). Programmable photonic circuits. *Nature*, *586*(7828), 207-216.
[2] Macho-Ortiz, A., López-March, R., Romero, P. M. C., Fraile-Peláez, F. J., & Capmany, J. (2026). Analog programmable-photonic information. *Advanced Photonics*, *8*(3), 036002-036002.
[3] Macho-Ortiz, A., Pérez-López, D., Azaña, J., & Capmany, J. (2023). Analog Programmable-Photonic Computation. *Laser & Photonics Reviews*, *17*(10), 2200360..

Angle-Insensitive High-Q Metasurface for Infrared

[1]Rahul, [1]Sherep Doma Dukpa, and [1,2,#]Sukanta Nandi
[1]Department of Electronics and Communications Engineering,
Indraprastha Institute of Information Technology, Delhi (IIIT Delhi), New Delhi 110020, India
[2]Center for Quantum Technologies,
Indraprastha Institute of Information Technology, Delhi (IIIT Delhi), New Delhi 110020, India
[#]sukanta@iiitd.ac.in

In this work, we present a high-Q germanium metasurface as an angle-insensitive device. The proposed metasurface exhibits angle insensitivity in the mid-infrared, maintaining an almost constant Q-factor over a range of incident angles. This robust performance makes it a promising platform for applications, such as in LiDAR.

In nanophotonics, low mode volume and high quality-factor (Q-factor) is of significant importance towards the quest of achieving high-performance miniaturized photonic devices. Recent advances in metasurfaces supporting bound states in the continuum and Fano resonances, among others, have enabled strong field confinement, leading to applications such as lasing, ultrasensitive sensing, and enhanced light-matter interactions.[1] Nevertheless, one crucial parameter that typically hinders many practical applications of these metasurfaces is their angle sensitivity to the incident light. This angle-sensitivity can be detrimental in the metasurface performance through drastically reduced amplitudes, large spectral shifts, and even sometimes complete disappearance of the high-Q mode. This limitation thus motivates us to design high-Q metasurfaces that are robust and insensitive to varying angles of incidence, and thereby, expanding their application domain under much robust conditions.[2,3]

In this work, we thus present our computational FDTD (Finite-Difference Time-Domain) results to demonstrate an angle-insensitive metasurface device. The metasurface is realized with germanium (Ge) dual void meta-atoms sitting on top of silica (SiO_2) substrate. Ge is particularly interesting due to its high-index (n~4) and transparency in the mid-infrared (MIR). The metasurface unit cell has a periodicity of ~1.4 μm (in both directions), comprising of a ~0.1 μm thick Ge layer patterned with two asymmetric air slots (void meta-atoms) on a SiO_2 substrate. Upon incidence of a plane-wave, a high-Q resonance with a Q-factor of ~10^2 is observed within the spectral range of ~2.3-2.6 μm. Upon varying the angles of incidence from 0-10°, the resonant response of the metasurface remains almost spectrally pinned with comparable Q-factors.

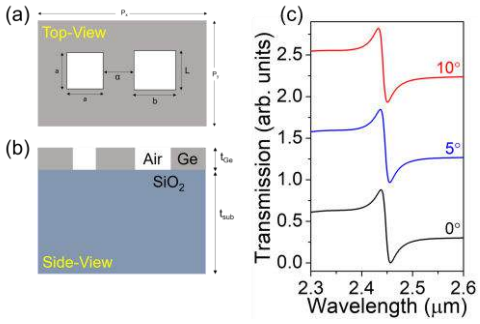


Fig. 1: Angle-Insensitive Metasurface. (a) Top and (b) side-view of the proposed Ge metasurface with dimensions as: P_x=P_y~1.4 μm, a ~0.3 μm, b ~0.3 μm, α ~0.4 μm, L ~0.4 μm, t_{Ge} ~0.1 μm, and t_{sub} ~3 μm. (c) Represents the transmission spectra of the metasurface under different angles of incidence.

To summarize, we propose a Ge metasurface design operating in the MIR and exhibiting a high-Q resonance. Our FDTD results show that the metasurface is robust against varying angles of incidence of the incident light, i.e., an *angle-insensitive metasurface*. The proposed metasurface thus has potential applications in the field of MIR sensing -relevant for sensing toxic gases and explosive chemicals. The other important application is in LiDAR (Light Detection and Ranging) for deployment in unmanned aerial vehicles (UAVs), for autonomous docking in spaceflight, robotics, and others.

SN acknowledges the financial support provided by the Institute Research Grant (IRG) at IIIT Delhi. The authors would like to acknowledge and thank Tidy3D (Flexcompute) for providing the FDTD access.

References:

[1] K. Koshelev, S. Lepeshov, M. Liu, A. Bogdanov, Y. Kivshar, *Physical Review Letters* 121 (2018) 193903.
[2] S. Z. Cohen, L. Sinitsky, S. Nandi, L. Singh, A. Sharoni, T. Lewi, *Nanophotonics* 15 (2026) e70169.
[3] Y. Liu, J. Lv, Y. Fan, M. Zong, S. Zhang, Z. Xu, *Chip* 4 (2025) 100121.

Design and Development of a 2×4 Optical Demultiplexer based on a Photonic Band Gap (PBG) Crystals

[1#]Debashri Saha, [1]Ayan Dey, [2]Suranjan Lakshan, [1]Sudipta Mazumder, [1]Vismaprovo Sinha and [3]Sourangshu Mukhopadhyay

[1]Department of Physics, The University of Burdwan, Golapbag, Purba Bardhaman, 713104, West Bengal, India

[2]Department of Science and Humanities, Vidya Vihar Institute of Technology, Maranga, Purnea, Bihar 854301

[3]Mahatma Gandhi University, Mahishadal, Purba Medinipur, 721628, West Bengal, India

[#]email id of the corresponding author: debashrisaha.2011@gmail.com

Recently, there is an increasing need for ultra-fast, all-optical optical processors in order to meet the growing requirements for superfast optical communications. The authors developed a '2x4' optical demultiplexing system based upon by the frequency characteristic using passband filters and the nonlinear properties of PC-SOAs used as optical switching elements.

Optical multiplexers are required to support fast optical communications in addition to very fast optical data processing. A single data output can be directed towards multiple receivers by controlling triggering input to each receiver channel. The proposed system is capable of routing information from one source towards multiple receivers as the result of proper operation in between the frequency encoded data and control signals both, along with active use of frequency-passing filters and Photonic crystal-based semiconductor-optical amplifiers (PC-SOAs). This increases transmission efficiency through amplification of the optical data. Therefore, these types of devices may also be used to extend performance of high-speed optical communication [1-3].

The proposed '2 x 4' Optical Demultiplexer uses distinct frequency assignments for a single data input and two control inputs. Frequency-selective filters (for example bandpass) allow to select desired control frequencies. Using PC-SOAs as the basis for optical switching allows to pass through the amplified data signal that is then routed to the correct output channel. **Fig. 1** provides an illustration of the block diagram for this proposed system. A summary of the complete operation of this system can be found in **Table 1**.

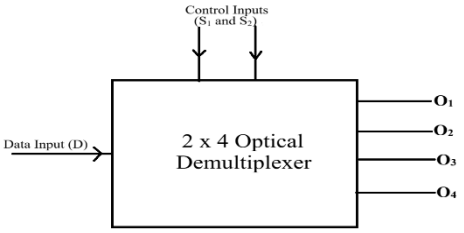


Fig.1. Block diagram of the 2 x 4 Optical Demultiplexer system (Here, O_1, O_2, O_3 and O_4 denote the output channels)

Table 1*. Truth Table of the overall operation of the proposed scheme of 2×4 optical demultiplexer system (Here* u_1 (λ_1) and u_2 (λ_2) are encoded as the two control inputs S_1 and S_2 respectively and u_3 (λ_3) is encoded as one data input)

Control Inputs		Data Input (D)	Outputs			
Signal 1	Signal 2		O_1	O_2	O_3	O_4
S_1 [u_1 (λ_1)]	S_1 [u_1 (λ_1)]	D [u_3 (λ_3)]	D [u_3 (λ_3)]	0	0	0
S_1 [u_1 (λ_1)]	S_2 [u_2 (λ_2)]	D [u_3 (λ_3)]	0	D [u_3 (λ_3)]	0	0
S_2 [u_2 (λ_2)]	S_1 [u_1 (λ_1)]	D [u_3 (λ_3)]	0	0	D [u_3 (λ_3)]	0
S_2 [u_2 (λ_2)]	S_2 [u_2 (λ_2)]	D [u_3 (λ_3)]	0	0	0	D [u_3 (λ_3)]

In future, the higher order demultiplexing systems are possible to develop using Photonic band gap (PBG) crystals.

The authors acknowledge the Centre for Advanced Studies (CAS) programme, Department of Physics, The University of Burdwan for providing software.

References:

[1] K. R. Chowdhury, P. P. Das, S. Mukhopadhyay, *Optical Engineering* **44** (3), 035201–035201-5 (2005).
[2] A. Pal, S. K. Pal, S. Mukhopadhyay, Optik, **125** (1), 304-307 (2014).
[3] F. Mehdizadeh, M. Soroosh, H. Alipour-Banaei, Optik, **127** (20), 8706-8709 (2016).

Designing Hyperbolic Metasurfaces for Enhanced Light-Matter Interaction and Efficient Radiation Outcoupling

[#]Faisal Ishaq, Mohammed Ashahar Ahamad, Mansoor Ahmed, and Faraz Ahmed Inam
Department of Physics, Aligarh Muslim University, Aligarh, Uttar Pradesh 202002, India
[#]ifaisal806@gmail.com

Photonic metasurfaces provide compact platforms for device miniaturization, near-field enhancement, and precise light control. Here, we propose a 2-D hyperbolic metasurface and investigate its optical response using analytical and COMSOL simulations. Mie scattering reveals a resonance at $\lambda = 637\ nm$, matching the NV center zero-phonon line and enabling light-matter interaction studies.

Hyperbolic metamaterials (HMM) have unusual electromagnetic properties due to their hyperbolic dispersion and large photonic density of states [1]. However, their optical implementation is limited by fabrication complexity and metallic losses. Converting bulk HMM into two-dimensional (2D) hyperbolic metasurfaces (HMS) offers reduced structural complexity and improved integration potential [2]. Here, we employ a semi-analytical Cartesian multipole approach to calculate the reflectance (R) and transmittance (T) using the following equations [3].

$$r = \frac{ik_d}{E_0\, 2S_L\varepsilon_0\varepsilon_d}\left(p_x - \frac{1}{v_d}m_y + \frac{ik_d}{6}Q_{xz} - \frac{ik_d}{2v_d}M_{yz} - \frac{k_d^2}{6}O_{xzz}\right) \quad (1)$$

$$t = 1 + \frac{ik_d}{E_0\, 2S_L\varepsilon_0\varepsilon_d}\left(p_x + \frac{1}{v_d}m_y - \frac{ik_d}{6}Q_{xz} - \frac{ik_d}{2v_d}M_{yz} - \frac{k_d^2}{6}O_{xzz}\right) \quad (2)$$

$$R = |r|^2, \text{and } T = |t|^2 \quad (3)$$

p_x, m_y, Q_{xz}, M_{yz} and O_{xzz} represent the electric dipole, magnetic dipole, electric quadrupole, magnetic quadrupole, and electric octupole moments, respectively. $S_L = D^2$ denotes the unit-cell area, where D is the lattice periodicity. The parameter v_d denotes the speed of light in the surrounding medium and $k_d = k_0\sqrt{\varepsilon_d}$, is the corresponding wave number, with ε_d being the relative permittivity of the surrounding medium.

The Ag and ZnS layers are 30 and 24 nm thick, respectively, and the structure is considered in vacuum [Fig. 1(a)]. Under (x)-polarized plane-wave excitation, R and T are calculated using ED, MD, EQ, MQ, and EO contributions. Analytical R and T spectra agree well with COMSOL results, validating the multipole model [Fig. 1(b)]. A rhombus-shaped HMS array on SiO_2 with 200-nm spacing [Fig. 1(c)], exhibits ED, MD, EQ, and MQ resonances near the 637-nm NV center ZPL [Fig. 1(d)], indicating potential for enhanced LDOS, spontaneous emission, and radiative outcoupling.

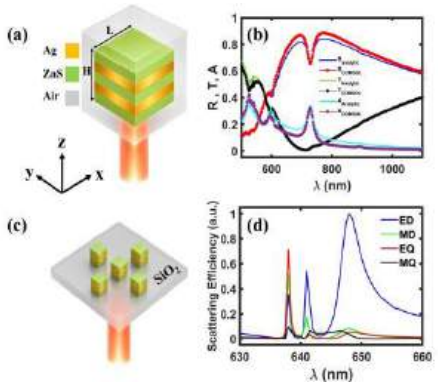


Fig. 1: (a) Ag/ZnS hyperbolic metasurface unit cell in vacuum excited with x-polarized plane-wave excitation with periodic boundaries. (b) Analytical and COMSOL simulated R, T, and A spectra. (c) Rhombus-shaped HMS on a SiO_2 substrate. (d) Mie-scattering modal response.

To summarize, the suggested HMS can support strong multipolar resonances at the NV emission wavelength, making it a suitable platform for increased light-matter interaction and efficient photon outcoupling.

Acknowledgement:

All authors would like to thank the Department of Science and Technology, India, for funding under the FIST Program 2020 and Core Research Grant CRG/2021/001167.

References:

[1] Poddubny, Alexander, et al. "Hyperbolic metamaterials." *Nature photonics* 7.12 (2013): 948-957.
[2] Zheng, Peng, et al. "Pyramidal Hyperbolic Metasurfaces Enhance Spontaneous Emission of Nitrogen-Vacancy Centers in Nanodiamond." *Advanced optical materials* 11.6 (2023): 2202548.
[3] Terekhov, Pavel D., et al. "Multipole analysis of dielectric metasurfaces composed of nonspherical nanoparticles and lattice invisibility effect." *Physical Review B* 99.4 (2019): 045424.

Quantifying the loss characteristics of a valley-assisted microwave beam splitter

[1,#]Geetanjali Jena, [1]Ravendra Kumar Varshney and [2]Dibakar Roy Chowdhury
[1]Department of Physics, Indian Institute of Technology Delhi, New Delhi 110016, India
[2]School of Engineering, Anurag University, Hyderabad, Telangana 500088, India
[#]*phz228023@iitd.ac.in*

Recently, valley photonic crystals have overturned the traditional wisdom that predicts noticeable losses at sharply curved regions of a propagation path. Herein, we verify the topological protection of a valley-assisted microwave beam splitter by introducing defect and disorder states and investigating its dispersion-loss characteristics through group-delay calculations.

Over the last few years, valley photonic crystals (VPCs) have emerged as a promising platform for exploring valley Hall physics [1,2]. To date, numerous works have substantiated the vision of topologically protected waveguides that exhibit unidirectional transmission, robust energy transport, backscattering-immune propagation and many more. In designing a topology-assisted beam splitter, there always exists an inherent trade-off between the excitation mechanisms, operational robustness, and working spectral window. This includes the demand of high-strength magnetic field to realize operationally robust edge state transport [3], while in others it utilizes complex designs operating in a relatively narrow spectral window [4]. Surprisingly, a detailed study on the loss and dispersion characteristics of the propagating edge state is so far missing, thereby leaving a critical gap in understanding the topological advantage of a photonic crystal. In view of this, we demonstrate a simple valley-assisted beam splitter, exhibiting dispersion-less and backscattering-immune wave propagation in the microwave frequency region. Figure 1(a) illustrates the schematic of our 1×2 topological beam splitter comprising two topologically distinct valley photonic crystals (VPCs) merged through a zigzag domain interface. The photonic bulk band study of the VPCs reveals the existence of a Dirac point at the K valley of the Brillouin zone, which is subsequently lifted to open up a Dirac-point derived bandgap hosting valley-assisted edge states. After confirming the existence of edge states, we verify the transmission response of our design in the presence of several defect and disorder states at the sharply curved region of the domain interface. In conventional photonic crystals, the curved region marks the critical region where significant transmission loss occurs due to mode mismatch. However, as shown in Fig. 1(b), our design exhibits minimal transmission fluctuations (<1 dB) as we increase the number of defect states from 0 to 4. A similar response is noticed for the disorder states, as shown in Fig. 1(c), with a negligible change in overall transmission. In addition, we study the propagation and bending-loss characteristics of our design, as shown in Fig. 1(d) and (e), which exhibit ultra-low propagation and bending-loss coefficients of 0.04 dB/cm and 0.2 dB/bend, respectively. Figure 1(f) further demonstrates the group delay of the propagating edge state across the two output ports. As shown, a low-dispersion region is observed, where the group delay exhibits near-flat, stable variation. Thus, our design can withstand the adverse effects of random disorder and defect states, with high-fidelity signal transmission and impressive loss characteristics. Benefitted from these unique properties, our design opens up new opportunities for the development of robust microwave photonic devices.

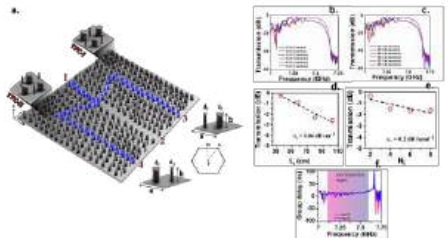


Fig. 1: (a) Schematic representation of our proposed valley-assisted beam splitter, with the left panel depicting the hexagonal unit cells of VPC-i and VPC-ii comprising aluminum rods of different diameters, and the right panel depicting the rhombohedral unit cell and its Brillouin zone. Effect of (b) defect, (c) disorder states on transmission spectra across the two output ports 3 and 4. (d) propagation loss, (e) bending loss, (f) Group delay variation across the two output ports.

References:

[1] G. Jena, N. Chourasis, R.K. Singh, R. K. Varshney, D.R. Chowdhury, *Journal of Physics D: Applied Physics* 59 (2026) 025101.
[2] Z. Gao, Z. Yang, F. Gao, H. Xue, Y. Yang, J. Dong, B. Zhang, *Physical Review B* 96 (2017) 201402.
[3] M. Mehdipoura, M. Moeini, V. Ahmadi, R. Poursalehi, *Scientific Reports* 14 (2024) 12905.
[4] Y.F. Mehdipoura, J.P. Sun, N. Xu, Z. Jiang, Q.C. Hou, H. Song, M.C. Jin, C. Zhang *Optics Communications* 483 (2021) 126646.

Half-Wave Plate Characteristics of 2A3NPCl in the Terahertz Range

[1]Sarang Joshi, [1]Shriganesh Prabhu, [2]Anurag Kumar Singh, [2]Atheena Pramod, [2]R.Nagalakshmi, and [2]Shashank G S

[1]Department of Condensed Matter Physics and Material Science, Tata Institute of Fundamental Research, Mumbai, India 400005

[2]Intermetallics and Nonlinear Optics Laboratory Department of Physics, National Institute of Technology (NIT), Tiruchirappalli, 620015, India

Email: sarang.joshi@tifr.res.in

Single crystals of 2-amino-3-nitropyridinium chloride (2A3NPCl) were grown by slow evaporation. X-ray diffraction confirmed a monoclinic non-centrosymmetric $P2_1$ structure. THz polarimetry (0.2–3 THz) verified birefringence and half-wave plate behavior near 0.8–1 THz ($\delta \approx \pi$), demonstrating its potential for THz polarization control.

2-amino-3-nitropyridinium chloride (2A3NPCl) is an organic nonlinear optical crystal grown via slow evaporation. X-ray diffraction confirms a monoclinic, non-centrosymmetric $P2_1$ structure, indicating its potential for polarization-dependent optical applications.

The polarization response of the crystal was investigated using a femtosecond laser-driven terahertz time-domain spectroscopy (THz-TDS) system over the frequency range of 0.2–3 THz, with electro-optic sampling using a ZnTe crystal[1]. A polarimetric configuration consisting of a fixed input polarizer, the sample, a rotating polarizer, and an analyzer was employed to probe the transmitted THz field.

Initial measurements confirmed birefringence[2] with a characteristic 90° symmetry. Subsequently, systematic polarimetric measurements were performed by rotating the polarization state from 0° to 360° for fixed sample orientations, followed by variation of the sample angle up to 90°. From the measured transmission data, optical parameters such as refractive index (n), extinction coefficient (k), permittivity (ε), and conductivity (σ) were extracted.

Further analysis yielded the polarimetric parameters a, b, and phase retardation δ. The contour profile of the amplitude ratio (b/a) as a function of frequency and polarization angle exhibits a distinct maximum near 0.8–1 THz around 45°, indicating strong polarization conversion. This corresponds to a phase difference of approximately π between orthogonal components, confirming that 2A3NPCl exhibits half-wave plate behavior in this frequency range.

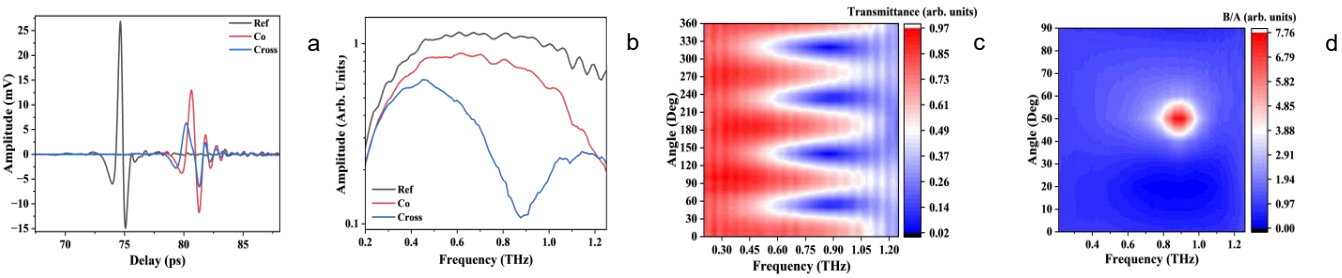


Fig 1: a) Time domain THz signal in co and cross configurations b) Frequency (THz) vs Amplitude in both the configurations c) contour of Transmittance wrt Angle(deg) at THz frequencies d) B/A contour wrt Angle(deg)

SSP acknowledges the support of the Department of Atomic Energy, Government of India, under Project Identification No. RTI4003.

References:

[1] Parkar, V., Haldankar, S., Narayan, M., Thamizhavel, A., Bhattacharya, A., & Prabhu, S. (2025, August). Terahertz Polarimetry of Nickel-Doped β-Ga_2O_3: Angle-dependent Resonance and Birefringence Studies. In *2025 50th International Conference on Infrared, Millimeter, and Terahertz Waves (IRMMW-THz)* (pp. 1-2). IEEE.

[2] Agarwal, S., Singh, A. K., Pramod, A., Faseela, F., Parkar, V., Haldankar, S., ... & Nagalakshmi, R. (2025). Comprehensive Terahertz Studies on Semi-organic 2-Amino-5-Nitropyridinium Chloride Crystal: Terahertz Generation and Birefringence. *Journal of Infrared, Millimeter, and Terahertz Waves*, *46*(10), 72.

Polarization-Independent All-Dielectric Metasurface-Based Ultra-Narrow Bandpass Filter in Telecom Band Regime

[1,#]*Chandan Kumar,* [2]*Debabrata Sikdar, and* [3] *Gagan Kumar*
[1]Department of Physics, Indian Institute of Technology Guwahati, Guwahati-781039 Assam, India
[2]Department of Electronics and Electrical Engineering, Indian Institute of Technology, Guwahati, Guwahati-781039 Assam, India
[3]*Department of Physics, Indian Institute of Technology Ropar, Punjab 140001, India*

[#]chandan.phy@iitg.ac.in

We propose a polarization-independent all-dielectric metasurface-based ultra-narrow bandpass filter operating in the telecom band. By exploiting guided mode resonance, the device exhibits high transmission, ultra-narrow linewidth, and excellent spectral selectivity. Moreover, its compact planar architecture offers a promising alternative to conventional multilayer interference filters for integrated photonic applications.

Ultra-narrow bandpass filters operating in the telecom band are crucial for numerous applications, including optical sensing, filtering, wavelength-division multiplexing (WDM), spectroscopy, and spectral imaging. However, most of the reported metasurface-based narrowband filters operate under a specific polarization of the plane-wave excitation, arising from the introduced in-plane asymmetry within the structure which limits their overall performance in applications. Also, there is a trade-off between resonance intensity and linewidth as asymmetry parameters vary. All-dielectric metasurfaces offer a low-loss and compact platform for realizing spectrally selective optical components. By leveraging this, we numerically demonstrate a polarization-independent ultra-narrow bandpass filter in the telecom band (1530-1565 nm) regime with wide out-of-band separation. The proposed metasurface comprises a periodically arranged array of silicon resonators with side-groove perturbations along all cardinal directions, exhibiting a sharp, high-Q resonance at 1552.4 nm with a full width at half-maximum of 1.9 nm. The optimized structure exhibits a narrow transmission passband with strong out-of-band suppression, indicating its suitability for wavelength-selective filtering applications. Furthermore, the meta-atom preserves in-plane C_{4v} symmetry, ensuring identical spectral responses for orthogonal linear x- and y-polarizations. Moreover, the device maintains high transmission under normal incidence, and this high-Q resonance can be passively tuned across the telecom band regime by scaling the meta-atom groove dimensions. Subsequently, the electric field distribution indicates strongly confined resonant trapped modes, resulting in a narrowband transmission formed by weakly radiating higher-order multipole oscillations. This ultra-thin device offers a promising solution for highly efficient spectral filters and could replace conventional thin-film interference filters.

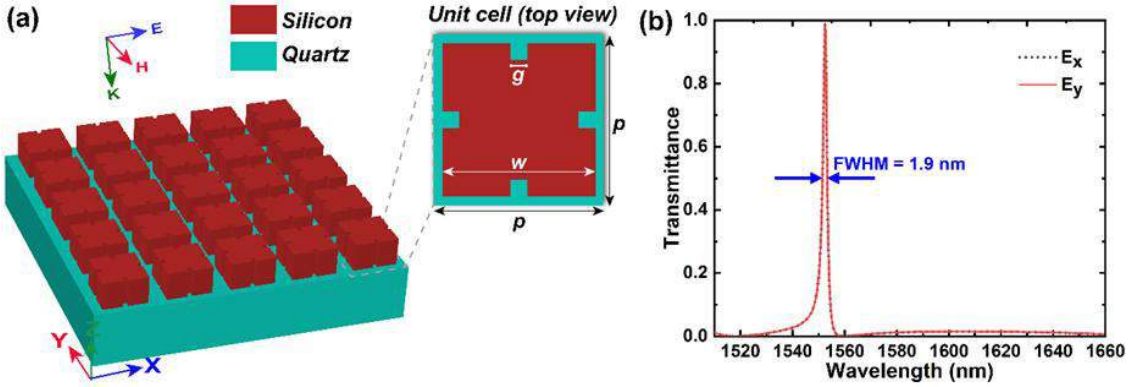


Figure 1: Schematic of metasurface design and transmission spectra exhibiting high-Q resonance within telecom band

References:

[1] Zheng, Ze, et al. "Planar narrow bandpass filter based on Si resonant metasurface." Journal of Applied Physics 130.5 (2021)
[2] Ng, Ryan C., et al. "Polarization-independent, narrowband, near-IR spectral filters via guided mode resonances in ultrathin a-Si nanopillar arrays." ACS Photonics 6.2 (2019)
[3] K. Koshelev, S. Lepeshov, M. Liu, A. Bogdanov, and Y. Kivshar. Asymmetric Metasurfaces with High-Q Resonanaces Governed by Bound States in the Continuum. Phys. Rev. Lett. 121,

Broadband Four-Winged Bowtie Metasurface for Passive Radiative Cooling through Enhanced Mid-Infrared Emissivity

Sanket Kumar, Praveen Chandra Pandey*

Department of Physics, Indian Institute of Technology (BHU), Varanasi, U.P 221005, India

* *Corresponding author, Email: - pcpandey.app@iitbhu.ac.in, Tel: - (+91)5427165473*

Abstract: *Passive daytime radiative cooling is demonstrated using a compact four-wing gold bowtie metasurface integrated with alternating TiO_2/SiO_2 dielectric layers. FDTD simulations reveal an average emissivity of **98%** within the 8-13 μm atmospheric window, corresponding to a theoretical net cooling power of approximately **105 W/m²**, highlighting its potential for energy-efficient thermal management.*

Passive daytime radiative cooling has emerged as an attractive solution for reducing energy consumption by dissipating thermal energy to the cold outer space through the atmospheric transparency window (8–13 μm). Conventional radiative coolers generally rely on thick multilayer dielectric coatings or complex photonic structures to achieve high emissivity and solar reflectance, making fabrication challenging. Metasurfaces provide an effective alternative because their resonant optical response can be engineered to achieve strong wavelength-selective thermal emission using compact nanostructures. In this work, a four-wing gold bowtie metasurface integrated with alternating TiO_2/SiO_2 dielectric layers is proposed to realize broadband infrared emissivity with a simplified multilayer architecture.

The proposed structure consists of a periodic four-wing bowtie resonator placed above alternating high- and low-refractive-index dielectric layers. The optical response was investigated using the finite-difference time-domain (FDTD) method in the wavelength range of 5–25 μm. The geometric dimensions of the bowtie and the thicknesses of the TiO_2/SiO_2 layers were optimized to maximize emissivity within the atmospheric transparency window. Strong electric-field localization in the nanoscale bowtie gaps excites multiple localized plasmonic resonances, while the dielectric multilayer provides efficient impedance matching between free space and the metasurface. The combined effect broadens the absorption bandwidth and enhances thermal emission over the desired infrared region.

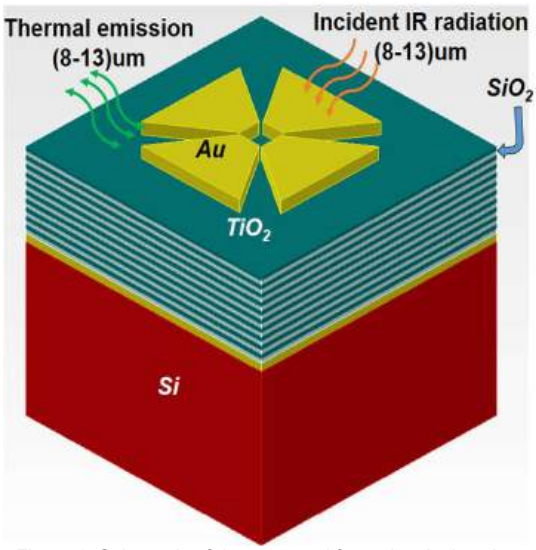


Figure 1: Schematic of the proposed four-wing Au bowtie metasurface supported by alternating TiO_2/SiO_2 dielectric layers on a silicon substrate.

The optimized metasurface exhibits an average absorptance (emissivity) of approximately **98%** across the 8–13 μm atmospheric window. At an operating temperature of **300 K**, the corresponding thermal emission is approximately **145 W m⁻²**, yielding a theoretical net radiative cooling power of approximately **105 W m⁻²** under ideal clear-sky conditions before considering solar absorption and non-radiative heat transfer. Compared with conventional multilayer radiative coolers requiring numerous dielectric layers, the proposed design achieves comparable cooling performance using a compact and fabrication-friendly architecture with reduced material consumption.

References:

[1] T. Feyisa, F. Tolessa, A. Belay, S. Asemare, G. Mathewos, J. Haji, *J. Opt.* **55** (2026) 1457–1469.
[2] T. Feyisa, A. Belay, F. Tolessa, et al., *Scientific Reports* **15** (2025) 43150.
[3] N. Pirouzfam, M.P. Menguc, K. Sendur, *Solar Energy Materials and Solar Cells* **253** (2023) 112225
[4] N. Pirouzfam, M.A. Kecebas, K. Sendur, *Optics Communications* **587** (2025) 131935

Transmittance Tunability in Topological Waveguide

[1]Santosh Kumar Nayak and [1,2] Akhilesh Kumar Mishra
[1]Department of Physics, Indian Institute of Technology Roorkee, Roorkee-247667, Uttarakhand, India
[2]Center for Photonics and Quantum Communication Technology, Indian Institute of Technology Roorkee, Roorkee-247667, Uttarakhand, India

santosh_kn@ph.iitr.ac.in, akhilesh.mishra@ph.iitr.ac.in

Topologically protected waveguides enable robust light transport at material edges. Although these waveguides are resistant to defects and bends, their transmittance depends on confinement characteristic of the waveguide. Here, we show that incorporating a thin graphene layer enhances transmittance and enables its tunability.

Several methods have been explored for valley photonic devices to control the transmittance. One of the such approaches is thermal tuning that uses integrated microheaters to change the silicon refractive index through the thermo-optic effect in silicon-based valley photonic crystals (VPC) [1]. Another approach is electrical tuning using liquid-crystal based valley photonic crystals (VPC), where an applied voltage changes the liquid crystal orientation, modifying the effective refractive index and light propagation in liquid-crystal based VPC [2]. Despite their effectiveness, these tuning methods have several limitations. Thermal tuning suffers from high power consumption, and thermal crosstalk issues, while liquid-crystal-based electrical tuning is constrained by polarization dependence, optical losses, fabrication complexity, and temperature sensitivity.

Graphene has emerged as a promising material for tunable photonic and optoelectronic applications due to its electrically controllable electronic band structure [3]. In bilayer and multilayer graphene, applying perpendicular electric field breaks the symmetry between the layers and opens a tunable band gap, enabling control over its optical and electronic properties [4].

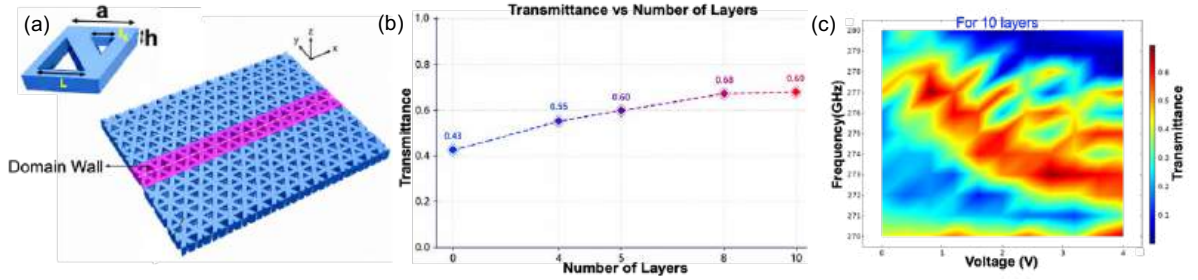


Figure 1 (a) Schematic picture of graphene coated TW (b) Variation of Transmittance with number of graphene layers (c) Transmittance tunability under external bias

Figure 1(a) shows the integration of a graphene layer at the interface of the topological waveguide. As shown in Figure 1(b), increasing the number of graphene layers from 2 to 10 enhances the transmittance by improving optical confinement and reducing edge-state leakage. Figure 1(c) demonstrates that an external bias tunes the operating frequency by modifying graphene's carrier concentration and refractive index [3].

In summary, in this work, we have demonstrated that incorporating graphene enhances the transmittance of the topological waveguide (TW). Furthermore, by applying an external bias, the transmittance was shown to be tunable over a frequency range a wide as 270–280 GHz. The proposed graphene-based tuning approach can also be extended to the development of other reconfigurable photonic devices, including tunable optical filters and optical switches.

Acknowledgement

S.K.N acknowledges support from GATE fellowship funded by the Ministry of Education, Government of India.

References:

[1] L.Sun et al. *Nanophtonics*, vol.13,issue 24. pp.4459-4470(2024)
[2] Y. Wang et al. *New Journal of Physics* 21 (2019)
[3] K.F. Mak et al. *Physical Review Letters* 102, 25405 (2009)
[4] E.V. Castro et al. *Physical Review Letters* 99, 216802 (2007)

An Orion-shaped Infrared Metamaterial Absorber for Greenhouse Gas Sensing Applications

Soorya P N, Ravi Varma M K, and N Yogesh*

Metamaterials and Photonic Structures Laboratory, Department of Physics, National Institute of Technology Calicut, Kozhikode - 673601, Kerala, India.

*yogesh@nitc.ac.in

Constellation-inspired geometries are innovative for the metamaterials (MTM) design. In this work, we have designed an Orion-shaped resonator with metallic strips for an MTM absorber at infrared frequencies. The proposed absorber shows 95% absorption efficiency at an IR frequency, making it useful for greenhouse gas sensing applications.

Metamaterials (MTM) in the Infrared regime find applications as sensors, filters, thermal imagers, and absorbers. The primary material structure of infrared absorbers can be a Metal-Dielectric-Metal/Metal-Insulator-Metal tri-layer stack or an all-dielectric metamaterial. We are focused on developing an IR absorber with a tri-layer stack of Metal-Dielectric-Metal. At Infrared frequencies, metal won't behave as a perfect conductor, unlike microwaves and radio waves. The plasma behavior of metal at IR frequencies can be modeled using the Drude model.

We have designed an IR MTM absorber using Orion-shaped metal patterns (Fig. 1(a)). The MTM absorber has three layers: a metallic ground plane (gold) modeled using the Drude model, an intermediate dielectric spacer (SiO_2), and a top metallic pattern consisting of an Orion-shaped resonator with metallic strips around it. The central patch geometry is a creative, constellation-inspired structure that resembles the classic stick-figure of the Orion constellation. Full-wave electromagnetic simulations are performed in CST Studio Suite to compute the absorbance of the proposed structure. It was found that the designed absorber has an absorption of 95.206% at the resonant frequency of 273.7607 THz (Fig.1(b)). We observed that the designed absorber can be used for greenhouse gas detection applications because greenhouse gases' absorption spectra lie in the IR range, and hence the shift in the resonance absorption frequency and the relative percentile change of the absorption for the presence of greenhouse gas species stuck on the IR MTM absorber are useful to sense different greenhouse gases.

1(a) 1(b)

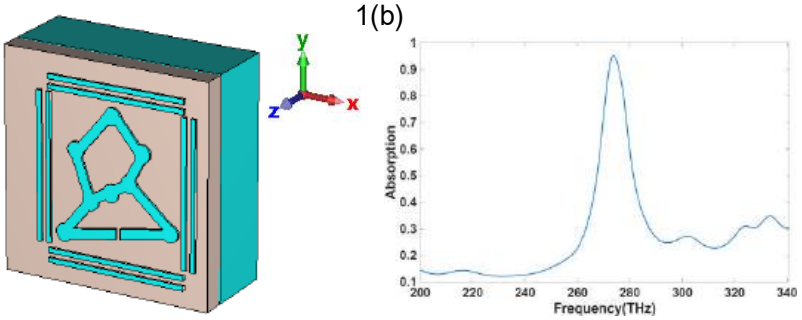


Fig.(1(a)): An Orion shaped resonator based IR absorber *Fig.(1(b)):Absorption Spectrum*

References:

[1] P.Wu et.al,*Results in Physics* 16(2020),102952.

[2] A.Hanif et al, *International Journal of optomechatronics,* ,18 (2024) 2299026

A Multipolar Decomposition Approach for Resonant Phase Control in All-Dielectric Metasurfaces

[1,#]Abhisek Roy, [1]Shanti Bhattacharya
[1]Department of Electrical Engineering, Indian Institute of Technology Madras, Chennai, India
[#]*ee25d012@smail.iitm.ac.in*

In this work, we use multipole decomposition of the scattered field from nanostructures acting as a unit building block (meta-atom) of a metasurface as an alternate method to calculate the resonant phase induced by an all-dielectric metasurface with varying radii. The result shows a high degree of similarity with the phase data obtained from finite element method (FEM) based simulations.

The resonance phase induced by a meta-atom is achieved by engineering its bulk properties like the array lattice (e.g., rectangular or hexagonal unit cells [1]) or the geometry. Obtaining an optimized shape through rigorous sweeping of the geometrical parameters without understanding the underlying physics makes the optimization a heuristic search rather than a systematic approach. In this work, we incorporate the multipole decomposition technique to obtain the resonant phase induced by individual meta-atoms by decomposing the scattered field which is different from its earlier applications in determining the polarization effects of multipole coupling on meta-atoms [2] and analyzing multi-resonant metasurfaces based on high-order multipole coupling [3].

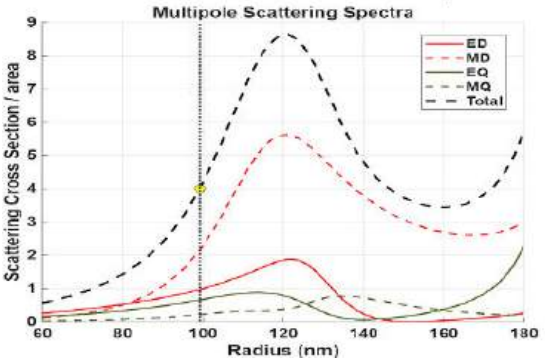


Fig. 1: The normalized scattering cross section with varying radius.

We model a cylindrical meta-atom of refractive index of 3.54 and determine its scattering cross section for different radius varied from 60 to 180 nm using analytical formulas. For a meta-atom illuminated by a normal incidence x-axis polarized "beam" and propagating along the z-axis, the complex transmitted field can be approximated as

$$t = 1 + \frac{(i\,k_s)}{(2S_L E_0 \varepsilon_0 \varepsilon_s)}\left(p_x + \frac{1}{v_s} m_y - \frac{i\,k_s}{6} Q_{xz} - \frac{i\,k_s}{2V_s} M_{yz} \cdots\right),$$

S_L is the unit cell area and E_0 is the electric field of the normally incident plane wave. ε_0 and ε_s are the permittivity of vacuum and medium, respectively. The terms p, m, Q and M are electric and magnetic dipole and quadrupole, respectively. The individual multipole moments were calculated using the expressions from the works by Alaee et al. [4]. A periodic boundary condition was defined across the unit cell. In the simulation, the analytical expression of the complex transmitted field was approximated up to the dipole terms.

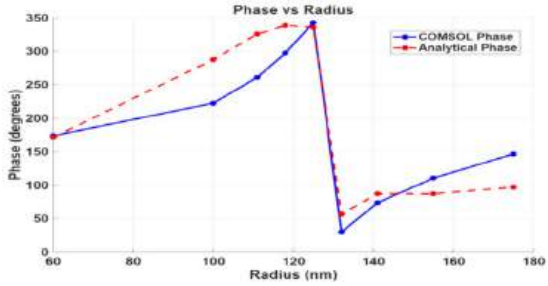


Fig. 2: The numerically (blue) and analytically (red) obtained phase induced by the unit cell of different radius.

The study shows that the phase profile obtained via FEM simulation closely aligns with the analytical results. From the analytical expression, it is evident that inclusion of higher order multipole terms will further reduce the disparity between the analytical and numerical data, representing a potential area for future study.

References:

[1] Zhang, Wenzhang, et al., IEEE access 8 (2020): 223797-223805.
[2] Zhu, Xiaosheng, et al., Optics Express 32.17 (2024): 30360-30379.
[3] Allayarov, Izzatjon, Andrey B. Evlyukhin, and Antonio Calà Lesina, Optics Express 32.4 (2024): 5641-5658.
[4] Alaee, Rasoul, Carsten Rockstuhl, and Ivan Fernandez-Corbaton, Optics Communications 407 (2018): 17-21.

Dielectric Chiral Metafoil Structures with Bisignate Circular Dichroism for Terahertz Waveband Applications

Siya Shahin Pallath[1] and N. Yogesh[2*]

[1]International School of Photonics, Cochin University of Science and Technology (CUSAT), Kochi - 682022, Kerala, India

[2]Metamaterials and Photonic Structures Laboratory, National Institute of Technology Calicut, Kozhikode-673601, Kerala, India

*yogesh@nitc.ac.in

A 3-D chiral metallic metafoil structure was previously reported. In this work, we numerically investigate all-dielectric chiral metafoils. A chiral metafoil formed by glass exhibited a bisignate circular dichroism of −0.73 at 2.4664 THz and +0.69 at 2.7796 THz, demonstrating its potential for frequency-selective THz polarization control and chiral sensing.

Imparting chirality has led to significant advancements in the THz regime owing to its ability to selectively transmit circularly polarized (CP) light. There has been tremendous evolution in chiral metamaterial architectures – from complex 3D helical and twisted structures to planar, substrate–free, free–standing metafoil configurations – that have enabled broadband circular dichroism (CD) with high extinction ratios [1]. Most existing chiral metafoils are metallic, which introduces ohmic losses and limits their potential for low-loss THz applications.

The geometry reported in [1] was adopted and investigated for different dielectric permittivities using CST Microwave Studio. Among the materials studied, MgO ($\varepsilon_r = 9.5$) exhibited the highest circular dichroism magnitude of approximately -0.8 at 2.0 THz, although without a distinct bisignate response. In contrast, a glass – like dielectric with ($\varepsilon_r = 5.5$) produced a clear bisignate circular dichroism spectrum, with extrema of -0.73 at 2.4664 THz and +0.69 at 2.7796 THz. The two lobes are separated by 0.313 THz with an intermediate zero – crossing frequency between them.

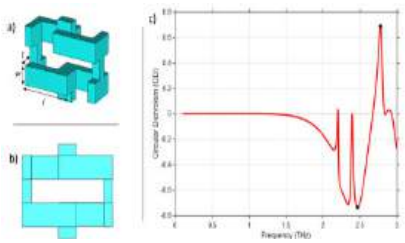


Fig. 1. (a) Three-dimensional view and (b) front view of the dielectric chiral metafoil unit cell with structural parameters l = 90 µm, w = 30 µm, and t = 17 µm, adapted from [1]. (c) Circular dichroism (CD = $|T_{++}|^2 - |T_{--}|^2$) of the glass (ε_r = 5.5) metafoil, exhibiting a bisignate response

To understand the origin of the observed behavior, electric field distributions corresponding to the CD extrema were analyzed. Different field localization patterns were observed for the two circular polarization states at resonance, leading to unequal transmission of LCP and RCP waves. Since the proposed structure is entirely dielectric, Ohmic losses associated with metallic metafoils are eliminated. This suggests potential applications as a frequency-switchable THz circular polarizer and as a chiral sensor based on the shift of the zero-crossing frequency between the lobes.

References:

[1] J. Wu, B. Ng, H. Liang, M.B.H. Breese, M. Hong, S.A. Maier, H.O. Moser, O. Hess, *Physical Review Applied* 2 (2014) 014005.

[2] Y. Zou, D. Wang, I. Afzal, D. Kong, R. Wang, T. Ma, *Optics and Lasers in Engineering* 196 (2026) 109456.

[3] S. Wang, H. Kuang, W. Li, Y. Wang, H. Luo, C. Li, H. Ge, Q. Wang, B. Jia, *Nanomaterials* 14(11) (2024) 979.

High-temperature photothermal conversion using a selective refractory metamaterial absorber for efficient solar energy harvesting

[1]Neha Singh, [2,#]Prof. P. C. Pandey
[1,2]Department of Physics, Indian Institute of Technology (Banaras Hindu University), 221005, India
[#]*email id:* pcpandey.app@iitbhu.ac.in

This work demonstrates a thermally robust, polarisation-insensitive metamaterial absorber that achieves near-unity absorption across the entire solar spectrum (200–2500 nm), thereby addressing spectral mismatch and radiative losses to enhance solar energy harvesting efficiency.

Solar energy has emerged as one of the most promising solutions for a sustainable energy transition. PV cells represent the most mature technology for solar energy conversion. However, due to spectral mismatch losses, they absorb only a limited wavelength range defined by their bandgap, thereby restricting their theoretical efficiency to the Shockley–Queisser limit (~30%) [1]. To enhance conversion efficiency, Swanson proposed a system incorporating a concentrator that focuses sunlight onto a high-temperature refractory radiator, which then emits thermal radiation toward a silicon PV cell, achieving 26% conversion efficiency. With optimised design, this efficiency can be further increased to 40–50%.

However, for effective operation, the system requires a spectrally selective absorber/emitter. In contrast, metamaterial absorbers offer a compelling alternative by enabling near-unity broadband absorption and tailored thermal emission for efficient Solar–thermal energy conversion [2,3].

Here, we propose a selective refractory metamaterial absorber (SRMA) with a three-layer structure (TiN-Si_3N_4-W). Simulation results demonstrate a weighted-average absorption efficiency of 96.70% under AM 1.5 solar illumination over the wavelength range 200-2500 nm using the Finite Element Method (FEM). To further assess its photovoltaic potential application, the short-circuit current density (J_{sc}) at different angles of incidence is evaluated for a solar cell configuration incorporating the proposed absorber, yielding an optimal value of 37.57 mA/cm^2. The proposed absorber exhibits a low emission of 9.7% at 375 K while sustaining high emission at elevated temperatures. It also demonstrates a photothermal conversion efficiency above 90% over a broad temperature range of 200-1200 K under high solar concentration.

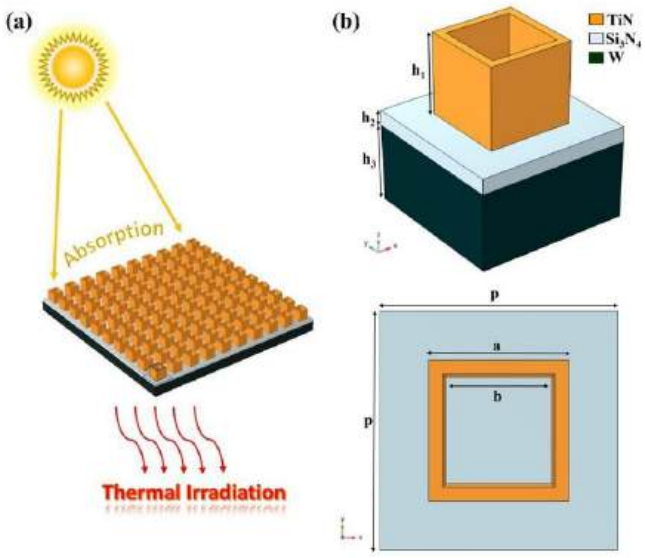


Fig. 1. (a) 3D periodic representation of the proposed metamaterial absorber. (b) a perspective view of the unit cell and (c) the top view of the unit cell

At the same time, the design is thermally stable, polarisation-insensitive, and angle-insensitive up to 60 ◦ across all polarisation states. These characteristics highlight the intrinsic spectral selectivity of the proposed absorber, making it a promising candidate for applications ranging from moderate-temperature solar thermal energy harvesting to high-temperature solar thermophotovoltaic (STPV) systems

References:

[1] W. Shockley, H. Queisser, Renewable Energy, vol. 2, Routledge, 2018, pp. 35–54.

[2] P. Wu, S. Dai, X. Zeng, N. Su, L. Cui, H. Yang , International Journal of Thermal Sciences 183 (2023) 107890.

[3] R. Kumar, R. Gupta, A.K. Mishra, N. Singh, P.C. Pandey, B.K. Singh, Plasmonics 20 (9), 7477-7494.

Four-Fold Symmetric Metasurface for Dual-Band Terahertz Near-Perfect Absorption

Riya Soni [1], Richa Sharma [2] and Kamal Kishor [1,*]

[1]TIFAC-Center of Relevance and Excellence in Fiber Optics and Optical Communication, Department of Applied Physics, Delhi Technological University, Delhi, 110042, India
[2]Department of Applied Physics, Delhi Technological University, Delhi, 110042, India

Coresponding Author email :- kishorkamal1@rediffmail.com

We propose a dual-band terahertz metamaterial absorber built on a copper–FR4–copper metal-insulator-metal structure. The four-fold symmetric resonator produces near-perfect absorption at two resonances, 7.4775 THz and 7.6225 THz, reaching a maximum absorptance of 0.9998. These characteristics make the design attractive for biosensing, terahertz sensing, and narrowband filtering.

The proposed metasurface absorber adopts a metal-insulator-metal (MIM) configuration with a copper resonator forming the top layer, FR4 acting as the dielectric substrate, and a copper ground plane, as shown in Figure 1. The geometrical parameters of the proposed structure are as follows: t_m denotes the thickness of the metallic layers, t_d is the thickness of the dielectric spacer (FR4), and P_x and P_y represent the periodicities of the unit cell along the x and y directions. All simulations were performed using the finite-element method in COMSOL.

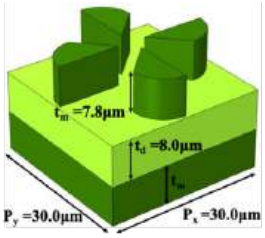


Figure 1. 3D side view

We examined the absorption response of the proposed structure across the terahertz band. The absorber exhibits two near-perfect absorption peaks at 7.4775 THz and 7.6225 THz with a maximum absorptance of 0.9998, as shown in Figure 2. This near-perfect absorption arises from the excitation of localized electromagnetic resonances and effective impedance matching between the metasurface and free space. The obtained results indicate the suitability of the proposed absorber for terahertz sensing and filtering applications. [1][2][3].

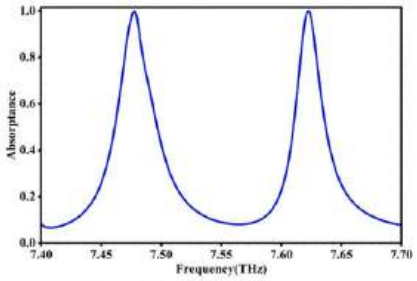


Figure 2. Absorption variation response

Conclusion

We have numerically demonstrated a dual-band terahertz metasurface absorber that achieves near-perfect absorption at 7.4775 THz and 7.6225 THz. The simple geometry, low-cost materials, and strong absorption characteristics make the proposed absorber a promising candidate for terahertz sensing and filtering applications.

Acknowledgment

Authors gratefully acknowledge the initiatives and support from the TIFAC-Centre of Relevance and Excellence in Fiber Optics and Optical Communication at Delhi College of Engineering, now DTU, Delhi, under the Mission REACH program of Technology Vision-2020, Government of India.

References

[1] W. Withayachumnankul, D. Abbott, Metamaterials in the terahertz regime, IEEE Photonics J. 1 (2009) 99–118. https://doi.org/10.1109/JPHOT.2009.2026288.

[2] S. Anwar, Dual-band detection based on metamaterial sensor at terahertz frequency, Opt. Rev. 30 (2023) 300–309. https://doi.org/10.1007/s10043-023-00808-w.

[3] J. Zhao, L. Zhang, H. Liang, Advances in Metasurface-Based Terahertz Sensing, Adv. Phys. Res. 3 (2024). https://doi.org/10.1002/apxr.202400077.

Graphene-Embedded all-dielectric metamaterial absorber

[1,#]Praveen Kumar Vishwakarma,[2]Raghwendra Kumar
Department of Physics, Patna University, Patna, Bihar-800005

[#]*Corresponding author e-mail address: pk31825@gmail.com*

A graphene-embedded all-dielectric metamaterial absorber is proposed for near-infrared refractive index sensing. It exhibits near-perfect absorption at 835.47 nm with a full width at high maxima (FWHM) of 19.96 nm, achieving a sensitivity of 560 nm/RIU and a figure of merit of 28, demonstrating excellent potential for high-performance optical sensing.

Metamaterial absorbers are engineered structures capable of controlling and absorbing electromagnetic waves with high efficiency. Through subwavelength resonant design, near-perfect absorption can be achieved, enabling applications in sensing, imaging, energy harvesting and photonic devices [1].

Metal-based absorbers exhibit strong plasmonic responses but suffer from optical losses, limiting their efficiency and resonance sharpness. Dielectric metamaterials overcome these limitations by providing low-loss electromagnetic confinement, resulting in improved quality factors, stable resonance characteristics, and better photonic integration [2,3]. Graphene, with its exceptional electrical, optical, and thermal properties, has emerged as a promising material for tunable photonic applications. Its adjustable surface conductivity enables dynamic control of light–matter interactions, while its high mobility and fabrication compatibility enhance the performance of graphene-integrated dielectric metamaterials for sensing applications [4,5].

In this work, a graphene-embedded all-dielectric metamaterial absorber is proposed for near-infrared refractive index sensing. The structure consists of periodically arranged silicon plus-shaped resonators placed on a graphene monolayer, supported by a silicon substrate. Simulations are performed using CST Microwave Studio under periodic boundary conditions, and absorptance is calculated using the relation, $A(\omega) = 1 - R(\omega) - T(\omega)$, where R(ω) is reflectance and T(ω) is the transmittance.

The optimized structure exhibits a narrow absorption resonance at 835.47 nm with nearly perfect absorption efficiency. The proposed absorber achieves a sensitivity of 560 nm/RIU and a figure of merit of 28. It can also differentiate various alcohols and hydrocarbon-based fuels through resonance wavelength shifts, demonstrating its potential for compact and highly sensitive optical sensing applications.

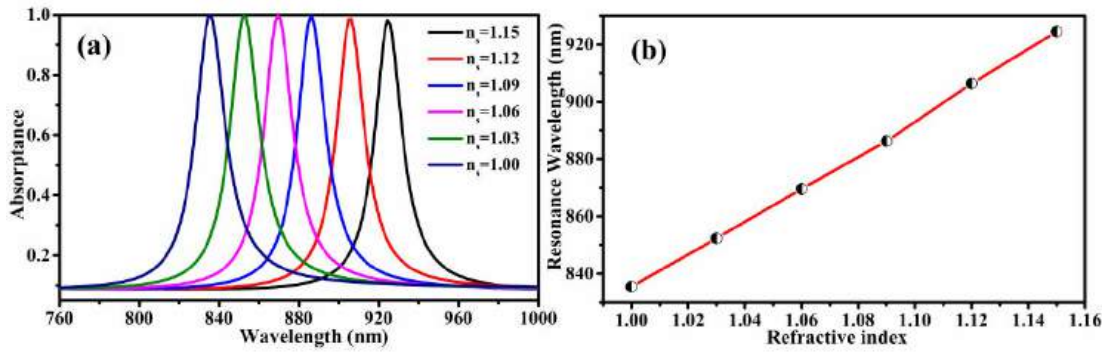


Fig.: (a) Absorptance spectra of the metamaterial absorber for different refractive index of the surrounding medium (n_s), and (b) Resonance wavelength as a function of refractive index of the surrounding medium (n_s).

References:

[1] N.I. Landy, S. Sajuyigbe, J.J. Mock, D.R. Smith, W.J. Padilla, Phys. Rev. Lett. 100 (2008) 207402.
[2] A.I. Kuznetsov, A.E. Miroshnichenko, M.L. Brongersma, Y.S. Kivshar, B. Luk'yanchuk, Science (1979). 354 (2016).
[3] M. Rahmani, B. Luk'yanchuk, M. Hong, Laser Photon. Rev. 7 (2013) 329–349.
[4] A.K. Geim, K.S. Novoselov, Nat. Mater. 6 (2007) 183–191.
[5] A. Kumar, P.K. Vishwakarma, R. Kumar, L. Jiang, Phys. Scr. 100 (2025) 115506.

Broadband Visible Region Absorber Using Dual-Shaped Tungsten Resonator Metasurfaces

[1,#]Rakesh Kumar, [2]Monica Pradhan, [3]Shubhanshi Sharma and [1]Shailendra Kumar Varshney
[1]Electronics and Electrical Communication Engineering, Indian Institute of Technology Kharagpur
[2]School of Nanoscience and Technology, Indian Institute of Technology Kharagpur
[3]Institute of Physics, Leibniz University Hannover, Germany

[#] *rakesh.raj091@gmail.com*

The proposed tungsten–SiO_2–tungsten multi-resonator metasurface provides a compact and robust platform for broadband visible-light absorption. Multiple resonant modes, effective impedance matching, and zero transmission collectively enable near-perfect absorption. These features make the design highly suitable for optical stealth, infrared suppression, thermophotovoltaic systems, advanced photonic devices, and high-temperature optical absorber applications.

A perfect absorber (PA) is an engineered electromagnetic structure that absorbs nearly all incident electromagnetic energy at selected wavelengths by minimizing both reflection and transmission. In visible-region applications, perfect absorbers have attracted considerable attention for optical camouflage, stealth technology, thermal emitters, photodetectors, photovoltaic systems, and sensing applications [1-3].

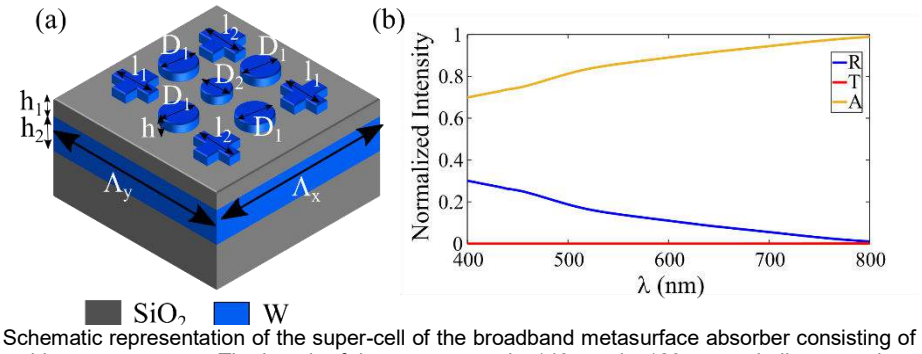


Figure 1: (a) Schematic representation of the super-cell of the broadband metasurface absorber consisting of nine resonant elements placed in a square array. The length of the crosses are l_1=140 nm, l_2=120 nm and all crosses have identical arm widths w = 50 nm, h_1 = 60 nm, h_2 = 150 nm, $\Lambda_x = \Lambda_y$ = 400 nm. The diameters of the circles are D_1=100nm, D_2=80 nm (b) Simulated reflectance, transmittance, and extinction spectra at normal incidence.

The proposed absorber consists of a metal–insulator–metal (MIM) configuration comprising an array of multiple tungsten (W) resonators on the top surface, a silicon dioxide (SiO_2) dielectric spacer, and a continuous tungsten ground plane. The upper metasurface consists of nine tungsten resonators of different geometrical dimensions arranged periodically within a single unit cell. Each resonator supports localized surface plasmon resonances (LSPRs) at different wavelengths. The variation in resonator dimensions produces multiple resonance modes that overlap within the visible spectrum, thereby significantly broadening the absorption bandwidth.The unit cell metasurface is shown in Figure 1. The periodicity of the unit cell is selected as 400 nm to ensure subwavelength operation throughout the visible spectrum. The thickness of resonators, spacer and ground plane is 50nm, 60nm and 100nm respectively. The intermediate SiO_2 spacer electrically isolates the resonators from the metallic ground plane while enabling strong magnetic resonance. The bottom tungsten layer is designed with thickness much greater than its optical skin depth, ensuring zero transmission throughout the visible region. Consequently, all incident optical energy entering the structure is confined within the resonator-spacer cavity and dissipated through dielectric and metallic losses, enabling absorption exceeding 90% over a broad wavelength range in the visible region (400 – 800 nm).

References:

1. Xinyu Liu, Kebin Fan, Ilya V. Shadrivov, and Willie J. Padilla, “Experimental realization of a terahertz all-dielectric metasurface absorber,” Opt. Express, 25(1), 191, (2017).
2. Gleb M. Akselrod, Jiani Huang, Thang B. Hoang, Patrick T. Bowen, Logan Su, David R. Smith, and Maiken H. Mikkelsen, “Large-Area Metasurface Perfect Absorbers from Visible to Near-Infrared,” Advanced materials, 27(48), 8028-8034, (2015).
3. Rasoul Alaee, Mohammad Albooyeh, and Carsten Rockstuhl, “Theory of metasurface based perfect absorbers,” Journal of Physics D: Applied Physics, 50(50), 503002, (2017).

Coherence control in Young's two-pinhole interferometer with incoherent electromagnetic fields

[1,#]Rajneesh Joshi
[1]Department of Physics, Government Degree College Danya, Almora, Uttarakhand, India
[#]*rajneeshjoshi077@gmail.com*

We theoretically demonstrate that the electromagnetic degree of coherence (EM DoC) can be modulated when spatially incoherent light is incident on a Young's two-pinhole interferometer. It is observed that the EM DoC depends on the degree of polarization at the pinholes as well as on the positions of the observation points. This is consistent with the van Cittert-Zernike theorem.

The interference of electromagnetic (EM) fields in a Young's two-pinhole interferometer depends on the correlation of the fields at the two-pinholes. In the space-frequency domain, the correlation properties are characterized by the coherence (two-point) Stokes parameters, defined as

$$S_n(\boldsymbol{\rho}_1, \boldsymbol{\rho}_2, \omega) = Tr[W_{jk}(\boldsymbol{\rho}_1, \boldsymbol{\rho}_2, \omega).\sigma_m],\ [n=0,1,2,3], \tag{1}$$

where, Tr denotes the trace, σ_m represents the unit matrix $(m = 0)$ and the Pauli spin matrices $(m = 1,2,3)$. Furthermore, $W_{jk}(\boldsymbol{\rho}_1, \boldsymbol{\rho}_2, \omega) =< E_j^*(\boldsymbol{\rho}_1, \omega)E_k(\boldsymbol{\rho}_2, \omega) >$, $(j,k = x,y)$,denotes the elements of the cross-spectral density matrix.

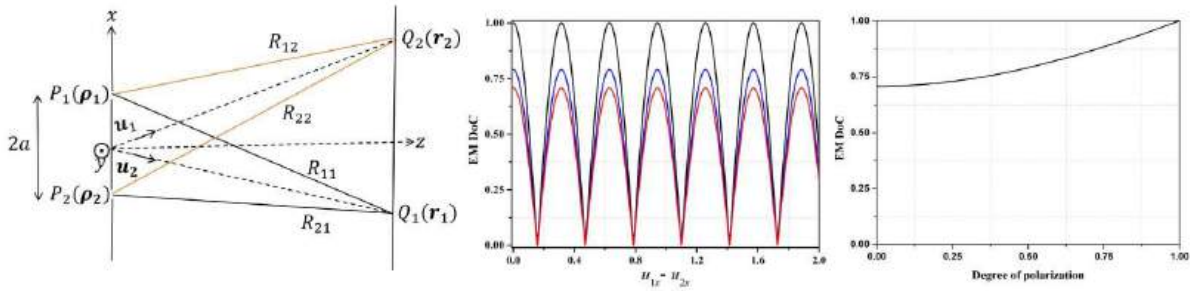


Fig. 1: Left: Schematic of Young's two-pinhole interference for two EM fields. Here, $2a$ denotes the pinhole separation, and $\boldsymbol{u}_1$ and $\boldsymbol{u}_2$ are unit vectors directed along $\boldsymbol{r}_1$ and $\boldsymbol{r}_2$, respectively. Middle: Variation of the EM DoC w.r.t. the difference between the x-components of the unit vectors. Right:Variation of the EM DoC w.r.t. to the degree of polarization at the pinholes.

For same spatial points, i.e., $\boldsymbol{\rho}_1 = \boldsymbol{\rho}_2 = \boldsymbol{\rho}$, the coherence Stokes parameters reduce to the polarization (one-point) Stokes parameters. In EM interference, the overall visibility depends on the visibilities associated with the modulation of all polarization Stokes parameters, $V_n(\omega) = |\eta_n(\boldsymbol{\rho}_1, \boldsymbol{\rho}_2, \omega)| = |S_n(\boldsymbol{\rho}_1,\boldsymbol{\rho}_2,\omega)/\sqrt{S_0(\boldsymbol{\rho}_1,\omega)S_0(\boldsymbol{\rho}_2,\omega)}|$. The EM DoC, which is equivalent to the electromagnetic visibility, quantifies the extent of coherence and is defined as

$$\eta^2(\boldsymbol{\rho}_1, \boldsymbol{\rho}_2, \omega) = 1/2 \sum_{n=0}^{n=3} |\eta_n(\boldsymbol{\rho}_1, \boldsymbol{\rho}_2, \omega)|^2. \tag{2}$$

The electric field vector at the observation plane can be expressed as

$$\boldsymbol{E}(\boldsymbol{r}, \omega) = K_1\boldsymbol{E}(\boldsymbol{\rho}_1, \omega)\, e^{ikR_1}/R_1 + K_2\boldsymbol{E}(\boldsymbol{\rho}_2, \omega)\, e^{ikR_2}/R_2. \tag{3}$$

By substituting $R_{mn} \approx r_n - \boldsymbol{\rho}_m.\boldsymbol{u}_n$, $(m,n = 1,2)$, and Eq. (3) into Eq. (1), we obtain the parameters as

$$S_n(\boldsymbol{r}_1, \boldsymbol{r}_2, \omega) = |K|^2/R^2\, e^{ik(r_2-r_1)}[S_n(\boldsymbol{\rho}_1, \boldsymbol{\rho}_1, \omega)e^{ika(u_{1x}-u_{2x})} + S_n(\boldsymbol{\rho}_2, \boldsymbol{\rho}_2, \omega)e^{-ika(u_{1x}-u_{2x})} + S_n(\boldsymbol{\rho}_1, \boldsymbol{\rho}_2, \omega)e^{ika(u_{1x}+u_{2x})} + S_n(\boldsymbol{\rho}_2, \boldsymbol{\rho}_1, \omega)e^{-ika(u_{1x}+u_{2x})}], \tag{4}$$

$$\eta_n(\boldsymbol{r}_1, \boldsymbol{r}_2, \omega) = e^{ik(r_2-r_1)}\frac{S_n(\boldsymbol{\rho}_1,\omega)e^{ika(u_{1x}-u_{2x})}+S_n(\boldsymbol{\rho}_2,\omega)e^{-ika(u_{1x}-u_{2x})}}{S_0(\boldsymbol{\rho}_1,\omega)+S_0(\boldsymbol{\rho}_2,\omega)},\ \eta^2(\boldsymbol{r}_1, \boldsymbol{r}_2, \omega) = 1/2\,[1 + (P_1+P_2)^2/4\,]. \tag{5}$$

Therefore, the EM DoC depends only on the input degree of polarization when $u_{1x} = u_{2x}$.

References:

[1] G.S. Agarwal, A. Dogariu, T.D. Visser, E. Wolf, Optics Letters 30 (2005) 120.
[2] T. Setala, J. Tervo, A. T. Friberg, Optics Letters 31 (2006) 2669.
[3] D. Kumar, R. Joshi, Gyaprasad, H. K. Singh, N.S. Bisht, Optics Communications 600 (2026) 132706.

High-Q Silicon Carbide Ring Resonator for Purcell-Enhanced Emission from Erbium Defect Centers at Telecom Wavelengths

[#]Mansoor Ahmed, Faisal Ishaq, and Faraz Ahmed Inam

Department of Physics, Aligarh Muslim University, Aligarh–202002, Uttar Pradesh, India

[#]mansoorahmed8261@gmail.com

We numerically study a silicon carbide (SiC) ring resonator coupled to a bus waveguide for integrated photonic applications. The resonator shows sharp transmission dips due to strong light confinement. A dipole emitter placed inside experiences enhanced spontaneous emission with a high Q-factor, demonstrating potential for quantum and photonic devices.

Silicon carbide (SiC) is a promising material for integrated photonic devices because of its high refractive index, low optical loss, wide transparency window, and compatibility with quantum emitters. SiC ring resonators can strongly confine light through total internal reflection and support enhanced light-matter interactions. Building on these properties, we investigate a SiC ring resonator coupled to a straight bus waveguide and evaluate its ability to confine light and enhance spontaneous emission.

As shown in **Fig. (a)**, the optimized geometry consists of a ring width (RW) of 1 μm, a waveguide width (WW) of 0.5 μm, a ring diameter (D) of 60 μm, and a uniform thickness (t) of 0.5 μm. The optical resonance condition determines the ring resonator's resonant wavelengths, as given by [1].

$$L\, n_{eff} = m\, \lambda_{res} \qquad (1)$$

where L is the optical path length of the ring, n_{eff} is the effective refractive index of the guided mode, m is the resonance order, and λ_{res} is the resonance wavelength.

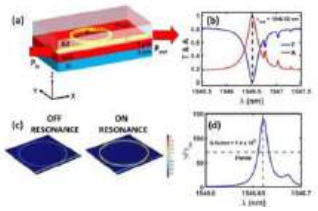


***Fig: (a)** Schematic of the SiC ring resonator coupled to a bus waveguide. **(b)** Simulated transmission and absorption spectra. **(c)** Simulated electric-field profiles showing weak coupling off resonance and strong coupling at resonance. **(d)** Purcell factor spectrum for an x-oriented dipole inside the resonator.*

Light enters the bus waveguide and travels toward the output port. At resonance, light couples efficiently into the ring and circulates inside it, creating a strong optical field. This reduces the transmitted power and produces sharp dips in the transmission spectrum. As shown in **Fig. (b)**, the resonance occurs at 1546.52 nm. **Fig. (c)** shows the simulated electric field profiles of the coupled waveguide-resonator system under off-resonance (left) and on-resonance (right) conditions, demonstrating strong optical confinement and field enhancement at the resonant wavelength.

To study light-emitter interaction, an x-oriented electric dipole was placed at the position of maximum electric field inside the ring resonator. The Purcell factor [2], shown in **Fig. (d)**, reaches about 142 times near the resonance wavelength, indicating strong coupling between the dipole and the resonant mode. This enhancement is due to the strong field confinement and low losses of the SiC cavity, which has a high Q-factor of ~1.4×10^5 [3].

In conclusion, the SiC ring resonator provides strong light confinement and enhances spontaneous emission. A resonance at 1546.52 nm and a maximum Purcell factor of about 142 were achieved. These results show its potential for integrated and quantum photonic applications [4].

Acknowledgement:

All authors would like to acknowledge the financial support provided by the DST-FIST grant.

References:

[1] A.K. Ghatak, K. Thyagarajan, *Optical Electronics*, Cambridge University Press, Cambridge (1989).
[2] L.C. Venuti, T. Albash, D.A. Lidar, P. Zanardi, *Physical Review A* 93 (2016) 032118.
[3] S. Sunder, A. Sharma, *Workshop on Recent Advances in Photonics, (WRAP 2019)* 19 (2019).

Effects of Anisotropic Atmospheric Turbulence on the Polarization Stability of C-Point and V-Point Vector Beams

Sagar[1] , Sanjay Kumar Mishra[3] and Akhilesh Kumar Mishra[1,2*]

[1]*Centre for Photonics and Quantum Communication Technology, Indian Institute of Technology Roorkee, Roorkee-247667, Uttarakhand, India*

[2]*Department of Physics, Indian Institute of Technology Roorkee, Roorkee-247667, Uttarakhand, India*

[3]*Adaptive Optics Group, Instruments Research and Development Establishment, Dehradun-248008, India*

Author e-mail address: sagar@cpqct.iitr.ac.in, akhilesh.mishra@ph.iitr.ac.in

Abstract: Vector beams carrying C-type and V-type polarization singularities are highly sensitive to atmospheric turbulence. This study examines the effects of anisotropic turbulence on Laguerre-Gaussian (LG) and circular airy vector (CAV) beams under vertical, slant, and horizontal propagation. Intensity evolution and spatial degradation are analyzed, while polarization behavior is evaluated using Stokes parameters and Poincaré sphere representation. Simulations show stronger depolarization for slant and horizontal paths, highlighting the importance of vectorial polarization analysis in realistic atmospheric conditions.

Structured vector beams carrying polarization singularities have attracted considerable interest for free-space optical (FSO) communication and advanced photonic applications due to their spatial-polarization coupling and enhanced information capacity. However, their performance is strongly influenced by atmospheric turbulence, particularly under an-isotropic conditions commonly encountered in ground-to-air links. While scalar beam propagation has been widely studied, a systematic analysis of vector beams with C-point (lemon) and V-point (azimuthal) singularities in an-isotropic turbulence remains limited. This work numerically investigates the propagation characteristics of LG and CAV beams along vertical, slant, and horizontal transmission paths in an-isotropic atmospheric turbulence. The propagation model is based on the angular spectrum method combined with a modified Von Kármán phase-screen[1] approach to simulate turbulence-induced refractive index fluctuations. The complex field evolution is described by

$$U(x, y, z + \Delta z) = \mathcal{F}^{-1}\{\mathcal{F}\{U(x, y, z + \Delta z) exp(exp[i\phi(x, y)])\} exp(-ik_z \Delta z)\}. \quad (1)$$

The aperture-averaged scintillation index (SI) is evaluated to measure intensity fluctuations with propagation distance [2]. Results indicate increasing scintillation and depolarization from vertical to horizontal paths, with LG beams exhibiting stronger fluctuations than circular Airy beams under an-isotropic turbulence.

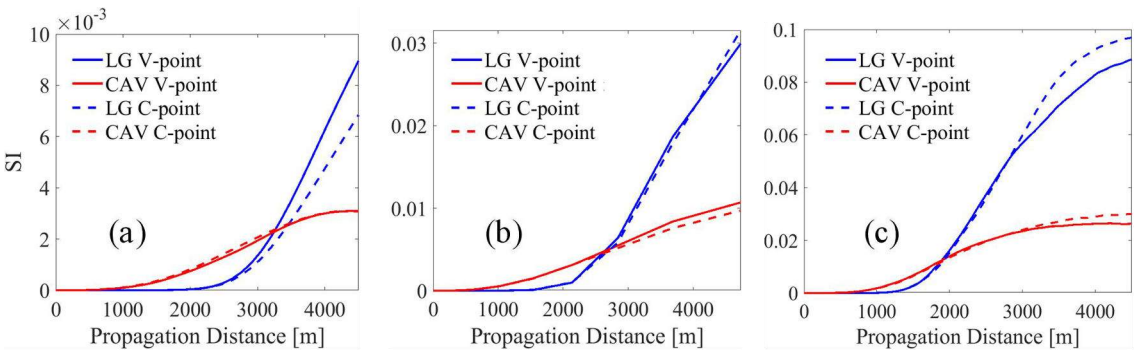


Fig. 1: The Variation of aperture averaged SI with propagation distance for LG and CAV beams, which carry C-point and V-point singularities, is analyzed after propagating through an-isotropic turbulence along uplinks paths. (a-c) corresponds to vertical, slanted and horizontal paths.

Conclusion: The results highlight the necessity of full vectorial modeling for realistic atmospheric analysis and indicate that CAV beams with C-point singularities offer improved robustness for long-distance FSO communication systems operating in an-isotropic turbulence.

[1] Khare *et. al.* "Orbital Angular Momentum States of Light" 1st ed. (*Bristol UK: IOP Publishing* 2020*)*

[2] S. Singh et. al. "Ring Pearcey vortex beam dynamics through atmospheric turbulence" J. Opt. Soc. Am. B (2023) 40 9

High Photon Pair Generation Rate in SiN Microring Resonator for O-Band Photonic Integrated Circuit

[#1]Jayeta Banerjee, [1]Suman Dey, [1]Soumyadip Mukherjee, [1]Pramod Watekar and [1]Shailendra K. Varshney
[1]Department of Electronics and Electrical Communication Engineering, Indian Institute of Technology, Kharagpur 721302, India
[#]*Email: j.banerjee87@yahoo.com*

The 1310 nm air-cladded SiN MRR serves as a promising integrated quantum photon source enabled by cavity-enhanced spontaneous four-wave mixing. With strong optical confinement, engineered dispersion, the device achieves a photon-pair generation rate in the order of 10^7 pairs/s, providing a pathway towards fiber-compatible entangled photon sources for quantum communication.

Silicon nitride (SiN) microring resonators (MRRs) have emerged as a promising platform for integrated quantum photon-pair generation benefiting from low optical loss, CMOS-compatible fabrication, and strong nonlinear response [1]. In this work, we present an air-cladded, dispersion-engineered SiN MRR specially designed for spontaneous four-wave mixing (SFWM) photon-pair generation in the O-band (~1310 nm), a wavelength regime that has received relatively limited attention compared with conventional telecom C-band quantum sources. The air-cladded configuration enables strong optical confinement and reduced effective mode area, enhancing nonlinear interaction strength while providing flexibility for dispersion engineering. The proposed SiN MRR consists of a 400 nm × 1200 nm waveguide cross-section, a radius of 60 μm, and an FSR of 350 GHz, optimized for phase-matched photon-pair generation near 1310 nm. The SFWM process is modeled by incorporating cavity enhancement, Kerr nonlinear interaction, and dispersion-induced phase matching. The resonator parameters include a group index of n_g=2.25, intrinsic loss of 0.5 dB/cm, effective mode area of 0.5 μm^2, SiN nonlinear index of $n_2=2.6\times10^{-19}$ m^2/W, and pump power of 5 mW. The calculated joint spectral intensity (JSI) [2], represented in the signal–idler resonance mode basis, describes the mode-resolved photon-pair correlations, while the photon-pair generation rate (PGR) evaluates the SFWM efficiency by considering cavity quality factors and dispersion-dependent phase matching [3]. The PGR reaches approximately 10^7 pairs/s for the 350 GHz FSR configuration and decreases with increasing mode index due to accumulated dispersion-induced phase mismatch. These results provide insight into the spectral correlation and generation efficiency of an O-band dispersion-engineered SiN MRR, indicating its potential as a fiber-compatible integrated entangled photon pair source.

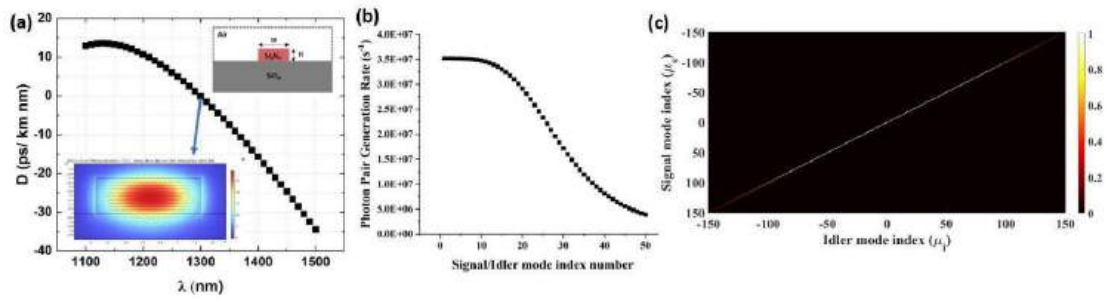


Fig1. *(a) Zero-dispersion-engineered SiN waveguide for O-band photon-pair generation, (b) mode-dependent photon-pair generation rate, and (c) cavity-enhanced joint spectral intensity demonstrating correlated signal–idler photon-pair generation.*

Acknowledgement: We would like to acknowledge the Department of Science and Technology (DST), Government of India, for financial support under the National Quantum Mission (NQM) Project.

References:

[1] Y. Hong, Y. Hong, J. Hong, G.W. Lu, *Photonics* 8 (2021), 161.
[2] K. Sugiura, Z. Yin, R. Okamoto, et al., *Appl. Phys. Lett.* 116, (2020) 224001.
[3] L. Duan,T. J. Steiner,P. Pintus, et al., *ACS Photonics* 12 (2025), 118−127.

Mid-Infrared Absorption Spectroscopy Using a Folded Quantum Nonlinear Interferometer

[1,†]Aadi Suketu Bharatia, [1,†] Muppalla Vidya Prakash, [2,#]Tanmoy Chakraborty and [1,#]Anshuman Kumar

[1]Department of Physics, Indian Institute of Technology Bombay, Mumbai-400076, India

[2]Light and Matter Physics, Raman Research Institute, Bengaluru-560080, India

[†] These authors contributed equally.

[#] *tanmoy@rri.res.in, anshuman.kumar.srivastava@gmail.com*

We demonstrate a folded single-crystal (PPLN) nonlinear interferometer based on Induced Coherence, having achieved interference fringes with a visibility of ∼36% while enabling wavelength-tunable mid-infrared absorption spectroscopy through visible (or near visible) photon detection.

The advent of Quantum Nonlinear Interferometry as a means to surpass the Standard Quantum Limit of phase sensitivity has led to its numerous applications in imaging, metrology and sensing. Moreover, the generation of correlated photon pairs via second order $(\chi^{(2)})$ processes have enabled nonlinear interferometers to become suitable platforms for observing a range of emergent quantum phenomena.

One such phenomenon is that of induced coherence [2], wherein phase information in the common aligned idler arm of two indistinguishable $\chi^{(2)}$ processes is encoded in the interferogram of the corresponding signal photons. The presence of an obstacle (sample) in the idler arm in between the two nonlinear sources reveals which-source information, reducing the extent of indistinguishability between the pair creation pathways and thus reducing the visibility of the signal photon interferogram. This allows for the probing of the sample's optical properties, detected as changes in interferogram visibility.

Here, we demonstrate signal interference with a visibility of 36% in a folded single-crystal nonlinear interferometric scheme [1], using a tunable Periodically Poled Lithium Niobate (PPLN) crystal which generates idler photons in the mid-infrared regime and signal photons in the visible (or near-visible) regime. We further establish the theoretical framework for extracting molecular absorption spectra from the measured visibility [3]. Conventionally, mid-infrared spectroscopy requires infrared detectors that are often expensive and cryogenically operated. Our nonlinear interferometer acts as a feasible platform for probing the infrared absorption spectra of molecules by detecting changes in the visible signal interferogram.

We use a continuous-wave 532 nm laser to pump a multi-grating PPLN crystal to produce non-degenerate photon pairs via SPDC, entangled by energy and momentum conservation relations. The signal photons are detected using a CCD spectrometer, while only the optical path (δ) of the undetected idler photons is modulated. The resulting signal-photon count rate is given by

$$R_s(\lambda, \delta) = R_0(\lambda) \left[1 + \mathcal{V}(\lambda) \cos\left(\frac{4\pi\delta}{\lambda_i}\right)\right] \quad (1)$$

where $\mathcal{V}(\lambda)$ denotes the wavelength-dependent interference visibility and λ_i denotes the idler wavelength. Fig. 1 (bottom) shows high-contrast interference fringes with 36% visibility, obtained by scanning the idler arm mirror.

The crystal's multi-grating architecture enables idler wavelength-tuning over a broad infrared range, allowing the setup to access the absorption bands of a wide variety of molecules via the visible regime. These results strongly encourage room-temperature quantum absorption spectroscopy and sensing in the mid-infrared using only silicon-based detectors.

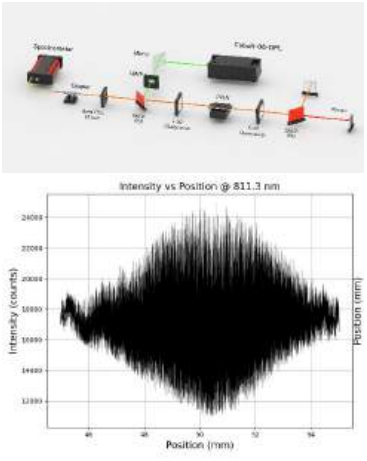


Fig. 1: (top) Folded single-crystal PPLN nonlinear interferometer. (bottom) Measured signal interferogram showing ∼36% visibility.

References:

[1] A.V. Paterova, H. Yang, C. An, D.A. Kalashnikov, L.A. Krivitsky, *Quantum Science and Technology* 3 (2018) 025008.

[2] X.Y. Zou, L.J. Wang, L. Mandel, *Physical Review Letters* **67**, 318–321 (1991).

[3] D.A. Kalashnikov, A.V. Paterova, S.P. Kulik, L.A. Krivitsky, *Nature Photonics* **10**, 98–101 (2016).

Pulse-Programmable Processing in Coulomb-Blockaded Triple Quantum Dots for Hybrid Quantum Optical Architectures

Harshita Bose
Dept. of Applied Physics, Delhi Technological University
Shahbad Daulatpur, New Delhi, 110042
harshitabose_23ep041@dtu.ac.in

We demonstrate a pulse programmable finite state machine using charge configurations in a Coulomb blocked triple quantum dot. Gate voltage pulses induce deterministic transitions between metastable states forming a directed state graph. The state space shows conceptual analogy to optical mode encoding in integrated circuits, enabling reconfigurable nanoscale computation.

Inspired by state encoding and reconfigurable information processing concepts in integrated optics and photonics, we investigate pulse driven charge state dynamics in a triple quantum dot (TQD) operated deep in the single electron Coulomb blockade regime [1,2]. In this regime, discrete charge configurations are metastable and can be deterministically switched by voltage pulses applied to individual plunger gates. Treating these configurations as computational states, we show that the resulting charge-transition graph defines a pulse-programmable finite-state machine (FSM).

A TQD system consists of three electrostatically defined potential wells, each capacitively coupled to plunger gates and weakly coupled to the coupled to electron reservoirs. First, consider a linear TQD defined electrostatically in a two-dimensional electron gas, consisting of left (L), center (C), and right (R) dots controlled by individual plunger gates and weakly coupled to source and drain leads (Fig.1). Let U_{LC} and U_{LC} be the nearest-neighbor inter-dot Coulomb interaction energies. It is also assumed that the U_{LC}, $U_{CR} >> k_BT$. Let the linear TQD, in a restricted low-energy regime, result in a state space given by

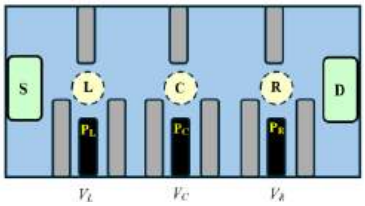


Fig. 1: Schematic for the linear TQD.

$$S = \{(1,0,0), (0,1,0), (0,0,1), (1,0,1)\}, \quad (1)$$

with the initial state as (1,0,0). Suppose we apply the voltage pulse on C followed by R, *i.e.*, $V_C \rightarrow V_R$. In that case, the state transition would be $(1,0,0) \xrightarrow{V_C} (0,1,0) \xrightarrow{V_R} (0,0,1)$. Next, we apply the voltage pulse on R followed by C, *i.e.*, $V_R \rightarrow V_C$. In the second case, the state transition would be $(1,0,0) \xrightarrow{V_R} (1,0,0) \xrightarrow{V_C} (0,1,0)$. We observe that the linear TQD system exhibits intrinsic memory and non-commuting transitions. This combination of state-dependent transitions and non-commuting pulse sequences enables the linear TQD as a minimal, pulse-programmable FSM.

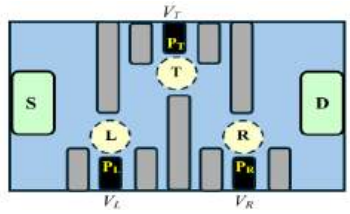


Fig. 2: Schematic for the triangular TQD.

Next, consider an extension of the concept to a triangular triple quantum dot (TTQD) geometry, as shown in Fig. 2. The TTQD geometry supports three charge configurations, (1,0,0), (0,1,0), and (0,0,1), corresponding to single-electron localization each quantum dot. By removing a preferred spatial direction, state transitions now occur along closed loops. For TTQD let us use the terminology left (L), top (T), and right (R) dots controlled by individual plunger gates. Let the initial state be (1,0,0). Suppose we apply the voltage pulse on T followed by R, followed by L, *i.e.*, $V_T \rightarrow V_R \rightarrow V_L$. Here, the state transition would be $(1,0,0) \xrightarrow{V_T} (0,1,0) \xrightarrow{V_R} (0,0,1) \xrightarrow{V_L} (1,0,0)$, thus enabling cyclic dynamics, e.g. modulo-3 operation.

Numerical simulations of the triple quantum dot system were performed using the Kwant Python library. It demonstrates the controlled the single-electron transport phenomenon through the linear TQD system. Peaks in the transmission corresponded to resonant tunnelling through discrete quantum dot states, providing quantitative identification of the metastable charge configurations.

This work suggests that Coulomb blockaded quantum dot networks can serve as electronic counterparts to integrated optical circuits, where discrete charge states play a role analogous to optical modes in reconfigurable information processing architectures.

References:

[1] S. Hiraoka et al., Applied Physics Letters 117 (2020) 074001.
[2] T. Aizawa et al., Physical Review B 110 (2024) 235421.

Quantum Weak-Value Amplification of Chiral Phase-SPR for Zeptomolar Enantiomer Detection

[1,#]Ipsita Chakraborty,and [1]Manik Pradhan
[1]Department of Chemical and Biological Sciences, S. N. Bose National Centre for Basic Sciences, JD Block, Sector 3, Salt Lake, Kolkata 700 106, India

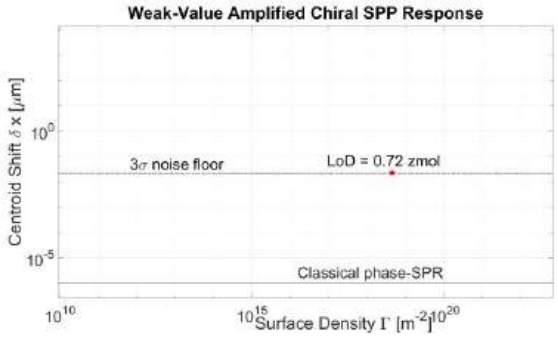
[#]ipsitachak2026@bose.res.in

We combine quantum weak measurement with plasmonic Kretschmann sensing to amplify chiral phase shifts while maintaining shot noise. Post-selecting polarization maps 0.55 mrad to 5.5 μm. The quantum Cramér-Rao bound with 10^8 photons achieves a 3σ detection limit of 10^{-22} mol, which is 10^4 times better than classical phase SPR and will enable single protein chirality read out.

Integrating quantum weak-value amplification (WVA) with plasmonic sensing has pushed surface plasmon resonance (SPR) biosensors toward quantum limits [1]. Weak measurements with SPP modes have resolved spin hall shifts. Chiral surface plasmons outperform chiral cavities by ~10 times in enantiomer detection, while achiral nanohole arrays achieve ~50 times circular dichroic enhancement [2]. Combining chiral phase SPR with quantum WVA remains unexplored and promising.

Novelty: This work provides: (1) WVA of Kretschmann chiral phase-SPR, mapping the Berreman 4×4 chiral phase to a post-selected beam shift with Aw ≈ 100; (2) Shot-noise-limited 0.17 zepto-molar LoD ~10^4 times below classical phase-SPR; (3) Deployable scheme using only HeNe, polarizers, and sCMOS with technical noise σ_{tech} = 2.8 μ◦/Aw = 0.5 nrad.

For SF11/Ag(50 nm)/chiral/water, Berreman 4×4 matrix with $\xi = \kappa/c \cdot l$, $\kappa_{chiral} = 1.42 \times 10^{-9}$ gives $\Delta\phi = \arg(r_{sp}) - \arg(r_{ps}) = 0.550$ mrad at 632.8 nm, $\theta = 57.21^\circ$.



WVA protocol:

1) Pre-select $|i\rangle = \frac{1}{\sqrt{2}}(|H\rangle + |V\rangle)$.

2) Weak SPP coupling

$\hat{U} = \exp\left(-i\Delta\phi\,\hat{A}\,\frac{\hat{k}_x}{\sigma_k}\right), \hat{A} = |H\rangle\langle H| - |V\rangle\langle V|.$

3) Post-select

$|f\rangle = \sin(\epsilon/2)|H\rangle - \cos(\epsilon/2)|V\rangle, \epsilon = 0.02\ \text{rad}.$

The weak value factor can be determined by $A_w = \frac{\langle f|\hat{A}|i\rangle}{\langle f|i\rangle} = -i\cot\left(\frac{\epsilon}{2}\right) \approx 0 + 100i$. Thus the centroid shifts by $\delta x = \frac{\lambda}{2\pi}\,\mathrm{Im}(A_w)\,\Delta\phi = 5.5\ \mu\text{m}$. Success probability is governed by $Ps \approx \frac{\epsilon^2}{4} = 10^{-4}$. Thus 1 mW power on detector recieving $N = 3 \times 10^{14}$ photons/s, yields $\sigma_{\Delta\phi} \geq \frac{1}{\sqrt{4N}} \sim 0.9$ prad. With $\frac{d\Delta\phi}{d\Gamma} = 2.75 \times 10^{-22}\ \text{mrad m}^2, \text{LoD}_{3\sigma} = 3 \cdot 3.2 \times 10^{-12}\ \text{rad}, \frac{d\Delta\phi}{d\Gamma} = 3.5 \times 10^{13}\ \text{m}^2$. For a detection area of $100\ \mu m^2$ the detection limit of the developed system will be ~ 3.5 × 10^3 molecules ~ 0.17 zepto-mole. Thus the developed system sensitivity is 10^4 times better than classical phase-SPR.

Quantum weak value amplification coupled with chiral plasmons breaks the zepto-molar barrier for short noise limited signals. This analysis reveals that by considering A_w = 100 we can convert 0.55 mrad to 5.5 μm shift of the centroid at the sCMOS plane which can be measured with standard optics. This platform will be immensely useful for the detection of chirality of single protein.

References

[1] Liping Xu. et al, Measurement of Chiral Molecular Parameters Based on a Combination of Surface Plasmon Resonance and Weak Value Amplification, ACS Sens. 2020, 5, 2398−2407

[2] Zhang, C., Hu, H., Ma, C. *et al.* Quantum plasmonics pushes chiral sensing limit to single molecules: a paradigm for chiral biodetections. *Nat Commun* **15**, 2 (2024).

A grating-chip cold-atom CPT clock with Raman phase mapping

[1,#]Rajnandan Choudhury Das,[1]Sean Dyer, [1]Erling Riis and [1]Paul F Griffin
[1]University of Strathclyde, Glasgow, United Kingdom

[#]*dr.rajnandan.phy@gmail.com*

We demonstrate a grating-chip cold-atom CPT clock with improved clock-signal SNR using Raman phase mapping. A Raman π/2 pulse replaces the conventional CPT readout pulse and maps the accumulated dark-state phase onto the ground-state population difference. Raman-induced light shifts are suppressed using a combined error signal technique.

Compact cold-atom clocks are attractive for applications requiring stable and portable frequency references. Coherent population trapping (CPT) clocks are particularly appealing because they interrogate the microwave hyperfine transition optically, avoiding the need for a microwave cavity [1]. Combining CPT interrogation with a grating magneto-optical trap further simplifies the laser-cooling geometry and supports compact system integration [2].

In this work, we demonstrate a grating-chip-based cold-atom CPT clock using the sequence: grating MOT loading, CPT preparation, dark-time evolution, Raman π/2 pulse, and D2 state-selective optical readout. Unlike a conventional Ramsey CPT clock, no CPT readout pulse is applied after the dark time. Instead, the Raman π/2 pulse maps the accumulated atomic phase onto the ground-state population difference, which is then detected optically.

This method improves the clock-signal SNR compared with conventional Ramsey CPT readout. We also investigate the light shift introduced by the Raman beam and suppress its contribution using a combined error signal technique [3]. These results provide a route towards improved short-term frequency stability in compact grating-chip cold-atom CPT clocks.

References:

[1] F.X. Esnault et al. *Phys. Rev. A* 88, 042120 (2013).
[2] R. Elvin *et al*. *Opt. Express* 27, 38359-38366 (2019).
[3] M. Shuker *et al*. *Appl. Phys. Lett.* 114, 141106 (2019).

Tuning the Dimensionality of NbTiN Meander Structures for Near-Infrared Single Photon Detection

[1,#]Rup Kumar Chowdhury, [1,2]Sameer Kumar Sahu, [1,3]Amaresh Ramachandran, [1]Abdul Wahid, [1]Majid Yousuf, [1]Rohan Patil, [1]Reena Kumari, [1]Ritu Srivastava, [1]R P Aloysius, [1]Venu Gopal Achanta

[1]CSIR-National Physical Laboratory, New Delhi 110012, India

[2]Indian Institute of Science Education and Research, Kolkata, West Bengal 741246, India

[3]Shiv Nadar Institution of Eminence, Gautam Buddha Nagar, Uttar Pradesh 201314, India

#rup.nplindia@csir.res.in

Optical absorption of niobium titanium nitride (NbTiN) meander structures are investigated as a function of line-width and inter-spacing distance using finite-difference time-domain (FDTD) method. The experimental spectroscopic ellipsometry data of ~5 nm NbTiN thin films are analyzed using Drude-Lorentz model to extend the FDTD calculations up to near-infrared (NIR) regime.

Single-photon detectors (SPDs) utilizing superconducting nanowire meander structures have become indispensable to modern quantum technologies, enabling critical advancements in both quantum key distribution (QKD) and quantum information science [1]. However, fabrication of such meander structures at nanoscale remains challenging via conventional photolithography process, therefore requires complex electron beam lithography (EBL) or focused ion beam (FIB) techniques. As a result, researchers are shifting their focus towards micron level meander structures. By keeping the thickness of the superconducting films below the coherence length (L_c < 10 nm), they achieved the single photon detection capabilities in micro-structured meander similar to the nanowire based SPDs [2,3]. These micron scale SPDs offer smaller kinetic inductance, higher bias currents, larger active area, and compatibility with commercial mask-less photolithographic processes, makes them suitable for wafer-scale superconducting SPD fabrication [3,4].
Here, we evaluate the ellipsometry data of ~5 nm NbTiN films using Drude-Lorentz model and extract the refractive index to simulate the optical absorption efficiency (η) up to 1.8 µm. The signal detection efficiency of a SPD is directly proportional to η of the superconducting meander structures. Using Ansys Lumerical FDTD, η is calculated as a function of width (W) and inter-spacing distance (S) of meander structure from 100 nm to 1 µm, while keeping the filling factor at 0.5 on 300 nm SiO_2 on Si substrate. Figure 1 shows the divergence in absorbance between the nanoscale and micro-scale NbTiN meander structures. At 1550 nm, η approaches to 45% for nanowires (W = 100 nm), which is in-line with the earlier report [2], whereas, η drops to ~25% for micron scaled (W = 1 µm) meanders. At nanoscale, meander structure induces strong local edge field enhancement due to confinement. In contrast, the micron level meander structures effectively behaves as macroscopic planar metal grating and scatters most of the light, resulting into a significant efficiency drop. In the future, it would be interesting to study the integration of nano-cavities or Bragg mirrors with the micron scaled meander structure that can enhance the absorption and detection efficiency by many-fold.

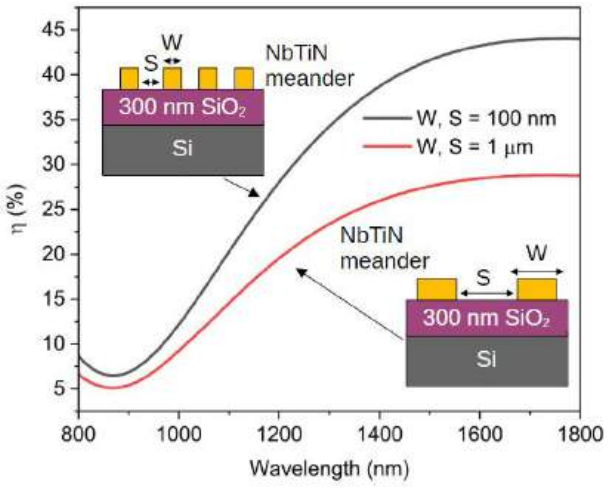


Fig. 1: The absorption efficiency (η) vs. wavelength plot with schematic diagrams of NbTiN meander structures showing the widths (W) and inter-spacing distances (S) of 100 nm & 1 µm (insets).

References:

[1] R. H. Hadfield, *Nature photonics*, *3* (12), 696-705 (2009).
[2] M. G. Tanner, C. M. Natarajan, V. K. Pottapenjara, J. A. O'Connor, R. J. Warburton, R. H., Hadfield, B. Baek, S. Nam, S. N. Dorenbos, E. B. Ureña, T. Zijlstra, *Appl. Phys. Lett.* 96, 221109 (2010).
[3] I. Craiciu, B. Korzh, A. D. Beyer, A. Mueller, R. M. Briggs, B. Bumble, M. Runyan, M. D. Shaw, O. Painter, A. Faraon, *Appl. Phys. Lett.* 122, 243506 (2023).
[4] R. Xu, C. Gu, X. Li, Y. Cheng, Z. Wang, T. Jia, L. You, *Photonics Research*, *9* (6), 958-967 (2021).

Optical Interferometer for Transferring Optical Carrier Frequency with High Stability

[#]Manoj Das, Vijesh K. R. and Subhasis Panja
Time & Frequency Metrology Division, CSIR-National Physical Laboratory, Dr. K. S. Krishnan Marg, New Delhi, 110012
[#]*manojdas.nplindia@csir.res.in*

Optical atomic clocks based on either single ion or multiple neutral atoms in an optical lattice clock, which are based on optical transitions offer accuracy at 18-digit level. The SI second redefinition based on optical atomic clocks is slated for the early 2030's. Such optical clocks require that the oscillator frequency needs to be transferred intra-laboratory from the source to the ion/atom trap chamber and then from chamber to the frequency comb counter without adding the channel's (*usually optical fibers*)*, own noise. In this paper, we discuss an interferometer-based setup to detect and cancel such channel-induced noise.*

At the Time and Frequency metrology laboratory at CSIR-NPL, work is being carried out on single ion Yb+ optical clock. The atomic clock consists of a pre-stabilized oscillator, an atomic reference, and a counter. Due to its potential to reach 10^{-18} accuracy and stability, the above three components needs to be linked using low-noise channel, usually a phase-stabilized optical fiber, whose noise level is below to that of the optical frequency being transferred.

The realization of such noise cancelled optical frequency transfer is carried out using a technique called phase compensated optical fiber transfer. The phase detector is a Michelson interferometer, where the measurement arm is the optical fiber which will transfer the optical clock frequency [1]. Proper transducers are then used to compensate the detected phase noise due to the fiber.

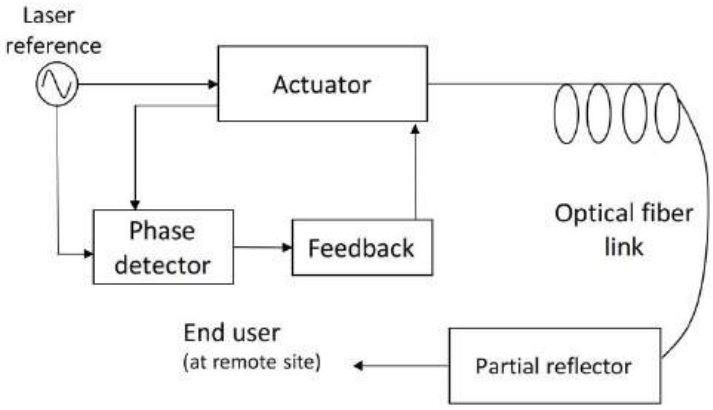


Figure 1 shows a typical setup for implementing such optical fiber induced noise cancellation system

In this paper, we will discuss the design and development of such setup at CSIR-NPL. We report on the progress made in setting up such an experimental system.

References:

[1] Ma LS, Jungner P, Ye J, Hall JL. Delivering the same optical frequency at two places: accurate cancellation of phase noise introduced by an optical fiber or other time-varying path. Opt Lett.1994;19:1777-1779.

Weak-Measurement Enhanced Two-Photon Polarization Spectroscopy of 5S-5D Transition in Rubidium

[1,2#]Purvesh V Garge, [1,2]Surya N Sahoo and [1,2]Ashok K Mohapatra
[1]School of Physical Sciences, National Institute of Science Education and Research, Bhubaneswar, India
[2]Homi Bhabha National Institute, Training School Complex, Anushaktinagar, Mumbai, India
[#]*purveshv.garge@niser.ac.in*

We develop weak-measurement-enhanced two-photon polarization spectroscopy in ^{87}Rb thermal vapor using a 780 nm probe and 776 nm pump. The method amplifies the nearly Doppler-free dispersive signal detected on a balanced photodetector, providing a sensitive modulation-free, continuously tunable error signal for off-resonant laser locking.

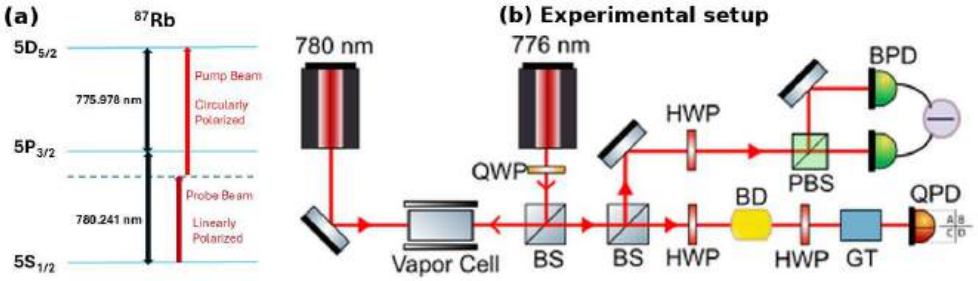


Fig. 1: (a) ^{87}Rb ladder system and (b) Experimental setup for weak-measurement-enhanced two-photon polarization spectroscopy.

Laser locking to atomic references is essential in precision spectroscopy and quantum optics. However, operation near fixed resonances can introduce absorption, scattering, optical pumping, and light shifts. Here, we investigate a modulation-free two-photon frequency-stabilization scheme in the ^{87}Rb $5S_{1/2} \rightarrow 5P_{3/2} \rightarrow 5D_{5/2}$ ladder system, where the relative detuning between the 780 nm probe and 776 nm pump is stabilized using a weak-measurement-enhanced dispersive polarization signal.

A heated ^{87}Rb vapor cell is maintained near 100 °C. A linearly polarized 780 nm beam is used as the probe and a stronger counter-propagating 776 nm beam as the pump. The circularly polarized pump induces circular birefringence and dichroism in the probe. After the cell, a polarization analyzer and balanced photodetector generate a dispersive two-photon error signal for relative frequency stabilization.

Tunability is obtained by co-detuning the 780 nm and 776 nm lasers while maintaining the two-photon resonance condition:

$$\delta_{2\gamma} = \Delta_{780} + \Delta_{776} + (k_{780} - k_{776})v \simeq 0$$

Because the wavelengths are close and counter-propagating, residual Doppler broadening is strongly reduced. This allows for relative stabilization of the 780 nm and 776 nm fields via atomic two-photon resonance, while both lasers are detuned from the strongly absorbing one-photon resonances.

Weak-measurement amplification enhances weak, far-detuned dispersive signals by increasing the readout slope through nearly orthogonal pre- and post-selection. We quantify the improvement using $SNR_{WM} \approx A_{eff}\ SNR_{BPD}/\eta_{tech}$, where $A_{eff} \approx 1/(2\varepsilon)$, ε is the post-selection offset, and η_{tech} accounts for technical-noise contributions from reduced transmitted power, detector noise, and post-selection imperfections. Weak-measurement readout outperforms conventional BPD detection when $A_{eff} > \eta_{tech}$, yielding $SNR_{WM} > SNR_{BPD}$. We will compare both SNRs and map the usable dispersive locking slope versus one-photon detuning, initially focusing on the 10–100 GHz range.

This scheme may provide a continuously tunable two-photon reference for relative frequency stabilization in far-detuned ladder spectroscopy, nonlinear optics, and precision measurements.

References:

[1] H.C. Busch et al., American Journal of Physics 93, 824 (2025);
[2] Y. Aharonov et al., Physical Review Letters 60, 1351 (1988).
[3] N.W.M. Ritchie, J.G. Story, R.G. Hulet, *Physical Review Letters* 66, 1107–1110 (1991).

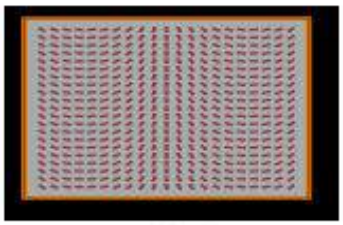
Pancharatnam-Berry Phase Metasurfaces for Two Entangled Photon State Generation

Shubham Ghosh,[1] Satya Pratap Singh,[2] Vinod Parmar,[2] Umesh Tiwari[2]
[1]*Department of Physics, National Institute of Technology Warangal, Warangal, India, 506004*
[2]*CSIR, Chandigarh, India*
**Email: physics_hod@nitw.ac.in*

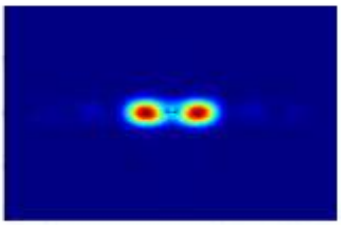
Abstract: We demonstrate a silicon-based Pancharatnam-Berry (PB) phase metasurface for generating two-photon NOON states from SPDC entangled photons. The structure introduces a linear phase gradient to efficiently route left- and right-circular polarizations into $\pm 10^{\circ}$ diffraction orders. Stokes parameter measurements confirm near-perfect circular polarization purity, validating the device's high spin-selectivity for quantum optics applications.

1. Introduction

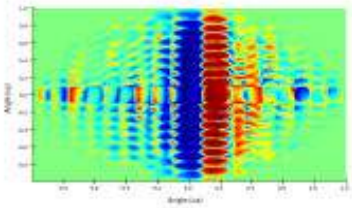
A metasurface is a 2D array of subwavelength nanostructures that locally engineers the amplitude, phase, or polarization of light [1]. The Pancharatnam-Berry (PB) phase metasurface specifically controls light via geometric phase by acting as a localized half-wave plate. It flips the handedness of circularly polarized light while imparting an extra geometric phase determined entirely by the nanofin's rotation angle. We start by pumping a nonlinear lithium niobate crystal with a laser of wavelength 775 nm; via Spontaneous Parametric Down-Conversion (SPDC), the crystal produces two 1550 nm polarization-entangled photons, one horizontally (H) and one vertically (V) polarized. Since linear polarization is inherently a superposition of left- and right-circular polarizations (LCP and RCP), the metasurface's linear phase gradient spatially separates the RCP and LCP components [1]. This effectively produces a two-photon NOON state, a maximally path-entangled quantum state where the photons remain inextricably linked regardless of the path taken.



(a) Metasurface Structure



(b) 2 beam represent LCP and RCP



(c) Stokes parameter, Red +1 RCP, Blue -1 LCP

2. Structure & Result

The Simulation metasurface uses high-aspect-ratio silicon nanofins (830 nm tall, 486 nm long, 201 ± 5 nm wide) sitting on a glass (SiO_2) substrate with a square lattice period of 667 nm. The rotation angle follows a linear Pancharatnam-Berry phase gradient, $\theta(x) = (\pi/\Lambda)x$, where Λ is the grating period. This linear variation gives the two circular helicities opposite geometric phases of $\pm 2\theta(x)$, which is what sends the left- and right-circularly polarized components into symmetric $\pm 10^{\circ}$ diffraction orders [1].

To confirm the polarization purity in each output channel, we ran a Stokes parameter characterization. Together, the four Stokes parameters (S_0, S_1, S_2, S_3) fully describe the polarization state of a light beam. S_0 is the total intensity, and everything else gets normalized against it. S_1 tells you whether the light leans horizontal (positive) or vertical (negative). S_2 does the same for diagonal, $+45^{\circ}$, versus anti-diagonal, -45°. S_3 is the circular polarization content, positive for right-circular (RCP) and negative for left-circular (LCP). Our measured normalized vector, $S = (1, -0.08, -0.06, 0.98)^T$, shows that nearly all the light intensity is circularly polarized. S_1 and S_2 sit close to zero, so the linear components are negligible, and $S_3 = 0.98$, near enough to the ideal $+1$, confirms the output beam is almost purely right-circularly polarized. That's the spin-selective behavior the metasurface was designed for.

References

[1] P. Georgi, M. Massaro, K.-H. Luo, B. Sain, N. Montaut, H. Herrmann, T. Weiss, G. Li, C. Silberhorn, and T. Zentgraf, "Metasurface interferometry toward quantum sensors," *Light: Science & Applications*, vol. 8, no. 1, p. 70, 2019.

Voltage-Controlled Quantum Coherence Engineering via Birefringence-Frequency Coupling in Nematic Liquid Crystals

[1,#] Gyaprasad
[1]Department of Physics, Government P. G. College Khair, Aligarh, Uttar Pradesh, India
[#]*gyaprasadamu@gmail.com*

We theoretically show that frequency-dependent birefringence in nematic liquid crystals (NLC) couples' polarization with frequency, leading to decoherence and a reduction in the quantum degree of polarization, which is further tuned by an applied voltage across NLC. These results highlight the potential of liquid crystals for electrically controlled quantum depolarization and coherence engineering.

Consider a general pure polarization state of a single photon $|\psi\rangle = \alpha|H\rangle + \beta|V\rangle$. When it passes through a birefringent Nematic liquid crystal cystal (NLC), the state becomes $|\psi\rangle = \alpha|H\rangle + \beta e^{i\delta}|V\rangle$, where $\delta = \frac{\omega}{c}\Delta n.L$, Δn is the birefringence, and L is the thickness of the NLC through which the light propagates. Changing the phase difference while keeping the frequency constant preserves the quantum degree of polarization ($QDoP$) but only rotates the polarization state. As a result, the quantum state remains pure. However, if ω changes, or in other words, if a broadband source is used for which Δn changes with frequency, then birefringence becomes coupled with frequency and can alter the correlation between the (H) and (V) modes. This coupling decoheres the polarization and hence can reduce the $QDoP$ which can be tuned by the applied voltage on NLC.

$$|\psi_{in}\rangle = |\psi_{pol}\rangle \otimes |\psi_{freq}\rangle = [\alpha|H\rangle + \beta|V]\rangle \otimes [\int d\omega\, f(\omega)\,|\omega\rangle] = \int d\omega\, f(\omega)\,[\alpha|H\rangle + \beta|V\rangle] \otimes |\omega\rangle. \quad (1)$$

If the quantum state passes through the NLC cell (homeotropic alignment in this case).

$$|\psi_{out}\rangle = \int d\omega\, f(\omega)\,[\alpha|H\rangle + \beta e^{i\delta}|V\rangle] \otimes |\omega\rangle. \quad (2)$$

Calculate the density matrix $\rho = |\psi_{out}\rangle\langle\psi_{out}|$. Since most detectors do not resolve frequency degree of freedom. The reduced polarization density matrix is obtained by tracing over the frequency degrees of freedom. we can calculate

$$\rho_{pol} = \begin{pmatrix} |\alpha|^2 & \alpha\beta^*\gamma \\ \alpha^*\beta\gamma^* & |\beta|^2 \end{pmatrix}, \quad (3)$$

where $\gamma = \int |f(\omega)|^2\, e^{-i\delta(\omega)}\, d\omega$. (4)

If $\alpha = \beta = \frac{1}{\sqrt{2}}$, $QDoP = \sqrt{2\,Tr(\rho)^2 - 1)} = |\gamma|$. (5)

Substituting $f(\omega) = \left(\frac{1}{2\pi\sigma^2}\right)^{\frac{1}{4}} e^{(-\frac{(\omega-\omega_0)^2}{4\sigma^2})}$ in Eq (4).

$\gamma = e^{i\delta_0}\, e^{\frac{1}{2}\sigma^2 D^2}$,

where $D(\omega,V) = \frac{d\delta(\omega,V)}{d\omega} = \frac{L}{c}\left[\Delta n(\omega,V) + \omega\frac{d\Delta n(\omega,V)}{d\omega}\right]$.

Hence, $QDoP(V) = e^{-\frac{1}{2}\sigma^2 D(\omega,V)^2}$. (6)

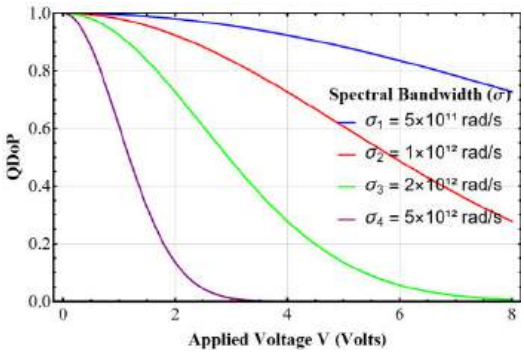


Fig. 1: The QDoP is plotted with respect to applied voltage V for four different values of photon spectral bandwidth σ.

For a photon centered at $\omega_0 \approx 2\pi \times 200\,THz$ which is typical for telecom applications, realistic bandwidth might be on the order of $\sigma \sim 10^{13}$ rad/s. This corresponds to a few nanometers of wavelength spread around $1550\,nm$. The $QDoP$ decreases exponentially which is shown in Fig.1. Assuming a voltage-dependent delay $D(V) = aV$ with $a = 10^{-13}\,s/V$. The applied voltage $V = 0 - 8\,V$. Applied voltage increases, birefringence grows, cause decoherence in polarization modes. This decoherence effect becomes more pronounced for photons with larger spectral bandwidth.

[1] Gyaprasad, R. Joshi, *Optics Communications*, 608 (2026) 132984.
[2] G. Björk, J. Söderholm, L.L. Sánchez-Soto, A.B. Klimov, I. Ghiu, P. Marian, *Optics Communications* 283 (2010) 4440.
[3] A. Luis, Physical Review A 66 (1) (2002) 013806.

Non-monotonic Dependence of the Angular Schmidt Spectrum on Crystal Thickness in Spontaneous Parametric Down-Conversion

[1,#]Harshal Jain, [2]Suman Karan and [3]Anand Kumar Jha
Department of Physics, Indian Institute of Technology Kanpur, Kanpur 208016, Uttar Pradesh, India

[#]*jainharshal52@gmail.com*

The dependence of the angular Schmidt spectrum on crystal thickness in spontaneous parametric down-conversion is investigated theoretically and experimentally. We observe a non-monotonic variation of the Schmidt number with crystal thickness, originating from spatial walk-off. Our experimental measurements closely follow the theoretical predictions obtained using the exact phase-matching model.

The orbital angular momentum (OAM) of photons provides access to a discrete and infinite-dimensional Hilbert space and has emerged as a promising resource for high-dimensional quantum information protocols. The dimensionality of OAM-entangled photon pairs generated via spontaneous parametric down-conversion (SPDC) is quantified through the angular Schmidt spectrum. Accurate prediction of the angular Schmidt spectrum requires retaining the exact phase-matching function inside the nonlinear crystal. Previous theoretical studies either employed approximate phase-matching conditions that neglect spatial walk-off or were restricted to thin crystals, predicting a monotonic decrease of the Schmidt number with increasing crystal thickness [1-4].

In this work, we investigate the crystal-thickness dependence of the angular Schmidt spectrum using the exact phase-matching formulation. By comparing the exact and approximate phase-matching models, we show that spatial walk-off qualitatively changes the crystal-thickness dependence of the Schmidt number. While the approximate formulation predicts the previously reported $1/\sqrt{L}$ decrease [3], the exact phase-matching model predicts a non-monotonic dependence on crystal thickness.

The theoretical predictions are verified experimentally using an interferometric technique for measuring the angular Schmidt spectrum [5]. Measurements are performed for different crystal thicknesses and phase-matching angles using type-I SPDC in a BBO crystal pumped by a 355 nm laser. The measured Schmidt numbers closely follow the theoretical trends and reproduce the predicted non-monotonic dependence on crystal thickness. The observed increase in the Schmidt number for larger crystal thicknesses is attributed to spatial walk-off inside the nonlinear crystal.

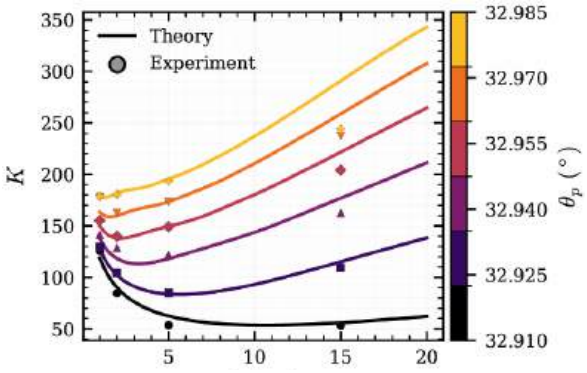


Fig. 1: Dependence of the Schmidt number on crystal thickness for different phase-matching angles. Solid curves denote theoretical predictions obtained using the exact phase-matching model, while symbols represent experimental measurements.

These results demonstrate that retaining the exact phase-matching function is essential for accurately describing the angular Schmidt spectrum. The present work provides the first experimental investigation of the dependence of the angular Schmidt spectrum on crystal thickness and highlights the important role of spatial walk-off in determining the dimensionality of OAM-entangled states and provides a foundation for reliable characterization of high-dimensional quantum light sources.

References:

[1] J. Torres, A. Alexandrescu, and L. Torner, Physical Review A 68, 050301 (2003).
[2] F. M. Miatto, A. M. Yao, and S. M. Barnett, Physical Review A 83, 033816 (2011).
[3] F. Miatto, D. Giovannini, J. Romero, S. Franke-Arnold, S. Barnett, and M. Padgett, The European Physical Journal D 66, 1 (2012).
[4] G. Kulkarni, L. Taneja, S. Aarav, and A. K. Jha, Physical Review A 97, 063846 (2018).
[5] G. Kulkarni, R. Sahu, O. S. Maga¯na-Loaiza, R. W. Boyd, and A. K. Jha, Nature communications 8, 1054 (2017).

Quantum Metrology with Displaced Squeezed vacuum state in Mach - Zehnder Interferometer

[1, #]K. Amrutha, [2]C. Sudheesh

1. Indian Institute of Space science and Technology, Thiruvananthapuram, 695547, India

amruthaezhur@gmail.com

This theoretical work investigates quantum-enhanced phase estimation in a Mach–Zehnder interferometer using coherent and displaced squeezed vacuum states. Phase sensitivity is evaluated using the Quantum Cramér–Rao Bound and different detection schemes. Results demonstrate sensitivity beyond the shot-noise limit, with displaced squeezed vacuum states providing superior phase-estimation performance and compare the result with coherent state mixing with squeezed displaced vacuum state.

High-precision measurement lies at the heart of modern physics, and quantum metrology offers a principled route to improving measurement sensitivity beyond what is achievable with classical resources. Among the available platforms, optical interferometric schemes most notably the Mach–Zehnder interferometer play a central role in precision phase estimation, with important implications for gravitational wave detection, rotation sensing, and precision monitoring of physical environments. The central objective of quantum enhanced interferometry is to infer an unknown phase shift ϕ with a precision that surpasses the standard quantum limit (SQL) or shot-noise limit (SNL) by exploiting non-classical states of light.

The phase sensitivity of a Mach–Zehnder interferometer is primarily determined by two factors: the quantum state injected into the input ports and the measurement strategy applied at the outputs. The use of non-classical resources—such as Fock states, squeezed vacuum states, N00N states, and Schr¨odinger cat states—can significantly enhance the interferometric sensitivity, enabling performance beyond the SQL In practice, the preparation of such nonclassical states and the implementation of optimal detection schemes remain technologically challenging. In this theoretical work, we explore the use displaced squeezed vacuum state (DSVS) and Squeezed displaced vacuum state (SDVS), which is then combined with a coherent state (CS), as inputs to the MZI. The aim is to enhance the phase sensitivity beyond SQL. The Quantum Cram´er–Rao Bound (QCRB) sets the ultimate limit on phase sensitivity in a Mach–Zehnder interferometer, independent of the particular measurement strategy. For the probe state considered here, we evaluate the QCRB and find that the achievable sensitivity lies below the shot-noise limit, indicating quantum-enhanced performance. In practice, however, the attainable precision also depends strongly on the detection scheme employed at the output ports. Quantum measurement techniques, such as homodyne and parity detection, generally provide better sensitivity than simple intensity-based methods. Nevertheless, these quantum detection schemes are often morecomplex and experimentally demanding, whichmakes conventional intensity detection attractivefor practical implementations. In this work, we therefore consider and compare the performance of parity detection, single-intensity detection, and intensity-difference detection schemes.

In this theoretical study, we demonstrate that, for a given coherent-state amplitude and squeezing parameter, the combination of a coherent state and a displaced squeezed vacuum state at the first beam splitter of the interferometer yields superior phase-estimation sensitivity compared to cases where the coherent state is combined with a squeezed vacuum state or a squeezed displaced vacuum state.

References:

[1] R. Birrittella and C. C. Gerry, J. Opt. Soc. Am. B, **31,** 586 (2014).
[2] S. Wang, X. X. Xu, Y. J. Xu, et al, Opt. Commun., **444,** 102 (2019).
[3] Zhao Z, Kang Q, Zhang H, Zhao T, Liu C and Hu L, Opt. Express, **32,** 28267 (2024).

Thickness Dependent Optical Effects in Hexagonal Boron Nitride

Swetha K, #Rajesh V. Nair

Quantum Photonics and Sensing Group, Department of Physics, Indian Institute of Technology Ropar, 140001, India

#rvnair@iitrpr.ac.in

We systematically investigate optical interference effects in exfoliated hexagonal boron nitride (hBN) to design efficient quantum photonic devices. We use micro-reflectivity and Raman measurements along with transfer matrix modelling and FDTD simulations for a quantitative understanding of thickness dependent electric field modulations in hBN.

Hexagonal Boron nitride (hBN) is a two-dimensional van der Waals material which is an emerging platform for quantum technologies [1]. The wide band gap of 6 eV enables it to host quantum emitters at room temperature which can also be spin active [2,3]. Due to the structural similarity to graphene, hBN is used as a thermal and electrical insulation layer for graphene based devices [1]. Its atomically flat and inert nature also enables it to be used as an encapsulation layer for transition metal dichalcogenide (TMDC) based gated devices [4]. The finite thickness and refractive index mismatch of this encapsulation layer introduces optical phenomena which effects the emission properties of the device. For single photon emitters hosted in hBN, the radiative emission dynamics is modulated by its vertical position in the flake. Hence, measuring thickness as well as refractive index of exfoliated hBN flakes is important to optimize their performance as a single photon source and for use in TMDC based opto-electronic devices.

Here we propose an aberration-free micro-reflectivity method to simultaneously estimate thickness (t) as well as refractive index (n) of hBN flakes using optical interference. The angle averaging induced by numerical aperture of the microscope objective in experiment is taken care in the theoretical modelling of measured spectra. The measurements are carried out at exactly the desired location which can be monitored using an in-situ camera. Since we are taking absolute reflectivity values, all the inhomogeneities on the flakes could be included in the measurements. We propose a theoretical model based on thin film matrix methods to support the measured reflectivity spectra. The t and n values are estimated for flakes with varying thickness and the estimated t values are complemented with that obtained from atomic force microscopy. We further perform Raman scattering measurements to support t value dependent intensity modulation. As Raman measurements shows an intensity variation, we perform FDTD simulations to investigate if similar effects exist for emission dipoles present at different depths in the flake. Even though a cavity like Purcell enhancement is not observed, a significant modulation of emission intensity is observed due to interference effects.

To conclude, we have studied optical interference effects in hBN flakes of varying thickness and observed an electric field intensity modulation across flake depth. Our results are useful in designing efficient quantum light sources, with enhanced emission and collection efficiency.

We thank INSPIRE Fellowship for the PhD program and funding from IIT Ropar, DST, SERB.

References:

[1] T. T. Tran, K. Bray, M. J. Ford, M. Toth, and I. Aharonovich, *Nature Nanotechnology*, **11** (2016) 37.

[2] A. Gottscholl, M. Kianinia, V. Soltamov, S. Orlinskii, G. Mamin, C. Bradac, C. Kasper, K. Krambrock, A. Sperlich, M. Toth, I. Aharonovich, and V. Dyakonov, *Nature Materials* **19** (2020) 540.

[3] A. Bhunia, P. Joshi, N. Singh, B. Chakraborty, and R. V. Nair, *Journal of Physics D: Applied Physics* **57** (2024) 395103.

[4] H. H. Fang., B. Han, C. Robert, M. A. Semina, D. Lagarde, E. Courtade, T. Taniguchi, K. Watanabe,T. Amand, B. Urbaszek, and M. M. Glazov, *Physical Review Letters*, **123** (2019) 067401.

Generation of Three-Component Mechanical Schrödinger Cat States in an Optomechanical Platform

Shahan Ulla Khan and #A. Kani
School of Physics, University of Hyderabad, Hyderabad, Telangana 500046, India.
Corresponding author's email: kanimohamed@uohyd.ac.in

We propose a protocol for generating robust three-component mechanical Schrödinger cat states in an optomechanical system by exploiting the intrinsic nonlinear radiation-pressure interaction, providing a promising route towards exploring macroscopic quantum phenomena with mechanical systems.

Engineering nonclassical quantum states in macroscopic systems is important for both fundamental quantum physics and quantum technologies [1]. Schrödinger cat states—superpositions of macroscopically distinct states—play a central role in testing fundamental quantum principles at macroscopic scales [2]. In optomechanical systems [3], the intrinsic nonlinear optomechanical interaction, when sufficiently strong, provides an efficient route for introducing tunable dispersive and dissipative nonlinearities into the mechanical element [4], which are essential for engineering nonclassical mechanical states. Here, we extend the approach of Hauer et al. [4] to realize a three-component mechanical Schrödinger cat state and characterize its nonclassical properties using the Wigner distribution.

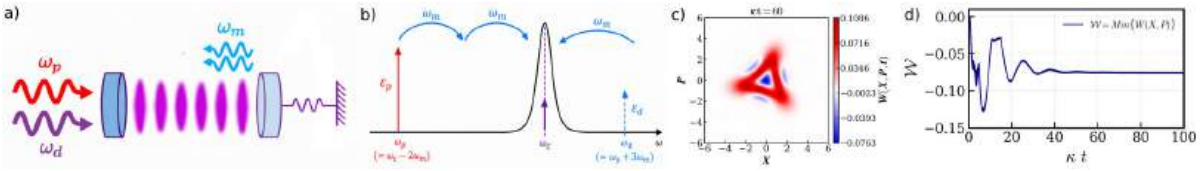


Figure 1: (a) Schematic of the system for generating three-headed mechanical cat state, (b) Frequency space including pumping scheme, (c) Mechanical resonator's Wigner distribution at $\kappa \mathbf{t} = 60$, (d) the minimal Wigner negativity of the mechanical state as a function of time. The parameters are $g_0 = 10\kappa$, $\omega_m = 50\kappa$, $\Gamma = 10^{-6}\kappa$, $\bar{n}_b = 0$, $\Delta_p = -2\omega_m$, $\Delta_d = -3\omega_m$, $\varepsilon_p = 30$, and $\varepsilon_d = 3$.

We consider a strongly coupled optomechanical system driven by a bichromatic field at appropriate frequencies, as shown in Fig. 1 (b). The effective optomechanical Hamiltonian describing the coherent evolution of the system is given by

$$\mathcal{H}/\hbar = \omega_c\, a^\dagger a + \omega_m\, b^\dagger b + g_0\, a^\dagger a(b + b^\dagger) + \varepsilon_p \left(a e^{i\omega_p t} + a^\dagger e^{-i\omega_p t}\right) + \varepsilon_d \left(a e^{i\omega_d t} + a^\dagger e^{-i\omega_d t}\right), \qquad (1)$$

where a (b) is the bosonic annihilation operator for the cavity (mechanical) mode with resonance frequency ω_c (ω_m), g_0 is the single-photon optomechanical coupling strength, and ε_p and ε_d are the amplitudes of the strong and weak drives at frequencies ω_p and ω_d, respectively. The dynamics of the system is governed by the Lindblad master equation,

$$\dot{\rho} = -\frac{i}{\hbar}[\mathcal{H}, \rho] + \kappa\mathcal{L}[a]\rho + \Gamma(\bar{n}_b + 1)\mathcal{L}[b]\rho + \Gamma\bar{n}_b\mathcal{L}[b^\dagger]\rho, \qquad (2)$$

where κ and Γ are the damping rates of the optical cavity and the mechanical resonator, respectively, and $\bar{n}_b$ is the mean thermal phonon occupation number of the mechanical mode at temperature T.

The numerical simulations of Eqn. 2 are shown in Fig. 1(c)(d). The strong drive which is red-detuned by twice the mechanical frequency with respect to cavity resonance ($\Delta_p = \omega_p - \omega_c \approx -2\omega_m$) mediates two-phonon cooling process. Along with the strong drive a blue-detuned weak drive which is detuned by thrice the mechanical frequency with respect to the strong drive ($\Delta_d = \omega_d - \omega_p \approx 3\omega_m$) mediates three-phonon driving and drives the mechanical state into a tricat state (Fig. 1(c)). The minimal Wigner negativity justifies the robustness of nonclassical states even at longer timescale (Fig. 1(d)).

By extending the protocol proposed by Hauer et al. [4] and by proper tuning of bichromatic optical drive, we have numerically shown that one can engineer robust mechanical tricat state.

[1] L. Pezzè, A. Smerzi, M. K. Oberthaler, R. Schmied, and P. Treutlein, *Rev. Mod. Phys.* 90, 035005 (2018).
[2] R. Howl, V. Vedral, D. Naik, M. Christodoulou, C. Rovelli, and A. Iyer , *Phys. Rev. X* 2, 010325 (2021).
[3] M. Aspelmeyer, T. J. Kippenberg, and F. Marquardt, *Rev. Mod. Phys.* 86, 1391 (2014).
[4] B. D. Hauer, J. Combes, and J. D. Teufel, *Phys. Rev. Lett.* 130, 213604 (2023).

Polarization Entanglement Distribution through Existing Fiber Infrastructure

Khushboo[1], Gourav Singh Rawat[1], Vivek Venkataraman[1,2,#], and Joyee Ghosh[1,*]
[1]Quantum Photonics Lab, Department of Physics, Indian Institute of Technology Delhi, New Delhi, 110016, India
[2]Department of Electrical Engineering, Indian Institute of Technology Delhi, New Delhi, 110016, India
*joyee@physics.iitd.ac.in, #Vivekv@ee.iitd.ac.in

We report polarization-entangled photon pair distribution over a 6 km dark fiber link at IIT Delhi using a fiber Sagnac interferometer with a Zn-indiffused MgO:PPLN ridge waveguide. Despite 31 dB total link loss, the $|\Phi^+\rangle$ Bell state yields 90.75% average two-photon visibility, 84.17% fidelity, and concurrence 0.68, demonstrating suitability for entanglement-based QKD over metropolitan fiber.

Deploying entangled photon sources over existing fiber infrastructure is essential for metropolitan quantum networks. Polarization-encoded qubits at 1550 nm are compatible with standard telecom fiber and DWDM components. However, deployed fibers experience environmental perturbations that cause time-varying polarization fluctuations that degrade entanglement fidelity. A common-path Sagnac geometry suppresses differential phase noise, providing intrinsic stability for field deployment [1, 2].
This work demonstrates the generation and distribution of polarization-entangled photon pairs using a type-0 Zn-indiffused MgO-doped periodically poled lithium Niobate (PPLN) ridge waveguide in Sagnac configuration. As shown in Figure 1a [3], a CW pump at 774.89357 nm (247 μW) generates broadband polarization-entangled photon pairs around 1550 nm at a phase-matching temperature of 36 °C. The photon pairs are demultiplexed using a 32-channel AWG, and the correlated channel pair C38–C31 is selected. Photons in C31 are transmitted through 6 km of deployed fiber (including a 5 km campus dark fiber loop and two 500m fiber spools) with a total channel loss of ∼31 dB, while C38 photons remain in the laboratory.

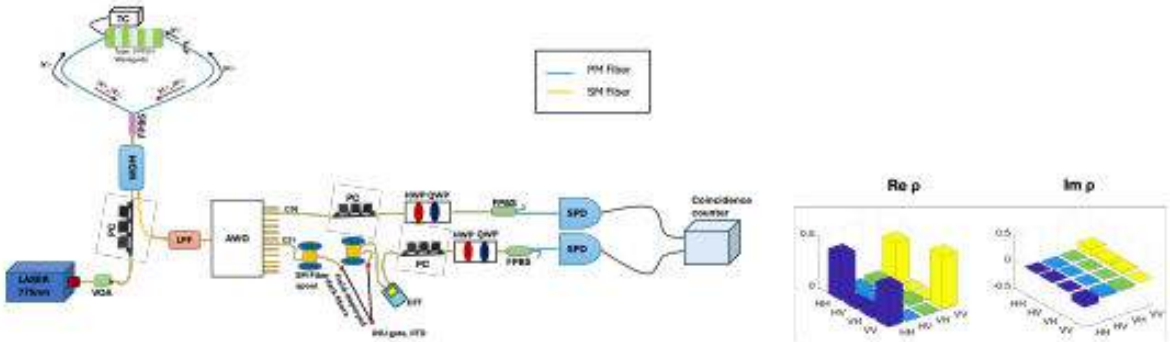


Figure 1: (a)Experimental setup for polarization-entanglement distribution through a field-deployed fiber link consisting of a 5 km dark fiber and two 500 m fiber spools [3].VOA: Variable optical attenuator,FPBS:fiber polarization beam splitter, WDM: wavelength division multiplexer, LPF: long pass filter, AWG: arrayed waveguide grating, DTF: digital tunable filter. (b) Reconstructed density matrix(Re ρ and Im ρ) obtained using quantum state tomography.

The two-photon interference experiment shows the fringe visibility in H-V basis is 89.5% and in D-A basis 92%, with SPAD at 35% QE, 5 μs DT, and a coincidence window of 256 ps of the time correlator.

Figure 1b shows the effective construction of the density matrix from quantum state tomography, illustrating that the state

$$|\Phi^+\rangle = \frac{1}{\sqrt{2}}\left(|H_s H_i\rangle + |V_s V_i\rangle\right) \tag{1}$$

is generated with Fidelity = 84.17% and Concurrence = 0.68.

These results establish that a fiber-integrated Sagnac PPLN source maintains high-fidelity polarization entanglement over a lossy metropolitan dark fiber link without active phase stabilization.

References

[1] J.-W. Pan, Z.-B. Chen, C.-Y. Lu, H. Weinfurter, A. Zeilinger, M. Żukowski, *Rev. Mod. Phys.* **84** (2012) 777.
[2] T. Kim, M. Fiorentino, F. N. C. Wong, *Phys. Rev. A* **73** (2006) 012316.
[3] V. Venkataraman, J. Ghosh *et al.*, *Opt. Commun.* **550** (2024).

Deterministic Single-Photon Emitter Arrays in Hexagonal Boron Nitride by Carbon-Assisted Focused Ion Beam Engineering

Rohit Kumar*, Mangababu Akkanaboina*, Brijesh Kumar*, Hrushikesh Gawali, Parul Sharma, Ikshvaku Shyam and Anshuman Kumar

Laboratory of Optics of Quantum Materials, Department of Physics, Indian Institute of Technology Bombay, Mumbai 400076, India

**Equal author contribution*
anshuman.kumar@iitb.ac.in

A lithography-free carbon-assisted focused ion beam technique is demonstrated for deterministic generation of single-photon emitter arrays in hexagonal boron nitride. The process combines Ga-ion milling, selective carbon incorporation, and thermal annealing, yielding 89% site-correlated emitters with dominant ZPLs around 581, 608, 630, 660 nm and high-purity single-photon characteristics, enabling scalable quantum photonic integration.

Scalable and deterministic single-photon emitters (SPEs) are fundamental for integrated quantum photonics. Hexagonal boron nitride (hBN) is a promising host for room-temperature SPEs; however, deterministic fabrication with high activation yield remains challenging. Here, we demonstrate a lithography-free approach based on Ga+ focused ion beam (FIB) milling, selective carbon deposition, and thermal annealing. Mechanically exfoliated hBN flakes were patterned using Ga-ion FIB followed by localized carbon deposition and annealing at 850 °C. Atomic force microscopy confirmed well-defined nanogrooves, while confocal photoluminescence mapping of 10×10 arrays revealed a site-correlated emitter yield of ~89%. Statistical analysis showed a dominant emitter family centred at 581–585 nm (≈28% of emitters), with additional emission groups near 604, 632, 640 and 660 nm.

Second-order autocorrelation measurements confirmed single-photon emission with $g^2(0)<0.5$, while the best emitter exhibited $g^2(0)=0.15\pm0.09$. The emitters showed excellent photostability, nanosecond-scale antibunching dynamics and high brightness. The proposed carbon-assisted FIB process provides a simple, reproducible and scalable route for deterministic hBN SPE arrays for future integrated quantum photonic devices.

References:
[1] A. Kumar, C. Cholsuk, A. Zand, M.N. Mishuk, T. Matthes, F. Eilenberger, S. Suwanna, T. Vogl, *APL Materials* **11** (2023) 071108.
[2] Aharonovich, D. Englund, M. Toth, *Nature Photonics* **10** (2016) 631–641.
[3] M. Luo, J. Ge, P. Huang, Y. Yu, I.C. Seo, K. Lu, H. Sun, J.K. Tan, B.K. Tay, S. Kim, W. Gao, H. Li, D. Nam, Nature Communications 16 (2025) Article 66314.

OAM-Induced Lattice Rotation Reveals a Fractional Optimum in Fault-Tolerant GKP Quantum Sensing

Simanshu Kumar and #Nandan S. Bisht

Department of Physics, D.S.B. Campus, Kumaun University, Nainital, Uttarakhand 263001, India

#*bisht.nandan@kunainital.ac.in*

Orbital angular momentum (OAM) encoding and Gottesman–Kitaev–Preskill (GKP) lattice geometry are structurally coupled. A fractional OAM charge $\ell = 1.5$ rotates the stabilizer lattice into a configuration reducing the logical error probability by $23.9\times$ over the square-lattice baseline, while quantum Fisher information is preserved to within 0.2% — without additional squeezing.

Gottesman–Kitaev–Preskill (GKP) codes [1] encode a logical qubit in the quadratures of a single bosonic mode and are among the most promising platforms for fault-tolerant quantum sensing. Their grid structure suppresses small displacement errors while preserving quantum Fisher information for precision phase estimation [2]. Conventional implementations adopt a square lattice, chosen for convenience rather than optimality under realistic loss and dephasing — raising the question of whether the lattice geometry can be tuned to suppress logical errors without compromising sensitivity.

We show that OAM and GKP lattice geometry are structurally coupled: imparting an OAM charge ℓ [3] — equivalent to a fractional Fourier transform of order $\alpha = \ell/2$ (for $\ell_{\max} = 4$) — continuously rotates the code lattice in phase space. A cylindrical-lens pair or spatial light modulator realizes the transform ($\alpha = 0.75$ for $\ell = 1.5$). Treating the rotation angle as a variational parameter, we derive a transcendental balance equation whose solution $\theta^*(\eta, \gamma, r)$ fixes the optimal geometry as a function of loss η, dephasing γ, and squeezing r. The full pipeline is a differentiable Strawberry Fields/TensorFlow program that jointly optimizes the logical error rate and quantum Fisher information via automatic differentiation [4].

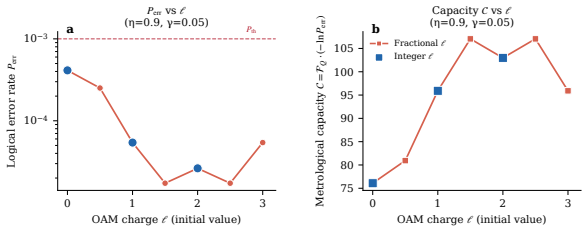


Fig. 1: (a) Logical error probability P_{err} and (b) metrological capacity $\mathcal{C} = \mathcal{F}_Q(-\ln P_{\mathrm{err}})$ vs. OAM charge ℓ at $\eta = 0.9$, $\gamma = 0.05$. The optimum is fractional: $\ell = 1.5$ reduces P_{err} by $23.9\times$ over the square lattice ($\ell = 0$) and raises capacity by $+41\%$, with $\mathcal{F}_Q$ unchanged to 0.2%.

Optimization reveals that the minimum logical error probability occurs not at an integer charge but at the fractional value $\ell = 1.5$. At this point, P_{err} is reduced by $23.9\times$ over the square-lattice baseline, while $\mathcal{F}_Q$ is preserved to within 0.2% — the metrological sensitivity is retained essentially for free. The combined benefit is captured by the metrological capacity

$$\mathcal{C} = \mathcal{F}_Q\,(-\ln P_{\mathrm{err}}), \tag{1}$$

which quantifies the joint sensitivity–fault-tolerance resource. At $\ell = 1.5$, $\mathcal{C}$ increases by 41% over the square lattice (Fig. 1).

Whereas GKP displacement sensing favours an axis-aligned lattice [5], phase estimation favours an oblique fractional geometry — the optimal lattice depends on the sensing task.

In conclusion, the OAM charge provides a continuous, physically natural handle on GKP lattice geometry, and the globally optimal configuration for fault-tolerant phase sensing is the fractional charge $\ell = 1.5$ — invisible to any integer-charge search yet accessible with standard mode-shaping optics and no additional squeezing. Lattice geometry thus emerges as a near-term, underused resource for noise-adaptive quantum sensing beyond the square-lattice paradigm. The authors acknowledge the Applied Optics & Spectroscopy Laboratory, S.S.J. University, Almora, Uttarakhand, India, for providing research infrastructure.

References:

[1] D. Gottesman, A. Kitaev, J. Preskill, *Phys. Rev. A* **64** (2001) 012310.

[2] S.L. Braunstein, C.M. Caves, *Phys. Rev. Lett.* **72** (1994) 3439.

[3] L. Allen *et al.*, *Phys. Rev. A* **45** (1992) 8185.

[4] S. Kumar, N.S. Bisht, arXiv:2605.13271 [quant-ph] (2026).

[5] L. Labarca *et al.*, *PRX Quantum* **7** (2026) 020301.

Robust Continuous-Variable Multipartite Entanglement Using Arrays of Nonlinear Waveguides

[1,#]Sugar Singh Meena, [2]David Barral, [1]Ankan Das Roy, [1]Sunita Meena and [1]Amit Rai
[1]School of Physical Sciences, Jawaharlal Nehru University, New Delhi 110067
[2]Quantum Materials and Photonics Research Group, Optics Area,
Department of Applied Physics, iMATUS, Faculty of Physics, Faculty of Optics and Optometry,
University of Santiago de Compostela, Santiago de Compostela, 15872, Spain
[3]Afflitiation with full address

[#] sugar15_sps@jnu.ac.in

We present a protocol for generating CV multipartite entanglement based on SPDC in a circular array of quadratic nonlinear waveguides. The circular geometry of our system is interesting: it has two zero-supermodes that remain squeezed and phase-matched during propagation, generating two sets of entangled states. The two entanglement layers – large spatially entangled states of odd modes and even modes – behave like parallel, minimally cross-talking quantum channels.

We establish a rigorous theoretical framework, provide comprehensive derivations of the propagation equations, and identify the regimes in which analytical solutions are possible. Physical ingredients, such as propagation eigenmodes and symmetry-based analytical solutions, enable the generation of two sets of large, distributable entangled states: one with odd modes and the other with even modes of the array. Moreover, based on three unique discrete symmetries of supermodes/Fourier modes, we derive orthonormality relations that can be exploited in circular arrays of nonlinear waveguides through suitable pumping. We used three different pump phase profiles to produce unique output correlations that can be calculated analytically.

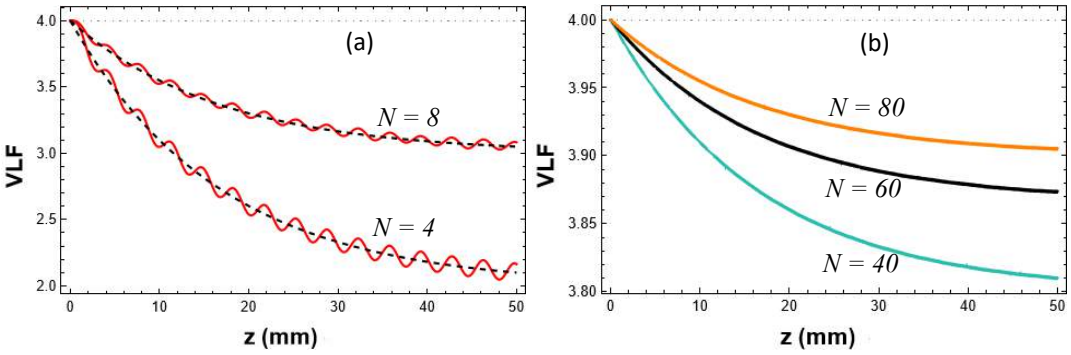


Fig. 1: Multipartite CV entanglement generation in the individual mode basis vs propagation distance (z) for a flat pump profile. (a) van Loock-Furusawa inequalities (VLF) for eight waveguides circular ANWs (Red). In the infinite coupling limit (dashed Black). We have two sets of multipartite entangled modes with identical results, 1-3-5-7 and 2-4-6-8, in the waveguide array with N = 8. (b) VLF inequalities in the infinite coupling limit for a large number of waveguides: N = 40 (Green), N = 60 (Black), and N = 80 (Orange). Simultaneous values under the threshold value (dotted), VLF = 4, imply CV multipartite entanglement.

These two sets of entangled spatial modes could be useful for parallel quantum computing [1] and crosstalk-resilient quantum communications [2]. This dichotomous nature of spatially guided modes adds an extra degree of freedom useful for engineering quantum resources [3]: one can mix every mode of one entangled set with every mode of the other, in contrast to multimode spectral strategies, giving rise to a new class of graph states. Crucially, our proposed setup enables active on/off switching of entanglement, offering a functional entanglement switch tailored for quantum networking applications. Our protocol stands out for its simplicity and robustness, as the efficient build-up of the propagation eigenmodes is independent of the specific values of coupling and nonlinearity.

References:

[1] T. W. Borneman, C. E. Granade, and D. G. Cory, Physical Review Letters 108, 140502 (2012).
[2] M. Azari, P. Polakos, and K. P. Seshadreesan, IEEE Transactions on Quantum Engineering 5, 1 (2024).
[3] M. Gu, C. Weedbrook, N. C. Menicucci, T. C. Ralph, and P. van Loock, Physical Review A 79, 062318 (2009).

Cavity Enhanced Steady State Quadrature Squeezing in Spontaneous Four-Wave Mixing Regime

[1,#] Soumyadip Mukherjee ,[1]Suman Dey and [1]Shailendra Kumar Varshney
[1] Department of Electronics and Electrical Communication Engineering, Indian Institute of Technology Kharagpur, India

[#] *isoumyadipm20@gmail.com*

We numerically demonstrate that steady-state joint amplitude quadrature vacuum squeezing of a first signal-idler pair increases with pump power in the spontaneous four-wave mixing regime, indicating improved squeezing performance while maintaining operation below the oscillation threshold of the ring-resonator which can be used as a squeezed quantum comb source.

Optical micro-resonator (MRR) based quantum frequency combs (QFCs) provide a versatile platform for investigating nonlinear quantum optical phenomena and have attracted significant interest for applications ranging from quantum metrology to high-resolution spectroscopy. Among these, squeezed quantum microcombs [1] have emerged as promising integrated sources of vacuum-noise-suppressed nonclassical light for quantum applications. In this work, we investigate the steady-state amplitude-quadrature squeezing characteristics of the first signal-idler Q-mode pair generated in the spontaneous four-wave mixing (SFWM) regime. The analysis is performed for a silicon nitride (Si_3N_4) MRR with an optical quality factor of approximately (Q =10^6).

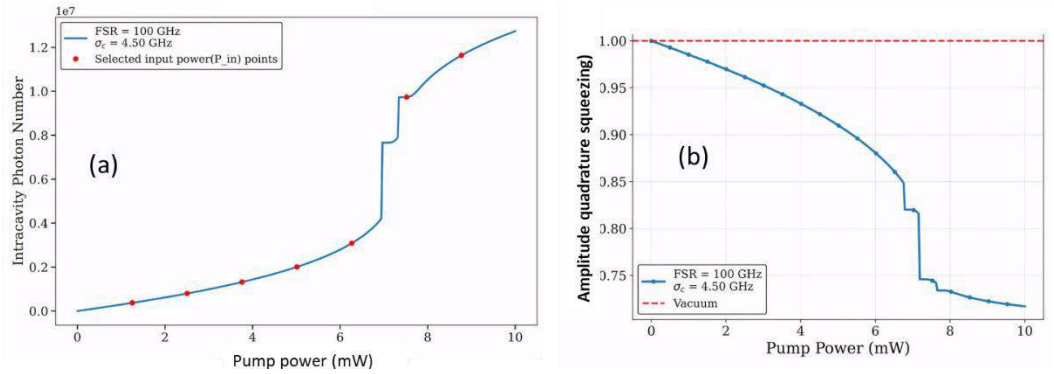


Fig 1: (a) Steady state intracavity photon number variation for fixed pump detuning (σ_c) and FSR. (b) Amplitude joint quadrature vacuum squeezing for the same detuning and FSR.

The threshold pump power (P_{th}) for stimulated four-wave mixing in the proposed Si_3N_4 MRR is estimated to be approximately 19 mW [2]. Therefore, we investigate the squeezing characteristics exclusively in the SFWM regime, with the maximum input pump power (P_{in}) limited to 10 mW, ensuring operation well below the oscillation threshold. By numerically solving the quantum Langevin equations [2] under continuous-wave pumping at 780 nm, while considering only the first signal-idler mode pair, we evaluate the steady-state intracavity photon number and the corresponding joint amplitude-quadrature vacuum squeezing, as presented in Fig. 1(a) and Fig. 1(b), respectively. Throughout the analysis, the pump detuning (σ_c= 4.5GHz) and the free spectral range (FSR = 100 GHz) are kept constant. As the P_{in} increases, the joint amplitude quadrature is progressively reduced below the vacuum noise level, demonstrating the enhancement of vacuum quadrature squeezing. The squeezing behavior indicates the direct dependency on the steady-state intracavity photon number throughout the SFWM regime, which can be further improved by local oscillator phase variation using homodyne detection angle. These results establish a promising foundation for realizing low-power integrated squeezed-light quantum sources for continuous-variable quantum computing, quantum-enhanced sensing, and precision quantum metrology.

Acknowledgements:

We would like to acknowledge the DST and Telecom Centres of Excellence, Government of India, for financial support under the National Quantum Mission (NQM) Project and Quantum Sources (Single photon and Entangled Photon Pair) (SRT) Project.

References:

[1] Z. Yang, M. Jahanbozorgi, D. Jeong, et al., *Nature Communications*, 12 (2021) 4781.
[2] Y. K. Chembo, *Physical Review A* 93 (2016) 033820.

Design of QPM crystal-based source for Quantum Ghost Imaging

[1,#]Uddipta Mukherjee,[2]O P Naraniya and [3]Unnikrishnan G
[1,2,3] Instruments Research and Development Establishment
Raipur Road, Dehradun - 248001
[#]*uddiptam2016@gmail.com*

Abstract:

Quantum ghost imaging requires entangled photon source. In Spontaneous Parametric Down-Conversion a pump photon splits two photons called signal and idler. One photon illuminates the object; and its twin is captured by a camera having spatial resolution. By correlating their detection, the object's image can be reconstructed from light that never interacted with the object.

Work Summary:

Quantum ghost imaging mostly uses photon pairs produced from Spontaneous Parametric Down-Conversion (SPDC) because it generates pairs of entangled photons that are strictly correlated in momentum and position [1]. This allows one photon to "sense" the object while the other, which never interacts with the object, provides the spatial information necessary to reconstruct the image through coincidence detection. For our design purpose, we are using laser source of 355 nm as pump and non-linear crystal Periodically Poled Stoichiometric Lithium Tantalate (PPSLT). The generated signal and Idler wavelengths are 460 nm and 1550 nm. The SPDC process and quasi-phase matching conditions have been simulated and optimized for the operational parameter in Python to calculate important crystal and beam parameters, including refractive indices, phase mismatch, poling period, beam waist, conversion efficiency etc. To determine the poling period, we have calculated phase mismatch given by

$$\Delta k = k_p - k_s \cos\theta_s - k_i \cos\theta_i,$$

where θ_s and θ_i are the emission angles of the signal and idler photons with respect to the pump propagation direction inside the nonlinear crystal. The grating period has been calculated as per the required non-collinear phase mismatch and its variation with respect to temperature of the crystal . Each wave vector is represented by

$$k_n = \frac{2\pi n(\lambda,T)}{\lambda}$$

where $n(\lambda,T)$ is calculated from temperature-dependent Sellmeier equation [2].

The simulation results for Crystal Length vs SPDC Output Power and Poling Period vs non-collinear angle are shown in fig.1 and fig. 2 respectively.

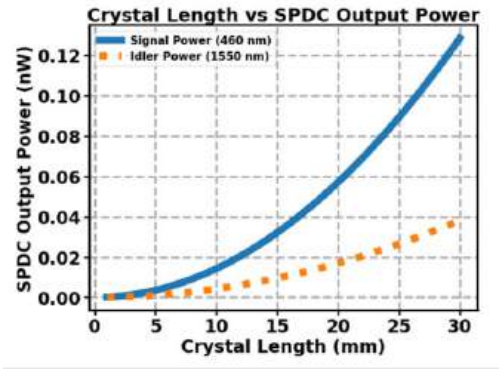


Fig.1 Crystal length vs SPDC Output Power

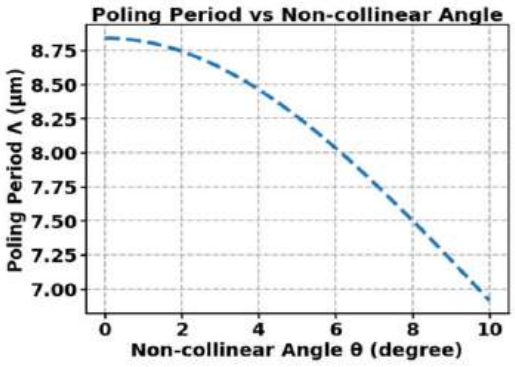


Fig.2 Poling Period vs Non-collinear Angle

References:

[1] R.W. Boyd, Nonlinear Optics, 4th ed., Academic Press, London (2020).

[2] D. H. Jundt, Opt. Lett. 22, 1553 (1997).

Purcell Enhancement of Green CdSe QDs Using a Bullseye Cavity

Sayan Nayak and #Souvik Ghosh
Electrical and Electronics Engineering, BITS Pilani K K Birla Goa Campus, India
#souvikg@goa.bits-pilani.ac.in

Efficient spontaneous emission control is demonstrated through the numerical optimization of a TiO_2 bullseye cavity coupled to green-emitting CdSe QDs. 3D FDTD simulations reveal a resonant Purcell enhancement of 71 with a Q-factor of 1325. The optimized cavity enables efficient light-matter interaction, offering a promising platform for integrated quantum photonic devices.

Controlling spontaneous emission is fundamental to cavity quantum electrodynamics and integrated quantum photonics. Colloidal CdSe quantum dots are promising solid-state emitters owing to their wavelength tunability, high quantum yield, and scalable integration [1]. However, their performance is limited by slow radiative emission, finite coherence, and inefficient omnidirectional photon extraction. Embedding a quantum emitter within an engineered optical cavity enhances the local density of optical states (LDOS), accelerating spontaneous emission through the Purcell effect while improving emission directionality [2].

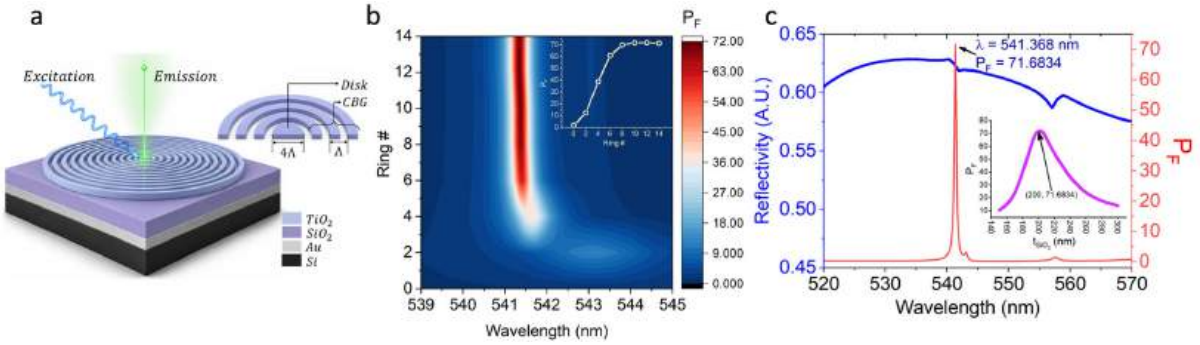


Figure 1: (a) Schematic of bullseye cavity comprising concentric circular Bragg grating (CBG) rings; (b) P_F as a function of wavelength and concentric ring $\#$, showing saturation after 10 rings (inset). (c) Reflection (blue) and P_F (red) spectra of the optimized cavity; inset shows the optimization of the SiO_2 spacer thickness.

In this work, a TiO_2 bullseye cavity is designed and optimized to enhance spontaneous emission from green-emitting CdSe QDs [3] through strong cavity-emitter coupling. The circular Bragg grating (CBG), comprising concentric TiO_2 rings, a SiO_2 spacer, and an Au reflector, provides azimuthally symmetric optical confinement and efficient coupling to in-plane dipole emitters. Satisfying the Bragg condition enables simultaneous in-plane mode confinement and vertical light extraction. Constructive interference between guided mode and reflected optical fields increases photon confinement within a small mode volume, thus resulting in enhanced electromagnetic field localization and a significantly increased LDOS at the emitter position. 3D FDTD simulations were performed to optimize the TiO_2 bullseye cavity by varying the central disk radius (R_{Disk}), grating period (Λ), duty cycle, spacer thickness, and number of concentric rings. The CBG period was designed using the Bragg condition, $\Lambda = m\lambda/2n_{eff}$, where n_{eff} is the guided mode effective index. The optimized cavity, comprising a central disk of $R_{Disk} = 620\,\mathrm{nm}$, $\Lambda = 310\,\mathrm{nm}$, 68% duty cycle, $200\,\mathrm{nm}$ SiO_2 spacer (Fig. 1(c) inset), and $150\,\mathrm{nm}$ Au reflector, achieved maximum optical confinement with ten concentric rings, Fig. 1(a), beyond which the Purcell enhancement saturated, Fig. 1(b). The cavity exhibits a resonant matched Purcell factor of 71.7 at QD emission wavelength, with a quality factor of 1325 and a sharp resonance linewidth of 0.408 nm. The Purcell enhancement is governed by, $P_F = RP_{cavity}/RP_{bulk}$, where RP represents the radiative dipole power. The P_F in Fig. 1(c) indicates that the simultaneous realization of a high-Q resonance and a small optical mode volume maximizes the spontaneous emission rate of CdSe QD. The reflection spectrum exhibits a pronounced resonant dip, signifying efficient excitation of the fundamental cavity mode and strong electromagnetic-field localization at the cavity centre. Spectral matching between the cavity resonance and the CdSe emission enhances the LDOS, thereby producing an approximately 72-fold increase in the spontaneous emission rate through cavity mediated light-matter interaction while maintaining efficient vertical photon extraction.

The proposed TiO_2 bullseye cavity combines strong optical confinement with efficient vertical photon extraction, enabling enhanced spontaneous emission from green CdSe QDs. The demonstrated high Purcell enhancement and scalable dielectric architecture establish a promising platform for compact quantum light sources, cavity quantum electrodynamics, and integrated quantum photonic circuits.

References:

[1] V. Manojkumar, G. K. Varier, R. Vathsan, P. Nandakumar, *Scientific Reports*, 15(1), 14639, (2025).
[2] R. Hekmati, J. P. Hadden, A. Mathew, S. G. Bishop, S. A. Lynch, A. J. Bennett, *Scientific Reports*, 13(1), 5316, (2023).
[3] M. L. Landry, T. E. Morrell, T. K. Karagounis, C. H. Hsia, C. Y. Wang, *Journal of Chemical Education*, 91(2), 274–279, (2014).

Schmidt-Mode Impurity as Visibility Ceiling in a Folded Nonlinear Interferometer with Undetected Photons

[1,†]Muppalla Vidya Prakash, [1,†] Aadi Suketu Bharatia, [2,#]Tanmoy Chakraborty and [1,#]Anshuman Kumar

[1]*Laboratory of Optics of Quantum Materials (LOQM), Department of Physics, Indian Institute of Technology Bombay, Mumbai-400076, India*

[2]Light and Matter Physics, Raman Research Institute, Bengaluru-560080, India

[†] These authors contributed equally.

[#] *tanmoy@rri.res.in, anshuman.kumar.srivastava@gmail.com*

We extract the joint spectral bandwidth of strongly non-degenerate SPDC ($810\,\mathrm{nm}/1.55\,\mu\mathrm{m}$*) from the coherence envelope of a folded PPLN nonlinear-interferometer path-length scan and cross check it against the Schmidt number obtained from unheralded* $g^{(2)}(0)$*, establishing a self-consistent modal characterization that requires only silicon-band detection.*

Every Fisher-information or Cramér–Rao-bound claim made on a nonlinear interferometer rests on knowing the effective mode content of the source. For non-degenerate SPDC this is awkward to characterize directly: the idler, here near $1.55\,\mu\mathrm{m}$, lies beyond convenient photon counting. We demonstrate that two *independent*, all-silicon measurements one interferometric and one statistical to determine the modal structure and check each other, with no infrared detector at any stage. Our source is a $1\,\mathrm{mm}$ type-0 congruent PPLN crystal pumped at $532\,\mathrm{nm}$ (CW) inside a folded Michelson-type nonlinear interferometer; the $810\,\mathrm{nm}$ signal is detected on Si SPADs and an Andor CCD spectrometer while the idler is retroreflected and never detected. Scanning the idler-arm mirror over the optical path difference (OPD) yields an interferogram whose fringe period in the folded geometry is $\lambda_i/2 \approx 775\,\mathrm{nm}$, and whose envelope, by the Wiener–Khinchin relation, is the Fourier transform of the joint down-conversion spectrum: the envelope width gives the coherence length l_c and hence the idler bandwidth $\Delta\lambda_i = \lambda_i^2/(2l_c)$ directly.

The statistical measurement uses the fact that the unheralded signal marginal of a multimode squeezed vacuum is thermal with a mode-diluted bunching peak [1],

$$K = \frac{1}{g^{(2)}(0) - 1}, \tag{1}$$

measured in a Hanbury Brown Twiss arrangement with two Si SPADs on the signal arm. Consistency between the spectral Schmidt number predicted from the measured bandwidth [2,3] and the K of Eq. (1) confirms a spectrally dominated mode structure; any excess of measured K over the spectral prediction quantifies spatial multimode contamination a diagnostic that directly informs mode filtering strategy. In our setup the achieved visibility $\sim$36% observed is tested with the Schmidt mode information obtained. The method is a general, low-overhead recipe: any laboratory operating an undetected-photon interferometer can characterize its mid-IR biphoton source bandwidth, coherence length, Schmidt number and purity using two silicon SPADs.

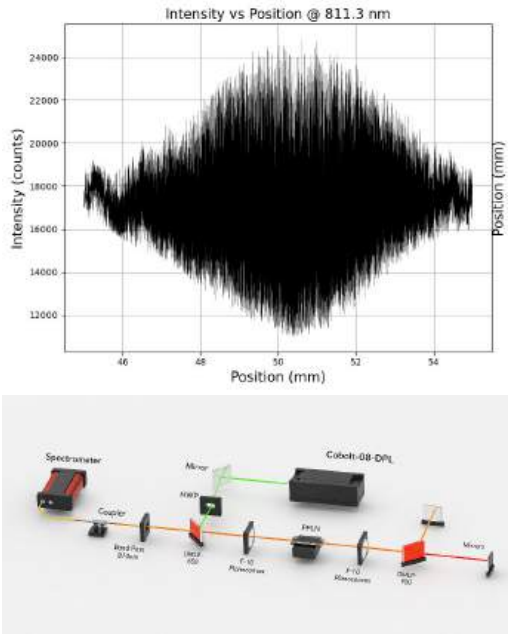


Fig. 1 Top: Measured interferogram envelope over the idler-arm scan; the envelope peak defines the zero-OPD anchor. Bottom: Schematic of the setup

References:

[1] AA. Christ, K. Laiho, A. Eckstein, K.N. Cassemiro, C. Silberhorn, *New Journal of Physics* (2010).
[2] W.P. Grice, A.B. U'Ren, I.A. Walmsley, *Physical Review A* (2001).
[3] P.J. Mosley, J.S. Lundeen, B.J. Smith, P. Wasylczyk, A.B. U'Ren, C. Silberhorn, I.A. Walmsley, *Physical Review Letters* (2008).
[4] M.V. Chekhova, Z.Y. Ou, *Advances in Optics and Photonics* 8 (2016).

Investigating the Emergence of Entanglement in an Atom-Cavity System

Siva Prasanna Karri, Mounika Sri Gudipati and #Nilakantha Meher
Department of Physics, SRM University AP, Amaravati 522240, Andhra Pradesh, India

#nilakantha.meher6@gmail.com

The emergence of entanglement in an atom-cavity system is investigated in terms of basis-dependent atomic coherence and energy exchange between the atom and the field. We find that, for certain field states, both mechanisms determine the entanglement. In contrast, for other field states, solely the energy exchange determines the entanglement.

The Jaynes-Cummings model predicts several interesting features of an atom-cavity system [1,2]. Here, we investigate the emergence of entanglement in such a system whose interaction is governed by the Jaynes-Cummings Hamiltonian [2,3]. By considering the atom in its excited state $|e\rangle$ and the cavity field in $|\psi_f\rangle = \sum_{n=0}^{\infty} c_n|n\rangle$, we get the amount of entanglement between the atom and the field at time t to be [2]

$$S(t) = -g_+(t)\log_2[g_+(t)] - g_-(t)\log_2[g_-(t)], \quad (1)$$

where

$$g_\pm(t) = \frac{1}{2}\left(1 \pm \sqrt{(C_{l_1}(\rho_a))^2 + (W(t))^2}\right). \quad (2)$$

Here, $C_{l_1}(\rho_a)$ is the l_1-norm of coherence of the atom with a reduced density matrix ρ_a, and $W(t)$ is the atomic population inversion that arises due to the energy exchange [2]. Based on the contributions of these two quantities to the entanglement, we classify the field states into two classes.

Class 1: In this class of states, we find $C_{l_1}(\rho_a) = 0$ for all t (See Fig. 1). Therefore, the entanglement between the atom and the field arises solely from the exchange of energy between them. This class includes Fock states, thermal states, even coherent states, odd coherent states, etc. Importantly, among these states, a few states display perfect collapse $W(t) = 0$ over an extended period. During this period, the entanglement between the atom and the field reaches its maximum value of unity (See Fig.1).

Class 2: In this class of states, the atomic coherence $C_{l_1}(\rho_a)$ becomes non-zero upon interaction with the field. Thus, the entanglement is determined by both the atomic coherence and the atomic population inversion. The entanglement becomes maximum if and only if they simultaneously vanish, which is highly unlikely. This class includes coherent states, Yurke-Stoller states, etc.

In summary, we investigated the emergence of entanglement in an atom-cavity system. For certain initial nonclassical field states, the entanglement between the atom and the field is determined by the l_1-norm of coherence and energy exchange. On the other hand, for other classes of field states, entanglement dynamics is governed by energy exchange only.

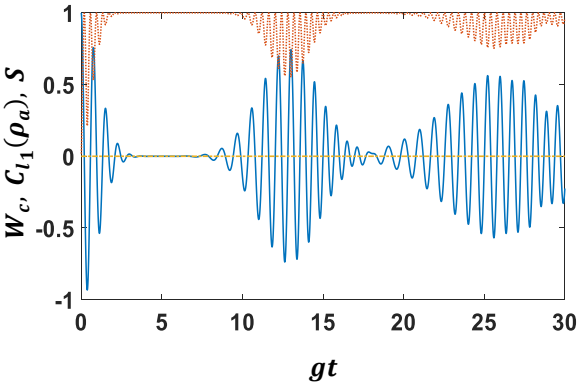


Fig. 1: The atomic population inversion (blue), von Neumann entropy (red-dot), and the l_1-norm of coherence of the atom (yellow-dashed) as a function of time, when the initial field is considered in an even coherent state with $\alpha = 4$.

References:

[1] E.T. Jaynes, F.W. Cummings, Proc. IEEE 51(1963), 89.
[2] Gerry C and Knight P L, *Introductory Quantum Optics,* Cambridge University Press, Cambridge (2004)
[3] N. Meher and S. Sivakumar, Eur. Phys. J. Plus 137 (2022) 985.

Towards Magnetically Tunable Laser Locking Using Polarization Spectroscopy of the Cs D_2 Line

[1,#]Rachana, [1]Pratiyush Vashisht and [1]Bodhaditya Santra

[1]Department of Physics, Indian Institute of Technology Delhi, New Delhi, 110016, India

[#][phz248484@physics.iitd.ac.in]

We report polarization spectroscopy of the $6S_{1/2}(F=4) \rightarrow 6P_{3/2}$ transition of the $^{133}Cs\ D_2$ line using an 852 nm DBR laser. A high contrast, background-free dispersive error signal with well-resolved hyperfine features is obtained to lock the laser to the F = 4 → F' transition. As a next step, we propose to investigate the effect of a controlled longitudinal magnetic field on the polarization spectroscopy signal to realize a magnetically tunable lock point.

Frequency-stabilized lasers are essential for laser cooling, trapping, and precision spectroscopy with caesium. Unlike saturated absorption spectroscopy, which often requires modulation to generate an error signal, polarization spectroscopy directly provides a background-free dispersive signal for robust modulation-free laser locking. Incorporating a controlled magnetic field can further enable a magnetically tunable lock point via the Zeeman effect, providing calibrated frequency offsets for applications such as laser cooling, repumping, and optical tweezers.

In our setup, counter-propagating pump and probe beams derived from a single 852 nm DBR laser pass through a room-temperature Cs vapour cell. The circularly polarized pump induces optical anisotropy, causing differential absorption of the $\sigma^+$and σ^-components of the linearly polarized probe. These components are separated using a PBS and detected by a balanced photodetector to generate a background-free dispersive error signal. Figure 1 shows the σ^+ and σ^- absorption profiles and the resulting error signal. The $F' = 4/5$ crossover and $F' = 5$ cyclic transitions exhibit the steepest zero-crossing slopes, making them suitable candidates for laser frequency locking.

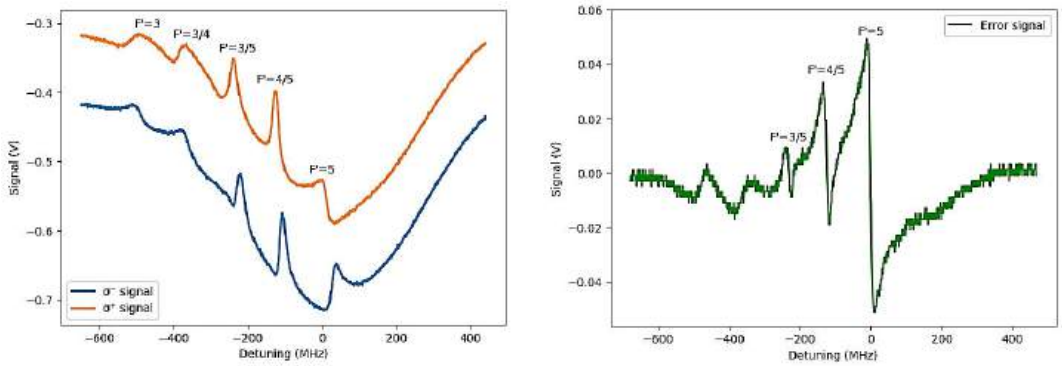


Fig. 1: (Left) σ⁺ and σ⁻ absorption profiles and (right) the corresponding polarization error signal for the Cs D2 F = 4 → F' manifold.

We further propose to study polarization spectroscopy under a controlled longitudinal magnetic field. Zeeman splitting of the atomic sublevels is expected to shift the σ^+ and σ^- transitions in opposite directions, altering the dispersive error signal and enabling a field-dependent lock point. By measuring the variation of the error-signal slope and zero-crossing with magnetic field, we aim to demonstrate a simple, magnetically tunable modulation-free laser locking scheme for generating controlled frequency detuning.

References:

1. C. P. Pearman, C. S. Adams, S. G. Cox, P. F. Griffin, D. A. Smith, I. G. Hughes, *Journal of Physics B: Atomic, Molecular and Optical Physics* 35 (2002) 5141.
2. M. L. Harris, C. S. Adams, S. L. Cornish, I. C. McLeod, E. Tarleton, I. G. Hughes, *Physical Review A* 73 (2006) 062509.
3. K. Pahwa, L. Mudarikwa, J. Goldwin, Optics Express 20 (2012) 17456.

Design and Optimization of a High-Resolution TOF Absorption Imaging System for a 2D Magneto-Optical Trap

[1,*#]Aryan Raj, [1,2]Mithlesh K Parit, [1]Mobassir Ahmad , [1]Niladri Sarkar, [1]Jatin and [1]Raghavan K Easwaran
[1]Indian Institute of Technology Patna, Bihta, Bihar, India

[2]Niels Bohr Institute, University Of Copenhagen, Denmark

[#]*aryanraj31482@gmail.com*

We report the optical design of an aberration-corrected imaging system for fluorescence and Time-of-Flight (TOF) absorption imaging of a two-dimensional rubidium magneto-optical trap. The optimized design achieves high spatial resolution and image fidelity, enabling accurate characterization of ultracold atomic clouds and quantitative measurements of their expansion dynamics..

Alkali atoms interacting with the resonant light give rise to Electromagnetically Induced Transparency (EIT) like interesting coherent phenomena. In the presence of a strong coupling light, the atomic media becomes transparent for a weaker probe light reducing the group velocity much slow compared to c making it a very suitable candidate for quantum memory (QM) unit. In this study, we show a theoretical model using the 2 dimensional magneto-optical trap (2D-MOT) to reduce down the temperature in micro Kelvin range, which makes a substantial changes in the atomic media to achieve slow slight (in the order of 101 in m/s).

Using this cold atomic system, we perform 1) fluorescence imaging and 2) Time of flight (TOF) absorption imaging. Time-of-flight (TOF) absorption imaging is a widely used technique for characterizing ultracold atomic clouds by recording their free expansion after release from a trapping potential. A resonant probe beam illuminates the expanding cloud, and the resulting absorption image is used to extract the optical density, atom number, and temperature. The imaging system must provide high spatial resolution, minimal optical aberrations, and accurate magnification to preserve quantitative measurements. In this work, we present the optical design and optimization of a high-resolution TOF absorption imaging system using achromatic doublets and ray-tracing simulations.

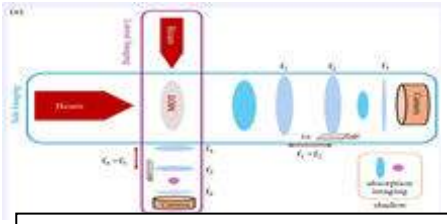


Fig1 shows the optical setup for TOF absorption imaging.

Further, we optimize the aberration of the imaging using commercially available lenses and Zeemax Opticstudio. The optimized imaging system provides aberration-corrected, high-resolution performance, enabling precise quantitative characterization of ultracold rubidium atoms for quantum technology applications. I acknowledge the funding from the National Quantum Mission, Department of Science and Technology, New Delhi, India, through grant number DST/QTC/NQM/QComm/2024/2(C).

References:

[1] S Bhushan,Raghavan K Easwaran Theoretical design for generation of slow light in a two-dimensional magneto optical trap using electromagnetically induced transparency,Indian Institute Of Technology Patna,2017.
[2] Developing and building an absorption imaging system for Ultracold Atoms , Tadas Pyragius, University of Nottingham, Department of Physics and Astronomy, NG7 2RD.
.

Helical Ince-Gaussian Beam Assisted Six-Wave Mixing in a Coherent Atomic Medium

#Naincy Shrivastava, Mobassir Ahmad, Niladri Sarkar and Raghavan K. Easwaran
Indian Institute of Technology Patna, Bihar, 801106

#naincy_2321ph07@iitp.ac.in

We theoretically investigate six-wave mixing in a coherent atomic medium using a Helical Ince–Gaussian as one of the coupling beams. The influence of the structured beam on the conversion efficiency is analyzed. Further we found that the spatial structure of the coupling beam is maintained in the generated beam.

A theoretical model of six-wave mixing in a coherent atomic medium is studied by solving the von Neumann equation under the density matrix formalism. The atomic coherences are then coupled with the Maxwell-Bloch equations to determine the evolution of the generated field and its corresponding Rabi frequency.

The analytical model is first studied to examine the generated field, atomic coherences, gain, and the normalized conversion efficiency. The analysis is subsequently extended by using Helical Ince-Gaussian (HIG) beam [2] as one of the coupling beam (Ω_c), allowing the influence of spatially varying beam profile on the six-wave mixing process.

A comparison between two cases showed that the HIG beam as a coupling beam yields a higher normalized conversion efficiency while preserving its elliptical beam profile and the spatial structure during nonlinear mixing process.

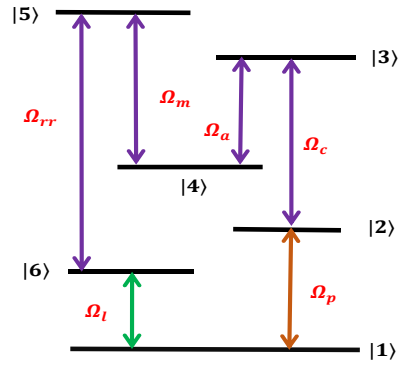


Figure 1: Energy levels for six wave mixing process [1]

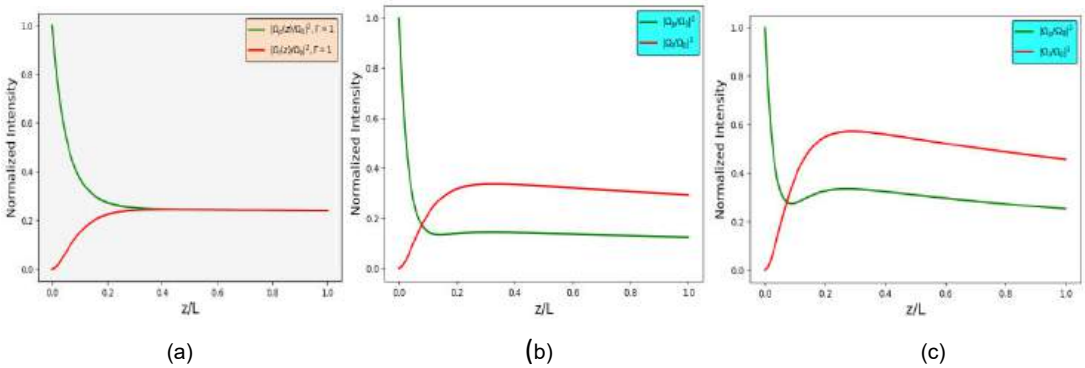


Figure 2: Normalized intensity of the probe and generated field (a) for analytical model, (b) and (c) when helical ince gaussian beam is used as coupling beam (Ω_c) having modes p = 9, m = 5 and p = 11, m = 9, respectively.

The present study provides a theoretical framework for investigating structured-light-assisted six-wave mixing and may serve as a basis for future experimental realization and optimization of coherent nonlinear frequency conversion. We acknowledge the funding from the National Quantum Mission, Department of Science and Technology, New Delhi, India, through grant number DST/QTC/NQM/QComm/2024/2(C).

References:

[1] VOGT, GROSS, HAN, PAL, LAM, KIFFNER, ANDLI PHYSICAL REVIEW A 99,023832 (2019)

[2] Bandres, Miguel & Gutierrez Vega, Julio. (2004). Ince–Gaussian beams. Optics Letters. 29. 144-146. 10.1364/OL.29.000144.

Height-Driven Modulation of Single-Photon Emission in $Al_{0.4}Ga_{0.6}As$ Bullseye Cavity

[1,*]Parul Singh,[1,*]Anurag Vishal, and [1,#]Jhuma Saha
[1] Indian Institute of Technology Gandhinagar, Gujarat. 382355
[*]Equal contribution

[#]*Correspoding author: parulsingh@iitgn.ac.in*

An $Al_{0.4}Ga_{0.6}As$ bullseye cavity incorporating an Au subshell is analyzed to examine the influence of emitter height on single-photon emission. Stable collection efficiency, pronounced Purcell modulation, and minimal resonance variation demonstrate a simple yet effective strategy for engineering high-performance integrated quantum light sources.

Single-photon sources are key components of quantum communication, quantum computing, and integrated quantum photonic systems [1]. Their performance depends on cavity characteristics including collection efficiency, Purcell enhancement, transmission, and resonant wavelength, which are strongly influenced by cavity geometry and emitter position. In this work, we investigate an $Al_{0.4}Ga_{0.6}As$ bullseye cavity incorporating an Au subshell to evaluate the influence of quantum-dot (QD) height on these optical properties. The simulation framework was first validated using the Fabry-Pérot cavity reported by *Huang et al*. [2]. The validated vertical layer stack was subsequently modified into a bullseye cavity by replacing the upper Ag and GaAs layers with an Au subshell to improve optical confinement and directional emission. The QD, modelled as an electric dipole, was displaced from 0 to 280 nm in 40 nm increments along the z-axis while maintaining an identical cavity geometry (Fig. 1(a)).

The proposed cavity achieves a maximum collection efficiency of 91% at NA = 1, remaining nearly unchanged over the investigated dipole positions (Fig. 1(b)), demonstrating robust photon extraction. In contrast, the Purcell factor exhibits a pronounced dependence on emitter height, increasing from 0.78 to 7.97 owing to variations in emitter-cavity mode overlap. Transmission follows a similar trend, increasing from 0.71 to 7.71 and confirming the strong influence of vertical emitter placement on cavity coupling. The resonant wavelength remains close to 881 nm for most dipole positions, indicating stable spectral behavior, but shifts to 800 nm near a dipole height of 160 nm, where the Purcell factor (0.78) and transmission (0.71) attain their minimum values, whereas the collection efficiency at NA = 0.65 reaches its maximum value of 72%.

These findings demonstrate that vertical QD positioning provides an effective means of engineering cavity performance without altering the device architecture. The ability to achieve nearly an order-of-magnitude modulation in Purcell enhancement while maintaining consistently high collection efficiency highlights the flexibility of the proposed bullseye cavity for optimizing spontaneous emission and photon extraction simultaneously. The presented design offers practical guidance for developing compact, experimentally realizable, and high-efficiency single-photon sources for future integrated quantum photonic platforms.

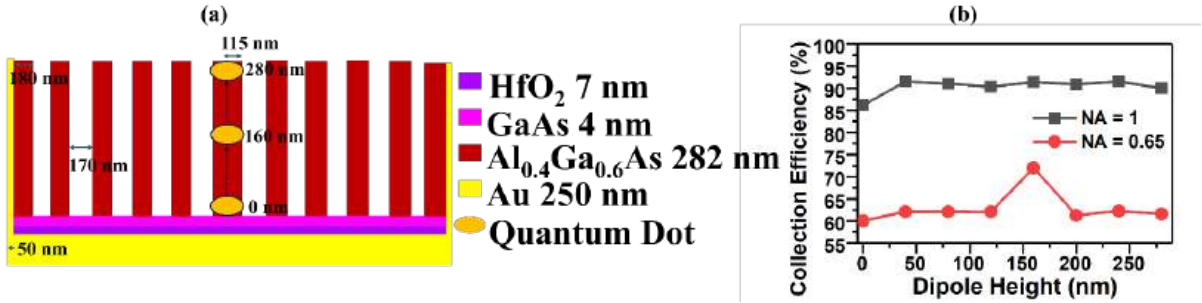


Fig. 1(a) Schematic of the proposed $Al_{0.4}Ga_{0.6}As$ bullseye cavity with Au subshell, showing all structural dimensions and layer thicknesses used in the simulation, and (b) Collection efficiency (%) as a function of dipole height for NA = 1 and NA = 0.65.

References:

[1] Gisin, Nicolas, and Rob Thew. "Quantum communication." Nature photonics 1.3 (2007): 165-171.
[2] Huang, Huiying, et al. "Bright single photon emission from quantum dots embedded in a broadband planar optical antenna." Advanced Optical Materials 9.7 (2021): 2001490.

Decoherence Analysis of $^{167}Er:Y_2SiO_5$ at the ZEFOZ Operating Point: Bath Regime Diagnostic and Motional Narrowing in a Telecom-Wavelength Quantum Memory

Shashank Srivastava[1], Anu Venugopalan[2]

Department of Physics, Netaji Subhas University of Technology, New Delhi, India

paradigm.shashank@gmail.com

Er:YSO is a leading telecom-wavelength quantum memory candidate. Using JAX automatic differentiation, the ZEFOZ point of the |14> to |15> transition of Site 2 is located exactly, reproducing a coherence time of 95.1 s. A six-check diagnostic shows the ^{89}Y bath is motionally narrowed, making this value a lower bound, not a ceiling.

A working quantum internet needs solid-state spin memories that hold coherence for 100 to 10,000 seconds, long enough to preserve a photonic qubit mapped onto a spin ensemble. Er:YSO, operating at its 1.53 μm telecom transition, is a strong candidate because its I = 7/2 nuclear spin gives rise to Zero First-Order Zeeman (ZEFOZ) points, where the transition frequency stops responding to first-order magnetic field noise. Matsuura et al. (2026) predicted T_2 = 95.3 s for the |14> to |15> hyperfine transition of Site 2 at $|B_0|$ = 633.52 mT, the highest value reported for any telecom-wavelength quantum memory.

This work verifies that result independently using JAX-based automatic differentiation. Exact sensitivity tensors S_1 and S_2 are computed by differentiating directly through the 16x16 Hermitian eigensolver, avoiding the truncation error of finite-difference methods. A Newton-Raphson search with the exact Hessian as Jacobian converges to the ZEFOZ point with residual $|S_1|$ = 3.70x10-14 MHz/mT. The result, T_2 = 95.1 s at |B0| = 633.527 mT, agrees with the reference to within 0.001% in field and 0.2% in coherence time.

A six-check diagnostic then tests whether the frozen-bath assumption behind T_2 = 95.1 s matches the actual 89Y bath dynamics. The bath correlation time, from the 89Y-89Y flip-flop rate, is tau_c = 27.72 ms, giving a timescale ratio T_2/tau_c = 3431. The Kubo parameter kappa = 5.83x10-4 rad sits three orders of magnitude below the crossover (kappa = 1), placing the system deep in the fast-modulation regime shown in Fig. 1. All six checks pass.

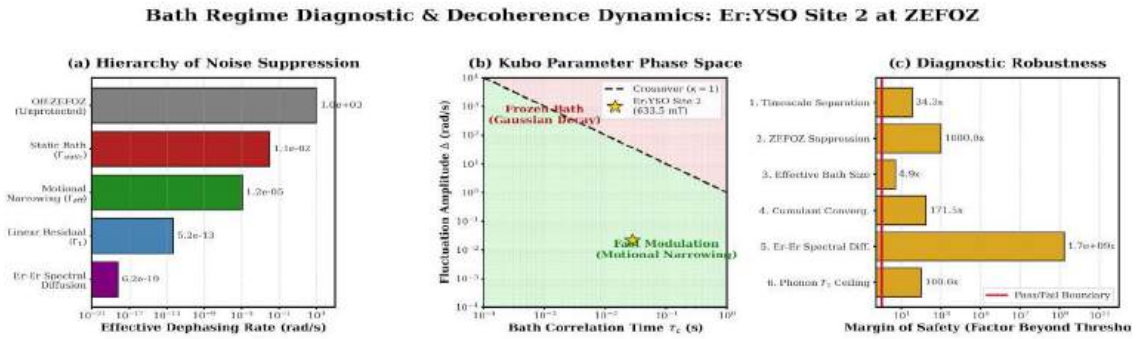


Fig. 1: Er:YSO in the fast-modulation regime of the Kubo phase space.

The main finding is that the 89Y dipolar network self-averages its own magnetic noise through motional narrowing, with no external pulse control needed. T_2 = 95.1 s is therefore a conservative lower bound, and the true coherence time is bounded above by the phonon limit of $2T_2$ = 19142 s. Er:YSO at 633.527 mT stands out as a strong, telecom-compatible quantum memory platform, motivating direct experimental verification of this regime.

References:

[1] Y. Wang, et al., Physical Review B 108 (2023) 174102.

[2] E. Fraval, M.J. Sellars, J.J. Longdell, Physical Review Letters 92 (2004) 077601.

[3] R. Kubo, Journal of the Physical Society of Japan 9 (1954) 935.

Interplay of Environmental and Target Reflectivity in Quantum Illumination

[#]Shilpi Srivastava and Shubhrangshu Dasgupta
Department of Physics, Indian Institute of Technology Ropar, Rupnagar, Punjab,140001, India

[#]*shilpi.22phz0008@iitrpr.ac.in*

A sequential interaction model for quantum illumination is investigated by analyzing the influence of the environmental and target reflectivities on the discrimination between the target-present and target-absent hypotheses. Using the quantum Chernoff bound, we identify a non-monotonic dependence on environmental reflectivity, revealing a regime of reduced distinguishability under strong signal-environment mixing.

Quantum illumination (QI) [1] is a quantum sensing protocol that exploits entanglement between the signal and idler modes generated via an SPDC source to reduce the error probability in detecting weakly reflecting targets embedded in noisy thermal environments. Existing QI models [2] often simplify the target-environment interaction by neglecting the target's intrinsic thermal emission or assuming a perfectly reflecting target, thereby limiting their applicability to realistic scenarios. Recently, a sequential interaction model [4] was introduced, in which the signal first interacts with a thermal environment and then with the target as shown in Fig.1. In this model, the environment and the target are represented by beam splitters with different reflectivities, while the target is allowed to have a temperature different from that of the surrounding environment.

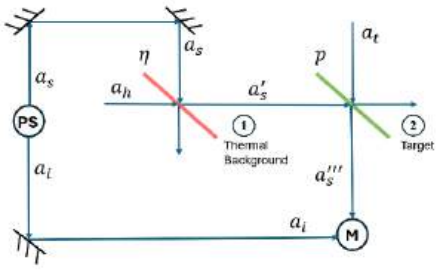


Fig.1 Schematic of QI

Using this framework, we investigate the effects of the environmental reflectivity η and target reflectivity p on the target discrimination performance. The analysis is carried out using the quantum Chernoff bound (QCB), which provides an asymptotically tight upper bound on the minimum error probability. The performance of QI with a two-mode squeezed state is compared with that of classical illumination employing a coherent state. Our results show a non-monotonic dependence of the QCB on the environmental reflectivity, with the largest values occurring at intermediate reflectivities and lower values near η→0 and η→1. Contour plots further reveal that the dependence of the QCB on the target reflectivity is strongly influenced by the environmental coupling. These results demonstrate that environmental coupling plays a key role in determining the target discrimination capability of sequential quantum illumination, irrespective of the probe state.

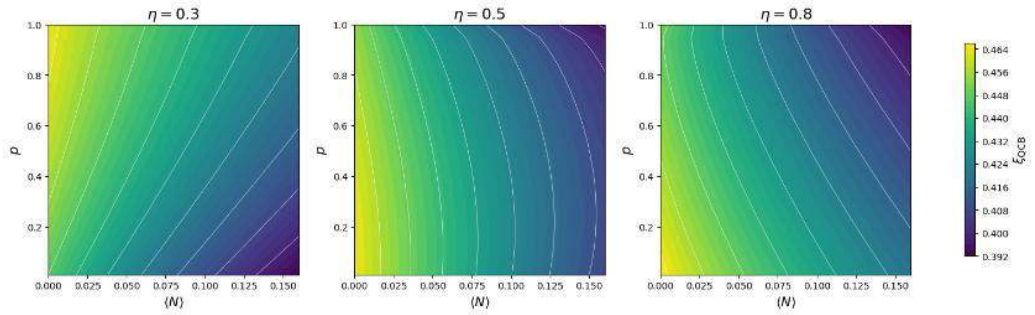


Fig.2 Contour plots showing the variation of QCB (ξ_{QCB}) with signal strength $\langle N \rangle$ and p for different η.

References:

[1] Lloyd, S. (2008). Enhanced sensitivity of photodetection via quantum illumination. *Science*, *321*(5895), 1463-1465.

[2] Fan, L., & Zubairy, M. S. (2018). Quantum illumination using non-Gaussian states generated by photon subtraction and photon addition. *Physical Review A*, *98*(1), 012319.

[3] Srivastava, S., & Dasgupta, S. (2026). Enhanced quantum illumination of a lossy target: A sequential interaction model. arXiv preprint arXiv:2604.12381.

Detection Parameter Optimization for Efficient Photon-Correlation Measurements

Vijay[1], Awanish Pandey[2], Vivek Venkataraman[1,3], and Joyee Ghosh[1,#]
[1]Quantum Photonics Lab, Department of Physics, Indian Institute of Technology Delhi, New Delhi-110016, India
[2]Optics and Photonics Centre, Indian Institute of Technology Delhi, New Delhi-110016, India
[3]Department of Electrical Engineering, Indian Institute of Technology Delhi, New Delhi-110016, India

[#]*joyee@physics.iitd.ac.in*

In this work, we have experimentally studied the effects of different operational parameters, such as detector quantum efficiency, dead time, and coincidence bin width, on photon-correlation measurements. The optimized parameters yield an efficient photon-correlation measurement, resulting in higher coincidence counts and a higher CAR.

Emerging photonic quantum technologies are promising for enhancing capabilities in secure communication, computing, metrology, and sensing [1]. To efficiently deploy these technologies, we need optimized operating parameters [2]. In this work, we explored different operating parameters, such as detector dead time, quantum efficiency (QE), and coincidence bin width, for our photon-pair source based on spontaneous four-wave mixing (SFWM) to find the optimal conditions for efficient photon-correlation measurement, yielding high coincidence counts and a high CAR (coincidence-to-accidental ratio).

In our experiment, the photon pairs are generated using SFWM, $\chi(3)$-based nonlinear process, in a SOI (silicon-on-insulator) nanowaveguide of length 2.5 mm. The waveguide is pumped at 1550.12 nm, and the output is channelized using a 100-GHz DWDM (dense wavelength-division multiplexing) module. Single-photon detectors based on avalanche diodes are used for photon detection, and the coincidences are measured using Swabian Time Tagger Ultra.

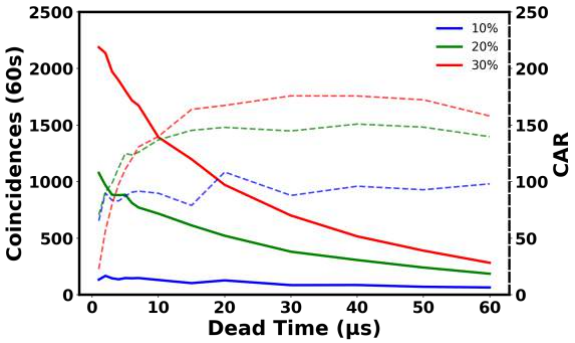


Fig. 1: Coincidences (left axis, solid lines) and CAR (right axis, dashed lines) as a function of detector dead time for three different detector quantum efficiencies (mentioned in the legend), with a coincidence bin-width of 256 ps.

Figure 1 shows the variation in coincidences, along with the corresponding CAR, as a function of detector dead time at three different quantum efficiencies (QEs), with a bin width of 256 ps. As is evident, both the coincidences and CAR increase with the increase in QE. The coincidences decrease with increasing detector dead time, while the CAR initially increases and then saturates at a dead time of ~5 μs. At small dead times, the CAR is low due to higher dark counts, which increase sharply at small dead times. Evidently, a higher quantum efficiency and appropriately small dead time, such that the adverse effect of high dark counts is absent, are desired for efficient photon-correlation measurement. We have also studied the effect of the coincidence bin width on the detected coincidences and the corresponding CAR. The coincidences first increase, then saturate, as the bin-width increases, while the corresponding CAR values decrease monotonically due to increasing noise correlations. An optimum bin width of ~200 ps sits at the sweet spot, leading to high coincidences and high CAR.

The analysis revealed optimal detection parameters for efficient photon-correlation measurement: QE 30%, dead time 5 μs, and coincidence bin width 200 ps, yielding high coincidences and high CAR.

References:

[1] Hui Wang, Timothy C Ralph, Jelmer J Renema, Chao-Yang Lu, and Jian-Wei Pan. Scalable photonic quantum technologies. Nature Materials, 24(12):1883–1897, 2025.
[2] Akanksha Angural and Joyee Ghosh. Enhancing quantum temporal cross-correlation measurements by manipulating detection parameters. Journal of Lightwave Technology, 2025.

Underwater topological charge detection of optical vortices

Gunjan Sinha & Praveen Kumar*

Department of Physics, Indian Institute of Technology Bhilai, Durg, Chhattisgarh, India

*praveen@iitbhilai.ac.in

This work investigates the identification of topological charge (TC) of underwater propagated vortex beam using polarization-based phase modulation method. The vortex beam is propagated through underwater environments, including turbid, and saline water, to examine the feasibility of this technique for reliable TC detection in varying underwater propagation conditions.

Optical vortex beams have attracted significant attention due to their ability to carry orbital angular momentum (OAM), which provides a large number of orthogonal states compared to the binary polarization states of the light. Their TC defined by the number of phase windings, is a key parameter for OAM-based applications. Several techniques, such as interferometry, diffraction, and polarimetry, have been reported for TC detection.

However, topological charge detection of underwater optical vortex beams has received limited attention. The underwater environment introduces scattering and absorption, making reliable TC detection more challenging. In this work, we propose a polarization-based method for the detection of the TC of underwater optical vortex beams.

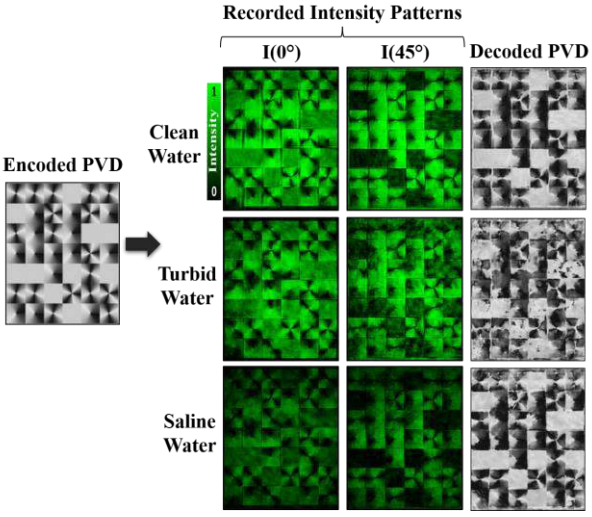


Fig. 1: Vortex array propagation in different underwater media

The proposed method determines the TC from the analysis of recorded intensity images. Its simple experimental implementation eliminates the need for critical alignment and complex optical field configurations, enabling reliable TC detection with improved stability against external disturbances and vibrations in underwater environments.

References:

1. Tripathi, K. K., Kumar, R., & Kumar, P., *Applied Physics B*, *132*(3) 30 (2026).
2. Kumar, P., Nishchal, N. K., *Optics Communications*, *459* (2020) 125000.
3. Yao, A. M., Padgett, M. J., *Advances in Optics and Photonics*, *3*(2) (2011).
4. Soskin, M. S., Gorshkov, V. N., Vasnetsov, M. v., Malos, J. T., Heckenberg, N. R., *Physical Review A*, *56*(5) 4064–4075 (1997).

Multi-Metric Analysis of Many-Body Quantum Interference in Integrated Photonic Boson Sampling

[1,#]Gaurav Kumar Yadav,[1]Chandan Pathak, [1]Ashutosh Kumar and [1]Mukesh Kumar

[1]Optoelectronic Nanodevice Research Laboratory (ONRL), Department of Electrical Engineering, Indian Institute of Technology Indore, Indore–453552, India
[#]*gauravyadav@iiti.ac.in*

Reliable benchmarking of photonic boson sampling remains challenging because no single metric fully characterizes quantum interference. A multi-metric framework integrating Total Variation Distance (TVD), Heavy Output Generation (HOG), Linear Cross-Entropy Benchmarking (XEB), and higher-order photon correlations provides robust validation of many-body interference in programmable integrated photonic circuits.

Boson sampling has emerged as a promising platform for near-term photonic quantum computing by exploiting many-body interference in linear optical networks [1]. As programmable photonic quantum processors continue to scale in circuit size and complexity, reliable verification of quantum interference becomes increasingly important for calibration, performance evaluation, and validation of computational advantage. Existing benchmarking protocols typically rely on individual observables, including cross-entropy benchmarking and heavy-output generation [2–3], each providing only a partial description of circuit performance. To address this limitation, a unified multi-metric benchmarking framework is presented that combines complementary quantum signatures for comprehensive validation of integrated photonic boson sampling circuits.

A programmable six-mode integrated photonic boson sampling circuit comprising cascaded beam splitters and phase shifters [4] is investigated to realize arbitrary unitary transformations. Three to five-photon Fock-state inputs are propagated through the interferometer, and the resulting output statistics are evaluated using four complementary benchmarking metrics. As shown in Fig. 1, the four metrics capture distinct aspects of many-body quantum interference. TVD quantifies the separation between quantum and classical output statistics, HOG measures the concentration of probability in interference-enhanced events, and XEB tracks the degradation of coherent evolution with increasing propagation time. Their complementary behaviour demonstrates that different metrics probe distinct signatures of many-body quantum interference, providing a more complete picture of interference dynamics during circuit evolution. The second and third-order photon correlation functions $g^{(2)}$ and $g^{(3)}$, quantify the emergence of many-body quantum correlations with increasing photon number. Together, these metrics provide a comprehensive assessment of interference dynamics and the transition from coherent quantum evolution to the classical crossover regime.

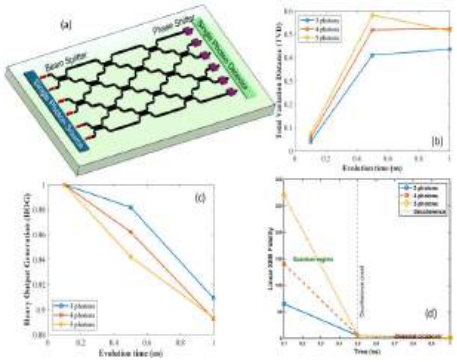


Fig. 1: Multi-metric benchmarking of a programmable six-mode photonic boson sampling circuit. (a) Schematic of the Boson sampling circuit. (b) Total Variation Distance (TVD), (c) Heavy Output Generation (HOG), and (d) Linear Cross-Entropy Benchmarking (XEB) for three to five-photon Fock-state inputs illustrating complementary signatures of quantum-classical separation, sampling fidelity, and coherence degradation during many-body quantum interference.

The multi-metric analysis reveals distinct interference regimes during circuit evolution, from coherent quantum dynamics to the quantum-to-classical crossover. Increasing photon number strengthens many-body interference while increasing sensitivity to phase dispersion and coherence loss. Together, TVD, HOG, XEB, and higher-order correlations provide deeper insight into quantum interference dynamics in programmable photonic boson sampling circuits, offering guidance for future NISQ photonic processors.

References:

[1] S. Aaronson, A. Arkhipov, Research in Optical Sciences, Optica Publishing Group (2014).
[2] C. Oh, L. Jiang, B. Fefferman, Physical Review Letters 131, 010401 (2023).
[3] A. Deshpande et al., Science Advances 8, eabi7894 (2022).
[4] W. R. Clements et al., Optica 3, 1460–1465 (2016).

Quantification of Weak Crystal Anisotropy Using Extreme Cross-Polarization Extinction

[1]Upasana Baishya and, [1#]Nirmal K Viswanathan
School of Physics, University of Hyderabad, Hyderabad, Telangana, India – 500046.

nirmalsp@uohyd.ac.in

Using the extreme cross-polarization extinction (EXE) technique, high-sensitivity quantification of weak residual crystal anisotropy is demonstrated. The null-intensity region of a spin-orbit-induced four-lobe pattern of a weakly diverging laser is exploited to measure residual elliptical birefringence in uniaxial optical crystals using the EXE technique. Experimental measurements for quartz and calcite are interpreted using Jones-matrix calculations, demonstrating extinction levels approaching 10^{-8} and enabling sensitive characterization of anisotropy.

Optical anisotropy plays an important role in polarization optics, crystal characterization, imaging, sensing, and photonic device engineering. Although linear and circular birefringence of crystals are routinely measured, weak residual elliptical birefringence is often assumed to be negligible when the optic axis is oriented parallel or perpendicular to the propagation direction. Quantifying such weak anisotropies remains challenging because the induced polarization changes are extremely small and often lie below the sensitivity of conventional polarimetric techniques.

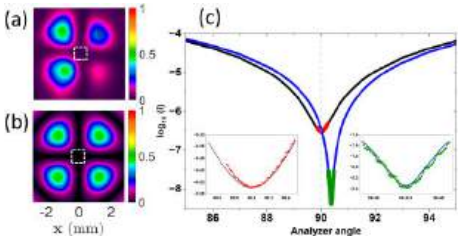


Fig. 1: (a) Experimental and (b) simulated EXE patterns and (c) corresponding extinction curve.

In this work, we demonstrate an Extreme Cross-polarization Extinction (EXE) technique for high-sensitivity characterization of residual crystal anisotropy [1]. A weakly divergent Gaussian beam from an Ar^+ laser (λ = 514.5 nm) is analyzed using a quarter-wave plate (QWP), an analyzer, and a CCD camera. Under optimized cross-polarization conditions, the beam exhibits a Hermite–Gaussian-like four-lobe structure with a dark-centered cross pattern arising from the spin-orbit interaction of light [2,3]. The perfectly dark central region provides a highly sensitive reference for all subsequent polarization measurements. By simultaneously adjusting the QWP and analyzer to achieve minimum intensity, the input polarization state of the beam is reconstructed from the null-intensity condition.

Quartz and calcite crystals, with their optic axes oriented parallel and perpendicular to the beam propagation direction, are introduced into the optical path and analyzed using the same EXE procedure. The reconstructed polarization states of the incident and transmitted beams are used to determine the linear and circular birefringence of the crystals. The extracted polarization ellipticity and ellipse orientation are subsequently related to the crystal anisotropy via Jones-matrix analysis, yielding an accurate measure of the refractive index difference (Δn). This enables quantitative characterization of weak anisotropy that is generally assumed to be negligible in these crystal orientations.

The experimentally measured intensity distributions, Stokes parameter maps, and extinction curves are compared with simulations based on the vectorial Richards–Wolf model and Jones-matrix formalism, showing excellent agreement. The extracted birefringence values for quartz and calcite are consistent with reported material parameters, validating the EXE approach [1]. In addition to providing a highly sensitive method for polarization-state reconstruction, the technique enables quantitative determination of weak crystal birefringence with extinction levels approaching 10^{-8} relative to the parallel-polarization intensity.

The demonstrated combination of high sensitivity, quantitative birefringence measurement, and simple experimental implementation makes the EXE technique a promising tool for characterizing weak optical anisotropy in crystals, ultrathin films, metasurfaces, and two-dimensional materials.

References:

[1] U. Baishya and N. K. Viswanathan, Extreme Cross-polarization Extinction Method for Quantification of Residual Crystal Anisotropy *APS Open Science* (2026) (under review).
[2] K. Y. Bliokh, F. J. Rodríguez-Fortuño, F. Nori and A. V. Zayats, *Nature Photonics 9* (2015) 796–808.
[3] K. Y. Bliokh and A. Aiello, *Journal of Optics 15* (2013) 014001.

Generation of Single-Photon Needle Beams Using a Flat Lens

[1]Sunny, [2]J. Bora, [2]A. D. Lad, [2]C.S. Yadav, [3]R. Menon and [1, #]V. Pal

[1]Department of Physics, Indian Institute of Technology Ropar, Ropar, Punjab 140001, India
[2]CQST, Indian Institute of Technology Mandi, Himachal Pradesh 175075, India
[3]Department of Electrical and Computer Engineering, University of Utah, Utah 84112, USA

[#]*vishwa.pal@iitrpr.ac.in*

We present the generation of single-photon needle beams using an inverse-designed, flat multi-level diffractive lens fabricated by grayscale lithography. Single photons produced via spontaneous parametric down-conversion (SPDC) are shaped into long-depth-of-focus beams with strong transverse confinement. These results highlight the potential of flat optics for enhanced light-mater interaction and quantum imaging.

Owing to the exceptional properties of structured light, significant interest has emerged in extending beam shaping techniques to the quantum domain for tailoring single photons for emerging quantum technologies [1]. Notable examples include the generation of quantum Airy photons [2], spatially entangled Airy photons [3], and spatiotemporal single-photon Airy bullets [4]. Light focusing plays a central role in numerous optical applications; however, tight focusing inherently results in a limited depth of focus due to diffraction. The resulting short axial confinement length restricts light-matter interaction and increases sensitivity to focal-plane misalignment. To overcome these limitations, optical needle beams, which combine an extended depth of focus (EDOF) with strong transverse confinement, have attracted considerable attention for applications requiring long interaction lengths, including enhanced light-matter interaction and quantum imaging [1,5].

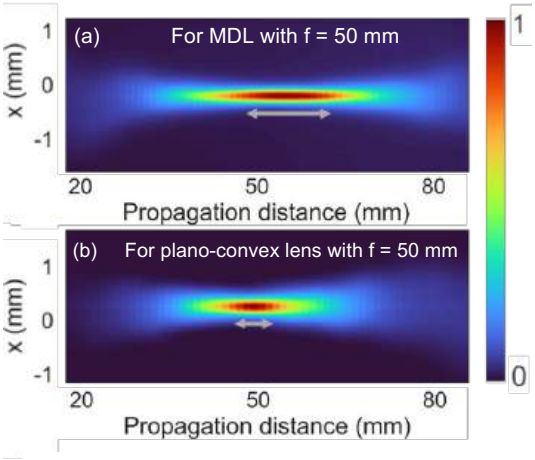


Figure 1. The photon distribution as a function of propagation distance captured using ICCD camera for (a) multi-level diffractive lens (MDL). (b) plano-convex lens

Conventional focusing of classical and quantum light relies on plano-convex or compound objective lenses, which are bulky, dispersion sensitive and fundamentally limited in depth of focus by diffraction. Here, we demonstrate the generation of single-photon needle beams using a compact, lightweight, highly transparent, flat multilevel diffractive lens (MDL). The MDL was designed through inverse-method and fabricated by grayscale lithography [5]. It comprises rings with a minimum lateral feature size of 2.5 μm and a maximum relief depth of 2.06 μm.

To experimentally demonstrate this approach, single photons generated via SPDC were focused using an MDL with a focal length of 50 mm, and the resulting focusing and EDOF characteristics were recorded with an ICCD camera, as shown in Fig. 1(a). The MDL generated a single-photon needle beam with an EDOF of approximately 10 mm and a focal spot size of 100 μm. For comparison, measurements were also performed using a planoconvex lens of the same focal length, demonstrating that the MDL provides a substantially extended depth of focus (Fig. 1(b)).

A comprehensive study was further performed using different MDLs with different design parameters to investigate the propagation dynamics and EDOF characteristics of single-photon needle beams. These results establish flat MDLs as an effective platform for shaping single photons, opening new avenues for enhanced light-matter interaction and high-resolution quantum imaging applications.

References:

[1] A. Forbes, F. Nothlawala, and A. Valles, Nat. Photon. 19, 1291 (2025).
[2] S. Maruca, S. Kumar, Y. M. Sua, J. Chen, A. Shahverdi, and Y. Huang, J. of Phys. B: At. Mo. Opt. Phys 51, 175501 (2018).
[3] O. Lib and Y. Bromberg, Opt. Lett. 45, 1399 (2020).
[4] J. Wang, Y. Zuo, X. Wang, D. N. Christodoulides, G. A. Siviloglou, and J. F. Chen, Phys. Rev. Lett. 132, 143601 (2024).
[5] S. Banerji, M. Meem, A. Majumder, B. Sensale-Rodriguez, and R. Menon, Optica 7, 214 (2020).

Comparative Study of Vector Beam Encoding Using Twisted Nematic and Parallel Aligned SLM

Bharat and Praveen Kumar
Department of Physics, Indian Institute of Technology Bhilai, Durg, India, 491002
*praveen@iitbhilai.ac.in

Vector beams have spatially varying polarization, which provides a higher degree of freedom for information encoding. The modulation characteristics and polarization response of the twisted nematic spatial light modulator (TNSLM) are investigated and used for vector beam encoding (VBE). A comparative study between TNSLM and parallel-aligned liquid crystal SLM is presented for VBE.

In optical encoding, vector beams provide an additional degree of freedom through their polarization distribution, enabling high-capacity and secure information encoding. Several VBE-based methods have been reported that use intensity measurement-based decoding; however, they require complex optical setups. Furthermore, arbitrary vector beam encoding (AVBE)-based methods have been reported that enable a simple decoding process using relatively simple optical setups, but they remain costly. In this work, we demonstrate AVBE using TNSLM to achieve a more compact and cost-effective system, and a comparative analysis with PASLM has been presented.

Input information in the form of phase value distribution (PVD) is encoded through polarization-dependent modulation of light using a TN SLM. The liquid crystal molecules in the TNSLM modulate both the phase and polarization state of the incident light. As a result, the encoded phase information is transformed into a spatially varying polarization distribution.

For decoding the PVD, the azimuthal angle distribution of the polarization ellipse is calculated from the captured intensity distribution at different analyzer orientations. To retrieve the actual PVD, the calculated azimuthal angle is mapped onto the phase response curve of the TN SLM, which was previously obtained. After the inverse Fourier transform of the obtained PVD, the actual plaintext is reconstructed. Also, a comparative analysis of VBE is presented between the TNSLM and PASLM. [1-5]

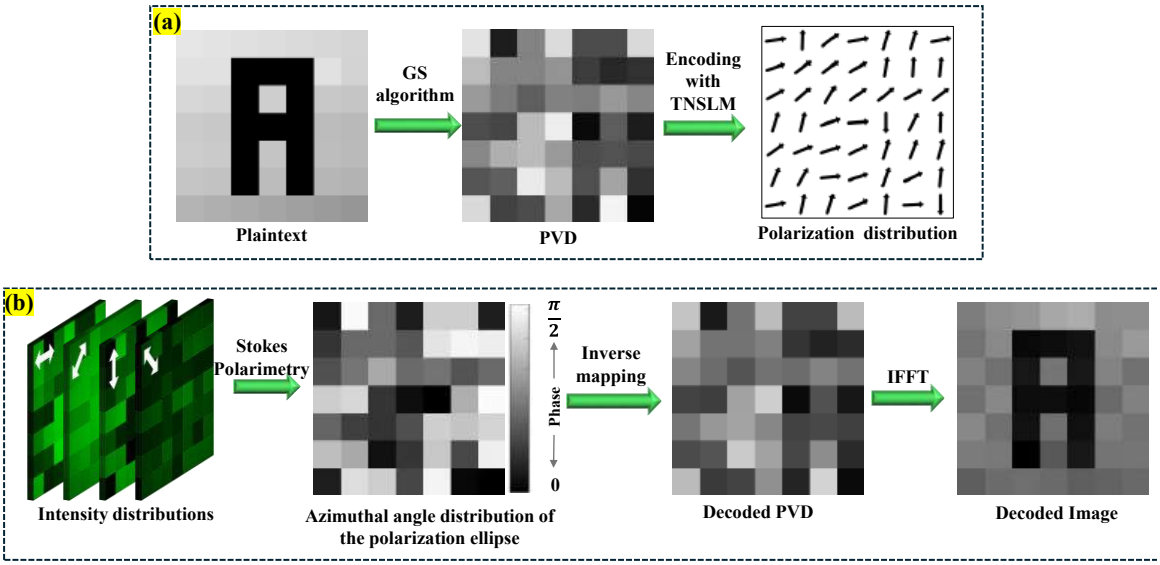


Fig. 1: Simulation result for arbitrary vector beam encoding using TNSLM (a) encoding process, (b) Decoding process.

References:

[1] Y. Zhao and J. Wang, Opt. Lett., vol. 40, no. 21, pp. 4843–4846, Oct. 2015.
[2] A. Fatima and N. K. Nishchal, Opt. Commun., vol. 417, pp. 30–36, Jun. 2018.
[3] C. Rosales-Guzmán, A. Forbes, SPIE Press,2017.
[4] V. Arrizón, Opt. Lett. Vol. 28, no. 15, pp. 1359-1361, 2003.
[5] P. Kumar; A. Fatima, and N. K. Nishchal, IEEE Photonics Technology Letters, vol. 33, no. 5, pp. 243-246, 2021.

Engineered Vector Vortex Beams with Multiple Radial Zones and Controllable Topological Charges

Neha Choudhary and *Naveen K. Nishchal
Department of Physics, Indian Institute of Technology Patna, Bihta, Patna 801106, India
*nkn@iitp.ac.in

An engineered vector vortex beam with multiple concentric radial zones and independently controllable topological charges is proposed for high capacity information encoding. The decoding is based on single-shot intensity recording eliminating the requirement of complex optical setup.

Optical communication systems have attracted significant attention owing to their high-speed transmission and parallel processing capabilities [1]. Structured light beams carrying orbital angular momentum (OAM) and possessing helical phase front, characterized by the topological charge (TC), l have been utilized for information encoding [2-4]. However, the reported vortex beams carry a single TC and therefore provide a single information channel within the optical field [3]. Although, several multiplexing and multiple image encryption schemes have been developed to enhance information capacity, they often suffer from cross-talk and complex optical architecture [5,6]. In this study, we address these challenges using an azimuthally polarized vector vortex beam with multiple radial zones and controllable TCs. In an azimuthally polarized vector vortex beams, the polarization direction of electric field changes along the azimuthal direction. An azimuthally polarized vector vortex beam is generated by passing the linearly polarized laser beam at 45° to *x*-axis through a phase-only spatial light modulator encoded with a specific phase-only function and passing through a quarter wave plate with slow axis oriented at 45° with respect to *x*-axis. The resulting intensity distribution is analyzed using a polarizer fixed at an angle θ and the corresponding intensity distribution is obtained as [7],

$$I(\theta) = \langle E_x E_x^* \rangle \cos^2\theta + \langle E_y E_y^* \rangle \sin^2\theta + \left(\langle E_x^* E_y \rangle + \langle E_x E_y^* \rangle\right) sin\theta cos\theta \quad (1)$$

where E_x and E_y represent the electric components and can be expressed as Jones matrix multiplication of quarter wave plate and encoded light field as [7],

$$\begin{bmatrix} E_x \\ E_y \end{bmatrix} = \frac{1}{2\sqrt{2}} \begin{bmatrix} 1-i & -1-i \\ -1-i & 1-i \end{bmatrix} \begin{bmatrix} \exp(i\beta(x,y)) \\ 1 \end{bmatrix} \quad (2)$$

The mathematical expression of the phase-only function to achieve a vector vortex beam with multiple radial zones is expressed as [7],

$$\beta(x,y) = Im[\exp\{il(r)\varphi\}] \quad (3)$$

Here, $l(r)$ is the radially varying TC and φ denotes the azimuthal angle.

The proposed engineered vector vortex beams provide compact, high capacity, and low cross-talk optical field for secure and high capacity information encoding.

Acknowledgement
The funding from the Council of Scientific and Industrial Research through grant Nos. 09/1023(18102)/2024-EMR-I and 03/1492/23/EMR-II and Anusandhan National Research Foundation (ANRF/ARG/2025/012264/PS), Govt. of India are acknowledged.

References:

[1] N. K. Nishchal, Optical Cryptosystems, IOP Publishing (2019).
[2] L. Allen, M.W. Beijersbergen, R.J.C. Spreeuw, J.P. Woerdman, Phys. Rev. A 45 (1992) 8185-8190.
[3] P. Kumar, N. K. Nishchal, A. AlFalou, IEEE Photon. Technol. Lett. 34 (2022) 521-524.
[4] A. Shikder, N. Choudhary, and N. K. Nishchal, J. Opt. 27 (2025) 065603.
[5] H. Tian, X. Zhuang, A. Yan, H. Zhang, Sci. Rep. 14 (2024) 19559.
[6] A. Hazer, R. Yıldırım, J. Opt. 23 (2021) 113501.
[7] N. Choudhary, A. Shikder, N.K. Nishchal, Opt. Commun. (2026) 133286.

Tightly focusing of circular airy femtosecond pulse with binary axicon

P. Gayathri[1], S. Kanishka[2], M. Lavanya[3], S. Arivandan[4],

K.B. Rajesh[1*]

[1]*Department of Physics, Chikkanna Government Arts College, Tirupur, Tamilnadu 641602, India*

[2,3]*Department of Physics, PSGR Krishnammal college for women, Coimbatore 641001, India*

[4]*Department of Physics, Chikkaiah Government Arts & College, Erode, Tamilnadu 638004, India*

[1*]*Department of Physics, Government Arts College, Coimbatore, Tamilnadu 641018, India*

rajeskb@gmail.com[1*]

*In this work, spin–orbital coupling in a femtosecond, tightly focused, radially polarized circular Airy vortex beam modulated by a binary axicon is investigated using Richards–Wolf vector diffraction theory. The effects of polarization, vortex phase, and focusing conditions on the angular momentum properties of the beam near focus are examined.*The study focuses on how the beam's intensity, phase, orbital angular momentum (OAM), spin angular momentum (SAM), and energy flow behave in both time and space near the focused region. The computed intensity distributions show spiral growth over time and asymmetric ring structures, which suggest dynamic interference between the orbital and spin components. Strong SOC is confirmed by the phase maps, which display distinct helical and twisted patterns with shifting singularities. The Poynting vector (energy flow) shows spiral patterns that indicate rotational energy transfer around the optical axis, while the SAM and OAM density plots show periodic angular momentum exchange between polarisation and spatial phase. All of the above results provide strong evidence of optical spin-orbit Hall effects and time-dependent SOC in ultrafast structured beams. The findings provide a physical understanding of how organised femtosecond fields can be designed for optical trapping, nanoscale photonic control, and light manipulation.

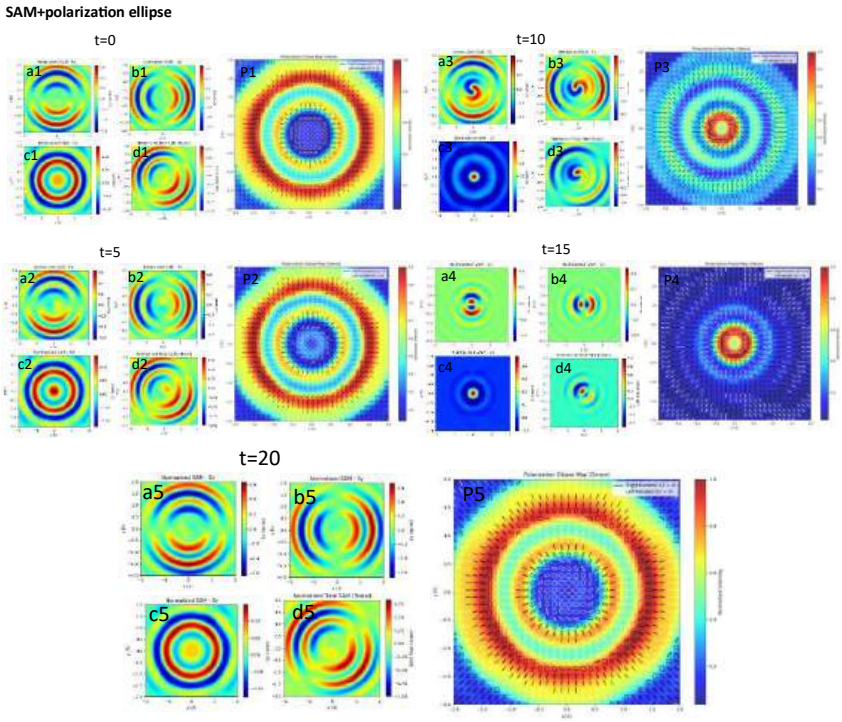


Fig.1 Figure a,b,c&d are spin angular momentum of E_x , E_y , E_z & E_{total}. P is the projection of polarization ellipse on the total intensity.

References:

[1] G. Lin, Z. Tang, Y. Wu, C. Liang, European Physical Journal Applied Physics 62 (2013) 31101.

[2] M. Chen, S. Huang, W. Shao, Optics Communications 402 (2017) 672–677.

[3] S.N. Khonina, A.P. Porfirev, Applied Physics B 124 (2018) 191.

Tailoring Orbital Angular Momentum Spectra with Angular Slit Masks

Aroma Indus[1,*], Kedar B. Khare[1], P. Senthilkumaran[1]

[1]Optics and Photonics Centre, IIT Delhi, India

[*]*indusaroma6@gmail.com*

Abstract. *Passive binary amplitude angular slit masks can tailor a beam's OAM spectrum without phase modulation. For arithmetic-progression slit spacing, the dominant modes follow* $\ell_{\text{peak}} = k\pi/\alpha$*, set only by the angular step, while slit number controls spectral concentration.*

Orbital angular momentum (OAM) provides an orthogonal modal basis for optical communication, quantum information, imaging and metrology [1, 2]. Existing OAM generators generally rely on active phase-modulating elements, whereas binary amplitude masks provide a simple passive alternative [3]. Here we explore a unified framework for engineering OAM spectra using angular multi-slit masks, where the OAM spectrum is determined solely by the angular arrangement of transmitting apertures.

From the Fourier relationship between angular position and OAM [4], the complex OAM amplitude for a mask of N identical slits of width $\Delta\phi$ centred at $\{\phi_m\}$ is

$$A(\ell) = \frac{\Delta\phi}{2\pi}\,\text{sinc}\left(\frac{\ell\Delta\phi}{2}\right)\sum_{m=0}^{N-1} e^{-i\ell\phi_m}, \tag{1}$$

Figure 1 shows the normalized modal power, $P_\ell \propto |A(\ell)|^2$; slit width sets the sinc envelope, while slit placement controls modal interference.

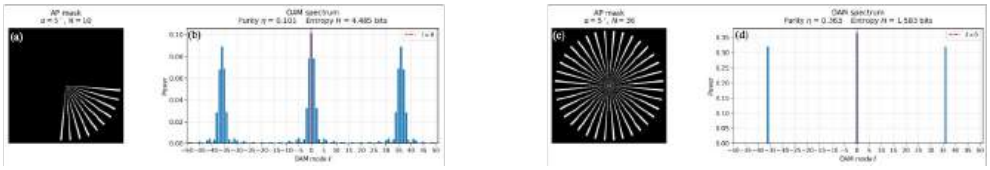


Figure 1: *Arithmetic-progression masks and corresponding OAM spectra for* $\alpha = 5°$*. Changing* N *from 10 to 36 improves spectral concentration without shifting the AP-determined peak positions.*

For an arithmetic-progression (AP) mask, the slit-centre angles are chosen as $\phi_m = p_m\alpha$, where $\{p_m\}$ is an arithmetic progression of integers and α is the angular step. In the examples studied here, $p_m = 2m+1$, so the slit centres are odd multiples of α, truncated within the interval $[0, 2\pi)$. The dominant mode positions are governed primarily by α, while the number of retained slits controls spectral sharpness, mode purity, and Shannon entropy [4]. The dominant spectral peaks satisfy $\ell_{\text{peak}} = k\pi/\alpha$, $k \in \mathbb{Z}$, demonstrating that the peak OAM mode can be engineered through angular spacing, while spectral purity can be adjusted independently through the slit number. This provides a simple geometrical rule for passive OAM spectral engineering using binary angular masks without phase modulation.

References

[1] C. He, Y. Shen, and A. Forbes *Light: Science & Applications*, vol. 11, p. 205, 2022.

[2] G. M. Gibson, J. Courtial, M. J. Padgett, M. V. Vasnetsov, V. A. Pas'ko, S. M. Barnett, and S. Franke-Arnold *Optics Express*, vol. 12, no. 22, pp. 5448–5456, 2004.

[3] S. Chava, R. Dharmavarapu, A. Vijayakumar, S. Jayakumar, A. Manthalkar, A. Dixit, *et al. Optical Engineering*, vol. 59, no. 4, p. 041205, 2020.

[4] B. Jack, M. J. Padgett, and S. Franke-Arnold *New Journal of Physics*, vol. 10, no. 10, p. 103013, 2008.

Frozen Whirlpools of Light: An Optical Analogue of Abrikosov Vortex Pinning Using Discrete Vortex Landscapes

[1,#]Aditya Narayana Jena, and [1]Vishwa Pal
[1]Laser Research Lab, Department of Physics, Indian Institute of Technology Ropar, Rupnagar, Punjab, India 140001.

[#]aditya.23phz0006@iitrpr.ac.in

Through controlled introduction of perturbations into discrete optical vortex landscapes, we reveal the emergence of localized singularity states that mimic the pinning behavior of magnetic flux vortices in Type-II superconductors. Our approach establishes structured light as a controllable testbed for exploring condensed-matter phenomena governed by topological defects and their interactions.

Vortex pinning governs the collective dynamics of topological defects across diverse quantum systems. However, direct observation of its microscopic mechanisms remains challenging owing to its complex vortex–defect interactions within inherently uncontrollable material defect landscapes. Therefore, the development of a programmable analogue platform capable of probing pinning dynamics in a controlled manner is highly desirable. Inspired by vortex pinning in Type-II superconductors, where Abrikosov vortices are immobilized by material defects, we investigate the dynamics of topological defects in a discrete optical vortex (DOV) system [1]. The deterministic control over phase singularities makes DOVs an ideal platform for emulating vortex-defect interactions. However, realizing an optical analogue that reproduces the perturbation-resilient pinning behavior of magnetic vortices remains largely unexplored. We demonstrate that, unlike conventional vortex beams where singularities evolve freely under diffraction, perturbed hexagonal DOVs preserve the topological identity of their phase singularities reminiscent of pinned Abrikosov vortices. Here, the optical field is synthesized from phase-locked lasers arranged in a hexagonal lattice with a prescribed topological charge (*m*) assigned to the array [2].

By introducing controlled perturbations into the propagated optical field [3], we emulate defect induced disturbances analogous to those experienced by magnetic vortices under external influences. Remarkably, we find that the perturbed phase singularities remain localized and preserve their topological identity during subsequent propagation, exhibiting a robust resistance to the perturbation. This persistence of singularity information at the perturbed site constitutes a striking optical manifestation of vortex pinning. Figure 1 depicts the evolution of the intensity and interference signatures of a perturbed discrete optical vortex composed of *N*=12 phase-locked laser beamlets arranged in a hexagonal geometry with *m*=1. The corresponding intensity and interference patterns reveal the recovery of the singularity after imposed perturbation highlighting the pinning-like dynamics of optical vortices during propagation. These observations establish a direct optical analogy to the trapping of magnetic vortices at defect sites in superconducting systems.

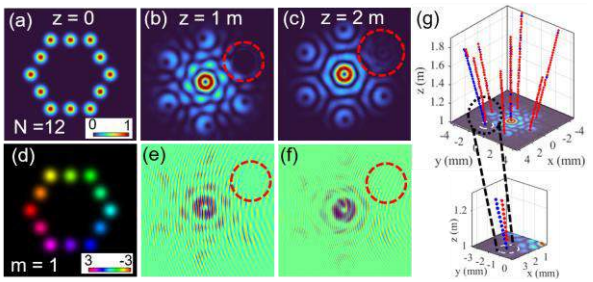


Fig. 1: **Demonstration of vortex pinning in a discrete optical vortex system**. (a–c) Intensity distributions at z = 0, 1m, and 2m, respectively, with a localized perturbation introduced at z=1m (red dashed circle). (d) Corresponding initial phase distribution of hexagonal array. (e-f) Interference fringes at z=1m and 2m, revealing the persistence of the phase singularity after perturbation. (g) Tracked singularity trajectories illustrating recovery of the perturbed singularity, evidencing Abrikosov-like vortex pinning. Blue and red dots trace the singularity trajectories of the unperturbed and perturbed lattices, respectively.

An extensive study was performed over a range of lattice configurations, perturbation scenarios, and propagation conditions, confirming the robustness of the observed vortex-pinning behavior. Our results establish structured DOVs as a versatile and controllable platform for exploring condensed-matter inspired phenomena, offering new opportunities to investigate the dynamics, stability, and interactions of topological defects in a purely optical setting.

References:

[1] M.S. Sidelnikov, A.V. Palnichenko, K.S. Pervakov et al., JETP Letters, 119, 523–528 (2024).
[2] V. Dev, V. Pal, Journal of the Optical Society of America B, 38, 3683–3696 (2021).
[3] P. Vaity, R.P. Singh, Optics Letters, 36, 2994–2996 (2011).

Dynamic Transformation of Optical Bimerons using Enantiomeric Excess

[1,#]Ankita Karmakar,[1]Abhishek Mandal and [1]Maruthi M. Brundavanam
[1]Indian Institute of Technology Kharagpur, Kharagpur, West Bengal, India-721302
[#]*ankita.emma123@gmail.com*

A common-path technique is experimentally demonstrated for the generation and dynamic topological transformation of optical bimerons using enantiomeric excess in an enantiomeric mixture. The optical rotation produced by the optically active medium transforms one bimeron to another using a wave-plate protecting the topology, and proves the robustness of the scheme.

The revolutionary discovery of Optical skyrmion [1] as a topologically protected quasiparticle in structured electric field has led to the creation of other quasiparticles with generalized topological states. One of the most promising topological textures is the optical bimeron (OB) [2]. The sophisticated texture of OB has found potential applications in communication, imaging, storage etc. Here, we propose the construction and dynamic transformation of OBs using the enantiomeric excess (EE) of an optically active (OA) medium.

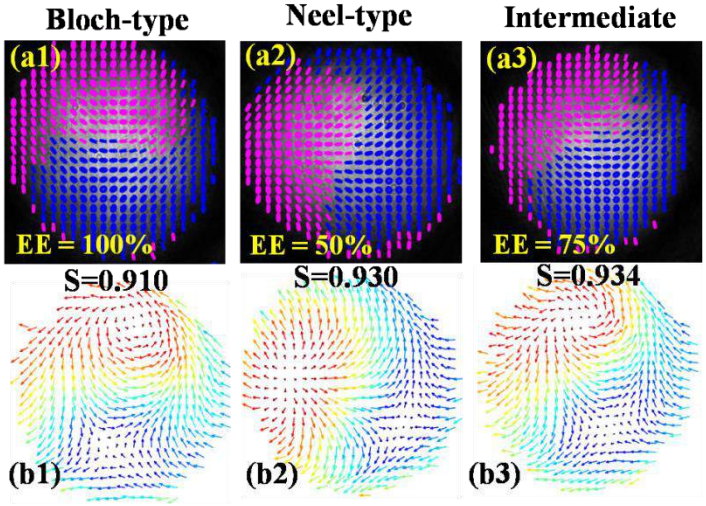


Figure 1: (a1-a3) Spatial polarization distribution of the VVBs, (b1-b3) Corresponding transverse vector with different textures (representing Bimerons) for different EE.

The OBs are constructed using the Stokes' vector from the vector vortex beams (VVBs) [3]. The stable VVBs generated in a common-path setup are represented in terms of optical skyrmionic structures which are transformed to different types of texture using EE. The properties of quarter wave plate are used to transform the generated textures to OB structures and EE is used to control the transformation of different OBs. The OA medium used here is an enantiomeric mixture of (+) and (-)-limonene with opposite specific rotations ($\pm 84.25^{O}$) and the excess amount of the (+)-limonene over the other is termed as EE. A concentration of 53.4% of the limonene with varying EE introduces the optical rotation (OR) of $\pm 90^{O}$ for a variation of EE from 100% to -100%. The VVBs that represent bimeron are characterized using the Stokes' polarimetry and the spatial distribution of polarization is reconstructed over the beam profile for different EEs as shown in Fig. 1(a1-a3). When the Stokes' vectors are mapped on to the transverse plane, they form two meron structure, one vortex (or, hedgehog) and another saddle, representing the texture for Bloch-type (or, Neel-type) OB. Without the presence of the OA medium, the texture forms a Bloch-type bimeron, whereas, an OA medium with EE=100% represents a Bloch-type. But when the EE is reduced to 50%, due to OR=45°, the Bloch-type transformed to a Neel-type texture. An intermediate EE can generate an intermediate type of bimeronic texture. The dynamic transformation of the bimerons using EE can be applied in chiral sensing and chiral sorting while preserving the skyrmion number [1, 2] that proves the robustness of the proposed methodology. The detailed experimental findings will be presented during the conference.

In conclusion, a robust and stable technique is demonstrated for the generation and dynamic transforms of OBs using EE of an OA medium.

AK thanks IIT Kharagpur for financial assistance. MMB thanks SERB for funding.

References:

[1] Yijie Shen *et al.*, Opt. Lett. 2021, 46, 3737–3740.
[2] Yijie Shen *et al.*, ACS Photonics 2022, 9, 296–303.
[3] Ankita Karmakar *et al.*, Opt. Lett. 2026, 51, 3116–3119.

Methods of Structured beam characterization

Laxminarayan, Kushal Kumar Tripathi and Praveen Kumar
Indian Institute of Technology Bhilai

**praveen@iitbhilai.ac.in*

Structured light with tailored phase, polarization, and amplitude distributions requires accurate yet simple characterization techniques. We present low-complexity approaches based on interferometry, diffraction, advanced Stokes polarimetry, and single-shot polarization analysis for beam characterization and wavefront sensing. These methods provide reliable performance across different propagation media and are promising for quantum communication, optical cryptography, and advanced photonic systems.

Structured light has emerged as a powerful tool in modern photonics because its amplitude, phase, and polarization can be tailored to encode and manipulate optical information. Such optical fields are commonly described by ($E = Ae^{i\ell\phi}$), where (A) represents the field amplitude and ($e^{i\ell\phi}$) defines the helical phase structure. The topological charge (ℓ) determines the wavefront helicity and is directly associated with the orbital angular momentum (OAM) of light, while the polarization state governs its spin angular momentum (SAM) [1]. These engineered degrees of freedom enable the realization of a broad range of structured and singular light fields for advanced photonic technologies. Although significant progress has been made in generating such beams using liquid-crystal spatial light modulators and other diffractive optical elements, their complete characterization remains a major challenge because it requires accurate determination of the phase, polarization, wavefront, and topological charge. In this work, we present a collection of simple and low-complexity characterization techniques based on interferometry, advanced Stokes polarimetry, and single-shot polarization analysis. These methods provide reliable characterization of structured light and facilitate wavefront sensing and topological charge detection, offering a practical framework for future developments in biomedical optics, optical communication, quantum photonics, and optical cryptography [2,3].

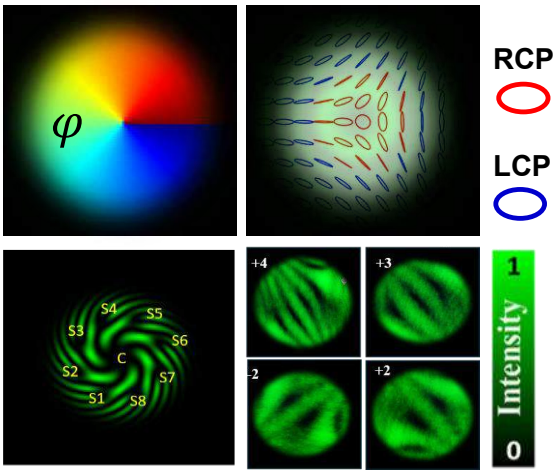


Fig. 1: Simulation and experimental results of characterization methods

References:

[1] Allen, L., Beijersbergen, M. W., Spreeuw, R. J. C., & Woerdman, J. P. Orbital angular momentum of light and the transformation of Laguerre-Gaussian laser modes. *Physical Review A*, *45*(11), 8185–8189, (1992).

[2] Laxminarayan, Allam, S. R., Omatsu, T., & Kumar, P. Singularity transformation through single-pass phase modulation of light. *Scientific Reports*, *15*(1), 8007, (2025).

[3] Nape, I., Sephton, B., Ornelas, P., Moodley, C., & Forbes, A. Quantum structured light in high dimensions. *APL Photonics*, *8*(5),(2023) .

Quantification of Rotational Speed Using Laser Speckle Contrast Imaging and 3D Convolutional Neural Networks

[1, #]Priya Malik, [1]Harsh Chatwani, [2]Arun Anand, [1]Gyanendra Sheoran
[1]Department of Applied Sciences, National Institute of Technology Delhi, Delhi 110036, India
[2]Department of Physics, Sardar Patel University, Vallabh Vidyanagar 388120, India

[#]priyamalik@nitdelhi.ac.in

Rotational speed is directly estimated from laser speckle image sequences using a three-dimensional convolutional neural network (3D-CNN), thereby eliminating the need for conventional decorrelation-time analysis. The proposed model achieved approximately 95% prediction accuracy on unseen datasets collected at 1-10 rotations per minute (RPM).

Laser Speckle Contrast Imaging (LSCI) is a simple, non-contact optical imaging technique that captures the dynamic fluctuations of speckle patterns produced by moving objects. Conventional quantitative LSCI estimates velocity through the speckle decorrelation time; however, the relationship between decorrelation time and velocity depends on several experimental parameters, making accurate quantitative measurements challenging. To overcome this limitation, we propose a deep learning framework that directly predicts rotational speed from raw laser speckle image sequences using a three-dimensional convolutional neural network (3D-CNN).

The experimental setup is shown in Fig. 1. A 532 nm green diode laser illuminated a rotating ground-glass diffuser driven by a stepper motor controlled using an Arduino Uno and a TB6600 motor driver, generating rotational speeds from 1 to 10 RPM in 0.5 RPM increments. The resulting dynamic speckle patterns were recorded using a CMOS camera. For each speed, 45 consecutive speckle images were acquired, and a suitable region of interest (ROI) was selected to reduce computational cost. The resulting image stack was used to train a 3D CNN with a 70:30 training-testing split and a learning rate of 0.001.

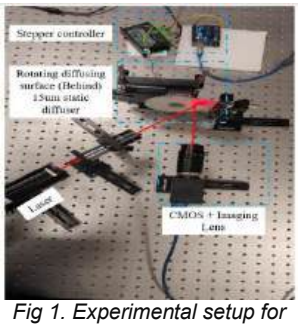


Fig 1. Experimental setup for quantification of RPM using LSCI and Neural Network

The prediction results are shown in Fig. 2. The proposed model accurately predicted rotational speeds across three independent datasets, with predicted RPM values closely matching the experimental values. An overall prediction accuracy of approximately 95% was achieved, demonstrating that raw speckle image sequences can be used for direct rotational speed estimation without decorrelation-time analysis.

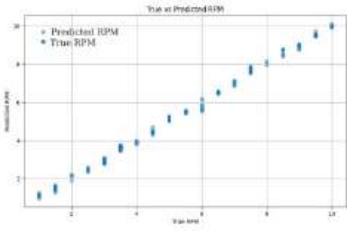


Fig. 2. Comparison of true and predicted rotational speeds using the proposed 3D-CNN.

The proposed approach combines the simplicity of LSCI with the learning capability of deep neural networks to enable accurate, calibration-free rotational speed measurement. The methodology can be extended to flow measurement and other industrial applications where conventional decorrelation-time analysis is difficult to implement.

The authors acknowledge research funding through the Department of Science and Technology (DST-INSPIRE) under Grant No. IF210399.

Reference:

[1] A.F. Fercher, J.D. Briers, Optics Communications 37 (1981) 326–330.

[2] J. Senarathna, A. Rege, N. Li, N.V. Thakor, *IEEE Reviews in Biomedical Engineering* **6** (2013) 99–110.

[3] P. Malik, N. Barak, N. Chhiller, G. Dwivedi, S. Sharma, A. Anand, G. Sheoran, Measurement 258 (2026) 119338.

Propagation characteristics of scattered Hermite-Gaussian beams

[1,#]MD Haider Ansari,[1]Ganesh Velagala, [1]Ravi Kumar, and [1,#]Gangi Reddy Salla
[1]Department of Physics, SRM University-AP, Neeru Konda, Amaravathi, 522240, Andhra Pradesh, India

[#]haideransari_md@srmap.edu.in, gangireddy.s@srmap.edu.in

We study the propagation characteristics of scattered Hermite-Gaussian (HG) beams and retrieve mode information from the 2-D autocorrelation profiles of the corresponding speckle pattern. The indices can be extracted from a single short recording of the speckle pattern for that mode. These results demonstrate the effectiveness of HG beams for communication, as they are robust against scattering.

Hermite-Gaussian (HG) beams are an important class of structured light beams with orthogonal transverse modes that are widely used in optical communication, laser resonators, particle manipulation, gravitational-wave detection, and bio-optical imaging [1]. Their unique spatial intensity distribution makes them attractive for mode-division multiplexing and information encoding. Compared with higher-order orbital angular momentum (OAM) modes, HG beams exhibit lower divergence and improved resilience to atmospheric turbulence, making them promising candidates for free-space optical communication [2]. However, accurate determination of HG mode indices becomes challenging after propagation through random or scattering media, where the beam is distorted into speckle patterns. Existing techniques for determining the mode information of HG beams are limited in these scenarios. This article explores the propagation characteristics of HG beams and implements a method for analyzing perturbed HG beams by employing a 2-D autocorrelation function and utilizing the intensity lobes and zero points present in the autocorrelation profiles along the two transverse directions with propagation distance for spatial mode information.

The field distribution of the HG beam at the source plane, which can be written mathematically as [3]:

$$E_{m,n}(x,y,0) = H_m\left(\frac{\sqrt{2}}{\omega_0}x\right) H_n\left(\frac{\sqrt{2}}{\omega_0}y\right) e^{-\left(\frac{x^2+y^2}{\omega_0^2}\right)}, \quad (1)$$

where $\mathrm{H_m}$ and $\mathrm{H_n}$ represent the Hermite polynomials of orders *m* and *n*, respectively, and ω_0 is the beam waist of the Gaussian beam used to generate the HG beams.

The autocorrelation function can be written in terms of Laguerre polynomials as:

$$\Gamma(\Delta X;\Delta Y) = \frac{\pi\omega_0^2 2^{m+n+1} m!n!}{\lambda^2 z^2} \exp\left[\frac{-k^2\omega_0^2}{8z^2}(\Delta X^2+\Delta Y^2)\right] L_m\left(\frac{k^2\omega_0^2}{4z^2}\Delta X^2\right) L_n\left(\frac{k^2\omega_0^2}{4z^2}\Delta Y^2\right), \quad (2)$$

The autocorrelation function contains the *m* number of zero-points along the X-direction and *n* number of zero points along the Y-direction, which are in match with the mode indices. With this, we confirm that the mode indices are equal to the number of zero-points present in two transverse directions of the intensity lobes.

We started with an analytical expression for the HG beam and further experimentally calculated the 2-D spatial autocorrelation function using speckle patterns of the HG beam. Figure 1 shows the speckle patterns (first row) and the corresponding theoretical (second row) and experimental (third row) autocorrelation profiles of HG (0,0), HG (0,4), and HG (4,0). It is clear from the figure that the number of zero points along the transverse directions is equal to the mode indices. The experimental results are well supported by the analytical results, demonstrating a robust, purely intensity-based technique for characterizing HG beams in random-scattering environments relevant to free-space optical communication systems.

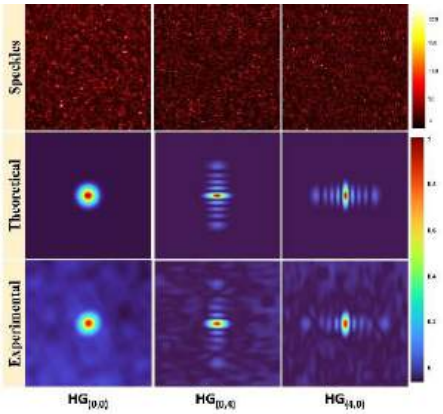


Figure 1: The speckle patterns, theoretical and experimentally obtained autocorrelation intensity profiles for HG beams with (m, n)= (0,0), (0,4), and (4,0) at z=20 cm.

References:

[1] C. Tan, Y. Wang, X. Li, *et al.*, Commun. Nonlinear Sci. Numer. Simul. 140, 108375 (2025).

[2] L. R. Hofer, L. W. Jones, J. L. Goedert, and R. V. Dragone, J. Opt. Soc. Am. A 36, 936–943 (2019).

[3] C. Rosales-Guzmán, B. Perez-Garcia, and M. A. Cox, J. Phys. Photonics 6, 043004 (2024)

Formation of High-Order Hollow Vector Beams with Invariant Dark-Core

Brijesh Kumar Mishra, and Brijesh Kumar Singh*
Department of Physics, Central University of Rajasthan, 305817, Ajmer (Rajasthan)
*brijeshsingh@curaj.ac.in, 2020phdph004@curaj.ac.in

Here, we introduce a numerical method based on vector diffraction theory using a multi-zone amplitude DOE to redistribute the energy of R-TEM$_{21}$ and R-TEM$_{31}$ high-order radially polarized modes. This enables the generation of hollow vector beams with a uniform dark-core size across numerical apertures (NA) ranging from low to high, while the intensity and width of the ring decreases with increasing NA.

Optical hollow beams exhibit a donut-shaped intensity profile characterized by a zero- or low- intensity central dark core surrounded by a high-intensity ring [1]. Hollow beams can be generated using axicons [2], spatial light modulators [3], diffractive optical elements (DOEs) and computer-generated holograms [4]. Despite recent advances, existing methods exhibit energy loss, NA sensitivity, and mode-specific optimization, while systematic control of dark-core size, beam width, and NA effects remains limited. In this work, we present a comprehensive numerical method based on vector diffraction theory and a multi-zone amplitude DOE to redistribute the energy of high-order radially polarized R-TEM$_{21}$ and R-TEM$_{31}$ modes. The proposed approach generates hollow vector beams with a uniform dark-core width across modes and various NA while enabling tuning of the high-intensity ring width through the focusing lens NA. These doughnut-shaped hollow beams may find applications in optical trapping [5], particle manipulation [6], ring-shaped ablation, and optical microscopy. Here, we modulate the high order mode with multizone amplitude mask given by Eqn. 1

$$T(\theta) = \begin{cases} 0 & 0 \le \theta < \theta_1, \quad \theta_2 \le \theta < \theta_3, \\ 1 & \theta_1 \le \theta < \theta_2, \quad \theta_3 \le \theta < \alpha \end{cases} \qquad (1)$$

Where, the focusing half-angle $\alpha = \sin^{-1}(NA)$ dividing into four angular zones θ_i (θ_1, θ_2, θ_3, $\theta_4 = \alpha$), such as $\theta_i = \sin^{-1}(r_i\ NA)$, which provides angular segmentation of the pupil.

Figure 1 illustrates the effect of the amplitude mask on the normalized intensity profiles of the high-order radially polarized R-TEM$_{21}$ and R-TEM$_{31}$ modes. The first column shows the unmodulated profile for NA = 0.35 as a reference, while the second and third columns present the corresponding modulated profiles for NA = 0.35 and 0.75, by proposed amplitude mask, respectively. The first and third rows display the 2D transverse intensity profiles, whereas the second and fourth rows show the corresponding 1D intensity profiles along the x-axis at z = 0. Simulation results for the hollow-beam formation of the R-TEM$_{21}$ mode are presented in the first and second rows of Figure 1(a-f). The transverse dark-core diameter remains invariant across all NAs, with a constant value of 28.56 λ, while the FWHM of the intensity ring decreases from 2.60 λ at NA = 0.35 to 0.80 λ at NA = 0.75. A similar trend is observed for the R-TEM$_{31}$ mode in the third and fourth rows of Figure 1(g-l), where the FWHM of the intensity ring decreases from 6.06 λ at NA = 0.35 to 0.81 λ at NA = 0.75. Overall, increasing NA form low to high reduces the intensity and width of ring while maintaining a nearly invariant dark-core diameter of 28.56 λ for both the high order modes.

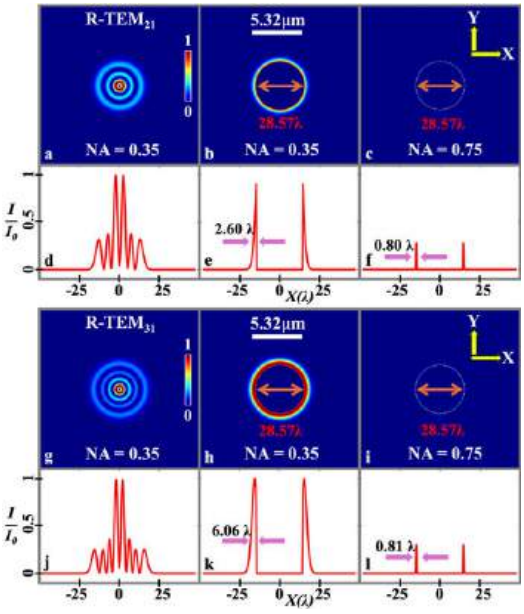


Figure 1. Simulation results for normalized hollow intensity distributions of amplitude-modulated high-order radially polarized beams for the R-TEM$_{21}$ and R-TEM$_{31}$ modes.

The invariant dark-core formation is attributed to the proposed multi-zone amplitude DOE, which redistributes the angular field of the incident R-TEM modes and modifies the interference conditions near the optical axis. The dark core is formed by destructive interference between the transverse and longitudinal field components, while the proportional scaling of the opaque and transparent angular zones preserves this interference balance, making the dark-core diameter nearly independent of NA despite the natural tendency of increasing NA to shrink the focal structure.

Funding. University Grants Commission (UGC), India.

References:

1. H. Ye, C. Wan, K. Huang, T. Han, J. Teng, Y. S. Ping, and C.-W. Qiu, Opt. Lett. **39**, 630 (2014).
2. Y. Zhang, Opt. Commun. **281**, 508–514 (2008).
3. F. K. Fatemi and M. Bashkansky, Opt. Lett. **31**, 864-866 (2006).
4. V. Pavelyev, V. Osipov, D. Kachalov, S. Khonina, and B. Chichkov, Appl. Opt. **51**, 4215-4218 (2012).
5. Z. Zhang, D. Cannan, J. Liu, P. Zhang, D. N. Christodoulides, and Z. Chen, Opt. Express **20**, 16212-16217 (2012).
6. V. G. Shvedov, A. V. Rode, A. S. Desyatnikov, W. Krolikowski, and Y. S. Kivshar, Phys. Rev. Lett. **105**, 118103 (2010).

Non-Contact detection of small deflection on a Cantilever Beam Using Laser Speckle Pattern Imaging

Lucky [1,2], Aman[1,2], Prashant Agnihotri[1,2], Nayanshree[2,3], Vikas[2,4],Kuldeep[2,4] Kamal Tewari[2,4], Surya Kumar Gautam[2,4], and Rajesh Kumar[2,4]

[1]GB Pant DSEU Campus- 1, Okhla, Delhi.

[2] CSIR-National Physical Laboratory (CSIR-NPL), New Delhi, Delhi 110012, India

[3] Delhi Skill and Entrepreneurship University, Okhla, Campus-2.

[4] Academy of Scientific and Innovative Research (AcSIR), Ghaziabad, 201002, India

Corresponding E-mail: (kamalt.nplindia@csir.res.in)

Abstract: The objective of this work was to measure the very small deflection in a cantilever beam using a non-contact optical technique known as Laser Speckle Pattern Imaging (LSPI). Unlike existing displacement sensors, this method detects tiny beam deformation without physically touching the specimen.

Experimental Setup: The setup consists of an ABS-fabricated cantilever beam using 3D printing, which is fixed at one end and has a small hole at the free end through which a thin thread is attached. Calibrated micro weights were applied to load the beam, whose surface was illuminated using a 532 nm green laser. The speckles were captured using a high-resolution CMOS camera which were then postprocessed on a computer using a Python-based image processing algorithm.

Working Principle: When coherent laser light illuminates the rough beam surface, scattered light interferes to form a random laser speckle pattern. Applying a small load causes slight beam bending, producing minute surface deflection, shifting the speckle pattern. These tiny shifts are captured by the CMOS camera and contain information about beam deformation. The captured reference (without weights) and loaded images (with weights) are processed using a Fourier Transform-based Python algorithm. Phase information is extracted, the speckle shift is determined, the bending angle is calculated, and calibration is used to relate the bending angle to the applied force. The measured bending angle varies linearly with load.



Fig 1: Setup and Schematic diagram

Results: The experimental results demonstrate accurate measurement of micro-scale beam deflections. The force-bending angle relationship was found to be highly linear in the chosen regime. The method enables precise deflection measurement without attaching any physical sensor to the beam.

Conclusion: LSPI was found to be a highly sensitive, accurate, and non-contact method for measuring very small cantilever beam deflections. As a lightweight load is applied to the free end of the beam, the resulting deformation causes a shift in the laser speckle pattern. A high-resolution CMOS camera captured these changes, and a Fourier Transform-based Python algorithm converted the speckle shift into beam deflection. This technique provides a simple, reliable, and precise alternative to conventional contact-based measurement methods.

References: [1] Simulation and Modelling of a Precision Method for Static Low Force Measurement V. Kumar, M.Jewariya · S. S. K. Titus · S. K. Gautam, *The Society for Experimental Mechanics, Inc 2024*

[2] Goodman, J. W. (2005). Introduction to Fourier Optics (*Englewood, CO: Roberts & Co.*).

[3] Timoshenko S et al (1959) Theory of Plates and Shells, vol 2. *McGraw-Hill, New York*

Generation of Homogeneous Polarization Singularity Array

[1,#]Sushanta Kumar Pal and [2]Rudrashis Panda
[1]Department of Physics, Centre for Quantum Science and Technology (CQST), Faculty of Engineering and Technology (ITER), Siksha 'O' Anusandhan Deemed to be University, Bhubaneswar 751030, Odisha, India
[2]Department of Physics, School of Applied Sciences, Kalinga Institute of Industrial Technology, Patia, Bhubaneswar 751024, Odisha, India

[#]*sushantapal@soa.ac.in*

We adopt an interferometric technique to synthesize customizable polarization singular fields embedded with homogeneous polarization singularities. In this work, we demonstrate generation of polarization singular fields embedded with I_C=1/2 C-points of uniform handedness in a triangular geometry for right-handed polarization.

Optical fields characterized by spatially varying polarization distributions have found diverse applications, including edge enhancement, robust laser beam engineering, chirality measurements etc [1]. These spatially varying optical fields are categorized into two primary classifications: ellipse fields and vector fields [2]. This categorization dictates that the fields are grouped based on the predominant polarization distributions manifest within the paraxial electromagnetic field. Within two-dimensional ellipse fields, the generic polarization singularities are classified as star, lemon, and monstar topologies. In these spatially variant polarization distributions, such singularities constitute isolated critical points where the major axis of the polarization ellipse is indeterminate. The local state of polarization at these critical points is circular, leading to their name as C-points. Characterized by the surrounding polarization morphology enclosing the critical point, the C-points can possess either positive or negative, as well as integral or half integral, polarization singularity indices. Furthermore, these C-points can exhibit either left- or right-handedness [3] and can occur at any intensity values.

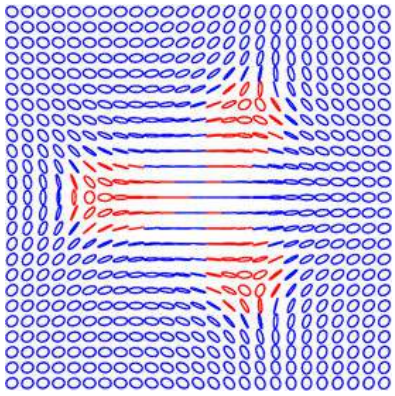


Fig. 1: Polarization morphology showing I_C=1/2 polarization singularity array with right-handed C-points arranged in a triangular geometry.

Generally, an optical field embedded with multiple polarization singularities is found to host C-points of opposite handedness, possessing either identical or opposite topological indices. Although it has been demonstrated that an elegant phase-engineering technique within a multiple-beam interference scheme can be employed to generate C-point lattice fields with homogeneous handedness [4], dynamically controlling and customizing the exact number of C-points in the resulting field remains highly challenging using that approach. In this work, we utilize the coaxial superposition of a right-circularly polarized Gaussian beam and a left circularly polarized, customizable complex field hosting three off-axis vortices arranged symmetrically about the beam axis. This superposition leads to the formation of optical fields embedded with homogeneous polarization singularity arrays. Figure 1 depicts the polarization morphology of a spatially varying paraxial optical field containing three right-handed C-points arranged in a triangular geometry around the beam axis. More importantly, both the density of C-points and their spatial arrangement in the resulting polarization morphology can be precisely controlled by customizing the complex field with the desired phase and amplitude profiles. This study may find applications in optical signal processing, structured illumination microscopy, and optical chirality measurements.

References:

[1] P. Senthilkumaran, *Singularities in Physics and Engineering*, IOP Publishing, London (2023).
[2] I. Freund, M. S. Soskin, A. I. Mokhun, *Opt. Commun*. 208 (2002) 223.
[3] S. K. Pal, G. Arora, Ruchi, P. Senthilkumaran, *Appl. Phys. Lett.* 119 (2021) 221106.
[4] S. K. Pal, P. Senthilkumaran, *OSA CONTINUUM* 1 (2018) 193.

Vortex Evolution in Composite Optical Field

[1]Rudrashis Panda,[2]Rakesh Mohan Das and [3,#]Sushanta Kumar Pal
[1]Department of Physics, School of Applied Sciences, Kalinga Institute of Industrial Technology, Patia, Bhubaneswar 751024, Odisha, India
[2]Department of Physics, School of Applied Sciences, Centre of Innovation and Research for Quantum Technology, Kalinga Institute of Industrial Technology, Patia, Bhubaneswar 751024, Odisha, India
[3]Department of Physics, Centre for Quantum Science and Technology (CQST), Faculty of Engineering and Technology (ITER), Siksha 'O' Anusandhan Deemed to be University, Bhubaneswar 751030, Odisha, India

[#]*sushantapal@soa.ac.in; sushanta1985@gmail.com*

This study examines the evolution of optical vortices embedded in a composite optical field generated via the coaxial superposition of two Laguerre–Gaussian beams. By systematically varying the fractional orbital angular momentum, we demonstrate the controlled generation of peripheral vortices. These findings provide a robust framework for advancements in structured light engineering.

An optical vortex is characterized by zero-intensity and undefined phase in the optical field [1, 2]. The coherent superposition of Laguerre-Gaussian (LG) beams with distinct orbital angular momentums (OAMs) can produce a composite vortex beam [3]. The composite beam hosts both on-axis and off-axis vortices. The number of off-axis vortices in the composite field is directly proportional to the difference of the OAMs of the interfering fields. In this work, we investigate the evolution of the off-axis vortex during the continuous increase of the topological charge of the one of the interfering beams from an integer value to the next integer value through fractional topological states [4], revealing the formation of composite vortices.

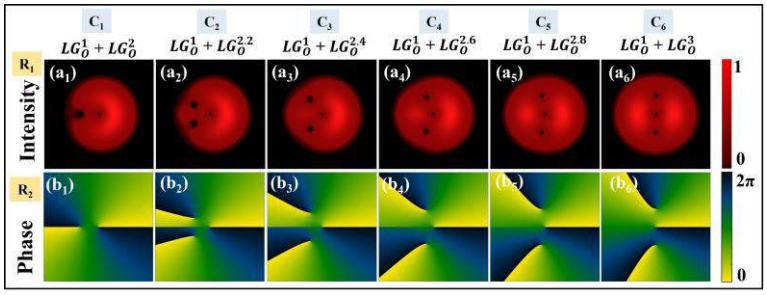


Fig 1: Composite vortex field by the coherent superposition of two LG beams with unequal OAMs and the evolution of off-axis vortices in the composite field.

The simulation results presented in this paper are evaluated for a wavelength of 633 nm and a beam waist radius of 1 mm, with the observation plane located at the beam waist (z = 0 plane). Figure 1 illustrates the evolution of the composite vortex beam during the coaxial superposition of LG_0^1 with LG_0^2, $LG_0^{2.2}$, $LG_0^{2.4}$, $LG_0^{2.6}$, $LG_0^{2.8}$ and LG_0^3 successively. The intensity distributions are presented in the first row (R_1) as Figs. 1(a_1)–1(a_6), while the corresponding phase distributions are shown in the second row (R_2) as Figs. 1(b_1)–1(b_6). For the composite field (LG_0^1 + LG_0^2), a single off-axis vortex is observed together with an on-axis vortex, which correspond to the topological charge difference $|l_2 - l_1| = 1$. As the topological charge of the second beam is increased continuously through fractional values, an additional off-axis phase singularity is formed and it gradually moves away from its point of origin. The angular separation between off-axis vortices in the case of integral OAM values are determined by $\frac{2\pi}{(l_2 - l_1)}$, where as it is $\frac{\pi}{(l_2 - l_1)}$ between the on-axis and an off-axis vortices. Our results demonstrate the importance of fractional OAM in the effective controlling and the formation of optical vortices in a composite optical field. The current work may be useful for applications such as structured light engineering, optical communication and quantum information processing.

References:

[1] M. J. Padgett, *Opt. Express* 25 (2017) 11265–11274.
[2] Ruchi, P. Senthilkumaran, S. K. Pal, *Int. J. Opt.* 2020 (2020) 2812803.
[3] S. Huang, Z. Miao, *Opt. Laser Eng.* 78 (2016) 132-139.
[4] V. V. Kotlyar, A. A. Kovalev, A. G. Nalimov, A. P. Porfirev, *Phys. Rev. A* 102 (2020) 023516.

Non-Contact detection of small deflection on a Cantilever Beam Using Laser Speckle Pattern Imaging

Aman[1,2], Lucky[1,2], Prashant Agnihotri[1,2], Nayanshree[2,3], Vikas[2,4], Kuldeep Kumar[2,4], Kamal Tewari[2,4], Surya Kumar Gautam[2,4], and Rajesh Kumar[2,4]

[1]GB Pant DSEU Campus- 1, Okhla, Delhi.

[2] CSIR-National Physical Laboratory (CSIR-NPL), New Delhi, Delhi 110012, India

[3] Delhi Skill and Entrepreneurship University, Okhla, Campus-2.

[4] Academy of Scientific and Innovative Research (AcSIR), Ghaziabad, 201002, India

Corresponding E-mail: (kamalt.nplindia@csir.res.in)

Abstract: The objective of this work was to measure the very small deflection in a cantilever beam using a non-contact optical technique known as Laser Speckle Pattern Imaging (LSPI). Unlike existing displacement sensors, this method detects tiny beam deformation without physically touching the specimen.

Experimental Setup: The setup consists of a stainless steel-fabricated cantilever beam which is fixed at one end and has a small hole at the free end through which a thin thread is attached. Calibrated micro weights were applied to load the beam, whose surface was illuminated using a 532 nm green laser. The speckles were captured using a high-resolution CMOS camera which were then post processed on a computer using a Python-based image processing algorithm.

Working Principle: When coherent laser light illuminates the rough beam surface, scattered light interferes to form a random laser speckle pattern. Applying a small load causes slight beam bending, producing minute surface deflection, shifting the speckle pattern. These tiny shifts are captured by the CMOS camera and contain information about beam deformation. The captured reference (without weights) and loaded images (with weights) are processed using a Fourier Transform-based Python algorithm. Phase information is extracted, the speckle shift is determined, the bending angle is calculated, and calibration is used to relate the bending angle to the applied force. The measured bending angle varies linearly with load.



Fig 1: Setup and Schematic diagram

Results: The experimental results demonstrate accurate measurement of micro-scale beam deflections. The force-bending angle relationship was found to be highly linear in the chosen regime. The method enables precise deflection measurement without attaching any physical sensor to the beam. The results were found to be repeatable as seen from Fig 2.

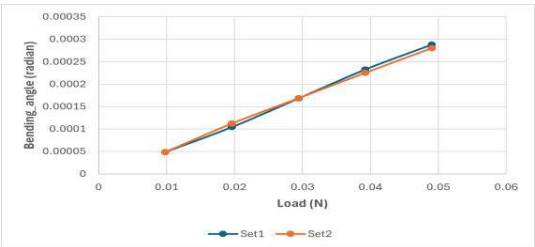


Fig 2: The relationship between force and bending angle

Conclusion: LSPI was found to be a highly sensitive, accurate, and non-contact method for measuring very small cantilever beam deflections. As a light weight load is applied to the free end of the beam, the resulting deformation causes a shift in the laser speckle pattern. A high-resolution CMOS camera captured these changes, and a Fourier Transform-based Python algorithm converted the speckle shift into beam deflection. This technique provides a simple, reliable, and precise alternative to conventional contact-based measurement methods.

References: [1] Kumar, V., et al. "Simulation and modelling of a precision method for static low force measurement." Experimental Techniques 49.3 (2025): 415-424.

[2] Vikas, et al. "Robust and precision small-angle measurement through the speckle pattern imaging technique." Applied Optics 64.9 (2025): 2195-2202.

Interferometric Complex-Field Approach for Reconstruction Through Scattering Media

[1,#]Yukti Pandey, [2]Raj Kumar and [1,3]Nandan Singh Bisht

[1]Applied Optics & Spectroscopy Laboratory, Department of Physics, Soban Singh Jeena University Campus Almora, 263601, India

[2]Optics & Photonics Instrumentation, CSIR–Central Scientific Instruments Organisation, Sector 30 C, Chandigarh 160030, India

[3]Department of Physics, D.S.B. Campus, Kumaun University Nainital, 263001, India

[#]*yuktipandyphysics@ssju.ac.in*

An interferometric complex-field correlation approach is proposed for reconstruction through scattering media. The method combines speckle-field recovery with calibrated modal matching to estimate object information and phase from a static scattering response.

Coherent light passing through a scattering medium forms a random-looking speckle pattern at the observation plane. Although this speckle appears disordered, it still carries information about the incident object or structured optical field. However, intensity-only detection loses the phase of the scattered field, which limits phase-sensitive reconstruction. Speckle formation has been widely studied in coherent optics [1], and wavefront shaping studies have shown that deterministic information can be accessed through fixed scattering media [2,3]. Motivated by this, we consider an interferometric complex-field approach in which the scattered signal is combined with a coherent reference beam before detection.

The input field is expressed as a modal superposition,

$$E_{\mathrm{in}}(x,y) = \sum_k c_k M_k(x,y), \tag{1}$$

where $M_k(x,y)$ represents a known modal basis and c_k are complex coefficients. For a static scattering medium, each mode produces a repeatable complex speckle fingerprint. The signal speckle $E_s(x,y)$ is recovered interferometrically using a clean reference field $E_r(x,y)$. For four-step phase shifting,

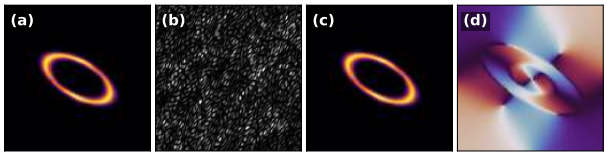


Figure 1: Preliminary numerical result for complex-field reconstruction through a static scattering medium. (a) Input structured-field intensity, (b) scattered speckle intensity, (c) reconstructed object intensity, and (d) reconstructed object phase.

$$H = (I_0 - I_{180}) + i(I_{90} - I_{270}), \tag{2}$$

from which $E_s(x,y) = H/4E_r^*(x,y)$ is obtained.

The recovered complex speckle is compared with calibrated modal fingerprints using phase-resolved modal correlation. The dominant modal components are selected from the correlation response, and the object field is estimated using a regularized modal fit,

$$\mathbf{c} = (\mathbf{D}^\dagger\mathbf{D} + \alpha\mathbf{I})^{-1}\mathbf{D}^\dagger\mathbf{y}. \tag{3}$$

The reconstructed field is then obtained as $E_{\mathrm{rec}}(x,y) = \sum_k c_k M_k(x,y)$, from which the object intensity and phase are estimated.

Preliminary numerical studies were performed using a static random phase diffuser and a dictionary of structured modes, including Laguerre-Gaussian, Hermite-Gaussian, perfect optical vortex, and anisotropic perfect optical vortex fields. As shown in Fig. 1, the input structured field is converted into a scattered speckle pattern, while the proposed complex-field reconstruction retrieves the object intensity and phase. These observations suggest that interferometric complex-field correlation can provide a route toward phase-sensitive reconstruction through static scattering media.

References:

[1] J.W. Goodman, *Speckle Phenomena in Optics*, Roberts and Company, Colorado (2007).

[2] I.M. Vellekoop, A.P. Mosk, *Optics Letters* 32, 2309–2311 (2007).

[3] A.P. Mosk, A. Lagendijk, G. Lerosey, M. Fink, *Nature Photonics* 6, 283–292 (2012).

Topological and Polarization Effects in the Tight Focusing of Hybrid Vector Vortex Beams through Uniaxial Crystals

[1]Sakthi Maheswari R,[1]T.K. Lena Shree, [1]Kanishka S,[1]Amal M,[2]K.B. Rajesh,[1#]Lavanya M

[1]Department of Physics, PSGR Krishnammal College for Women,641001
[2]Department of Physics, Government Arts College, Coimbatore,641018

[#]*lavanyam@psgrkcw.ac.in*

Hybrid vector vortex beams (HVVBs) with independently varying topological indices were investigated in isotropic and uniaxial media using vectorial diffraction theory. Birefringence significantly modified the focal field, producing larger focal shifts, anisotropic energy transport, enhanced longitudinal fields, and increasingly complex polarization structures with increasing beam order.

The propagation of vector vortex beams (VVBs) in anisotropic media, particularly uniaxial crystals, offers additional possibilities for structured-light control through birefringence [1,2]. However, the tight focusing of hybrid vector vortex beams (HVVBs) characterized by two independently varying topological indices, m and n, remains relatively unexplored, particularly with respect to focal shift, polarization topology, and energy transport.

In this work, the focusing characteristics of HVVBs in isotropic and uniaxial media are investigated using vectorial diffraction theory [3]. The indices $m$and $n$are independently varied from $-10\ to\ +10$, and the resulting focal intensity, axial focal shift, polarization structure, orbital and spin flows, total energy flow, and longitudinal field intensity are analyzed. The results show that crystal birefringence produces pronounced anisotropic focal deformation and significantly modifies the axial focal position compared with isotropic media [2,4].

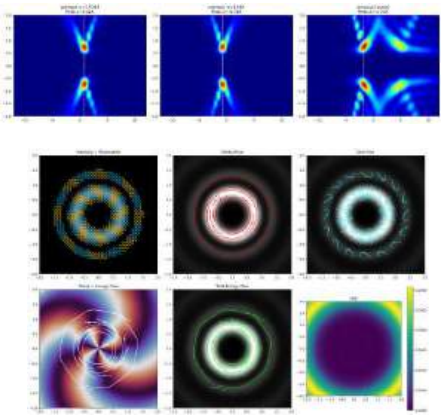


Fig. 1: Focal-field characteristics of a hybrid vector vortex beam in isotropic and uniaxial media for $(m,n) = (4,-4)$

Increasing the beam order broadens the vortex structure and enlarges the central dark core [5], while producing increasingly complex polarization and energy-flow distributions. Alternating left- and right-handed polarization domains become more spatially modulated at higher orders. The orbital flow retains a predominantly circulating character, whereas the spin flow becomes progressively fragmented. Reversal of the topological charge mainly alters the spin-flow topology with comparatively minor changes in the focal intensity distribution.

These results demonstrate that beam topology and crystal birefringence jointly govern the focal position, polarization structure, and energy transport of tightly focused HVVBs. The observed behavior provides a potential route for structured-light manipulation in singular optics, optical trapping, beam shaping, and photonic information processing.

Acknowledgement: The authors acknowledge financial support from ANRF-SERB, Government of India, under the CRG scheme.

References:

[1] V. Aita, M. Shevchenko, F. Rodríguez-Fortuño, A. Zayats, *Physical Review B* 109 (2024) 125433.
[2] S. Stallinga, *Journal of the Optical Society of America A* 18 (2001) 2846–2859.
[3] R. Kumar, D. Gupta, N. Ghosh, A. Banerjee, *Proceedings of SPIE* 12152 (2022) 121520.
[4] B. Ge, Q. Zhang, R. Zhang, J.-T. Lin, P.-H. Tseng, C.-W. Chang, C. Dong, R. Zhou, Z. Yaqoob, I. Bischofberger, P. So, *ACS Photonics* 8 (2021) 3440–3447.
[5] X. Dai, Y. Li, L. Liu, *Optics Communications* 426 (2018) 46–53.

Vectorial Diffraction Analysis of Tightly Focused Hybrid Poincaré Beams Through an Oil Immersion Objective

[1]Kanishka S, [1]Sakthi Maheswari R, [1]T.K. Lena Shree, [1]Amal M, [2]K.B. Rajesh, [1#]M Lavanya

[1]Department of Physics, PSGR Krishnammal College for Women, Coimbatore, 641001.

[2]Department of Physics, Government Arts College, Coimbatore, 641018.

[#]*Corresponding author Email id: lavanyam@psgrkcw.ac.in*

The tight focusing of Hybrid Poincaré beams through an oil immersion objective is investigated using the vectorial Richards–Wolf diffraction formalism. Incorporating Fresnel transmission and refractive-index mismatch, the model reveals focal intensity, polarization, energy-flow, and chiral optical force characteristics, providing a versatile framework for structured-light engineering and high-resolution immersion microscopy.

High-numerical-aperture oil immersion objectives are widely used in microscopy to improve spatial resolution and light collection. However, refractive-index mismatch at the oil–coverslip–water interfaces introduces immersion-induced aberrations that alter the focal field. Hybrid Poincaré beams, possessing spatially varying polarization and coupled spin–orbital angular momentum, provide an attractive platform for studying vectorial focusing in such optical systems. In this work, the tight focusing of Hybrid Poincaré beams through an oil immersion objective is investigated using the vectorial Richards–Wolf diffraction formalism.

The incident beam is formed by the superposition of two orthogonally polarized vortex beams carrying topological charges m and n. Fresnel transmission coefficients and the phase aberration caused by refractive-index mismatch are incorporated into the Richards–Wolf model to calculate the focused field,

$$E(r,z) \propto \int_0^{\alpha} T(\theta) \sin\theta \; A(\theta) \; J_p(kn_2 r \sin\theta_t) e^{i[kn_2 z \cos\theta_t + \Phi(\theta)]} d\theta \qquad (1)$$

The focal field is analyzed through the intensity distribution, Stokes parameters, polarization ellipses, energy flow, and optical force distributions.

Fig.1 shows the transverse focal-field characteristics for m = n = 5. The focused beam exhibits an annular intensity profile with spatially varying polarization ellipses. The spin and orbital energy flow distributions display distinct circulation around the optical axis, while their superposition determines the total energy flow.Fig. 2 presents the corresponding achiral and chiral optical force distributions. The achiral force is concentrated near regions of high intensity gradient, whereas the chiral force exhibits handedness-dependent behavior. The dominance maps identify regions where the chiral contribution exceeds the achiral force.

The proposed numerical model provides a framework for investigating the vectorial focusing of Hybrid Poincaré beams in oil immersion systems and offers insight into structured-light engineering, optical manipulation, and high-resolution microscopy.

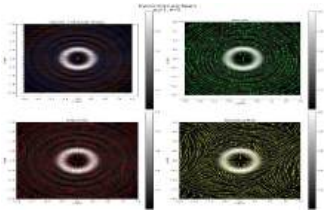


Fig. 1: Transverse focal-field characteristics for m = n = 5.

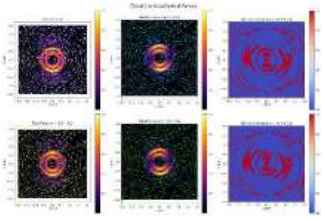


Fig. 2: Achiral and chiral optical force distributions

References:

[1] X. Dai, Y. Li, L. Liu, *Optics Communications* 426 (2018) 46–53.
[2] A. S. Marathay, J. R. McCalmont, *J. Opt. Soc. Am. A* 18 (2001) 2585–2593.
[3] P. Suresh, C. Mariyal, R. C. Saraswathi, K. B. Rajesh, T. V. S. Pillai, Z. Jaroszewicz, *Optik* **125** (2014) 1264.

Programmable Liquid Crystal Vortex Beam Generation Using Independently Addressable Ring Sector Electrodes

[1]Rohit Shimpi,[2*]Kedar Khare and [3*]Aloka Sinha
[1]Department of Physics, Indian Institute of Technology Delhi, New Delhi 110016, India
[2]Department of Physics, Indian Institute of Technology Delhi, New Delhi 110016, India
[3]Department of Physics, Indian Institute of Technology Delhi, New Delhi 110016, India

We propose a programmable liquid crystal vortex beam generator employing independently addressable ring sector electrodes for simultaneous radial and azimuthal phase modulation. A model based on electrostatic and Oseen Frank is used to investigate voltage controlled orbital angular momentum generation, demonstrating the potential of compact electrically reconfigurable structured light devices for computational imaging and integrated photonics.

Orbital angular momentum (OAM) beams have emerged as a powerful tool for applications in optical communication, computational imaging, optical manipulation and beam shaping. Although spatial light modulators (SLMs) offer versatile wavefront control, their pixelated architecture, bulky optical setup and high cost limit their use in compact integrated systems. Liquid crystal (LC) phase modulators provide a promising alternative owing to their low power consumption, compactness and electrical tunability. However, conventional LC vortex generators employing spiral or sector electrodes primarily control only the azimuthal phase, restricting the range of achievable optical wavefronts.

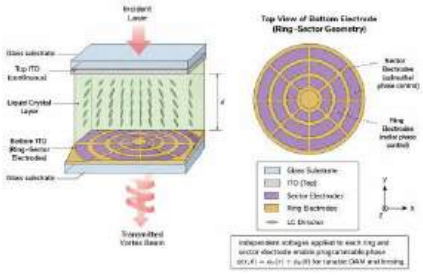


Fig. 1: Proposed ring sector electrode architecture for voltage controlled liquid crystal vortex and vortex lens beam

In this work, we propose a programmable LC vortex beam generator based on independently addressable concentric **Ring–Sector (annular pizza-slice)** electrodes. The sector electrodes generate the azimuthal phase required for OAM, while the concentric ring electrodes independently control the radial phase, enabling synthesis of generalized phase profiles given by $\phi(r,\theta) = \phi_r(r) + \phi_\theta$, where ϕ_θ governs the vortex phase and ϕ_r introduces a programmable radial phase for electrically tunable lensing. Unlike conventional sector-only geometries, the proposed architecture provides independent control over both radial and azimuthal phase distributions, enabling dynamic generation of vortex-lens wavefronts within a single LC device. The proposed device is investigated using a physics-based numerical model incorporating electrostatic field computation, Oseen Frank elastic theory for liquid-crystal director reorientation, optical phase accumulation and Fourier propagation. Device performance is evaluated through far field intensity distributions, OAM spectrum, vortex purity, diffraction efficiency, mode overlap and phase error. The proposed ring sector architecture provides an additional degree of freedom for programmable phase engineering and offers a compact electrically reconfigurable platform for structured-light generation with potential applications in computational imaging, adaptive optics and integrated photonics.

Overall, a programmable ring sector liquid-crystal electrode architecture is proposed for voltage controlled structured light generation. Independent radial and azimuthal phase modulation offers greater wavefront design flexibility than conventional sector only LC devices while maintaining a compact analog architecture. Numerical modelling demonstrates the potential of the proposed geometry for electrically tunable vortex beam generation and programmable vortex-lens operation.

The authors acknowledge the Department of Physics, Indian Institute of Technology Delhi, for providing computational and research facilities

References:

[1] J. Albero, P. Garcia-Martinez, N. Bennis, E. Oton, B. Cerrolaza, I. Moreno, and J.A. Davis, *J. Lightwave Technol*. (2012) 30, 3055–3060.

[2] T. Jankowski, A. Walewska, N. Bennis, et al., Proc. SPIE 13595, *Novel Optical Systems, Methods, and Applications* (2025) 13595, 135950V1-135950V5

Secure Optical Image Authentication Based on C-Point Singularities

Tileshwar and Praveen Kumar
Department of Physics, Indian Institute of Technology Bhilai, Durg, 491001, India
*praveen@iitbhilai.ac.in

We present an optical image authentication scheme based on the topological stability and uniqueness of C-point polarization singularities in vector light fields. The proposed method utilize the topological and polarization degrees of freedom (DOFs) of C-points for multi-data encoding and image authentication. Intensity-based verification eliminates the need for interferometric detection and phase retrieval techniques, providing a simple and robust approach for optical security applications.

Optical authentication has emerged as an effective approach for protecting visual information by exploiting the physical parameters of light, such as amplitude, phase, and polarization. Recent advances in structured light have introduced additional DOF, making it possible to improve the security and capacity of optical cryptographic systems. In particular, vector light fields containing polarization singularities provide unique topological features that are well suited for secure information encoding and authentication [1-2].

Existing structured-light-based cryptographic techniques typically require multiple spatial light modulators or complex phase-modulation schemes, which increase the complexity and cost of optical implementation. In this work, we present an optical image authentication scheme based on topologically stable C-point polarization singularities [3-4].

The proposed method utilize the topological stability and uniqueness of C-points to encode and authenticate images through intensity-based verification, eliminating the need for interferometric detection. The resulting approach provides a simple, compact, and robust framework for high-security optical authentication [5].

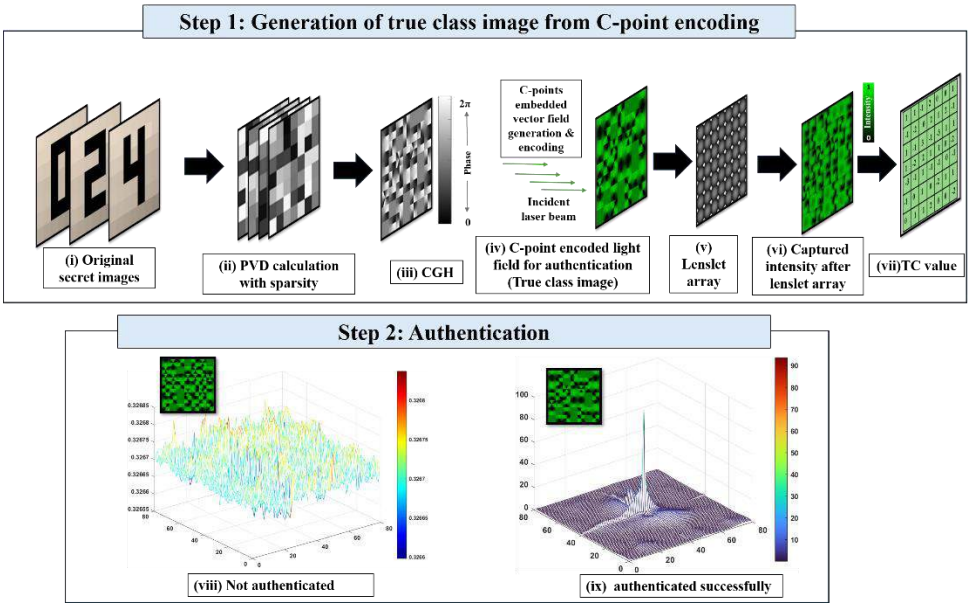


Figure 1. Overview of the proposed C-point-based optical image authentication process.

References:

[1] B. Javidi, Optical and Digital Techniques for Information Security, Springer, Berlin (2005).
[2] N.K. Nishchal, Optical Cryptosystems, IOP Publishing, Bristol, UK (2020).
[3] M. Baliyan, N.K. Nishchal, Opt. Lasers Eng. 180 (2024) 108337.
[4] P. Kumar, N.K. Nishchal, A. Alfalou, J. Opt. 24 (2022) 064017.
[5] Tileshwar, P. Kumar, Appl. Opt. **65** (2026) 4708-4716.

*****

Optimized simultaneous generation of dual-wavelength phase and polarization singularities

[1]Kushal Kumar Tripathi, [1]Laxminarayan, [2]Sudheesh K. Rajput, [3,#]Yasuhiro Awatsuji and [1]Praveen Kumar
[1]Department of Physics, Indian Institute of Technology Bhilai, Durg, 491002, Chhattisgarh, INDIA
[2]Department of Engineering Physics, Koneru Lakshmaiah Education Foundation (KLEF), Vaddeswaram, 522302, Guntur, AP, India
[3]Faculty of Electrical Engineering and Electronics, Kyoto Institute of Technology, Matsugasaki, Sakyo-ku, Kyoto 606-8585, Japan

[#]*awatsuji@kit.ac.jp*

Simultaneous generation of phase and polarization singularities at dual wavelengths is achieved using an optimized SLM configuration. A wavelength-specific gray-level optimization strategy enables accurate wavefront modulation at 532 nm and 635 nm, resulting in high-fidelity generation of phase and polarization singularities through experimental validation.

Phase and polarization singularities are widely used in optical communication, beam shaping, optical trapping, and quantum photonics. However, simultaneous wavefront modulation at multiple wavelengths is challenging because the phase response of liquid crystal spatial light modulators (SLMs) varies with wavelength. In this work, an optimized SLM configuration is proposed for simultaneous generation of dual-wavelength phase and polarization singularities at 532 nm and 635 nm using a single phase-only SLM. To compensate for wavelength-dependent phase errors, a wavelength-specific gray-level optimization strategy was developed based on the calibrated phase response of the SLM. The phase modulation introduced by the device is expressed as

$$\phi(g,\lambda) = \frac{2\pi}{\lambda}\Delta n(V_g)d. \tag{1}$$

where g is the gray level, λ is the operating wavelength, $\Delta n(V_g)$ is the voltage-dependent birefringence, and d is the liquid crystal layer thickness. Optimized gray-level maps were encoded onto separate regions of the SLM to achieve simultaneous phase modulation at both wavelengths.

Experimental results demonstrate that the proposed gray-level optimization effectively compensates wavelength-dependent phase errors, enabling accurate generation of dual-wavelength phase and polarization singularities.

The proposed technique provides a simple and efficient platform for dual-wavelength structured-light generation with potential applications in optical information processing, beam shaping, optical manipulation, and quantum photonics.

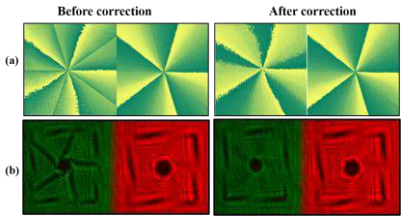


Fig. 1: Comparison of azimuthal phase and vortex beam intensity before and after phase correction. Row (a) shows the azimuthal phase, while row (b) shows the corresponding vortex beam intensity. Columns (i) and (ii) indicate the results before and after phase correction, respectively.

Acknowledgement: The authors acknowledge the financial support provided by the Ministry of Education, Government of India, and the research facilities provided by the Indian Institute of Technology Bhilai.

References:

[1] K.K. Tripathi, Laxminarayan, S.K. Rajput, Y. Awatsuji, P. Kumar, Scientific Reports 16 (2026) 20647.

[2] C.R. Guzman, A. Forbes, Structured Light with Spatial Light Modulators, CRC Press, Boca Raton (2024).

[3] M. Born, E. Wolf, Principles of Optics, 7th ed., Cambridge University Press, Cambridge (1999).

Point singularities in Spectral Interference.

[1,#]Athira T S,[2]Harikrishnan P and [3]Dinesh N Naik
[1]Govt KNM Arts and Science college, Thiruvananthapuram
[2,3]Applied and Adaptive Optics Laboratory, Department of Physics, Indian Institute of Space Science and Technology, Thiruvananthapuram

[#]*athiratsoptics@gmail.com*

This work demonstrates the possibility of generating the first spectral vortex by engineering the spectral properties of interfering fields. The inherent one-dimensional spectral information is transformed into a two-dimensional topological representation to reveal phase singularities. Simulations confirm the formation of point singularities in spectral interference.

Optical vortices have been a significant area of research in optical interferometry for several decades. They are phase singularities characterized by a helical wave front with a phase variation 2π around the singular point. Optical vortices are typically observed as two-dimensional topological structures in an optical field and can be generated using various techniques, including spiral phase plates, interferometric methods, forked holograms, and spatial light modulators [1]. The regions containing these singularities exhibit nonlinear phase accumulation, which can be identified through three-beam interference [2]. Similar singular behavior and nonlinear phase accumulation are also present in spectral interference. However, unlike spatial optical fields, spectral data are inherently one-dimensional. Therefore, to visualize spectral singularities in a manner analogous to spatial vortices, the one-dimensional spectral data must be represented as a two-dimensional topological distribution. This is achieved by stacking one-dimensional spectral information over a long path-delay range, resulting in line singularities in a two-dimensional topological representation, as experimentally demonstrated in [3]. By transforming these line singularities into point singularities, the first spectral phase vortex can be revealed.

Line singularities in spectral interference can be generated through the interference of two Gaussian fields with slightly different mean frequencies. These line singularities can be transformed into phase singularities by applying an equal and opposite linear phase delay that compensates for the phase delay introduced by the time delay τ. Let $E_1(\omega,t)$ and $E_2(\omega,t)$ are Gaussian fields with center frequencies ω_{01} and ω_{02} and width $\Delta\sigma_\omega$ as shown in the figure 1(a).

$$E_1(\omega,t) = E_{01} exp\left(-\frac{(\omega-\omega_{01})^2}{2\Delta\sigma_\omega^2}\right) exp(i\omega\tau) exp\left(i\frac{\pi}{2}\right) \quad (1)$$

$$E_2(\omega,t) = E_{02} exp\left(-\frac{(\omega-\omega_{02})^2}{2\Delta\sigma_\omega^2}\right) exp(-i\omega\tau) exp\left(-i\frac{\pi}{2}\right) \quad (2)$$

The interference of the two fields now produces a spectral vortex and associated phase singularity, as shown in the figure 1(b) and 1(c). Thus, by modifying the spectral properties of the interfering fields, we successfully introduced a phase singularity into the spectral interference pattern. This topological transformation creates a unique singular point in the optical field with distinctive phase characteristics, which has the potential to enhance measurement sensitivity in a range of optical sensing and metrological applications.

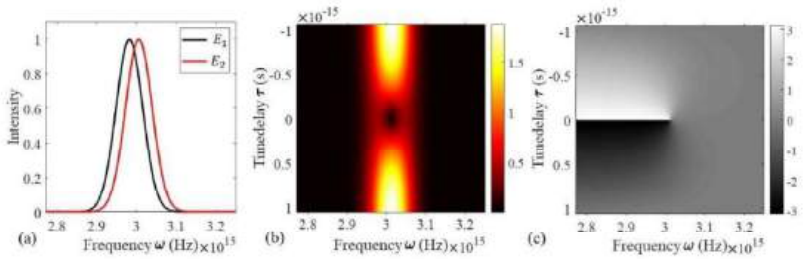


Fig. 1: (a)The interfering Gaussian spectral field $E_1(\omega,t)$and $E_2(\omega,t)$ (b)The intensity of interference shows the point singularity (c) The phase of interference.

References:

[1] G. J. Gbur, Singular Optics *Singular Optics*, CRC Press, Boca Raton (2016).
[2] T. S. Athira and D. N. Naik, *Journal of Optics*, 23(11), 115606 (2021).
[3] T. S. Athira and D. N. Naik, *Physica Scripta,* 98(6), 065509 (2023).

Tailoring the properties of coherence vortices: control functional engineering of Laguerre-Gaussian beams.

[1,#]Ganesh Velagala,[1]Md. Haider Ansari, [1]Ravi Kumar, and [1,#]Gangi Reddy Salla
[1]Department of Physics, SRM University-AP, Amaravathi 522240, Andhra Pradesh, India

[#]ganesh_velagala@srmap.edu.in , gangireddy.s@srmap.edu.in

In this work, we generate tunable coherence vortices from the intensity correlation of speckle patterns produced by scattering functionally engineered Laguerre-Gaussian beams. We demonstrate that coherence vortex radius and ring width can be tailored via controlled speckle engineering, offering a flexible approach for structured-light applications in imaging and optical communications.

The field distribution of the lowest radial order (p=0) Laguerre-Gaussian (LG) beam can be mathematically expressed in cylindrical coordinates as [1]:

$$E(\rho,\theta,0) \propto \left(\frac{\rho\sqrt{2}}{w_0}\right)^{|\ell|} \exp\left(-\frac{\rho^2}{w_0^2}\right) \exp(-i\ell\theta), \qquad (1)$$

We have generated tunable LG beams by introducing the scaling function $f(\ell)$ into the beam waist of the above equation, i.e. $w_0 \rightarrow w_0 f(\ell)$. Furthermore, four different vortex beams have been generated using different scaling functions. After that, we have scattered these tunable beams across a rough surface, such as a ground glass plate (GGP), and captured the resulting speckle patterns at different propagation distances. The coherence vortices are generated by cross-correlating the speckle patterns of tunable beams of different TCs. The correlation function can be expressed as [2]:

$$\Gamma = \frac{2\pi}{\lambda^2 z^2} e^{\frac{ik}{2z}(r_1^2 - r_2^2)} (-i)^{m-} \frac{(\beta e^{i\phi_s})^{m-} (|\ell_1|)! e^{\frac{-\beta^2}{4\alpha}}}{2^{m-+1} \alpha^{|\ell_2|+1}} L_{|\ell_1|}^{(m_-)} \left(\frac{\beta^2}{4\alpha}\right) \qquad (2)$$

where = $m_- = |\ell_2| - |\ell_1|, \beta = \frac{k\Delta r}{z} and\ \alpha = 2/w_0^2 (f(\ell))^2$. The size of the coherence vortex is calculated from Eq. (2) and can be written as:

$$\Delta r = \frac{\sqrt{8R_l^m}}{k w_0 f(l)} z \qquad (3)$$

From the above equation, we confirm that the size of the coherence vortex can be controlled through the scaling function $f(l)$.

We started with the analytical expression for the tunable LG beams and then experimentally computed the 2-D spatial cross-correlation function using speckle patterns from these beams. Fig. 1 shows the coherence vortices of four beam types: (a) constant beam, (b) corrected beam, (c) sinusoidal, and (d) Gaussian-modulated vortex beams with order of vortices m = 1, 3, and 5.

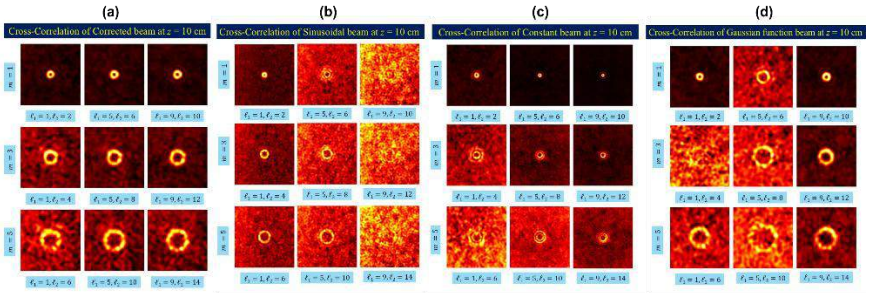


Figure 1:Experimentally generated coherence vortices of (a) corrected, (b) Constant, (c) Sinusoidal, and (d) Gaussian-modulated beams at the propagation distance z=10 cm

The figure clearly shows that the size of the coherence vortices varies with the scaling function. For the corrected beam, the size is independent of the initial input TC ℓ_1 and $\ell_2$whereas for other beams it follows the scaling function. This dependence of the size of coherence vortices arises from the speckle size of the beams, which is controlled by the scaling function [3].

References:

1. V. Cocotos, A. Forbes, Journal of Optics, 27, 7, 07LT01 (2025).
2. P. Gangwani, H. Ansari, R. Kumar, S.G. Reddy, S. Prabhakar, J. Banerji, R.P. Singh, Optics and Lasers in Engineering, 194, (2025).
3. G. Velagala, M.H. Ansari, R. Kumar, S. Prabhakar, S.G. Reddy, Journal of Optics, 28, 6, 065604 (2026).

Spatiotemporal Enhancement of Dynamic Laser Speckle Activity Maps for Low-Contrast Fine Structural Visualisation

[1#]Ashwani Verma,[2#]Anil Kumar Nirala

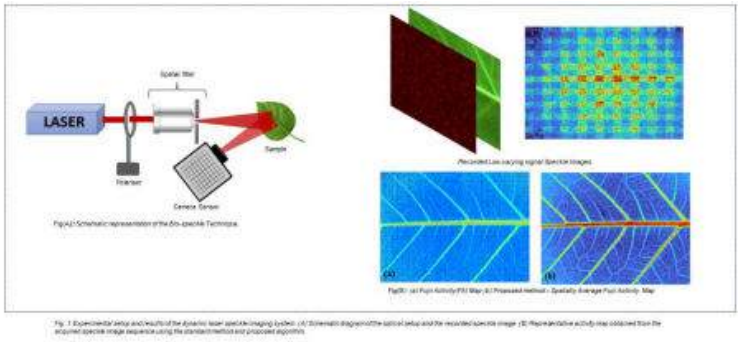
[1]Biomedical Optics Laboratory, Department of Physics, Indian Institute of Technology (ISM), Dhanbad, Jharkhand 826004, India

[2]Biomedical Optics Laboratory, Department of Physics, Indian Institute of Technology (ISM), Dhanbad, Jharkhand 826004, India

[#]22dr0064@iitism.ac.in,aknirala@iitism.ac.in

Dynamic laser speckle imaging is often limited by low visual contrast, hindering the visualisation of fine vascular structures and weak activity patterns. The proposed spatiotemporal framework uses local statistical correlations to reduce stochastic speckle fluctuations to improve the robustness of activity estimates and the delineation of weakly active fine vascular structures in low-contrast regions.

This experimental work demonstrates that raw sequential speckle images exhibit low visual contrast, making the direct observation of fine vascular structures difficult. To address these issues, a spatially averaged Fujii index that leverages spatiotemporal information via temporal smoothing and spatial neighbourhood averaging is proposed.



The successive speckle frames are temporally smoothed using a three-frame moving average. The absolute intensity difference and intensity summation between subsequent frames are then used to compute the numerator and denominator of the Fujii index. To incorporate neighbourhood information while suppressing random intensity fluctuations, local spatial averaging is then applied to both components using a normalised $(5x5)$ averaging kernel $'K'$ before activity estimation.

The proposed method is as follows:

The Fujii sequence is $$F(x,y,k) = \frac{N_S(x,y,t)}{D_S(x,y,t)} = \frac{K*N}{K*D} = \sum_{i=1}^{5}\sum_{j=1}^{5}\frac{K(i,j)*N(x+i,y+i,t)}{K(i,j)*D(x+i,y+i,t)} \quad (1)$$

where (x,y) is the spatial coordinate and 't' is the time frame.

A normalised averaging kernel satisfies, $K(i,j) = \frac{1}{w^2}, \quad 1 \le i,j \le w$

The Spatially Averaged Fujji Activity Map $(SAFA)$ is given as:

$$SAFA(x,y) = F_{RMS}(x,y) * W(x,y) \quad (2)$$

Where, $W(x,y)$ is the weight map.

In a nutshell, this approach retains activity information while minimising stochastic speckle alterations. In addition to the traditional Fujii index Activity Map, it produces more reliable activity assessment by improving the depiction of weakly active, low-contrast fine vascular structures.

The authors thank the Biomedical Optics Laboratory and the Department of Physics at the Indian Institute of Technology (ISM) Dhanbad for providing the research facilities.

References:

[1] C. Koley, A. K. Nirala, *Laser Phys*. 32, (2022) 075603.
[2] N. Kumar, A. K. Nirala, *Optik* 274, (2023) 170518.
[3] M. Z. Ansari, A. K. Nirala, *Eur. Phys. J. Appl.* Phys. 70, (2015) 21201.
[4] E. Colin, E. Garcia-Caurel, K. Adeline, A. Plyer, X. Orlik, *Photonics* 11, (2024) 1086.

Fourier-Space Theory of Turbulence Broadening and Scintillation Reduction in Vortex Beams

Shouvik Sadhukhan

Applied and Adaptive Optics Laboratory, Department of Physics, Indian Institute of Space Science and Technology (IIST), Valiamala, Thiruvananthapuram, Kerala, India
Corresponding author: shouvikphysics1996@gmail.com

A Fourier-space framework is developed to explain how atmospheric turbulence broadens the transverse momentum spectrum of Gaussian beams and how a vortex phase plate redistributes turbulence-induced fluctuations among orbital angular momentum channels. The analysis reveals that scintillation reduction arises from modal redistribution and spectral averaging rather than turbulence removal, providing insight for resilient free-space optical communication systems.

Atmospheric turbulence degrades optical beam propagation by introducing random phase distortions that broaden the beam spectrum and generate intensity scintillation, limiting the performance of free-space optical systems. In this work, a Fourier-space framework is developed to analyze turbulence-induced spectral broadening and to investigate how a vortex phase plate redistributes optical energy among orbital angular momentum modes, leading to reduced scintillation through modal averaging.

Atmospheric turbulence acts as a broadband random phase modulator that broadens the transverse momentum spectrum of an optical beam, transferring energy from low to high spatial frequencies and increasing momentum variance. This spectral broadening strengthens with turbulence intensity and induces coupling from a fundamental Gaussian beam into higher-order Hermite–Gaussian, Laguerre–Gaussian, and orbital angular momentum modes, providing a physical explanation for turbulence-induced modal mixing.

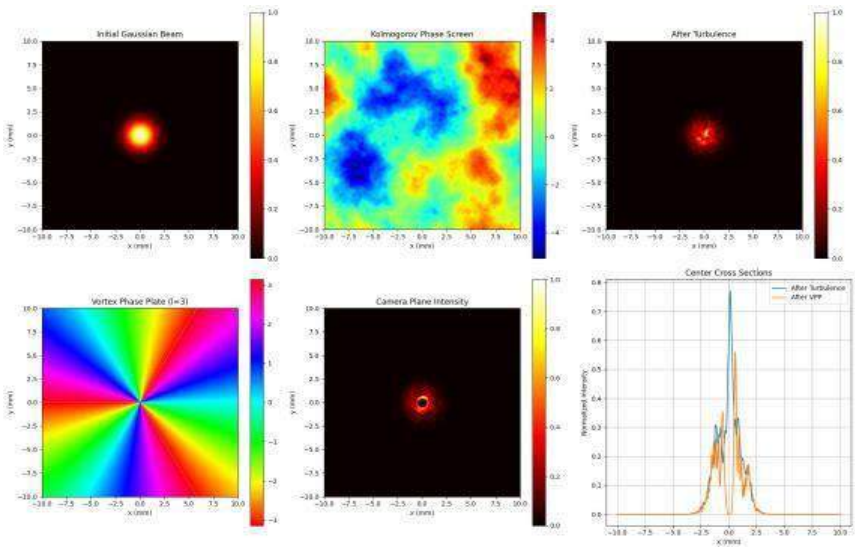


Figure 1: Results before and after beam shaping. Both are after turbulence impact.

A Fourier-space framework shows that a vortex phase plate redistributes turbulence-induced spectral fluctuations among orbital angular momentum modes, reducing scintillation through modal averaging and thereby improving the robustness of free-space optical beam propagation.

References:

1. S. Sadhukhan and C. S. Narayanamurthy, “Turbulence impacted wavefront corrections using beam modulation technique,” Opt. Commun. 567, 130716 (2024).
2. R. Sharma, J. S. Ivan, and C. S. Narayanamurthy, “Wave propagation analysis using the variance matrix,” J. Opt. Soc. Am. A 31, 2185–2191 (2014).

Development of a Reflectance Speckle Contrast Optical Spectroscopy System for Quantitative Flow Imaging

[1]Sriya Vaitheeswaran,[1]Raveena A, [1]Sameer B, [1]Sarfaraz Mirza, [1]Mahima Sharma, [1]Parth Pal and [1,#]Renu John

[1]Medical Optics and Sensors, Department of Biomedical Engineering, Indian Institute of Technology Hyderabad, India

[#]*renujohn@bme.iith.ac.in*

This work presents the development of a Speckle Contrast Optical Spectroscopy system for quantitative blood-flow imaging. Multi-exposure speckle contrast measurements were acquired using a custom SCOS system from tissue-mimicking flow phantoms at varying flow rates, enabling flow reconstruction. A deep learning-based temporal super-resolution framework is also proposed for real-time evaluation.

Speckle Contrast Optical Spectroscopy (SCOS) is a non-invasive optical imaging modality that exploits the temporal fluctuations of laser speckle patterns to visualize and quantify flow dynamics in highly scattering media, such as tissues [1]. SCOS has been extensively studied in applications involving blood flow assessment and brain imaging. The technique enables non-invasive measurement of blood flow by analyzing speckle contrast variations, providing high temporal resolution to dynamic changes in tissue perfusion. In this work, a reflectance SCOS system was developed and validated using tissue-mimicking phantoms

Speckle images were acquired over a range of controlled flow rates (5, 8 and 10 µl/min) and multiple camera exposure times (300 to 1500 µs) to capture the spatiotemporal dynamics of the scattered light. The system was validated on an agar-based phantom with a 0.3 mm cylindrical tube embedded at a depth of 2 mm from the surface. A schematic representation of the experimental setup is shown in Fig. 1. A 785nm fiber-coupled laser illuminated the phantom through a collimator, while intralipid solution was circulated through the embedded tube using a syringe pump to simulate blood flow. The diffusely reflected light was collected using a 50 mm imaging lens and captured using a CMOS camera. The acquired multi exposure speckle image were analyzed to evaluate the dependence of speckle contrast on flow velocity. For a given exposure time, the speckle contrast (K) was calculated as shown in Eqn.1, where σ_I is the standard deviation of the speckle intensity, and $\langle I \rangle$ is the mean intensity.

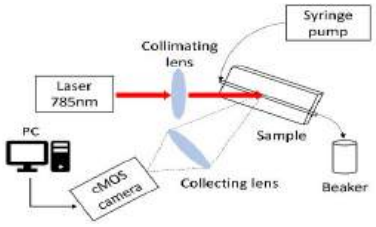


Fig. 1: Experimental Schematic of the SCOS system

$$K = \frac{\sigma_I}{\langle I \rangle} \tag{1}$$

The speckle contrast can also be expressed using the Siegert relation as

$$K(T,\tau_c) = \{\beta\rho^2 \frac{e^{-2x}-1+2x}{2x^2} + 4\beta\rho(1-\rho)\frac{e^{-x}-1+x}{x^2}\}^{1/2} \tag{2}$$

where $x = \frac{T}{\tau_c}$, $\rho = \frac{I_f}{I_f+I_c}$ is the fraction of dynamically scattered light, β is the experimental coherence factor, T is the exposure time, and τ denotes the correlation delay [2]. The exposure-dependent speckle contrast ($K^2(T,\tau_c)$) was fitted to estimate the speckle correlation time (τ_c), which is inversely proportional to flow velocity. The developed SCOS system was evaluated using tissue-mimicking phantoms at different flow velocities and compared with static phantoms. The estimated correlation times were subsequently used to obtain quantitative 2D flow maps of the embedded flow channel.

References:

[1] H.M. Varma, C.P. Valdes, A.K. Kristoffersen, J.P. Culver, T. Durduran, *Biomedical Optics Express* 5 (2014) 1275-1289.

[2] A.B. Parthasarathy, W.J. Tom, A. Gopal, X. Zhang, A.K. Dunn, *Optics express 16* (2008) 1975-1989.

Finite Difference Vector Analysis of the Arbitrary Waveguides

[1]Ramesh Kumar,[2,#]Anurag Sharma and [3]Pratiksha Chaudhary
[1]PI Gandhi Govt. college for Women Jind, Haryana
[2]Indian Institute of Technology Delhi, New Delhi
[3]Afflitiation with full address

[#]asharma@physics.iitd.ac.in

A New method is presented for full vector analysis of any arbitrary waveguide. The method is based on the finite difference approach with higher order series expansion of the derivative terms. These derivative operators are directly used in the eigenvalue equation.

The modelling and analysis of the waveguiding structure converges the loop of fabrication, testing and refabrication till the desired structure is achieved. All structures can't be analyzed with the analytical methods. This necessitates the essence of the numerical methods to analyze such structures. There are methods based on the requirements of the applications of the structure such as scalar, semi-vectorial and vectorial. The scalar methods[1] are effective when the refractive index difference is very small. Semi-vector[2] approach is used for moderate refractive index contrast structures. The full vector methods[3] are used to analyze the high refractive index contrast structures. The full vector methods are the most accurate methods to find all components of the electromagnetic field for the structures. The proposed method uses the finite difference approach. The derivative terms are expressed as the series terms which strengthen the accuracy of the method. These derivative operators are directly used in the eigenvalue equation for the compact formulation. Moreover, this method has no constraints of the symmetry and therefore any structure can be analyzed using this method. The suppression the appropriate terms converts the method into the semi-vector and scalar methods.

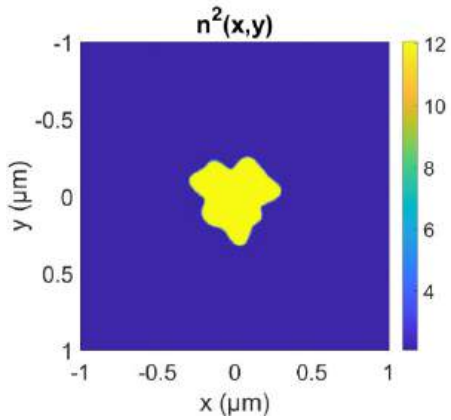


Fig. 1: Refractive index profile of 2D arbitrary structure.

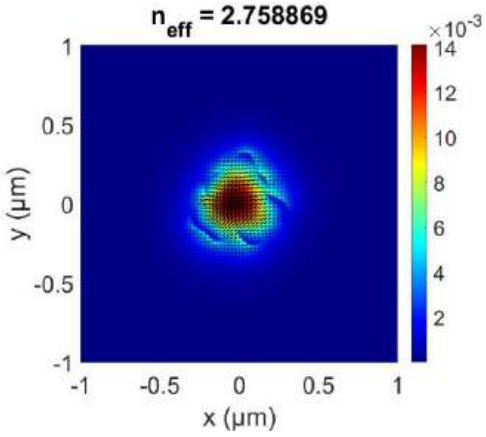


Fig. 2: Modal field intensity corresponding to highest effective index.

We have shown the refractive index profile and modal field intensity of highest n_{eff} of the structure which is having refractive index arbitrary boundary. The refractive index of core and cladding are 3.45 and 1.44, respectively. In step index structure we can't always make the exact waveguide at the refractive index interface. This is a discretization issue therefore the actual waveguide is minutely different when the number of points are changed. The subpixel averaging was used to get rid of the discretization issue. The wavelength of operation was 1.55 micrometer. The first four effective indices of the structure are 2.758869, 2.742519, 1.885164, 1.549656. The number of finite difference points used in the analysis were 501 in both horizontal and vertical extent of the structure. The numerical parameters were optimized for a simple square waveguide structure which matches well with the COMSOL results. The more results will be presented in the conference.

References:

[1] A. Sharma, "Collocation method for wave propagation through optical waveguiding structure," in Methods for Modeling and Simulations of Guided-Wave Optoelectronic Devices, vol. 11, S. March (Ed.), pp. 143–198, 1995.
[2] K. Gehlot and A. Sharma, "Optimization of Si slot waveguide using approximate semianalytical method," Optics Express, vol. 24, no. 5, pp. 4722–4729, Mar. 2016.
[3] A. Agrawal and B. M. A. Rahman, Finite Element Modelling Methods for Photonics. Norwood, MA, USA: Artech House, 2013.

Dual-Adaptive Physics-Informed Neural Networks for Optical Waveguide Eigenvalue Problems

[1,#]Geetanjli, [1] Kirankumar R Hiremath

[1]Department of Mathematics, Indian Institute of Technology Jodhpur, Rajasthan 342030, India

[#]*Corresponding author: p23ma0007@iitj.ac.in*

This work presents a dual-adaptive physics-informed neural network for optical-waveguide Helmholtz eigenvalue problems. The method combines residual-based collocation-point redistribution with adaptive learning of the propagation constant. Tested on different 1D and 2D waveguides, it improves stability, accuracy, and convergence, especially for higher-order TE and TM modes.

The computation of guided modes in optical waveguides involves solving Helmholtz eigenvalue problems with material discontinuities on unbounded domains. Classical mesh-based methods, such as finite-difference and finite-element techniques, require domain truncation and artificial absorbing boundaries, which introduce discretization errors, increase computational cost, and reduce flexibility in parametric studies. Physics-Informed Neural Networks (PINNs) [1] offer a mesh-free alternative by embedding the governing differential equations directly into the training objective. However, standard PINN formulations struggle to accurately enforce radiation conditions in open waveguide configurations, often leading to spurious reflections and inaccurate modal fields.

In this work, Perfectly Matched Layers (PMLs) are incorporated into the PINN framework through a complex-stretched Helmholtz equation posed on a finite computational domain. The PML attenuates outgoing and evanescent fields near the truncated boundaries, thereby approximating the open-domain radiation condition without requiring a conventional computational mesh.

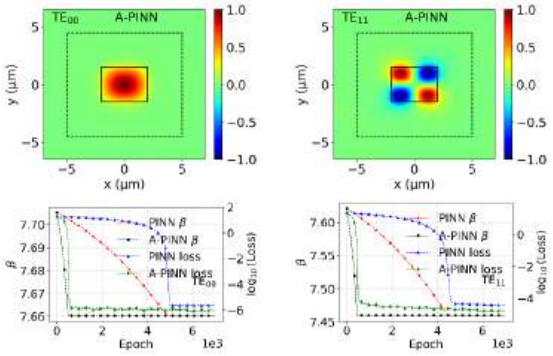


Figure 1: A-PINN modal fields and the corresponding propagation-constant and loss convergence histories for the TE_{00} *and* TE_{11} *modes.*

To improve the simultaneous learning of the modal field and propagation constant, a dual-adaptive strategy is introduced. The first adaptive mechanism employs residual-based collocation refinement, in which training points are progressively concentrated in regions with large PDE residuals, particularly near material interfaces and rapidly varying or evanescent field regions. The second mechanism assigns an adaptive learning rate to the trainable propagation constant [3], allowing its updates to be controlled independently of the neural-network parameters and thereby reducing oscillations, slow convergence, and convergence toward undesired eigenvalue branches.

As demonstrated in Fig. 1, the resulting dual-adaptive PINN–PML framework accurately predicts transverse-electric guided modes and their propagation constants in rectangular 2D waveguides while achieving faster and more stable convergence of the propagation constant than the standard PINN.

The authors acknowledge the support provided by the host institution.

References:

[1] M. Raissi, P. Perdikaris, G.E. Karniadakis, *Journal of Computational Physics* (2019).

[2] Geetanjli, K.R. Hiremath, *IOP Science Machine Learning: Engineering* (2026).

Quantum Simulator for RC Circuit Analysis using Unitary Dilation and Strang Splitting

[1,#]Aayush Deole, [2]J. T. Andrews, [3]A. S. Bais

[1]Dept. of Electronics and TeleCommunication, COEP Technological University, Pune, India
[2]Dept. of Physics, SGSITS, Indore, India
[3]Dept. of Computer Science, SGSITS, Indore, India

[#]aayush.deole@gmail.com

We present a quantum simulator for RC circuit analysis that resolves the conflict between unitary quantum evolution and dissipative classical dynamics using ancilla-based unitary dilation. Decomposing the state matrix into skew- and symmetric parts and applying Strang splitting, we achieve near machine-precision fidelity (~0.9999) validated against classical time-domain and Bode-plot results in Qiskit.

RC networks are fundamental to filtering, coupling and delay circuits, but their governing ODE is dissipative: the resistor irreversibly bleeds energy as heat, giving a strictly decaying eigenvalue. Quantum gates, by contrast, are unitary and norm-preserving, so the dissipative evolution cannot be applied directly as a quantum circuit. This work builds an exact quantum simulator for a single-stage RC low-pass filter that resolves this mismatch through ancilla-based unitary dilation, implemented and validated in Qiskit.

The augmented state matrix A (encoding Vc and the sinusoidal source) is split into a skew-symmetric part K, which generates an exact unitary evolution, and a symmetric part S, which generates the non-unitary, contractive dissipative dynamics. S is diagonalized ($S = VDV^T$) and its negative-shifted eigenvalues are encoded as controlled-RY rotations onto a single ancilla qubit; post-selecting the ancilla in $|0\rangle$ recovers the contraction exactly, with the residual global scale factor tracked classically. A Strang-split sandwich, $\exp(K\Delta t/2)\cdot[\text{ancilla-dilated } S]\cdot\exp(K\Delta t/2)$, raises the scheme to second-order accuracy, $O(\Delta t^2)$ global error, at negligible extra cost.

The full 50 ms, 5000-step evolution (R = 1 kΩ, C = 1 μF, f = 100 Hz) was validated against scipy.integrate.odeint: relative RMS error < 0.5%, average state fidelity 0.99996, and Frobenius-norm discrepancy of 2.7×10^{-16} against the exact non-unitary Trotter step. The reconstructed Bode magnitude reproduces the expected −20 dB/decade roll-off with cutoff fc ≈ 159.2 Hz (Fig. 1). The main practical cost is the post-selection success probability, which decays geometrically with simulation length, motivating future work on amplitude amplification and multi-node extensions.

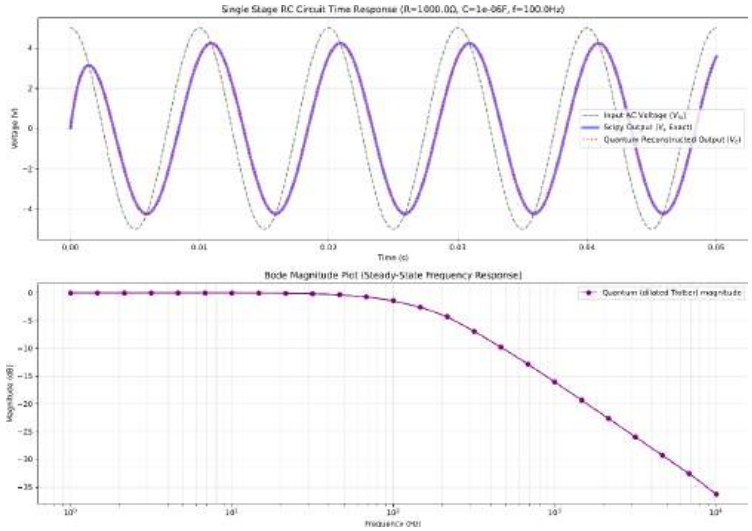


Fig. 1: *Time-domain response and Bode magnitude plot of the single-stage RC circuit — quantum-reconstructed output vs. exact SciPy solution.*

References:

[1] A. Zaman, H. J. Morrell, H. Y. Wong, IEEE Access (2022), doi:10.1109/ACCESS.2022.0122113.
[2] B. Zanger, C. B. Mendl, M. Schulz, M. Schreiber, arXiv:2012.09469v2 (2021).
[3] D. W. Berry, G. Ahokas, R. Cleve, B. C. Sanders, arXiv:quant-ph/0508139 (2006).

Inverse designed non-volatile phase change varifocal metalens at the edge of the visible spectrum

[1,2]Subrahmanyam S.G. Mantha,[1]Kannal Amudhu K and [1,#]Harish N.S. Krishnamoorthy

[1]Tata Institute of Fundamental Research, Hyderabad 500046, India

[2]Birla Institute of Technology and Science Pilani, KK Birla Goa Campus Sancoale 403726, India

[#]harishk@tifrh.res.in

We present a switchable varifocal metalens enabled by a phase-change material platform, designed via a combined finite element and inverse design strategy. Operating at the visible spectrum edge, the metalens dynamically switches focal states with superior performance – focusing efficiencies of ~40% and Strehl ratios of 0.80/0.78 in amorphous/crystalline states, indicating near-diffraction-limited performance.

Metalenses comprise of subwavelength nanophotonic entities that offer precise control over wavefront shaping, polarization and phase. Traditionally they are static in nature, with their optical properties such as focal length, operational spectral range fixed once designed. However, tunable characteristics of these designed metalenses are critical for advanced imaging systems such as adaptive optics, biomedical imaging and wearable vision technologies [1]. This reconfigurability can be achieved through either mechanical or non-mechanical ways. Among the non-mechanical approaches, phase change materials exhibit the distinct advantage of faster switching speeds between two states and are good candidates for varifocal metalenses.

In this work, a reconfigurable metalens was designed using Sb_2S_3 at a working wavelength of 795 nm with two different focal lengths 150 *μm* and 200 *μm* for two states. Sb_2S_3 was chosen due to high contrast in refractive index between its crystalline and amorphous states, and having low losses at the working wavelength and enables non-volatile reconfiguration with fast and reversible switching between the two states. The constituent meta-atoms consist of two rectangular nano-pillars, for which the required phase modulation was achieved by the geometric phase approach. The phase map was discretized into 4 levels for practical reasons. An Indium Tin Oxide (ITO) layer was added beneath the nano-pillars. Being conductive in nature, it serves as a microheater and helps in switching between the two states [2].

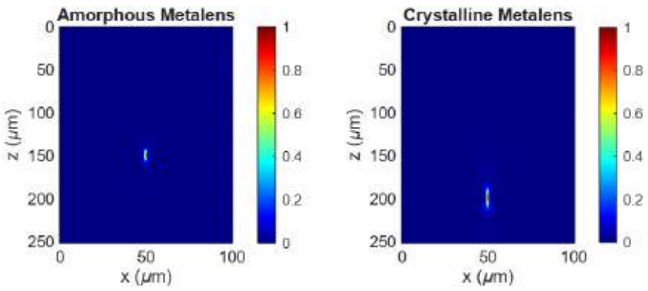


Fig. 1: Normalized axial(x-z) intensity profiles computed by beam propagation method, indicating the shift in the focal position from z ≈ 150 μm in the amorphous state to z ≈ 200 μm in the crystalline state.

To achieve reasonable performance of metalens in both states, an inverse design approach was used to generate a library of meta-atom geometries by using finite-element based computation combined with genetic algorithm. Genetic algorithm is based on the process of natural selection which aids in generating a meta-atom library by optimizing the objective functions (transmission) while maintaining the constraints. The chosen meta-atoms are then further rotated to impart required geometric phase.

The metalens operation was simulated using beam propagation method, from which Strehl's ratio and focusing efficiencies were computed. Strehl's ratio, an indicator of diffraction-limited performance, must be greater than 0.8 for a lens to be regarded as diffraction limited. The optimized varifocal Sb_2S_3 based metalens demonstrated reasonably good focusing efficiencies of 42% and 40%, and Strehl ratios of 0.80 and 0.78 in the amorphous and crystalline states, respectively, indicating near-diffraction-limited performance.

References:

[1] Mantha, Subrahmanyam SG, and Harish NS Krishnamoorthy, *arXiv preprint* (2026) arXiv:2604.00760.

[2] Taghinejad, Hossein, Sajjad Abdollahramezani, Ali A. Eftekhar, Tianren Fan, Amir H. Hosseinnia, Omid Hemmatyar, Ali Eshaghian Dorche, Alexander Gallmon, and Ali Adibi. Optics Express 29, no. 13 (2021): 20449-20462.

Spectral Characterization of Large Hollow-Core Bragg Fibers: A New Approach

[1]Ajay Kumar and [2, #]Anurag Sharma
[1]*Department of Physics, Indian Institute of Technology Delhi, New Delhi, 110016*
[2]*Optics & Photonics Centre, Indian Institute of Technology Delhi, New Delhi, 110016*
[#]*asharma@iitd.ac.in*

We present a new technique to compute the confinement loss, and propagation, and spectral characteristics of LP_{01} in liquid-filled large hollow core Bragg fibers by analyzing the field in the Bragg layers and calculating the power flow through these layers.

The large hollow-core Bragg fibers are vital for sensing because their oversized hollow core allows filling and refilling of desired liquids with ease. By guiding light through photonic bandgaps, they enable highly sensitive chemical and biological detection without the constraints of lower cladding index [1]. We model large core Bragg fibers using a variable transformed radial collocation method. This technique uses azimuthal symmetry to reduce 2D problems into a 1D eigenvalue problem and transformation crucially distributes the sample points in core and Bragg layers [2,3]. We consider the hollow core Bragg fiber with index profile is written as

$$n(r) = \begin{cases} n_c & r \le r_c \\ n_h & r_c + N\Lambda < r < r_c + N\Lambda + d_h \\ n_l & otherwise \end{cases} \quad (1)$$

where $n_c = 1.333\ to\ 1.378, n_h = 1.59,\ n_l = 1.49,\ r_c = 400\ \mu m,\ d_h = 0.13\ \mu m,\ \Lambda = 0.5\ \mu m$ and N=0 to 24. We have obtained the LP_{01} for wavelengths in the range of $0.4 - 0.8\ \mu\mathrm{m}$ [1]. This fiber has 25 bilayers of high and low index over a radial distance of $12.5\ \mu m$.

To quantify the mode confinement behavior with wavelength for a particular core refractive index $(n_c = 1.3330)$, we have computed the power flow through the layers from the core. Evidently, more power flow would mean less confinement in the core, and vice versa. To quantify this power flow, the ratio of the modal field intensity in last Bragg layer to first Bragg layer and hence, confinement loss (CL) is calculated using the formula as below.

$$P_{flow} = \frac{\int_{r_c+(N-1)\Lambda}^{r_c+N\Lambda} |\psi_\lambda|^2 r dr}{\int_{r_c}^{r_c+\Lambda} |\psi_\lambda|^2 r dr} \text{ and } \text{Confinemet Loss (CL)} \propto \log_{10}(\mathrm{P_{flow}}) \quad (2)$$

The results obtained by our method have the minimum confinement loss about central wavelength (λ_c) corresponding to the Bragg condition of reflection from the layers [4].

$$\lambda_c = 2 \times \left[d_h \sqrt{n_h^2 - n_c^2} + d_l \sqrt{n_l^2 - n_c^2} \right] \quad (3)$$

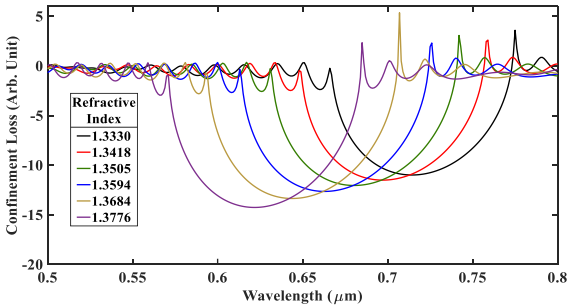


Fig.1: Confinement loss of LP_{01} mode with different RI of core.

Figure 1 shows the spectral variation of this ratio for different core indices of the core liquid. The results obtained are similar to results obtained by transfer matrix method (TMM), as reported in literature [1]. The wavelength band for "mode-like" behavior has the minimum loss. This correlates quite well with the spectral loss behavior. We have compared our results with TMM and experimental reported results [1,3]. This approach is simple for the estimation of spectral behavior of leakage loss or the window of leakage loss. All these results are obtained from the modal field in the first and last Bragg layer without involving any calculations in complex domains as in TMM. More results will be presented at the conference.

A. Sharma, a NASI Distinguished Chair Professor, acknowledges support from National Academy of Sciences, India (NASI).

References:

[1] H. Qu and M. Skorobogatiy, *Applied Physics* Letter 98, 201108 (2011).
[2] A. Kumar, A. Sharma, *Conference on SCOPOSIS-2025*, (SCOPOSIS 2025) 221 (2025)
[3] A. Kumar and A. Sharma, *Journal of the Optical Society of America A* 43, D141-D148 (2026)
[4] M. Skorobogatiy, *Optics Letters* 30, 2991-2993 (2005).

Design and Stray Light Simulation of Star Sensor Baffle for Interplanetary Missions

[1,] Arvind Kumar Sharma, [2]Rajnish Kumar Singh and [3]Aditya Toley
[1]Laboratory for Electro-Optics System (LEOS), ISRO, Bengaluru, Karnataka
[2]Laboratory for Electro-Optics System (LEOS), ISRO, Bengaluru, Karnataka
[3]Manipal Institute of Technology, Udupi, Karnataka

rajnish.singh@leos.gov.in

An Optical Baffle for Stray Light Attenuation in Star Sensor for Interplanetary mission is being developed. This paper will discuss the need aspect of such baffles and the Optical performance and Opto-Mechanical design of the baffle through simulations.

Attitude Sensors like the Star Sensor play crucial role in satellites by providing information to the attitude and orbital control systems which control the spacecraft. The sensors have to detect very faint signals coming from Star. They are also subjected to unwanted off-axis signals originating from various celestial bodies like the Sun, Moon. An external conical structure known as the 'baffle' is required for the attenuation of these unwanted signals. To maintain sensor accuracy, the design of the baffle is subjected to many constraints including the Field of View, Solar Constant, Attenuation factor Requirement and Thermal loading conditions.

For interplanetary missions closer to the sun there is a substantial increase in the Solar Constant, Attenuation Factor and Thermal Loads. The value of Solar Constant for Earth bound missions is taken as 1 but now considering mission requirement a Solar Constant of 2 is taken into account. Stray light attenuation requirement has increased from an order of $10e^{-7}$ to $10e^{-8}$ and thermal loads will drastically vary from atmosphere to atmosphere. A new baffle structure has been designed to tackle the increase in demand to maintain sensor accuracy in interplanetary missions. The challenges are to maintain optical accuracy while keeping our exclusion angle to a minimum in comparison with our field of view so that sensor performance is not affected and stray light can be attenuated properly.

Optical Design decides the Attenuation Factor of the Baffle and whether the Baffle is capable of handling the stray light that is primarily originating from the Sun. Optical Design depends on majorly three factors the overall length, vane spacing and vane depth. Based on the given requirement Initial estimate is done within CAD modeling itself. Once a configuration is selected, it is rigorously optimized for increase in attenuation factor and reduction in length and weight. The performance of the system is calculated using Advance System Analysis Program (ASAP) which utilizes mechanical and optical surfaces to calculate low light flux reaching the detector. The system calculates stray light in terms of Point Source Transmittance (PST) by tracing a set number of rays through our system. A few million rays are traced in order to evaluate the performance of the Baffle. Once Optical Optimization is completed Structural Design and Simulation begins for varying boundary conditions.

Validation of both the Optical and Structural Performance is completed through simulations in this paper.

References:

[1] Arvind Kumar Sharma, *IX Control Instrumentaion System Conference(CISCON-2012)* 16-17 November 2012.
[2] Robert P.Breault, Hand Book of Optics, Volume-1
[3] Gary L.Peterson, SPIE, Vol. 3780, pp 132-137, 1999
[4] Francis Reininger, SPIE, Vol. 2260, pp 17-28, 1994

Numerical Investigation of Enhanced Alpha-Particle Generation in Laser-Driven Proton-Boron Fusion

[1,#]Anupam Shaw, [1]R. M. Arun Kumar and [1]Bhuvanesh Ramakrishna
[1]Department of Physics, Indian Institute of Technology Hyderabad, Telangana-502285, India

[#]*es26resch01001@iith.ac.in*

Laser-driven proton–boron fusion was numerically investigated using EPOCH PIC and FLUKA simulations. Optimized proton acceleration from a gold pitcher target via target normal sheath acceleration (TNSA) yielded an enhanced alpha-particle flux from a boron catcher, demonstrating the potential of compact laser-driven sources for aneutronic fusion and medical isotope production.

Laser-driven proton–boron (p–^{11}B) fusion is an attractive aneutronic fusion scheme owing to its production of energetic alpha particles and its potential applications in advanced energy systems, medical radioisotope production, and laboratory astrophysics [1]. Recent advances in high-intensity lasers have enabled the acceleration of protons to initiate these fusion reactions. In this work [2], we investigate alpha-particle generation in a pitcher–catcher configuration [3] using a sub-μm gold target as the proton source and a solid boron catcher target.

Proton acceleration from the gold pitcher target is studied using the EPOCH particle-in-cell (PIC) code, while subsequent proton–boron fusion and alpha-particle production are modelled using the FLUKA Monte Carlo (MC) framework. Our results demonstrate that the high-Z nature and high density of the $2\ \mu\mathrm{m}$ gold target resulted in an intense quasi-static sheath field, generating a highly collimated proton beam with a cutoff energy of ~11 MeV. Crucially, this configuration yields proton counts up to 10^4 times higher within the key p–^{11}B fusion resonance cross-sections (0.6–0.75 MeV and 1.2–1.5 MeV) compared to traditional plastic (CH) or aluminium pitcher targets [4]. The accelerated protons subsequently interact with the boron catcher, resulting in efficient alpha-particle generation.

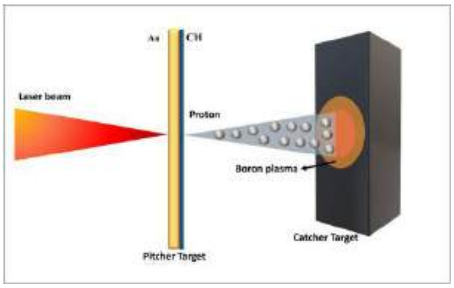


Fig. 1: Schematic of the pitcher-catcher target geometry. The pitcher is gold with a CH contaminant layer, and the catcher is boron.

The FLUKA simulations, which self-consistently account for proton transport, energy loss, and resonance crossing, predict an alpha-particle flux of $2.67 \times 10^{11}\ \alpha/\mathrm{MeV/sr}$, representing an enhancement of approximately two orders of magnitude over the highest flux previously reported for pitcher–catcher experiments [5]. The enhanced alpha-particle yield is primarily attributed to the high proton flux $(\sim 10^{18}\ \mathrm{MeV}^{-1})$ and the extended stopping range of higher-energy protons within the boron catcher. As the protons propagate through the target and gradually lose energy, they repeatedly sample the p–^{11}B resonance region, thereby increasing the effective fusion probability and the resulting alpha-particle yield. An analytical treatment based on stopping power and energy-dependent fusion cross sections corroborates the Monte Carlo results.

These findings establish important numerical benchmarks for future experimental validation and highlight the potential of laser-driven aneutronic fusion as a compact, high-flux alpha-particle source for applications in nuclear science, medical isotope production, and fusion energy research.

References:

[1] M. Scisciò, T. Carrière, H. Larreur, et al., *Matter and Radiation at Extremes* 10 (2025) 037402.
[2] R.M. Arun Kumar, A. Shaw, and B. Ramakrishna, *AIP Advances* 16 (2026) 045036.
[3] C. Labaune, C. Baccou, S. Depierreux, et al., *Nature Communications* 4 (2013) 2506.
[4] J. Bonvalet, Ph. Nicolaï, D. Raffestin, et al., *Physical Review E* 103 (2021) 053202.
[5] M. Huault, G. Petringa, Z. Zhu, et al., *Physics of Plasmas* 32 (2025) 013102.

Stability Analysis of the Effective index of Bent Optical Waveguide Operators with Perfectly Matched Layer

Deepanshi Singh[1] and Kirankumar R. Hiremath[1]

[1]Department of Mathematics, Indian Institute of Technology Jodhpur, India
Email: p22ma203@iitj.ac.in

We investigate the spectrum of a one-dimensional eigenvalue problem for bent optical waveguides, whose operator is non-self-adjoint. Domain truncation via PML introduces spurious modes alongside physical leaky modes. We employ ϵ-pseudospectrum analysis to assess robustness and sensitivity of TE modes under perturbations. Energy criteria used for distinguishing physically admissible modes from computational artifacts.

The computation of modal propagation constants in optical waveguides is commonly formulated as an eigenvalue problem for the Helmholtz operator on an unbounded domain with discontinuous refractive-index profiles. In bent optical waveguides, the governing operator is intrinsically non-self-adjoint [1], leading to complex-valued propagation constants associated with the leaky modes. The numerical treatment of such problems requires domain truncation, which is most often implemented using perfectly matched layers (PML) based on impedance matching condition [2]. However, the impact of PML truncation on the spectral properties of the discretized operator remains insufficiently understood.

Current PML-based approaches yield complex discrete spectra mixing physical modes, radiation continuum, and spurious PML eigenmodes. This spectral contamination obscures modal robustness, and sensitivity analysis—vital for design tolerance and perturbation resilience—is absent. We address this gap by employing ϵ-pseudospectrum [3] analysis to directly quantify n_{eff} sensitivity across the modal spectrum. Using second-order finite-difference discretization with split-field PML, we compute pseudospectra contours via resolvent-norm analysis, revealing which modes exhibit fundamental robustness and which are artifacts prone to perturbation.

Pseudospectra broaden progressively from fundamental to higher-order modes, demonstrating increasing sensitivity (see Fig(b) and fig(c)). Crucially, physically admissible modes remain comparatively stable under perturbations, whereas PML-induced spurious modes display pronounced spectral sensitivity (see Fig(a))—enabling post-hoc mode classification and reliability assessment without prior modal identification. Analysis is done to 1D cylindrical bent waveguides with specified refractive profiles; generalization to 2D and 3D structures requires further development. This study highlights the spectral contamination induced by PML truncation and underscores the need for carefully designed computational configurations to accurately and reliably compute leaky modes in bent waveguide eigenvalue problems.

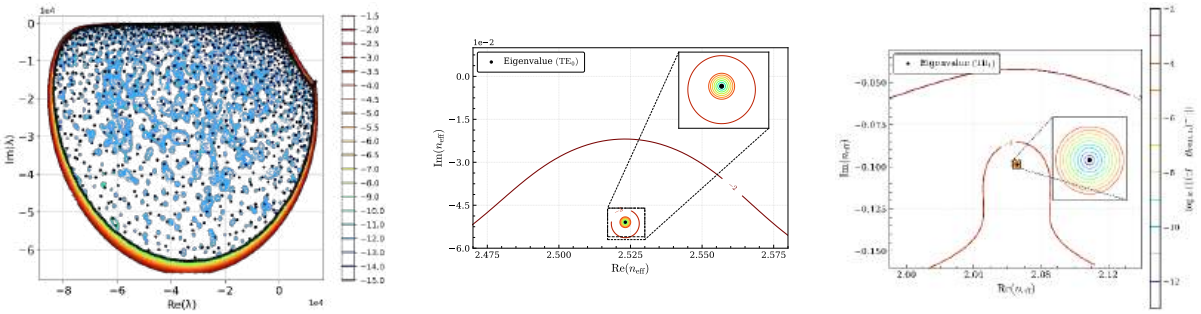


Figure 1: $\epsilon-$ pseudospectrum of (a)All eigenvalues(λ), (b)Fundamental mode eigenvalue and (c)First mode eigenvalue.

[1] R. Kumar and K. R. Hiremath. Non-self-adjointness of bent optical waveguide eigenvalue problem. *Journal of Mathematical Analysis and Applications*, 12(1):126024, 2022.

[2] J-P Berenger. A perfectly matched layer for the absorption of electromagnetic waves. *Journal of computational physics*, 114(2):185–200, 1994.

[3] L. N. Trefethen and M. Embree. *Spectra and Pseudospectra: The Behavior of Nonnormal Matrices and Operators*. Princeton University Press, 2005.

$NaBiF_4$:Yb, Er UCNPs: Temperature Sensing with off-resonant 1064 nm light

[1,#]Agniva Das,[2] Yamini S., and [3]Basudev Roy
[1]Department of Physics, Indian Institute of Technology Madras, India, 600036

[#]*agnivadas1@gmail.com*

Upconverting particles are typically excited with 975 nm laser light, but that is also the absorption resonance of water, leading to significant heating. We study the temperature-sensing of $NaBiF_4$:Yb, Er upconversion nanoparticles under 1064 nm excitation. They exhibit intense red emission and 22-fold higher sensitivity than $NaYF_4$, with minimal heating.

NaBiF4:Yb, Er upconversion nanoparticles (UCP) show intense red upconversion under 975nm and 1064nm NIR lasers. In this study, we observe the temperature sensing performance of NaBiF4 UCPs under 1064nm laser excitation in our optical tweezer setup. NaBiF4 UCPs show intense red luminescence with good chemical stability, making them suitable for temperature sensing applications. In comparison with NaYF4 UCPs, NaBiF4 offers approximately 22-fold higher temperature sensitivity, while exhibiting comparable heating behavior with a 975nm NIR laser. We observe that heating is significant with a 975nm laser compared to a 1064nm laser, because 975nm is a conventional exciting wavelength, and UCP is also an absorption resonance of water. With a 1064nm laser, the photo-thermal effect is also minimal, which makes NaBiF4 a highly promising material for precise, non-invasive nanoscale thermometry and biological optical manipulation. The key in this material is the broadband absorption of light, starting from 800 nm all the way to 1100 nm, around 975 nm, which is not the case for conventional UCP.

FIR values can be obtained, according to the Boltzmann distribution is [1]

. $$\text{FIR} = \frac{I_{550}}{I_{660}} = Be^{\left(\frac{-\Delta E}{k_B T}\right)} \quad (1)$$

Absolute sensitivity (Sa) and relative sensitivity (Sr)

$$S_a = \left|\frac{d\,FIR}{dT}\right| = FIR\,\frac{\Delta E}{k_B T^2} \quad (2)$$

$$S_r = \left|\frac{1}{FIR}\,\frac{d\,FIR}{dT}\right| = \frac{\Delta E}{k_B T^2} \quad (3)$$

References:

[1] L. Cao, L. Chen, Y. Wang, H. Zhu, X. Liu, X. Mi, Enhanced up-conversion luminescence and temperature sensing performance of $NaBiF_4$: Er^{3+}, Yb^{3+}, Al^{3+}, *Journal of Luminescence* 270 (2024) 120556.

Relativistic Compression Optimization of Negatively Chirped Super-Gaussian Laser Pulse in Plasma

[1]Km Shivani Bhardwaj, [1]Sintu Kumar
[1]Deen Dayal Upadhyaya Gorakhpur University, Gorakhpur, 273009, India
Email id: bhardwaj20shivani@gmail.com

This study numerically demonstrates a stable, ultra-short relativistic compression regime for a negatively chirped Super-Gaussian pulse in a pre-formed quadratic plasma channel. Coupling plasma-guided dispersion compensation with relativistic self-focusing yields simultaneous spatial confinement and temporal shortening, suppressing beam filamentation and offering a scalable route to stable, ultrashort relativistic light sources.

The generation of ultrashort, high intensity laser pulses remain central to high-field physics science. While conventional Gaussian pulses frequently undergo catastrophic filamentation and energy degradation under relativistic conditions, Super-Gaussian profiles offer mitigation due to their steep edges and uniform intensity plateau. By balancing relativistic electron mass corrections with group velocity dispersion (GVD), demonstrate a stable spatiotemporal compression regime. This mechanism suppresses structural beam degradation, resulting a robust framework for next generation relativistic light sources.

Laser envelope evolution in the plasma is modeled using a modified nonlinear Schrödinger equation. This framework couples transverse diffraction and longitudinal group velocity dispersion (GVD) with a quadratic density and relativistic self-phase modulation. The plasma electron density is defined quadratically [1] as

$$n_e(r) = n_0\left(1+\frac{r^2}{L_n^2}\right) \qquad (1)$$

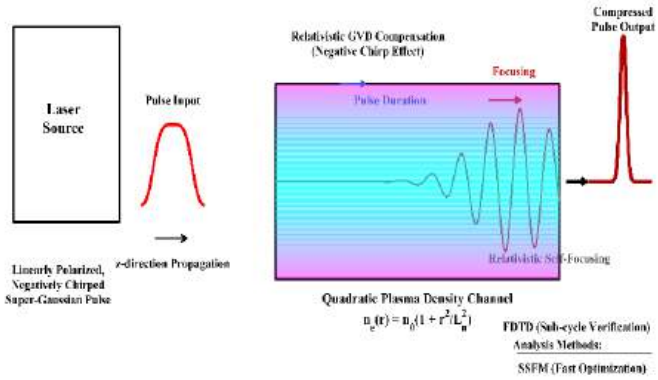


Figure 1: Schematic of relativistic spatiotemporal compression of a chirped Super-Gaussian in quadratic plasma density.

The initial profile of the Super-Gaussian pulse with an initial negative chirp parameter $\alpha_0 < 0$ at boundary condition $z = 0$

$$A(r,\xi,z=0) = A_0 \exp\left[-\frac{1}{2}\left(\frac{r}{r_0}\right)^{2N}\right]\exp\left[-\frac{\xi^2}{2\tau_0^2}(1+i\alpha_0)\right] \qquad (2)$$

The Super-Gaussian N > 1 [2] provides structural beam rigidity, implement a symmetric Split-Step Fourier Method (SSFM) for rapid parametric sweeps of the envelope evolution, then cross-validate it with a full-wave Finite-Difference Time Domain (FDTD) [3].

In conclusion, this framework demonstrates optimized spatiotemporal pulse contraction by coupling Super-Gaussian profile, this methodology provides an efficient design route for stable next generation light sources.

References:

[1] E. Esarey, C. B. Schroeder, and W. P. Leemans, "Physics of laser-driven plasma-based accelerators," *Reviews of Modern Physics*, 81(3), 1229 (2009).
[2] G. P. Agrawal, *Nonlinear Fiber Optics*, 5th ed. (Academic Press, San Diego, 2013).
[3] K. S. Yee, "Numerical solution of initial boundary value problems involving Maxwell's equations in isotropic media," *IEEE Transactions on Antennas and Propagation*, 14(3), 302-307 (1966).

Halide-Organic Spacer Interplay as energy funneling knob to tailor optical response in 2D Ruddlesden-Popper Perovskites

Mandeep[1], Balpratap Singh[2], SR Rondiya[2], N Mondal[1]

1. Department of Physics, Indian Institute of Technology Delhi, Hauz Khas, New Delhi 110016,

2. Department of Materials Engineering, Indian Institute of Science (IISc) Bangalore, Karnataka, 560012

phz258491@iitd.ac.in

2D hybrid organic–inorganic lead halide perovskites exhibit exceptional optoelectronic properties. Using the bithiophene-ethylammonium (BThEA$^+$) spacer, we reveal how halide substitution governs excited-state relaxation. Femtosecond transient absorption spectroscopy shows that bromide promotes efficient intersystem crossing and ultrafast triplet sensitization, generating long-lived molecular triplet and triplet excimer states.

To elucidate the energetic and dynamical interplay between the organic and inorganic components of two-dimensional (2D) hybrid perovskites, we performed steady-state and ultrafast optical spectroscopy on a series of halide-engineered systems by varying the inorganic halide composition from Br to I while maintaining an identical organic component. Steady-state optical measurements reveal strong quenching of the inorganic excitonic emission in the pure-Br system, unlike its pure-I counterpart, accompanied by broad emission bands characteristic of phosphorescence from the organic component. Notably, this phosphorescence is absent at room temperature for the isolated organic molecule, indicating that the perovskite framework activates an additional energy-transfer pathway.

To uncover the underlying mechanism, femtosecond transient absorption spectroscopy was performed following UV excitation. All compositions exhibit a pronounced excitonic bleach (XB) corresponding to the inorganic excitonic transition. While the pure-I system displays conventional exciton recombination on the hundreds-of-picoseconds timescale, the pure-Br system exhibits markedly accelerated XB recovery within tens of picoseconds, coinciding with strong quenching of excitonic photo-luminescence. These observations indicate efficient exciton transfer from the inorganic framework to the organic component, leading to rapid triplet sensitization. Furthermore, the pure-Br and mixed Br/I compositions, which exhibit pronounced phosphorescence, display an additional broadband photoinduced absorption (450–650 nm) that appears nearly instantaneously (Fig. 1). This feature closely matches the triplet excimer-like absorption observed in the isolated organic molecule, providing direct spectroscopic evidence for ultrafast triplet-state formation.

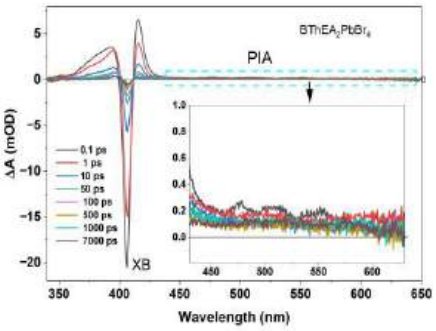


Fig.1 TA spectra of BThBr

Exciton-density-independent XB dynamics rule out nonlinear exciton–exciton annihilation, confirming that the fast recovery originates from triplet sensitization. Despite this rapid component, a long-lived nanosecond XB plateau persists, inconsistent with complete one-step Dexter energy transfer and instead suggesting a multistep mechanism involving a transient charge-transfer intermediate prior to triplet formation. Complementary control experiments further indicate that the heavy-atom effect of Br and enhanced spin–orbit coupling within the halide network promote ultrafast intersystem crossing, thereby increasing the triplet population and giving rise to the observed triplet excimer-like phosphorescence. These findings establish halide composition as a key parameter for controlling ultrafast energy transfer and triplet generation in 2D hybrid perovskites.

Refrences:

1. Tian et al. *J. Phys. Chem. Lett.* 2020, 11, 2247–2255.
2.Fujitsuka et al. *J. Chem. Soc., Faraday Trans.* 1998, 94, 3331–3337.

Harmonically Mode-Locked Bright-Dark-Bright Vector Soliton Complexes in an Erbium-Doped Fibre Laser

[1,#]Subrata Manna and [1]K. Nithyanandan

[1]Ultrafast Fiber Optics & Smart Photonic Technologies Laboratory, Department of Physics, Indian Institute of Technology Hyderabad, Kandi, Telangana 502285, India

[#]*id22resch11014@iith.ac.in*

We report the first observation of harmonic mode-locking of a three-component bright-dark-bright (BDB) vector soliton complex, sustained to the third harmonic of the 8.014 MHz fundamental in an anomalous-dispersion NPR erbium-doped fibre laser, the complex multiplying as an indivisible quasi-particle.

Mode-locked fibre lasers host localised states far beyond the conventional bright soliton, notably vector complexes in which dark and bright components are mutually trapped by cross-phase modulation (XPM), first predicted for the coupled nonlinear Schrödinger system [1]. Adding one component yields the BDB triplet — a central dark soliton clasping two bright satellites — reported only at the fundamental rate [2]. Harmonic mode-locking (HML) of hybrid states has been shown only for two-component pairs [3,4], and related composite states only at the fundamental rate in anomalous-dispersion NPR cavities, whether the BDB triplet survives harmonic multiplication is untested.

The laser is a 25 m all-fibre ring [Fig.1(a)], 3 m of erbium-doped fibre pumped at 976 nm, two polarisation controllers flanking a polarisation-dependent isolator, and 17 m of single-mode fibre. The net cavity dispersion of −0.17 ps² places operation deep in the anomalous regime and fixes the fundamental repetition rate at 8.014 MHz; mode-locking self-starts at 18 mW.

At a pump power of 240 mW, the laser exhibits a stable bright-dark (BD) soliton mode-locked state. By further increasing the pump power and adjusting the polarization controller (PC) orientations, we successfully achieved harmonic mode-locking of the BD soliton up to the sixth order, as depicted in Fig. 1(b). At 440 mw pump power the laser emits the BDB complex at the fundamental rate, each unit showing a central depression flanked by two bright components [Fig. 1(c)]. Raising the pump drives it into second- and third-order harmonic states, two and three complexes occupying one 124.8 ns round trip at exact sub-multiples of the fundamental period. Crucially, every unit retains the complete three-lobed structure: the complex multiplies as a rigid, indivisible entity rather than fragmenting. The spectra [Fig. 1(d)], centred near 1567 nm, remain invariant across all orders.

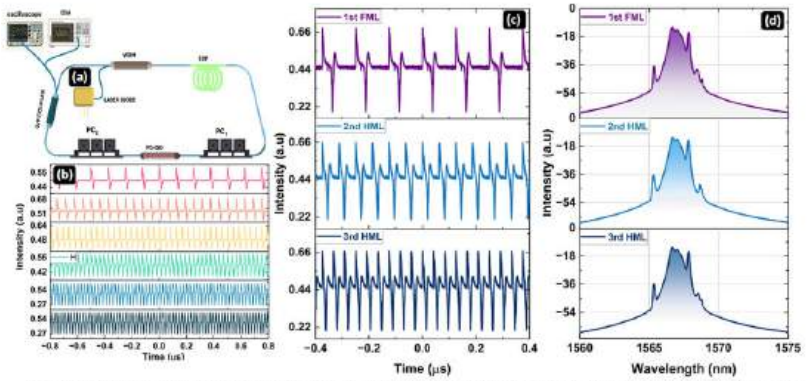


Fig. 1: (a) Laser Cavity. (b)HML of DB soliton up to 6th order.(c) BDB pulse trains at the fundamental (1st FML) and the 2nd and 3rd harmonic orders. (d) Corresponding optical spectra.

The generation of three-component vector solitons, such as bright-dark-bright (BDB) states, in passively mode-locked fiber lasers is governed by the interplay of linear cavity birefringence, cross-phase modulation (XPM), and saturable absorber (SA) nonlinearity. Inherent fiber birefringence naturally splits the propagating optical field into orthogonal polarization components. Subsequently, strong XPM nonlinearly couples these orthogonal axes, compensating for linear group-velocity mismatch and effectively locking the constituent pulses. This XPM-induced locking enables morphologically distinct pulses—such as an isolated bright pulse on one polarization axis and a dark-bright pair on the orthogonal axis—to co-propagate stably as a unified vector entity. Finally, XPM-mediated dynamic energy exchange mitigates intracavity gain competition within the active medium, preventing pulse splitting and preserving the temporal separation of the multicomponent soliton complex under varying pump intensities.

References:

[1] V.V. Afanasyev, Y.S. Kivshar, V.V. Konotop, V.N. Serkin, *Optics Letters* 14 (1989) 805.

[2] Q. Wu, Z. Wu, Y. Yao, X. Xu, L. Chen, Y. Zhao, K. Xu, *Optics Communications* 498 (2021) 127231.

[3] X. Li, S. Zhang, Y. Meng, Y. Hao, *Optics Express* 21 (2013) 8409.

[4] Z. Lv, H. Teng, S. Fang, H. Jia, L. Wang, J. Wang, Z. Wei, *Journal of Optics* 18 (2016) 065502.

Femtosecond Vortex Beam Nanostructuring of Plasmonic Silver Surface and Application in SERS-based Trace Detection

[1,2] Supriya Pradhan, [1]Niharika Pradhan, [1,2,*] Venugopal Rao Soma
[1]DRDO Industry Academia-Center of Excellence (DIA-CoE, formerly ACRHEM), University of Hyderabad, Telangana-500046, India
[2]School of Physics, University of Hyderabad, Telangana-500046, India

Corresponding author email: soma_venu@uohyd.ac.in

Surface nanostructuring of plasmonic materials using femtosecond vortex beam ablation (fs-VBA) has emerged as an exciting and rapidly growing research area. The unique wavefront and energy distribution of vortex beams enable intricate surface nanostructures. Such nanoscale architectures are highly desirable for sensing, catalysis and photonic applications [1].

In this study, we have used spiral phase plates (SPPs) to generate vortex beams (VBs) with topological charges 1 and 2 by interacting with the Gaussian beam (GB) output of a Ti: Sapphire laser system operating at a central wavelength of 800 nm (1 kHz, 50 fs). The laser-processed silver (Ag) surfaces exhibited well-defined laser-induced periodic surface structures (LIPSS) with low spatial frequencies [2]. A comparison with Ag surface nanostructure (NS) fabricated using conventional Gaussian beam revealed notable differences in the surface morphology and NS distribution. The resulting plasmonic Ag NSs were subsequently utilized as surface-enhanced Raman scattering (SERS) substrates for trace-level detection of hazardous compounds. We used a portable Raman system with a laser source of 785 nm to conduct the SERS studies and successfully detected trace levels of ammonium nitrate (AN) at 500 nM and picric acid (PA) at 100 nM [3]. These substrates demonstrated excellent SERS activity, providing strong signal enhancement and reliable trace-level detection and reusability. The findings highlight the potential of fs-VBA as an effective approach for tailoring plasmonic NSs with highly reproducible and efficient SERS performance.

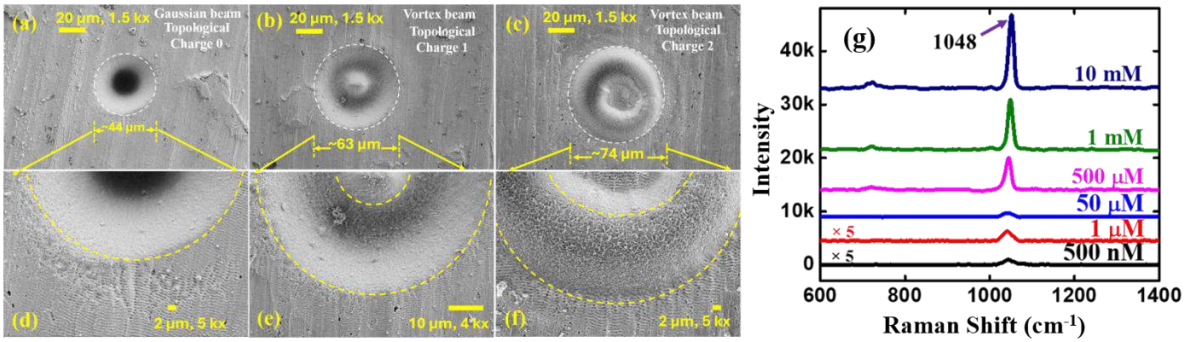


Fig. 1: (a-f) Single spot ablation by fs GB and VB. (g) SERS spectra of ammonium nitrate at different concentration.

References:

1. J.J.J. Nivas, S. He, A. Rubano, A. Vecchione, D. Paparo, L. Marrucci, R. Bruzzese, S. Amoruso, *Scientific Report* 5 (2015) 17929.
2. D. Banerjee, M. Akkanaboina, R. Kumar Kanaka, V.R. Soma, *Applied Surface Science* 616 (2023) 156561.
3. S. Pradhan, N. Pradhan, V.R. Soma, *Applied Surface Science* 719 (2026) 164980.

Intensity-dependent Nonlinear Optical Behavior of $MoSe_2$ Nanoparticles Prepared by Femtosecond Laser Ablation in Liquid

Tuhina Parvin Sultana,[1,2] Amrit Kumar,[1,2] and Venugopal Rao Soma[1.,2,#]
[1]School of Physics, University of Hyderabad, Telangana, India, 50046
[2]DRDO Industry Academia-Centre of Excellence (DIA-COE; formerly ACRHEM), University of Hyderabad, Telangana, India 500046

[#]E-mail of the corresponding author: ***soma_venu@uohyd.ac.in***

$MoSe_2$ nanoparticles were prepared by femtosecond laser ablation in liquid at different laser pulse energies. Detailed structural and optical studies revealed that the laser energy greatly influences the particle size, crystallinity and bandgap. The nanoparticles showed wavelength-dependent nonlinear optical properties, such as reverse saturable and saturable absorption, and positive nonlinear refraction, indicating their potential for tunable photonic and optical limiting applications.

Two-dimensional transition metal dichalcogenides (TMDCs), particularly $MoSe_2$, are promising candidates for advanced photonic and nonlinear optical applications owing to their strong light–matter interaction and tunable optical properties. In this work, we prepared $MoSe_2$ nanoparticles by femtosecond laser ablation in liquid at four different laser pulse energies (25, 50, 100, and 200 μJ) named as sample A, B, C and D. The structural and optical characterization revealed that the ablation energy has a great influence on the morphology, crystallinity and optical bandgap of the nanoparticles and the most optimized nanocrystalline nature is observed for sample B.

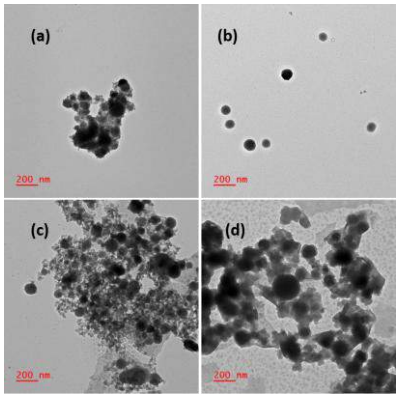


Fig. 1: TEM images of (a) Sample A, (b) Sample B (c) Sample C and (d) Sample D

The nonlinear optical properties were studied by femtosecond Z-scan technique at the excitation wavelengths of 400 nm, 800 nm and 1200 nm. All the samples exhibited reverse saturable absorption (RSA) at 800 nm. Samples A and B exhibited the RSA at 400 nm while samples C and D exhibited the saturable absorption (SA), which indicated the switch of optical behavior depending on the laser energy. All samples exhibited SA at lower excitation energy, while combined SA+RSA response was observed at higher excitation energy at 1200 nm. All the samples showed positive n_2 coefficients at all the wavelengths investigated.

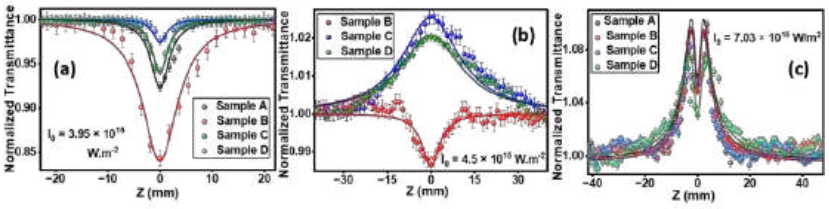


Fig. 2: Open-aperture Z-scan transmittance curves at (a) 800 nm, (b) 400 nm and (c) 1200 nm

These fluence and wavelength dependent nonlinear optical responses demonstrate the potential of fs-laser-synthesized $MoSe_2$ nanoparticles for tunable photonic and optical limiting applications.

All the authors would also like to acknowledge DIA-COE (formerly ACRHEM), University of Hyderabad for the experimental facilities. TPS thanks CSIR for providing JRF (# 241610224478) and VRS acknowledges ANRF for financial support through project (# ANRF/ARG2025/001189/PS dated 14.03.2026).

References:

[1] S. Pradhan, N. Pradhan, and V. R. Soma, Appl. Surf. Sci. 719 (2026) 164980
[2] A. Pandey, S.K. Saini, R.Kr. Singh, A. Kanjilal, T. Mohanty, Appl. Phys. A 132 (2026) 120.
[3] R. Rafi, K. Mani Rahulan, N.A. Little Flower, M. Abith, T.C. Sabari Girisun, A.S. Rajendran, ACS Appl. Nano Mater. 7 (2024) 11097–11106.

Synthesis of few layers WS_2 sheets via liquid assisted ultrafast laser ablation for SERS applications

[1,2]Aanchal Tyagi and [1,2,#]Venugopal Rao Soma

[1]School of Physics, University of Hyderabad, Telangana, India, 500046
[2] DRDO Industry Academia - Centre of Excellence (DIA-COE; formerly ACRHEM), University of Hyderabad, Telangana, India 500046

[#]E-mail of the corresponding author: ***soma_venu@uohyd.ac.in***

Conventional substrates such as Si wafer and plasmonic chips have been used for SERS based sensing. However, they show minimal reproducibility and longevity. Here, we propose WS_2/Ag-WS_2 synthesized using ultrafast laser ablation which gives better signal refinement, homogeneity and high enhancement factor.

Surfaced Enhanced Raman Spectroscopy (SERS) has been proven as an advanced technique in the detection of explosives, dyes, and pesticides. The significant factor in SERS based sensing measurement is directly dependent on the quality of the substrate being employed i.e., stability, reproducibility, longevity etc. In this work, we have used filter papers homogeneously decorated with 2D material nanoparticle colloid with Ag plasmonic which gives uniformity and better relative standard deviation of the Raman signal.

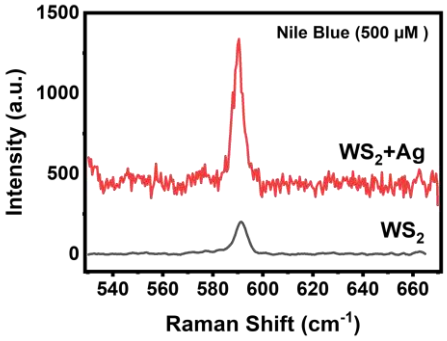


Fig. 1: *Comparison of SERS spectra of 500 μM Nile Blue with ablated WS_2/Ag-WS_2.*

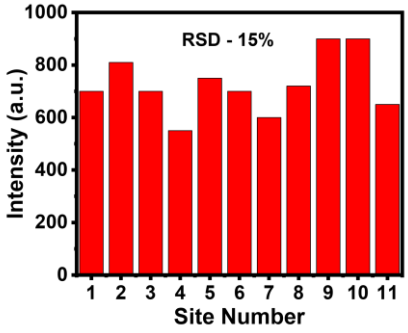


Fig. 2: *The Relative Standard Deviation (RSD) value for Nile Blue (500 μM) for Ag-WS_2 coated substrate.*

WS_2/Ag-WS_2 nanocolloids were synthesized using femtosecond laser via liquid assisted ablation technique. The Raman data of the bulk samples was recorded for the reference purpose. Further, we dip coated the filter papers with ablated WS_2 nanoparticles and Ag plasmonic components. Filter papers coated with WS_2 NPs and Ag NPs were used as the substrate to detect Nile Blue. We observed better signal refinement and high enhancement factor for our Ag-WS_2 (ablated) dip coated filter paper when compared with non-ablated WS_2 conjugates. The RSD value for Nile Blue (500 μM) is observed to be 19% for WS_2 and 15% for Ag-WS_2 substrate.

All the authors would also like to acknowledge DIA-COE (formerly ACRHEM), University of Hyderabad for the experimental facilities. VRS acknowledges the ANRF for financial support through project (# ANRF/ARG2025/001189/PS dated 14.03.2026).

References:

[1] N.R. Jana, *An Overall Account of Surface Enhanced Raman Spectroscopy*, CRC Press, Boca Raton (2025).
[2] Y. Yuan, P. Zuo, F. Li, G. Wang, K. Zhang, H. Tian, W.H. Rao, L. Lv, Y. Huo, R. Xu, S. Liu, *Advanced Engineering Materials* 27 (2025) 2501441.
[3] M.L. Mekonnen, W.N. Su, C.H. Chen, B.J. Hwang, *Analytical Methods* 9 (2017) 6823–6829.

Generation of few-micron thick liquid sheet using single jet impingement on knife-edge

Pooja chugh[1] , Kamal P. Singh [1]

[1]*Indian Institute of Science Education and Research, Mohali*
*Corresponding author: kpsingh@iisermohali.ac.in

We demonstrate few-micron liquid sheet generation via a single laminar water jet impinging on a knife-edge. This simple method provides a promising route for ultra-thin liquid target generation in ultrafast optical applications.

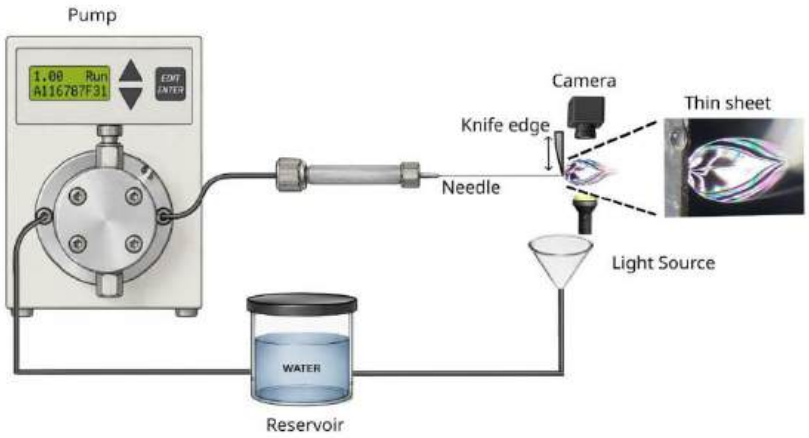


Fig.1 Schematic diagram of few-micron thin liquid sheet generation using a needle connected with HPLC pump and delivering a water jet which is impinging on a knife edge as a result leading to the formation of thin leaf-shaped water sheet.

Sub-micron to few-micron thick liquid targets are emerging as a good target to study the charge dynamics in matter using ultrafast lasers and find many applications in other fields as well. We demonstrate few-micron liquid sheet generated via a single laminar water jet impinging on a knife-edge. Apart from introducing a novel approach for generating micro thick water sheets using a knife edge geometry in conjunction with a single water jet we perform Quantitative analysis of the dependence of sheet width, length, area and other optimisable parameters , by calibrated imaging. Velocity estimation confirms consistent jet dynamics. White-light interference fringes were also obtained which indicate thickness variations, suggesting few-micron to sub-micron regions within the sheet. This simple method provides a promising route for ultrathin target generation in ultrafast optical applications. While existing techniques predominantly rely on impinging jet configurations, gas-dynamic acceleration, or converging microfluidic channels, the proposed knife edge approach offers potential advantages in terms of simplicity, cost-effectiveness, and controllability. Through extensive literature analysis, we identify the key parameters governing thin liquid sheet formation and highlight the uniqueness of the knife edge methodology. This work establishes the theoretical foundation and experimental considerations for implementing this novel water sheet generation technique.

References

[1] Taylor, Sir Geoffrey 1959a Proc. Roy. Soc. A, 253, 296.

[2] Akira WATANABE, Hiroshi SAITO Vol 71, number 5 Optics Comm.

[3] Christopher J. Crissman, et al DOI : 10.1039/d1lc00757b

Asymmetric frequency-mode coupling for discrete spectral diffraction

Nisha, Chanakya Kolli, Sushma Kumari, Varnam Sherawat, Priya Srivastava, Kushagra Chikara, Awanish Pandey

Optics and Photonics Center, IIT-Delhi - New-Delhi-110016,India

opz258496@iitd.ac.in

We demonstrate directional spectral discrete diffraction in waveguides using permittivity and conductivity modulation. The disparate time derivatives of these channels produce asymmetric frequency-mode coupling. By tuning the RF drive phase offset to $\pm\frac{\pi}{2}$ we achieve deterministic steering of the generated sideband energy distribution.

Starting from fundamental electromagnetic principles, we investigate a general framework for routing optical energy within discrete frequency modes. By utilizing a waveguide structure driven by periodic radio-frequency (RF) signals, energy is dynamically shifted into discrete spectral sidebands. The wave propagation under time-varying material properties can be directly derived from Maxwell's equations as follows:

$$\nabla \times \nabla \times \mathbf{E} = -\mu_0 \epsilon_s \frac{\partial^2 \mathbf{E}}{\partial t^2} - \mu_0 \frac{\partial^2}{\partial t^2} \left[\delta\epsilon(\mathbf{r}, t)\mathbf{E}\right] - \mu_0 \frac{\partial}{\partial t} \left[\sigma(\mathbf{r}, t)\mathbf{E}\right] \tag{1}$$

where ϵ_s is the static permittivity. Within one composite modulator section of RF phase φ, the two drives occupy distinct spatial profiles $\hat{u}_p(\mathbf{r})$ and $\hat{u}_a(\mathbf{r})$ (separate electrodes) and are offset by the phase ψ:

$$\delta\epsilon(\mathbf{r}, t) = \delta\epsilon\, \hat{u}_p(\mathbf{r}) \cos(\Omega t + \varphi) \tag{2}$$

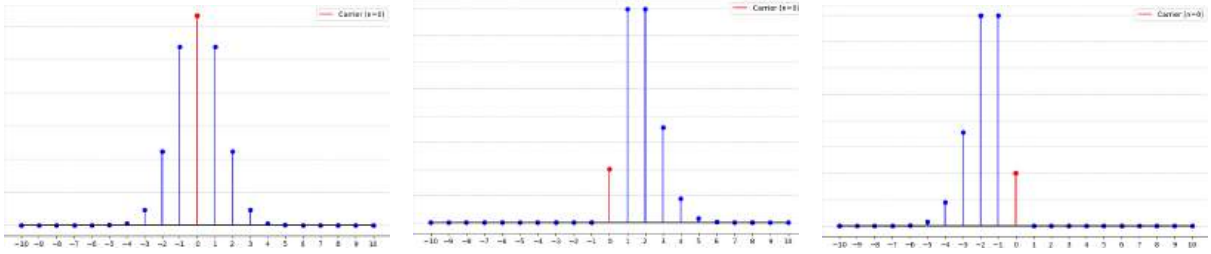
$$\sigma(\mathbf{r}, t) = \sigma_0\, \hat{u}_a(\mathbf{r}) + \sigma_1\, \hat{u}_a(\mathbf{r}) \cos(\Omega t + \varphi + \psi) \tag{3}$$

In Eq. 1, the permittivity term undergoes a double time derivative (∂_t^2), yielding a real factor scaled by $-\omega_n^2$, whereas the conduction term undergoes a single time derivative (∂_t), yielding an imaginary factor proportional to $+i\omega_n$. This intrinsic mathematical disparity naturally introduces a quadrature relation between the phase and loss channels. The spatial evolution of the co-propagating sideband amplitudes along the propagation direction x can be modeled by the following coupled-mode equations:

$$i\frac{da_n}{dx} = g_n^{(+)} e^{i\phi} e^{iKx} a_{n-1} + g_n^{(-)} e^{-i\phi} e^{-iKx} a_{n+1} - i\alpha_0 a_n, \tag{4}$$

$$g_n^{(\pm)} = \frac{\mu_0 \omega_n}{4\beta_n} \left[\omega_n \delta\epsilon \Theta_p - i\sigma_1 \Theta_a e^{\pm i\psi_i}\right], \quad \alpha_0 = \frac{\mu_0 \sigma_0 \omega_n}{2\beta_n} \Theta_{0a}. \tag{5}$$

These expressions define the spatial transport of the sideband amplitudes a_n, where the coupling between adjacent modes is governed by the asymmetric hopping coefficients $g_n^{(\pm)}$ outlined in Eq. 5. To evaluate the spectral transport behavior, we map the optical intensity across the generated frequency sidebands. By tailoring the relative RF drive phase offset ψ to 0°, 90°, and -90°, a clear directional steering of the spectral energy distribution becomes manifest.



(a) $\psi = 0°$ *(b)* $\psi = 90°$ *(c)* $\psi = -90°$

Figure 1: Shift in the energy distribution of generated sidebands.

References:

[1] Q. Lin, J. Wang, S. Fan, Optics Letters 44 (2019) 2240.

[2] L. Yuan, Q. Lin, M. Xiao, S. Fan, *Optica* 5 (2018) 1396.

[3] C.R. Doerr, N.K. Fontaine, L.L. Buhl, *Optics Letters* 36 (2011) 2013.

Primary Vibration Calibration Using Laser Interferometer

[,#]Shailesh Mohine, Naveen Garg and Chitra Gautam
CSIR-National Physical Laboratory, New Delhi, India-110 012

[#]*smohine.nplindia@csir.res.in*

Abstract- This paper illustrates the framework and measurement uncertainty for primary vibration calibration based on sine approximation method as per ISO 16063-11. CSIR-NPL has upgraded the primary vibration calibration facility that measures the accelerometer complex sensitivity and phase measurement using laser interferometer and optical encoder. The paper is also highlighting multipoint laser positioning and digital signal processing technique to enhance the measurement accuracy.

This paper reports the methodology and measurement uncertainty in primary vibration of vibration sensors in the frequency range of 0.1 Hz to 20 kHz using the sine approximation method as per ISO 16063 Part 11 [1]. CSIR-NPL has recently upgraded its facility with the replacement of a high-frequency shaker (PCB396C11), measurement data acquisition at a higher sampling rate, and digital bandpass filtering. The study illustrates the measurement uncertainty in the determination of accelerometer complex sensitivity, including phase determination using a laser interferometer and optical encoder in the frequency range of 0.5 Hz to 20 Hz. A multipoint laser positioning approach is followed to circumvent non-rectilinear and rocking modes, etc., if any. The quadrature signals are online monitored and acquired through the National Instruments NI PCI6251 card, and both displacement and voltage signals are processed via the latest version of 9155C-575 software. Future efforts are in progress to upgrade the low-frequency shaker and replace the laser interferometer with a new one. Also, efforts are targeted for the inclusion of vibration CMCs in the Key Comparison Database of BIPM Paris.

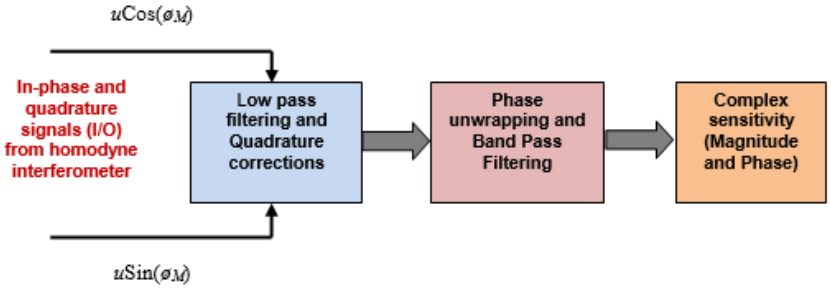


Fig. 1: Methodology to determine the complex sensitivity of accelerometer

The methodology to determine the complex sensitivity of accelerometer is shown below in Fig.1 [2-3]. The homodyne interferometric signals: in-phase (I) and quadrature (Q) generated are analyzed to form a Lissajous figure which is a perfect circle. The lack of quadrature is corrected by least square ellipse fitting technique stipulated by Heydemann, and digital band pass filtering is implemented to enhance the signal-to-noise ratio and circumvent any gain fluctuations and distortion, noise and hum in the measurements. The analogue quadrature signals corrected by Heydemann approach are demodulated using arc-tangent function with appropriate phase unwrapping and band pass filtering in order to obtain the accelerometer complex sensitivity (magnitude and phase).

References:

[1] ISO 16063-11:1999 Methods for the Calibration of Vibration and Shock Transducers, Primary vibration calibration by laser interferometry.

[2] Garg, Naveen, and M. Singh. "Measurement uncertainty in primary calibration of accelerometer complex sensitivity at low frequencies." MAPAN 36.4 (2021): 821-831.

[3] Veldman, C. S. "A novel implementation of an ISO standard method for primary vibration calibration by laser interferometry." *Metrologia* 40.2 (2003): 1-8.

Characterization of Off-Axis Aspheric Mirrors of Three Mirror Anastigmatic (TMA) Telescope

B.S. Bhargava Ram#, Mandeep Kiran, Rakesh Lakshman, B. Vishweshwar Rao and R. Venkateswaran

Laboratory for Electro Optics Systems, 1st Cross, 1st Stage, Peenya Industrial Estate, Bengaluru, India-560058

#email id: bhargav2011iitd@gmail.com

The off-axis TMA telescope is a promising configuration for attaining high-resolution imaging over a wide-field of view. Its configuration nature demands tight fabrication tolerances on individual mirrors. Here, we discuss the characterization difficulties, various(CGH-Null-test, Profilometry)methods used for assessing the off-axis aspheric mirror (Primary, Tertiary)parameters with the required accuracies.

The off-axis Three Mirror Anastigmatic (TMA) telescope system is an advanced optical configuration, opted for space exploration and remote sensing applications, offering high-resolution unobscured imaging with wide-field of view (FoV) requirements [1]. The off-axis TMA telescope system is prone to be sensitive for misalignments (axial separations, de-centers and tilts) due to lack of rotational symmetry. The off-axis nature of the system configuration demands tighter tolerances on individual mirror parameters. Controlling and measuring the mirror parameters to the required accuracy with high precision is very challenging during fabrication. Here we discuss the characterization difficulties and various methods for assessing the two off-axis aspheric (Primary and Tertiary) mirrors of an off-axis TMA telescope. The required mirror parameters are provided in Table 1.

Table 1: Mirror Parameters

Parameter	Primary Mirror	Results	Tertiary Mirror	Results
Shape & Size	Circular; Dia 170.2mm; Off-axis concave hyperboloid	170.1mm	Rectangular; 570mm x 144mm; Off-axis concave Ellipsoid	569.9mm X143.9mm
RoC (R) in mm	1422.23±1	1422.389	692.522±0.5	692.272
Conic K	-2.0038±0.001	-2.0035	0.2325±0.0001	0.23256
OAD in mm	96.345	96.439	84.007±0.1	84.016
SFE @ λ=632.8nm	λ/40= 15.82nm	λ/41.46= 15.26 nm	λ/40= 15.82nm	λ/41.40= 15.66 nm

Due to lack of rotational symmetry, testing and characterization of off-axis aspheric mirrors becomes challenging task in optical metrology [2]. The six degrees of freedom (DoF) alignment requirements of the unit under test (UUT) makes it complex; any misalignment in 6 DoFs triggers a false assessment of the true surface. For example, lateral misalignment (de-center) introduces a false astigmatism and coma. Traditionally, Null-Lens technique [3] is used for testing the aspheric mirrors. However, it requires mechanical aligning aids for placing the off-axis mirror precisely at the designated off-axis distance (OAD). A diffractive optical element, called, Computer Generated Hologram (CGH) is another technique [3] where the wavefront from the Null pattern can be made matching the surface profile of the UUT. Along with the Null pattern, the CGH possesses alignment and fiducial patterns assisting the alignment procedure for locking the UUT at the designated location. Here, we use a multi-region CGH to mitigate the possible false assessments arising due to the misalignments.

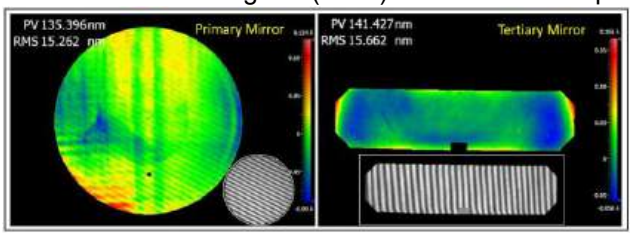


Figure 1. Phase profile and the corresponding interferograms of the Primary (Left) and Tertiary (Right) Mirrors.

Results: An independent interferometric test configurations were established to check the surface figure error (SFE) of Primary and Tertiary mirrors using the corresponding multi-region CGHs. The inter-separation metrology data is used for calculating the RoC and Conic (k) constants. An in-house program is developed to compute the OAD from the tactile profilometry (Sagitta) data [3]. The corresponding results are shown in Table 1 and Fig 1 conforming to the requirements. The individual mirrors are ready for integrated system level performance check in the telescope configuration.

References:

[1] B. V. Rao, K. V. Sriram, C. S. Narayanamurthy, *Optik* 311 (2024) 178952.

[2] B.S. B Ram, B. V. Rao, B. Raha, R. Lakshman, R. Venkateswaran, K.V. Sriram, (*Chap. 19) Advances in Biophotonics, Nanofabrication, Optical Metology and Nonlinear and Ultrafast Photonics. Photonics 2023. Lecture Notes in Electrical Engineering, Springer* 1242 (2025)161-170.

[3] Malacara D, *Optical Shop Testing*, Wiley-Interscience (2007).

Effect of Nonlinearity in branched flow of light in quasi-periodic photonic lattices

[1]Snehita Ghosh, [1]Snehashis Sadhukhan, [1]Dushyant Kumar[#] and [2]Somnath Ghosh[*]
[1] *Department of Physics, Indian Institute of Technology Jodhpur, Rajasthan-342030, India*
[2] *Department of Physics, Ecole Centrale School of Engineering, Mahindra University, Hyderabad-500043, India*

[*]somiit@rediffmail.com, [#]dushyantkumar@iitj.ac.in

Abstract: Waves propagating through a weakly disordered medium split into multiple channels of varying intensities, giving rise to the branched flow of light. These branches can induce extreme nonlinear events during propagation. Here, we construct a quasiperiodic nonlinear photonic lattice that exhibits self-focusing and self-defocusing of the propagating branches.

The phenomenon of branched flow (BF) was first observed in a two-dimensional electron gas [1], later in microwave resonators [2], and more recently with laser light propagating through thin soap membranes [3]. In photonic lattices, transverse disorder is known to induce Anderson localization, while the addition of longitudinal disorder produces BF. Previous studies have primarily focused on BF in the linear regime. However, the intense filaments formed during branched flow can initiate extreme nonlinear phenomena by concentrating optical energy into localized regions. Motivated by this, we investigate the influence of Kerr nonlinearity on the dynamics of BF in photonic lattices.

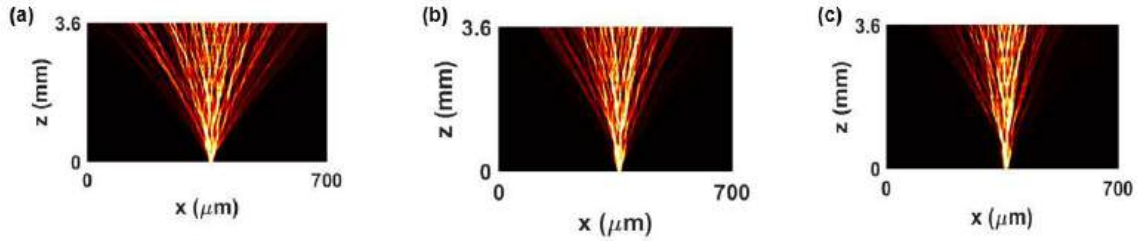


Fig.1 Normalized intensity distribution of the branching channels in a QP lattice: (a) an enhanced branching effect due to the gradual decrease in the refractive index of the lattice structure(self-defocusing), (b) branching phenomena in the linear regime when there is no change in the refractive index of the lattice while propagation, (c) a spatially confined branch phenomenon when refractive index increases with the propagation of light(self-focusing).

Here, we introduce a Kerr-type nonlinearity characterized by the Kerr coefficient n_2, which determines the strength of the nonlinear response, and an operating parameter σ, which specifies the nature of the nonlinearity. The propagation of light in the nonlinear QP lattice is governed by Eq. (1), where A denotes the slowly varying envelope of the electric field, $\Delta n(x,z)$ represents the refractive-index variation and k_0 is the free-space wave number

$$i\left(\frac{\partial A}{\partial z}\right)+\left(\frac{1}{2k}\right)\left(\frac{\partial^2 A}{\partial x^2}\right)+k_0\Delta n(x,z)A+\sigma\left(\frac{k}{n_0}\right)n_2|A|^2A=0 \quad (1)$$

The refractive index of the lattice varies quasi-periodically along the longitudinal direction, yet the transverse profile of the lattice is kept perfectly periodic The lattice material is chosen such that it exhibits an intrinsic Kerr nonlinear response at the operating wavelength. For $\sigma=-1$, the branches spread over a larger region, characteristic of a self-defocusing nonlinear response [Fig.1(a)]. For $\sigma=0$, the system reproduces the branched-flow dynamics of the linear regime [Fig.1(b)]. In contrast, for $\sigma=+1$, the branches become increasingly localized, exhibiting self-focusing [Fig.1(c)]. These observations indicate that the introduction of self-focusing nonlinearity leads to highly intense, localized branches with enhanced energy density, whereas self-defocusing nonlinearity promotes a more pronounced branching phenomenon by increasing the number of propagation channels and facilitating a more uniform distribution of energy throughout the lattice.

References:
1. S. E. J. Shaw, “Propagation in smooth random potentials,” Ph.D. thesis, Harvard University, Cambridge, MA (2002).
2. R. Hohmann, U. Kuhl, H.-J. Stöckmann, L. Kaplan, and E. J. Heller, “Freak waves in the linear regime: A microwave study,” *Phys. Rev. Lett.* 104, 093901 (2010).
3. A. Patsyk, U. Sivan, M. Segev, and M. Bandres, “Observation of branched flow of light,” *Nature* **583**, 60–65 (2020).
Acknowledgements: Snehita acknowledges the Ministry of Education (MoE), Government of India, for financial support.

Fiber Bragg gratings in Multi-mode ZBLAN fiber for environmental temperature sensing

[1]Priyanshu Singh, [2,#] Anuj K. Sharma
[1]Physics Division, Department of Applied Sciences, National Institute of Technology Delhi, India, 110036

[#]priyanshusingh@nitdelhi.ac.in

Abstract: *This work presents the design and simulation of multi-mode fiber Bragg gratings (MMFBG) in ZBLAN fluoride fiber for environmental temperature sensing applications, using Ansys Lumerical. The simulated results of the proposed sensor show a sensitivity of 12 pm/°C, high linearity of 99.6% and a fine limit of detection (LOD) of 0.002 °C.*

Temperature sensing is crucial in environmental monitoring and device health monitoring. Most of the temperature sensors are prone to electromagnetic interference (EMI) and are energy inefficient, failing to perform effectively in applications that require high-precision sensing. FBG offers an EMI-immune and efficient alternative for such applications [1]. FBG is characterized by the Bragg wavelength given in Equation 1, where ∧ is the periodicity of the grating and n_{eff} is the effective refractive index of the FBG. The sensing principle involves measurement of temperature-induced Bragg wavelength shift.

$$\lambda_B = 2n_{eff}\,\Lambda \tag{1}$$

The use of Silica-based FBGs results in a narrow operation window and high non-radiative loss due to

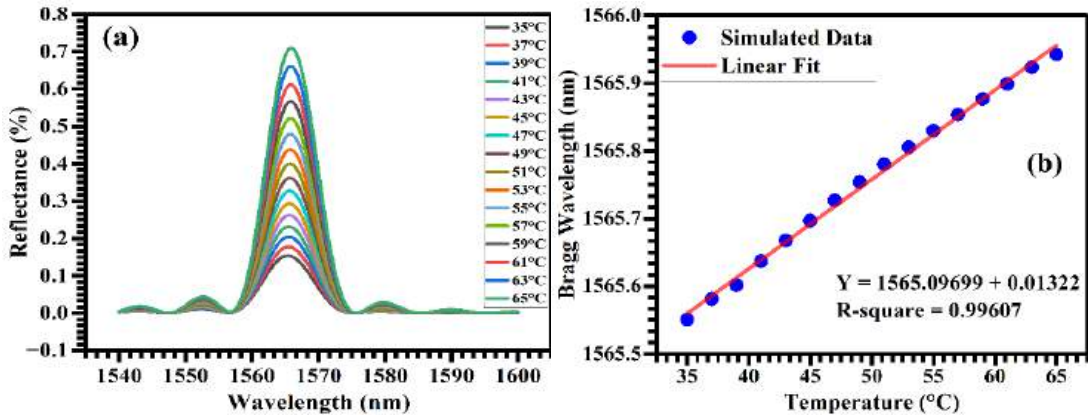


Fig. 1 (a) Spectral Response of the MMFBG under temperature variation from 35-65 °C, and (b) Linearity of the simulated MMFBG structure

the high phonon energy of silica (~ 1100 cm^{-1}), while ZBLAN offers a larger transparency window and has much lower phonon energy (~500 cm^{-1}) than silica in the near-IR region of the EM spectrum, which makes it more efficient to use for sensing applications [2,3]. Also, the use of MM fiber makes the components cost-effective, can be coupled effectively and offer high power transfer.

The study shows that the proposed sensor exhibits a red shift in the Bragg wavelength with increasing temperature in the range 35-65 °C, as shown in Fig. 1(a). The MMFBG exhibits thermal sensitivity of 12 pm/°C, high linearity of 99.6%, as shown in Fig. 1(b), and a fine LOD of 0.002 °C, which are better than the current state-of-the-art MMFBG temperature sensors. The reflection peak of the spectrum also shows a linear increase with an increase in temperature. The proposed MMFBG sensor will further help in the development of fluoride fiber-based sensing systems.

References:

[1] **R. Rohan, · K Venkadeshwaran, · Prakash Ranjan, 53 (2024) 282–293.**

[2] **A.K. Sharma, J. Gupta, IEEE Sens. J. 19 (2019) 8775–8780.**

[3] **R. Liu, Z. Luo, L. Wu, J. Ran, Y. Wang, C. Lv, S. Qin, Z. Bai, Y. Wang, S. Liu, C. Liao, Y. Wang, Journal of Lightwave Technology 43 (2025) 4429–4434.**

Tunable Bandgap-Assisted Nonadiabatic Dynamics in an Optomechanical Array

Divya Mishra and Parvendra Kumar
Optics and Photonics Centre, Indian Institute of Technology Delhi, New Delhi, India
Emails: opz228593@opc.iitd.ac.in & parvendra@opc.iitd.ac.in

Controllable bandgaps in optomechanical systems are key to realizing tunable non-reciprocal devices. We theoretically show that the synthetic magnetic flux induced by the driving-laser phase dynamically tunes the bandgap between hybridized eigenmodes, thereby controlling their nonadiabatic dynamics and mode transitions.

Radiation pressure force-induced optomechanical (OM) coupling between optical and mechanical modes has been extensively utilized for entangling these modes, inducing non-reciprocal effects in the propagation of photons and phonons, and investigating non-adiabatic dynamics in many-body systems [1]. This type of coupling can be achieved in various systems, including microwave-optomechanical circuits, microdisk resonators, and photonic crystal cavities [2, 3]. This work focuses on a one-dimensional array of coupled optomechanical resonators, theoretically examining how laser phase modulation influences the dynamics of eigenmodes, the band structure, and photon-phonon conversion [4]. In this system, the optomechanical sites support localized optical and mechanical modes. A continuous wave laser drives the optical modes with a site-dependent phase. We demonstrate that phase modulation allows for control over the net excitation transfer between the two eigenmodes during nonadiabatic evolution.

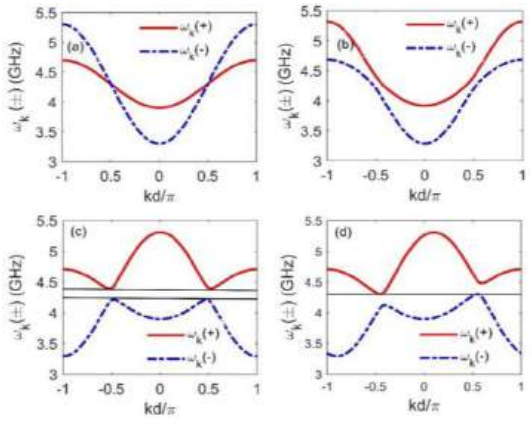


Fig. 1 The Band structure of the hybrid eigen modes with enhanced optomechanical coupling variation (a)$g = 0, \theta = 0$,(b) $g = 0.1GHz, \theta = 0$ with phase variation (c), $g = 0.1GHz, \theta = \pi$ (d) $g = 0.1GHz, \theta = 0.8\pi$.

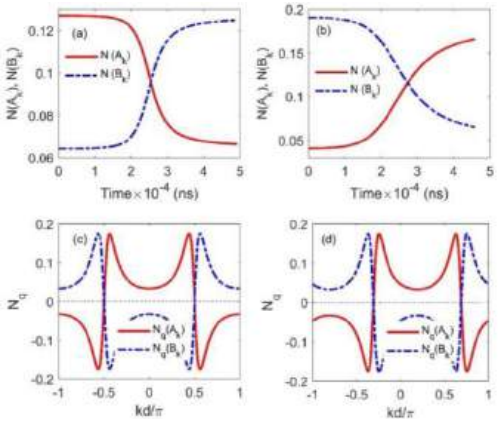


Fig. 2 Dynamics (a, b) for $\theta = 0, \theta = \pi$ and net excitations (c, d) for $\theta = \pi, \theta = 0.8\pi$ of the eigen modes due to sudden change of optomechanical coupling from positive to negative: $g\ to - g$.

First, we computed the linearized Hamiltonian of the coupled optomechanical array and analytically calculated the eigenmodes, which are hybridized due to the optomechanical coupling. We also employed the Magnus expansion method to investigate the dynamics of the eigenmodes in response to sudden changes in the optomechanical coupling. The dynamics of the eigenmodes, illustrated in Fig. 1, indicate that the bandgap of these modes can be controlled by adjusting the phase of the driving laser. Figure 2 presents the population dynamics and net excitations of the eigenmodes. Notably, we can observe the phase-dependent net excitations of the eigenmodes, especially at the minimum bandgap, during nonadiabatic evolution.

References

[1] M. Aspelmeyer, T. J. Kippenberg, and F. Marquardt, Rev. Mod. Phys. **86,** 1391 (2014).
[2] C. Yang, X. Wei, J. Sheng and H. Wu, Nat. Comm. **11**, 4656 (2020).
[3] H. Hu and E. Zhao, Phys. Rev. Lett. 124, 160402 (2020).
[4] D. Mishra and P. Kumar, J. Opt. Soc. Am. B 42, 1934–1946 (2025).

Measurement of displacement using shadow-based Opto-Mechanical Analysis

Prashant Agnihotri[1,2], Nayanshree Mishra[2,3], Lucky [1,2], Aman[1,2],Vikas[2,4], Kamal Tewari[2,4], Surya Kumar Gautam[2,4], and Rajesh Kumar[2,4]

[1]GB Pant DSEU Campus- 1, Okhla, Delhi.

[2] CSIR-National Physical Laboratory (CSIR-NPL), New Delhi, Delhi 110012, India

[3] Delhi Skill and Entrepreneurship University, Okhla, Campus-2.

[4] Academy of Scientific and Innovative Research (AcSIR), Ghaziabad, 201002, India

Corresponding E-mail: (kamalt.nplindia@csir.res.in)

Abstract: This work presents a non-contact displacement monitoring technique based on geometric shadow projection. The relationship between applied displacement and shadow distortion was investigated for a stiffened aluminum plate. A known displacement was applied to the Al disc using positioning stages, and changes in the disc's shadow diameter were recorded with a lens and a high-resolution CMOS camera.

Introduction: Conventional contact sensors may alter structural behavior and are unsuitable for inaccessible locations. This work uses shadow projection to convert induced displacement into measurable optical changes.

Working Principle: A point light source positioned in the line of sight of the specimen was used to cast a shadow on the screen. As known vertical deflections ($\boldsymbol{\Delta h}$) were applied via micro positioning stages, the changes in the shadow boundary were captured using CMOS camera with suitable magnification via lens. Given the distance from the light source ($\boldsymbol{h1}$) and the projection plane ($\boldsymbol{h2}$), the magnification of the shadow is defined by the ratio of these distances.

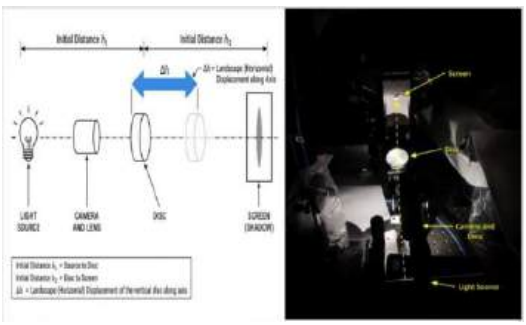


Fig: - Setup and Schematic diagram

Equations:

$$\boldsymbol{\Delta h} = \frac{\boldsymbol{F}}{\boldsymbol{k}} \quad (1)$$

$$\boldsymbol{D(shadow)} = \boldsymbol{D(disc)} \times \frac{\boldsymbol{h1+h2-\Delta h}}{\boldsymbol{h1+\Delta h}} \quad (2)$$

Results and Analysis: The shadow edges moved proportionally to the induced displacement given using the micro positioning stage, demonstrating that a suitable transducer can be fabricated for metrological applications using this principle.

Conclusion: This study validates the feasibility of using shadow geometry as a proxy for metrological applications for non-contact sensing applications. This provides a robust basis for a low-cost, non-contact monitoring system for varied applications.

References: 1. A Shadow-Based Nano Scale Precision Force Sensor Hongyu Lu, Yelong Zheng, Jile Jiang, Wei Yin, Yonggang Meng, and Yu Tian *IEEE SENSORS JOURNAL, VOL. 19, NO. 6,* MARCH 15, 2019
2. A disturbance suppression micro-Newton force sensor based on shadow method Yang [a], Meirong Zhao [a], Dantong Li [a], Moran Tao [a], Chunyuan Zhu [a], Yelong Zheng [a], Yu Tian [b] *Tianjin University, Tianjin, 300072, China*

A Portable Low-Cost Smartphone-Based Microspectrophotometer for Integrated Microscopic Imaging and Spectroscopy

[1, #] Biprav Chetry,[1] Pratik Dhar and [1] Pabitra Nath
[1] Applied Photonics and Nanophotonics Laboratory, Department of Physics, Tezpur University, Sonitpur, Assam-784028, India.
[#] *Corresponding Author: biprav.chetry@gmail.com*

A portable, low-cost smartphone-based microspectrophotometer is demonstrated for integrated microscopic imaging and spectroscopy. Designed system utilizes rear and front smartphone cameras combined with optical components, achieving 2.19 µm lateral resolution and 0.43 nm/pixel spectral dispersion, with development cost of ~$290. System performance is validated using different samples.

Microspectrophotometers (MSPs) combine microscopy and spectrophotometry within a single instrument to provide morphological and spectroscopic information from the same microscopic sample region [1]. However, conventional laboratory MSPs require sophisticated optical and optomechanical assemblies, making them expensive, bulky, and inaccessible in resource-constrained settings. Although smartphone-based microscopy and spectroscopy have been demonstrated independently [2-3], fully standalone smartphone-based MSPs remain limited [4]. Herein, a compact, low-cost smartphone-based MSP is presented, employing the smartphone's rear and front cameras within a shared optical architecture to integrate microscopy and spectroscopy in a single device. Constructed from off-the-shelf optical components, the standalone system enables imaging and spectral acquisition without external microscopic or spectrometric modules.

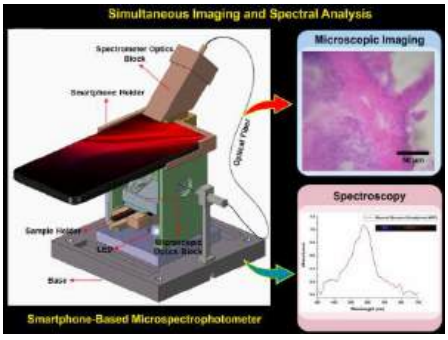


Fig. 1: Graphical abstract for the MSP

The developed system consists of microscopic imaging and spectrophotometric units enclosed within a 3D-printed housing. The microscopic unit employs a compact optical imaging configuration using a ball lens and a plano-convex lens as the magnifying optics to relay the image onto the smartphone's rear camera, while the spectrophotometric unit operates in a transmission optical configuration. A 50:50 R/T beam splitter positioned in the shared optical path divides the light transmitted through the sample between the imaging and spectroscopic channels, enabling both units to acquire information from approximately the same sample region. In the spectroscopic channel, the transmitted light is coupled into an optical fiber, focused by a cylindrical lens, dispersed by a 1200 grooves/mm transmission diffraction grating, and recorded by the smartphone's front camera. The standalone system measures ~120 × 130 × 170 mm, weighs ~383 g, and costs ~US$290.

The microscopic unit achieved an optical magnification of ~175× with an experimental lateral resolution of 2.19 µm by resolving Group 7, Element 6 of a 1951 USAF resolution test target and provided a usable field of view of ~410 µm. Representative biological specimens, including 5 µm microbeads, Leishman-stained blood smear, *Rhizopus*, and *Paramecium*, were successfully imaged, demonstrating the system's microscopic imaging capability. The spectrophotometric unit achieved a linear pixel-to-wavelength calibration (R^2 = 0.99), a spectral dispersion of 0.43 nm/pixel, an average wavelength deviation of ~3.9 nm, and an average spectral resolution of ~6.5 nm. Spectral analysis of Rhodamine B showed good agreement with a laboratory-grade UV-Vis spectrophotometer, confirming reliable wavelength-resolved measurements. Furthermore, the developed MSP enabled integrated microscopic imaging and spectrophotometric analysis from the same region of biological specimens. Comparative evaluation with a laboratory-grade MSP demonstrated good agreement in both imaging and spectral measurements, validating the proposed system as a compact, low-cost alternative for integrated microspectrophotometric investigations.

References:

[1] P. Martin, *Microscopy Today* 21.1 (2013): 22-26.
[2] B. Roy, A. Maikap, S. Das, S. Chakraborty, *Biosensors and Bioelectronics* 276 (2025): 117259.
[3] D. Rabha, A. Sarmah, P. Nath, *Journal of microscopy* 276.1 (2019): 13-20.
[4] G. Chen, H.H. Chai, J.J. Fu, L. Yu, C. Fang, *Analytical Methods* 12.33 (2020): 4166-4171.

Portable Electrochemiluminescence Sensor with Smartphone-Controlled Imaging for Antioxidant Capacity Determination

[1,#]Chunuranjan Dutta and [1]Pabitra Nath
[1]Applied Photonics and Nanophotonics Laboratory, Department of Physics, Tezpur University, Sonitpur, Assam, India-784028
[#]*email id of the corresponding author: chunuranjandutta1@gmail.com*

We report a smartphone-based electrochemiluminescence platform using pencil graphite electrodes for total antioxidant capacity determination. Synchronization of voltage triggering and image acquisition improved reproducibility, yielding an RSD of 2.47%. The platform achieved an LOD of 56.7 μM for Trolox as a representative antioxidant and correlated strongly with conventional DPPH assay.

Total antioxidant capacity (TAC) is an important analytical parameter for nutritional assessment, screening of natural sources of bioactive compounds, evaluation of food quality and pharmaceutical research [1]. Conventional methods for TAC determination often involve bulky, time-consuming and expensive instrumentation that limits their application to laboratory settings. Electrochemiluminescence (ECL) offers an attractive alternative due to its low background interference, high sensitivity and relatively simple instrumentation [2]. The optical nature of ECL signal makes it especially suitable for miniaturized CMOS camera-based detection. However, due to the transient nature of ECL signals, the commonly used portable ECL systems suffer from compromised reproducibility when voltage trigger and image acquisition are not synchronized.

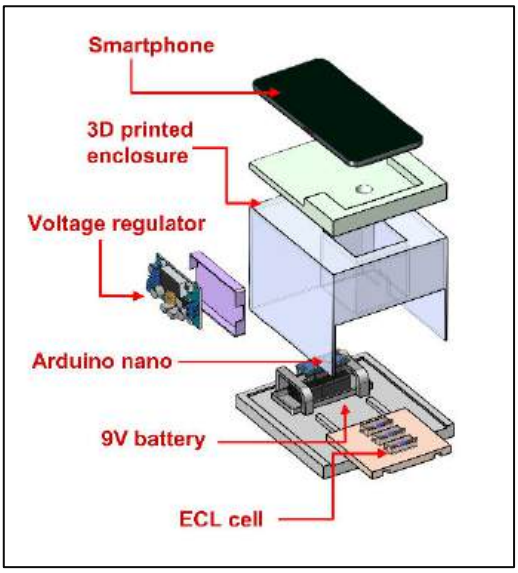


Fig. 1: Exploded view of the designed ECL sensor for TAC determination

In this work, a low-cost smartphone-based ECL platform has been developed for TAC determination using Trolox as a representative antioxidant standard. The sensing system employed a pencil graphite electrode (PGE) inserted into a custom 3D-printed reaction cell. TAC determination is based on the radical-scavenging property of antioxidants. Electrochemical oxidation of luminol in the presence of H_2O_2 produces reactive intermediates that generate blue ECL emission with a maxima at ~425 nm. Antioxidants such as Trolox scavenge these reactive intermediates and consequently decrease the ECL intensity [3]. Therefore, the extent of ECL quenching can be correlated with antioxidant capacity determination.

The ECL reaction was initiated by applying a voltage through a simple electronic control circuit connected to the smartphone through its USB-OTG port. The electronic system consisted of an Arduino Nano, a voltage regulator, a MOSFET switching circuit and a 9 V battery power supply. An Android application regulates synchronized voltage application with automated camera acquisition with the help of this peripheral circuit. The captured images are subsequently transferred to PC and analyzed using ImageJ. The analytical response was obtained from the mean gray values of the selected region of interest of the captured images. The voltage-synchronized acquisition mode produced a relative standard deviation of blank signal 2.47% for ten replicate measurements. Under optimized conditions, Trolox progressively quenched the luminol ECL emission and showed a linear analytical response over the range of 0-300 μM Trolox, with a limit of detection of 56.7 μM. The ECL-derived TEAC values showed good agreement with those obtained using the conventional DPPH radical-scavenging assay. These results demonstrate the feasibility of quantitative and portable ECL analysis using a smartphone camera without conventional detection and control instrumentation, such as photomultiplier tubes, CCD detectors, or electrochemical workstations.

References:

[1] J. Flieger, W. Flieger, J. Baj, R. Maciejewski, *Materials* 14 (2021) 4135.
[2] C. Ma, Y. Cao, X. Gou, J. J. Zhu, *Analytical Chemistry* 92 (2019) 431–454.
[3] N. Nagatani, Y. Inoue, A. Araki, H. Ushijima, G. Hattori, Y. Sakurai, *Electrochimica Acta* 222 (2016) 580–586

Interferometric Force Measurement System Based on Fringe Displacement Tracking

[1, 2, #]Surya Kumar Gautam, [1, 2]Kuldeep Kumar, [1,2]Vikas, [1,2]Kamal Tewari, [1,2]Mukesh Jewariya, [1,2]Rajesh Kumar
[1]CSIR-National Physical Laboratory (CSIR-NPL), New Delhi, Delhi 110012, India.
[2]Academy of Scientific and Innovative Research (AcSIR), Ghaziabad, 201002, India.
[#]*Corresponding author: suryagautam89@gmail.com*

Simple interferometric force measurement system based on fringe displacement tracking is presented. Applied force induces displacement of a spring mounted mirror, causing measurable interference fringe shifts. Experimental results demonstrate a clear correlation between fringe position and applied force, highlighting the potential of the proposed technique for precise optical force sensing.

Most conventional load cells and force transfer standards operate on the principle of displacement measurement, wherein the elastic deformation induced by an applied force is converted into an electrical, optical, capacitive, or strain dependent signal. Displacement is the fundamental physical quantity from which force is indirectly, yet accurately, determined in the majority of mechanical and electromechanical force measurement systems.

The experimental setup is shown in Fig. 1. A plane mirror (M1) is mounted on a spring loaded assembly, allowing controlled vertical displacement under an applied force and returning to its initial position upon force removal. A horizontally aligned laser beam is directed downward by a beam splitter (BS), which generates the object and reference beams. The transmitted beam is reflected by a stationary mirror (M2) to form the reference beam, while the reflected beam is directed to the movable mirror (M1) to generate the object beam. The two beams are recombined at the beam splitter and interfere at a camera positioned above the BS, where the interference fringes are recorded.

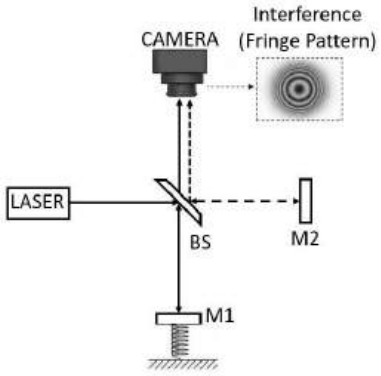


Figure 1



Figure 2

Interference patterns were recorded for applied forces ranging from 0 to 3.5 N in increments of 0.5 N using calibrated weights. The applied force displaced the spring mounted mirror, introducing an optical path difference between the object and reference beams, which caused the interference fringes to shift progressively toward the center. The x-coordinate of a selected fringe was tracked for each force level and exhibited a monotonic increase with the applied force. Fig. 2 illustrates the relationship between the fringe position and the applied force, demonstrating the feasibility of the proposed interferometric method for force measurement.

References:

[1] P. Hariharan, Optical Interferometry, 2nd ed., Academic Press, Amsterdam (2003).
[2] D. Malacara (Ed.), Optical Shop Testing, 3rd ed., John Wiley & Sons, Hoboken, NJ (2007).
[3] J.W. Goodman, Introduction to Fourier Optics, 4th ed., W.H. Freeman, New York (2017).
[4] H.J. Tiziani, Optics and Lasers in Engineering 9 (1988) 115–130.
[5] International Organization for Standardization, ISO 376:2011 Metallic Materials Calibration of Force Proving Instruments Used for the Verification of Uniaxial Testing Machines, ISO, Geneva (2011).

Investigation on Post-Processing of Diamond-Turned Chalcogenide Glass using Chemical Mechanical Polishing

[1]Md Ataul Haque, [2]Md Talha Ateeque, [3]Kundan Kumar Prasad and [4#,]Gufran S Khan
[1] Centre for Sensors, INstrumentation and Cyber-physical Systems Engineering (SeNSE)
Indian Institute of Technology Delhi
Hauz Khas, New Delhi

[#]*gufranskhan@sense.iitd.ac.in*

Chalcogenide glass ($Ge_{23}Sb_{14}Se_{63}$) is a key material for infrared imaging systems. However, its poor machinability limits achieving lower surface roughness with reduced subsurface damage. Moreover, periodic tool marks formed during machining further degrade optical performance. To address this, a chemical mechanical polishing (CMP) process has been developed to polish the diamond-turned finished surface. The process effectively removes residual tool marks and enhances overall surface quality.

The finished chalcogenide glass substrate using single-point diamond turning (SPDT) typically retains periodic tool marks and mid-spatial-frequency errors. These increase stray light effects and reduce image quality in infrared optical systems. To overcome these, a chemical mechanical polishing (CMP) process has been developed for the post-processing of diamond-turned chalcogenide glass.

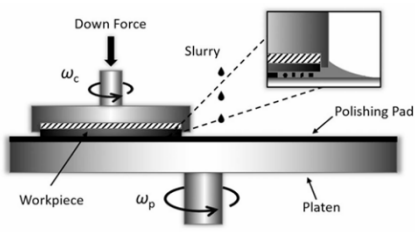


Fig 1: Schematic of CMP process

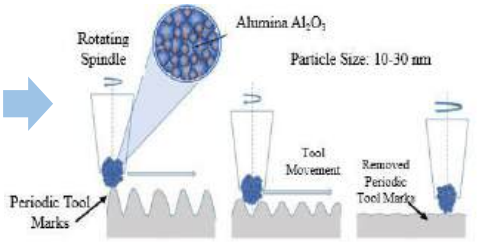


Fig 2: Material removal mechanism

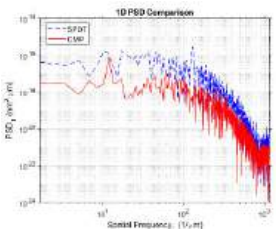


Fig 3: PSD analysis

The experiments have been performed on an HM 300 (make OptoTech) numerical control (NC) based CMP polishing. Fig 1 depicts the experimental setup, which consists of a polishing pad, a slurry delivery system, and the chalcogenide glass substrate mounted on a fixture. Fig 2 shows the polishing mechanism used for material removal, including the relative motion between the pad, the workpiece, and the slurry feed arrangement onto the contact zone. During polishing, the workpiece is held in continuous contact with the pad under a controlled applied pressure, while the slurry of varying pH (acidic, neutral, and alkaline) is continuously supplied to sustain the chemical-mechanical interaction at the interface. Based on the slurry composition and process requirements, the polishing process parameters, including pad rotational speed, applied pressure, and polishing duration, are analyzed. The diamond-turned chalcogenide glass surface has been polished with the selected slurry formulation, process parameters, and the CMP setup, resulting in effective removal of residual diamond turning feed marks. The present study shows that the CMP process effectively minimizes periodic tool marks generated during machining. The effectiveness of this process is validated by the PSD analysis shown in Fig. 3, which characterizes surface errors across different spatial frequencies. Specifically, the periodic tool marks from SPDT appear as distinct peaks at specific frequencies, whereas their suppression after CMP confirms effective removal of these features and improved surface quality across the frequency spectrum.

$$PSD_1 = \frac{\Delta}{m} \left| \sum_{k=0}^{M-1} (z(k) \exp(-i2\pi f_m k\Delta) \right|^2,$$

where $z(k)$ is the surface contour function of the measured surface with points sampled at intervals of $\Delta; L = M.\Delta$ is the sampling length, m is the spatial frequency index, and $f_m = {}^{m}/_{L}$ is the spatial frequency.

References:

[1] Tang, B., Yang, Y., Fan, Y., Zhang, *Journal of Materials Science & Technology*, *26*(6) (2010), 558-563.
[2] Owen, J. D., et al., *CIRP annals,* 64.1 (2015): 113-116.
[3] Xue, Dongbai, Yiqin Ji, and Peng Wang, *Procedia CIRP,* 71 (2018): 172-176.

Estimation of spectral mismatch factor for broadband UV radiometers

[1,#]V.K. Jaiswal, [2]Shibu Saha, [3]Parag Sharma
[1,2,3]Academy of Scientific and Innovative Research (AcSIR), Ghaziabad 201002, India
[1,2,3]Optical Radiation Metrology, CSIR-National Physical Laboratory, New Delhi 110012, India

[#]*email id: jaiswalvk.nplindia@csir.res.in*

Broadband UV radiometers, economic and small sized as compared to spectroradiometers, often ends up giving erroneous results, due to non-ideal responsivity, when measuring light sources other than the one spectral profile they are calibrated with. To reduce this error, it requires spectral mismatch correction factor to correct the estimated result.

Apart from other parameters, a detector is mainly characterized with its sensitivity spectral range and the relative spectral responsivity profile which is generally matched with the action spectrum of a photobiological or photochemical effect under study.

The integrated responsivity $\mathfrak{R}$ of a broadband radiometer in spectral range (λ_1, λ_2) can be expressed as $\mathfrak{R} = \frac{\int_{\lambda_1}^{\lambda_2} R(\lambda).S(\lambda)d\lambda}{\int_{\lambda_1}^{\lambda_2} S(\lambda)d\lambda}$; R(λ): General radiometric spectral responsivity of radiometer, S(λ) is spectral irradiance of the light source on the detector surface. Though an ideal or flat R(λ) results in a constant integrated responsivity $\mathfrak{R}$ however, the integrated or effective responsivity $\mathfrak{R}$, of a radiometer therefore, critically depends on the choice of spectral profile of the source. Hence the information of source spectral profile S(λ) makes it essential for correct measurement with a broadband radiometer having non-flat spectral responsivity [1-4]. Hence a broadband radiometer, calibrated against a spectral profile of standard light source, when deployed to measure test lamp having different spectral profile often results in erroneous measurements despite being calibrated and traceable.

Study on numerical estimation of spectral mismatch correction factor (SMCF) has been presented for different spectral profile UV lamps, available in labs and used for UV irradiation and measurements.

In the study four lamps, namely, FEL (tungsten), Deuterium, Mercury (Hg), and a LED lamp were deployed and all lamps were theoretically measured at constant distance using a typical broadband UVC radiometer (calibrated against the standard Mercury lamp) with typical spectral responsivity profile as shown in Fig.1. The Spectral Mismatch Correction Factor (SMCF) was then evaluated for each lamp as stated in Ref [2] and are listed in the Table 1.

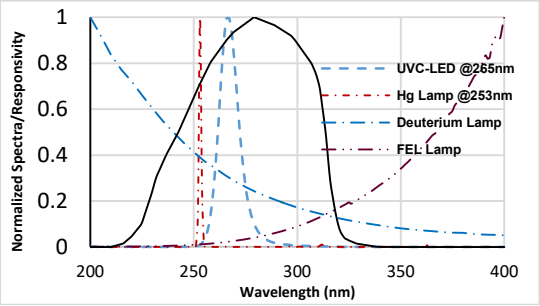


Fig. 1: *Typical spectral responsivity of radiometer*

Test lamp spectrum	Spectral Mismatch Correction Factor (SMCF)
FEL lamp	12.10
Deuterium lamp	1.77
Mercury (Hg) lamp (253 nm)	1
UVC LED lamp (265 nm)	0.77

Table 1: *Estimated Spectral mismatch factors*

The study specifically highlights the inevitability of SMCF for different lamps, even the radiometer used is pre-calibrated.

Acknowledgement: Authors acknowledge support and continuous encouragement received from the Director, CSIR-NPL to carry out this study.

References:

[1] CIE 202: 2011: Spectral Responsivity Measurement of Detectors, Radiometers and Photometers
[2] CIE 220: 2016: Characterization and Calibration Methods of UV Radiometers
[3] A. Gugg-Helminger, CIE 220: 2016- Characterization and calibration method of UV radiometers. IUVA News, 19 (2), 18–23 (2017)
[4] P. Sharma, V. K. Jaiswal, S. Saha and D. K. Aswal, Metrological Traceability and Crucial Detector Characteristics for UVC Metrology in UVGI Applications, MĀPAN-J. Metrol. Soc. India, 37(2), 237–249 (2022).Cambridge (1989).

Optoelectronic arrangement and beat frequency measurement of the optical pressure standard

[1,2]Elizabeth Jeessa James, [1,2]Adarsh Mishra, [1,2]Megha Singh, [1,2]Ashok Kumar

[1] Academy of Scientific and Innovative Research (AcSIR), Ghaziabad, 201002, India

[2] Pressure, Vacuum & Ultrasonic Metrology, Physico-Mechanical Division, CSIR-National Physical Laboratory, New Delhi, 110012, India.

Email: ashok553.nplindia@csir.res.in

Global trends in quantum metrology are transforming SI pressure standards. CSIR-NPL India has been working towards creating an Optical Pressure Standard (OPS) using optical interferometry. Stabilized lasers locked to a dual Fabry-Perot cavity measure beat frequency to determine gas refractivity, enabling quantum-traceable pressure determination through fundamental physical constants.

The OPS setup at CSIR-NPL is based on a 150 mm long dual Fabry-Perot (FP) cavity arrangement. This FP cavity is made up of ULE glass for minimizing any physical changes, and it is mounted within a copper box and aluminum outer case to isolate it from temperature and vibrational effects. We utilize Pound-Drever-Hall (PDH) locking to stabilize lasers to the cavities, with the resulting beat frequency as well as temperature with respect to time is recorded by an integrated data logging system. The fundamental theory relies on the precise relationship where gas refractivity shifts the beat frequency; this shift allows for the determination of pressure through quantum-traceable physical constants, effectively bypassing the need for traditional mechanical standards

To evaluate the environmental stability of the OPS, the beat frequency and cavity temperature were continuously monitored over time. The recorded data reveal a clear inverse correlation between temperature and beat frequency, indicating that even small thermal fluctuations produce measurable frequency shifts. As shown in Fig. 1, the beat frequency exhibits a systematic inverse variation with temperature, confirming the thermal sensitivity of the dual Fabry-Perot cavity. Following compensation for the temperature-induced beat frequency shift, the system exhibits stable frequency response consistent with readings obtained from calibrated pressure devices.

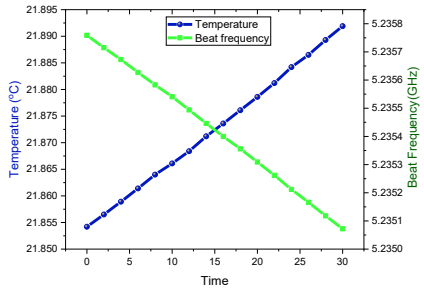


Figure 1. Variation of beat frequency and cavity temperature with time during stability measurements of the optical pressure standard, illustrating the thermal dependence of the dual Fabry-Perot cavity.

This characterization enables determination of the cavity's thermal sensitivity, provides insight into long-term frequency stability, which may affect the accurate calculation of pressure and forms the basis for implementing temperature compensation to improve pressure measurement accuracy. With the implementation of an active temperature-control system, the OPS is expected to realize a primary pressure standard covering the 1 Pa–150 kPa range with high accuracy and full SI traceability. So, establishment of the OPS at CSIR-NPL represents a transformative step for Indian pressure metrology and demonstrates India's commitment to the global quantum-SI transition. Authors would thank, CSIR, UGC and Dr. Venu Gopal Achanta Director NPL for their encouragement and support.

References

1. Das, M., Ghosh, S.K., Kumar, K. *et al.* Laser-based optical interferometer manometer design for primary pressure standard in India. *J Opt* 53, 1957–1963 (2024). https://doi.org/10.1007/s12596-023-01347-y

2. James, E.J., Rab, S., Singh, M. *et al.* Pressure-induced deformation in ultra-low expansion dual fabry–perot cavities. *J Opt* (2026). https://doi.org/10.1007/s12596-026-03135-w

Theoretical Analysis of Pressure Dependent Beat-Frequency Sensitivity in Optical Refractometry: Helium and Nitrogen

[1,2]Adarsh Mishra, [1,2]Elizabeth Jeessa James and [1,2,#]Ashok Kumar
[1] Academy of Scientific and Innovative Research (AcSIR), Ghaziabad, 201002, India
[2] Pressure, Vacuum & Ultrasonic Metrology, Physico-Mechanical Division, CSIR-National Physical Laboratory, New Delhi, 110012, India.
[#] Corresponding Author Email: ashok553.nplindia@csir.res.in

Pressure-dependent beat-frequency sensitivity in a Fabry–Pérot optical refractometer is theoretically studied for helium and nitrogen using virial-based refractivity models at 633 nm and 1550 nm. Refractivity, beat-frequency shift, and sensitivity are evaluated from 1 mPa to 100 kPa to support the design of optical pressure standards using suitable gases wavelengths.

The realization of the pascal based on optical refractometry has emerged as a promising alternative to mercury manometers by relating gas pressure directly to refractive index through fundamental physical constants. In a dual FP cavity refractometer, pressure is determined from the beat frequency between lasers locked to a reference cavity maintained under vacuum and a measurement cavity filled with gas[1,4]. Since the measurement sensitivity determines the achievable pressure resolution, a quantitative understanding of its pressure dependence is essential for the design and optimization of next-generation optical pressure standards.

In this work, helium (He) and Nitrogen (N_2) are studied at **633 nm** and **1550 nm** using the virial expansion of the equation of state and the Lorentz-Lorenz equation. The pressure-dependent beat frequency is expressed as [4]

$$\frac{\Delta f}{\nu} = [c_1 - (d_m + d_r)]P + (c_2 - c_1 d_m)P^2 + (c_3 - c_2 d_m)P^3 \quad (1)$$

and the sensitivity is defined as

$$S(P) = \frac{d(\Delta f)}{dP} \quad (2)$$

The required refractivity and density virial coefficients were taken from published literature, and all the calculations were carried out using custom C++ programs.

Table 1. Calculated low pressure beat-frequency sensitivity

Gas (Wavelength)	**Sensitivity (MHz/Pa)**
He (633 nm)	0.149
He (1550 nm)	0.0605
N_2 (633 nm)	1.256
N_2 (1550 nm)	0.507

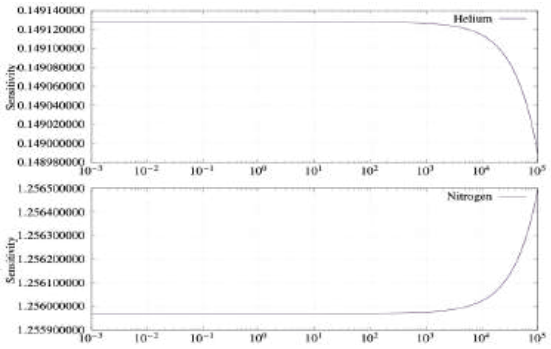


Figure 2. Pressure-dependent sensitivity for helium and nitrogen.

The calculated sensitivity for nitrogen at 633 nm agrees with published optical pressure standards [2,3].

The results show that nitrogen provides higher sensitivity, while helium offers a more linear response over a wide pressure range. The model can be used to estimate the performance of optical pressure standards before experiments and to help select suitable gases and operating wavelength for future optical pressure metrology.

References:

[1] M. Egan, J. A. Stone, J. R. Hendricks, *Nature Physics*, **13**, 807–811 (2017).
[2] Y. Yang, T. Rubin, J. Sun, *Vacuum*, **194**, 110598 (2021).
[3] H. W. Song, J. H. Kim, S. Y. Woo, *Journal of the Korean Physical Society*, **78**, 124–129 (2021).
[4] P. F. Egan, J. A. Stone, J. H. Hendricks, *Optics Letters* **40**, 3945 (2015).

Polarization-multiplexed dual-frequency finite-difference discriminator for frequency locking

[1,2,#]Nandini Mondal,[1,2]Surya N Sahoo and [1,2]Ashok K Mohapatra
[1]National Institute of Science Education and Research, Bhubaneswar, India
[2]Homi Bhabha National Institute,Training School Complex, Anushaktinagar, Mumbai, India
[#]*nandini.mondal@niser.ac.in*

We introduce and experimentally demonstrate a polarization-multiplexed dual-frequency finite-difference (PMDF) discriminator for frequency stabilization. The technique employs two frequency-offset, orthogonally polarized probe beams that sample cavity transmission, while a balanced detection scheme generates a dispersion-like error signal without phase modulation. The discriminator exhibits tunable slope, enabling stable top-of-fringe locking.

Laser frequency stabilization is essential for precision spectroscopy, optical metrology, quantum technologies, and quantum communication. Among the available techniques, Pound–Drever–Hall (PDH) locking provides excellent sensitivity but requires phase modulation and is susceptible to residual amplitude modulation [1,2]. Modulation-free locking schemes offer simpler implementations, but many require careful alignment or additional experimental constraints, limiting their general applicability. Here, we demonstrate a polarization-multiplexed dual-frequency finite-difference (PMDF) discriminator that generates a dispersion-like error signal using only intensity measurements, eliminating the need for phase modulation [3].

The PMDF technique employs two frequency-offset, orthogonally polarized probe beams derived from a single laser source. After reflection from the optical cavity, the two beams are separated using polarization optics and detected with a balanced photodetector. Their intensity difference generates a dispersion-like error signal whose zero crossing correspon-ds to the cavity resonance. The discriminator slope can be continuously tuned by varying the probe frequency separation and remains applicable to both symmetric and asymmetric cavity resonances. Closed-loop operation is demonstrated by stabilizing both the laser frequency to the cavity resonance and, independently, the cavity resonance to the laser frequency using conventional PID controllers. A direct comparison with PDH locking under identical experimental conditions shows comparable locking performance, while shot-noise analysis indicates the same shot-noise-limited sensitivity scaling as PDH.

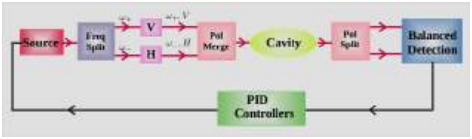


Fig. 1: Conceptual block diagram for implementation of PMDF locking schme

Overall, the finite-difference discriminator provides a conceptually simple alternative for frequency stabilization in systems where optical phase modulation, cavity birefringence, or higher order spatial modes are undesirable. This method avoids some of the practical limitations of established frequency-locking techniques without any significant increase in experimental complexity, and thereby makes it attractive for many optics and atomic physics experimental setup. A detailed description of the theoretical model and experimental validation is presented in [3].

NM acknowledges the Chankya Doctoral Fellowship (DST), SNS acknowledges the Inspire Faculty Fellowship Grant (DST). All authors acknowledge the financial support from DAE through the project No – RIN4001.

References:

[1] R. W. P. Drever, J. L. Hall, F. V. Kowalski, J. Hough, G. M. Ford, A. J. Munley & H. Ward, *Appl. Phys. B* 31, 97–105 (1983).

[2] Edward A. Whittaker, Manfred Gehrtz, and Gary C. Bjorklund, *J. Opt. Soc. Am. B* 2, 1320-1326 (1985)

[3] Nandini Mondal, Surya N. Sahoo, and Ashok K. Mohapatra, *Opt. Lett.* 51, 3941-3944 (2026)

An Indigenously Developed Photodiode Preamplifier Array For Reliable And Sustainable Operation Of A Laser- Cooled Cesium Primary Frequency Standard

Ojaswi[1], Sidhant Sahoo[1], Harupjit Singh[1,2], Anjali Bisht[1,2], Poonam Arora*[1,2]
CSIR- National Physical Laboratory, New Delhi-110012
The Academy of Scientific and Innovative Research, Ghaziabad- 201002
arorap.nplindia@csir.res.in

A two-stage photodiode preamplifier circuit developed for the optical setup of a cesium fountain primary frequency standard is presented. It continuously monitors laser beam power at the magneto-optical trap and at fibre-coupled points along the beam path, enabling real-time fault detection needed to sustain the long, uninterrupted fountain runs required for a valid TAI contribution.

A caesium fountain primary frequency standard relies on a fairly elaborate laser system, and keeping it running reliably matters as much as the underlying physics. In our setup, a small fraction of the laser beams going to the magneto-optical trap (MOT) are picked off and monitored continuously by a SI photodiodes. Similarly photodiodes are also placed at other points along the optical path to catch power fluctuations or fibre-coupling faults early. This matters because a contribution to TAI requires the fountain to run continuously for at least ten days, and an unnoticed lapse in laser performance during that window means the run has to be discarded. Therefore, a preamplifier circuit was developed that converts photodiode small output current into usable monitoring signal i.e. voltage' for continuous monitoring of laser power.

As shown in Fig. 1, the circuit with two amplification stages was designed. The photodiode itself is reverse-biased i.e. photoconductive mode. The first stage has a transimpedance amplifier built around a precision op-amp (IC1, OP07CR). Here, feedback resistor R1 (1 MΩ) does the real work, turning the photodiode's small current into a proportional voltage, and the OP07CR's low input-referred noise keeps this conversion clean even for weak signals.

Therefore, the signal passes through a simple low-pass filter (R2, C1) that knocks down high frequency noise before reaching the second stage was another OP07CR (IC2), was wired as a non-inverting amplifier. Resistors R3, R4 and R5 set the gain here, boosting the signal to a level that downstream data-acquisition or timing electronics could read/record effectively. The final output is brought out at connector JP2, labelled detector out.

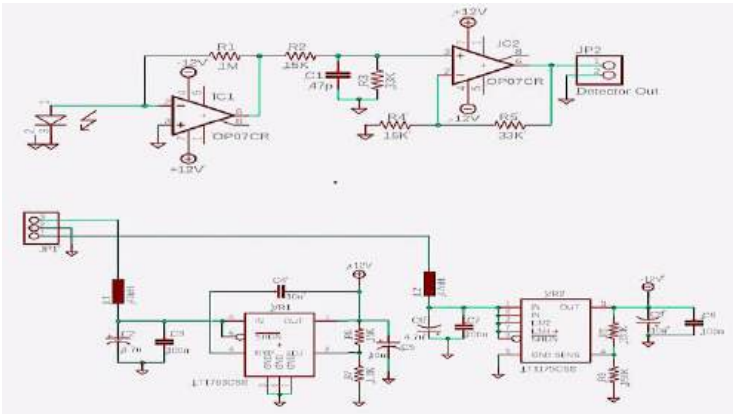


Fig. 1: Photodiode preamplifier circuit diagram

Further, for getting clean power signal the circuit includes its own regulation stage: an LT1763CS8 for the positive rail and an LT1175CS8 IC for the negative one. Both low-noise linear regulators were backed up by filter capacitors and inductors networks. Together these turn the input supply into well-regulated ±12 V rails, keeping power-line noise from creeping into the sensitive preamplifier stages.

This preamplifier is now a routine part of the caesium fountain's optical setup, monitoring laser beam powers at the MOT and other points along the beam path, supporting fibre coupling, and flagging faults early enough to protect the long continuous runs on which a TAI contribution depends. A closer look at its bandwidth and noise performance is the next step.

References:

[1] Analog Devices, OP07 Precision Operational Amplifier, Data Sheet.
[2] UDT Sensors (OSI Optoelectronics), PIN-13DI Silicon PIN Photodiode Datasheet.
[3] Analog Devices, LT1763 / LT1175 Low Noise Micro power Regulators, Data Sheets.

A Systematic Comparison of Retroreflective Background-Oriented Schlieren and Retroreflective Shadowgraph Imaging

[#]Diganta Rabha and Manish Kumar
Centre for Sensors, Instrumentation and Cyber-Physical System Engineering (SeNSE)
Indian Institute of Technology Delhi, Hauz Khas, New Delhi-110016

[#]*diganta.iitd@gmail.com*

We systematically compare retroreflective background-oriented schlieren (RBOS) and retroreflective shadowgraph (RS) techniques using a co-aligned experimental configuration. Results demonstrate that RS consistently resolves finer spatial structures, whereas RBOS achieves higher sensitivity. This trade-off provides evidence-based guidance for selecting the optimal technique based on specific application requirements.

Background-Oriented Schlieren (BOS) and shadowgraph imaging are the two predominant large-scale optical visualization techniques for seeing flow in transparent media [1, 2]. Among these, shadowgraph imaging is simpler and requires fewer resources. Nonetheless, BOS is popular for its quantitative flow measurement capabilities. Recent reports have compared both techniques and highlighted shadowgraph imaging as superior to the BOS for flow visualization [3]. However, one needs to be careful when comparing the two approaches directly. The experiments must be performed under identical conditions with no room for hidden biases. The comparison should further clearly distinguish between qualitative and quantitative metrics.

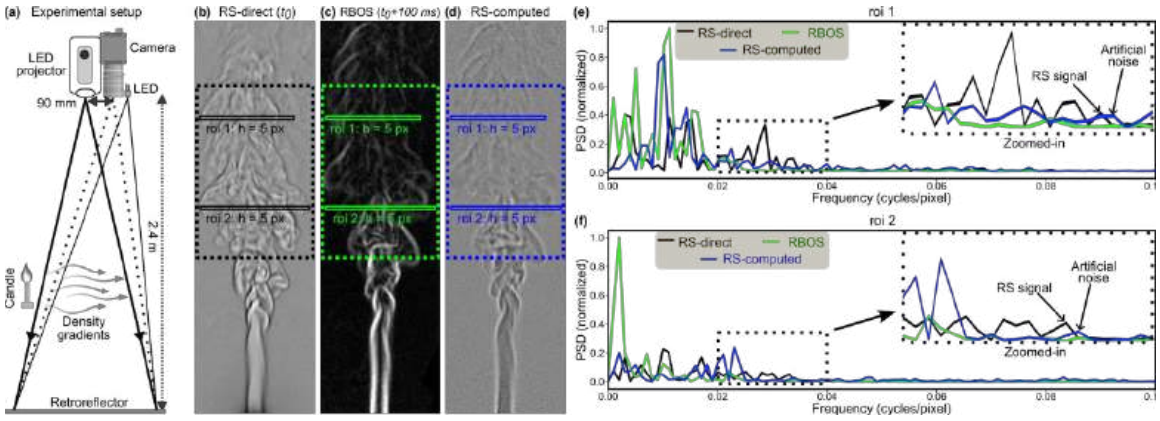


Fig. 1: Alternate RBOS and RS system. (a) Experimental configuration. (b), (c), and (d) Lighter plume captured using direct RS, RBOS, and computationally reconstructed RS from RBOS data, respectively. (e) and (f) spectral analysis plots of the selected regions.

Here, we develop a co-aligned experimental configuration that integrates both techniques using the same camera under identical illumination, as shown in Fig. 1a. We capture alternate RBOS and RS images of a density gradient field. The comparison is made between the RBOS, direct RS, and the computationally reconstructed shadowgram derived from the RBOS (Fig. 1b-d). We show that although the retroreflective implementations of both visualization techniques capture identical flow fields, as revealed by Fourier analysis (Fig. 1e-f), RS consistently resolves finer spatial structures. However, the sensitivity analysis shows that RBOS is more sensitive than RS. We quantify this trade-off by imaging the density-gradient field induced by the combustion plume. This trade-off is shown to be intrinsic to how each technique responds to density gradients. It provides clear evidence-based guidance that the choice of technique may depend on the specific resolution and sensitivity requirements of a given application.

Acknowledgment: DR and MK acknowledge ANRF and IIT Delhi for funding.

References:

[1] G. S. Settles, *Schlieren and shadowgraph techniques: visualizing phenomena in transparent media*, Springer Science & Business Media (2001).
[2] D. Rabha, D. Saini, A. Kumar, V. Kumar, and M. Kumar, *Experiments in Fluids* 66 (2025) 147.
[3] K. M. Talluru, H. Kleine, *Measurement Science and Technology* 34(3) (2023) 035201.

A Hot-Extractive Fourier Transform-based UV-DOAS System for SO_2, NO and NH_3 Monitoring in Industrial Plants

[1,#]Anirban Roy,[1]Yashwant Rajeshirke and [1]S K Karthick Kumar
[1]R&D, Forbes Marshall Pvt. Ltd., Kasarwadi, Pune, India - 411034

[#]*anirbanroy@forbesmarshall.com*

We report the development and validation of a highly sensitive differential optical absorption spectroscopy-based system for hot-extractive measurement of sulphur dioxide (SO_2), nitric oxide (NO) and ammonia (NH_3) concentration in industrial flue gas.

Sulphur dioxide (SO_2), nitric oxide (NO) and ammonia (NH_3) are among the most common pollutants that need to be monitored in hostile industrial environments. A major challenge faced while designing these measurement systems is that flue gas is generally at a high temperature and is laden with large quantities of water vapour. More importantly, it is necessary to operate at a wavelength region where the line strength of the absorption lines is high enough to achieve the desired sensitivity. Fortunately, the electronic transitions in the UV region satisfy both these requirements - (i) they lie in a region which has negligible spectral interference from water vapour, and (ii) their transition probabilities are few orders of magnitude higher than that of vibrational transitions [1]. Maintaining the integrity of the flue gas while making measurements is another concern. In this regard, the hot-extractive approach retains the integrity of flue gas better than the cold-extractive approach. In this paper, we report the development of a hot-extractive Differential Optical Absorption Spectroscopy (DOAS) [2] system for accurate long-term monitoring of SO_2, NO and NH_3 in industrial stacks.
We use a 2W Xenon flash lamp (Excelitas) as the optical source in the sensor. The light from the lamp passes through a multipass gas cell which has an effective optical path length of 1.6 m. The light is then detected by a UV spectrometer (Oto Photonics). Heaters with PID control are provided on the multipass cell to maintain the gas temperature at 150°C. The spectra of SO_2, NO and NH_3 obtained from the spectrometer are shown in Fig. 1(a). The spectra are processed and gas concentrations are calculated using a novel Fast Fourier Transform (FFT)-based algorithm in LabVIEW. The performance of the system is evaluated through measurement of calibrated gases in laboratory conditions. The error in measurement is below 1% for the measurement range of 0-100 ppm. The response time (T_{90}) of the sensor is then evaluated as shown in Fig. 1(b). The plots show a response time of 48 s for SO_2, 51 s for NO and 150 s for NH_3. These values conform to the performance criteria outlined in the EN 15267-3 standard. Our focus at present is to deploy the system at multiple industrial plants and test its on-field performance at boiler stacks.

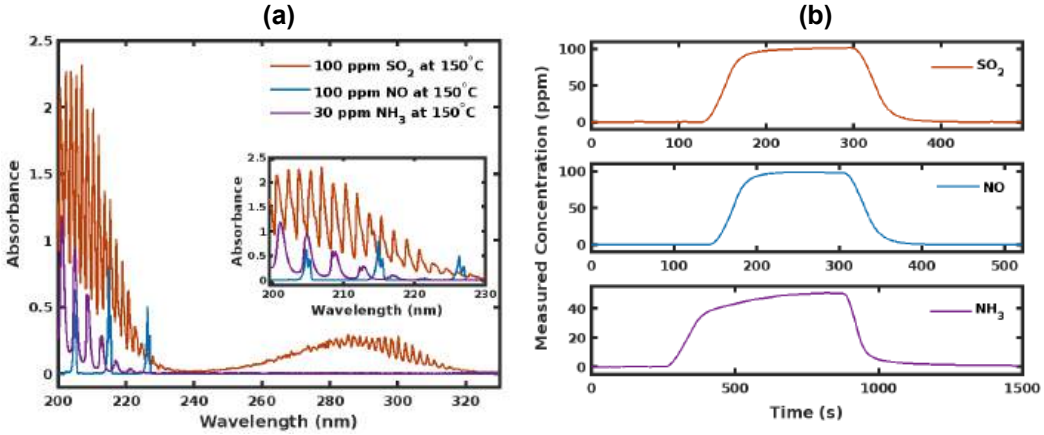


Fig. 1. (a) Absorption spectra of SO_2, NO and NH_3 obtained from the UV spectrometer. The inset shows the 200-230 nm region where there is significant spectral congestion. (b) Response time of the flue gas analyser for measurement of SO_2, NO and NH_3 recorded while flowing calibrated gases through the multipass gas cell.

References:

1. J. Shao, L. Lathdavong, P. Thavixay and O. Axner, "Detection of nitric oxide at low ppb·m concentrations by differential absorption spectrometry using a fully diode-laser-based ultraviolet laser system," J. Opt. Soc. Am. B **24**, 2294-2306 (2007).
2. U. Platt, "Air Monitoring by Differential Optical Absorption Spectroscopy," Encyclopedia of Analytical Chemistry (Wiley, 2017).

Blue Light Hazard Measurement Facility for Photobiological Safety Assessment of Lamps, Luminaires and Electronic Display Devices

[1,#]Shibu Saha,[1]Rajat Kr. Mukherjee. [1]V. K. Jaiswal and [1]Parag Sharma
[1]Optical Radiation Metrology, CSIR-National Physical Laboratory, Dr. K. S. Krishnan Marg, Delhi-110012

[#]*ssaha.nplindia@csir.res.in*

Blue light hazard assessment has become increasingly important with widespread use of LED lighting and display devices. The work presents establishment of a standardized spectroradiometric measurement facility for blue light hazard evaluation in accordance with IS 16108:2012 and demonstrates its application to representative lighting and display technologies for safety assessment.

Widespread adoption of LED technology has made it the dominant source of artificial illumination in lighting and display devices. White LEDs exhibit a pronounced spectral emission peak in the blue wavelength region. As blue light plays an important role in regulating human circadian rhythm, excessive exposure to artificial LED illumination and prolonged viewing of displays are linked with potential photobiological effects. Consequently, reliable assessment of blue light hazard through standardized measurement has become increasingly important [1,2]. However, these capabilities remain limited in India, emphasizing the need for traceable measurement facilities.

IS 16108:2012 (IEC 62471:2006) specifies the methodology for assessing the photobiological safety of light products [1]. Blue light hazard assessment relies on accurate measurement of spectral radiance, followed by application of the blue light hazard spectral weighting function, B(λ), which represents the relative spectral effectiveness for blue-light-induced retinal photochemical injury (shown in inset of Fig. 1) [1]. The quantitative assessment of blue light hazard depends directly on accurate spectral radiance measurements, measurement geometry, and other metrological aspects.

A blue light hazard measurement facility has been established in accordance with IS 16108:2012 (IEC 62471). The facility consists of an SI-traceable spectroradiometer, and precision field-of-view optics conforming to the 100 mrad requirement of the standard. Representative measurements have been carried out on LED lighting sources, mobile phone displays, computer monitors, and other visual display devices. Spectral radiance distributions for sample LED sources with CCTs of 2700 K, 4000 K and 6500 K are shown in Fig. 1, from which their blue-light-hazard-weighted radiance values were calculated to be 11.6, 26.5, and 39.2 $W \cdot m^{-2} \cdot sr^{-1}$, respectively, indicating increased blue-light-hazard-weighted radiance for higher CCTs, while remaining well within the Exempt Group limit.

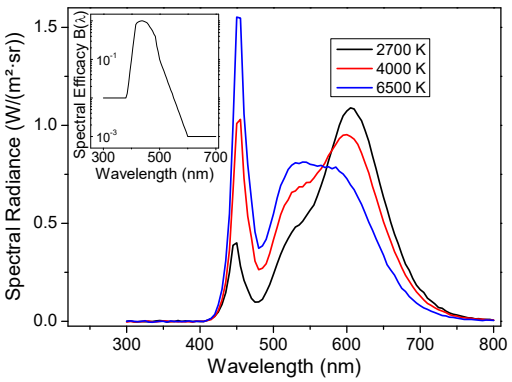


Fig 1: Spectral Radiance of LED light sources of various CCTs (Inset shows spectral weighting function, B(λ))

The established SI-traceable measurement capability provides a standardized framework for blue light hazard assessment of modern lighting products and electronic display devices. It would support product development, photobiological safety evaluation, conformity assessment, and testing laboratories engaged in optical radiation measurements. The facility is expected to facilitate wider adoption of standardized blue light hazard assessment in India and strengthen national metrology capabilities for photobiological safety evaluation of LED sources.

Financial supports from BEE, Min. of Power, GoI and CSIR are thankfully acknowledged.

References:

[1] Bureau of Indian Standards, IS 16108:2012 Photobiological Safety of Lamps and Lamp Systems.
[2] A.T. Jaadane, P. Boulenguez, S. Chahory, M. Carré, O. Savoldelli, P. Martinsons, *Free Radical Biology and Medicine* 84 (2015) 373.

Investigation of Optical Polishing of Single-Crystal Sapphire and Polycrystalline Spinel

H.P. Singh[1], Santosh Shah[1], B. Poddar[1], M.P. Singh[1], Neeraj Pandey[1], L.M. Pant[1]

[1]Instruments Research & Development Establishment, Dehradun- 248008

hpsingh.drdo@gov.in

This study evaluates float polishing of single-crystal sapphire and polycrystalline spinel for high-performance optical applications. Surface form improved from 4500 nm to 183 nm for sapphire and 5000 nm to 929 nm for spinel, with the central region reaching 445 nm. Minimum roughness values of 2.66 nm and 2.42 nm demonstrate excellent optical surface quality.

Single-crystal sapphire (Al_2O_3) (Fig.1) and transparent polycrystalline spinel ($MgAl_2O_4$) (Fig. 2) are advanced optical ceramics used in IR and electro-optical applications, including aerospace and defence systems [1]. Their high hardness, transparency, and mechanical strength make precision polishing essential for achieving optical-grade surfaces. However, orientation-dependent behaviour in sapphire and grain structure in spinel influence material removal, surface finish, and subsurface damage, requiring optimized diamond-abrasive polishing processes.

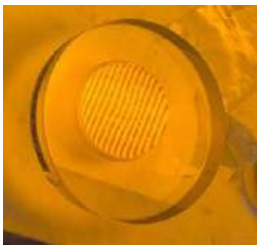


Fig. 1: Sapphire sample

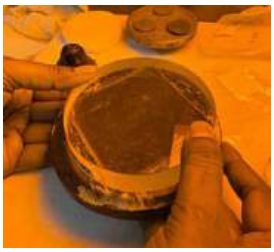


Fig. 2: Spinel sample

Single-crystal sapphire (Ø50 mm, Circular) and polycrystalline spinel (75 × 75 mm, rectangular) specimens (Fig. 3) were polished using float polishing with a 1 µm diamond slurry on a tin-alloy lap. Each specimen underwent more than 100 hours of polishing, during which the surface form was monitored approximately ten times using a Fizeau interferometer to guide the polishing process and maintain the desired optical surface form and finish [3]. After polishing, the final surface form was measured using the Fizeau interferometer, while the surface roughness was evaluated using the optical profilometer or white light interferometer [2]. Optical Polishing using 1 µm diamond slurry successfully produced optical-quality surfaces on sapphire and polycrystalline spinel, demonstrating substantial improvements in surface form and roughness. Sapphire achieved a surface form of 183 nm PV, while spinel improved significantly from 5000 nm to 929 nm PV, with 445 nm PV (Ø70 mm, Circular) measured in its central region (Fig. 4). The surface roughness reached 2.66 nm for sapphire and 2.42 nm for spinel, confirming the effectiveness of the precision polishing process.

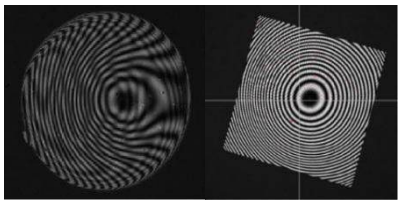


Fig. 3: Interferograms showing the initial surface form of sapphire and spinel before polishing.

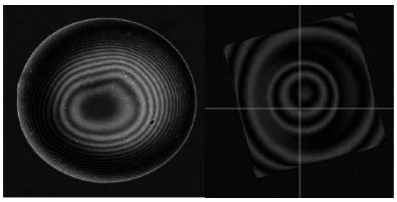


Fig. 4: Interferograms showing the final surface form of sapphire and spinel after polishing.

Authors are highly thankful to Director IRDE for their constant motivation and guidance.

References:

1. D. F. Harris, Materials for Infrared Windows and Domes: Properties and Performance, SPIE Press (1999).
2. Zygo Corporation, *White Light Interferometry and Optical Surface Metrology: Application Notes. Zygo Corporation*.
3. J. C. Wyant, K. Creath, Basic Wavefront Aberration Theory for Optical Metrology, in Applied Optics and Optical Engineering, Vol. 11, R. Kingslake, Ed., Academic Press, 1–53 (1992).

Single - layer silicon-nitride edge coupler for short-wavelength NIR PIC architecture

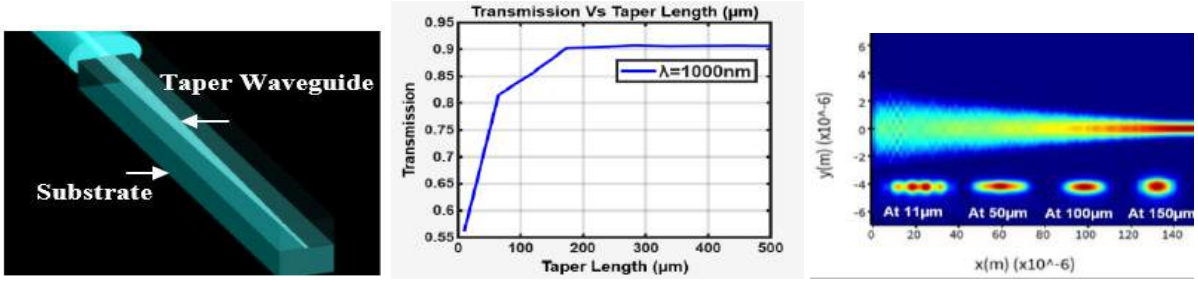
[1,#]Binshati Chatterjee,[1]Pramod R Watekar [1]Shailendra K Varshney
[1]Department of Electronics and Electrical Communication Engineering, Indian Institute of Technology, Kharagpur, West Bengal, India

[#]*email id of the corresponding author:* binshatichatterjee@gmail.com

This paper presents an edge coupler based on silicon nitride (Si_3N_4) material. It provides a transmission efficiency of 90% and smooth beam-propagation at the wavelength of 1000nm. The combination of high transmission efficiency, good beam-propagation and compact design demonstrate the potential of the proposed edge coupler for efficient fiber-to-waveguide coupling.

The large-scale integration of photonic circuits on a single chip has been a key driving force behind the development of Photonic Integrated Circuit (PIC) technology. The PIC has shown use cases in various fields, including information technology, optical communications and quantum computing [1-3]. One of the major challenges in PIC is achieving high optical intensity on-chip, where edge couplers play a crucial role in efficiently coupling light between optical fibers and photonic devices. Most previous studies have focused on edge coupler designs operating in the visible spectrum or the C-band wavelength range [4,5]. Therefore, this work aims to design and optimize an edge coupler for operation in the short-wavelength near-infrared (NIR) region.

The primary objective of an optical coupler design is to achieve efficient coupling between an optical fiber and an on-chip waveguide. The basic structure of the proposed coupler and its performance is shown in Fig. 1. The coupler consists of a silicon nitride (Si_3N_4) core and SiO2 substrate. The designed edge coupler provides a constant 90% transmission after particular taper length. The beam propagation has simulated and mode-field-distributions are obtained using Lumerical MODE solution at propagation lengths of 11 µm, 50 µm, 100 µm, and 150 µm, respectively, as shown in the inset of Fig.1(c).



(a) (b) (c)

Fig.1. (a) The schematic of the forward tapered edge coupler (b) Transmission vs Taper Length (c) The beam propagation with mode distributions through the edge coupler at 1000nm wavelength

The forward tapered edge coupler has been designed and its performance analysis has been carried out in terms of transmission efficiency and electric field propagation. The coupler mainly couples the light from the lensed fiber to the waveguide. The designed architecture is capable to provide the transmission efficiency of 90% at the wavelength of 1000nm. The high transmission efficiency, fabrication-friendly design and good mode distribution shows the efficient energy transfer from the fiber to the waveguide.

Acknowledgement: I would like to acknowledge the National Quantum Mission (NQM), Govt. of India, for funding this research work.

References:

[1] Carmelo Mordini, Alfredo Ricci Vasquez, Yuto Motohashi, Mose Müller, Maciej Malinowski, Chi Zhang, Karan K. Mehta, Daniel Kienzler, and Jonathan P. Home, Physical Review X, 15, 011040 (2025).
[2] Moon-Hyeok Lee, Simon Nellen, Francisco Soares, Martin Moehrle, Wolfgang Rehbein, Moritz Baier, Bjoern Globisch, and Martin Schell, Optic Express, 30, 20149, (2022).
[3] Shengjie Xie, Yang Zhang, Yiwen Hu, Sylvain Veilleux, Mario Dagenais., ACS Photonics 7, 1009–1015 (2020).
[4] Xiheng Ai, Maxwell Wei Xuan, Yang Zhang, Wei-Lun Hsu, Sylvain Veilleux, and Mario Dagenais, Optic Express, 33, 16253, (2025).
[5] Zijun Yao, Yuhang Wan, Yu Zhang, Xinxuan Ma, Zheng Zheng, Optics Communication,475, 126301, (2020).

Rapid Designing of Silicon Nitride Frequency Combs via Integrated Tidy3D and PyLLE Simulations

[1]Divyanshu Tiwari, [2]Esraaj Sarkar Gupta, [1]Satyam Verma, and [1#]Anshuman Kumar

[1]Laboratory of Optics of Quantum Materials (LOQM), Department of Physics, IIT Bombay, Mumbai, India

[2]Plaksha University, Mohali, India

[#]anshuman.kumar.srivastava@gmail.com

A Python based package integrating Tidy3D and PyLLE is developed for the rapid design and simulation of frequency combs in silicon nitride ring resonators. Finite-difference simulations extract precise dispersion parameters, which seamlessly feed into Lugiato Lefever equation solvers, enabling high-throughput optimization of micro-resonator geometries.

The development of on-chip optical frequency combs in high-Q micro-resonators has revolutionized fields ranging from ultra-broadband telecommunications to quantum information processing. Silicon nitride (SiN) has emerged as a premier platform for these devices due to its wide transparency window and negligible two-photon absorption in the telecom band. However, achieving deterministic soliton generation requires precise engineering of the anomalous group velocity dispersion (GVD), which is highly sensitive to nanoscale geometric variations. Simulating these systems traditionally involves a decoupled, computationally heavy two-step process: executing exhaustive electromagnetic mode-solving followed by independent nonlinear spatiotemporal dynamics modeling. In this work, we present an open-source Python package that unifies these steps by seamlessly interfacing cloud-based Finite-Difference Time-Domain (FDTD) solvers with nonlinear micro-cavity simulation frameworks.

The integrated package utilizes the high-performance Tidy3D cloud infrastructure to rapidly compute the modal properties and chromatic dispersion of SiN channel waveguides. The extracted resonance frequencies ω_μ and the free spectral range (D_1) are dynamically formatted and injected directly into PyLLE, a robust solver for the Lugiato-Lefever Equation (LLE).

By eliminating manual data translation between the electromagnetic mode-solver and the nonlinear dynamics engine, the package enables rapid, automated closed-loop optimization. Users can specify target comb characteristics, such as bandwidth, repetition rate, or specific soliton states, and the framework automatically sweeps the geometric landscape to locate stable operating regimes. This parallelized workflow reduces the optimization time significantly, offering a powerful tool for the rapid prototyping of next-generation quantum photonic chips. The authors gratefully acknowledge funding from Technical Group 3 of the Quantum Materials Hub under India's National Quantum Mission.

References

1. *Kippenberg, T. J., Holzwarth, R., & Diddams, S. A. (2011). Microresonator-Based Optical Frequency Combs. Science, 332, 555-559. https://doi.org/10.1126/science.1193968*
2. *Liu, Z., & Poon, J. K. S. (2025). Comparison of Lumerical FDTD and Tidy3D for three-dimensional FDTD simulations of passive silicon photonic components. arXiv. https://doi.org/10.48550/arxiv.2506.16665*
3. *pyLLE: a Fast and User Friendly Lugiato-Lefever Equation Solver arXiv:1903.10441 https://arxiv.org/abs/1903.10441*
4. *Lugiato, L. A., & Lefever, R. (1987). Spatial Dissipative Structures in Passive Optical Systems. Physical Review Letters, 58, 2209-2211. https://doi.org/10.1103/physrevlett.58.2209*

Dispersion-Engineered Asymmetric Directional Coupler on InP for Routing 1310 nm and 1550 nm

[1#]Vogirala Nithin and [2]M. R. Shenoy

[1] Department of Physical and Chemical Sciences, Sri Sathya Sai University for Human Excellence Kalaburagi, Navanihal - 585313, Kalaburagi, India

[2] Formerly at Department of Physics, Indian Institute of Technology Delhi, New Delhi - 110016, India

[#] *email id: nithin.v@sssuhe.ac.in*

We present a planar wavelength router on InP separating 1310 nm and 1550 nm using an asymmetric directional coupler of two lattice-matched InGaAsP ridge waveguides. Supermode analysis yields a 96.4 μm coupling length, achieving 99.3% power transfer to the drop port at 1550 nm with negligible crosstalk at 1310 nm.

The InGaAsP/InP platform supports monolithic integration of amplifiers, lasers, modulators, and photodiodes with passive routing [1]. Conventional InP-based asymmetric directional couplers (ADCs) usually phase-match the shorter wavelength and deliberately mismatch the longer one. Because the 1550 nm mode field is wider than at 1310 nm, such ADCs often require long interaction regions, extra epitaxial layers, or aggressive confinement engineering to suppress C-band leakage. Recently fabricated InP-based 1310/1550 nm MMI demultiplexer measured 7.1 dB and 5.9 dB extinction at the C-band and O-band, respectively [2].

We instead use a planar ADC where the ridges are made of InGaAsP of different composition and of slightly different widths. Figure 1 shows the cross-section: Waveguide 1 (through arm) is lattice-matched 1295Q InGaAsP (the subscript Q denotes a quaternary InGaAsP alloy, named by its bandgap wavelength in nm), 1.0 μm wide and 1.0 μm high. Waveguide 2 (drop arm) is 1100Q InGaAsP, 1.2 μm wide and 1.0 μm high; the inter-waveguide separation is 0.12 μm. InP is the substrate and Benzocyclobutene (BCB) is the cover. The design targets transverse-magnetic (TM) polarization, consistent with the dominant gain polarization of InGaAsP-based active devices.

Alloy contrast and unequal widths make the effective indices n_{eff} of the two isolated ridges meet near 1550 nm and stay far apart at 1310 nm (Fig. 2). At 1310 nm the index difference is about 0.087, so cross-coupling is suppressed. At 1550 nm the guides are nearly phase-matched, so power can transfer from WG1 to WG2 over a short length.

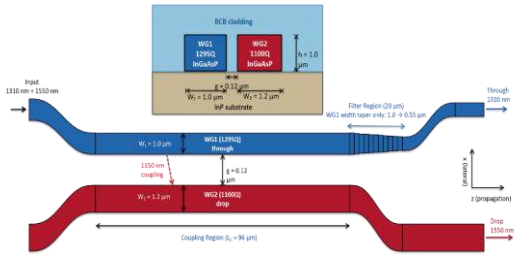


Fig. 1. Device layout. Top: cross-section of WG1 (1295Q, 1.0 μm × 1.0 μm) and WG2 (1100Q, 1.2 μm × 1.0 μm), gap 0.12 μm, BCB cladding. Bottom: top view with coupling region (L ≈ 96 μm) and output taper on WG1.

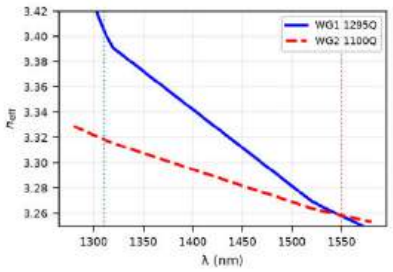


Fig. 2. Effective index of each isolated ridge vs. wavelength (TM). Curves cross near 1550 nm (phase-matched) and stay apart at 1310 nm

Using two-dimensional MIT Photonic Bands (MPB) eigenmode simulation at 64 pixels/μm, we solve for the symmetric and antisymmetric supermodes of the coupled waveguides. At 1550 nm, the half-beat coupling length is L_c = 96.4 μm and the drop fraction is 99.3% (0.03 dB); about 0.7% stays on WG1. At 1310 nm, the large mismatch keeps the coupling fraction well below 0.01%, so isolation is better than 40 dB.

By considering fabrication width error ±20 nm and height error ±10 nm, the worst case 1550 nm drop is 88.4% (0.53 dB), with 11.6% left on WG1. To increase the isolation at the through port, a width taper (from a width of 1.0 μm to a width of 0.55 μm) on the WG1 output can be included in the layout (see Fig.1), so that residual 1550 nm light approaches cutoff while 1310 nm stays guided.

References:

[1] M. K. Smit, K. A. Williams, J. van der Tol, APL Photonics 4 (2019) 056508.
[2] F. Guo, D. Lu, H. Song, Y. Niu, D. Zhou, L. Zhao, Photonics 11 (2024) 232.

Hollow Core ARROW Waveguide

Poonam Yadav [1, *], and Deepak Jain [2]

[1] Optics and Photonics Centre, Indian Institute of Technology Delhi

[2] Optics and Photonics Centre, Indian Institute of Technology Delhi

*opz238621@iitd.ac.in

A rectangular hollow-core anti-resonant reflecting optical waveguide (ARROW) with alternating Si/SiO_2 multilayer cladding is proposed and numerically analyzed using the finite element method. The effects of waveguide geometry on optical confinement and propagation loss are investigated. The analysis further reveals that lower waveguide heights broaden the cladding-mode band around the resonance wavelength, resulting in additional core–cladding modal coupling, whereas increasing the waveguide height leads to well-defined resonance bands and reduced coupling.

Hollow-core anti-resonant reflecting optical waveguides(ARROWs) have attracted significant attention for integrated photonic applications owing to their ability to guide light within a low-refractive-index medium while minimizing material absorption and scattering losses. In this work, we present the design, optimization and numerical simulation of an on-chip hollow-core waveguide using COMSOL Multiphysics. For efficient light guidance through ARROW guidance, we first consider a closed hollow-core structure surrounded by a cladding of micro structured silicon (Si) and silica (SiO_2) layers. Systematic optimization of the geometrical parameters (core width, layer thicknesses of silicon and silica, index contrast, number of cladding rings) greatly reduces leakage losses. For a design of 7 rings ($N = 7$), a core width ($a = 15\ \mu m$), a silica layer thickness ($t_{(SiO_2)} = 0.325\ \mu m$), and a silicon layer thickness ($t_{Si} = 0.1\ \mu m$), low propagation loss of $0.25\ dB/cm$ is obtained.

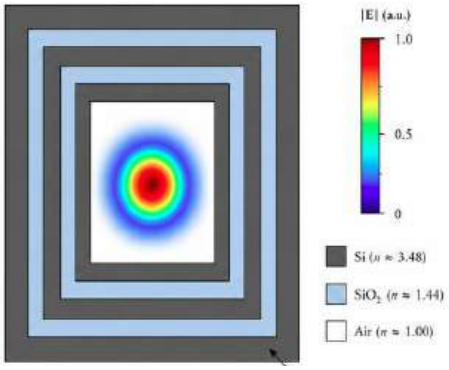


Fig. 1: Cross-sectional view of the proposed hollow-core ARROW

For the hollow core waveguide, analysis of the power fraction loss over a spectral range for lower heights shows that the resonant condition of wavelength:

$$\lambda = \frac{\left(2t\sqrt{(n_2^2 - n_1^2)}\right)}{m} \qquad (1)$$

is not satisfied perfectly, inducing additional modal couplings. Similarly, when the cladding-modes n_{eff} versus wavelength characteristics were plotted over the same wavelength range, the modes formed a band spread over a range around the resonance wavelength calculated using Eq. (1).

For lower waveguide heights, this band was observed to be broader, resulting in additional coupling between the core mode and cladding modes. These additional coupling events are reflected as multiple coupling peaks in the power fraction graph. As the waveguide height increases, the cladding modes gradually converge and form a well-defined band centered around the resonance wavelength, thereby reducing the additional coupling effects. This behavior can be attributed to the assumptions made during the derivation of the resonance wavelength formula. The analytical expression is derived under the assumption that the fiber radius is sufficiently large. For the proposed rectangular waveguide, the waveguide height represents the corresponding characteristic transverse dimension analogous to the circumference ($2\pi r$) of the circular anti-resonant fiber used in the derivation. Therefore, for smaller waveguide heights, the assumptions underlying the analytical model are less accurately satisfied, leading to a broader distribution of cladding modes around the predicted resonance wavelength. As the waveguide height increases, the assumptions become more closely satisfied, resulting in better convergence of the cladding modes around the resonance wavelength predicted by Eq. (1).

Analysis of Kerr lens modelocking Ti:Sapphire femtosecond laser under CW operation

[#]Gayathri A Nair, Harikrishnan P and Dinesh N Naik
Applied and adaptive optics laboratory, Department of Physics, Indian Institute of Space Science and technology, Thiruvananthapuram,Kerala 695541, India

[#]*gayathrianair.25@res.iist.ac.in*

The wavelength-tuning characteristics of a Kerr-lens modelocked(KLM) Ti:Sapphire laser were investigated using intracavity wavelength tuning elements(WTEs) to optimise cavity alignment for modelocking. During continuous tuning, spectral discontinuities corresponding to mode hopping were observed. The behaviour is analysed using resonator stability theory.

KLM Ti: Sapphire femtosecond lasers are the cornerstone of ultrafast science. The modelocking process in such a laser (Coherent Mira 900-F femtosecond laser) arises from the complex interplay between cavity parameters, including mirror alignment, cavity geometry, dispersion compensations, pump conditions and nonlinear optical effects. Due to this multidimensional nature, the conditions leading to stable modelocking are not predictable in advance.

In such lasers, the optical cavity in CW operation has two stability zones [1], defined by the resonator stability condition, $|A + D| < 2$, where A and D are the matrix elements of the ABCD matrix of the cavity. Since the matrix depends only on geometric distances and mirror curvatures, the stability regions are wavelength independent. Now, the wavelengths which oscillate in the stability regions of the cavity are defined by the cavity's resonance condition, $m \cdot \lambda = 2 \cdot n(\lambda) \cdot L(opl)$. So by reducing the alignment freedom to WTEs, we can investigate the behaviour of the spectra under CW operation.

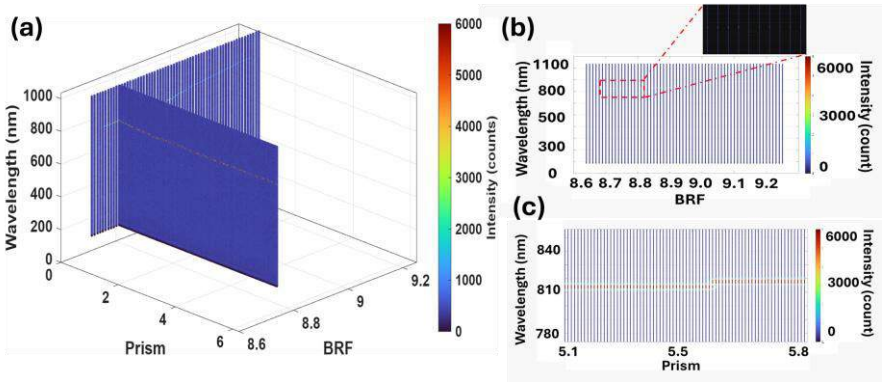


Fig. 1: Dynamics of the spectra. a) Wavelength tuning by BRF and main cavity prism. b) Mode hopping induced by prism translation. c) Mode hopping induced by BRF rotation.

Wavelength tuning in KLM Ti:Sapphire laser is achieved by WTEs such as birefringent filters (BRFs) and Brewster prism pairs. In CW operation, a BRF can tune the wavelength across the Ti:Sapphire emission range, while a prism tunes a narrow region around the cavity's central wavelength. We investigated whether a single WTE could restore the wavelength that the other had disturbed. For a particular mirror arrangement of the optical cavity setup[2], after achieving a peak intensity wavelength(or any wavelength) from the coupled effect of WTEs, we tuned the wavelength using the prism in the main cavity and tried to recover the original peak-intensity wavelength using the BRF. During BRF tuning, mode hopping was observed at certain wavelengths, and the intensity decayed as the wavelength approached the peak-intensity wavelength.

Wavelength tuning by prism is associated with the change in the optical path length of the cavity, but tuning by BRF is associated with polarisation-dependent interference [3]. The effect of one is not compensated by the other. The operating point achieved by the cavity is unique. The underlying mechanism behind modehopping, its association with WTEs and its effects on cavity's stability

References:

[1] Yefet, Shai, and Avi Pe'er. *Applied Sciences* 3.4 (694-724)(2013).
[2] Rodríguez, A. A., et al. Fifth Symposium Optics in Industry. Vol. 6046. SPIE,(2)(2006).
[3] Wei, Jiao, et al. *Photonics*. Vol. 10. No. 11. MDPI, (2-5)(2023).

.

V-shaped millibot integrated with FRET-assisted random lasing tip

[1,#]Nikita Choudhary,[1]Diksha Sharma and [1,2]Anjani Kumar Tiwari
[1]Department of Physics, Indian Institute of Technology Roorkee, Roorkee, 247667, Uttarakhand, India
[2]Centre for Photonics and Quantum Communication Technology, Indian Institute of Technology Roorkee, Roorkee 247667, Uttarakhand, India

[#]*n_choudhary@ph.iitr.ac.in*

We present a V-shaped millibot and integrate its tip region with a FRET-assisted random lasing microlayer. Upon optical illumination, the millibot's arm undergoes bending deformation, which is used to navigate it to a predefined target point. Upon reaching the target point, the millibot's tip generates efficient FRET-assisted random lasing signals.

Liquid crystal elastomers (LCEs) are smart materials that integrate the elastic behavior of polymers with the anisotropic properties of liquid crystals [1]. LCEs exhibit extraordinary characteristics, including soft elasticity, birefringence, and reversible actuation under external stimuli [2-4]. These properties make them suitable for tunable photonic devices, soft actuators, and mimicking versatile locomotion.

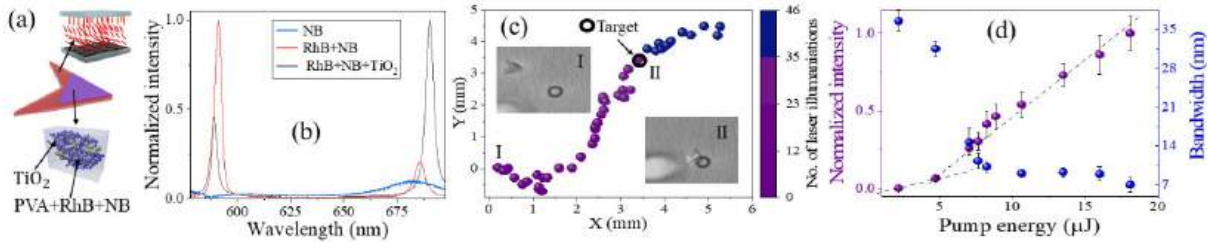


Fig. 1: (a) Schematic of the V-shaped millibot. (b) Emission spectrum of the NB, RhB + NB, *and* RhB + NB + TiO_2 nanoparticles *embedded in a PVA matrix. (c) Trajectory of the light controlled millibot on a plane surface. (d) Plot of the emission intensity and bandwidth of the FRET-assisted random lasing signal.*

In this work, we realize a V-shaped LCE millibot and coat its tip region with a Förster resonance energy transfer (FRET)-assisted random lasing film. Fig. 1(a) shows the schematic of the millibot, fabricated from LCE having molecular alignment in the splayed fashion. The tip region of the millibot is coated with a polyvinyl alcohol (PVA) solution containing a mixture of Rhodamine B (RhB), Nile blue (NB), and TiO_2 nanoparticles. Since the emission spectrum of RhB and the absorption spectrum of NB overlap significantly, the right concentration of these molecules enables efficient FRET signals. To systematically characterize FRET, three separate films of PVA containing NB, RhB+NB, and RhB + NB + TiO_2 were prepared. The films were excited using the second harmonic (532 nm) of a sub-nanosecond Nd:YAG laser. Figure 1(b) shows the single-shot emission spectra from these films. The PVA film doped with NB shows a weak fluorescence. In the RhB+NB film, an enhancement in the NB emission is observed. The addition of TiO_2 nanoparticles in the RhB+NB film provides multiple-scattering feedback, leading to the emergence of a sharp, narrow peak at 690 nm. The optimized PVA mixture of RhB + NB + TiO_2 was coated onto the tip region of the LCE millibot. Due to the splay alignment of the molecules, upon laser illumination, the arm of the LCE millibot exhibits bending deformation. By cyclic illuminations of the arms, the V-shaped LCE milibot was remotely navigated to the desired target point. Fig. 1(c) shows the X–Y displacement of the composite millibot parked at (3.8 mm, 3.7 mm) position. The inset shows the snapshots of the composite millibot for the 1st and 35th ON/OFF laser illumination cycles. After the 35th illumination, the millibot reaches the predefined target point. At the target point, the emission spectra from the tip region are collected at different pump energies. The random lasing threshold of the FRET signal is identified at 4.7 μJ as shown in Fig. 1(d). Above this threshold, the emission intensity increases sharply, and the spectral bandwidth collapses, indicating the onset of FRET-assisted random lasing in the tip region.

References:

[1] M. Warner and E. M. Terentjev, Liquid Crystal Elastomers, Oxford University Press 120, (2007).
[2] O.M. Wani, H. Zeng, and A. Priimagi, Nature communications 8 (2017) 15546.
[3] N.Choudhary, D.S. Gaur, D. Sharma, A. K. Tiwari, and N. K. Gupta, Scientific Reports 15 (2025) 35779.
[4] N. Choudhary, D. Sharma, J. Mandal, and A. K. Tiwari, Optics Letters 51 (2026) 1041-1044.

Breaking Plastic with Light: Resonant Energy Transfer-Driven Near-Infrared Degradation of PET Polymer

Christy Antony P and N. Yogesh*

Metamaterials and Photonic Structures Laboratory, Department of Physics, National Institute of Technology, Kozhikode-673601, Kerala

*Corresponding Author: yogesh@nitc.ac.in

*Plastic waste accumulation has become a major environmental challenge, necessitating the development of efficient, sustainable strategies for polymer degradation. In this work, poly (ethylene terephthalate) (PET) degradation was achieved using near-infrared (NIR) and suitable photosensitizers based on a **resonant energy transfer** (RET) mechanism.*

We created and verified a quick technique that uses light to break down plastic into tiny molecular pieces. This technique uses near-infrared (NIR) laser light to break down particles with the least energy. For this investigation, polyethylene terephthalate (PET) was used as the model polymer. A photosensitizer is required to absorb NIR light, as PET shows no absorption in this region. To meet the criteria for selecting photosensitizers, materials must have energy levels that absorb near-infrared light. When the energy collected by the photosensitizer is transferred to the bond dissociation limit of the targeted chemical bonds in the polymer, PET breakdown begins. Three distinct photosensitizers were employed in this study: graphite, titanium diboride (TiB_2), and magnesium diboride (MgB_2). We determined the lowest unoccupied molecular orbital (LUMO) levels of the photosensitizers using cyclic voltammetry. Among the three photosensitizers, MgB2's LUMO level is nearly equal to the bond-dissociation limit for PET. Therefore, if the energy transfer between MgB_2 and PET is resonant, polymer degradation will occur even at standard temperature and pressure with a moderate level of light intensity. We demonstrate 60% mass loss of PET using a MgB2 photosensitizer and a 3 W NIR laser. Gas chromatography-mass spectrometry (GC-MS) analysis was used to confirm the PET's degradation in the presence of the MgB_2 photosensitizer. Thus, the exhibited NIR laser-assisted PET degradation utilizing photosensitizers serves as one of the green photonics solutions to the PET plastic challenges.

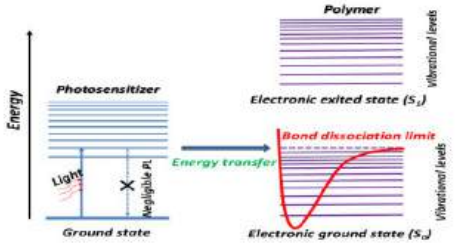


Fig. 1: Resonant energy transfer mechanism

References:

[1] Christy Antony, P., Yogesh, N. Near-infrared laser-induced plastic (polyethylene terephthalate (PET)) degradation with photosensitizers based on resonant energy transfer mechanism. Sci Rep (2026). https://doi.org/10.1038/s41598-026-59732-z

[2] H.F. Son, I.J. Cho, S. Joo, H. Seo, H.Y. Sagong, S.Y. Choi, S.Y. Lee, K.J. Kim, Rational Protein Engineering of Thermo-Stable PETase from Ideonella sakaiensis for Highly Efficient PET Degradation, ACS Catal 9 (2019) 3519–3526.9.

Experimental and theoretical understanding on the role of Xenon in laser gas mixture towards sealed off CO_2 laser development

[1, #]Avantika Gautam,[1]Tirumala Rao B,[2]Sunil Verma and [1]Manoj Kumar
[1]CO_2 Laser Technology Section
[2]Photonic Materials Technology Section, Raja Ramanna Center for Advanced Technology, Indore, Madhya Pradesh 452 013

[#]*avantika@rrcat.gov.in*

A CO_2:N_2:He gas mixture (1:1:8) with xenon concentrations ranging from 0.5% to 2% was investigated by measuring voltage between two probes inserted in the glow discharge. The decreased probe voltage with xenon content indicates that a positive effect of xenon for sustaining discharge at low E/N for improving the life of gas mixture. This is further supported from theoretical calculations using BOLSIG+ solver-based analysis.

Sealed-off CO_2 lasers are widely used in industrial, medical, and scientific applications due to their compact design, reliability and long operational lifetime. The performance of these lasers is strongly influenced by the composition of the active gas mixtures, which governs the discharge characteristics. In this work, the effect of xenon (Xe) addition on the discharge behavior of the laser gas mixture was investigated through experimental and theoretical simulations.

Fig 1a presents the schematic of experimental set up consisting of two electrostatic probes inserted into the discharge region separated by a gap of 2.25 cm. The experiments were carried out using a sealed discharge tube filled with the gas mixture in the ratio of CO_2:N_2:He as 1:1:8.The measurements were conducted at three gas pressures of 10, 20, and 30 mbar with discharge currents of 20 and 30 mA at each pressure. The role of xenon was studied by introducing it at three different quantities of 0.5%, 1%, and 2% by adjusting the helium gas content. Fig 1b presents the measured probe voltage at 20 and 30 mbar at 30 mA current. It shows that at higher pressure the probe voltage is more and also with increase of xenon, a systematic decrease in the probe voltage has been noticed. This is because, xenon gas having lower ionization potential [1], favours the lower sustained reduced electric field. Fig 1c presents the influence of xenon at 20 mA and 20 mbar, it also reveals that similar trend observed in previous case. Further To understand the effect of pressure and current at fixed xenon concentration the obtained results at 0.5 % xenon is shown in Fig1d.To validate these experimental observations, theoretical simulations were performed using the BOLSIG+ solver and python code. The electron energy distribution function (EEDF) was obtained over a reduced electric field (E/N) in range of 1–100 Td from BOLSIG+. Using this information, the steady-state reduced electric field corresponding to the self-sustained glow discharge condition was obtained via balancing the production and loss of electrons. The corresponding electric field was then calculated using the gas number density, and then the probe voltage was estimated from the relation (V = E\d), where (d) is the probe gap. These theoretical results are also shown in the above figures which are well aligned with the experimental results. This study demonstrates that a small fraction of xenon plays an important role by sustaining the glow discharge at lower E/N value. A key factor for improving the longevity of the sealed off laser operation with optimum power.

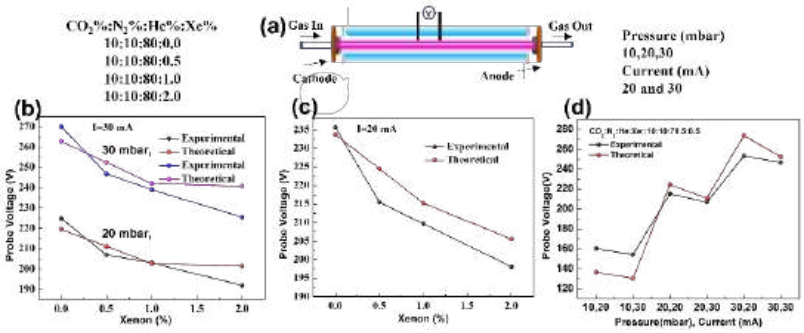


Fig.1 Probe Voltage set up and measurements.

References:

[1] A. M. Razhev · E. S. Kargapol'tsev, *Applied Physics B* (2022) 128:115

Analytical Evaluation of Atmospheric Propagation for High-Power CW and Pulsed Lasers

Ipshit Ghosh[1], P. Prem Kiran[1], and Ashok Vudayagiri[1]

[1]School of Physics, University of Hyderabad, Hyderabad, Telangana 500046, India

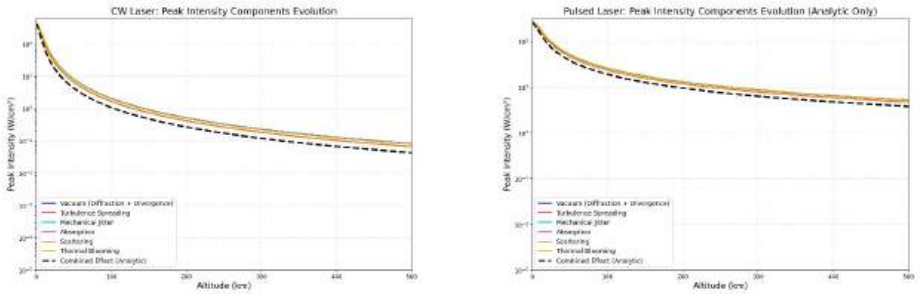
ghosh_sopra@uohyd.ac.in

We evaluate the atmospheric propagation of 300 kW continuous-wave and 5 J nanosecond pulsed lasers (1064 nm) over a 500 km vertical path. The continuous-wave beam is heavily attenuated by thermal blooming and centroid drift, whereas the pulsed beam avoids hydrodynamic expansion, resulting in higher peak intensity at the target.

Ground-based lasers designed for orbital debris interaction encounter significant atmospheric distortion during lower-altitude propagation. The physical loss mechanisms depend largely on whether a continuous-wave (CW) or pulsed architecture is used. CW lasers deposit thermal energy continuously, which initiates non-linear thermal blooming. This heating produces a refractive index gradient that behaves as a diverging lens, deflecting the beam laterally when a cross-wind is present. Nanosecond pulsed lasers avoid this macroscopic acoustic expansion because the pulse passes through the air before the medium can hydrodynamically react. Consequently, their beam spread is mainly limited by diffraction and turbulent phase modulations.

An analytical model was developed to compare these propagation regimes along a vertical-up path to 500 km. We modeled a 300 kW CW laser ($M^2 = 3.5$) and a 5 J, 10 ns pulsed laser ($M^2 = 8.5$) at 1064 nm. The calculations account for standard atmospheric profiles, optical extinction, and mechanical pointing jitter. Optical turbulence is treated using the Andrews-Phillips formulation via the Fried parameter to compute dynamic beam spreading:

$$\theta_{\text{turb}} = \frac{\lambda}{\pi w_0} \left(\frac{w_0}{r_0} \right)^{5/6} \tag{1}$$



Peak intensity evolution: CW laser with thermal defocusing (left) and Pulsed laser (right).

The results show a clear difference in beam centroid stability. The CW laser yields a centroid drift of approximately 200 m at the 500 km target altitude. This is caused by the interaction of the cross-wind with the thermal blooming gradient, steering the beam off-axis. The 10 ns pulsed laser does not suffer from wind-induced thermal steering. Its centroid drift is approximately 7.6 m, which is limited by the modeled mechanical jitter (1.0 μrad) and atmospheric turbulence.

This stability affects the final focused intensity. At 500 km, the CW laser's peak intensity decreases to roughly 10^3 W/m^2 due to thermal defocusing. The pulsed beam, which is governed mostly by geometric divergence and its M^2 diffraction limit, maintains a peak intensity near 10^6 W/m^2. These findings indicate that avoiding steady-state thermal blooming is advantageous for short-pulse architectures delivering energy over vertical space propagation paths.

References:

[1] C.R. Phipps et al., Adv. Space Res. 49 (2012) 1283.

[2] F.G. Gebhardt, Appl. Opt. 15 (1976) 1479.

[3] L.C. Andrews, R.L. Phillips, Laser Beam Propagation through Random Media, SPIE Press, Bellingham (2005).

Thin Meta-lens for Enhanced Depth of Focus at 10μm Wavelength

[1,#]Kriti Gupta and [1,2]Akhilesh Kumar Mishra
[1]Department of Physics, Indian Institute of Technology Roorkee, Roorkee-247667, Uttarakhand, India
[2]Centre for Photonics and Quantum Communication Technology, Indian Institute of Technology Roorkee, Roorkee-247667, Uttarakhand, India

[#]kriti_g@ph.iitr.ac.in

We present a transmissive meta-lens design using germanium (Ge) nanocylinders on a zinc selenide (ZnSe) substrate that operates at 10μm wavelength. The meta-atoms are sized to provide full 0 to 2π phase coverage with a wide transmission window. The diameter of the meta-lens is 2.97 mm and focal length is 78.57 mm. The lens yields a depth of focus of 24.7619 mm.

Meta-lenses are advanced optical devices composed of artificial nano-antenna arrays. Its flat, light-weight, ultra-thin, compact, customizable, and easy-to-integrate advantages enable wide potential applications [1]. By precisely engineering the phase, amplitude, and polarization of light at the nanoscale, meta-surfaces can manipulate light in ways that are not possible with conventional optical materials [2].

(a)

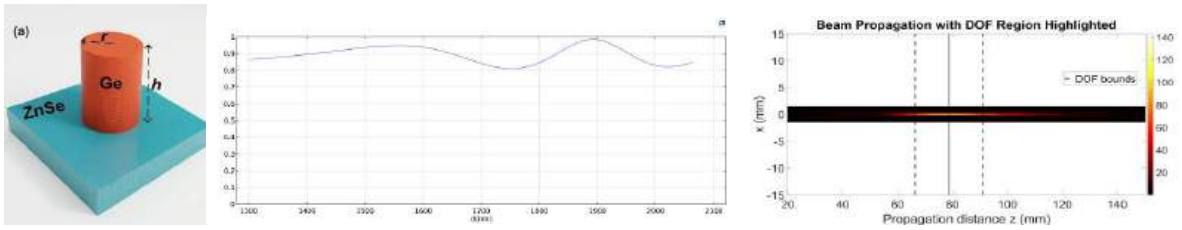


Fig. 1: (a) the meta-atom cell of the meta-lens. (b) variation of transmittance with cylinder diameter d, and (c) longitudinal view of the beam focusing.

The meta-lens focusing formula for the focusing phase is shown below:

$$\varphi(r,\lambda) = -\left[\frac{2\pi}{\lambda}\left(\sqrt{(r^2+f^2)}-f\right)\right]$$

where φ is the phase requirement, r is the distance away from the meta-lens center, λ is the working wavelength, and f is the focal length of the meta-lens.

High refractive index of Ge provides strong Mie-type resonance enabling efficient and precise manipulation of electromagnetic waves at the nanoscale [3]. The diameter of the Ge-cylinder in meta-atoms is varied from $1300\ nm$ to $2067\ nm$ with a $3.3\ \mu m$ period to optimise the transmittance and the optimised height is $7.9\ \mu m$. The schematic of the meta-atom of the thin lens is shown in fig. 1(a) and the variation of the transmittance with Ge-cylinder diameter is depicted in fig. 1(b). Fig. 1(c) reveals a distinct line-focused hot spot extending from $z = 66.2657\ mm$ to $z = 91.0276\ mm$ which gives the value of the depth of focus as $24.7619\ mm$ and the measured focal length is 78.57 mm.

This study may find applications in thermal imaging and terahertz imaging.

References:

[1] Mu Ku Chen et.al., Meta-Lens in the Sky, IEEE Access, (2022)
[2] YONGCAN ZENG et.al., Extended depth of focus meta-lens toward the entire long-wave infrared spectrum through inverse design framework, Optics Express, (2025)
[3] E. Aslan, "Germanium hollow nano-disk resonator for magnetic dipole decay rate enhancement in near-infrared," *Microw. Opt. Technol. Lett.*,vol. 63, no. 1, pp. 279–285, Jan. 2021.

Studies on the Effect of Nanosecond Pulse Laser Irradiation on Layered Mylar Sheet

[1,#]Deepti Joshi, [1]S. Veerabuthiran, [2] P. Prem Kiran, [1]Jagannath Nayak, [1]M. Sahu, [2] Pruthwin P.B and [2]G.S. Sasank
[1]Center for High Energy Systems and Sciences, DRDO, Hyderabad 500069, India
[2] School of Physics, University of Hyderabad, Hyderabad -500046, India
deeptijoshi.chess@gov.in

Mylar sheets are used for protection of various space based payloads. In this article experimental procedure and observation of nanosecond pulse laser irradiation (Nd:YAG laser, pulse duration 10 ns, pulse repetition rate 10 Hz) on a Layered Mylar sheet having total thickness of 0.32 mm in free standing mode are presented.

Mylar sheets are a form of Multi-Layer Insulation (MLI), designed to manage extreme temperatures in space. In general, MLI is a type of high-performance insulator which uses multiple radiation-heat transfer barriers to retard the flow of energy. MLI consists of lightweight reflective films assembled into thin layers that range in thickness [1]. Mylar sheet has total 11 layers namely golden color Kapton (2 layers), silver color aluminum (4 layers) and Mesh net (5 layers). Studies suggest that Laser Induced Damage Threshold (LIDT) of any structure is influenced by the material surface morphology, incident light intensity, wavelength, pulse width, number of laser shots, etc. [2-3]. In this article, we discussed the MLI disruption mechanisms by illuminating a 1064 nm nanosecond pulse laser systematically. The MLI surface disruption thresholds under different conditions were studied. Initially fluence of 5 J/cm2 was incident on the sample which resulted no characteristic changes in the surface of Mylar. Morphological changes on the Mylar sheet started occurring when a single shot of laser energy fluence reached 10J/cm^2 and above. A threshold damage test for the layered Mylar sample was performed by focusing the laser pulse at the same spot with increase in no of shots. An experimental analysis followed by a brief discussion regarding the results of the experimental observations is reported. The schematic of the experimental setup is shown in Fig. 1(a). A pulsed laser (Amplitude Technologies Ltd, Model: TITAN, PL-2250, 2015) was used. The laser pulse energy varied depending on the requirements. The pulse repetition frequency of the source can be varied from a single pulse to 5 Hz. Laser was focused on the target using focal length – 750 mm making 1mm spot size on the target. On laser irradiation the Gaussian-like intensity profile leaves a 1 mm spot size on the surface film, with a fluence-variant irregular crater as shown in Fig 1 (b).

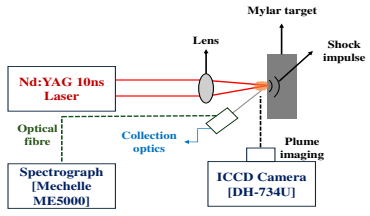


Fig.1: (a) Block diagram of experimental set up.

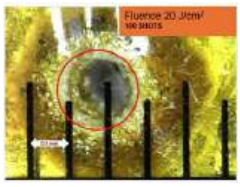


Fig. 1: (b) The impact of the laser irradiation on the Mylar sheet damage

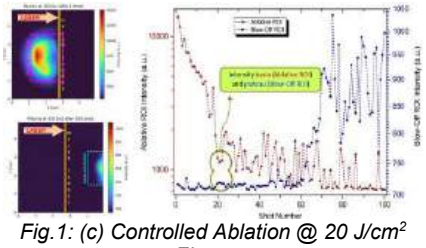


Fig.1: (c) Controlled Ablation @ 20 J/cm^2 Fluence

Experimental results suggest a single shot of nanosecond pulse laser can physically damage the Mylar sheet if it has laser energy density equal or above of 10J/cm^2. A threshold damage test for the layered Mylar sample was also performed by analyzing plasma plume for intensity tracking. The intensity was tracked by ablative ROI and blow-off ROI. Plasma plume images were captured from 500 ns after the ablative event till 5 µs in steps of 500 ns. Plasma Plume Evolution at 20 J/cm^2 fluence is shown in Fig 1 (c). Further the effect of laser fluence with respect to the no of shots was also studied. At fixed laser fluence 5J/cm^2 increasing the no of shots till 610 shots no piercing (damage of all 11 layers) was observed. For laser fluence 10J/cm^2 and 20J/cm^2 piercing observed at 80 shots and 60 shots respectively.

References:

[1] M.M. Finckenor, D. Dooling, *NASA/TP*—1999-209263, April (1999).
[2] F. Dahmani, T Kerdja, *Physical Review A* 44 (1991).
[3] I. Vladoiu, M. Stafe, C. Negutu, I.M. Popescu, *Journal of Optoelectronics and Advanced Materials* 10 (2008)3177.

Competing Noise-Driven Operating Regimes in a Free-Running GHz-rate Actively Harmonic Mode-Locked Fiber Laser

[1,2,#]Dixit Kumar, [1,2]Amol Choudhary, and [1]Vivek Venkataraman
[1]Ultra Fast Optical Communications & High-performance Integrated Photonics (UFO-CHIP) group, [2]Department of Electrical Engineering, IIT Delhi, New Delhi (110016), India

[#]*eez228202@iitd.ac.in*

Two mutually exclusive operating regimes are experimentally demonstrated in a free-running harmonic mode-locked fiber ring laser. Simulations identify competition between cavity supermode fluctuations and ASE induced phase noise as the underlying mechanism, producing either stable temporal pulses or coherent optical frequency combs and providing insight into the free-running laser dynamics.

Actively harmonic mode-locked (AHML) fiber lasers are attractive sources of multi-GHz pulse trains and optical frequency combs (OFCs) owing to their electronic tunability and compact architecture [1-3]. Although cavity stabilization is employed to simultaneously obtain stable pulse trains and coherent OFCs, the behavior of free-running AHML lasers remains of considerable interest for understanding their intrinsic cavity dynamics [1][2]. Here, a free-running AHML fiber ring laser was developed to investigate these dynamics, leading to the observation of two distinct and mutually exclusive operating regimes.

The experimental system comprises a non-polarization-maintaining fiber ring laser employing a C-band Er/Yb-doped fiber amplifier (EYDFA) as the gain medium and a dual-drive Mach-Zehnder modulator (DDMZM) for active mode locking. The cavity free spectral range is ~3.96 MHz, while the DDMZM is driven at the 1578th harmonic (~6.25 GHz) with ~24 dBm RF power. Polarization controllers placed before the DDMZM, and the EYDFA adjust the intracavity operating condition.

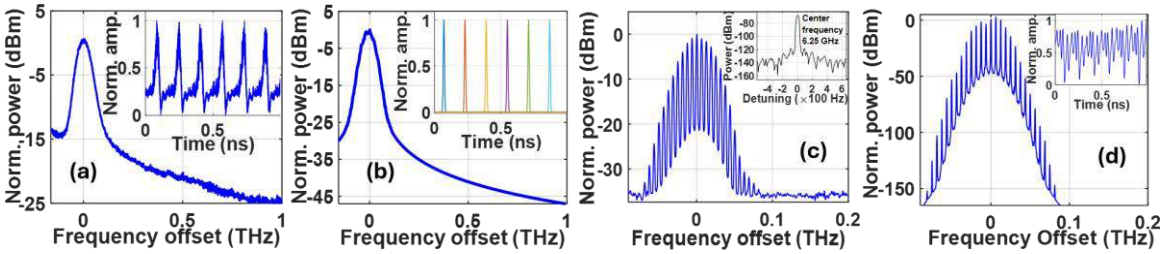


Fig. 1: Experimental output (a) and simulation (b) of the state with temporal pulse train with supermode noise. Experimental output (c) and simulation (d) of the frequency comb state with noisy/chaotic temporal characteristics.

For one polarization setting, the laser generates ~40 ps pulses with a smeared optical spectrum of bandwidth of ~67 GHz (Fig. 1(a)). The RF beat spectrum exhibits pronounced supermode noise, indicating cavity mode hopping [2][4]. For another polarization setting, a coherent OFC is obtained while the temporal waveform becomes unstable. In this regime, supermode noise is suppressed below the noise floor of the electronic spectrum analyzer, and the RF beat note exhibits a resolution-limited linewidth of ~29 Hz (Fig. 1(c)). The experimentally observed operating regimes are explained by simulations through incoherent superposition of cavity supermodes with random temporal phases with gain near the cavity threshold condition (Fig. 1(b)) and by incorporating ASE-induced random spectral phase with random cavity round-trip phase fluctuations in the higher gain beyond threshold (Fig. 1(d)).

The combined experimental and numerical results reveal competing noise mechanisms governing the two-operating state of the free-running laser. Dominant cavity supermode fluctuations preserve stable temporal pulse formation while averaging the optical spectrum through cavity mode hopping. In contrast, dominant ASE-induced phase fluctuations destabilize the pulse train while maintaining mutual coherence among the comb lines, resulting in a coherent OFC. These findings provide new insight into the intrinsic dynamics of free-running AHML fiber lasers and establish useful design guidelines for realizing simultaneously stable pulse trains and high-coherence OFCs through cavity stabilization or optical injection locking.

Acknowledgment: Department of Telecommunications (DoT), India through Advanced Optical Communications Testbed Project.

References:

[1] J. Wu *et al.*, *Journal of Lightwave Technology*, vol. 43, no. 24, pp. 11037-11042, 15 Dec.15, 2025.
[2] D. C. Kirsch, A. Bednyakova, and M. Chernysheva, *Laser Photonics Rev*19, no. 23 (2025).
[3] H. A. Haus, *IEEE Journal of Selected Topics in Quantum Electronics*, vol. 6, no. 6, pp. 1173-1185, Nov.-Dec. 2000.
[4] K. -P. Ho and J. M. Kahn, IEEE Photon. Technol. Lett., 5, 721-725 (1993).

Metal-nanoparticle assisted simultaneous self-assembly and phase change at air-water interface

[1]Mrutyunjaya Rath, and [1,#]Basudev Roy
[1] Department of physics, Indian institute of technology, Madras, Chennai, 600036
[#]*basudev@iitm.ac.in*

Laser light induced heating at air-water interface of a sessile water droplet, drives self-assembly of nanoparticles through convection current. Introducing metal nanoparticles, increases heating thus accelerates self-assembly and inducing solidification of Soft Oxometallate (SOM) dispersions. The resulting structure exhibits birefringence, can simultaneously incorporate micron size particles and mobile in nature.

The self-assembly of materials and nanoparticles has emerged as a powerful strategy for additive manufacturing with unique optical and mechanical properties. At air-water interface, it provides a lithography-free, bottom-up approach to fabricate materials with unique mechanical and anisotropic optical properties. Because of fluid flow, thermophoresis, and Marangoni convection, migration of particles happens and thus self-assembly.

There are studies, where people rely on direct laser heating or using Upconverting particles for the self-assembly[1]. At the same time, people have also showed mesoscopic pattern formation on a glass slide by heating Soft Oxometallate (SOM) solution by moving laser hotspot [2]. Going one step further, this study utilizes gold nanoparticles (Au-NPs) as localized heating agents, leveraging their exceptional stability and tunable plasmonic properties. By optimizing nanoparticle size, surface chemistry, and assembly condition, we elucidate the mechanics of interfacial properties to fabricate structurally birefringent solid masses for applications in photonics, optical sensors, and flexible electronics.

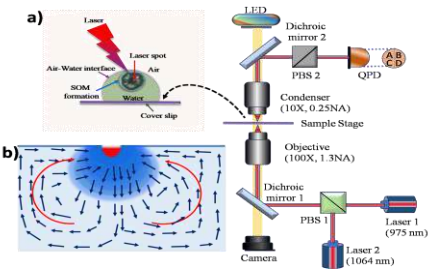


Figure 1: This figure shows the schematic representation of the optical tweezer setup that is used in the experiment. While Fig. 1(a) highlights the magnified picture of SOM formation at the air-water interface in the sample plate, Fig. 1(b) displays the fluid flow due to a temperature gradient in a steady-state condition

In summary, we have demonstrated gold nanoparticle-assisted light-induced self-assembly of mesoscopic materials, resulting in the formation of a stable and floating solid mass at the air–water interface. We used the same technique using UCPs and found out that the rate of formation of solid mass is higher in case of Au-NPs assisted. The solid mass formed using gold nanoparticles remained mobile in nature, floating freely at the air–water interface even after the laser was switched off, indicating that it was not attached to any supporting surface. Furthermore, the assembled structure exhibited signatures of structural birefringence, suggesting an ordered internal arrangement. The mobility and stability of this floating solid mass make it a promising candidate for transport and manipulation using techniques that can be explored in future studies.

We thank the Indian Institute of Technology, Madras, India, for their seed and initiation grants to Basudev Roy. This work was also supported by the DBT/Wellcome Trust India Alliance Fellowship IA/I/20/1/504900 awarded to Basudev Roy.

References:

[1] Goswami, J.; Nalupurackal, G.; Lokesh, M.; Roy, S.; Chakraborty, S.; Bhattacharya, A.; Mahapatra, P. S.; Roy, B. The Journal of Physical Chemistry B (2023), 127, 8487–8495, PMID: 37733383

[2] Roy, B.; Arya, M.; Thomas, P.; J¨urgschat, J. K.; Venkata Rao, K.; Banerjee, A.; Malla Reddy, C.; Roy, S.Langmuir (2013), 29, 14733–14742, PMID: 24171640...

The Effect of CW Laser on Silicon Based Optical Sensor

[#]Kethiri Narsimha Reddy, Sourav Paul, Madhuchhanda Sahu, S Veerabuthiran,
Rahul Kumar, Ajay K Sharma and Jagannath Nayak
Center for High Energy Systems and Sciences, DRDO, Hyderabad, India, 500058.

[#]*n.reddy@gov.in*

High-definition imaging systems with optical sensors are often used for optical surveillance. These systems can be easily disrupted by illuminating the laser. Depending upon the incident fluence, the sensor can be dazzled or damaged. This paper presents an experimental procedure and observations of CW laser irradiance on optical sensors. The aim is to detect the threshold irradiance required to blind and damage the optical sensors.

Recent technical advancements have made optical sensors capable of imaging with magnificent resolution. These cameras are widely used for detection, tracking, identification, inspection and specially for military surveillance. Mostly silicon-based CMOS and CCD cameras are used and operated in visual, NIR and IR regime of spectrum for surveillance. As a consequence, these sensors are highly sensitive to strong laser light irrespective of their wavelength band of operation. CW laser Irradiation of CCD/CMOS systems with sufficient intensity can overflow the well capacity of photodetectors with photoelectrons and degrade the spectral responsivity and detectivity and thereby the signal to noise ratio. If the power density of the incident light beam is exceeding the failure threshold (filling the potential well and clipping the pixels) the sensors get saturated, dazzled or even damaged. When the entire pixels of the sensor are saturated, blinding of sensor occurs and thermal ablation of micro lens, Bayer filters or few forward layers of the silicon substrate in pixels causes damaging [1].

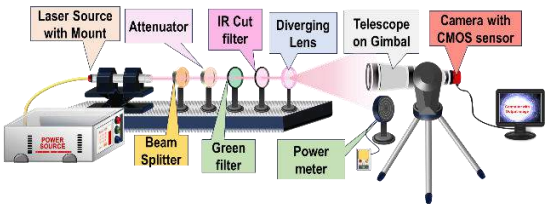


Fig. 1: Optical scheme of experimental setup



Fig. 2: (a) Complete saturation in output image of CMOS, (b) Microscopic image of physical damage on sensor.

A laboratory experiments were conducted as per the scheme shown in Fig. 1. In this experiment, continuous wave (CW) fiber laser (Model: IPG photonics (Pvt. Ltd. 2010)) operating at 1070 nm was used. For regulating the intensity of the incident laser beam, attenuators, green filters and IR cut filter have been used. Power meter is placed to measure the incoming laser beam power. Diverging lens was used to increase the spot size of the laser beam to ensure that it overfills the exit pupil of the Optics which serves as the front-end optics of the camera. ZWO Astro camera (CMOS) ASI224MC was placed about 10 m away from the laser source and was connected to a computer for image acquisition. The telescope focusses the incoming laser beam to a small, intense point on the electronic array of sensor. This intense laser focal spot can blind the underneath and surrounding pixels, increasing the photoelectron current or damage the electronic array by depositing thermal energy (optical heating) depending on the intensity [2]. The variation in power was done by inserting/omitting the optical elements mentioned above from optical path. The captured image or video has the resolution of 1304 × 976 pixels. Analyzing the dazzled area in captured images, the number of pixels dazzled has been deduced.

In Fig 2, it was observed that more that 90% of pixel gets dazzled when the intensity reaches above 23 W/cm^2 on the sensor (Fig.2 (a)). Pixel damaged spot was observed at an intensity of 4 – 5 kW/cm^2 with short (~ ms) exposure time as shown in Fig. 2(b). However, with long exposure time at 2 – 3 kW/cm^2 intensity on the sensor point damage was observed (Fig. 2(b)).

References:

[1] S Veerabuthiran, Sourav Paul, Jagannath Nayak, Optik; Volume 348, 2026, 172698.
[2] J. R. Meyer, M. R. Kruer, F. J. Bartoli, J. Appl. Phys. 51, 5513 (1980).

Realization of Optical Bench for Intersatellite Laser Communication Terminal

#[1]Priyabrata Senapati, [1]Amit Kumar, [1]K A Lohar and [1]Ravikumar Keshavappa
[1]Laboratory for Electro-Optics System (LEOS), ISRO, Bengaluru, Karnataka

#*psenapati@leos.gov.in*

An optical bench for an intersatellite laser communication terminal was designed and experimentally validated for a 2.5 Gbps Geostationary Earth Orbit (GEO) communication link. The integrated transmitter and receiver optics were aligned with an alignment accuracy of 15 arcseconds, demonstrating stable optical performance and validating the system's suitability for future high-speed space-based laser communication missions.

The increasing demand for high-capacity satellite communication has accelerated the development of optical wireless communication systems capable of supporting multi-Gbps data rates. Compared with conventional radio frequency (RF) systems, laser communication provides higher bandwidth, lower size, weight, and power (SWaP), improved security, and better spectral efficiency. Consequently, intersatellite laser communication has become a key technology for next-generation space communication networks, requiring highly precise optical terminals. Laser communication systems rely on several key technologies to establish reliable high-speed optical links. These include Pointing, Acquisition, and Tracking (PAT) systems for accurate beam alignment, advanced modulation and coding techniques for efficient and robust data transmission, and optical and opto-mechanical technologies comprising lasers, collimators, beam splitters, fine steering mirrors, detectors, and precision optical benches for stable beam generation, steering, and reception.

One of the most critical challenges in realizing the optical bench was the design, fabrication, and integration of opto-mechanical mounts capable of catering stringent alignment requirements for spaceborne laser communication. The optical bench is the structural platform of the laser communication terminal, providing a rigid and stable base for integrating the transmitter and receiver collimators, fine steering mirror (FSM), quarter-wave plate, beam splitter, polarizing beam splitter (PBS), and detector Each optical component required a specific mount with required degree-of-freedom to enable sub-arcminute alignment while maintaining high mechanical rigidity and long-term stability. The cumulative effect of machining tolerances, assembly errors, and mounting-induced stresses demanded a highly controlled alignment methodology.

The optical bench alignment was verified through staged optical power measurements during subsystem- and system-level integration using a high-resolution autocollimator and precision plane reflecting targets. Iterative opto-mechanical adjustments compensated for assembly-induced errors, and the measured optical power budget and angular deviation confirmed alignment accuracy better than 15 arcseconds. The developed optical bench demonstrated stable optical performance and high-precision integration, validating its suitability for future intersatellite laser communication systems. The authors acknowledge the support of the development team and technical staff for their contributions to fabrication, alignment, metrology, and system integration.

References:

[1] Hemmati, H. (Ed.). *Deep Space Optical Communications*. Wiley-Interscience, 2006.
[2] Toyoshima, M. “Trends in satellite communications and the role of optical communications.” *Optical Engineering*, 50(9), 091302, 2011.
[3] Kaushal, H., & Kaddoum, G. “Optical communication in space: Challenges and mitigation techniques.” *IEEE Communications Surveys & Tutorials*, 19(1), 57–96, 2017.
[4] Giggenbach, D., & Horwath, J. “Optical inter-satellite communication links.” *Proceedings of SPIE*, Free-Space Laser Communications XIV, 2014.
[5] Bloom, S., et al. “Understanding the performance of free-space optical communication systems.” *Journal of Optical Networking*, 4(7), 178–200, 2005.

Investigation of Damage Morphology in Multilayer Dielectric Mirrors Induced by High-Power Laser Irradiation

Purva Sharnagat*, Arpit Gupta, Deblina Sabui, Basant Kumar, Jasleen Lugani, Gufran S Khan
Centre for Sensors, Instrumentation and Cyber-physical Systems Engineering, IIT Delhi, India
[2]Centre for High Energy Systems and Sciences, Hyderabad, India

idz218511@iitd.ac.in

This study investigates the damage morphology of multilayer dielectric mirrors subjected to 1070 nm continuous-wave laser irradiation. Transient thermal simulations indicate that ppm-level absorption leads to localized heating. Laser-induced damage threshold (LIDT) testing reveals that defects, thermo-mechanical stress, crack propagation, delamination, and catastrophic failures escalate at elevated power densities.

Summary: Multilayer dielectric mirrors are the key components of the high-power laser systems owing to their high reflectivity, low absorption and high laser-induced damage threshold. Despite absorption in the hundreds of parts per million (ppm) range, prolonged exposure to high-power continuous-wave (CW) lasers can induce significant thermal loading, ultimately leading to catastrophic coating failure. Understanding the underlying thermo-optical damage mechanisms is therefore essential for the reliable design and deployment of multilayer dielectric components in high-power laser applications.

In this study, the damage morphology of ion beam sputtered (IBS) highly reflecting multilayer dielectric mirrors is experimentally investigated under CW laser irradiation. LIDT testing utilised a continuous-wave laser at 1070 nm, achieving power densities from tens to hundreds of kW/cm² to study thermally induced damage with increasing energy loading.

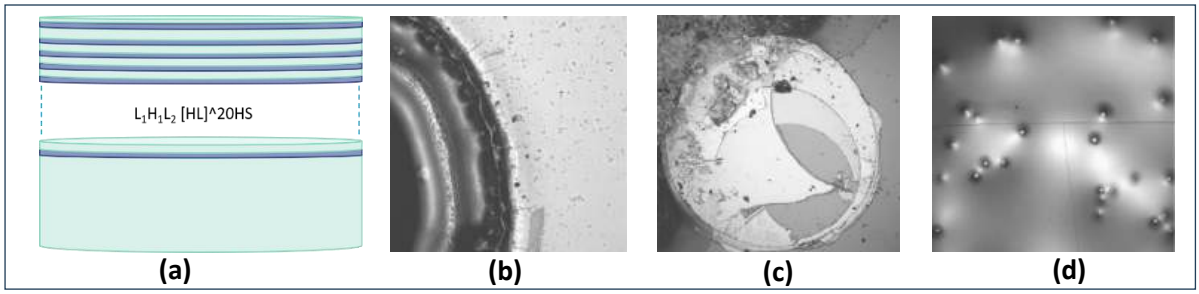


Figure 1 (a) Multilayer dielectric mirror configuration, (b) Peripheral damage and crack formation, (c) Catastrophic delamination, (d) Crack propagation and substrate damage

Transient thermal simulations of the dielectric mirror revealed that the simulated ideal surface did not show any failure, at high incident power densities. In contrast, experimental results indicated a failure threshold significantly lower than that observed in the simulations. Figure 1 presents the progressive damage morphology of the multilayer dielectric mirror under continuous-wave laser irradiation. Figure 1(a) shows the schematic of a multilayer dielectric mirror, and Figure 1(b) illustrates the initiation of damage at the coating, accompanied by localized coating degradation and debris formation. Figure 1(c) exhibits extensive crack propagation and coating delamination due to the accumulation of thermo-mechanical stresses. Figure 1(d) represents catastrophic failure, where the damage extends through the multilayer coating into the fused silica substrate. At this stage, severe crack propagation, substrate crater formation, and blister-like surface features are observed, indicating intense localised heating, substrate softening, and irreversible thermo-mechanical failure caused by sustained high-power laser irradiation.

The study establishes a direct correlation between localised optical absorption, transient heat generation, thermo-mechanical stress development, and the resulting damage morphology. The comparison between simulated thermal behaviour and experimentally observed damage highlights the critical role of non-ideal factors, such as foreign impurities and fabrication defects, in determining the practical laser damage threshold of multilayer dielectric mirrors.

References:

[1] Xia, Jingjing, et al. "Research progress and prospects of laser coating technology." Light: Advanced Manufacturing (2026)
[2] Xu, Jiao, et al. "Continuous-wave laser damage mechanism of a spectral combining grating." *Applied Optics* (2019)
[3] Sharnagat, Purva, et al. "Optical and thermal performance analysis of multilayer dielectric grating as a spectral beam combiner." *Optics & Laser Technology* 196 (2026)

Picosecond Laser Pulse Propagation Through Aerosols Under Atmospheric Conditions

[1] Hasna Sherin K T,[2]Pruthwin P B, and [3 #] P. Prem Kiran
[1,2, 3]School of Physics, University of Hyderabad, Gachibowli, Hyderabad, Telangana, 500046,

[#]*prem@uohyd.ac.in*

Propagation of 30 ps, 532 nm laser pulses through atmospheric-like absorbing and scattering media in liquid and aerosol phases was studied. Spectral and spatial characterization revealed resonance-enhanced Raman scattering, scattering-induced suppression of nonlinear interactions, and increased beam instability in aerosols, improving the understanding of laser propagation through complex atmospheric media.

Laser beam propagation through complex media is important in remote sensing, LIDAR, and free-space optical communication systems [1]. The interaction of short laser pulses with particulate environments can lead to both linear attenuation and nonlinear optical effects, depending on the pulse intensity and medium characteristics [2]. While linear absorption and scattering are well understood [3], [4], the influence of high-intensity picosecond pulses in such media requires further controlled experimental investigation.

In this experiment, 30 ps pulses at 532 nm with 10 Hz repetition rate were propagated through different ink solutions (Red, Blue, and Black) at different concentrations, which serve as absorbing-type media, and different concentrations of NaCl solutions, which serve as scattering-type media, and a mixture of both, in liquid phase as well as in aerosol phase. The pulse energy was varied from 1 mJ to 14 mJ.

The transmitted spectra recorded show clear signatures of nonlinear interaction in the absorbing and scattering media. Stokes peaks were observed in the transmitted spectra; their intensities increased with increasing pulse energy. The Red ink solution exhibited the highest Stokes gain compared to the other ink samples, as shown in **Fig. 1**.

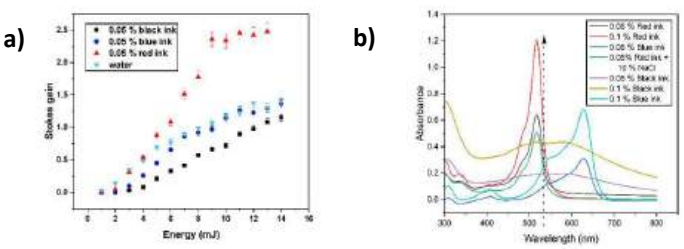


Fig. 1: a) Stokes gain V/S Energy graph for 0.05% Red, Blue, and Black ink solutions b) UV-Visible absorption spectra of samples. The vertical dashed line represents the excitation wavelength of 532 nm.

The enhanced Raman response in red ink is due to resonance between its absorption spectrum and the excitation wavelength of 532 nm [2]. This was further supported by UV-Visible absorption spectrum analysis, which showed that the red ink's absorption peak is strongest near 532 nm.

The addition of NaCl suppressed the Raman signal, indicating that increased scattering limits the effective nonlinear interaction. In the aerosol phase, no distinct Raman features were observed because of the reduced interaction length and lower effective particle density compared to the liquid phase. Aerosol samples exhibited larger beam jitter than the input beam and liquid samples, confirming that scattering by aerosol particles induces fluctuations in beam stability during propagation. These results demonstrate the significant roles of absorption and scattering in governing picosecond laser pulse propagation through atmospheric-like media.

References:

[1] The study can improve the understanding of laser propagation through complex atmospheric media.
[2] R. W. Boyd, Nonlinear Optics, 3rd ed. (Academic Press, New York, 2008).
[3] E. Hecht, Optics, 5th ed. (Pearson, England, 2017).
[4] C. F. Bohren and D. R. Huffman, Absorption and Scattering of Light by Small Particles, 2nd ed. (John Wiley & Sons, New York, 2005).

Laser Power Beaming through Multi-spectral Multi-beam Power Transfer

#Swati Verma, C.K. Joshi, Reshmi Kumari, Arpan Majhi, Shailendra S. Yadav
Instruments Research and Development Establishment
#swativerma.irde@gov.in

***Abstract**: We report a laser wireless power transfer system using multi-spectral, multi-beam laser architecture. This set-up reduces laser thermal management challenges while optimizing receiver recombination. Employing an interconnected silicon array, greater than 5000 mW power was transmitted over a 4.0 meter free-space link for a sustained duration exceeding 10 minutes.*

Introduction: Laser power beaming (LPB) has recently emerged as a promising solution for long range energy harvesting to provide perpetual energy supplies to electronic equipments [1]. It can be transformative in providing continuous power to aerospace platforms, remote sensors, and off-the-grid places and hard to reach disaster encountered areas.

This paper demonstrates a sustainable solution for optical wireless power transfer utilizing a multi-spectral, multi-beam laser system. When single monochromatic laser is incorporated for irradiating the receiver, the thermal load becomes quite high for laser transmitter and also induces localized hot spots on PV receiver [2]. By distributing power across multiple discrete wavelengths, this approach significantly mitigates localized thermal loads by optimizing the spectral matching to the band-gap of a mono-crystalline Silicon photovoltaic (PV) array and stimulates layers at different depths of PV array [3]. This structural distribution besides reducing hot spots also preserves the device's open-circuit voltage (V_{oc}) by throttling the temperature dependent increase in reverse saturation current.

Experimental Set-up: Laser transmitter consisting of four different lasers of wavelengths 808 nm, 885 nm, 976 nm and 1064 nm was aligned in a manner as to illuminate an interconnected 2x2 silicon PV array as shown in the figure 1. The distance between laser transmitter and receiver is 4 m and is constrained by the laboratory spatial restrictions. The PV array is connected to a power connector circuit and a load/ battery. Minimal convectional cooling is done using fans. The laser beam irradiates the PV array and is converted into electrical power, which is then managed by power converter module. The converter can transmit this power either to a load or store it in a battery.

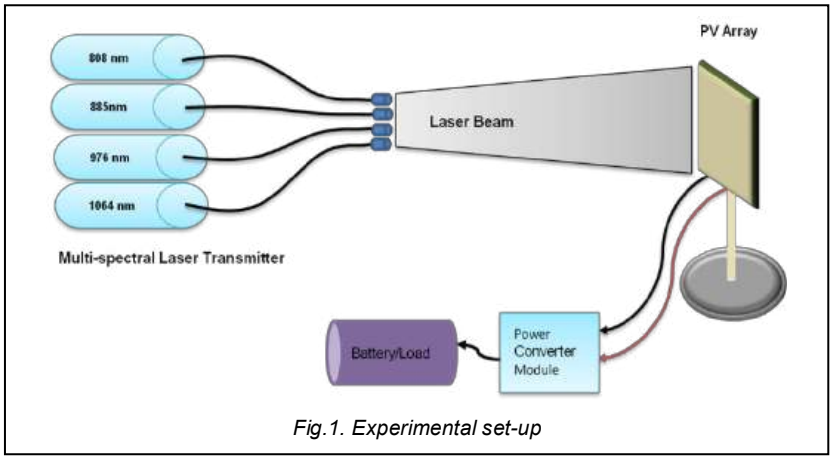


Fig.1. Experimental set-up

Result: This multi-spectral laser architecture was able to generate an output power greater than 5000 mW beamed for a sustained period of more than 10 minutes with laser input power of approx. 50 Watt. The results are depitcted in figure 2. This approach provides a scalable and feasible framework for long range laser wireless power transfer.

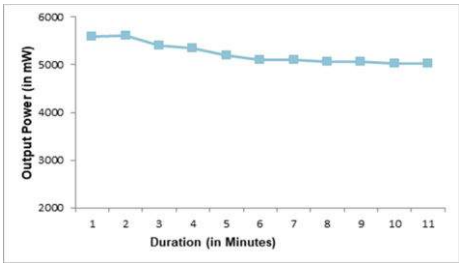


Fig. 2. Output Power measured Vs. Time

References:

[1]L. Sun, J.Kang, Y. Bai, P. Jin, *Photonics*, 1, 12, 30 (2025)
[2] C. Algora, I. Garcia, M. Delgado, R. Pena, C. Vázquez, M. Hinjosa, I. Rey-Stolle, *Joule*, 2, 6, 314-332 (2022)
[3] M.A. Green, *Solar Energy Materials and Solar Cells*,11, 92, 1305-1310 (2008)

Terahertz Antiferromagnetic Resonance Tuning in Zn-Doped NiO via Cationic Doping and Temperature

[#1,2]Khushboo Bishnoi, [1]Aryan Singh Kushwah, [1]Sarang Joshi, [1]Amitkumar Pandey,[1]Parvathy J.P, [1]Sudeep Tiwari and [1]S.S. Prabhu

[1]Department of Condensed Matter Physics and Material Science, Tata Institute of Fundamental Research, Colaba, Mumbai ,400005, India

[2]Department of Applied Physics ,Defence Institute of Advanced Technology, Girinagar ,Pune, 411025, India

[#]*Khushboobishnoi9229@gmail.com*

Zn-doped NiO ($Ni_{1-x}Zn_xO$; x=0, 0.02, 0.04) was investigated for terahertz antiferromagnetic resonance (AFMR) using CW-THz transmission spectroscopy. Zn doping red-shifted the AFMR frequency from 1.004 THz to 0.929 THz and broadened the linewidth, while further softening and damping occurred with rising temperature (313-413 K), demonstrating wide, controllable tunability of AFM dynamics for THz spintronic applications.

Polycrystalline $Ni_{1-x}Zn_xO$ (x = 0, 0.02, 0.04) pellets were synthesized by solid-state reaction and characterized by PXRD with Rietveld refinement (single-phase cubic Fm-3m, Vegard's-law lattice expansion), SEM-EDX, and SQUID ZFC-FC magnetometry confirming antiferromagnetic order near room temperature. Room-temperature CW-THz transmission spectroscopy (0.05-1.2 THz, <10 MHz resolution) was performed after removing Fabry-Perot interference from internal reflections, revealing a clear AFMR absorption dip in every composition.

The AFMR frequency follows the Kittel relation below, with γ the gyromagnetic ratio and H_E, H_A the exchange and anisotropy fields. Since H_E (~1000 T in NiO) H_A, small doping- or temperature-induced changes in either field shift ω_r markedly, placing NiO's AFMR in the THz rather than the GHz range typical of ferromagnets.

$$\omega_r = \gamma\sqrt{(2H_EH_A)} \quad (1)$$

At room temperature, fr decreased monotonically with Zn content: 1003.7(1), 970.7(1) and 928.8(1) GHz for NiO, $Ni_{0.98}Zn_{0.02}O$ and $Ni_{0.96}Zn_{0.04}O$, a ~7.5% redshift for only 4% Zn. Linewidth broadened from 8.1 to 14.3 GHz and Q (=fr/Δf) fell from 123 to 65. These trends reflect non-magnetic Zn^{2+} diluting the Ni^{2+}-O_2--Ni^{2+} superexchange network (lowering H_E) and lattice expansion weakening Ni-O orbital overlap and perturbing H_A.

Temperature-dependent measurements (313-413 K) showed a further, continuous redshift of fr, consistent with reduction of sublattice magnetization and weakening of AFM exchange. Pronounced broadening at 393-413 K reflects enhanced magnon damping via magnon-phonon and two-magnon scattering. Together, doping and temperature give complementary, wide-range control of both AFMR frequency and Q-factor.

This work establishes non-magnetic Zn^{2+} doping, together with temperature, as an effective route to engineer the AFMR frequency and damping of NiO, providing design guidelines for tunable THz antiferromagnetic/magnonic devices for post-5G/6G applications.

References:

[1] V. Baltz, A. Manchon, M. Tsoi, T. Moriyama, T. Ono, Y. Tserkovnyak, *Rev. Mod. Phys.* 90 (2018) 015005.
[2] T. Moriyama, K. Hayashi, K. Yamada, M. Shima, Y. Ohya, T. Ono, *Phys. Rev. Mater.* 4 (2020) 074402.
[3] K. Nawa, A. Gumarilang, T. Moriyama, K. Nakamura, *Phys. Rev. Appl.* 21 (2024) 034040.

THz Plasmonic Photoconductive Antennas on Semi-Insulating and Ion-Implanted GaAs: Fabrication and Characterisation

[1,3,#]Parvathy J P, [1,3]Aryansingh H. Kushwah, [1]Sarang Joshi, [1]Khushboo Bishnoi, [2]Nilesh Mhatre, [1]Sudeep Tiwari, [2]Deepankar Mishra, and [1]S.S Prabhu

[1]Department of Condensed Matter Physics and Material Science, Tata Institute of Fundamental Research, Colaba, Mumbai, 400005

[2]Department of Nuclear and Atomic Physics, Tata Institute of Fundamental Research, Colaba, Mumbai, 400005

[3] Department of Physics, Indian Institute of Science Education and Research Berhampur, Odisha, 760003

[#]*parvathyjp05@gmail.com*

This study investigates THz signal generation in plasmonic photoconductive antennas fabricated on semi-insulating and ion-implanted GaAs. The influence of ion implantation on THz emission was evaluated through output amplitude and bandwidth, highlighting the role of defect engineering in enhancing PCA performance.

Photoconduction is one of the most widely used techniques for generating pulsed terahertz (THz) radiation. In a photoconductive antenna (PCA), an ultrafast optical pulse excites charge carriers in a biased semiconductor substrate, producing a transient photocurrent that emits THz radiation. The carrier dynamics of the substrate strongly influence the amplitude, bandwidth, and overall performance of the emitted THz pulse.

The performance of PCAs can be tailored through substrate engineering. Ion implantation introduces defect states that act as carrier-capture and non-radiative recombination centres, modifying the carrier lifetime and electric-field distribution within the photoconductor. These changes influence the characteristics of the generated THz radiation and provide a route for optimizing device performance [1,2].

In this work, plasmonic and conventional bowtie photoconductive antennas with a 15 µm electrode gap were fabricated on semi-insulating GaAs using electron beam lithography. The devices were subsequently subjected to ion implantation to engineer defects within the substrate. THz emission spectroscopy was performed using an 800 nm femtosecond laser under varying optical pump powers and bias voltages. Time-domain THz waveforms were recorded and transformed to the frequency domain using fast Fourier transform (FFT) to evaluate the emission characteristics. A comparative analysis of the fabricated devices was carried out to investigate the influence of plasmonic enhancement and defect engineering on THz emission performance.

References:

[1] N.M. Burford, M.O. El-Shenawee, Optical Engineering 56 (2017) 010901.
[2] M. Tonouchi, Nature Photonics 1 (2007) 97–105.

Fabrication, Characterization, and Comparative Study of Unimplanted and Ion Implanted GaAs-Based Terahertz Photoconductive Antennas

[#1,3]Aryansingh H. Kushwah,[1,3]Parvathy J P, [1]Sudeep Tiwari, [1]Khushboo Bishnoi, [1]Sarang Joshi, [2]Nilesh Mhatre, [2]Deepankar Mishra and [1]S.S Prabhu

[1]Department of Condensed Matter Physics and Material Science, Tata Institute of Fundamental Research, Colaba, Mumbai, 400005, India
[2]Department of Nuclear and Atomic Physics, Tata Institute of Fundamental Research, Colaba, Mumbai, 400005, India
[3]Department of Physics, Indian Institute of Science Education and Research Berhampur, Odisha, 760003
[#]*Kushwah21@iiserbpr.ac.in, aryanthe01@gmail.com*

GaAs-based bowtie terahertz photoconductive antennas were fabricated and characterized before and after ion implantation. The influence of implantation on THz emission performance was evaluated by comparing output amplitude, bandwidth, and signal quality. The study highlights the trade-offs introduced by defect engineering for optimizing photoconductive THz sources.

Terahertz (THz) photoconductive antennas (PCAs) are widely used for broadband THz generation owing to their coherent and time-resolved operation. Their performance is strongly influenced by the carrier dynamics of the photoconductive material, making defect engineering an effective approach for performance optimization [1,2]. In this work, GaAs-based bowtie photoconductive antennas were designed, fabricated, and experimentally characterized. Controlled defect engineering was employed to tailor the carrier recombination dynamics through ion implantation. The devices were characterized using a THz emission setup, where an ~800 nm femtosecond laser was used as the optical pump to generate broadband THz radiation from the photoconductive antenna. The same laser wavelength was used as the probe, and THz detection was performed using electro-optic sampling. A comparative study was carried out between unimplanted and ion-implanted devices by analyzing their time- and frequency-domain THz responses under different optical excitation powers and applied bias voltages. Key performance parameters, including THz emission amplitude, spectral bandwidth, temporal response, signal-to-noise ratio, and saturation behaviour, were investigated to understand the influence of defect engineering on the performance of GaAs-based photoconductive antennas.

References:

[1] N.M. Burford, M.O. El-Shenawee, *Optical Engineering* 56 (2017) 010901.

[2] M. Tonouchi, *Nature Photonics* 1 (2007) 97–105.

Dual-Resonant Graphene Split-Ring Metamaterial for Terahertz Refractive Index Sensing

[1, #]Shakti Mahato, [1]Himanshi Saini, [1,2]Vipul Rastogi
[1]Department of Physics, Indian Institute of Technology Roorkee, INDIA 247667
[2]Centre for Photonics and Quantum Communication Technology, Indian Institute of Technology, Roorkee, Uttarakhand, INDIA 247667

[#]*sp_mahato@ph.iitr.ac.in*

In this work, a dual-resonant terahertz (THz) refractive index (RI) sensor based on a graphene split-ring structure is proposed. The proposed sensor achieves a maximum sensitivity of 1611.4 (GHz/RIU) and a figure of merit (FoM) of 6.44 RIU^{-1}, respectively.

Terahertz (THz) radiation has gained significant interest in recent years because of its unique electromagnetic characteristics, including non-ionising nature and ability to probe material-specific spectral signatures. Consequently, THz devices have been extensively explored for sensing, switching, imaging, detection, and spectroscopic applications [1]. Various metamaterial (MM) structures have the advantage of narrowband responses and higher sensitivity. For more accurate measurements and sensitive applications, it is better to use multi-band absorption [2]. Graphene has emerged as one of the most promising materials for terahertz (THz) applications owing to its exceptional electromagnetic, optical, chemical, and mechanical properties. Moreover, it exhibits low optical loss and strong field confinement in the THz regime, which can help to improve the detection efficiency and sensitivity of the sensor [3].

The proposed design is a periodic structure, and the schematic of the unit cell is shown in Fig. 1(a). Silica (SiO_2) layer of permittivity 3.9 placed on top of the gold reflector. A Graphene layer is placed on the silica in the shape of a split ring. Figure 1(b) shows the reflection spectra obtained from COMSOL Multiphysics simulations for various refractive index (RI) values (n_a) of the test analyte. Here, we observe two resonance dips in the reflectance spectra at 4.1 THz and 7.55 THz for n_a=1. At 4.1 THz, the electric field is strongly confined within the split gaps of the graphene ring. This field enhancement results from the accumulation of opposite-polarity charge at the gap edges, producing a capacitive response and indicating the excitation of graphene plasmons. The higher-frequency resonance at 7.55 THz originates from a higher-order plasmonic mode, where the electric field extends along the ring boundaries in addition to the split gaps.

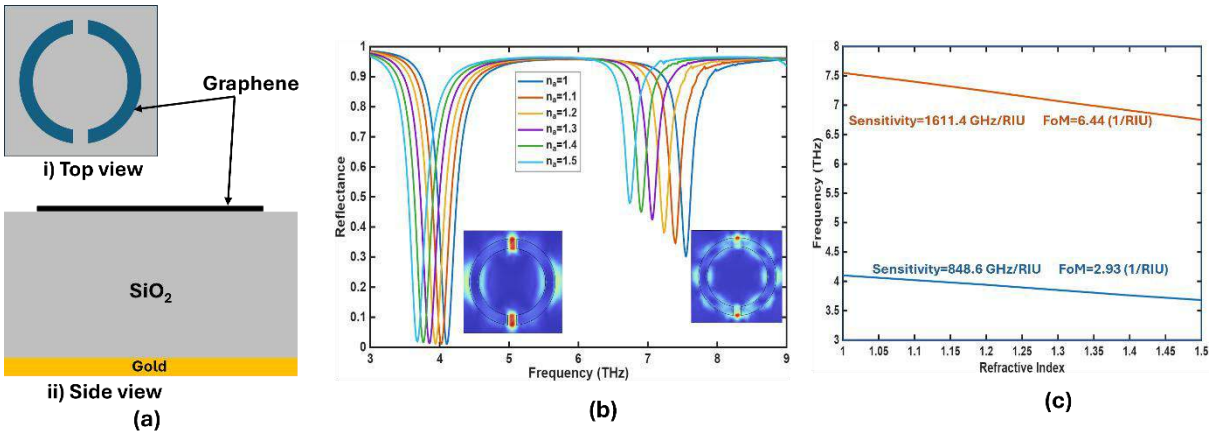


Fig. 1: (a) Schematic of the top and side view of the unit cell. (b) The reflectance spectrum when RI changes from 1 to 1.5. and (c) Variations of the resonance frequencies with changing RI.

Figure 1(c) shows the variation of resonance frequencies with changing RI, yielding sensitivity values of 848.6 GHz/RIU and 1611.4 GHz/RIU for the two modes. Based on the simulated performances, the designed sensor is a good candidate for medical and biosensing applications.

References:

[1] S. Ghafari, M.R. Forouzeshfard, Z. Vafapour, *IEEE Sensors J*. 20 (6) (2019) 3235–3241.
[2] X. Liu, G. Liu, P. Tang, G. Fu, G. Du, Q. Chen, et al., *Carbon* 140 (2018) 362–367.
[3] Z. Vafapour, H. Ghahraloud, A. Keshavarz, et al, *IEEE Sensors J*. 21 (12) (2021) 13786–13793.

A High Resolution Switchable and Tunable Microwave Photonic Multi-Notch Filter

[1,#]Neha Ahlawat, [2]Bhavisha Daryani and [3]Ravi Pant
Laboratory for Phoxonics and Nonlinear Optics in Nanostructures (PHONON), School of Physics, Indian Institute of Science Education and Research (IISER), Thiruvananthapuram, Kerala, 695551

[#]*neha23@iisertvm.ac.in*

Agile-frequency radar systems, Bluetooth, and other wireless communication systems require rapid switching among multiple carrier frequencies. In this work, we propose a multi-frequency switch based on coherent Brillouin interactions in the radio-frequency (RF) domain.

Microwave Photonic Notch Filters (MWPNFs), because of their various applications, are crucial components in RF signal processing. Although single-notch MWPNFs, including those based on Brillouin interactions, have been extensively investigated [1], [2], experimental demonstrations of multi-frequency MWPNFs remain limited [3]. However, multi-notch filters with switching capability enable applications such as frequency hopping, agile radar systems, and the simultaneous suppression of multiple interfering signals. Here, we demonstrate a switchable, high-resolution (on the order of tens of MHz), multi-notch filter based on coherent Brillouin interactions.

The experimental setup used to validate the proposed concept is shown in Fig. 1(a), employing a conventional pump–probe configuration. In the probe arm, an intensity modulator (IM) was used to control the phase difference between the Stokes and anti-Stokes sidebands. In the pump arm, the optical carrier was modulated to generate multiple pump tones, which were amplified and launched into a 50 m long polarization-maintaining (PM) fiber for stimulated Brillouin scattering (SBS). The backscattered signal was detected using a vector network analyzer (VNA), enabling characterization frequency response of notch filter. The operating principle of the proposed filter is illustrated through simulations in Fig. 1(b), which shows the amplitude response with multiple crossings along with the corresponding frequency response. A phase difference of 180° was introduced between the Stokes and anti-Stokes components to achieve destructive interference, resulting in a notch filter response. By varying the IM bias voltage, the notch frequencies can be switched, as shown by the blue and grey curves in Fig. 1(b,c,d). The measured frequency response demonstrating the switchable single-notch filtering operation is presented in Fig. 1(c). The response shows resolution of 8 MHz by tuning the bias voltage applied to IM. The same concept was implemented to multi-frequency notch by modulating the pump and the corresponding frequency response is shown in Fig. 1(d).

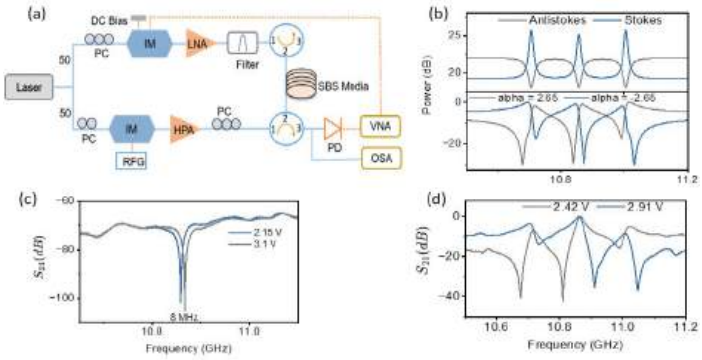


Fig. 1: (a) Experimental setup for demonstration of proposed filter. (b) Experimentally measured frequency response showing switchable single notch filter. (c) Simulated amplitude and frequency response for modulated pump (with frequency of 150MHz) showing multiple notches. (d) Measured frequency response of the proposed multi-notch switchable filter, showing agreement with the simulated response.

In conclusion, we have demonstrated a switchable multi-notch microwave photonic filter based on stimulated Brillouin scattering. Since on-chip stimulated Brillouin scattering has already been demonstrated [4], the proposed filter can be readily extended to integrated photonic platforms, paving the way for compact microwave photonic systems.

References:

[1] Ge, J., & Fok, M. P. (2015). Scientific reports, 5(1), 17263.
[2] Shakthi, S. A., Varun, M. K., & Pant, R. (2021). IEEE Journal of Selected Topics in Quantum Electronics, 27(6), 1-13.
[3] Garrett, M., Liu, Y., Merklein, M., Choi, D. Y., Yan, K., Madden, S. J., & Eggleton, B. J. (2021). Journal of Lightwave Technology, 40(6), 1672-1680.
[4] R. Pant, C. G. Poulton, D.-Y. Choi, H. Mcfarlane, S. Hile, E. Li, L. Thevenaz, B. Luther-Davies, S. J. Madden, and B. J. Eggleton, Optics express, vol. 19, no. 9, pp.8285–8290, 2011.

High-Q Terahertz Electromagnetically Induced Transparency in Silicon Metamaterials

[1,2] Shivansh Sharma,[2] Prof. Prem Pal and [1,#] Dr. Yogesh Kumar Srivastava
[1] Ultrafast Terahertz Photonics Laboratory, Department of Physics, Indian Institute of Technology Hyderabad, Kandi, Sangareddy 502284, India
[2] MEMS & Micro/Nano Systems Laboratory, Department of Physics, Indian Institute of Technology Hyderabad, Kandi, Sangareddy 502284, India

[#]*yogesh.srivastava@phy.iith.ac.in*

This work demonstrates electromagnetically induced transparency (EIT) phenomenon using an all-silicon-based metamaterial. The dielectric resonators enable excellent loss engineering by suppressing ohmic losses, resulting in a high-quality factor (Q) and enhanced group delay in the THz regime. Furthermore, the all-silicon platform simplifies fabrication, making it promising for practical THz photonic applications.

Electromagnetically Induced Transparency (EIT) is a quantum interference phenomenon arising from the interaction between a bright mode and a dark mode. Its classical analogue can be realized in metamaterials, where metallic split ring resonators (SRRs) [1] based metamaterials have previously demonstrated EIT-like responses over a broad frequency range. However, metallic metamaterials suffer from significant ohmic losses, limiting the achievable Q-factor and group delay. All-dielectric metamaterials [2], [3] overcome these limitations by reducing dissipative losses, enabling high-Q resonances and enhanced slow-light effects.

In this work, an all-silicon membrane metamaterial operating in the THz regime is proposed and demonstrated. The device exhibits a high Q-factor and a nanosecond order group delay. The use of a single-material silicon platform simplifies fabrication and ensures excellent process control through mature silicon microfabrication technology.

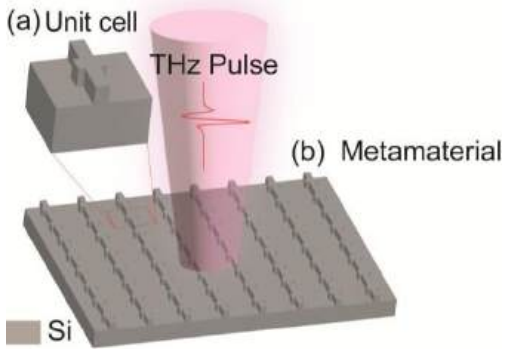


Figure 1. Schematic illustration of the proposed silicon (Si) metamaterial. (a) unit cell (b) all Si membrane type metamaterial illuminated by a normally incident terahertz (THz) pulse.

Figure 1 illustrates the schematic of the unit cell and the corresponding all-dielectric silicon metamaterial array exhibiting an EIT response.

EIT response in the proposed metamaterial originates from the near-field coupling between a directly excited bright mode and an indirectly excited dark mode, as verified using the coupled harmonic oscillator model [2]. By employing loss engineering in an all-silicon metamaterial platform, we achieve a high-Q EIT resonance with a quality factor of approximately 3000, accompanied by a group delay of about 2 ns, demonstrating significant slow-light performance. The proposed design provides a promising route toward low-loss THz devices for slow-light, filtering, sensing, and integrated photonic applications.

References:

[1] R. G. Meher, S. Sharma, Mikhila M, G. Dayal, Y. K. Srivastava *J. Appl. Phys.* 28 October 2025; 138 (16): 163106.
[2] Yang, Y., Kravchenko, I., Briggs, D. *et al. Nat Commun* **5**, 5753 (2014).
[3] Tian Ma, Qiuping Huang, Hongchuan He, Yi Zhao, XIaoxia Lin, and Yalin Lu, Opt. Express 27, 16624-16634 (2019).

A WDM-RoF Framework for Hybrid Wired-Wireless Networks

[1,2#]Shruti,[2,3]Abhishek Dixit and [1,2,3]Amol Choudhary
[1]Ultrafast Optical Communications and High-performance Integrated Photonics (UFO-CHIP)
[2]Bharti School of Telecommunication Technology and Management
[3]Department of Electrical Engineering, Indian Institute of Technology (IIT) Delhi, India
[#]*shruti@dbst.iitd.ac.in*

We present a WDM-RoF framework based on a hardware-efficient hybrid modulation scheme, which simultaneously transmits an RF and a baseband signal on each WDM channel. The performance is evaluated through the simulation and experimental setups for a two-channel WDM-RoF link.

Integrated wired-wireless optical links support simultaneous transmission of baseband and RF signals over a shared fiber infrastructure, while wavelength-division multiplexing(WDM)-radio-over-fiber (RoF) further improves link utilization [1-2]. We present a WDM-RoF framework that employs a hybrid modulation scheme in which each optical carrier is sequentially modulated by baseband and RF signals, requiring only one additional MZM in a conventional intensity-modulation direct-detection (IMDD) link. The baseband and RF signals on each channel are recovered using a single photodetector (PD), with baseband-RF beat interference mitigated through a simple subtraction-based technique [3].

Fig. 1(a) illustrates the proposed WDM-RoF system and corresponding spectra at various stages of the link. We experimentally demonstrate a two-channel WDM link employing ITU-grid channels H35 (193.55 THz) and C35 (193.50 THz), generated using continuous wave (CW) lasers. Each channel is modulated by baseband and RF signals using cascaded Mach-Zehnder modulators (M1 and M2). The resulting wired-wireless signals are multiplexed using an arrayed waveguide grating (AWG), transmitted over a standard single-mode fiber (SSMF), demultiplexed using a second AWG, and detected using one PD per WDM channel. The baseband signal is extracted using a low-pass filter (LPF-1), the RF signal is demodulated using coherent detection, and the impact of baseband-RF signal beating on the RF signal is mitigated. Due to hardware limitations, the experiment is conducted at a data rate of 500 Mbps per signal, with an RF carrier at 3 GHz each, and 10^4 bits are transmitted per signal. The BER is evaluated using bit-to-bit comparison, resulting in a minimum measurable BER of zero/10^{-4} for no/one error.

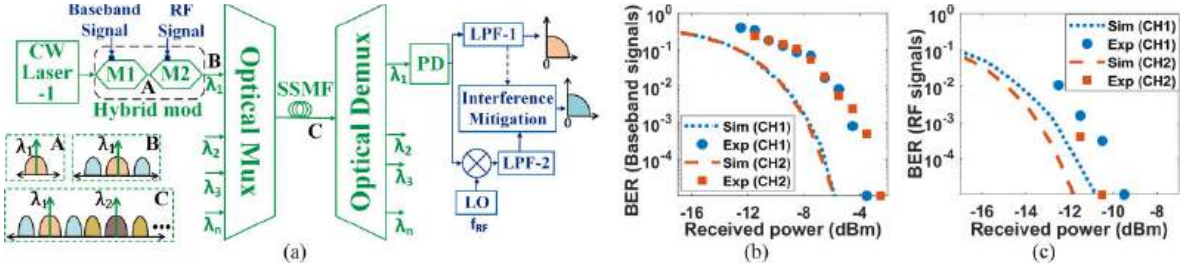


Fig. 1: (a) Principle of the WDM-RoF framework using hybrid modulation scheme, Simulation and experimental results for variation of BER with power received on PD, for (b) baseband signals, and (c) RF signals. M1, M2: Mach-Zehnder Modulators, SSMF: standard single-mode fiber, PD: photodetector, LO: local oscillator, LPF: low-pass filter.

The experimental results are obtained for optical powers of -3 dBm to 6 dBm launched into a 10 km fiber, resulting in received powers of -12.5 to -3.5 dBm at channel-1 PD, and -11.5 dBm to -2.5 dBm at channel-2 PD. Figs. 1(b) and 1(c) show that the experimental results follow the simulation results with ~2 dB penalty at a BER of 10^{-4}, attributed to imperfections in experimental components, cables, and connectors, that are not fully accounted for in simulations. For baseband signals, a BER of 10^{-4} is achieved at received powers of -3.5 dBm and -2.5 dBm at CH1 and CH2, respectively. For RF signals, a BER of 10^{-4} is obtained at -9.5 dBm and -10.5 dBm, respectively. The slight variation across the WDM channels is due to the wavelength dependence of optical components and fiber impairments. The results validate the proposed WDM-RoF setup, which can be extended to mmWave signal transport using high-bandwidth components, making it suitable for 5G and beyond networks.

Acknowledgment: Department of Telecommunications (DoT), India, through Advanced Optical Communications Testbed Project.

References:

[1] L. Li et al.," IEEE Journal of Lightwave Technology 39(5), 1278-1288 (2021).
[2] G. Pandey, A. Choudhary, and A. Dixit, IEEE Journal on Selected Areas in Communications 39(9), 2789–2803 (2021).
[3] S. Shruti, R. Dhawan, A. Choudhary, A. Dixit, Optical Fiber Technology 94, 104368 (2025).

Effect of Length and Conductivity of PCM VO_2 on the Performance of the On-Chip Guided Wave THz Modulator

Ram Ashish Yadav[1], Geert Morthier[2], and Rajesh Kumar[1,3,#]
[1]Department of Physics, Indian Institute of Technology Roorkee, Uttarakhand 247667, India.
[2]Photonics Research Group, Department of Information Technology (INTEC) Ghent University–imec, Ghent 9052, Belgium.
[3]Centre for Photonics and Quantum Communication Technology, Indian Institute of Technology Roorkee, Roorkee, Uttarakhand 247667, India.
[#]rajesh.kumar@ph.iitr.ac.

Along with variations in the length of PCM VO_2, the contrasting change in IMT-induced conductivity of VO_2 determines the THz modulator's output transmission. This manuscript investigates the effects of PCM VO_2 length and conductivity on electromagnetic performance of a VO_2-based on-chip THz modulator operating in the 0.5-0.6 THz frequency range.

Phase change material Vanadium dioxide (VO_2) has recently been widely used to design absorbers and THz modulators operating across the visible-to-THz frequency range [1-2]. A recently reported on-chip guided-wave THz modulator that utilizes the volatile phase-change property of VO_2 has been reported [1]. The schematic of the modulator integrating PCM VO_2 on top of the dielectric THz waveguide is presented in Fig. 1(a). Using frequency-dependent transmission of modulator for insulating ($T_{High(\omega)}$) and metallic ($T_{Low(\omega)}$) phases of VO_2, the modulation depth (MD =[($T_{High(\omega)}$−$T_{Low(\omega)}$)/ $T_{High(\omega)}$] ×100%) and the insertion loss (IL = −10 × log ($T_{High(\omega)}$) dB) of the modulator are evaluated. A change in dielectric permittivity with conductivity, as well as the physical dimensions of the VO_2, primarily determines the values of $T_{High(\omega)}$ and $T_{Low(\omega)}$. The present study investigates the effect of the structural phase transformation and the physical dimension (length) of VO_2 on the MD and IL of the proposed modulator.

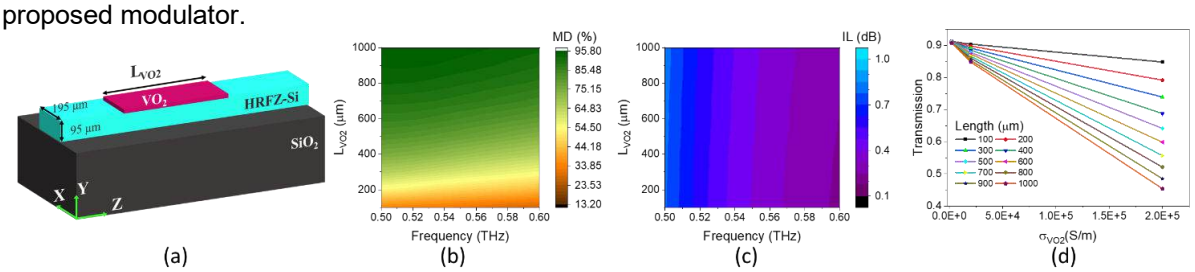


Fig.1: (a) Schematic of proposed THz modulator. (b) Modulation depth and (c) Insertion loss of the modulator as a function of VO_2 length. (d) The transmission of the modulator as a function of the conductivity of VO_2 for its various lengths. The width and thickness of VO_2 are 195 μm × 0.150 μm.

The variation in the MD and IL of the modulator with VO_2 length at a fixed width and thickness of 195 μm × 150 nm is shown in Fig. 1(b) and Fig. 1(c), respectively. For a 1000 μm long VO_2, the modulator exhibits an almost uniform MD of more than 90% with an IL of less than 1 dB. The transmission of the modulator with VO_2 conductivity at various lengths is shown in Fig. 1(d). As the length and conductivity of VO_2 increase, the modulator's transmission decreases significantly. The interaction between the guided THz wave and the lossy VO_2 increases with the length of the VO_2, thereby increasing the absorption of the guided THz wave and decreasing the modulator's transmission, thereby increasing the MD. For the insulating phase of VO_2, the imaginary part of its dielectric permittivity is quite low, which results in an IL of less than 1 dB. Furthermore, for a fixed length and thickness of VO_2, the imaginary part of the dielectric permittivity of VO_2 increases with its conductivity. These material characteristics translate into the modulator's transmission characteristics shown in Fig. 1(d).

Acknowledgment: DST, India (DST/QTC/NQM/QMD/2024/4); MOE, India (GIAN program (IIT/GIAN/S-18/1465)); SERB, India (CRG/2023/001094).

References:

[1] T. Xu, W. Zhang, Q. Song, Z. Yi, C. Ma, et al., Thermotunable mid-infrared metamaterial absorption material based on combined hollow cylindrical VO_2 structure, Surfaces and Interfaces 52, 104868 (2024).
[2] Y. Wang, Y. Chen, F. Liu, L. Chen, K. Ji, X. Wang, X. Ji., Vanadium dioxide enabled polarization insensitive tunable broadband terahertz metamaterial absorber, Scientific Reports 15, 10140 (2025).
[3] R. A. Yadav, V.B. Palekar, G. Morthier, R. Kumar, Electro-thermally driven vanadium dioxide based guided wave THz modulator, Advanced Theory and Simulations 9, e01200 (2026).

Engineering a Quartz-Supported Terahertz Gold Nano rod Metasurface for Enhanced Refractive Index Sensing

[1#]Sapana Yadav, [1]Parinda Vasa

[1]Department of Physics, Indian Institute of Technology Bombay, Mumbai 400076, India

*Email: yadavphysapana8@gmail.com (Sapana Yadav), parinda@iitb.ac.in (Parinda Vasa)

In this work, a gold nanorod Metasurface fabricated on a quartz substrate is numerically investigated for refractive index sensing. The resonance frequency exhibits systematic shifts with variations in analyte refractive index. The proposed design demonstrates highest sensitivity with a resonance linewidth (FWHM) indicating its potential for THz dielectric sensing.

The terahertz spectral region offers significant opportunities for non-invasive detection of biological and chemical materials owing to their characteristic dielectric properties [1]. Metasurfaces provide an effective platform for enhancing light–matter interaction through localized electromagnetic fields confined around subwavelength resonators. In this study, a periodic array of gold nanorods on a quartz substrate is designed and analyzed as a refractive index sensor in the THz regime.

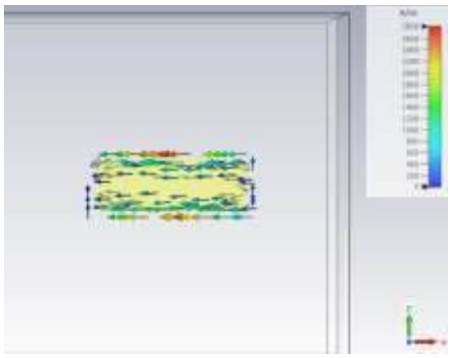


Fig. 1: Surface Current Distribution

Numerical simulations are carried out using CST Studio Suite with periodic boundary conditions over the frequency range of THz. Variations in analyte refractive index produce measurable shifts in the transmission resonance, which form the basis of the sensing mechanism [2].

The optimized metasurface exhibits a highest sensitivity and corresponding to an estimated figure of merit of ~0.34 RIU^{-1}. Electric-field analysis shows that the resonant field is strongly localized near the edges of the gold nanorods, leading to enhanced interaction with the surrounding analyte and enabling reliable refractive index detection [3].

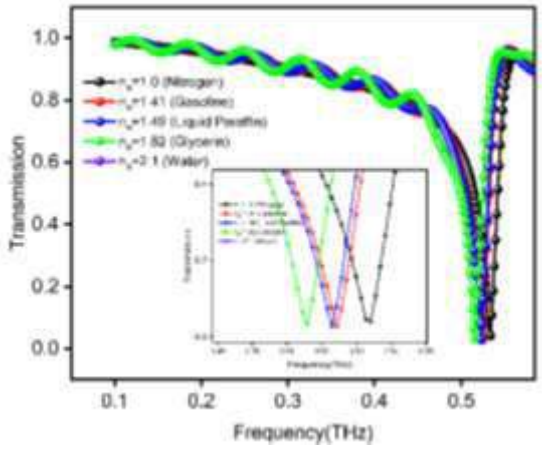


Fig. 2: Transmission spectrum corresponding to different RI

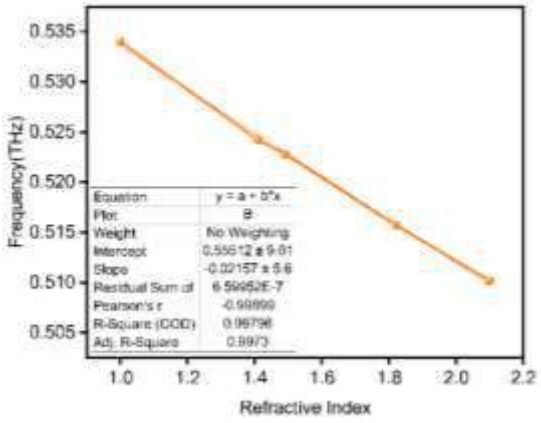


Fig. 3: Fitting relationship between resonance freq and RI

References:

[1] Dongxu Wang, Kai-Da Xu, Siyuan Luo, Yuqing Cui, Liuyang Zhang, Jianlei Cui; *Nanoscale* 2023; 15 (7): 3398–3407.

[2] Xin Tang, Haoduo Jia, Lanbin Li, Ming Li, Dai Wu, Kui Zhou, Peng Li, Weijun Wang, Jitao Li, and Dingyu Yang, *Photon. Res*. 12, 1574-1582 (2024).

[3] Zarrabi, F.B., Islam, M.T., Alenezi, A.M. and Soliman, M.S., 2026, *Ain Shams Engineering Journal*, 17(1), p.103832.

Terahertz Investigation of Tunable Natural Ferromagnetic Resonance in Rare Earth Substituted $CoFe_2O_4$

[#]Amitkumar D. Pandey, Sarang Joshi, Sudeep Tiwari, S. S. Prabhu
Tata Institute of Fundamental Research, Mumbai, India

[#]*pandeyamitkumar0207@gmail.com*

$CoFe_2O_4$ exhibits strong magnetocrystalline anisotropy, making it an excellent platform for probing sub-THz spin dynamics. Temperature-dependent terahertz time-domain spectroscopy reveals systematic tuning of natural ferromagnetic resonance through Nd^{3+} substitution at the Fe^{3+} site, demonstrating cation-engineered control of magnetic anisotropy and exchange interactions for field-free THz spintronic and magnonic applications.

The is a hard ferrimagnetic spinel oxide possessing large magnetocrystalline anisotropy, moderate saturation magnetization, and excellent chemical stability, making it attractive for high-frequency spintronic and magnonic devices [1]. Among its low-energy magnetic excitations, natural ferromagnetic resonance (NFMR), which originates from intrinsic magnetic anisotropy without the application of an external magnetic field, is particularly attractive for realizing field-free THz functionalities [2]. Although theoretical considerations predict NFMR in CFO within the sub-THz regime at low temperatures, experimental investigations remain limited [3]. In the present work, pure and Nd-substituted $CoFe_2O_4$ samples containing 2% and 5% Nd at the Fe site (CFN2 and CFN5) are investigated to understand the influence of rare-earth substitution on sub-THz spin dynamics.

Temperature-dependent terahertz time-domain spectroscopy measurements were performed between 40 and 200 K. Distinct absorption resonances emerge below approximately 180 K in all samples. The transmission contour maps (Fig. 1) reveal well-defined NFMR modes within the 0.25–0.45 THz frequency range. At 40 K, the resonance frequencies are approximately 0.44 THz, 0.40 THz, and 0.29 THz for CFO, CFN2, and CFN5, respectively. Upon increasing temperature, the resonance frequencies progressively soften to approximately 0.18 THz, 0.13 THz, and 0.12 THz, accompanied by linewidth broadening arising from enhanced thermal spin fluctuations and magnon–phonon interactions. The systematic reduction of resonance frequency with temperature reflects the weakening of magnetocrystalline anisotropy, while Nd^{3+} substitution provides an effective means of tailoring both anisotropy and exchange interactions, thereby enabling controlled tuning of the NFMR.

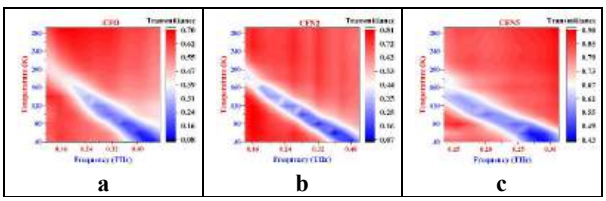


Fig. 1: *Transmission plot CFO, CFN2 and CFN5*

The experimental observations are further supported by temperature-dependent magnetization measurements and quantitative modeling using the Brukhatov–Kirensky description of magnetocrystalline anisotropy. The combined experimental and analytical results establish rare-earth cation substitution as an effective strategy for engineering field-free sub-THz magnetic excitations in cobalt ferrite, highlighting its potential for tunable THz spintronic and magnonic devices.

S. S. Prabhu acknowledges financial support from the Department of Atomic Energy, Government of India, under Project Identification No. RTI4003.

References:

[1] K. Pradhan, D. Chemate, V. Parkar, S. Haldankar, S. Prabhu, S. Shukla, S. P. Duttagupta, *MRS Advances* **9** (2024) 929–935.
[2] E. A. Gorbachev, M. V. Soshnikov, L. N. Alyabyeva, E. S. Kozlyakova, A. S. Fortuna, A. Ahmed, R. D. Svetogorov, L. A. Trusov, *Physics of the Solid State* **63** (2021) 99–107.
[3] S. Joshi, A. Pandey, P. J. P. Parvathy, A. Kushwah, A. Mondal, S. S. Meena, S. Tiwari, S. S. Prabhu, *Journal of Infrared, Millimeter, and Terahertz Waves*, under review.

In-situ SERS detection of gaseous benzaldehyde: A prospective breath analysis method

[1]Mahadeva Prasad KS, [2]Aswini Kumar Mohapatra and [1#]Aseefhali Bankapur

[1]Manipal Institute of Applied Physics, Manipal Academy of Higher Education, Manipal, 576104, India

[2]Department of Respiratory Medicine, Kasturba Medical College, Manipal Academy of Higher Education, Manipal 576104

[#]asif.bankapur@manipal.edu

Breath analysis is a non-invasive diagnostic approach for detecting potential lung cancer biomarkers, like benzaldehyde. Although SERS can detect trace levels of benzaldehyde, the substrates pose limitations. We report an in-situ approach for simultaneous sampling and SERS detection of gaseous BA in colloidal solutions, achieving detection sensitivity of 4.95 ppb.

Human exhaled breath contains numerous volatile organic compounds (VOCs) and gases, and studies have highlighted VOCs such as benzaldehyde (BA), typically present at 10–100 ppb, as promising biomarkers for early-stage lung cancer detection [1-2]. Metal-organic frameworks (MOFs), such as ZIF-8 and MIL-100, have been transformed into surface-enhanced Raman spectroscopy (SERS) substrates, enabling the successful detection of BA at ppb concentrations [3,4]. Despite its promise, the MoF-based approach is limited by structural heterogeneity, environmental instability, reduced plasmonic activity, complex fabrication, surface contamination, lack of in-situ nanogap control, and the need for signal-optimization scans, all of which restrict its clinical applicability. In this work, a colloidal solution of 4-ATP-functionalized gold nanoflowers (AuNFs@4-ATP) confined within a sample cell has been used for *in situ* sampling and detection of gaseous BA as a proof of concept (PoC) for in-situ breath analysis. Surface plasmon polariton (SPP)-assisted dynamic assembly of AuNFs@4-ATP inside the sample cell facilitated efficient SERS detection by forming multiple hotspots in 3-dimensional space. The system and method successfully enabled gaseous BA detection by exposing the benzaldehyde vapor to AuNFs@4-ATP colloid for 5 minutes, achieving an estimated sensitivity of 4.95 ppb. The interference experiment showed high specificity for benzaldehyde and excellent batch-to-batch reproducibility, with an RSD of ~4.2%. The authors acknowledge financial support from the Department of Science and Technology (DST), Govt. of India, under grant SP/YO/2019/882 (G).

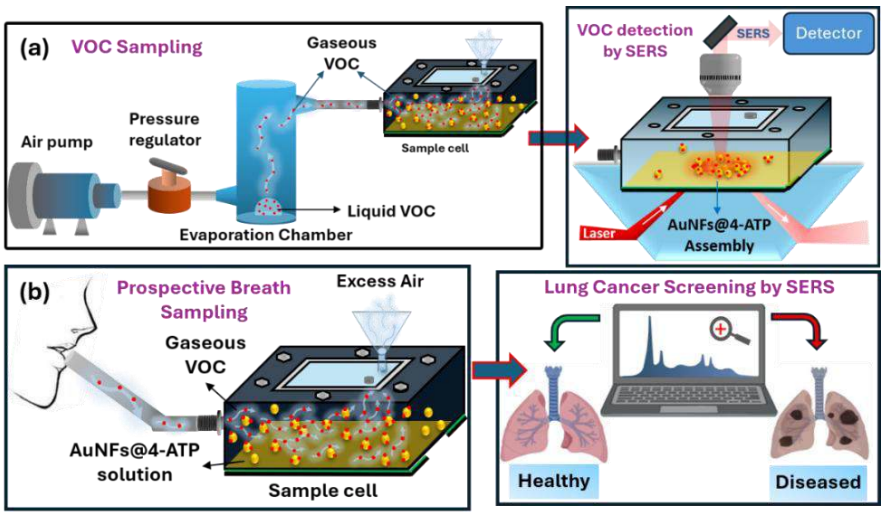


Figure 1. (a) The schematic representation of the in-situ VOC collection and detection, and (b) the working of the prospective breath analysis and lung cancer screening method.

References:

[1] Z. Xia, D. Li, and W. Deng, *Analytical Chemistry*, 93 (2021), 4924-4931.
[2] M. A. Floss, T. Fink, F. Maurer, T. Volk, S. Kreuer, and L. M. Müller-Wirtz, *Molecules*, 27 (2023), 5258
[3] J. Xu, J. Xu, Y. Xu, J. Li, J. Zhao, X. Jian, J. Xu, Z. Gao, and Y. Song, *ACS Sensors*, 8 (2023), 3487-3497.
[4] G. Fang, X. Lin, J. Wu, W. Xu, W. Hasi, and B. Dong, *Small*, 21 (2025), 2408670.

Machine Learning assisted Graphene-Coated Quantum-Enhanced Photonic Crystal Waveguide Biosensor for blood Cancer Detection

[1, #]Soumita Chakraborty & [1]Rajib Chakraborty

Affiliation: Department of Applied Optics & Photonics, JD Block, Sector 3, Saltlake, , Kolkata 700106 , INDIA,

[#] *socaop_rs@caluniv.ac.in*

This work presents a Machine Learning (ML) assisted graphene coated rib ridge photonic crystal waveguide biosensor for blood cancer detection. FDTD calibrated optical responses, quantum enhanced readout, and optimized graphene parameters are integrated for classification and sensitivity improvement. Ensemble models achieved robust discrimination, lower LOD operating conditions for early blood cancer detection.

A graphene-coated rib ridge photonic crystal waveguide biosensor detects blood cancer progression by sensing Refractive Index(RI) changes from normal blood, RI = 1.376, to cancerous blood, RI = 1.390 [1]. Graphene enhanced light matter interaction and squeezed light quantum readout improve resonance estimation and LOD without changing the sensor geometry [2].

To extend the framework toward intelligent diagnosis, ML is incorporated as a post-processing and decision-support layer. ML analysis demonstrates that the proposed graphene-coated rib–ridge photonic crystal waveguide biosensor can be effectively interpreted through classification, progression prediction, regression based surrogate modeling, explainable AI, and multi-objective optimization. The ML dataset is prepared from the proposed sensor parameters, where refractive index, cavity length, graphene thickness, graphene chemical potential, photon number, and squeezing level are varied. The corresponding optical and quantum-response parameters include resonance shift, FWHM, Q-factor, effective sensitivity, wavelength uncertainty, and LOD, with normal blood labeled as 0 and cancer-progressed blood labeled as 1 [3]. Random Forest, Gradient Boosting, and Support Vector Machine were analysed for normal vs cancer classification. Random Forest and Gradient Boosting achieved perfect performance, with accuracy, precision, recall, F1-score, and ROC-AUC equal to 1.00, whereas SVM showed moderate performance with 0.65 accuracy and 0.8075 ROC-AUC, as shown in Fig. 1. Sensor optimization further identified the best condition at cavity length = 1.5 μm, graphene thickness = 0.34 nm, chemical potential = 0.375 eV, photon number = 1×10^8, and squeezing level = 10 dB, yielding sensitivity = 1803.797 nm/RIU, FWHM = 5.234657 nm, Q-factor = 607, and LOD = 3.51×10^{-7} RIU. Overall, the proposed photonic–quantum–ML framework enables automated classification and parameter optimization for early cancer detection.

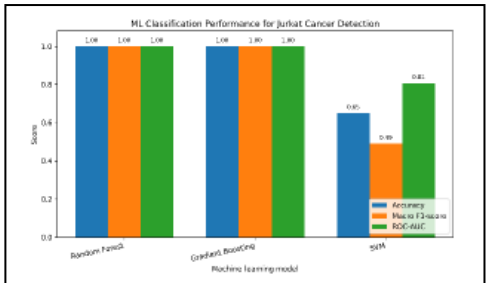


Fig. 1:ML classification normal vs cancer

References:

[1]M.A. Jabin, K. Ahmed, M.J. Rana, B.K. Paul, M. Islam, D. Vigneswaran, M.S. Uddin, IEEE Photonics Journal 11 (2019) 1-10.
[2]S. Chakraborty, R. Chakraborty, *Journal of the Optical Society of America B* **43** (2026) B301–B309.
[3] H. Raji, M. Tayyab, J. Sui, S.R. Mahmoodi, M. Javanmard, *Biomedical Microdevices* **24** (2022) 26.

Fourier investigation of Surface-Plasmon Polariton coupled Emission

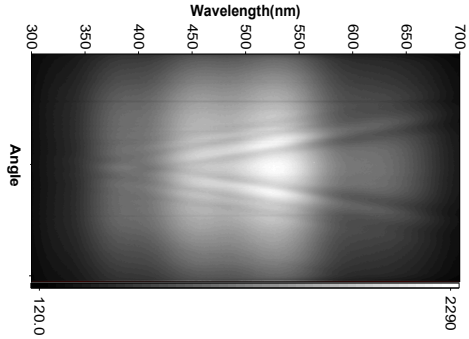
[1,] Satyam Dalmiya,[2]Sahil Rathi and [3]Satyendra Nath Gupta
[1]AMOPH Division, Physical Research Laboratory, Ahmedabad - 380009, India
[2]Indian Institute of Technology, Gandhinagar - 382055, India

[#]*satyamd@prl.res.in*

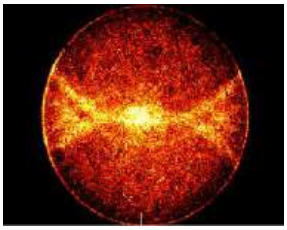
Silver gratings on ITO enable surface plasmon polariton (SPP)-mediated directional emission from colloidal quantum dots. Back focal plane microscopy links white-light reflection dispersion with QD emission for gratings of 250–500 nm periods. Measured emission angles at 610 and 645 nm closely match predicted SPP coupling angles, confirming plasmon-mediated directionality.

Imposing directionality and spectral content in spontaneous emission from quantum emitters is a long-standing goal in nanophotonics, with applications ranging from efficient single-photon sources to directional light-emitting diodes and sensing platforms. Metallic-dielectric interfaces that support surface plasmon polaritons (SPPs) could be an ideal candidate for this goal since SPPs are bound electromagnetic wave modes at the interface between two materials (metal-dielectric interfaces). SPPs have in-plane wave vectors that are larger in magnitude than those of the corresponding free-space wave at the same frequency, and therefore, do not radiate into the far field directly unless a momentum-matching structure (usually a periodic grating) is inserted. When an emitter is placed near a SPP-supporting periodic metallic structure, a significant fraction of its near-field emission can couple into the bound surface plasmon polariton (SPP) mode. The periodic grating provides the additional momentum required to scatter into free-space radiation, producing directional emission at angles determined by the SPP dispersion and the grating momentum-matching condition.

This work demonstrates that rather than engineering radiative suppression, the grating period can be tuned to maximise and direct the emission of colloidal quantum dots (QDs). The resulting directional emission pattern can be quantitatively predicted from an independent white-light dispersion measurement on the same structure. We fabricate silver gratings of periods of 250–500 nm directly on optically transparent indium tin oxide (ITO)-coated substrate. We map the SPP dispersion of each bare grating in reflection, and then to image the BFP emission pattern of two colloidal QD species (peak emissions at 610 nm and 645 nm) deposited on the same gratings. By comparing the SPP coupling angles predicted from the white-light measurement to the emission lobe angles observed for each QD species and grating period, we establish a direct, period-resolved cross-validation of SPP-mediated directional emission. We acknowledge the financial support from the Department of Space, Government of India.



(a)Dispersion map of 300nm period of grating obtained via Back Focal Imaging



(b) Back focal plane image of quantum dots emission pattern

References:

[1] I. C. Seo, S. Kim, B. H. Woo, I.-S. Chung, and Y. C. Jun, *Nanophotonics*, (2020).
[2] S. Cueff, L. Berguiga, and H. S. Nguyen, *Nanophotonics*, (2020).[

Fourier domain imaginary weak value amplification of small birefringence effects

Ritwik Dhara[1#], Arani Maity[1], Srijita Biswas[1], Jeeban Kumar Nayak[2], Paras N. Prasad[3], Alexander Baev[3], Nirmalya Ghosh[1]

[1]Department of Physical Science, Indian Institute of Science Education and Research Kolkata, 741246 Mohanpur, Nadia, India

[2] Nanophotonics and Metrology Laboratory (NAM), Swiss Federal Institute of Technology Lausanne (EPFL), Lausanne 1015, Switzerland

[3] Institute for Lasers, Photonics and Biophotonics, University at Buffalo, New York 14260, USA

[#]rd21ip025@iiserkol.ac.in

Polarization properties such as birefringence and optical rotation are fundamental material characteristics. This work develops a non-destructive weak-value amplification device for highly sensitive and accurate measurement of weak polarization effects.

We tried to recreate the interferometer formalism in a $4-f$ Fourier arrangement to achieve greater stability than in the Mach-Zehnder-based arrangement. The idea behind the $4-f$ setup is that when we do a Fourier transform of an electric field in the Fourier space, it is decomposed into corresponding spatial frequencies of the incident field. Which acts like individual sources that again interfere with each other by going through another Fourier transform. For simplicity, let's say we have an incident electric field with a transverse cosine profile, $E_{in} = Ecos(k'x)$, that decomposes into two delta functions $\delta(+k')$, $\delta(-k')$ at $+k'$ and $-k'$ positions in the momentum plane. These two delta functions act like two point sources that interfere with each other and produce $cos(k'x)$ after going through another Fourier transform.

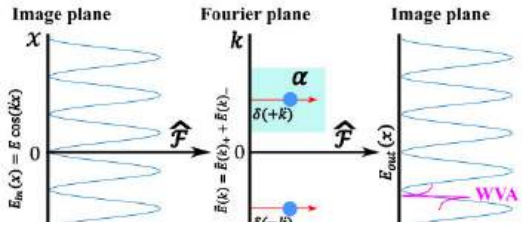


Fig. 1: Schematic representation of the theoretical background of our work of measuring the weak value of polarization anisotropies in a $4-f$ Fourier arrangement setup. Here, we introduce a small anisotropy effect α in one of the sources, while keeping the other intact.

Introducing a small polarization anisotropy in one point source while leaving the other unaffected creates an effective Mach–Zehnder-like configuration, establishing weak coupling between spatial frequency and polarization. The resulting polarization effects are weak-value amplified in the near-destructive interference region, with different Stokes-vector components amplified depending on the input polarization and type of anisotropy [1].

For a Gaussian input, the same formalism applies, with multiple Fourier-plane point sources interfering to form the image. Introducing the anisotropy in half of the Fourier plane produces similar amplification of optical rotation and linear birefringence in the corresponding Stokes-vector elements. For Gaussian beams, amplification occurs near the circumference, while for LG beams it occurs in the central dark region, both corresponding to near-destructive interference.

References:

1. Modak, Niladri, Athira BS, Ankit Kumar Singh, and Nirmalya Ghosh. "Generalized framework of weak-value amplification in path interference of polarized light for the enhancement of all possible polarization anisotropy effects." *Physical Review A* 103, no. 5 (2021): 053518.

Engineering of a Perovskite-based Ultrasensitive Multilayer Plasmonic Sensor

[1]Divyanshu Suthar,[2,3,*]Sagar Kumar Verma
[1]Indian Institute of Science Education and Research, Bhopal, 462066, Madhya Pradesh, India
[2]Department of Physics, Indian Institute of Technology Jodhpur, Jodhpur-342037, Rajasthan, India
[3]Medical Technology Center, Indian Institute of Technology Jodhpur, Jodhpur-342037, Rajasthan, India
[*]sagarkv@iitj.ac.in

A perovskite-based plasmonic sensor was engineered by following the wavelength interrogation approach. The inclusion of a selected perovskite ($MAPbI_3$) layer in the conventional prism-based plasmonic sensor enhances refractive index sensitivity by increasing the plasmonic volume. Such a plasmonic sensor shows an ultrahigh RI sensitivity of 4996 nm/RI.

Surface Plasmon Resonance (SPR) is one of the widely used nanophotonic phenomena to develop optical sensors for detecting microscopic changes in the analyte medium [1]. The sensing mechanism in SPR devices depends on surface plasmon modes generated at the metal-dielectric interface for TM-polarized incidence [1]. Any change in the analyte's refractive index alters the resonance conditions, leading to a measurable shift in the resonance angle/wavelength [2]. The conventional SPR sensors provide decent sensitivity, which could be enhanced by inclusion or addition of advanced materials like 2D materials or perovskite materials because they enhance light-matter interaction [2, 3]. In the present work, a multilayer SPR was investigated by incorporation of a perovskite layer.

A schematic illustration of the proposed SPR sensor is shown in Fig. 1(a). The proposed sensor consists of an SF11 coupling prism, a silver (Ag) thin film, a $MAPbI_3$ layer, and the analyte medium. Using the Transfer Matrix Method (TMM), the optimized geometrical parameters were obtained as Ag thickness of 46.7 nm and a $MAPbI_3$ thickness of 5 nm under wavelength interrogation at a fixed incident angle of 53.5°. The sensing performance was evaluated in terms of refractive index (RI) sensitivity. In Figure 1(b), the reflectance spectra have been plotted to present the performance comparison between the conventional SPR configuration as SF11/Ag/Analyte and the proposed configuration as SF11/Ag/$MAPbI_3$/Analyte. For the optimized thickness of 5nm, the proposed SPR configuration gives the minimum reflectance (R_{min}) of 0.0038 at the resonance wavelength (λ_{res}) 654nm while the conventional sensor has R_{min} of 0.068 at λ_{res} of 532nm. The lower value of R_{min} corresponds to the maximum SPR mode coupling, having a larger plasmonic volume, which leads to the sensitivity enhancement. Fig. 1(c) shows the red shift in reflectance spectra for the change in analyte RI values from 1.330 to 1.335. The values of λ_{res} corresponding to different RI values were extracted from Fig. 1(c) and plotted in Fig. 1(d) to show the sensor response and estimate the maximum RI sensitivity as 4996 nm/RIU by linear fit. The conventional SPR sensor without MAPbI3 shows the maximum RI sensitivity of 2800 nm/RIU. The inclusion of $MAPbI_3$ results in extreme sensitivity.

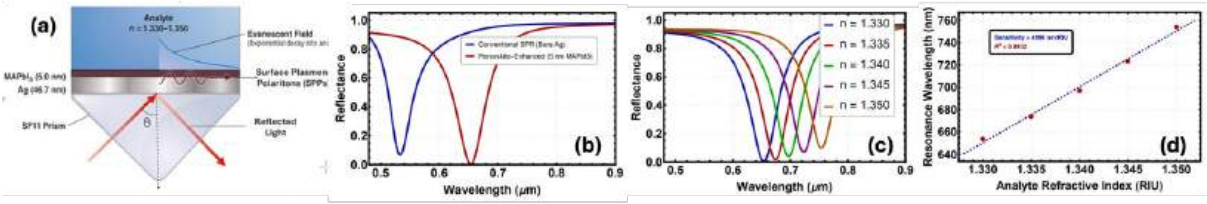


Fig. *1(a) Schematic of multilayer perovskite-based plasmonic sensor; (b) Reflectance spectra for the configurations SF11/Ag/Analyte compared with SF11/Ag/$MAPbI_3$/Analyte, (c) Reflectance spectra with SF11/Ag/$MAPbI_3$/Analyte for different RI values of analyte medium, (d) RI sensitivity estimation for the sensor configuration SF11/Ag/$MAPbI_3$/Analyte*

References:

[1] S. K. Srivastava, R. Verma, and B. D. Gupta, "Theoretical modeling of a self-referenced dual mode SPR sensor utilizing indium tin oxide film," Optics Communications, vol. 369, pp. 131–137, 2016
[2] A. Bansal and S. K. Srivastava, "High-performance SPR sensor using 2-D materials: A treatise on design aspects, material choice and figure of merit," Sensors and Actuators A: Physical, vol. 369, p. 115159, 2024.
[3] S. Roy, N. Mondol, D. Kundu, A. A. Meem, M. R. Islam, M. A. Hossain, and M. B. Hossain, "Numerical investigation into impact of halide perovskite material on the optical performance of prism-loaded hybrid surface plasmon resonance biosensor: A strategy to increase sensitivity," Sensing and Bio-Sensing Research, vol. 43, p. 100630, 2024.

Slot-Engineered Split Cylindrical TiO_2 Metasurfaces for Enhanced Refractive Index Sensing

Mohammed Eesa S M, Vanniya Balan, Srijith Kanakambaran[#]
Department of Electronics and Communication Engineering
IIITDM Kancheepuram, Chennai 600127, India

[#]*email id: srijith@iiitdm.ac.in*

A TiO_2 dielectric cylindrical metasurface with a central slot is proposed for refractive index sensing and analyzed using COMSOL Multiphysics software. The effects of varying the slot width on the resonance characteristics and sensitivity is investigated. The results demonstrate that the slot geometry effectively tunes the sensitivity of two resonance modes, enabling improved sensing performance.

Metasurfaces are two-dimensional arrays of subwavelength structures, known as meta-atoms, that enable precise tailoring of amplitude, phase and polarization of incident light [1]. Dielectric metasurfaces are particularly attractive for sensing applications because their low optical losses support high quality factor resonances with narrow linewidths [2]. These characteristics make them well suitable for applications such as biosensing, environmental monitoring and chemical detection.

In this work, a TiO_2 dielectric metasurface incorporating a central slot is investigated for refractive index sensing. The proposed structure consists of a cylindrical TiO_2 meta-atom placed on a SiO_2 substrate and periodically arranged with a lattice periodicity(Λ) of 600 nm in the XY plane, as shown in Fig.1. a. The cylindrical meta-atom has a radius(*R)* of 180 nm and a height(*H)* of 90 nm, while air is considered as the surrounding medium. The optical response of the metasurface is analysed using COMSOL Multiphysics software under normal incidence of x-polarized light over the wavelength range of 700–835 nm. The transmission spectrum exhibits two distinct resonance modes at 735 nm and 796 nm as shown in Fig.1. b.

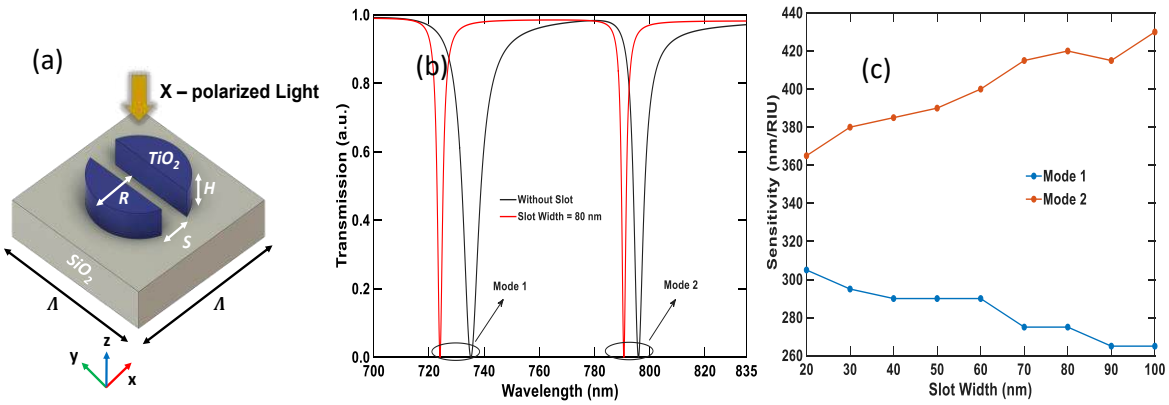


Fig. 1: (a) Metasurface Unit-Cell (b) Transmission Spectra (c) Sensitivity vs Slot Width plot

To investigate the influence of the structural geometry, a slot is introduced into the cylindrical meta-atom, and its width(*S*) is varied from 20 nm to 100 nm. The transmission spectra of the structures with and without the slot are compared to examine the effect of the slot on the resonance characteristics as shown in Fig.1. b. Both the lower resonance (mode 1) and the higher resonance (mode 2) exhibit a blue shift upon the introduction of the central slot. To evaluate the sensing performance, the refractive index of the surrounding analyte is varied from 1.33 to 1.41, and the resulting shifts of both resonance modes is then monitored for different slot widths and sensitivity values are estimated. Fig 1. c shows that increasing the slot width gradually decreases the sensitivity of Mode 1 from 305 nm/RIU to 265 nm/RIU, whereas the sensitivity of mode 2 increases from 365 nm/RIU to 430 nm/RIU. This behavior demonstrates that the slot geometry has a significant influence on the resonance response with an enhancement of around 18% of mode 2 sensitivity.

References:

[1] Dishniya Vishnuramkumar, Danveer Singh, *ACS Applied Optical Materials* 4 (2), 314-324(2026)
[2] Dhananjoy De, Vijaya R, *Frontiers in Photonics* 4:1234060(2023)

Engineering of Multimode Excitation on Multilayer Flat Plasmonic Geometry by Integrating with Spherical Nanoparticles

[1]Hemant Beniwal,[2,3,*]Sagar Kumar Verma

[2]Department of Physics, Sardar Vallabhbhai National Institute of Technology, Surat-395007, Gujarat, India

[2]Department of Physics, Indian Institute of Technology Jodhpur, Jodhpur-342037, Rajasthan, India

[3]Medical Technology Center, Indian Institute of Technology Jodhpur, Jodhpur-342037, Rajasthan, India

[*]sagarkv@iitj.ac.in

A periodic arrangement of nanoparticles near the metal layer in plasmonic Nano architectures leads to the excitation of multiple resonances because of the coupling of surface plasmon polaritons (SPPs) with localized surface plasmons (LSPs). The study demonstrates the excitation of triple resonances that can be tailored by controlling the arrangement of NPs.

LSP resonance was first observed in 1908 by Gustav Mie for light passing through various gold nanoparticles (NPs) to understand the light absorption and scattering [1]. The nanophotonic architectures integrated with NPs provide strong electromagnetic (EM) field enhancements by their confinement around the junctions due to the near-field coupling between the NPs and the induced image charge within the metal film [2,3]. The continuous placement of the NPs near the metal layer helps to couple the SPP with the LSP modes, resulting in SPP and LSP coupling and other resonances [4]. In this work, a prism-based plasmonic structure was proposed to integrate with AgNPs and simulated by COMSOL Multiphysics software.

The schematic diagram shown in Fig. 1 (a) represents a prism, an Ag layer, and a 1D array of Ag nanoparticles (AgNP) with a diameter of 5 nm. The distance of the AgNP from the Ag layer and the inter-particle distance between AgNPs are considered as g (nm) and d (nm), respectively. The design of a multi-layered flat geometry structure is performed to study the multiple-mode excitation. The design has been optimized for triple mode resonances with fixed values of transverse magnetic (TM) polarized light of wavelength 633nm, and Ag layer thickness of 43nm. Figures 1(b) and 1(c) show the reflection spectra for different combinations of g and d values to excite the triple resonances. These spectra show that increasing values of g result in decreases in reflectivity, and with the increase in d values result in excitation of two other modes at 59.8° and 73.5° respectively. Figures (d), (e), and (f) represent the electric field profiles at all three resonant angles, 54°, 59.8° and 73.5°, respectively, for the generation of triple surface plasmon resonance modes with g = 0 and d = 1.

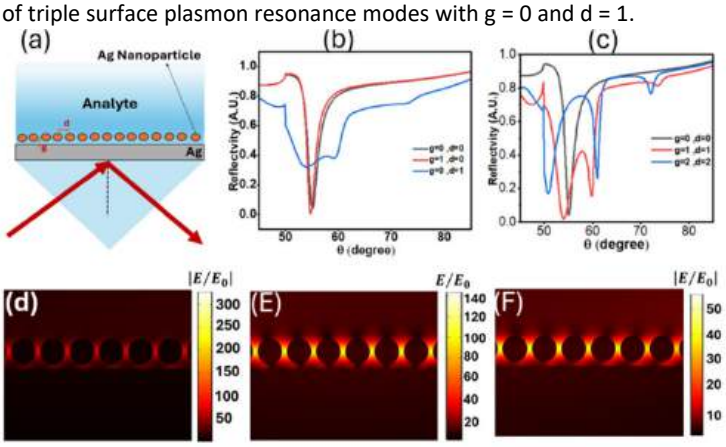


Fig. *1(a) Schematic of multilayer plasmonic geometry by integrating AgNPs,(b)&(c) for (g) Height of nanoparticles and (d) distance between AgNPs; Electric field profiles for surface plasmon modes excited at: (d)* 54°, *(e)* 59.8° *(f)* 73.5°

References:

1. G. Mie., Annalen der Physik, 1908, 330(4), 377–445.
2. S. Mubeen, S. Zhang, N. Kim, S. Lee, S. Krämer, H. Xu and M. Moskovits, Nano Lett., 2012, 12, 2088–2094.
3. P. Nordlander and E. Prodan, Nano Lett., 2004, 4, 2209–2213.
4. M. Sarkar, M. Besbes, J. Moreau, J. F. Bryche, A. Olivéro, G. Barbillon, A. L. Coutrot, B. Bartenlian and M. Canva, ACS Photonics, 2015, 2, 237–245

Integrated Long-Period Grating-Coupled SPR Sensor for High-Sensitivity Refractive Index Sensing

[1]Sourabh Jain,[1]Dharmendra Shakya, and [2,#]Rahul Kumar Gangwar
[1] Department of Electronics and Communication Engineering, Indian Institute of Information Technology, Bhopal, Madhya Pradesh, Bhopal, India
[2]Department of Physics, Indian Institute of Information Technology, Bhopal, Madhya Pradesh, Bhopal, India
[#]rahul.gangwar@iiitbhopal.ac.in

A long-period grating-coupled SPR sensor with Au-TiO_2-analyte interfaces is proposed for detecting water adulteration in milk by monitoring the resonance dip shift corresponding to refractive index changes (1.33–1.35). The sensor exhibits a high-sensitivity of 550 nm/RIU.

Integrated photonics has emerged as a promising platform for miniaturized optical sensing owing to its strong light-matter interaction. Recent efforts have largely focused on sub-wavelength grating (SWG) enhanced Surface Plasmon Resonance (SPR) based photonic structures to achieve compact, highly integrated optical sensors with enhanced light–matter interaction [1]. Nevertheless, long-period gratings (LPGs) provide more effective alternative for SPR sensing by enabling efficient coupling between guided modes and surface plasmon polaritons without requiring sub-wavelength patterning [2]. Their relatively large grating periods simplify fabrication, facilitate efficient light coupling under relaxed alignment conditions, and make them attractive for compact and multiplexed sensor arrays [3]. In LPG-assisted SPR sensors, the periodic grating facilitates phase-matched coupling between the guided core mode and surface plasmon polaritons, resulting in enhanced light-matter interaction and improved refractive index sensitivity.

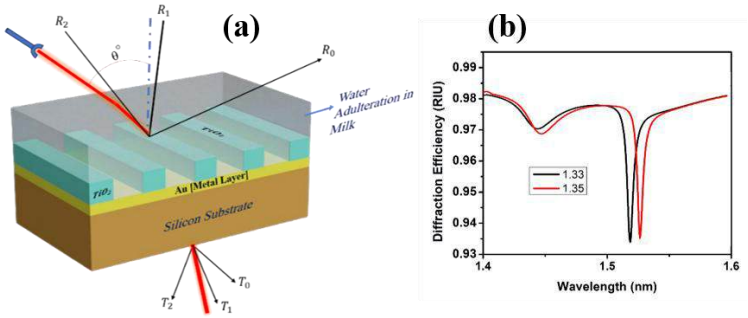


Figure 1. (a) 3D schematic of the SPR sensor featuring a TiO_2-Analyte grating on Au-coated Si substrate, along with diffraction order mapping (R_0-R_2, T_0-T_2) under TM-polarized incident light. (b) Reflectance spectrum for RI = 1.33 (water) and RI = 1.35 (milk) showing shift from 1.509 µm to 1.520 µm.

As shown in Fig. 1(a), the proposed grating-enhanced SPR sensor consists of a Si substrate, a 107 nm thick Au film, and a 692 nm thick TiO_2 grating. The grating has a period of 1.5 µm, a duty cycle of 44%, and is infiltrated with the analyte. The optical response of the structure is analyzed using Rigorous Coupled-Wave Analysis (RCWA) method [4]. The angle of incidence, Θ^0, is optimized at 52°, and the free-space wave vector k_0 is defined as $2\pi/\lambda$. The structure exhibits a strong resonance response in the near-infrared wavelength range. This architecture is specifically designed to detect ultra-narrow RI changes, such as those caused by water adulteration in milk. Fig. 1(b) shows that the resonance wavelength shifts from 1.509 µm to 1.520 µm when the analyte is changed from pure water to milk. The observed 11 nm wavelength shift serves as a measurable indicator of the refractive index (RI) change, corresponding to a sensitivity of 550 nm/RIU, as determined from $S=\Delta\lambda/\Delta n$.

The simulated diffraction order analysis signifies energy distribution among the R_0, $R_{\pm1}$, T_0 and $T_{\pm1}$ modes under varying refractive index conditions. As the RI changes from 1.33 to 1.35, the field strength in the analyte region increases, indicating stronger plasmon excitation. The redistribution of energy into higher diffraction orders signifies enhanced coupling efficiency. These behaviors confirm that the sensor not only detects RI changes through resonance shift but also reflects deeper physical changes in the mode propagation and energy localization. Additionally, a large free spectral range ensures single-dip resonance within the detection window, enabling unambiguous, high-resolution, and noise-free refractive index sensing which makes it an ideal platform for biochemical or food quality applications. The authors acknowledge MPCST support under Grant No. 3852/CST/R&D/Phy.&Engg. and Pharmacy/2025–26.

References:

[1] S. Jain, et al., Applied Physics Reviews, 12.1 (2025): 011337.
[2] S. Jain, et al., Plasmonics 21.1 (2026): 1295-1306.
[3] C. Trono, Trends in Analytical Chemistry (2024): 117875.
[4] J. Schlipf, Jon, and I. A. Fischer, Optics Express, 29.22 (2021): 36201-36210.

Engineering of Extraordinary Transmission via Fano Resonance for Selective Wavelength Filtering with Ultra-high Q-factor

[1]Bablu Jatav,[1,2,*]Sagar Kumar Verma
[1]Department of Physics, Indian Institute of Technology Jodhpur, Jodhpur-342037, Rajasthan, India
[2]Medical Technology Center, Indian Institute of Technology Jodhpur, Jodhpur-342037, Rajasthan, India
[*]sagarkv@iitj.ac.in

A 1-D Plasmonic metasurface was engineered to work as a wavelength-selective transmission filter with an ultra-high Q-factor. The proposed filter follows the phenomena of Fano-resonant mode excitation, which support the extraordinary optical transmission of IR light. The maximum transmission efficiency of 9% was achieved at $\theta = 3^o$ with Q-factor of 6440.

Fano-resonance was discovered by Ugo Fano in 1961 during the quantum mechanical study of auto-ionising states of an atom [1]. The resulting in an asymmetric spectra, which is originated from the interference between super-radiant (broad bright) plasmonic modes and sub-radiant (narrow dark) modes [2,3]. Extraordinary optical transmission (EOT) is a phenomenon in which the transmission efficiency of the light is much higher than the intensity of the light incident on the plasmonic nanostructure itself, while such a nanostructure contains sub-wavelength periodic openings with specific geometry, size and orientation [4]. First time in 1998, Ebbesen and his co-workers discussed and experimentally demonstrated the EOT by following the concept of surface plasmons, and they observed that EOT only occurs on plasmonic interfaces [4]. However, during the early investigations of EOT, the transmission efficiency remained relatively low due to the weak coupling between the surface plasmon (SP) modes and the incident radiation itself [5,6]. The current study mainly focuses on the possibility of EOT by the excitation of Fano resonant modes.

A schematic of the proposed plasmonic metasurface (PM) has been shown in Figure 1(a). For the engineering of the shown PM, the rigorous coupled wave analysis (RCWA) has been followed. This PM consists of a 1D patterned Gold (Au) array on Yttrium oxide (Y_2O_3) substrate with optimized geometrical parameters such as period $(\Lambda) = 2100\text{nm}$, groove width $(W) = 220\text{nm}$, and height of Au (D)=1040nm The controlled engineering was performed for the incidence of transverse magnetic (TM) polarized light on PM. In Figure 1(b), the transmission efficiency spectra have been plotted for different values of `D` varying from 1020nm to 1060nm. This graph indicates that the proposed PM exhibits maximum transmission at D=1040nm, and the transmission efficiency decreases when the 'D' either decreases or increases. In Figure 1(c), the transmission efficiency spectra have been plotted for different values of `W` varying from 190nm to 260nm. The maximum transmission efficiency has been obtained for W=220nm. In Figure 1(d), transmission efficiency spectra have been plotted for different values of incident angle (θ) varying from 0° to 6°. The maximum transmission efficiency of 9% was achieved at θ=3° with the maximum value of its Q-factor as 6440.

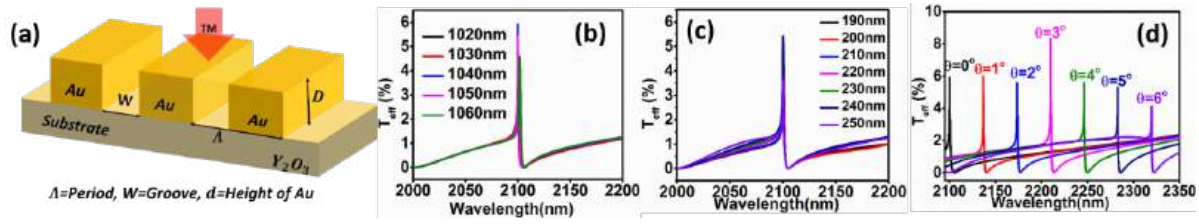


Fig. *1(a) Schematic of EOT based PM filter; Transmission efficiency spectra for: (b) D variation, (c) W variation, (d) θ variation*

References:

[1] U. Fano, Physical Review 124, 1866–1878 (1961).
[2] A. Lovera, B. Gallinet, P. Nordlander, J. O. F Martin, ACS Nano, 7, 4527–4536 (2013).
[3] S. K. Verma and S. K. Srivastava, Journal of the Optical Society of America B 41, 356- 363 (2024).
[4] T. W. Ebbesen, H. J. Lezec, H. Ghaemi, T. Thio, and P. A. Wolff, Nature, 391, 667 (1998).
[5] H.A. Bethe Physical Review, 66, 163–182 (1944).
[6] O.M. Mendez, M.Cadilhac, and R. Petit Journal of the Optical Society of America A, 73, 328–331 (1983).

Analyte Thickness Engineering for Enhanced Localized Plasmonic Sensing through Resonance Hybridization

[1]Aashirya Kanwar,[1,#]Dr. Ankit Arora
[1]Department of Electronics Engineering, IIT (BHU) Varanasi, Varanasi, India – 221005.
[#]*ankit.ece@itbhu.ac.in*

We demonstrate that analyte thickness, a largely unexplored yet easily tunable design parameter in plasmonic biosensing, can be exploited to control plasmonic-photonic resonance hybridization and significantly enhance the performance of localized plasmonic sensing without modifying the plasmonic nanostructure. By tuning the analyte-supported guided-mode resonance (GMR) across a localized surface plasmon resonance (LSPR), the resonance linewidth is reduced by more than 60%, resulting in an approximately threefold enhancement in the sensing figure of merit (FOM) compared with the conventional semi-infinite analyte configuration, while preserving nearly identical refractive-index sensitivity (RIS). These results demonstrate that linewidth engineering through resonance hybridization, rather than increasing the intrinsic RIS, provides a simple and effective route toward high-performance LSPR sensors.

The proposed sensor consists of a 400 nm thick silver grating with a period of 420 nm, groove depth of 110 nm and a duty cycle of 90%, covered by a dielectric analyte layer of finite thickness, as shown in Fig. 1(a). The electromagnetic response of the structure was simulated using the FEM solver COMSOL Multiphysics. While the LSPR is weakly affected by analyte thickness as it depends on grating shape[1], the dielectric layer supports a guided-mode resonance whose spectral position can be continuously tuned by varying the analyte thickness(refractive index=1.3)[2]. As the GMR is swept across the LSPR, a pronounced avoided crossing is observed in the reflectance spectra (Fig. 1(b)), confirming resonance hybridization and the formation of hybrid plasmonic–photonic modes. Two representative operating points corresponding to analyte thicknesses of 250 nm and 300 nm on the upper hybridized branch were selected to investigate the influence of mode hybridization on sensing performance.

The sensing performance was evaluated by calculating the sensing FOM defined as RIS normalized with the resonance linewidth, for analyte refractive indices ranging from 1.30 to 1.50. As summarized in Fig. 1(c), the hybridized resonances exhibit substantially narrower linewidths than the conventional semi-infinite analyte configuration, whereas the RIS remains nearly unchanged. The electric-field distributions, shown in Fig. 1(e), reveal that the hybridized resonance retains strong plasmonic localization around the grating ridges and inside the grooves while simultaneously exhibiting enhanced field penetration into the analyte layer due to its increased GMR character. This enables stronger light-matter interaction without sacrificing subwavelength field confinement. Consequently, the optimized 300 nm analyte thickness achieves the highest FOM, demonstrating that analyte-thickness-induced resonance hybridization provides a practical and experimentally accessible strategy for improving plasmonic biosensors without redesigning the underlying nanostructure.

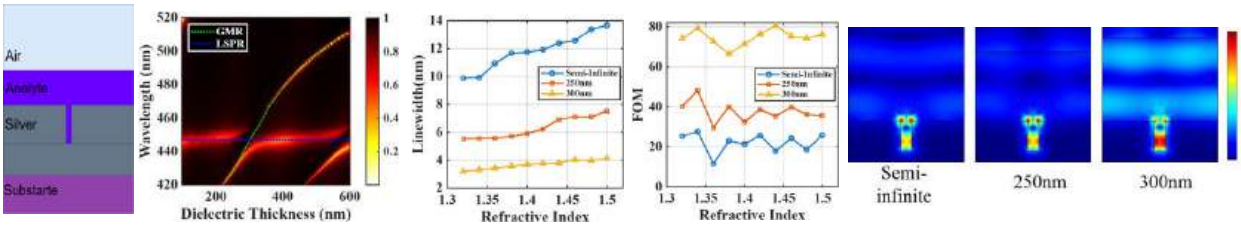


Figure 1: *(a) Schematic of the hybrid plasmonic–photonic sensor consisting of a silver grating covered by a dielectric analyte layer of finite thickness. (b) Simulated reflectance dispersion as a function of analyte thickness, showing the interaction between the LSPR and GMR, resulting in an avoided crossing and the formation of hybridized modes. (c),(d) Comparison of the resonance linewidth and sensing FOM for the semi-infinite analyte configuration and the hybridized resonances corresponding to analyte thicknesses of 250 nm and 300 nm. (e) Normalized electric-field intensity distributions of the three operating points, illustrating the evolution from a predominantly plasmonic mode to a hybrid plasmonic-photonic mode with enhanced field penetration into the analyte while preserving strong field localization around the grating.*

References:

[1] V. G. Kravets, A. V. Kabashin, W. L. Barnes, and A. N. Grigorenko, "Plasmonic Surface Lattice Resonances: A Review of Properties and Applications," *Chemical Reviews*, vol. 118, no. 12, pp. 5912–5951, 2018.
[2] H. S. Bark and T.-I. Jeon, "Dielectric film sensing with TE mode of terahertz guided-mode resonance," *Optics Express*, vol. 27, no. 2, pp. 500–509, 2019.

Scalable Reproduction of Plasmonic Quasicrystals via Thermal Nanoimprint Lithography for Label-Free Detection of Cotinine

[1,#]Deepak Kumar,[2]Sibashish Chakraborty and [3]Satish Kumar Dubey
[1]SeNSE, Indian Institute of Technology Delhi, Hauz Khas, New Delhi ,
[2]satishdubey@sense.iitd.ac.in

Plasmonic quasicrystals (PlQCs) fabricated by electron-beam lithography offer strong, broadband SERS enhancement but are expensive and limited in scale. Here, we demonstrate the replication of PlQC masters using ***thermal nanoimprint lithography (NIL)*** *followed by* ***gold sputtering*** *to achieve large-area, low-cost plasmonic substrates. Both EBL and NIL substrates were tested for label-free* ***cotinine detection*** *down to* ***5 ng/mL****, revealing comparable enhancement and uniformity. Principal component analysis confirmed consistent molecular discrimination. This work highlights NIL as a viable, scalable fabrication method for high-performance, reproducible SERS substrates suitable for practical biosensing of nicotine biomarkers*.

Passive smoking poses a serious health risk. It is reported that passive smoking increases the risk of lung cancer and onset of cardiovascular diseases. We developed a highly sensitive method to assess exposure to active and passive smoking using Surface Enhanced Raman Spectroscopy (SERS). SERS is a powerful technique for detecting biomolecules at ultra-trace levels. Efficient SERS analysis requires substrates that are highly sensitive, uniform, and molecule-specific. In this work, we demonstrate a scalable replication of EBL-fabricated PlQC masters using thermal nanoimprint lithography (NIL), followed by gold sputter deposition, to realize low-cost and reproducible SERS-active substrates. The NIL-replicated PlQC substrates retain the quasiperiodic geometry of the master pattern and exhibit broadband plasmonic behavior across the visible spectrum. Both master and NIL-replicated substrates were evaluated for label-free detection of cotinine, a primary biomarker for nicotine exposure, down to 5 ng/mL concentration. SERS spectra reveal strong and well-defined cotinine vibrational peaks, with the NIL-replicated substrates showing comparable enhancement and spatial uniformity to the EBL master, despite simpler and scalable fabrication route. Principal component analysis (PCA) confirms reliable molecular discrimination from blank controls across all measured sites.

This study establishes thermal NIL replication of PlQC structures as a practical and high-throughput alternative to EBL for producing uniform, broadband plasmonic SERS substrates. The ability to achieve cotinine detection at nanogram levels using replicated substrates highlights their potential for cost-effective, field-deployable biosensing platforms for passive smoking exposure assessment and beyond.

Author's description: Deepak Kumar received a Gold Medal in M.Sc. Applied Physics from Delhi Technological University, India. He is currently a research scholar at the Centre for Sensors, Instrumentation, and Cyber-Physical Systems Engineering (SeNSE), IIT Delhi. His research focuses on the design, fabrication, and application of nano-plasmonic structures for surface-enhanced Raman spectroscopy (SERS)-based analyte detection.

References:

1. Chakraborty, S., Vij, R., Goel, R. *et al.* PlQC based highly sensitive and reproducible novel SERS active substrate for biomolecule detection with high specificity. *Sci Rep* 14, 29186 (2024). https://doi.org/10.1038/s41598-024-74528-9.

Protein detection in real-time using whispering gallery modes and comparative analysis of modes and photonic nanojets in bare and multilayer dielectric microspheres

#Shubham Kumar Mahanta, and *Venkata Ramanaiah Dantham
Department of Physics, Indian Institute of Technology Patna, Patna, Bihar – 801103
#*Presenting author: shubham_2421ph15@iitp.ac.in*
**Corresponding author: dantham@iitp.ac.in*

Real-time detection of protein markers associated with dangerous diseases is crucial in the field of biosensing. Therefore, the detection of protein markers of a few diseases using whispering-gallery modes of photonic microresonators (dielectric microspheres) in aqueous media will be presented. In addition, a comparative theoretical analysis of the optical modes and photonic nanojets in bare and multilayer dielectric microspheres will also be presented at the conference.

Early detection of dangerous diseases is very important for effective treatment and can save patients' lives. At the early stage, the protein biomarkers (or protein molecules) related to diseases appear in the bodily fluids (such as blood, serum, saliva, etc.) at an ultralow concentration (order of femtomolar). The typical size of most of the protein markers is lower than 20 nm. Therefore, detecting protein molecules is an extremely difficult task. This detection is possible only with biosensors that have ultrahigh sensitivity and resolution. Therefore, there is a tremendous need to develop biosensors for detecting protein markers in real time. Therefore, the real-time detection of cancer and heart attack protein biomarkers using whispering-gallery mode (WGM) photonic microresonators is demonstrated in an aqueous medium. The detection has been demonstrated by monitoring the wavelength shift of the WGM of the microresonator upon adsorbing protein markers on its surface. Moreover, from the wavelength shift of the WGM, one can estimate crucial information, such as the size, mass/molecular weight, and number of amino acids, of the protein markers. These can be considered as unique advantages of these WGM photonic microresonators. The experimental setup for real-time protein detection is shown in Fig. 1. Fabrication details of the microresonators, experimental results, and analysis will be presented at the conference.

It is to be noted that the dielectric microspheres support WGMs upon resonant optical illumination. Interestingly, these microspheres generate intense photonic nanojets (PNJs) upon non-resonant optical illumination. These PNJs have been found to be useful in several applications, ranging from medical surgery to optical storage. The length, width, and electric field of the PNJs strongly depend upon the size, shape, and relative refractive index of the dielectric microsphere. These parameters can be tuned precisely by coating the microspheres with different dielectric layers with appropriate thickness. Therefore, a theoretical investigation of multilayered dielectric microspheres is conducted to understand the characteristics of optical modes and PNJs using the Generalized Mie theory, and a comparative analysis of modes and PNJs in bare and multilayer dielectric microspheres (Fig. 2) will be presented at the conference.

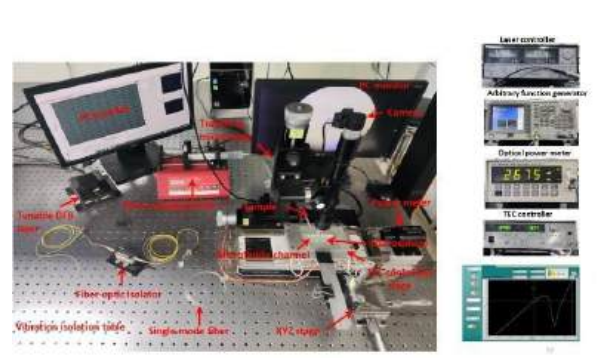


Fig. 1. Experimental setup for demonstrating the real-time detection of protein markers using a photonic microresonator.

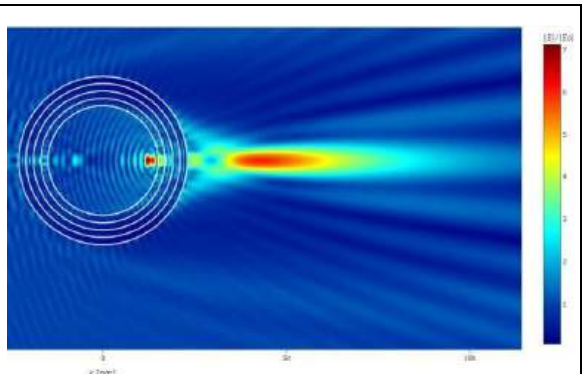


Fig.2. Generation of a PNJ from the shadow side of a multilayered dielectric microsphere upon non-resonant illumination.

References:

[1] S. W. Koireng, S. Sahoo, V.R. Dantham, *Optical and Quantum Electronics* 58 (2025) 25.
[2] A. Mandal, P. Tiwari, P.K. Upputuri, V.R. Dantham, *Scientific Reports 12* (2022) 173.
[3] P. Patar, S. Roy, V.R. Dantham, *Optics Communications* 577 (2025) 131467.

Probing the Broken Spatial Symmetry of a Stratified Medium with Structured Light

[1,#] Arani Maiti,[1]Sauvik Roy , [1]Nirmalya Ghosh,[1] Ayan Banerjee and [1,2]Subhasish Dutta Gupta
[1]Department of Physical Sciences, IISER-Kolkata, Mohanpur 741246, India
[2]Tata Institute of Fundamental Research, Hyderabad, Telangana 500046, India
[#]*arani2331maitiray@gmail.com*

We investigate near-symmetric resonant stratified media to demonstrate ultrasensitive detection of minute spatial symmetry breaking using structured light with or without orbital angular momentum. Resonantly enhanced and weak-value-amplified Goos–Hänchen and Imbert–Fedorov shifts enable nonreciprocal, sign-reversing responses, providing a versatile platform for ultra-high-precision optical sensing.

We investigate nonreciprocal beam shifts arising from broken spatial symmetry and explore their potential for sensing minute variations in length, refractive index(RI) etc. We consider a folded Kretschmann-like configuration supporting coupled fundamental guided modes, illuminated from either end by a light beam. Spatial symmetry is broken by a slight translation or refractive-index mismatch of the guiding layers, producing asymmetric phase winding for opposite propagation directions and, consequently, nonreciprocal beam shifts. To analyze the beam shifts, we employ a generalized angular spectrum formalism based on the framework of Bliokh and Aiello[1], extended to incorporate a broader transverse momentum distribution for an accurate description of non-paraxial effects.

We first break the spatial symmetry by introducing a small translation of 0.0005μm between the coupled guiding layers [2]. The reflected gaussian beam profiles for forward and backward illumination exhibit positive and negative GH shifts for *s*-polarized input, respectively, with magnitudes comparable to the beam spot size for different beam waists. For tightly focused beams, slight beam distortion accompanied by weak secondary lobes is also observed. We next consider a configuration in which the spatial symmetry is broken by introducing a slight refractive-index mismatch between the guiding layers. Similar to the previous case, we again observe direction-dependent positive and negative beam shifts, demonstrating the potential of this configuration for RI sensing applications.

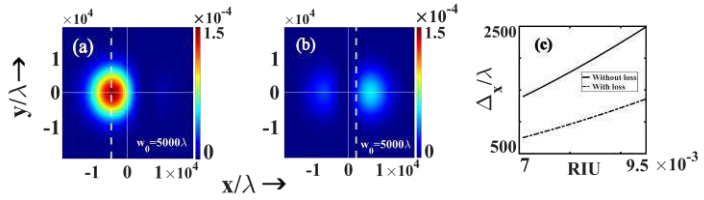


Fig. 1: Results for RI mismatch induced asymmetry: (a) and (b) Represent beam profiles for the forward and backward directions. (c) Differential GH shift Δ_x between GH shifts for forward and backward illumination as a function of RI change for a structure without (solid) and with loss (dashed).

Finally we investigate the effect of symmetry breaking on the IF shift under different polarization measurement schemes. For conventional IF measurements with left- or right-circularly polarized Gaussian beams, the forward–backward difference is small and difficult to resolve experimentally. This motivates the use of polarization-selective detection and weak-value amplification(WVA) [3] to enhance the underlying nonreciprocal transverse shift. WVA is perform by setting input state $(0,1)^T$ and the reflected beam is post-selected onto a nearly orthogonal state $(1,\epsilon)^T$.

In conclusion, we have studied the nonreciprocal effects in both GH and IF shifts when the spatial and temporal symmetry of a coupled waveguide structure is slightly disturbed.

References:

[1] K. Y. Bliokh and A. Aiello, Journal of Optics 15, 014001 (2013).
[2] S. D. Gupta, N. Ghosh, and A. Banerjee, in Wave Optics (CRC Press, 2015).
[3] M. R. Dennis and J. B. G¨otte, New Journal of Physics 14, 073013 (2012).

In-Situ Detection of Micro/Nano Plastics in Water Using Surface Enhanced Raman Spectroscopy

[1]Meenakshi, [1]Anjika Kumari, [1]Dalip Singh Mehta* and [1]Kanchan Saxena*
[1]Biophotonics and Green-Photonics Laboratory, Department of Physics, Indian Institute of Technology Delhi, Hauz Khas, New Delhi 110016, India
*mehtads@physics.iitd.ac.in *Saxena.mehta@gmail.com *meenakshisingh2997@gmail.com

Abstract: *A rapid SERS approach using colloidal Ag nanoparticles and anisotropic Ag nanodendrites was developed for sensitive micro/nanoplastic detection in water. PVC, PVA and PS were identified through intrinsic Raman fingerprints. Trace detection and successful analysis of PS in tap and river water demonstrate the potential of portable SERS for in-situ environmental screening.*

Micro/Nano plastics are persistent aquatic contaminants that are challenging to detect at trace levels. Raman spectroscopy provides label-free molecular fingerprints but suffers from weak signal intensity. Surface-enhanced Raman spectroscopy (SERS) overcomes this limitation through plasmonic enhancement. Here, spherical Ag NPs and anisotropic Ag NDs were comparatively investigated for detecting PVC, PVA, and PS in water[1,2].

Raman and SERS spectra were acquired using a portable 785 nm Raman spectrometer. Ag NPs showed an average diameter of ~80 nm, while Ag NDs exhibited sharp, multibranched structures. Using R6G, enhancement factors of 1.09×10^6 and 4.67×10^6 were achieved for Ag NPs and Ag NDs, respectively, with higher enhancement from Ag NDs due to their anisotropic morphology and dense hotspots. Comparative SERS measurements enabled PVC detection down to 1 nM with Ag NPs and 0.1 nM with Ag NDs shown in Fig.1. PVA was detected to 10 mM using Ag NPs and 5 mM using Ag NDs. For 1 µm PS beads, a detection limit of 10^{-6} M (26 µg mL^{-1}) was achieved. Unlike PVC and PVA, PS showed stronger enhancement with spherical Ag NPs, indicating that analyte–nanostructure surface contact and adhesion are important in addition to hotspot density. Characteristic polymer bands provided intrinsic, label-free specificity [3,4]

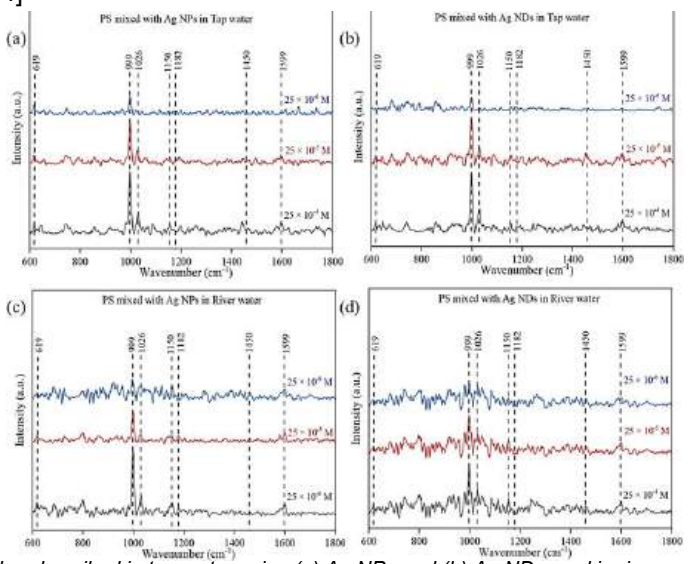


Fig. 1: SERS spectra of PS beads spiked in tap water using (a) Ag NPs and (b) Ag NDs, and in river water using (c) Ag NPs and (d) Ag NDs.

The method was further evaluated in complex real-water matrices. PS-spiked tap and river water retained characteristic PS Raman signatures, although spectral interference increased in river water because of dissolved organic and inorganic constituents. Detection limits of 26 µg mL^{-1} in tap water and 260 µg mL^{-1} in river water were obtained. These results establish a simple, cost-effective and portable SERS strategy for sensitive in-situ identification of micro/nanoplastics in aquatic environments. Meenakshi acknowledges UGC-JRF India for financial support.

References:

[1] L. Lv, L. He, S. Jiang, et al., Science of the Total Environment 728 (2020) 138449.
[2] G. Xu, H. Cheng, R. Jones, et al., Environmental Science & Technology 54 (2020) 15594–15603.
[3] Q.T. Lê, N.H. Ly, M.-K. Kim, et al., Journal of Hazardous Materials 402 (2021) 123499.
[4] Meenakshi, S. Das, A.K. Verma, et al., Environmental Science and Pollution Research 31 (2024) 49255–49266.

Optics of Finite Self-Assembled Disordered Sphere Arrays

Srikant Moharana*, Nikhil Shrivas‡, Venkata Jayasurya Yallapragada†
*skm20@iitk.ac.in, ‡snikhil21@iitk.ac.in, †jayasurya@iitk.ac.in.
Indian Institute of Technology Kanpur, Kanpur, U.P,208016, India

Many biological structures exhibit structural colours due to the light matter interaction produced by nano structures[1] present in them. This coloration is due to the short-range and long-range positional correlations among the constituent particles[2]. The investigation of how the density and arrangement of spheres within a material can impact optical phenomena is central to the study of these disordered sphere packed structures. The longitudinal width of the sphere assembly significantly impacts its reflection efficiency and spectrum. In this work, we have modelled the disordered sphere packing by using Monte-Carlo simulations followed by Finite-Difference Time-Domain (FDTD) analysis to get the optical behaviour of the disordered assembly. For experiments, we self-assembled a colloidal suspension in a wedge shaped spacer of desired thickness to get the disordered assembly of polystyrene spheres.

The randomly packed structure was generated using molecular dynamics simulations by varying parameters such as the initial velocity and growth rate of particles[3]. Finite difference time domain (FDTD) numerical method was used to get the optical response of these structures having different longitudinal features. Using this simulation data, we compared the reflectance of two assemblies having different thicknesses. Fig:1 shows reflection peak for a 2.71µm thick assembly of particles whereas complete transmission for a 4.27µm thick assembly. For the relatively thick structure there are a lot of scattering events which disperse all the light in all directions preventing us from seeing any peaks in the reflection corresponding to structural effects, but in case of a packing having finite width, the scattering events are fewer, and we can observe a distinct peak in the reflection spectrum.

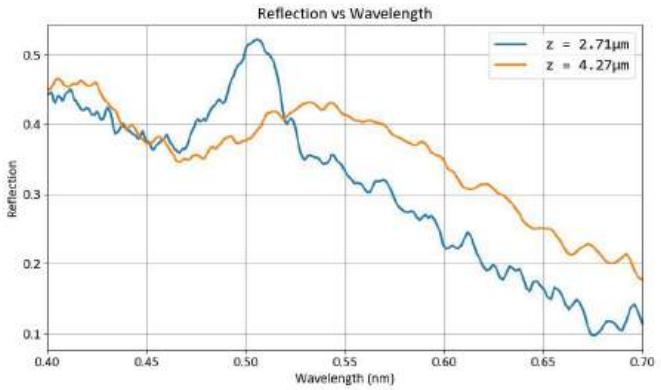


Fig. 1: shows the comparison of reflection spectra of two assemblies of particles having a thickness of 2.71µm and 4.27µm.

To observe the qualitative predictions of the calculations, we have performed colloidal self- assembly of polystyrene nanospheres of radius ~200 nm. We placed a dense suspension of the spheres between two glass coverslips supported by spacer along one of the edges to form a wedge. We scanned the wedge at different positions along one the edge to get reflection spectra for different thicknesses for the assembly. Preliminary results indicate that confining disordered assemblies leads to an increased reflectance at specific wavelength bands.

1. References

[1] Shavit, Keshet, et al. "*A tunable reflector enabling crustaceans to see but not be seen.*" *Science* 379.6633 (2023): 695-700.
[2] Markkanen, J., et al. *"Scattering and absorption in dense discrete random media of irregular particles."* *Optics letters* 43.12 (2018)
[3] Ghossein, Elias, and Martin Lévesque. "*A fully automated numerical tool for a comprehensive validation of homogenization models and its application to spherical particles reinforced composites.*" International Journal of Solids and Structures 49.11-12 (2012): 1387-1398
[4] Spheres Ziwei Deng, Min Chen, Shuxue Zhou, Bo You, and Limin Wu, "A Novel Method for the Fabrication of Monodisperse Hollow Silica", Langmuir 2006, 22, 6403-6407
[5] Victoria Hwang,et.al. "*Effects of multiple scattering on angle-independent structural color in disordered colloidal materials*", Phys. Rev. E 101, 012614(2020)

Free-Carrier Tunable and Reconfigurable Mid-Infrared Meta-Atoms

[1]Sherep Doma Dukpa, [3]Naama Moyal, [3,*]Tomer Lewi, and [1,2,#]Sukanta Nandi
[1]Department of Electronics & Communication Engineering, and
[2]Centre for Quantum Technology,
Indraprastha Institute of Information Technology Delhi (IIIT-Delhi), New Delhi 110020, India
[3]Faculty of Engineering and Institute of Nanotechnology and Advanced Materials,
Bar-Ilan University, Ramat Gan 5290002, Israel

*tomer.lewi@biu.ac.il, #sukanta@iiitd.ac.in

Ultrafast dynamic tuning of meta-atoms- the fundamental building blocks of metasurfaces, is crucial for the design and realization of on-demand nanophotonic components. In this work, we investigate and demonstrate the active tunability and reconfigurability of high-index (n~6) lead telluride (PbTe) hoppercube meta-atoms via optically-induced free-carrier generation. Optical pumping above the bandgap of PbTe leads to refractive-index modulation via free-carrier generation, resulting in an ultrafast (~200ps) amplitude and spectral tunability of ~40% and ~35nm, respectively.

In photonics, the active control of light at subwavelength scales provides a promising route for the development of next-generation nanophotonic and quantum nanophotonic devices. Mechanisms such as thermal and electrical tuning enable dynamic control over the amplitude, phase, and polarization of light. Unlike plasmonics, dielectric Mie-resonators demonstrate better tunability and energy efficiency owing to their intrinsically low optical losses. In this work, we demonstrate the active tunability and reconfigurability of narrow bandgap (~0.32eV) lead telluride (PbTe) hoppercube (HC) meta-atoms through optically-induced free-carrier generation. The generated free-carriers tunes the plasma frequency of PbTe, eventually leading to the modulation of refractive-index.

PbTe is a particularly attractive material for the mid-infrared (MIR) owing to its direct bandgap- thus ideal for optical pumping, high refractive index (n~6), and negative thermo-optic coefficient. Here, crystalline PbTe HCs were synthesized via a scalable hydrothermal method [1] and their active tunability was investigated using ultrafast pump-probe nanospectroscopy integrated with a commercial scattering-type scanning near-field optical microscopy (s-SNOM) system (Attocube systems AG, Fig. 1a). Non-resonant optical excitation produced a reflectance modulation of ~16% at the HC edges (Fig. 1b) with the centers showing ~5 times lower modulation. On the other hand, resonant excitation of a high-Q (Q~100) mode demonstrated a dynamic and reconfigurable behavior with ~40% amplitude and ~35nm spectral modulation with an ultrafast (~200ps) reconfigurability (Fig. 1c).[2,3]

To summarize, we present the first study demonstrating the dynamic and reconfigurable tunability of hierarchical PbTe Mie resonators through free-carrier generation. Our results reveal that the tunable optical response of these chemically scalable resonators is strongly dependent on their morphology and size. These findings establish PbTe as a promising material platform for MIR nanophotonic and metaphotonic applications.

Acknowledgements: TL would like to thank the Israel Science Foundation (ISF) for funding this work under Grant No 523/23. SN acknowledges the financial support provided by the Institute Research Grant (IRG) at IIIT-Delhi.

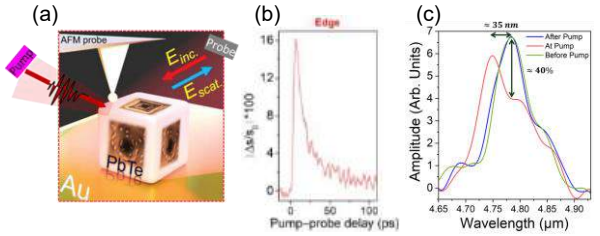


Fig. 1: Free-carrier induced tunability in PbTe HC meta-atoms. (a) Schematic illustration of the ultrafast pump-probe nanospectroscopy using s-SNOM. (b) Ultrafast pump-probe nanospectroscopy showing the normalized reflectance modulation as a function of pump-probe delay. (c) Amplitude and spectral modulation of a higher-order Mie-resonance in a HC resonator, induced by free-carrier excitation.

References:

[1] S. Nandi, T. Shimoni, E. Yitzchaik, T. Lewi, *Advanced Optical Materials* 12 (2024) 2400646.
[2] S. Nandi, T. Lewi, *The European Conference on Lasers and Electro-Optics, Optica Publishing Group* (2025) ck_13_5.
[3] S. Nandi, T. Lewi, *Ultrafast Phenomena and Nanophotonics XXX, SPIE* 13894 (2026) 39.

Influence of Analyte Thickness on Refractive Index Sensing Performance of Silicon Cylindrical Metasurfaces

Anagha Peter[1], Vanniya Balan[2], Srijith Kanakambaran[2#]
[1]Department of ECE, Govt. Engineering College Palakkad, Sreekrishnapuram, Kerala 678633
[2]Department of ECE, IIITDM Kancheepuram, Chennai 600127
[#]*email id:* srijith@iiitdm.ac.in

A silicon cylindrical metasurface on an SiO_2 substrate is numerically investigated using COMSOL Multiphysics for refractive index sensing. The effects of analyte thickness and refractive index on transmission resonance are analyzed. Resonance exhibits a blue shift with increasing thickness, while sensitivity peaks at 250–300 nm before saturating beyond 500 nm.

Dielectric metasurfaces composed of subwavelength resonant structures have emerged as a promising platform for manipulating electromagnetic waves and developing compact, high-performance optical sensors [1]. Their low optical losses, strong light-matter interactions, and high-quality resonances make them particularly suitable for refractive index sensing applications, where small variations in the surrounding medium can produce measurable shifts in the resonance wavelength [2]. In this work, we investigate a metasurface comprising a silicon cylindrical resonator with a radius (R) of 300 nm and a height (H) of 100 nm, positioned at the center of a SiO_2 substrate. The resonators are periodically arranged with a periodicity of 700 nm in the x–y plane, as illustrated in Fig.1. The analyte thickness is varied from 101 nm to 700 nm, while its refractive index is changed from 1.33 to 1.35 to investigate the combined influence of geometrical and optical parameters on the resonance characteristics of the metasurface through numerical simulations performed using COMSOL Multiphysics under Y-polarized normal plane-wave as the excitation source.

The resonance wavelength was determined from the minimum transmission point of each transmission spectrum, and the corresponding resonance shifts were analyzed for different analyte thicknesses and refractive indices. The resonance wavelength exhibits a blue shift with increasing analyte thickness from 101 nm to 400 nm and gradually approaches a constant value beyond 500 nm, as shown in Fig. 2. Increasing the analyte refractive index from 1.33 to 1.35 produces a systematic red shift in the resonance wavelength.

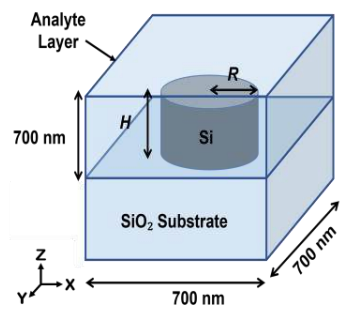


Fig. 1: Metasurface unit-cell schematic

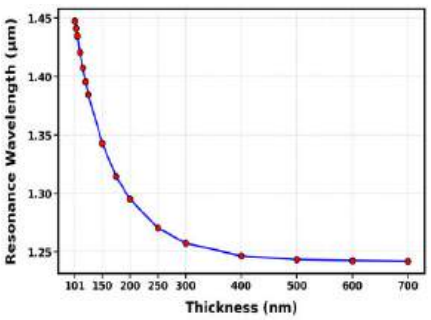


Fig. 2: Resonance Wavelength vs Thickness

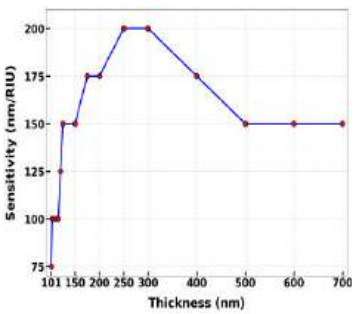


Fig. 3: Sensitivity vs Thickness

The refractive-index sensitivity, shown in Fig. 3, initially increases with analyte thickness, reaches a maximum value of approximately 200 nm/RIU for a thickness of 250-300 nm, and then gradually decreases before stabilizing at approximately 150 nm/RIU for thicknesses above 500 nm. The results demonstrate that analyte thickness significantly influences the refractive-index sensitivity of the proposed metasurface sensor.

References:

[1] Chen, Wenjie, Li, Ming, Zhang, Wenhao and Chen, Yuhang, *Nanophotonics*, vol. 12, no. 6(2023)
[2] Tom van Loon, Minpeng Liang, Thomas Delplace, Bjorn Maes, Shunsuke Murai, Peter Zijlstra, and Jaime Gómez Rivas, *Optics Express* 32, 14289-14299 (2024)

Spin-split dispersion in symmetric and symmetry-broken plasmonic Metasurfaces

Sujit Rajak[1*], Dheeraj Yadav[1], Adway Banerjee[1], Nishkarsh Kumar[2], Suman Mandal[1], Jeeban K Nayak[3], Ayan Banerjee[1], Subhasish Dutta Gupta[1,4], Olivier Martin[3], and Nirmalya Ghosh[1]

[1]Department of Physical Sciences, Indian Institute of Science Education and Research Kolkata, Mohanpur, 741246, W.B., India

[2]Department of Physics, University at Buffalo, SUNY,Buffalo, NY 14260, United States

[3]Nanophotonics and Metrology Laboratory (NAM), Swiss Federal Institute of Technology Lausanne (EPFL), Lausanne, 1015, Switzerland.

[4]Tata Institute of Fundamental Research, Hyderabad 500046, Telangana, India

**sr23rs061@iiserkol.ac.in*

We present Rashba-like spin-split dispersion in an inversion-symmetric 1-D plasmonic grating metasurface and a symmetry-breaking geometric phase gradient metasurface (GPGM) using momentum (k)-domain Mueller matrix analysis. We show how the evolution from structural symmetry to engineered symmetry breaking fundamentally modifies the spin–orbit interaction in the momentum-domain and the resulting spin-split dispersion leaky surface plasmon modes of the spatially plasmonic metasurfaces.

Using a custom-built dark field Fourier-domain Mueller matrix polarimetry system, spin-dependent dispersion of leaky surface plasmon mode is investigated in an inversion-symmetric one-dimensional plasmonic (gold - Au) grating system and a symmetry-breaking geometric phase gradient metasurface (GPGM). For the symmetric grating metasurface, momentum-domain polarization Mueller matrix analysis revealed a transverse momentum-dependent linear birefringence–linear diattenuation (geometric LB–LD) effect arising from the sequential polarization interaction of the structured optical field of tightly focused polarized light and the anisotropic plasmonic crystal as the origin of the observed Rashba-like spin-split dispersion of the leaky plasmon modes. The resulting geometric phase gradient produces spin-dependent transverse momentum shifts, giving rise to symmetric spin-split dispersion in the (M_{14}) and (M_{41}) elements of the (k)-domain Mueller matrix (shown in Fig.1a). In contrast, the phase-gradient metasurface introduces a spatially varying Pancharatnam–Berry phase gradient that deliberately breaks the momentum-space symmetry and imparts additional opposite momentum shifts to left- and right-circularly polarized light, leading to asymmetric spin-selective dispersion(shown in Fig.1b). Detailed analysis of the momentum domain Mueller matrix demonstrated a clear transition from geometry-induced spin splitting in a inversion symmetric metasurface to engineered spin splitting in a symmetry-breaking metasurface, providing a unified framework for understanding and controlling Rashba-like spin-dependent dispersion in plasmonic metasurfaces. The details of the k-domain Mueller matrix analysis, and the results of the analysis of the observed spin-split dispersion will be presented.

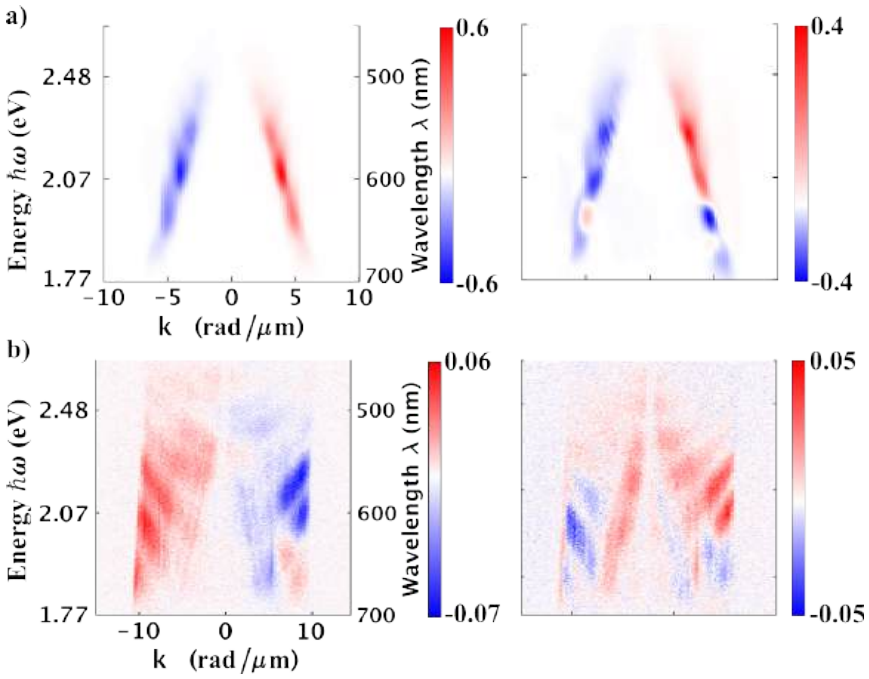


Fig. 1: Spin-dependent dispersion in inversion symmetric (a) and symmetry-breaking (b) plasmonic crystal metasurface. spin-momentum locking of light arising from spin–orbit interaction is clearly manifested as spin (circular polarization)-selective dispersion branches in the M_{14} and M_{41} Mueller matrix elements.

Acknowledgement: The authors gratefully acknowledge the Indian Institute of Science Education and Research (IISER) Kolkata for research facilities, the CSIR–UGC, India, for fellowship support, and the Anusandhan National Research Foundation (ANRF) through the SUPRA Project (Project No. SPR/2023/000 451) for financial support.

References

[1] Sujit Rajak, Nishkarsh Kumar, Dheeraj Yadav, Suman Mandal, Jeeban Kumar Nayak, Ayan Banerjee, Subhasish Dutta Gupta, Olivier J F Martin, and Nirmalya Ghosh. Rashba-like spin splitting in inversion symmetric plasmonic meta- surface. Reports on Progress in Physics, 2026.

[2] J.K.Nayak, H.Suchiang, S.K.Ray, S.Guchhait, A.Banerjee, S.D.Gupta, and N.Ghosh. ". Spin-direction-spin coupling of quasiguided modes in plasmonic crystals". Phys. Rev.Lett., 131:193803, Nov 2023.

Exploring Resonant Metasurfaces for Extreme Light Matter Interaction

[1]Ananya Rout, [2]Ameya Parab, [1]Prashant K. Singh, [2]G. Ravindra Kumar and [1#]Harish N. S. Krishnamoorthy

[1]Tata Institute of Fundamental Research Hyderabad, Hyderabad, Telangana 500046
[2]Tata Institute of Fundamental Research Hyderabad, Mumbai, Maharashtra 400005

[#]*harishk@tifrh.res.in*

Metasurfaces offer a promising platform for coherent in-situ control of electron dynamics in intense laser–plasma interactions. We report the design, fabrication, and optical characterization of a resonantly absorbing plasmonic metasurface optimized for excitation with an 800 nm, 30 fs laser system. Supporting experimental and simulation studies are also presented.

Extreme intense laser-matter interaction with ordered nano-structured targets has significantly improved laser energy coupling and influence the acceleration and directionality of relativistic electrons. A recent study by Dulat et al. [1] demonstrated that we can have in-situ control over the direction of relativistic electrons by using a subwavelength grating target. However, the potential of subwavelength metasurfaces to control such interactions remains largely unexplored. Plasmonic metasurfaces support localized surface plasmon resonances that confine light and tailor the optical response at the nanoscale. Their resonant absorption enables efficient laser energy coupling, while their periodic arrangement of nanometer size meta-atoms can steer the relativistic electrons. In this work we present the design, fabrication, and optical characterization of a plasmonic metasurface optimized for resonant absorption at an excitation wavelength of 800 nm, demonstrating its capability to manipulate the electron emission dynamics.

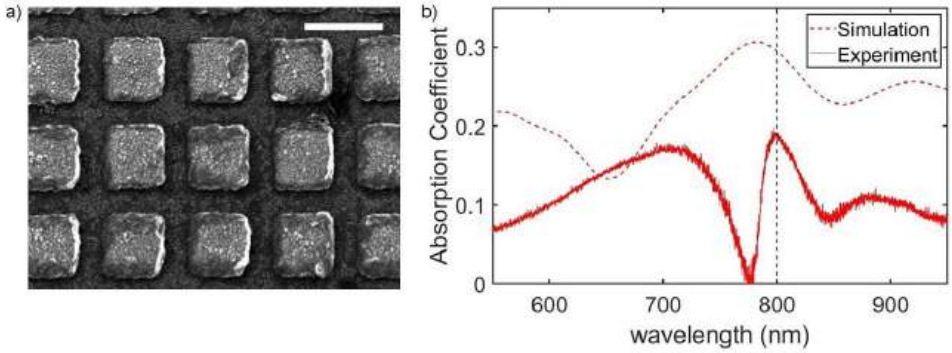


Fig 1: a. SEM image of the fabricated metasurface (top view), (nominal dimensions: w_1=400 nm, w_2=150 nm, height =30n m). There is a ±5% deviation in the size of the meta-atoms from the nominal values. Scale bar = 500 nm. b. Simulated and measured absorption coefficient of the metasurface. The deviation between the two plots may be ascribed to various factors including increased surface roughness resulting from the lithography process and non-uniformity in the sizes of the different meta-atoms which were not considered in the simulation.

The metasurface consists of periodic square gold nano bars fabricated on an ITO-coated glass substrate (fig. 1a). Numerical electromagnetic simulations were performed using FDTD analysis to optimize the geometry for maximum optical absorption at 800nm, followed by fabrication using electron beam lithography. The optical response was experimentally characterized through transmission and reflection spectroscopy, from which the absorption spectrum was determined. The fabricated metasurface showed a peak absorptance of 19% at 800 nm (fig. 1b). Laser excitation experiments were carried out using a Ti-Sapphire laser delivering 150 TW peak-power, 800 nm, 30 fs pulse. Preliminary observations indicate relativistic electron emission along the optical diffraction direction, in addition to the specular reflection and surface propagation modes, upon irradiation at an angle of incidence (AOI) of 25° with approximately 300 mJ pulse energy focused to a 10 μm spot. The enhancement in laser energy coupling is currently under investigation. Ongoing studies focus on understanding the role of resonant plasmonic and all-dielectric metasurfaces in controlling laser–matter interactions in non-linear and extreme non-linear regime.

References:

[1] A. Dulat, S. Rakeeb, S. Dam, A.D. Lad, Y.M. Ved, S. Kruk, G.R. Kumar, Laser & Photonics Reviews 19 (2025) 2401570.

Multichannel photon correlation simulation of fast spectral dynamics of single fluorophores

[1]Nikhil Shrivas, [1]Abhishek Yogi , [1]Venkata Jayasurya Yallapragada
[1]Department of Physics, Indian Institute of Technology Kanpur, Kanpur 208016, India

Email: snikhil21@iitk.ac.in

We demonstrate a computational framework to simulate and analyze multichannel photon timestamping experiments. This enables us to visualize and differentiate between the effects of different physical processes within the emitter, and the artefacts that shows up in these types of fast spectral diffusion based experiments and justify results from real experiments.

Experiments using photon correlations soon became popular in studying properties of emitted light, which is a route to obtaining information about the photo-physical processes within an emitter[1]. One of the interesting applications of these multichannel based photon-correlation experiment is the study of fast spectral dynamics in single quantum dots (QDs). Spectrally resolved photon correlation measurements using SPAD arrays[2], where is spectrum from a single QD is spread over several pixels of SPAD arrays provide a route to uncovering fast intensity and spectral fluctuations in quantum dots. Here it is crucial to know how various processes in the QD and artefacts in the detection manifest themselves in such higher order-based photon correlation study. However, analytical models of emitters under study become difficult to formulate for multi-channel photon correlation experiments.

A Monte Carlo simulation was performed to model the response of a typical photo-luminance experiment performed on a QD. Each process can be simulation by sampling events from there respective statistical distribution. For example, absorption can be sampled from Poissonian distribution, which emission can be sampled from exponential distribution. We then include spectral contribution form the inherent temperature broadening and quantum confined stark effect (QCSE) [3] which plays major role in the spectrum diffusion. The emitted photons from the QD then go through different channels from the grating to individual pixels of SPAD arrays. We then include various artefacts of SPAD arrays like dark counts, non-uniform time binning, detection efficiency, etc.

With this simulation we are able to point out how various processes manifest themselves in a realistic experiment by taking the data of the simulation and finding higher order auto-correlation data w.r.t. time and energy. With this we show how QCSE leads to broadening of higher order auto-correlation data, which verifies the results from a real spectral resolved photon correlation experiment.

References:

[1] Lubin, Gur, et al. "Photon correlations in spectroscopy and microscopy." ACS photonics 9.9 (2022).

[2] G. Lubin, R. Tenne, A. C. Ulku, I. M. Antolovic, S. Burri, S. Karg, V. J. Yallapragada, C. Bruschini, E. Charbon, D. Oron, *Nano Letters* (2021).

[3] S. A. Empedocles, M. G. Bawendi, Quantum-Confined Stark Effect in Single CdSe Nanocrystallite Quantum Dots.Science (1997).

Optical properties of single magnetic micro and nanoparticles using a transmission-based darkfield microscope

Arya Kumar Siddharth and #Venkata Ramanaiah Dantham
Department of Physics, Indian Institute of Technology Patna, Bihar 801106, India

#dantham@iitp.ac.in

Magnetic micro- and nanoparticles have attracted considerable interest for biomedical and photonic applications because of their excellent biocompatibility and unique optical properties.[1-3] This work presents the absorption and scattering characteristics of individual magnetic particles together with wavelength-dependent electric and magnetic field intensity distributions for different particle sizes, providing insight into their optical resonances.

This work presents a comprehensive optical characterization of individual magnetic micro- and nanoparticles using a transmission-mode dark-field microscope. The particle morphology is first examined by atomic force microscopy (AFM), followed by UV–Vis absorption and fluorescence spectroscopy to investigate their ensemble optical properties.

The optical response of single particles is then investigated by recording far-field scattering images (as shown in Fig. 1) and scattering spectra using a transmission-based dark-field optical microscope. From these measurements, the resonance wavelengths and full widths at half maximum (FWHM) of individual particles are determined, enabling quantitative analysis of their optical resonances. Furthermore, the

influence of the polarization state of the incident light on the scattering characteristics and resonance behavior of single magnetic particles is systematically investigated. Numerical calculations of the electric and magnetic field intensity distributions inside and around the particles are also presented to support the experimental observations. Representative dark-field scattering images of individual magnetic nanoparticles will be included to illustrate the measured optical response.

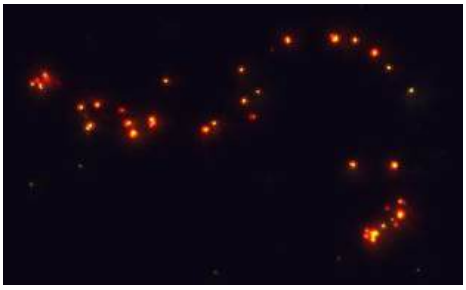


Fig 1. The dark field scattering image of magnetic nanoparticles

This study demonstrates that transmission-mode dark-field microscopy provides a powerful, non-destructive approach for probing the optical properties of single magnetic micro- and nanoparticles, offering valuable insights for their applications in optical sensing, bioimaging, and nanophotonics.

References:

[1] K. McNamara, S.A. Tofail, *Advances in Physics: X* 2 (2017) 54–88.
[2] L.R. Hirsch, R.J. Stafford, J.A. Bankson, S.R. Sershen, B. Rivera, R.E. Price, et al., *Proceedings of the National Academy of Sciences* 100 (2003) 13549–13554.
[3] Q. Tian, J. Hu, Y. Zhu, R. Zou, Z. Chen, S. Yang, et al., *Journal of the American Chemical Society* 135 (2013) 8571–8577.

Graphene-Coated Nanomatryoshka for Cholesterol Detection

[1,#]Alok Singh, and [1]Laksh Sharma
[1]Department of Physics, JSS University, Noida
[#]*aloksinghphy@gmail.com*

An ultrasensitive graphene assisted transition metal nitride nanomatryoshka is proposed for cholesterol biosensing in the near-infrared region. Strong Fano resonance and enhanced exhibits a linear red shift with cholesterol concentration, demonstrating excellent potential for biomedical sensing applications.

Cholesterol is important biomarker associated with cardiovascular diseases, atherosclerosis, and stroke. Therefore, rapid and reliable cholesterol detection is essential for early diagnosis and healthcare monitoring. In this work, graphene-coated TiN nanomatryoshka operating in the near-infrared (NIR) region is investigated as plasmonic cholesterol sensor [1]. The proposed structure consists of a SiO_2 core (R_1=85nm), TiN shell (R_2=95nm), and monolayer graphene (t_G =0.34 nm) embedded in the sensing medium. Adsorption of cholesterol, resulting in a measurable plasmonic resonance shift. The optical response is analyzed using Mie scattering theory [2]. The scattering efficiency is expressed as

$$Q_{sca} = \frac{2}{\rho^2}\sum_{n=1}^{\infty}(2n+1)\,(|\,A_n\,|^2 + |\,B_n\,|^2) \quad (1)$$

where ρ denoted the size parameter and A_n and B_n are the electric and magnetic coefficients, respectively. The resonance wavelength corresponds to the maximum scattering peak is monitored to evaluate sensing performance. Strong coupling between the TiN plasmonic mode and graphene induced varies from 1.33840 to 1.34529, the resonance wavelength shifts from 1046.24 nm to 1050.52 nm. The observed wavelength shift of 4.28 nm corresponds to sensitivity of 617.64 nm/RIU. The nearly linear variation of resonance wavelength with refractive confirms stable sensing characteristics and reliable analyte detection.

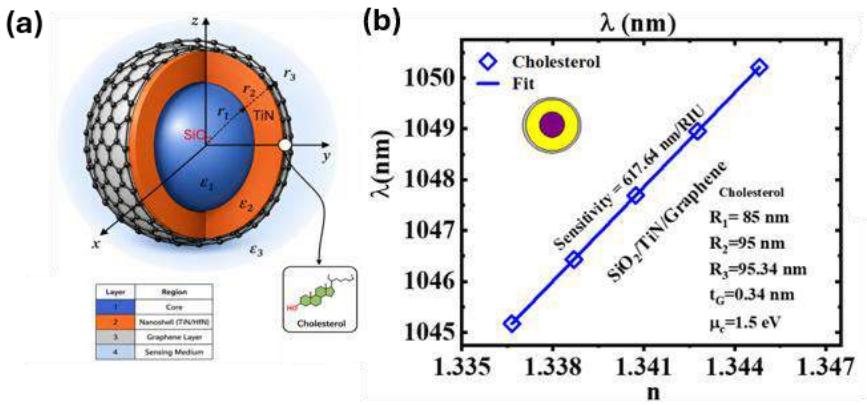


Fig. 1. (a) Graphene-assisted TiN nanoshell structure for cholesterol biosensing. (b) Resonance wavelength shift with refractive index, showing a sensitivity of 617.64 nm/RIU in the near-infrared region.

The enhanced sensing performance originates from strong electromagnetic field localization at the graphene-TiN interface and excellent adsorption capability of monolayer graphene. The proposed sensor combines high sensitivity label-free operation and thermal stability making it a promising platform for next-generation cholesterol diagnostics and point-of-care biomedical monitoring.

Acknowledgements: A. Singh thanks Dr. Manmohan Singh Shishodia (GBU, Greater Noida, India) for his valuable guidance.

References:

[1]. A. Singh, M. S. Shishodia, D. Agarwal, and P. Kumar, Appl. Phys. A 129, 366 (2023).
[2]. A. Singh, P. Rajput, R. Verma, J. Appl. Phys 139, 13 (2026).

Dual-mode SEIRA detection of microplastics from disposable paper cups using a plasmonic metagrating

Ojasvi Singh[1], Sachin Kumar Srivastava[1,2,*]

[1]Department of Physics, Indian Institute of Technology Roorkee, Haridwar, UK 247667, India
[2]Center for Photonics and Quantum Communication Technology, Indian Institute of Technology Roorkee, India
sachin.srivastava@ph.iitr.ac.in

A plasmonic metagrating supporting dual mode sensing is demonstrated. Microplastics in paper cups are detected using absorption dependent molecular mode and refractive index dependent Fano mode with sensitivities of 0.386 Abs./μg and 558.9 cm^{-1}/μg.

Infrared absorption can be enhanced when molecules are adsorbed on surfaces supporting localized electromagnetic radiation, a phenomenon known as surface enhanced infrared absorption (SEIRA) [1]. One approach to realize SEIRA is through surface plasmon resonance (SPR). Artificially designed plasmonic nanostructures, like metagratings can enhance localized electromagnetic fields. In present work, a flexible plasmonic aluminum (Al)- metagrating (FPM) template was fabricated in a single step directly from a commercial compact-disc on a scotch tape. Varying masses of HDPE (m) were deposited on the FPM and absorption (Abs.) spectra were recorded using a Fourier transform infrared spectrometer in transverse magnetic (TM) mode at an angle of incidence at 80^0, as shown in Fig.1(a).

A sharp vibrational molecular mode near 2913cm^{-1} (ν_{2913}) was observed [2]. Its strength depends on the number of molecules interacting with the incident light and hence is proportional to m as shown in Fig.1(b). Additionally, in Fig. 1(a), a Fano mode (ν_{Fano}) corresponding to FPM whose spectral position depends on the effective refractive index (n_{eff}) near the FPM surface is also observed. It shows a red shift in wavenumber with decreasing m. Furthermore, solutions were made by spiking the solvent with mp from 200ml of water in disposable paper cups at 80^0C for 15 minutes. The response curve of spiked solutions was likewise plotted for both the modes as shown in Fig.1(b,c). For same response value, the difference in m values for spiked and unspiked values gives the leached mp (u) from paper cups. The sensitivity (S) of a sensor is given by the slope of the response curve. For ν_{2913} and ν_{Fano}, the S values come out to be 0.386 Abs./μg and 558.9 cm^{-1}/μg respectively.

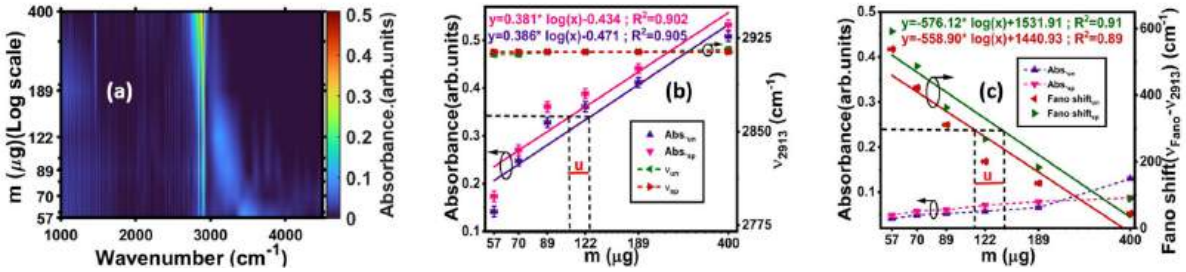


Fig.1. (a) Abs. spectra of various m of mp deposited on FPM. Response curve for (b) ν_{2913} – (c) ν_{Fano}- modes

FPM supporting two simultaneous modes of sensing with distinct sensing mechanism was used to detect leaching of mp in disposable paper cups. Through difference of spiked and unspiked solutions, the amount of mp leached in 200ml of hot water exposed for 15min is estimated to be approx. 25μg.

Funding from MoE-STARS(STARS/APR2019/NS/713); SERB-(SRG/2020/002518); DST India (INT/Korea/JNC /CPS) is thankfully acknowledged. Ojasvi Singh thanks MoE and IITR for a research fellowship.

References:

[1] Kozuch, Jacek, Kenichi Ataka, and Joachim Heberle, NLM/ISO 4:**70** (2023).
[2] Julie Charles. Asian J. Chem. 21(6):4477 (2009).

Numerical Analysis of Pd/$HfSe_2$ Based Surface Plasmon Resonance Biosensor with Enhanced Sensitivity for Biomolecular Detection

[1]S Subanya ,[1]T K Lena Shree, [1]M Lavanya, [2#]K B Rajesh
[1]Department of Physics, PSGR Krishnammal College for Women, Peelamedu, Coimbatore – 641 004
[2]Department of Physics, Government Arts College, Coimbatore – 641 018
[#]*rajeshkb@gmail.com*

Surface plasmon resonance (SPR) technology has gained significant attention for high-performance, label-free biosensing owing to its ability to detect minute refractive index variations. In this work, a multilayer SPR sensor is designed and computationally investigated using the Transfer Matrix Method (TMM). The influence of the multilayer architecture on plasmonic behavior is systematically examined by evaluating sensitivity, figure of merit (FoM), and detection accuracy. The optimized structure, comprising 34 nm Silver (Ag), 15 nm Palladium (Pd), and 1 nm Hafnium Diselenide ($HfSe_2$), achieves better sensor parameters within a refractive index range of 1.335–1.351. The improved optical response indicates that the proposed configuration is well suited for the detection of subtle biomolecular interactions and shows promise for biomedical diagnostics, disease biomarker analysis and environmental sensing.

Surface plasmon resonance (SPR) biosensors have emerged as powerful label-free optical platforms for real-time detection of biomolecular interactions owing to their high sensitivity and rapid response. In this work, a Kretschmann configuration-based multilayer SPR biosensor comprising a Cesium Fluoride (CsF) prism, silver (Ag) layer, palladium (Pd) layer, hafnium diselenide ($HfSe_2$) transition metal dichalcogenide (TMD) layer, and sensing medium is proposed and numerically investigated [1-2]. The selected materials provide complementary optical characteristics that enhance surface plasmon excitation and strengthen light–matter interactions, thereby improving sensing performance. The optical response of the proposed structure is analyzed using the Transfer Matrix Method (TMM) based on Maxwell's electromagnetic boundary conditions. Sensor performance is evaluated in terms of sensitivity, detection accuracy (DA), and figure of merit (FoM) over a refractive index range of 1.335–1.351. In the Fig.1 among the investigated configurations, the optimized structure consisting of a CsF prism, 34 nm Ag layer, 15 nm Pd layer, and 1 nm $HfSe_2$ layer exhibits a maximum sensitivity of **407.793125°/RIU**, a detection accuracy of **0.254226**, and a figure of merit of **103.671615**, demonstrating superior sensing performance. The enhanced response is attributed to the synergistic plasmonic behavior of the Ag/Pd bilayer and the excellent optical properties of the $HfSe_2$ nanolayer, which improve confinement of the electromagnetic field at the metal–dielectric interface.

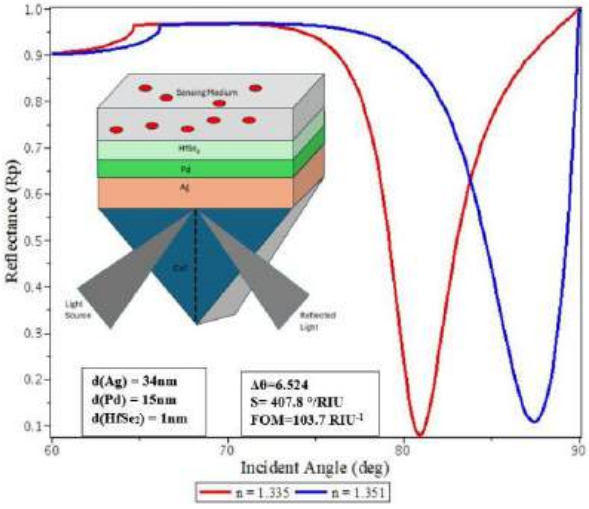


Fig. 1: Reflectance spectrum for the optimized configuration

The proposed sensor exhibits excellent capability for detecting minute refractive index variations associated with biomolecular interactions, making it a promising candidate for clinical diagnostics, disease biomarker detection, pathogen identification, drug discovery, food safety analysis, environmental monitoring, and point-of-care biomedical applications.

References:

[1] Ritesh Singh Shah, Rahul Kumar Singh, Rajeev Kumar. *Plasmonics* (2025) 20:4811–4820
[2] Bhishma Karki, Amrindra Pal, Partha Sarkar, Ram Bharos Yadav, Gaurav Dhiman, Arjuna Muduli. *Plasmonics (2023)*

Modelling Surface Plasmon Polaritons in double layers Graphene Elliptical Waveguide

Ramnarayan, Ravindra Singh and #Surendra Prasad
Department of Physics, Institute of Science, Banaras Hindu University, Varanasi-221005

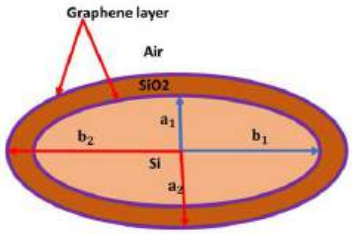
#prasads@bhu.ac.in

The dispersion characteristics of surface plasmon polaritons (SPPs) supported in the double layers graphene elliptical waveguide has been simulated using Comsol Multiphysics. It is observed that the fundamental mode exhibits higher effective index as compared to the first and second order modes.

The SPPs are surface electromagnetic waves that propagate along the interface between a metal and a dielectric medium [1]. SPPs are instrumentals in the development of highly compact and efficient photonic components, viz. orthogonal mode couplers, metamaterial-based ring resonators, and refractive index sensors [2]. As metals have poor surface mode confinement in the mid-infrared frequency regime as its real permittivity becomes less negative [3]. So, graphene is being used to overcome this limitation. Also, it provides additional parameters such as chemical potential, temperature, and operating frequency to tune its conductivity, hence permittivity [4]. Moreover, compared to conventional planar and cylindrical waveguide, elliptical shaped waveguide provides more structure parameters to control the SPPs properties. An elliptical dielectric nanowire coated with monolayer graphene has demonstrated enhanced confinement and longer propagation length compared to its cylindrical counterpart fabricated from the same material system [5]. Hence, in this manuscript, dispersion properties of SPPs supported in the double layer elliptical graphene waveguide are simulated.

The double layer graphene waveguide structure is consisted of two graphene ribbons, separated by a dielectric material, as shown in the figure 1. The ribbons form an elliptical shape, characterized by their semi-minor and semi-major axes. The interior and exterior semi-minor axes are labelled as a_1 and a_2 respectively, while the interior and exterior semi-major axes are denoted by b_1 and b_2. The separation between the two graphene layers is defined as $d_1 = a_2 - a_1$ for the semi-minor axes and $d_2 = b_2 - b_1$ for the semi-major axes. Graphene is modelled as an infinitely thin material with surface conductivity, which is described by the Kubo formula [4].

Fig.1: Schematic diagram of waveguide



The simulation work has been performed using the Electromagnetic Waves, Frequency Domain interface from the RF Module in the Comsol. The waveguide structure has been divided into three regions depending on the relative permittivity of the dielectrics: ε_1= 11.9, ε_2= 2.09, ε_3= 1. The effective mode index ($\frac{Re(k_z)}{k_0}$) is plotted with frequency for SPPs modes, where k_z is the wave vector of SPPs modes in the z-direction and k_0 is the wave vector of light in free space. It is observed that increase in the temperature of waveguide affect the effective modes of fundamental (solid),first (dash) and second (circles) order modes as shown in the figure 2. It is concluded that the proposed waveguide supports tunable SPPs mode, whose dispersion chracterisics strongly depend on the temperature.

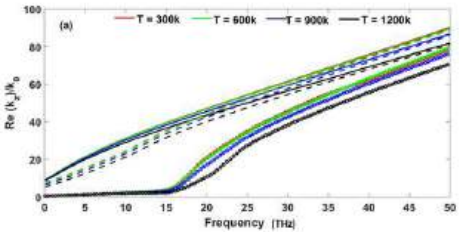


Fig. 2: Variation of effective mode index with T

References:

[1] W. L. Barnes, A. Dereux, T.W. Ebbesen, *Nature* 424(2003) 824.
[2] A. K. M. Rakib, A. T. Bin Siddique, M.S. Sakib, M. O. Faruque, R. H. Sagor, *Optics Communications* 530 (2003)129205.
[3] P. Liu, X. Zhang, Z. Ma, W. Cai, L. Wang, J. Xu, *Optics Express* 21 (2013)32432–32440
[4] M. Jablan, H. Buljan, M. Soljačić, *Physical Review B* 80 (2009) 245435
[5] X. Cheng, W.R. Xue, Z. Z. Wei, H. Y. Dong, C. Y. Li (2019), *Acta Physica Sinica* 68 (2019)058101

Design Optimization of Plasmonic Metasurfaces for Sensing Applications

[1]Charu Rajput,[1,2]Vinod Parmar and [1,2,#]Umesh Kumar Tiwari
[1]Optics & Photonics Instrumentation, CSIR-Central Scientific Instruments Organisation, Chandigarh – 160030, India
[2]Academy of Scientific & Innovative Research (AcSIR), Ghaziabad – 201002, India

[#]*Email id of the corresponding author:* umeshtiwari.csio@csir.res.in

***Abstract**: This paper investigates the effect of plasmonic spokes in design of plasmonic meta-surfaces on its resonance behavior and sensing performance using FDTD simulations. In contrast to the conventional four spoke design, six and eight spoke geometries exhibit higher transmission values and lower losses with almost same resonant wavelengths.*

Plasmonic metasurfaces have attracted significant attention for optical sensing because of their ability to confine electromagnetic energy through localized surface plasmon resonance (LSPR). Plasmonic metasurfaces are primarily made from array of meta-atoms which consists of metallic nanostructures whose optical response are governed by the particle plasmon resonance they support [1]. In a time-varying external field, the collective motion of conduction band electrons can be described as a Lorentzian oscillator, with its characteristic peak in the displacement amplitude (polarizability) around the resonance frequency accompanied by a π phase shift over the spectral width of the resonance [1].

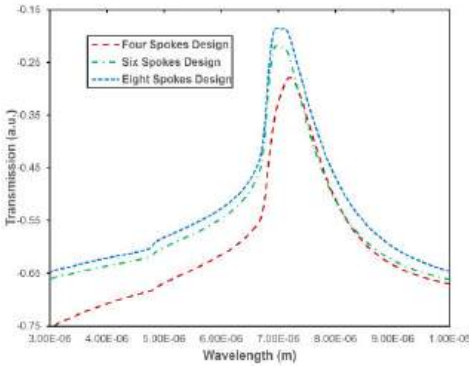


Fig. 1: Transmission spectra of distinct design of plasmonic metasurfaces depicting the resonance

In this work, we have designed the plasmonic metasurfaces with four, six, and eight spokes (metallic nanostructures on base substrate) and the field effect from the various design of plasmonic nanostructures were analyzed using Finite-Difference Time-Domain (FDTD) simulations to investigate the influence of spoke configuration on resonance behavior, transmission characteristics, and localization of electric-field around the spokes.

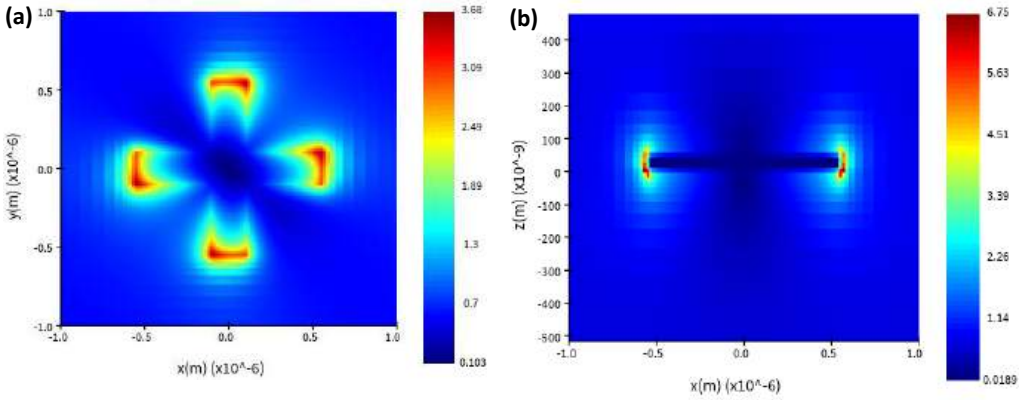


Figure 2. The electric field profile obtained from the 4-spokes design of plasmonic metasurfaces: (a)Top-view of electric field intensity distribution (b) Side-view of electric field distribution.

The transmission spectra show that increasing the number of spokes improves the interaction between incident light and the metallic nanostructure. The aforementioned results indicate enhanced electromagnetic confinement and stronger optical resonance. The Electric-field distributions further validate these observations. The localized hotspots at the metallic edges due to plasmon excitation, while the top-view field distribution demonstrates strong field concentration around the spoke tips and central coupling region. These results confirm that increasing the spoke number enhances light confinement and suggests improved refractive-index sensing performance, making multi-spoke plasmonic metasurfaces promising candidates for high-performance plasmonic sensors.

References:

[1] N. Meinzer, W. L. Barnes, I.R. Hooper, *Nature Photonics* 8, 889-898 (2014)..

Performance Analysis of SPR Biosensor for Colorectal Cancer Diagnosis Using TMDC layers

[1]T.K. Lena Shree, [1]S Subanya, [1]R. Sakthi Maheswari, [1]M. Amal, [1]S. Kanishka,
[2]K.B. Rajesh, [1#]M. Lavanya

[1]Department of Physics, PSGR Krishnammal College for Women, Coimbatore-641004
Department of Physics, Government Arts College, Coimbatore-641018
[#]lavanyam@psgrkcw.ac.in

Colorectal cancer is a major global health concern, and early diagnosis is essential for improving patient survival. Existing diagnostic methods are often invasive or have limitations in detecting the disease at an early stage. This study proposes a highly sensitive, non-invasive surface plasmon resonance (SPR) sensor using a carefully designed multilayer structure to improve biomarker detection. The multilayer SPR is designed using Kretschmann configuration incorporating in the calcium fluoride CaF_2 prism, a silver (Ag) layer, an Aluminum antimonide (AlSb)/ nickel phosphorus trisulfide ($NiPS_3$), Hafnium diselenide ($HfSe_2$)/ tantalum diselenide ($TaSe_2$) *transition metal dichalcogenide (TMD) sensing medium achieves the high sensitivity.*

Colorectal cancer (CRC) is one of the most prevalent malignancies worldwide and ranks among the leading causes of cancer-related deaths, with millions of new cases and hundreds of thousands of fatalities reported annually. Early diagnosis is crucial for improving patient survival; however, conventional diagnostic techniques such as colonoscopy and tissue biopsy are invasive, time-consuming, and may cause patient discomfort. Non-invasive methods, including fecal immunochemical tests (FIT), fecal occult blood tests (FOBT), stool DNA testing, and medical imaging, offer less discomfort but often face limitations in sensitivity, specificity, or early-stage detection. In this regard, a surface plasmon resonance (SPR) sensor based on the Kretschmann configuration presents a promising solution, offering label-free, real-time, diagnosis of colorectal cancer.

The proposed surface plasmon resonance (SPR) sensor is designed based on the Kretschmann configuration, incorporating a calcium fluoride (CaF_2) prism, a silver (Ag) plasmonic metal layer, an aluminum antimonide (AlSb)/nickel phosphorus trisulfide ($NiPS_3$) semiconductor enhancement layer, and a hafnium diselenide ($HfSe_2$)/tantalum diselenide ($TaSe_2$) transition metal dichalcogenide (TMD) sensing layer [1-2]. Each material is carefully selected for its unique optical properties, enabling enhanced light–matter interaction and improved plasmonic performance. The multilayer architecture is strategically optimized to exploit the complementary advantages of these materials, thereby enhancing the sensor's detection capability. The performance of the proposed SPR sensor is numerically analyzed using the Transfer Matrix Method (TMM) based on Maxwell's electromagnetic boundary conditions. The sensing performance is evaluated in terms of key parameters, including sensitivity, figure of merit (FoM), and detection accuracy, to assess its suitability for the non-invasive detection of colorectal cancer biomarkers. The results demonstrate that the proposed SPR sensor configuration, consisting of a CaF_2 prism, silver layer, aluminum antimonide (AlSb) layer, and hafnium diselenide ($HfSe_2$) layer, exhibits high sensitivity, as evidenced by the reflectance curve. This enhanced sensing performance highlights its potential as a promising platform for the early and non-invasive detection of colorectal cancer.

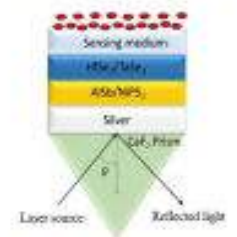
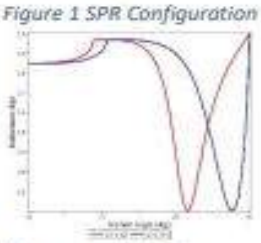


Figure 1 SPR Configuration



These computational techniques enable precise optimization of the sensor's structural parameters, thereby enhancing its sensitivity to subtle refractive index variations associated with the early stages of colorectal cancer. The optimized design demonstrates improved detection performance by effectively responding to minute biomolecular changes.

References:

[1] Bhishma Karki, Amrindra Pal, Gaurav Dhiman, Mohammad Z. Ahmed, *Microchimica Acta* (2025) 192:126
[2] Manaswi Kilaru, Jaswitha Bode, Yesudasu Vasimalla, Ragini Singh, Santosh Kumar, *Microchemical Journal* 224 (2026) 117439

Fourier domain enhancement of Chiro-optical signal in Plasmonic Nanostar using Structured light

[1,*]**Dheeraj Yadav**, [1]Sujit Rajak, [1]Nimish Sharma, [1]Adway Banerjee, [2]Nishkarsh Kumar, [1]Ujjal Karmakar, [2]Jojo P. Joseph, [2]Alexander Baev, [1,3]Subhasish Dutta Gupta, [2]Paras N. Prasad, [1]Nirmalya Ghosh

[1]Indian Institute of Science Education and Research Kolkata, Mohanpur, 741246, W.B., India
[2]University at Buffalo SUNY, New York, New York 14260, United states
[3]Tata Institute of Fundamental Research, Hyderabad, 500046, Telangana, India

[*]*dy23ip012@iiserkol.ac.in*

Chiro-optical effects are central to wide variety of applications ranging from molecular characterization to chemical and bio-sensing. We demonstrate that structured optical field of a focused vortex and Gaussian beam in a Fourier-domain configuration significantly enhances chiro-optical signal from a chiral polymer with plasmonic gold nanostar. A theoretical framework combining modified chiral Mie theory and angular spectrum approach unravels the underlying mechanisms.

Chiro-optical interactions are intrinsically weak because the differential interaction of matter with left- and right-circularly polarized light arises from higher-order light-matter coupling. Here, we demonstrate that these weak chiro-optical responses can be significantly enhanced using tightly focused circularly polarized Laguerre-Gaussian (LG) beams carrying both spin and orbital angular momentum (OAM) of light. We have used a momentum (Fourier)-domain Stokes polarimetry experimental embodiment to measure the polarization response of an annealed P*AuNS film (gold nanostar embedded in a chiral polymer) [1]. A band-pass filter (480–510 nm) isolated the absorbance region of chiro-optical signal, while varying numerical aperture (NA = 0, 0.1, and 0.3) controlled the vectorial structure of the incident field. We experimentally observed a systematic enhancement of the spin-vortex-locked dichroism, defined as the normalized differential response between opposite spin (circular polarization)-OAM states, with increasing numerical aperture. In order to comprehend and understand the underlying mechanism of the enhancement of chiro-optical response, we have developed a theoretical model combining a modified chiral Mie scattering formalism [2] with a generalized angular spectrum approach for modeling focusing of vector vortex beams [3]. The simulated circular differential absorption agrees well with the experimental observations. Multipolar decomposition further reveals that, unlike conventional Gaussian-beam ($l = 0$) illumination, spin-vortex excitation strongly enhances higher-order multipolar resonances, particularly the quadrupole and octupole modes of the plasmonic nano-scatterer. Differential contributions of such multipolar resonances for left and right circularly polarized vortex beams with opposite topological charges governs the observed enhancement of chiro-optical signal. The details of the experimental results and their theoretical modeling will be presented

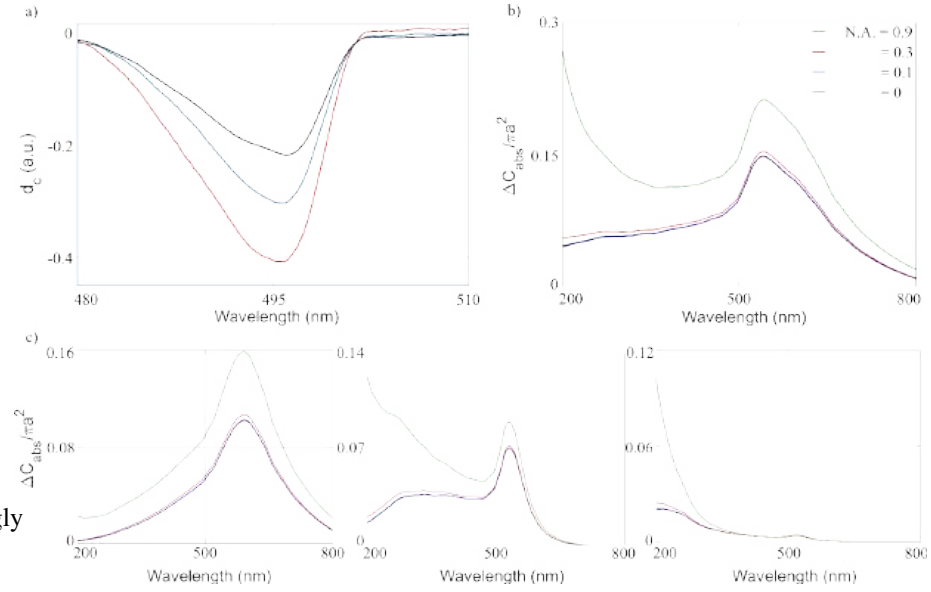


*Figure 1: (a) Experimentally determined spin–vortex-locked dichroism obtained from the Fourier (momentum -k)-domain Stokes vector measurements on the annealed P*AuNSs film under high-NA structured beam illumination. (b) Corresponding simulated spin–vortex circular dichroism calculated using a modified Mie scattering formalism combined with a generalized angular spectrum approach for modeling tight-focusing of vector vortex beams. (c) Multipolar decomposition of the spin–vortex circular dichroism into dipole (left), quadrupole (center), and octupole (right) contributions, revealing the dominant role of higher-order multipoles in the observed chiro-optical signal enhancement with structured light.*

Acknowledgements: The support from IISER-K and Scheme for Promotion of Academic and Research Collaboration (SPARC) is acknowledged.

References:
[1] S. Sunder, A. Sharma, *S.R. Abraham, J.P. Joseph, B.M. Rajapakse, A. Dutta, R.K. Das, A. Kuzmin, A. Baev, L. Velarde, P.N. Prasad, M.T. Swihart, Advanced Optical Materials* 12 (2024) 2400914.
[2] S.J. Yoo, Q.-H. Park, *Scientific Reports 5*, 14463 (2015).
[3] L.C. Venuti, T. Albash, D.A. Lidar, P. Zanardi, *B. Richards, E. Wolf, Proceedings of the Royal Society of London A* 253 (1959) 349–379.

Investigating Optical Excitons in Two-Dimensional Inorganic-Organic Hybrid Perovskites

[1]Naveen Yadav,[2]Mohammad Adnan, [1]Kanaka Ravi Kumar, and [1, #]G. Vijaya Prakash

[1]Department of Physics, Indian Institute of Technology Delhi, New Delhi 110016, India
[2] Department of Physics, Aligarh Muslim University Aligarh 202002 India

[#] gaddam.vijaya.prakash@gmail.com

Self-assembled 2D inorganic–organic hybrid semiconductor heterostructures have been synthesized for nanophotonic applications. The novel phenomenon of self-assembly has been explored for making hybrid alternate layers of organic and inorganic moieties and displayed strong exciton emission. The nonlinear optical (NLO) studies reveal details on multiphoton absorption and other associated effects.

Recently, inorganic–organic (IO) hybrid perovskites have attracted significant attention due to combined effects of both inorganic and organic moieties present as layered structures forming 2D semiconductors heterostructures (SHs) [1]. The respective stacking exhibits strong exciton emission in the visible region displaying significant role of alternate bandgaps in the confined structure [2]. In this present work, we are interested in a particular organic compound, Chlorobenzyl amine (n-Cl-$C_6H_4CH_2NH_2$, whose amine group is positioned differently in each compound forming 2-, 3-, and 4-Chlorobenzyl amine. This, as an organic combined with inorganic PbI_2 in presence of HI makes a complete I-O hybrid SHs (hereafter CBPI) under controlled experimental conditions. The as formed I-O hybrid products are thoroughly washed in appropriate solvent to remove excess HI and allowed to dry under ambient conditions. Figure 1 represents the overall experimental workflow and initial confirmations of exciton emission. It has been observed that there is a significant variation in PL intensities observed from 2-,3-, and 4-CBPI thin films prepared on glass substrate. The observed variations in optical characteristics are interpreted based on self-assembled structure formation and inter-molecular bonding between inorganic and organic moieties. Further, the nonlinear optical (NLO) studies have been performed to investigate the multiphoton absorption phenomenon among these I-O hybrid structures. Overall, the results obtained so far demonstrate the strong relationship between molecular structure and optical response highlighting the significant role of organic compound (Chlorobenzyl amine) in CBPI-based IO hybrid perovskites. This has great potential in photonics and near future optoelectronic device applications. Details of all the characterizations and results will be discussed in the presentation/paper.

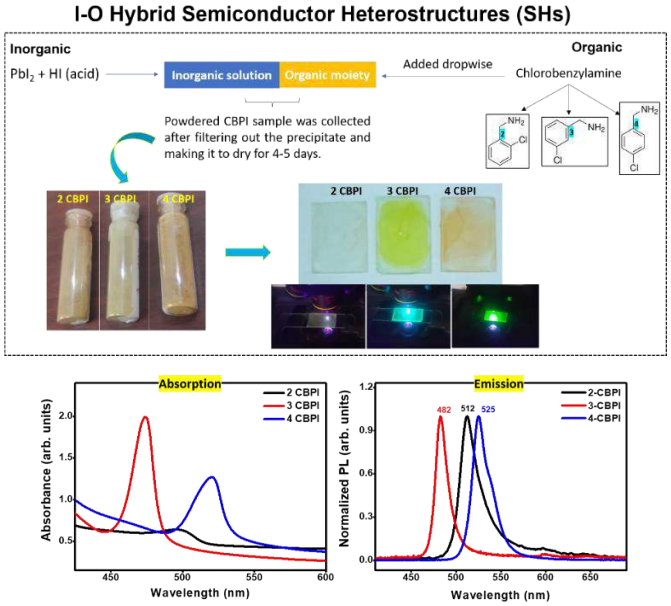


Fig. 1: Schematics of the experimental workflow and corresponding optical characteristics of CBPI thin films.

References:

[1] P. Steeger, M. Adnan, T. Deilmann, X. Li, S. Müller, K. Skrzyńska, M. Hanfland, E. Kolesnikov, J.Kösters, T. Block, R. Schmidt, I. Kupenko, C. Sanchez-Valle, G. Vijaya Prakash, S. M. Vasconcellos, and R. Bratschitsch, *J. Am. Chem. Soc.* 146 (2024) 23205-23211.

[2] M. Adnan, J. J. Baumberg, and G. Vijaya Prakash, *Sci. Rep.* 10 (2020) 2615.

Tailoring soft cavities for robust molecular strong coupling

[1]Siddharaj M. Gadge and [1,#]Adarsh B. Vasista
[1]Department of Physics, Indian Institute of Science Education and Research Bhopal, Bhopal 462066, Madhya Pradesh, India
[#]*avasista@iiserb.ac.in*

Conventional cavity figures of merit overlook the asymmetry between cavity and molecular linewidths. Studying TDBC coated polystyrene microspheres, we introduce $\chi = g/\max(\kappa, \gamma)$*, which peaks when* $\kappa \approx \gamma$*. This dissipation matching condition sets the optimal soft cavity size for robust molecular strong coupling, independent of the emitter linewidth and its resonance wavelength.*

Optical cavities reshape molecular absorption, emission and energy transfer through light–matter coupling. Once the coupling strength g overcomes the dissipative rates, hybrid light–matter states, polaritons, form, opening a route to modify transport, reactivity and energy transfer [1]. Dielectric microspheres are appealing here: they support spectrally narrow whispering gallery modes (WGMs) while remaining chemically open, giving direct access to the confined mode [2]. Cavity suitability is usually judged by $Q/\sqrt{V}$ or by the cooperativity $C = g^2/(\kappa\gamma)$, with κ and γ the cavity and molecular linewidths. Neither describes what happens when κ and γ differ substantially, as is generic for organic emitters in dielectric cavities. Since many soft cavities already satisfy the conventional threshold, which size is optimal?

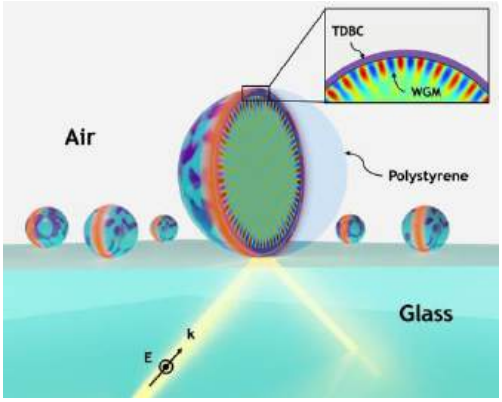


Fig. 1: Schematic of the molecule–cavity system: a TDBC coated polystyrene microsphere on glass probed by broadband evanescent excitation.

We model this with a two dimensional finite element simulation (COMSOL Multiphysics) of a polystyrene microsphere on glass, excited evanescently in the Kretschmann geometry (Fig. 1). An 8 nm shell, four layers of J-aggregated TDBC, coats the sphere; its permittivity follows a Lorentz oscillator with λ_{exc} = 582 nm and γ_{exc} = 43 meV [3]. Since WGMs are morphology dependent, the cavity energy is swept across the stationary exciton by varying the diameter from 1.5 to 4.0 μm, and g is extracted from multimode coupled oscillator fits to the simulated dispersions [4].

Every diameter satisfies the conventional criterion $2g > (\gamma_{exc} + \kappa)$, yet the parameters vary strongly: g falls from ≈ 79 to ≈ 23 meV across the sweep, following $g \propto 1/\sqrt{V} \propto 1/R$, while κ drops nearly an order of magnitude, from 64.7 to 8.7 meV. Because coherent exchange is throttled by the faster decay channel, not by the mean, we compare g against the dominant loss,

$$\chi = g / \max(\kappa, \gamma_{exc}) \quad (1)$$

which identifies the process actually limiting the polariton lifetime. For TDBC, χ peaks sharply at $D \approx$ 2.0 μm, where κ = 40.6 meV matches γ_{exc} = 43 meV: g still retains ≈ 85% of its maximum while κ has reached the molecular floor, so further growth only dilutes the mode volume. Reducing γ_{exc} to 20 meV shifts the maximum to $D \approx$ 3.0 μm, again at the crossing $\kappa(D) = \gamma_{exc}$, and detuning the emitter to 550 or 640 nm leaves the optimum at $D \approx$ 2.0 μm. The optimum is thus set by the balance of the two loss channels, not by oscillator strength or exciton wavelength; cooperativity, by contrast, identifies no optimum.

Linewidth matching is therefore not just a criterion for spectral visibility but a dissipation matching condition, analogous to impedance matching: when neither subsystem dominates as a sink for coherence, reversible light–matter exchange is most robust. Cavity selection then reduces to a fabrication free rule: pick the diameter where the bare cavity linewidth equals the molecular one. We acknowledge ANRF PMECRG (ANRF/ECRG/2024/006239/PMS) and I-STEM for COMSOL access.

References:

[1] T.W. Ebbesen, *Acc. Chem. Res.* 49 (2016) 2403.
[2] A.B. Vasista, W.L. Barnes, *Nano Lett.* 20 (2020) 1766.
[3] M.S. Bradley, J.R. Tischler, V. Bulović, *Adv. Mater.* 17 (2005) 1881.
[4] K.J. Vahala, *Nature* 424 (2003) 839.

Electric Double Layer–Driven Flow Focusing in Laser-Induced Liquid Microjets

[1] Rakshith Kamath, and [1,#]Kailash C. Jena
[1]Department of Physics, Indian Institute of Technology Ropar, Rupnagar, Punjab-140001, India
[#]*kcjena@iitrpr.ac.in*

Laser-induced liquid microjet generation in confined silica microchannels is governed by flow focusing. We show that the electric double layer formed above the silica point of zero charge modifies flow focusing, while ionic screening weakens this effect. Below the point of zero charge, electrostatic screening is negligible, leaving jet characteristics essentially unchanged.

Laser-induced liquid microjets (LILMs) generated in confined silica microcapillaries are widely used in needle-free drug delivery, inkjet printing, and microfluidics. A focused laser pulse generates a cavitation bubble whose pressure pulse accelerates the liquid meniscus into a high-speed jet through flow focusing. Although jet formation is known to depend on laser energy, capillary geometry, and meniscus shape, the role of the silica–water interface has remained unexplored. Since silica develops a pH-dependent surface charge, an electrical double layer (EDL) forms at the interface and may influence jet dynamics.

Microjets were generated in borosilicate microcapillaries (400 μm inner diameter) using a 28 ps Nd:YAG laser (532 nm). High-speed imaging was used to measure jet evolution while varying solution pH (1–12) and NaCl concentration (0.01–0.1 M).

Jet acceleration, terminal velocity, and jet length increased with increasing pH. Above the point of zero charge (pH ≈ 2), deprotonation of silanol groups produces a negatively charged silica surface and a well-developed EDL. The results suggest that the interfacial electric field modifies the near-wall boundary condition, enhancing flow focusing and increasing jet velocity. Increasing NaCl concentration compressed the EDL through electrostatic screening, reducing jet acceleration and terminal velocity while increasing the acceleration time. In contrast, below the point of zero charge, where the silica surface is weakly charged, ionic strength produced negligible changes in jet dynamics. These observations identify two distinct operating regimes governed by interfacial electrostatics.

This work demonstrates that the electrical double layer provides a simple means of controlling laser-induced microjets through solution chemistry, establishing a direct link between molecular-scale interfacial electrostatics and macroscopic flow focusing.

References:

[1] B. Rana, R. Kamath, M. Mishra, K.C. Jena, *Physics of Fluids* 36 (2024) 033319.
[2] B. Rehl, E. Ma, S. Parshotam, E.L. Dewalt-Kerian, T. Liu, F.M. Geiger, J.M. Gibbs, *Journal of the American Chemical Society* 144 (2022) 16338–16346.
[3] K.C. Jena, P.A. Covert, D.K. Hore, *Journal of Physical Chemistry Letters* 2 (2011) 1056–1061.
[4] B. Rana, D.J. Fairhurst, K.C. Jena, *Journal of the American Chemical Society* 145 (2023) 9646–9654.

Beaconless Adaptive Wavefront Shaping by MEMS-based Deformable Mirror

[#]Arnab Bhattacharyya, Soumya Kumari, Prateek Agrawal, Sarita, Rakesh Kumar Singh

Laboratory of Information Photonics & Optical Metrology, Department of Physics, Indian Institute of Technology (Banaras Hindu University), Varanasi, Uttar Pradesh 221005, India

[#]*arnabbhattacharyya.rs.phy23@itbhu.ac.in*

This work demonstrates adaptive correction of wavefront distortion and laser beam focusing through scattering media without a beacon by incorporating an iterative optimization technique on a deformable mirror. This method eliminates the need for direct detection of wavefront aberrations, thereby enabling potential applications across various areas.

Wavefront distortion occurs when light propagates through scattering or inhomogeneous media, causing higher-order aberrations that degrade image quality and transmitted information. Traditional beacon-based Adaptive Optics [1], comprising a wavefront sensor, a deformable mirror (DM), and a reconstructor, is widely used for beam correction. This work presents a beacon-free adaptive correction using the Stochastic Parallel Gradient Descent Algorithm (SPGD), an iterative optimization technique for controlling DM and maximizing beam focusing [2].

A laser beam (532.8 nm) is passed through a diffuser, and the subsequently scattered beam hits a DM. Then the beam is reflected from DM, and the distorted beam is then recorded by the camera. We have used a DM (DM140A-35-P01) comprising 140 actuators; each actuator's voltage ranges from 0V to 222V. The surface deformation of DM, governed by the influence function of each actuator, corrects the distortions present in the beam propagating through scattering media. Optimal surface deformation of DM is achieved by iteratively optimizing actuator voltages using SPGD [3]. An initial bias voltage is applied at the start. A small perturbation voltage Δu is applied to actuators and a certain image contrast metric J is measured from the observed image in the camera; in our case, we choose the intensity at the central region of the camera as J. We measured J_+ and J_- for positive and negative perturbation, respectively, and calculated $\Delta J = J_+ - J_-$ which is then used to calculate a new set of voltages,

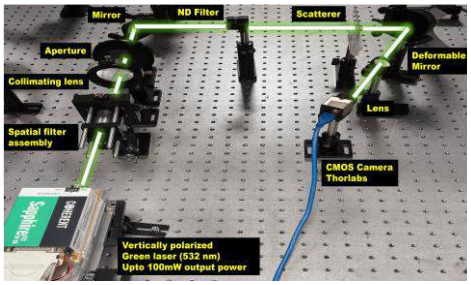


Fig. 1: Experimental Setup

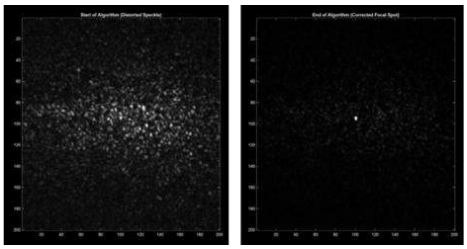


Fig. 2: Beam Convergence after SPGD Optimization

$$u_{i+1}^{N} = u_i^{N} + \gamma \Delta J \Delta u$$

where u_{i+1}^{N} is the voltage at N^{th} actuator in the next loop, u_i^{N} is the voltage at N^{th} actuator in the previous loop and γ is the gain coefficient, tuned as per the experimental requirement. After several iterations, we got a bright spot at the central region (Fig 2).

Thus, we showed that we do not require direct detection of wavefront aberrations via any wavefront sensor, nor any reference beacon for beam focusing. Hence, the experimental complexity and cost are highly reduced. This technique can be highly effective in defense applications where beaconless target detection is highly required. This technique is also very useful in microscopic depth imaging of biological tissue and in underwater communication radar systems.

Support is acknowledged from projects DRDO: DGTM/DFTM/GIA/24-25/426 and UPEIDA: R&D/UPEIDA/D.Corridor/2018-19/01/Phy/813.

References:

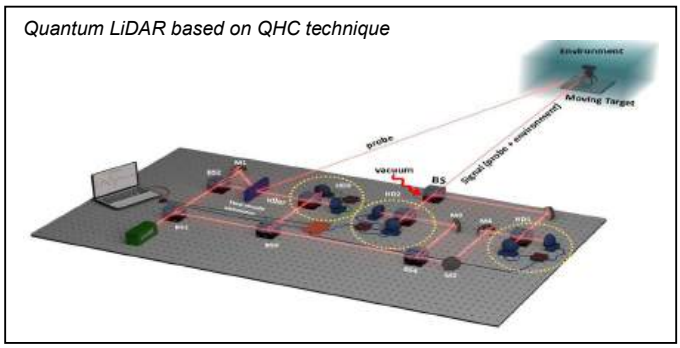
[1] R.K. Tyson, *Principles of Adaptive Optics*, CRC Press, Boca Raton (2010).
[2] N. Miyamura, *Proc. SPIE* 10410 (2017) 1041003.
[3] Q. Xu, H. Yang, Y. Wu, H. Yang, *Proc. SPIE* 11338 (2019) 113383J.

Entanglement based LiDAR for ranging moving targets

[1,]Greeshma Gopinath, and [1#] Sankar Davuluri
[1] Department of Physics, Birla Institute of Technology and Science, Pilani, Hyderabad Campus, Jawahar Nagar, Kapra Mandal, Medchal District, Telangana 500078, India
[#]*sankar@hyderabad.bits-pilani.ac.in*

A moving target continuously alters the frequency and phase of the LiDAR probe reflected from it. This makes it impossible to achieve phase lock with the probe and finding the LiDAR probe spectral component in large environment. Our theoretical design overcomes these problems for building a practical quantum LiDAR.

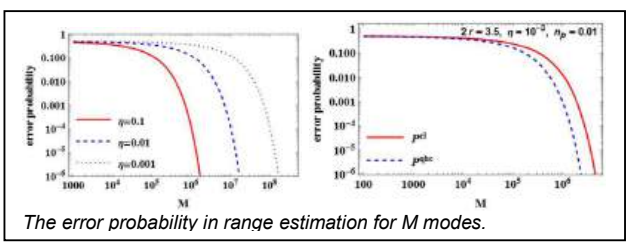
Decoherence has been a primary problem for almost all quantum technologies. In 2008, Lloyd's[1] proposed quantum illumination (QI) technique which proved that quantum advantage can be preserved even in presence of large thermal noise. While initial investigations on QI are motivated for building quantum radar, abundance of quantum resources at optical frequencies naturally shifted the scientific community towards quantum LiDAR.



We developed a quantum LiDAR based on quantum homodyne cross-correlation (QHC) technique [2,3]. In this method, we entangle idler and probe fields. The idler field is sent into homodyne and the output is measured. On the other hand, the probe field is reflected from a target of unknown reflectivity η. The target actively tries detection by using jamming field which is represented by anhillation operator $\hat{E}$. In practical LiDAR scenario, $(1-\eta)\langle \hat{E}^{\dagger}\hat{E}\rangle \gg \langle \hat{a}^{\dagger}\,\hat{a}\rangle$, so that the entanglement is destroyed by the time probe field reaches the LiDAR receiver. Moreover, the moving target alters the probe frequency through Doppler effect which changes the LiDAR receiver from a homodyne to heterodyne detection. In QHC LiDAR, we implement a conjugate homodyne design for simultaneous measurement of range and velocity. The conjugate homodyne is similar to heterodyne [4] in quantum information theory. However, it eliminates the phase dependence of the output. The final ranging output C_r and variance σ_r^2 , for estimation of moving target distance, in the QHC LiDAR is

$$C_r = \sqrt{\eta I\, I_r 2\, n_p\left(1+n_p\right)}\,,\ \ \sigma_r = \sqrt{n_{th} I\, I_r\left(1+2\,n_p\right)}, \qquad (1)$$

where, n_p, n_{th}represents the average photon number of the probe field and the background thermal noise, while I and $I_r$denote the intensities of the reference fields in the homodyne detectors, respectively. Similarly the expectation C_v and variance σ_v^2 in estimation of target's velocity is given as $C_r/2$ and $\sigma_r^2/2$ respectively. The limit for simultaneous estimation of position and velocity of the moving target is given as $\sigma_r\sigma_v = 1/4$ for $n_{th} \ll 1$ and $n_p \ll 1$.



The error probability in range estimation for M modes.

References:

[1] S. Lloyd, Science 321 (2008) 1463–1465.
[2] S. Davuluri, G. Gopinath, S. Subhash, M.J. Woolley, Applied Physics Letters 127 (2025) 094001
[3]G. Gopinath, S. Davuluri, Long range stealth probing quantum LiDAR for simultaneous position and velocity measuremen with spoofing immunity and 3 dB quantum advantage, (In Submission).
[4] M. Reichert, Q. Zhuang, M. Sanz, Physical Review Letters 133 (2024) 130801.019).

Rapid laser beam focusing and lateral scanning through scattering media using a gradient descent algorithm

[1,2, #]Sayantan Gantait, [1]Sarita, [2]Atul Kumar, [1]Rakesh Kumar Singh
[1] Laboratory of Information Photonics and Optical Metrology, Department of Physics, Indian Institute of Technology (Banaras Hindu University), Varanasi, India – 221005
[2] Department of Electronics Engineering, Indian Institute of Technology (Banaras Hindu University), Varanasi-221005, India

[#]*sayantangantait.rs.phy25@itbhu.ac.in*

Wavefront shaping and laser beam focus steering have recently attracted research interests owing to applications in defense and beam shaping. Herein, we report fast, noise-resilient laser beam focusing and lateral scanning through scattering media using a phase SLM controlled by stochastic parallel gradient descent. Simulated and experimental results are presented.

Laser beam distortion caused by turbulence remains a major challenge in practical systems, including astronomy, biomedical imaging, remote sensing, free-space optical communication, and defense applications. Thus, preserving laser beam quality during propagation through random media is essential for efficient focusing and accurate retrieval of object information [1]. Optical wavefront shaping is a promising technique that enables focusing of light through scattering media by iteratively altering the incident beam profile via a feedback loop positioned downstream of the scatterer. Here, we employ a phase-only spatial light modulator (p-SLM) to modulate the incident light, guided by a gradient-based optimization algorithm that processes active feedback from a CMOS camera [2,3].

Numerical simulations were performed in MATLAB using a random phase diffuser. A p-SLM is used to implement the stochastic parallel gradient descent (SPGD) algorithm [2,4], in which random perturbations are applied to the control parameters, and the feedback intensity is iteratively maximized. The actuator phase update is given as $u_{l,m}^{n+1} = u_{l,m}^{n} + \gamma S_{l,m}(J_n^+ - J_n^-)$, where $u_{l,m}^{n}$ is initial phase for each actuator, $\varepsilon = \pi/10$ is the magnitude of the perturbation, $J_n^{+/-}$corresponds to the fitness function value, and γ is the gain coefficient. The initial speckle pattern obtained in simulation (Fig. 1(b)) is corrected using an efficient feedback cost function with GPU-based parallel processing. A focused spot is obtained after 5000 SPGD iterations within 1-2 minutes, demonstrating faster convergence (Fig. 1(c)). By adding a linear phase gradient to the final optimized mask [5], the focused spot is steered toward the desired region of interest (ROI) without re-running the entire optimization process (Fig. 1(d)).

Fig. 1(a) shows the experimental setup. A collimated laser beam of wavelength 532 nm (Coherent Sapphire, SF NX 100mW) is incident on a p-SLM (Holoeye LCOS Pluto 2.1), and the modulated beam is directed through the scattering medium. The transmitted speckle intensity is recorded by a camera (Thorlabs, Model no: DCC3240M) and used as feedback for SPGD optimization. To achieve optimal focus with Strehl ratio (>0.96) and high peak-to-background ratio, a rigorous parametric analysis was performed. The initial speckle pattern produced by the Thorlabs 600-grit ground glass diffuser (DG100X100-600) in Fig. 1(e) is corrected, and a bright, focused spot is obtained at the center in 4-5 minutes. Lateral focus shifting was illustrated in the experiment (Fig. 1(g)).

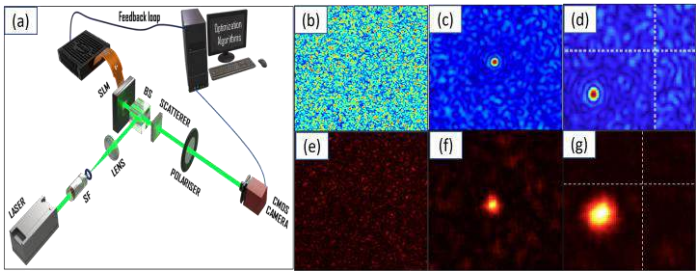


Fig 1: (a) Schematic of the experimental setup. Simulation results (b)speckle pattern, (c)optimized focus, (d)focus shifted diagonally; Experimental results (e)speckle pattern, (f)optimized focus at the center, (g)focus shifted diagonally

In conclusion, our work demonstrates rapid, high-quality beam focusing and controlled lateral beam scanning at any desired ROI through strong scattering media. The authors acknowledge the support from IIT (BHU), Varanasi, and the DRDO project (DGTM/DFTM/GIA/24-25/426).

References:

[1] Tyson, R.K., Principles of Adaptive Optics, CRC Press, (2010).
[2] Vorontsov, M. A., Carhart, G. W., & Ricklin, J. C. Optics letters, 22(12), 907-909 (1997).
[3] Vellekoop, I. M. & Mosk, A. P. Focusing coherent light through opaque strongly scattering media. Opt. Lett. 32,(2007).
[4] Nelson, W., Palastro, J. P., Wu, C., & Davis, C. C. Optics Letters, 41(6), 1301-1304 (2016).
[5] Sanjeev, A., Trivedi, V., & Zalevsky, Z. Scientific Reports, 12(1), 6387 (2022).

Design & Development of Minimum Resolvable Temperature Difference (MRTD) Test Station for Field Performance Evaluation of Thermal Imagers

[1]Lt Colonel Kabir Kohli
[1]*Instructor, Faculty of Optronics & Instrumentation Technology, EME School, Vadodara*
kabirkohlieme@gmail.com

*Thermal imaging systems operating in MWIR (3-5 µm) and LWIR (8-12 µm) bands enable night vision and high-contrast electro-optical sensing. Their performance is assessed through Minimum Resolvable Temperature Difference. Portable **TRINETRA** brings field-level MRTD testing, providing rapid GO/NO-GO evaluation, reducing repair delays, minimizing downtime and improving operational readiness through real-time diagnostics.*

Thermal imagers are the principal night-vision sensors used across armoured vehicles, weapon sights, artillery and surveillance systems, providing long-range target detection in darkness and degraded conditions. Their performance depends on spatial resolution and thermal sensitivity and is expressed in detection, recognition and identification (DRI) ranges based on Johnson's criterion. In laboratories, this capability is evaluated through MRTD, which defines the smallest temperature contrast required to resolve a standard pattern. Existing facilities are ex-import, expensive, bulky and restricted to higher repair echelons, resulting in limited field diagnostics, extended downtime and a higher repair load. Indigenous Trinetra Test Station enables field-level GO/NO-GO MRTD testing for eight thermal imaging systems of the Indian Army. In the way ahead, adaptive resolution strategies that enable thermal systems to dynamically adjust spatial and thermal accuracy in response to operational requirements [1] for enhancing target detection are being studied and explored.

The test employs a four-bar target with a differential blackbody that establishes one isothermal temperature for the four-bar target and another for the conjugate background. The target is imaged on the TI display and viewed by an observer while the temperature difference, initially zero, is increased until the bars are just distinguishable; this threshold defines the MRTD. Under these conditions, the spatial temperature distribution of each bar is measured remotely, ensuring that the mean temperature of individual bars does not vary from others by more than the measured MRTD. The background temperature and spatial frequency are specified for every measurement. MRTD indicates the ability of a thermal imager to resolve scene detail and enables comparison between systems, thereby enabling field-level MRTD testing in GO/NO GO MODE [2] under real-time conditions.

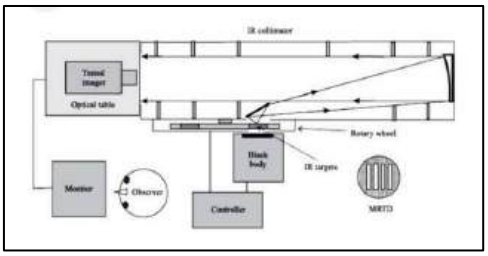


Fig.1: Schematic of MRTD Measurement Test Set-Up

Successful laboratory trials have been conducted wherein multiple TI were systematically evaluated using the test station installed within the faculty premises. These trials provided a controlled framework to assess critical performance parameters of thermal imaging systems under repeatable and measurable conditions. The results confirm that MRTD performance depends strongly on target–background thermal contrast, with a reduction in detection as the temperature difference nears zero, which gives a GO/NO GO assessment of MRTD performance at a particular spatial frequency [3]. Resolvability remains stable at low spatial frequencies but worsens at higher ones. The results link resolution and NETD to detection capability, showing MRTD as a standardised tool for both laboratory validation and reliable field-performance prediction.

The field army operates cooled thermal imagers whose performance requires periodic verification. MRTD is a key measure of fine-detail resolution in darkness and obscured conditions. An indigenous MRTD Test Station enables self-reliant field evaluation, ensuring the timely availability of fully serviceable thermal imaging systems for operations

References:

[1] Kohli, K. *Int. J. Innov. Sci.Res.Technol.*,2025,10(8),1107–1115. https://doi.org/10.38124/ijisrt/25aug556
[2] R. Braddick and Ludlow, SPIE Vol. 2224, pp 291-296
[3] G.C.Holst, JCD Publishing,1993.

Parametric Studies of an Optical Telescope System for Tracking of Low Earth Space Objects

[1,2,#]Sourav Paul,[2]Mayukh Pahari,[1]Kethiri Narsimha Reddy,[1]S Veerabuthiran, and [1]Jagannath Nayak
[1]Center for High Energy Systems and Sciences, DRDO, Hyderabad, India
[2]Indian Institute of Technology, Hyderabad
[#] *n.reddy@gov.in*

This study presents a parametric analysis of an optical telescope system for Low Earth Orbit object tracking, evaluating the requirements of telescope aperture and focal length along with typical slew rate, tracking accuracy, encoder resolution, and optical design. Results show that a telescope with a 35 cm aperture satisfies all performance criteria, making it highly suitable for tracking the low earth satellite upto height of 2000 km under twilight conditions.

The increasing number of satellites and space debris in Low-Earth Orbit (LEO) has created a growing demand for accurate ground-based optical tracking systems capable of supporting space situational awareness and orbit determination. The performance of such systems is governed by a combination of orbital dynamics, telescope optics, detector characteristics, and mount control capabilities. This work presents a parametric analysis of an optical ground station designed for long range object such LEO objects detection and tracking and evaluates the suitability of a telescope system with 35 cm aperture and F number 3. The analysis aims to identify the critical system requirements needed to achieve precise tracking and reliable detection of space objects over a wide range of orbital altitudes.

Detection performance depends on object brightness, atmospheric transmission, detector quantum efficiency, telescope aperture and focal ratio. The reflected-light phase function combines diffuse and specular scattering components, while the received photon flux is estimated from the apparent magnitude of the object. The dependency of detectable size (D) on optical design is given as,

$$D = \frac{\sqrt{2.755 \times 10^{-21}\omega.SNR.R^2.f'\sqrt{d_{optic}^2 QE\tau_{optic}y_{pix}t\pi L_b + 4f'^2e_{read}^2 + d_{optic}^2 e_{read}^2}}}{P(\rho,\psi).QE.y_{pix}\tau_{optic}\tau_{atm}d_{optic}^2\pi\sqrt{d_{optic}^2 + 4f'^2}}$$

Where, d_{optic} is the aperture (35 cm) and f' is the focal length which is 3 times of aperture in our case. Other symbols stand for suitable parameters as referred by Wagner et. al. [1,2]. The SNR can be also quantified as a function of focal ratio (F#). Fig. 1 shows, the variation of detectable target diameter i.e. object size with aperture size and Fig. 2 shows the variation of SNR of target with focal ratio. It is evident that a telescopic system with 35 cm aperture and focal ratio 3 can detect 12 cm object with good SNR.

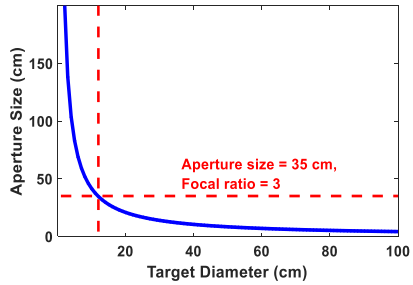


Fig. 1: Variation of object size with aperture size. Target distance = 700 km, exposure = 0.02 ms and Pixel = 3.75 µm

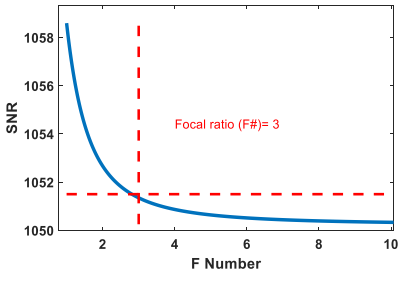


Fig. 2: Variation of SNR with Focal ratio. Target distance = 700 km, exposure = 0.02 ms and Pixel = 3.75 µm.



Fig. 3: Tracking of Satellite at height of about 700 km.

Fig. 3 shows the preliminary results of an image of a satellite at 700 km height with telescopic system (35 cm Aperture, Focal ratio 3). The satellite's streak image was captured under staring mode. This observation directly validates the approach of the parametric analysis mentioned in this paper.

References:

[1] P. Wagner, T. Hasenohr, D. Hampf, F. Sproll, L. Humbert, J. Rodmann, W. Riede, German Aerospace Center, Institute of Technical Physics, Pfaffenwaldring 38-40, 70569.
[2] James R. Shell, US Air Force, Space Innovation and Development Center 24 Talon Way, Schriever AFB, CO 80912.

Effect of Maritime and Terrestrial Atmospheric Turbulence on Coherent Beam Combination

[1]P M Pooja, [1]Khushboo Soni, [1,#]Nithyanandan Kanagaraj

[1]Directed Energy Systems And Applications Laboratory, Department of Physics, Indian Institute of Technology Hyderabad, India – 502 284

[#] *nithyan@phy.iith.ac.in*

We evaluate the performance of coherent beam combination under maritime and terrestrial turbulence using the same refractive index structure parameter ($C_n^2 = 10^{-13}\ m^{-2/3}$)*, using Power in the Bucket (PIB) as evaluation metric. The results show that PIB is lower under maritime turbulence* ($PIB = 0.538$) *than under terrestrial turbulence* ($PIB = 0.554$)*, indicating that the combined beam experiences more distortion in maritime turbulence.*

A seven gaussian beam array in a hexagonally packed configuration of identical beam waist and power was considered. Band limited angular spectrum method was used to propagate the beam array to get the far field intensity distribution at 1000m. Adagrad optimizer was used in phase synchronization as shown in Fig. 1.

Turbulence phase screen of both maritime in Eq. (1) and terrestrial in Eq. (2) were generated by Monte Carlo method using their respective PSD models. For comparison sake, we assumed $C_n^2 = 10^{-13}\ m^{-2/3}$, outer ($L_0 = 5m$) and inner scale ($l_0 = 6mm$) of turbulence same for both [1].

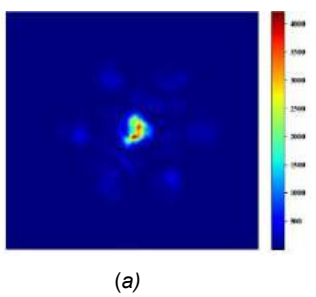
$$\Phi_n^{Mar}(\kappa) = 0.033 C_n^2 \left[1 - 0.061\left(\frac{\kappa}{\kappa_H}\right) + 2.836\left(\frac{\kappa}{\kappa_H}\right)^{7/6}\right] \frac{\exp(-\kappa^2/\kappa_H^2)}{(\kappa^2 + \kappa_0^2)^{11/6}} \tag{1}$$

$$\Phi_{\mathrm{n}}^{\mathrm{Ter}}(\kappa) = 0.033\ \mathrm{C}_{\mathrm{n}}^2\ \frac{\exp(-\kappa^2/\kappa_{\mathrm{m}}^2)}{(\kappa^2 + \kappa_0^2)^{11/6}} \tag{2}$$

The performance was evaluated using Power in the Bucket (PIB) metric [2] in Eq. (3).

$$PIB = \iint \mathrm{I}(\hat{\mathrm{x}}, \hat{\mathrm{y}}).\,\mathrm{dS} \Big/ \iint \mathrm{I}(\mathrm{x}, \mathrm{y})\mathrm{dS} \tag{3}$$

It is observed that the PIB is lower in maritime turbulence (PIB=0.538) than in terrestrial turbulence (PIB=0.554) under the same turbulence conditions as shown in Fig. 2.



(a) (b)

Fig. 1 (a) Far field intensity under terrestrial turbulence (b) Far field intensity under maritime turbulence

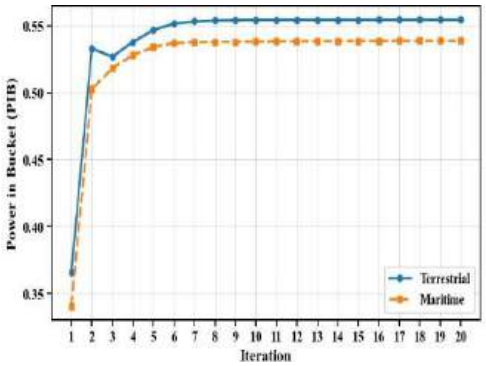


Fig. 2 PIB under maritime and terrestrial turbulence

References:

[1] M. Li, M. Cvijetic, *Applied Optics* 54 (2015) 1453–1462

[2] A. D. Thomas, K. Soni, K. Nithyanandan, *Journal of Lightwave Technology* 43 (2025) 824–831

Narcissus analysis of a Ge-free Mid Wave Infrared Cooled System

[1,#]Krishnendu Roy,[2]Neelam Verma and [3]Dr.Ravinder Reddy M
[1,2 & 3] PDIC, Bharat Electronics Limited, Bengaluru

[#]*krishnenduroy@bel.co.in*

Narcissus effect correction in cooled infrared systems is one of the advanced optical design improvements done in the pen-ultimate design stages. This paper enumerates a thermal optics design for a cooled mid wave thermal detector. The kernel of the paper focuses on the narcissus analysis of a cooled mid-wave infrared system and divulges method to blur it.

Thermal imagers using cryogenically cooled detectors are preferred for their low NETDs and sensitivity. These detectors are highly sensitive to temperature differences in the surroundings as a result any stray thermal radiations can create a ghost image and drastically degrade the imaging of the detector. The narcissus effect in thermal imagers can be briefly understood as the image formed by the cooled detector due to the stray light reflected by its own imaging optics at incident angle less than the angular airy radius of the optical system.

Fig. 1. depicts a cross section of an optical design for a cooled MWIR thermal detector. The optical system is optimized for 640 x 512 x 15 micron pitch detector using combination of diffractive optical element and aspheric lenses. The lens materials used for the design are strictly Ge-free like silicon and chalcogenide glasses.

Narcissus induced temperature difference (NITD) distribution across the thermal detector plane can be visualized utilizing simulation softwares like Zemax or Code V. The ghost image generated by the stray light makes any impact on the thermal detector imaging, can be checked by the NITD plots. In thermal optical design, the stray light falling on the detector is blurred by controlling the ray height, refractive index and ray incident angle at each optical surface.

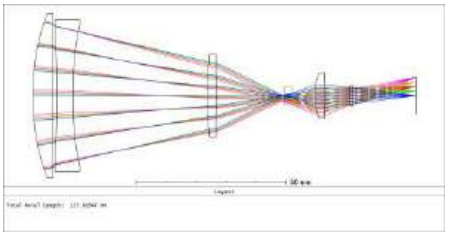
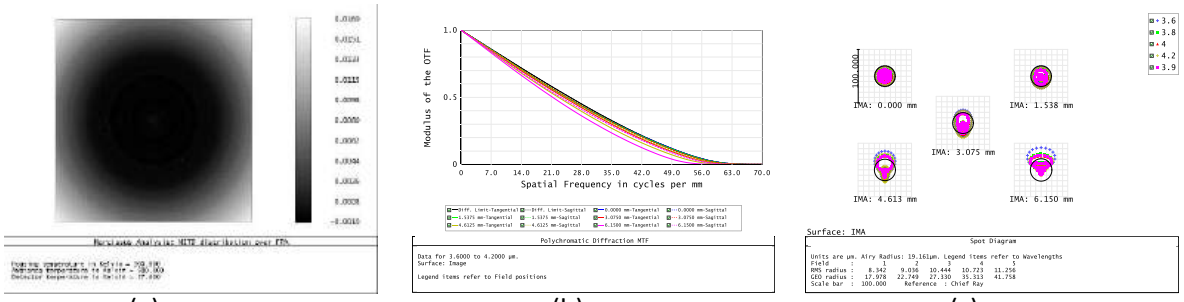


Fig. 1: Cross section of Cooled MWIR Imager Optics



(a) (b) (c)

Fig 2. (a), (b) & (c). describes Reduction of Narcissus effect in the optical system, MTF plot and Spot diagram of the optical system respectively.

Infrared cooled imaging systems with excellent system performance still may suffer severely due to presence of narcissus effect. The reduction of the narcissus effect is not an option but a crucial thermal optics design aspect. The paper demonstrates a thermal optics design and its system performance. It also emphasizes about the narcissus analysis technique and its correction.

References:

[1] M. Nadeem Akram, *Simulation and control of narcissus phenomenon using non sequential ray tracing*, *Applied Optics/Vol.49, No.6*
[2] Serhat Hasan, *Opticstudio narcissus analysis macro*, *Ansys Learning Hub*.
[3] Donald Dilworth, *Lens Design-Automatic and quasi-autonomous computational methods and techniques, ISBN 978-0-7503-1609-5*.

A High-Speed Time Interleaved Photonic-Assisted Analog-to-Digital Converter (Ph-ADC) Architecture for Defense Applications

#Naresh Sothuku, Thejna Ros Joseph, Rupam Biswas, Chiranjeevi Damacherla and Ranu Tyagi
Central Research Laboratory, Bharat Electronics Limited, Jalahalli, Bengaluru - 560013
#*nareshsothuku@bel.co.in*

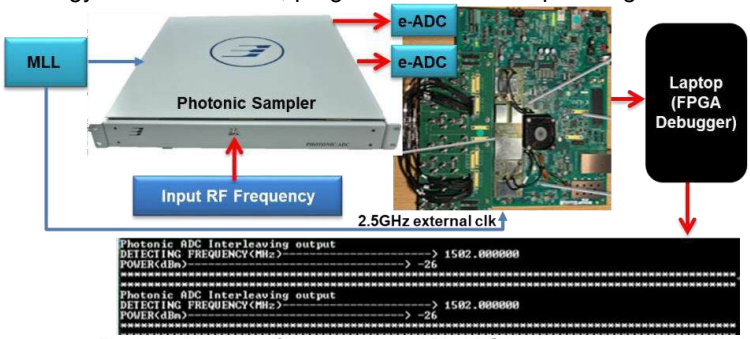
This paper presents a high-speed, time-interleaved photonic-assisted ADC achieving 5 GSpS. Using a mode-locked laser as a low-jitter unified reference clock for both the photonic sampler and electronic quantizer, a digital interleaving algorithm is implemented in RFSoC to obtain 5GSps sampling rate, providing a viable solution for radar and millimeter-wave applications.

Worldwide, Photonic Analogue-to-Digital Converters (Ph-ADCs) are key enablers in next generation defense systems powered by photonics technologies[1]. A Ph-ADC architecture employing photonic sampling and electronic quantization utilizes advantages of both photonic and electronics domains[2]. Photonic sampling can bypass the bandwidth and jitter limitations inherent in electronic sampling. However, photonic quantization is still under development.

In this implementation, a low-jitter 2.5GHz repetition rate Mode-Locked Laser (MLL) at 1560nm with femtosecond pulse train acts as the reference clock. A two-channel time-wavelength mapped 5GHz optical clock is generated from the MLL pulses and is used as the optical sampling clock. 5GSps optical sampling of the input RF signal is realized by the amplitude modulation of the 5GHz optical pulse train by a photonic modulator. By performing sampling in the optical domain, the system achieves ultra-wideband (20GHz) and high speed signal acquisition with ultra-low aperture jitter (<30fs) compared to conventional electronic-only architectures. Optically sampled signals are further converted to electrical domain and digitized using electronic ADCs.

To ensure phase coherence across the hybrid optical-electronic interface, a 2.5GHz RF clock generated from MLL pulses is used as the external clock for RFSoC. Electronic quantization and conversion to digital domain is performed by two independent 2.5GSps ADCs in RFSoC. A custom digital time interleaving algorithm implemented in the FPGA logic recombines these two streams, effectively doubling the sampling rate to 5GSps**.** The results of the interleaved data streams, capturing the detected frequency, power of interleaved signal are displayed via debugger. This digital reconstruction is critical for the elimination of interleaving artifacts, errors typically induced by channel mismatch thereby ensuring an Effective Number of Bits (ENOB) exceeding 7. Fig.1 shows the complete architecture of the time-interleaved Ph-ADC implementation along with the achieved specifications.

By delegating high-bandwidth sampling to the Mach-Zehnder Modulator (MZM) and complex digital reconstruction to the RFSoC, this system successfully combines the vast bandwidth of optical technology and the versatile, programmable landscape of digital electronics.



Achieved Specifications

No.	Parameter	Value
1.	Input RF frequency	Upto 20 GHz
2.	Input RF power	[-5, -60] dBm
3.	Sampling rate	5 GSa/s
4.	ENOB	>7
5.	Sampling Jitter	< 30 fs

Fig. 1: Architecture of time-interleaved Ph-ADC implementation along with the achieved specifications

References:

[1]. A. Khilo, S.J Spector, M.E Grein et al, "Photonic ADC: overcoming the bottleneck of electronic jitter," in Optics Express, vol 20, no. 4, February 2012.
[2]. Guang Yang, Weiwen Zou, Lei Yu, Kan Wu and Jianping Chen, "Compensation of multi-channel mismatches in high-speed high-resolution photonic analog-to-digital converter," Optics Express, Vol.24, No.21, 2016.

Visible-Near Infrared Photodetection using large area grown SnS_2 Thin Film on Quartz Substrate

[1,2,#]Aditya Khudiwal, [1,2]Rahul Kumar, [1,2]Pooja Rani,[1,2,3]Bharti, [1,2,*]Mukesh Jewariya, [1,2,*]Sunil Singh Kushvaha

[1]CSIR- National Physical Laboratory, Dr. K.S. Krishnan Road, New Delhi,110012, India

[2]Academy of Scientific and Innovative Research (AcSIR), Ghaziabad, 201002, India

[3] DRDO- Solid State Physical Laboratory, Timarpur, New Delhi 110054, India

Corresponding authors E-mail: jewariyam.nplindia@csir.res.in, kushvahas.nplindia@csir.res.in

The developed SnS_2 thin-film metal-semiconductor-metal (MSM) photodetector (PD) exhibits effective dual-band visible-near infrared (Vis-NIR) photodetection with self-powered operation under NIR light. A remarkable photoresponse was observed, demonstrating the potential of large area CVD grown SnS_2 thin film as a low-cost, eco-friendly material for next-generation broadband optoelectronic and self-powered sensing applications.

PDs are essential optoelectronic devices that convert incident light into electrical signals, serving critical roles in diverse realms. TheVis-NIR PDs are particularly important for everyday imaging, autonomous vehicles, night vision, optical communication, and healthcare devices [1]. Two-dimensional (2D) layered materials have gained significant attention for high-performance photodetectors owing to their tunable band gaps, strong light-matter interaction, and mechanical flexibility. Among them, SnS_2, a metal dichalcogenide with a hexagonal CdI_2-type structure and ~2.2 eV band gap, stands out as a promising candidate for Vis-NIR PD [2].

The growth of uniform SnS_2 thin films is crucial for high-performance electronic and optoelectronic devices. The conventional methods like exfoliation and solvothermal synthesis face several limitations like uniformity, scalability, and reproducibility [3]. To overcome this, we employ a simple two-step sputtering and CVD sulfurization strategy. This approach ensures excellent thickness control and large-area uniformity. The choice of quartz substrate can enhance device performance through high optical transparency, chemical stability, and reduced interfacial defects. These result in low-noise, stable, and efficient self-powered NIR photodetectors [4].

In this study, SnS_2 thin films were grown on quartz substrates via a two-step sputtering and CVD sulfurization process for large-area uniformity. The structure, morphology, and elemental composition of the SnS_2 thin films were studied using Raman spectroscopy, X-ray diffraction, field-emission scanning electron microscopy, and X-ray photoelectron spectroscopy. From the UV-Vis absorption studies, the band gap was obtained as 2.27 eV. MSM photodetectors were fabricated, achieving responsivities of ~250 mA/W (visible) and ~120 mA/W (NIR) at 10 V bias. The devices also exhibited self-powered behavior under NIR illumination, owing to enhanced light absorption from the nanostructured morphology. These results establish SnS_2 as a promising material for future applications in electronics, optical communication, broadband imaging, and self-powered sensing systems.

References:

1. J. Xia, D. Zhu, L. Wang, B. Huang, X. Huang, X.M. Meng. *Advanced Functional Materials* 25 (2015) 4255.
2. X. Jia, C. Tang, R. Pan, Y. Long, C. Gu, J. Li. *ACS Applied Materials & Interfaces* 10 (2018) 18073.
3. G. Ham, S. Shin, J. Park, J. Lee, H. Choi, S. Lee, H. Jeon. *RSC Advances* 6, (2016) 54069.
4. Y. Sun, J. Chen, Y. Sun, Y. Luo, R. Huo, M. Che, H. Zhang, R. Wen, W. Lei, C. Zhou. *Laser & Photonics Rev.* 20 (2025) e01848.

Disposable microplasma generating chip for aqueous sample analysis, fabricated on a PET substrate

Manjeet Kumar and Bhaskar Mitra
Indian Institute of Technology Delhi, India

Manjeet.Kumar@ee.iitd.ac.in

A disposable, low-cost, portable microplasma optoelectronic device based on glow-discharge optical emission spectroscopy (GDOES) was developed for liquid-phase ion detection. Fabricated on a flexible PET substrate using UV lithography, generates atmospheric-pressure plasma in open air without vacuum or external gases. It detects Li and Na ions < 1 mM using optical emission spectroscopy.

An optoelectronic device based on microplasma discharge technology has been fabricated using a microfabrication approach, featuring a compact footprint of 3 mm × 5 mm on a flexible PET substrate. The device is composed of metallic electrodes coated with micro/nanostructured metal nanoflowers, which facilitate effective liquid sampling and function as wetted cathodes upon contact with analyte solutions.

Optical emission spectroscopy (OES) is a commonly used technique for metal analysis in liquid samples, where plasma excitation produces characteristic emission spectra corresponding to individual elements [1]. However, conventional OES systems are often large, costly, and unsuitable for portable or field-deployable applications. To address these challenges, several miniaturized plasma-based OES approaches have been investigated. Wilson and Gianchandani introduced microfluidic OES platforms employing liquid electrodes and later developed glass-frit channel-based designs, reducing fabrication complexity and sample requirements while maintaining analytical performance [2,3]. Other reported developments include flexible atmospheric-pressure glow-discharge devices utilizing screen-printed carbon electrodes on paper substrates [4], wet plasma dielectric barrier discharge (DBD) systems with laser-patterned copper electrodes [5], and inkjet-printed thin-film electrodes on flexible PET substrates for plasma generation [6]. These advancements highlight the promise of compact, cost-effective OES platforms for portable and on-site chemical analysis.

In this study, a disposable and miniaturized microplasma device was developed on a flexible polyethylene terephthalate (PET) substrate, using a UV lithography process. The device consists of silver nanoflowers containing numerous nanoscale voids that enable efficient delivery of liquid into the glow-discharge region, together with a micropatterned copper ribbon electrode. The fabricated device is compact in size and has an inter-electrode gap of 70 µm. It produces a stable wet plasma glow under atmospheric conditions (1 atm) in open air. With a sample consumption of only 0.4 µL, the device was successfully applied to lithium-ion detection in lithium hydroxide solutions, providing a linear detection range of 1–5 mM and a limit of detection (LOD) of 0.159 mM. The analytical performance was further verified using real water samples, achieving a lithium recovery of 97.133%. These findings demonstrate the capability of the developed device as a low-cost, portable alternative to conventional large-scale analytical techniques, such as inductively coupled plasma atomic emission spectroscopy (ICP-AES).

References:

[1] P. Kuznietsov, O. Biedunkova, I. Statnik and V. Korbutiak*, Water Sci. Springer*, 40, 3 (2026).
[2] C.G. Wilson, Y.B. Gianchandani, *IEEE Transactions on Electron Devices*, vol.49, no.12, (2002).
[3] B. Mitra, B. Levey and Y. B. Gianchandani*, IEEE Transactions on Plasma Science*, vol. 36, no. 4 (2008).
[4] C. -C. Hsu, J. -H. Tsai, Y. -J. Yang, Y. -C. Liao and Y. -W. Lu, *Journal of Microelectromechanical Systems*, vol. 21, no. 5, (2012).
[5] A. K. Bose, D. Maddipatla, B. B. Narakathu, B. J. Bazuin and M. Z. Atashbar, *IEEE FLEPS*, (2019).
[6] Jinwoo Kim, Sanghoo Park and Wonho Choe, *Nature Scientific Reports*, (2021)

Synergistic Improvement of Narrow Bandgap PbS Quantum Dot Solar Cells through Surface Ligand Engineering and Enhanced Electrode Transparency

Anjali Sharma and Dr. Arup Kumar Rath*
Physical and Material Chemistry Division, CSIR-National Chemical Laboratory, Pune 411008
Academy of Scientific and Innovative Research (AcSIR), Ghaziabad 201002, India
Email id – aj.sharma@email.ncl.res.in and ak.rath.ncl@csir.res.in

This study presents a hybrid ligand engineering approach combining cadmium halide and organic thiols to enhance narrow bandgap PbS quantum dot solar cells. Improved surface passivation reduces aggregation and trap states. Optimized ITO electrode transparency in the near-infrared enables power conversion efficiencies up to 12.4% under AM1.5G illumination.

The tunability of the energy bandgap in the near-infrared (NIR) range uniquely positions colloidal lead sulfide (PbS) quantum dots (QDs) as a versatile material to enhance the performance of existing perovskite and silicon solar cells in tandem architectures. The desired narrow bandgap (NBG) PbS QDs exhibit polar (111) and nonpolar (100) terminal facets, making effective surface passivation through ligand engineering highly challenging. Despite recent breakthroughs in surface ligand engineering, NBG PbS QDs suffer from uncontrolled agglomeration in solid films, leading to increased energy disorder and trap formation [1]. The limited NIR transparency of commonly used indium-doped tin oxide (ITO) electrodes further compromise the true performance of NBG PbS QDs in solar cells. Here, we employ a hybrid ligand strategy based on inorganic cadmium halide and organic thiol molecules, leading to the partial substitution of surface Pb atoms with Cd heteroatoms. This hybrid ligand strategy substantially reduces undesired QD fusion in solid films, improving the photophysical and electronic properties. By modulating the thickness of the ITO layer and managing refraction loss through a ZnO layer coating, we improved NIR transparency to above 80%. Enhancements in surface passivation of QDs, improvements in NIR transparency of electrodes help us achieve solar cell power conversion efficiencies of 12.4%, 4.48%, and 1.37% under AM 1.5G, perovskite filter, and silicon filter illuminations, respectively. A record open-circuit voltage (*V*oc) of 0.54 V and short-circuit current density (*J*sc) of 38.5 mA/cm2 are achieved under AM 1.5G illumination [2].

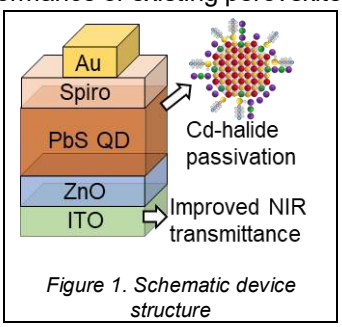


Figure 1. Schematic device structure

References:

[1] C. Mahajan, A. Sharma, A.K. Rath, *ACS Applied Materials and Interfaces* 2020, 12 (44), 49840-49848.
[2] A. Sharma, D. D. Shinde, C. Mahajan, N. V. Dambhare, A. Biswas, A. Mitra, V. S. Girade, A. K. Rath, *ACS Applied Materials and Interfaces* 2025, 17 (4), 6614-6625.